

## ALICE: Physics Performance Report, Volume II

This article has been downloaded from IOPscience. Please scroll down to see the full text article.

2006 J. Phys. G: Nucl. Part. Phys. 32 1295

(<http://iopscience.iop.org/0954-3899/32/10/001>)

View [the table of contents for this issue](#), or go to the [journal homepage](#) for more

Download details:

IP Address: 200.37.69.79

The article was downloaded on 07/11/2010 at 21:30

Please note that [terms and conditions apply](#).

# ALICE: Physics Performance Report, Volume II

ALICE Collaboration<sup>14</sup>

**B Alessandro<sup>1</sup>, F Antinori<sup>2</sup>, J A Belikov<sup>3</sup>, C Blume<sup>4</sup>, A Dainese<sup>2</sup>,  
P Foka<sup>5</sup>, P Giubellino<sup>1</sup>, B Hippolyte<sup>6</sup>, C Kuhn<sup>6</sup>, G Martínez<sup>7</sup>,  
M Monteno<sup>1</sup>, A Morsch<sup>3</sup>, T K Nayak<sup>3</sup>, J Nystrand<sup>8</sup>, M López Noriega<sup>3</sup>,  
G Paić<sup>9</sup>, J Pluta<sup>10</sup>, L Ramello<sup>11</sup>, J-P Revol<sup>3</sup>, K Šafařík<sup>3</sup>, J Schukraft<sup>3</sup>,  
Y Schutz<sup>3</sup>, E Scapparín<sup>1</sup>, R Snellings<sup>12</sup>, O Villalobos Baillie<sup>13</sup> and  
E Vercellin<sup>1</sup> (editors)**

<sup>1</sup> Dipartimento di Fisica dell'Università and Sezione INFN, Turin, Italy

<sup>2</sup> Dipartimento di Fisica dell'Università and Sezione INFN, Padua, Italy

<sup>3</sup> Physics Department, CERN, Geneva, Switzerland

<sup>4</sup> Institut für Kernphysik, Johann Wolfgang Goethe Universität, Frankfurt, Germany

<sup>5</sup> Gesellschaft für Schwerionenforschung (GSI), Darmstadt, Germany

<sup>6</sup> Institut de Recherches Subatomiques (IReS), IN2P3-CNRS and Université Louis Pasteur, Strasbourg, France

<sup>7</sup> Laboratoire de Physique Subatomique et des Technologies Associées (SUBATECH), IN2P3-CNRS and Université de Nantes, Nantes, France

<sup>8</sup> Department of Physics and Technology, University of Bergen, Bergen, Norway

<sup>9</sup> Instituto de Ciencias Nucleares, Universidad Nacional Autónoma de México, Mexico City, Mexico

<sup>10</sup> Institute of Physics, University of Technology, Warsaw, Poland

<sup>11</sup> Facoltà di Scienze dell'Università and INFN, Alessandria, Italy

<sup>12</sup> National Institute for Nuclear and High Energy Physics (NIKHEF), The Netherlands

<sup>13</sup> School of Physics and Space Research, University of Birmingham, Birmingham, UK

Received 5 May 2006

Published 13 September 2006

Online at [stacks.iop.org/JPhysG/32/1295](http://stacks.iop.org/JPhysG/32/1295)

## Abstract

ALICE is a general-purpose heavy-ion experiment designed to study the physics of strongly interacting matter and the quark–gluon plasma in nucleus–nucleus collisions at the LHC. It currently involves more than 900 physicists and senior engineers, from both the nuclear and high-energy physics sectors, from over 90 institutions in about 30 countries.

The ALICE detector is designed to cope with the highest particle multiplicities above those anticipated for Pb–Pb collisions ( $dN_{\text{ch}}/dy$  up to 8000) and it will be operational at the start-up of the LHC. In addition to heavy systems, the ALICE Collaboration will study collisions of lower-mass ions, which are a means of varying the energy density, and protons (both pp and pA), which primarily provide reference data for the nucleus–nucleus collisions. In addition, the pp data will allow for a number of genuine pp physics studies.

<sup>14</sup> A complete listing of the members of the ALICE Collaboration and external contributors appears on pages 2010–7.

The detailed design of the different detector systems has been laid down in a number of Technical Design Reports issued between mid-1998 and the end of 2004. The experiment is currently under construction and will be ready for data taking with both proton and heavy-ion beams at the start-up of the LHC.

Since the comprehensive information on detector and physics performance was last published in the ALICE Technical Proposal in 1996, the detector, as well as simulation, reconstruction and analysis software have undergone significant development. The Physics Performance Report (PPR) provides an updated and comprehensive summary of the performance of the various ALICE subsystems, including updates to the Technical Design Reports, as appropriate.

The PPR is divided into two volumes. Volume I, published in 2004 (CERN/LHCC 2003-049, ALICE Collaboration 2004 *J. Phys. G: Nucl. Part. Phys.* **30** 1517–1763), contains in four chapters a short theoretical overview and an extensive reference list concerning the physics topics of interest to ALICE, the experimental conditions at the LHC, a short summary and update of the subsystem designs, and a description of the offline framework and Monte Carlo event generators.

The present volume, Volume II, contains the majority of the information relevant to the physics performance in proton–proton, proton–nucleus, and nucleus–nucleus collisions. Following an introductory overview, Chapter 5 describes the combined detector performance and the event reconstruction procedures, based on detailed simulations of the individual subsystems. Chapter 6 describes the analysis and physics reach for a representative sample of physics observables, from global event characteristics to hard processes.

**Contents**

<b>Colour figures I–VI</b>	<b>1300</b>
<b>Summary and overview</b>	<b>1306</b>
<b>5. Detector performance</b>	<b>1315</b>
5.1. Track finding with central detectors	1315
5.1.1. Primary-vertex reconstruction	1315
5.1.2. Track-finding strategy	1323
5.1.3. Track finding in the TPC	1326
5.1.4. Track finding in the ITS	1337
5.1.5. Track finding in the TRD	1350
5.1.6. Combined track finding	1356
5.1.7. Secondary vertex reconstruction	1362
5.2. Track finding in the forward muon spectrometer	1374
5.2.1. Coordinate reconstruction	1374
5.2.2. Track reconstruction	1377
5.3. High-Level Trigger reconstruction	1381
5.3.1. TPC reconstruction	1381
5.3.2. ITS reconstruction	1387
5.3.3. Dimuon reconstruction	1388
5.4. Charged-particle identification	1395
5.4.1. Particle identification with ITS	1395
5.4.2. Particle identification with TPC	1399
5.4.3. Particle identification with TRD	1401
5.4.4. Particle identification with TOF	1407
5.4.5. Particle identification with HMPID	1419
5.4.6. Combined particle identification	1429
5.5. Neutral-particle identification	1435
5.5.1. Photon spectrometer	1435
5.5.2. Photon multiplicity detector	1477
<b>6. ALICE physics performance</b>	<b>1484</b>
6.1. Event characterization	1485
6.1.1. Introduction	1485
6.1.2. Centrality determination using the ZDCs	1486
6.1.3. Multiplicity determination using the SPD and the FMD	1504
6.1.4. Multiplicity vs. centrality: a physics performance study	1518
6.1.5. Global event properties in pp collisions	1523
6.1.6. Event centrality in pA collisions	1540
6.2. Particle production	1548
6.2.1. Overview of current results	1548
6.2.2. Identified particle spectra	1571
6.2.3. Topological identification of strange and multi-strange particles	1591
6.2.4. Reconstruction of the $\rho^0$ signal	1606
6.2.5. Detection of $\phi \rightarrow K^+K^-$	1613

6.2.6.	Reconstruction of the $K^*(892)^0$ signal	1622
6.2.7.	Search for strange dibaryons	1629
6.3.	Momentum correlations	1635
6.3.1.	Introduction	1635
6.3.2.	Formalism of two-particle correlations	1635
6.3.3.	Momentum correlations in heavy-ion collisions	1637
6.3.4.	Software tools for the simulation of momentum correlations	1646
6.3.5.	Two-pion momentum correlation analysis	1650
6.3.6.	Other potential analyses and particular aspects of momentum correlation analyses	1665
6.3.7.	Conclusion	1670
6.4.	Flow	1671
6.4.1.	Radial flow	1672
6.4.2.	Anisotropic flow	1672
6.4.3.	Methods of anisotropic flow measurement	1674
6.4.4.	Results on flow from lower energies	1681
6.4.5.	Flow measurements in ALICE	1689
6.4.6.	Summary	1701
6.5.	Event-by-event physics	1701
6.5.1.	Introduction	1701
6.5.2.	Lattice predictions	1702
6.5.3.	Correlations and fluctuations	1705
6.5.4.	Event-by-event measurements in ALICE	1708
6.5.5.	Centrality selection for fluctuation studies	1709
6.5.6.	Temperature fluctuations	1710
6.5.7.	$\langle p_t \rangle$ fluctuations	1712
6.5.8.	Multiplicity fluctuations	1714
6.5.9.	Fluctuations in particle ratio and strangeness	1717
6.5.10.	Fluctuations of conserved quantities	1720
6.5.11.	Balance functions	1724
6.5.12.	Fluctuations in azimuthal anisotropy	1733
6.5.13.	Disoriented chiral condensates	1734
6.5.14.	Fluctuations in intermediate and high $p_t$ sector and jets	1744
6.5.15.	Long-range correlations	1749
6.5.16.	Summary	1751
6.6.	Charm and beauty	1753
6.6.1.	Physics motivations	1753
6.6.2.	Current experimental results on heavy-quark hadroproduction	1764
6.6.3.	Charm and beauty production at the LHC	1768
6.6.4.	Charm reconstruction in the $D^0 \rightarrow K^- \pi^+$ channel	1784
6.6.5.	Perspectives for the study of charm quenching	1811
6.6.6.	Testing QCD with charm production in pp collisions	1813
6.6.7.	Beauty detection in Pb–Pb collisions in the semi-electronic decay channels	1816
6.6.8.	Beauty detection in Pb–Pb collisions with the ALICE muon spectrometer	1828
6.6.9.	Outlook: ongoing studies and future directions	1838

---

6.7. Quarkonia production	1843
6.7.1. General considerations	1843
6.7.2. Quarkonia detection in the dimuon channel: Pb–Pb collisions	1852
6.7.3. Quarkonia detection in the dimuon channel: pp collisions	1868
6.7.4. Quarkonia detection in the dimuon channel: pA collisions	1873
6.7.5. Quarkonia detection in the dielectron channel: Pb–Pb collisions	1874
6.8. Jet physics	1882
6.8.1. Introduction	1882
6.8.2. Jet production rates at the LHC	1883
6.8.3. Jet quenching at the LHC	1886
6.8.4. Monte Carlo production	1890
6.8.5. Characteristics of the background from the underlying event	1898
6.8.6. Jet reconstruction in central Pb–Pb collisions	1904
6.8.7. Jet-analysis results from full simulation	1916
6.8.8. Level 1 jet triggering with the ALICE EMCal	1923
6.8.9. Leading particle correlations	1928
6.8.10. Conclusions	1933
6.9. Photons	1934
6.9.1. Direct high- $p_t$ photons	1935
6.9.2. Direct low- $p_t$ photons	1944
6.9.3. Low-mass lepton pairs	1953
6.9.4. Photon–jet correlations	1959
6.9.5. Photon–pion momentum correlations	1963
6.10. Ultra-peripheral collisions	1967
6.10.1. Physics of ultra-peripheral collisions	1967
6.10.2. Results from lower energy	1973
6.10.3. Ultra-peripheral collisions in ALICE	1975
6.11. Cosmic-ray physics	1982
6.11.1. Contributions of ALICE to cosmic-ray physics	1982
6.11.2. Hadronic interaction models in cosmic rays	1983
6.11.3. The ALICE environment	1986
6.11.4. Physics topics of interest	1990
6.11.5. Use of the TOF and TPC for the detection of atmospheric muons	1999
6.11.6. Use of atmospheric muons for ALICE detector alignment and calibration	2007
<b>7. Conclusions</b>	<b>2009</b>
<b>ALICE Collaboration</b>	<b>2010</b>
<b>External Contributors</b>	<b>2017</b>
<b>Acknowledgments</b>	<b>2017</b>
<b>References</b>	<b>2018</b>

### Colour figures I–VI

Various figures are in colour throughout the online edition but only Figures I–VI are in colour in the print edition.

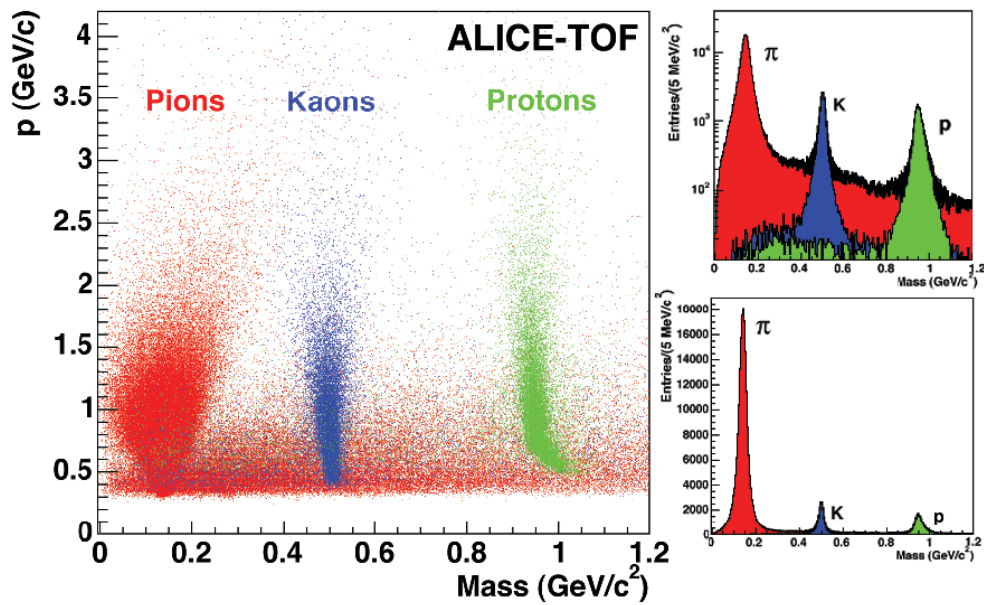


**Figure I.** Mass separation as a function of momentum with the TOF detector, for 200 HIJING central Pb–Pb events and with a simulated overall TOF time resolution of 80 ps. The corresponding mass distribution for  $0.5 < p < 4.2 \text{ GeV}/c$  is shown on the right, on a logarithmic (upper plot) and linear (lower plot) scale. The distributions from pions, kaons and protons are respectively indicated by the labelled histograms, while the black histogram represents the inclusive distribution from all particle species.

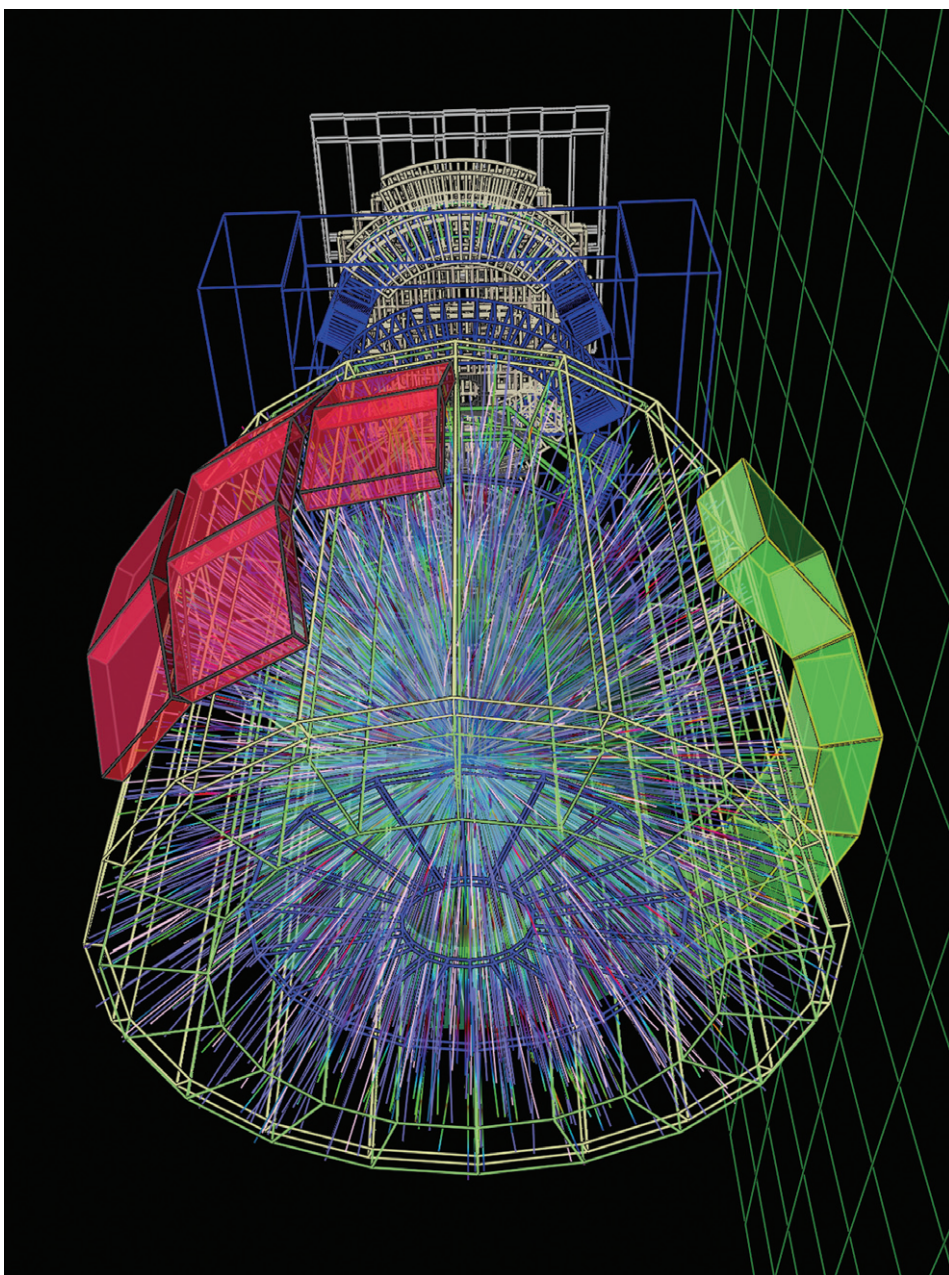


**Figure II.** AlRoot representation of the ALICE detector.

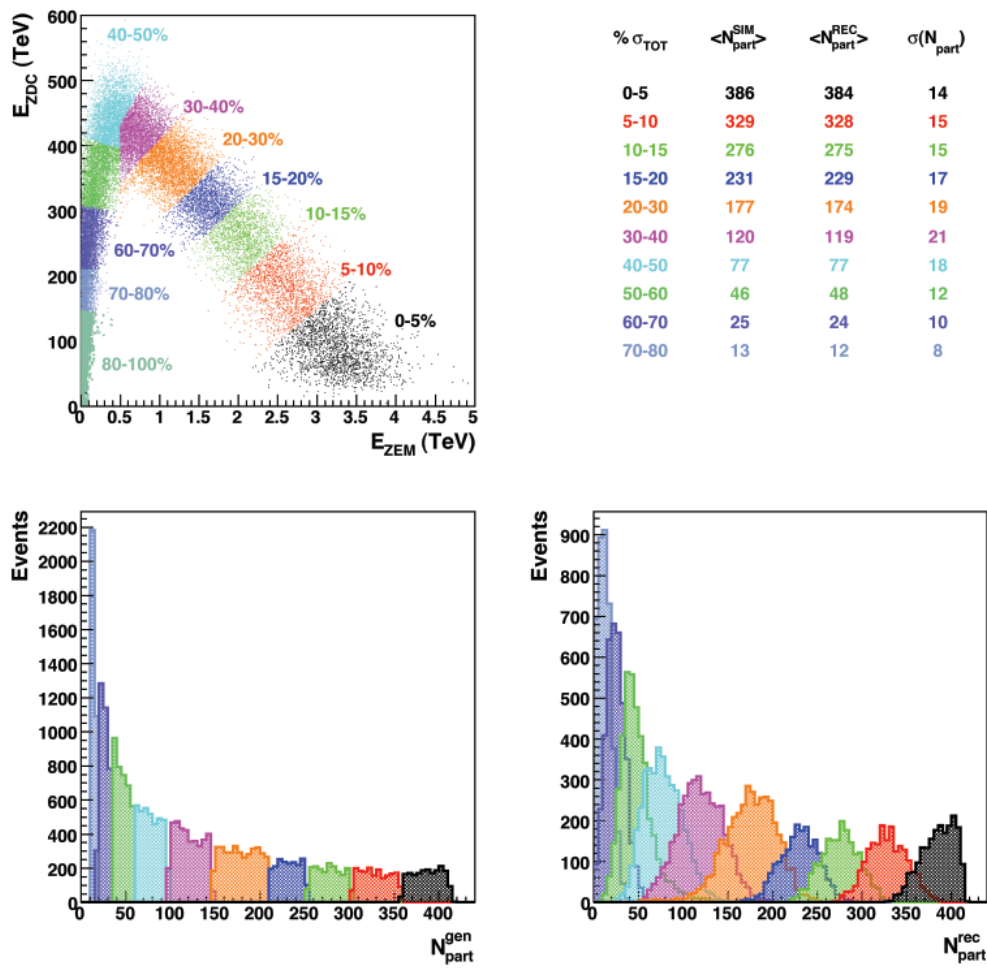


**Figure III.** The correlation between the energy in the hadronic ZDCs (ZN, ZP) and the energy in the forward electromagnetic calorimeter (upper plot). A possible centrality binning is indicated. In the lower plots we show the corresponding  $N_{part}$  distributions with and without taking into account the resolution on the energy measurement.

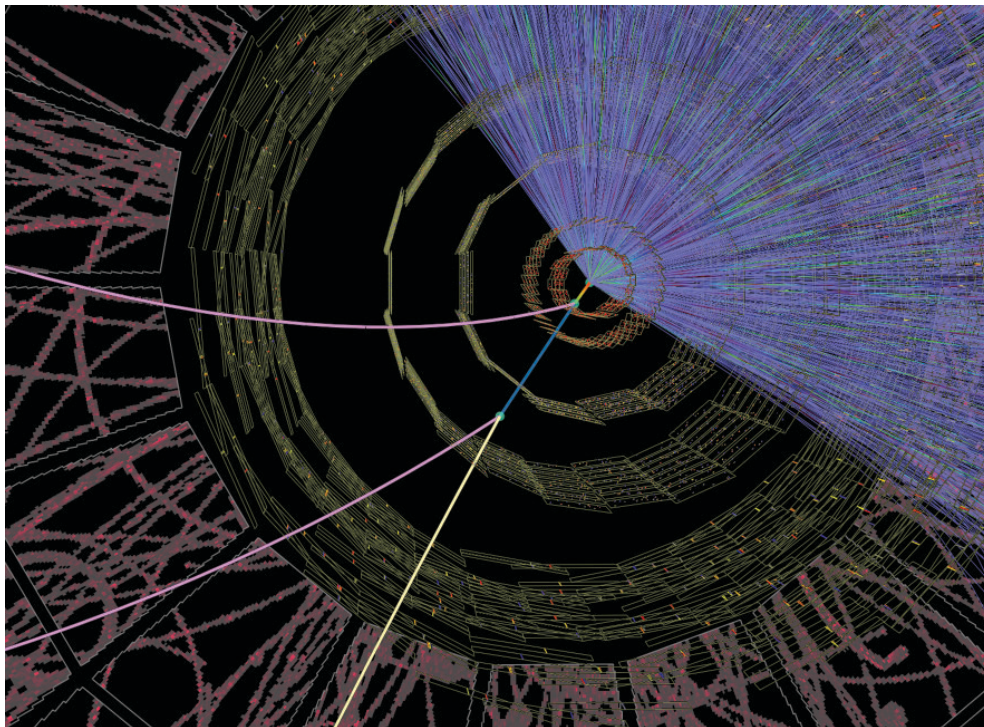
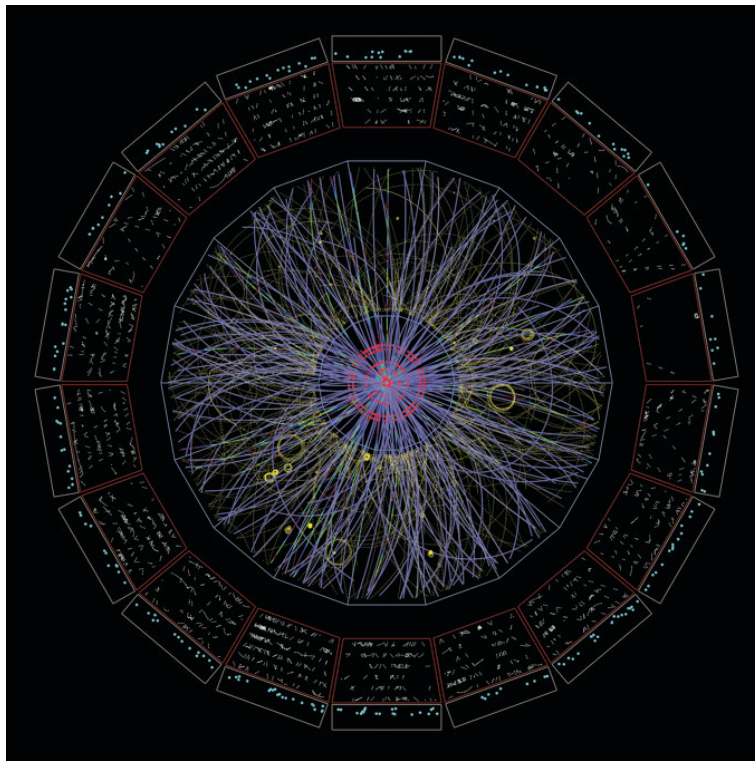


**Figure IV.** Top: A fraction of Pb–Pb event in the central barrel detectors. Bottom: Close-up of the ITS. Identification of a cascade weak decaying particle in the central region of the ALICE detector. The reconstruction is performed from its three charged daughters tracked with the ITS and TPC subsystems.

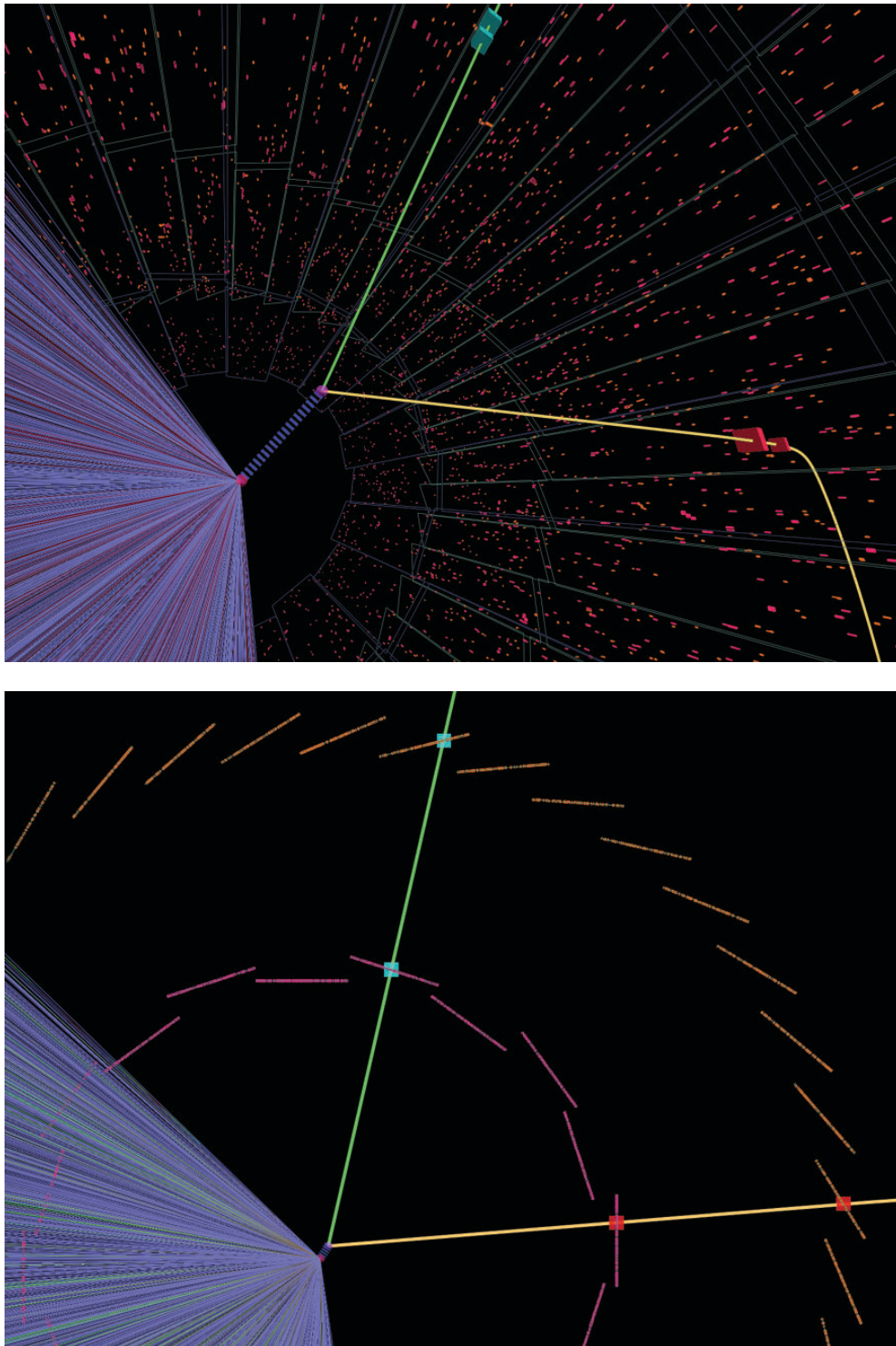


**Figure V.** Event display of a  $D^0 \rightarrow K^- \pi^+$  decay in a central Pb–Pb collision (perspective projection (top) and transverse projection (bottom)). The digits in the two layers of Silicon Pixel Detectors of the ITS are visualized. The trajectories of the particles from the Pb–Pb collision are shown for a limited azimuthal angle only. The value of the magnetic field is set to zero.

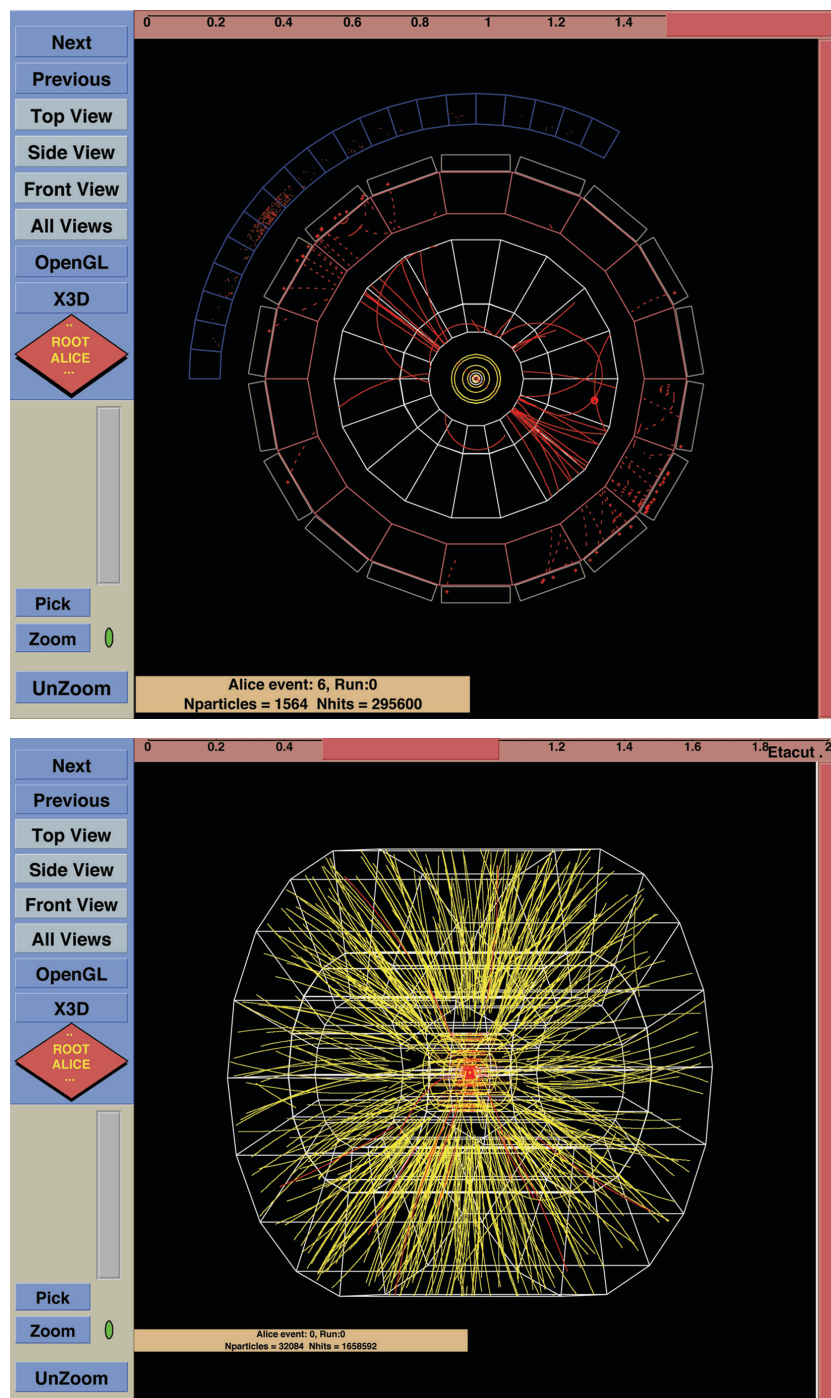


**Figure VI.** Display of the simulation of a 100 GeV dijet event in a pp interaction (upper) and a Pb-Pb collision (lower). Tracks from the jet have been marked red. Only tracks with  $p_t > 1.5$  GeV are shown.

## Summary and overview

ALICE is a general-purpose heavy-ion experiment designed to study the physics of strongly interacting matter and the quark–gluon plasma in nucleus–nucleus collisions at the LHC. It currently involves more than 900 physicists and senior engineers, from both the nuclear and high-energy physics sectors, from over 90 institutions in about 30 countries.

The ALICE detector is designed to cope with the highest particle multiplicities anticipated for Pb–Pb collisions ( $dN_{\text{ch}}/dy$  up to 8000) and it will be operational at the start-up of the LHC. In addition to heavy systems, the ALICE Collaboration will study collisions of lower-mass ions, which are a means of varying the energy density, and protons (both pp and pA), which primarily provide reference data for the nucleus–nucleus collisions. In addition, the pp data will allow for a number of genuine pp physics studies.

The detector consists of a central part, which measures event-by-event hadrons, electrons and photons, and of a forward spectrometer to measure muons. The central part, which covers polar angles from  $45^\circ$  to  $135^\circ$  over the full azimuth, is embedded in the large L3 solenoidal magnet. It consists of: an Inner Tracking System (ITS) of high-resolution silicon detectors; a cylindrical Time-Projection Chamber (TPC) a single-arm electromagnetic calorimeter (PHOS); and three particle identification arrays of: Time-Of-Flight (TOF) detector, Transition Radiation Detector (TRD); and a single-arm ring imaging Cherenkov (HMPID). The forward muon arm (covering polar angles  $171^\circ$ – $178^\circ$ ) consists of a complex arrangement of absorbers, a large dipole magnet, and fourteen planes of tracking and triggering chambers. Several smaller detectors (ZDC, PMD, FMD, T0, V0) for global event characterization and triggering are located at forward angles. An array of scintillators (ACORDE) on top of the L3 magnet will be used to trigger on cosmic rays.

The detailed design of the different detector systems has been laid down in a number of Technical Design Reports issued between mid-1998 and the end of 2004. The experiment is currently under construction and will be ready for data taking with both proton and heavy-ion beams at the start-up of the LHC.

Since the comprehensive information on detector and physics performance was last published in the ALICE Technical Proposal in 1996, the detector, as well as simulation, reconstruction and analysis software have undergone significant development. The Physics Performance Report (PPR) provides an updated and comprehensive summary of the performance of the various ALICE subsystems, including updates to the Technical Design Reports, as appropriate.

The PPR is divided into two volumes. Volume I, published in 2004 (CERN/LHCC 2003-049, ALICE Collaboration 2004 *J. Phys. G: Nucl. Part. Phys.* **30** 1517–1763), contains in four chapters a short theoretical overview and an extensive reference list concerning the physics topics of interest to ALICE, the experimental conditions at the LHC, a short summary and update of the subsystem designs, and a description of the offline framework and Monte Carlo event generators.

The present volume, Volume II, contains the majority of the information relevant to the physics performance in proton–proton, proton–nucleus, and nucleus–nucleus collisions. Following an introductory overview, Chapter 5 describes the combined detector performance and the event reconstruction procedures, based on detailed simulations of the individual subsystems. Chapter 6 describes the analysis and physics reach for a representative sample of physics observables from global event characteristics to hard processes.

The work described in this document spans a period of several years which saw substantial progress in the simulation, reconstruction, and analysis software. While an effort

has been made to update some of the earlier results, it is inevitable that in some cases different versions of the ALICE simulation and reconstruction software have been used to estimate the physics performance.

### ***Detector performance***

Chapter 5 of the PPR describes the performance of the ALICE detector and the reconstruction software.

#### *Track finding with the central detectors*

The primary vertex is found using the clusters reconstructed in the two innermost ITS layers, made of the Silicon Pixel Detector (SPD). In central Pb–Pb collisions, the vertex position is reconstructed with a precision of about  $5\ \mu\text{m}$  in the beam direction and about  $25\ \mu\text{m}$  in the transverse plane. For pp collisions, the precision on the vertex position is about one order of magnitude worse. However, due to the very low track multiplicity in pp events, this deterioration of the vertex precision does not have a significant impact on the reconstruction of physics signals, such as  $D^0$ 's,  $V^0$ 's, etc.

The track finding in the central detectors starts in the TPC. For tracks with a sufficient number of hits and  $p_t$  above  $0.2\ \text{GeV}/c$ , the TPC track-finding efficiency is almost 100%, even for charged-particle densities of central Pb–Pb collisions. The effective TPC track-finding efficiency is lower, around 85% (and around 90% for tracks with  $p_t$  above  $1\ \text{GeV}/c$ ), because of particle decays and the dead zones between the TPC sectors. The momentum resolution of tracks reconstructed in the TPC is about 0.7% (at  $p_t = 1\ \text{GeV}/c$  and the magnetic field  $0.5\ \text{T}$ ), and the  $dE/dx$  resolution is about 6%. These resolutions depend only slightly on event multiplicity.

The tracks reconstructed in the TPC are then prolonged to the ITS. Using the ITS measurements, the track impact-parameter resolution at primary vertex is improved to  $\sim 50\ \mu\text{m}$  for  $1\ \text{GeV}/c$  tracks in central Pb–Pb collisions. At the same momentum, the impact-parameter resolution in pp events is about  $100\ \mu\text{m}$ , because of the worse resolution of the primary-vertex position in low-multiplicity events.

Including the ITS measurements and, to a lesser extent, also the TRD data in the track reconstruction significantly improves the momentum resolution at high  $p_t$ , at  $p_t = 100\ \text{GeV}/c$  the momentum resolution is around 3.5% in magnetic field  $B = 0.5\ \text{T}$ . However, in this case the effective tracking efficiency is reduced to about 60%, because of particle absorption in the TRD and in the support structure.

In the last step, the reconstruction algorithm searches for secondary vertices from  $V^0$ 's, cascades, and kinks. The  $V^0$  and cascade decays are reconstructed within the fiducial volume between  $\sim 1\ \text{cm}$  from the primary vertex and the TPC inner radius. Typical reconstruction efficiencies are  $\sim 60\%$  for  $K_S^0$ 's,  $\sim 40\%$  for  $\Lambda$ 's, and  $\sim 5\%$  for  $\Xi$ 's. The kinks (i.e. charged pion or kaon decays on the flight) are reconstructed inside the TPC in the fiducial volume  $120 < r < 220\ \text{cm}$ . The kink reconstruction efficiency for charged kaon decays is about 70% in pp collisions and about 40% in central Pb–Pb collisions for kaons with  $p_t$  up to  $\sim 20\ \text{GeV}/c$ .

#### *Track finding in the forward muon spectrometer*

The reconstruction quality in the muon arm depends on the level of the background. However, even for the worst background scenario (using the pile-up of two highest multiplicity events), the muon-arm track-finding efficiency is about 95% and the resolution in the reconstructed  $\Upsilon$  mass is better than the requirement of  $100\ \text{MeV}/c^2$ .

### *High-Level Trigger reconstruction*

A reliable and efficient High-Level Trigger (HLT) is of great importance for ALICE. It reduces the data volume (e.g. by data compression) and the event rate (by triggering), resulting in a significant reduction of the overall data rate. The HLT will process data from both the central ALICE detectors and the forward muon spectrometer. The track reconstruction is based on HLT-specific algorithms as well as on algorithms developed for the offline software. To achieve better timing performance, the offline implementation has to be modified, however, at a cost of some decrease in the track-finding efficiency, particularly at lower momenta. The typical HLT track-finding efficiency in the central detectors is about 90% at 1 GeV/c, and the momentum resolution is  $\sim 3\%$  at the same momentum (in the magnetic field 0.5 T). The typical time needed to reconstruct a central Pb–Pb event ( $dN_{\text{ch}}/d\eta = 6000$ ) is about 10 s on a standard 1.3 kSPECint PC. The HLT algorithm for the muon reconstruction improves the muon- $p_t$  resolution by a factor  $\sim 2$  compared to the resolution obtained with the muon trigger chambers, and this allows for a sharper  $p_t$  cut before data recording. The corresponding timing is below 1 s on a standard 1 kSPECint PC. A farm of about 1000 CPU's will be able to perform the reconstruction task in the real time.

### *Charged-particle identification*

The identification of charged hadrons is done by combining the PID information provided by the ITS, TPC, TDR, TOF, and HMPID detectors. Assuming the particle production ratios as given by the HIJING event generator, the efficiency of the PID algorithm is above 95% up to  $p \sim 6$  GeV/c for pions, above 60% up to  $p \sim 3$  GeV/c for kaons, and above 70% up to  $p \sim 5$  GeV/c for protons, in all cases the contamination with wrongly-identified particles is below 30%. The overall effective PID efficiency is limited by particle decays and absorption in the material. It is about 50% for pions and protons, and about 40% for kaons, integrated over momentum. Electrons with momentum above 1 GeV/c are identified by the TRD with the efficiency above 90% and with the pion-rejection factor of about 100.

### *Neutral-particle identification*

The PHOS spectrometer detects and identifies photons with high energy- and position resolutions. In the low-momentum range, below  $\sim 20$  GeV/c, the direct-photon spectrum is obtained by subtracting, from the overall identified-photon spectrum, the contribution from decay photons, mainly from the light neutral mesons ( $\pi^0$ ,  $\eta$ ,  $\omega$ , etc.). The yields of these mesons are measured by an invariant-mass analysis. In the high-momentum range, above 20 GeV/c and up to  $\sim 100$  GeV/c, direct photons are identified on an event-by-event basis, by the shower-shape and the isolation-cut discrimination techniques. The identification efficiency for photons ( $0.5 \text{ GeV} < E_\gamma < 40 \text{ GeV}$ ) in pp collisions is above 90%. In central Pb–Pb collisions this efficiency is above 50%. The contamination from misidentified particles (electrons, charged hadrons, long-lived neutral mesons, neutrons and antineutrons) remains below 3%. For even higher-energy photons ( $40 \text{ GeV} < E < 120 \text{ GeV}$ ) the detection efficiency decreases to about 40%, however, the contamination from non-resolved  $\pi^0$ 's is smaller than 10%.

The Photon Multiplicity Detector (PMD) counts photons in the forward pseudorapidity region  $2.3 < \eta < 3.5$ . The photon-reconstruction efficiency is a function of the pseudorapidity with a maximum of  $\sim 70\%$  at  $\eta \sim 2.6$ . The purity of the sample of reconstructed photons is above 60% in the whole pseudorapidity range.

## *ALICE physics performance*

Chapter 6 of the PPR describes the analysis and physics reach for a representative sample of physics observables from global event characteristics to hard processes.

### *Event characterization*

The initial geometry of the collisions is determined by measuring the global event properties. This measurement allows also to study how the available centre-of-mass energy is redistributed in phase space.

The collision geometry can be estimated using several observables. One way is to use the information from the Zero-Degree Calorimeters (ZDCs). The number of participant nucleons  $N_{\text{part}}$  is determined with the resolution  $\sigma_{N_{\text{part}}} \sim 15$ , roughly independent of centrality.

The charged-particle multiplicity and the charged-particle pseudo-rapidity distribution can be measured over almost 8 units in  $\eta$ , by means of the Forward Multiplicity Detector (FMD), and of the innermost layers of the ITS. A simplified tracking algorithm has been used in the ITS to measure multiplicity in a robust way, defining ‘tracklets’ by associating clusters of hits in the two silicon pixel detector planes. In Pb–Pb collisions, the charged-particle multiplicity is measured with very good accuracy for all centralities. In the mid-rapidity region, even for very peripheral events, the resolution on multiplicity is better than 10%, and it becomes progressively smaller for more central collisions.

The same algorithm has been used to investigate the multiplicity distributions in pp collisions. It is possible to efficiently select minimum-bias pp collisions with a negligible trigger bias and small contamination of background events (e.g. beam–gas interactions). It exploits the trigger capabilities of the V0 and SPD. The initial study will include the measurements of charged-particle multiplicity,  $p_t$  spectrum, and correlation between mean  $p_t$  and charged-particle multiplicity.

In pA collisions the event centrality can be determined by measuring the so-called ‘grey tracks’ (having momentum between 250 MeV/c and 1 GeV/c) in the ZDCs. At least four centrality bins can be defined, without a significant overlap between adjacent bins.

### *Particle production*

The comprehensive measurements of particle ratios and momentum spectra are an important part of the ALICE physics programme. They are important both in the low- $p_t$  region, where a thermal and chemical analysis of freeze-out conditions is the main aim, and at intermediate and high  $p_t$ , where the role of radial flow, quark recombination, and, eventually, hard processes, becomes apparent.

By combining the information from different PID detectors, stable charged hadrons (pions, kaons, and protons) can be identified and measured from very low momentum (hundreds of MeV) up to at least 50 GeV. Secondary vertices are used to identify charged and neutral kaons as well as hyperons up to, and beyond 10 GeV. Baryon production will be measured in the central region ( $p$ ,  $\bar{p}$ ,  $\Lambda$ ,  $\bar{\Lambda}$ ,  $\Xi^-$ ,  $\Xi^+$ ,  $\Omega^-$ , and  $\bar{\Omega}^+$ ) to study the baryon number transfer in rapidity both in Pb–Pb and pp collisions.

Resonances bring additional information about the final stages of the collision. Three resonances have been investigated so far, the  $\rho(770)^0$ , the  $K^*(892)^0$ , and the  $\phi(1020)$ . In addition to production spectra, ALICE will be able to measure to some extent variations in the resonance parameters (mass, width, line shape), which may arise from the restoration of chiral symmetry.

### *Momentum correlations*

The space–time geometry of the particle-emitting source created in ultra-relativistic heavy-ion collisions can be studied by the analysis of two-particle intensity interferometry. Possible experimental effects and biases are simulated and discussed in detail, the necessary tools to either remove them or to correct for them have been implemented.

ALICE will contribute to the existing results of HBT analysis in heavy-ion collisions as well as open the possibility for new analysis, such as direct-photon interferometry or event-by-event HBT analysis. Data from the LHC may help to clarify the ‘RHIC HBT puzzle’ by extending the excitation function to much higher energy and particle multiplicities, and by making precise measurements of the shape and the anisotropy of the particle-emitting source as given by azimuthally-sensitive HBT analysis. It will also extend the existing investigations to a larger number of different hadron species, which will help to better understand the particle emission, and therefore the geometry and evolution of the system.

### *Flow*

High-accuracy measurements of anisotropic flow are very important for understanding the dynamics of the heavy-ion collisions at the LHC.

The determination of the reaction plane, a prerequisite for the measurement of anisotropic flow, will benefit from the possibility to be done independently by the different subsystems of the ALICE detector, and by different analysis methods. At mid-rapidity, making use of the elliptic flow signal ( $v_2$ ), we will be able to determine the reaction plane for a very wide range of particle multiplicities and magnitudes of the elliptic flow. At beam-rapidity, using the directed flow signal ( $v_1$ ), we will get an independent determination of the reaction plane from the ZDCs. A systematic comparison between different methods and different subsystems in ALICE will allow us to estimate non-flow contributions to the anisotropic flow and will be crucial for a quantitative interpretation of the results.

The expected precision of the reaction-plane determination will allow for anisotropic-flow measurements with unprecedented accuracy for both charged and identified particles in a momentum range from a few hundred MeV/ $c$  up to well above 10 GeV/ $c$ . These measurements are expected to provide constraints on the equation of state (low  $p_t$ ), collective motion of the constituent quarks (intermediate  $p_t$ ), and parton-energy loss (high  $p_t$ ).

### *Event-by-event physics*

Fluctuations of thermodynamic quantities are fundamental to the study of the QGP phase transition. The ALICE experiment is well suited to precise event-by-event measurements of various observables. Fluctuations in these observables can be studied in order to understand the physics of bulk properties of matter as well as high- $p_t$  particles and jets. Recent lattice calculations have shown that interesting fluctuation patterns might be present also at the small chemical potential, which will prevail at LHC energies. The capability of the ALICE detector is explored in terms of measurement of temperature and  $\langle p_t \rangle$  fluctuations, multiplicity and strangeness fluctuations, fluctuations of conserved quantities including net-charge fluctuation, balance functions, fluctuation in azimuthal anisotropy, fluctuation in space–time parameters from correlation measurements, disoriented chiral condensates, importance of jets and mini-jet production in fluctuation measurements and long-range dynamical correlations.

### *Charm and beauty*

LHC is the first machine where heavy quarks will be produced abundantly in heavy-ion collisions. The study of heavy-flavour production in both pp and nucleus–nucleus collisions down to almost zero transverse momentum will allow a sensitive comparison with QCD predictions and a study of the in-medium quenching of heavy quarks compared to massless partons (light quarks and gluons). The benchmark decay channel  $D^0 \rightarrow K^- \pi^+$  has been studied in detail. In one LHC year at nominal luminosity, we expect to cover, in  $|\eta| < 0.9$ , the transverse-momentum range  $1 \text{ GeV}/c < p_t < 18 \text{ GeV}/c$  in central Pb–Pb collisions and  $0.5 \text{ GeV}/c < p_t < 18 \text{ GeV}/c$  in pp and pPb collisions, with statistical errors smaller than 15–20% at high  $p_t$  in all cases.

Beauty production in central Pb–Pb collisions can be measured via semi-leptonic decays. Identified electron tracks displaced from the primary vertex provide a measurement of the b-hadron cross section above a given  $p_t^{\text{min}}$ . ALICE can cover the range  $2 \text{ GeV}/c < p_t^{\text{min}} < 30 \text{ GeV}/c$  (in  $|\eta| < 0.9$ ) with statistical errors of order 10% or less. Single muons and opposite-sign dimuon pairs allow a measurement of open-beauty production with high statistics in the forward pseudorapidity region  $-4 < \eta < -2.5$  in the transverse-momentum range  $2 \text{ GeV}/c < p_t^{\text{min}} < 22 \text{ GeV}/c$ .

Additional channels are currently under investigation, such as  $D^+$  reconstruction, electron–muon and multi-muon correlations, beauty production via displaced  $J/\psi$ 's from B decays and the perspectives for the measurement of W-boson-decay muons (which will be useful as a medium-blind reference to study the production of heavy flavour).

### *Quarkonia*

At LHC, the complete spectrum of heavy quarkonia states ( $J/\psi$ ,  $\psi$ ,  $\Upsilon$ ,  $\Upsilon'$ , and  $\Upsilon''$ ) is accessible and will allow a very detailed study of both suppression phenomena (due to deconfinement, which should affect members of both the charm and beauty family) and possible enhancement (due to recombination, significant only for the charmonium states). Quarkonia are detected in ALICE at mid-rapidity ( $-0.9 < \eta < 0.9$ ) in the dielectron channel, and at forward rapidity ( $-4.0 < \eta < -2.5$ ) in the dimuon channel.

In the central-rapidity region, the  $J/\psi$  production cross section will be measured down to  $p_t = 0 \text{ GeV}/c$  in the minimum-bias data sample. The data triggered with high- $p_t$  electrons have the  $p_t$  threshold for  $J/\psi$  acceptance of about  $5 \text{ GeV}/c$ . The production of  $\Upsilon$  states is measured over the full transverse-momentum range in both minimum-bias and triggered data samples. The mass resolutions are  $\sigma_m \approx 30 \text{ MeV}/c^2$  for the  $J/\psi$  and  $\sigma_m \approx 80 \text{ MeV}/c^2$  for the  $\Upsilon$ . About  $10^5 J/\psi$  and  $10^3 \Upsilon$  will be measured in central Pb–Pb collisions during one year of data taking.

Quarkonia measured at forward rapidity allow measurement of parton distributions at  $x$  values as small as  $10^{-5}$ . The modest transverse-momentum cut on single muons applied at the trigger level extends quarkonia detection down to zero transverse momentum. The number of detected  $J/\psi$  is about  $7 \times 10^5$  per year, allowing for a detailed study of  $J/\psi$  production as a function of centrality and transverse momentum. Similar studies can be carried out for the  $\Upsilon$ , but with significant statistical errors, since the expected yearly statistic is about 10 000  $\Upsilon$ s.

Reference pp data will be usually taken at  $\sqrt{s} = 14 \text{ TeV}$ . In one year the expected statistic for  $J/\psi$  ( $\Upsilon$ ) is about  $5 \times 10^6$  ( $4 \times 10^4$ ). The statistic collected in a special pp run of  $10^6$  s, at the nominal heavy-ion energy  $\sqrt{s} = 5.5 \text{ TeV}$ , is about  $2 \times 10^5$  and  $2 \times 10^3$  for  $J/\psi$  and  $\Upsilon$ , respectively.

Data in pPb collisions are needed to measure nuclear effects (shadowing and nuclear absorption). Preliminary results indicate that in a dedicated run of  $10^6$  s the statistics is adequate to perform these measurements.

### *Photons*

Direct *prompt photons* at high  $p_t$  allow the study of hard processes in the dense medium without any final-state modification. In the low- $p_t$  domain, *thermal photons* trace the thermal evolution of the system and, in particular, of the hot and early phase of the reaction.

The photon spectrum will be measured in ALICE with the PHOS spectrometer. Hard photons will be identified on an event-by-event basis using shower-shape and isolation-cut analyses. In this energy domain, the systematic errors due to misidentified neutral mesons will be of the order of a few per cent. Statistics will limit the measurement in the high-energy part of the spectrum to about 100 GeV both in pp and in Pb–Pb collisions. Prompt photons will be used to tag charged jets emitted in the opposite direction in order to study jet-fragmentation functions. In-medium modification of the fragmentation function will be measured with an accuracy of the order of a few per cent. Various correlations, such as photon–hadron and photon–photon correlations will provide additional information on the medium modified di-jet structure.

In the low-energy domain direct photons will be identified as an excess of identified photons (with shower-shape analysis) when compared with the spectrum of decay photons. The systematic error on the measurement of the excess will be about 8%. This excess has several origins, including thermal photons from the QGP and hadron gas, photons generated by fast partons traversing the medium, and prompt photons.

An alternative way to measure photons consists in measuring electron pairs from photon conversions. Conversions will be identified in the central tracking system and in the PHOS spectrometer, and they will be measured up to about 30 GeV/ $c$  both in pp and in Pb–Pb collisions, limited by statistics. The production of low-mass dielectrons will be measured with the central tracking system for masses between 0.2 GeV/ $c^2$  (to avoid the  $\pi^0$  Dalitz decay) and 0.6 GeV/ $c^2$  (to avoid the low-mass vector meson decays). The  $p_t$  range, limited by statistics, extends to about 10 GeV/ $c$ .

### *Jet physics*

Properties of the hot and dense medium produced in nucleus–nucleus collisions can be studied via the energy loss experienced by fast partons in the medium (*jet quenching*). The highest sensitivity to the medium properties is expected when measuring the longitudinal and transverse fragmentation functions of jets both at large and at small relative momentum fraction  $z$ .

In central Pb–Pb collisions at LHC, jet rates within the ALICE acceptance are sufficient to map out the energy dependence of jet fragmentation over a very wide kinematic range, up to  $E_t \simeq 200$  GeV. However, jet reconstruction in nuclear collisions has to cope with the large background from the underlying event, therefore, jet reconstruction has to be limited to small cone sizes in the range  $0.3 < R_c < 0.5$ . In addition, a transverse momentum cut in the range  $1 \text{ GeV}/c < p_t < 2 \text{ GeV}/c$  has to be applied to reduce the background. As a consequence, even for perfect calorimetry, the energy resolution is limited to  $\Delta E_t/E_t \simeq 20\%$ .

Jets with energies in the range from 20 GeV to 200 GeV have been embedded into HIJING events and passed through the full detector simulation and reconstruction chain. The energy spectrum and jet-structure observables are reconstructed and compared to unmodified

jets as measured in pp collisions. Only for cone energies below  $\simeq 40$  GeV fake jets do influence the quality of the reconstruction.

In its present design, ALICE can measure only the charged particles within the jets, limiting the jet-energy resolution to 40–50%. Nevertheless, at high  $E_t$ , charged-jet reconstruction is shown to be much superior to studying high- $p_t$  parton fragmentation using leading particles only, because the bias in the fragmentation function is significantly reduced. Whereas the high- $p_t$  and high- $j_t$  (momentum transverse to the jet axis) regions of the leading parton remnants are essentially background free and will be measured very well in ALICE, the spectra of particles originating from radiated gluons have to be extracted mostly from kinematic regions, where background dominates the signal ( $S/B = 10^{-1}$ – $10^{-2}$ ). In such domain the low- $p_t$  tracking capabilities of ALICE are essential and unique, and allow a study of this region (including PID information) on a statistical basis.

In the low- $E_t$ -jet region, jet-structure modifications will be studied with inclusive spectra of identified particles and particle correlations, as shown by the RHIC experiments. These studies require excellent low- $p_t$  and PID capabilities and ALICE will extend them to heavy-ion collisions at the LHC.

The proposed electromagnetic calorimeter for ALICE will improve the jet-energy resolution, increase the selection efficiency and further reduce the bias on the jet fragmentation. Furthermore, it will add a jet trigger which is needed to increase the statistics at high  $E_t$ . The low- and high-transverse-momentum tracking capabilities combined with electromagnetic calorimetry represent an ideal tool for jet-structure modification studies at the LHC over a wide kinematic region of jet and associated-particle momenta.

### *Ultra-peripheral collisions*

In ultra-peripheral collisions, where the impact parameter is larger than the sum of the nuclear radii, particles can be produced in photon-induced interactions because of the strong electromagnetic fields of heavy ions. The photon can also interact with a parton in the target nucleus, for example via photon–gluon fusion, leading to the production of jets and heavy quark pairs. Ultra-peripheral interactions will require different trigger and analysis techniques compared with hadronic interactions. The TOF and the SPD detectors can provide a Level-0 multiplicity trigger for the ALICE central barrel, and the forward muon spectrometer can provide a Level-0 trigger for the dimuon decay channel. The higher trigger levels will be used to reduce the trigger rates by suppressing the background. Simulations show that the rates for exclusive production of heavy vector mesons ( $J/\psi$  and  $\Upsilon$ ) and for production of heavy-quark pairs are sufficient for meaningful measurements.

### *Cosmic-ray physics*

Energies available in pp and A–A collisions at the LHC correspond to a proton of  $E \sim 10^{17}$  eV interacting with a fixed target. This will allow, for the first time with an accelerator, accessing a region well above the knee in the cosmic-ray spectrum ( $E \sim 3 \times 10^{15}$  eV) and may contribute to the understanding of its nature. The possibility to measure in detail the properties of minimum-bias collisions, including particle identification, will improve the knowledge of hadronic interactions, and provide a consistency check of model predictions in an energy domain relevant for the latest-generation cosmic-ray surface experiments.

A cosmic-ray trigger, intended for calibration and alignment of the central detectors, will also be used to make genuine cosmic-ray measurements. The excellent tracking performance of the TPC, improved by TRD, can be employed to detect atmospheric muons produced after

---

the collision of a primary cosmic ray with a nucleus of the atmosphere. This will be one of the first experiment in cosmic-ray physics allowing to analyze multimMuon events, measuring with very high resolution the number of muons crossing the apparatus, including their directions and energies. In one year of data taking, corresponding to 30 days of live time, statistics should be sufficient to investigate the unexpected high-multiplicity muon events found by the ALEPH experiment. A detailed measurement of the inclusive muon spectrum up to TeV energies will be performed over a period of several years.

## 5. Detector performance

### 5.1. Track finding with central detectors

In this section we focus on the track and vertex reconstruction in the central part of the ALICE detector, which includes Inner Tracker System (ITS), Time Projection Chamber (TPC), Transition Radiation Detector (TRD), Time-Of-Flight detector (TOF), High Momentum Particle Identification Detector (HMPID) and Photon Spectrometer (PHOS).

Track reconstruction is one of the most challenging tasks in this experiment. It is of great importance to precisely determine the momentum of particles as close as possible to the point of their generation (main interaction point or secondary decay vertices). Also, the track reconstruction procedure should be capable of a precise extrapolation of the tracks to the detectors providing the particle identification information (TOF, HMPID, PHOS) that are, in the case of ALICE, situated far away from the main interaction point.

For various kinds of physics analysis of the data, knowledge about the position where the particle was generated (the primary and secondary vertices) is necessary. The reconstruction software should provide such information.

Wherever it is not specified explicitly as different, we refer to the ‘global ALICE coordinate system’. It is a right-handed coordinate system with the  $z$  axis coinciding with the beam-pipe axis and going in the direction opposite to the muon arm, the  $y$  axis going up, and the origin of coordinates defined by the intersection point of the  $z$  axis and the central-membrane plane of TPC.

We also use the following terms:

- *Digit*: This is a digitized signal (ADC count) obtained by a sensitive pad of a detector at a certain time.
- *Cluster*: This is a set of adjacent (in space and/or in time) digits that were presumably generated by the same particle crossing the sensitive element of a detector.
- *Reconstructed space point*: This is the estimation of the position where a particle crossed the sensitive element of a detector (often, this is done by calculating the centre of gravity of the ‘cluster’).
- *Reconstructed track*: This is a set of five parameters (such as the curvature and the angles with respect to the coordinate axes) of the particle’s trajectory together with the corresponding covariance matrix estimated at a given point in space.

The details of the reconstruction procedure are described below. We should mention that exactly the same software is to be used for reconstructing both pp and Pb–Pb events. However, to achieve the best performance, the program parameters have to be tuned to a given track multiplicity. With its present status, the reconstruction takes into account the non-uniformity of the longitudinal component of the magnetic field, but the corrections for the misalignment and miscalibration of the involved detectors are not yet implemented.

*5.1.1. Primary-vertex reconstruction.* The reconstruction of the primary-vertex position in ALICE is done using the information provided by the silicon pixel detectors, which constitute the two innermost layers of the ITS.

The vertex diamond at the LHC can be parametrized by Gaussian shapes along the  $z$ -axis (with  $\sigma_z = 5.3$  cm) and in the  $x$ ,  $y$  directions. The width parameter in the transverse plane,  $\sigma_{x,y}$ , reported as  $15 \mu\text{m}$  in all previous ALICE documents [1], will, however, depend on the choice of the beam parameter  $\beta^*$ , which also affects the beam luminosity and lifetime. In particular, since  $\sigma_{x,y} = \sqrt{\varepsilon\beta^*}$ , where  $\varepsilon = 0.57$  nm rad is the beam emittance, larger values of

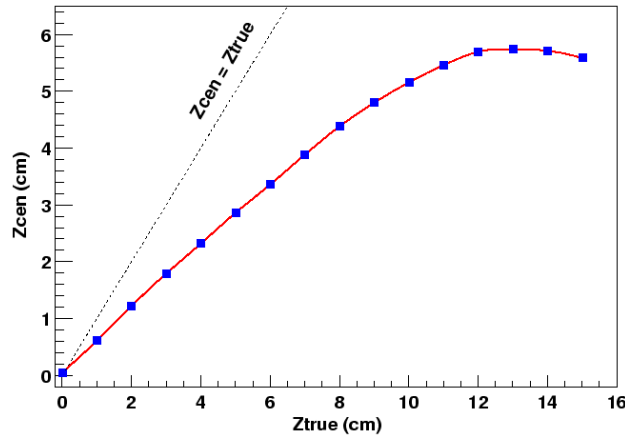


**Figure 5.1.** Correlation between the centroid of the  $z$  distribution,  $z_{\text{cen}}$ , and the true position of the primary vertex,  $z_{\text{true}}$ .

$\beta^*$  (of the order of 10 m), will give a width parameter  $\sigma_{x,y}$  of about  $75 \mu\text{m}$  [2]. Moreover, different fillings of the LHC will give average beam positions in the transverse plane which may differ by several millimetres.

It is important to evaluate the effect that such beam displacements may have on the overall vertex reconstruction and to design a full 3D algorithm for vertex-position determination.

**5.1.1.1. Simulations.** All the studies reported here were carried out using the ALICE offline simulation and reconstruction framework AliRoot (Volume I [3]). In the case of central Pb–Pb events, the parametrized HIJING event generator was used, with a primary charged-particle multiplicity in the full phase space of  $N_{\text{ch}} = 84\,210$  ( $dN_{\text{ch}}/d\eta)_{\eta=0} = 8000$ ). Events were also generated at lower particle densities. The position of the primary vertex along the  $z$  axis was varied from  $z = -15$  cm to  $z = +15$  cm, while in the transverse plane radial displacements up to 10 mm were used. All the physical processes in GEANT3 were switched on, with an energy cut-off equal to 1 MeV everywhere except for the pixel-detector sensitive volumes, where it was set to 70 keV. The response of the pixel detectors was simulated in detail.

**5.1.1.2. Primary-vertex finding using ITS pixel layers.** The algorithm starts with looking at the distribution of the  $z$  coordinates of the reconstructed space points in the first pixel layers. At a vertex  $z$  coordinate  $z_{\text{true}} = 0$  the distribution is symmetric and its centroid ( $z_{\text{cen}}$ ) is very close to the nominal vertex position. When the primary vertex is moved along the  $z$  axis, an increasing fraction of hits will be lost and the centroid of the distribution no longer gives the primary vertex position. However, for primary vertex locations not too far from  $z_{\text{true}} = 0$  (up to about 12 cm), the centroid of the distribution is still correlated to the true vertex position, as can be seen from Fig. 5.1. The saturation effect at large  $z_{\text{true}}$  values of the vertex position ( $z_{\text{true}} = 12$ –15 cm) is, however, not critical, since this procedure is only meant to find a rough vertex position, in order to introduce some cut along  $z$ .

A monotonic relationship, through a polynomial fit, was used to evaluate a first approximated value ( $z_v^0$ ) of  $z_v$  from the centroid of the  $z$  coordinate distribution of the reconstructed space points.

Referring to Fig. 5.2, once  $z_v^0$  has been estimated, the confidence region around  $z_v^0$ , ( $z_v^{\text{min}}, z_v^{\text{max}}$ ) was evaluated by  $z_v^{\text{min,max}} = z_v^0 \pm \Delta z$  where  $\Delta z$  was assumed to depend on the

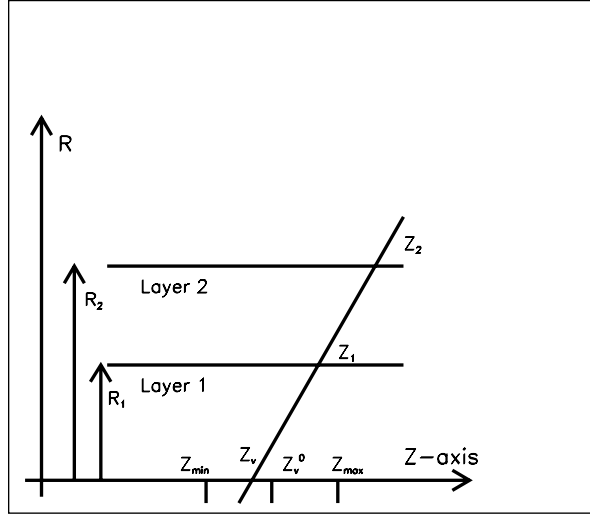


**Figure 5.2.** Geometrical sketch of the algorithm used to correlate the points in the two pixel layers. A rough estimation of the vertex location,  $z_v^0$  is made first, using the  $z$  distribution of the reconstructed points in the innermost pixel layers. The correlation of the points  $z_1, z_2$  in the two layers is then considered, selecting only those pairs which give a vertex position  $z_v$  within the confidence region  $(z_{\min}, z_{\max})$  around  $z_v^0$  and having a difference of the position azimuthal angles in the transverse plane smaller than a preselected value.

estimated vertex position as  $\Delta z = a + bz_v^0 + c(z_v^0)^2$  to account for a larger uncertainty in the vertex position at large  $z_v^0$  values.

To find the final vertex position, the correlation between the points  $z_1, z_2$  in the two layers (Fig. 5.2) was considered, as was already done in the ITS TDR [1] and described in more detail in the internal notes [4, 5]. When the primary vertex lies outside the  $x = y = 0$  axis, the radial distances between the vertex and the points on the two layers are slightly different from the average values of the pixel layers radii  $r_1, r_2$ . The correct radial distances are taken into account by estimating them with a rough vertex determination in the transverse plane from the  $x$  and  $y$  distributions of the points. Leaving only those points  $z_1$ , for each point  $z_2$ , which give a  $z_v$  between  $z_v^{\min}$  and  $z_v^{\max}$ , the correlation between  $z_1$  and  $z_2$  results in a  $z_v$  spectrum as reported in Fig. 5.3. A careful choice of these ( $z_v^0$ -dependent) cuts is able to reduce the combinatorial background to a large extent, especially outside the true correlation peak, leaving only a small fraction of the possible  $N_1 N_2$  pairs, where  $N_1$  and  $N_2$  are the numbers of space points reconstructed on the two layers.

The distribution shown in Fig. 5.3 can be fitted to a sum of a constant and a Gaussian function  $f(z_v) = B + Y \exp[-(z_v - z_{\text{found}})^2 / 2\sigma_z^2]$ , where  $B, Y, z_{\text{found}}$  and  $\sigma_z$  are the free parameters. The quality of the applied cuts can be characterized by the ratio  $Y/B$  which is proportional to the ratio of the point pairs (coming from the real tracks) and the combinatorial pairs. Substantial reduction of the combinatorial background comes from the cut on  $\Delta\varphi = \varphi_2 - \varphi_1$ , where  $\varphi_1$  and  $\varphi_2$  are the azimuthal angles (in the transverse plane) of the two space points. The distribution of this quantity depends on the distribution of the curvature of the tracks selected for this procedure. It depends also on the amount of multiple scattering and, thus, on the material budget traversed by particles on the way from the primary vertex to the second pixel layer. A value of  $\Delta\varphi = 0.1^\circ$  was adopted in most cases. However, such an optimization have to be carried out for each particle density and magnetic field setting.

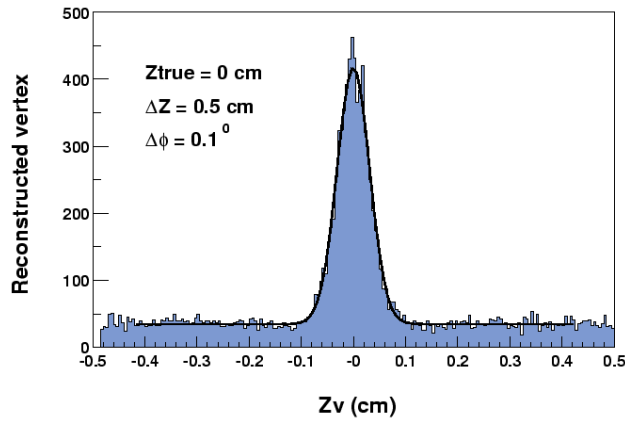


**Figure 5.3.** Distribution of  $z_v$  for a central Pb–Pb collision. After fitting the distribution to the sum of a Gaussian and a constant, the centroid of the Gaussian is used as the estimate of the primary vertex position.

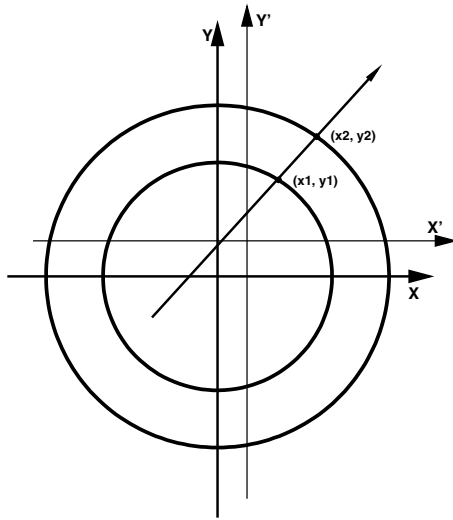


**Figure 5.4.** Geometrical sketch of the two pixel layers with the reconstructed points in the transverse plane. Correlation between the points  $(x_1, y_1)$  and  $(x_2, y_2)$  can be used to determine the distribution of the intercepts with axes  $X', Y'$  (estimated from a first-order evaluation of the vertex coordinate).

A similar approach can be applied to the reconstruction of the vertex position in the transverse plane. Because of the small average radii of the pixel layers (4 cm and 7 cm), the deviation of the track projection from a straight line is small, and a reasonable result can be obtained even with a linear approximation, especially for the high-momentum particles. Also, the combinatorial background can be reduced nearly to zero, once a good knowledge of the vertex location along the beam axis has been achieved. We selected only the point pairs giving the intersection with the  $z$  axis within  $4\sigma_z$  around the estimated vertex location  $z_v$  and a  $\Delta\phi$  cut dependent on the magnetic field. The distribution of the intersections of all the straight lines connecting the points  $(x_1, y_1)$ ,  $(x_2, y_2)$  with the axes  $X', Y'$  (Fig. 5.4) has its minimum

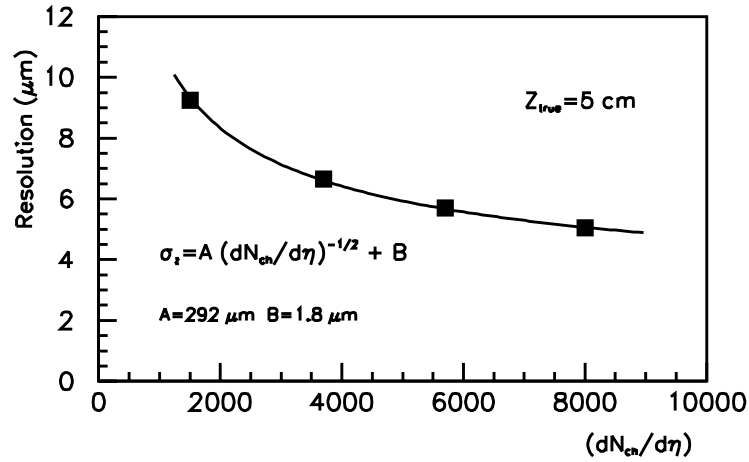


**Figure 5.5.** Resolution of the reconstructed vertex position as a function of the particle density for  $B = 0.2$  T. The solid line is a fit through the parametrization given in the figure (see text).

width (best resolution) at the values  $X'$ ,  $Y'$  close to the true vertex coordinates that can be found through an iterative procedure. No more than 2–3 iterations were needed, since after that the limiting factor was the straight line approximation itself.

By taking the centroids of the  $x_v$ ,  $y_v$  and  $z_v$  distributions, it is possible to estimate the location of the primary vertex in three dimensions [6, 7].

#### 5.1.1.3. Results for the central Pb–Pb events

*Dependence on the vertex location.* For the case of the highest particle density  $dN_{ch}/d\eta = 8000$ , for  $B = 0.2$  T, the method gives a resolution of about  $5 \mu\text{m}$  along the  $z$  axis. When the primary vertex is away from  $z = 0$ , the algorithm tends to slightly overestimate (by a few  $\mu\text{m}$ ) the absolute value of its position. This is due to the difference in the left and right background tails of the  $z_v$  spectrum. Such small effect however has been corrected by including this observed trend as a part of the estimation process. The results showed that it is possible to obtain a very good resolution (in the order of  $5 \mu\text{m}$  along the  $z$  axis), even in case of beam displacements off the  $z$  axis, up to radial distances of 10 mm. The resolution in the transverse plane was found to be about  $25 \mu\text{m}$  at  $B = 0.2$  T. Such values are good enough for the track reconstruction purposes.

*Dependence on the particle density.* The capability to reconstruct the vertex location was also investigated for different particle multiplicities, down to a value of  $N_{ch} = 17000$  in the full phase space ( $dN_{ch}/d\eta \sim 1500$ ). For low particle multiplicity the combinatorial background is very low; however the loss in statistics results in a slightly worse vertex resolution. This can be seen from Fig. 5.5, which shows the dependence of the vertex resolution on the particle density.

If the vertex resolution is plotted against the particle density, a power law

$$\sigma_z = \frac{A}{\sqrt{dN_{ch}/d\eta}} + B$$

can be fitted to the data, obtaining  $A = 292 \mu\text{m}$  and  $B = 1.8 \mu\text{m}$ . The result also shows that a good vertex finding can be obtained even with a reduced number of tracks (down to 1/4 of the expected maximal number of tracks). This could help where a fast vertex reconstruction

**Table 5.1.** LHC parameters for pp and Pb–Pb runs at the ALICE intersection point.

Parameter	pp	Pb–Pb
Energy per nucleon (TeV)	7	2.76
$\beta^*$ (m)	10	0.5
$\sigma_{x,y}^{\text{bunch}}$ ( $\mu\text{m}$ )	71	16
$\sigma_z^{\text{bunch}}$ (cm)	7.5	7.5
$\sigma_{x,y}^{\text{vertex}}$ ( $\mu\text{m}$ )	50	11
$\sigma_z^{\text{vertex}}$ (cm)	5.3	5.3

is needed, since the amount of CPU time scales approximately as the square of the number of tracks.

*Dependence on the number of dead pixels.* Several detector-related factors (like noisy channels or misalignment) may affect the ideal primary vertex reconstruction. Only the effect of dead pixels or chips was investigated in a simple approach.

The switching off of a pixel, due to charge sharing, does not necessarily lead to a loss of efficiency, since sometimes the cluster can still be reconstructed (although with a reduced resolution). However, in our case, we assumed that if a track crosses a dead pixel, the corresponding cluster is always lost.

We found that the resolution does not change too much, even when the number of dead pixels increases up to 10% of the total. If a full chip is masked, the effect may be different, depending on the position of the chip with respect to the vertex location. However, we verified that the absolute value of such an effect is small, even for a large fraction of dead chips, randomly distributed over the two pixel layers.

*Effect of the magnetic field.* Increasing the magnetic field leads to a higher occupancy, which in turn increases the combinatorial background and worsens the resolution. Also, for the higher field setting, the straight line track approximation may become unsatisfactory. We verified that the resolution does not significantly change with the increase of the magnetic field, from 0.2 T to 0.5 T. For example, the resolution in the reconstructed  $z$  position only changes from  $5 \mu\text{m}$  to about  $8 \mu\text{m}$ , whereas the resolution in the transverse plane varies between  $25 \mu\text{m}$  and  $35 \mu\text{m}$  going from 0.2 T to 0.5 T.

*5.1.1.4. Primary vertex reconstruction in pp collisions.* Precise information on the primary vertex position is necessary for the reconstruction. However, precision of about 1 mm is enough for reconstruction purposes. The real limitation comes from the physics considerations. Indeed, the detection of open charm and open beauty particles like  $D^0$  ( $c\tau \simeq 123 \mu\text{m}$ ) or B mesons ( $c\tau \sim 500 \mu\text{m}$ ) requires the primary vertex position to be reconstructed with a precision better than  $50 \mu\text{m}$  in the bending plane.

In Table 5.1 we recall the LHC machine nominal parameters at the ALICE intersection point for pp and Pb–Pb (see Chapter 2 of the ALICE PPR [3]).

For the Pb–Pb runs, beams will be well focused in the transverse plane, and the transverse position of the vertex will be known from the machine monitoring with a resolution of  $\simeq 10 \mu\text{m}$ . For the pp runs, the nominal luminosity of  $5 \times 10^{32} \text{cm}^{-2} \text{s}^{-1}$  will have to be reduced to  $< 3 \times 10^{30} \text{cm}^{-2} \text{s}^{-1}$ , in order to limit the pile-up in the TPC and in the Silicon Drift Detector (SDD). Such a reduction can be achieved in two ways: either by increasing the value of  $\beta^*$  or by displacing the two beams in the transverse plane to make a collision between the tails of the particle distributions. If the first option is chosen,  $\beta^*$  might be increased up to 100 m; this would broaden by a factor  $\sqrt{100 \text{m}/10 \text{m}} \simeq 3$  the transverse size of the interaction

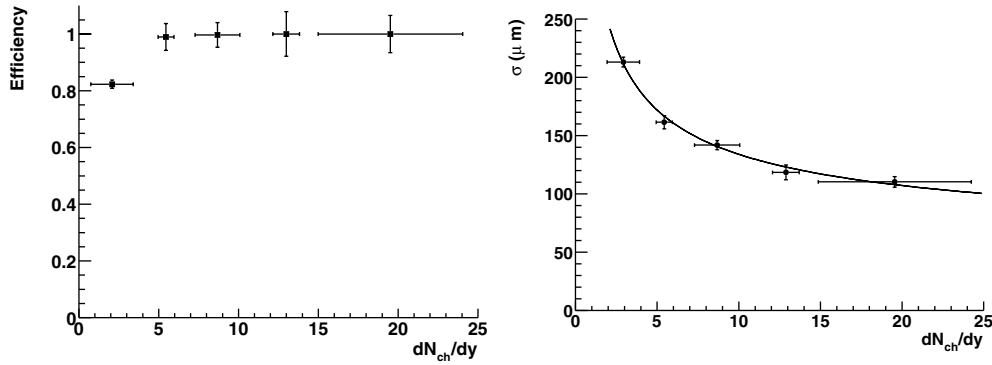


**Figure 5.6.** Resolution and efficiency of the vertex reconstruction along the beam direction using the SPD as a function of  $dN_{\text{ch}}/dy$  for the case of pp interactions. The resolution has been fitted to the expression  $A/\sqrt{dN_{\text{ch}}/dy} + B$ .

‘diamond’, up to  $\simeq 150 \mu\text{m}$ . If the second option is necessary, the beams might be displaced to a distance of  $\simeq 4-5\sigma_{x,y}^{\text{bunch}}$  and the collisions would occur in the tails at  $4-5\sigma$  from the centre of the beams: these tails will most likely be non-Gaussian and the size of the interaction ‘diamond’ may be even larger than  $150 \mu\text{m}$ .

We conclude that the position of the primary vertex has to be reconstructed in 3D, event-by-event, for pp runs.

*Reconstruction of the vertex position along the beam direction using the Silicon Pixel Detectors.* The algorithm ([4] and [5]) applied for the Pb–Pb events can be adapted also to the low-multiplicity environment of pp interactions: the position of the vertex along the beam direction ( $z$ ) is reconstructed by exploiting the correlation between the reconstructed points in the two innermost detector layers (silicon pixels) of the ITS.

All details about the optimization of the parameters and its behaviour in the case of pp events are described in Ref. [8]. Here we only present the main results (for the magnetic field 0.4 T). As one can see in Fig. 5.6, the efficiency saturates at 100% for  $dN_{\text{ch}}/dy \simeq 6$ , where the resolution is  $155 \mu\text{m}$ . As expected, the resolution decreases as the multiplicity increases. The fit to the expression  $A/\sqrt{dN_{\text{ch}}/dy} + B$  gives

$$\sigma_z(dN_{\text{ch}}/dy) = \left[ \frac{(290 \pm 16)}{\sqrt{dN_{\text{ch}}/dy}} + (42 \pm 6) \right] (\mu\text{m}). \quad (5.1)$$

When only one tracklet is found, the vertex position can still be estimated although the error cannot be given. The simulations showed that for such events the resolution is  $\sim 400 \mu\text{m}$ , which is in fair agreement with what is expected from detector geometry and spatial resolution. In cases where no tracklets pass the cuts, the primary vertex position is not reconstructed.

*3D reconstruction of the vertex position using tracks.* The precision of the primary vertex reconstruction in the bending plane required for the reconstruction of D and B mesons in pp events can be achieved only after the tracking is done. The method is discussed in Ref. [8].

Each track, reconstructed in the TPC and in the ITS, is approximated with a straight line at the position of the closest approach to the nominal primary vertex position (the nominal vertex position is supposed to be known with a precision of  $100-200 \mu\text{m}$ ). Then, all possible track pairs ( $i, j$ ) are considered and for each pair, the centre  $C(i, j) \equiv (x_{ij}, y_{ij}, z_{ij})$  of the segment

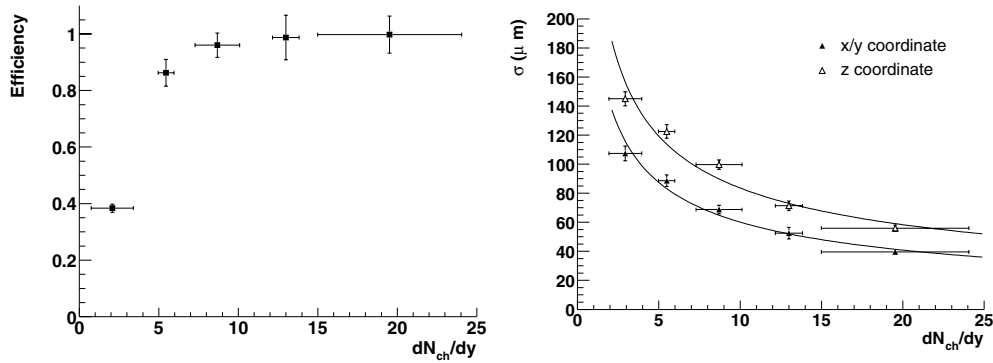


**Figure 5.7.** Efficiency and resolutions for the primary vertex reconstructed in 3D from tracks as a function of  $dN_{ch}/dy$  for the case of pp events.

of minimum approach between the two lines is found. The coordinates of the primary vertex are determined as

$$x_v = \frac{1}{N_{\text{pairs}}} \sum_{i,j} x_{ij}, \quad y_v = \frac{1}{N_{\text{pairs}}} \sum_{i,j} y_{ij}, \quad z_v = \frac{1}{N_{\text{pairs}}} \sum_{i,j} z_{ij},$$

where  $N_{\text{pairs}}$  is the number of track pairs. This gives an improved estimate of the vertex position.

Finally, the position  $\mathbf{r}_v = (x_v, y_v, z_v)$  of the vertex is reconstructed minimizing the  $\chi^2$  function (see Ref. [9]):

$$\chi^2(\mathbf{r}_v) = \sum_i (\mathbf{r}_v - \mathbf{r}_i)^T \mathbf{V}_i^{-1} (\mathbf{r}_v - \mathbf{r}_i), \quad (5.2)$$

where  $\mathbf{r}_i$  is the global position of the track  $i$  (i.e. the position assigned at the step above) and  $\mathbf{V}_i$  is the covariance matrix of the vector  $\mathbf{r}_i$ .

In order not to spoil the vertex resolution by including in the fit tracks that do not originate from the primary vertex (e.g. strange particle decay tracks), the tracks giving a contribution larger than some value  $\chi_{\text{max}}^2$  to the global  $\chi^2$  are removed one-by-one from the sample, until no such tracks are left. The parameter  $\chi_{\text{max}}^2$  was tuned, as a function of the event multiplicity, so as to obtain the best vertex resolution.

As for the reconstruction of the vertex  $z$  position with the SPD, the performance of the algorithm was evaluated as a function of  $dN_{ch}/dy$  (Fig. 5.7).

The efficiency of the vertex reconstruction shows trend similar to that observed for the SPD, namely, the vertex is always reconstructed in events with  $dN_{ch}/dy > 10$ . The resolutions in all three directions as a function of  $dN_{ch}/dy$  can be fitted to the expression

$$\sigma(dN_{ch}/d\eta) = \frac{A}{\sqrt{dN_{ch}/dy}} + B. \quad (5.3)$$

The results of the fit are reported in Table 5.2.

As discussed later in Section 5.1.6.3, the uncertainties of the primary vertex position reconstructed with this method do not dramatically deteriorate the resolution on the track impact parameters, thus allowing a good performance for the identification of charm and beauty (see Section 6.6).

**Table 5.2.** Parameter values obtained by fitting to the formula the  $A/\sqrt{dN_{\text{ch}}/dy} + B$  dependence of the primary vertex position reconstructed using tracks.

Parameter ( $\mu\text{m}$ )	$x/y$	$z$
$A$	$208 \pm 13$	$272 \pm 13$
$B$	$-6 \pm 4$	$-3 \pm 4$

*5.1.2. Track-finding strategy.* Depending on the way the information is used, the tracking methods can be divided into two large groups: global methods and local methods. Each group has advantages and disadvantages.

With the global methods, all the track measurements are treated simultaneously and the decision to include or exclude a measurement is taken when all the information about the track is known. Typical algorithms belonging to this class are combinatorial methods, Hough transform, templates, conformal mappings. The advantages are the stability with respect to noise and mismeasurements and the possibility to operate directly on the raw data. On the other hand, these methods require a precise global track model. Such a track model can sometimes be unknown or does not even exist because of stochastic processes (energy losses, multiple scattering), non-uniformity of the magnetic field etc. In ALICE, global tracking methods are being extensively used in the High-Level Trigger (HLT) software (see Section 5.3). There, we are mostly interested in the reconstruction of the high-momentum tracks only, the required precision is not crucial, but the speed of the calculations is of great importance.

Local methods do not need the knowledge of the global track model. The track parameters are always estimated ‘locally’ at a given point in space. The decision to accept or to reject a measurement is made using either the local information or the information coming from the previous ‘history’ of this track. With these methods, all the local track peculiarities (stochastic physics processes, magnetic fields, detector geometry) can be naturally accounted for. Unfortunately, the local methods rely on sophisticated space point reconstruction algorithms (including unfolding of overlapped clusters). They are sensitive to noise, wrong or displaced measurements and the precision of space point error parametrization. The most advanced kind of local track-finding methods is Kalman filtering which was introduced by P. Billoir in 1983 [10].

Kalman filtering is quite a general and powerful method for statistical estimations and predictions. The conditions for its applicability are the following. A certain ‘system’ is determined at any moment in time  $t_k$  by a state vector  $x_k$ . The state vector varies with time according to an evolution equation

$$x_k = f_k(x_{k-1}) + \varepsilon_k.$$

It is supposed that  $f_k$  is a known deterministic function and  $\varepsilon_k$  is a random vector of intrinsic ‘process noise’ which has a zero mean value ( $\langle \varepsilon_k \rangle = 0$ ) and a known covariance matrix ( $\text{cov}(\varepsilon_k) = Q_k$ ). Generally, only some function  $h_k$  of the state vector can be observed, and the result of the observation  $m_k$  is corrupted by a ‘measurement noise’  $\delta_k$ :

$$m_k = h_k(x_k) + \delta_k.$$

The measurement noise is supposed to be unbiased ( $\langle \delta_k \rangle = 0$ ) and have a definite covariance matrix ( $\text{cov}(\delta_k) = V_k$ ). In many cases, the measurement function  $h_k$  can be represented by a certain matrix  $H_k$ :

$$m_k = H_k x_k + \delta_k.$$

If, at certain time  $t_{k-1}$ , we are given some estimates of the state vector  $\tilde{x}_{k-1}$  and of its covariance matrix  $\tilde{C}_{k-1} = \text{cov}(\tilde{x}_{k-1} - x_{k-1})$ , we can extrapolate these estimates to the next time slot  $t_k$  by means of formulas (this is called ‘prediction’):

$$\tilde{x}_k^{k-1} = f_k(\tilde{x}_{k-1}), \quad \tilde{C}_k^{k-1} = F_k \tilde{C}_{k-1} F_k^T + Q_k, \quad F_k = \frac{\partial f_k}{\partial x_{k-1}}.$$

The value of the predicted  $\chi^2$  increment can be also calculated:

$$(\chi^2)_k^{k-1} = (r_k^{k-1})^T (R_k^{k-1})^{-1} r_k^{k-1}, \quad r_k^{k-1} = m_k - H_k \tilde{x}_k^{k-1}, \quad R_k^{k-1} = V_k + H_k \tilde{C}_k^{k-1} H_k^T.$$

The number of degrees of freedom is equal to the dimension of the vector  $m_k$ .

If at the time  $t_k$ , together with the results of prediction, we also have the results of the state vector measurement, this additional information can be combined with the prediction results (this is called ‘filtering’). As a consequence, the estimation of the state vector improves:

$$\tilde{x}_k = \tilde{x}_k^{k-1} + K_k (m_k - H_k \tilde{x}_k^{k-1}), \quad \tilde{C}_k = \tilde{C}_k^{k-1} - K_k H_k \tilde{C}_k^{k-1},$$

where  $K_k$  is the Kalman gain matrix  $K_k = \tilde{C}_k^{k-1} H_k^T (V_k + H_k \tilde{C}_k^{k-1} H_k^T)^{-1}$ .

Finally, the next formula gives us the value of the filtered  $\chi^2$  increment:

$$\chi_k^2 = (r_k)^T (R_k)^{-1} r_k, \quad r_k = m_k - H_k \tilde{x}_k, \quad R_k = V_k - H_k \tilde{C}_k H_k^T.$$

It can be shown that the predicted  $\chi^2$  value is equal to the filtered one:

$$(\chi^2)_k^{k-1} = \chi_k^2. \quad (5.4)$$

The ‘prediction’ and ‘filtering’ steps are repeated as many times as we have measurements of the state vector.

When applied to the track-reconstruction problem, the Kalman-filter approach has many attractive properties:

- It is a method for simultaneous track recognition and fitting.
- There is a possibility to reject incorrect space points ‘on the fly’, during the only tracking pass (see Eq. 5.4). These incorrect points can appear as a consequence of the imperfection of the cluster finder. They may be due to noise or they may be points from other tracks accidentally captured in the list of points to be associated with the track under consideration. In the other tracking methods one usually needs an additional fitting pass to get rid of incorrectly assigned points.
- In the case of substantial multiple scattering, track measurements are correlated and therefore large matrices (of the size of the number of reconstructed points) need to be inverted during a global fit. In the Kalman-filter procedure we only have to manipulate up to  $5 \times 5$  matrices (although as many times as we have reconstructed space points), which is much faster.
- One can handle multiple scattering and energy losses in a simpler way than in the case of global methods.
- It is a natural way to find the extrapolation of a track from one detector to another (for example from the TPC to the ITS or to the TRD).

In ALICE we require a good track-finding efficiency and a reconstruction precision for tracks down to  $p_t = 100 \text{ MeV}/c$ . Some of the ALICE tracking detectors (ITS, TRD) have a significant material budget. Under such conditions one can not neglect the energy losses or the multiple scattering in the reconstruction. There are also rather big dead zones between the tracking detectors which complicates finding the continuation of the same track. For all

these reasons, it is the Kalman-filtering approach that has been our choice for the offline reconstruction since the very beginning.

The reconstruction software for the ALICE central tracking detectors (ITS, TPC and TRD) shares a common convention on the coordinate system used. All the clusters and tracks are always expressed in some local coordinate system related to a given sub-detector (TPC sector, ITS module etc). This local coordinate system is defined as the following (see also Fig. 5.9, page 1329):

- it is a right handed-Cartesian coordinate system;
- its origin and the  $z$  axis coincide with those of the global ALICE coordinate system;
- the  $x$  axis is perpendicular to the sub-detector's 'sensitive plane' (TPC pad row, ITS ladder, etc).

Such a choice reflects the symmetry of the ALICE set-up and therefore simplifies the reconstruction equations. It also enables the fastest possible transformations from a local coordinate system to the global one and back again, since these transformations become simple single rotations around the  $z$ -axis.

The reconstruction begins with cluster finding in all of the ALICE central detectors (ITS, TPC, TRD, TOF, HMPID and PHOS). Using the clusters reconstructed at the two pixel layers of the ITS, the position of the primary vertex is estimated and the track finding starts. As described later, cluster-finding as well as the track-finding procedures performed in the detectors have some different detector-specific features. Moreover, within a given detector, because of high occupancy and a big number of overlapped clusters, the cluster finding and the track finding are not completely independent: the number and positions of the clusters are finally determined only at the track-finding step.

The general tracking strategy is the following. We start from our best tracker device, i.e. the TPC, and from the outer radius where the track density is minimal. First, the track candidates ('seeds') are found. Because of the small number of clusters assigned to a seed, the precision of its parameters is not enough to safely extrapolate it outwards to the other detectors. Instead, the tracking stays within the TPC and proceeds towards the smaller TPC radii. Whenever possible, new clusters are associated with a track candidate in a 'classical' Kalman-filter way and the track parameters are more and more refined. When all of the seeds are extrapolated to the inner limit of the TPC, the tracking in the ITS takes over. The ITS tracker tries to prolong the TPC tracks as close as possible to the primary vertex. On the way to the primary vertex, the tracks are assigned additional, precisely reconstructed ITS clusters, which also improves the estimation of the track parameters.

After all the track candidates from the TPC are assigned their clusters in the ITS, a special ITS stand-alone tracking procedure is applied to the rest of the ITS clusters. This procedure tries to recover the tracks that were not found in the TPC because of the  $p_t$  cut-off, dead zones between the TPC sectors, or decays.

At this point the tracking is restarted from the vertex back to the outer layer of the ITS and then repeated towards the outer wall of the TPC. For the track that was labelled by the ITS tracker as potentially primary, several particle-mass-dependent, time-of-flight hypotheses are calculated. These hypotheses are then used for the particle identification (PID) with the TOF detector (see Section 5.4). Once the outer radius of the TPC is reached, the precision of the estimated track parameters is sufficient to extrapolate the tracks to the TRD, TOF, HMPID and PHOS detectors. Tracking in the TRD is done in a similar way to that in the TPC. Tracks are followed till the outer wall of the TRD and the assigned clusters improve the momentum resolution further. Next, the tracks are extrapolated to the TOF, HMPID and PHOS, where they acquire the PID information. Finally, all the tracks are refitted with the

Kalman filter backwards to the primary vertex (or to the innermost possible radius, in the case of the secondary tracks).

The tracks that passed the final refit are used for the secondary vertex ( $V^0$ , cascade, kink) reconstruction. There is also an option to reconstruct the secondary vertices ‘on the fly’ during the tracking itself. The potential advantage of such a possibility is that the tracks coming from a secondary vertex candidate are not extrapolated beyond the vertex, thus minimizing the risk of picking up a wrong track prolongation. This option is currently under investigation.

The reconstructed tracks (together with the PID information), kink,  $V^0$  and cascade particle decays are then stored in the Event Summary Data (ESD).

### 5.1.3. Track finding in the TPC

**5.1.3.1. Cluster finding.** Before reconstructing the tracks, two-dimensional clusters in pad row–time planes are found. The reconstructed positions of the clusters are interpreted as the crossing points of the tracks and the centres of the pad rows. We investigate the region of  $5 \times 5$  bins in  $z$  (drift) and  $y$  (pad) directions around the central bin with maximum amplitude. This is bigger than the typical size of a cluster, which is  $\sigma \sim 0.75$  bins in both directions.

*Reconstruction of the cluster positions.* The position of a cluster is reconstructed as its centre of gravity (COG). The COG of a cluster, as well as the cluster width, is affected by systematic distortions induced by the threshold effect.

To correct for this effect, the signals below threshold are replaced by a virtual charge according to some interpolation. If the virtual charge is above the threshold value, it is replaced with amplitude equal to the threshold value. This method gives results comparable to a Gaussian fit of the cluster and it is much faster. Moreover, the COG position is less sensitive to the gain fluctuations.

The cluster width obtained with this method is then used for calculation of the cluster-position errors and for tagging clusters that are potentially overlapped.

*Parametrization of the cluster-position errors.* The errors  $\sigma_{z_{\text{COG}}}^2$  and  $\sigma_{y_{\text{COG}}}^2$  of the cluster position are calculated according to the following formulas [11]:

$$\begin{aligned}\sigma_{z_{\text{COG}}}^2 &= \frac{D_L^2 L_{\text{Drift}}}{A} \cdot \frac{G_g(A)}{k_{\text{ch}}} + \frac{\tan^2 \alpha L_{\text{pad}}^2}{12A} \cdot \frac{G_{\text{Lfactor}}(A)}{k_{\text{prim}}} + \sigma_{\text{noise}}^2, \\ \sigma_{y_{\text{COG}}}^2 &= \frac{D_T^2 L_{\text{Drift}}}{A} \cdot \frac{G_g(A)}{k_{\text{ch}}} + \frac{\tan^2 \beta L_{\text{pad}}^2}{12A} \cdot \frac{G_{\text{Lfactor}}(A)}{k_{\text{prim}}} + \sigma_{\text{noise}}^2.\end{aligned}\tag{5.5}$$

The first term in these formulas describes the contribution from the diffusion, where  $D_L$  is the diffusion coefficient,  $L_{\text{Drift}}$  is the drift length,  $A$  is the charge of the cluster and  $G_g(A)$  is the gas gain fluctuation factor. The second term comes from the angular effect, where  $L_{\text{pad}}$  is the pad length,  $\alpha$  is the track inclination angle with respect to the pad plane,  $\beta$  is the angle between the tangent to the track projection to the pad plane and the pad rows, and  $G_{\text{Lfactor}}(A)$  is the secondary ionization factor. The last term in the formulas,  $\sigma_{\text{noise}}^2$ , reflects the noise of the read out electronics. The  $k_{\text{ch}}$  and  $k_{\text{prim}}$  are free parameters.

Since the track inclination angles  $\alpha$  and  $\beta$  require knowledge about the track, the calculation of the cluster-position errors is done during the track finding.

Finally, an additional correction for the cluster shape and overlap factor is applied according to the formula:

$$\sigma_{\text{COG}} \rightarrow \sigma_{\text{COG}}(A) \times \left( 1 + \text{const} \times \frac{\text{RMS}_m - \text{RMS}_e}{\text{RMS}_e} \right),\tag{5.6}$$

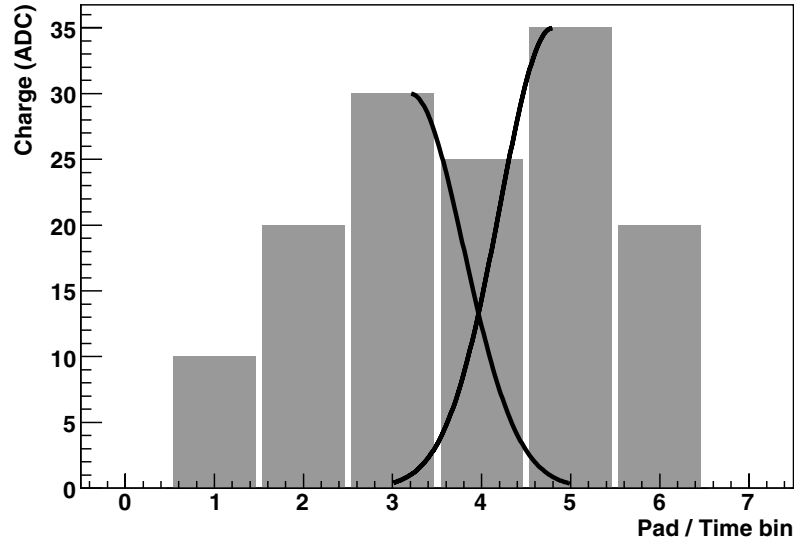


**Figure 5.8.** Unfolding of a typical cluster with two local maxima (see the explanation in the text).

where errors in  $z$  and  $y$  directions,  $\sigma_{\text{COG}}(A)$ , are calculated by means of the formulas (5.5). The  $\text{RMS}_m$  is the measured r.m.s. and the  $\text{RMS}_e$  is the expected parametrized r.m.s. of the cluster (see Ref. [11]).

In principle, the cluster positions can be also corrected for the cluster asymmetry, but the simulations showed that the resulting improvement was negligible. It is also questionable how well such a correction would work on the real data.

*Cluster unfolding.* Since the expected occupancies reach 40% in the inner sectors of the TPC and about 20% in the outer sectors, clusters from different tracks may overlap. Therefore, a certain number of clusters are lost, and the others can be significantly displaced. These displacements are rather hard to take into account. Moreover, these displacements are strongly correlated depending on the distance between two tracks.

To reduce the impact of the overlapped clusters on the track reconstruction we try to unfold the clusters having several local maxima. The fast spline method is used here. We require the charge to be conserved in this method. Overlapped clusters are supposed to have the same r.m.s., which is equivalent to the same track angles. If this assumption is not fulfilled, tracks diverge very rapidly.

The general idea of the unfolding algorithm is as follows. Let us consider a cluster made of six amplitude measurements  $C_i$  (as shown in Fig. 5.8) and having one of its local maxima (left) at position 3 and the second local maximum (right) at position 5.

First, the contribution  $A_{L4}$  from the left side to the charge measured in bin 4 is calculated using polynomial interpolation, assuming the contribution  $A_{L5}$  and from the left (and its derivative  $A'_{L5}$ ) to be 0. The amplitudes  $A_{L2}$  and  $A_{L3}$  are considered to be not affected by the overlap ( $A_{L2} = C_2$  and  $A_{L3} = C_3$ ).

Then, the contribution from the right to the charge in bin 4,  $A_{R4}$ , is calculated in a similar way.

Finally, the contributions from the left and from the right are renormalized, so that the sum of the contributions is equal to the measured charge ( $C_4 = A_{R4} + A_{L4}$ ):

$$A_{L4} \rightarrow C_4 \frac{A_{L4}}{A_{L4} + A_{R4}} \quad \text{and} \quad A_{R4} \rightarrow C_4 \frac{A_{R4}}{A_{L4} + A_{R4}}.$$

As additional criterion for unfolding one can use the cluster asymmetry. Let us denote  $\mu_i$  the  $i$ -th central momentum of the cluster, which was created by overlapping from two sub-clusters with unknown positions and deposited energy (with momenta  ${}^1\mu_i$  and  ${}^2\mu_i$ ).

Let  $r_1$  be the ratio of two cluster amplitudes:

$$r_1 = {}^1\mu_0 / ({}^1\mu_0 + {}^2\mu_0)$$

and the track distance  $d$  is equal to

$$d = {}^1\mu_1 - {}^2\mu_1.$$

Assuming that the second moments for both sub-clusters are the same ( ${}^0\mu_2 = {}^1\mu_2 = {}^2\mu_2$ ), the distance between the sub-clusters  $d$  and the ratio of their amplitudes  $r_1$  can be estimated:

$$R = \frac{(\mu_3^6)}{(\mu_2^2 - {}^0\mu_2^2)^3},$$

$$r_1 = 0.5 \pm 0.5 \times \sqrt{\frac{1}{1 - 4/R}},$$

$$d = \sqrt{(4 + R) \times (\mu_2^2 - {}^0\mu_2^2)}.$$

In order to trigger unfolding by using the shape information additional information about track and mean cluster shape over several pad rows is needed. This information is available during the track-finding procedure.

**5.1.3.2. Track finding.** The reconstructed TPC tracks and clusters are expressed in the local coordinate system of one of the TPC sectors. This coordinate system was already defined in Section 5.1.2. The  $y$  and  $z$  coordinates of the intersection point of a track and a pad row at a given  $x$  coordinate are then given by the equations:

$$y(x) = y_0 - \frac{1}{C} \sqrt{1 - (Cx - \eta)^2},$$

$$z(x) = z_0 - \frac{\tan \lambda}{C} \arcsin(Cx - \eta), \quad \eta \equiv Cx_0,$$

where  $C$  (see Fig. 5.9) is the curvature of the track projection on the pad plane,  $\lambda$  is the ‘dip’ angle between the track and the pad plane,  $(x_0, y_0)$  are the coordinates of the centre of the curvature of the track projection on the pad plane, and  $z_0 \equiv z(x_0)$ .

The track ‘state vector’  $\mathbf{x}^T$  used in the Kalman-filter calculations is then chosen as

$$\mathbf{x}^T = (y, z, C, \tan \lambda, \eta).$$

With this choice of the track parametrization, only two of the five components of the ‘state vector’ (the local track position  $y$  and  $z$ ) change as the track is propagated from one pad row to another. These calculations are done about 160 times (number of TPC pad rows) per a track. When a track is leaving one sector and is entering another, the coordinate system is rotated, then three components ( $y$ ,  $z$  and  $\eta$ ) of the ‘state vector’ have to be changed (see Fig. 5.9). However, in the worst case this happens 2–3 times per track, and the majority of the tracks, being contained entirely within the same sector, do not require this transformation at all.

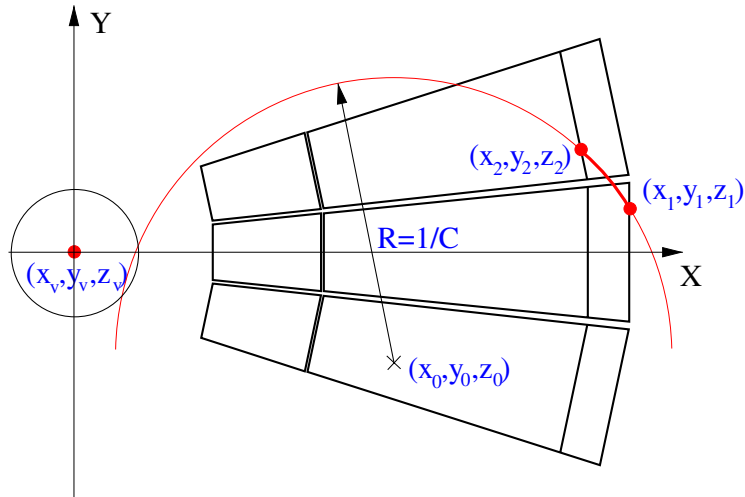


**Figure 5.9.** Track-finding coordinate system, track parameters and the schematic view of the ‘seeding’ with the vertex constraint.

*Seed finding.* The Kalman-filter track finding relies on the determination of a good initial approximation for the track parameters and their covariance matrix (so called track ‘seeds’). Since none of other detectors have so far been able to provide the seeds for the track reconstruction in the TPC, the seed finding is done using the TPC data. This very important part of the whole reconstruction chain is described in detail below.

Two different seed-finding strategies are used: seed finding with the primary vertex constraint and without any constraint.

The first seed finding is done with the vertex constraint. It begins with a search for pairs of points at a pad row  $i$  and at a pad row  $j$  closer to the interaction point ( $i - j = 20$  at present), which can project to the primary vertex. For each point at the outer pad row  $i$ , points at the inner pad row  $j$  are checked only within a given window in the  $(x, y)$  plane, defined by some  $p_t$  cut-off, and a given window in the  $z$  direction defined by the requirement of pointing to the primary vertex. This significantly reduces the number of possible combinations. The position of the primary vertex is reconstructed, with high precision, from hits in the ITS pixel layers, independently of the track determination in the TPC.

When a reasonable pair of clusters is found, parameters of a helix going through these points and the primary vertex are calculated, and an occurrence of a cluster near the crossing point of this helix and a ‘middle’ pad row  $k = j + (i - j)/2$  is checked. If such a cluster is found, the parameters of this helix are taken as an initial approximation of the parameters of the potential track. The corresponding covariance matrix is evaluated by using the point pair errors and applying some big uncertainty to the primary vertex position. This is the only place where the (moderate) vertex constraint is introduced. Later on, tracks are allowed to have any impact parameters at primary vertex in both the  $z$  direction and in the  $(x, y)$  plane.

Using the calculated helix parameters and their covariance matrix, the Kalman filter is started from the outer pad row  $i$  to the inner pad row  $j$ . If at least half of the possible points between the initial ones are successfully associated with this track candidate, it is saved as a seed, and we continue to look for another pair of initial points.

Although efficient for the primary tracks, the seed finding with the vertex constraint penalizes the secondary tracks. Therefore, two algorithms for track seeding without vertex

constraint have also been developed. With the first algorithm, for each cluster at the middle pad row  $k$ , the two nearest clusters at the pad rows  $k + 1$  and  $k - 1$  are found. These three points are fit to a straight line. This line is prolonged to the pad rows  $k + 2$  and  $k - 2$ , where again the two nearest to the line clusters are found. The linear fit is replaced by polynomial after the track candidate is assigned seven clusters. The algorithm continues until the pad rows  $i$  and  $j$  are reached. If more than half of the possible clusters are found, the track parameters and their covariance are calculated and the candidate is saved as a seed. The efficiency of this algorithm rapidly decrease for low- $p_t$  tracks because of the angular effect, which correlates the cluster-position distortions between neighbouring pad rows.

To increase seed-finding efficiency and seed quality, a second algorithm, using non-correlated clusters, was implemented. For each pair of clusters selected at the pad row  $i$  and within some window at the pad row  $j$  ( $i - j = 7$  in this case) the algorithm tries to find a third cluster at the ‘middle’ pad row  $k = j + (i - j)/2$  near the crossing between the pad row  $k$  and the straight line connecting the two clusters selected at the pad rows  $i$  and  $j$ . If such a cluster is found, the cluster triplet is fit to a helix. Using the calculated helix parameters and their covariance matrix, the Kalman filter starts from the outer pad row  $i$  to the inner pad row  $j$ . If at least half of the possible clusters are successfully associated with the track candidate, it is saved as a seed.

The sizes of the ‘windows’ for all the seed-finding approaches are fixed with a compromise between the efficiency,  $p_t$  cut-off, and the required CPU time.

The efficiency of the seed finding can be increased by repeating the procedure at different pad rows (changing the pad row  $i$ ). Unfortunately, some of the tracks are very close each to other on a long path. The seed finding at different pad rows cannot in this case be considered as independent. The efficiency quickly saturates at some value. Another problem with repetitive seed finding is that occupancy increases towards the lower pad row radius and thus the efficiency of a single seed finding is a decreasing function of the pad row radius.

To maximize the track finding-efficiency for secondary tracks, especially for the kinks, it is necessary to perform almost ‘continuous seed finding’ inside sensitive volume of the TPC. This, of course, requires additional computing resources (memory size and the CPU power). The compromise between efficiency and resource consumption can be achieved using the following strategy:

- Reconstruction of the tracks seeded with the vertex constraint (the CPU time is minimal and about 90% of the primary tracks are reconstructed):
  - Three seedings with the constraint in the outermost pad rows in steps of six pad rows and the cut on the curvature corresponding to  $p_t > 200 \text{ MeV}/c$ .
  - Nine seedings with the constraint in the outermost pad rows in steps of two pad rows for  $p_t > 500 \text{ MeV}/c$ .
  - Ten seedings with the constraint scanning the full TPC in steps of 10 pad rows towards to innermost pad row and decreasing the  $p_t$  cut.
- Reconstruction of the tracks seeded without the vertex constraint:
  - Three seedings starting at three outermost pad rows (to maximize the kink finder efficiency).
  - Six seedings in steps of five pad rows.
  - Five seedings scanning the outer sectors in steps of 10 pad rows towards the innermost pad row and decreasing the  $p_t$  cut.

The reconstructed tracks are classified according to their quality. The quality parameter is defined by the normalized  $\chi^2$  and the ratio of the number of found clusters to the number of

possible clusters (the number of possible clusters is considered to be equal to the number of track crossings with the pad rows when the track is not in a dead zone). The mean value and the sigma of the distribution of the quality parameter is then calculated. If the quality parameter of a given track falls within the  $3\sigma$  range from the mean value, the assigned clusters are marked as ‘used’. Such clusters are not used in the subsequent seedings, but they can still be assigned to other tracks during the track following.

*Track following.* Each of the seeded tracks is followed down to the innermost TPC pad row or until it is lost. The prolongation to the next pad row is calculated according to the current estimation of the track parameters. During this step we take into account multiple scattering (by adding the corresponding matrix to the track covariance matrix) and mean energy loss (by means of the Bethe–Bloch formula) assuming that the actual particle is a pion. Then on this pad row we define a ‘window’ along the pad direction inside which we look for a cluster to be associated with the track. The width of the window is set to  $\pm 4\sigma$  where  $\sigma$  is calculated taking into account the track position errors (given by the track parameter covariance matrix) and expected cluster-position errors (given by formulas (5.5) and (5.6) and some additional ‘safety factor’ to account for possible cluster overlapping).

Each cluster is ordered according to its  $y$  coordinate, and the clusters within the window are quickly selected using the binomial search. The cluster nearest to the track is then taken as the most probable one belonging to the track. The errors of the estimation of the nearest cluster position are calculated using the formulas (5.5) and (5.6). The cluster is finally accepted if the residuals in both direction are smaller than the estimated  $3\sigma$ , and the track parameters and their covariance matrix are updated.

It can happen that a track leaves one TPC sector to enter another. In such a case the track parameters and the covariance matrix are recalculated (rotated) so that they are always expressed in the local coordinate system of the sector containing the track.

A special value, the local cluster density, is defined as a ratio of the accepted clusters to all the potential ones in a region of several pad rows. Tracks with low local cluster density are not completely removed (since secondary tracks may have low cluster density), they are marked and left for the subsequent passes.

Since the same track can potentially be seeded many times, an additional value, the ‘track overlap factor’, is defined as the ratio of the clusters shared between two track candidates and the number of all clusters. If for two track candidates the overlap factor is bigger than some value (currently 0.6), the track candidate with higher  $\chi^2$  or lower number of assigned cluster is removed. This is the compromise between the maximal track finding efficiency and the minimal number of multiple found tracks.

### 5.1.3.3. Performance of the TPC track finding

*Track-finding quality.* The quality of the track-finding procedure can be characterized by many different parameters.

The ratio of the number of clusters associated with a track to the number of pad rows crossed by this track is shown in Fig. 5.10. For the case of pp collisions this distribution is sharply peaked at 100%. For high-track-multiplicity events (central Pb–Pb collisions), tracks start losing clusters, however, the percentage of associated clusters is still rather high (about 90%).

Track-finding quality can also be characterized by the pulls. The pull of a track parameter is defined as the difference between the reconstructed and generated value of the parameter divided by the estimation of the corresponding error. Under ideal conditions the pulls are distributed normally (i.e. with zero mean value and sigma equal to 1). Figure 5.11 shows

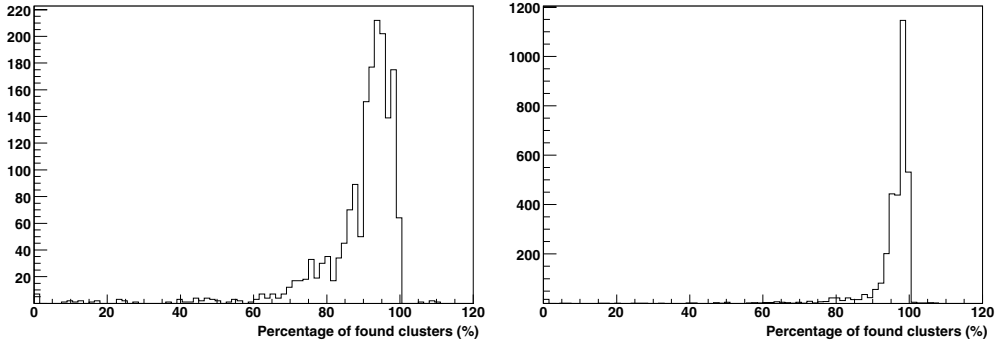


**Figure 5.10.** Ratio of the number of clusters associated with a track to the number of pad rows crossed by this track. Left: central Pb-Pb collisions ( $dN_{ch}/d\eta = 6000$ ). Right: pp collisions.

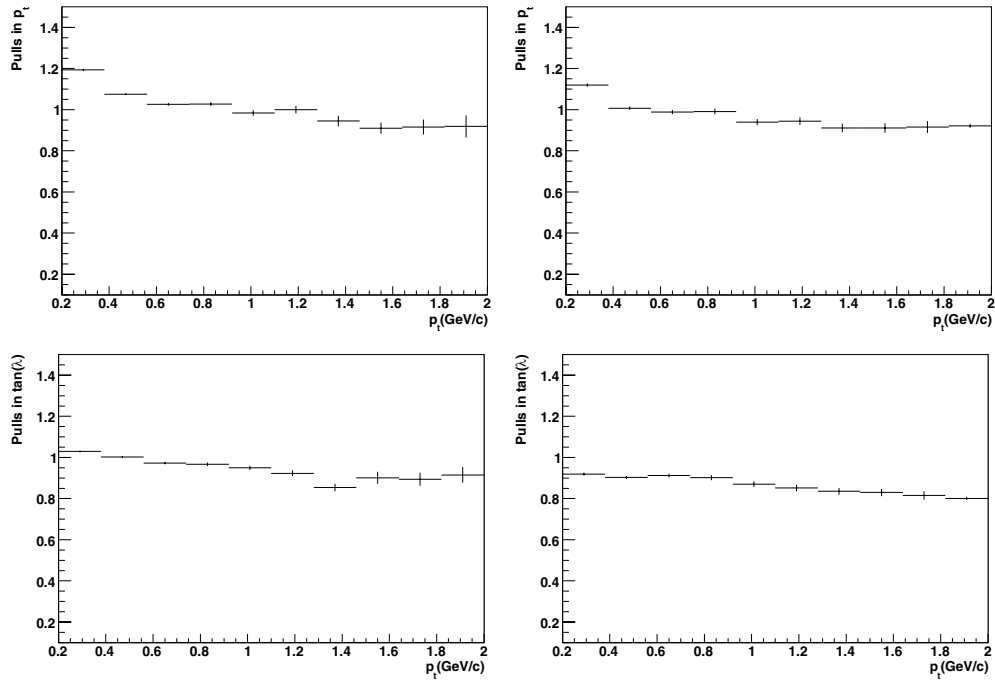


**Figure 5.11.** Pulls in track momentum and dip angle as a function of particle transverse momentum. Left: central Pb-Pb collisions ( $dN_{ch}/d\eta = 6000$ ). Right: pp collisions.

the sigmas of the pulls in the transverse momentum and the track dip angle as a function of particle transverse momentum.

*Track finding efficiency.* In the following we distinguish two kinds of track-finding efficiency: The efficiency of track-finding software and the ‘physical’ efficiency that includes also all other factors such as dead zones in the detectors, inefficiency of the electronics, decays, etc.

The software track-finding efficiency is defined as the ratio of the number of ‘good found’ tracks to the number of ‘good generated’ tracks, while the probability to produce a fake track is expressed by the number of ‘fake found’ tracks normalized in the same way. We use here

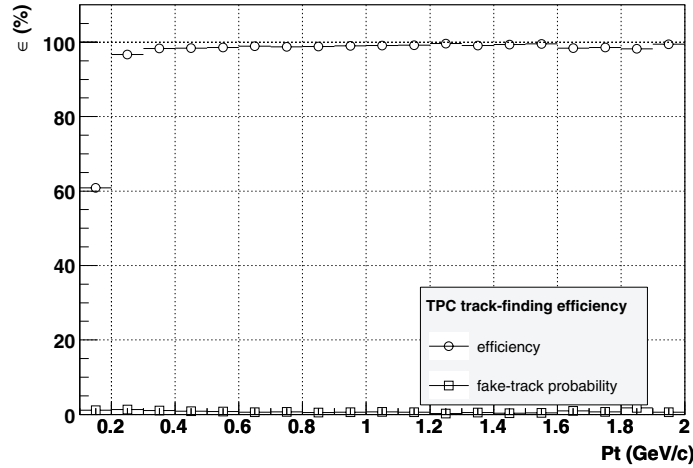


**Figure 5.12.** Efficiency of the TPC track-finding software as a function of particle transverse momentum for central Pb–Pb collisions ( $dN_{\text{ch}}/d\eta = 6000$ ).

the following definitions:

1. ‘Good generated’ track is a track which crosses at least 50% of all pad rows.
2. ‘Good found’ track is a track with the number of assigned clusters larger than 50% of the number of crossed pad rows. In addition, we require that more than 90% of assigned clusters belong to this track, and that at least half of the innermost 10% of clusters are assigned correctly.
3. If the requirement on the number of assigned clusters is satisfied, but the requirements on the number of correctly assigned clusters are not satisfied, such a track is considered as ‘fake found’.

As shown in Fig. 5.12, no significant dependence of the software track-finding efficiency on particle transverse momentum has been found. Even in the case of central Pb–Pb collisions ( $dN_{\text{ch}}/d\eta = 6000$ ), it is about 100% practically everywhere and goes down only in the low-momentum region  $p_t < 0.2 \text{ GeV}/c$ .

The physical track finding efficiency is defined as ratio of the number of tracks reconstructed with the pulls in momentum and the two emission angles less than 4 to the number of tracks that were generated within the beam pipe and emitted within the TPC acceptance. This efficiency is shown in Fig. 5.13 (left). The decrease at low momenta is due to the energy loss, interactions with the material, and particle decays.

The presence of the dead zones between the TPC sectors leads to losses of the physical efficiency too. The dependence of the physical track-finding efficiency on the azimuthal angle  $\varphi$  within a TPC sector is shown in Fig. 5.13 (right). When a high-momentum track goes near the edge of a sector ( $\varphi \sim 0^\circ$  or  $\varphi \sim 20^\circ$ ) a large part of the track is lost in a dead zone. Thus, the probability of missing such a track is high. The low-momentum tracks are less affected by the dead zones because in this case only a small part of a track is lost in a dead zone.

The physical track-finding efficiency is different for different particle species (see Fig. 5.14). For the case of secondary particles, it is also a function of the radial position of the point where the secondary particle is generated (see Fig. 5.15).

*Track-finding resolutions.* The transverse-momentum and dip-angle resolutions for the case of central Pb–Pb collisions and pp collisions are shown in Fig. 5.16. The obtained resolutions

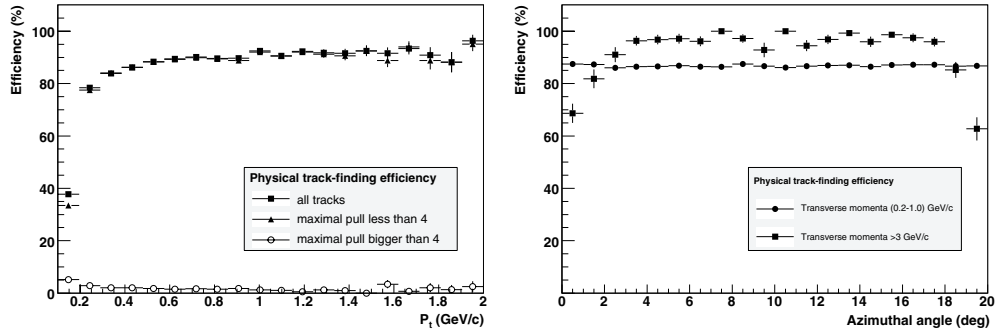


**Figure 5.13.** Physical TPC track-finding efficiency as a function of particle transverse momentum (left) and as a function of the track azimuthal angle within a TPC sector (right) for central Pb–Pb collisions ( $dN_{\text{ch}}/d\eta = 6000$ ).

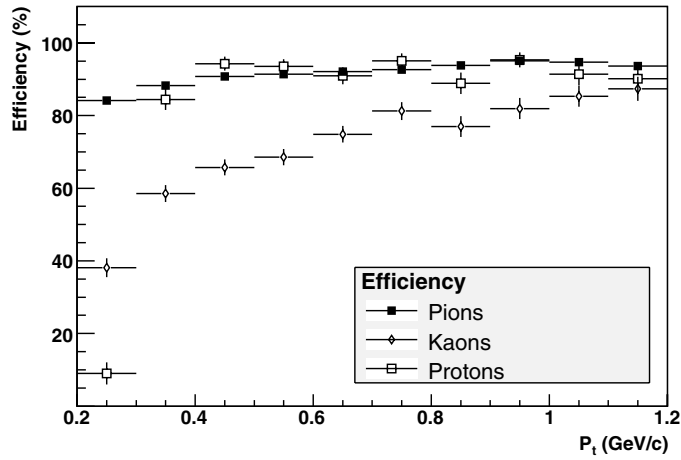


**Figure 5.14.** Physical TPC track-finding efficiency for different particle species as a function of particle transverse momentum for central Pb–Pb collisions ( $dN_{\text{ch}}/d\eta = 6000$ ).

are well within the theoretical expectations and the difference in resolutions for the two limiting cases of proton-proton and Pb–Pb collisions is negligible.

*dE/dx measurement.* The most natural way to perform the  $dE/dx$  analysis would be to use the total charge deposited in the clusters. However, it has also been found that for the tracks which are within the TPC acceptance, one can successfully use the amplitudes at the local maxima of the clusters. This method is less sensitive to the overlapped clusters. For each cluster associated to a track, the amplitude at the local maximum is divided by the length of the corresponding track segment, and then the overall  $dE/dx$  value is estimated using the truncated mean method. Under our conditions, the best resolution is achieved if we discard 2% of the smallest signals and 40% of the largest ones. Clusters which are shared between tracks are not used for  $dE/dx$  calculation.

For the case of pp events, when the tracks are well separated and almost all of possible clusters are assigned to tracks, the achieved  $dE/dx$  resolution is 5.4%, which is in good agreement with theoretical expectations. Under high-track-multiplicity conditions, the  $dE/dx$  resolution becomes about 6.8% (see Fig. 5.17).

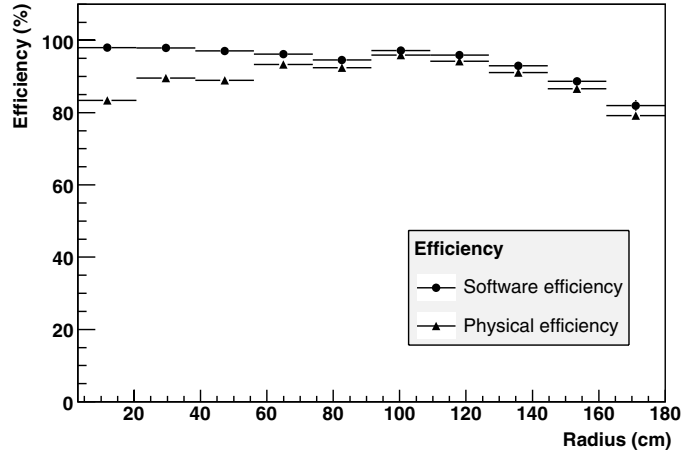


**Figure 5.15.** Physical and software track-finding efficiency of the TPC as a function of particle vertex position for central Pb–Pb collisions ( $dN_{\text{ch}}/d\eta = 6000$ ).

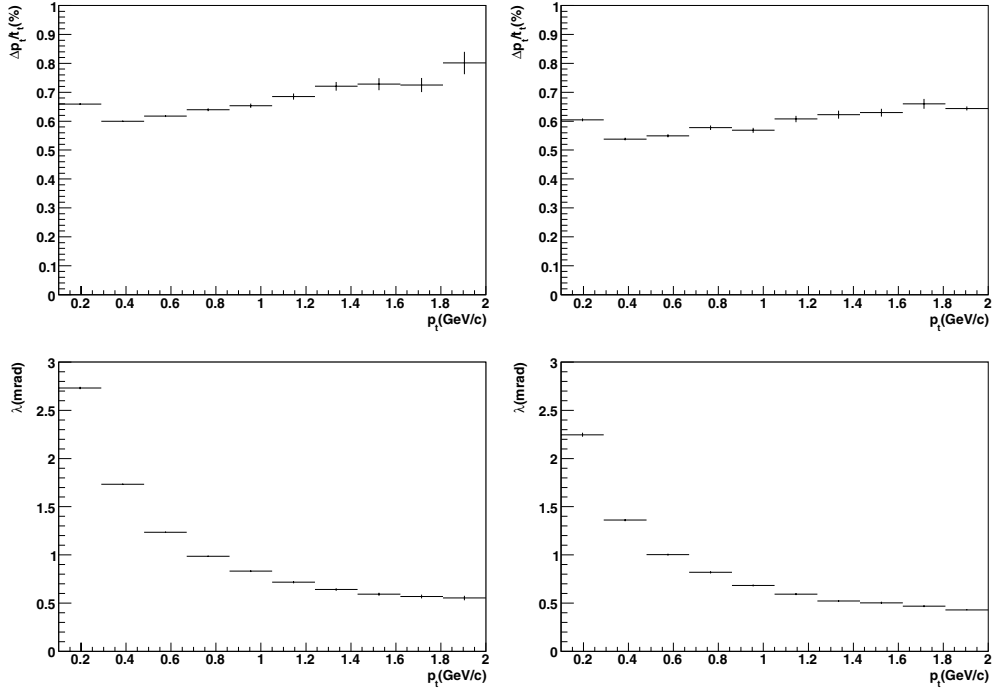


**Figure 5.16.** Momentum and dip-angle resolutions as a function of particle transverse momentum. Left: central Pb–Pb collisions ( $dN_{\text{ch}}/d\eta = 6000$ ). Right: pp collisions.

The dependence of the  $dE/dx$  resolution on the track dip angle for the tracks within the TPC acceptance ( $-1 < \tan\lambda < 1$ ) is weak. The resolution deteriorates for the larger dip angles, because the tracks start leaving the TPC via the end-caps and thus they cross fewer pad rows (see Fig. 5.18).

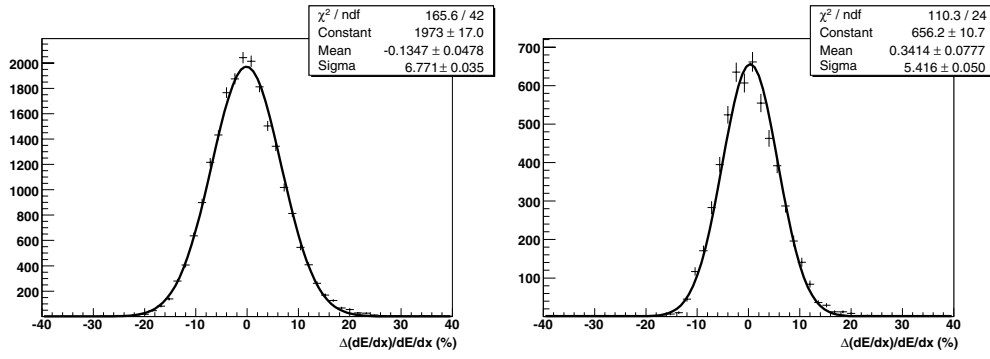


**Figure 5.17.**  $dE/dx$  resolution. Left: central Pb–Pb collisions ( $dN_{ch}/d\eta = 6000$ ). Right: pp collisions.

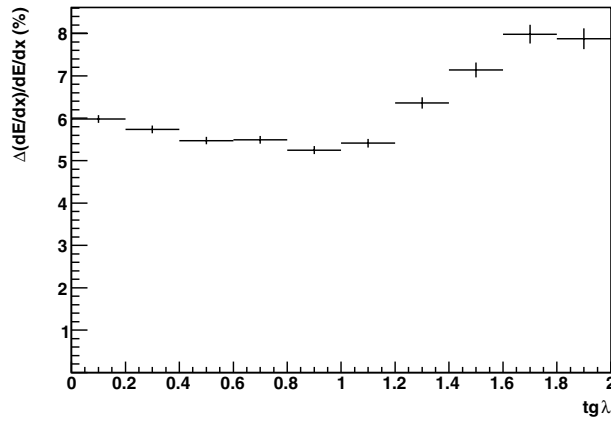


**Figure 5.18.**  $dE/dx$  resolution as a function of dip angle (pp collisions).

No significant dependence of the  $dE/dx$  resolution on the transverse momentum of the particles was observed, whereas the resolution certainly improves with an increase of the number of assigned clusters (see Fig. 5.19).

*Two-track efficiency.* If the distance between two tracks becomes small, the clusters are no longer resolved. With the approach described above, one of two track candidates sharing a big number of common clusters is removed. This leads to a decrease of the number of reconstructed tracks with close parameters. On the other hand, some of the tracks may change their direction (due to multiple scattering), can be lost by the track following and reconstructed again as a separate track from another seed, which increases the number of (wrongly) reconstructed tracks with close parameters. Thus, the two-track efficiency, being of a great importance for some kinds of physics analysis (like HBT), is not a function of the single track-finding efficiency, and so it must be investigated separately. A careful consideration of the shape of clusters can potentially improve the two-track efficiency. The possibility to use this information is currently under study. However, one can expect here a big increase of the computational time with only a modest improvement of the two-track efficiency.

The two-track efficiency of the TPC track finding will be discussed in detail in Section 6.3.5 of this Physics Performance Report.

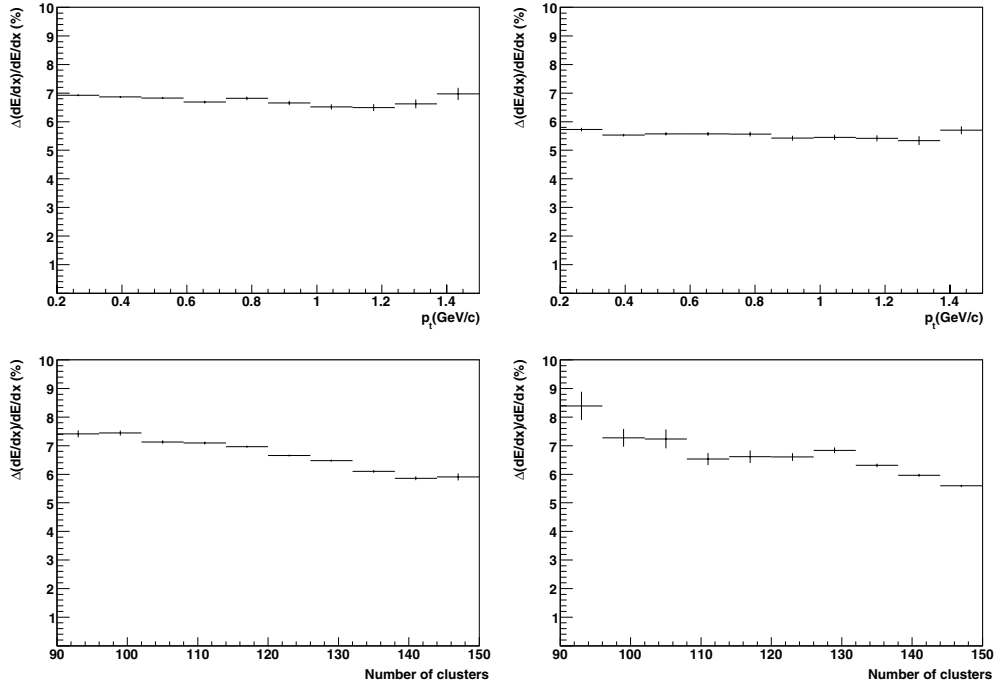


**Figure 5.19.**  $dE/dx$  resolution as a function of particle transverse momentum and number of clusters used. Left: central Pb–Pb collisions ( $dN_{ch}/d\eta = 6000$ ). Right: pp collisions.

**5.1.4. Track finding in the ITS.** The ALICE Inner Tracking System (ITS) is designed to reconstruct the primary vertex (with a precision better than  $100 \mu\text{m}$ ), the secondary vertices from  $V^0$  and cascade hyperon decays as well as D and B meson decays. In addition, it improves the momentum and angular resolution for the tracks that are also reconstructed in the TPC and contributes to the particle identification by  $dE/dx$  measurements with the two strip and two drift-detector layers.

As already outlined in Section 5.1.2, the ITS reconstruction software tries to find a prolongation for all the tracks found by the TPC. The algorithm of this prolongation is based on the Kalman filter approach with a few (but very important) modifications described below.

About 10% of the total number of reconstructed tracks are missed in the TPC due to the dead zones between the TPC sectors, decays, and the  $p_t$  cut-off. Such tracks are reconstructed by the stand-alone ITS track-finding software as discussed in this section.

**5.1.4.1. Cluster finding.** Before the track finding starts, two-dimensional clusters in ITS layers are found. Then the positions of the corresponding space points are reconstructed and are interpreted as the crossing points of tracks and middle planes of the subdetectors. The errors of the estimations of space-point positions are supposed to be proportional to the cluster width.

In the Silicon Strip Detectors (SSDs), one-dimensional clusters on the P and N sides of the detector are, first, localized. The clusters having an extended shape (more than four strips) are split into two clusters. Next, the one-dimensional clusters from the sides of the detector are combined together, creating two-dimensional space points. To minimize the number of ghost clusters, the correlation between the charges collected in one-dimensional P- and N-side clusters is taken into account. In the simplest case, when the difference between the charges

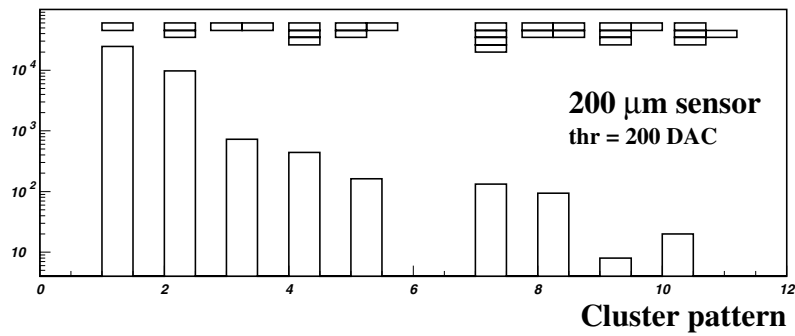


**Figure 5.20.** Frequency of different cluster patterns on the test plane for threshold setting of 200 DAC units.

of a given one-dimensional cluster and another cluster on the opposite side is less than  $3\sigma$ , and there is no other matching candidate with the charge difference less than  $6\sigma$ , only one two-dimensional space point is created. Otherwise, the space points made of all possible pairs of one-dimensional clusters are kept.

In the case of the central Pb–Pb collisions, the occupancy at the Silicon Drift Detector (SDD) layers is not negligible. Thus, the unfolding of the overlapped clusters is important. The method of cluster unfolding in SDD was inspired by the TPC cluster finding. First, for each group of neighbouring digits with signals above the zero-suppression level, the positions of the local maxima are found. Then, for each of the local maxima, a space point is reconstructed as a centre of gravity of all the digits around the maximum that have signals higher than the signal at the saddle point between this maximum and the nearest one.

For the Silicon Pixel Detectors (SPDs), a cluster is a group of neighbouring activated pixels. The position of the space point is calculated as its centre of gravity. When tracks happen to cross the SPD closely, the corresponding clusters can overlap. Therefore, the clusters with unusually big numbers of activated pixels are unfolded. For each such cluster, the number of activated pixels is calculated. The rectangle, defined by the number of activated pixels in both directions, is divided into subrectangles defined by the cluster size for an isolated track. For each of the subrectangles, a space point is created.

The performance of the SPD was studied in detail in dedicated beam tests. The results of these studies are presented below.

*Beam-test performance of the SPD.* The prototype assemblies for the ITS SPD were tested at the SPS beams in 2002 and 2003 [12, 13]. The beam-test geometry, together with a detailed cluster analysis of the hits, allowed a study of the intrinsic spatial precision of the planes under test and their detection efficiency [14, 15]. Since the SPD ladders are currently under production with  $200\ \mu\text{m}$  thick sensors, we briefly discuss the 2002 beam-test results that were obtained with this sensor thickness.

The space point precision (the difference between the reconstructed and measured track position) was found to be a function of the cluster pattern, electronic threshold, and the track incidence angle. The frequency of different cluster patterns on the test plane, at 200 DAC units threshold (corresponding to about 3000 electrons [16]) and for normal incidence tracks, is shown in Fig. 5.20.

To disentangle the intrinsic spatial precision of the detector from the width of the measured residual distribution, we took into account the track reconstruction precision. As

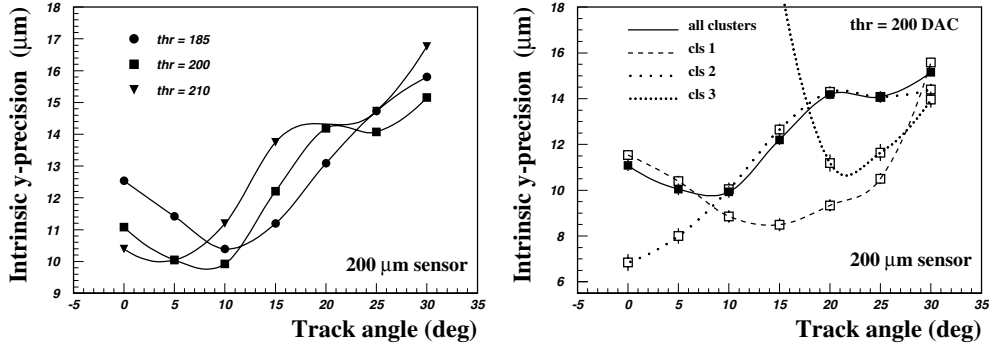


**Figure 5.21.** Intrinsic precision in the  $y$  coordinate as a function of the track incidence angle on the detector: at different threshold settings (left) and at 200 DAC units threshold for the main cluster patterns separately (right).

an approximation (see also Ref. [17]) we assumed the following expression:

$$\sigma_{\text{pixel}}^2(y) = \sigma_{\text{resid}}^2(y) - \sigma_{\text{track}}^2(y),$$

where  $\sigma_{\text{resid}}(y)$  is the sigma of the Gaussian fit to the measured  $y$ -residual distribution (along the  $50 \mu\text{m}$  pixel side), while  $\sigma_{\text{track}}(y)$  is estimated to be about  $6 \mu\text{m}$  for the 2002 beam test set-up [15]. A similar expression was used also for the  $x$  coordinate (along the  $425 \mu\text{m}$  pixel side) in the analysis of the 2003 test data for the thicker sensor detector, where a good tracking precision was available in both  $x$  and  $y$  coordinates [14].

After subtracting the uncertainty on the track position prediction, the global detector precision (averaged over all the cluster patterns) is found to be  $\sigma_{\text{pixel}}(y) = (11.1 \pm 0.2) \mu\text{m}$ , while the corresponding values for the two main cluster patterns (see Fig. 5.20) separately are found to be

$$\sigma_{\text{pixel}}^{\text{cls1}}(y) = (11.5 \pm 0.2) \mu\text{m} \quad \text{and} \quad \sigma_{\text{pixel}}^{\text{cls2}}(y) = (6.8 \pm 0.3) \mu\text{m}.$$

In a wide plateau around the mentioned threshold setting the detector efficiency was found to be above 99%.

Results of the study on the spatial precision as a function of the track incidence angles are shown in Fig. 5.21. In the left-hand panel, we see that the precision curves reach the minimum around  $5\text{--}10^\circ$  of incidence angle: for each threshold that minimum occurs at the angle for which the fractions of single and double- $y$  pixel clusters are roughly equal [15].

The precision also degrades for all the threshold settings with the increasing track angle, as expected when higher cluster topologies are involved. On the right-hand panel of Fig. 5.21, the intrinsic precision is shown together with the contributions due to the main pixel cluster patterns separately, for the case of 200 DAC threshold setting. These results can be particularly useful in the tuning of the tracking errors to be associated to the SPD clusters, both in the simulation and in the real data analysis.

The beam-test results discussed here were also used to validate the Monte Carlo simulations of the SPD. Two SPD models were tested against the data: the geometrical model and the diffusion model. In the geometrical model the deposited charge is divided among the pixels proportionally to the linear path length in each of the pixels. In the diffusion model the charge is shared simulating the diffusion of the electron-hole cloud. The models are described in detail in Refs. [18–23].

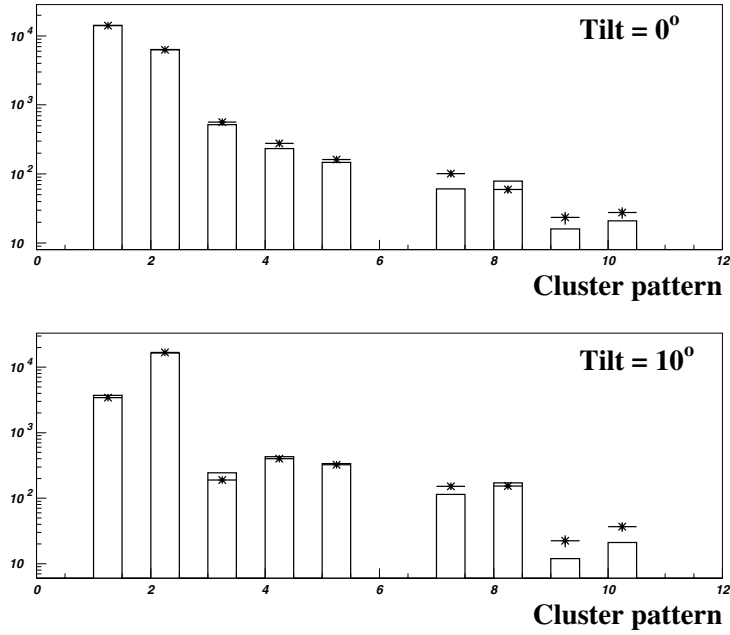


**Figure 5.22.** Comparison of cluster pattern distributions between real data (marker points) and the Monte Carlo diffusion model (full histogram), for tracks at normal incidence (top) and for tracks with a tilt angle of 10 degrees with respect to the normal (bottom). The threshold settings correspond to 190 DAC units and 3220  $e^-$  for the real data and the Monte Carlo calculations, respectively.

A detailed comparison of the SPD performance in beam tests with the results obtained with the two simulation models can be found in Ref. [24]. The geometrical model reasonably reproduces the behaviour of an ideal digital detector with a response independent of the particle impact coordinates on each sensor cell yielding the intrinsic spatial precisions given by  $\sigma_{r\varphi} = L_{r\varphi}/\sqrt{12} \approx 14 \mu\text{m}$  ( $y$  coordinate in the beam test) and  $\sigma_z = L_z/\sqrt{12} \approx 123 \mu\text{m}$  ( $x$  coordinate in the beam test). It is also significantly (15 times) faster than the diffusion model. This model has been used for the SPD simulations for this Physics Performance Report.

On the other hand, the diffusion model gives a fairly good description of the real detector response. In particular, it can reproduce the main features of the spatial precisions (with a quite good qualitative agreement), the efficiency and the distribution of cluster type as a function of either the threshold or the bias voltage or the track incidence angle [24]. As an example, in Fig. 5.22 we show a comparison of the cluster pattern distributions between the diffusion model and the real data, for tracks at normal incidence (top) and for tracks with a tilt angle of 10 degrees with respect to the normal (bottom). A fairly good agreement is observed also for larger tilt angles.

After some additional tuning of the parameters, the diffusion model can be used to compute the corrections in the physics analysis of real data.

**5.1.4.2. Track finding.** The track finding in the ITS starts with the TPC–ITS matching. This is difficult, because the distance between the inner wall of the TPC and the outer layer of the ITS is rather large and the track density inside the ITS is so high that the naive continuation of the track-finding procedure used for the TPC would be ineffective. In this case there is a

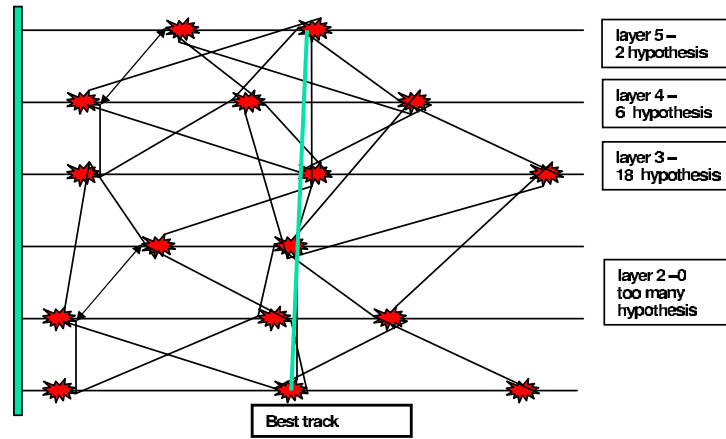


Figure 5.23. Building of the track hypothesis tree.

high probability of assigning a wrong hit to the track if we use just the criterion of minimal  $\chi^2$  in a given ITS layer. Therefore we have implemented a few modifications of the Kalman filter procedure.

First, we try to assign to the track, one by one, all the hits within the predicted window having a  $\chi^2$  below a given limit, and not only the one with minimal  $\chi^2$ . This way we are building from each TPC track a candidate tree through all the ITS layers. To speed up the building of the track hypothesis tree, the branches are sorted after each layer according to  $\chi^2$  and only a restricted amount of the best branches are propagated further down (see Fig. 5.23). Finally, we choose the most probable track candidate (i.e. the path along the tree) taking into account the following information:

- sum of the  $\chi^2$ s;
- probability that a track is in a dead zone;
- dead channels of the readout electronics;
- probability to have a cluster with a charge below the threshold;
- for the secondary tracks, the probability of missing some of the layers (as a function of the longitudinal and transverse impact parameters);
- the clusters that are potentially shared (as a function of the cluster shape).

The clusters assigned to the best track hypothesis are marked as belonging to that track. Each cluster can be marked by several track candidates. The clusters marked by more than one track candidate are treated by a special ‘symmetric’ cluster assigning procedure (see below).

A certain amount of the best short track candidates are also kept as potentially coming from  $V^0$  decays.

Another improvement is that we use the primary vertex constraint [1]. If the best constrained track hypothesis gives the  $\chi^2$  bigger than some critical value, the procedure is repeated without vertex constraint.

When propagating from one ITS layer to another, the track parameters and their covariance matrix are corrected for the mean energy loss and the multiple scattering. The most probable mass hypothesis provided by the  $dE/dx$  measurements in the TPC is used for these calculations.

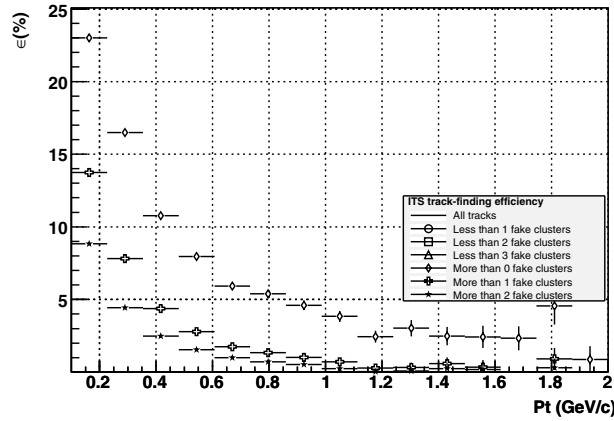


**Figure 5.24.** The fake-track probability (see the text) as a function of particle momentum ( $dN_{ch}/d\eta = 6000$ ).

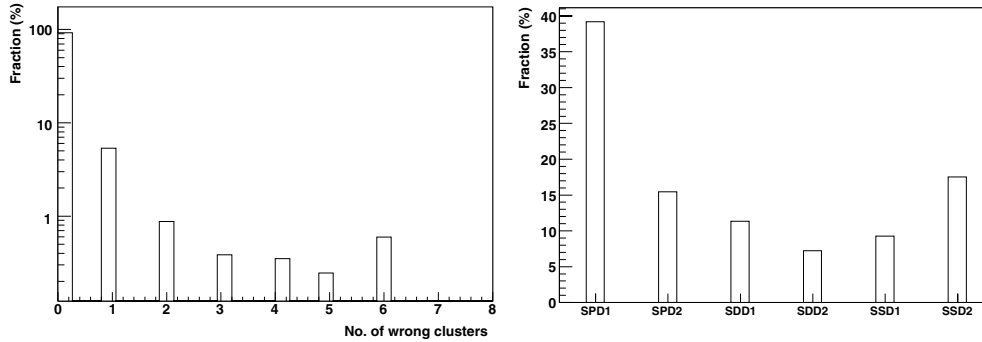


**Figure 5.25.** Distribution of the number of wrong clusters per track (left), and per layer (right).

*Asymmetric and symmetric algorithms of assigning clusters to the tracks.* In the high track multiplicity environment there is always a high probability of assigning a wrong hit to a track. The probability of assigning the wrong hit is proportional to the space density of these hits and to the track position uncertainty. In the following, we call a track a ‘fake’, if at least one of the assigned clusters does not in fact belong to this track.

The probability of obtaining such fake tracks as a function of particle momentum is shown in Fig. 5.24. This probability decreases rapidly with the particle momentum, since the contribution of the multiple scattering to the track position uncertainty becomes smaller. Above  $\sim 1\text{GeV}/c$ , where the track position uncertainty is dominated by the extrapolation errors, the fake track probability saturates.

Most of the reconstructed tracks do not have any wrongly assigned clusters, and the biggest part of the fake tracks has only one such cluster (see Fig. 5.25, left). The probability of assigning a wrong cluster is maximal at the innermost layer (SPD1), where the cluster density is the highest. This probability is also rather big at the outermost layer (SSD2), because, after the extrapolation through the dead zone between the TPC and the ITS, the track position is not precisely defined (see Fig. 5.25, right).

To minimize the probability of assigning a wrong hit to a track, two algorithms were implemented: the ‘asymmetric’ algorithm and the ‘symmetric’ algorithm.

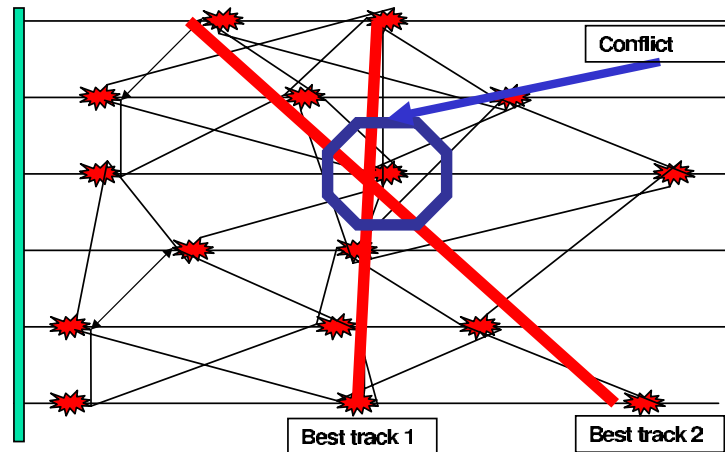


Figure 5.26. Symmetric algorithm of cluster assigning.

The following assumptions were used in the asymmetric algorithm:

- The reconstructed hits can not be shared between different tracks.
- When a hit can potentially belong to several tracks, it is assigned to the track with the smallest track position uncertainty.

This approach gives worse results than the symmetric algorithm. However, it is faster. Therefore, this approach can be applied for the High Level Trigger reconstruction (see Section 5.1.3).

The assumptions used in the symmetric algorithm are the following:

- The reconstructed space points can be shared between two tracks. The probability that a space point was created by two different tracks is a function of the deviation of the cluster shape from the expected shape.
- When a hit can potentially belong to several tracks, the track with the smallest track position uncertainty has the biggest probability to be associated with this hit. However, for other tracks, this probability is also not zero.
- The minimization of combined  $\chi^2$  of pairs of tracks is sufficient, because most of the fake tracks have only one wrongly assigned cluster.

If for two best track-prolongation hypotheses, originating from two different tracks reconstructed in the TPC, the number of common clusters is bigger than a certain value (see Fig. 5.26), the corresponding two trees of possible track prolongations are investigated once more. During this investigation, all the possible pairs of branches (one branch from one of the trees, another branch from another tree) are checked again trying to find the pair giving the minimum 'combined  $\chi^2$ '. Such a pair of branches is registered as a final pair of reconstructed tracks.

In the case of primary track candidates, this combined  $\chi^2$  of two tracks is the weighted sum of the following parameters: the space  $\chi^2$  of the two tracks, the number of skipped clusters, and the number of shared points. For the secondary track candidates (those having big impact parameters), the penalty term for the skipped clusters is reduced by a special factor that parametrizes the probability to decay at this radius as a function of the track impact parameters.

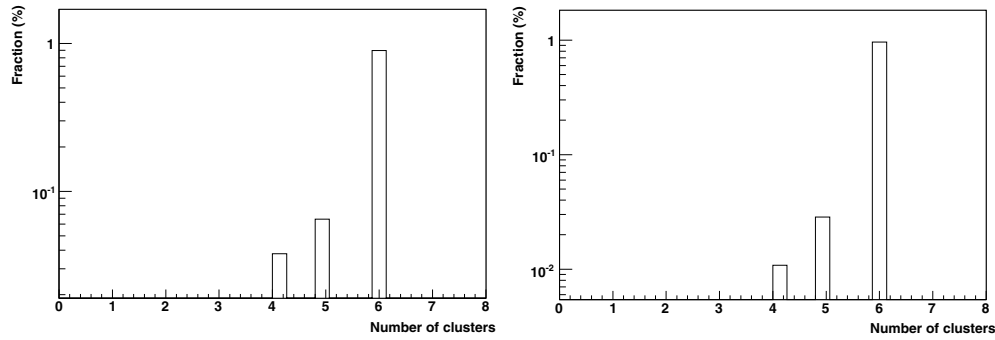


**Figure 5.27.** Distribution of the number of assigned clusters per an ITS tracks. Left: Central Pb-Pb collisions ( $dN_{\text{ch}}/d\eta = 6000$ ). Right: pp collisions.

All the weights in the combined  $\chi^2$  formula are tuned to minimize the probability of a wrong cluster assignment and to maximize the track finding efficiency.

With the symmetric algorithm the fake track probability is reduced by a factor of about 0.6 for the case of the primary tracks. The improvement factor for the secondary tracks is more than 2.

The remaining part of the fake tracks is still quite significant. The main part of these tracks (more than 50%) is due the hits that do not belong to any of the tracks reconstructed in the TPC. Such hits can not be treated correctly by any of the two described cluster assigning mechanisms.

*Performance of the ITS track finding.* The majority of the tracks prolonged in the ITS have clusters assigned at all the six layers (see Fig. 5.27). However, this does not mean that the ITS track-finding efficiency is as high as in the TPC, because some of the assigned clusters do not in fact belong to those tracks. The tracks having more than one wrongly assigned ITS cluster (or more than 10% of wrongly assigned TPC clusters) are not counted as properly reconstructed. Such tracks are considered as ‘fake’.

The combined TPC+ITS track-finding efficiency as a function of momentum is shown in Fig. 5.28. The efficiency is normalized to the number of so-called findable tracks. The definition of a findable track is as follows:

- more than 60% of pad rows crossed in the TPC;
- all six layers crossed in the ITS.

For low-track-multiplicity events the efficiency does not depend strongly on the particle momentum and is about 100%. In the high-multiplicity environment the efficiency is lower. It decreases with decrease of the momentum. This decrease is mainly due to a higher probability of the wrong cluster assignment. This probability is about 10% at 0.2 GeV/c.

The efficiency and fake track probability for different definitions of fake tracks (different number of wrong clusters before the track is considered as ‘fake’) is shown in the Fig. 5.29. Different track parameters are differently affected by the presence of the wrongly associated clusters (see Fig. 5.30). Thus, the  $p_t$  resolution is affected only marginally. As for the transverse impact parameter, almost 98% of the tracks with zero wrongly assigned clusters point to the vertex within 3 sigmas. For the tracks with one wrong cluster, it is about 85%. For the case of tracks with two wrong clusters it is about 65%.

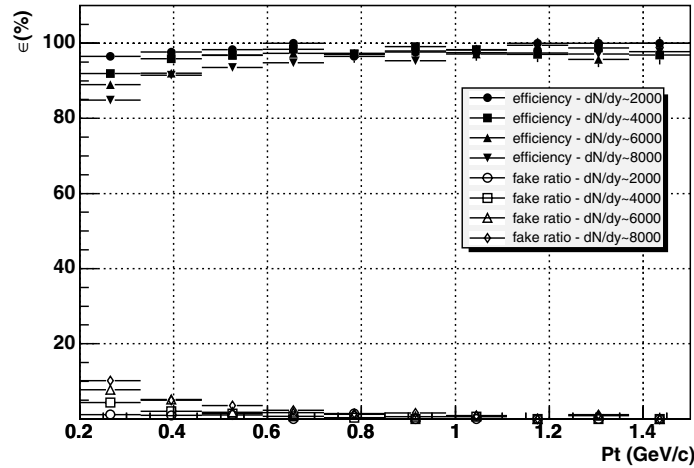


Figure 5.28. TPC+ITS track-finding efficiency and fake-track probability as the function of transverse momentum for different track multiplicities.

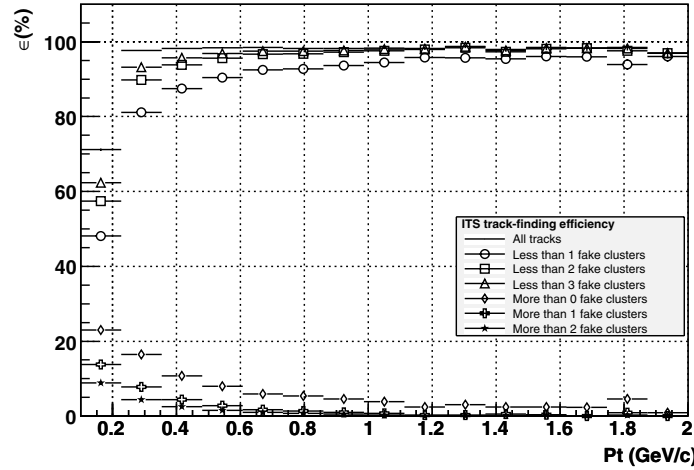
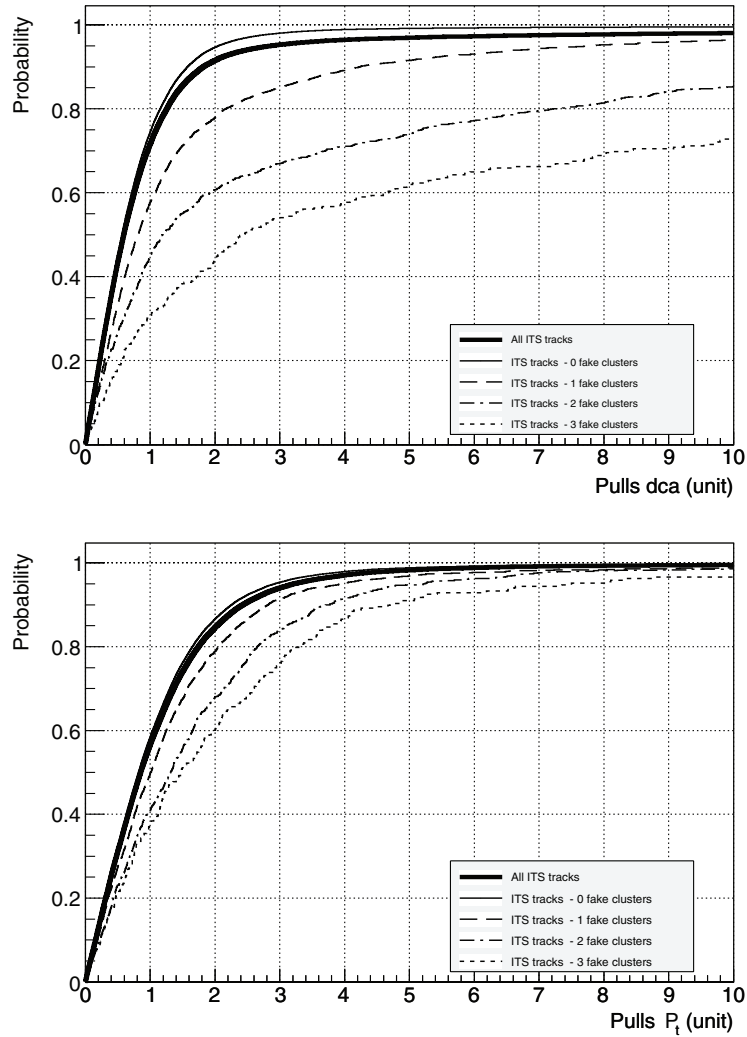


Figure 5.29. ITS+TPC track-finding efficiency and fake-track probability for different numbers of wrongly associated ITS clusters ( $dN_{ch}/d\eta = 6000$ ).

**5.1.4.3. Stand-alone ITS track finding.** The ITS stand-alone track finding software is aimed at reconstructing the high-momentum tracks going entirely inside the dead zones between the TPC sectors, decaying between the ITS and the TPC and, if possible, the low-momentum tracks (below 100 MeV/c). Such tracks can not be found in the TPC and thus they are not reconstructed by the ITS track finding described above.

ITS stand-alone track finding is a complicated task. The tracks are represented by a small number of points (at most six points) available for the reconstruction, the points are seriously displaced by the multiple scattering and the space density of these points is high. Therefore, the strategy is as follows. First, we run the standard TPC+ITS track reconstruction and remove from the event all the ITS points that are associated with the reconstructed tracks. The number of the remaining ITS points (those that can not be associated with any of the tracks found in the TPC) becomes 3–4 times lower as compared with the initial number of points. The



**Figure 5.30.** The cumulative function of the pull in the transverse impact parameter and of the pull in  $p_t$ , for different number of wrongly assigned clusters.

stand-alone track finding is performed on this set of the remaining points. We briefly outline two possible implementations of the ITS stand-alone trackers that have been developed so far.

*Neural network stand-alone track finder.* This approach, fully described in Ref. [25], is based on the Denby–Peterson method for pattern recognition [26]. The algorithm simulates the behaviour of a Hopfield neural network (NN) [27] with the improvement of the Mean Field Theory (MFT) [28].

The mapping of the track finding into this scheme consists in associating a neuron  $N_{ij}$  to an oriented segment between two space points  $i$  and  $j$  lying in two consecutive ITS layers. The synaptic weight  $W_{ijkl}$  between neurons  $N_{ij}$  and  $N_{kl}$  is defined according to geometrical correlations based on the physical shape of the tracks to be recognized. In this kind of NN, correlations between neurons are expressed by positive weights, and competitions by negative ones. Here a correlation is present when two neurons form a ‘chain’, as in Fig. 5.31(a): this

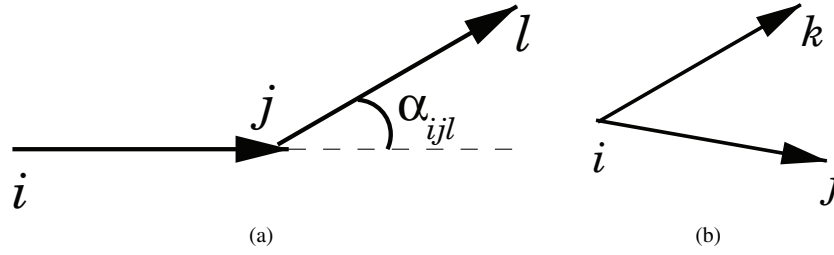


**Figure 5.31.** The typical configurations which can appear in the neural network track-finding scheme described in the text. Figure (a) represents a correlation, because the segments are chained together, while figure (b) represents a competition, because two segments start from the same point.

represents a possible guess for a track element. When two neurons form a bifurcation, as in Fig. 5.31(b), this is a competition. If two neurons are completely separated, a zero weight is set. Then, the weight is defined as

$$W_{ijkl} = A(1 - \sin \alpha_{ijl})^n \delta_{jk} - B(\delta_{ik} + \delta_{jl}),$$

where Kronecker symbols are set to zero if neither  $j = k$  nor  $i = k$  nor  $j = l$ . Parameters  $A$  and  $B$  are free parameters whose optimal values have been adjusted in order to get the best performance. The angle  $\alpha_{ijl}$  is the one formed by the oriented segments  $i \rightarrow j$  and  $j \rightarrow l$ . With this expression, a strong contribution comes only when the two ‘chained’ segments are well aligned. The exponent  $n$  has the purpose of modifying the strength of the alignment requirement for the two neurons. The larger the exponent, the faster the weight will fall to zero when  $\alpha_{ijl}$  increases.

In order to minimize the ‘confusion’ that can arise from creating too many neurons starting from a cluster and ending in it, and in order to optimize also the execution time, some cuts have been introduced. To improve the track-finding efficiency, a recursive algorithm has been implemented where a set of curvature cuts is defined and the NN operates on the same ensemble of space points in many steps. At the end of each step, all ‘used’ points are saved and removed and the curvature cut is enlarged. Another improvement, which turns out to be useful in decreasing the computing time, is an azimuthal sectioning of the whole ITS barrel. The choice of 20 sectors has been found to be a good compromise between CPU time and efficiency. With this choice, the track-finding procedure takes at maximum roughly 1–2 minutes of CPU time with a 1 GHz Pentium III processor.

The final answer of the NN consists in a binary map where all neurons are turned ‘on’ or ‘off’. Track candidates are extracted as polygonal lines composed of chains of neurons turned ‘on’. These candidate tracks are then fitted by means of a Kalman-filter procedure, to obtain the track physical parameters, which are essentially the components of the impact parameter and momentum vector. The obtained resolution for the transverse momentum is 7.4%, and the resolution for the dip angle and azimuthal angle of the momentum vector is smaller than 2 mrad. The resolution for the impact parameter is  $\sim 70 \mu\text{m}$  in the transverse direction and  $\sim 160 \mu\text{m}$  in the longitudinal direction.

The algorithm has been tested with different samples of Pb–Pb events generated with a parametrized HIJING generator [29] at different multiplicities ( $dN_{\text{ch}}/d\eta = 4000$  and 8000) and different magnetic fields (0.2 T and 0.4 T). First, the standard Kalman-filter TPC+ITS

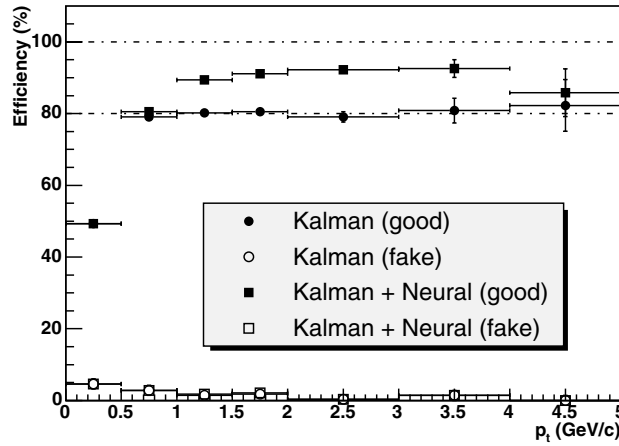


**Figure 5.32.** Track-finding efficiency and fake track probability for the standard TPC+ITS (Kalman) track finding and for the combination of the standard and the stand-alone (neural) track finding, as a function of the transverse momentum.

**Table 5.3.** Averaged track-finding efficiency and fake probability for all charged particles having  $p_t > 1$  GeV/c. The second column reports the values related to the standard TPC+ITS (Kalman) track finding and the third column reports the values related to the combined standard TPC+ITS and neural track finding. Increase of the efficiency is shown in the last column.

	Kalman (%)	Combined (%)	Increase (%)
Efficiency	$80.0 \pm 0.3$	$90.0 \pm 0.5$	$10.0 \pm 0.6$
Fake track probability	$1.7 \pm 0.1$	$2.1 \pm 0.1$	$0.4 \pm 0.1$

track finding is run. Then, all the ITS clusters which have been assigned to tracks are removed from the initial set. Finally, the neural track finding is performed on the remaining space points.

As an example, Fig. 5.32 shows the track-finding efficiency and the fake track probability, as a function of the transverse momentum, for the standard TPC+ITS track finding (Kalman filter) and for the combined track finding for events with the particle multiplicity  $dN_{ch}/d\eta = 4000$  and the magnetic field 0.4 T. The circles in this figure refer to the efficiency of the standard TPC+ITS track finding only, while the squares refer to the efficiency obtained summing up the tracks coming from TPC+ITS track finding and neural track finding on the remaining clusters. Averaged values of track-finding efficiency for  $p_t > 1$  GeV/c and of fake track probability are also summarized in Table 5.3.

The track-finding efficiency is defined here as the ratio of number of ‘good’ and ‘findable’ tracks. A track is considered ‘findable’ if it has at least five reconstructed space points in the ITS. A found track is called ‘good’ if at least five of its points are related to the same particle, otherwise it is considered as ‘fake’. The fake track probability is then defined as the ratio of number of ‘fake’ tracks to the number of ‘findable’ tracks.

One can observe that the described procedure increases the efficiency by 10%, while the fake track probability augments by a negligible amount.

*Cluster grouping stand-alone track finder.* This approach was inspired by the method described in Ref. [30], where it is referred to as ‘grouping algorithm’. The general idea is as follows. Since the high- $p_t$  tracks are only slightly bent by the magnetic field, the  $(\theta, \varphi)$

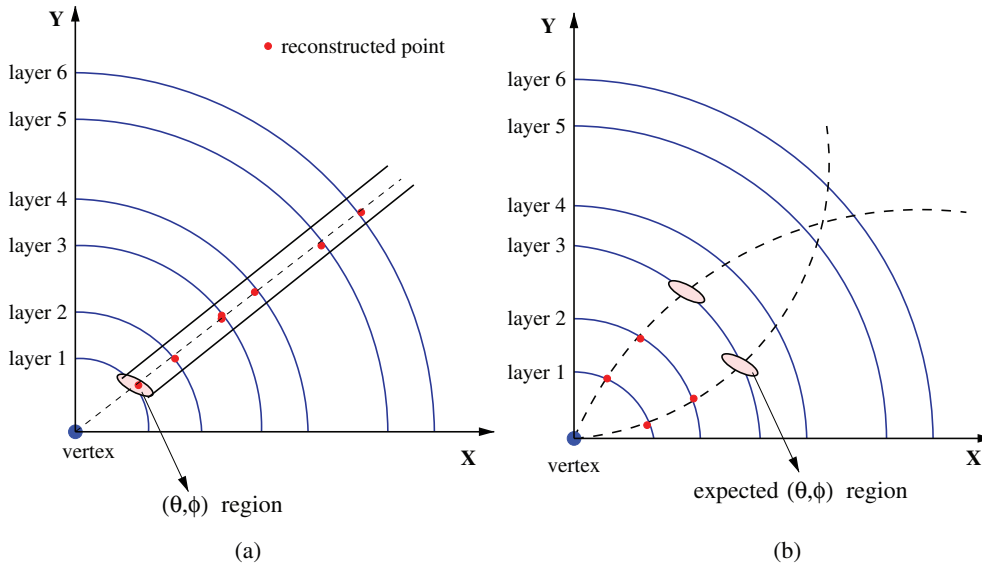


**Figure 5.33.** Schematic of the track-finding procedure, for high- $p_t$  tracks (a) and the optimized procedure for low- $p_t$  tracks (b).

coordinates of the clusters belonging to the same track do not change from layer to layer. The angles  $(\theta, \varphi)$  are defined as

$$\theta = \arctan \frac{z}{\sqrt{x^2 + y^2}},$$

$$\varphi = \arctan \frac{y}{x},$$

where  $(x, y, z)$  are the coordinates of a cluster in the global coordinate system. A schematic view of this track-finding procedure for high- $p_t$  tracks is shown in Fig. 5.33(a). A group of reconstructed points found on all the layers within the same  $(\theta, \varphi)$  window is considered as a track candidate.

The algorithm described here is similar, but it is optimized for lower- $p_t$  tracks. In this case, the  $\varphi$  window is not the same for all the layers (see Fig. 5.33(b)). For each couple of points belonging to the two innermost layers in the same  $(\theta, \varphi)$  window the curvature of the track is estimated using also the position of the primary vertex. The expected value of  $\varphi$  on layer 3 ( $\varphi_3$ ) is calculated, and the next point is searched in the  $(\theta, \varphi_3)$  window. The same procedure is performed for all the layers, using the last three found points for estimating the track curvature. The track candidate is considered as ‘good’ if it has one reconstructed point for each of the layers. In a less restrictive approach, a track candidate is allowed to miss a cluster at one of the layers.

The algorithm starts with finding the high- $p_t$  tracks. Then, tracks with decreasing  $p_t$  are successively found. The procedure is repeated increasing the size of the  $(\theta, \varphi)$  window. A track candidate may have more than six associated clusters, since more than one reconstructed point may enter the  $(\theta, \varphi)$  window on the same layer. This redundancy is eliminated by the fitting procedure described below. The clusters successfully fitted to a track candidate are removed from the initial set.

The track candidates are fitted by the same Kalman-filter method as for the main TPC+ITS reconstruction. The initial values of the track parameters and their covariance matrix

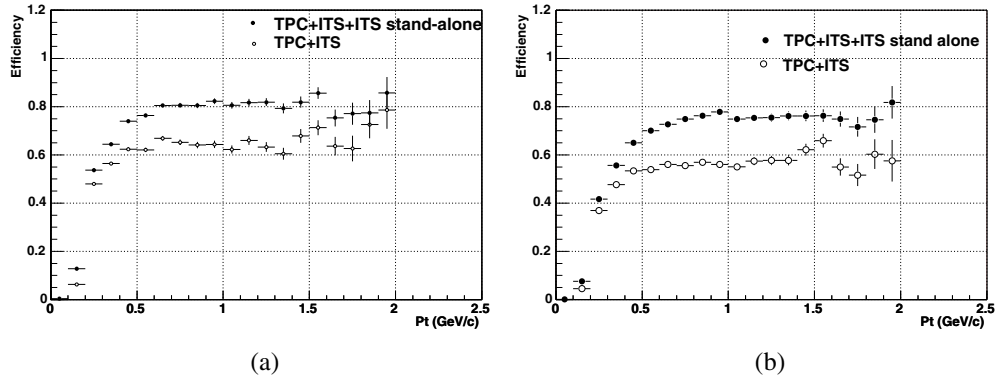


**Figure 5.34.** Comparison between the efficiency obtained with and without the ITS stand-alone procedure, in the case of four HIJING events at  $dN_{\text{ch}}/d\eta = 4000$  (a) and  $dN_{\text{ch}}/d\eta = 6000$  (b).

are calculated using the positions of the two clusters at layers 1 and 2 and the primary vertex. Since a track candidate may have more than six associated points, the fit is performed on all the possible combinations of points and the combination giving the lowest  $\chi^2$  is stored as the final result.

The efficiency was evaluated combining the stand-alone algorithm with the main TPC+ITS track finding. The stand-alone procedure was performed after the TPC+ITS track finding, to recover the tracks which could not be prolonged from the TPC. The track-finding efficiency is defined as the ratio between the number of found ‘good’ tracks and the number of ‘trackable’ tracks. A ‘trackable’ track is defined as a track having all six points (one for each layer of the ITS). A reconstructed ‘fake’ track is therefore defined as a track with one, or more, points that do not belong to this track.

The algorithm was tested using parametrized HIJING events with different multiplicities in the pseudo-rapidity region  $-8 \leq \eta \leq 8$  and the magnetic field of 0.4 T.

The track-finding efficiencies obtained for the combined track finding are shown in Fig. 5.34(a) and (b) for the particle multiplicities  $dN_{\text{ch}}/d\eta = 4000$  and  $dN_{\text{ch}}/d\eta = 6000$ , respectively. They are compared with the efficiencies obtained with the main TPC+ITS track finding. In this case the ‘good’ tracks are defined requiring six points out of six in the ITS. The ‘trackable’ tracks must have six clusters in the ITS with no special requirement in the TPC.

One can see that the stand-alone track finding reconstructs about 10% of tracks in addition to the tracks found by the main TPC+ITS track-finding procedure.

### 5.1.5. Track finding in the TRD

#### 5.1.5.1. Cluster finding

*Cluster position reconstruction.* The ionization electrons in the TRD chambers drift radially, and the clusterization is done in the (pad, pad row) planes. For each time bin the radial ( $x$ ) position of a cluster is defined by the centre of this time bin. Because of the big pad size in the  $z$  (pad row) direction (about 9 cm), the charge sharing between the adjacent pad rows is not essential, and thus no clustering is performed in that direction. Therefore, like for the  $x$  direction, the  $z$  position of a cluster is given by the centre of the corresponding pad row.

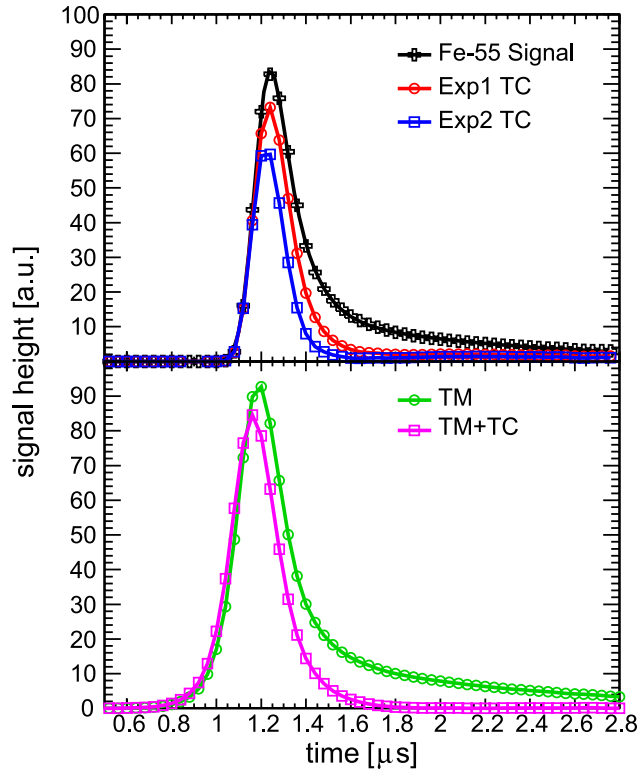


**Figure 5.35.** Time dependence of the average pulse height for  $^{55}\text{Fe}$  X-rays. Because of the point-like charge deposit of the X-rays, this signal is almost identical to the time response function. The upper panel shows the original signal and the signal after applying a tail cancellation with one and two exponential functions. The lower panel shows the effect of adding the short tail component to the left (tail making), and of subsequent tail cancellation (long component).

The TRD cluster-finding algorithm searches for adjacent pads with a signal above threshold only in the  $y$  (pad) direction. A typical cluster consists of signals from two or three pads. A good precision of the cluster position reconstruction is mandatory for the momentum measurement. This can be done either by calculating the centre of gravity of the charge distribution inside a cluster or by using a pre-built look-up table. Such a table contains the deviations of the cluster position from a pad centre as a function of signals on the three adjacent pads. This method generally provides a better resolution.

The reconstructed cluster positions are affected by several kinds of distortions [31]. Slowly moving positive ions produced in electron avalanches near the anode wires induce long-tail signals on the pads of the TRD chambers. These tails change the charge values measured in subsequent time bins and lead to strong correlations between those measurements. This effect can be partially corrected by applying (before the cluster finding) a special deconvolution procedure, ‘tail cancellation’ (see Fig. 5.35).

The drift length to the nearest anode wire is different for electrons produced at different  $z$  positions (see Fig. 5.36, left). Also the strength of the electric field (and so the drift velocity) inside the amplification region of the chamber is a strong function of the  $z$  coordinate. Thus, the reconstructed  $x$  position of the clusters becomes the function not only of the time bin (and the nominal drift velocity) but also of the  $z$  coordinate.

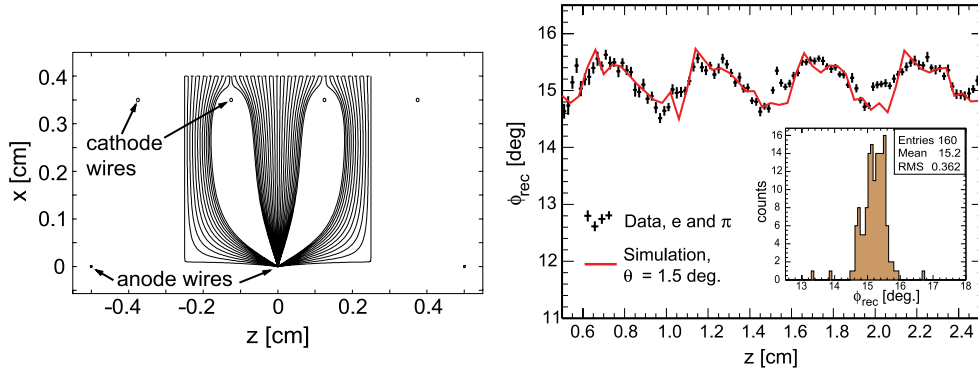


**Figure 5.36.** Left: Ideal drift lines for electrons coming from the drift region (from the top) at different  $z$  positions. Right: Systematic variation of the reconstructed angle  $\phi_{\text{rec}}$  with the  $z$  coordinate (across the wires). We show measured (crosses) and simulated results (solid line). The insert shows a projection of the measured data on the  $\phi_{\text{rec}}$  axis.

The same effects are responsible for the systematical errors in the reconstructed  $y$  position (or the azimuthal  $\varphi$  coordinate) of the clusters (see Fig. 5.36, right).

The reconstructed clusters are corrected for these distortions. However, because of the big pad size in the  $z$  direction (about 9 cm), such corrections are possible only in average.

*Cluster unfolding.* In the high multiplicity environment of the ALICE experiment, the occupancy in the TRD chambers, defined as the percentage of detector ‘pixels’ (pad  $\times$  time bin) above the 2 ADC count threshold, becomes non-negligible (about 40% for events with the multiplicity  $dN_{\text{ch}}/d\eta = 8000$ ). Thus we have to implement some cluster unfolding procedure. Currently, only clusters containing signals from five pads are unfolded in a way similar to that used for the TPC (see Section 5.1.3), using the pad response function as an estimator for the cluster shape. The cluster shape depends on the track parameters. The response function and diffusion contributions to the cluster r.m.s. are known during clustering. This is not true for an angular contribution to the cluster width. The cluster finder should be optimized for high-momentum particles coming from the primary vertex.

An additional improvement of the cluster unfolding can be achieved at the track reconstruction step, when the contributions to the cluster shape can be estimated better.

The ‘quality’ of the unfolded clusters is usually not good enough, and the chances of biasing the estimation of the track momentum are high. That is why, from the point of view of obtaining the best possible momentum resolution, it is often preferable not to include some of the unfolded clusters in the fit.

*5.1.5.2. Track reconstruction.* Offline track finding in the TRD is based on the Kalman filtering approach, which we have chosen because of its successful implementation for track finding in the TPC and ITS and the similarities of the track finding environment in the ALICE TPC and in the TRD. As mentioned in Section 5.1.2, one of the advantages of the Kalman filter concept is that it provides a straightforward way to propagate track segments between sub-detectors, in our case between the adjacent TRD layers as well as between the TRD and the TPC.

The implementation of the TRD track finding shares many features developed for the ALICE TPC track finding described in detail in Section 5.1.3 of this report. The track candidate from the TPC is followed inside the drift volume of the TRD chambers in steps

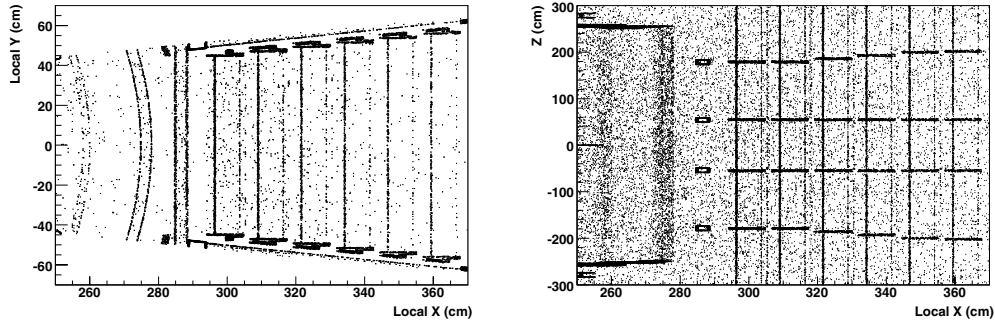


**Figure 5.37.** Space distribution of the points of particle interactions with the material between the TPC and TOF.

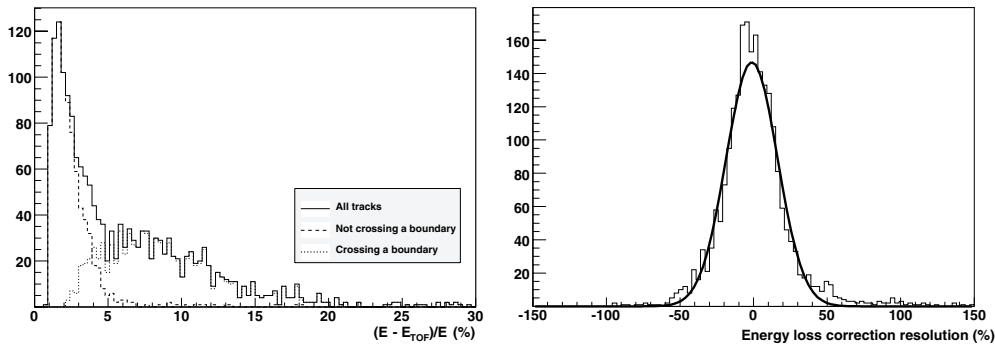


**Figure 5.38.** Left: Relative energy losses in the material between the TPC and the TOF (HIJING particle momentum spectrum). Right: Energy loss fluctuations remaining after the most probable energy loss corrections.

which correspond to the effective radial distance between two consecutive time bins. At each extrapolation the track helix parameters and covariance matrix are re-evaluated using information about the expected multiple scattering and energy loss.

There are some differences between the TPC and TRD track finding that are described below.

*Interactions with the detector material.* A significant fraction of tracks traversing the TRD interacts with the detector material. When a particle hits some high density element of the TRD (electronics, cooling, space frame) it either scatters and loses a significant amount of its energy or may even be absorbed. The space distribution of the points of particle interactions with material between the TPC and the TOF is shown in Fig. 5.37.

Because of the bending in the magnetic field, the amount of material crossed by a particle depends on the particle momentum. The typical particle energy loss can easily be as big as 10% of the initial energy (see Fig. 5.38, left). The TRD track reconstruction software takes into account these losses, however, the particle energy can be corrected only for the most probable energy loss. After this correction is done, the remaining statistical uncertainty of the particle energy is still rather high (see Fig. 5.38, right). This gives the uncertainty in the reconstructed momentum of about 2%, which is bigger than the momentum resolution that is already achieved for this track after the reconstruction in the TPC and ITS.

Therefore, the TRD track reconstruction acts differently in the following two situations. If a track does not cross areas with a high material concentration, its parameters are updated each time a new TRD cluster is assigned to this track until the outer wall of the TRD is reached. Such tracks are then propagated to the TOF and the final refit towards the TPC is done using the track parameters stored at the outer wall of the TRD. The tracks crossing big amounts of material are still propagated to the surface of the TOF. However, for the final backward refit, we use the track parameters stored at the point before entering the zone with the high material concentration.

*Tracklet finding.* The Kalman filter algorithm uses extrapolation of track parameters to the next propagation layer. The distances between the TRD chambers are bigger than the distances between TPC pad rows. In the case of the TPC, a cluster with the minimal distance to the predicted track extrapolated position is taken as the next measurement. However, in the case of the TRD, the track position uncertainty is comparable to the mean distance between the clusters. In the high multiplicity environment, there is a significant probability of taking incorrect clusters. The situation is even more complicated, because the  $z$  coordinate of the cluster is known only with precision of about 3 cm (given by the pad length of about 9 cm).

Therefore, the cluster-search mechanism was replaced by a tracklet-search mechanism. A tracklet is a set of clusters and we try to combine the track extrapolation information with the local tracklet informations. We search for tracklets with minimal  $\chi^2$  distance to the track. The  $\chi^2$  distance is given not only by the tracklet position but also by the tracklet angle. The information on the  $z$ -position is also used in the tracklet-finding algorithm. For tracks with the tangent of deep angle less than 1 (all primary tracks), the number of changes in pad row direction can not exceed one.

In order to find tracklets with minimal  $\chi^2$  distance to the track, a full combinatorial search can be used. However, such an algorithm uses a lot of CPU time. Instead, an iterative approach was chosen. In a first approximation, the closest clusters to the track are taken. Afterwards, the closest tracklets to the track are found in several iterations:

- The tracklet position, angle and their uncertainty are calculated.
- The new weighted mean cluster position is calculated (tracklet + track).
- If the  $\chi^2$  of the current tracklet is smaller than the  $\chi^2$  of the best previous tracklet and the number of pad row changes are less than or equal to the best previous, the current tracklet is chosen.
- The clusters closest to the new weighted mean position are taken.

*Tracklet and cluster error parametrization.* The cluster position uncertainty can be estimated using the r.m.s. of the tracklet-cluster residuals. This so-called intrinsic resolution is determined mainly by signal-to-noise ratio and angular effects. The cluster errors inside one layer are strongly correlated. To take the correlation into account two approaches were implemented and tested:

- We update the track parameters with the tracklet measurement, as the error correlation between the tracklet measurements is negligible.
- We update the track parameters using the cluster position measurements corrected for the systematic effects mentioned above.

The track-parameter resolution obtained using both approaches is similar. The main advantage of the first approach is that it is several times faster. Moreover, in this approach the correction for the centre of gravity in the radial (drift) coordinate can be applied. The

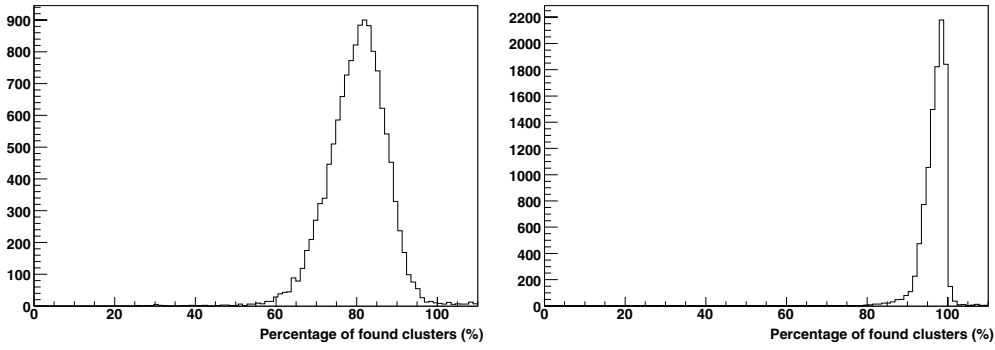


**Figure 5.39.** Ratio of the number of associated clusters to the number of pad rows crossed. Left: central Pb–Pb collisions ( $dN_{\text{ch}}/d\eta = 6000$ ). Right: pp collisions.

disadvantage of this approach is that it would require some modifications in the underlying track reconstruction equations. Therefore, the second approach is currently used.

In this approach, the resulting cluster uncertainty  $\sigma_y^2$  used in the Kalman filter is calculated in the following way:

$$\sigma_y^2 = \text{r.m.s.} + (\sigma_{dt} \tan \alpha)^2 N_{\text{cl}}, \quad (5.7)$$

where  $\sigma_{dt}$  is a parameter corresponding to the uncertainty in time position and  $N_{\text{cl}}$  is the number of clusters in the tracklet. The value of the parameter  $\sigma_{dt}$  is obtained normalizing pulls of the error distribution to one, independently of the tracklet angle.

The space point resolution for overlapped clusters is an order of magnitude worse than the space point resolution obtained for isolated clusters, even if the clusters are unfolded. Consequently, additional correction factors are added to the cluster uncertainty  $\sigma_y^2$ , corresponding to the mean cluster shape for the tracklet and the number of pad row changes. The correction factors were chosen by normalizing the pulls of the error distribution to one, independently of the mean shape factor and the number of pad row changes.

*Tuning of the tracker parameters.* To improve the space and momentum resolution and the track-finding efficiency, several parameters (the drift velocity, the shape of the ion tail, the time offset) have to be tuned. These effects depend on the hit position. Unfortunately, the precision of the track space measurement is not sufficient in the coordinate that is important here ( $z$ ) to be able to make an efficient correction for these effects. Instead, an effective drift velocity, an effective tail cancellation, and an effective time offset are used as parameters.

To tune these parameters in offline reconstruction, the local matching between the TRD tracklets from different TRD planes is required.

### 5.1.5.3. Performance of the TRD track finding

*Track finding quality.* In high track multiplicity events many clusters are overlapped, and their reconstructed positions are significantly displaced. Usually, such clusters do not fall into the  $\pm 4\sigma$  window around the extrapolated track position and, thus, these clusters are not assigned to tracks. The ratio of the number of clusters associated to a track to the number of pad rows crossed by this track is shown in Fig. 5.39.

*Track-finding efficiency.* As usual, the efficiency of track-finding software is defined as a ratio of number of ‘good found’ tracks to the number of ‘good generated’ tracks, whereas the

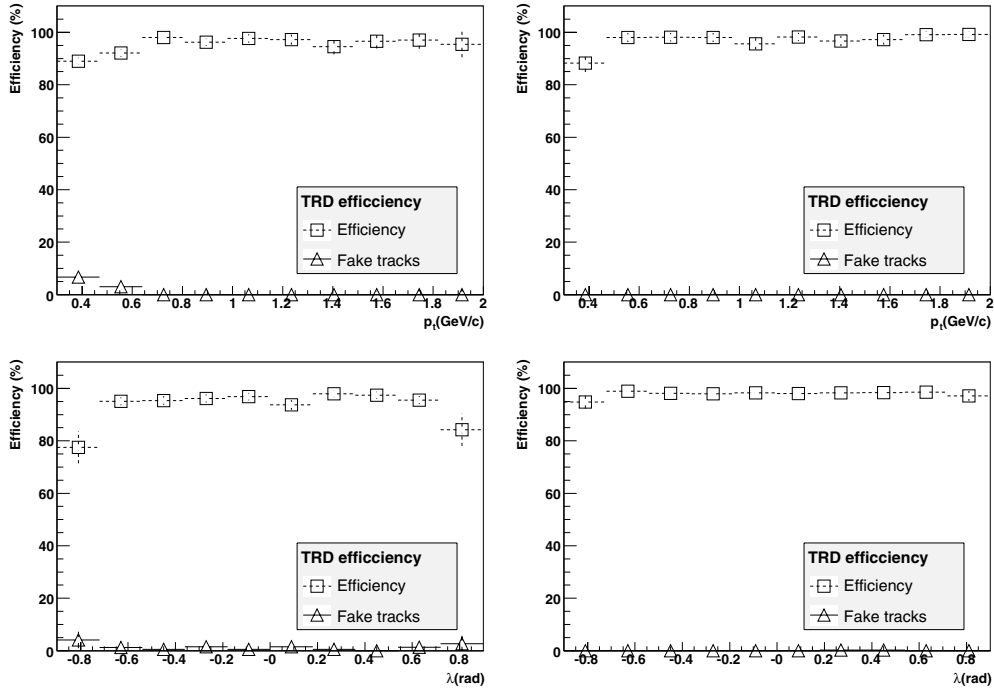


**Figure 5.40.** TRD software track-finding efficiency as a function of particle transverse momentum and dip angle. Left: central Pb–Pb collisions ( $dN_{\text{ch}}/d\eta = 6000$ ). Right: pp collisions.

probability to obtain a fake track is expressed by the number of ‘fake found’ tracks divided by the number of ‘good generated’ track.

In case of the TRD we define:

- ‘Good generated’ track as a track that crosses more than three TRD chambers.
- ‘Good found’ track as a track having the number of assigned clusters larger than 50% of the expected number of pad rows crossed. In addition, we require such tracks to have not more than 10% of incorrectly assigned clusters, and at least half of the innermost 10% of clusters have to be assigned correctly.
- ‘Fake found’ track as a track with a sufficient number of assigned clusters, but having a bigger percentage of incorrectly assigned clusters.

No significant dependence of the software track-finding efficiency on the transverse momentum of the particles was found (see Fig. 5.40).

*Precision of the reconstructed track position.* The efficiency of matching the tracks with the TOF detector is affected by the precision with which the position of a track is reconstructed at the outer wall of the TRD. This precision depends on the particle momenta and also on the track multiplicity as can be seen in Fig. 5.41.

### 5.1.6. Combined track finding

*5.1.6.1. Overall track-finding efficiency.* Every detector, if it contributes to the reconstruction of a track, improves the reconstruction quality of this track. However, the requirement of being reconstructed in as many detectors as possible reduces the statistics of such tracks.

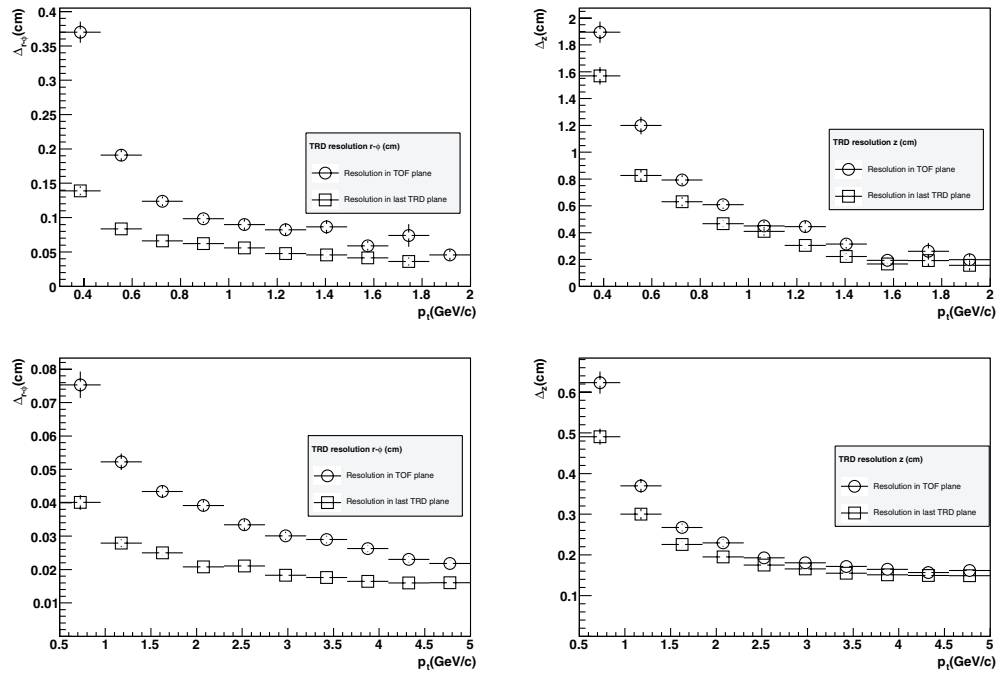


**Figure 5.41.** Precision of the track position reconstructed at the outer wall of the TRD in  $xy$  plane (left) and  $z$  direction (right) for central Pb–Pb collisions  $dN_{ch}/d\eta = 6000$  (top) and pp collisions (bottom).

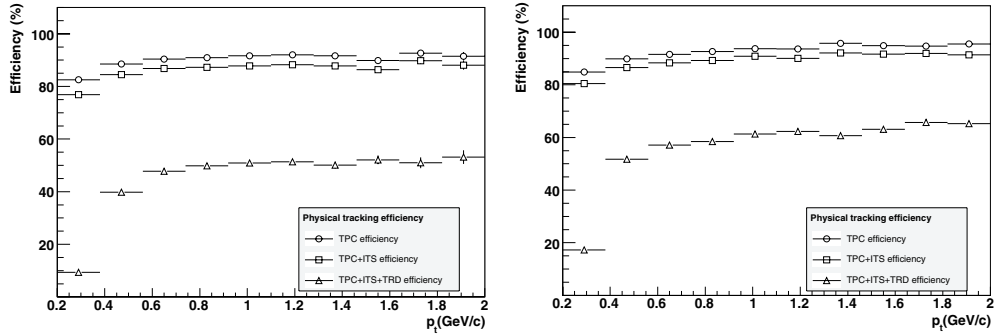


**Figure 5.42.** Physical track-finding efficiency for different combinations of the tracking detectors. Left: Central Pb–Pb collisions ( $dN_{ch}/d\eta = 6000$ ). Right: pp collisions.

The overall software track-finding efficiency is still rather high (about 90% practically at any momenta), but the physical track-finding efficiency is much more dependent on the number of contributing detectors. This is true both for the case of the high multiplicity events (see Fig. 5.42, left) and pp events (Fig. 5.42, right), because, as already discussed above, the physical efficiency is mainly defined by the particle decays, presence of dead zones, and interactions with the material.

**5.1.6.2. Overall momentum and angular resolutions.** As can be seen from Fig. 5.42, the biggest loss of the combined track-finding efficiency happens in the TRD. However, this

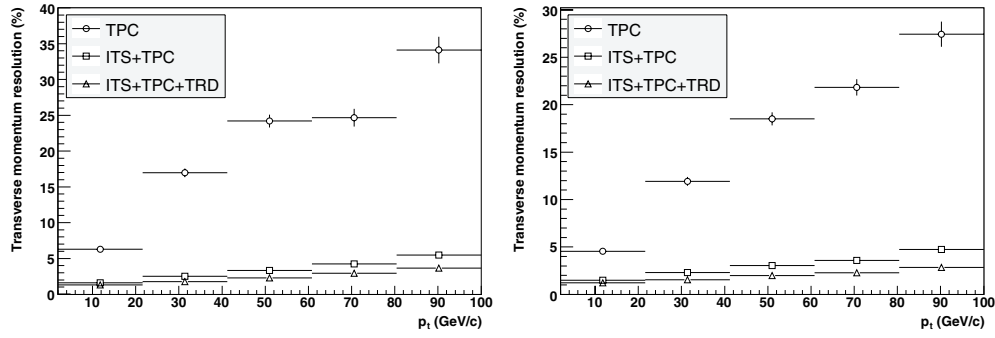


**Figure 5.43.** Transverse-momentum resolution for different combinations of the tracking detectors. Left: Central Pb-Pb collisions ( $dN_{ch}/d\eta = 6000$ ). Right: pp collisions.

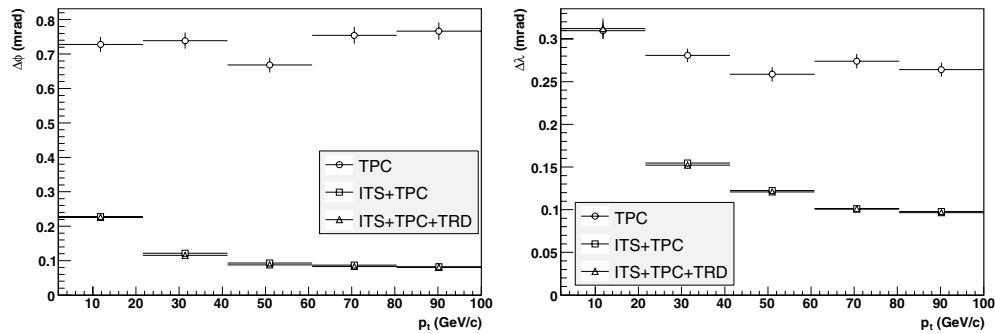


**Figure 5.44.** Azimuthal-angle resolution ( $\Delta\phi$ ) and dip-angle resolution ( $\Delta\lambda$ ) for different combinations of the tracking detectors (central Pb-Pb collisions,  $dN_{ch}/d\eta = 6000$ ).

detector is indispensable for electron identification (see Section 5.4.3) and, in addition, it improves the overall momentum resolution, especially at higher momenta (see Fig. 5.43).

The best overall momentum resolution is achieved for low track multiplicity events (pp collisions) for the combination ITS+TPC+TRD. The resolution is as good as  $\sim 3.5\%$  at 100 GeV/c (see Fig. 5.43, right). This will, however, require very accurate corrections for the energy losses in the material and precise alignment of the detectors.

The angular resolutions for different combinations of the tracking detectors are shown in Fig. 5.44. At lower momenta the angular resolutions are defined by the multiple scattering on the material between the last space point assigned to a track and the primary vertex. At higher momenta, where the influence of multiple scattering becomes negligible, the angular resolution is defined by the space point precision of the contributing tracker detectors. As pointed out in Ref. [32] the best results are achieved by combining the TPC and ITS. The obtained resolutions are in good agreement with the ones that can be estimated from the thickness of the inner pixel ITS layer and the beam pipe, and the space point precision of the detectors.

There is no significant dependence on the track multiplicity.

**5.1.6.3. Track impact-parameter resolution.** The impact parameter of a track is defined as the distance of closest approach of the track to the interaction vertex. The measurement of the track impact parameter is crucial for the study of the physics signals characterized by the presence of a secondary vertex with a small displacement from the interaction vertex.

This is, in particular, the case for the detection of particles with open charm and open beauty (Section 6.6). We consider separately the two projections of the impact parameter in the plane transverse to the beam direction and along the beam direction, respectively:

$$d_0(r\varphi) = \rho - \sqrt{(x_v - x_0)^2 + (y_v - y_0)^2} \quad \text{and} \quad d_0(z) = z_{\text{track}} - z_v, \quad (5.8)$$

where  $\rho$  and  $(x_0, y_0)$  are the radius and the centre of the track projection in the transverse plane,  $(x_v, y_v, z_v)$  is the position of the primary vertex, and  $z_{\text{track}}$  is the  $z$  position of the track after it has been propagated to the distance of closest approach in the transverse plane. Clearly, the  $d_0$  resolutions are a convolution of the track position resolution and of the primary vertex position resolution.

In ALICE, the information on the impact parameter is mainly provided by the Inner Tracking System, and, in particular, by the two layers of Silicon Pixel Detectors, which have fine granularity and are positioned close to the interaction point. In the following we summarize simulation results [32] on the dependence of the impact parameter resolution on particle kinematics and particle type. We consider the nucleus–nucleus and proton–proton cases separately.

*Impact parameter resolution in Pb–Pb collisions.* As discussed in Section 5.1.1, the transverse size of the interaction region during LHC nucleus–nucleus runs will be of about  $10 \mu\text{m}$ . Since the position of the centres of the beams will be stable for a given run (of a duration of a few hours), the mean position of the interaction point during each run can be measured with very high precision, by integration over a long time interval. Therefore, the uncertainty on the vertex position in the transverse plane can be assumed to be given by the size of the interaction region, i.e. about  $10 \mu\text{m}$ . The  $z$  position of the vertex can be reconstructed, before tracking, exploiting the correlation between clusters in the two pixel layers. The resolution is about  $5\text{--}7 \mu\text{m}$  for multiplicities in the range  $dN_{\text{ch}}/d\eta = 3000\text{--}6000$ . The uncertainty on the primary vertex position is, therefore, much smaller than the track position resolution for tracks with  $p_t$  up to about  $10 \text{ GeV}/c$ , in nucleus–nucleus collisions.

For the evaluation of the  $d_0$  resolutions, track reconstruction was performed using the standard Kalman filter in the TPC and in the ITS, with two iterations in the latter. During the first iteration, the information on the primary vertex position (nominal beam position) is used for primary track finding; in the second step, the vertex constraint is released to allow for secondary (displaced) track finding. Afterwards, all found tracks are refitted without vertex constraint in order not to bias the measurement of the impact parameter. At first we consider tracks with a cluster in each layer of the ITS; as detailed in the following, the impact parameter resolution is strongly dependent on the number of clusters associated to track in the ITS, and, in particular, on the presence of the clusters in the two pixel layers.

Figure 5.45 presents the resolutions as a function of  $p_t$  for electrons ( $e^\pm$ ), pions ( $\pi^\pm$ ), kaons ( $K^\pm$ ) and protons (p and  $\bar{p}$ ) with  $|\eta| < 0.9$ . The  $p_t$ -dependence reflects what is expected from a momentum-independent contribution due to the spatial resolution of the detectors added to a momentum-dependent contribution due to multiple scattering. We fitted the  $d_0(r\varphi)$  resolution for charged pions to the expression

$$\sigma_{d_0(r\varphi)} (\mu\text{m}) = 10 + \frac{53}{p_t (\text{GeV}/c) \sqrt{\sin \theta}}, \quad (5.9)$$

where  $\theta$  is the polar angle of the track (for the functional form of the  $p_t$  and  $\theta$  dependence of the multiple scattering term, see, for example, the appendix of Ref. [8]). Given that the multiple scattering angle depends on  $1/\beta$ , for low momenta, where this is the main contribution to the impact parameter resolution, the resolution itself depends on the particle type, being worse for heavier particles. For  $p_t > 1 \text{ GeV}/c$  the resolutions for kaons (protons)

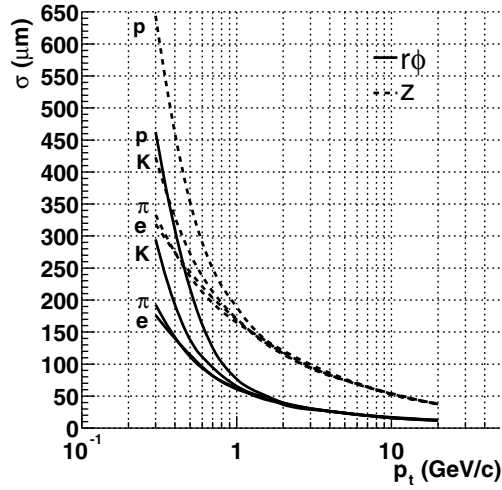


**Figure 5.45.** Impact parameter resolutions in central Pb–Pb collisions for electrons, pions, kaons and protons as a function of the transverse momentum. An assigned cluster in each of the six ITS layers is required.

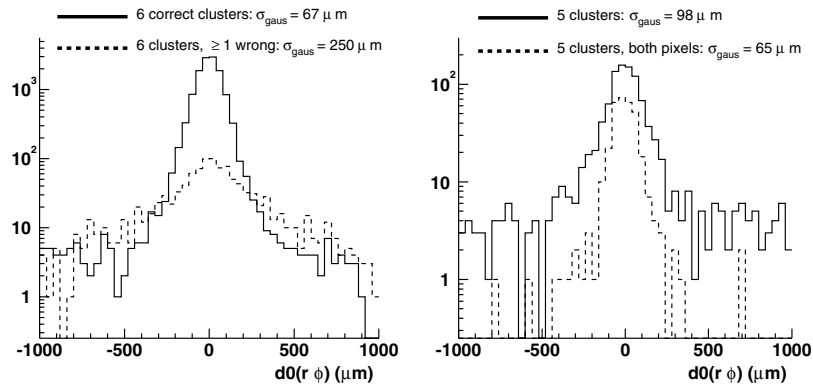


**Figure 5.46.** Distributions of the  $r\phi$  impact parameter for primary pions with  $0.9 < p_t < 1.1$  GeV/ $c$ . On the left, tracks with six correctly assigned ITS clusters (solid) and ‘fake’ tracks, with at least one misassigned cluster (dashed). On the right, tracks with five ITS clusters (solid) and tracks with five clusters but with clusters in the pixel layers (dashed). We report the resolutions estimated with a Gaussian fit.

are the same as for pions. The separation at low  $p_t$  between pions and electrons is not well defined, because the latter can suffer from energy loss due to the bremsstrahlung process; even if the probability is quite low ( $\sim 1\%$  at  $p_t = 1$  GeV/ $c$ ), this spoils both the momentum and the impact parameter resolutions.

We now consider the effect on the impact parameter resolution of misassigned or missing clusters in the ITS layers. We focus on the  $r\phi$  impact parameter for pions with  $0.9 < p_t < 1.1$  GeV/ $c$ . Figure 5.46 (left) shows that the distribution of the impact parameters for ‘fake’ tracks (at least one misassigned cluster) is much broader than that for tracks with six correctly assigned clusters. However, since the fraction of fake tracks is about 2–3% at  $p_t = 1$  GeV/ $c$  and it rapidly vanishes as the  $p_t$  increases, for relatively high  $p_t$  tracks, the effect due to

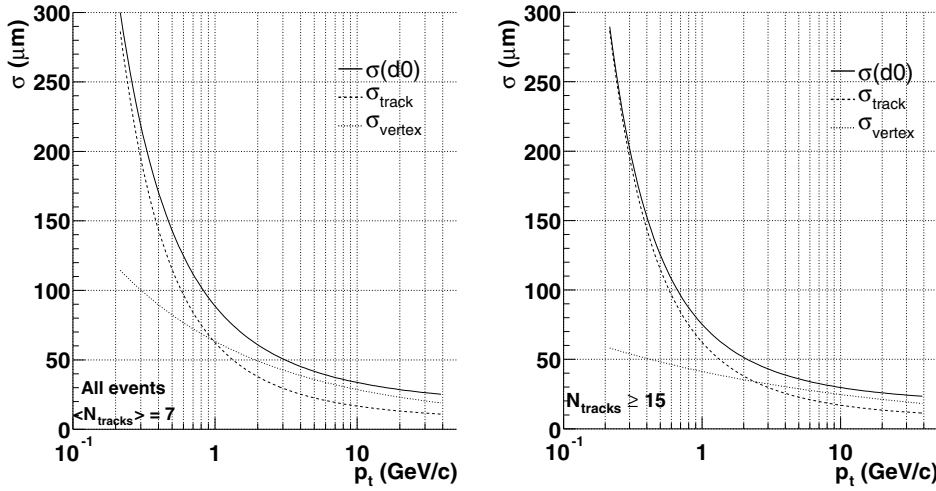


**Figure 5.47.** Impact-parameter resolution in the transverse plane as function of the transverse momentum in pp collisions.

misassigned clusters is very small, if six ITS clusters are required. As can be seen in Fig. 5.46 (right), for tracks with only five clusters in the ITS, the resolution is still good if there is a cluster in each of the pixel layers. Therefore, for the physics studies requiring an optimal impact-parameter resolution, the loosest track-quality condition is to have at least five clusters in the ITS and the two clusters in the pixel layers.

*Impact parameter resolution in proton–proton collisions.* In Section 5.1.1 we argued that the primary vertex position in pp collision will have to be determined on an event-by-event basis and we showed that the resolutions achieved with an algorithm that uses reconstructed tracks depend on the event multiplicity and are of  $60 \mu\text{m}$  for the transverse coordinates and  $90 \mu\text{m}$  for  $z$ , on average. Therefore, in pp collisions the impact parameter resolution will have a significant contribution from the uncertainty in the primary vertex position, which is about one order of magnitude larger than in the Pb–Pb case.

The resolution on the track position in the transverse plane—the main contribution to the impact parameter resolution—is essentially the same in pp and in Pb–Pb, if one cluster per ITS layer is required [32]. This is not surprising, having already verified that the effect due to the presence of fake tracks in Pb–Pb is quite small. Figure 5.47 presents the  $r\phi$  impact parameter resolution in pp collisions for charged pions. On the left, we show the resolution integrated over a large sample of PYTHIA events (for this sample the average number of reconstructed tracks is  $\langle N_{\text{tracks}} \rangle = 7$ ). On the right, we consider only high-multiplicity events with  $N_{\text{tracks}} \geq 15$ . We plot the resolution  $\sigma_{d_0}$  on the impact parameter (solid line), the resolution  $\sigma_{\text{track}}$  on the track position (dashed line), and the ‘equivalent’ resolution on the vertex position (dotted line), obtained as  $\sigma_{\text{vertex}} = \sigma_{d_0} \ominus \sigma_{\text{track}}$  (for all quantities we consider the  $r\phi$  component). From the analysis of these plots, we observe that the worsening in the  $d_0$  resolution w.r.t. the case of perfect knowledge of the vertex position,  $(\sigma_{d_0} - \sigma_{\text{track}})/\sigma_{\text{track}}$ , is negligible for very low  $p_t$  tracks, of the order of 30% for  $p_t = 1 \text{ GeV}/c$ , and of the order of 50% for  $p_t = 10 \text{ GeV}/c$ . However, the impact of the uncertainty on the vertex position is not too dramatic for medium- and high-momentum tracks, since these tracks are always produced

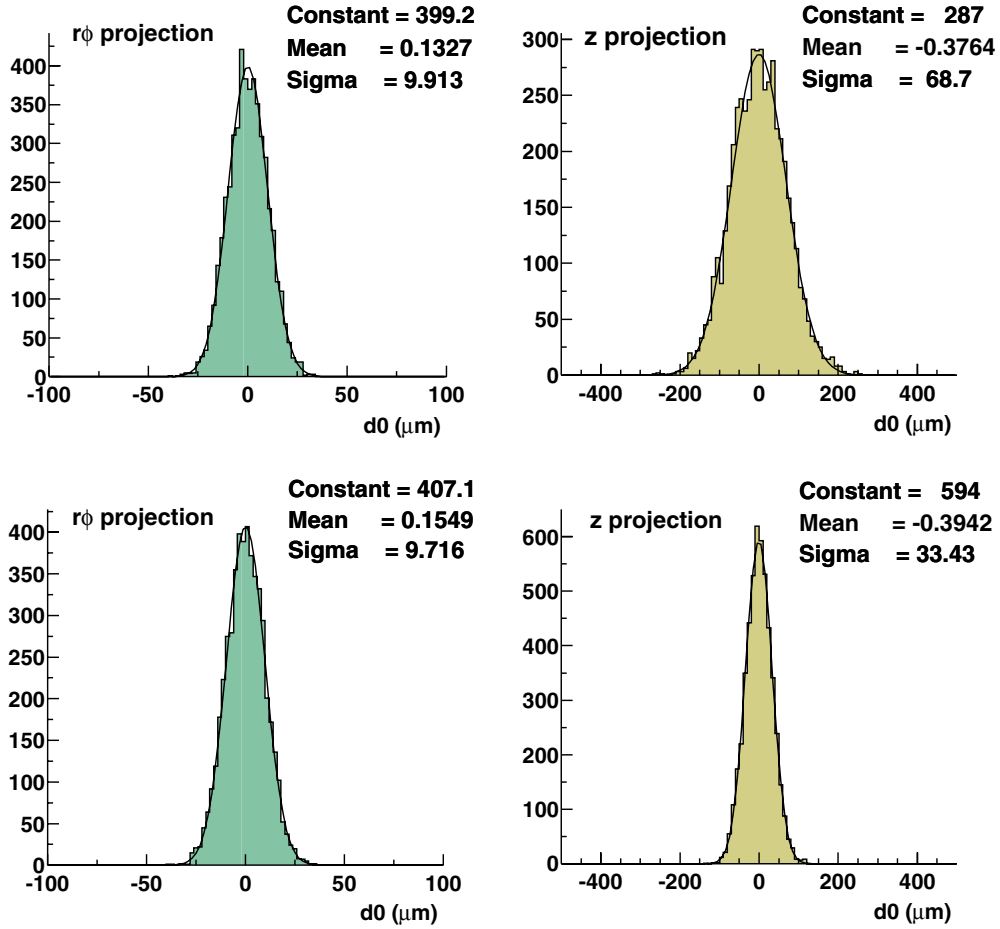


**Figure 5.48.** Impact-parameter resolutions for tracks with  $p_t > 20 \text{ GeV}/c$  reconstructed with the ITS only (upper panels) and with the combination TPC+ITS (lower panels).

in events with large multiplicity, in which the vertex can be reconstructed quite precisely; this is clearly shown by the strong  $p_t$  dependence of the ‘equivalent’ vertex resolution,  $\sigma_{\text{vertex}}$ .

*Impact-parameter resolutions for high-momentum tracks.* As demonstrated in Ref. [32], in the high momentum-limit, where the multiple scattering is negligible, the TPC contribution to the longitudinal  $z$  impact-parameter resolution becomes essential (see Fig. 5.48). This can be explained by observing that the impact-parameter resolutions are strongly dependent on the angular resolutions which are, especially for the dip angle, better if the TPC space points are included in the reconstruction.

**5.1.7. Secondary vertex reconstruction.** In this subsection we describe the ALICE capabilities to reconstruct  $V^0$ , cascade and kink topologies.

**5.1.7.1.  $V^0$  and cascade finding procedure.** The  $V^0$  finding procedure starts with the selection of secondary tracks: tracks which have a too small impact parameter with respect to the primary vertex are eliminated. Then, one has to combine each ‘secondary’ track with all

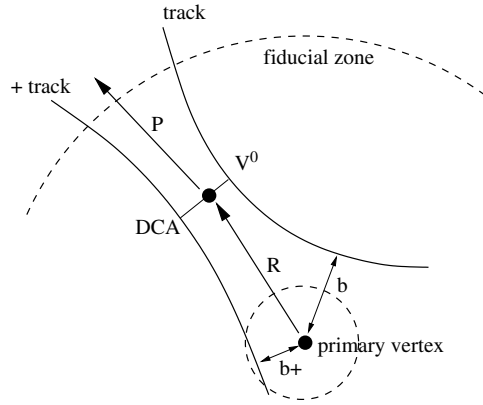


Figure 5.49. Geometrical selections for secondary vertex reconstruction.

the other ‘secondary’ tracks having an opposite charge. Two different cuts are applied for the positive track ( $b+$ ) and the negative track ( $b-$ ) impact parameters (see Fig. 5.49).

Such pairs of tracks are rejected if the distance of closest approach (DCA) in space between the two tracks is larger than a given value. The minimization of the distance between the tracks is performed numerically using a 3-dim helix track parametrization. There is also a possibility to minimize a ‘normalized DCA’ which takes into account the possible difference in the reconstructed track position in the transverse plane and along the beam direction. This increases slightly the precision of the reconstructed  $V^0$  position, especially for the high-momentum  $V^0$ ’s. This position is supposed to be on the line corresponding to the DCA while the distance between a track and the vertex is proportional to the norm of the covariance matrix of the track parameters.

Once the vertex position is defined, only the secondary vertices inside a given fiducial volume are kept. The inner boundary of this fiducial area is limited by the expected particle density and the tracking precision which, in turn, is mainly defined by the multiple scattering on the pixel layers of the ITS. It can be shown that, assuming a particle density of  $dN_{ch}/d\eta = 4000$  and being given the current material budget together with the present tracking software, one can hardly go deeper than 0.9 cm from the primary interaction point. The outer limit was initially imposed by the radius of the beam pipe (3 cm), however there is a possibility to extend this limit up to the inner radius of the TPC.

Finally, the  $V^0$  finding procedure checks whether the momentum of the  $V^0$  candidate points well back to the primary vertex. Hence we extrapolate the two tracks of this candidate to the points of the DCA and calculate the  $V^0$  momentum as the sum of the track momenta taken at those points. Then we apply a cut on the cosine of the angle (pointing angle) between the  $V^0$  momentum ( $P$ ) and a vector ( $R$ ) connecting the primary vertex and the  $V^0$  vertex positions ( $\cos \Theta_p$ ).

The cascade finding procedure, used to reconstruct the  $\Xi^-$  and  $\Omega^-$  baryons and their corresponding antiparticles, starts with looking for all  $V^0$  candidates. The method is illustrated in Fig. 5.50 for the  $\Xi^-$  and the  $\Omega^-$  cases. Since the  $\Lambda$ ’s we want to reconstruct here come from a cascade particle decay, they do not have to point on the main collision vertex. The condition on the pointing angle is consequently loose. In order to achieve a substantial background suppression at this level, we select only the  $V^0$  candidates having a large impact parameter ( $b_{V^0}$ ).

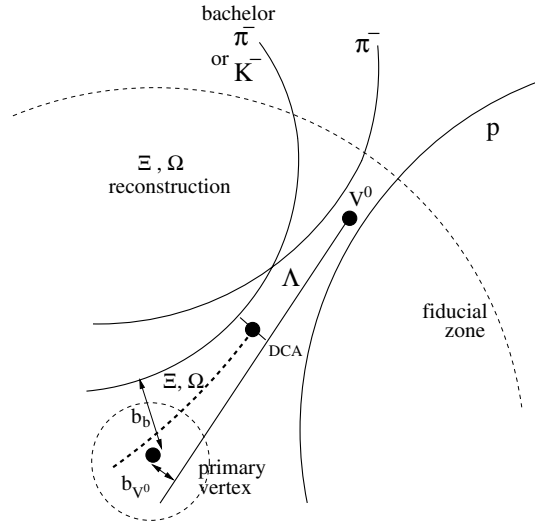


**Figure 5.50.** Geometrical selections for cascade reconstruction.

Then, the  $V^0$  candidates found within the  $\Lambda$  mass window have to be combined with all possible secondary tracks (bachelor candidates). The impact parameter ( $b_b$ ) of the bachelor must also be large enough to have a good rejection of primary particles. A  $V^0$  bachelor association is accepted if the distance of closest approach (DCA) between the bachelor track (helix) and the  $V^0$  mother trajectory (straight line) is small enough.

Finally, we check whether this cascade candidate points well back to the primary vertex. The cascade finding is limited to the same fiducial region as the one used for  $V^0$  reconstruction. Hence, both the cascade decay and the successive  $\Lambda$  decay have to be between  $r = 0.9$  cm and a variable upper limit.

*Estimation of the reconstruction quality.* The precision of the reconstruction is calculated using the difference between the reconstructed parameters and the generated ones.

The efficiency of the reconstruction ( $\varepsilon_{\text{good}}$ ) and the probability to get a fake vertex ( $\varepsilon_{\text{fake}}$ ) are defined in the following way:

$$\varepsilon_{\text{good}} = \frac{\text{number of good found}}{\text{number of good generated}},$$

$$\varepsilon_{\text{fake}} = \frac{\text{number of fake found}}{\text{number of good generated}}.$$

A vertex is called ‘good’ generated (or, in other words, ‘findable’) if it:

- is inside the fiducial volume;
- consists of ‘good’ tracks, hence findable tracks;
- comes from  $K_S^0 \rightarrow \pi^- \pi^+$ ,  $\Lambda^0 \rightarrow \pi^- p$ ,  $\Xi^- \rightarrow \pi^- \Lambda^0 \rightarrow \pi^- \pi^- p$  and  $\Omega^- \rightarrow K^- \Lambda^0 \rightarrow K^- \pi^- p$  and the corresponding antiparticle decays.

A ‘good’ found vertex must be:

- inside the fiducial volume;
- within a certain window around the particle mass;
- coming from a real decay;
- have a correct mass hypothesis.

Finally, ‘fake’ found vertices are those which do not come from a real decay or are assigned a wrong mass hypothesis, even if they are found inside the fiducial area and within the window around the searched particle mass.

The acceptance of the reconstruction chain is defined as follows:

$$A = \frac{\text{number of good generated}}{\text{total number of generated in } 45^\circ < \theta < 135^\circ}.$$

The results presented in the next section were obtained using the ‘microscopic’ simulator for the TPC and the ITS. The amplitude of the magnetic field was set at 0.5 T. The quality of the  $V^0$  and cascade reconstruction was estimated for events characterized by a particle multiplicity of  $dN_{ch}/d\eta \sim 4000$ . The hyperons were generated with a momentum distribution following  $m_T$ -scaling and mixed in the background parametrized HIJING events (Section 4.2.1.2 in Volume I [3]).

*Current results.* The first strategy that we applied consists in limiting the hyperon reconstruction to a very narrow fiducial zone, inside the beam pipe (between 0.9 cm and 2.9 cm), in order to reduce the background as much as possible. In this case, good tracks must have six clusters in the ITS (one per layer). Because of these constraints, the number of findable secondary tracks is small. Consequently, the acceptance for  $V^0$  is only about 5%. On the other hand, we are able to reach a good efficiency for  $V^0$  finding ( $\sim 30\text{--}40\%$ ), while the background stays at a very low level ( $S/B \sim 10$ ). This is due to the fact that we can apply tight reconstruction cuts (for  $\Lambda$ :  $b+ > 300 \mu\text{m}$ ,  $b- > 600 \mu\text{m}$ ,  $DCA < 600 \mu\text{m}$  and  $\cos \Theta_p > 0.9995$ ) because the track parameters are determined with a very good precision (including all ITS layers) and the nearest possible from the secondary vertices. Besides, the fact that the reconstruction is limited to the region inside the beam pipe allows to avoid all the background coming from secondary interactions in the material. The situation becomes more difficult in the case of cascade hyperons. Here, the rate of losses during the secondary vertex reconstruction is higher. These losses are due to the rather severe cuts that have to be applied in order to keep the signal-to-background ratios at an acceptable level.

The second strategy consists of keeping for the  $V^0$  reconstruction all the tracks which have been found in the TPC, regardless of the number of clusters they contain in the ITS (from zero to six). In this case, the reconstruction region can be extended up to the TPC. Taking the case of  $\Lambda$ 's, this leads to a substantial gain in the acceptance (25.5%). The price to pay is an increase of the background. The reconstruction cuts have to be optimized in order to reduce it as much as possible ( $S/B > 1$ ) without deteriorating the efficiency since the aim of this last strategy is to approach the best possible reconstruction rate. Actually, the  $V^0$  finding efficiency can even be improved, the reason being that fewer secondary tracks are lost since the assignment of clusters in the ITS layers is not required anymore. The tracking efficiency for secondaries goes up to about 80–90%. A ‘good’  $V^0$  can actually be found only if its two daughters are ‘good’ tracks which are correctly reconstructed (i.e. ‘good’ found tracks). Being given this tracking efficiency of about 80–90% for secondary tracks, the number of such  $V^0$ 's, taking the case of  $\Lambda$ 's, represents about 70% of the ‘good’ ones. Hence, the maximum  $\Lambda$  finding efficiency that we may hope to get is approximately 70%. If the reconstruction cuts are reasonably loose (minimum impact parameters  $b+$  and  $b-$  of  $200 \mu\text{m}$ , a maximum

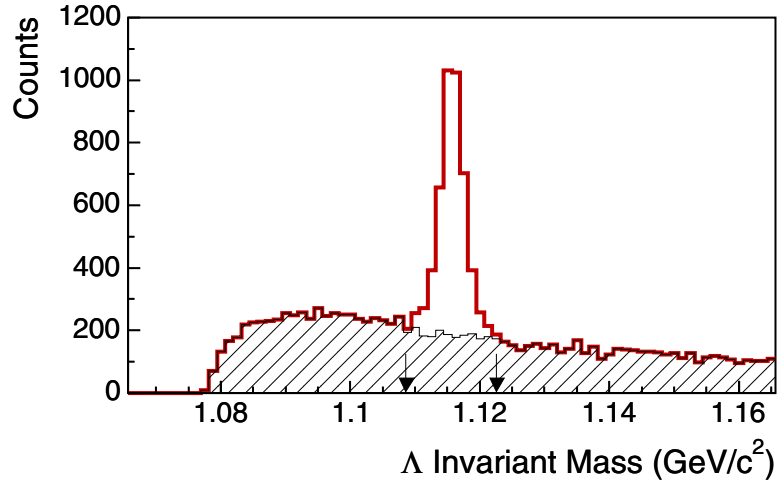


**Figure 5.51.**  $\Lambda$  invariant mass spectrum corresponding to the reconstruction of 300 HIJING events.

DCA at 1 cm and a maximum pointing angle at  $6^\circ$  ( $\cos \Theta_p > 0.995$ ), we are able to reach this value. Indeed, less than 1% of the  $V^0$ 's get lost during the reconstruction procedure. In other words, the intrinsic efficiency of the reconstruction method is larger than 99%. But to keep the background at an acceptable level, we have to use tighter cuts which deteriorate the efficiency.

As a compromise, the  $\Lambda$  invariant mass spectrum, obtained after the reconstruction of 300 HIJING events ( $dN_{ch}/d\eta = 4000$  and  $100 \Lambda$ 's/event within  $45^\circ < \theta < 135^\circ$ ) is shown in Fig. 5.51. The geometrical cuts used here ( $b^- > 0.15$  cm,  $b^+ > 0.1$  cm,  $DCA < 0.5$  cm,  $\cos \Theta_p > 0.999$ ) lead to an efficiency of 42.5% and a S/B of about 1.4.

The rate of reconstructed  $V^0$ 's (acceptance  $\times$  efficiency) is substantially improved with respect to the first strategy, since it reaches 11% for  $\Lambda$ 's.

Of course, depending on the kind of analysis one has to perform, one can tolerate different levels of background. If a pure signal is mandatory, then we can reach a low level of noise by applying more severe cuts which in turn reduce the reconstructed  $\Lambda$  rate.

An example, corresponding to  $b^- > 0.15$  cm,  $b^+ > 0.1$  cm,  $DCA < 0.1$  cm,  $\cos \Theta_p > 0.9997$ , is shown in Fig. 5.52. Here, the efficiency (22.5%) and the reconstruction rate (5.7%) are reduced by a factor 2 but the S/B ratio is larger than 6.

The same kind of study has been conducted for the reconstruction of  $K_S^0$ . The results are summarized in Table 5.4. The reconstruction rate of  $K_S^0$  is comparable to that of  $\Lambda$  particles.

Concerning  $\Xi$  reconstruction, the global acceptance is of about 10%. For this reconstruction, the selection of secondary  $\Lambda$ 's uses minimum impact parameter values close to the ones used for primary  $\Lambda$ 's ( $b^- > 0.2$  cm,  $b^+ > 0.06$  cm) but the condition on the DCA of the  $\Lambda$  daughters is strengthened ( $< 0.1$  cm) while the cut on the  $V^0$  pointing angle is obviously loose ( $\cos \Theta_p > 0.995$ ). A minimum impact parameter of 1 mm is also required for the  $\Lambda$ .

The maximum impact parameter of the bachelor is of 1.2 mm and the maximum DCA allowed between the bachelor and the  $V^0$  trajectory around 1 mm, while the pointing angle of the reconstructed cascade must be smaller than  $2^\circ$  ( $\cos \Theta_p > 0.9995$ ). The invariant mass spectra obtained with this set of cuts for  $\Xi$  particles is shown in Fig. 5.53. The efficiency of the reconstruction is 5%. The yield of reconstructed  $\Xi$ 's is 0.075/event.

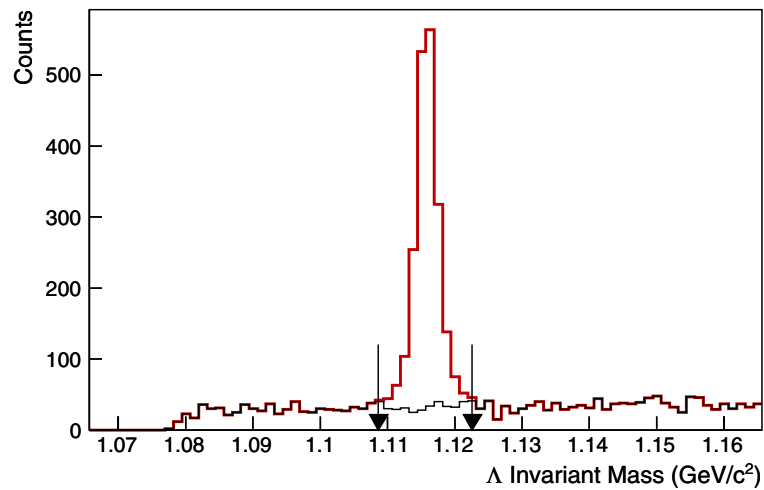


**Figure 5.52.**  $\Lambda$  invariant mass spectrum corresponding to the reconstruction of 300 HIJING events, using tight cuts on the DCA and  $\cos \Theta_p$ .

**Table 5.4.** Reconstruction precisions, efficiency, and integrated acceptance normalized to the production in the range  $45^\circ < \theta < 135^\circ$ .

	Position resolution (mm)	Angular resolution (mrad)	Momentum resolution (%)	Efficiency $\varepsilon_{\text{good}}$ (%)	Acceptance $A$ (%)
$K_S^0$	0.3	5.0	1.5	58	20
$\Lambda^0$	0.4	3.5	1.2	42.5	25.5

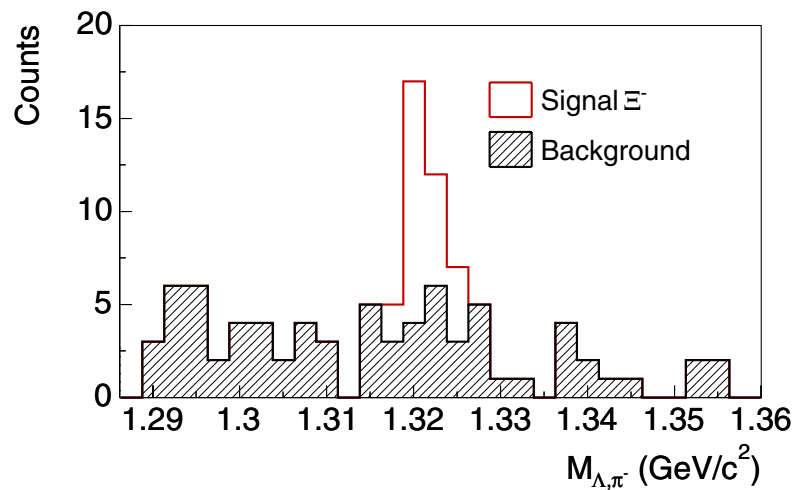


**Figure 5.53.**  $\Xi$  invariant mass spectrum obtained with the reconstruction of 300 HIJING events.

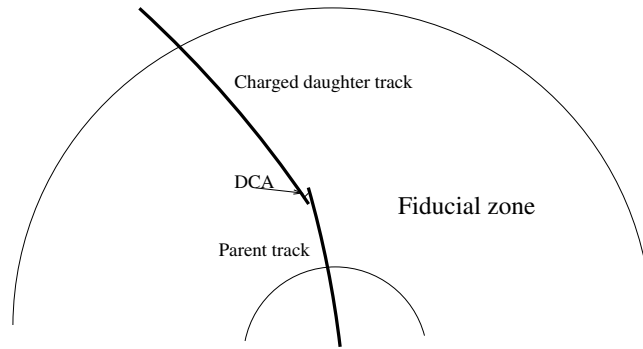


**Figure 5.54.** Geometrical selections in the  $r\phi$  projection used for the kink reconstruction.

The main advantage of the large acceptance available within this second reconstruction strategy is that it allows for a substantial extension of the measurable transverse momentum range, while the efficiency for high- $p_t$  hyperon reconstruction can also be improved a lot by applying  $p_t$  dependent cuts. This will be discussed in detail in Chapter 6.

**5.1.7.2. Kink reconstruction.** Kinks are topological signatures of 1-prong decays. The final objective for kink reconstruction is to identify kaons over a wide momentum range. The most frequent sources of kinks are the muonic decays of charged  $\pi^-$  and K-mesons:  $\pi^- \rightarrow \mu^- \nu$  (branching 99.98%),  $K^- \rightarrow \mu^- \nu$  (branching 63.26%). Since both mesons have a large  $c\tau$ , 780.4 cm and 371.3 cm, respectively, and momentum in the central region of ALICE in a range from few MeV/c to few tens of GeV/c, we concentrate on the search for kinks inside the volume of the TPC. However, the performance of the kink finder will be improved by including the information from the other two tracking detectors in the central barrel, the ITS and TRD.

*The kink-finding algorithm (large decay angles).* Large-decay-angle kinks are reconstructed by associating pairs of tracks that intersect (within some tolerances) in space and have the same charge. The tracks that cross the entire TPC volume are rejected. Each of the tracks left is paired with all the other tracks passing a set of selection criteria: the tracks should not pass far from each other (i.e. should pass through the same or one of the neighbouring sectors and closer than 60 mm in the  $z$  projection), should have the same charge, and the summed number of clusters associated to the two tracks should be within certain boundaries.

For each track pair we find the distance of closest approach (DCA) in the bending plane (or the intersection points) and, if it does not happen inside a specified fiducial region in  $r$ , such a pair is rejected (see Fig. 5.54 for the possible configuration). The fiducial region at this step may exceed the TPC coverage. Then one calculates analytically in linear approximation the distance in space between the tracks at the position of the DCA found in the previous step, and imposes stronger constraints on the fiducial region and the newly calculated value of the DCA. Next, the decay vertex is reconstructed by a numerical minimization of the distance in space between the two helices representing the tracks in a way similar to that used for the  $V^0$  reconstruction (see Section 5.1.7.1 of this document).

Only pairs having the reconstructed kink position within the final fiducial volume are kept. This fiducial volume is limited by the track precision, which in TPC is mainly defined

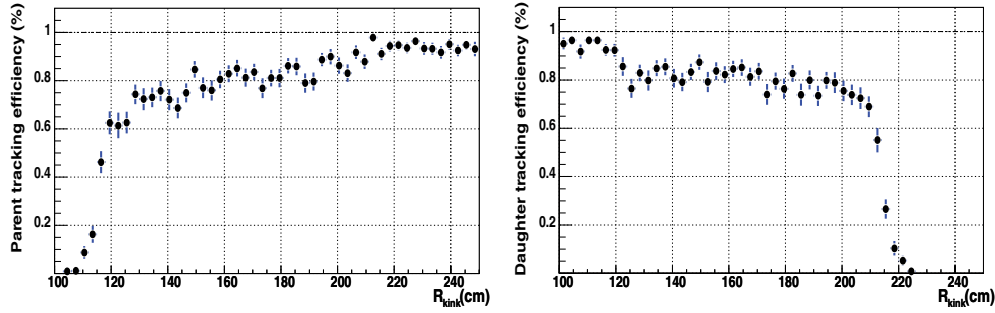


**Figure 5.55.** Left: Tracking efficiency for parent tracks as function of the radial coordinate of the decay vertex. Right: tracking efficiency for daughter tracks as a function of the radial coordinate of the decay vertex.

by the length of the track, and the tracking efficiency. The inner boundary of the fiducial zone is further limited by an increased (with respect to the outer pad rows) occupancy. One can see from Fig. 5.55 that the fiducial area can hardly be extended outside the  $R = 120\text{--}220$  cm range.

In order to further decrease the number of wrong track pairs, the track cluster densities, before and after the DCA position, are calculated for each track in the pair and a set of cuts on these track cluster densities is applied. Further, we compare the cluster densities before the DCA position for the two tracks in order to associate the correct track to the decaying particle and apply an upper limit cut on the curvature for the decaying particle.

Finally, for all the selected kink candidates, we refit the tracks towards the decay vertex, and additional rejection of improbable configurations is achieved by applying a cut on the decay angle. If a track can potentially belong to several kink candidates, only the best combination (the longest tracks, the highest cluster density, the smallest DCA) is kept.

*The kink-finding algorithm (small decay angles).* The second part of the kink-finding algorithm starts with the selection of track candidates for breakpoint analysis. Low-momentum tracks ( $p_t < 1.4$  GeV/c), tracks that are associated to any of the kink candidates found previously, tracks that share at least half of their associated clusters with tracks that belong to a kink candidate, and tracks which have less than a certain number (80) of associated clusters are rejected. For each of the track candidates we obtain at every hit on the track away from the ends (about 20 pad rows) three fits for the track parameters at that hit: a fit to the part of the track upstream, a fit to the part of the track downstream, and a fit to the whole track. Instead of using the classical test-statistics based on the  $\chi^2$  of the mismatch of all the forward–backward parameters at each hit, we explicitly search for a change in direction.

Thus we use the upstream and the downstream parts of the track to define a kink for which we require that its decay vertex be inside the fiducial volume. We define the track breakpoint at the location of the kink for which we register the biggest change in track direction. Once the kink is thus defined, it will be stored if our selection criteria are met. These selection criteria require that the number of clusters associated to the two track segments is higher than certain values (at least 30 clusters for mother and at least 20 clusters for daughter), the decay vertex position is inside the fiducial volume and the DCA between the tracks is less than 0.5 cm, and that the  $p_t$  of the mother is not below 1.4 GeV/c.

The final set of cuts, aimed to reduce the number of found kinks that do not come from a real decay, involve parameters that are well defined only after the last tracking pass including

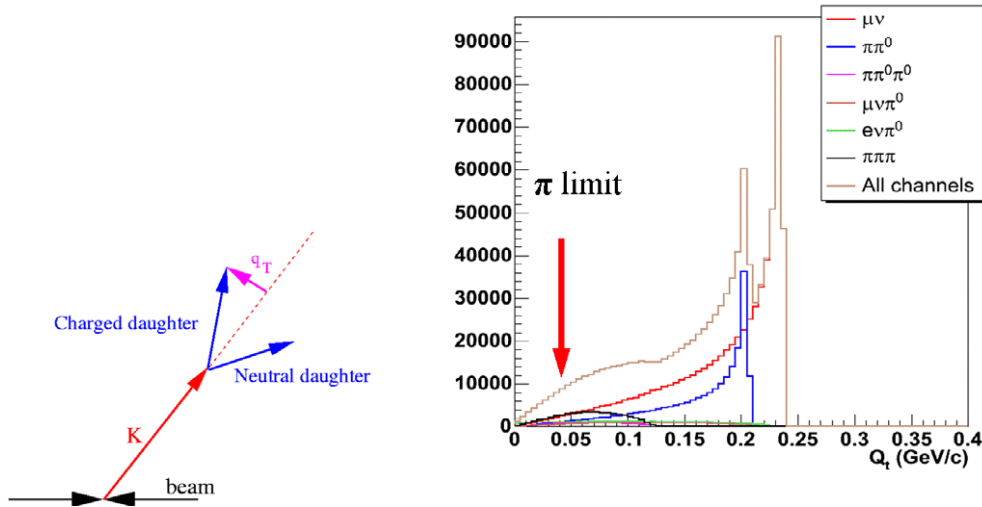


**Figure 5.56.** Left: Definition of the  $q_t$ -value of the charged daughter. Right: The  $q_t$ -value distributions of charged daughters for different kaon decay channels. The branching ratios were taken into account. The arrow indicates the  $q_t$  limit of the pion decays ( $30 \text{ MeV}/c$ ).

the information from the other tracking detectors is performed and the kink parameters are updated accordingly. They include the decay angle and its associated reconstruction error, the DCA, and the transverse momentum of the charged daughter calculated in the rest system of the decaying particle. The pion decays and the bulk of low-momentum accidental crossings between unrelated tracks are rejected by cutting on the transverse charged daughter momentum calculated in the centre-of-mass system ( $q_t$  value, see Fig. 5.56, left panel) of the particle which decays. The right panel of Fig. 5.56 shows the  $q_t$  distributions of charged daughters for different kaon decay channels and the  $q_t$  limit for pion decays.

To improve further the signal-to-background level, one has to check for unrejected accidental crossings. We thus introduce a  $p_t$ - and event-multiplicity-dependent cut on the decay angle by requiring that the kink angle be not smaller than a certain critical angle parametrized in terms of decay angle reconstruction error. Also we require that tracks associated to the decaying particle pass through the ITS and survive the back propagation to the TPC, both parent and daughter tracks are in the TPC acceptance and do not curl back inside the TPC, the impact parameter of the parent track is smaller than some value, and that the distance between the last hit of the parent and the kink vertex position does not exceed a given limit.

Since kaons have a  $p_t$  threshold to pass through the ITS material and TPC cannot track well below  $100 \text{ MeV}/c$ , lower limit cuts on the  $p_t$  of the parent track and on the daughter momentum help to reject more background. The main selection parameters and their final cut values are listed in Table 5.5.

*Estimation of the reconstruction quality.* The quality of the reconstruction can be characterized by its precision, efficiency and probability of obtaining a fake decay vertex. Precision is naturally defined as the width of the distribution of the differences between a true (simulated) parameter, such as momentum or vertex position, and the reconstructed one. Efficiency of the kink finding and the probability of obtaining a fake decay vertex is

**Table 5.5.** Kink selection parameters and cut values.

Selection parameter	Cut value
Fiducial region ( $R$ )	$120 < R < 220$ cm
$q_t$	$> 50$ MeV
Distance of closest approach (DCA)	$< 2$ mm
Decay angle	$> 3\sigma_{\theta_{\text{kink}}}$
$\theta_{\text{parent}}$	$45^\circ < \theta < 135^\circ$
$d_{\text{parent}}$	$< 2$ cm
$d_{\text{daughter}}$	$> 2$ cm
$p_{\text{daughter}}$	$> 100$ MeV/ $c$
$p_{\text{parent}}$	$> 300$ MeV/ $c$

defined as:

$$\varepsilon_{\text{good}} = \frac{\text{number of good found}}{\text{number of good generated}},$$

$$\varepsilon_{\text{fake}} = \frac{\text{number of fake found}}{\text{number of good generated}}.$$

In the above definitions, a ‘good’ (‘findable’) generated decay vertex fulfils the following conditions:

- it is inside the fiducial volume;
- it is inside the TPC acceptance range  $45^\circ < \theta < 135^\circ$ ;
- it comes from a  $K^\pm \rightarrow \mu^\pm \nu$  decay;
- the decay happens in the forward direction;
- it consists of ‘good’ tracks (each of the two tracks has left signals in at least 15 different pad rows).

A ‘good’ found vertex must be:

- inside the fiducial volume;
- coming from a real  $K^\pm \rightarrow \mu^\pm \nu$  decay.

Finally, a found decay vertex is ‘fake’ if it does not come from a real kink decay.

The acceptance of the reconstruction chain is defined in the same way as for the  $V^0$  and cascade particles:

$$A = \frac{\text{number of good generated}}{\text{total number of generated in } 45^\circ < \theta < 135^\circ}.$$

The estimates of the quality of kink reconstruction were obtained using the the detailed TPC simulations and ‘signal enriched’ events for different particle multiplicities and different tracking detectors configurations. The ‘signal enriched’ events were obtained by mixing within realistic HIJING events (central Pb–Pb,  $b$ : 0–2 fm) pure K signal events generated in samples of 500 kaons (50%  $K^+$  and 50%  $K^-$ ) in the TPC acceptance in intervals of 0.5 GeV/ $c$  covering a wide range in transverse momentum, with full momentum and pseudo-rapidity distributions fixed by HIJING model parametrizations, and forced to decay in the TPC fiducial volume ( $120 \text{ cm} < R < 220 \text{ cm}$ ) to the  $K \rightarrow \mu \nu$  decay channel. The mixing was done at the level of ‘summable digits’ (see Chapter 4 of Volume I [3] for details on signal+background event merging technique). The amplitude of the magnetic field was set to 0.2 T. The results are presented below.

**Table 5.6.** Averaged over the interval  $0 < p_t < 7$  GeV/c: The kink radial position resolution ( $\sigma_R$ ), position resolution along the Z-axis ( $\sigma_Z$ ), kink angle resolution ( $\sigma_{\theta_{\text{kink}}}$ ),  $q_t$  resolution ( $\sigma_{q_t}$ ), momentum resolution of the decaying particle ( $\sigma_p$ ), kink-reconstruction efficiency, pion contamination ( $\varepsilon_{\text{good}}$  and  $\varepsilon_{\text{fake}}$ ), and the acceptance ( $A$ ) obtained using the TPC stand-alone.

	$\sigma_R$ (mm)	$\sigma_Z$ (mm)	$\sigma_{\theta_{\text{kink}}}$ (mrad)	$\sigma_{q_t}$ (MeV/c)	$\sigma_p$ (GeV/c)	$\varepsilon_{\text{good}}$ (%)	$\varepsilon_{\text{fake}}$ (%)	$A$ (%)
pp	3.7	1.3	1.7	20.	5.9	70.	0	2.4
Pb–Pb	6.4	2.5	3.3	33.	11.	40.	2.0	2.4

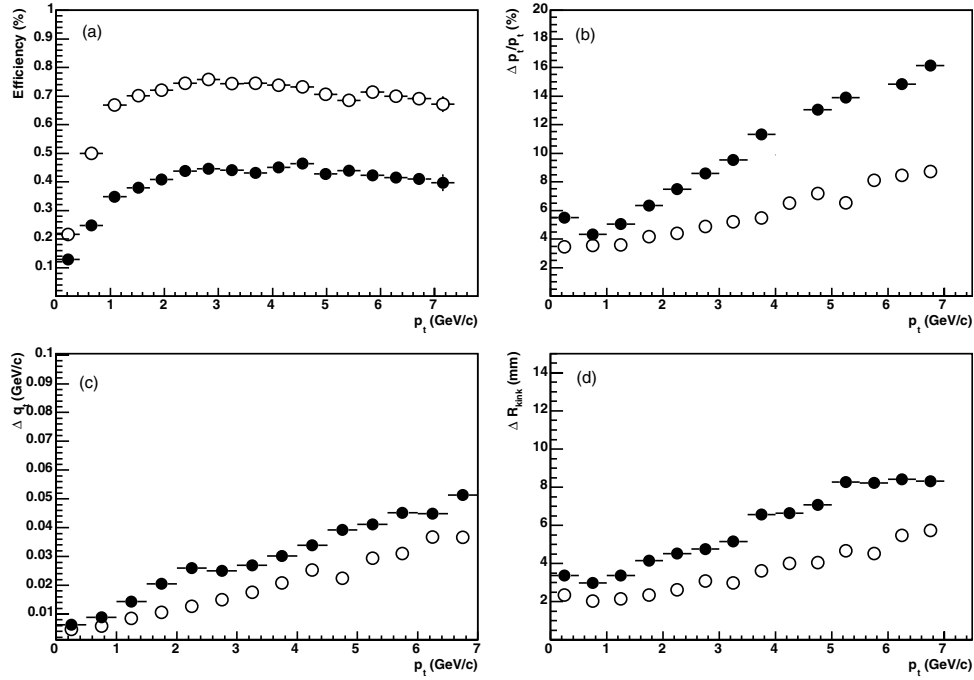


**Figure 5.57.** Efficiency and resolutions of different reconstructed kink parameters reconstructed with the TPC stand-alone as a function of the momentum. Full circles: central Pb–Pb collisions ( $dN_{\text{ch}}/d\eta = 6000$ ). Empty circles: pp collisions.

*Kink reconstruction performance: current results.* In this section we present the performance of the kink reconstruction algorithm, i.e., we address the questions of kink-finding efficiency, of decay vertex position, kink angle,  $q_t$  and kaon momentum resolutions, the question of how the efficiency of the kink finder depends on the momentum of the kaon, on the decay radius, and on the kink angle, and finally the question of pion contamination and background levels.

The kink reconstruction precision and efficiency using the TPC stand-alone for particle densities corresponding to pp and central Pb–Pb collisions are summarized in Table 5.6. The results were obtained for the fiducial zone  $120 < R < 220$  cm.

The values in Table 5.6 depend on the momentum of the decaying meson. This dependence is illustrated in Fig. 5.57. The curves marked by empty circles correspond to the pp low multiplicity. The full circles mark the values obtained for high particle densities expected in central Pb–Pb collisions.

**Table 5.7.** Averaged over the interval  $0 < p_t < 15$  GeV/c (for  $0 < p_t < 7$  GeV/c, in parentheses): The kink radial position resolution ( $\sigma_R$ ), position resolution along the Z-axis ( $\sigma_Z$ ), kink angle resolution ( $\sigma_{\theta_{\text{kink}}}$ ),  $q_t$  resolution ( $\sigma_{q_t}$ ), momentum resolution of the decaying particle ( $\sigma_p$ ), kink reconstruction efficiency, pion contamination ( $\varepsilon_{\text{good}}$  and  $\varepsilon_{\text{fake}}$ ), and the acceptance ( $A$ ) obtained using the ITS, TPC and TRD combined together.

	$\sigma_R$ (mm)	$\sigma_Z$ (mm)	$\sigma_{\theta_{\text{kink}}}$ (mrad)	$\sigma_{q_t}$ (MeV/c)	$\sigma_p$ (GeV/c)	$\varepsilon_{\text{good}}$ (%)	$\varepsilon_{\text{fake}}$ (%)	$A$ (%)
pp	5.3 (2.9)	1.8 (1.1)	0.97 (1.2)	13. (9.6)	5.8 (4.9)	74. (77.)	0	1.5
Pb–Pb	7.5 (4.4)	2.7 (1.6)	1.6 (1.8)	23. (16.)	6.7 (5.3)	42. (45.)	2.9 (2.2)	1.5

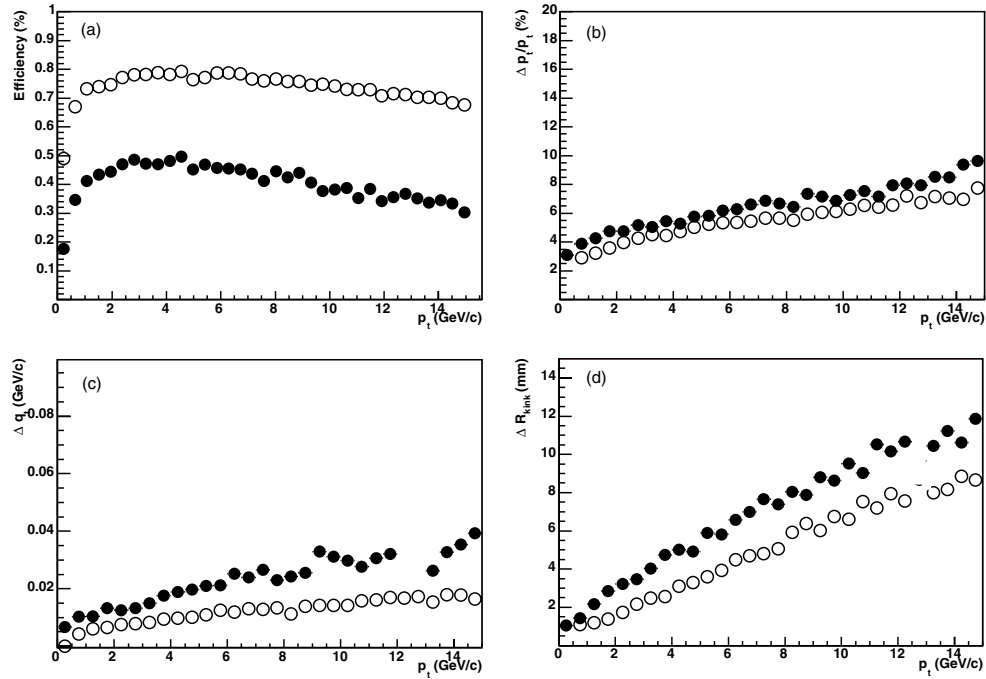


**Figure 5.58.** Efficiency and resolutions of different reconstructed kink parameters reconstructed with the ITS, TPC and TRD combined together. Full circles: central Pb–Pb collisions ( $dN_{\text{ch}}/d\eta = 6000$ ). Empty circles: pp collisions.

Figure 5.57 (d) shows that over the whole  $p_t$  range the position resolution of the decay vertex is below the 1 cm limit (which is roughly the size of the TPC pads). The resolution of the charged daughter transverse momentum in the rest system of the decay, see  $\Delta q_t$  in Figure 5.57 (c), worsens with the increase of the  $p_t$  of the decaying particle mainly due to the decrease in resolution of the momentum of the charged daughter.

Evidently, the addition of the ITS and TRD significantly reduces the uncertainties of the kink parameters. This is due to the fact that both mother and daughter tracks are in this case reconstructed over a large length and so with a better precision. The results are shown in Table 5.7 and Fig. 5.58. The numbers shown in parentheses in Table 5.7 correspond to values averaged over the same  $p_t$  interval as the values shown in Table 5.6.

One can see that including the TRD improves the  $q_t$  resolution by almost a factor 2. Similarly, for particle densities expected in central Pb–Pb collisions, the momentum resolution of the decaying kaon is improved almost by a factor 2 if we add the ITS into the reconstruction.

Thus we found that in a very high track-density environment, the momentum range over which we can use kink reconstruction to identify kaons with momentum resolution better than 10% extends up to 15 GeV/c compared to about 3 GeV/c, when only the TPC information is used. Likewise, in a low-multiplicity environment, we can extend this momentum range from 8 GeV/c, up to about 20 GeV/c by using the combined tracking information. The kink reconstruction efficiency increases only slightly, about 3%.

## 5.2. Track finding in the forward muon spectrometer

**5.2.1. Coordinate reconstruction.** As described in Ref. [33], cathode pad chambers have been chosen as tracking detectors of the forward muon spectrometer with both the cathode planes being read out. In order to reconstruct particle coordinates from pad charge distributions two methods have been developed.

**5.2.1.1. Traditional method.** The ‘traditional’ cluster-finding method [34] is based on a ‘common-sense’ approach and implements the following model. The charge released by a charged particle passing through a chamber induces signals on cathode pads. The pad charge distribution can be described by a two-dimensional integral of the Mathieson function [35]. Therefore, in case of a single particle, its coordinates can be extracted from the fit of the pad charge distribution by a Mathieson-function-based expression. If there are several close particles the number of fit parameters must be increased accordingly, and the number of particle candidates is estimated from the number of local maxima in the pad charge distribution.

The pad sizes of the chambers are defined by the requirement to have the expected occupancy of  $\sim 5\%$ . However, given the uncertainty in the extrapolation of the existing data on particle multiplicities at high rapidities in heavy-ion collisions to the LHC energy, one might see higher than expected chamber occupancies. For high background levels the amount of events with significant overlapping of signal- and background-induced pad charges can become significant. In this case, the estimation of the number of particles from the local maxima is not sufficiently accurate and results in deterioration of the coordinate resolution. The situation is even more complicated since pad charges from both cathodes should be combined during the reconstruction and pad sizes on both cathodes are different for most of the chamber surface. Therefore, a more sophisticated coordinate reconstruction algorithm, based on the pad charge unfolding, is desirable and has been developed as described below.

**5.2.1.2. EM-based method.** The new approach [36] exploits the so-called Maximum Likelihood–Expectation Maximization (MLEM or EM) deconvolution technique [37] (also known as the Lucy–Richardson method [38, 39] or Bayesian unfolding [40]). The essence of the method is that it iteratively solves the inverse problem of a distribution deconvolution. It was widely used in nuclear medicine for tomographic image reconstruction, and was also successfully tried for hit finding in silicon drift detectors [41].

The algorithm starts by finding groups of adjacent pads on one cathode and overlapping them with pads on the other cathode which together form a ‘precluster’ (Fig. 5.59). For a given precluster an array of pixels in the anode plane is built with the size defined by the overlap of pads on both cathodes. It is assumed that each pixel contains a track (Fig. 5.60). If the initial value of energy released by a track  $j$  (i.e. pixel intensity) was  $q_j^0$  (usually all  $q_j^0$ ’s are set to 1) then the following iterative procedure will update its value:

$$q_j^{k+1} = \frac{q_j^k}{\sum_{i=1}^{N_{\text{pads}}} c_{ij}} \sum_{i=1}^{N_{\text{pads}}} c_{ij} \frac{Q_i}{f_i^k} \quad \text{with} \quad f_i^k = \sum_{j=1}^{N_{\text{pix}}} c_{ij} q_j^k,$$

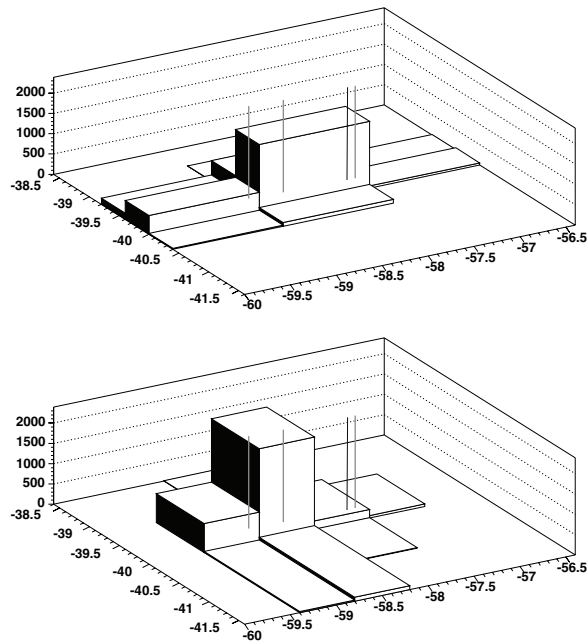


**Figure 5.59.** Example of a ‘precluster’. The lines indicate hit positions. The right-most two lines show the simulated and reconstructed muon hits (horizontal axes: coordinates of the pad centres (cm), vertical axis: charge (ADC)).

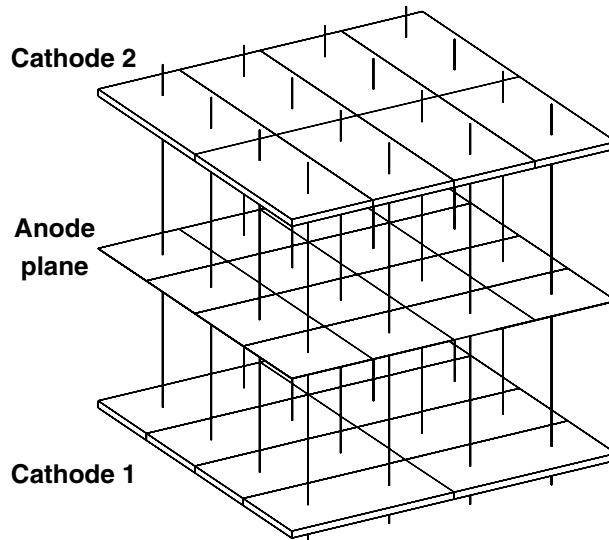


**Figure 5.60.** Initial pixel array in the anode plane built for a two-cathode precluster.

where  $f_i^k$  is the expected signal on pad  $i$  if the pixel intensity was  $q_j^k$  (at the  $k$ -th iteration),  $Q_i$  is the measured signal on pad  $i$ ,  $c_{ij}$  is the pixel-to-pad coupling (given by the Mathieson integral), and  $N_{\text{pix}}$  is the number of pixels in the array.

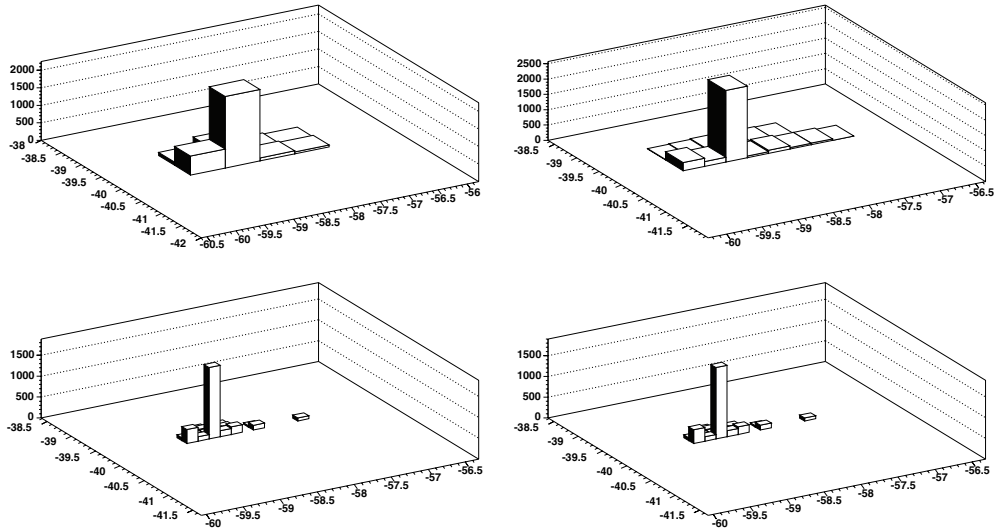


**Figure 5.61.** Pixel arrays found by the MLEM method on each pass for the precluster from Fig. 5.59.

After several iterations (10–15) the larger pixel dimension is decreased by two and pixels with the lowest intensity are removed if the total number of pixels exceeds the number of pads. This is necessary in order to ensure the unique solution of the system. Then the iterative procedure is performed again. The algorithm stops when the pixel size becomes sufficiently small (1 mm) (see Fig. 5.61). After that, the resulting pixel clusters are used as fitting seeds for the fitting procedure.

Thus, the proposed method transforms the ‘two-cathode fixed-pad-size’ problem into the ‘one-anode-plane variable-pixel-size’ one. Effectively, it improves the detector segmentation offering better conditions for making a decision about complex cluster splitting.

Owing to the iterative character of the proposed procedure, and the necessity to perform several passes in order to achieve the required pixel size, the algorithm is expected to be ‘intrinsically slow’. However, if it is applied only for complex clusters (with large enough size) one can reduce the processing time.

*5.2.1.3. Cluster reconstruction results.* The results presented below were obtained for dimuons with  $180^\circ - \theta = 2-9^\circ$  from  $\Upsilon$  decays. The effect of the background was simulated by summing hits from HIJING-generated [42] central events with 6000 charged particles per rapidity unit. Two such events summed together made one so-called nominal background event. The merged (signal+background) events were processed with the described reconstruction methods. Figure 5.62 shows coordinate residuals (difference between reconstructed and simulated coordinates) for the bending plane in different tracking stations. One can see that for a high background level, where the probability for charges from different particles to overlap is large (the percentage of the muon activated pads, contaminated by the background originated charge, is presented in Fig. 5.63), the EM-based algorithm outperforms the traditional method on account of its better ability to resolve complex clusters with a similar processing time.

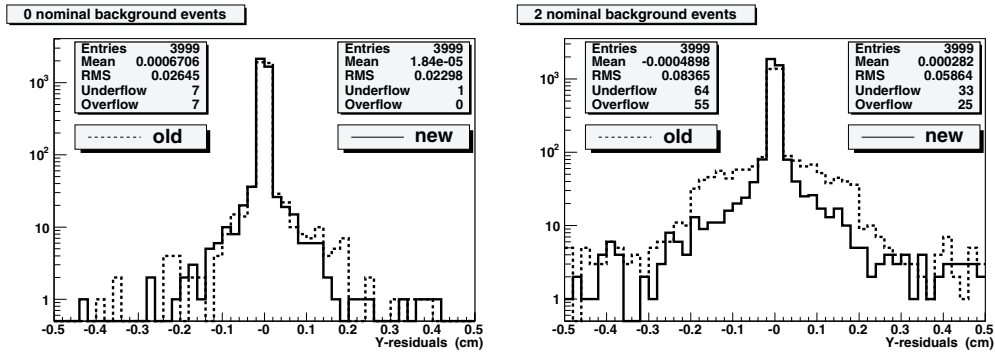


**Figure 5.62.** Coordinate residuals for the bending plane for the first station (closest to the interaction point). The solid histogram shows results for the EM-based (new) cluster finder, dashed for the traditional (old) one. Left: only muons from upsilon decays are simulated. Right: two nominal background events are added.

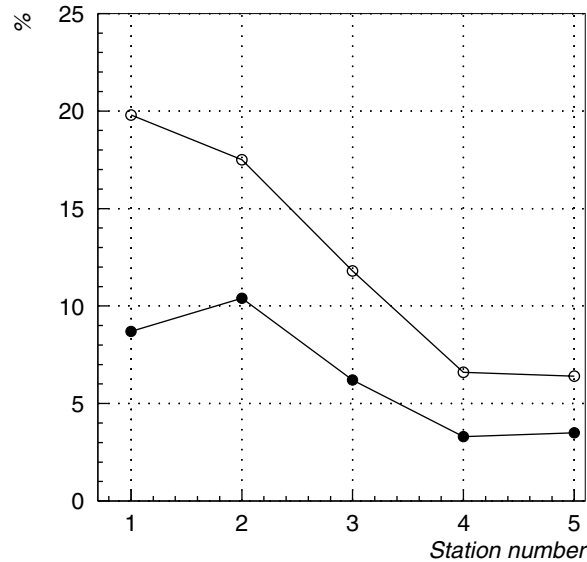


**Figure 5.63.** Average percentage of pads containing charge from muons from upsilon decays overlapped with background-originated charges relative to the total number of muon activated pads versus chamber station number: closed circles for one nominal background event, open circles for two. Lines are drawn to guide the eye.

**5.2.2. Track reconstruction.** Since the muon spectrometer geometry is quite different from that of the central detectors (notably, the large distance (up to 2.5 m) between consecutive measurements), it was not obvious from the beginning that the Kalman filter (see, for example, [43]) would demonstrate the best performance possible as compared with other methods. That is why another algorithm was developed originally which further served as a reference point for Kalman filter studies.

**5.2.2.1. Original track reconstruction method.** The ‘original’ method [44] is motivated by the Kalman filter strategy, i.e. implements a combined track-finding and fitting approach as

follows. Track candidates start from segments (vectors) found in the last two tracking stations, where a segment is built from a pair of points from two chamber planes of the same tracking station. Then each track is extrapolated to the first station and segments or single hits found in the other stations are added sequentially. For each added station, the track candidate is refitted and the hits, giving the best fit quality, are kept. In order to increase the track finding-efficiency the procedure looks for track continuation in the first two stations in direct and reverse order. A track is validated if the algorithm finds at least three hits (out of four possible) in the detector planes behind the dipole magnet, at least one hit (out of two) in the station located inside the magnet and three hits (out of four) in the chambers before the magnet.

Because of the repeated track-fitting procedure (which is done explicitly) one can expect the method to be somewhat slow.

*5.2.2.2. Kalman filter.* A Kalman track seed is created for all track segments found in detector stations 4 and 5 (as for the previous method). Tracks are parametrized as  $(y, x, \alpha, \beta, q/p)$ , where  $y$  is a coordinate in the bending plane,  $x$  is a non-bending coordinate,  $\alpha$  is a track angle in the bending plane with respect to the beam line,  $\beta$  is an angle between the track and the bending plane,  $q$  and  $p$  are the track charge and momentum, respectively.

A track starting from a seed is followed to station 1 or until it is lost (if no hits in a station are found for this track) according to the following procedure. It propagates the track from the current  $z$ -position to a hit with the nearest  $z$ -coordinate. Then for given  $z$  it looks for the hits within certain window  $w$  around the transverse track position. After this there are two possibilities. The first one is to calculate the  $\chi^2$ -contribution of each hit and consider the hit with the lowest contribution as belonging to the track. The second possibility is to use a so-called track branching and pick up all the hits inside the acceptance window. Efficiency and mass resolution tests have shown that the second way gives a better result [45, 46] and so is used in the current implementation.

After propagation to chamber 1 all tracks are sorted according to their quality  $Q$ , defined as

$$Q = N_{\text{hits}} + \frac{\chi_{\text{max}}^2 - \chi^2}{\chi_{\text{max}}^2 + 1},$$

where  $\chi_{\text{max}}^2$  is the maximum acceptable  $\chi^2$  of tracks. Then duplicated tracks are removed, where duplicated means having half or more of their hits shared with another track with a higher quality.

Despite the modifications, for high-background levels, the Kalman filter showed somewhat lower tracking efficiency with respect to the original method. It was claimed in Ref. [47] that the introduction of the smoothing technique into the Kalman filter should extend its capabilities and make it a more flexible and efficient tracking tool. Smoothing means the evaluation of track parameters at any point along the track after its reconstruction, i.e., using information from all the measured points belonging to the track. Thus, the smoother provides the most optimal conditions for a detection of wrongly assigned hits.

Given that the smoother procedure exists, the following tracking strategy can be proposed. If the background conditions are heavy and result in loss of efficiency, the size of the window used to accept measurements during the direct track propagation should be increased. This allows one to find track continuation in the detector geometry with large distances between consecutive measurements even when the assumed measurement error is underestimated in some cases (as usually happens for overlapped clusters). Then the found track should be passed through the smoother in order to reject measurements with  $\chi^2$  above certain cut (outliers).

**Table 5.8.** Performance results of the original track-finding method and the Kalman filter for particle coordinates reconstructed with the traditional method. The background level is expressed in terms of the nominal background events. The single-track efficiency is shown, defined with respect to the number of fully contained tracks (see the text). The mass resolution is taken from the fit to the Gaussian in the  $0.5 \text{ GeV}/c^2$  range around the peak position. Results for the Kalman filter are shown for two sets of parameters: ‘tight’ muons with  $w$  and  $\chi_{\text{cut}}^2$  equal to  $8\sigma$  and 25 and ‘loose’ muons (in parentheses) with  $12\sigma$  and 100 (with additional constraint  $w_y < 5 \text{ cm}$ ).

Original tracking, 2500 $\Upsilon$ 's			
Background level	0	1	2
Efficiency (%)	98.8	94.7	85.9
Mass resolution ( $\text{MeV}/c^2$ )	$95.3 \pm 2.4$	$108.4 \pm 4.3$	$153.6 \pm 7.1$
CPU time/event (s)	0.9	3.7	8.1
Kalman filter, 2500 $\Upsilon$ 's			
Background level	0	1	2
Efficiency (%)	98.0	87.8	70.6
	(98.9)	(93.5)	(83.6)
Mass resolution ( $\text{MeV}/c^2$ )	$90.7 \pm 2.2$	$95.3 \pm 3.1$	$107.2 \pm 3.2$
	( $98.2 \pm 2.6$ )	( $109.2 \pm 3.7$ )	( $137.2 \pm 5.2$ )
CPU time/event (s)	0.4	1.3	4.9
	(0.4)	(1.4)	(7.6)

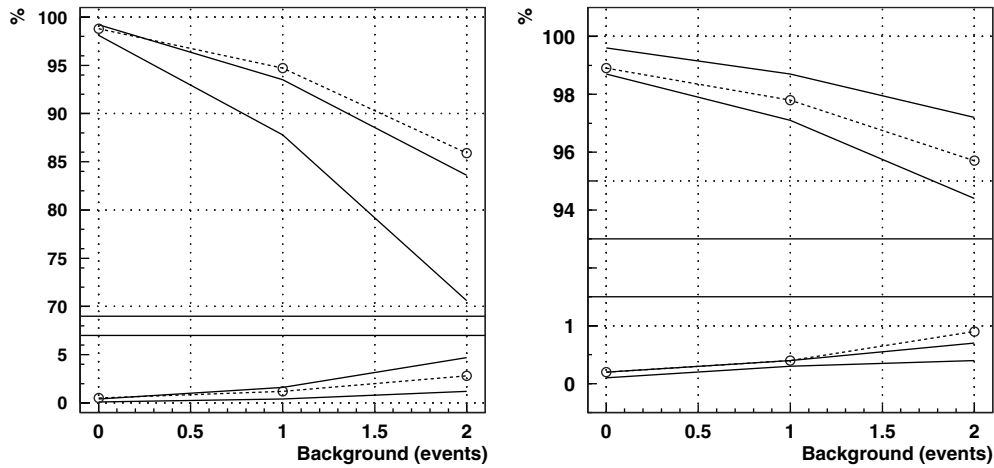


**Figure 5.64.** Track-finding efficiency (upper part) and percentage of ‘bad’ tracks (lower part) versus occupancy, expressed in terms of the number of added nominal background events, after the traditional coordinate reconstruction method (left) and EM-based coordinate reconstruction (right). Closed circles: original tracking; the bands show results for Kalman filter for different algorithm parameters. Lines are drawn to guide the eye.

The price to pay for the smoother is the extra information to be kept for each point of the track candidate (vectors of extrapolated and filtered track parameters, extrapolated and filtered covariance matrices and propagation matrix) and additional processing time due to wider acceptance windows. However, since there are about 10 points per track on average, the amount of extra information is quite moderate. In addition, by changing two correlated parameters (acceptance window  $w$  and outlier rejection criterion  $\chi_{\text{cut}}^2$ ) it is possible to tune

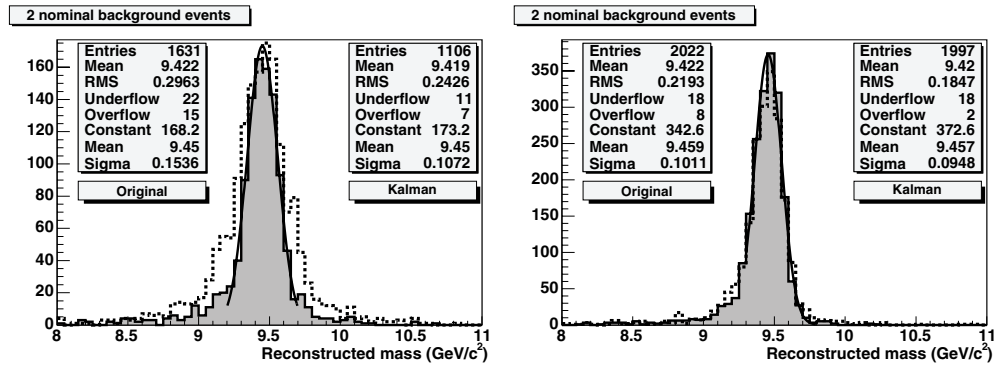


**Figure 5.65.** Reconstructed dimuon invariant mass after the traditional coordinate reconstruction method (left) and EM-based coordinate reconstruction (right): histograms are for the Kalman filter (‘tight’ muons), dashed lines for the original method.

**Table 5.9.** The same as in Table 5.9 for hits reconstructed with the EM-based method. ‘Tight’ muons with  $w = 4\sigma$  and  $\chi_{\text{cut}}^2 = 25$  and ‘loose’ muons with  $8\sigma$  and  $100$  ( $w_y < 5$  cm).

Original tracking, 2500 $\Upsilon$ 's			
Background level	0	1	2
Efficiency (%)	98.9	97.8	95.7
Mass resolution (MeV/c <sup>2</sup> )	91.0±2.2	96.4±2.6	101.1±2.9
CPU time/event (s)	0.7	3.6	8.2
Kalman filter, 2500 $\Upsilon$ 's			
Background level	0	1	2
Efficiency (%)	98.7 (99.6)	97.2 (98.7)	95.0 (97.2)
Mass resolution (MeV/c <sup>2</sup> )	88.6±2.1 (92.4±2.3)	91.6±2.2 (98.6±2.8)	94.8±2.4 (99.3±2.9)
CPU time/event (s)	0.4 (0.4)	1.3 (1.4)	4.3 (7.4)

the algorithm to have a high tracking efficiency with good track quality and reasonable CPU consumption.

**5.2.2.3. Track reconstruction results.** The performance of the track reconstruction methods has been tested for dimuons from  $\Upsilon$  decays. The single-track efficiency was defined with respect to the number of fully contained tracks, i.e. tracks passing through all the tracking chambers (in order to exclude the geometrical acceptance effect at the detector edges).

The results [48] for coordinates reconstructed with the traditional method are summarized in Table 5.8 and Fig. 5.64 (left), where the single-track efficiency and percentage of ‘bad’ tracks are plotted for different background levels. ‘Bad’ is defined as a track having at least one wrong hit assignment. The track reconstruction quality can be evaluated from the dimuon invariant mass distribution (Fig. 5.65 (left)), which also shows the impact on one of the physics cases (possibility to resolve  $\Upsilon$  states). One can see that by varying the Kalman filter parameters it is possible to approach the single-track efficiency obtained in the original method having still higher track quality, which gives results satisfactory from the physics point of view ( $\Upsilon$  mass resolution below 100 MeV/c<sup>2</sup>). When the more sophisticated

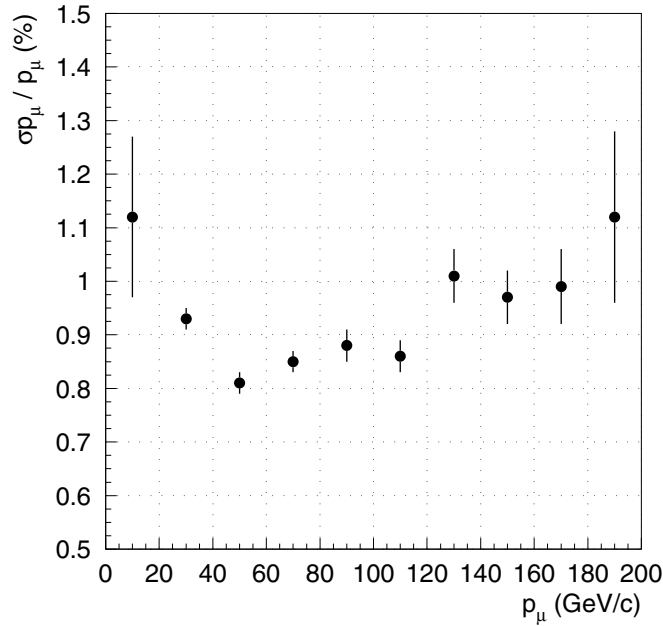


Figure 5.66. Relative momentum resolution vs. momentum for muons from upsilon decays.

EM-based hit-finding algorithm was used the situation became much easier, and the results were close to the ones obtained for GEANT smeared hits (see Table 5.9 and Figs. 5.64 (right) and 5.65 (right)).

*5.2.2.4. Conclusions.* The results presented demonstrate that the muon spectrometer parameters and reconstruction methods allow us to achieve the expected performance (see also Fig. 5.66) for the current estimate of particle multiplicity with a large safety margin.

### 5.3. High-Level Trigger reconstruction

The High-Level Trigger (HLT) combines and processes the full information from all major detectors in a large computer cluster. Data rate reduction is achieved by reducing the event rate by selecting interesting events (software trigger) and by reducing the event size by selecting sub-events (e.g. pile-up removal in pp interactions) and by advanced data compression. The overall processing and data flow architecture of the system is driven by the inherent readout granularity and the requirement for a complete event reconstruction and trigger decision. The internal topology will have a tree-like structure, where the result from the processing on one layer (e.g. track segments on the sector level) will be merged at a higher layer (sector merging and track fitting). Finally all local results will be collected from the sub-detectors (e.g. TPC and ITS) and combined on a global level where the complete event can be reconstructed and trigger decisions can be issued. Reconstruction chains for the barrel detectors and the forward muon spectrometer have been developed and benchmarked.

*5.3.1. TPC reconstruction.* The main processing task for the central barrel detector system is to reconstruct the tracks in the TPC, and in a final stage combine the information from all

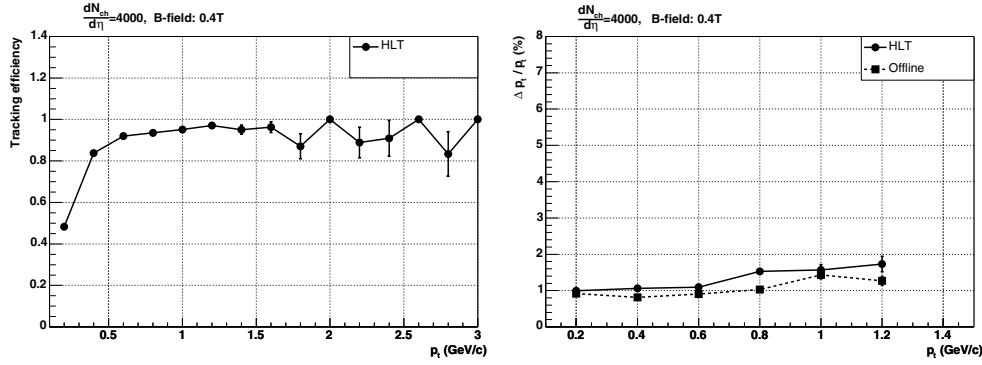


**Figure 5.67.** Performance of the HLT track-finding algorithms: CF and TF efficiency (left) and relative transverse momentum resolution (right) as a function of the transverse momentum for a pseudorapidity density of 4000.

central detectors. Given the uncertainties of the anticipated particle multiplicities, different approaches are being considered for the TPC track reconstruction.

**5.3.1.1. TPC cluster finder and track follower.** The conventional approach of TPC track reconstruction consists of a Cluster Finder (CF) and a subsequent Track Follower (TF). In a first step the Cluster Finder reconstructs the cluster centroids from the generated two-dimensional charge distributions in the TPC pad row planes. Together with the position of the pad row planes the centroids are interpreted as three-dimensional space points along the particle trajectories, and serve as an input for the Track Follower which connects the space points into track segments. A final helix-fit of the track segments provides the track parameters and thus the kinematic properties of the particles.

Such an approach has been implemented and evaluated on simulated TPC data [49]. The algorithms were originally developed for the STAR L3 trigger [50] and consist of a straightforward centre-of-gravity calculation of cluster centroids, and a Track Follower which applies conformal mapping on the space points. The latter enables the circular tracks to be fitted by a linear parametrization, thereby significantly reducing the computational requirements. The purpose of the Track Merger is to merge multiple-track segments belonging to the same particle trajectory. This is necessary if track finding is performed independently in the different TPC sectors.

The overall measured performance of the reconstruction chain represented by the track finding efficiency and the relative transverse momentum resolution as a function of the transverse momentum are shown in Fig. 5.67.

The track-finding efficiency for  $dN_{ch}/d\eta \leq 4000$  is similar to that achieved by the standard offline reconstruction chain—albeit at the cost of a slightly higher fake rate (Fig. 5.68). The algorithm is one order of magnitude faster than the off-line one. It is well suited for the lower multiplicity regime. For higher multiplicities the observed track-finding performance deteriorates. This is due to the increasing detector occupancy which gives rise to a significant amount of overlapping clusters. In such a scenario the Cluster Finder fails to reconstruct the cluster centroids because of its incapability to deconvolute overlapping charge distributions.

The track-finding performance discussed above was determined exclusively for primary tracks. In order to get an estimate of the reconstruction capabilities of secondary particles like K and  $\Lambda$  particles, a second pass was done during the track-finding step, where

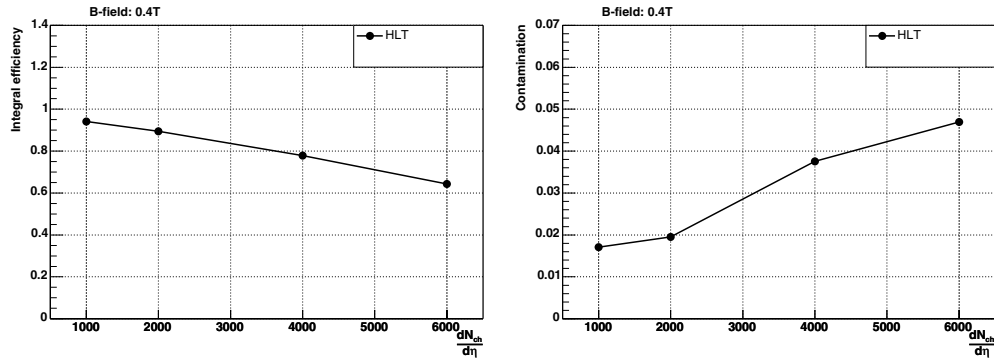


**Figure 5.68.** Performance of the HLT track-finding algorithms: CF and TF integral efficiency and contamination of fake tracks as a function of multiplicity.

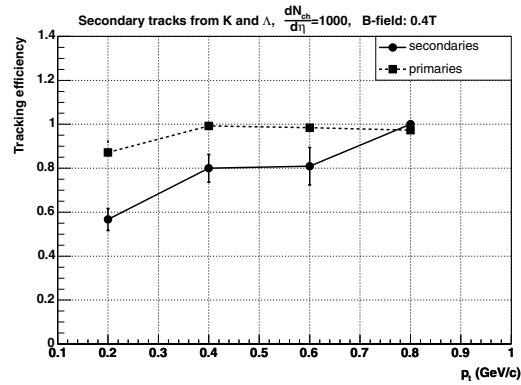


**Figure 5.69.** Track finding efficiency of secondary tracks from decay of K and  $\Lambda$  particles.

the second track-finding pass took the unused clusters from the first pass as input. No vertex constraint was imposed on these secondary tracks, and thus the conformal mapping of the space points was calculated relative to the first assigned cluster to a track. In Fig. 5.69 the resulting efficiency as a function of  $p_t$  is shown for events with multiplicity of  $dN_{ch}/d\eta \leq 1000$ . The track-finding efficiency is  $\sim 60\%$  for the low-momentum bin, while at higher  $p_t$  it increases to  $>80\%$ . It should be noted that the current HLT algorithm was not tuned for the detection of secondary tracks with the exception of the second track-finding pass adaptation.

**5.3.1.2. Iterative track-finding and cluster deconvolution.** In the sequential track-finding approach described in the previous section, the cluster centroids are obtained using a straightforward centre-of-gravity calculation. Such an algorithm has obvious limitations when applied to a high occupancy environment, since the lack of information about the tracks biases the centroid calculation in the case of overlapping charge distributions. The main objective of iterative track-finding is to provide the track information prior to the cluster finding in order to better fit and unfold the overlapping clusters. From this the correct cluster centroids should be obtained.

In this approach, the pattern recognition scheme consists of two main parts: track-candidate finding and cluster fitting. In a first step an implementation of the Hough transform

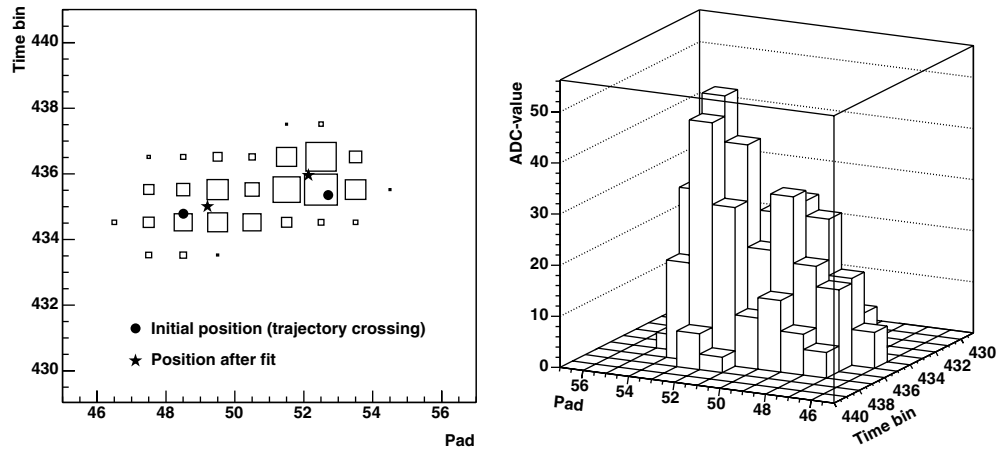


**Figure 5.70.** Illustrating fitting and deconvolution of overlapping clusters. Left: The circles mark the initial position given as input to the fitting routine, while the star marks the best-fit values returned from the fit. Right: Same clusters shown using a lego plot.

is applied to the raw ADC data in order to obtain a list of track candidates. These track segments serve as input for the Cluster Fitter, which reconstructs the cluster centroids along the particle trajectories by fitting the respective charge distributions to a parametrized shape. Finally, the assigned clusters are fitted to a helix in order to obtain the best estimate of the track parameters.

The shape of the clusters is given by the convolution of the response functions of the readout pads. Both the pad and time response functions have a close to Gaussian shape. The spread of the electron clouds due to diffusion is also Gaussian. The cluster model can thus to a good approximation be described with a two-dimensional Gaussian distribution whose widths depend on the geometry of the pads and the track parameters. A total of five independent parameters are needed to fully describe the model. These parameters vary for each cluster, so without any prior knowledge they would all have to be fitted for. In the case of overlapping clusters such a fitting procedure would be a very demanding task as no information about the number of contributing tracks, nor the shape for each individual charge distributions, is known. Any prior knowledge of track parameters could provide the fitting procedure with an improved initial guess of the parameters, or even reduce the number of parameters to vary in a fit. The procedure can also be extended to other models for the cluster shape, e.g. to account for asymmetric Gaussian distributions. In that case the two-dimensional Gaussian given above may be replaced with an alternative model, and the fitting procedure is done accordingly. An example of deconvolution of two overlapping clusters is shown in Fig. 5.70. In this case the input to the fitting routine is the two sets of five initial parameters, each consisting of the position in the pad row plane (illustrated by the circle markers), the widths of the distribution in two dimensions, and the amplitude. The initial values of these parameters are determined from the results obtained by the preceding track-finding algorithm. The initial positions are taken as the crossing point of the computed tracks with the pad row plane.

**5.3.1.3. Hough transformation.** For large particle multiplicities clusters in the TPC start to overlap, and deconvolution becomes necessary in order to achieve the desired track-finding efficiencies. The cluster shape is highly dependent on the track parameters, and in particular on the track crossing angles with the pad row and drift time. In order to properly deconvolute

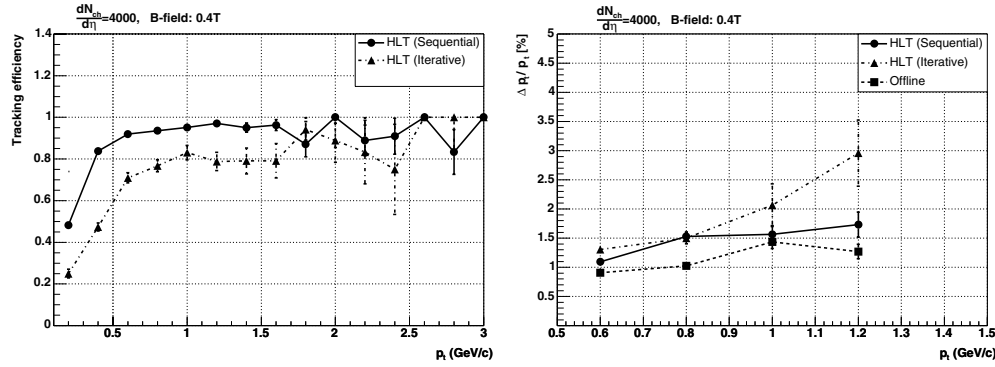


**Figure 5.71.** Track-finding efficiencies (left) and relative transverse-momentum resolution (right) as a function of the transverse momentum for  $dN_{ch}/d\eta = 4000$ . All tracks with  $p_t \geq 0.15$  GeV/c have been included in the evaluation.

the overlapping clusters, knowledge of the track parameters that produced the clusters is necessary. The Hough transform is well suited for that purpose, as it can be applied directly on the raw ADC data thus providing an estimate of the track parameters. If extracted track parameters are sufficiently accurate they can be used for event reconstruction directly, or optionally refitted after a cluster deconvolution step.

The Hough transform is a standard tool in image analysis that allows recognition of global patterns in an image space by recognition of local patterns (ideally a point) in a transformed parameter space. The basic idea is to find curves that can be parametrized in a suitable parameter space. In its original form one determines a curve in parameter space for a signal corresponding to all possible tracks with a given parametric form to which it could possibly belong [51]. All such curves belonging to the different signals are drawn in parameter space. That space is then discretized and entries are stored in a histogram. If the peaks in the histogram exceed a given threshold, the corresponding parameters are found.

In our case the local track model is a helix. In order to simplify the transformation, the TPC is divided into sub-volumes in pseudo-rapidity. If one restricts the analysis to tracks originating from the vertex, the circular track in the  $\eta$ -volume is characterized by two parameters: the emission angle with the beam axis  $\psi$ , and the curvature  $\kappa$ .

*Grey-scale Hough transformation.* Each ADC value above a certain threshold is transformed from  $(R, \varphi)$  space to  $(\psi, \kappa)$  space using the following equations:

$$R = \sqrt{x^2 + y^2} \quad \varphi = \arctan \frac{y}{x} \quad \kappa = \frac{2}{R} \sin(\varphi - \psi). \quad (5.10)$$

Each ADC creates a sinusoidal curve extending over the whole  $\psi$  range of the parameter space. All the corresponding bins in the histogram are incremented with the corresponding ADC value. The superposition of these point transformations produces a maximum at the circle parameters of the track. The track recognition is now done by searching for local maxima in the parameter space.

Figure 5.71 shows the track-finding efficiency as a function of the transverse momentum for a multiplicity of  $dN_{ch}/d\eta = 4000$ . All primary particles with  $p_t \geq 0.15$  GeV/c were included in this evaluation, and the boundaries of the parameter space were adapted accordingly. The efficiency is lower than for both the HLT sequential and offline track-reconstruction algorithms. In particular, the efficiency drops in the low-momentum region for  $p_t \leq 0.5$  GeV/c.

The main reason for the moderate performance of the grey-scale Hough transform approach is the presence of too many fake track candidates.

*Fast Hough transformation.* A better approach is the so called ‘counting’ Hough transform track-finding procedure [52]. The method combines a linear Hough transformation with fast filling of the parameter space. Taking into account that the TPC is a continuous track-finding device and therefore all pad rows have to contribute to a good track candidate, the method is based on the counting of the number of gaps (empty pad rows) along the track candidate trajectory. Parameter space bins with large gaps are identified as fake-track candidates and removed immediately from the rest of the filling procedure. The counting procedure also allows one to perform the Hough transformation only for the cluster (identified as a sequence of signals located on neighbouring pads) borders, and the whole algorithm becomes several times faster. In addition, the parameter space is linearized using a conformal mapping transformation of the Cartesian coordinate system:

$$x \rightarrow \alpha = \frac{x}{x^2 + y^2}, \quad y \rightarrow \beta = \frac{y}{x^2 + y^2}. \quad (5.11)$$

In this way, track trajectories become straight lines and can be parameterized by their position  $\beta_1, \beta_2$  on two straight lines parallel to the  $\beta$  axis. Then the  $(\psi, \kappa)$  space defined in Eq. (5.10) is replaced by the  $(\beta_1, \beta_2)$  space and the Hough transformation becomes linear:

$$\beta_1 = A + B \beta_2. \quad (5.12)$$

Moreover, since the coefficients  $A$  and  $B$  depend only on the pad position, they are calculated in advance and used through look-up tables during the filling process. The position of the two straight lines in the conformal mapping space and the order in which the pad rows are processed were chosen so as to optimize both the track finding and time performances of the algorithm.

The methods described above speed up drastically the transformation and result in a simple peak structure in the parameter space (Fig. 5.72). The obtained track-finding efficiency as a function of track transverse momentum is shown in Fig. 5.73 (left). The efficiency is better than 95% for  $p_t \geq 0.6$  GeV/c and does not depend on the event multiplicity. The rate of fake-track candidates is less than 5%. Three main sources of inefficiency were identified:

- overlapping or merging of track candidate peaks in the parameter space;
- division in sub-volumes of pseudorapidity;
- geometrical effects near the dead zone between TPC sectors.

As expected, the binning of the parameter space dominates the resolution and implies the relative transverse momentum resolution which rises linearly with the transverse momentum (Fig. 5.73, right). Note the fact that the resolution shows no significant dependence on the event multiplicity.

*5.3.1.4. Timing performance.* The overall computing time needed for the TPC track finding for different multiplicities is shown in Table 5.10. The reference platform was an Intel Pentium 4 (2.8–3 GHz) which corresponds to a performance rating of approximately 1 kSPECint. The CF + TF approach produces track parameters as well as space points for refitting and  $dE/dx$  analysis, while the fast Hough transform just results in track parameters. Assuming a multiplicity of  $dN_{ch}/d\eta = 2000\text{--}4000$ , as predicted by many models based on RHIC results, a farm of about 1000 CPUs would suffice to solve the pattern recognition task within the time budget of about 5 ms.

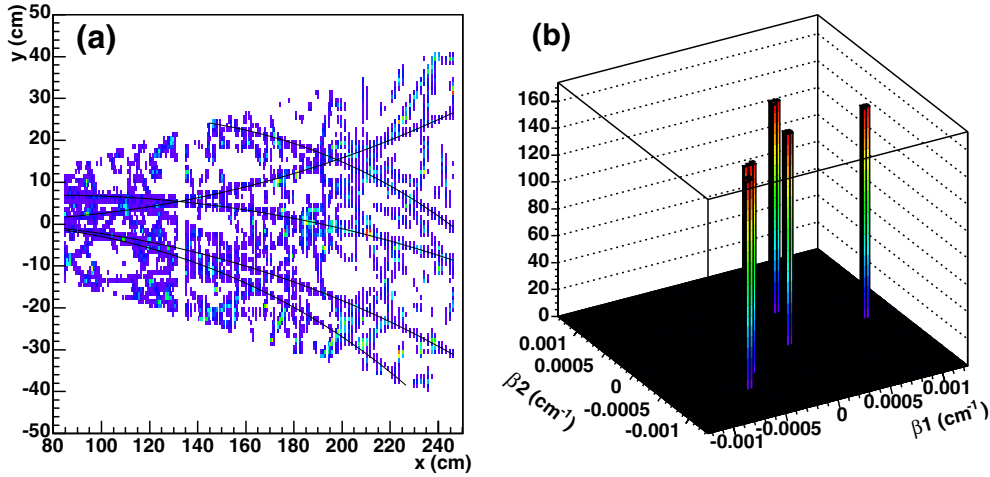


**Figure 5.72.** (a) One pseudorapidity slice of single-TPC-sector data. The reconstructed tracks are shown as solid curves; (b) The corresponding parameter space histogram. The peaks represent the reconstructed tracks.

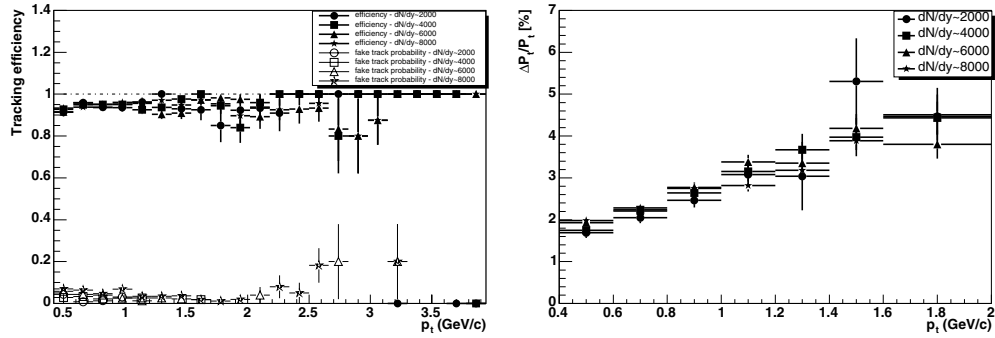


**Figure 5.73.** Performance of the HLT track-finding algorithms: fast Hough transform efficiency and fake-track abundance for different pseudorapidity densities (left) and the transverse-momentum resolution as functions of the transverse momentum (right).

**Table 5.10.** Timing measurements of the TPC track-finding codes. The benchmarks were performed on a 1 kSPECint machine (Intel Pentium 4, 2.8 GHz).

$dN_{ch}/d\eta$	0	2000	4000	6000	8000
CF+TF (s)		6.3	13.2	21.2	
Fast HT (s)	0.8	3.5	5.8	8.7	11.8

**5.3.2. ITS reconstruction.** The tracks found in the TPC are propagated into the Inner Tracking System (ITS). The offline code was adapted for the processing of the ITS data and the track finding. The ITS vertex reconstruction uses the clusters found in the two layers of the Silicon Pixel Detector (SPD). It provides the longitudinal vertex position to the Hough transform track finding in the TPC. Two versions of the ITS track reconstruction have been studied—with and without the two Silicon Drift Detector (SDD) layers. There are several reasons to consider an ITS track finding without SDD. The first one is the fine segmentation of the SDD readout and hence the large amount of hardware resources with

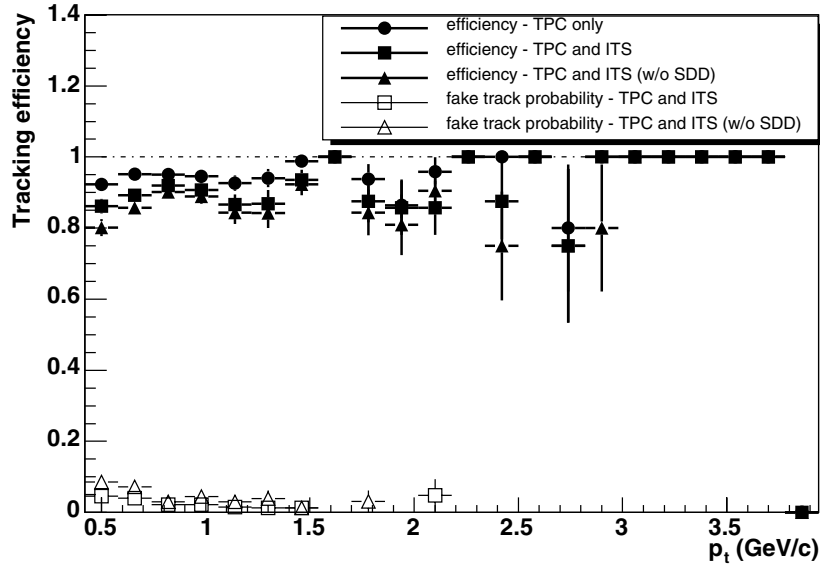


**Figure 5.74.** Performance of the HLT ITS track finding: Combined fast TPC Hough transform and ITS track-finding efficiency (filled markers) and fake track abundance (open markers) as a function of the transverse momentum for a pseudorapidity density of 4000.

which the HLT system has to be equipped. The second reason is related to the possible misalignment and miscalibration effects which might appear during the online processing of the SDD data. In addition, an ITS reconstruction without SDD allows one to speed up significantly both the cluster finding and track reconstruction. The efficiency of the combined track finding (fast Hough transform and ITS) for a pseudo-rapidity density of 4000 is shown in Fig. 5.74. As can be seen, the prolongation of the TPC tracks into the ITS results in about 5% loss in the efficiency. The exclusion of the SDD leads to an acceptable performance deterioration of between 2% and 5% depending on the transverse momentum. As expected, the angular and impact parameter resolutions of the prolonged tracks are dominated by the ITS SPD and therefore they are comparable to the offline results. For example, the transverse impact-parameter resolution for tracks with  $p_t \sim 1 \text{ GeV}/c$  is about  $60 \mu\text{m}$ . Based on this impact-parameter resolution, it becomes possible to select track candidates stemming from a secondary vertex and build an efficient  $D^0$  trigger for the HLT. For the purpose, an optimized for time performance version of the offline  $D^0$  finder code is used to process HLT-tracks. The  $D^0$  invariant-mass resolution is found to be  $35 \pm 5 \text{ MeV}/c^2$  for  $D^0$  transverse momentum of  $2 \text{ GeV}/c$  — about 2–3 times larger than the offline result. Then the expected background rate using the offline reconstruction [53] leads to a rough estimate of the HLT background rejection factor of about 20. The efficiency of the HLT  $D^0$  trigger is under investigation.

The computing time needed by the ITS processing and track finding and the  $D^0$  finder for different event multiplicities is shown in Table 5.11. The reference platform was a 1.3 kSPECint machine. Only the silicon pixel and silicon strip detectors were included in the HLT processing. The processing is fast, both for the ITS part and the open charm trigger.

**5.3.3. Dimuon reconstruction.** The primary goal of the dimuon High-Level Trigger (dHLT) is to improve the sharpness of the  $p_t$  cut over that performed by the L0 electronics. The sharper  $p_t$  cut improves low- $p_t$ -background particle rejection and allows finer tuning of the

**Table 5.11.** Timing measurements of the ITS track finding code (without SDD) and the  $D^0$  trigger. The benchmarks were performed on a 1.3 kSPECint machine.

$dN_{ch}/d\eta$	2000	4000	6000	8000
Clusterer (s)	0.53	0.61	0.70	0.79
Vertexer (s)	0.04	0.08	0.13	0.18
Tracker (s)	0.26	0.54	0.90	1.38
$D^0$ finder (ms)	10	30	90	160

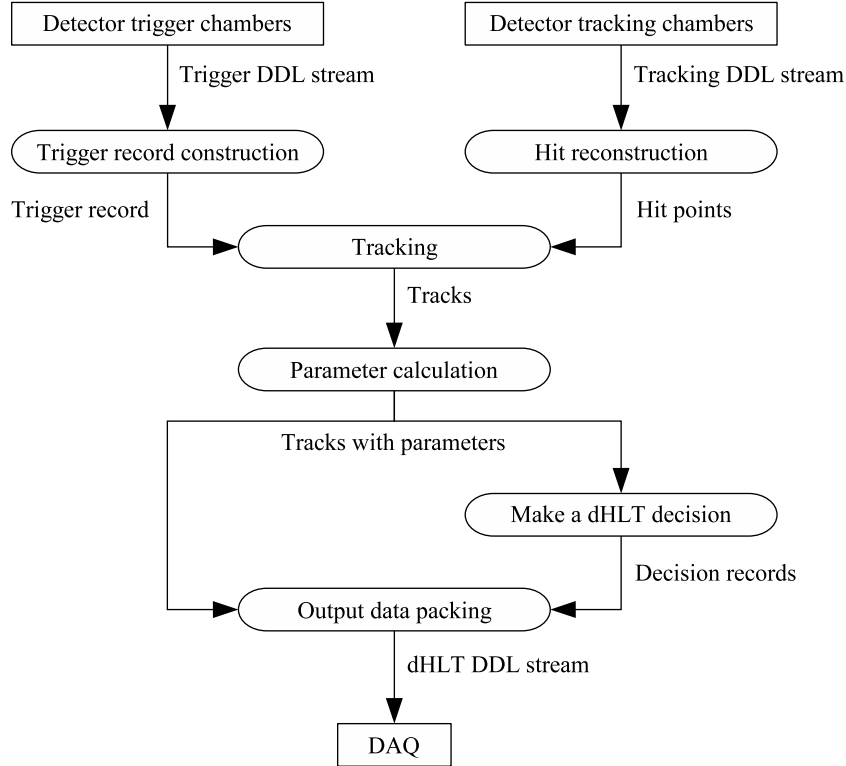


**Figure 5.75.** Data flow through the dHLT system and the relation between the six general processing stages.

cut parameter. The  $p_t$  cut is made sharper by tracking through the front absorber, thereby eliminating scattering and energy loss effects induced by the absorber. This allows one to improve the momentum resolution for the particles passing through the detector. The dHLT algorithm is composed of six general stages shown in Fig. 5.75.

*Trigger record construction.* This step is simply a data transformation. The transformation involves converting hardware addresses and bit patterns into a data structure that can be used by the tracking algorithm internally. The bit pattern received from the front-end trigger electronics is described in Ref. [54].

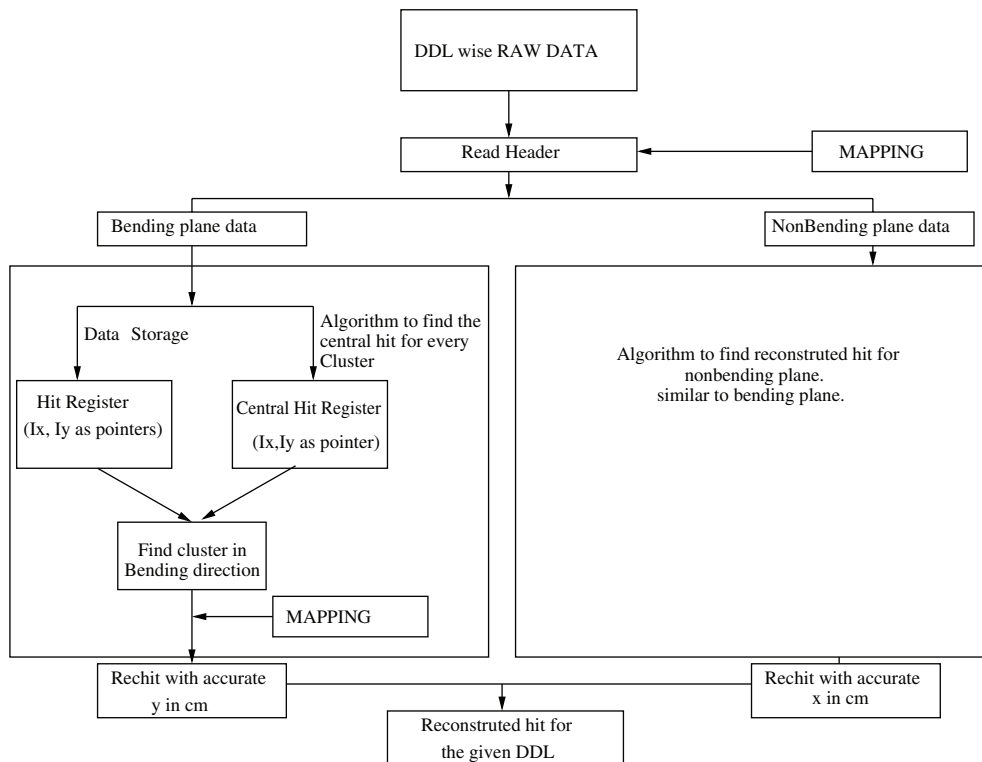


**Figure 5.76.** Flow chart of hit reconstruction and cluster-finder algorithm.

*Hit reconstruction.* Hit reconstruction involves pattern recognition on the level of individual channel signals, to try and find charge clusters that are induced by particles traversing the tracking chambers. This step is performed by the Cluster Finder.

*Track finding.* The track-finding stage performs pattern recognition on the level of reconstructed hit points and trigger records to try and identify all particle tracks in the forward muon spectrometer.

*Parameter calculation.* Here we compute an estimate for the transverse momentum from the found tracks.

*Making a dHLT decision..* The dHLT decision is similar to the trigger decision produced by the trigger electronics. It involves marking tracks that pass the low and/or high  $p_t$  cut, then counting like- and unlike-sign particle pairs.

*Packing output data.* The last step involves packing the reconstructed tracks and decision records into a DDL binary stream to be sent to the DAQ. Data compression can optionally be put into this stage.

**5.3.3.1. Cluster Finder.** The hit reconstruction algorithm for dHLT will be implemented on the RORC card which will receive DDL-wise raw data from stations 4 and 5. So, the first step is to separate the bending and the non-bending plane data by utilizing the DDL-wise mapping files of station 4 and 5. The flow chart of the algorithm is given in Fig. 5.76.

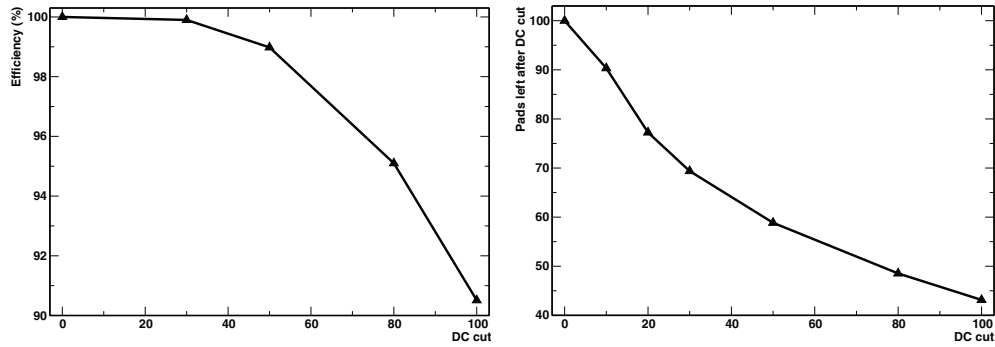


**Figure 5.77.** Efficiency of central hit reconstruction (right) and the rejection of not central hits (left) as a function of the DC cut.

It is proposed to identify each cluster by its central pad (pad carrying the maximum charge for a given cluster) which is the unique property of the cluster.

For every plane of a DDL we book two registers—one for storing only central hits and other for storing all pad hits. The logical pad positions  $(ix, iy)$  are used as pointers in these registers.

In order to identify the central pads, a DC cut of 50 ADC channel is used which introduces an inefficiency of only 1% for finding the central hits (shown in Fig. 5.77, left). However, this DC cut allows us to reject 40% of the pad hits (Fig. 5.77, right) that are not central pads.

For an event, all the central pad hits are identified and stored in the central hit register according to their  $(ix, iy)$  values. Once a central hit for a cluster is known, the centre of gravity (COG) of the pad charges of the central pad and its two immediate neighbours is found, which gives the reconstructed hit position. As stations 4 and 5 are essentially strip chambers, the COG of the charge distribution is only considered along the direction that gives position resolution, i.e. along the  $y$  direction for the bending plane and along the  $x$ -direction for the non-bending plane.

Figure 5.78 shows the accuracy of hit reconstruction for this algorithm. We have used the digitized data from AliRoot and the histogram is the difference between the reconstructed hit and GEANT hit. It is observed from the figure that more than 90% of the clusters are reconstructed within 100  $\mu\text{m}$  accuracy.

Figure 5.79 shows the average time taken to reconstruct the bending plane of an event with a varying number of particles. For a Pb–Pb event the average number of particle hits on stations 4 and 5 is around 150. The reconstruction time is calculated with a simulated raw data file which had all the features of real raw data. It is observed from the figure that for a central Pb–Pb event the reconstruction time for bending plane is around 1.1 ms, which is quite within the acceptable limit.

The merging of the bending and non-bending plane data has not been yet implemented.

**5.3.3.2. Tracker.** The dHLT track-finding algorithm performs only partial track reconstruction through tracking stations 4 and 5 and is the one originally developed by Manso [55]. It is a ‘follow-your-nose’ type algorithm that uses conic search regions to follow the track, hit by hit. A 2/4ths coincidence selection is applied by requiring at least one reconstructed hit to be found on either chamber of each tracking station.

The algorithm’s reconstruction efficiency reaches about 83% as shown by the high  $p_t$  saturation in Fig. 5.80. The plots shown were generated with 200 simulated primary muons

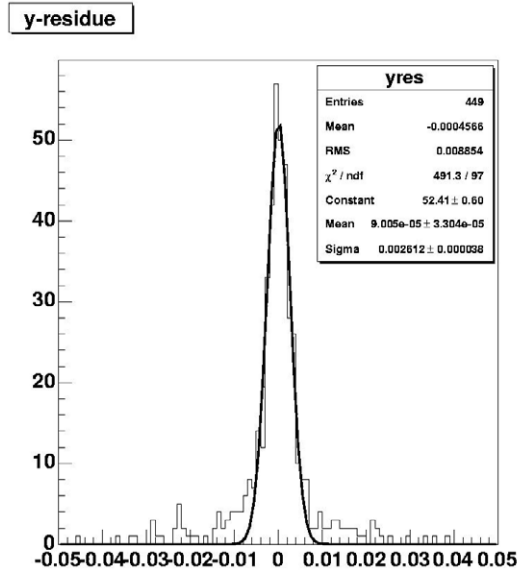


Figure 5.78. Coordinate residuals in the bending plane.

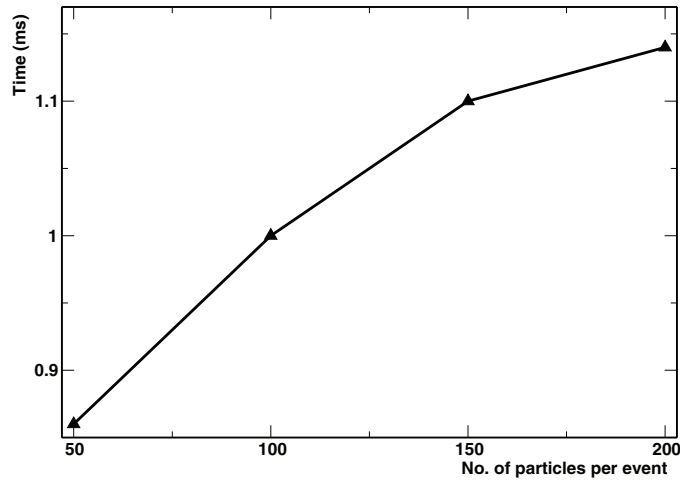
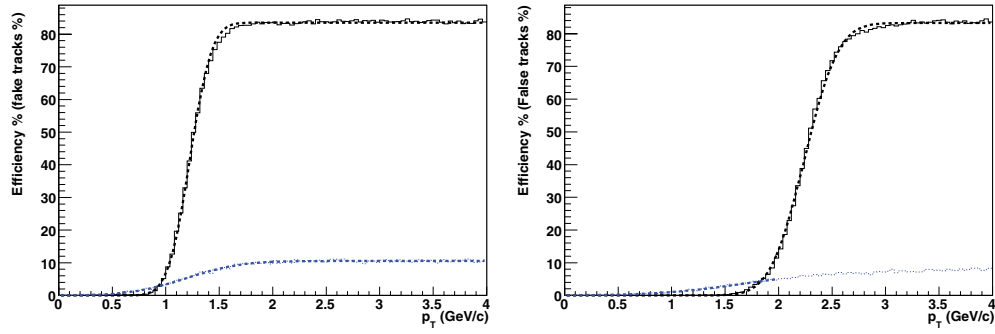


Figure 5.79. Timing of the hit reconstruction in the bending plane.

in the spectrometer per event. The hits were smeared with a Gaussian with nominal standard deviations of  $150 \mu\text{m}$  in the bending plane and  $1 \text{ mm}$  in the non-bending plane. Since the track finding is performed only up to stations 5 and 4 the algorithm is fairly prone to creating fake tracks. At 10% false hits this is still manageable, especially considering that the algorithm is only for triggering.

The histograms are fitted with

$$f(p_t) = \frac{1}{2} \varepsilon \left( 1 + \operatorname{erf} \frac{p_t - \mu}{\sqrt{2}\sigma} \right), \quad (5.13)$$



**Figure 5.80.**  $p_t$  efficiency cut functions for 1 GeV/c  $p_t$  cut (left), 2 GeV/c  $p_t$  cut (right). For both figures the solid line is the efficiency and the dotted line is the percentage of fake tracks. The fitted function (dashed lines) parameters are presented in Table 5.12. Note that the  $p_t$  correction due to the 4 GeV/c momentum loss in the front absorber was not applied. This was to clearly show the shift in the  $p_t$  cut spectrum.

**Table 5.12.** Fitted efficiency and  $p_t$  cut parameters.

No. of particles per event	Applied $p_t$ cut (GeV/c)	Efficiency $\varepsilon$ (%)	Fitted $p_t$ cut $\mu$ (GeV/c)	Std. dev. $\sigma$ (GeV/c)
100	1	83.48	1.227	0.162
200	1	83.52	1.226	0.161
300	1	83.51	1.228	0.164
100	2	83.33	2.242	0.252
200	2	83.27	2.242	0.251
300	2	83.24	2.241	0.250
% Fake tracks				
100	1	5.37	1.191	0.412
200	1	10.53	1.191	0.409
300	1	14.42	1.182	0.419
100	2	3.85	1.703	0.627
200	2	7.57	1.718	0.653
300	2	10.34	1.712	0.643

where  $\varepsilon$  is the efficiency amplitude,  $\mu$  is the  $p_t$  cut mean and  $\sigma$  is the standard deviation of the underlying momentum resolution uncertainty. The fitted parameters can be found in Table 5.12. There we also present fits for 100 and 300 muons per event for which the histograms follow the same form as in Fig. 5.80.

We also see the comparison between the L0  $p_t$  cut function and the dHLT cut function for a 2 GeV/c  $p_t$  cut, Fig. 5.81. Approximately a factor of 2 improvement in cut quality is visible.

The timing of the algorithm on an Intel Pentium 4 2.6 GHz processor (about 0.933 kSpecFp units [56]), is about  $300 \pm 45 \mu\text{s}$  for a central HIJING event with  $dN_{\text{ch}}/d\eta = 8000$ . For a flat spectrum of muons we see a steady rise of processing time per trigger (Fig. 5.82). This is a result of a linearly increasing chance with track density of finding more than one hit in the algorithm's search region. In such cases the algorithm tries to resolve the tracks by creating a new track through each hit in the search region. Clearly more time is required. The initial sharp rise on the left is a result of the finite processing time of overhead code, which is not directly associated with the algorithm code. There is also some room for improvement

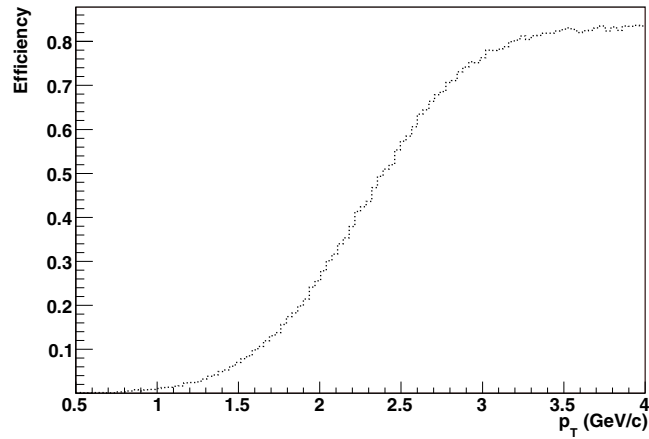


**Figure 5.81.** Comparison between L0  $p_T$  cut efficiency (dotted line) and dHLT (solid line) for a 2 GeV/c  $p_T$  cut.

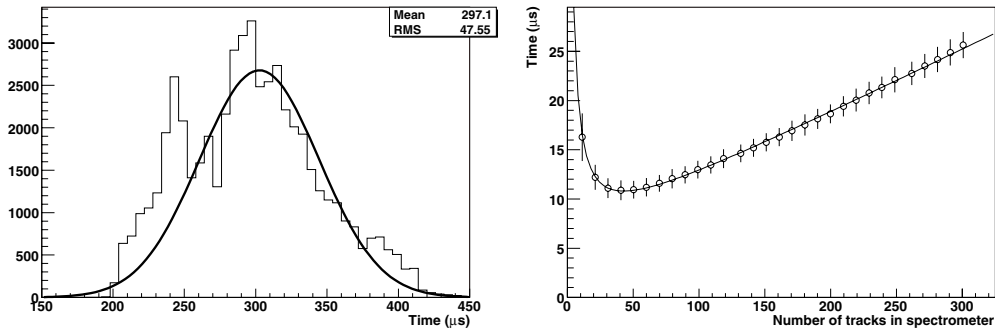


**Figure 5.82.** Processing time required by the dHLT algorithm for central HIJING events. The fitted Gaussian has a mean of 302.6  $\mu\text{s}$  and sigma of 42.0  $\mu\text{s}$  (left). Processing time required per trigger for various track densities. The fitted equation is given by:  $y = 5.20 + 1.2/x + 6.55x$  (right).

since the implementation does not sort or index the reconstructed hits in any way. Thus it defaults to an  $O(n^2)$  algorithm where a presort of the data could easily improve this to an  $O(n \log(n))$  algorithm. Sorting of two-dimensional coordinate data is somewhat complicated however.

**5.3.3.3. Momentum resolution.** The transverse momentum of the particle is estimated by fitting the space points associated with the track as described in Ref. [34] Section 3.1.2. This  $p_T$  needs to be corrected for the  $\sim 4$  GeV energy loss caused by the muon-arm front absorber. The correction is estimated from the residual histogram and added to the calculated  $p_T$ .

The momentum resolution is given by the residual distribution between the  $p_T$  of simulated tracks and the reconstructed  $p_T$ . Such a histogram is shown in Fig. 5.83. We clearly see an improvement in the momentum resolution capabilities of the dHLT over the trigger electronics.

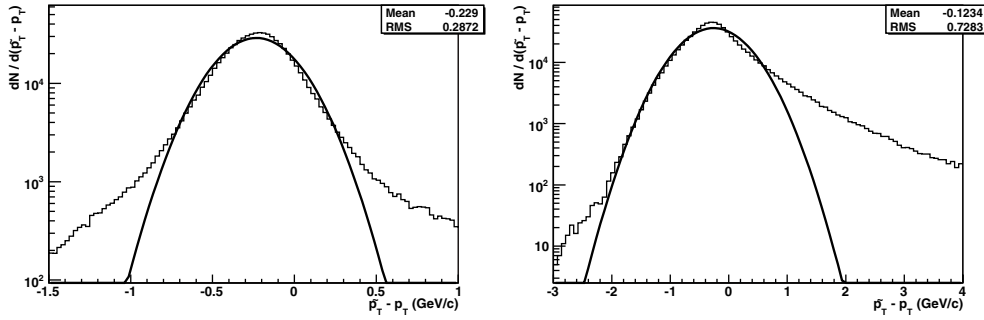


**Figure 5.83.**  $p_T$  residual histograms for the dHLT algorithm, with the fitted Gaussian having a mean of  $-0.232$  GeV/ $c$  and sigma of  $0.233$  GeV/ $c$  (left). Similar  $p_T$  residual histogram for L0 momentum resolution, with the fitted Gaussian having a mean of  $-0.261$  GeV/ $c$  and sigma of  $0.504$  GeV/ $c$  (right).

#### 5.4. Charged-particle identification

The ALICE experiment is able to identify particles with momenta from about  $0.1$  GeV/ $c$  and up to a few GeV/ $c$  by combining different detecting systems that are efficient in some narrower and complementary momentum sub-ranges, and up to a few tens GeV/ $c$  by using the  $dE/dx$  relativistic rise in the TPC (see Section 6.2.2). In this Section we discuss the charged particle identification (PID) capabilities of the central ALICE detectors: The ITS, TPC, TRD, TOF and the HMPID. In the cases when some of the tracks are reconstructed in more than one detector simultaneously, the particle identification can be improved by combining the single detector PID information in some special way that will also be described at the end of this section.

**5.4.1. Particle identification with ITS.** The measurement of the energy loss in thin silicon detectors can be used for particle identification (PID) in the non-relativistic ( $1/\beta^2$ ) region. Four of the six ITS layers (two silicon strip and two drift detector layers) provide the  $dE/dx$  measurement that can be combined with the other PID detector measurements. In the case of low-momentum particles or particles that are not reconstructed in the TPC, the ITS is the only source of the PID information.

Some results of the particle identification with the ITS were already presented in the ALICE TP (see Section 11.4.1 of Ref. [33]), in the ALICE ITS TDR (Section 5.3 of Ref. [1]) and in the ALICE Internal Note [57]. Here we present an update obtained with the latest version of the ITS simulation and reconstruction software.

**5.4.1.1. ITS simulations.** The ITS simulations are a part of the common ALICE simulation/reconstruction framework (AliRoot). The GEANT3 transport code generates energy losses according to the Landau distribution, the corresponding charge is collected on a number of anodes/strips (i.e. a cluster is produced) and transformed into the electronics ADC count. The distribution shape of this signal differs from the Landau one depending on the detector electronics response. There exist very detailed simulations of the ITS electronics response.

Figure 5.84 (a) and (c) show, respectively, the ADC signal and the energy loss,  $dE/dx$ , distributions for the SDD in the narrow momentum interval ( $830$ – $930$  MeV/ $c$ ) for pions. The same distributions but in the MIP (Minimum Ionization Particle) units are presented in the same figure (b) and (d). The maxima of these distributions were normalized to one MIP. One can see from the figures (b) and (d) some influence of the electronics response to the

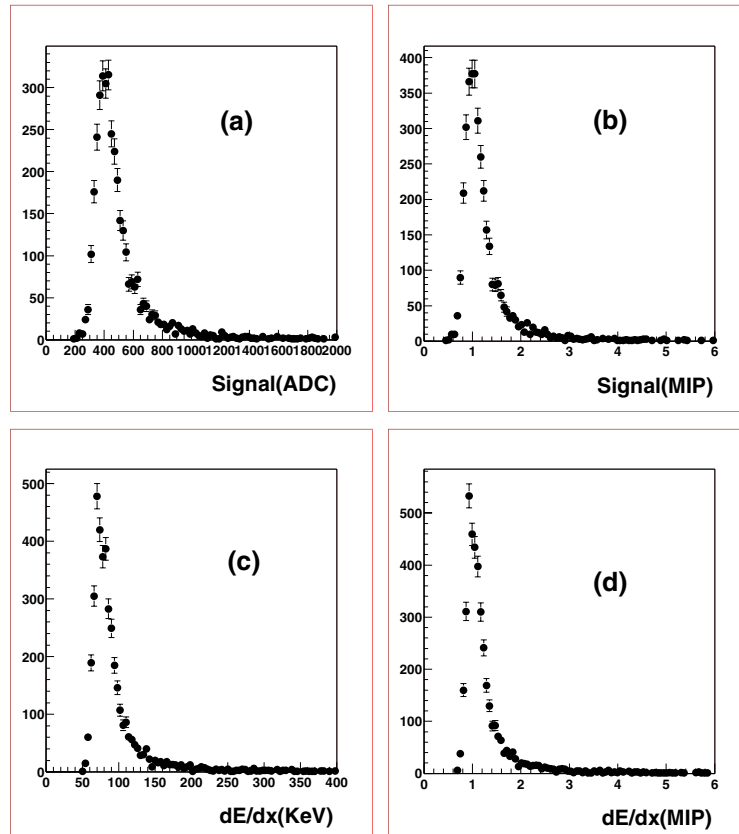


**Figure 5.84.** Detector signal and  $dE/dx$  distributions for pions in the momentum interval 830–930 MeV/ $c$  for the SDD.

distribution shape (this influence is very small for the SSD). We note that the dynamical range is fixed by the 8 MIP per two dimensional cell (anode  $\times$  time bucket) for the SDD and 12 MIP per one strip for the SSD. It is enough to detect the signal up to 25–30 MIP corresponding to protons at lowest momentum of 300–400 MeV/ $c$ .

**5.4.1.2. Particle identification.** For each track reconstructed in the ITS a truncated mean  $dE/dx$  is calculated (two out of four or, sometimes, three out of four  $dE/dx$  measurement). A special correction for the different path length inside the silicon was applied to the cluster charges before calculating the truncated mean.

Figure 5.85 shows the distribution of the truncated mean  $dE/dx$  calculated for tracks reconstructed in 250 HIJING events with momentum from 400 to 425 MeV/ $c$ . The magnetic field was 0.4 T. The curves are the results of Gaussian approximations. The quasi realistic particle ratios generated by HIJING are seen. One can also see some additional kaon and proton contamination on the left from the corresponding Gaussians. This effect decreases with an increase of particle momentum and is conditioned by wrong signal values obtained for the ‘fake’ tracks which contain one or more reconstructed space points belonging to the other tracks (mostly to the pion ones).

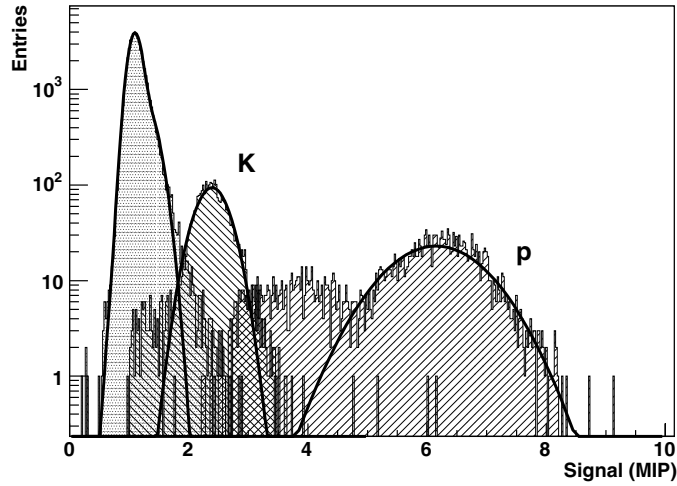


**Figure 5.85.** Distributions of the truncated mean SDD and SSD signals (MIP units) obtained with the HIJING generator for pions, kaons and protons at the reconstructed momentum of 400–425 MeV/c. The curves are results of Gaussian approximations.

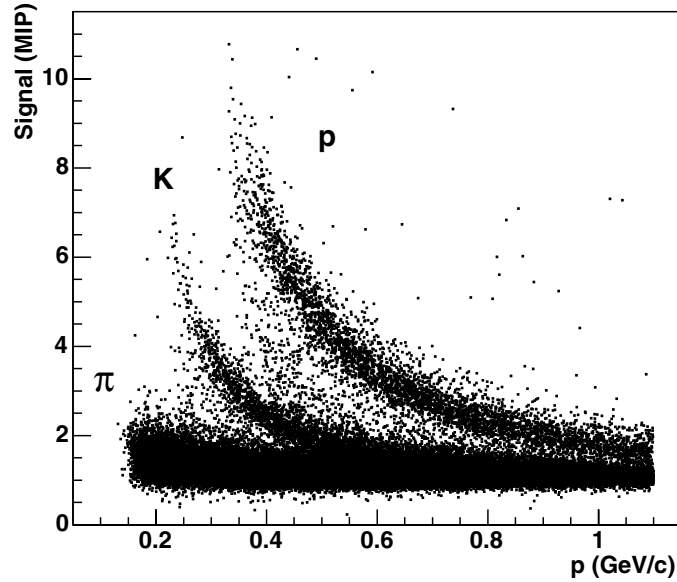


**Figure 5.86.** Correlation plot of the specific SDD/SSD signals (MIP units) calculated by the truncated mean method vs. particle momentum obtained from the TPC+ITS tracking for different particle species.

Figure 5.86 shows signal–momentum correlation plot for the tracks reconstructed in the same HIJING events as in Fig. 5.85. Gamma conversions and other secondary particle productions are included. The separated bands are clearly seen for the different particle species.

The separation between the particle species can be made in a certain momentum interval using the PID probability for each type of particle. The PID probabilities were obtained from

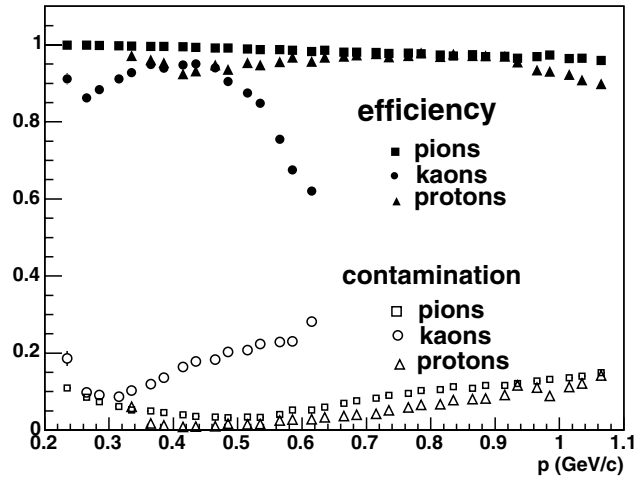


**Figure 5.87.** Momentum dependences of the PID efficiencies and contaminations (see text) for pions, kaons and protons (250 HIJING events).

approximations of the signal distributions by a sum of several Gaussian functions. These Gaussian functions, for example, are shown in Fig. 5.85 for pions, kaons and protons. The PID probability for each particle type at the given signal is the ratio of  $g_i/G_s$ , where  $g_i$  is the Gaussian value for particle type  $i$  and  $G_s$  is a sum of the Gaussian values for all particle types.

The momentum dependence of PID efficiencies, the ratios of the correctly identified particle numbers to the ones submitted to the PID procedure, are shown in Fig. 5.87 for all particle species (the full points: squares for pions, circles for kaons, triangles for protons). Also the residual contaminations, the ratios of the misidentified particle numbers to the all identified ones, are presented as well (the open points: squares for pions, circles for kaons, triangles for protons). The particles were selected by the maximum PID probability. One can see that the kaon and proton separation with the efficiency  $\geq 90\%$  and at the contamination level 10–20% for kaons and 2–10% for protons is possible in the momentum intervals 0.35–0.50 GeV/ $c$  and 0.35–0.90 GeV/ $c$  for kaons and protons, respectively. The strong decrease of the kaon efficiency at lower momenta is a consequence of the migration of some kaon signals to the pion region because of the ‘fake’ track influence discussed above. A similar but smaller effect is seen also for protons in the momentum region 0.4–0.6 GeV/ $c$ . The other consequence of this effect is the additional contamination of protons by kaons and kaons by pions at low momentum ( $p < 0.3$  GeV/ $c$ ). The main part of the contamination to pions comes, in this low-momentum region, from muons and electrons that can not be identified by the  $dE/dx$ . At particle momenta above 0.5 GeV/ $c$ , the kaon  $dE/dx$  band begins to overlap with the pion one (see Fig. 5.86). However, the pions are still identified with high efficiency and low contamination because they are much more abundant than other particle species.

Finally, we demonstrate one possibility to decrease the ‘fake’ track influence using different algorithms of the truncated mean calculation in the low-momentum region where the signals of different particle types are far enough from each other. Such a possibility is demonstrated in Fig. 5.88 where the efficiencies and contaminations obtained by the standard truncated mean method are shown by the full and open squares, respectively. To increase the efficiencies we removed two points with the maximum signals and one point with the minimum one for kaon separation and removed one point with the maximum signal and two

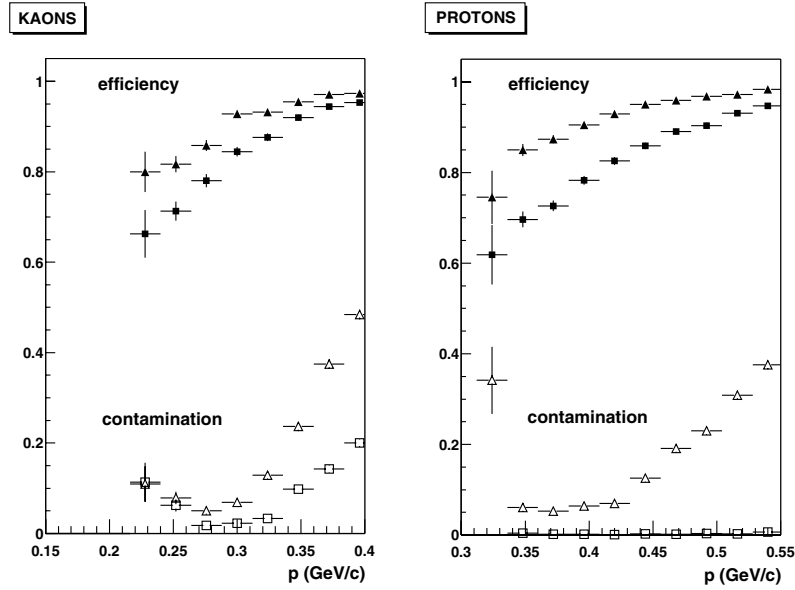


**Figure 5.88.** Momentum dependences of the PID efficiencies and contaminations for kaons and protons. Square and triangular points were obtained, respectively, by the standard and different (see text) algorithms of the truncated mean calculation.

points with the minimum ones for proton separation. The results are shown in Fig. 5.88 by the full and open triangles for the efficiencies and contaminations, respectively. One can see that for both kaons and protons the efficiencies increase significantly, but, on the other hand, the contaminations also increase. Hence, the algorithm has to be chosen as a function of the measurement desired.

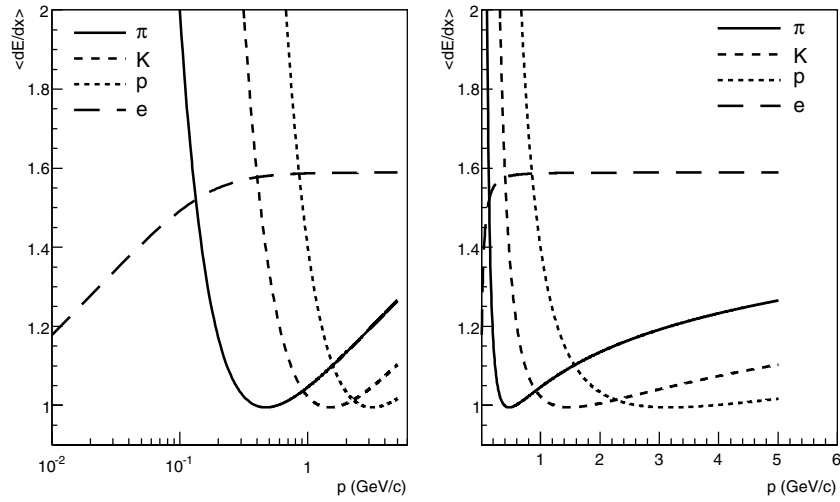
**5.4.2. Particle identification with TPC.** Charged particles travelling through the TPC ionize the detector's gas. The Bethe–Bloch equation

$$\langle dE/dx \rangle = C_1/\beta^2 (\ln(C_2\beta^2\gamma^2) - \beta^2 + C_3)$$

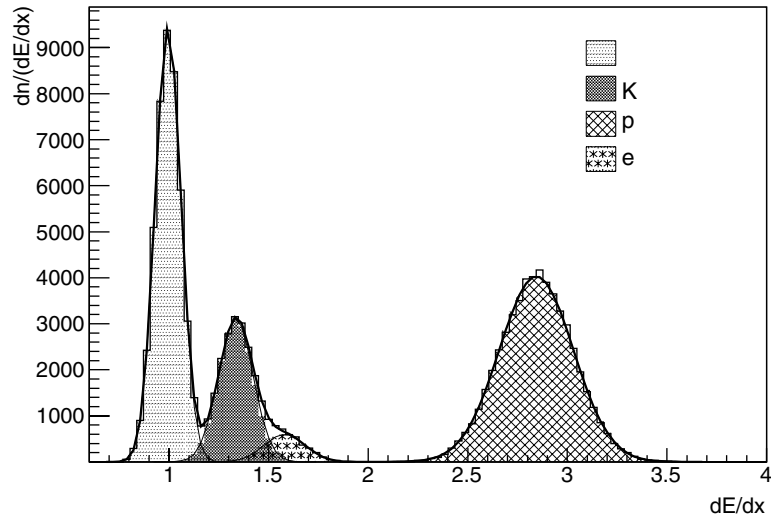
with  $\gamma = 1/\sqrt{1 - \beta^2}$  and detector-specific constants  $C_1$ ,  $C_2$ , and  $C_3$ , relates the mean energy loss per path length,  $\langle dE/dx \rangle$ , to the velocity  $\beta$  of the particle. Combining the momentum information with the measured  $dE/dx$  value yields the particle mass, its identity.

Figure 5.89 shows the dependence of the mean energy loss in the momentum range  $0.1 \text{ GeV}/c < p < 5 \text{ GeV}/c$  for electrons, pions, kaons, and protons reconstructed in the ALICE TPC. To be independent of the detector settings, the energy loss in this figure has been normalized to unity for minimum-ionizing particles. The particle identification in the TPC at larger momenta is discussed in detail in Section 6.2.2.

The calculation of the  $dE/dx$  value from the sample of clusters assigned to a track is discussed in Section 5.1.3. The mean value of the  $dE/dx$  distribution at a fixed momentum is Gaussian with the standard deviation  $\sigma$  determined by the detector properties and the quality of a reconstructed track. The simulations give a resolution (defined as the standard deviation divided by the mean value) of about 6.5% in the case of central Pb–Pb events. At lower track densities, in peripheral Pb–Pb collisions or in pp collisions, the resolution is about 5.5%. To achieve this resolution under experimental conditions, a careful analysis and calibration of the detector response will be required.



**Figure 5.89.** Momentum dependence of the mean energy loss ( $dE/dx$ ) for pions, kaons, protons, and electrons according to the parametrization of the Bethe–Bloch formula adapted to the ALICE TPC. The mean energy loss is normalized to unity for minimum ionizing particles.



**Figure 5.90.** Monte Carlo simulated  $dE/dx$  distribution of electrons, pions, kaons, and protons with  $p = 0.5$  GeV/c. The solid line indicates the result of the fit to a sum of four Gaussians. The shaded areas correspond to the contributions from different particle species.

Assuming the resolution of 6.5%, Fig 5.90 shows a Monte Carlo simulated  $dE/dx$  distribution for particles with the momentum  $p = 0.5$  GeV/c. In this example, the particle ratios have been chosen arbitrarily. Fitting the sum of four Gaussian functions to this distribution allows one to extract contributions from the individual particle types.

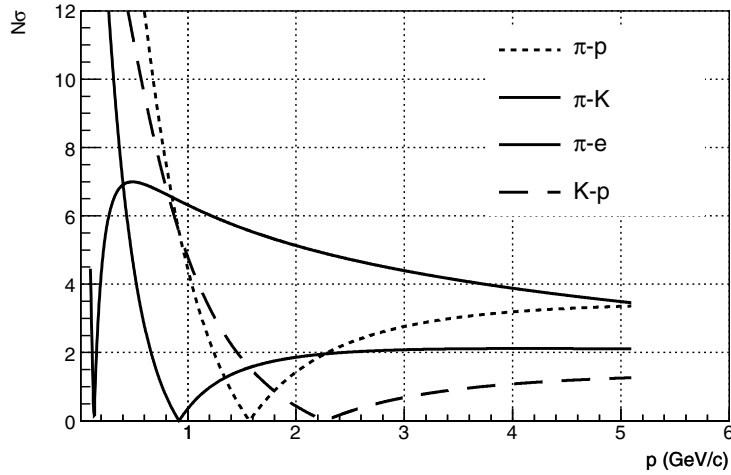


**Figure 5.91.** Momentum dependence of the  $\langle dE/dx \rangle$  separation for most important particle combinations in units of the energy loss resolution assuming a constant resolution of 6.5%.

The general way to quantify the separation power between particle types A and B is to give the distance of the mean energy loss values in units of relative resolution:

$$N\sigma_{A,B} = \frac{\langle dE/dx \rangle_A - \langle dE/dx \rangle_B}{(\sigma_A + \sigma_B)/2}.$$

Figure 5.91 shows the dependence of  $N\sigma_{\pi-p}$ ,  $N\sigma_{K-p}$ ,  $N\sigma_{\pi-K}$ , and  $N\sigma_{\pi-e}$  on momentum in the range from  $p = 0.1 \text{ GeV}/c$  up to  $p = 5 \text{ GeV}/c$ . If  $N\sigma$  vanishes the two particle species are not distinguishable. At  $N\sigma = 2$ , if the  $dE/dx$  cut selecting 90% of particles of a given type is applied, only 27% of the particles of other types contaminate the sample. At the momentum ranges where the separation between particle types becomes small, particle identification based on other detectors is foreseen (see Section 5.4.6).

Once the resolution and the mean ionization at a given momentum are known, the PID probabilities to be a particle of a certain kind can be assigned on a track-by-track basis, using, for example, the Bayesian approach (see Section 5.4.6).

#### 5.4.3. Particle identification with TRD

*Electron identification.* An important task of the TRD is to supplement the TPC electron/pion identification by a pion rejection factor of the order of 100 at momenta in excess of  $1 \text{ GeV}/c$  [58, 59]. In addition, by measurement of energy loss [60], the TRD will improve the identification of other charged particles. Here we briefly review the method and performance of the detector concerning electron/pion identification. The main emphasis is put on the achieved performance in measurements with detector prototypes [61] and on the comparison of the measurements with simulations.

In the TRD, the detector signal is digitized in about 20 time bins, each 100 ns. This is mainly determined by the tracking performance (also at the trigger level), and helps substantially to improve the  $e/\pi$  separation, as will be shown here. In Fig. 5.92 we present the measured average signals as a function of drift time for pions and electrons (with and without radiator), for the momentum of  $2 \text{ GeV}/c$ . For our nominal drift field of  $0.7 \text{ kV}/\text{cm}$ , the detector signal is spread over about  $2 \mu\text{s}$  (the time zero is arbitrarily shifted). The peak at small drift times originates from the amplification region, while the plateau is from the drift

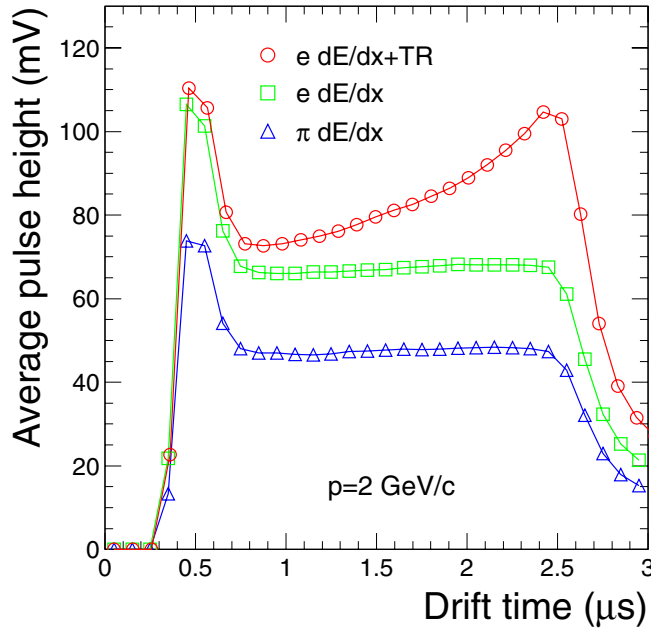


**Figure 5.92.** Average pulse height as a function of drift time for pions and electrons (with and without radiator). The time zero is shifted by about  $0.3 \mu\text{s}$ .

region. For the electrons, the contribution of transition radiation (TR), which is preferentially absorbed at the entrance of the detector (corresponding to large drift times), is evident.

The distributions of measured integrated energy deposit in one layer of the detector are shown in Fig. 5.93 for pions and electrons of  $2 \text{ GeV}/c$ . The measured data [61] are compared with calculations, which include ionization energy loss [60] and, in the case of electrons, transition radiation. For TR production we employ a parametrization of a regular radiator [62], which we tune to describe the electron spectra. The calculations include TR absorption in the radiator reinforcement as well as in the detector volume. As seen in Fig. 5.93, we can achieve a good agreement with the measurements with a reasonable (but not unique) set of parameters ('foil' thickness  $d_1 = 10 \mu\text{m}$ , gap  $d_2 = 80 \mu\text{m}$ , number of 'foils'  $N_f = 180$ ). The measured data for pure TR [63] are described equally well by this parametrization.

The commonly used method for particle identification in TRDs is the likelihood method. The likelihood (to be an electron) is defined as

$$L = \frac{P_e}{P_e + P_\pi}, \quad P_e = \prod_{i=1}^N P(X_i|e), \quad P_\pi = \prod_{i=1}^N P(X_i|\pi), \quad (5.14)$$

where the products run over the number of detector layers,  $N$ .  $P(X_i|e)$  and  $P(X_i|\pi)$  are the probabilities that a detector signal  $X_i$  recorded in layer  $i$  was produced by an electron or a pion, respectively. The detector signal most commonly used is the integrated energy deposit. We explore this simplest case in some detail below.

The likelihood distributions for six layers, based on the total energy deposit in one layer (Fig. 5.93) are shown in Fig. 5.94 for the momentum of  $2 \text{ GeV}/c$ . Cuts of given electron efficiency are imposed on the likelihood value and the pion efficiency,  $\pi_{\text{eff}}$ , is calculated (the pion rejection power is  $1/\pi_{\text{eff}}$ ). The dependence of the pion efficiency on the electron

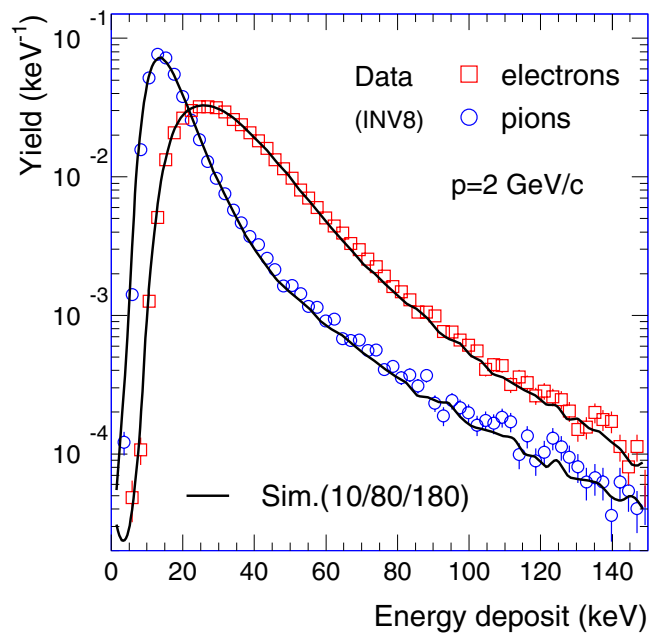


**Figure 5.93.** Integrated energy deposit for pions and electrons for a momentum of  $2 \text{ GeV}/c$ . The symbols represent the measurements, the lines are calculations.

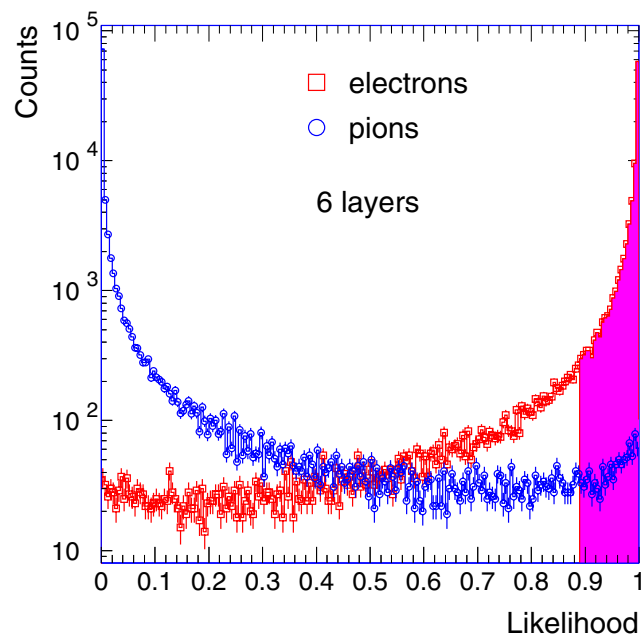


**Figure 5.94.** Distributions of the likelihood (to be an electron) for electrons and pions of  $2 \text{ GeV}/c$ , obtained from the total energy deposit. The shaded area corresponds to 90% electron efficiency.

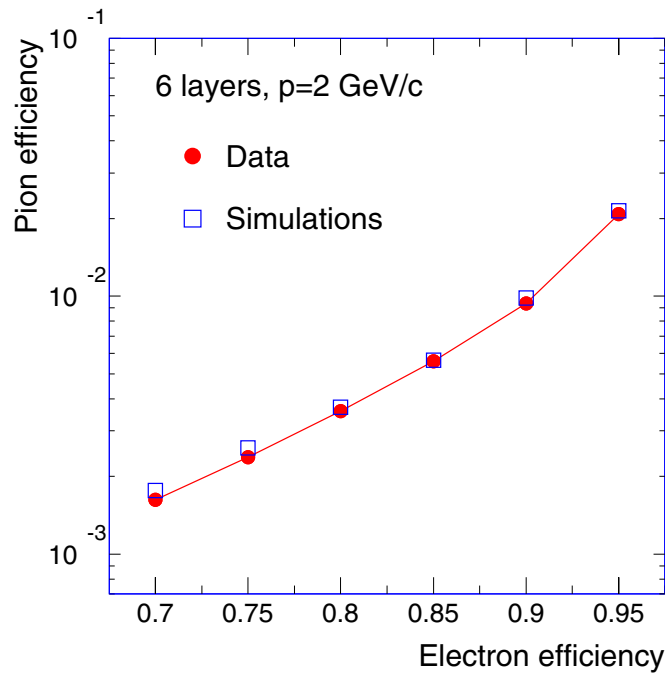
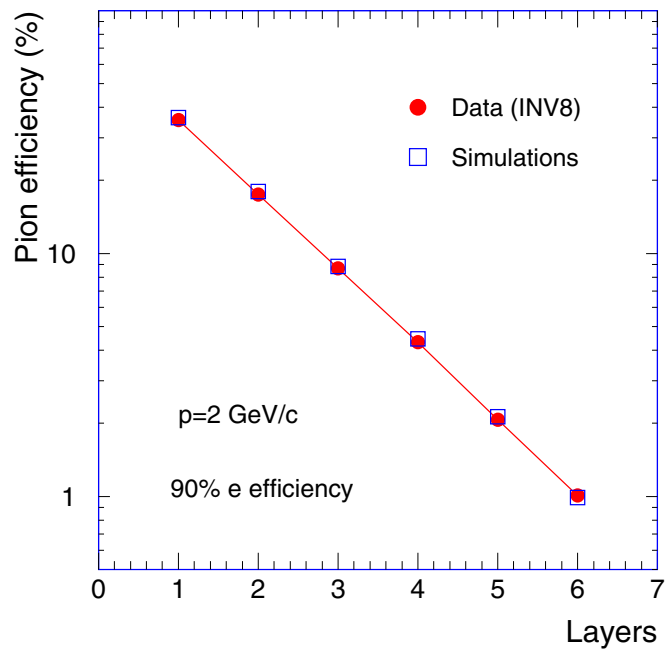


**Figure 5.95.** Pion efficiency as a function of electron efficiency for a six-layer likelihood on total energy, for momentum of 2 GeV/c. The values corresponding to measured data are compared to simulations.

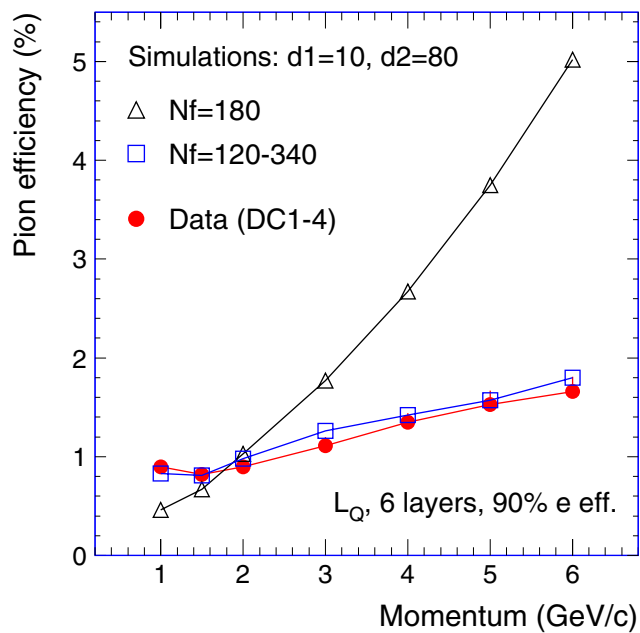
efficiency is presented in Fig. 5.95 for 2 GeV/c momentum. For 90% electron efficiency (which is a baseline value) a pion efficiency down to 1% (pion suppression of 100) is achieved. This value improves substantially for lower electron efficiencies. However, because of the quadratic dependence of the quarkonia yield on the electron efficiency, working at lower electron efficiencies is undesirable in most cases. Following from the agreement seen for the charge spectra, the simulations reproduce very well the measured pion efficiencies.

Figure 5.96 shows the measured and simulated pion efficiency as a function of the number of layers included in the likelihood calculation. Given the strong dependence of the pion rejection on the number of layers (roughly a factor 2 per layer), a reduced but not negligible rejection is achieved for tracks that are only partially in the geometrical acceptance of the detector.

The momentum dependence of the pion rejection is shown in Fig. 5.97. Beyond 2 GeV/c, a steady degradation of the pion rejection is observed. A factor of about 2 worse rejection is measured at 6 GeV/c compared to 2 GeV/c. In this regime, the TR yield, which roughly saturates, can no longer compensate the pion relativistic rise in  $dE/dx$  (see Ref. [60] and references therein). The simulations cannot reproduce the measurements, unless we employ a momentum-dependent parametrization of the radiator, namely by varying the effective number of foils. The value  $N_f = 180$ , which reproduce the measurements at 2 GeV/c, leads to a much steeper pion rejection degradation as a function of momentum than seen in the data. The calculations predict a TR yield saturation already at 2 GeV/c, while the measurements indicate a steady increase in TR yield up to 6 GeV/c [61]. Given our highly irregular radiator (composed of two types of randomly distributed interfaces, fibers and foams, [59]) it is not surprising that a regular radiator parametrization is not able to reproduce the measurements consistently. Efforts are under way to understand this behaviour and to find alternative TR



**Figure 5.96.** Pion efficiency as a function of the number of layers for a momentum of 2 GeV/c.



**Figure 5.97.** Measured and simulated pion efficiency as a function of momentum.

descriptions (for irregular radiators) which could reproduce the measurements. Also, the contribution of bremsstrahlung, not included in the present simulations, is being investigated. Our recent measurements of pure TR spectra up to 10 GeV/c, which are currently under evaluation, will shed more light on these aspects.

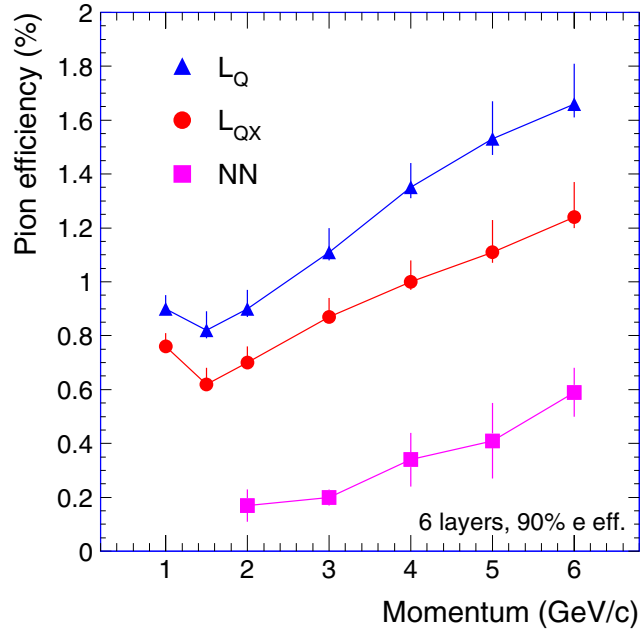


**Figure 5.98.** Measured pion efficiency as a function of momentum for three methods: likelihood on total charge ( $L_Q$ ), bidimensional likelihood on charge and position of the maximum time bin amplitude ( $L_{QX}$ ), and neural networks (NN).

The likelihood on total energy deposit is a straightforward method, but it does not use all the recorded information in the TRD. A so-called bidimensional likelihood [64], for which the distribution over the drift time of the time bin with the maximum measured amplitude is used together with the integrated charge measurement ( $L_{QX}$ ) [61] can also be used in a simple way, namely as a multiplicative probability in the likelihood calculation, Eq. (5.14). Owing to the preferential absorption of TR (Fig. 5.92), an improvement of the pion rejection by a factor up to 1.4 is achieved with this method compared to the likelihood on total energy deposit ( $L_Q$ ), as illustrated in Fig. 5.98. The pion rejection can be further enhanced by exploiting the amplitude measurement in each time bin. Because of the correlation between time bins, arising from the intrinsic detector signal, convoluted with the response of the preamplifier/shaper, the signal in each time bin cannot be used in a simple way in a likelihood method. To overcome this, we have recently performed an exploratory study on a neural network (NN) approach to  $e/\pi$  identification, which showed that a factor of up to 3 better pion rejection compared to the  $L_{QX}$  method can be achieved [65]. A comparison of the three methods is presented in Fig. 5.98.

All the results presented above are for the ideal case of isolated tracks. However, for real events in ALICE a degradation of the identification performance is expected [59]. A study of this effect with the most updated detector response implemented in AliRoot is under way. We expect that the NN method will provide a good safety factor for the performance in real events, but the application of this method for high-multiplicity events also needs to be investigated.

*Hadron identification.* In addition to the electron identification, the TRD will also improve the identification of the hadrons. This is done by measuring the  $dE/dx$  in a way similar to that used for the ITS and the TPC. For comparison with these detectors, Fig. 5.99 shows the  $dE/dx$  distribution for minimum-ionizing pions truncated over the six TRD chambers.

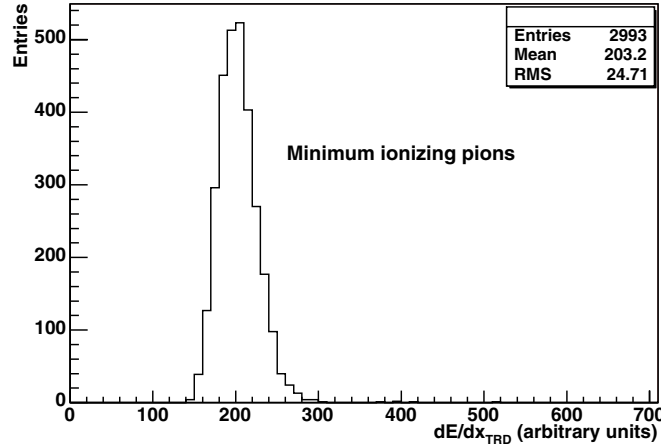


**Figure 5.99.** Truncated mean  $dE/dx$  distribution of minimum-ionizing pions from TRD.

The actual PID procedure in the TRD does not use the truncated mean method because the transition radiation information, which is important for electron identification, is lost in such a procedure. Instead, for each of the six TRD planes the distribution of the energy deposit for electrons, pions, muons, kaons, and protons is obtained. The PID weights  $P_i^k$  ( $i = e, \mu, \pi, K, p$ ;  $k = 1, 2, \dots, 6$ ) are calculated for each of the planes using these distributions (often referred to as the PID ‘response functions’). The combined (over all the six planes) PID probability  $p_i$  to be a particle of the type  $i$  is then given by

$$P_i = \frac{\prod_{k=1}^6 P_i^k}{\sum_{j=e,\mu,\pi,\dots} \prod_{k=1}^6 P_j^k}, \quad i = e, \mu, \pi, K, p.$$

As an example, we show in Fig. 5.100 the PID efficiencies and contaminations as a function of particle momentum for pions, kaons and protons for the case of generated low multiplicity events containing equal number of particles of these types. The PID efficiency is defined as the ratio of the number of correctly identified particles to the number of particles of this type submitted the PID procedure. The contamination is defined as the ratio of the number of misidentified particle to the number of all identified ones.

**5.4.4. Particle identification with TOF.** In this section we illustrate the PID performance of the Time-Of-Flight (TOF) detector, which is designed to identify charged particles at intermediate momenta in the ALICE central acceptance ( $|\eta| < 0.9$ ). More details can be found in [66]. In Section 5.4.4.1, we summarize the characteristics of the Monte Carlo samples and of the TOF detector simulation used for the results presented here. The algorithm used for the matching of the reconstructed tracks with the time signals measured on the TOF system is then described in Section 5.4.4.2. Finally, the TOF PID procedure and its performance are discussed in Section 5.4.4.3. Results are reported for both simulated Pb–Pb events at different centralities, and for pp minimum-bias collisions.

**5.4.4.1. Monte Carlo event samples and detector simulation.** The Pb–Pb events were generated with the HIJING 1.36 Monte Carlo simulation program [67] in five independent

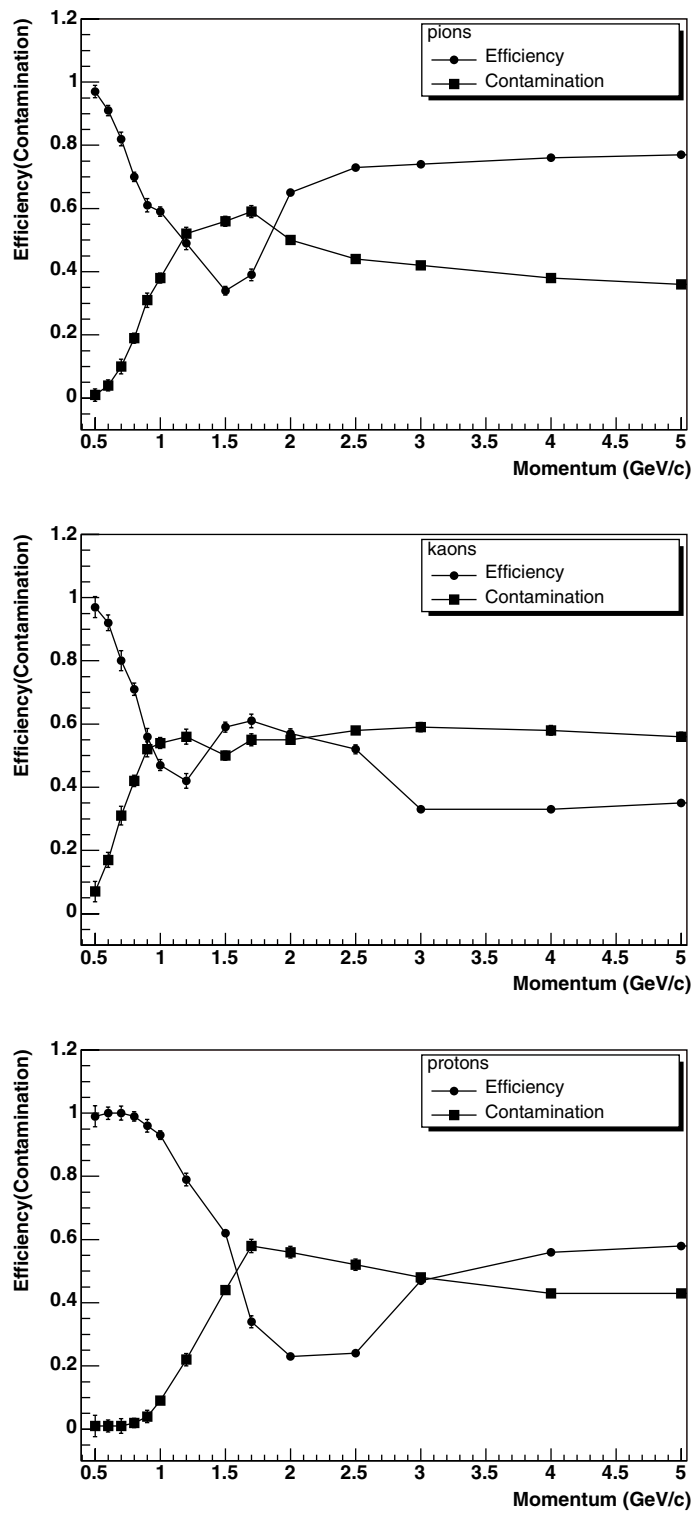


Figure 5.100. PID efficiencies and contaminations for pions, kaons and protons obtained with the TRD.

bins of the impact parameter of the collision,  $b$ . The sample with the highest generated statistics (200 events) consists of central Pb–Pb collisions ( $0 \leq b \leq 5$  fm), which are taken as the main reference for the optimization of the TOF reconstruction and PID, and in the evaluation of their performances. The rest of the HIJING Pb–Pb events are used to study the TOF PID in peripheral collisions, and consist of four samples of 30 events each, generated in impact-parameter bins of equal cross-section between 5 and 15 fm<sup>1</sup>. In addition, to quantify explicitly the sensitivity of the TOF PID performance to different charged track environments, three sets of 60 Pb–Pb collisions with a predefined number of charged tracks per unit rapidity were simulated with *HijingParam*, a parametrization of the pseudo-rapidity and transverse-momentum distributions of charged and neutral hadrons, (see Section 4.2.1.2 in Ref. [3] for more details). Charged track densities of  $dN_{\text{ch}}/d\eta = 2000, 5000$  and  $8000$ , safely covering the uncertainty on the expectations for the charged-particle multiplicity in central Pb–Pb collisions at LHC energies, were selected in the simulation. Finally, a sample of 15000 minimum-bias proton–proton events at  $\sqrt{s} = 14$  TeV, generated with the PYTHIA Monte Carlo [68], were used to evaluate the performance of the TOF PID in pp collisions.

Particle tracking, signal generation and detector response were simulated with GEANT3 [69]. The geometry of the TOF detector used in the simulation is the same as described in Ref. [3], except that in the five TOF azimuthal sectors covering the region  $220^\circ \leq \varphi \leq 320^\circ$ , the central modules<sup>2</sup> have been removed to minimize the amount of material in front of the PHOS detector. This configuration corresponds to a reduction of  $\sim 5\%$  in the TOF geometrical acceptance.

Particle signals at the GEANT level were digitized according to a Gaussian time response. Border effects, like the sharing of the particle signal between neighbouring pads and the dependence of the Multi-gap Resistive-Plate Chamber (MRPC) time resolution on the impact point of the particle within a pad, were parametrized according to test-beam results and have been included in the simulation in the same way as described in Ref. [70]. The overall TOF time resolution assumed in the simulation ( $\sigma_{\text{TOF}} = 80$  ps) takes into account different sources of uncertainty:

$$\sigma_{\text{TOF}}^2 = \sigma_{\text{MRPC}}^2 + 2\sigma_{\text{TDC}}^2 + \sigma_{\text{Cal}}^2 + \sigma_{\text{Clock}}^2 + 2\sigma_{\text{CITRM}}^2 + \sigma_{\text{T0}}^2,$$

coming, respectively, from the detector intrinsic resolution  $\sigma_{\text{MRPC}}$ , the HPTDC time resolution  $\sigma_{\text{TDC}}$ , the channel-to-channel calibration uncertainty  $\sigma_{\text{Cal}}$ , the clock distribution jitter via the TTC system  $\sigma_{\text{Clock}}$ , the jitter  $\sigma_{\text{CITRM}}$  introduced when distributing the clock in the TRM, and the uncertainty  $\sigma_{\text{T0}}$  on the collision time (see Ref. [70] for more details). The values used in the simulation for each of the contributions mentioned above are listed in Table 5.13. The estimates for  $\sigma_{\text{MRPC}}$  and  $\sigma_{\text{TDC}}$  reflect the results obtained for the intrinsic MRPC time resolution<sup>3</sup> and the HPTDC performance in the latest test beams [71]. The uncertainties related to the quality of the clock distribution through the electronic chain,  $\sigma_{\text{Clock}}$  and  $\sigma_{\text{CITRM}}$ , were estimated on the basis of the most recent lab-bench tests [72]. Concerning the uncertainty  $\sigma_{\text{Cal}}$ , related to the knowledge of the channel-to-channel relative timing and of the time slewing corrections, it is foreseen that it will be kept well below 30 ps by means of online/offline calibrations. Finally, an uncertainty  $\sigma_{\text{T0}}$  below 50 ps is expected to be reached on the absolute time of the collision, which will be precisely monitored in ALICE by the T0 detector. With a TOF time resolution of 80 ps, the system is expected to provide a  $\pi/K$

<sup>1</sup> The four bins in the impact parameter  $b$  are respectively [5, 8.6], [8.6, 11.2], [11.2, 13.2] and [13.2, 15] fm.

<sup>2</sup> As described in Ref. [3], each of the 18 azimuthal sectors of the TOF detector is segmented in five units along the  $z$  coordinate. In each sector, the central module covers the region close to  $\eta \sim 0$ , defined by  $|z| < 58$  cm,  $z$  being the coordinate along the beam direction.

<sup>3</sup> The value quoted in Table 5.13 refers to the intrinsic MRPC time resolution measured at the centre of the TOF pad.

**Table 5.13.** Individual contributions to the TOF time resolution used in the simulation of the TOF detector response, for the three overall time resolutions  $\sigma_{\text{TOF}} = 80, 120$  and  $60$  ps.

TOF time resolution (ps)	$\sigma_{\text{MRPC}}$ (ps)	$\sigma_{\text{TDC}}$ (ps)	$\sigma_{\text{Cal}}$ (ps)	$\sigma_{\text{Clock}}$ (ps)	$\sigma_{\text{CITRM}}$ (ps)	$\sigma_{\text{T0}}$ (ps)
80	40	20	30	15	10	50
120	60	50	50	35	10	50
60	40	20	30	15	10	15

and K/p separation better than  $3\sigma$  up to a track momentum  $p \simeq 2.5$  GeV/c and  $p \simeq 4$  GeV/c, respectively.

In addition to the baseline resolution of 80 ps, the TOF detector response in the most central HIJING events was also simulated assuming an overall TOF time resolution  $\sigma_{\text{TOF}}$  of 120 ps and 60 ps. As shown in Table 5.13, the 120 ps simulation, which can be regarded as a ‘worst case’ scenario, assumes very conservative estimates for the intrinsic MRPC and HPTDC resolutions (implying also an increased uncertainty on the TOF channel-to-channel calibration), and for the jitter introduced in the clock distribution via the TTC system. An overall TOF resolution of 60 ps is instead obtained when the uncertainty  $\sigma_{\text{T0}} = 50$  ps on the start time of the collision is replaced with the improved accuracy  $\sigma_{\text{T0}} = 15$  ps that the T0 detector is expected to reach in central Pb–Pb events. In this respect, a comparable precision is actually foreseen to be achieved, at the offline stage, using the TOF system alone. In particular, ongoing studies show that, in central Pb–Pb events, it will be possible to measure the time of the collision with a resolution  $\sigma_{\text{T0}} \simeq 5$  ps, using a combinatorial algorithm based on the comparison of the measured and the calculated times of flight of well reconstructed tracks.

*5.4.4.2. Track–TOF signal matching.* The starting sample for the track-TOF signal-matching procedure consists of all the TPC tracks which can be successfully extrapolated from the TPC outer wall (at a radius  $R \sim 2.6$  m) to the TOF inner radius ( $R \sim 3.7$  m). As discussed in Section 5.1.5, track extrapolation to the TOF is performed by track reconstruction in the TRD. In general, the use of the TRD spatial information allows one to further constrain the track trajectory, thereby improving the quality of the track extrapolation and its association to the time signals on the TOF system. However, owing to the quality criteria applied during track reconstruction in the TRD, which cause the track extrapolation to be stopped when regions with a relevant amount of passive material are crossed (in particular, close to the boundaries between TRD modules), a sizable fraction of the tracks releasing a signal on the Time of Flight system actually fails to be extrapolated to the TOF inner radius. As that would imply a significant loss of efficiency in the TOF PID procedure, a further extrapolation step is applied to recover the tracks stopped during the TRD reconstruction. In this case, the extrapolation is performed without applying the requirements mentioned above, and using average values of the density and the radiation length of the material crossed to take into account the effects from energy loss and multiple scattering. Following this procedure, nearly 100% of the TPC tracks which have released a signal on the TOF system are eventually included in the starting sample of the track-TOF signal matching algorithm. This is illustrated in Fig. 5.101 (a), which shows, as a function of the track momentum, the fraction of the tracks which have released a signal on TOF and are extrapolated by the TRD tracking algorithm (dark-shaded histograms), and by the additional extrapolation step described above (light-shaded histograms), in central Pb–Pb collisions. Figure 5.101 (b) shows the same quantities as a function of the track pseudorapidity  $\eta$ . In terms of the performance of the matching algorithm, presented later in this section, the inclusion of the latter set of tracks translates to a substantial gain in the association efficiency

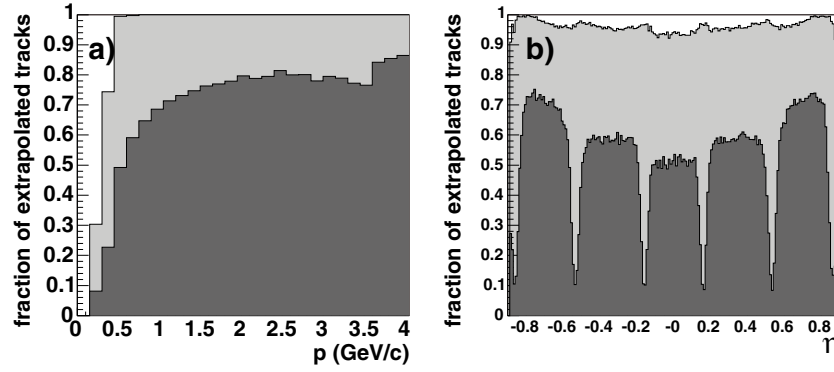


**Figure 5.101.** The momentum (a) and pseudo-rapidity (b) dependence of the fraction of TPC tracks which release a signal on TOF and are extrapolated to the TOF inner radius by the TRD tracking algorithm (dark-shaded histograms), and by the additional propagation step described in the text (light-shaded histograms), in central Pb–Pb collisions.

(a factor  $\sim 1.3$ – $2$ , depending on the track momentum), with only a limited increase (a factor  $\sim 1.1$ ) in the rate of fake associations. Note that an extrapolation procedure complementing the one performed by the TRD track reconstruction will be even more necessary in the case of a reduced geometrical acceptance of the TRD, as foreseen for the experiment start-up phase.

After extrapolation to the TOF inner radius, the tracks are sorted according to their curvature, so that the matching procedure is first applied to the highest momentum tracks. The ordering in momentum contributes to reducing the contamination from fake associations. After that, a window  $[d\varphi, dz]$  in the azimuthal and longitudinal coordinates (which depends on the track parameters and their errors) is opened for each track, and TOF pads that have given a signal are searched for within this window. These pads are preselected as candidates for the association. The matching procedure is then organized in two stages:

- In the first step, each track is propagated through the TOF detector, until its extrapolation crosses one of the preselected TOF pads. The time signal of this pad is then associated to the track.
- In the second step, the same procedure, but with a looser criterion, is applied to all those tracks whose extrapolation did not fall within the active area of any of the preselected TOF pads. In particular, the TOF signal closest to the track trajectory is associated, provided that its distance is smaller than a predefined value  $d_{\max}$ . In Pb–Pb collisions, a distance  $d_{\max} = 3$  cm, which optimizes the ratio between the matching efficiency and contamination in central events, is used. In the case of pp collisions, which are characterized by a much lower charged track density, a more inclusive cut is applied,  $d_{\max} = 9$  cm.

During both steps, the association of the tracks is performed according to the ordering in momentum mentioned above; moreover, once a TOF signal is assigned to a track, it is flagged to prevent any further association to other tracks, to avoid ambiguous track-time assignments.

The performance in central Pb–Pb collisions of the association algorithm described above is presented in Fig. 5.102, showing, for primary pions, kaons and protons, the dependence on the track momentum  $p$  of the matching efficiency  $\varepsilon^m$  and contamination  $c^m$ , which are defined as:

$$\varepsilon^m = \frac{N_{m,t}}{N_{\text{reco,TOF}}}, \quad c^m = \frac{N_{m,f}}{N_{m,t} + N_{m,f}}. \quad (5.15)$$

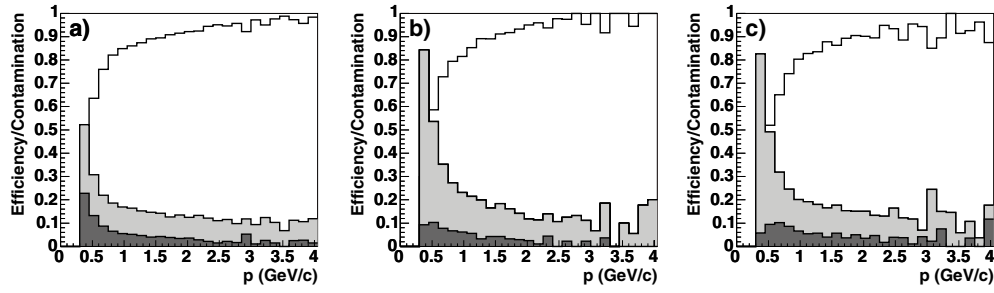


**Figure 5.102.** The momentum dependence of the efficiency (empty histograms) and the contamination (shaded histograms) of the TOF matching procedure in central Pb–Pb collisions, for primary particles of different species ((a): pions, (b): kaons, (c): protons). The contamination coming from tracks having and not having released a signal on TOF are shown separately as the dark and light-shaded histograms, respectively. A slightly lower efficiency and higher contamination is observed for kaons and protons with respect to pions, as expected from the increased effect of multiple scattering.

Here,  $N_{\text{reco,TOF}}$  is the number of the TPC reconstructed tracks which release a hit on TOF, and  $N_{\text{m,t}}$  and  $N_{\text{m,f}}$  are, respectively, the number of tracks associated with the correct TOF signal, and with a signal coming from a different particle in the event. For all three particle species, the matching efficiency increases with increasing track momentum, as expected from the correspondingly decreasing effect of multiple scattering on the extrapolation of the track to the TOF sensitive volume. For the matching contamination, two distinct sources of track mis-associations can be distinguished. The main component, shown by the light-shaded histograms in Fig. 5.102, is related to the tracks which did not reach the TOF because of the interaction in the material (or because of decays, in the case of kaons). These tracks were nevertheless extrapolated to the TOF sensitive volume, and then associated, in most of the cases, to an uncorrelated TOF signal. The other component (dark-shaded histograms) comes from tracks which have actually reached and released a signal on TOF, but are mis-associated to the signal from another particle in the event because of an incorrect extrapolation of the track. Still, for the matching contamination in central Pb–Pb collisions, it is worth mentioning that, in  $\sim 10\%$  of the cases, the track is actually associated to a TOF signal generated by one of its secondaries (from either decay or interaction). In this case, the correlation between the measured time and the time calculated from tracking (once the right mass hypothesis is assumed) is to some extent preserved, and these particles, although being mis-associated according to the definition in (5.15), are likely to be identified by the TOF PID procedure in a correct way.

In Fig. 5.103, the performance of the association algorithm in central Pb–Pb collisions is also shown in terms of the fraction of primary pions (a), kaons (b) and protons (c), generated in the  $|\theta - 90^\circ| < 45^\circ$  region, which have been associated with the correct (light-shaded histograms) or with a wrong (dark-shaded histograms) TOF signal. As a reference, the fraction of primary particles which reach the TOF sensitive volume and release a hit on the detector (empty histogram) is also shown. The observed loss in the TOF acceptance is due to the TOF dead space ( $\sim 15\%$  of the full  $|\eta| < 0.9$  acceptance), to the interaction of particles in the material in front of the TOF detector (equivalent to  $\sim 0.18$  absorption lengths, mostly due to the TRD material), and to particle decays (in the case of kaons). The momentum threshold for particles to reach the TOF is instead directly related to the magnetic field,  $p_{\text{min}} \sim 300 \text{ MeV}/c$  with  $B = 0.5 \text{ T}$ , being slightly higher (respectively  $\sim 350$  and  $\sim 450 \text{ MeV}/c$ ) for kaons and protons, due to the increased effect of the energy loss.

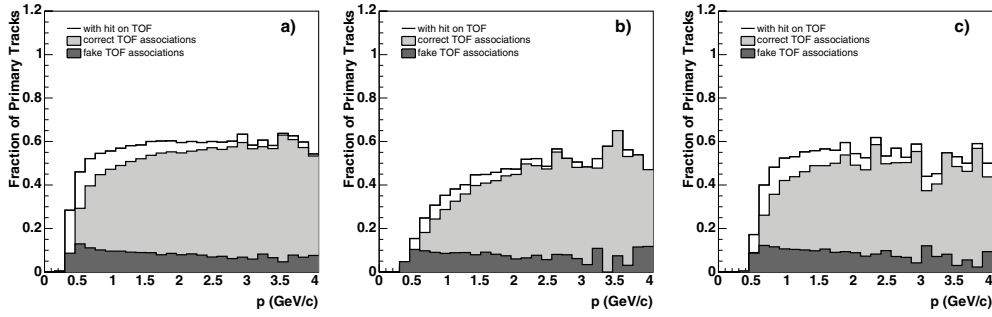


**Figure 5.103.** The fraction of primary pions (a), kaons (b) and protons (c), generated in the  $|\theta - 90^\circ| < 45^\circ$  region, which are associated to a correct (light-shaded histograms) and incorrect (dark-shaded histograms) signal on TOF, in central Pb–Pb collisions. The empty histogram indicates the fraction of primary particles which reach the TOF sensitive volume and release a hit on the detector.

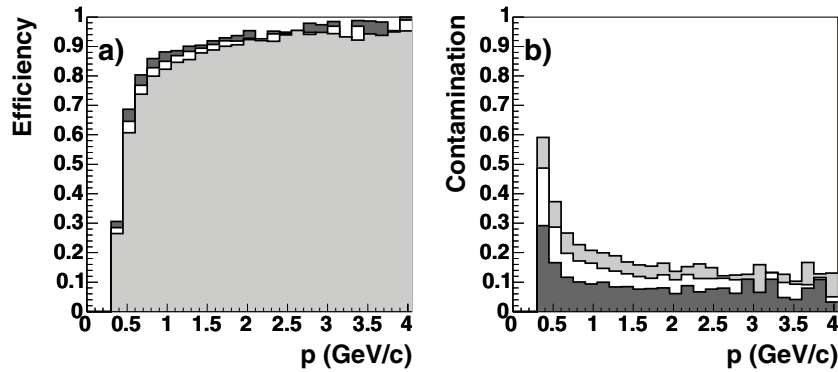


**Figure 5.104.** Track–TOF signal matching efficiency (a) and contamination (b) versus momentum, averaged over all hadron species ( $\pi$ , K, p), for different charged-track densities in the event. The dark-shaded, empty and light-shaded histograms correspond to Pb–Pb collisions generated with charged-track multiplicities per unit rapidity of  $dN_{\text{ch}}/d\eta = 2000, 5000$  and  $8000$ , respectively.

The quality of the track–TOF signal association procedure is expected to be sensitive to the track density characterizing the event. Figure 5.104 shows the association efficiency and contamination, averaged over all hadron species, for the three different charged-track densities  $dN_{\text{ch}}/d\eta = 2000, 5000$  and  $8000$  assumed in the simulated Pb–Pb collisions. Going from the highest to the lowest simulated multiplicity, variations of the order of a few per cent are observed in the efficiency, while the contamination decreases by approximately a factor two. The sensitivity to the track density is also at the origin of the dependence of the TOF matching algorithm performance on the centrality of the collision. This is illustrated in Fig. 5.105 (a) and (b), where the matching efficiency and contamination (integrated over the momentum range  $0.45 < p < 6 \text{ GeV}/c$ , and averaged over all hadron species) are shown as a function of the average charged-track multiplicity per unit rapidity observed in samples of Pb–Pb events generated at different centralities (see Section 5.4.4.1). In the most peripheral Pb–Pb collisions, where the predicted charged track multiplicity per unit rapidity is about 100, the overall matching efficiency is  $\sim 10\%$  higher, with a factor  $\sim 8$

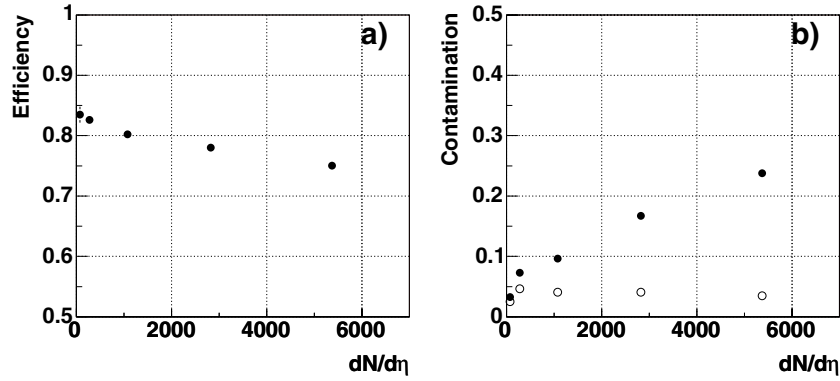


**Figure 105.** Track-TOF signal matching efficiency (a) and contamination (b) as a function of the average  $dN_{\text{ch}}/d\eta$  observed in Pb-Pb events generated at different centralities (full dots). The open symbols indicate the contamination from tracks associated with TOF signals coming from their secondaries.

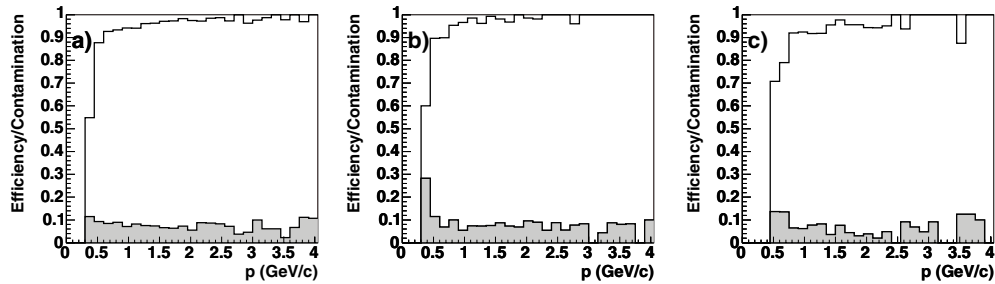


**Figure 5.106.** The momentum dependence of the efficiency (empty histograms) and the contamination (shaded histograms) of the TOF matching procedure for primary particles of different species in pp minimum-bias collisions ((a): pions, (b): kaons, (c): protons).

smaller fraction of mis-associated tracks with respect to the case of central events, where  $dN_{\text{ch}}/d\eta \approx 6000$ . As far as the matching contamination in particular is concerned, it can be noticed that the component of the contamination coming from the associations of the tracks to the secondaries produced in their decays or interactions (indicated in Fig. 5.105 (b) as open symbols) is essentially independent of  $dN_{\text{ch}}/d\eta$ , and becomes the dominant contribution when  $dN_{\text{ch}}/d\eta \lesssim 1000$ . The remaining part of the contamination, related to associations with TOF signals uncorrelated to the tracks, is instead consistent with scaling as the  $dN_{\text{ch}}/d\eta$  in the event.

Indeed, in the case of proton-proton interactions, where  $dN_{\text{ch}}/d\eta$  is expected to be three orders of magnitude lower than in central Pb-Pb events, the track-TOF signal matching procedure is particularly efficient and pure, as can be seen from Fig. 5.106. Notice that in this case a looser association criterion ( $d_{\text{max}} = 9$  cm) has been used. This leads to an increase of about 10% in the association efficiency, with a factor  $\sim 2$  increase in the contamination (which is, in any case, still very limited).

**5.4.4.3. Particle identification.** After the track-TOF signal matching step, the procedure for TOF Particle Identification (PID) is applied to all the reconstructed tracks that have been

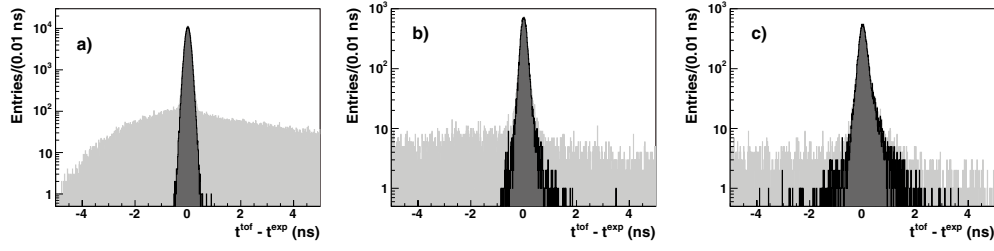


**Figure 5.107.** The difference between the measured time  $t^{\text{TOF}}$  and the time-of-flight  $t^{\text{exp}}$  calculated from tracking for (a) pions, (b) kaons, and (c) protons, in central Pb–Pb collisions. The dark and light-shaded histograms show the contribution from correctly and incorrectly associated tracks, respectively.

associated to a signal on the TOF system. As an illustrative example of the PID capabilities of the TOF detector in central Pb–Pb collisions, Colour Figure I shows, for all the reconstructed tracks matched with a signal on the TOF system, the correlation between the track momentum and the mass:

$$M = \frac{p}{\beta\gamma} = p \sqrt{\frac{(ct^{\text{TOF}})^2}{l^2} - 1}$$

calculated from the measured time-of-flight  $t^{\text{TOF}}$ , the reconstructed track length  $l$ , and the track momentum  $p$ . To translate such capabilities into a Particle Identification procedure, the Bayesian method described in Section 5.4.6 has been used.

The measured time-of-flight  $t^{\text{TOF}}$  is chosen as the PID discriminating variable, and the Gaussian

$$g_i(t^{\text{TOF}}) \sim \frac{1}{\sigma} \exp\left\{-\frac{(t^{\text{TOF}} - t_i^{\text{exp}})^2}{2\sigma^2}\right\} \quad (5.16)$$

is taken as the TOF ‘detector response function’ for different mass hypotheses  $m_i$  ( $i = e, \mu, \pi, K$  and  $p$ ). Besides the measured time-of-flight, the response function  $g_i$  depends on other two parameters, the expected time-of-flight  $t_i^{\text{exp}}$  for the  $i$ -th mass hypothesis and the overall time-of-flight resolution  $\sigma$ .

The expected time of flight  $t_i^{\text{exp}}$  is calculated during track reconstruction by summing up at each tracking step the time-of-flight increments:

$$\Delta t_k = \frac{\sqrt{p_k^2 + m_i^2}}{p_k} \Delta l_k,$$

$p_k$  being the local estimate of the track momentum and  $\Delta l_k$  the track length increment along the trajectory<sup>4</sup>. Additional details on the calculation of the expected time-of-flight  $t_i^{\text{exp}}$  can be found in Ref. [73].

The distribution of the difference between the measured time-of-flight  $t^{\text{TOF}}$  and the expected time  $t^{\text{exp}}$  for pions, kaons and protons is shown in Fig. 5.107, for central Pb–Pb collisions. The contribution from correctly associated tracks, shown as the dark-shaded histograms, is well described by a Gaussian in the case of pions, while non-Gaussian tails become increasingly more significant in the case of kaons and protons, because of the enhanced effects of the energy loss and multiple scattering. The light-shaded histograms

<sup>4</sup> To ensure a reliable calculation of the expected time of flight, the track is required to have a good extrapolation to the primary vertex; for primary particles, this requirement has an efficiency of  $\sim 95\%$ .

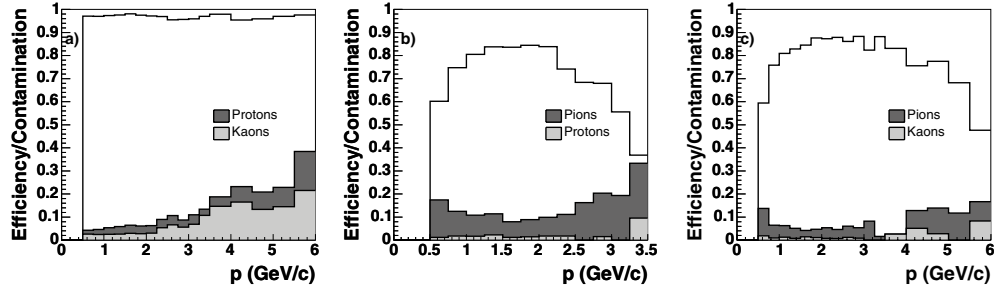


**Figure 5.108.** The momentum dependence of the efficiency and contamination of the PID algorithm for primary charged particles of different species ((a): pions, (b): kaons, (c): protons), in central Pb–Pb collisions. The empty histograms refer to the efficiency, the dark and light-shaded histograms show respectively the contamination coming from other particle species.

indicate the component from mis-associated tracks, which spreads over time differences of several nanoseconds.

The overall time-of-flight resolution,  $\sigma = \sqrt{\sigma_{\text{TOF}}^2 + \sigma_{\text{reco}}^2}$  includes both the time resolution of the TOF system,  $\sigma_{\text{TOF}}$ , and the uncertainty  $\sigma_{\text{reco}}$  related to the reconstruction of the momentum and of the track length. The latter uncertainty, which depends on the track momentum and on the particle type (see again Ref. [73]), is, on average,  $\sim 30$  ps.

On the basis of the response function  $g_i$  defined in Eq. (5.16), the conditional probability  $P_i(t^{\text{TOF}})$  to be a particle of type  $i$  is then assigned to each track weighting  $g_i$  by the *a priori* probability  $C_i$  for a track to be a particle of type  $i$ :

$$P_i(t^{\text{TOF}}) = \frac{C_i g_i(t^{\text{TOF}})}{C_e g_e(t^{\text{TOF}}) + C_\mu g_\mu(t^{\text{TOF}}) + C_\pi g_\pi(t^{\text{TOF}}) + C_K g_K(t^{\text{TOF}}) + C_p g_p(t^{\text{TOF}})},$$

$i = e, \mu, \pi, K, p.$

The identity of the track is defined by the highest among the probabilities  $P_i$ . For the results presented here, in the case of both Pb–Pb and pp collisions the *a priori* probabilities were respectively set to  $C_\pi = 0.85$ ,  $C_K = 0.10$ ,  $C_p = 0.05$  and  $C_e, C_\mu = 0.01$ , close to the generator-level particle concentrations observed in the HIJING and PYTHIA Monte Carlos. In central Pb–Pb collisions, no attempt to identify electrons was made because of a high background, while in the case of pp minimum-bias events, the particularly clean track environment allows for some level of separation, as will be shown later in this section.

The performance in central Pb–Pb collisions of the TOF PID algorithm is presented in Fig. 5.108, which shows the PID efficiency  $\varepsilon^{\text{PID}}(i)$  and contamination  $c^{\text{PID}}(i)$  for pions, kaons and protons ( $i = \pi, K, p$ ) as a function of the track momentum. The efficiency and the contamination are defined as

$$\varepsilon^{\text{PID}}(i) = \frac{N_{\text{id}}^{\text{l}}(i)}{N(i)}, \quad c^{\text{PID}}(i) = \frac{N_{\text{id}}^{\text{w}}(i)}{N_{\text{id}}^{\text{l}}(i) + N_{\text{id}}^{\text{w}}(i)},$$

$N(i)$  being the number of particles of type  $i$  ( $i = \pi, K, p$ ) associated with a signal on the TOF system,  $N_{\text{id}}^{\text{l}}(i)$  the number of particles of type  $i$  which are correctly identified, and  $N_{\text{id}}^{\text{w}}(i)$  the number of non-type  $i$  particles misidentified as particles of type  $i$ . While a very high ( $>95\%$ ) identification efficiency is observed for pions, approximately constant

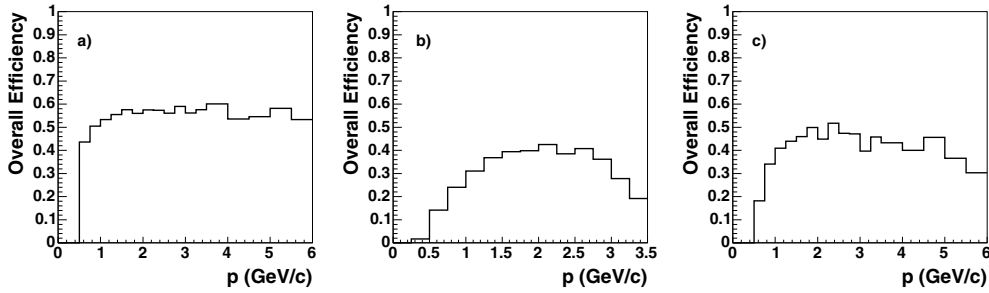


**Figure 5.109.** The momentum dependence of the overall PID efficiency for primary charged particles of different species (a): pions; (b): kaons; (c): protons), generated in the  $|\theta - 90^\circ| < 45^\circ$  region, in central Pb–Pb collisions.

over the momentum range  $0.5 < p < 6 \text{ GeV}/c$ , the efficiencies for kaons and protons are generally lower (at most 85%) and momentum-dependent. At low momenta, the main factor limiting the kaon and proton efficiencies is related to track–TOF signal mis-associations (and decays, in the case of kaons), while at high momenta it is also due to the decrease of the  $\pi/K$  and  $K/p$  separation power of the time-of-flight system. The pion efficiency is less sensitive to these effects, being the most abundant particle species. For PID contamination, in case of pion identification the fraction of incorrect particle-type assignments (coming predominantly from kaons) ranges from a few per cent to  $\sim 30\%$  over the momentum interval  $0.5 < p < 6 \text{ GeV}/c$ . A comparably low level of contamination (from a few per cent to 15%, coming mostly from pions) is observed for protons in the same momentum range, while kaons are identified with a contamination varying from 20% to 10% (again, mostly from pions) in the range  $0.5 < p < 3 \text{ GeV}/c$ . As in the case of the efficiency, at low momentum the PID contamination originates predominantly from track–TOF signal mis-associations, while at high momenta it is also related to the decrease of time-of-flight separation power.

Figure 5.109 shows the corresponding overall TOF PID efficiencies with respect to primary tracks generated in the  $|\theta - 90^\circ| < 45^\circ$  region. Notice that in this case, in addition to the efficiency of the PID algorithm, all the factors coming from the track reconstruction efficiency, the effect from TOF dead space, the losses due to the particle decays or interactions and the efficiency of the track-TOF association procedure (see Section 5.4.4.2) are included. On average, in a central Pb–Pb collision simulated with HIJING, about 1600 primary pions and about 100 kaons and protons are expected to be reconstructed and correctly identified by the TOF system.

The quality of the TOF PID at high momenta depends significantly, as expected, on the time resolution of the TOF system. This can be seen from Fig. 5.110, which shows, as an example, the kaon PID efficiency and contamination for the three different TOF time resolutions of 80, 120 and 60 ps. The PID performance is also affected by the charged-track density in the event. This is demonstrated in Fig. 5.111, where the kaon PID efficiency and contamination are shown for simulated Pb–Pb collisions with  $dN_{\text{ch}}/d\eta = 2000, 5000$  and 8000. As expected, the sensitivity of the TOF PID performance to the charged-track density is most significant in the low-momentum region, where the contribution of mis-associated tracks is predominant.

Finally, it should also be remarked that, with respect to the results presented here, the actual level of the PID contamination in central Pb–Pb collisions may change significantly if the relative particle concentrations for pions, kaons and protons at the LHC are different from

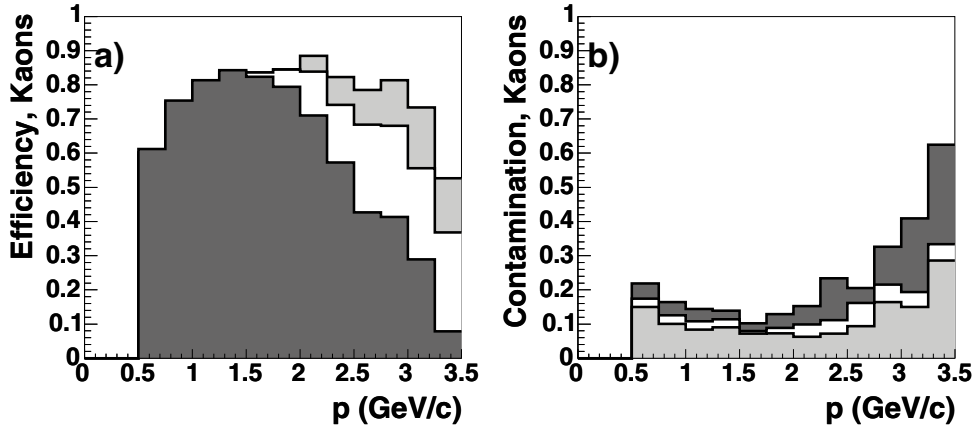


**Figure 5.110.** The momentum dependence of the (a) algorithmic PID efficiency and (b) contamination for three different TOF time resolutions of 80, 60 and 120 ps (empty, light and dark-shaded histograms, respectively), for primary kaons in central Pb–Pb collisions.

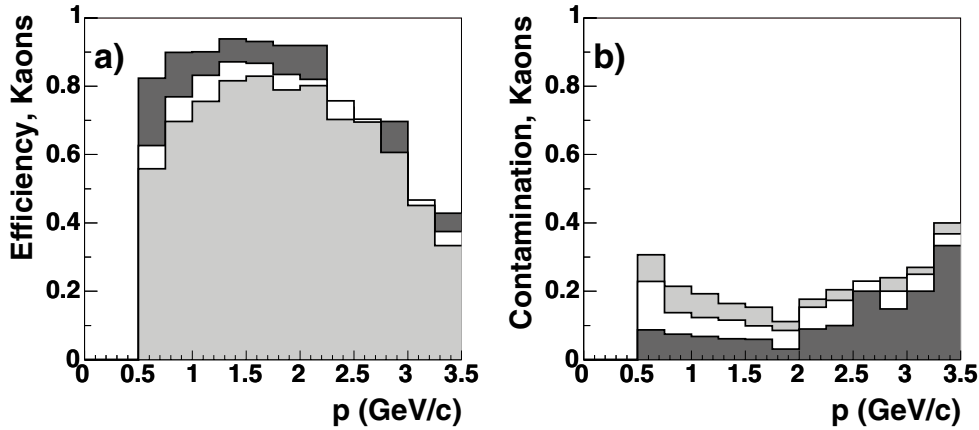


**Figure 5.111.** The momentum dependence of the algorithmic PID efficiency (a) and contamination (b) for primary charged kaons, for three different charged track multiplicities per unit rapidity  $dN_{ch}/d\eta = 2000, 5000$  and  $8000$  (dark-shaded, empty and light-shaded histograms). The simulated TOF time resolution is 80 ps.

those predicted by HIJING. In particular, a substantial improvement in the kaon identification is expected if the production rates of pions, kaons and protons become comparable for momenta  $\gtrsim 1.5$  GeV/c, as currently indicated by the results on the charged hadron spectra obtained at RHIC [74]. To be more independent of the particle ratios simulated in the Monte Carlo, the TOF PID performance in central Pb–Pb collisions is also presented in terms of the probability for particles of type  $i$  to be mistagged as a particle of type  $j$ , ( $i \neq j$ ), for a fixed identification efficiency (here 85% has been chosen) for particles of type  $j$  ( $i, j = \pi, K, p$ ). The results are shown in Fig. 5.112.

The performance of the TOF PID improves in case of peripheral collisions, owing to the reduction of the level of track–TOF signal mis-associations with decreasing charged-track density in the event. This can be seen from Fig. 5.113, which shows the kaon PID

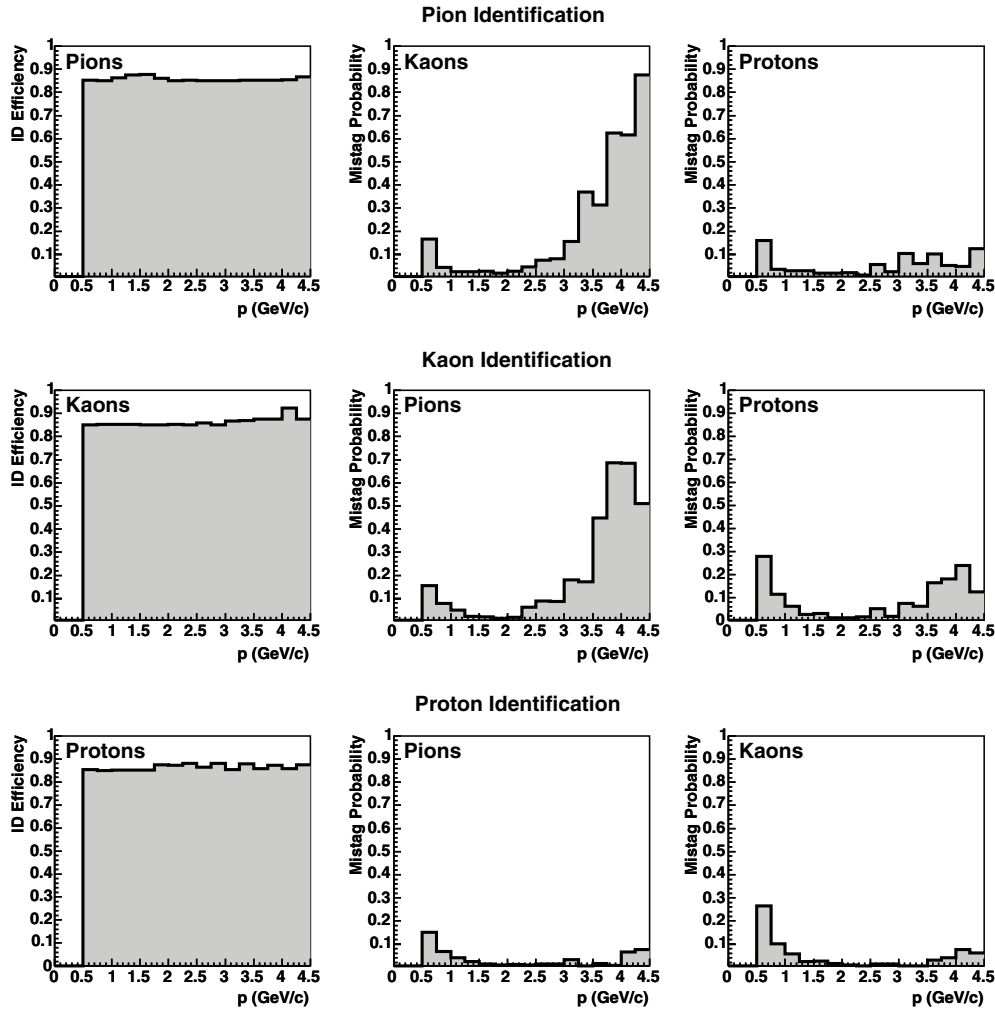


**Figure 5.112.** PID efficiencies (fixed at 85%, see text) and mistag probabilities in case of pion (top), kaon (middle) and proton identification (bottom), for pions, kaons and protons in central Pb–Pb collisions.

efficiency and contamination, integrated over the momentum range  $0.5 < p < 3$  GeV/c, as a function of the charged-track multiplicity per unit rapidity observed in Pb–Pb collisions at different centralities. A substantial improvement in the PID performance is also observed in pp collisions (Fig. 5.114); the TOF algorithmic PID efficiency is above 90% over a considerable fraction of the momentum range even for kaons, with a contamination of some relevance only at high momenta. Moreover, as mentioned before in this section, the particularly clean track environment which is expected in pp collisions may even allow one to identify low-momentum electron tracks via a time-of-flight measurement (see Fig. 5.114 (d)).

**5.4.5. Particle identification with HMPID.** The hadron identification at high transverse momenta ( $1 < p < 3$  GeV/c for  $\pi$  and K,  $1 < p < 5$  GeV/c for p), in the ALICE experiment will be achieved by the HMPID (RICH) detector.

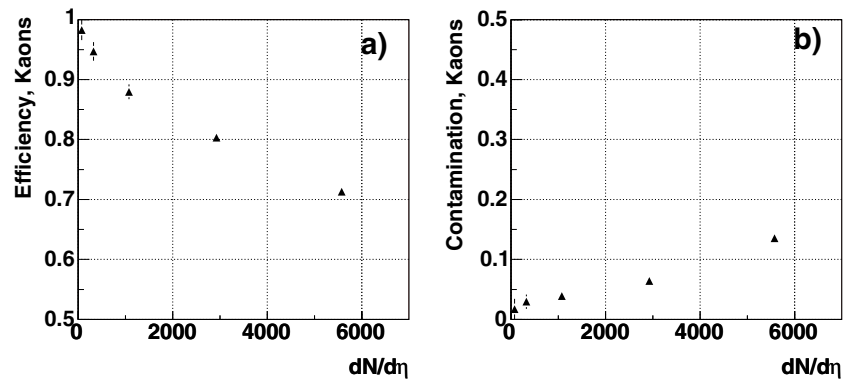


Figure 5.113. PID efficiency (a) and contamination (b) for kaons, integrated over the momentum interval  $0.5 < p < 3 \text{ GeV}/c$ , as a function of the charged-track multiplicity per unit rapidity in Pb–Pb events at different centralities.

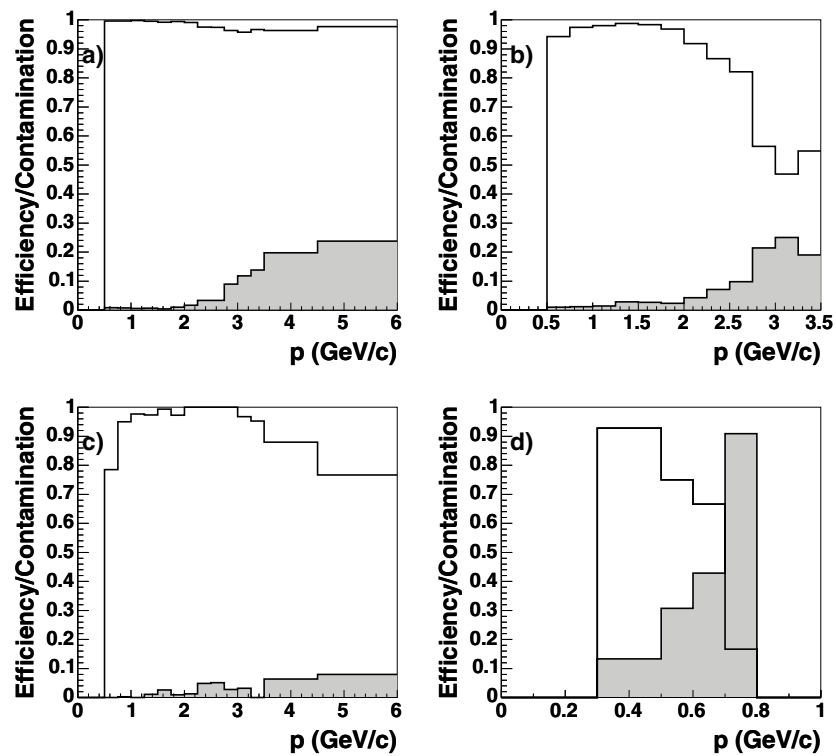
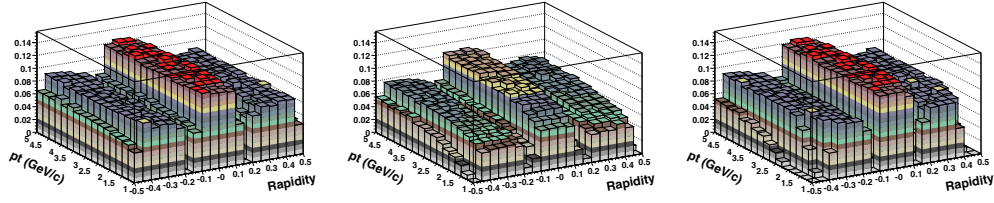


Figure 5.114. The momentum dependence of the PID efficiency and the PID contamination for primary charged particles of different species ((a): pions, (b): kaons, (c): protons and (d) electrons) in pp minimum-bias collisions. The empty histograms refer to the efficiency, while the shaded histograms indicate the PID contamination.



**Figure 5.115.** The HMPID acceptance for pions (left), kaons (centre) and protons (right). In the case of kaons, the mean lifetime has been taken into account. The magnetic field is 0.5 T and uniform.

In the acceptance region covered by the HMPID (about 5% of the full central) the maximum particle density reaches  $100 \text{ m}^{-2}$  (including the expected background) with incident angle ranging from  $0^\circ$  to  $15^\circ$  [75]. The tracking capability of the ALICE apparatus allows a satisfactory reconstruction of the impact, and of the incident angle for charged particles impinging on HMPID modules. Nevertheless, the high global multiplicity onto the photocathodes (track impacts, Cherenkov and feedback photons etc.) and the dependence of Cherenkov images from the track's incident angle make the pattern recognition and the Cherenkov angle reconstruction very complex.

All the details about the HMPID reconstruction can be found in Ref. [76]. Below we report the main results.

**5.4.5.1. HMPID acceptance for charged particles.** In Fig. 5.115, the detector acceptances for pion, kaons and protons, respectively, as a function of rapidity and transverse momentum are shown (magnetic field is 0.5 T). A charged particle is accepted by the detector if it passes through the sensitive MWPC volume of the detector creating a cluster at the pad plane.

In the central rapidity region ( $|y| < 0.15$ ), covered by three modules, the acceptance is the factor of 1.5 more than that on the sides ( $|y| > 0.15$ ) covered by two modules only. The dead zones between the modules are seen. In the calculations of the acceptance for each of the modules, the dead zones between the photocathodes were taken into account. In the case of the acceptance for kaons, the finite mean lifetime of the particles was considered.

**5.4.5.2. Matching algorithm with HMPID.** The identification of the charged particles in the HMPID requires tracks from the central tracking devices (ITS, TPC, TRD) to be extrapolated and associated with an ionization cluster in the HMPID cathode plane [77]. Therefore, the first step in the analysis procedure is the discrimination between a photon and a given MIP cluster. This selection is made by applying a threshold cut on the cluster charge (depending on the gain of the HMPID chamber).

In Fig. 5.116 (top) the minimum distance  $d_{\min}$  between the extrapolated track point on the HMPID photocathode plane of a given chamber and the coordinate of the nearest centroid, of a charge compatible with a MIP cluster, is shown. The distribution clearly shows that the majority of the events are within one pad size ( $8.0 \times 8.4 \text{ mm}^2$ ). A selection of  $d_{\min} < 1 \text{ cm}$  can be applied, with about 80% of the particles selected. It has been estimated that about 8% of the distribution, representing part of the tail of the distribution, comes from the decay of charged kaons.

In the distribution of Fig. 5.116 (bottom), it is evident how the multiple scattering contributes to  $d_{\min}$ ; for high momenta ( $p \simeq 5 \text{ GeV}/c$ ) the selection on  $d_{\min}$  to define a good matching may be less.

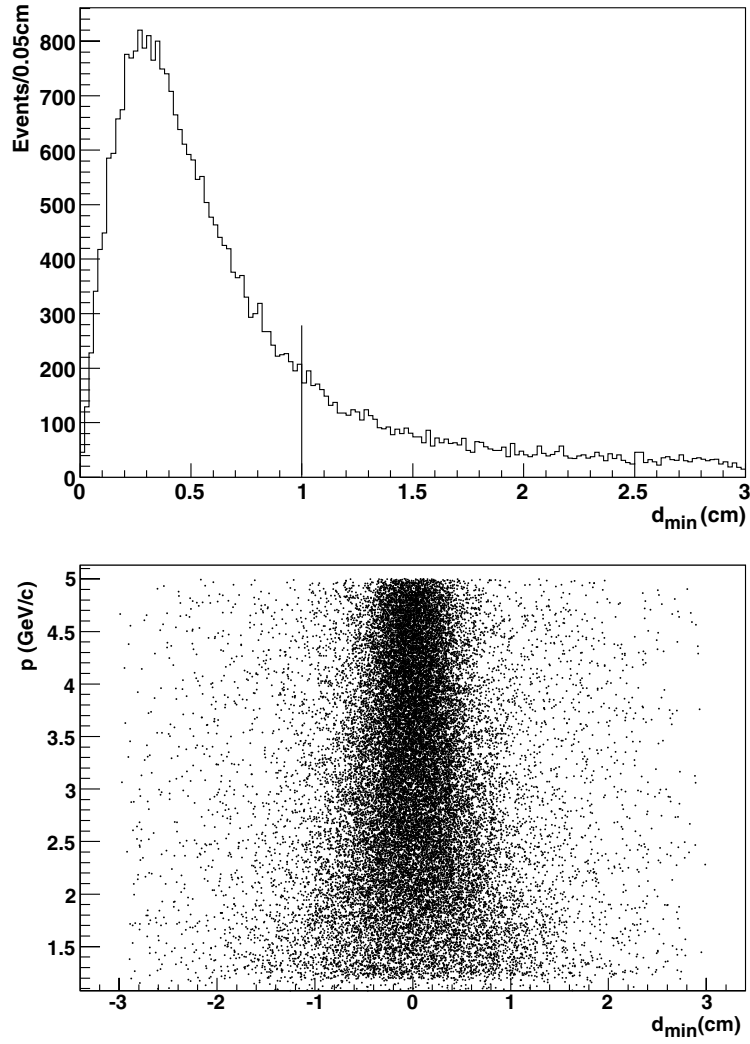


**Figure 5.116.** Distribution of the distance  $d_{\min}$  between the extrapolated track position at the HMPID photocathode plane and the nearest MIP centroid ( $Q_{MIP} < 100$  ADC). Central HIJING events ( $dN_{ch}/d\eta = 6000$ ).

It is important to point out that the inclination angle  $\theta_p$  has to be known with high precision. In fact it determines the shape of the ring and then affects systematically the value of the single Cherenkov angle  $\theta_c$ . Therefore, in order to reduce the error on the inclination angle  $\theta_p$  of impact of the track, the selection  $d_{\min} < 1$  cm has been applied in the whole range of  $p_t$ . This cut reduces the probability of mismatching of a track with the MIP cluster of another particle (the cut is of the order of the pad size), even if the efficiency will decrease. Figure 5.117 shows the distribution of the  $\Delta\theta_p$ , difference between the  $\theta_p^{\text{sim}}$  of the simulated track and the  $\theta_p^{\text{rec}}$  of the reconstructed track. A value of  $\sigma = 2.8$  mrad has been obtained from the fit of the distribution. This accuracy on the  $\theta_p$  implies an indetermination less than 3% on  $\theta_c$ .

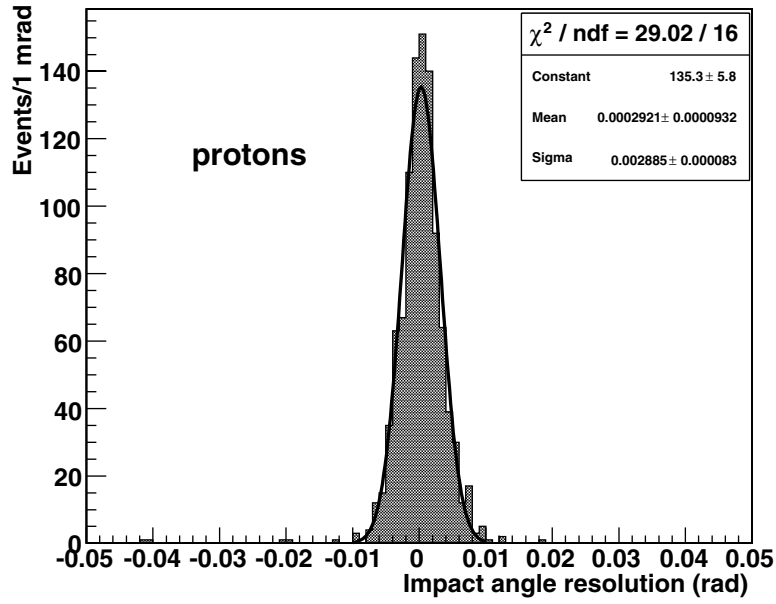


**Figure 5.117.** Difference between the angles of impact on the HMPID, with respect to the normal at the detector, for the simulated and the reconstructed track. The distributions refers to protons in central HIJING events ( $dN_{\text{ch}}/d\eta = 6000$ ).

In Fig. 5.118 the matching efficiency, as a function of the  $p_t$  for pions, kaons and protons is shown. The loss of efficiency at lower transverse momenta is due to the multiple scattering and the cut  $d_{\text{min}} < 1$  cm. The probability of mismatching, similar for the three particle types, is also shown.

**5.4.5.3. Extraction of the mean Cherenkov angle: the Hough transformation method.** The Hough Transformation Method (HTM) is an efficient implementation of a generalized *template matching* strategy for detecting complex patterns in binary images. This is achieved by analyzing the parameters which characterize these patterns and looking for local maxima in a *feature parameter space*. The main advantage of the Hough transform is that it is relatively unaffected by topological gaps in curves and by high noise background in spot-like images. Let us assume that we transform a Cartesian space to a feature space:

$$\mathbf{x} \rightarrow (\mathbf{a}, T(\mathbf{x}, \mathbf{a})) \quad (5.17)$$

where  $\mathbf{a}$  is a parameter vector and  $T(\mathbf{x}, \mathbf{a})$  its relative transform. For each thresholded contribution of  $T(\mathbf{x}, \mathbf{a})$  in the parameter space, the value of a corresponding variable  $HCS(T(\mathbf{x}, \mathbf{a}))$  gets incremented according to the following scheme:

$$HCS(T(\mathbf{x}, \mathbf{a})) \rightarrow HCS(T(\mathbf{x}, \mathbf{a})) + w. \quad (5.18)$$

This counting procedure defines the function  $HCS(T(\mathbf{x}, \mathbf{a}))$  in the so-called *Hough Counting Space*. The incrementation function  $w = w(\mathbf{x}, \mathbf{a})$  allows one to use other relevant information associated with a given feature point. If the incrementation quantity  $w$  is assumed unitary, a simple counting of the number of contributions as a function of the *feature vector*  $\mathbf{a}$  is performed. Nevertheless the incrementation strategy of Eq. (5.18) can be refined further by applying an incrementation function:

$$w = w(\mathbf{x}, \mathbf{a}). \quad (5.19)$$

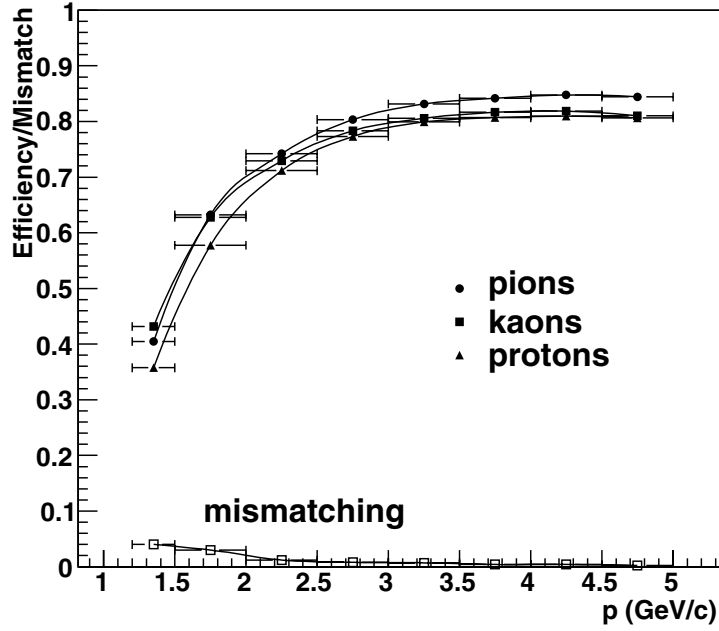


**Figure 5.118.** Track–MIP cluster matching efficiency and the probability of mismatching (open squares) as a function of the momentum for pions, kaons and protons.

In this way a weighting policy can be applied in order to use other relevant informations associated with a given feature point. The Hough estimator for the feature vector is given by the bin value in *HCS* with the highest frequency in the parameter space.

For Cherenkov patterns, the starting point of the analysis consists of a bidimensional map with the impacts  $(x_p, y_p)$  of the charged particles, impinging the detector plane with known incidence angles  $(\theta_p, \varphi_p)$ , and of the coordinates  $(x, y)$  of hits due to both Cherenkov photons and background sources. A Hough counting space has to be constructed for each charged particle, according to:

$$(x, y) \rightarrow ((x_p, y_p, \theta_p, \varphi_p), \eta_c). \quad (5.20)$$

Since the feature vector  $\mathbf{a} = (x_p, y_p, \theta_p, \varphi_p)$  is provided by the tracking of the charged particle, the transform will reduce the problem to a solution in a one-dimensional mapping space. The transformation which provides the parameter  $\eta_c$  for a given  $\mathbf{a}$  vector is the *geometrical backtracing algorithm* to extract the Cherenkov angle associated to each photon pad.

The *HCS* in this case represents the photon Cherenkov angle  $\eta_c$  spectrum and, indeed, a Hough estimator for the Cherenkov angle  $\theta_c$  of the particle is chosen as the highest peak provided by all the photons which fall in that angle bin. Thus, the *HCS* accumulates the contributions from several Cherenkov photons according to the expression (5.18). The analysis procedure can be easily extended and made more effective if the weight function (5.19) is used to take into account other factors like the background evaluation or the charge contribution for each Cherenkov photon.

The basic HT method applied for the HMPID has been enhanced in such a way as to be less influenced from the background caused from several noise sources.

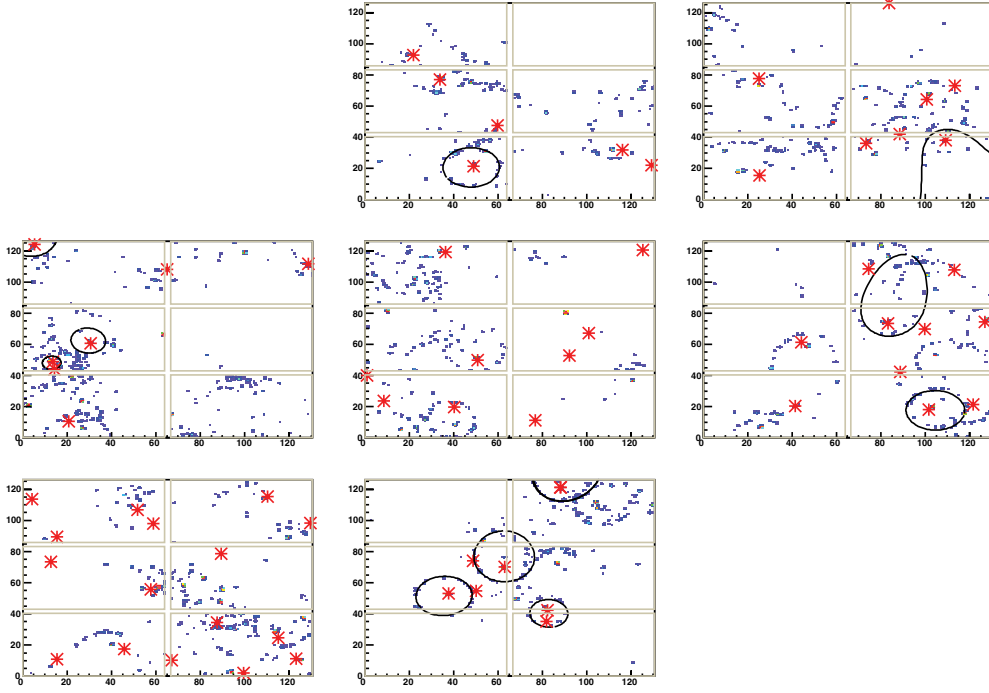


**Figure 5.119.** An offline event display of a central Pb–Pb HIJING event ( $dN_{\text{ch}}/d\eta = 2500$ ) in the HMPID. Reconstructed rings with relative photon cluster (star) are shown for associated tracks.

For each photon there is a spread in the Cherenkov angle to be taken into account, which makes it harder to achieve a good resolution  $\sigma_{\eta_c}$  in the Cherenkov angle identification. In order to enhance statistically as much as possible the signal in the  $\eta_c$  spectrum, the incrementation expression (5.18) has been modified as described in the following.

The following integration in the  $\eta_c$  space over a ‘sampling band’  $b$  has been applied:

$$HCS'(\eta_c) = \int_{\eta_c - \frac{b}{2}}^{\eta_c + \frac{b}{2}} HCS(\eta'_c) d\eta'_c, \quad (5.21)$$

which in the discrete case, where  $d\eta_c = 1$  mrad (i.e.  $\eta_c(k) = k d\eta_c$ ,  $k$  integer), transforms into the correlation:

$$HCS'(\eta_c(k)) = \sum_{i=\eta_c(k) - \frac{b}{2}}^{\eta_c(k) + \frac{b}{2}} HCS(i). \quad (5.22)$$

The  $HCS$  has been calculated using  $w = W_{\text{bkg}}(\eta_c)$  defined by Eq. (5.19) as the incrementation function. The sampling band in the correlation has been determined at 45 mrad for the smallest  $\sigma_{\eta_c}$  value.

Figure 5.119 shows an offline display of an event, where the reconstructed rings associated to tracks are also shown.

*Improvements to the Cherenkov angle reconstruction.* Several improvements in the method described above have been implemented [78]. In central Pb–Pb central events, where the HMPID occupancy is more than 10%, the background mainly due to photons coming from other charged particles, becomes relevant. In order to take into account the background,

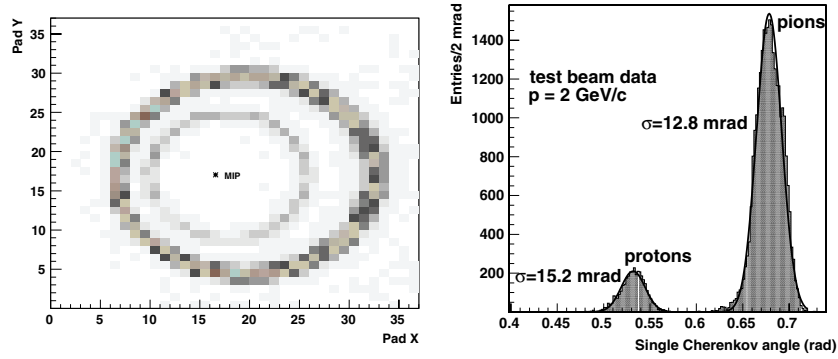


**Figure 5.120.** Left: Pad map of the Cherenkov photons for protons (inner ring) and pions (outer ring), with  $p = 2 \text{ GeV}/c$  (the MIP cluster has been removed). The particles cross the HMPID detector with an incidence angle  $\theta_p = 4^\circ$  with respect to the normal at the detector. Right: Single Cherenkov angle distribution for pions and protons. Experimental data have been collected from a PS test beam (beam composition: 11% protons, 89% pions).

supposed to be uniformly distributed on the photocathode, the photon density is calculated introducing a weight equal to  $1/A$  in Eq. (5.19), where  $A$  is the area allowed to that photon falling in the given search band.

To minimize the propagation errors of the track parameters  $(x_p, y_p, \theta_p, \varphi_p)$  on the reconstruction of the Cherenkov angle of the single photon, the extrapolated coordinates of the track  $(x_p, y_p)$  are replaced by the coordinate of the MIP cluster, representing a better estimate of the impact point. In addition, an iterative procedure to improve the knowledge of the impact angles of the track  $(\theta_p, \varphi_p)$  to the HMPID is applied. In fact, after having tagged  $N$  candidate photons to a given ring, a minimization of  $\sigma/\sqrt{N}$  (where  $\sigma$  is the r.m.s. of the tagged photon distribution), with the impact angles as free parameters, is performed. If  $N$  changes, the Hough algorithm is applied again by using the new angles. The iteration stops when no change in the number of photons occurs. It has been estimated, by simulation, that this improves the reconstructed Cherenkov angle resolution by about 20%.

**5.4.5.4. Response function of the HMPID detector.** The HMPID group has investigated in detail the response of the HMPID detector to charged particles, by analyzing data coming from different test beam sessions [79]. It was possible to study the performance of the HMPID detector as a function of the beam energy, the beam type (pions and protons), the inclination angle to the detector, the impact point on the photocathode, gain of the MWPC. The response of the detector has been studied in terms of different variables (i.e. mean number of photons); in particular the evaluation of the standard deviation  $\sigma_{\text{photon}}^{\text{single}}$  of Cherenkov angle  $\theta_c$  for single photon is fundamental to be confident to the response of the detector in terms of identification probability.

At fixed momenta and inclination angle  $\theta_p$ , the distribution of the single Cherenkov angle  $\theta_c$  is well described by a Gaussian. In Fig. 5.120 (left) data from beam tests show the typical ring pattern for pions and protons with  $p = 2 \text{ GeV}/c$  and  $\theta_p = 4^\circ$ , while on the right of Fig. 5.120, the distributions of the  $\theta_c$  for pions and protons are clearly of Gaussian shape.

The  $\sigma_{\theta_c}$  has been parametrized as a function of the following parameters:

$$\sigma_{\theta_c} = \sigma_{\theta_{c,i}}(p, \theta_p, \varphi_p, \varphi_{\text{ring}}), \quad i = \pi, K, p,$$

where  $p$  is the momentum of the charged particle,  $(\theta_p, \varphi_p)$  are the particle impact angles to the HMPID module, and  $\varphi_{\text{ring}}$  is the azimuthal angle of the single Cherenkov photon around the MIP.

The parametrization has been obtained in the following way. From the test beam data, the  $\sigma_{\theta_c}$  has been found by fitting the distributions of the single Cherenkov angle  $\theta_c$  at different momenta, impact angle  $\theta_p$ . Other values of  $\sigma_{\theta_c}$ , not available from experimental data, have been interpolated by the results obtained from Monte Carlo simulation.

The Cherenkov angle  $\theta_c$  for single photon is mainly affected by the following errors:

$$\sigma_{\theta_c}^2 = \sigma_{\text{chrom}}^2 + \sigma_{\text{geom}}^2 + \sigma_{\text{loc}}^2,$$

where:

- $\sigma_{\text{chrom}}$  is the chromatic error, related to the variation of the radiator refractive index  $n$  with the photon energy  $E$ . It is generated by the dispersion  $dn/dE$  of the radiator medium index and by the spread of the detector response over the effective photon energy range. The detector response, in turn, is determined by the convolution of the CsI photocathode (PC) quantum efficiency (QE) with the transmission of the media traversed by the Cherenkov photons inside the detector.
- $\sigma_{\text{geom}}$  is the geometrical error, related to the spread of the emission point along the particle path in the Cherenkov radiator.
- $\sigma_{\text{loc}}$  is the localization error, related to the precision with which the photon and particle impact coordinates can be measured. It is determined by the photodetector geometry (pad size, sense wires pitch) and by the photon feedback.

While the chromatic and geometrical error are intrinsic, respectively, to the radiator properties and to the proximity focusing technique, the latter is determined by experimental conditions, such as the photodetector gain  $A_0$ .

In Fig. 5.121 the dependence of  $\sigma_{\text{chrom}}$ ,  $\sigma_{\text{geom}}$  and  $\sigma_{\text{loc}}$  with the photons azimuthal angle  $\varphi_{\text{ring}}$ , for a proton of  $p = 5 \text{ GeV}/c$  and impact angles  $\theta_p = 0^\circ$  and  $\theta_p = 7.5^\circ$ , respectively, is shown. The results on the  $\sigma_{\theta_c}$  are a good fit to the data coming from beam tests.

However, as discussed in 5.4.5.2 the error on  $\theta_p$ , due to the precision of the tracking devices, as well as the pad occupancy (that implies a certain probability of cluster overlapping), can affect the measurement of  $\sigma_{\theta_c}$ . The integrated effect has been estimated to be of the order of 10%. The influence of the occupancy on the  $\sigma_{\theta_c}$  is, however, still under study.

**5.4.5.5. PID with HMPID.** The PID procedure for the HMPID [76] is the following. The probability that a given reconstructed  $\theta_c$  belongs to the probability density function (pdf) of the particle type  $i = \pi, K, p$  and falls in the interval  $[\theta, \theta + d\theta]$  is

$$P(\theta_c)d\theta = \text{Gauss}(\theta_c, \sigma_{\theta_{c,i}})d\theta,$$

where  $\theta_{c,i}$  can be found from the knowledge of the response function of the detector. Finally, the probability that a given particle with  $\theta_c$  is of the type  $i = \pi, K, p$  is

$$P_i = \frac{\text{Gauss}(\theta_c, \sigma_{\theta_{c,i}})}{\sum_{i=\pi, K, p} \text{Gauss}(\theta_c, \sigma_{\theta_{c,i}})}, \quad i = \pi, K, p.$$

It is possible to choose a significance level (typically 0.10, 0.05, and 0.01) to identify a particle. The significance level, however, will affect the efficiency and the contamination.

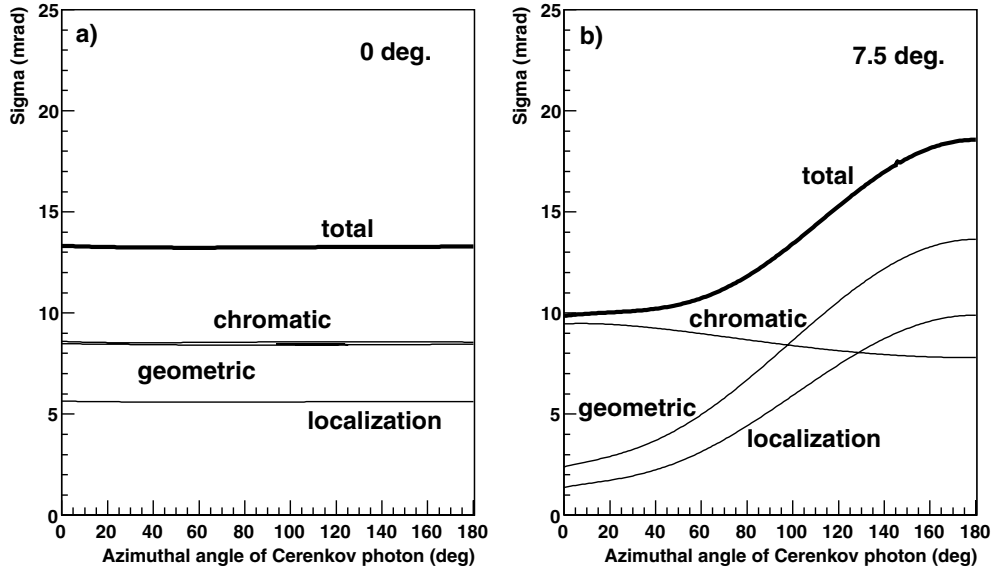


**Figure 5.121.** Different contributions to the Cherenkov angle  $\sigma_{\theta_c}$  for single Cherenkov photon, emitted by protons of  $p = 5 \text{ GeV}/c$  as a function of the azimuthal angle  $\varphi_{\text{ring}}$ , at the particle angles (a)  $\theta_p = 0^\circ$  and (b)  $\theta_p = 7.5^\circ$ .

**5.4.5.6. Analysis and results.** The reconstructed Cherenkov angle as a function of the track momentum measured by the tracking devices is shown in Fig. 5.122. Clear bands of events around the predicted curves for  $\pi$ , K and p are visible with low background.

The performance of the recognition strategy of circular Cherenkov patterns based on the Hough transformation, in fully simulated central Pb–Pb ALICE events ( $dN_{\text{ch}}/d\eta = 6000$ ), was studied in terms of particle identification efficiency and particle contamination [80].

In order to study a set of ring patterns at fixed momentum and incidence angle in the ALICE multiplicity environment, central Pb–Pb events ( $\sim 13\%$  of pad occupancy) were simulated in the ALICE setup for a charged-particle multiplicity of  $dN_{\text{ch}}/d\eta = 6000$ . First the total response (charged particles and photons) of a HMPID module was generated and then a track with its Cherenkov photons at a given momentum and incidence angle was generated and merged with the event.

The procedure was repeated for pions, kaons, and protons reaching the central HMPID module, in the momentum range between 1.2 and 5 GeV/c, until a satisfactory statistics was reached for each particle type. The tracks were reconstructed including ITS, TPC and TRD; in addition, for further studies on combined PID, the charged track was accepted if detected by the TOF detector. The pattern recognition method was applied to obtain the respective distributions of the reconstructed Cherenkov angle [76], so that efficiency and contamination for the three species of hadrons could be examined. For efficiency  $\varepsilon_i$  and contamination  $c_i$  concerning the particle of type  $i = \pi, K, p$  at a fixed momentum value, the following definition was employed:

$$\varepsilon_i = \frac{N_i^{\text{found}}}{N_i^{\text{tot}}}, \quad c_i = \frac{N_j^{\text{found}} + N_k^{\text{found}}}{N_i^{\text{found}} + N_j^{\text{found}} + N_k^{\text{found}}}, \quad i \neq j \neq k \quad (i = \pi, K, p),$$

where  $N_i^{\text{found}}$  denote the number of the reconstructed rings with Cherenkov angle in a selected range, while  $N_i^{\text{tot}}$  is the number of the total simulated rings for particle of  $i$  type.

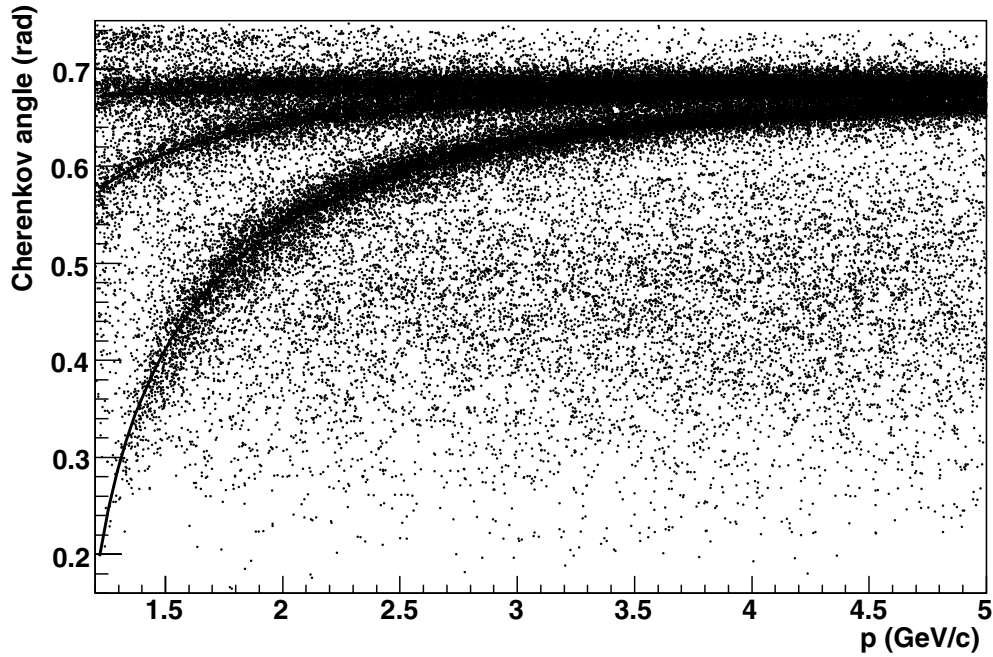


**Figure 5.122.** Reconstructed Cherenkov angle in the HMPID as a function of the track momentum. Equal concentrations of pions, kaons, and protons have been merged with HIJING events ( $dN_{\text{ch}}/d\eta = 6000$ ). Solid lines indicate the predicted curves for  $\pi$ , K and p.

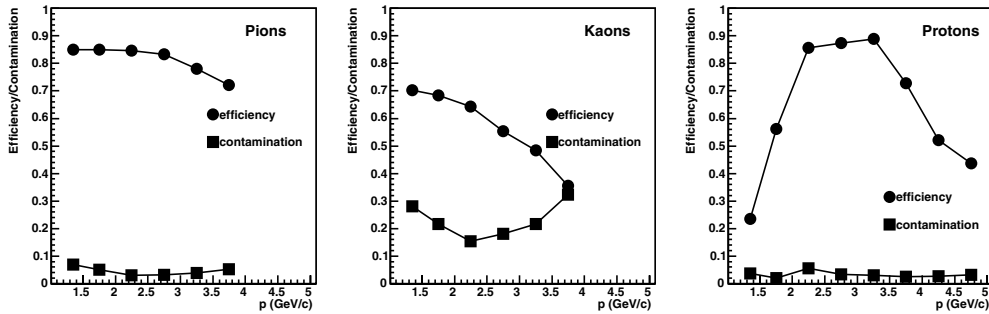


**Figure 5.123.** Efficiency and contamination for pions, kaons, and protons.

The dependence of expected particle production ratios from the momentum, estimated with HIJING, have been taken into account to calculate  $c_i$ .

The cuts made in the analysis reflected the best compromise between efficiency and contamination. It is only indicative since cuts will depend on the physics signal under study with the HMPID. Figure 5.123 reports the efficiencies and contaminations, computed for  $\pi$  in the momentum range 1.2–4 GeV/c, for K in the momentum range 1.2–3 GeV/c and for p in the momentum range 1.2–5 GeV/c. The identification of charged particles with the HMPID detector was performed on simulated central Pb–Pb events ( $dN_{\text{ch}}/d\eta = 6000$ ).

**5.4.6. Combined particle identification.** Having to combine the PID information coming from different detecting systems implies dealing, in some common way, with PID signals of

a different nature (e.g.  $dE/dx$  and time-of-flight measurements). The situation is additionally complicated by the amount of data to be processed (about  $10^7$  events with about  $10^4$  tracks in each). Thus the particle identification procedure should be as much as possible automatic and should also be capable of combining signals distributed according to quite different probability density functions.

We will demonstrate here that combining PID signals in a Bayesian way satisfies all these requirements. The method described in the following is similar to that in Ref. [81].

*5.4.6.1. Bayesian PID with a single detector.* Let  $r(s|i)$  be a conditional probability density function to observe in some detector a PID signal  $s$  if a particle of type  $i$  ( $i = e, \mu, \pi, K, p, \dots$ ) is detected. The probability to be a particle of type  $i$  if the signal  $s$  is observed,  $w(i|s)$ , depends not only on  $r(s|i)$ , but also on how often this type of particles is registered in the considered experiment (*a priori* probability  $C_i$  to find this kind of particle in the detector). The corresponding relation is given by Bayes's formula:

$$w(i|s) = \frac{r(s|i)C_i}{\sum_{k=e,\mu,\pi,\dots} r(s|k)C_k}. \quad (5.23)$$

Under some reasonable conditions,  $C_i$  and  $r(s|i)$  are not correlated so that one can rely on the following approximation:

- The functions  $r(s|i)$  reflect only properties of the detector ('detector response functions') and do not depend on other external conditions like event and track selections.
- On the contrary, the quantities  $C_i$  ('relative concentrations' of particles of type  $i$ ) do not depend on the detector properties, but do reflect the external conditions, selections etc.

The PID procedure is done in the following way. First, the detector response function is obtained. Second, a value  $r(s|i)$  is assigned to each track. Third, the relative concentrations  $C_i$  of particle species are estimated for a subset of events and tracks selected in a specific physics analysis. Finally, an array of probabilities  $w(i|s)$  is calculated (see Eq. (5.23)) for each track within the selected subset.

The probabilities  $w(i|s)$  are often called PID weights.

*Obtaining the conditional probability density functions.* The conditional probability density function  $r(s|i)$  (detector response function) can always be parametrized with sufficient precision using available experimental data.

Let us consider, for example, the ALICE TPC. Currently, the ALICE reconstruction software uses the following parametrization. For each track reconstructed in the TPC,  $r(s|i)$  ( $s$  is the assigned  $dE/dx$  measurement) is Gaussian with centroid  $\langle dE/dx \rangle$  given by the Bethe–Bloch formula and width calculated as  $\sigma = \kappa \langle dE/dx \rangle$ , where the coefficient  $\kappa$  is approximately constant over all the momentum region and for all the particle species and, in case of simulated central HIJING [67] Pb–Pb  $\sqrt{s_{NN}} = 5.5$  TeV events, it is about 0.07 (see Fig. 5.124).

*Obtaining the a priori probabilities.* In the simplest approach, the *a priori* probabilities  $C_i$  (relative concentrations of particles of  $i$ -type) to observe a particle of  $i$ -type can be assumed to be equal.

However, in many cases one can do better. Thus, for example in ALICE, when doing PID in the TPC for the tracks that are registered both in the TPC and in the TOF detector, these probabilities can be estimated using the measured time-of-flight. One simply fills a histogram of the following quantity:

$$m = \frac{p}{\beta\gamma} = p\sqrt{\frac{c^2t^2}{l^2} - 1}, \quad (5.24)$$

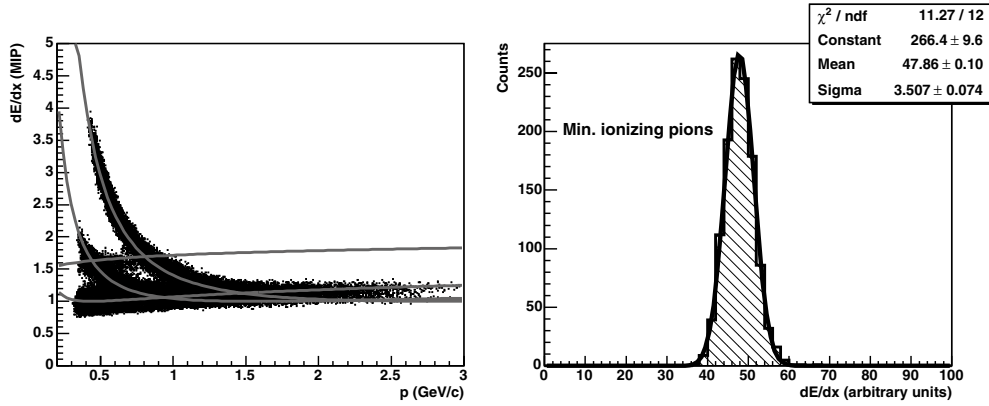


**Figure 5.124.**  $dE/dx$  response of the ALICE TPC (left) and its profile for minimum-ionizing pions (right) for simulated central HIJING Pb–Pb  $\sqrt{s_{NN}} = 5.5$  TeV events.

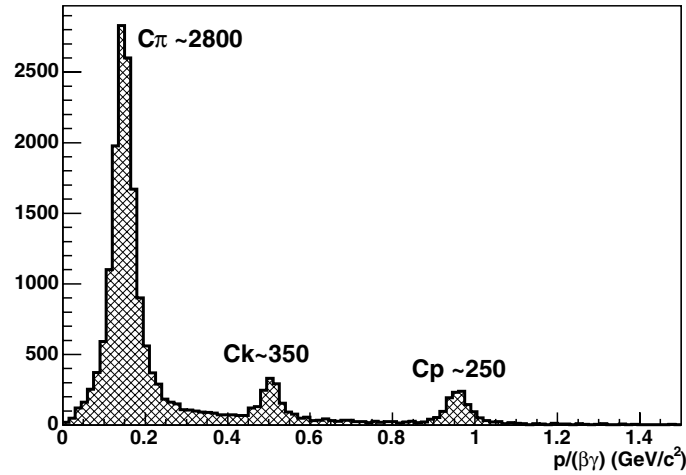


**Figure 5.125.** *A priori* probabilities  $C_i$  estimated using time-of-flight measurements (see the text).

where  $p$  and  $l$  are the reconstructed track momentum and length and  $t$  is the measured time-of-flight. Such a histogram peaks near the values  $m$  that correspond to the masses of particles.

Under ALICE conditions, because the width of the peaks is mainly defined by the time resolution and is almost the same for all the particle types (see Fig. 5.125), the counts at the maxima of the histogram are proportional to the  $C_i$ . The absolute normalization of  $C_i$  is not important (see Eq. (5.23)). Therefore, one can use straightaway  $0 < C_e < 10$ ,  $0 < C_\mu < 100$ ,  $C_\pi \sim 2800$ ,  $C_K \sim 350$  and  $C_p \sim 250$  for the case (event and track selection) shown in Fig. 5.125.

Forcing some of the  $C_i$  to be exactly zeros excludes the corresponding particle type from the PID analysis and such particles will be redistributed over other particle classes (see Eq. (5.23)). This can be useful for the kinds of analysis when, for the particles of a certain type, one is not concerned by the contamination but, at the same time, PID efficiency is of particular importance.

5.4.6.2. *PID combined over several detectors.* This method can be easily applied for combining PID measurements from several detectors. Considering the whole system of  $N$  contributing detectors as a single ‘super-detector’ one can write the combined PID weights  $W(i|\bar{s})$  in the form similar to that given by Eq. (5.23):

$$W(i|\bar{s}) = \frac{R(\bar{s}|i)C_i}{\sum_{k=e,\mu,\pi,\dots} R(\bar{s}|k)C_k}, \quad (5.25)$$

where  $\bar{s} = s_1, s_2, \dots, s_N$  is a vector of PID signals registered in the first, second and other contributing detectors,  $C_i$  are the *a priori* probabilities to be a particle of the type  $i$  (the same as in Eq. (5.23)) and  $R(\bar{s}|i)$  is the combined response function of the whole system of detectors.

If the single detector PID measurements  $s_j$  are uncorrelated (which is approximately true in the case of the ALICE experiment), the combined response function is the product of single response functions  $r(s_j|i)$  (the ones in Eq. (5.23)):

$$R(\bar{s}|i) = \prod_{j=1}^N r(s_j|i). \quad (5.26)$$

One obtains the following expression for the PID weights combined over the whole system of detectors:

$$W(i|s_1, s_2, \dots, s_N) = \frac{C_i \prod_{j=1}^N r(s_j|i)}{\sum_{k=e,\mu,\pi,\dots} C_k \prod_{j=1}^N r(s_j|k)}. \quad (5.27)$$

In the program code, the combined response functions  $R(\bar{s}|i)$  do not necessarily have to be treated as analytical. They can be ‘procedures’ (C++ functions, for example). Also, some additional effects like probabilities to obtain a mis-measurement (mis-matching) in one or several contributing detectors can be accounted for.

Equation 5.27 has the following useful features:

- If for a certain particle momentum one (or several) of the detectors is not able to identify the particle type (i.e.  $r(s|i)$  are equal for all  $i = e, \mu, \dots$ ), the contribution of such a detector cancels out from the formula.
- When several detectors are capable of separating the particle types, their contributions are accumulated with proper weights, thus providing an improved combined particle identification.
- Since the single-detector response functions  $r(s|i)$  can be obtained in advance at the calibration step and the combined response can be approximated by Eq. (5.26), a part of PID (calculation of the  $R(\bar{s}|i)$ ) can be done track-by-track ‘once and forever’ by the reconstruction software and the results can be stored in the Event Summary Data (ESD). The final PID decision, being dependent via the *a priori* probabilities  $C_i$  on the event and track selections, is then postponed until the physics analysis of the data.

And so the combined PID procedure in ALICE consists of three parts:

- First, the single-detector PID response functions  $r(s|i)$  are obtained. This is done by the calibration software.

- Second, for each reconstructed track the combined PID response  $R(\bar{s}|i)$  is calculated and effects of possible mis-measurements of the PID signals can be accounted for. The results are written to the ESD and, later, are used in all kinds of physics analysis of the data. This is a part of the reconstruction software.
- And finally, for each kind of physics analysis, after the corresponding event and track selection is done, the *a priori* probabilities  $C_i$  to be a particle of a certain  $i$ -type within the selected subset are estimated and the PID weights  $W(i|\bar{s})$  are calculated by means of Eq. 5.27. This part of the PID procedure belongs to the analysis software.

Such a procedure takes naturally into account the fact that, owing to different event and track selection, the PID depends on a particular kind of performed physics analysis. It is capable of combining, in a common way, signals from detectors having quite different shapes of the PID response functions (silicon, gas, time-of-flight, transition radiation and Cherenkov detectors), and it is fully automatic. No interactive multidimensional graphical cuts are involved.

**5.4.6.3. Combined PID results.** Let us define the efficiency of the PID as  $N_{\text{corr}}/N_{\text{true}}$  and the contamination as  $N_{\text{incorr}}/(N_{\text{incorr}} + N_{\text{corr}})$ , where  $N_{\text{corr}}$  is the number of correctly identified,  $N_{\text{incorr}}$  the number of mis-identified particles, and  $N_{\text{true}}$  is the true number of particles of a certain type in the PID procedure. These efficiencies and contaminations were estimated using the ALICE simulation/reconstruction framework AliRoot [3] for central HIJING Pb–Pb  $\sqrt{s_{\text{NN}}} = 5.5$  TeV events.

The results of identifying charged kaons using the ALICE ITS, TPC and the TOF as stand-alone detectors (see Eq. 5.23) and the result for the combined PID (see Eq. (5.27)) are shown in Fig. 5.126. Only tracks reconstructed simultaneously in all the detectors were selected for the analysis, and the set of *a priori* probabilities was  $C_e = 0$ ,  $C_\mu = 0$ ,  $C_\pi = 0.70$ ,  $C_K = 0.15$  and  $C_p = 0.15$ .

One can see from this picture that:

- The efficiency and the contamination of the combined PID are significantly weaker functions of the momentum than in the case of a single-detector particle identification.
- The efficiency of the combined result is always higher (or equal) than in the case of any of the detectors working stand-alone.
- The combined PID contamination is always lower (or equal) than the contaminations obtained with the single-detector PID procedures.

The approach can easily include the PID information provided by the TRD. This will improve the PID quality for all the particle types (by using the  $dE/dx$  measurements) and, in particular, for the electrons (by using the additional transition radiation signal (see Section 5.4.3)). The corresponding software is under development.

Because of the small geometrical acceptance and a high  $p_t$  cut-off, the studies of the HMPID performance in the context of the combined PID required special simulations. The conditions for these simulations were as follows.

Two types of events were simulated: parametrized-HIJING events for the identification of pions and kaons, and a ‘cocktail’ of seven protons (one per each HMPID module) superimposed on parametrized-HIJING events. In both cases, 2000 events with 600 particles in the geometrical acceptance of the HMPID ( $-0.5 < \eta < 0.5$  and  $0^\circ < \varphi < 60^\circ$ ) were generated. The magnetic field was 0.5 T.

The first obtained results are shown in Fig. 5.127. The particles were identified as kaons or protons if the corresponding combined PID probability was higher than 85%. In these calculations, the following set of *a priori* probabilities was used:  $C_e = 0.11$ ,  $C_\mu = 0.13$ ,

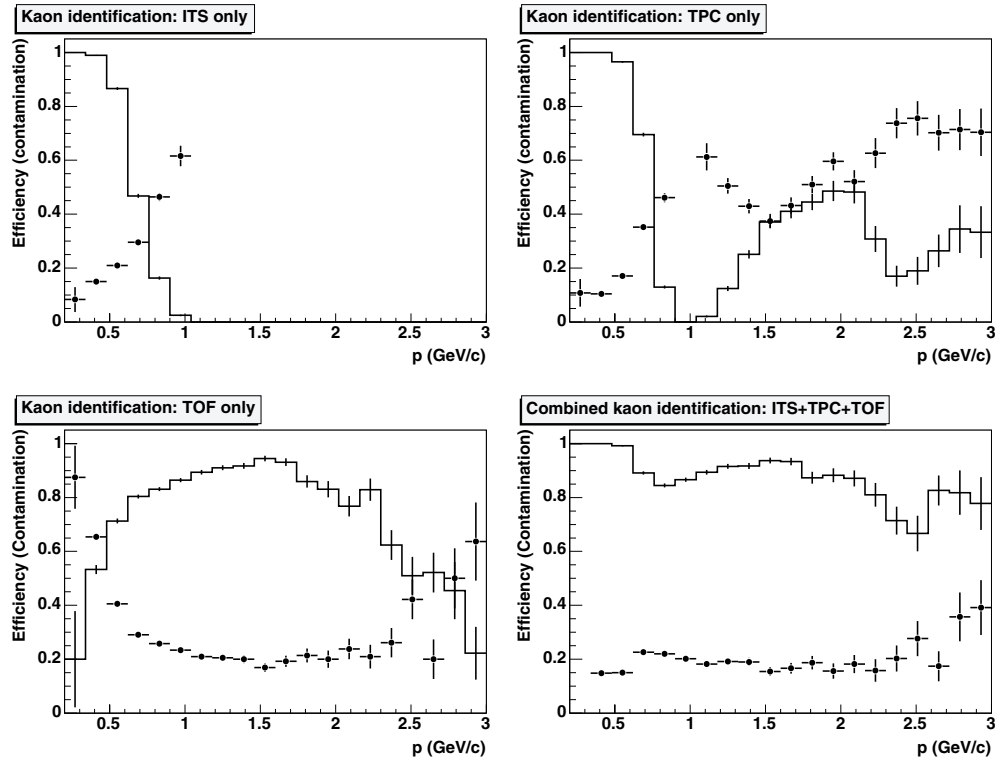


**Figure 5.126.** Single-detector efficiencies (solid line) and contaminations (points with error bars) of the charged kaon identification with the ITS, TPC and TOF stand-alone and the combined efficiency and contamination using all the detectors working together.

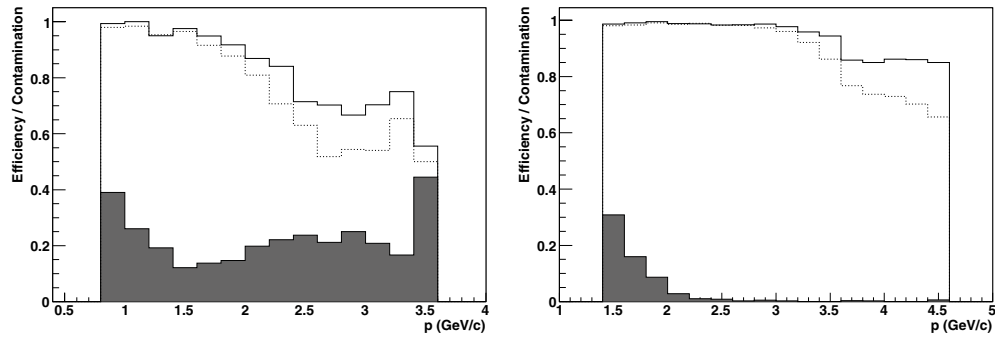


**Figure 5.127.** The combined PID results for kaons (left) and protons (right) with and without including the HMPID in the PID procedure. The solid-line histograms show the PID efficiency for the combination ITS+TPC+TOF+HMPID, the corresponding contamination is demonstrated by the filled histograms. For comparison, the dotted-line histograms show the PID efficiency for the combination of ITS+TPC+TOF. The results were obtained in dedicated HMPID simulations (see the text).

$C_\pi = 0.68$ ,  $C_K = 0.05$ , and  $C_p = 0.04$ . An improvement in the PID efficiency at high  $p$  can be seen, whereas there is no significant increase of the contamination.

Additional studies in this direction are currently under way.

Since the results of the PID procedure explicitly depend on the choice of the *a priori* probabilities  $C_i$  (and, in fact, this kind of dependence is unavoidable in any case), the question of stability of the results with respect to the almost arbitrary choice of  $C_i$  becomes important.

Fortunately, there is always some momentum region where the single-detector response functions for different particle types of at least one of the detectors do not significantly overlap, and so the stability is guaranteed. The more detectors that enter the combined PID procedure, the wider this momentum region becomes and the results are more stable.

Detailed simulations using the AliRoot framework show that results of the PID combined over all the ALICE central detectors are, within a few per cent, stable with respect to variations of  $C_i$  up to at least 3 GeV/c.

## 5.5. Neutral-particle identification

*5.5.1. Photon spectrometer.* The role of the PHOTon Spectrometer (PHOS) in the ALICE experiment is to detect and identify real photons and measure with high resolution their 4-momentum with the prospect of performing the physics programme exploiting direct photons and light neutral mesons ( $\pi^0$  and  $\eta$  mesons mainly) as privileged probes. The unique ability of the PHOS to measure and identify particles over a broad dynamic range in transverse momentum will enable us to access key information on the soft and hard processes occurring in pp, pA and AA collisions at LHC energies. Although the detection of photons is straightforward, their unambiguous identification, among the abundantly produced particles, constitutes a first challenge. A second one is the discrimination between direct and decay photons, which are mixed in a ratio of about one to ten. To respond to these challenges the PHOS has been designed to match the following requirements:

- high discrimination power between photons and any other kind of particle, charged and neutral baryons, charged hadrons and electrons;
- high energy and position resolution and consequently a high mass resolution in the two-photon invariant mass spectrum;
- geometrical acceptance sufficient to measure neutral mesons down to low transverse momenta and to collect statistically-significant data for the rare high-momentum particles.

We shall first describe the characteristics of the PHOS which allow these criteria to be met. We shall then discuss the various steps to simulate the PHOS response: hits from the tracking algorithm are converted into digits which in turn are processed by the reconstruction algorithm to produce reconstructed particles. The simulated intrinsic properties of the PHOS, matched to data from in-beam measurements, are presented. We examine how the various parameters are modified in the realistic environment of the ALICE experiment. Finally we discuss identification methods for neutral mesons and direct photons.

*5.5.1.1. Description.* The photon spectrometer PHOS is optimized for the measurement, with high energy and spatial resolution, of photons and of light neutral mesons ( $\pi^0$  and  $\eta$ ) through their two-photon decay. Particles will be efficiently identified over a wide dynamic range, spanning the domain from a few hundreds of MeV/c up to several tens of GeV/c. The PHOS, acting as a calorimeter, also gives access to global observables of interest for event characterization, such as the electromagnetic transverse energy and multiplicity at mid-rapidity. The PHOS is described in detail in Refs. [3, 82]. It consists of five modules, each with an electromagnetic calorimeter composed of 64 (across the beam direction) by 56 (along the beam direction) lead-tungstate  $\text{PbWO}_4$  scintillator crystals (EMC) [82], and a charged-particle detector (multiwire proportional chambers with cathode pad readout) acting as a veto (CPV) [82, 83].

5.5.1.2. *Simulation parameters.* The exact geometry of PHOS is implemented in the AliRoot simulation package. The energy deposition in the active materials is calculated by the tracking algorithm (GEANT3) and is converted into digitized information comparable to real raw-data.

- The algorithm records at each step of the tracking a hit described by the deposited energy, the position, the time and the primary particle which has generated the hit. The deposited energy,  $E_d$ , is converted into a signal amplitude. The mean number of scintillation photons,  $\langle N_\gamma \rangle$ , collected by the Avalanche Photo-Diod (APD) is calculated as

$$\langle N_\gamma \rangle = E_d \tilde{N}_\gamma \varepsilon_{\text{APD}} \exp(-Ad),$$

where  $\tilde{N}_\gamma = 4.7 \times 10^4 \gamma \text{ GeV}^{-1}$  is the average number of scintillation photons per unit of deposited energy,  $\varepsilon_{\text{APD}} = 0.0266$  is the APD photo-efficiency,  $A = 0.0045$  is the attenuation factor of scintillation photons and  $d$  is the distance of the hit to the APD. The amplitude,  $\mathcal{A}$ , of the APD signal is calculated from  $n_\gamma$ , randomly selected according to a Poisson distribution with mean value  $\langle N_\gamma \rangle$ :

$$\mathcal{A} = n_\gamma G_{\text{APD}} C,$$

where  $G_{\text{APD}} = 300$  is the APD photo-electron gain factor and  $C = 0.13418/\tilde{N}_\gamma$  a calibration factor that converts photo-electrons into GeV. Since particles entering the calorimeter develop an electromagnetic shower and thus a huge number of tracks and hits, the PHOS algorithm stores only one hit per primary particle and per active volume. A PHOS hit thus corresponds to the summed energy deposited by a given primary particle in a single crystal and the time corresponds to the time at which the particle entered the volume: a primary particle can generate several hits in different volumes and there can be several hits in a single volume originating from different primary particles.

The energy  $E_d$  deposited by an ionizing particle in the active gas volume of CPV, is proportional to the ionization charge  $Q$  collected around the nearest anode wire:  $Q = A E_d$ . The collected charge is expressed in arbitrary units, and for simplicity  $A$  is taken equal to 1. When the track is inclined, several anode wires can collect a charge which is proportional to the projection of the inclined track onto the CPV cathode plane. The charge distribution on the cathode plane is calculated according to the electrostatic formula:

$$\sigma(x') = \frac{Q}{\pi} \sum_{i=0}^{\infty} (-1)^i \frac{2i+1}{x'^2 + (2i+1)^2},$$

where  $x' = x/d$ ,  $x$  is a distance from the charge on the cathode plane,  $d$  is the anode-to-cathode distance and  $i$  is the pad number. This charge distribution function allows one to calculate the charge induced in each pad. The CPV hits are calculated from this distribution.

- Summable digits are constructed as a copy of hits. For hits with a deposited energy below a given threshold ( $E_{\text{th}}^{\text{prim}} = 1 \text{ MeV}$ ) the reference to the primary particle is omitted to reduce the number of primary particles attached to the same digit.
- To construct digits, first a random Gaussian noise (with a mean value of 4 MeV equivalent deposited energy for EMC and 0.01 units for CPV) is added to all active elements, whether they have been hit or not. Summable digits in the same active volume are merged into a single digit by summing the deposited energy. The time is calculated in a way that mimics the function of a leading-edge discriminator with a rise of  $t_{\text{rise}} = 1 \text{ ns}$ , an energy crossing-threshold that defines the time zero,  $E_{\text{cross}} = 1 \text{ MeV}$  and a time zero jitter,  $t_{\text{jit}} = 0.5 \text{ ns}$ . Only EMC digits with an energy that surpasses a 12 MeV noise threshold, and CPV digits with the charge above 0.09 units are recorded. The energies in EMC are digitized in 16 bit words

(which corresponds to a gain of 1.5 GeV/channel and to an overflow at 90 GeV), and the times in 12 bit words (gain 1 ps/channel). The charges in CPV are digitized in 12 bits words (gain of 0.001 units/channel and overflow at 5 units).

**5.5.1.3. Reconstruction algorithm.** The reconstruction algorithm processes the EMC and CPV digits in three steps: to produce reconstructed points, track segments, and reconstructed particles. The first step is performed separately on EMC digits and CPV digits whereas the two last steps combine the information collected by the two detectors. The particle identification can take into account additional information from the global tracking in ALICE.

**Clustering.** The algorithm clusters neighbouring digits, taken from a list ordered according to the digit location, to form reconstructed points. Two modules or cells are declared neighbours if they have a common edge or a common corner. Any EMC digit with an energy above a threshold selected above the energy deposited by minimum-ionizing particles is considered as a seed of a new cluster. Clusters with several local maxima, due in general to overlapping showers, are unfolded following the algorithm described in Ref. [82]. A local maximum is defined as a digit in the cluster with an energy which differs from the energy of surrounding digits by more than a value of  $E_{\text{th}}^{\text{lm}} = 30$  MeV. The fitting procedure takes into account the measured electromagnetic-shower profile. Such clusters are split into a set of reconstructed points with one local maximum, and the digit energy is shared in proportion given by the fitting result.

The energy  $E$  and the position of the clusters in the  $(x, z)$  plane of the module reference frame, are calculated, respectively, as the sum of the digit energies  $e_i$ , and the centre of gravity with a logarithmic weight:

$$\bar{s} = \frac{\sum_{\text{digits}} s_i w_i}{\sum_{\text{digits}} w_i}, \quad (5.28)$$

where  $\bar{s}$ , either  $\bar{x}$  or  $\bar{z}$ , is the coordinate of the cluster centre-of-gravity,  $s_i$ , either  $x_i$  or  $z_i$  is the coordinate of the digit and the sum extends over all digits forming the cluster. The weight  $w_i$  is defined by

$$w_i = \max \left[ 0, p + \log \left( \frac{e_i}{E} \right) \right], \quad (5.29)$$

where  $e_i$  is the digit energy and  $p$  is a parameter whose value has been empirically determined (4.5 for EMC and 4.0 for CPV). Since the edges of the crystals in a module (except for the central crystal) are not parallel to the momentum direction of particles emerging from the interaction vertex, the centre of gravity of EMC clusters with the energy  $E$  is further corrected for the incidence direction,  $(\theta, \varphi)$ , of the primary particle:

$$x' = x - (A + B \log E) \sin \varphi, \quad z' = z - (A + B \log E) \cos \theta, \quad (5.30)$$

where the parameters  $A$  and  $B$  have been determined empirically from simulation (see Eq. (5.35)), and the energy  $E$  is measured in GeV.

Clusters in EMC are characterized by the digit multiplicity (Fig. 5.128), which is a function of the particle type, energy and selected digit threshold.

A few additional parameters that characterize the shape of the clusters are calculated:

- The lateral dispersion,  $d$ , in the  $(x, z)$  plane measured on the surface of EMC:

$$d = \frac{\sum_{\text{digits}} w_i [(x_i - x)^2 + (z_i - z)^2]}{\sum_{\text{digits}} w_i}.$$

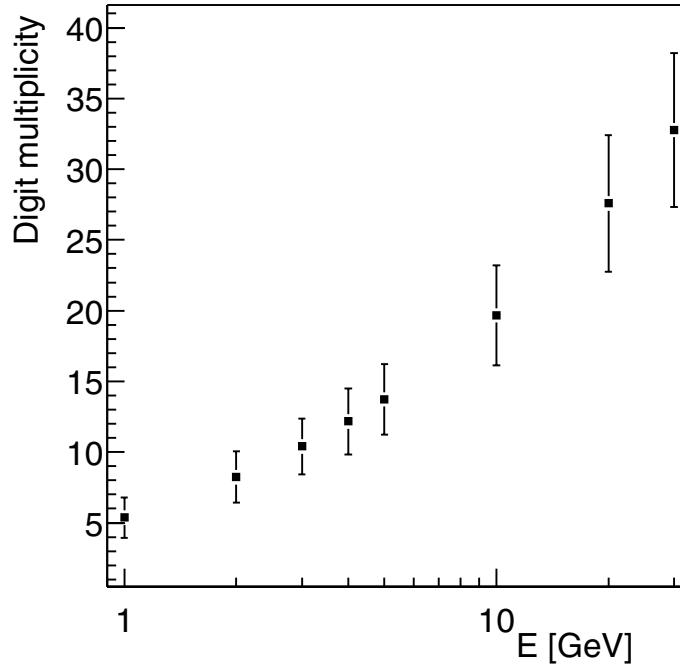


**Figure 5.128.** Digit multiplicity of EMC clusters from simulated mono-energetic photons with energies between 1 and 30 GeV. The error bars indicate the width (r.m.s.) of the multiplicity distribution.

- The shape of the surface, intersection of the cone containing the shower with the front plane of the calorimeter (Fig. 5.129). This surface can be expressed in terms of the covariance matrix:

$$S = \begin{pmatrix} s_{xx} & s_{zx} \\ s_{xz} & s_{zz} \end{pmatrix}, \quad (5.31)$$

where

$$s_{xx} = \langle (x - \bar{x})^2 \rangle = \frac{\sum_{\text{digits}} w_i x_i^2}{\sum_{\text{digits}} w_i} - \left( \frac{\sum_{\text{digits}} w_i x_i}{\sum_{\text{digits}} w_i} \right)^2,$$

$$s_{xz} = \langle (x - \bar{x})(z - \bar{z}) \rangle = \frac{\sum_{\text{digits}} w_i x_i z_i}{\sum_{\text{digits}} w_i} - \frac{\sum_{\text{digits}} w_i x_i \times \sum_{\text{digits}} w_i z_i}{\left( \sum_{\text{digits}} w_i \right)^2},$$

and corresponding definitions for  $s_{zz}$ ,  $s_{zx}$ . Here  $\langle \rangle$  denotes averaging with logarithmic weights  $w_i$  (Eq. (5.29)),  $\bar{x}$  and  $\bar{z}$  are the centre of gravity of the cluster (Eq. (5.28)),  $(x_i, z_i)$  are the positions of a crystal  $i$  belonging to the cluster. Diagonalization of this covariance matrix defines the main axes of the shower surface,  $\lambda_1$  and  $\lambda_2$ , as the square root of the eigen vectors of the covariance matrix.

- The sphericity parameter defined from the major axes  $\lambda_1$  and  $\lambda_2$ :

$$S = \frac{|\lambda_1 - \lambda_2|}{\lambda_1 + \lambda_2}.$$

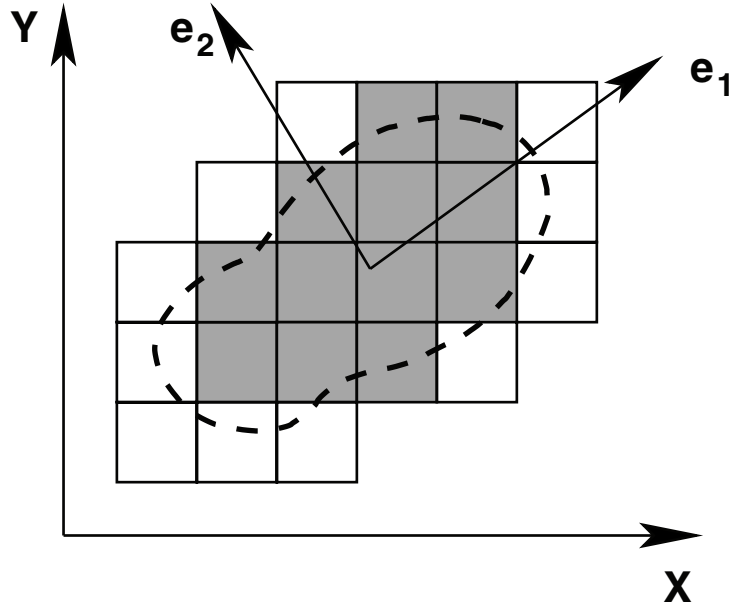


**Figure 5.129.** Example of a shower profile and its main axes  $e_1$  and  $e_2$ .

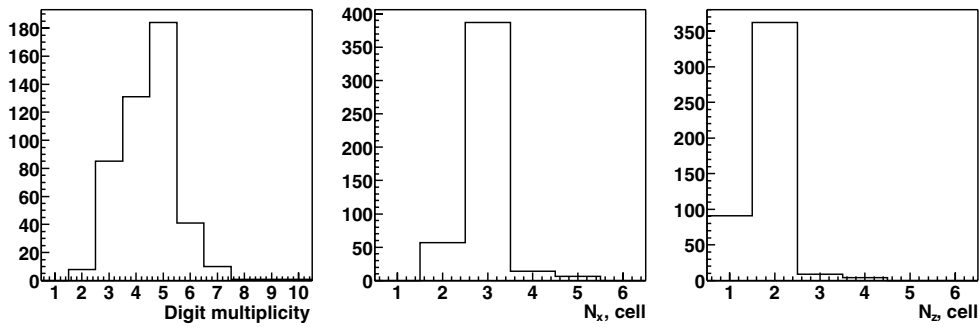


**Figure 5.130.** Digit multiplicity and cluster extension  $N_x$  and  $N_z$  along the  $x$  and  $z$  directions of the CPV cluster generated by a single charged track.

- The largest fraction of the cluster energy deposited in a single crystal.
- The core energy corresponds to the summed energy of digits within a given radius ( $R_{\text{core}} = 3$  cm) around the largest digit. From the experimentally established shower profile, the fraction of energy deposited by an electromagnetic shower beyond this distance is less than 2%. The core energy is thus less subject to fluctuations because of background which might contribute to the cluster or because of overlapping showers.
- The time of the cluster is selected as the shortest time among the digits making the cluster.

The CPV cluster is characterized by the digit multiplicity induced by a single track, and by its extension  $N_x$  and  $N_z$ , in units of a cell, along the  $x$  and  $z$  directions in the detector reference system. These values (Fig. 5.130) were measured experimentally during in-beam tests [83], and the reconstruction procedure was tuned to coincide with the experimental data.

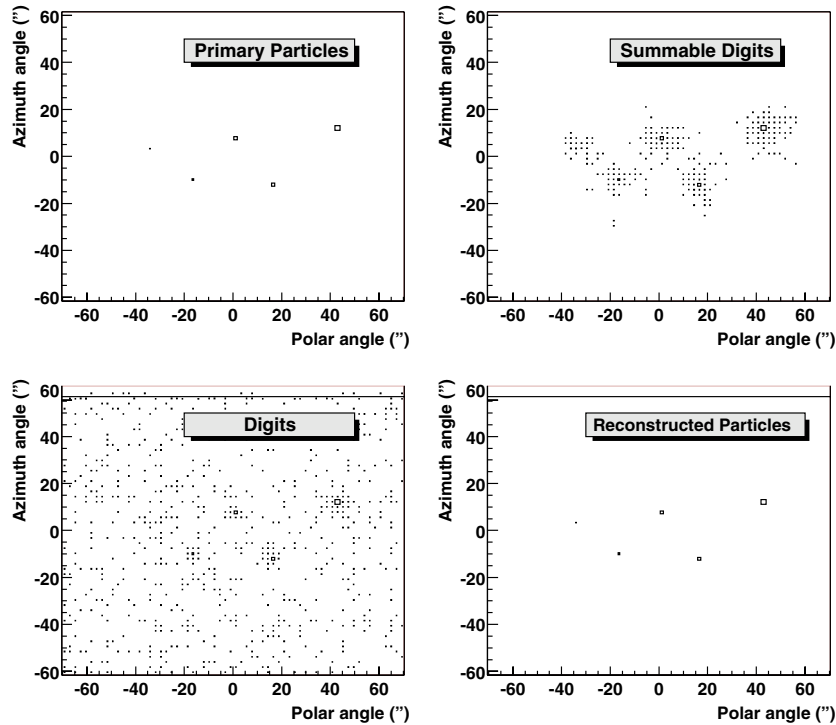


**Figure 5.131.** Event display in one EMC module demonstrating the simulation, digitization and the reconstruction algorithm.

*Construction of track segments.* A track segment in PHOS is made up by at most two reconstructed points, one in CPV and one in EMC. First the algorithm searches for all possible pairs that are distant by less than a given distance ( $d_{\text{th}}^{\text{link}} = 10$  cm). For a given EMC reconstructed point, the associated track segment is defined either as the pair including the considered EMC reconstructed point and the closest CPV reconstructed point among all possible pairs, or the EMC reconstructed points alone. A CPV reconstructed point can be used only once in a track segment.

*Particle identification.* Every track segment constitutes the seed of a reconstructed particle. Its energy is taken as the energy of the EMC reconstructed point and its momentum is taken either by the direction passing through the EMC reconstructed point and the CPV reconstructed point or the direction passing through the EMC reconstructed point and the interaction vertex, depending on the number of reconstructed points that constitute the track segment. The particle type is determined following the measured parameters which characterize the track segment. Three criteria are used to identify particles: (i) the Time of Flight (time elapsed between the time of the interaction and the impact of the particle on the calorimeter); (ii) the charged particle rejection with the CPV and EMC; and (iii) the shape of the shower that develops the particle in the calorimeter. The details on the particle identification and several identification methods will be discussed in Sections 5.5.1.8 to 5.5.1.11.

The simulation, digitization and reconstruction algorithm is demonstrated in Fig. 5.131. It shows the event display in one EMC module represented in the module local coordinate

**Table 5.14.** Parameters of the function  $f(p_t)$  of Eq. (5.32) which fits the acceptance vs.  $p_t$  for photons,  $\pi^0$ - and  $\eta$ -mesons.

Accept. vs. $p_t$	$p_0$	$p_1$	$p_2$	$p_3$
$\gamma$ ( $p_t$ 100 GeV/c)	0.0694±0.0002			
$\pi^0$ ( $p_t$ 10 GeV/c)	0.042±0.002	0.0013±0.0003	0.55±0.07	1.25±0.16
$\pi^0$ ( $p_t$ 100 GeV/c)	0.064±0.002	0.000012±0.000027	-14±6	12±4
$\eta$ ( $p_t$ 10 GeV/c)	0.002±0.002	0.00131±0.00015	0.75±0.07	2.3±0.9
$\eta$ ( $p_t$ 100 GeV/c)	0.0196±0.0007	0.000052±0.000010	2.2±0.8	86.0±9.0

**Table 5.15.** Parameters of the function  $g(y)$  of Eq. (5.33) which fits the acceptance vs.  $y$  for photons,  $\pi^0$ - and  $\eta$ -mesons.

Accept. vs. $y$	$q_0$	$q_1$
$\gamma$ ( $p_t$ 100 GeV/c)	0.2451 ± 0.0009	
$\pi^0$ ( $p_t$ 10 GeV/c)	0.1801 ± 0.0011	393.0 ± 13.0
$\pi^0$ ( $p_t$ 100 GeV/c)	0.2324 ± 0.0013	57.0 ± 17.0
$\eta$ ( $p_t$ 10 GeV/c)	0.0348 ± 0.0005	146.0 ± 4.0
$\eta$ ( $p_t$ 100 GeV/c)	0.0828 ± 0.0008	86.0 ± 9.0

system. The generated event (upper left) contains five photons with energy between 1 and 10 GeV. The corresponding summable digits (upper right), digits (lower left) and the reconstructed particles (lower right) are calculated with the PHOS-AliRoot simulation algorithm as explained above.

**5.5.1.4. Acceptance.** The photon acceptance is defined as a probability that a photon, radiated from the interaction point within rapidity interval  $|y| < 0.5$  and azimuth angle  $0 < \varphi < 2\pi$ , hits PHOS. The PHOS acceptance for photons depends neither on their transverse momentum nor on their rapidity, the acceptance being about 0.7 and 0.25, respectively. The acceptance for  $\pi^0$ - and  $\eta$ -mesons detected in the  $\gamma\gamma$  decay channel is defined as a probability that both decay photons hit PHOS when the mesons are radiated from the interaction point within rapidity interval  $|y| < 0.5$  and azimuth angle  $0 < \varphi < 2\pi$ . This acceptance is small at low  $p_t$  owing to the wide opening angle between the decay photons. For  $p_t < 2$  GeV/c, the acceptance as a function of  $p_t$  is smaller than 0.03 for  $\pi^0$  and  $10^{-3}$  for  $\eta$ . There is an increase of the acceptance with increasing transverse momentum which reflects the narrowing of the relative angle between the decay photons. The acceptance saturates for  $\pi^0$  at  $p_t > 20$  GeV/c (acceptance about 0.06). For  $\eta$ -mesons the acceptance does not reach its maximum value even at 100 GeV/c (acceptance about 0.024 for  $p_t = 100$  GeV/c).

The dependences of the acceptance on  $p_t$  and  $y$  in the range  $-0.13 < y < 0.13$  can be fitted by the parametric functions:

$$f(p_t) = (p_0 + p_1 p_t) \exp\left(-\frac{p_t - p_2}{p_3}\right), \quad (5.32)$$

$$g(y) = q_0 - q_1 y^4, \quad (5.33)$$

with the parameters  $p_i$  listed in Tables 5.14 and 5.15.

The PHOS installation schedule foresees the possibility to install the detector gradually; for the first ALICE run only one module will be installed with the number of modules increasing by one in the following runs. According to this schedule, the acceptance of the PHOS detector with 1, 2 and 3 modules was studied compared to all the 5 modules.

Acceptance of such reduced PHOS geometry to single photons is simply proportional to the number of modules. The same effect is expected for high- $p_t$   $\pi^0$ -mesons. Neutral mesons at lower  $p_t$  will be more affected by the reduced geometry, and the optimization of the relative modules position is needed in this case. Adjacent module installation as well as installation with gaps between modules were studied. More reduction of the  $\pi^0$ -acceptance in the PHOS geometry with gaps between the module is observed for  $p_t < 3$  GeV/ $c$ . For  $\eta$ -mesons in the  $\gamma\gamma$ -decay mode, there is a more profound suppression for the module installation with gaps between them at low  $p_t$  up to 15 GeV/ $c$ . In conclusion, in the case of reduced PHOS geometry in the first ALICE runs, all available modules should be installed adjacently to avoid the acceptance loss.

*5.5.1.5. Intrinsic performances.* We shall now discuss the response functions of the EMC and CPV subdetectors of the PHOS.

#### *EMC performance*

*Response to electromagnetic particles.* The parameters that describe the response of the EMC spectrometer and play the most important role for photon identification are the energy, the position, and the time-of-flight resolutions. The energy resolution depends on the ability of the spectrometer to collect most of the energy in the electromagnetic shower, the scintillation efficiency and the light transport through the crystal, the APD photo efficiency, and photo-electron gain-factor. The position resolution depends on the segmentation of the spectrometer and on the energy resolution of the individual EMC crystals.

*Energy resolution.* The parameters of the simulation were tuned to match the calculated response function to measurements performed with electron beams of energy ranging from 0.6 to 4.5 GeV. The central module of an array of  $3 \times 3$  crystals was irradiated. The energy resolution was determined from the total energy  $E$  collected in the array. The resulting resolution  $\sigma/E$  was compared to that obtained by the simulation performed in exactly the same conditions as the experiment. The following parametrization was adjusted to the experimental resolution:

$$\frac{\sigma}{E} = \sqrt{\frac{a^2}{E^2} + \frac{b^2}{E} + c^2}, \quad (5.34)$$

where  $E$  is in units of GeV,  $a$  represents the contribution of the electronic noise,  $b$  the stochastic term, and  $c$  the constant term. The values of the three parameters  $a$ ,  $b$  and  $c$  are determined by the simulation parameters (Section 5.5.1.2), while the stochastic term  $b$  depends also on the clustering algorithm parameters (Section 5.5.1.3). The fitted values of these parameters are summarized in Table 5.16. The experimental energy resolution of a  $3 \times 3$  PbWO<sub>4</sub> array for electrons of energy between 0.6 GeV and 120 GeV is compared in Fig. 5.132 with the simulated resolution for photons.

Switching from the static clustering, i.e., summing the energy deposited in the  $3 \times 3$  array, to the dynamic clustering as in the reconstruction algorithm (see Section 5.5.1.3), the resulting resolution is slightly improved (see Table 5.16) through a lower value of the stochastic term.

The response (Fig. 5.133) to mono-energetic photons, with energies ranging from 0.6 to 100 GeV, impinging on the centre of a PHOS block indicate that, for photon energies larger than 10 GeV, on average close to 94% of the photon energy is contained in the cluster found by the reconstruction algorithm. The parameters of the function which describes the energy resolution are reported in Table 5.16. At high photon energies (larger than 10 GeV) the constant term dominates and the resolution remains almost constant and equal to 1.3%.

**Table 5.16.** Parameters obtained by adjusting Eq. (5.34) to the resolution of the measured energy collected in a  $3 \times 3$  array of EMC crystals upon the impact of mono-energetic electrons (0.6 to 4.5 GeV) and of the calculated energy from simulations of mono-energetic photons (0.6 to 10 GeV or 0.6 to 100 GeV) performed in identical conditions. In the static reconstruction the energy is collected in the  $3 \times 3$  array of neighbouring detector whereas in the dynamic reconstruction the standard clustering method is applied.

	$a$ (GeV)	$b$ (GeV <sup>1/2</sup> )	$c$
Electron beam	0.022	0.028	0.013
Static reconstruction	$0.014 \pm 0.03$	$0.0365 \pm 0.0012$	$0.0067 \pm 0.0010$
Dynamic reconstruction (0.6–10 GeV)	$0.017 \pm 0.002$	$0.0334 \pm 0.0013$	$0.0071 \pm 0.0010$
Simulation dynamic (0.6–100 GeV)	$0.0255 \pm 0.0011$	$0.0272 \pm 0.0010$	$0.01290 \pm 0.00017$

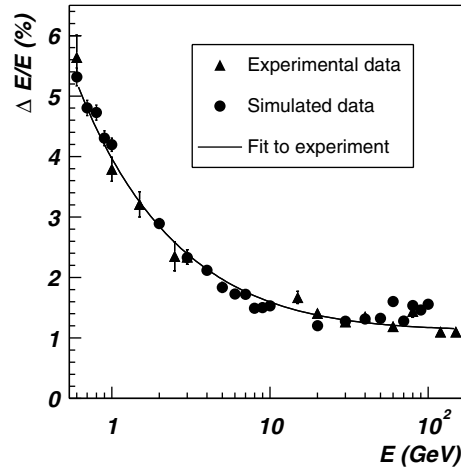


**Figure 5.132.** Energy resolution of a  $3 \times 3$  PbWO<sub>4</sub> array measured in response to mono-energetic electrons (▲) or calculated with simulations of mono-energetic photons (●). The continuous line represents the result of the fit of Eq. (5.34) to the experimental data.

We conclude from this study that photons can be measured in good conditions up to energies of the order of 100 GeV where the yield (estimated by considering the LHC running conditions and expected cross-sections extrapolated from systematics [84]) will reach the limit of statistical significance.

*Position resolution.* The impact position on PHOS, transverse ( $x$ ) and longitudinal ( $z$ ) to the beam direction, is reconstructed, as described in Section 5.5.1.3, by calculating the position of the centre of gravity of the reconstructed cluster. This position is further corrected for the incidence direction of the impinging photon according to Eq. (5.30). The test beam measurements were extended to verify the incidence on the position resolution by tilting the array of EMC modules by  $\alpha = 0, 3, 6$  and  $9^\circ$ .

Before applying the position correction (5.30), the shift of the reconstructed point with respect to the photon impact onto the EMC surface is simulated for several incidence angles and for several photon energies. Figure 5.134 shows the difference between the reconstructed point ( $x_{\text{rec}}$ ) and the impact coordinate ( $x_{\text{in}}$ ) versus the sine of the incidence angle for various

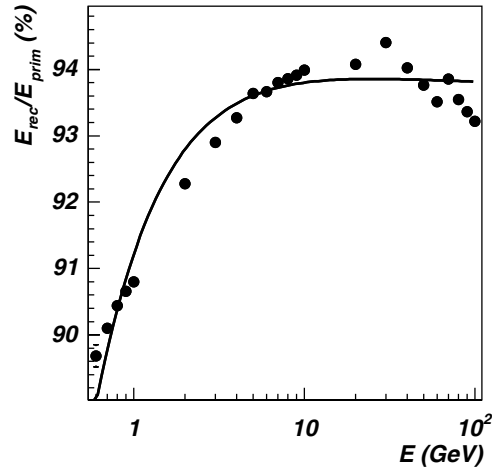


**Figure 5.133.** Fraction of the energy contained in the cluster obtained by the reconstruction algorithm for simulated mono-energetic photons impinging on the centre of a PHOS block (points). The line is a fit to the points by the equation  $p_0/E + p_1/\sqrt{E} + p_2$ .

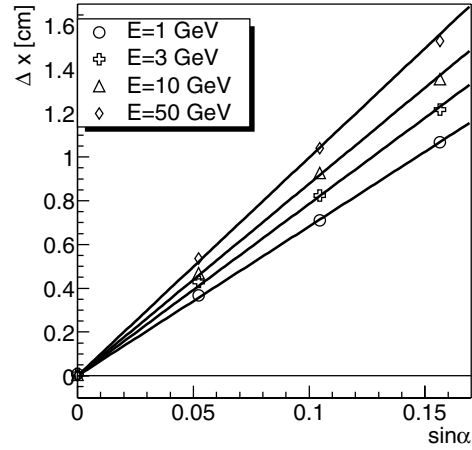


**Figure 5.134.** Difference between the reconstructed point position ( $x_{\text{rec}}$ ) and the impact coordinate ( $x_{\text{in}}$ ) on a PHOS module versus the  $\sin\alpha$  for incidence angle  $\alpha = 0, 3, 6, 9^\circ$  and for the photon energies 1, 3, 10 and 50 GeV.

photon energies. The linear dependence with  $\sin\alpha$  of the shift  $x_{\text{rec}} - x_{\text{in}}$  is parametrized as

$$x_{\text{rec}} - x_{\text{in}} = t_{\text{eff}} \sin \alpha ,$$

where  $t_{\text{eff}}$  is the effective maximum depth at which the shower develops in the crystal for inclined photon tracks. Its energy dependence (Fig. 5.135) has been studied for photon energies from 1 to 50 GeV and is described by the function

$$t_{\text{eff}} = A + B \log E ,$$

where the photon energy  $E$  is measured in GeV and parameters  $A$  and  $B$  are equal to

$$A = 7.02 \pm 0.04 , \quad B = 0.75 \pm 0.01 . \quad (5.35)$$

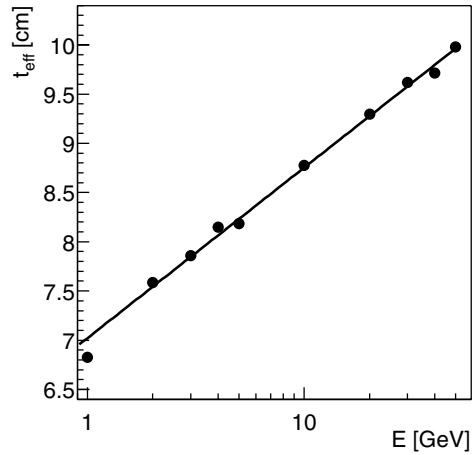


**Figure 5.135.** Dependence with photon energy of the effective maximum depth at which the shower develops in EMC crystals.

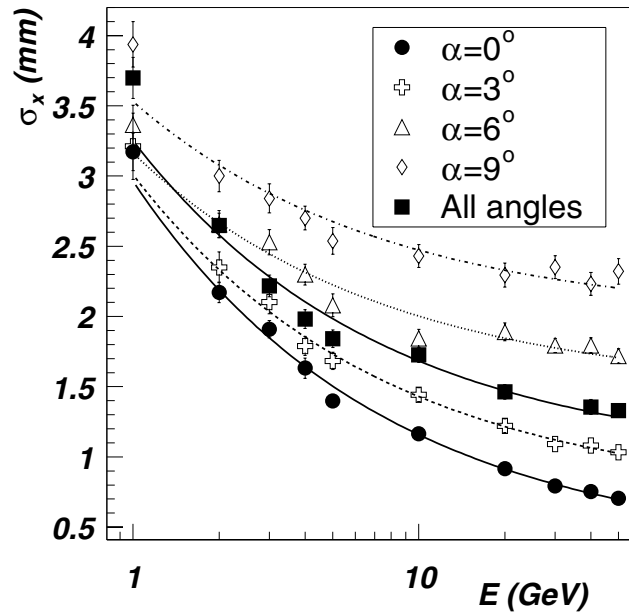


**Figure 5.136.** Position resolution versus the photon energy for the incidence angles on a PHOS module  $\alpha = 0, 3, 6$  and  $9^\circ$  and the average for all possible incidences in the ALICE layout.

The position of the reconstructed points is corrected for this effect according to Eq. (5.30).

The width of the  $x_{\text{rec}} - x_{\text{in}}$  distribution defines the spatial resolution. It was studied (Fig. 5.136) for several incidence angles and photon energies. The better position-resolution obtained when the photon energy increases is mostly the consequence of the increasing digit multiplicity and thus a more accurate determination of the centre of gravity. The position-resolution strongly depends on the incidence angle.

**Table 5.17.** Parameters  $A_x$  and  $B_x$  of Eq. (5.36) for the incidence angles  $\alpha = 0, 3, 6$  and  $9^\circ$  as well as for all possible incidence angles.

$\alpha$ (degree)	$A_x$ (cm)	$B_x$ (cm GeV <sup>1/2</sup> )
$0^\circ$	0.032	0.264
$3^\circ$	0.070	0.231
$6^\circ$	0.147	0.170
$9^\circ$	0.198	0.155
all angles	0.096	0.229

The function

$$\sigma_{x,z} = \sqrt{A_{x,z}^2 + \frac{B_{x,z}^2}{E}} \quad (5.36)$$

was adjusted to the experimentally measured position-resolution of electrons. These results were then compared to simulations where photons from the interaction vertex illuminate entirely a PHOS module, i.e., make an incidence angle with the direction perpendicular to the surface of the EMC modules continuously distributed between  $0$  and  $8.75^\circ$ . The resolution calculated from the simulated data compares with the experimental results and is intermediate between the values obtained for  $0^\circ$  and  $13^\circ$  incidence angle. The parameters obtained by fitting Eq. (5.36) to the position resolution obtained for photons between 1 and 50 GeV (Fig. 5.136) for different incidence angles are reported in Table 5.17.

*Time of flight.* Currently, there exists no measurement of the time of flight (TOF) and we base our study exclusively on simulations. The resolution of TOF depends on the jitter in the time pick-up for the start (the trigger) and the stop signal (the time from the EMC crystal). In our simulations, we have neglected the jitter on the start time. With the guess made on the timing parameters, a resolution of 500 ps can be achieved. This value compares well with, for example, the one achieved with the PHENIX calorimeter [85].

The TOF resolution required to discriminate photons (and electrons) from massive particles can be deduced from Fig. 5.137.

Applying the TOF criterion to identify photons will mainly reject the heaviest particles with an efficiency depending on the final TOF resolution. This is illustrated by the spectra of identified photons (Fig. 5.138) with the changing neutron and anti-neutron contamination as the TOF resolution changes.

*Response to hadrons.* Hadrons produced at LHC energies enter PHOS with minimum-ionizing energies. They therefore deposit in the EMC a constant energy that depends only on the amount of traversed material. The average value of the energy deposited in a single EMC module has been estimated from GEANT3 simulations of charged pions, with energy between 0.5 and 10 GeV, emitted from the ALICE vertex, and irradiating one EMC module. It is found equal to  $227 \pm 3$  GeV. However, a fraction (51% of the hadrons deposit an energy larger than 350 MeV) of the hadrons trigger a shower inside the calorimeter, through hadron–nucleus interactions.

With antiprotons and antineutrons, the situation is particular, since these particles annihilate inside the crystals and may deposit more energy than protons and neutrons. The annihilation of antinucleons produces most likely charged pions, we do not expect that antinucleons deposit the 2 GeV corresponding to the mass of the two annihilated baryons. Moreover, since antinucleons travel a given distance before annihilating (the nuclear interaction length in PbWO<sub>4</sub> is 19.5 cm), the impact position obtained from the clustering

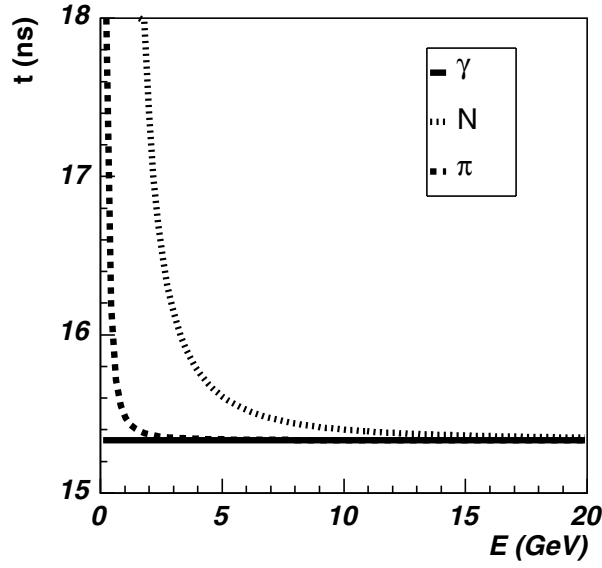


Figure 5.137. Time of flight of photons,  $\pi$ -mesons and nucleons from the interaction point to the PHOS surface versus particle energy.

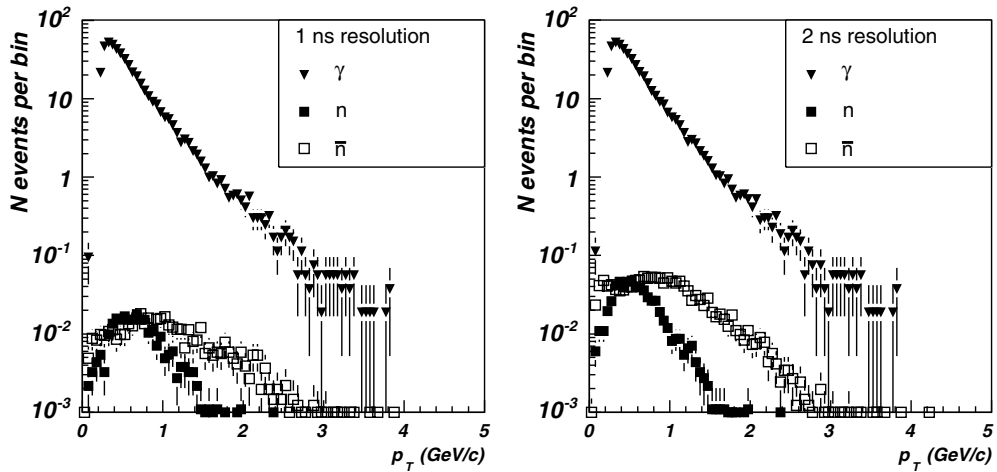
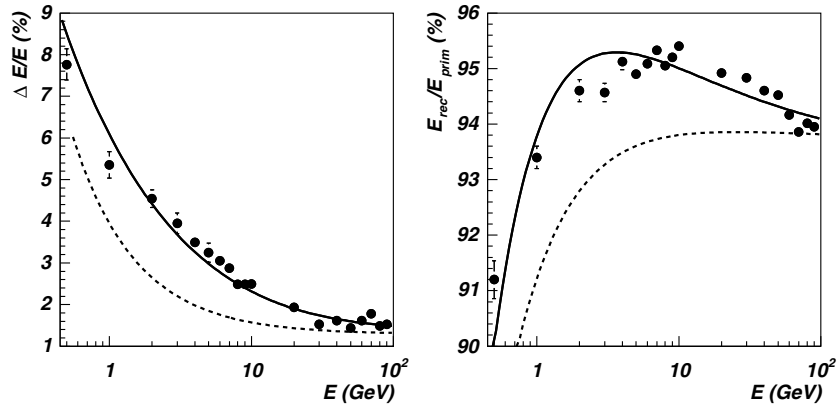


Figure 5.138. Spectra of photons ( $\blacktriangledown$ ), neutrons ( $\blacksquare$ ) and anti-neutrons ( $\square$ ) generated by central Pb-Pb HIJING [67] events, identified as low-purity photons by the TOF criterion (see Section 5.5.1.8) for time resolutions of 1 and 2 ns.

algorithm for oblique tracks is different from the true impact position. This effect deteriorates the identification of antiprotons by correlating hits in the CPV and EMC.

The response of PHOS to hadrons depends on several factors like the hadron type and energy and the detector occupancy by other particles. The spectrum of primary hadrons can be obtained by unfolding the spectrum of reconstructed hadrons with the help of the reconstructed energy  $E_{\text{rec}}$  versus the primary energy  $E_{\text{prim}}$ , however, this unfolding has not been done yet.



**Figure 5.139.** Energy resolution (left) and fraction of energy contained in the cluster (right) found by the reconstruction algorithm for simulated mono-energetic photons impinging on the centre of a PHOS block and embedded in a central heavy-ion collision environment with charged particle density at mid-rapidity of 8000. The dashed curves represent the values obtained for photons in a particle-free environment (Figs. 5.132 and 5.133). Solid lines on the left and right figures are a fit to the points by Eq. (5.34) and equation  $p_0/E + p_1/\sqrt{E} + p_2$ , respectively.

### CPV performance

*Response to ionizing particles.* The CPV detector is sensitive to any particle which triggers an ionization process in the CPV gas volume. Therefore it will detect charged particles with almost any momentum. The only parameter which defines the response of the CPV is the position resolution of the charged track passing through the detector.

*Position resolution.* The impact position on CPV is reconstructed directly as the centre of gravity of the cluster made of neighbouring pads with non-zero deposited energy. In-beam tests were carried out at the CERN PS accelerator with beams of different charged particles (electrons, hadrons, muons) in the momentum range 1–5 GeV/c [83]. To measure the position resolution experimentally, a gas strip-detector (GSP) with position resolution of 60  $\mu\text{m}$  was used as a reference detector. The effective spatial resolution of CPV was measured as  $\sigma_x = 0.138$  cm (across the wires) and  $\sigma_z = 0.154$  cm (along the wires). AliRoot simulations reproduce the coordinate resolution of the CPV.

*5.5.1.6. Modifications in the colliding heavy-ion environment.* In the high-particle-multiplicity environment created in ALICE by heavy-ion collisions, the intrinsic performances, energy and position resolution of EMC will deteriorate. By how much the performances will degrade depends obviously on the occupation of EMC; the larger the occupancy the more probable the overlapping of an electromagnetic shower and a charged particle impact, or hadronic shower. This effect has been studied by embedding mono-energetic photons in a central heavy-ion collision event. The central event was generated using the parametrized HIJING [67] and setting the particle density at central rapidity equal to 8000. The change in energy resolution and in the fraction of reconstructed energy are displayed in Fig. 5.139. Because of shower overlapping, the energy resolution is noticeably degraded, the effect being the largest for low-energy photons. The new parameters fitting the energy resolution dependence with the photon energy (Eq. (5.34)) are as follows (cf. Table 5.16):  $a = 0.00(6)$  GeV,  $b = 0.0593(12)$  GeV<sup>1/2</sup> and  $c = 0.0136(2)$ .

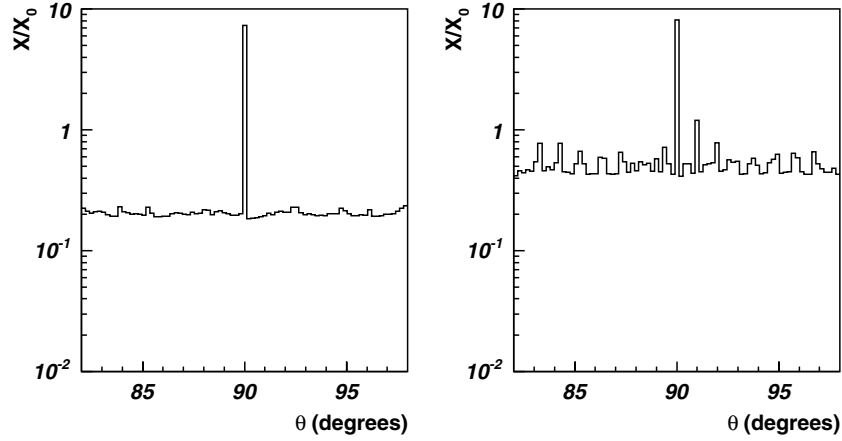


**Figure 5.140.** Radiation length of all material in front of PHOS vs. polar angle  $\theta$  for ‘holes’ configuration (left) and for ‘no holes’ (right) configurations.

*5.5.1.7. Modifications due to the ALICE environment.* The previously discussed performances will be modified when PHOS is incorporated in the ALICE experiment. Several effects will contribute to performance degradation, e.g. conversion and scattering of photons in the material between the interaction point and PHOS and particles not originating from the vertex. The above simulations have been repeated to study the impact on the energy resolution of material in front of PHOS [86]. Writing the change in the resolution with and without material as

$$\frac{\sigma_E^w}{\sigma_E^{wo}} = 1 + d,$$

we find that the degradation  $d$  approximately scales with two times the interaction probability:  $d \sim 2P_I$ , with the following relations linking interaction probability and the material thickness,  $X$ :

$$P_I^{\gamma} = 1 - \exp(-7X/9X_0) \quad \text{for photons,}$$

$$P_I^e = 1 - \exp(-X/X_0) \quad \text{for electrons.}$$

The material budget in front of PHOS in terms of radiation length  $X$  has been studied for two ALICE geometry options. In one geometry only ITS and TPC detectors are installed between the interaction point and PHOS while in other central detectors TOF and TRD there are holes in the aperture of PHOS (so called ‘holes’ geometry). Another geometry configuration has no holes in TOF and TRD (referred to as ‘no holes’ geometry). The radiation length distribution of the material in front of PHOS versus the polar angle  $\theta$  for these two geometries are shown in Fig. 5.140. In the case of ‘holes’ geometry the average radiation length in front of PHOS is equal to  $0.2X_0$  except a high peak at  $\theta = 90^\circ$  because of the TPC central electrode. With TOF and TRD installed in front of PHOS, the average radiation length increases by a factor 2.5 and becomes  $0.5X_0$  with several peaks up to  $0.7X_0$  due to internal structures of TOF and TRD. Such high values will degrade the energy resolution so badly that the accuracy with which the spectrometer measures neutral mesons will be reduced by a

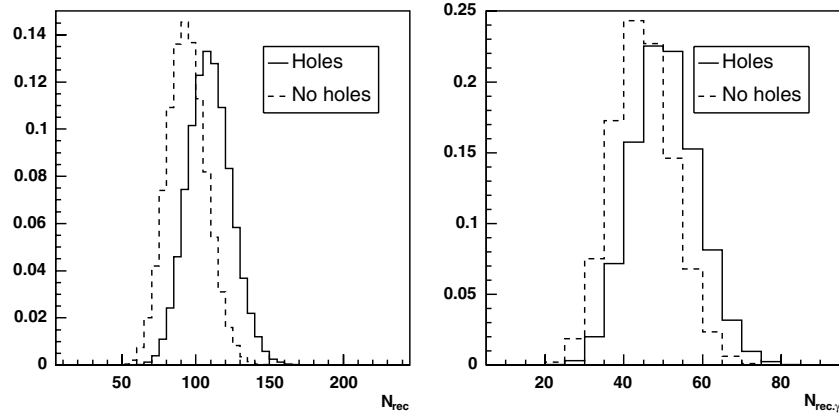


**Figure 5.141.** Distributions of all reconstructed particle numbers (left) and of reconstructed photons (right) in PHOS in central Pb–Pb collisions for ‘holes’ and ‘no holes’ configurations.

factor of 4 [87]. Installation of TOF and TRD in the PHOS aperture also increases the nuclear absorption length by a factor of 3, from about  $0.05\lambda_I$  to  $0.14\lambda_I$ .

Installation of extra material between the interaction point and PHOS by covering the PHOS aperture by TOF and TRD deteriorates the PHOS capability to reconstruct and identify particles. The distributions of reconstructed particle multiplicity in PHOS in the most central Pb–Pb collisions ( $b < 2$  fm) calculated for ‘holes’ and ‘no holes’ geometries (Fig. 5.141) indicate that the average number of all reconstructed particles in PHOS (left plot) is reduced due to TOF and TRD from 109 to 94 particles per event, and the average number of reconstructed and identified photons (right plot) is reduced from 51 to 45, i.e. ‘no holes’ detector configuration leads to 12% loss of particles in PHOS. Dependence of the reconstructed photon and  $\pi^0$  spectra on transverse momentum in the central Pb–Pb collisions is shown in Figs. 5.142 and 5.143, respectively. The left plots of these figures show the  $p_T$ -spectra of reconstructed photons and  $\pi^0$ -mesons, and the right plots show the ratios of the reconstructed spectra with the ‘no holes’ configuration to the spectra with ‘holes’. From the ratios of spectra one sees that the loss of photons at  $p_T > 1$  GeV/ $c$  is about 20%, and the loss of  $\pi^0$ ’s is about 40% in the ‘no holes’ configuration.

**5.5.1.8. Particle identification.** In this subsection, the details of the particle identification in PHOS are discussed. Photons are identified according to three quality classes, defined with respect to efficiency and purity. The efficiency is defined as the ratio of the number of reconstructed particles identified as photons to the number of primary (generated) photons. The purity is defined as the ratio of the number of reconstructed particles identified as photons, which are indeed produced by photons, to the total number of reconstructed particles identified as photons. The following criteria are used for particle identification: time of flight, CPV and EMC identification of charged particles, and shower shape analysis.

**Charged particle identification with the CPV.** Showers in EMC can be initiated by photons as well as by charged particles. Electromagnetic charged particles (electrons and positrons) will produce electromagnetic showers in the calorimeter, while charged hadrons can produce hadronic showers or minimal-ionizing signals. The CPV capability to identify showers produced by charged particles can be determined by matching the positions of CPV and EMC

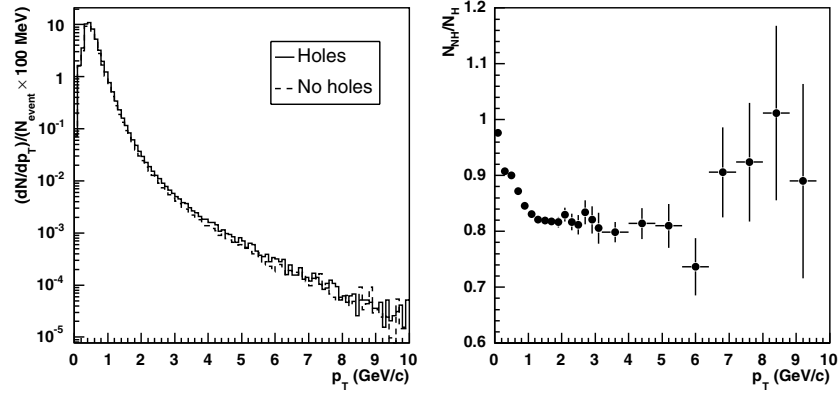


**Figure 5.142.** Left: Spectrum of reconstructed photons per one central Pb–Pb collision for the ‘holes’ and ‘no holes’ configurations. Right: Ratio of the reconstructed photon spectrum in the ‘no holes’ configuration to that in the ‘holes’ configuration.

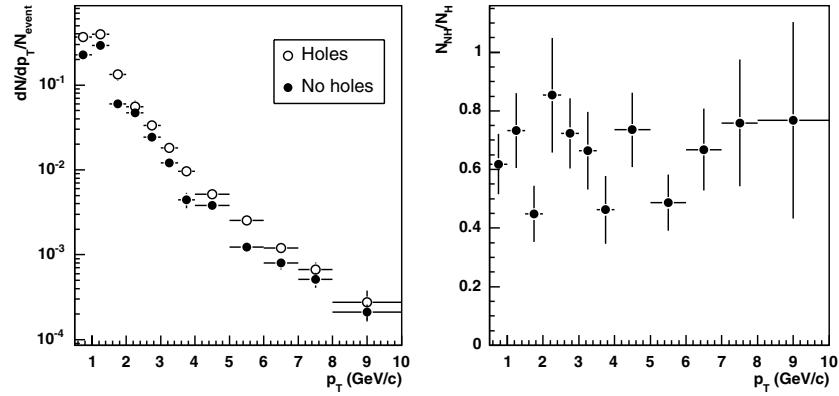


**Figure 5.143.** Left: Spectrum of reconstructed  $\pi^0$ -mesons per one central Pb–Pb collision for the ‘holes’ and ‘no holes’ configurations. Right: Ratio of the reconstructed  $\pi^0$  spectrum in the ‘no holes’ configuration to that in the ‘holes’ configuration.

reconstructed points. The width of the distributions of the relative distance, measured within the ALICE environment, is about 1 cm, and it is larger for pions.

We use this criterion to identify charged particles in the ALICE environment and obtain the relevant efficiencies (Fig. 5.144). The probability to misidentify photons as charged particles is about 10% over the whole energy range and results from the photon conversion into  $e^+e^-$  pairs in the material budget in front of PHOS. The probability of electron identification as charged particles is only about 90% because of losses due to bremsstrahlung in the material. The probability of charged pion identification as charged particles is less than that for electrons because pions that deposit the minimum-ionizing energy are not recorded by EMC.

In the reality, the situation will be different for electromagnetic particles, which deposit essentially all their energy in EMC, and hadrons, which deposit only a small fraction. Therefore what counts for hadrons is the dependence of the CPV–EMC distance rms  $\sigma$  on the reconstructed energy (Fig. 5.145). This dependence in the two directions  $x$  and  $z$  can be

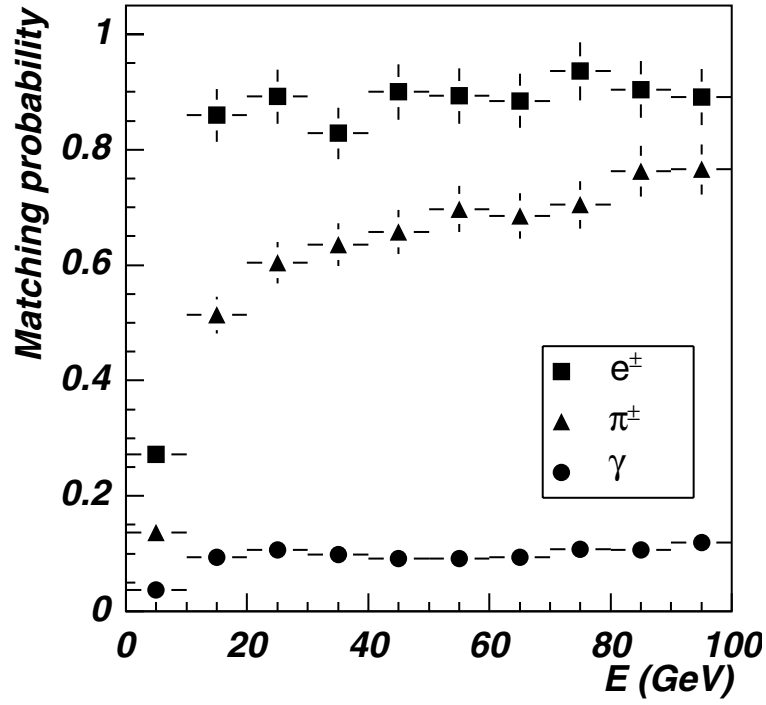


**Figure 5.144.** Probability to accept the EMC reconstructed impact point as a charged particle versus the incident particle energy for photons (●), electrons (■) and charged pions (▲).

described by the function

$$\sigma = a + \exp(b - Ec), \quad (5.37)$$

where  $\sigma$  is measured in cm, the reconstructed energy  $E$  is expressed in GeV and the parameters  $a$ ,  $b$  and  $c$  are equal to:

axis	$a$ (cm)	$b$	$c$ (GeV <sup>-1</sup> )
$x$	0.64	0.44	0.30
$z$	0.54	0.14	0.42

The identification is performed using three criteria depending on the purity quality one aims to achieve. Three definitions of a neutral particle purity are introduced in the particle identification in PHOS: low, medium, and high purity which identify a neutral particle if there is no matching reconstructed point in CPV within a rectangular defined by 1, 2, and 3 standard deviations, respectively. Formally the condition for a neutral particle selection is expressed by the following inequalities:

$$|x_{\text{EMC}} - x_{\text{CPV}}| > \kappa \sigma(\Delta x), \quad |z_{\text{EMC}} - z_{\text{CPV}}| > \kappa \sigma(\Delta z), \quad \kappa = 1, 2, 3,$$

where the factor  $\kappa$  defines the purity: low, medium, and high, respectively.

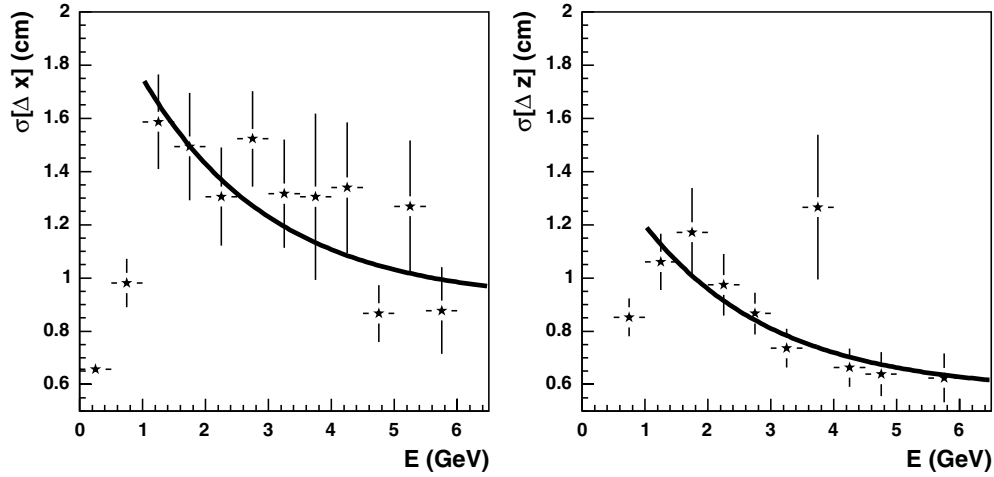


**Figure 5.145** Standard deviation of the distance between the reconstructed impact points in the CPV and EMC along the  $x$ -axis and  $z$ -axis (along the beam) for charged pions produced with a uniformly distributed energy from 0 to 100 GeV vs. the reconstructed energy. The lower points between 0 and 1 GeV correspond to minimum-ionizing particles which have larger energy and therefore smaller widths.

*Time of flight.* A reconstructed particle is qualified as photon-like if its time of flight is consistent with that of a photon, i.e. 15.3 ns. Two qualities of photon-like particles are considered, high purity (TOF < 16.5 ns) and low purity (TOF < 17.0 ns).

*Shower shape analysis in the PCA approach.* The shower generated in the calorimeter is characterized by the following seven parameters, already defined in Section 5.5.1.3: lateral dispersion, two ellipse axes, sphericity parameter, core energy, largest fraction of energy deposited in a single crystal; and digit multiplicity of the shower. Ideally one could define selection criteria on this multidimensional surface, but that would be a tedious task with no guarantee of finding the absolute minimum. A set of seven statistically independent parameters, referred to as the principal components, can be obtained by diagonalizing the covariance matrix of the original seven parameters. Thus showers produced by different kinds of particles, can be recognized in the space of the principal components within an approach known as the Principal Component Analysis (PCA) [88]. The two most significant principal components, i.e. the two components which correspond to the largest eigen values of the covariance matrix, were used to identify showers (Fig. 5.146) in the two-dimensional space spanned over these two principal components.

Variable contours depending on the EMC cluster energy and on the particle identification quality one desires to achieve, have been defined. Particles inside this contour are tagged as photons, and those outside as any other particle. These two-dimensional distributions were fitted by a two-dimensional Gaussian function

$$f(p_0, p_1) = \exp[-R(p_0, p_1)],$$

$$R(p_0, p_1) = \left(\frac{p_0 - x_0}{a}\right)^2 + \left(\frac{p_1 - x_1}{b}\right)^2 + C \frac{(p_0 - x_0)(p_1 - x_1)}{ab}, \quad (5.38)$$

where the parameters  $a$ ,  $b$ ,  $c$ ,  $x_0$  and  $x_1$  depend on the reconstructed energy. The evolution of these parameters with energy is shown in Ref. [89]. Three classes of photon purity  $\kappa$

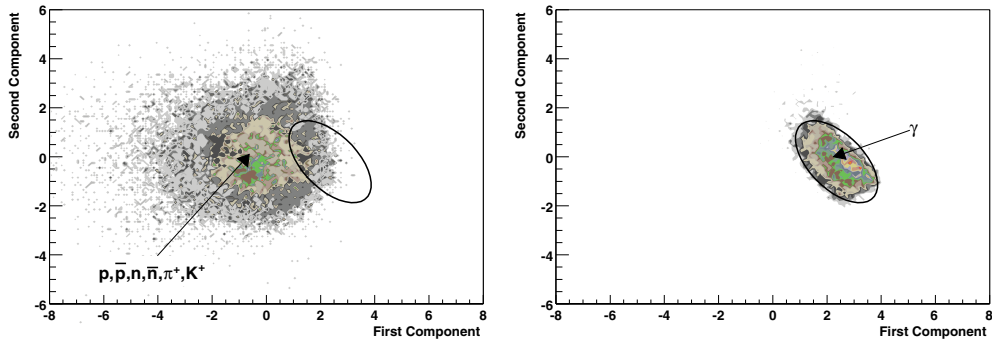


**Figure 5.146** First and second components from the principal component analysis. The analysis was performed for single-particle events of photons (right-hand side), charged pions, charged kaons, protons, antiprotons, neutrons and antineutrons (left-hand side plot). Their transverse momentum was uniformly distributed between 0.5 and 100 GeV/c. The particles pointed in PHOS acceptance. The contour on the figure corresponds to the photon identification cut with high efficiency (95%) and low purity (79%).

are defined: high, medium, and low purities which correspond to the reconstructed particles occupying the areas in the  $(p_0, p_1)$  space defined by the argument  $R$  of Eq. (5.38):

$$R(p_0, p_1) < \kappa/2$$

with  $\kappa = 1, 4, 9$ , respectively, defining 1, 2, and 3 standard deviations from the shower centre in the  $(p_0, p_1)$  space.

#### Particle-identification probabilities

*Single photons.* The identification probability (Fig. 5.147) was calculated for photons generated with a uniform energy distribution from 0.5 to 120 GeV, with two different intervals, 0.5 to 10 GeV and 0.5 to 120 GeV, and tracked inside the ALICE set-up. It is defined as the ratio between the spectrum of the reconstructed particles identified as photons and the spectrum of all reconstructed particles. The three identification criteria (CPV, TOF and PCA) were applied simultaneously and the probability for the three purity classes was obtained.

*Photons in the heavy-ion environment.* The high occupancy of PHOS in heavy-ion collisions induces a significant number of overlapping showers. In central HIJING Pb–Pb collisions ( $b < 2$  fm), about one third of the EMC reconstructed points are associated to more than one primary particle, as observed in Fig. 5.148. To avoid identification ambiguities in the simulations, we have assigned to each reconstructed point the primary particle that contributes with the largest fraction of energy to it. We studied two centralities,  $b < 2$  fm and  $b < 5$  fm ( $dN_{\text{ch}}/d\eta \approx 6000$  and 3500 charged particles per pseudorapidity unit, respectively).

*Low-energy photons in the heavy-ion environment.* The probability for the three purity classes is calculated combining the three criteria (TOF, CPV, and PCA). They are taken separately first and then combined. To evaluate the contamination of the identified photon spectrum we consider charged pions, protons, neutrons, and their antiparticles. We summarize the main results when we apply the identification criteria separately (more details in Ref. [89]):

The identification probability by TOF indicates that TOF measurements alone cannot discriminate photons from nucleons for reconstructed energies larger than 1.5 GeV. This threshold is higher for anti-nucleons because they deposit additional energy through their

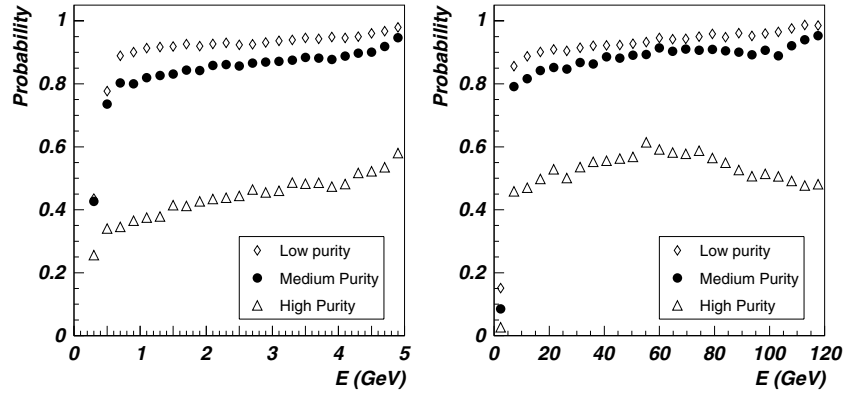


**Figure 5.147** Photon-identification probability for soft, 0.5 to 10 GeV, (left) and hard, 0.5 to 100 GeV, (right) photons plotted as a function of the energy of the reconstructed particle. The probability is represented for three purity classes.

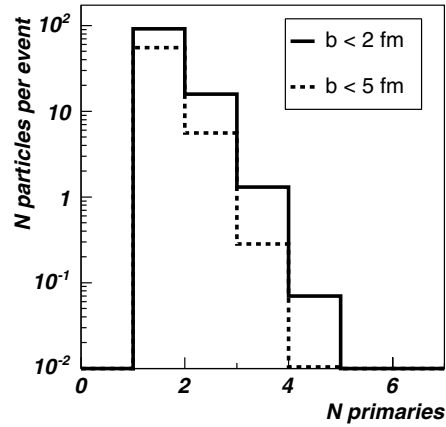


**Figure 5.148** Number of primary particles associated with one reconstructed particle in HIJING events.

annihilation. Charged  $\pi$ -mesons cannot be discriminated from photons for energies higher than 0.5 GeV.

Charged particles are efficiently discriminated by the CPV criterion from neutral particles for reconstructed energies higher than 1 GeV. Soft hadrons are significantly deflected by the magnetic field so that the distance of their impact point in CPV and EMC is sufficiently large to produce their misidentification as photons. We observe that neutral particle identification probabilities are well below 100% (between 90 and 50% depending on the purity class and centrality of the collision). This is due to a mismatch in the tracking between the CPV and the EMC produced by the HIC environment. This effect increases with the particle multiplicity of the event; for  $b < 2$  fm the probability of misidentifying neutral particles is about 10% worse than for  $b < 5$  fm.

The PCA identification criterion is efficient for reconstructed energies  $E > 1$  GeV, although a strong dependence of the identification probability with the particle multiplicity

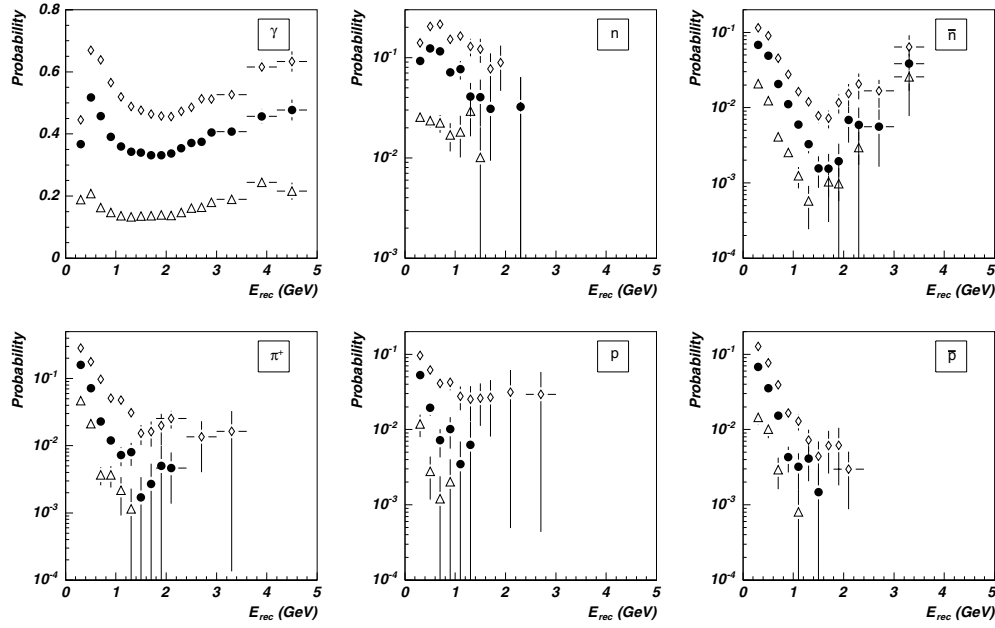


**Figure 5.149** Probability of identifying a particle as a photon with high ( $\Delta$ ), medium ( $\bullet$ ) and low ( $\diamond$ ) purity level by the TOF, CPV, and PCA criteria as a function of the reconstructed energy for  $\gamma$ ,  $n$ ,  $\bar{n}$ ,  $p$ ,  $\bar{p}$  and  $\pi^\pm$  generated by HIJING simulations for Pb–Pb collisions at 5.5A TeV and  $b < 5$  fm.

is observed. Hadrons are misidentified as photons with a high probability for reconstructed energies lower than 0.5 GeV, but for higher energies the probability is small. The comparison of the identification probabilities for each of the three identification criteria alone allows us to conclude that for energies  $E < 1$  GeV the TOF criterion is the most efficient. The CPV criterion rejects charged hadrons for  $E > 1$  GeV, while the PCA criterion rejects charged and neutral hadrons for  $E > 1$  GeV.

In Fig. 5.149 the results for the three identification criteria combined are plotted for centralities of  $b < 5$  fm, for  $b < 2$  fm the photon identification probability descends 10% and hadron misidentification probability increases by 10%.

We observe that the probability of identifying photons has a maximum at low energies and then decreases reaching a minimum at about 1.5 GeV. If this probability is compared to the probability obtained by merging photons of energy uniformly distributed with HIJING events, shown in Fig. 5.150 left, we see that these probabilities are quite different. This difference is due, on one hand, to the shape of the photon spectrum in HIJING events which is exponential and on the other hand, to the overlapping clusters produced in HIJING events. In these figures, we observe a maximum of the identification probability at low energies and a decrease with energy which is more pronounced for HIJING events. This decrease is due to the overlapping of showers of different particles which produces reconstructed particles with higher energy than the original particle, and photons identified as hadrons. Consequently, the probability denominator, which is the number of clusters generated by photons, is enhanced at higher energies. In the case of single HIJING events, the probability decreases with the energy even faster owing to the exponential shape of the HIJING photon spectrum. This effect is smaller and saturates for uniform energy photon distributions. On the other hand,

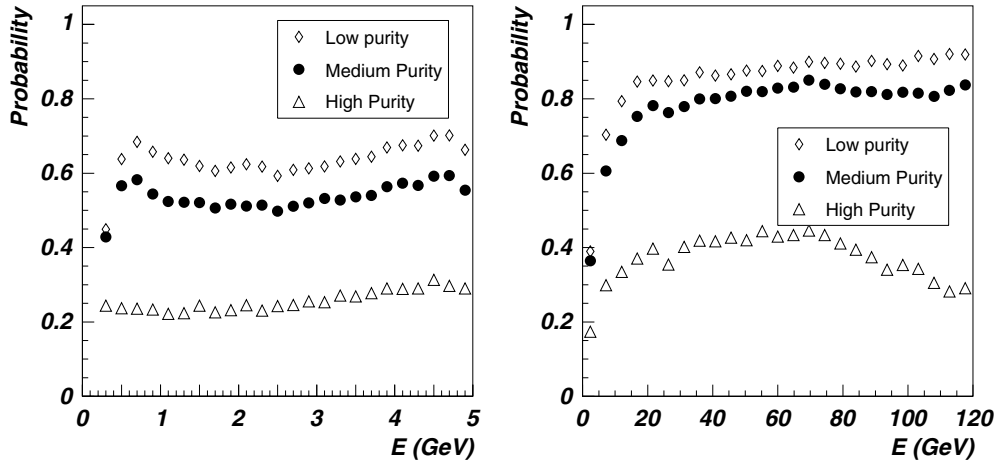


**Figure 5.150** Probability of identifying photons generated with energy uniformly distributed from 0 to 5 GeV (left) and from 0.5 to 120 GeV (right), and merged with HIJING events as a function of the reconstructed energy with high ( $\Delta$ ), medium ( $\bullet$ ) and low ( $\diamond$ ) purity level, for TOF, CPV and PCA criteria simultaneously required. Results for impact parameter  $b < 5$  fm are shown.

if the photon spectrum is exponential, there are comparatively fewer high-energy photons and an abrupt drop of the probability takes place.

The purity  $\mathcal{P}$  of the identified photons is defined as the ratio of the number of reconstructed particles actually generated by photons and the total number of particles identified as photons. Similarly, the hadron contamination  $C$  is defined as the ratio of the number of reconstructed particles identified as photons but generated by hadrons and the total number of particles identified as photons ( $C = 1 - \mathcal{P}$ ). About 97–99% of all the particles identified as photons are indeed photons. The contamination of photons is displayed in Fig. 5.151.

*High-energy photons in the heavy-ion environment.* The identification of high-energy photons in a HIC environment was studied with built-up test cases, simulated by mixing single hard photons of energy generated by a uniform distribution between 0.5 to 120 GeV with central Pb–Pb HIJING events ( $b < 2$  fm and  $b < 5$  fm). The identification probabilities of hard photons for heavy-ion collisions are plotted in Fig. 5.150 (right) for  $b < 5$  fm. For  $b < 2$  fm, the probability descends 10–20%. The hard photon identification probability decreases by 10% compared with the single-particle case due essentially to the failure of the CPV criterion.

#### 5.5.1.9. $\pi^0$ detection in PHOS

*Invariant-mass analysis of single  $\pi^0$ 's.* Neutral mesons are identified by measuring in PHOS the two decaying photons and by applying the invariant-mass analysis. The average mass resolution at the  $\pi^0$  mass (Fig. 5.152) in PHOS is 3–6 MeV/ $c^2$  depending on the  $\pi^0$  energy. The probability (Fig. 5.153) to reconstruct  $\pi^0$ 's by invariant-mass analysis, i.e. to distinguish the two decay photons and measure their invariant mass, was evaluated from  $\pi^0$ 's generated with a uniform energy distribution between 0 and 100 GeV and oriented toward PHOS so that both decay photons enter into the PHOS acceptance.

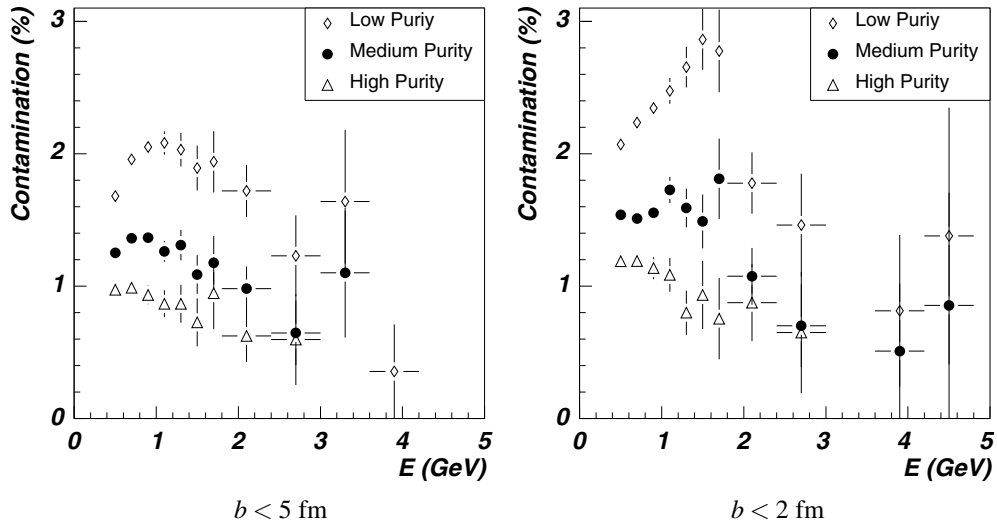


**Figure 5.151** Hadron contamination of the spectrum of reconstructed particles identified as photons in HIJING events for  $b < 5$  fm (left) and  $b < 2$  fm (right), with high ( $\Delta$ ), medium ( $\bullet$ ) and low ( $\diamond$ ) purity level.

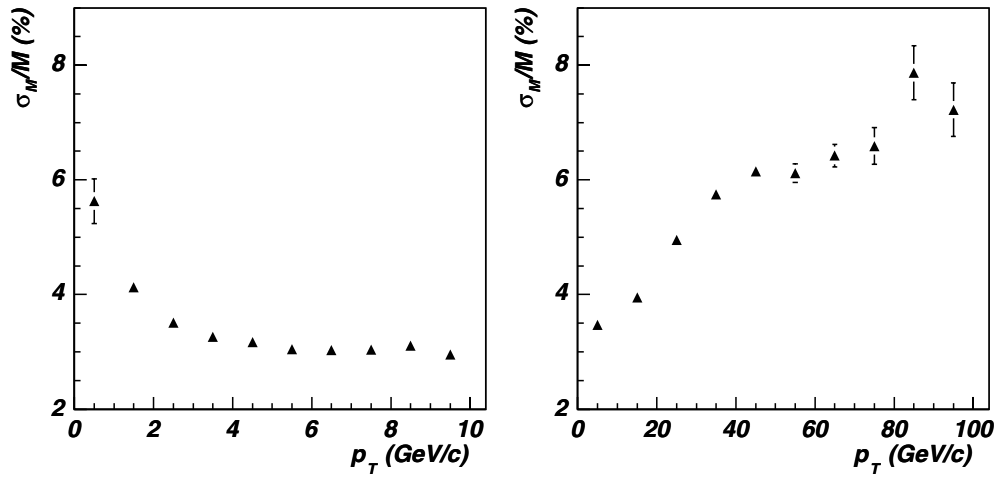


**Figure 5.152** Invariant-mass resolution calculated for  $\pi^0$ 's of energy uniformly distributed between 0.5 and 100 GeV.

The reconstruction probability was studied for different gradual selections:

- without any selections (denoted as a bare efficiency);
- after applying a fiducial-volume cut, i.e. taking into account only those photons which are located at least 2 cells apart from the EMC edge;
- after applying a cut on two-photon invariant mass  $|M_{\gamma\gamma} - M_{\pi^0}| < 2\sigma_{M_{\gamma\gamma}}$ ;
- after the asymmetry cut on the photon energies  $E_1$  and  $E_2$ :  $A = |E_1 - E_2|/(E_1 + E_2) < 0.8$ ;
- and, finally, after the photon identification with low, medium, and high purities.

We conclude that the  $\pi^0$  spectrum can be measured in PHOS with a fairly good efficiency up to  $\pi^0$  transverse momentum  $p_t < 30$  GeV/c. Beyond this momentum value, the efficiency

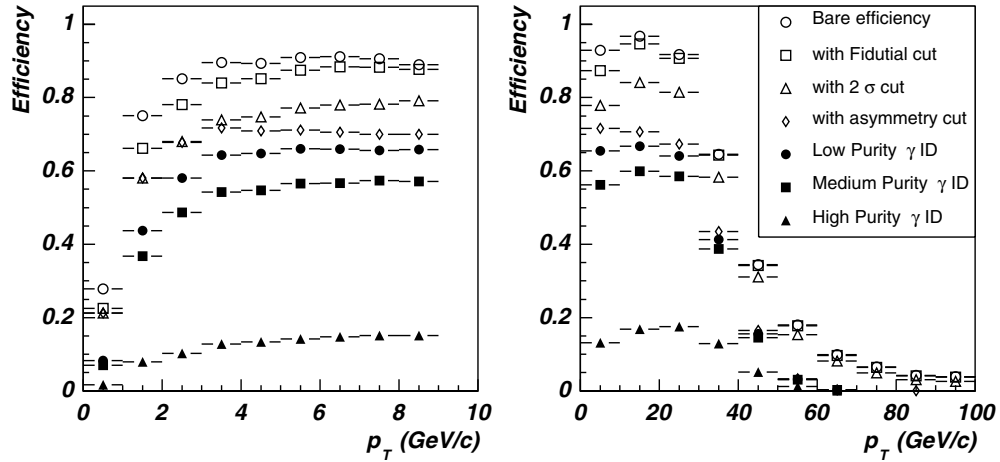


**Figure 5.153** Probability of reconstructing  $\pi^0$ 's by invariant-mass analysis with different conditions.

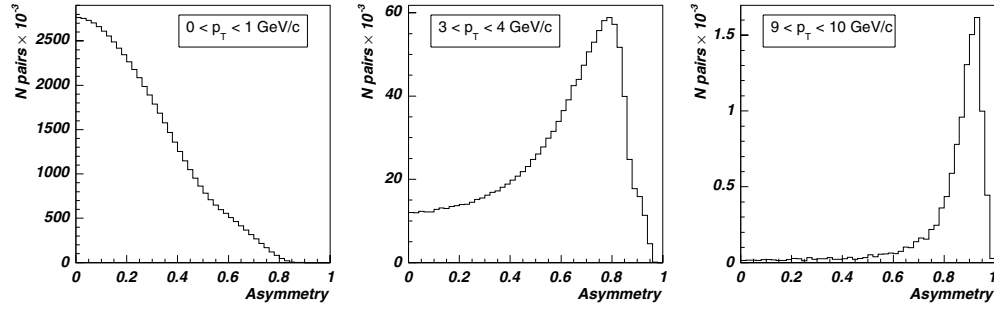


**Figure 5.154** Energy asymmetry parameter  $A$  calculated for all reconstructed pairs generated in HIJING events and with transverse momenta  $0 < p_t < 1$  GeV/c,  $3_t < p < 4$  GeV/c and  $9 < p_t < 10$  GeV/c.

drops steeply and it vanishes above  $p_t = 50$  GeV/c. This decrease is explained by the fact that the two decay photons merge into a single reconstructed point which cannot be unfolded anymore.

*Invariant-mass analysis of  $\pi^0$ 's in the heavy-ion environment.* The high  $\pi^0$  multiplicity in a heavy-ion environment generates a combinatorial background in the invariant-mass spectrum constructed by combining by pairs all the detected photons. The background underlying the  $\pi^0$  peak must be statistically subtracted. In central Pb–Pb HIJING collisions generated at impact parameter  $b < 2$  fm, on account of high combinatorial background, no peak at the  $\pi^0$ -mass is observed until pair transverse-momenta  $p_t = 10$  GeV/c. This is because of the large contributions of hadrons which can be suppressed by applying a selection on the energy asymmetry parameter  $A$ . The decay-photon asymmetry distribution is uniform due to the isotropic  $\pi^0$  decay. The distribution measured for all reconstructed particles in a HIJING event (Fig. 5.154) exhibits a strong enhancement at large asymmetries and for large transverse momentum of a pair. This is explained by the combinations of very asymmetric particle pairs, where one particle is most probably a hadron. Eliminating pairs with these large asymmetries

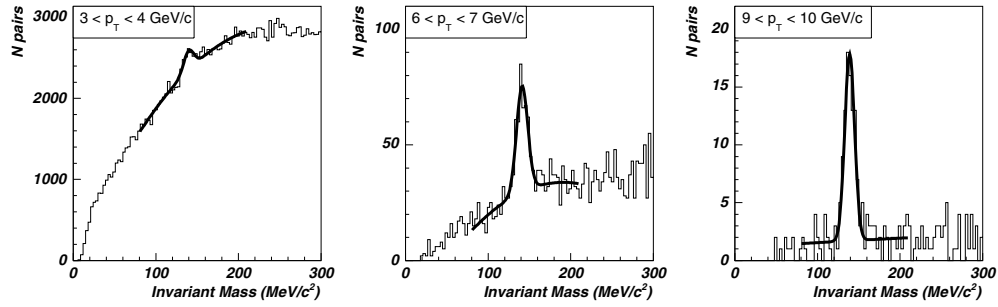


**Figure 5.155** Invariant-mass spectra in HIJING events of any reconstructed particle pairs with asymmetry  $A < 0.75$  in the ranges  $3 < p_t < 4$  GeV/c,  $6 < p_t < 7$  GeV/c and  $9 < p_t < 10$  GeV/c.

$A > 0.75$  reduces (Fig. 5.155) the combinatorial background significantly while the  $\pi^0$  peak is suppressed by only 25%.

The procedure of the combinatorial background subtraction was demonstrated to be very efficient in the WA98 experiment [90] in Pb–Pb collisions at 158A GeV. According to this procedure, the combinatorial background is constructed in the event-mixing technique when all photon pairs for the invariant mass calculation are taken from different events to exclude any correlations. Applied to the ALICE heavy-ion environment, the procedure of the combinatorial background subtraction allows one to extract the  $\pi^0$  spectrum above  $p_t$  of 0.5 GeV/c. As a demonstration, the invariant-mass spectrum of all reconstructed particle pairs identified as low-purity photons, in 200 000 events of central Pb–Pb collisions at  $b < 2$  fm, is shown in Fig. 5.156 (a) in the  $p_t$ -bin  $1.0 < p_t < 1.5$  GeV/c. Owing to the large combinatorial background the  $\pi^0$  peak is not visible. Figure 5.156 (b) shows the invariant-mass spectrum of reconstructed low-purity photons taken from 10 mixed events. The ratio of the invariant-mass spectrum in Pb–Pb events to that spectrum in mixed events in Fig. 5.156 (c) reveals a clearly visible peak at the  $\pi^0$  mass. This ratio in the region of uncorrelated pairs between  $\pi^0$  and  $\eta$ -meson peaks equal to  $R = 0.0584$  is a scaling factor which normalizes mixed-event invariant-mass spectrum to the mass spectrum in Pb–Pb events. The result of subtraction of the normalized mixed-event spectrum from the two-photon spectrum is shown in Fig. 5.156 (d). The statistical errors of the latter spectrum are propagated from the statistical errors of the spectra (a) and (b). The final two-photon mass spectra after the combinatorial background are fitted by the Gaussian, the dispersion of which is shown in Fig. 5.157 versus the  $\pi^0$  transverse momentum.

The  $\pi^0$  spectrum can be correctly reconstructed as demonstrated by comparison of generated and reconstructed spectra (Fig. 5.158).

*5.5.1.10. Event-by-event photon and  $\pi^0$  identification.* At high momenta,  $\pi^0$ 's are *a priori* identified as photons because the photons from  $\pi^0$  decay merge into a single reconstructed point. Several approaches have been developed to discriminate these  $\pi^0$ 's from photons. They are all based on the shower-shape analysis.

*One-dimensional shower-shape analysis.* In addition to the parameters already defined for the photon/hadron discrimination, a few more have been introduced for the  $\gamma/\pi^0$  identification. They are the various moments of the cluster tensor, among which the second moment  $M_{2x}$ , or the largest eigen value of the covariance matrix (Eq. (5.31)) is the most discriminant one (Fig. 5.159). At moderate  $p_t$ , the distributions of the moment  $M_{2x}$  for photon and  $\pi^0$  are well separated with only a slight overlap, while at higher  $p_t$  they merge.

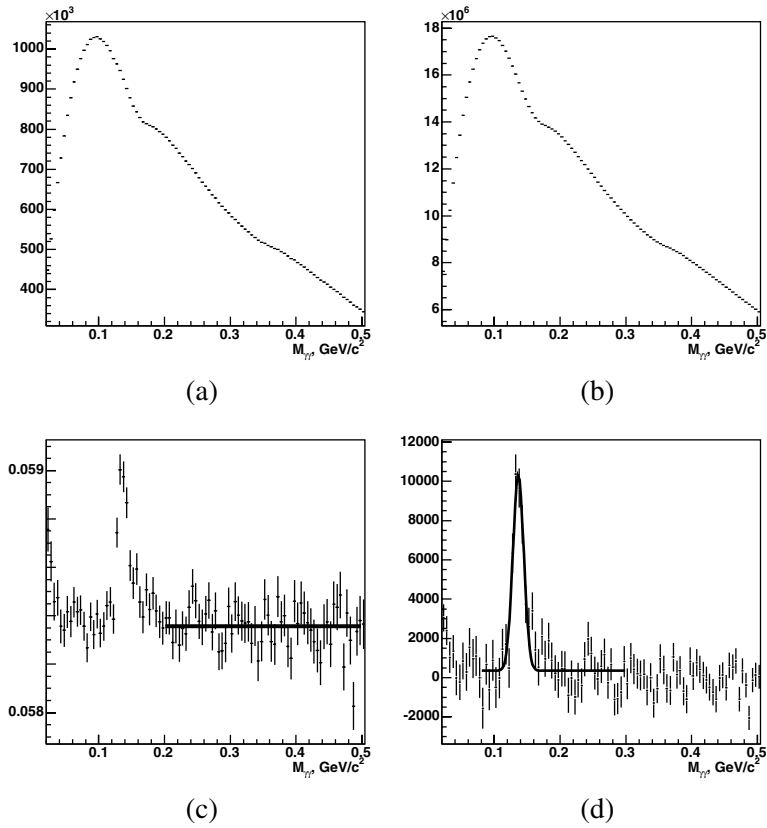


**Figure 5.156** Two-photon invariant-mass distributions in central Pb-Pb events (a), in mixed events (b), their ratio (c) and difference of the invariant-mass distribution and the combinatorial background (d). Transverse momentum of the  $\gamma\gamma$  pairs in  $1.0 < p_t < 1.5 \text{ GeV}/c$ . Statistics corresponds to 200 000 events.

To distinguish photons and  $\pi^0$ -mesons, the optimal border  $M_{2x}^0$  between the two moment distributions is found, which maximizes the ratio of the true particle identification probability to the misidentification probability. To have a reasonably high value of the true identification probability, we restrict the search of this optimal border by the interval between the mean values of the photon and  $\pi^0$  moments (Fig. 5.159), and demand that the misidentification probability need not be less than 3%. The value of  $M_{2x}^0$  can be different for photons and  $\pi^0$ .

The photon identification probability  $P(\gamma, \gamma)$  is defined as a fraction of single-photon events with the moments  $M_{2x} < M_{2x}^0$ , and the misidentification probability  $P(\gamma, \pi^0)$  of  $\pi^0$  as a photon is a fraction of  $\pi^0$  events with the moments in the same range (Fig. 5.160, left). Similarly the  $\pi^0$  identification probability  $P(\pi^0, \pi^0)$  and the photon misidentification probability as a  $\pi^0$   $P(\pi^0, \gamma)$  are defined as the fraction of  $\pi^0$  events and the fraction of single-photon events within  $M_{2x} > M_{2x}^0$ , respectively (Fig. 5.160, right). The ratios  $P(\gamma, \pi^0)/P(\gamma, \gamma)$  and  $P(\pi^0, \gamma)/P(\pi^0, \pi^0)$  (Fig. 5.161) demonstrates that the misidentification is suppressed compared with the true identification to the level of a few percent at moderate  $p_t$  and is not higher than 10–20% at the highest  $p_t = 120 \text{ GeV}/c$ .

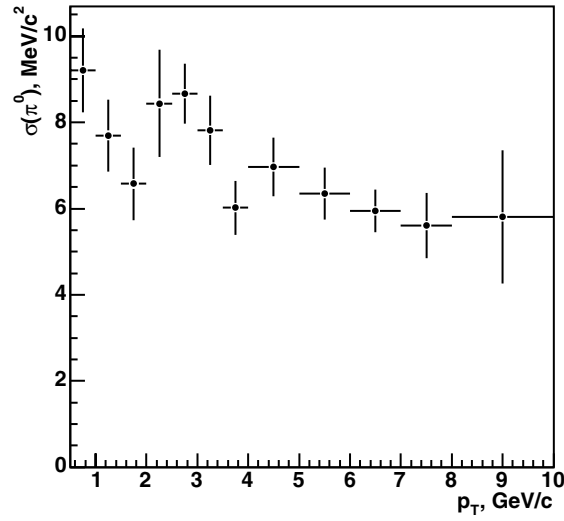


Figure 5.157 Width of  $\pi^0$  peak in central Pb–Pb collisions vs.  $p_T$ .

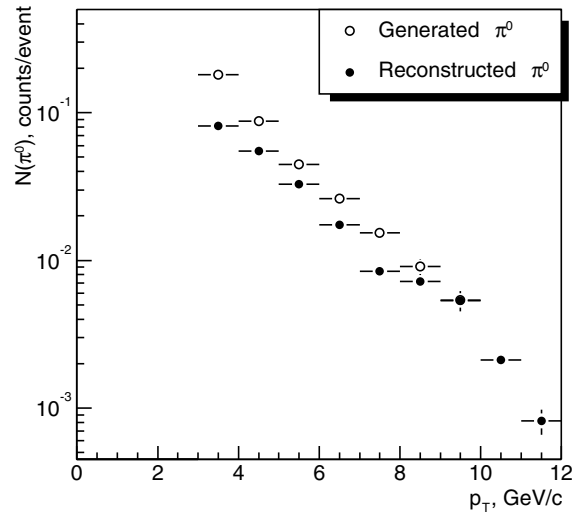


Figure 5.158  $p_T$  spectrum of generated and reconstructed  $\pi^0$  per HIJING event.

*Recognition of photons and  $\pi^0$ 's by PCA.* Another approach to distinguish photons and  $\pi^0$ -mesons is based on comparison of the showers in the space of principal components within the principal component analysis (PCA) described in Section 5.5.1.8. A prominent difference between photon and  $\pi^0$  showers is observed at lower energies, while both particles overlap in this space at higher energies (see Ref. [89] for more details).

The probabilities of true identification and misidentification  $P(\gamma, \gamma)$ ,  $P(\pi^0, \pi^0)$ ,  $P(\gamma, \pi^0)$  and  $P(\pi^0, \gamma)$  are defined analogously to the methods described in Section 5.5.1.8 and shown in Figs. 5.162 and 5.163.

In the heavy-ion environment, the efficiency of  $\pi^0$  identification was studied in the same way as for hard photons, as described in Section 5.5.1.8. Events with  $\pi^0$ -mesons with

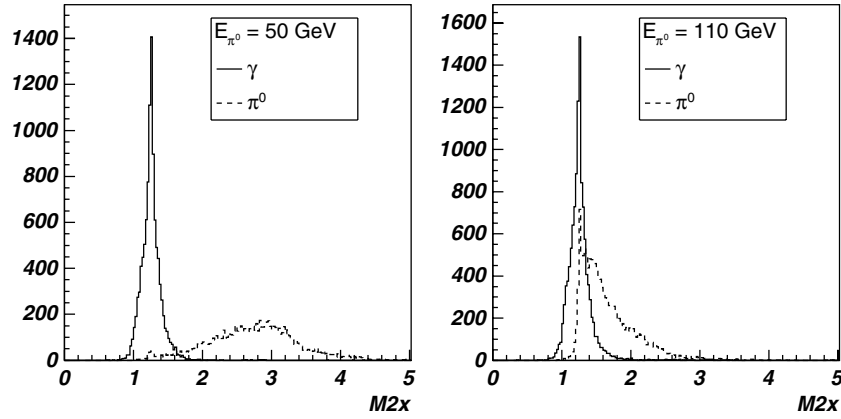


Figure 5.159  $M_{2x}$  for photons (solid line) and  $\pi^0$ 's (dashed line) of 50 and 110 GeV of energy.

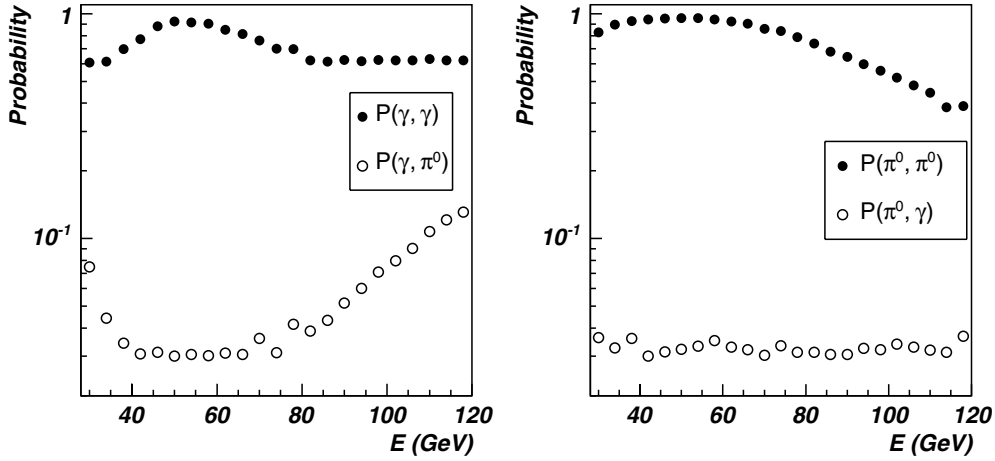


Figure 5.160 Probability of the photon identification and misidentification of photons as  $\pi^0$ 's (left plot) and that of the  $\pi^0$  identification and misidentification of  $\pi^0$ 's as photons (right plot).

transverse momenta uniformly distributed in the range  $30 < p_t < 120$  GeV/ $c$  were merged with HIJING events of central Pb–Pb collisions, then the identification criteria including TOF, CPV and PCA were applied. We see that the identification probabilities are only about 10% smaller than those of single  $\pi^0$  identification due essentially to the CPV matching failure, as observed for single hard photons, which means that the high detector occupancy existing in a heavy-ion environment does not modify significantly the capability of discriminating hard  $\pi^0$ 's from photons by the PCA analysis.

*Recognition of photons and  $\pi^0$ 's by a neural network.* The discrimination between photons and  $\pi^0$ -mesons has been studied also in the Artificial Neural Network (ANN) approach [91] which has already been recognized as a powerful tool for different applications in high-energy physics, see Refs. [92–97].

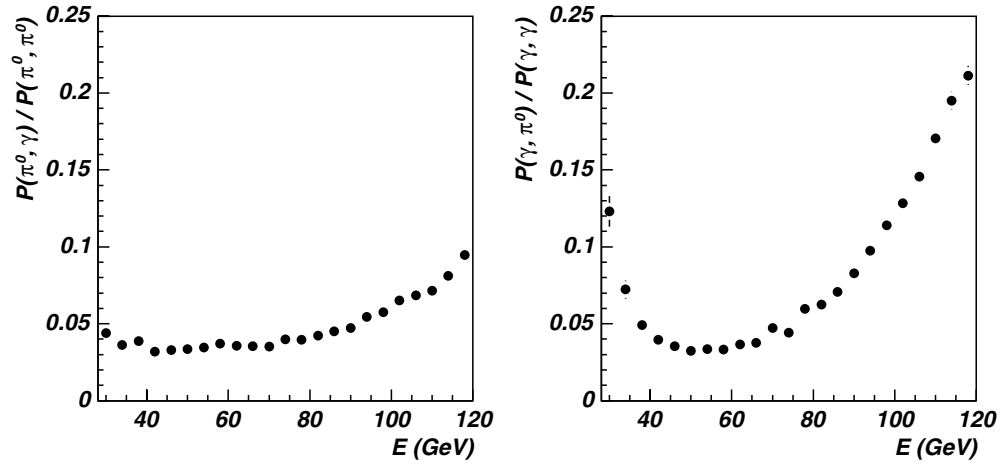


Figure 5.161 Ratios  $P(\gamma, \pi^0)/P(\gamma, \gamma)$  (left plot) and  $P(\pi^0, \gamma)/P(\pi^0, \pi^0)$  (right plot).

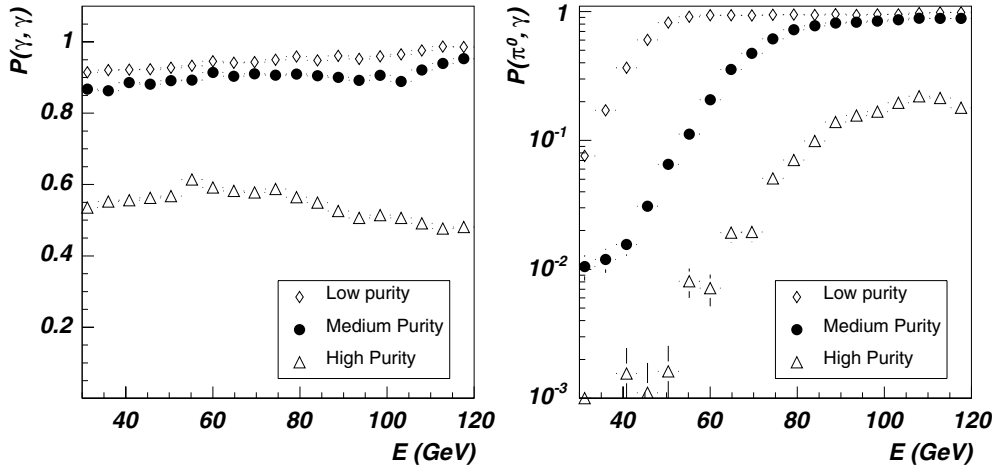
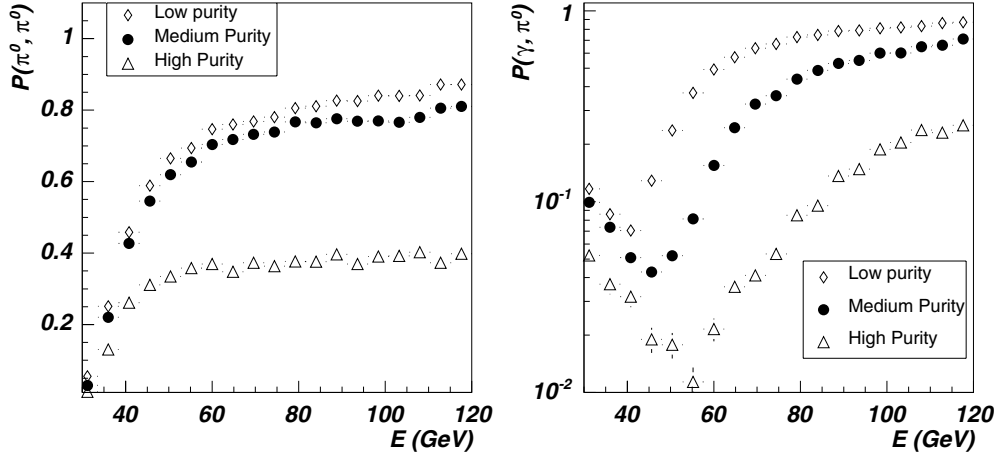


Figure 5.162 Probability of correct single-photon identification (left) and misidentification as  $\pi^0$  (right) by PCA for high ( $\Delta$ ), medium ( $\bullet$ ) and low ( $\diamond$ ) identification purity levels.

The reconstruction program of the PHOS provides data as a set of clusters characterized by the amplitudes of signals and relevant coordinates of cluster cells in the detector plane. Our approach to  $\gamma/\pi^0$  selection with the ANN method is based on a limited number of characteristic variables which nevertheless carry the major information about the cluster profile independent of its size. At the first stage the  $2 \times 2$  matrix  $Q_{ij}$  (tensor) for each cluster is introduced as follows:

$$Q_{ij} = \sum_k x_i^{(k)} x_j^{(k)} E_k, \quad (5.39)$$

where index  $k$  runs over all cluster cells,  $i, j = 1, 2$ ,  $\vec{x}^{(k)} = (x_1^{(k)}, x_2^{(k)})$  is the vector of the cell coordinates in units of the crystal transverse size. The tensor (5.39) is similar to the cluster covariance matrix (5.31), but with the linear energy weights and without averaging.



**Figure 5.163** Probability of correct single  $\pi^0$  identification (left) and misidentification as photons (right) by PCA for high ( $\Delta$ ), medium ( $\bullet$ ) and low ( $\diamond$ ) identification purity levels.

This energy-profile tensor depends on the number of photon showers glued in the cluster as well as on the inclination angle of photons to the detector surface. To avoid the latter effect, or to decrease its influence, calculation of the matrix  $Q_{ij}$  was made after compression of the cluster cell coordinates relative to the central point  $\vec{X}_0$  of the cluster defined as the centre of cell with maximal signal in the cluster. The compression is defined by the angle  $\Theta$  between the normal to the PHOS module surface and the direction of photon propagation according to the transformation

$$\vec{x} \rightarrow R(-\varphi_0) \cdot E_c(\Theta) \cdot R(\varphi_0) \cdot (\vec{x} - \vec{X}_0) + \vec{X}_0, \quad (5.40)$$

where  $\vec{x} = (x_1, x_2)$  is the radius-vector of an arbitrary cell in the cluster,  $R$  and  $E_c$  are rotation and compression matrices, respectively:

$$R(\varphi_0) = \begin{pmatrix} \cos \varphi_0 & \sin \varphi_0 \\ -\sin \varphi_0 & \cos \varphi_0 \end{pmatrix}, \quad E_c = \begin{pmatrix} \cos \Theta & 0 \\ 0 & 1 \end{pmatrix}, \quad (5.41)$$

and  $\varphi_0$  is a polar angle of the point  $\vec{X}_0$  in the coordinate system with origin in the centre of the PHOS module.

After compression two eigen values of matrix  $Q_{ij}$  were calculated and ordered as  $\lambda_1 \geq \lambda_2$ , and corresponding eigen vectors  $\vec{e}_1$  and  $\vec{e}_2$  were found. The matrix can be reduced then to the diagonal form

$$\begin{pmatrix} \lambda_1 & 0 \\ 0 & \lambda_2 \end{pmatrix} \quad (5.42)$$

in the coordinate system defined by the eigen vectors. In the new coordinate system the moments  $M_{mn}$  were calculated according to the formula

$$M_{mn} = \sum_k (x_1^{(k)})^m \cdot (x_2^{(k)})^n E_k, \quad (5.43)$$

where index  $k$  runs over all cluster cells. The centre of a cell with a maximal signal was taken as the origin of the local coordinate system for calculation of the moments  $M_{mn}$  (5.43). Note, that such important variables as effective mass of two photons  $M_{\gamma\gamma}$  can be expressed in terms of moments  $M_{mn}$  (5.43), see details in Refs. [98, 99].

One additional variable is also useful for event analysis by the ANN method. This is an angle  $\varphi$  between the eigen vector  $\vec{e}_1$  and the vector  $\vec{X}_0$  directed from the geometrical centre of the PHOS module to the cluster centre:

$$\varphi = \arccos(\vec{e}_1, \vec{X}_0/|\vec{X}_0|). \quad (5.44)$$

This variable increases the quality of  $\gamma/\pi^0$  selection mainly in the peripheral region of PHOS modules.

Thus an input vector  $\vec{P}^{(\text{in})}$  of event features for ANN is filled with the following variables: energy  $E = M_{00}$  of the cluster, eigen values  $\lambda_1$  and  $\lambda_2$ , momenta  $M_{10}$ ,  $M_{30}$ ,  $M_{40}$  and  $M_{04}$ , distance  $d$  between the hits of two photons at the PHOS surface, effective mass  $M_{\gamma\gamma}^2$  and angle  $\varphi$ .

The ANN for  $\gamma/\pi^0$  selection was composed of three layers: input, hidden, and output. The input layer consists of  $N$  nodes, where  $N$  is the dimension of vector  $\vec{P}^{(\text{in})}$  of the event features; the hidden layer is built of  $2N+1$  nodes; and finally, a one-node output layer provides the neural-net response  $S_{\text{NN}} \in (0-1)$  used for the final classification of the events.

The net was trained with two event samples, i.e. clusters from direct photons, and those from background (clusters produced by overlapped photons from decay  $\pi^0 \rightarrow 2\gamma$ ). Each sample contained 10 000 events (clusters) passing pre-selections. Upon training the net, we tested its efficiency on another two statistically independent samples, each consisting of 30 000 events also passing the pre-selections.

The data for the analysis were simulated within the ALICE framework for the simulation, reconstruction and data analysis, AliRoot v.3.06.02. Isolated photons and neutral pions (with following decay  $\pi^0 \rightarrow \gamma\gamma$ ) were emitted from the interaction point with uniformly distributed transverse momentum in the range  $0 < p_t < 120$  GeV/ $c$  within the solid angle defined by the uniformly distributed azimuth angle  $210^\circ < \varphi < 330^\circ$  and polar angle  $80^\circ < \theta < 100^\circ$ . The solid angle of the emitted particles was chosen to be a bit larger than that of the PHOS detector to avoid various border effects.

The noise with  $\sigma_{\text{noise}} = 10$  MeV was applied to the digits, after which the digits were passed through the 50 MeV threshold cut. The remaining digits with common side were grouped into the clusters. Only clusters with total energy greater than 500 MeV were accepted.

The achieved  $\gamma/\pi^0$  discrimination power of the ANN after net training is shown in Fig. 5.164 for the event feature vectors  $(E, \lambda_1, \lambda_2, M_{30}, M_{04}, \varphi)$ . This figure shows the probability  $\varepsilon(\gamma, \gamma)$  of true photon identification and misidentification  $\varepsilon(\gamma, \pi^0)$  of  $\pi^0$ -meson as a photon in the energy interval of generated photons and neutral pions from 3 GeV to 120 GeV, as well as a coefficient of  $\pi^0$ -background suppression relative to the photon identification probability, i.e.  $\varepsilon(\gamma, \pi^0)/\varepsilon(\gamma, \gamma)$ .

From this figure one can see that the probability of misidentification of a neutral pion as a photon is on the level of a few per cent in the energy range of pions of 3–120 GeV with relatively high efficiency of the correct photon identification as isolated photons in the same energy range.

We compare our results with the data of Ref. [100] where the coefficient  $\varepsilon(\gamma, \pi^0)$  was estimated for the STAR experiment as 0.15 at 20 GeV and 0.45 at 40 GeV. The efficiency of the  $\gamma/\pi^0$  recognition was also calculated for the CMS set-up in the note [101] with values  $\varepsilon(\gamma, \pi^0)$  about 0.5 at 20 GeV and 0.55–0.60 at 100 GeV. This comparison shows that the ALICE set-up with the PHOS spectrometer is more adequate for the goal of  $\gamma/\pi_0$  selection than the mentioned experiments.

*5.5.1.11. Bayesian approach for the identification of particles detected with PHOS.* In this section we present another identification approach, based on Bayes's theory of probabilities

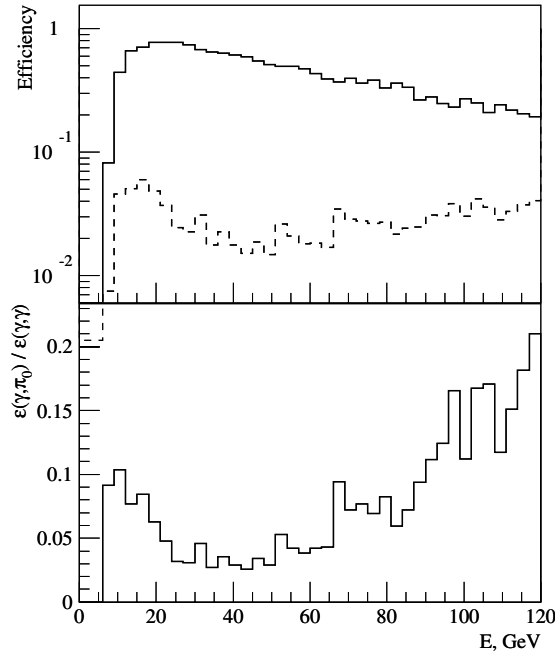


**Figure 5.164** Probability  $\epsilon(\gamma, \gamma)$  of true photon identification (solid lines), and misidentification  $\epsilon(\gamma, \pi^0)$  of  $\pi^0$ -meson as a photon (dotted lines), and coefficient of  $\pi^0$ -background suppression relative to detection efficiency of direct photons  $\epsilon(\gamma, \pi^0)/\epsilon(\gamma, \gamma)$ .

where PID weights are assigned, on an event-by-event basis, to every reconstructed particle. Combining these weights with similar PID weights derived from the ALICE central tracking system provides a global PID of all particles, both charged and neutral, emitted within the PHOS acceptance. This method is widely discussed in Ref. [102].

In this method, the PID of particles detected with PHOS relies on three independent identification parameters derived from the data collected by the detectors: (i) the time-of-flight (*tof*); (ii) the distance between the CPV and the calorimeter ( $d_{CE}$ ); and (iii) the lateral dispersion of the shower which develops in the calorimeter (*dis*).

PID weights are assigned to each reconstructed particle. The weights represent the probability that the detected particle is of a given type, among photon  $\gamma$ , electron  $e^\pm$ , charged hadron  $h^\pm$ , neutral hadron  $h^0$  and high- $p_t$   $\pi^0$ . The weights are calculated according to the following steps:

- First, charged ( $\pi^\pm$ ,  $K^\pm$ ,  $\bar{p}$  and  $p$ ) and neutral ( $K_L^0$ ,  $\bar{n}$  and  $n$ ) hadrons are generated with realistic exponential energy distribution and tracked through the ALICE detection systems. Since, at variance with the previously listed hadrons, photons and high- $p_t$   $\pi^0$ 's (generating a single electromagnetic cluster in PHOS) always develop an electromagnetic shower in the calorimeter, they can be generated with an uniform energy distribution. The reconstructed particle spectra constitute the particle response function of the detector and are used as input of the next step.
- The density distribution,  $P(\text{parameter}|\text{particle type})$ , of the probability to identify a given particle type is calculated for each particle in the above list and for each one of the three identification parameters, *tof*,  $d_{CE}$  and *dis*. Either Landau or Gaussian distributions are used to parametrize these distributions. Combining the probability obtained for each

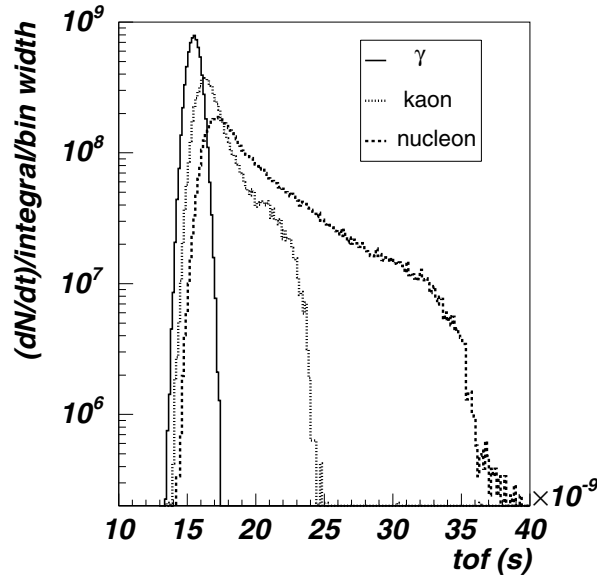


**Figure 5.165** Time-of-flight probability density distributions for different particle species, photons, kaons and nucleons, integrated from 0 to 2 GeV reconstructed energy.

identification parameter, the final weights are calculated giving the probabilities for a reconstructed particle to be of the types listed above.

- Finally, the method is tested by applying the algorithm to particles in HIJING events and in events with a single photon, electron or high-energy  $\pi^0$  merged in a HIJING event simulating a realistic heavy-ion collision environment.

#### Probability density distributions

*Time-of-flight.* Massive hadrons can be identified and discriminated from electrons and photons by measuring their time-of-flight ( $tof$ ) from the collision vertex to the PHOS. The measurement is discriminating up to transverse momenta of about 2 GeV. For larger values, all particles move at almost the speed of light and can no longer be identified. Therefore, the  $tof$  parameter will be considered for PID only for particles with a reconstructed energy smaller than 2 GeV. However, the  $tof$  discriminating power will be limited by hadrons with transverse momenta larger than 2 GeV showering in the calorimeter and depositing only a fraction of their energy.

The  $tof$  probability density distributions,  $P(tof|i)$  (Fig. 5.165), are calculated as the  $tof$  distribution for the particle of type  $i$  (as listed in the previous section), and for all reconstructed energy up to 2 GeV. The distributions are normalized to the total number of reconstructed events. The distributions are then parametrized with either a Gaussian or a Gaussian plus a Landau distribution (in the case of kaons and nucleons).

*CPV-EMC distance.* Electrons can be distinguished from other charged particles by measuring the distance between the impact of the particle in CPV and the impact in EMC. The probability density distributions  $P(d_{CE}|i)$ , are calculated for the  $d_{CE}$  components projected to the PHOS surface, parallel to the beam axis ( $z$ ) and perpendicular to the beam axis<sup>5</sup> ( $x$ )

<sup>5</sup> Charged particles are bent in the direction of the  $x$ -axis.

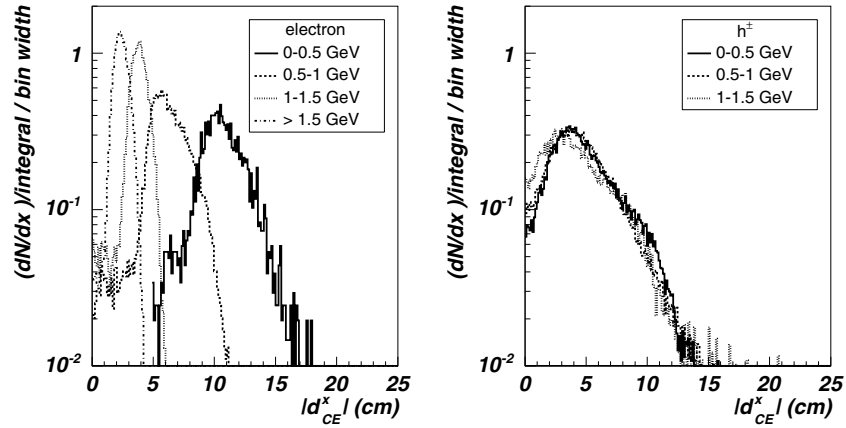


**Figure 5.166** Probability-density distributions of the distance between the impact on the CPV and on the EMC projected on the surface of the PHOS along the  $x$  axis measured for electrons (left), and charged hadrons ( $p$ ,  $\bar{p}$ ,  $\pi^\pm$  and  $K^\pm$ , right) and for different reconstructed energies.

distance and for electrons, pions, kaons and anti-protons reconstructed with different energy values. For low reconstructed energies and for a given value of the energy, the measured  $x$ -component of the distance,  $d_{CE}^x$ , is larger for electrons than for hadrons (Fig. 5.166). This is due to the fact that the electron energy is well measured with PHOS, whereas for hadrons only a fraction of the energy is measured, so that a low reconstructed energy originates from more energetic hadrons whose track has a small curvature. In addition, the measured fluctuation of the  $z$ -component,  $d_{CE}^z$ , distributions (centred at 0 for all energies) is smaller for electrons than for charged hadrons because hadronic showers cannot be as well localized as electromagnetic showers in PHOS. The distributions are parameterized with Gaussian distributions.

Given the  $d_{CE}$  value measured along the  $x$  and  $z$  axis, the probability densities,  $P(d_{CE}^{xz}|i)$ ,  $i$  being either  $e^\pm$  or  $h^\pm$ , are calculated as the product  $P(d_{CE}^x|i) \cdot P(d_{CE}^z|i)$ , of the pre-established distributions. A particle is identified as a neutral particle if  $P(d_{CE}^{xz}|i)$  for  $e^\pm$  and  $h^\pm$  is smaller than  $10^{-5}$ .

*Shower lateral dispersion.* Photons and electrons can be distinguished from hadrons by the difference in the shape of the showers which develop in the calorimeter. In addition, high- $p_t$   $\pi^0$ 's which are detected through their two decay-photons merging into a single electromagnetic cluster in the calorimeter can be distinguished from photons up to a limiting  $p_t$  value of about 100 GeV/ $c$ . We characterize the shower by its lateral dispersion (see Ref. [89]) and we calculated the probability density distribution  $P(dis|i)$  for photons, hadrons, and high- $p_t$   $\pi^0$  shown in Fig. 5.167.

The lateral dispersion is not significant when the cluster multiplicity (number of hit calorimeter cells which contribute to the cluster) is below four. For photons with reconstructed energies below 0.5 GeV, the average number of clusters is three (Fig. 5.168), setting the limit of applicability of this selection criterion. The probability density distribution is parametrized by Gaussian distributions for photons and high- $p_t$   $\pi^0$ 's and by Landau distributions for hadrons.

*Hadron reconstruction probability.* The probability that a hadron develops a shower in the PHOS is also taken into account. This probability depends on the initial hadron energy

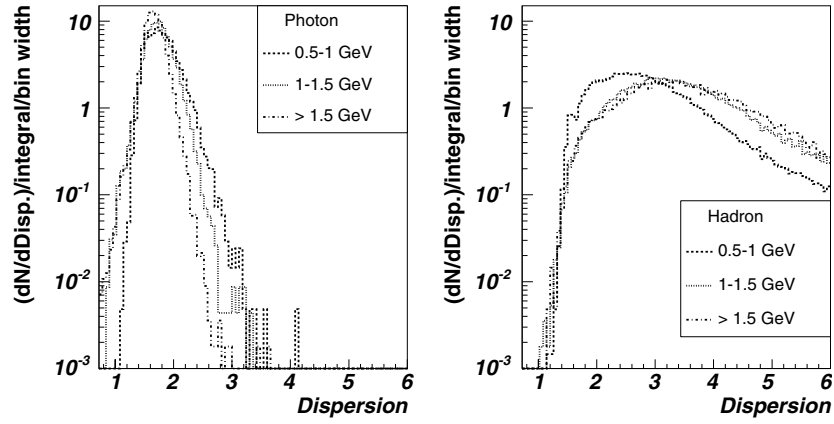


**Figure 5.167** Probability density distributions of the shower lateral-dispersion measured for photons (left) and hadrons (right) and for different reconstructed energies.

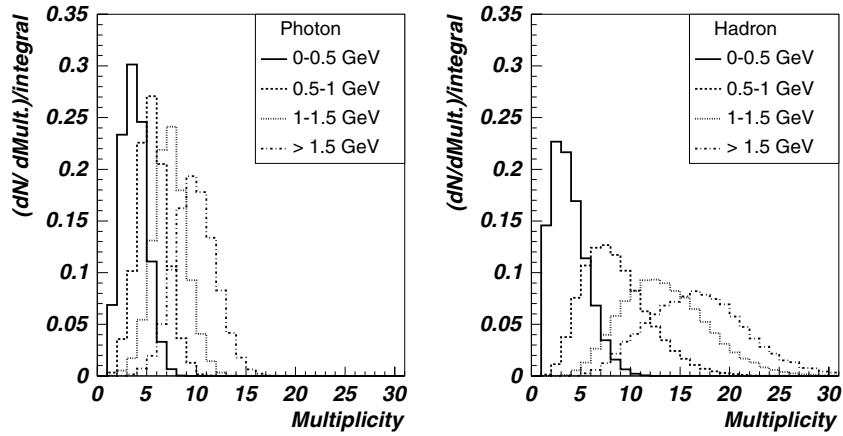


**Figure 5.168** Cluster multiplicity measured with the PHOS for photons (left) and hadrons (right) with different reconstructed energies.

and hadron type, and as an upper limit it was calculated from the response function of the PHOS to mono-energetic charged pions of 100 GeV. The response, normalized to one, and displayed in Fig. 5.169, gives the probability density distribution  $P(rec|i)$  for hadrons as the two exponential fit of the figure. The probability density is set to 1 for  $\gamma$ ,  $e^\pm$  and high- $p_t$   $\pi^0$ 's.

*PID weight.* From the probability density distributions calculated for particles of type  $\gamma$ ,  $e^\pm$ ,  $h^0$ ,  $h^\pm$  and high- $p_t$   $\pi^0$ 's and parametrized as described in the previous section, and for each measured reconstructed particle characterized by a  $tof$  value, a  $d_{CE}$  value and a  $dis$  value, a PID weight  $W(i)$ , ranging from 0 to 1, for particle species  $i$  is calculated as the product of the four probability density distributions for the particle  $i$  normalized to the sum of these products

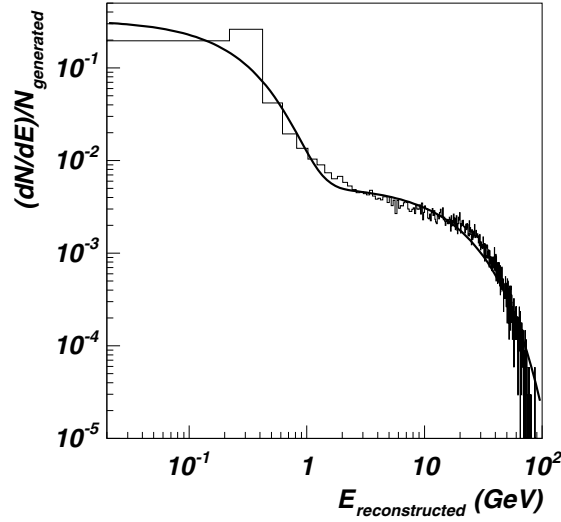


Figure 5.169 Simulated PHOS response function to 100 GeV/c  $\pi^\pm$ .

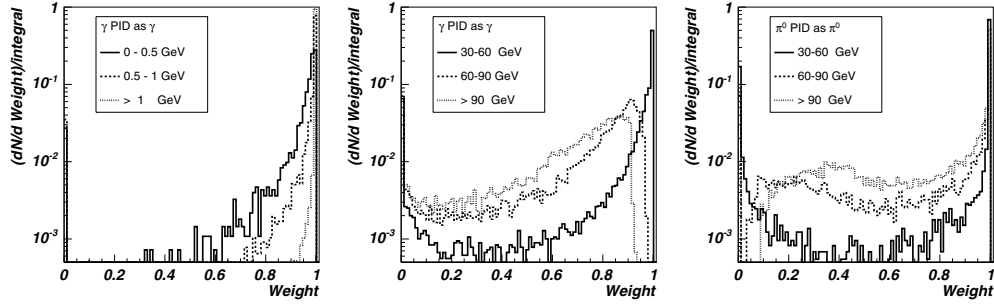


Figure 5.170 Distributions of PID weights calculated for single photons (left and middle) and  $\pi^0$ 's, and for different reconstructed energy bins. Photons were generated with an uniform energy distribution between 0 and 5 GeV (right) and 5 and 120 GeV (middle) and neutral pions were generated with an uniform energy distribution between 30 and 120 GeV.

for all the particle species, being  $s = \gamma, e^\pm, h^0, h^\pm$  and high- $p_t \pi^0$ 's:

$$W(i) = \frac{P(\text{tof} | i) \cdot P(d_{\text{CE}}^{xz} | i) \cdot P(\text{dis} | i) \cdot P(\text{rec} | i)}{\sum_s [P(\text{tof} | s) \cdot P(d_{\text{CE}}^{xz} | s) \cdot P(\text{dis} | s) \cdot P(\text{rec} | s)]}. \quad (5.45)$$

We have applied this PID procedure to single photons, electrons and  $\pi^0$ 's, generated with an uniform energy distribution, merged or not into HIJING events (Pb–Pb collisions at 5.5A TeV,  $b < 2$  fm) mimicking the heavy-ion collision (HIC) environment. Without the HIJING event, photons reconstructed with energies below 30 GeV are well identified with a PID weight equal to 1 (Fig. 5.170).

For energies below 0.5 GeV, where the shower shape criterion is not effective, the neutral hadron weight becomes large, i.e., photons can be misidentified as neutral hadrons. For energies larger than 30 GeV, photons can be misidentified as high- $p_t \pi^0$ . This misidentification probability increases with increasing reconstructed energy. Electrons are usually well

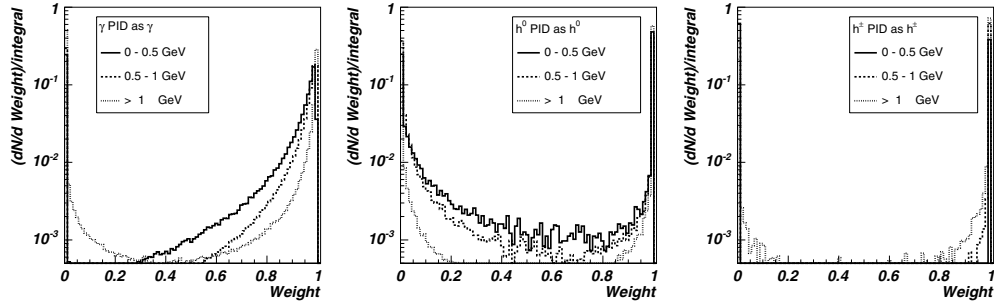


**Figure 5.171** Distributions of PID weights calculated for photons (left), neutral hadrons (middle) and charged hadrons (right), and for different reconstructed energy bins. These particles were taken from HIJING events (Pb–Pb collisions at 5.5A TeV,  $b < 2$  fm).

identified with a weight equal to one for reconstructed energies larger than 0.5 GeV. For single and merged high- $p_t$   $\pi^0$ 's, with reconstructed energies in the range  $30 < E_{\text{rec}} < 120$  GeV (Fig. 5.170, left), the PID photon weight is significant and increases with the reconstructed energy.

Applying the procedure to all detected particles in HIJING events (Fig. 5.171), photons, neutral hadrons and charged hadrons are well identified.

*PID efficiency and contamination.* We define the PID efficiency as the probability to correctly identify particles of type  $i$ , i.e., the ratio of the spectrum of reconstructed clusters generated by the particles of type  $i$ , and identified with a PID weight  $W(i)$  larger than a given threshold value  $W^{\text{th}}(i)$  and of the spectrum of all reconstructed clusters generated by the same type of particles, without condition on  $W(i)$ . Two energy bins have been considered: particles with energy ranging from 0 to 5 GeV and particles with energy ranging from 5 to 120 GeV (from 30 to 120 GeV for  $\pi^0$ 's).

The contamination is defined as the ratio of the spectrum of reconstructed clusters not generated by particles of type  $i$ , but identified as particles of type  $i$ , and of the spectrum of all reconstructed clusters identified as particles of type  $i$ .

*Low-energy particles.* Single electrons and photons are identified with an efficiency of almost 100% (Fig. 5.172) for particles reconstructed with energies larger than 1 GeV. This efficiency decreases to about 40–50% when photons and electrons are merged into central HIJING events ( $b < 2$  fm). A small dependence with  $W^{\text{th}}(i)$  is observed.

The contamination of wrongly identified particles in HIJING events (Fig. 5.173) does not show a strong variation with reconstructed energy or with the event particle multiplicity. It is small, ranging from 3.5 to 1.5% in the  $b < 2$  fm case and from 2.5 to 1% in the  $b < 5$  fm case.

*High-energy particles.* The PID efficiency obtained for high-energy particles from 0 to 120 GeV (neutral pions from 30 to 100 GeV) shows only a small dependence with the value of  $W^{\text{th}}(i)$  for single electrons (Fig. 5.174). The PID efficiency for single electrons is larger than 85% and is reduced by 5–10% when electrons are merged in a HIC environment.

The PID efficiency for high-energy photons (Fig. 5.175) is the same as that obtained for low-energy photons ( $2 < E_{\text{rec}} < 5$  GeV) up to reconstructed energies of 30 GeV. Beyond 30 GeV, the contribution of photons wrongly identified as  $\pi^0$ 's becomes important showing a strong dependence with the  $W^{\text{th}}(i)$  value. The optimum value of  $W^{\text{th}}(i)$  is found by constructing PID efficiency ratios of correct particle identification to misidentification and

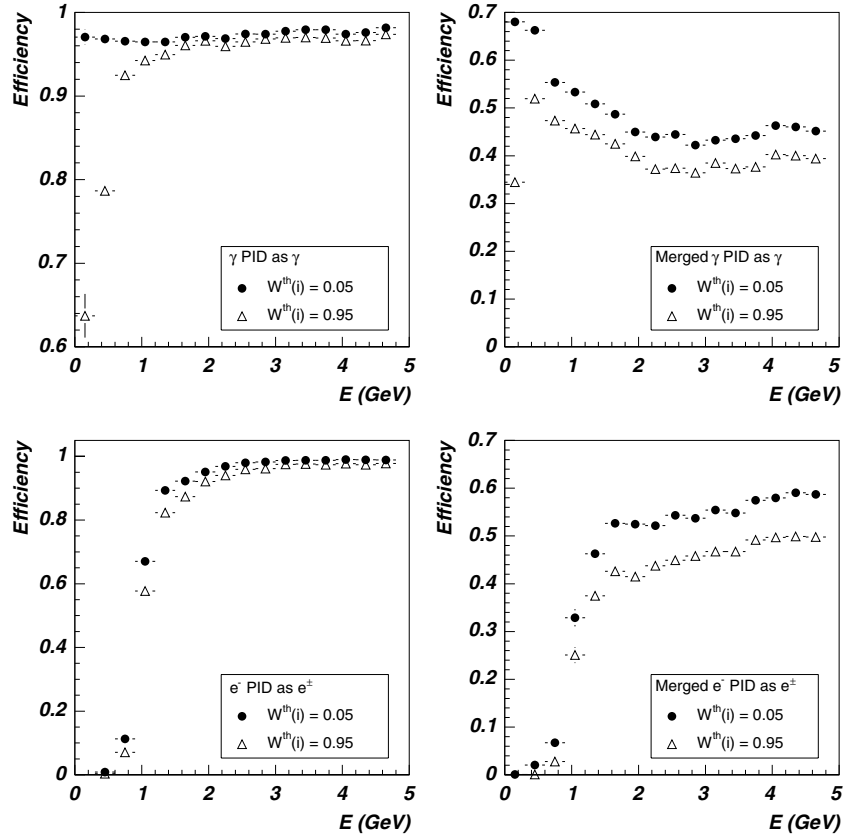


**Figure 5.172** PID efficiency for photons (upper) and electrons (lower) as a function of the reconstructed energy. Right frames: efficiency for single particles, left frames: particles merged into HIJING events (Pb–Pb collisions at 5.5 A TeV,  $b < 2$  fm). Particles were generated with an uniform energy distribution between 0 and 5 GeV.

minimizing them. Using the values of  $W^{\text{th}}(i)$  deduced in Fig. 5.176, the final PID efficiency and contamination of wrongly identified particles are calculated (Fig. 5.177).

Assuming that photons and  $\pi^0$  are produced in the collision in the same amount, background-to-signal ratios have been constructed (Fig. 5.178). For photons, the background ( $\pi^0$ 's identified as photons) to signal (photons identified as photons) is smaller than 0.2 independent of whether photons are within a HIC environment or not. However, the ratio changes strongly with the photon reconstructed energy.

*5.5.1.12. Identification of high-energy photons converted into electron pairs.* The presence of the TRD and TOF detectors in front of the PHOS will perturb the photon yield detected in the PHOS, as discussed in Section 5.5.1.7. Photons can interact with the material of these detectors and produce conversion electrons ( $\gamma \rightarrow e^-e^+$ ). High-energy photons converted into electron pairs can be identified with the method presented in this section. The need of a configuration with holes in the TRD and TOF to obtain reliable data with the PHOS is discussed. See Ref. [89] for complete details.

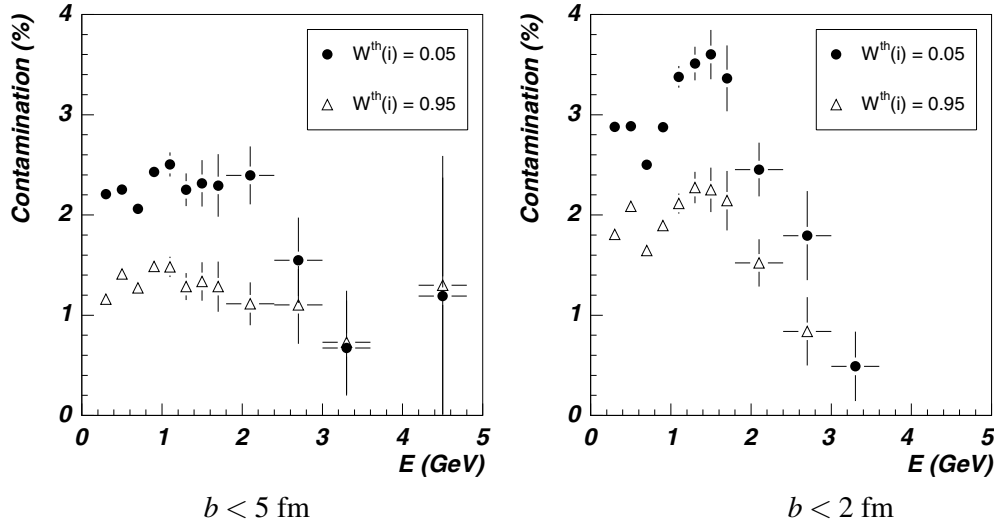


**Figure 5.173** PID contamination of wrongly identified photons as a function of the particle reconstructed energy in HIJING events for Pb-Pb collision at 5.5 A TeV,  $b < 5$  fm (right) and  $b < 2$  fm (left).

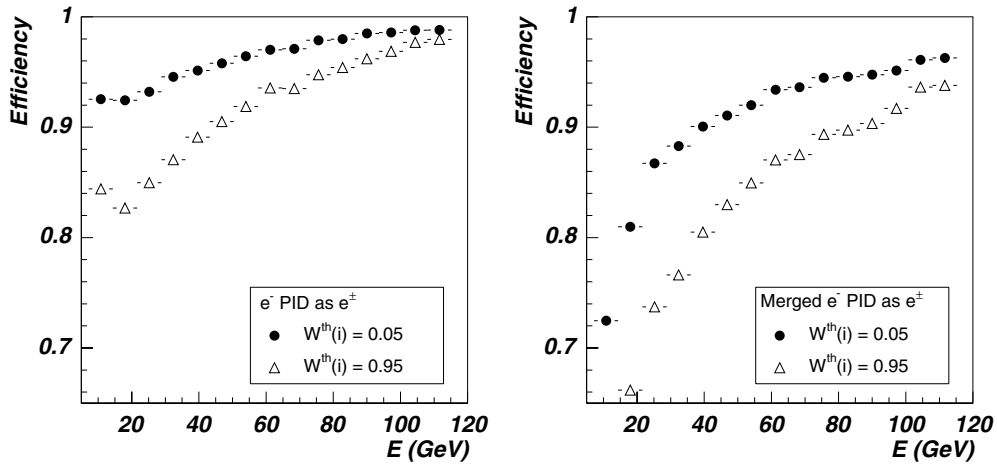


**Figure 5.174** PID efficiency for high-energy electrons as a function of the reconstructed energy. Left: single electrons. Right: electrons merged in HIJING events (Pb-Pb collisions at 5.5 A TeV,  $b < 2$  fm).

*Converted-photon reconstruction.* The electrons created by a photon converted in the material between the TPC and PHOS can be identified because there is no matching track in the TPC pointing to the hit produced by those electrons in the CPV of the PHOS. To minimize random matching in the heavy-ion environment, it is important to control accurately the matching criteria. For this purpose, electrons with energies between 10 and 40 GeV were simulated and the distance between the TPC track and CPV signal was studied. The maximum distance is about 2 cm but we have set the maximum to 4 cm in the matching algorithm to ensure that low-energy electrons which are more bent by the magnetic field, are not rejected.

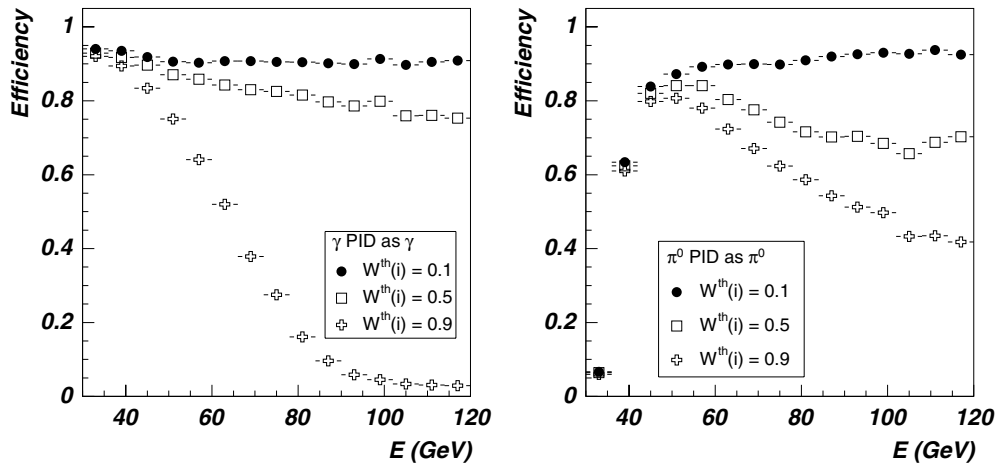


**Figure 5.175** PID efficiency as a function of the reconstructed energy for single high-energy photons (left) and  $\pi^0$ 's (right).

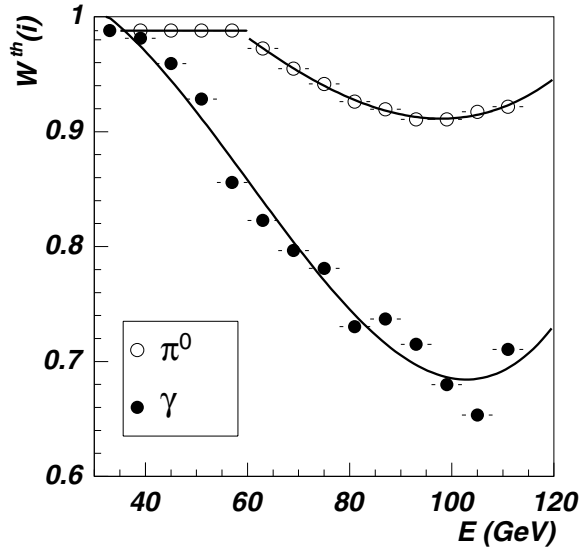


**Figure 5.176** Values of  $W^{th}(i)$  for which the ratios of correct identification to misidentification probabilities for photons ( $\bullet$ ) and for neutral pions ( $\circ$ ) are minimum. Points were fitted by a third-order polynomial.

More accurate simulations are needed to find the optimum value of the maximum matching distance.

In order to study the reconstruction of electrons produced by photon conversion, photons were generated with energy uniformly distributed between 10 and 40 GeV for the set-ups with and without holes. Particles identified as charged particles by the CPV but not detected by the TPC and identified as photons by the PCA were tagged as *conversion electrons*. In this section, particles are identified as photons with low-purity level; electrons are identified as low-purity photons by the PCA and as charged particles by the CPV and the TPC. The probability

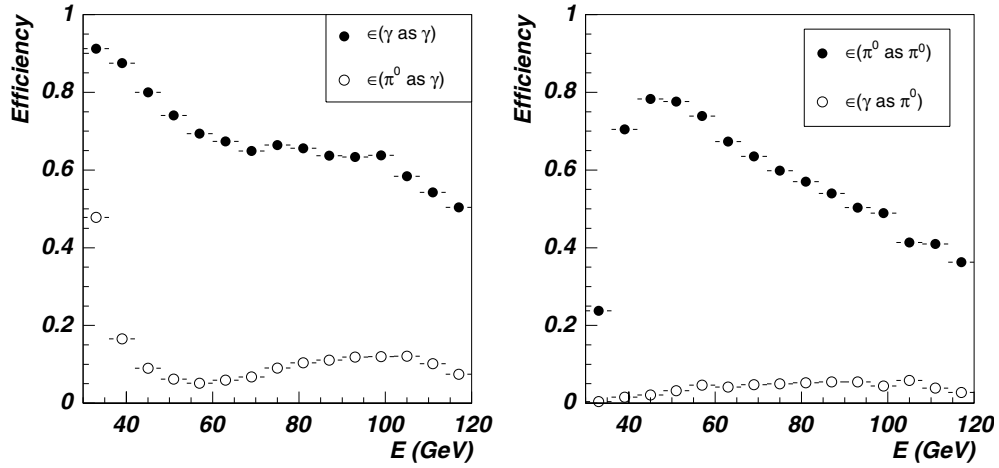


**Figure 5.177** PID efficiency for a single high-energy photon or  $\pi^0$  to be identified as a hard photon (left) or hard  $\pi^0$  (right) with  $W^{\text{th}}(i)$  given by fits in Fig. 5.176 as a function of the particle reconstructed energy. Photons are generated with an uniform energy distribution between 5 and 120 GeV for photons, and between 30 and 120 GeV for  $\pi^0$ 's.

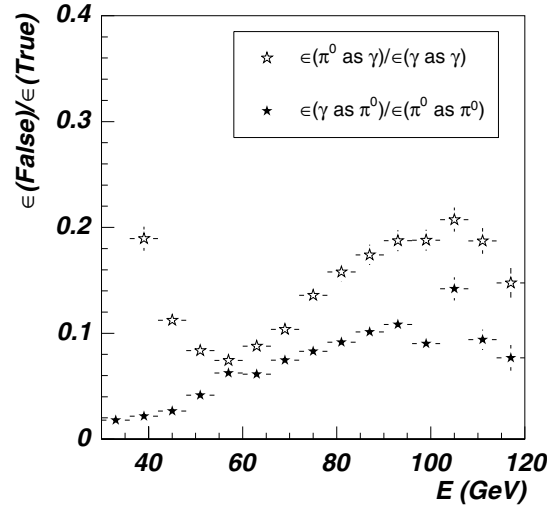


**Figure 5.178** Ratios of the PID contamination of wrongly identified hard  $\pi^0$ 's ( $\gamma$ ) to the PID efficiency of  $\gamma$  ( $\pi^0$ 's) as a function of the reconstructed energy.  $W^{\text{th}}(i)$  given by fits in Fig. 5.176. Photons are generated with an uniform energy distribution between 5 and 120 GeV for photons, and between 30 and 120 GeV for  $\pi^0$ 's.

of identifying conversion electrons as single photons is about 50–60% in the energy range  $E < 40$  GeV.

In order to recover the original photons from the conversion electrons, the invariant mass of all possible pairs of identified conversion electrons was calculated. If the invariant mass was small, the pair likely came from a photon of energy close to the total energy of the pair. If only an isolated conversion electron was detected, we assumed that both electrons fly very close to each other and PHOS cannot separate them, so the energy of this isolated electron was

taken as the energy of the parent photon. For single photons, the invariant mass distribution peaks at 0–0.2 MeV/ $c^2$  ending at 20 MeV, for reconstructed energies between 10 and 40 GeV. In the case of a HIC environment, the invariant-mass distribution is broader and we identified as photons conversion pairs of invariant mass smaller than 20 MeV/ $c^2$ .

*Photon identification probability.* Generated photons with energy between 10 and 40 GeV were identified in the PHOS as stated above. In the configuration with holes, about 10% of the photons suffer conversion somewhere between the interaction point and the CPV. Conversion electrons produced in the TPC are tagged mostly as electrons. In the configuration without holes, about 30% of the photons are converted into electrons, of which 20% are converted in the TRD and TOF. Between 10 and 20% of the photons can be recovered by conversion-pair identification. If we add the identified conversion pairs to the identified photons, the identification probabilities for the configuration with and without holes are close.

*5.5.1.13. Conclusions.* The PHOS detector provides a good capability to detect and identify photons, electrons and  $\pi^0$ -mesons, and measure their 4-momenta with high precision.

PHOS simulation reproduces the beam-test experimental data which is confirmed by comparison of energy and position resolutions of the PHOS sub-detectors.

Reconstruction algorithms of the PHOS were adjusted to reduce systematics error in measuring the coordinates and energy of reconstructed points.

Implemented particle identification methods allow one to identify photons and electrons and distinguish them from hadrons in a wide energy range from 0 to 100 GeV. The neutral pion spectrum can be measured in PHOS statistically by the invariant-mass analysis in the energy range from 0 to 40 GeV, and on an event-by-event basis by particle identification at higher energies up to 100 GeV. Several methods of photon- $\pi^0$  recognition at high energies were developed, and all of them demonstrate high identification efficiency of these particles up to 100 GeV.

*5.5.2. Photon multiplicity detector.* The Photon Multiplicity Detector (PMD) measures the multiplicity and the spatial ( $\eta$ - $\varphi$ ) distribution of photons on an event-by-event basis. In the region where large particle density forbids a measurement using calorimetric techniques, the photon production can be studied using a preshower detector of high granularity. The physical features of the PMD are described in Volume I of the Physics Performance Report [3]. It will have full azimuthal coverage in the pseudorapidity region  $2.3 \leq \eta \leq 3.5$  on the positive rapidity side in ALICE.

*5.5.2.1. Physics goals of PMD.* The measurement of event-by-event photon multiplicity, rapidity and azimuthal distribution of photons in the PMD would enable us to:

- determine the reaction plane and study probes of thermalization via studies of azimuthal anisotropy and flow;
- study critical phenomena near the phase boundary leading to fluctuations in global observables like multiplicity and pseudorapidity distributions;
- search for signals of chiral-symmetry restoration (disoriented chiral condensates) through the study of the observable  $N_\gamma/N_{\text{ch}}$  (in conjunction with the charged particle detector FMD);
- understand the reaction dynamics, through the scaling of photon multiplicity with the number of participant nucleons and number of collisions;
- estimate the transverse electromagnetic energy, useful for event characterization.

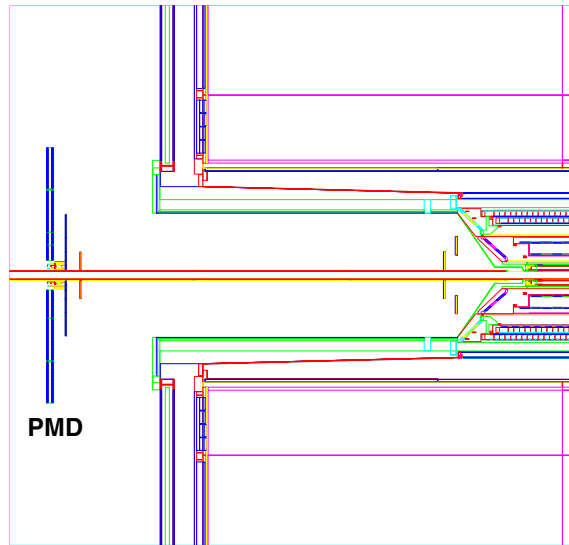


**Figure 5.179** AliRoot picture of detectors and services in front of the PMD. Only the positive rapidity part of ALICE is shown.

The capability of the PMD for addressing the above physics goals has been described in Refs. [103, 104].

*5.5.2.2. Simulation framework.* The measurement of photon multiplicity and spatial distribution is affected by the environment of the detector. The results are presented for the intrinsic performance of the detector (i.e., a ‘standalone’ PMD in air with no other detector around) and for the performance in the ALICE environment where particles falling on the PMD may have to traverse the material of several other detectors in front of it.

*PMD in AliRoot.* The PMD consists of two planes of highly segmented sensitive media (detectors) placed on both sides of the 15 mm thick lead plate and 5 mm stainless-steel plate. The lead and steel plates together constitute a  $3 X_0$  thick converter for photons. The detector plane which faces the interaction point is called the ‘charged particle veto’ and the one behind the converter is called the ‘preshower’ plane.

Figure 5.179 shows the detectors and service elements in front of the PMD in the AliRoot framework.

*Event generator.* The parametrized HIJING event generator, which is an integral part of the AliRoot, has been used for all the simulation to study photon reconstruction efficiency, purity of photons in the detected sample, and the effect of upstream material. For most of the studies presented here, it is assumed that a central Pb–Pb collision at the LHC energy will have a maximum charged-particle pseudorapidity density of 8000 at  $\eta = 0$ . The total number of photons within the acceptance of the PMD in such a case is 4500. The performance of the detector for lower particle densities has also been studied; these lower densities may arise because of the change in centrality, the use of lighter ions or lower particle production even in central Pb–Pb collisions as extrapolated from RHIC data [105].

*5.5.2.3. Particle density and occupancy.* The PMD positioned in the forward region in ALICE faces a very high particle density. This is shown in the left panel of Fig. 5.180 for

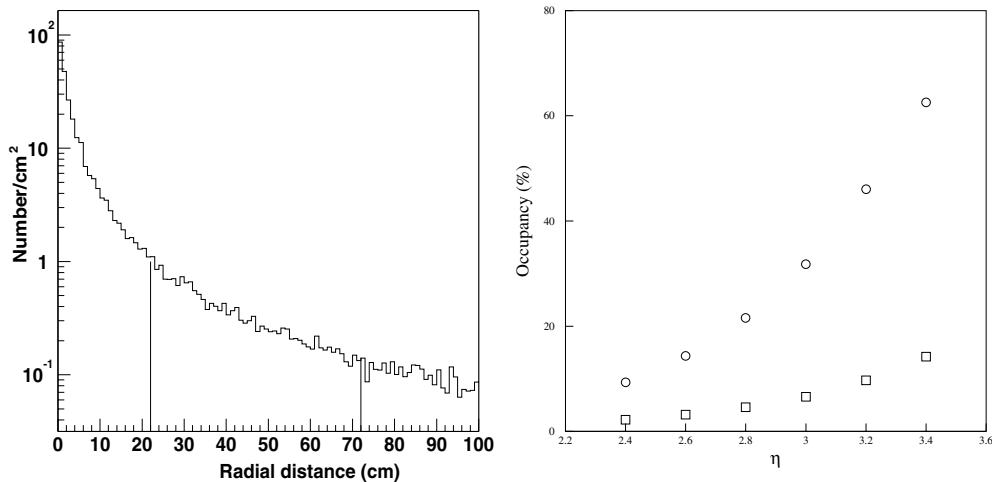


**Figure 5.180** Left: Density of photons (particles/cm<sup>2</sup>) falling on the PMD. The vertical lines denote the two  $\eta$ -limits. Right:  $\eta$ -distribution of occupancy on the PMD: preshower plane (open circles), veto plane (open squares).

photons falling on the PMD. An almost similar number of charged particles also fall on the detector within the same acceptance. The large particle density and the fact that the shower of the incident photons spreads to an average of about four cells leads to a very high occupancy in the preshower plane of the PMD.

The cell occupancies for the two planes of the PMD in the standalone case are shown on the right panel in Fig. 5.180 as a function of pseudorapidity, with a bin size of 0.2 units. The occupancy on the preshower plane varies from 10% to more than 60% and that on the veto plane is about a factor of five lower.

**5.5.2.4. Reconstruction.** Simulated data produce events with a set of hit cells having some energy deposition (EDEP). Before reconstruction, the simulated data format is made identical to the experimental data format by converting the EDEP values to ‘ADC’ values using relations derived from beam tests. A noise threshold, equivalent to 20% of the energy deposition by a minimum-ionizing particle, is applied uniformly to all the cells. For photon reconstruction, the hits above the noise threshold are first converted into clusters and then a suitable algorithm is used to reject charged hadron hits.

**Clustering.** The clustering is done in two steps. In the first step, the data is organized in descending values of ADC. Starting from the largest ADC, cells having nonzero ADC and having at least one cell with nonzero ADC are collected together to form a super cluster. This is repeated with the next largest ADC (provided it is not a member of and already formed super cluster) till all the cells with nonzero ADC are exhausted. If the number of particles falling on the PMD is small enough, each super cluster has fewer cells and one directly proceeds to label the clusters using a photon–hadron discrimination algorithm. When the number of particles is large, one has very large super clusters containing hundreds of cells, and these need to be broken up into smaller clusters.

For breaking up of super clusters, we assume that a cluster can be characterized by a Gaussian with the centre coordinate, strength and width. The super cluster is then formed by a number of overlapping Gaussians with their centres, strengths and widths to be determined by

a minimization procedure. The total strength of all Gaussians must add up to the sum of the ADC values of all the cells included in the super cluster. To estimate the number of Gaussians, we arrange the cell ADCs in descending order and starting from the cell with largest ADC, choose the cell as a cluster centre if the nearest cluster centre is more than one cell unit away and it forms a local maximum. The cluster centres, their strengths and widths are then varied in the minimization procedure. The final result is a set of cluster positions (two coordinates), strengths and widths.

*Association.* Each cluster is then associated with an incoming track. If there are two or more clusters belonging to the same incoming track, the cluster having larger ADC and less deflection (see Section 5.5.2.7 below) is considered assigned to the track, other(s) being labelled as contaminants.

*Photon-hadron discrimination.* For the results presented here, we have used a simple photon-hadron discrimination algorithm based on direct association of hits in the veto and preshower planes. It is assumed that charged hadrons hit only one cell in both the veto and preshower planes and that these cells are located just opposite each other in the two detector planes. Before clustering, the preshower hits opposite to veto hits are set to zero. A threshold on cluster signal is applied to remove split clusters. Any split cluster surviving the cut is treated as a contaminant. Clusters which are shifted by a large amount (see Section 5.5.2.7) are also labelled as contaminants.

5.5.2.5. *Photon reconstruction efficiency and purity.* The result of photon-hadron discrimination is a set of clusters which are labelled as  $\gamma$ -like, the total number of such clusters is  $N_{\gamma\text{-like}}$ .

The photon reconstruction efficiency  $\varepsilon_\gamma$  and the purity of the photon sample  $f_p$  are defined by the following relations:

$$\varepsilon_\gamma = N_{\text{cls}}^{\gamma,\text{th}} / N_{\text{inc}}^\gamma, \quad f_p = N_{\text{cls}}^{\gamma,\text{th}} / N_{\gamma\text{-like}},$$

where  $N_{\text{inc}}^\gamma$  is the number of incident photons from the event generator and  $N_{\text{cls}}^{\gamma,\text{th}}$  is the number of clusters from photon tracks after the application of the discrimination algorithm,  $(1 - f_p)$  is the fractional contamination in the  $N_{\gamma\text{-like}}$  sample.

For the measurement of photon multiplicity, the total number of photons incident on the detector in a given acceptance is estimated from the  $N_{\gamma\text{-like}}$  clusters obtained from data by using the above two equations,  $N_{\text{inc}}^\gamma = N_{\gamma\text{-like}} \cdot f_p / \varepsilon_\gamma$ , and employing the estimated values of photon reconstruction efficiency and purity from simulation studies.

5.5.2.6. *ALICE environment : Material distribution in front of the PMD.* The PMD, being situated at 361.5 cm in ALICE from the nominal collision point, sees the inner detectors like ITS, TPC, FMD, V0 in front. Although great care has been taken to minimize the structural material of these detectors and their supports and services, the total upstream material seen by the PMD is non-negligible. Full optimization of this upstream material with design modifications in the structures is still under way. For the results presented here it is assumed that the upstream material will have the  $\eta$  distribution shown in Fig. 5.181. In the smaller  $\eta$  region the thickness of the upstream material goes up to about  $1 X_0$ . The  $\varphi$  distribution is assumed to be uniform. We shall use the term ‘ALICE environment’ when referring to this type of upstream material.

5.5.2.7. *Effect of upstream material: Deflection of original photon track.* Scattering and conversion in the upstream material result in the deflection of the original photon tracks. If the incoming particle tracks are deflected substantially from their original position, then

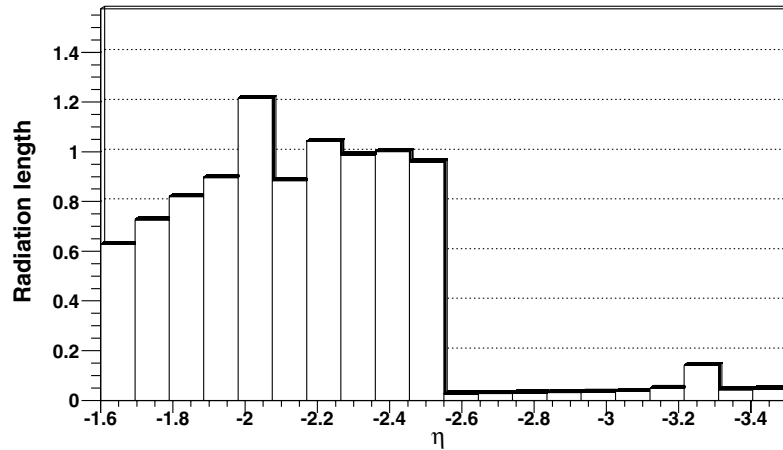


**Figure 5.181** Assumed  $\eta$  distribution of material (in units of radiation length) in front of the PMD.

the detector cannot be used for studying the event structure and correlations at smaller length scales where the deflection may have distorted the underlying structure. Cosmic-ray observations by the JACEE Collaboration suggest pairing and clustering of tracks at scales  $\delta\eta \sim 0.2$  and  $\delta\varphi \sim 30^\circ$  [106].

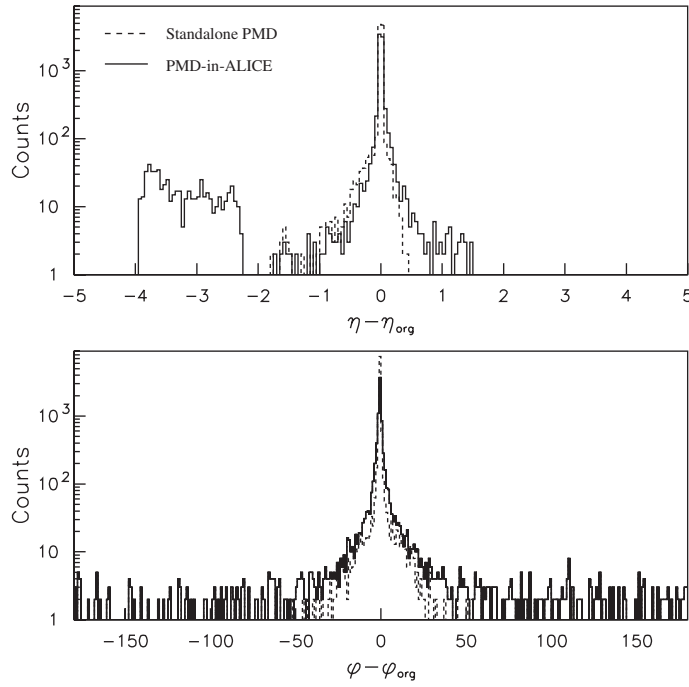
The effect of upstream material is demonstrated by plotting the distribution of  $\delta\eta (= \eta - \eta_{\text{orig}})$  and  $\delta\varphi (= \varphi - \varphi_{\text{orig}})$ , which denote the deviation of incoming photon tracks with the identified cluster location on the detector. Here  $(\eta, \varphi)$  are the reconstructed positions of the photon track and  $(\eta_{\text{orig}}, \varphi_{\text{orig}})$  are the original positions of the same track on the detector. The  $(\delta\eta, \delta\varphi)$  plot for photon clusters is shown in Fig. 5.182 for the case of standalone PMD and for PMD in the ALICE environment. The small bump on the left in the  $\delta\eta$  distribution results from tracks originating from vertex at large pseudorapidities ( $\eta > 5$ ) due to back scattering from the stainless-steel structure behind the PMD (bellows, flanges and the stainless-steel section of the ALICE vacuum chamber).

Table 5.18 summarizes the effect of deflection of tracks for the standalone PMD and for the PMD in the ALICE environment by considering two pseudorapidity regions in terms of the percentage of photon tracks having  $|\delta\eta| \leq 0.1$  and  $|\delta\varphi| \leq 10^\circ$ . For the standalone detector, there is no difference in the percentage of accepted tracks. But in the ALICE environment the effect of upstream material results in fewer clusters (tracks) being accepted in the lower pseudorapidity region.

For the estimation of photon reconstruction efficiency and purity we have considered all clusters having  $\delta\eta > 0.1$  or  $\delta\varphi > 10^\circ$  as contaminants.

#### 5.5.2.8. Results on photon reconstruction efficiency and purity

*Average values.* The average values of photon reconstruction efficiency and purity are presented in Table 5.19 for the standalone PMD and for the PMD in the ALICE environment. The results are given for two multiplicities of the events, having maximum pseudorapidity density at  $\eta = 0$  ( $\rho_0$ ) of 8000 and 4000. The latter may be the more likely scenario if the particle production is lower at the LHC energy, as may be extrapolated from RHIC measurements [105]. For the higher particle density, the photon reconstruction efficiency of  $\sim 55\%$  and purity of  $\sim 65\%$  are achieved. Studies of photon production at



**Figure 5.182** ( $\delta\eta$ ,  $\delta\varphi$ ) distribution for the standalone PMD (dashed line) and PMD in the ALICE environment (solid line).

**Table 5.18** Percentage of accepted tracks within  $|\delta\eta| \leq 0.1$  and  $|\delta\varphi| \leq 10^\circ$ .

$\eta$ range	Environment	
	Standalone	PMD in ALICE
2.3–2.5	94	84
2.9–3.1	94	88

**Table 5.19** Average values of photon reconstruction efficiency and purity for various cases for two values of pseudorapidity density ( $\rho_0$ ).

	$\rho_0 = 8000$		$\rho_0 = 4000$	
	Efficiency	Purity	Efficiency	Purity
Standalone PMD	57	70	69	70
PMD in ALICE environment	54	65	64	68

forward rapidities were carried out with similar efficiencies earlier at the SPS and the RHIC [107, 108].

Efficiency of up to 65% and purity of 70% may be obtained if the event multiplicity were lower by a factor of two.

*$\eta$ -dependence.* The pseudorapidity dependence of photon reconstruction efficiency and purity is displayed in Fig. 5.183. For the standalone PMD the efficiency falls to below 40% at the highest  $\eta$  region due to very large occupancy. This happens as the cell size is kept the same throughout the  $\eta$  region of the detector although the particle density varies by more than a factor of 5 over that region. The purity values are almost uniform throughout the entire  $\eta$  range.

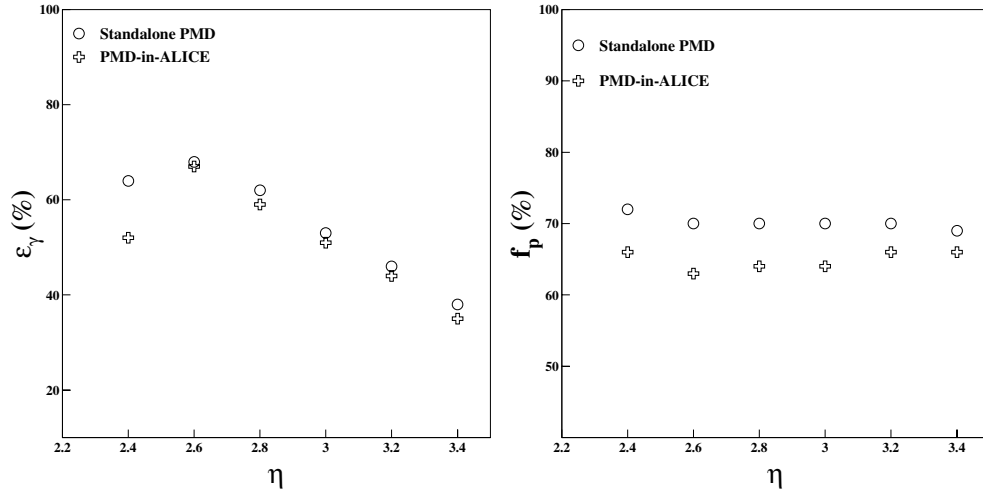


**Figure 5.183**  $\eta$  dependence of photon reconstruction efficiency ( $\epsilon_\gamma$ ) (left) and purity ( $f_p$ ) (right) for the standalone PMD and for the PMD in the ALICE environment.

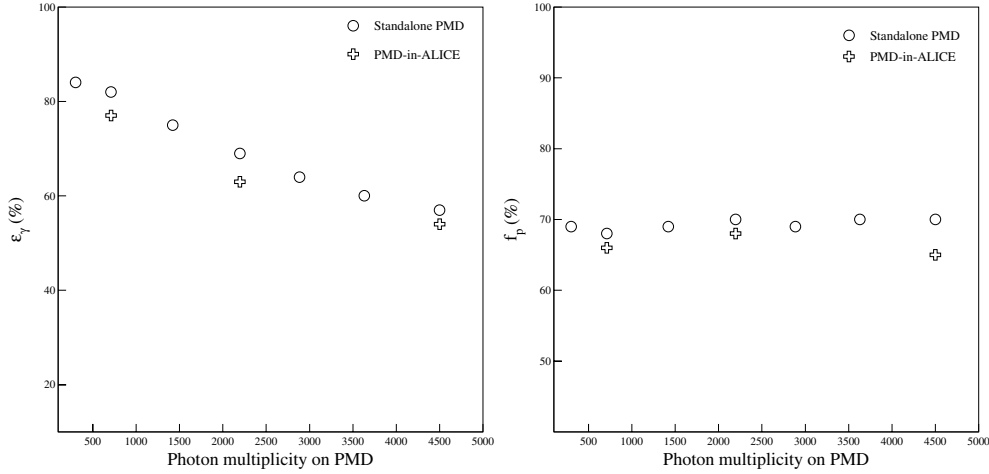


**Figure 5.184** Multiplicity dependence of efficiency (left) and purity (right) for the standalone PMD (circles) and for the PMD in the ALICE environment (cross).

The efficiency is slightly lower in all  $\eta$  regions for the PMD in the ALICE environment as compared to that of the standalone PMD. At the lowest  $\eta$  bin the effect of upstream material becomes significant and the efficiency drops by  $\sim 10\%$ . Purity values are lower by  $\sim 5\%$  in all  $\eta$  regions in the ALICE environment.

*Multiplicity dependence.* Figure 5.184 shows the multiplicity dependence of average photon reconstruction efficiency and purity for standalone PMD and for the PMD in the ALICE environment. Lower multiplicity may correspond to a larger impact parameter of collision or it may arise in the case of light ion collisions. While the purity is almost unaffected by a change in the number of particles falling on the detector, photon reconstruction efficiency slowly increases at lower particle densities as the occupancy reduces, reaching values around

80% in the lowest multiplicity case studied. The rate of increase is similar for standalone PMD and for PMD in ALICE environment. However, the values of reconstruction efficiency are about 5% lower for the PMD in the ALICE environment than for the standalone PMD at all multiplicities.

Purity values in the case of PMD in ALICE environment are lower by about 5% than the values for the standalone PMD. The behaviour with multiplicity is similar in both cases.

**5.5.2.9. Summary.** The simulation results on the reconstruction of photon hits on the PMD suggest that a reconstruction efficiency of about 55% associated with a purity of 65% is achievable for the assumed maximum pseudorapidity density of 8000 at midrapidity in Pb–Pb collisions at LHC energy for the PMD in the ALICE environment. The  $\eta$  dependence of purity is almost uniform. However, the reconstruction efficiency falls sharply at larger  $\eta$ , the difference between the maximum and minimum values being about 25%. If the particle production process follows the systematics established up to RHIC energies, the particle density at the LHC may be much lower and the performance of the PMD will improve with higher reconstruction efficiency. The deflection of photon tracks in the upstream material is small enough to permit correlation studies at length scales  $\delta\eta \sim 0.2$  and  $\delta\varphi \sim 30^\circ$ .

## 6. ALICE physics performance

This chapter summarizes the current results of the physics performance studies in a number of representative examples. These studies have evolved in parallel and reached different levels of sophistication. Some have started only very recently (e.g. the studies of jet quenching) and are in a preliminary state. Others are more mature but none can be considered complete and work will be ongoing in all areas in order to prepare reconstruction and analysis software for the actual data taking period.

Some of the studies were reported already in the ALICE Technical Proposal and in the Technical Design Reports using approximate methods, fast simulations, and various rough estimates. We have developed now a very detailed simulation of the ALICE detector and its response, which is used for the majority of present performance investigations. The event display produced by these up-to-date simulations is shown in Colour Figure II.

Some of the physics assumptions, which influence the performance, have evolved in time. The predictions for particle densities produced in central Pb–Pb collisions at LHC energies span the very large range  $dN_{\text{ch}}/d\eta = 1500\text{--}8000$  at mid-rapidity. After RHIC, the lower values are more likely today but significant uncertainties still exist when extrapolating to LHC energies, related in particular to the amount and effects of jet quenching. Therefore we have tested the basic detector performance, like tracking, up to charged-particle densities  $dN_{\text{ch}}/d\eta = 8000$  at mid-rapidity, which should include some significant safety margin. In the physics studies we typically list the performance from pp values  $dN_{\text{ch}}/d\eta = 5\text{--}7$  up to  $dN_{\text{ch}}/d\eta = 6000$ .

Largely for historical reasons, different values of the magnetic field are assumed in the central part of the detector in the L3 magnet. The field setting of  $B = 0.2\text{ T}$  is used for some studies of soft-physics observables, because it lowers the  $p_t$  cut-off for slow-particle detection down to  $100\text{ MeV}/c$  or even below. Most of the recent studies have been done using a magnetic field of  $B = 0.4\text{ T}$  or  $B = 0.5\text{ T}$ , the latter being the nominal setting which will be used for standard data taking. The stronger magnetic field is especially beneficial for the hard probes and observables because it significantly improves the measurement precision.

## 6.1. Event characterization

**6.1.1. Introduction.** In heavy-ion collisions, the study of the global properties of the final state plays an important role, since it allows one to determine both the initial geometry of the collisions and the way in which the initial available centre-of-mass energy is redistributed in the accessible phase space. The global observables discussed in this section are charged-particle multiplicity and zero-degree energy distributions [109].

In ion–ion collisions, the determination of the variables that characterize the geometry of the collision is an essential prerequisite to the study of any physics observable. The impact parameter  $b$  and other quantities related to it by geometry (e.g. number of participant nucleons  $N_{\text{part}}$  or number of nucleon–nucleon collisions  $N_{\text{coll}}$ ) can be extracted in a rather model-independent way from either charged-particle multiplicity or from zero-degree energy distributions. It is possible to define the centrality of each event and to select head-on interactions where the maximum energy density can be reached. Having determined the centrality of the collision, it becomes possible to perform studies of various physics observables as a function of  $b$  or  $N_{\text{part}}$ . In particular, by studying sensitive signals as a function of these variables, it may be possible to locate the onset of the phase transition from hadronic to deconfined matter [110].

The study of the multiplicity distributions as a function of centrality is also sensitive to the ‘hard’ or ‘soft’ nature of the particle production [111]. By using theoretical models which link observables such as the  $dN_{\text{ch}}/dy$  shape and the  $p_t$  distributions to the energy density and to the temperature attained in the collision [112, 113], one can give a complete characterization of the global aspects of the event.

In pp collisions, ALICE will study the global properties of minimum-bias events [114], extending by about an order of magnitude the accessible  $\sqrt{s}$  region with respect to the highest energies available today (Tevatron). Of particular interest may be the shape of the inclusive multiplicity distribution, which has been linked to the observation of the transition between non-perturbative and perturbative regimes [115].

This section is organized as follows. First we discuss the study of the centrality variables in heavy-ion collisions at ALICE. After a short introduction on the general method of these measurements, we will analyse the possible centrality estimators, and their accuracy, within ALICE.

Then, we briefly review the results obtained up to now at the SPS and RHIC in the study of the multiplicity distributions [105, 116–122]. Concerning ALICE, we define various possible estimators of the total hadron multiplicity, involving essentially the Inner Tracking System (ITS) [1] and the Forward Multiplicity Detector (FMD) [123] and we analyse their properties.

The centrality and multiplicity estimators are then correlated, leading to a full simulation of the performance of ALICE in the determination of the centrality dependence of hadron multiplicity for Pb–Pb collisions. With such an analysis it is possible to qualitatively determine the contribution of hard processes to the particle production mechanism. This measurement, not requiring particle identification capabilities, can be performed in ALICE with a limited subset of detectors, namely the Zero-Degree Calorimeter (ZDC) [124] and the silicon pixel layers (SPD) of the ITS. Owing to its relative simplicity, it will be one of the first physics results accessible at the LHC. We present here a first version of this analysis, using event-generator data (HIJING [150]) as input.

Then, we address the study of the global event properties for pp collisions in ALICE. We first show how it is possible to define, through the use of the V0 [123] and SPD detectors, a pp trigger with the highest possible efficiency and lowest possible bias. We then analyse the performance of the multiplicity estimators for the low multiplicity expected in pp collisions.

Finally, we turn to the problem of the centrality determination in pA collisions, that are also going to be studied in ALICE. We begin with a short introduction describing the methods and the underlying physics, developed at lower energies. Then, we show the results of a Monte Carlo simulation, basically involving the ZDCs, which shows that such an analysis is indeed feasible with the foreseen ALICE set-up.

In the simulations described throughout this section, the event generation, the tracking, and the reconstruction of the considered variables have always been carried out using the ALICE offline framework, AliRoot [125], in order to take properly into account the experimental acceptance and detector effects.

*6.1.2. Centrality determination using the ZDCs.* Several measurable quantities are correlated with the centrality of the collision, which is usually characterized through the geometrical variable  $b$ , the impact parameter, or through the number of participant nucleons  $N_{\text{part}}$ . In past heavy ion experiments, the centrality has been estimated starting from three kinds of observables: (i) the zero-degree energy  $E_{\text{ZDC}}$ , corresponding to the energy carried by spectator nucleons, (ii) the charged hadron multiplicity  $N_{\text{ch}}$  and (iii) the transverse energy  $E_{\text{t}}$ , measured around mid-rapidity. For the first quantity, the relationship with  $N_{\text{part}}$  is rather obvious. At fixed target experiments, it is simply given by  $N_{\text{part}} = 2 \times (A - E_{\text{ZDC}}/E_{\text{A}})$ , where  $E_{\text{ZDC}}$  is the energy due to projectile spectators hitting the ZDC,  $A$  is the mass number of the ion and  $E_{\text{A}}$  is the beam energy per nucleon. Concerning  $E_{\text{t}}$  and  $N_{\text{ch}}$ , they give the same kind of physics information, since they have been experimentally shown to be proportional to each other. Furthermore, since, up to SPS energies, the particle production mechanism is essentially soft, they are also directly proportional to  $N_{\text{part}}$  [126].

Obviously, an accurate determination of the  $b$  and  $N_{\text{part}}$  distributions starting from experimental quantities requires a careful treatment of the detector effects (acceptance, resolution) and the knowledge of nuclear density distributions. Usually, the calculations are performed in the frame of the Glauber model [127]. In this approach, the nucleus–nucleus collision is seen as a superposition of independent N–N interactions, the main parameters of the model being simply the inelastic N–N cross section  $\sigma_{\text{N}}$  and the nuclear density distribution  $\rho(r)$  [128]. The model gives the relationship between  $b$  and  $N_{\text{part}}$  ( $N_{\text{coll}}$ ) and allows one to calculate  $d\sigma/db$  and  $d\sigma/dN_{\text{part}}$ . By using the relation between  $E_{\text{ZDC}}$ ,  $E_{\text{t}}$  or  $N_{\text{ch}}$  and  $N_{\text{part}}$ , and taking into account the detector resolution, it is then possible to calculate  $d\sigma/dE_{\text{ZDC}}$ ,  $d\sigma/dE_{\text{t}}$  and  $d\sigma/dN_{\text{ch}}$  and compare them with the measured distributions. In practice, the measured distributions are often fitted with an analytical function of  $N_{\text{part}}$ . With this approach, the spectra are usually well reproduced, showing that the relation between centrality variables and measured quantities has been correctly chosen. One can then divide the experimental distribution in classes, by defining sharp cuts on  $E_{\text{ZDC}}$ ,  $E_{\text{t}}$ , or  $N_{\text{ch}}$ , which will correspond to well-defined intervals of the centrality variables. The number of classes that one can define is connected with the resolution one can achieve on that variable. In general, centrality classes are defined such that the separation between the central values of  $b$  and  $N_{\text{part}}$  for two adjacent classes is significantly larger than the resolution on that variable.

An alternative approach is to use an event-generator to simulate the experimental spectra. If a good agreement is found, one can use the relationship between centrality variables and measured quantities as given by the model. At the SPS, the two approaches give comparable results [119].

The procedure outlined above can, in principle, be adopted also for ALICE, where both multiplicity and forward energy will be measured. It is still generally true that  $N_{\text{ch}}$  is correlated with  $N_{\text{part}}$ . However, a simple linear relationship is no longer expected at the LHC. This is essentially due to the particle production mechanism, which, around mid-rapidity, will probably

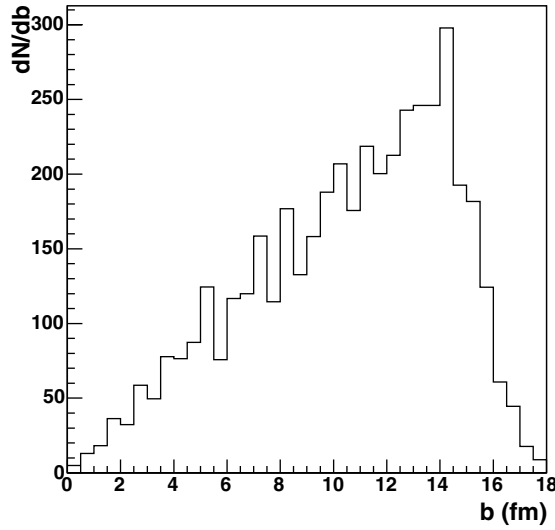


**Figure 6.1** Impact parameter distribution, weighted by the interaction probability, for the events generated with HIJING 1.36.

be dominated by hard processes, scaling with the number of N–N collisions  $N_{\text{coll}}$ . This change of behaviour already sets in at RHIC energies [129], where however soft processes are still sizeable. The zero-degree energy will not be affected by the onset of hard physics; it is still directly connected, through the energy released by the spectators, to  $N_{\text{part}}$ . However, in a collider experiment, some spectator nucleons will be bound into light nuclear fragments and escape detection. This effect becomes quantitatively important for peripheral events. As a consequence, the relation between  $E_{\text{ZDC}}$  and  $N_{\text{part}}$  will neither be linear nor, in fact, monotonic.

A possibility, already adopted by the RHIC experiments, is to correlate the ZDC measurement with another quantity that has a rather broad, but monotonic, relation with  $N_{\text{part}}$ . It is then possible to define, along this correlation, classes of events corresponding to given fractions of the total Pb–Pb inelastic cross section. One can then assign to each class the  $N_{\text{part}}$  range corresponding to such fractions, calculated using the Glauber model or an event generator.

In the following, we show in detail how the outlined methods can be applied to the determination of the centrality of the collision in ALICE. In particular we concentrate on the use of  $E_{\text{ZDC}}$  for such a study, suitably complemented with inputs from other detectors.

*6.1.2.1. Use of ZDCs for centrality selection.* The design of ZDCs, as well as their integration in the set-up and the achievable energy resolution have already been described in detail in the ZDC TDR [124] as well as in Chapters 3 [3] and 5 of this document. Therefore, in the following, we will essentially discuss the methods used to reconstruct the centrality variables, starting from the simulated response of the ALICE ZDCs (see also Ref. [130]).

For this study about  $10^3$  events were generated with HIJING 1.36 [42, 131]. The generation was performed in various centrality bins, covering the impact parameter range  $0 < b < 18$  fm. In Fig. 6.1 we plot the impact parameter distribution of the generated events, weighted by the interaction probability.

Each event is generated at the nominal interaction point (I.P.) since the possible smearing of the vertex position due to the finite length of the diamond has no practical effect on the response of the ZDCs, positioned at 115 m from the I.P. In ALICE, two sets of zero-degree

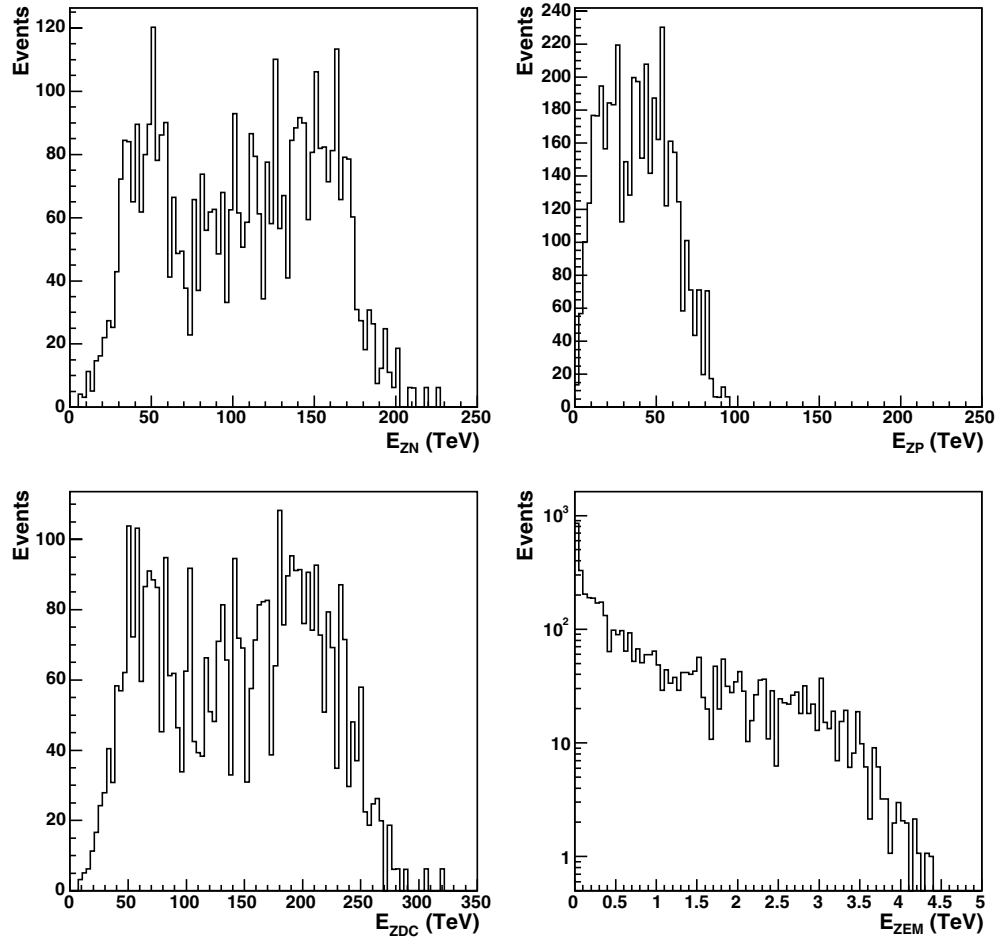


**Figure 6.2** The reconstructed energy distributions for the neutron ( $E_{ZN}$ ) and proton ( $E_{ZP}$ ) ZDCs and for the forward electromagnetic calorimeter ( $E_{ZEM}$ ). The total hadronic energy  $E_{ZDC} = E_{ZN} + E_{ZP}$  is also shown.

calorimeters, symmetrically positioned with respect to the I.P., will be used. Each set is composed by two devices, one for spectator neutrons (ZN), and one for spectator protons (ZP). The hadronic calorimeters are complemented by a set of two very-forward electromagnetic calorimeters (ZEM), covering the pseudo-rapidity range  $4.8 < \eta < 5.7$ . For this study, only one of the two sets of hadronic calorimeters has been simulated, because of technical problems connected with the use of a very long set-up inside the GEANT [132] simulation package. The advantages coming from the use of two sets of ZDCs in the experiment will be discussed later in Section 6.1.2.7.

The response of the detector, corresponding to the number of photoelectrons produced in each detector for that event, is then digitized to ADC channels, taking into account the electronic noise. Then, the incident energy is reconstructed using, for ZN and ZP, the calibration point obtained from the position of the single neutron and proton peak, corresponding to  $E = 2.7$  TeV. These signals will indeed be available in the experiment, on account of the large cross section for the electromagnetic dissociation process [133, 134] (see also Ref. [124]). In Fig. 6.2 we show the reconstructed energy spectra for ZN, ZP and ZEM.

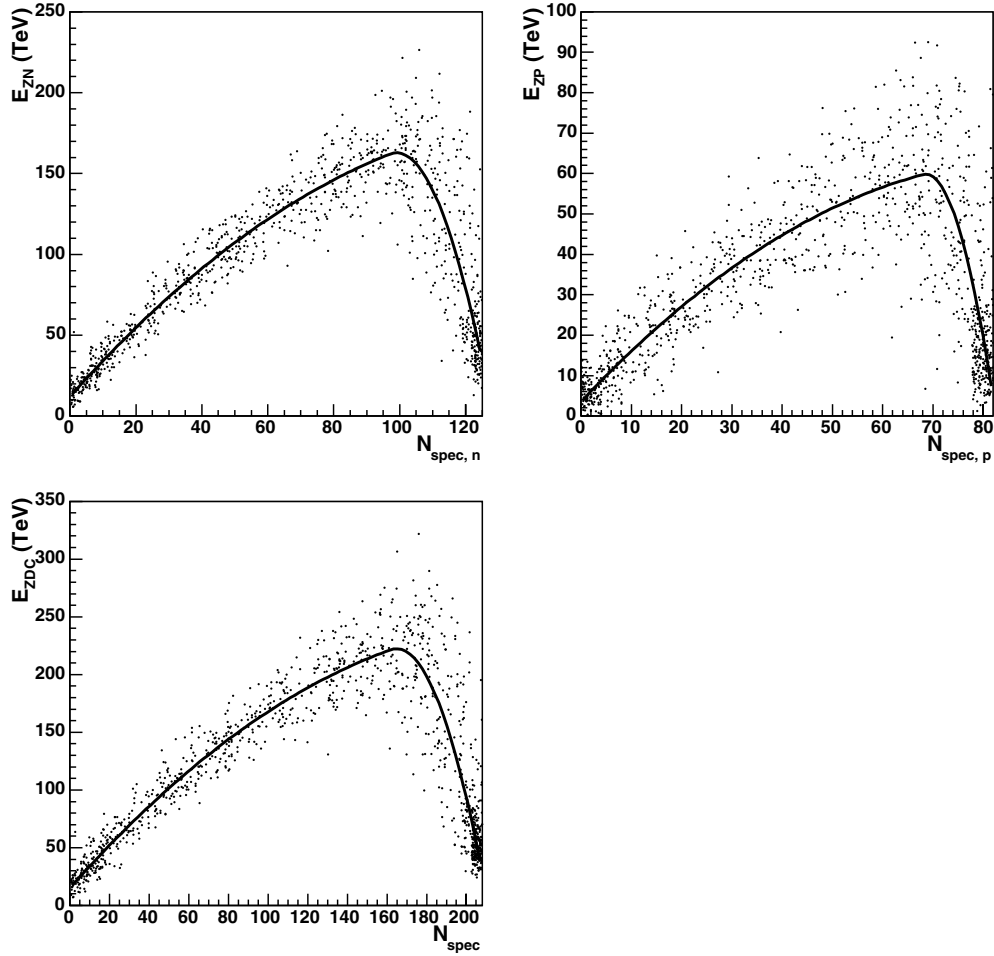


**Figure 6.3** Fit of the correlations between the number of generated spectators and the detected energy.

*6.1.2.2. Event-by-event determination of the centrality.* The first procedure investigated makes use of the correlations between the reconstructed energy in the ZDCs and the centrality variables  $b$  and  $N_{\text{part}}$  as simulated in HIJING. As a first step the correlations between the number of spectators neutrons  $N_{\text{spec},n}$  and protons  $N_{\text{spec},p}$ , and the energies  $E_{\text{ZN}}$  and  $E_{\text{ZP}}$  reconstructed in ZN and ZP respectively, have been considered (see Fig. 6.3).

As it is well known, because of the incomplete fragmentation of spectator nucleons [135, 136] (see also [124]), the correlation between  $E_{\text{ZN}}$  and  $E_{\text{ZP}}$  and the centrality variables is no more monotonic, but exhibits two different branches, one of them corresponding to events from central to semi-peripheral, and the other one to peripheral events.

To take into account this effect, the two branches of the correlations  $E_{\text{ZN}}$  versus  $N_{\text{spec},n}$ ,  $E_{\text{ZP}}$  versus  $N_{\text{spec},p}$  and  $E_{\text{ZDC}} (= E_{\text{ZN}} + E_{\text{ZP}})$  versus  $N_{\text{spec,tot}} = N_{\text{spec},n} + N_{\text{spec},p}$  have been fitted with two polynomial functions, imposing the condition that the two functions assume the same value for the abscissa corresponding to the value of the number of spectators where the two branches meet (see Fig. 6.3). Then, the functions have been inverted so that each of them describes one of the two branches of the correlation between detected energy and the

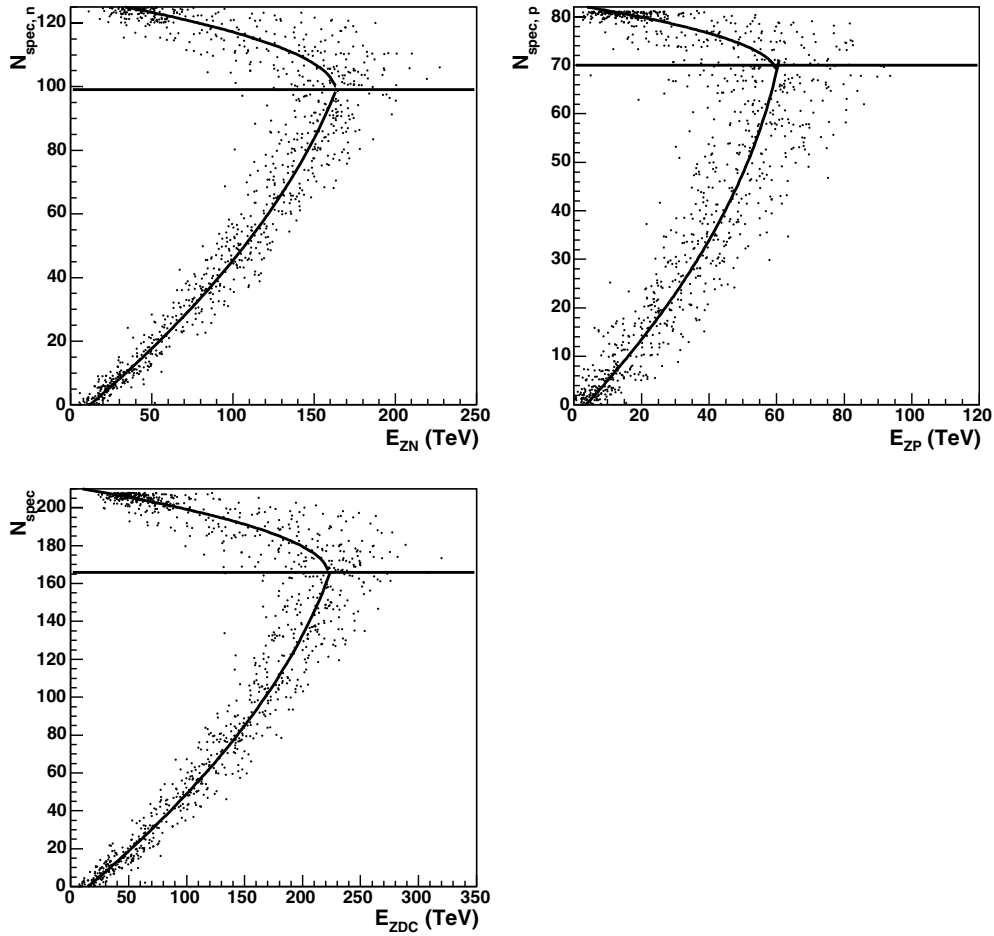


**Figure 6.4** Correlations between incident energy and the number of generated spectators in ZN (upper left), in ZP (upper right) and in both hadronic ZDCs (bottom). The horizontal lines represent spectator values in which the two functions are linked (see text for the values).

number of generated spectators. The resulting functions are plotted in Fig. 6.4 on top of the corresponding correlations. The horizontal line in the plots indicates the number of spectators  $N_{\text{spec},n}^j$  and  $N_{\text{spec},p}^j$  corresponding to the junction of the two branches. We get  $N_{\text{spec},n}^j = 100$  and  $N_{\text{spec},p}^j = 70$ . The corresponding energy values are  $E_{\text{ZN}} = 162$  TeV and  $E_{\text{ZP}} = 59.8$  TeV.

In this way, each energy value in the ZDCs can correspond to two different values for the number of spectators. The information provided by the forward electromagnetic calorimeters allows us to remove this ambiguity. In practice, the correlation between the number of spectators and the energy detected in the electromagnetic calorimeters was also fitted with a polynomial function (see Fig. 6.5). The value of  $E_{\text{ZEM}}$  corresponding to  $N_{\text{spec}}^j = N_{\text{spec},n}^j + N_{\text{spec},p}^j$  is  $E_{\text{ZEM}} = 420$  GeV. This value can be used as a threshold value for discriminating, at fixed  $E_{\text{ZDC}}$ , between the two branches of  $N_{\text{spec}}$  vs.  $E_{\text{ZDC}}$  correlations.

Using the correlations defined in this section it is possible, from the three values  $E_{\text{ZN}}$ ,  $E_{\text{ZP}}$  and  $E_{\text{ZEM}}$  reconstructed in each event, to estimate the number of spectator nucleons corresponding to that event. The number of participants is then readily obtained by subtraction:  $N_{\text{part}} = A - N_{\text{spec}}$ .

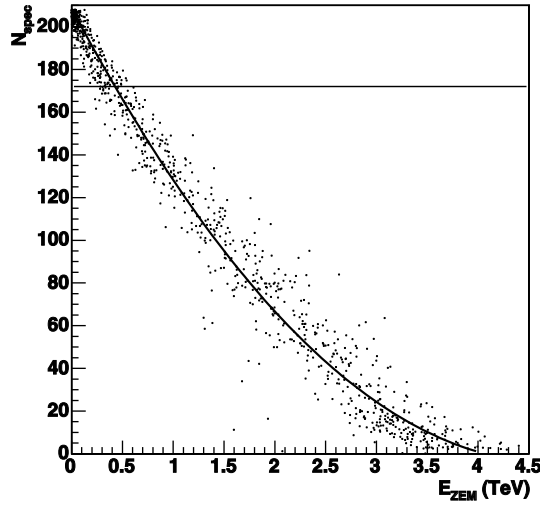


**Figure 6.5** Correlation between the number of generated spectators and the energy detected in ZEM. The horizontal line corresponds to the number of spectators for which the correlation  $E_{ZDC}$  vs.  $N_{\text{spec}}$  has a maximum. The corresponding  $E_{ZEM}$  value is  $\sim 420$  GeV.

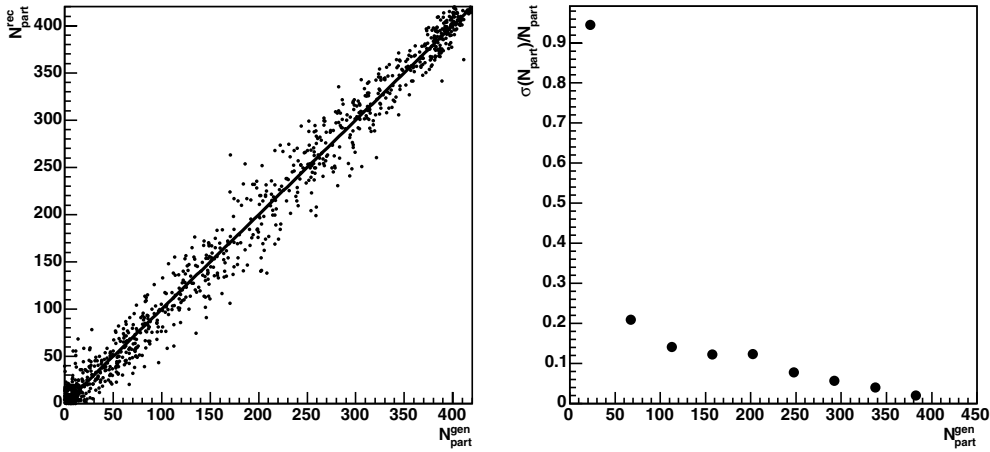


**Figure 6.6** Reconstructed number of participants as a function of the generated one (left), and resolution on the  $N_{\text{part}}$  measurement (right).

Concerning the impact parameter, a similar procedure has been adopted, starting from the correlations between the reconstructed energies in the ZDCs and the impact parameter given, event by event, by HIJING.

The quality of the results obtained with the described reconstruction procedure can be tested comparing, event by event, the values obtained for  $b$  and  $N_{\text{part}}$  to the corresponding generated values.

Concerning  $N_{\text{part}}$ , we plot in Fig. 6.6 the correlation between the reconstructed ( $N_{\text{part}}^{\text{rec}}$ ) and the generated ( $N_{\text{part}}^{\text{gen}}$ ) number of participants. One can see that, for all centralities,  $N_{\text{part}}^{\text{rec}} \sim N_{\text{part}}^{\text{gen}}$ , i.e., there is no significant bias in our procedure. The  $N_{\text{part}}^{\text{rec}}$  resolution, as a function of centrality is also shown in Fig. 6.6. It is below 10% for  $N_{\text{part}} \gtrsim 250$  and becomes larger than 50% only for very peripheral events ( $N_{\text{part}} < 25$ ). Concerning  $b$ , we also have a good

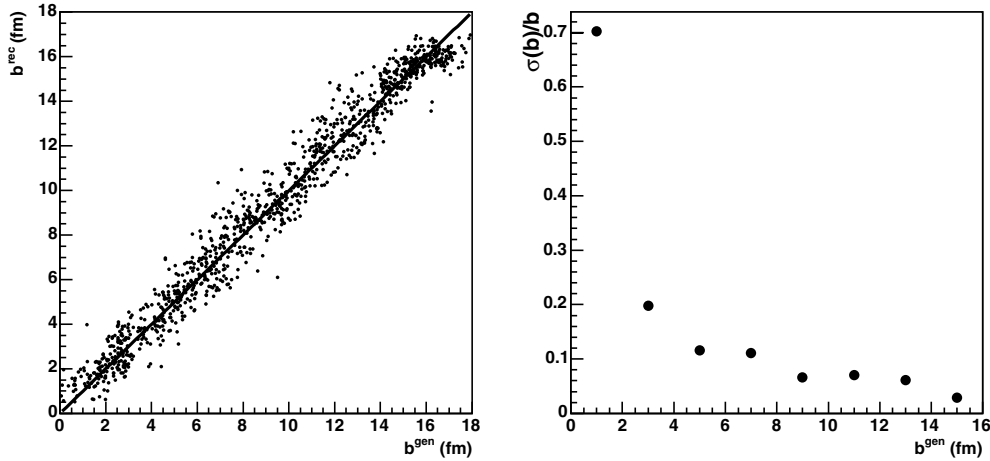


**Figure 6.7** Impact parameter reconstruction: correlation with simulated  $b$  (left), resolution on  $b$  as a function of the generated impact parameter (right).

agreement between  $b^{\text{rec}}$  and  $b^{\text{gen}}$  (see Fig. 6.7 (left)), for all centralities. The resolution on the reconstructed values of  $b$ , as can be deduced from Fig. 6.7 (right), is of the order of 1 fm over the whole centrality range.

**6.1.2.3. Centrality classes in the event-by-event method.** The generated events were divided into six centrality classes using the following  $b^{\text{gen}}$  ranges:

- class 1:  $0 < b < 3$  fm
- class 2:  $3 < b < 6$  fm
- class 3:  $6 < b < 9$  fm
- class 4:  $9 < b < 12$  fm
- class 5:  $12 < b < 15$  fm
- class 6:  $15 < b < 18$  fm.

With the method described in the previous section we can easily obtain the corresponding centrality classes in the  $b^{\text{rec}}$  variable. The event distributions vs.  $b^{\text{gen}}$  and  $b^{\text{rec}}$  are shown in Fig. 6.8. In Table 6.1 the mean value and r.m.s. of  $b^{\text{sim}}$  and  $b^{\text{rec}}$  for each class are reported.

For each class,  $\langle b^{\text{rec}} \rangle$  and  $\langle b^{\text{gen}} \rangle$  differ by less than 0.3 fm, showing that this method does not induce any significant bias in the centrality determination. We can note that the r.m.s. for each class is significantly smaller than the separation between consecutive classes, i.e., the overlap between the centrality bins is rather limited. In fact, the small number of bins chosen for this analysis is mainly due to the rather small statistics available. As will be seen later in Section 6.1.2.7, a larger number of bins can be safely defined, still keeping a reasonable separation between adjacent centrality classes.

A similar exercise has been carried out for  $N_{\text{part}}$ , using the following definitions for the six  $N_{\text{part}}^{\text{gen}}$  classes:

- class 1:  $378 < N_{\text{part}} < 414$
- class 2:  $278 < N_{\text{part}} < 378$
- class 3:  $143 < N_{\text{part}} < 278$
- class 4:  $50 < N_{\text{part}} < 143$
- class 5:  $8 < N_{\text{part}} < 50$
- class 6:  $0 < N_{\text{part}} < 8$ .

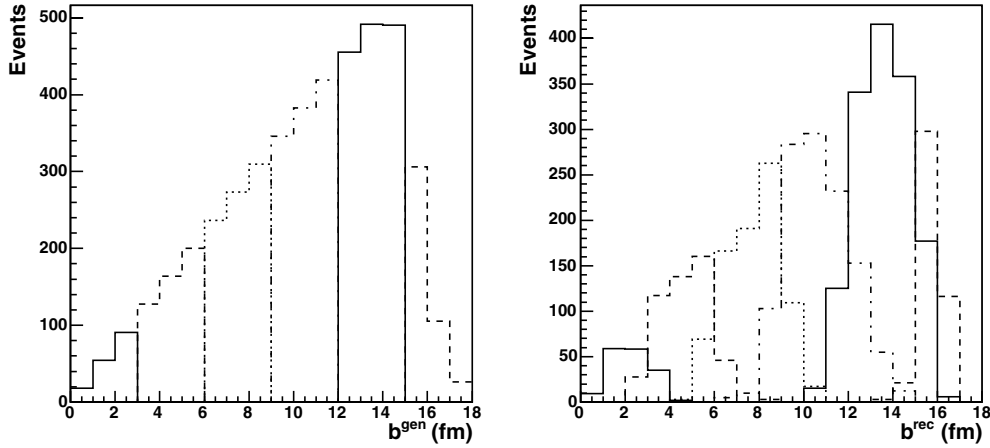


**Figure 6.8** Left: centrality classes defined on the generated event sample. Right: the same centrality classes as obtained with the event-by-event reconstruction.

**Table 6.1** Mean value and r.m.s. of simulated and reconstructed impact parameter in six centrality classes.

$b$ range (fm)	$\langle b^{\text{gen}} \rangle$ (fm)	$\langle b^{\text{rec}} \rangle$ (fm)	r.m.s. $b^{\text{gen}}$ (fm)	r.m.s. $b^{\text{rec}}$ (fm)
0–3	2.0	2.3	0.7	0.8
3–6	4.6	4.7	0.8	1.1
6–9	7.6	7.9	0.9	1.4
9–12	10.6	10.5	0.8	1.5
12–15	13.5	13.4	0.8	1.5
15–18	15.8	15.7	0.6	0.5

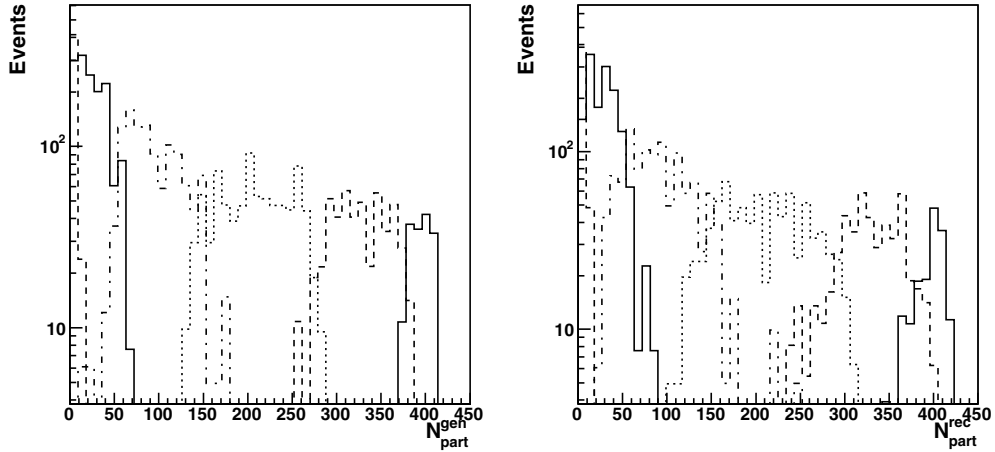


**Figure 6.9** Generated (left) and reconstructed (right) centrality classes in  $N_{\text{part}}$  variable.

The width of these classes was chosen in such a way that each class selects the same fraction of the total hadronic cross section selected in the corresponding  $b$  classes defined before. In Fig. 6.9 we show the event distributions vs.  $N_{\text{part}}^{\text{gen}}$  and  $N_{\text{part}}^{\text{rec}}$ . In Table 6.2 the mean value and RMS of  $N_{\text{part}}^{\text{gen}}$  and  $N_{\text{part}}^{\text{rec}}$  for each class are reported.

**Table 6.2** Mean value and r.m.s. of the simulated and reconstructed number of participants in the six centrality classes defined.

$N_{\text{part}}^{\text{gen}}$ range	$\langle N_{\text{part}}^{\text{gen}} \rangle$	$\langle N_{\text{part}}^{\text{rec}} \rangle$	r.m.s. $N_{\text{part}}^{\text{gen}}$	r.m.s. $N_{\text{part}}^{\text{rec}}$
378–414	393	392	12	17
278–378	317	315	27	38
143–278	207	209	40	47
50–143	93	110	31	53
8–50	24	29	16	30
0–8	3	5	3	3

**Table 6.3** Mean values of the reconstructed  $N_{\text{part}}$  for the three different simulated backgrounds.

$N_{\text{part}}^{\text{sim}}$ range	$\langle N_{\text{part}}^{\text{sim}} \rangle$	$\langle N_{\text{part}}^{\text{rec}} \rangle$ HIJING	$\langle N_{\text{part}}^{\text{rec}} \rangle$ $0.5 \times \text{HIJING}$	$\langle N_{\text{part}}^{\text{rec}} \rangle$ $2 \times \text{HIJING}$
378–414	393	392	402	379
278–378	317	315	338	309
143–278	207	209	221	192
50–143	93	110	97	103
0–50	18	21	20	22

The centrality selection shown here is based on sharp cuts on the impact parameter value. There are of course several ways of defining centrality intervals. Another common choice is to define centrality bins as fractions of the inelastic Pb–Pb cross section. An example of such a selection will be discussed later, in Section 6.1.2.7.

*6.1.2.4. Discussion on the event-by-event determination of centrality.* As we have shown, the method described allows an event-by-event estimation of centrality. However, since it is based on the parametrization of simulated correlations, it is, in principle, sensitive to the choice of the event generator. Therefore, we tried to estimate to which extent the reconstructed values of  $b$  and  $N_{\text{part}}$  depend on the assumed model. For this purpose we made a very simple test, consisting in varying the size of the HIJING ‘background’ contribution, i.e., the fraction of the signal in the ZDCs not due to spectators. Then we reconstructed again, event-by-event,  $b$  and  $N_{\text{part}}$ , without re-fitting the  $b$  vs.  $E_{\text{ZDC}}$  and  $N_{\text{part}}$  vs.  $E_{\text{ZDC}}$  correlations. This is equivalent to considering a situation where the experimental background is different from the simulated one. We have performed two tests, respectively doubling and halving the HIJING background levels. We find that the contribution to the ZDC signal due to background is sizeable for central events only. For such events, the number of participants and secondaries emitted within ZDC pseudo-rapidity acceptance is the highest and the number of spectators is low.

The consequences on the reconstructed values of  $b$  and  $N_{\text{part}}$  are negligible, except for very central events. This can be seen by looking at Table 6.3, where we compare, for five  $N_{\text{part}}$  classes (we have grouped for this study the more peripheral bins), the average value of  $N_{\text{part}}^{\text{gen}}$  with the  $N_{\text{part}}^{\text{rec}}$  values obtained for the three background simulations (HIJING,  $0.5 \times \text{HIJING}$ , and  $2 \times \text{HIJING}$ ). The bias on the determination of  $\langle N_{\text{part}} \rangle$  is always below 5%. Moreover, the resolution on  $N_{\text{part}}$  is not significantly worsened. We conclude, therefore, that the proposed method has a slight dependence on the event generator used for simulation, but it can be safely used to provide an event-by-event evaluation of the centrality of the event.

*6.1.2.5. Determination of centrality from the  $E_{\text{ZDC}}$  vs.  $E_{\text{ZEM}}$  correlation.* The centrality of the collision can also be estimated by making use of the correlation between the reconstructed

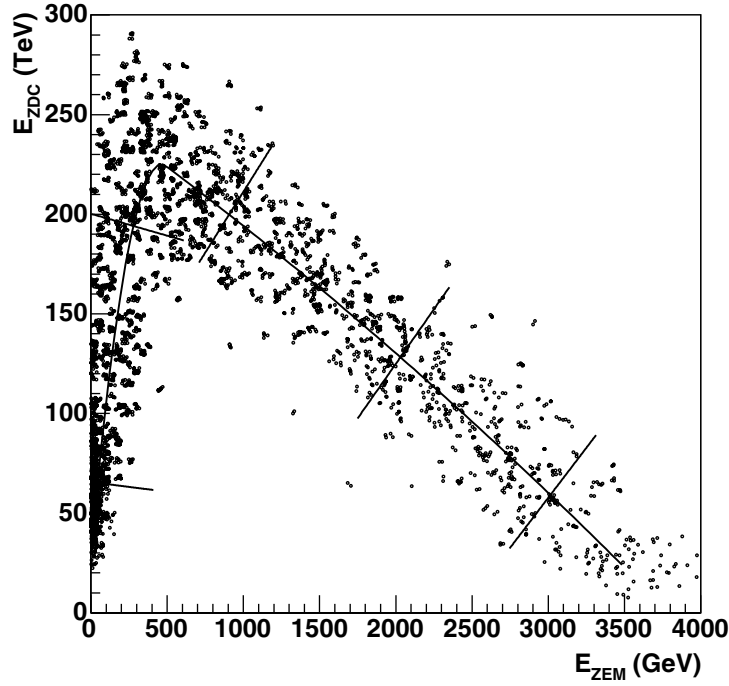


**Figure 6.10** Correlation between  $E_{ZDC}$  and  $E_{ZEM}$ . The cuts used to define the six centrality classes are also indicated.

$E_{ZDC}$  and  $E_{ZEM}$  values. The underlying assumptions are that the most central events correspond to the region where  $E_{ZEM}$  reaches its maximum and  $E_{ZDC}$  is very low, and that, starting from that region and following the shape of the correlation,  $b$  increases monotonically (or alternatively,  $N_{part}$  decreases monotonically). In practice, one defines centrality classes by means of cuts perpendicular to the  $E_{ZDC}$  versus  $E_{ZEM}$  correlation. In this way, it is possible to create centrality classes corresponding to well-defined percentiles of the total hadronic cross section:

$$\int_{E_{ZEM,i}} \int_{E_{ZDC,i}} \frac{d^2\sigma}{dE_{ZEM}dE_{ZDC}} dE_{ZEM}dE_{ZDC} = \int_0^{b_i} db \frac{d\sigma}{db} = x_i \times \sigma_{tot},$$

where  $i$  refers to the selected region in the  $E_{ZDC}$ – $E_{ZEM}$  plane, corresponding to an impact parameter range  $0 < b < b_i$ , and  $x_i$  is the selected fraction of the total (inelastic) cross section. The corresponding number of participants,  $N_{part,i}$ , can be calculated using the Glauber model or from the HIJING event generator.

To compare the performance of this method directly with the event-by-event method, six classes have been defined, each one selecting fractions of the total cross section corresponding to the same  $b$  values used in the study of the event-by-event method. In Fig. 6.10 the  $E_{ZDC}$  versus  $E_{ZEM}$  correlation is shown, together with the cuts used to select the five centrality classes.

The  $b$  and  $N_{part}$  distributions obtained for the five classes are plotted in Fig. 6.11. In Table 6.4 the mean values obtained for each centrality class are compared to the simulated ones. One can see that the reconstructed and simulated  $\langle b \rangle$  and  $\langle N_{part} \rangle$  are in good agreement for both methods.

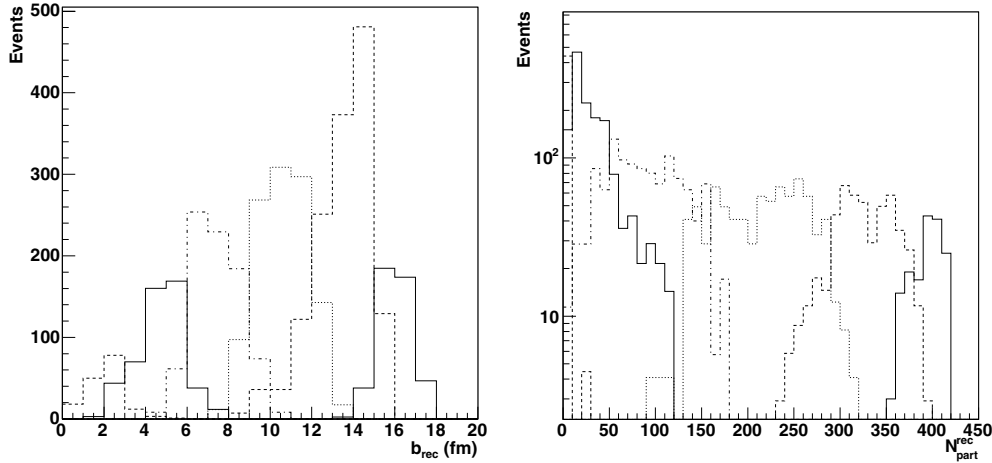


**Figure 6.11**  $b$  and  $N_{\text{part}}$  classes defined using the  $E_{\text{ZDC}}$  vs.  $E_{\text{ZEM}}$  correlation.

**Table 6.4** Impact parameter and number of participants, as reconstructed from the six centrality classes defined with the  $E_{\text{ZDC}}$  vs.  $E_{\text{ZEM}}$  correlation.

$\sigma/\sigma_{\text{inel}}$ (%)	$b_{\text{gen}}$ range	$\langle b_{\text{gen}} \rangle$ (r.m.s.)	$\langle b_{\text{reco}} \rangle$ (r.m.s.)	$\langle N_{\text{part}}^{\text{gen}} \rangle$ (r.m.s.)	$\langle N_{\text{part}}^{\text{reco}} \rangle$ (r.m.s.)
0–3.6	0–3 fm	2.0 (0.7)	2.2 (0.8)	393 (12)	393 (15)
3.6–14.6	3–6 fm	4.6 (0.8)	4.7 (1.1)	317 (27)	323 (33)
14.6–32.8	6–9 fm	7.6 (0.9)	7.4 (1.1)	207 (40)	217 (45)
32.8–58.3	9–12 fm	10.6 (0.8)	10.6 (1.2)	93 (31)	94 (41)
58.3–90.3	12–15 fm	13.5 (0.8)	13.4 (1.3)	24 (16)	37 (52)
90.3–100	15–18 fm	15.8 (0.6)	16.0 (0.8)	3 (3)	4 (2)

It should be underlined that this method, being exclusively based on experimental quantities, does not depend on the particular model used for the simulation and is essentially not sensitive to the level of background contamination.

**6.1.2.6. Comments on the determination of  $N_{\text{part}}$ .** In the previous section we showed a way of relating the differential cross section  $d^2\sigma/dE_{\text{ZEM}}dE_{\text{ZDC}}$  in the measured variables  $E_{\text{ZEM}}$  and  $E_{\text{ZDC}}$  to the differential cross section in the  $b$  variable. On account of the geometrical meaning of such variable, the shape of  $d\sigma/db$  is, except for very peripheral events, model-independent and simply given by  $d\sigma/db = 2\pi b$ . This allows a robust determination of the  $b$  interval relative to a certain event sample. If one wants to determine the corresponding  $N_{\text{part}}$  interval, one can either rely on the Glauber model or use a Monte Carlo event generator like HIJING. Comparing the correlation between  $b$  and  $N_{\text{part}}$  calculated in these two ways, we find that HIJING gives, at fixed  $b$ , a slightly larger  $N_{\text{part}}$  (see Fig. 6.12). The detailed reason for such a discrepancy is still under investigation. Anyway, also RHIC experiments have found that the calculation of some geometrical quantities related to nucleus–nucleus collisions (e.g. eccentricity) gives different results when performed in an analytical Glauber calculation or via a Monte Carlo implementation of the Glauber model. For the time being, we have quantified the influence of this systematic shift on the determination of  $\langle N_{\text{part}} \rangle$  corresponding to a certain centrality class.

Using the correlations provided by the two different models, we calculated for each of the centrality classes defined in the previous sections the difference  $\Delta N_{\text{part}}$  between the estimated

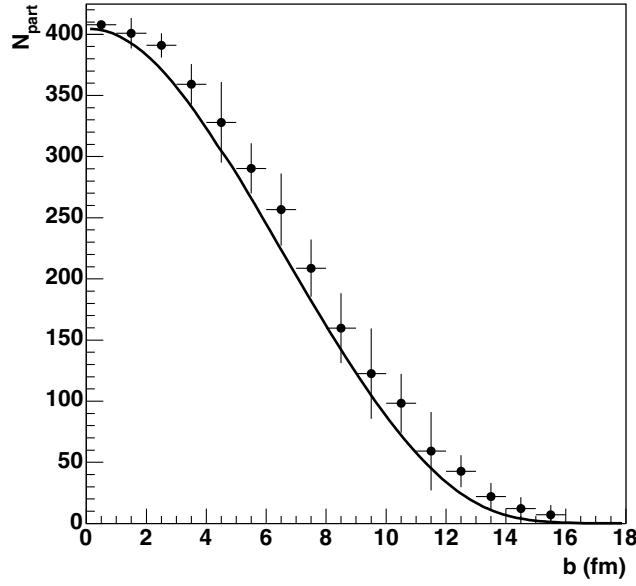


**Figure 6.12** Number of participants as a function of the impact parameter for Pb–Pb collisions at  $\sqrt{s_{NN}} = 5.5$  TeV: Glauber model (solid line) and HIJING (points).

**Table 6.5**  $N_{\text{part}}$  reconstruction using Glauber and HIJING models.  $|\Delta N_{\text{part}}^{\text{reco}}|$  is calculated as:  $|\Delta N_{\text{part}}^{\text{reco}}| = ((N_{\text{part}}^{\text{reco}})_{\text{HIJING}} - (N_{\text{part}}^{\text{reco}})_{\text{GLAUBER}}) / (N_{\text{part}}^{\text{reco}})_{\text{HIJING}}$ .

$N_{\text{part}}$ range	$ \Delta N_{\text{part}}^{\text{reco}} $
378–414	2%
278–378	6%
143–278	11%
50–143	20%
0–50	21%

average number of participants. We find that  $\Delta N_{\text{part}}$  is negligible for central events and reaches  $\Delta N_{\text{part}} = 20$  for centrality classes corresponding to intermediate  $b$  values. The result is shown in more detail in Table 6.5, for five centrality bins. We conclude that, although the effect is small, it must be taken into account when comparing, for example, the experimental results with the output of theoretical models.

**6.1.2.7. Fast simulation of the ZDC response.** The full simulation used in the previous sections for the study of the centrality determination is somewhat limited by the event statistics. It is therefore desirable to develop a tool for a more accurate investigation of the physics performance of the apparatus. This has been done by preparing a fast simulation of the ZDC response, based on the parametrization of the results obtained in the full simulation. One of the possible applications of the fast simulation is the study of the physics issues related to the availability of two identical sets of ZDCs, positioned at opposite sides with respect to the I.P. As already noted in Section 6.1.2.1, in the full simulation only one set of detectors was taken into account, because of technical problems connected with the extremely large length ( $\sim 250$  m) of the set-up that would have to be used otherwise inside GEANT.

**Table 6.6** Parameter values for the ZN, ZP and ZEM response.

$i, j$	$a$	$b$	$c$
ZN,n ( $N_{\text{spec},n} \leq 100$ )	-0.07269	2.287920	11.921710
ZN,n ( $N_{\text{spec},n} > 100$ )	-0.190932	37.812280	-1709.259672
ZP,p ( $N_{\text{spec},p} \leq 70$ )	-0.007283	1.321353	3.550697
ZP,p ( $N_{\text{spec},p} > 70$ )	-0.310786	42.643308	-1402.945615
ZEM,tot	0.030790	-23.678061	3551.461324

$i, j$	$\alpha$	$\beta$	$\gamma$	$\delta$
ZN,n	$4.2 \times 10^{-5}$	$-0.4986 \times 10^{-2}$	0.249020	6.268601
ZP,p	$3.0 \times 10^{-5}$	$-0.2730 \times 10^{-2}$	0.198875	3.573390
ZEM,tot	0	$-0.1592 \times 10^{-2}$	-1.414557	397.308402

The fast simulation is based on the parametrization of the response of ZN, ZP and ZEM, as a function, respectively, of the number of spectator neutrons  $N_{\text{spec},n}$ , spectator protons  $N_{\text{spec},p}$  and their sum  $N_{\text{spec},\text{tot}}$ . For each detector we parameterize the average detected energies  $\langle E_{\text{ZN}}(N_{\text{spec},n}) \rangle$ ,  $\langle E_{\text{ZP}}(N_{\text{spec},p}) \rangle$ ,  $\langle E_{\text{ZEM}}(N_{\text{spec},\text{tot}}) \rangle$ , and their r.m.s.  $\sigma_{E_{\text{ZN}}}(N_{\text{spec},n})$ ,  $\sigma_{E_{\text{ZP}}}(N_{\text{spec},p})$  and  $\sigma_{E_{\text{ZEM}}}(N_{\text{spec},\text{tot}})$ . The parametrization of the average energies is of the following kind:

$$\langle E_i(N_{\text{spec},j}) \rangle = a \times (N_{\text{spec},j})^2 + b \times N_{\text{spec},j} + c \quad (6.1)$$

while their dispersions are given by

$$\sigma_{E_i}(N_{\text{spec},j}) = \alpha \times (N_{\text{spec},j})^3 + \beta \times (N_{\text{spec},j})^2 + \gamma \times N_{\text{spec},j} + \delta. \quad (6.2)$$

The parameter values are listed in Table 6.6.

We assume that the response of the ZDCs on the two sides of the I.P. can be parametrized by the same set of functions. This assumption should be not too far from reality, in view of the substantial symmetry of the set-up and of the fact that the detectors are identical. Small differences might be expected only for the ZPs, on account of the slight asymmetry of the beam optics elements on the two sides (muon arm dipole on one side vs. set of correcting magnets on the other side).

Having parametrized the detector response, a large event sample can be simulated generating Pb–Pb events with an event generator, without tracking any particle in the set-up. To test the fast simulation,  $4 \times 10^4$  events were generated using HIJING. By using the above-defined parametrizations, it is possible to build the  $E_{\text{ZDC}}$  vs.  $E_{\text{ZEM}}$  correlation, where  $E_{\text{ZDC}} = E_{\text{ZN}} + E_{\text{ZP}}$ . Such a correlation, as explained in Section 6.1.2.5, can be directly used to define centrality classes corresponding to various fractions of the inelastic cross section  $\sigma_{\text{PbPb}}^{\text{inel}}$ . As in that section, we have selected event classes by means of cuts perpendicular to the axis of the correlation, following its typical pattern ( $E_{\text{ZEM}}$  decreases monotonically from central to peripheral events, while  $E_{\text{ZDC}}$  first increases and then decreases because of the increasing loss of nuclear fragments). The correlation corresponding to the sum of the ZDC energies on the two sides was used. The centrality bins are shown in Colour Figure III. For the most central events (from 0% to 20% of the inelastic cross section) a finer binning was chosen, followed by a relatively coarser selection.

For each centrality bin it is possible to calculate the theoretical  $N_{\text{part}}$  distribution by simply selecting, in the generated  $N_{\text{part}}$  plot, event classes corresponding to the various percentages of  $\sigma_{\text{PbPb}}^{\text{inel}}$  that one wants to investigate. These  $N_{\text{part}}$  classes can then be compared to the  $N_{\text{part}}$  distributions relative to each of the bins defined on the  $E_{\text{ZDC}}$  vs.  $E_{\text{ZEM}}$  correlation.

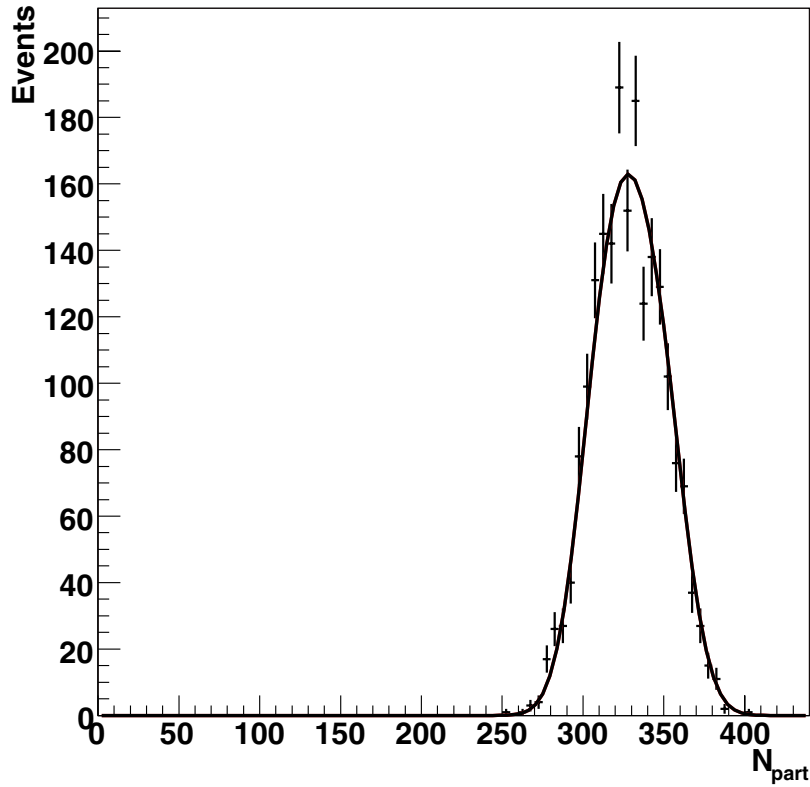


**Figure 6.13.** The  $N_{\text{part}}$  distribution measured for the 5–10% centrality sample. The curve represents a fit, obtained starting from the corresponding theoretical  $N_{\text{part}}$  distribution, enlarged by introducing a certain  $\sigma_{N_{\text{part}}}$ , which is the fit parameter. For this bin we get  $\sigma_{N_{\text{part}}} = 15$ .

Such distributions include the smearing effects due to the energy resolution of the calorimeter. The comparison is shown in Colour Figure III.

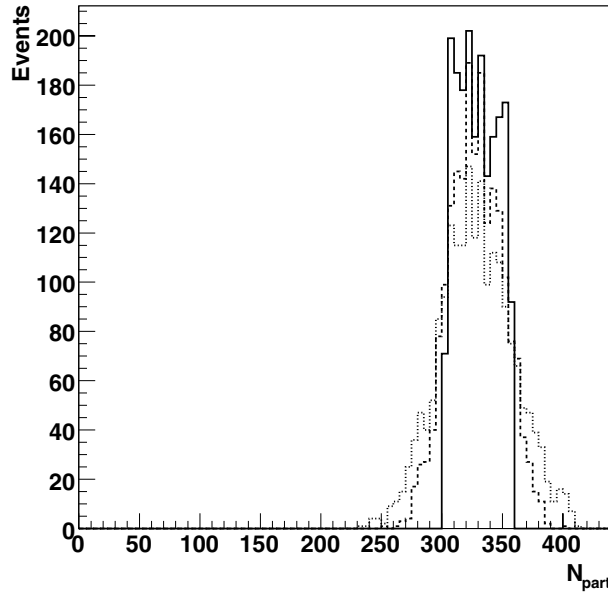
It can be seen that, in spite of the observed smearing of the  $N_{\text{part}}$  classes, a clear separation between adjacent classes is visible. To quantify the resolution on the  $N_{\text{part}}$  measurement, we have calculated, bin per bin, the smearing that has to be applied to each of the distributions contained in the left plot in Colour Figure III in order to get the smeared distributions. This has been done by means of a fitting procedure, whose result is shown, for one centrality bin, in Fig. 6.13. Finally, in Table 6.7, we show for the various centrality bins the simulated and reconstructed average  $N_{\text{part}}$  values, together with the estimated centrality resolution.

It can be seen that the  $\langle N_{\text{part}}^{\text{REC}} \rangle$  values are always in good agreement with the corresponding  $\langle N_{\text{part}}^{\text{SIM}} \rangle$ , indicating that the adopted method for the bin selection (cut on the  $E_{\text{ZDC}}$  vs.  $E_{\text{ZEM}}$  correlation) is substantially correct. Concerning the centrality resolution, the values range from  $\sim 4\%$  for central events to  $\sim 60\%$  for very peripheral events. This loss of resolution in the peripheral region should be ascribed mainly to the ‘bending’ of the correlation due to the formation of nuclear fragments. Anyway, with the chosen bin size, the separation between adjacent classes still looks satisfactory.

Finally, it must be noted that it would be interesting to perform the same kind of study with other combinations of centrality-related observables. In this respect, the most promising

**Table 6.7.** Results of the fast simulation for the  $N_{\text{part}}$  binning.

$\sigma_{\text{PbPb}}^{\text{inel}} (\%)$	$\langle N_{\text{part}}^{\text{SIM}} \rangle$	$\langle N_{\text{part}}^{\text{REC}} \rangle$	$\sigma(N_{\text{part}})$
0–5	386	384	14
5–10	329	328	15
10–15	276	275	15
15–20	231	229	17
20–30	177	174	19
30–40	120	119	21
40–50	77	77	18
50–60	46	48	12
60–70	25	24	10
70–80	13	12	8

**Figure 6.14.** Starting from the theoretical  $N_{\text{part}}$  distribution for the 5–10% centrality sample (continuous lines), the corresponding distributions from the  $E_{\text{ZDC}}$  vs.  $E_{\text{ZEM}}$  correlation are shown, with  $E_{\text{ZDC}}$  corresponding to the sum of the hadronic energy on the two sets of ZDCs (dashed line) or to the energy on one side only (dotted line).

possibility is the study of the correlation between  $E_{\text{ZDC}}$  and the charged multiplicity  $N_{\text{ch}}$ , calculated with the SPD information using the algorithms described in Section 6.1.3.1. Such a study is foreseen and will be performed in the near future.

**6.1.2.8. Correlations between the response of the two sets of ZDCs.** The use of two symmetrically positioned sets of ZDCs offers several advantages. First of all, by detecting spectator nucleons on the two sides, it is possible to increase the resolution on the  $N_{\text{part}}$  determination, since the event-by-event effect of the relative fluctuations between the number of spectator nucleons for the two nuclei is minimized. This effect is shown in Fig. 6.14 where we plot, for the 5–10% centrality bin, the reconstructed  $N_{\text{part}}$  distributions using either one or two sets of ZDCs to define  $E_{\text{ZDC}}$ . The increase in resolution deriving from the use of the two sets of ZDCs is clearly visible.

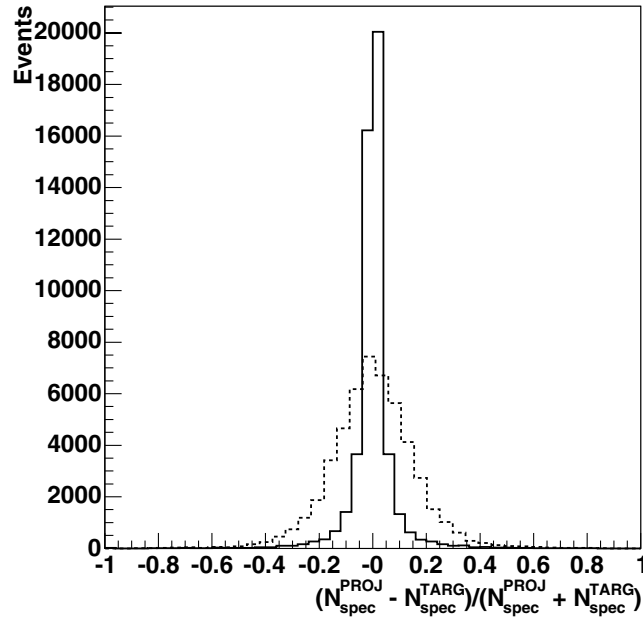


**Figure 6.15.** The asymmetry in the number of spectators for the two colliding Pb ions, for minimum-bias collisions. The continuous line is the HIJING distribution, the dashed line represents the same quantity for the free spectator nucleons, i.e., the ones not bound into nuclear fragments.

On the other hand, we have investigated the possibility of studying the correlations between the number of spectator nucleons  $N_{\text{spec}}^1$  and  $N_{\text{spec}}^2$  for the two colliding nuclei. Using HIJING as an event generator, we have tried to see if possible asymmetries between the spectator emission on the two sides can be detected with a reasonable resolution. Unfortunately, it turns out that such effects are heavily masked by the (stochastic) formation of nuclear fragments that removes a considerable number of spectator nucleons from the ZDC acceptance. As an example, in Fig. 6.15 we show the relative asymmetry between the number of spectator nucleons on the two sides, both at the generator level and after the formation of nuclear fragments. It can be seen that the small asymmetry present in the HIJING event sample is largely washed out when one looks at the asymmetry between the detected spectator nucleons, i.e., the ones that are not bound into fragments. Therefore, the accuracy with which asymmetries between the spectator emission on the two sides can be detected appears rather limited. Only for central events, where the formation of nuclear fragments is less important, could one reasonably look for emission asymmetries. However, the small number of nucleons emitted in this case makes it difficult, even in this case, to distinguish genuine correlation effects from trivial stochastic fluctuations.

**6.1.2.9. Determination of the reaction plane with the ZDC.** The ZDCs can provide information not only on the magnitude of the impact parameter vector, and therefore on the centrality of the collisions, but also on its direction.

Thanks to the four tower segmentation, the neutron zero-degree calorimeter (ZN) can be considered as a rough position sensitive device. This localizing capability can be used to reconstruct, event by event, the centroid of the spectator neutrons spot on the ZN front-face. The centroid coordinate is sensitive to the directed flow  $v_1$  (“bounce off”) of the spectator neutrons and therefore its measurement allows to reconstruct the 1<sup>st</sup>-order event plane. The event plane

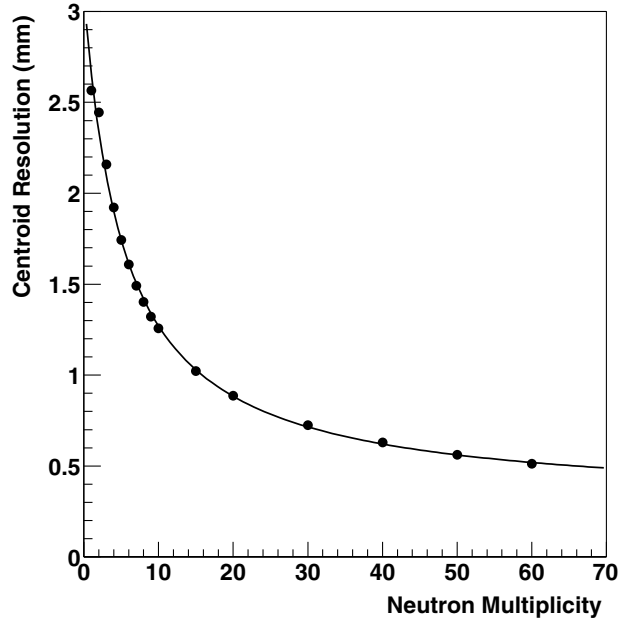


**Figure 6.16.** Resolution on the  $x$ -coordinate of the centroid as a function of the neutron multiplicity.

resolution that the ZN calorimeter will provide depends on the magnitude of the directed flow  $v_1$  of spectator neutrons, which is expected to be quite large ( $\approx 20\%$ ) and independent of beam energy. WA98 at the SPS measured a directed flow of protons of the order of 20% in the target fragmentation region [137]. Furthermore, STAR measurements of  $v_1$  among charged particles [138] are in good agreement at forward rapidities with NA49 measurements [139], when plotted as a function of  $y - y_{\text{beam}}$ . This observation is consistent with the hypothesis of ‘limiting fragmentation’ [140] in this region and may suggest that  $v_1$  among spectator nucleons could be independent of beam energy between SPS and RHIC [141].

The first information we need in order to estimate how well the reaction plane can be estimated by means of the ZN calorimeter, is the resolution on the centroid of the spectator neutrons spot on the ZN. The centroid resolution is estimated by means of a simulation, where spectator neutrons (2.76 TeV) are generated with a momentum distribution taking into account Fermi momentum and a transverse Pb beam divergence at the interaction point of  $30 \mu\text{rad}$ . A GEANT-based simulation code tracks the neutrons in the calorimeter, where the hadronic shower deposits light in the four towers. The centroid of the spectator neutron spot on the ZN front-face is estimated by means of the relations [142]:

$$x = c \frac{\sum_{i=1}^4 x_i w_i}{\sum_{i=1}^4 w_i}, \quad y = c \frac{\sum_{i=1}^4 y_i w_i}{\sum_{i=1}^4 w_i}, \quad \text{with } w_i = E_i^\alpha, \quad (6.3)$$

where  $x_i$  and  $y_i$  are the coordinates of the centre of the  $i$ -th tower and  $E_i$  is the light in the  $i$ -th tower.  $\alpha$  and  $c$  are free parameters introduced in order to get accurate reconstructed impact coordinates. The difference between the centroid reconstructed by the ZN and the true one, known from simulation, is calculated for the  $x$  and  $y$  coordinate for different neutron multiplicity. The resolution on the centroid coordinate, which is the RMS of these distributions, decreases as the neutron multiplicity grows, as shown in Fig. 6.16. A centroid resolution less than 1 mm can be achieved for neutron multiplicity greater than 20.

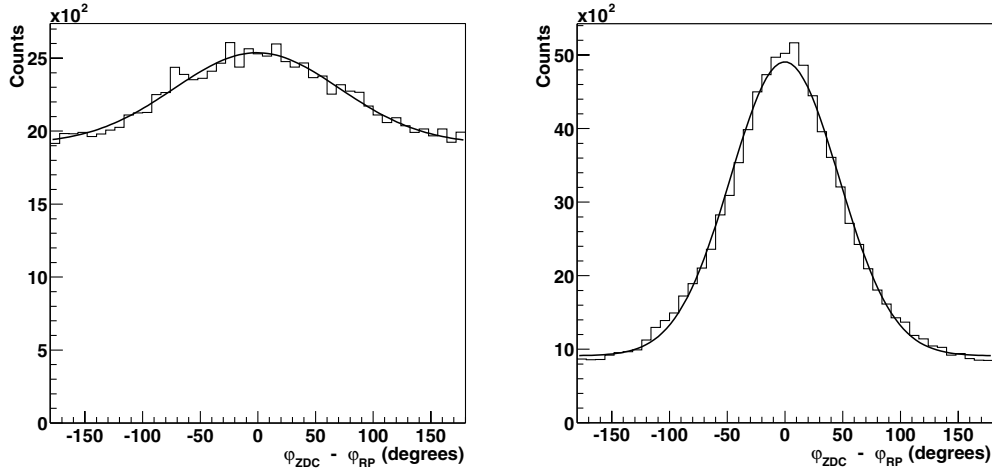


**Figure 6.17.** Event plane resolution: on the left  $v_1 = 5\%$  and  $n_{\text{neutr}} = 5$ , on the right  $v_1 = 20\%$  and  $n_{\text{neutr}} = 40$ .

The information on the centroid resolution was used in a fast simulation in order to estimate the resolution on the event plane reconstructed by means of the ZN calorimeter. Spectator neutrons (2.76 TeV) on one side of the interaction point (I.P.) are generated with a momentum distribution that takes into account Fermi momentum, a transverse beam divergence at I.P. =  $30 \mu\text{rad}$  and a transverse beam size at I.P. =  $16 \mu\text{m}$ . A random reaction plane azimuth ( $\varphi_{\text{RP}}$ ) is assigned to each event and a directed flow of spectator neutrons  $v_1$  is introduced following standard prescriptions [143]. By means of this simulation a parametric study of the event plane resolution as a function of the neutron multiplicity  $n_{\text{neutr}}$  was performed for three different values of the directed flow of spectator neutrons  $v_1 = 5\%$ ,  $10\%$ ,  $20\%$ . Figure 6.17 illustrates two examples of distributions of the difference between the event plane azimuth, measured from the reconstructed centroid of the spectator neutrons spot on the ZN ( $\varphi_{\text{ZDC}}$ ), and the input reaction plane azimuth ( $\varphi_{\text{RP}}$ ). The distributions are fitted with the superposition of a Gaussian plus a constant function. The event plane resolution, i.e. the variance of the Gaussian function, is  $72^\circ$  when  $v_1 = 5\%$  and  $n_{\text{neutr}} = 5$  and  $47^\circ$  when  $v_1 = 20\%$  and  $n_{\text{neutr}} = 40$ . The corresponding r.m.s. values for the two distributions are  $100^\circ$  and  $75^\circ$ .

The results of the parametric study are summarized in Fig. 6.18, where two estimators of the event plane resolution, the variance of the gaussian fit of the distribution  $\varphi_{\text{ZDC}} - \varphi_{\text{RP}}$  (left) and the mean cosine of the angular difference  $\langle \cos(\varphi_{\text{ZDC}} - \varphi_{\text{RP}}) \rangle$  (right), are plotted as a function of  $n_{\text{neutr}}$ . We study six different  $n_{\text{neutr}}$  values, from 5 up to 60, which is roughly the maximum number of emitted neutrons, when the production of nuclear fragments in the collision is taken into account. As expected the event plane resolution depends on the magnitude of  $v_1$  and on a lesser extent on the neutron multiplicity.  $\langle \cos(\varphi_{\text{ZDC}} - \varphi_{\text{RP}}) \rangle$  is of the order of 0.40 in the case  $v_1 = 20\%$  and  $n_{\text{neutr}} = 30$ , slightly better than the value calculated for the STAR ZDC-SMD ( $\approx 0.34$ ) [141]. In summary, an event plane reconstruction algorithm, which makes use of one ZN calorimeter, has been presented and the resolution on its determination has been calculated via Monte Carlo. In ALICE, thanks to the availability of two such detectors, it will also be possible to estimate the event plane resolution directly from the experimental data. This will be done through the well-known sub-event technique, using the information from each ZN as sub-event.

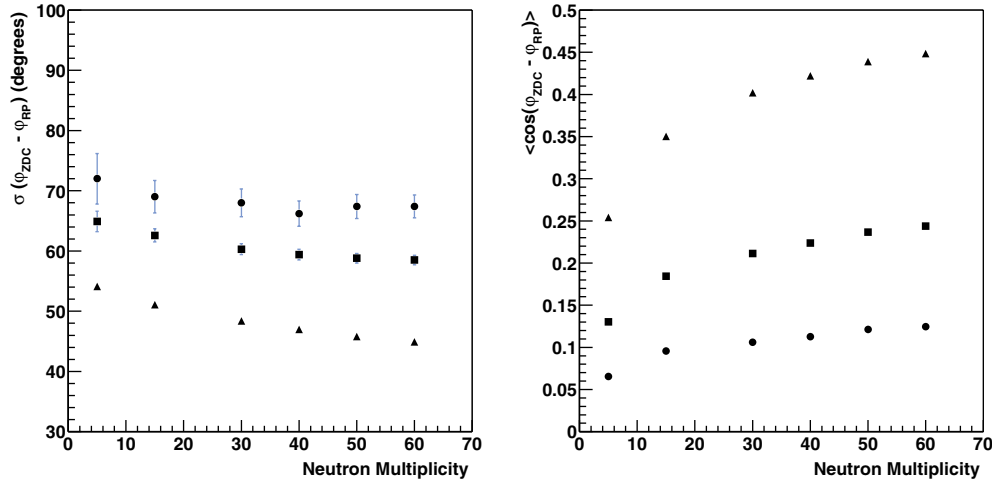


**Figure 6.18.** Event plane resolution expressed as the variance of the  $\varphi_{\text{ZDC}} - \varphi_{\text{RP}}$  gaussian fit (left) and as  $\langle \cos(\varphi_{\text{ZDC}} - \varphi_{\text{RP}}) \rangle$  (right), as a function of neutron multiplicity. Circles, squares and triangles correspond to  $v_1 = 5\%$ ,  $10\%$ ,  $20\%$  respectively.

**6.1.3. Multiplicity determination using the SPD and the FMD.** The hadron multiplicity is an essential observable for the study of the event characterization in heavy-ion physics. The way the initial energy available in the reaction is redistributed for producing particles in the final state is strictly linked with the energy density  $\varepsilon$  reached in the early phase of the collision. It is usually estimated through the Bjorken formula [112]:

$$\varepsilon_{\text{Bj}} = \frac{\langle m_t \rangle}{2\pi R_A^2 \tau_{\text{th}}} \left( \frac{dN_{\text{ch}}}{dy} \right)_{y=0}, \quad (6.4)$$

where  $\langle m_t \rangle$  is the average transverse mass of the produced particles,  $R_A$  is the nuclear radius,  $\tau_{\text{th}}$  is the thermalization time, and  $(dN_{\text{ch}}/dy)_{y=0}$  is the charged multiplicity at mid-rapidity. This formula can be used in ALICE, since the appropriate conditions for its application (the presence of a baryon-free mid-rapidity region, and a corresponding plateau in the multiplicity distributions) should indeed be met. Of course, a suitable value of  $\tau_{\text{th}}$ , an essential ingredient in the calculation of  $\varepsilon$ , will have to be provided by theory.

Furthermore, the multiplicity information allows to constrain the hadroproduction models. By studying the  $\sqrt{s}$  dependence of charged particle multiplicity, in various rapidity ranges, one can get informations on the underlying dynamics of the particle production mechanism, including an estimate, for example, of the relative contributions of hard parton-parton scattering processes, governed by perturbative QCD, and of soft processes, which can be described by phenomenological non-perturbative approaches. Theory predictions for the multiplicity usually vary in a considerable way. At RHIC, for example, the estimate of the various models for  $dN_{\text{ch}}/d\eta$  at mid-rapidity ranged from  $\sim 600$  to  $\sim 1300$  [144], and most of them predicted values much higher than the actual measured value. Therefore an experimental measurement of multiplicity is a top priority for an experiment like ALICE, which will explore a still uninvestigated energy range.

Concerning lower energy experiments, many experimental measurements are currently available, from AGS [145], SPS [116–119] and RHIC [105, 120–122, 129]. At SPS energies ( $\sqrt{s} \sim 20$  GeV/nucleon), the  $N_{\text{part}}$  dependence of the multiplicity per participant pair at mid-rapidity,  $dN_{\text{ch}}/dy|_{y=0}/(0.5 \cdot N_{\text{part}})$ , has been found to be rather flat. By parametrizing the

scaling of  $dN_{\text{ch}}/dy$  as

$$\left. \frac{dN_{\text{ch}}}{dy} \right|_{y=0} = a \cdot N_{\text{part}}^{\alpha}, \quad (6.5)$$

$\alpha$  values ranging from 1.00 to 1.10 were obtained. At SPS energy, the approximate scaling with  $N_{\text{part}}$  of the multiplicity at mid-rapidity is usually understood as an indication that hard scattering does not play an appreciable role. The numerical values of  $dN_{\text{ch}}/dy|_{y=0}/(0.5 \cdot N_{\text{part}})$  range from  $\sim 1$  at low SPS energy ( $\sqrt{s} \sim 9$  GeV/nucleon) to  $\sim 2$  at high SPS energy ( $\sqrt{s} \sim 17$  GeV/nucleon).

At RHIC ( $\sqrt{s} = 65\text{--}200$  GeV/nucleon), the multiplicity per participant is obviously higher, due to the higher  $\sqrt{s}$ , with values ranging from  $\sim 2.5$  at  $\sqrt{s} = 65$  GeV/nucleon, to  $\sim 3.7$  at  $\sqrt{s} = 200$  GeV/nucleon, for central collisions. These data indicate an approximately logarithmic scaling of the multiplicity per participant as a function of  $\sqrt{s}$ . Furthermore, the multiplicity per participant shows a clear increase with centrality. At  $\sqrt{s} = 200$  GeV/nucleon, for example, PHOBOS measures a  $\sim 35\%$  rise in this quantity between peripheral and central events [129]. This result shows that new features appear in the particle production mechanism at RHIC with respect to the SPS. Various theoretical models have been developed, in order to explain these new features. In a first, phenomenological approach, Kharzeev and Nardi [111] have expressed the measured  $dN_{\text{ch}}/d\eta|_{|\eta|<1}$  as the sum of two terms, one proportional to  $N_{\text{part}}$  (soft component) and one proportional to the number of nucleon–nucleon collisions  $N_{\text{coll}}$  (hard component):

$$\frac{dN_{\text{ch}}}{d\eta} = (1-x)n_{\text{pp}} \frac{N_{\text{part}}}{2} + xn_{\text{pp}}N_{\text{coll}}, \quad (6.6)$$

where  $n_{\text{pp}}$  is the pseudo-rapidity density of charged particles, measured in pp collisions at the same nucleon–nucleon centre-of-mass energy. By fitting the measured data as a function of centrality, they found  $x = 0.09$  at  $\sqrt{s} = 130$  GeV. In the spirit of this simple model this means that 37% of the observed multiplicity has been produced in hard processes.

A more conceptual approach, based on the parton saturation concept, has been successively developed and has been found to describe rather well the RHIC data [146]. Basically, in the low- $x$  regime probed at RHIC energies, an incoming parton probes a transverse area  $1/Q^2$  inversely proportional to the momentum transfer  $Q^2$ . When  $Q^2$  is lower than a certain value  $Q_s^2$ , the parton system starts to appear dense to the incoming probe (saturation), and a different theoretical approach, based on the so-called classical Chromo-Dynamics, must be adopted. In this framework, the multiplicity scales in first approximation with the number of participants, but there are important logarithmic corrections from the evolution of the parton structure functions with the saturation scale  $Q_s^2$ . It turns out that also this approach reproduces in a satisfactory way the observed centrality dependence of charged multiplicity, showing that high density QCD effects probably play an important role in determining the global event features of at RHIC energies.

In the following sections we will show how relatively simple estimators of the charged multiplicity can be built, and we will study their properties. For the central pseudo-rapidity region, the two innermost layers of the ITS [1] will be used for the determination of the density of charged particles, while in the forward region the FMD [123] will be used.

**6.1.3.1. Measurement of multiplicity and  $dN_{\text{ch}}/d\eta$  in ITS.** The measurement of the charged particle multiplicity and the reconstruction of the pseudo-rapidity  $\eta$  in the barrel region can be efficiently performed with the two SPD layers of the ITS.

In the following we consider the reconstruction of the pseudo-rapidity ( $\eta$ ) distribution and the measure of the multiplicity for charged particles in the central ( $|\eta| < 0.5$ ) and in the full

acceptance regions ( $|\eta| < 2$  for layer 1,  $|\eta| < 1.4$  for layer 2). The resolution is determined as a function of the multiplicity.

Two different methods are considered:

1. Counting of the number of clusters  $N_c$  for each layer, where a cluster is defined by a number of contiguous pixels with a signal exceeding a defined threshold.
2. Counting of the number of tracklets  $N_t$ , where each tracklet is defined by the association of the clusters in the two layers. The association is done by considering a straight line extrapolated to the primary vertex, assumed to be known [147], and within a fiducial window. This window is defined by the cuts on the longitudinal and radial residuals, i.e. the differences between the coordinates of the centre of the cluster with respect to the expectation from the straight line. This method is somewhat similar to the one used by PHOBOS [105] for multiplicity studies at RHIC.

In both cases the pseudo-rapidity  $\eta$  is evaluated by considering a straight line to the vertex. Measurement errors and resolutions are then reported for both methods.

The simulation requires a complete description of the detector response, and an algorithm for clusters identification [19, 20].

In principle, a special running session with the L3 magnetic field off will offer the best configuration for this measure. For this reason most of the simulations were performed without magnetic field. Subsequently, the effect of the field was studied with a dedicated simulation, with different field values.

A sample of about 1000 events was generated with HIJING 1.36 and tracked in the ALICE apparatus. The impact parameter was generated with a flat distribution in order to increase the statistics in the central class, then the appropriate weights were introduced in order to reproduce a minimum bias distribution. A special sample of very low-multiplicity events was also generated using a HIJING parametrization. As the acceptance and then the measured multiplicity depend on the vertex longitudinal position  $z_v$ , a scan on several  $z_v$  values was also performed.

The correlation between the generated and the reconstructed multiplicities is shown in Fig. 6.19 for  $z_v = 0$ . Here  $dN/d\eta$  indicates the charged multiplicity in the central unit of  $\eta$ .

The reconstructed  $dN/d\eta$  is evaluated by counting the number of clusters  $N_c$  in either layer 1 or layer 2 (top and middle plots), or by counting the number of tracklets (bottom). The statistical errors are smaller than the size of the symbols in figure. The hit multiplicities  $N_h$  produced by the primary particles are also reported, where a hit is defined as the crossing of a particle on a layer through its sensitive volume. There is almost no difference between  $N_c$  and  $N_h$  in layer 1 (upper plot), both being slightly lower than the ideal value (the straight line, corresponding to the diagonal) due to small geometrical losses and cluster merging at high multiplicity. On the contrary,  $N_c$  is enhanced in layer 2 (central plot) by the secondaries produced in the inner layer and by the double hits of the tracks due to the ‘turbo geometry’. In such a geometry, the pixel ladders are not perpendicular to the radial direction, but slightly tilted. In this way there is a superposition between the edges of adjacent ladders.

The situation for the tracklets is close to that of layer 1, but at high multiplicity some inefficiency is visible (bottom plot). In principle, the second method (tracklets) should be cleaner, allowing for background rejection (noise, secondary particles), but the association efficiency decreases as a function of the multiplicity. On the contrary, the first method is more reliable at high multiplicity, as the statistical fluctuations become negligible. However, the level of background can have a large influence on the cluster number. Similar results are observed considering the full  $\eta$  range.

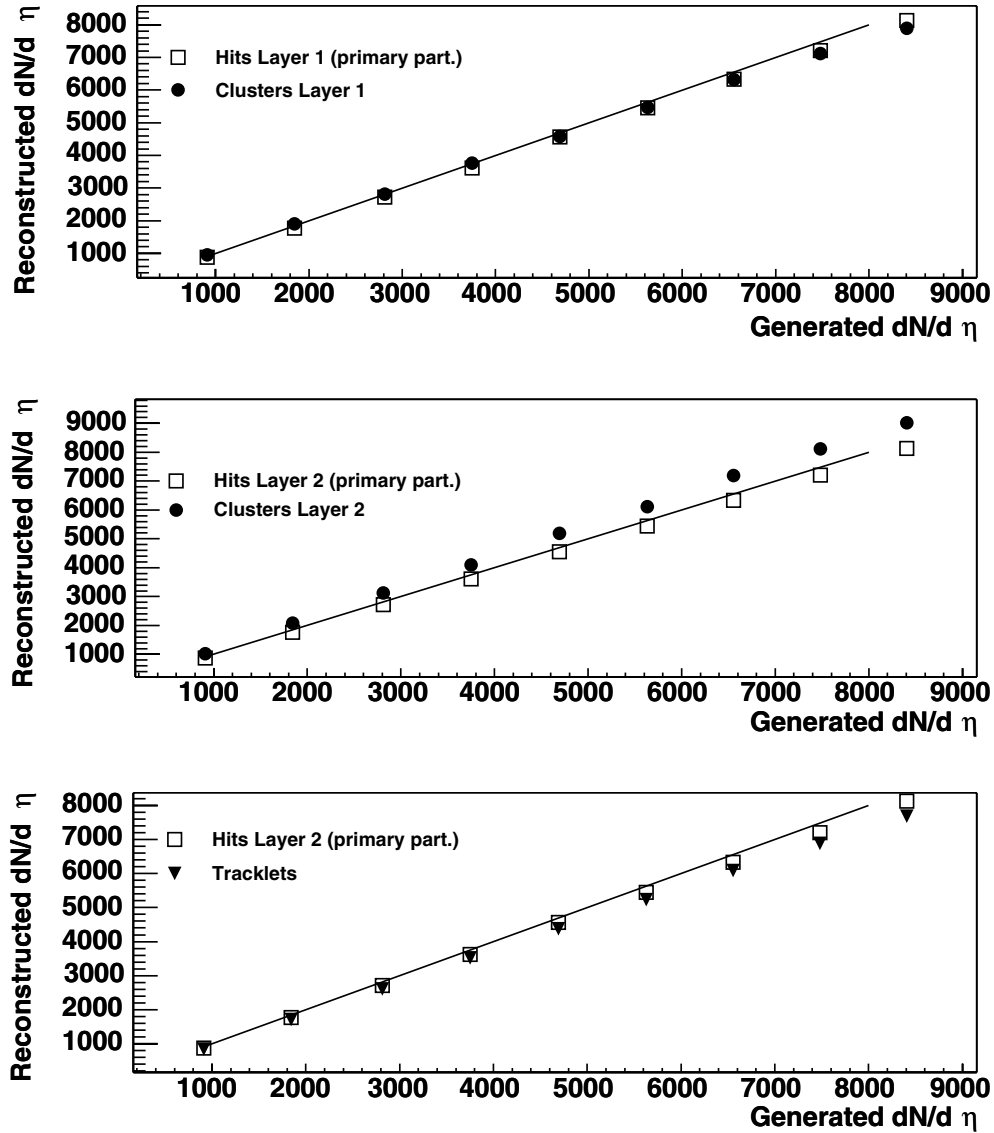


**Figure 6.19.** Number of hits and clusters for layer 1 (top) and 2 (centre) and number of tracklets (bottom) in the central unit of  $\eta$  as a function of the generated multiplicity. The straight line corresponds to the diagonal. The longitudinal vertex position is fixed to zero.

In order to study the dependence on the vertex position, Pb–Pb events were generated with different  $z_v$  from 0 up to  $\pm 10$  cm (about two times the expected standard deviation of the primary vertex diamond). The resulting acceptances for the two layers are shown in Fig. 6.20 where the ratio between the number of hits on the detector and the number of generated particles is shown as a function of  $z_v$ . We note also that due to the vertex spread, the acceptance in  $\eta$  for the second layer can be increased up to about  $|\eta| < 1.5$ .

In Fig. 6.21 and 6.22 the number of clusters and tracklets is reported as a function of the noise level for low ( $dN/d\eta = 40$ ) and high ( $dN/d\eta = 3750$ ) multiplicity, respectively. The

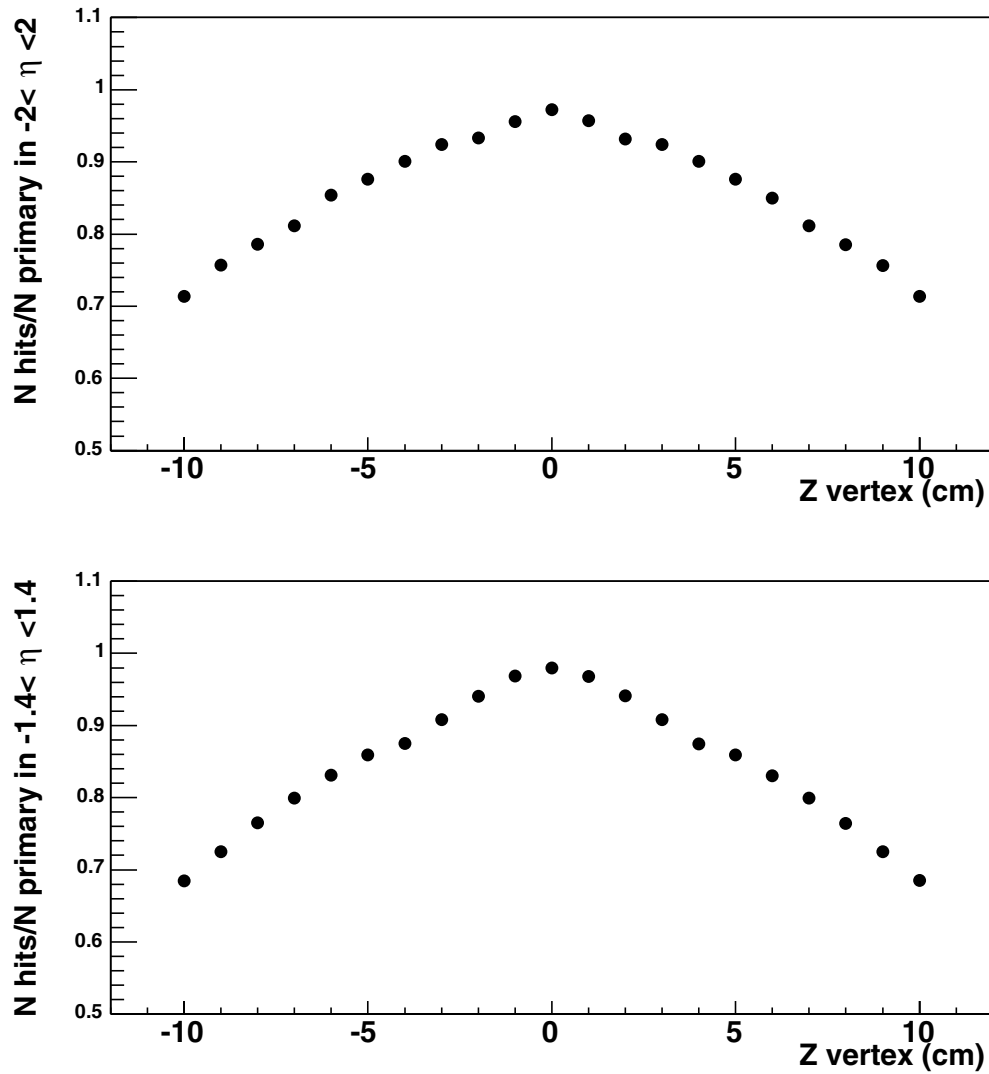


**Figure 6.20.** Ratio between the number of hits and the number of generated particles as a function of the vertex longitudinal position, for the first (up) and second layer (bottom) respectively.

expected value of the noise corresponds to the first point of the plots (280 electrons); the considered range goes to very high noise level in order to study our sensitivity up to the worst conditions.

It can be seen that when the noise level exceeds a value of about 550 electrons the multiplicity of the clusters starts to increase, in particular for layer 2. At low multiplicity the number of tracklets remains almost constant up to the larger noise level (Fig. 6.21). As the tracklets are constructed starting from the clusters on layer 1 and looking for a corresponding cluster in layer 2 within a fiducial window [148], at low multiplicity even a loose selection of the fiducial window is enough to reject the background. However, at higher multiplicity, the number of tracklets follows the increase of the number of clusters in layer 1 (Fig. 6.22, full triangles). A more severe window definition is therefore needed in order to reject the

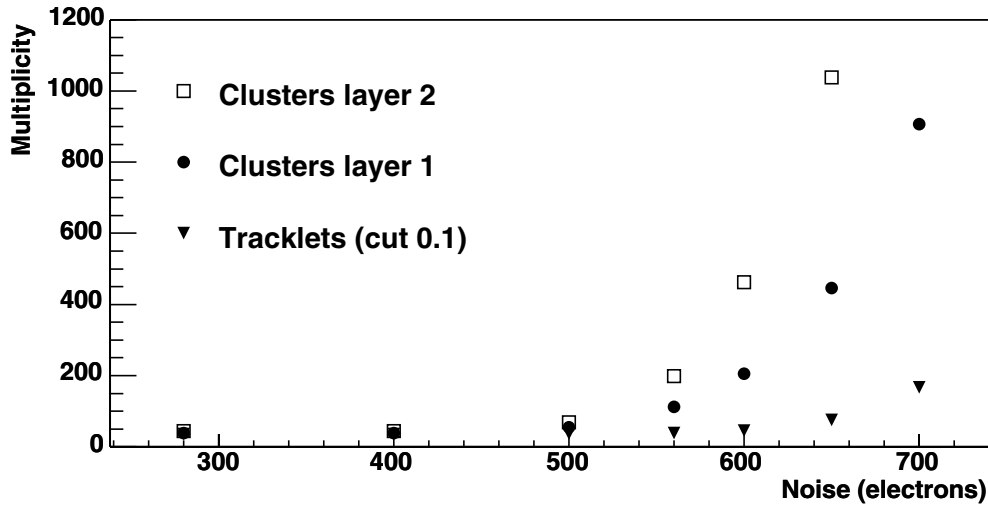


**Figure 6.21.** Number of clusters and tracklets as a function of the noise level for a low multiplicity event.

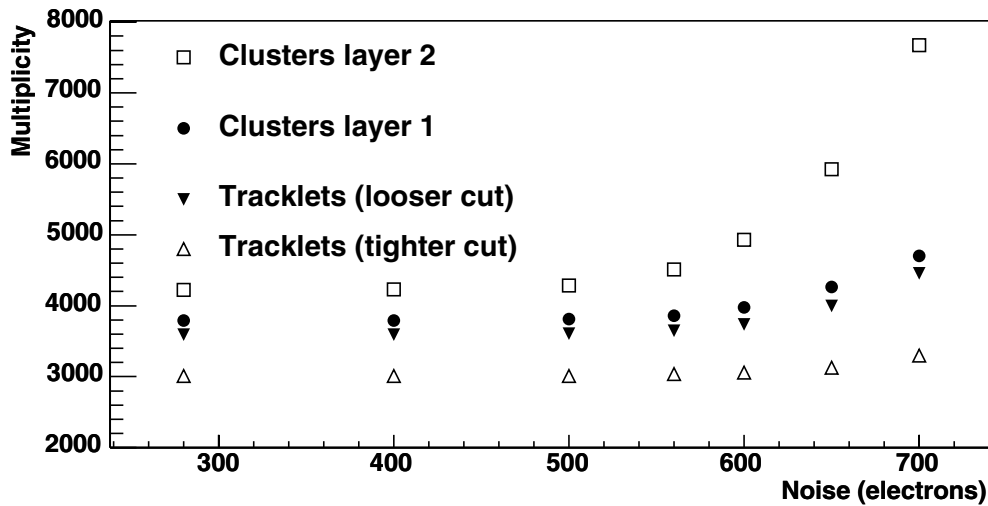


**Figure 6.22.** Number of clusters and tracklets as a function of the noise level for a high multiplicity event. Two different sizes of the tracklet fiducial window are considered.

noise, even if the overall efficiency is strongly decreased (Fig. 6.22, open triangles). As the clusters associated to the tracks in layer 2 are with more probability made of more than one pixel (because of the ‘turbo’ geometry), while the noise typically excites single pixels, one could avoid the use of single pixel clusters of layer 2 for the tracklets construction. This selection removes almost all the noise with a global decrease of the efficiency (as some true tracks are also removed) in a way much similar to the previous case. Finally, we note that the noise due to electronic cross talk is negligible. A more detailed study of the tracklets efficiency in different conditions and with different methods can be found in Ref. [148].

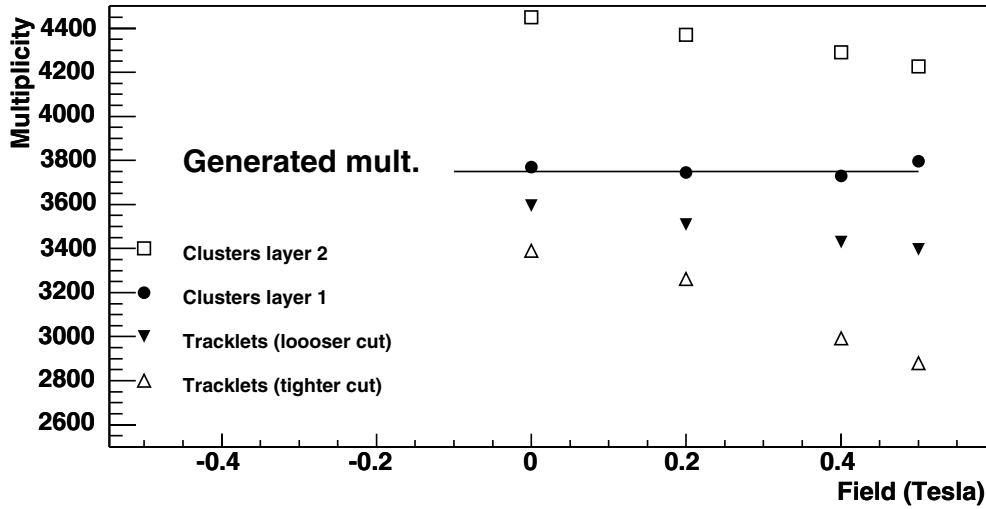


**Figure 6.23.** Reconstructed multiplicity as a function of the magnetic field intensity. For tracklets two different cuts on the fiducial window are considered.

The previous analysis was performed under the condition of no magnetic field. In Fig. 6.23 the measured multiplicity is reported as a function of the magnetic field intensity. The field values are those foreseen to be used in the ALICE experiment (0.2, 0.4 and 0.5 Tesla). It can be seen that the number of clusters in the first layer is insensitive to the field, whereas the number of clusters in the second layer and therefore the number of tracklets is slowly decreasing with increasing field strength. This is mainly due to the tracks of very low momentum which are unable to hit the second layer.

For tracklets two different cuts on the fiducial window are used. It can be seen that in the presence of the magnetic field the efficiency strongly depends on the size of the fiducial window.

An example of  $dN/d\eta$  reconstruction is reported in Fig. 6.24 for multiplicity  $dN/d\eta \simeq 3000$  and  $B = 0.4$  T. Events were generated with random vertex longitudinal position in the range  $\pm 5$  cm. The full line corresponds in both plots to the generated  $\eta$  distribution. In the upper picture the distributions obtained with hits (squares) and clusters (points) in the first layer are shown. A clear discrepancy between the distributions which increases with  $|\eta|$  can be seen, as a consequence of the displacement of the main vertex. Also, some background is present in the clusters, again increasing with increasing  $|\eta|$ .

In the bottom picture the generated distribution is compared with the reconstruction performed with the tracklets, with and without the geometrical acceptance correction (triangles and open circles respectively). A good agreement is obtained in this last case, also outside  $|\eta| < 1.4$ , which is the geometrical limit corresponding to  $z_v = 0$ . The underestimation of the central  $dN/d\eta$  observed for the uncorrected distribution is due to the presence of several geometrical holes, corresponding to the junctions of the ladders. They occur at pseudo-rapidity  $\eta = \pm 1.35$  (first layer),  $\eta = \pm 0.8$  (second layer) and  $\eta = 0$  (both layers).

At high multiplicity the statistical fluctuations are completely negligible compared with the systematic effects (see Figs. 6.19 on page 1507 and 6.37 on page 1521). These effects are accounted for by the simulation, the main source being the production of background secondaries.

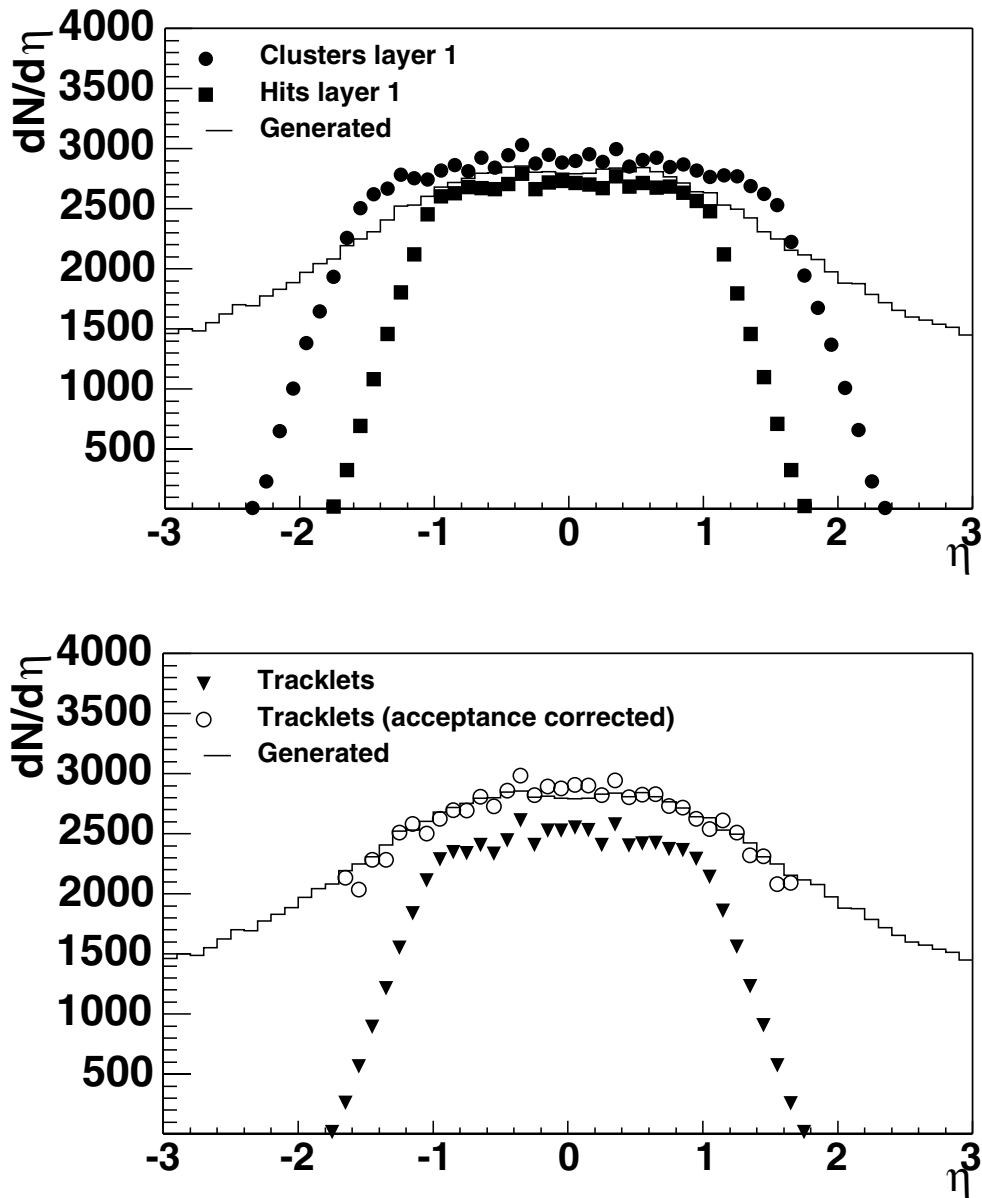
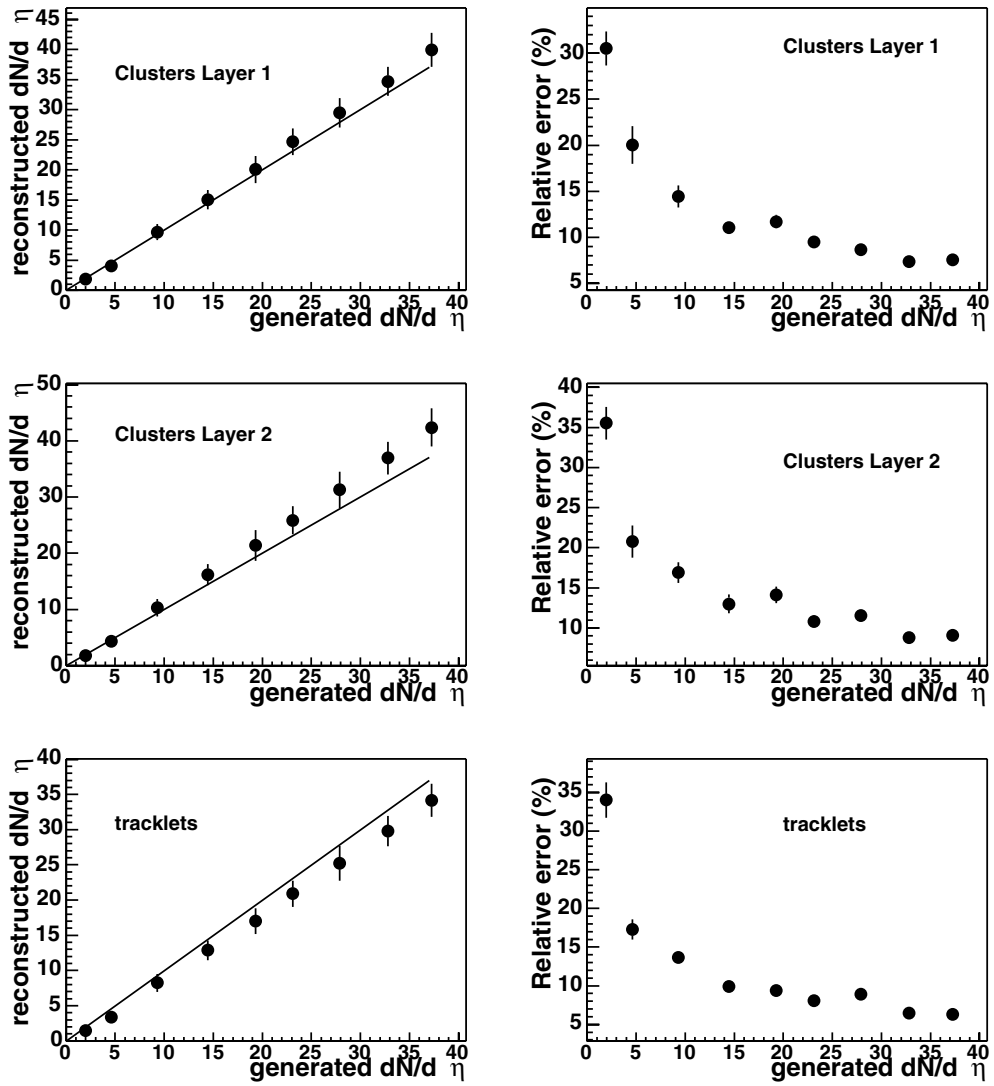


Figure 6.24. Generated and reconstructed  $\eta$  distribution, for  $B = 0.4$  T.

At very low multiplicity fluctuations become dominant, as shown in Fig. 6.25, where on the left side the reconstructed  $dN/d\eta$  is shown as a function of the generated  $dN/d\eta$ , for each method. Two hundred events were generated for each multiplicity bin, and the distribution of the difference between reconstructed and generated  $dN/d\eta$  was fitted by a Gaussian. The resulting  $\sigma$  parameter is plotted as error bar on the same plot. The corresponding relative error  $\sigma/(dN/d\eta)$  is shown in the same figure (right side). It can be seen that a very low  $dN/d\eta$  ( $\simeq 10$ ) can be measured within a 10% relative error.



**Figure 6.25.** Spread of the reconstructed  $dN/d\eta$  as a function of the generated  $dN/d\eta$  (left), and relative error as a function of the generated  $dN/d\eta$  (right).

The resolution on the determination of the single track pseudo-rapidity can be seen in Fig. 6.26, where a track-by-track distribution of the differences between generated and reconstructed  $\eta$  is shown. A Gaussian fit gives  $\sigma = 0.002$   $\eta$ -units.

**6.1.3.2. Multiplicity reconstruction by the Forward Multiplicity Detector (FMD).** The charged particle multiplicity measurement, which will be performed in ALICE by several detector systems like ITS, FMD and PMD has several physics purposes. In Pb–Pb collisions, the primary goal is to obtain information on the pseudo-rapidity density of charged particles produced in the collisions, but interesting information on non-statistical fluctuation in the particle yield as well as on the centrality of the collision can also be extracted.

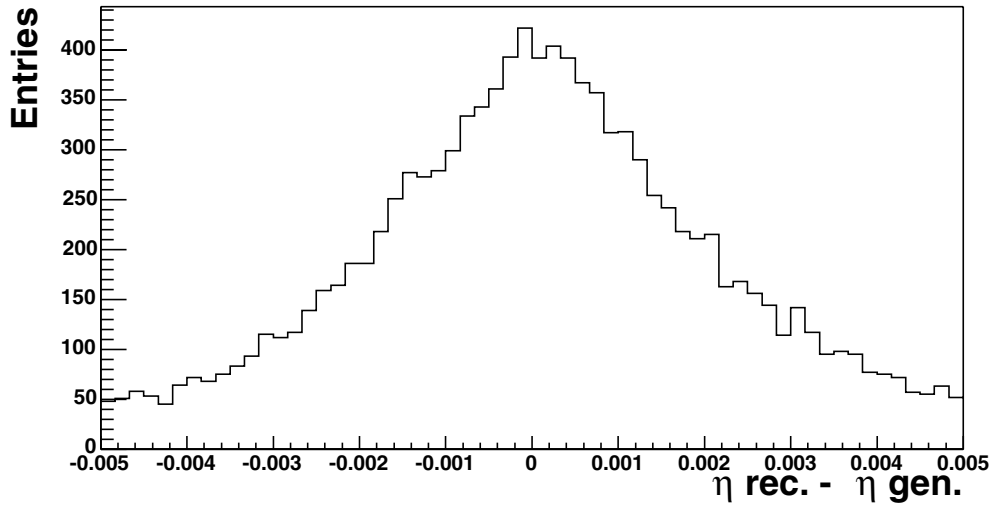


Figure 6.26. Distribution of the differences between generated and reconstructed  $\eta$ .

It is well known that high values of the number of participant nucleons  $N_{\text{part}}$ , corresponding to the most central collisions, can be extracted by selecting events with high charged multiplicity  $N_{\text{ch}}$ . However, the systematic ambiguities in the correlation between  $N_{\text{ch}}$  and  $N_{\text{part}}$  impose an accuracy not worse than 10% in the determination of  $N_{\text{ch}}$  in order to have a meaningful physics measurement.

In order to reach such an accuracy for the FMD, a high granularity is obviously required. In the final layout of the detector 512 rings and 20 sectors are foreseen for the inner crowns, while the outer crown will be subdivided into 256 rings and 40 sectors (see Chapter 3 of Volume I [3] for details). Unfortunately, even with this granularity it turns out that the occupancy in the detector for central events will be of the order of 100% or even larger. Using HIJING for Pb–Pb collisions, we estimate an occupancy between 0.8 and 2.2 particles per pad for the Si1 detector (inner) and between 0.4 and 0.9 for the other detectors. Therefore, it will not be possible to determine the multiplicity by simply counting the pads which have fired, due to the large contribution of hits from more than one incident particle.

A possibility to overcome this problem is to estimate the multiplicity per pad from the measurement of the total deposited energy in that pad. This method might be affected from sizeable systematic errors, due to the importance of the tails of the Landau energy loss distribution. However, a special algorithm, tuned for an occupancy per pad between 4 and 8 particles was developed for the multiplicity estimate from deposited energy in order to reduce these uncertainties. In this approach the charged particle multiplicity measured in a strip or in a group of strips is obtained by dividing the total detected signal by the average signal deposited by a single particle. Then, to give an estimate of the primary multiplicity, the measured multiplicity must be corrected for the contribution of secondaries, as estimated from a Monte Carlo simulation. The relative accuracy of the multiplicity determination can be increased by adding signals from several strips, e.g. by summing over strips with different azimuthal angles but with similar rapidities, or integrating over rapidity by grouping strips in a given azimuthal sector.

The simulations were done by using a single central HIJING event for Pb–Pb, integrating over strips in the interval  $1.71 < \eta < 3.58$ . The energy loss spectrum was generated by assigning Landau responses to each detector hit. The reconstructed multiplicity was then

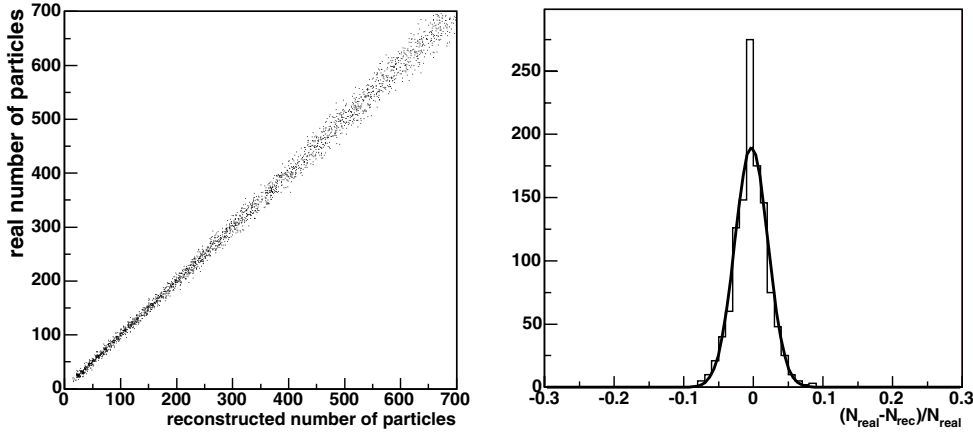


**Figure 6.27.** Comparison between HIJING generated and reconstructed number of particles on the Si1 detector (integrated over the detector acceptance).

obtained by counting the number of hits in energy intervals  $\Delta E_n$  around the  $n$ -th peak. An iterative procedure was used to determine such intervals. In the first step the energy loss corresponding to one particle was defined as the interval from zero to the minimum of the sum of the Landau distributions corresponding to two particles hit on the pad ( $\Delta E_2$ ). Similarly, double hits were defined as energy deposited in the interval from  $\Delta E_2$  to  $\Delta E_3$ , the latter being the minimum of the sum of three Landau distributions, and so on. In the following step, the set of interval boundaries  $\Delta E_2, \Delta E_3, \dots$  were adjusted in order to minimize the difference between the generated and reconstructed multiplicity distributions. With this method, the relative accuracy of reconstruction in different pseudo-rapidity intervals is of the order of 5%.

An alternative method, based on the counting of empty pads, was also developed. The simulations show in fact that with the present geometry and granularity of the FMD, and for a mean occupancy per pad ranging from 0.4 to 2.2, there is a statistically significant number of empty pads when one considers 0.1 unit-wide pseudo-rapidity bins. Therefore, using the Poisson statistics, the average occupancy  $\lambda$  can be determined as:  $\lambda = -\ln P(0)$ , where the probability  $P(0) = N_e/N_{\text{tot}}$  is the ratio of the number of empty pads  $N_e$  to the total number of pads  $N_{\text{tot}}$  in a certain  $\Delta\eta = 0.1$  interval. Then, the total multiplicity  $n$  can be simply calculated as  $n = \lambda \times N_{\text{tot}}$ .

In the present algorithm for the reconstruction of multiplicity in the FMD we assume that the pad is empty when the ADC signal is below a given threshold, that will be chosen in order to be below the signal of the minimum ionising particle, but higher than the noise level. The fine tuning of the threshold must then be chosen in order to have a reconstructed multiplicity as close as possible to the real one. The accuracy of this method is better than 3% as shown in Fig. 6.27, where the comparison of the reconstructed and total generated particles (including secondaries) is presented.

In order to obtain from the measured multiplicity the real primary multiplicity it is necessary to subtract the contribution from secondary particles. It turns out that most of it comes from the ITS detector structure and from the beam pipe. The correction coefficients as a function of  $\eta$  have been determined using a simulation based on a sample of 200 HIJING events with an impact parameter range  $0 < b < 11.2$  fm. The results are shown in Fig. 6.28 for the complete  $\eta$  range covered by the FMD. The error bars plotted on this figure represent the r.m.s. deviations of the reconstructed  $dN/d\eta$  distributions for a single event. The errors

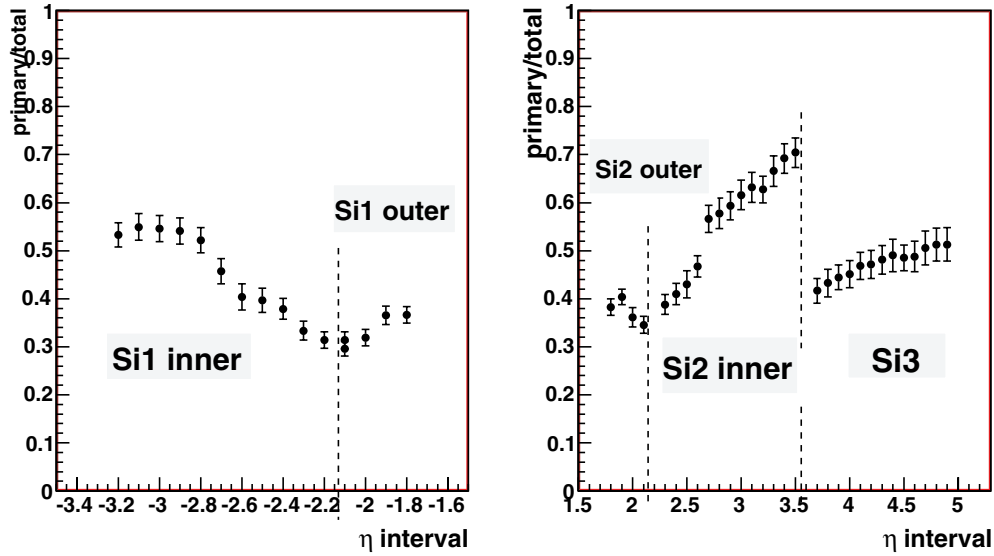


Figure 6.28. Rapidity dependence of the primary to total particles ratio.

on the mean values of the ratio primary/total (not plotted) are inversely proportional to the square root of the number of simulated events.

The background correction procedure could be refined using the information from the ITS detector. By determining the position of secondary re-interaction vertices and tracking the corresponding background particles down to the FMD one could subtract their contribution from the estimated multiplicity.

The apparent break in Fig. 6.28 at  $\eta = -3.6$  is due to the different  $z$ -position of Si2 inner ( $z = -83.4$  cm) and Si3 ( $z = -345$  cm) detectors. For Si2 the contamination by secondary particles turns out to be smaller since this detector is closer to the interaction point. Finally, when the ratios of Fig. 6.28 are computed for various centrality bins, the r.m.s. deviations are much smaller for the most central events sample, since in this case the multiplicity per event is large, leading to a smaller statistical error in the estimate of the ratio primary/total.

In Fig. 6.29 we show the reconstructed vs. generated primary multiplicity for some specific rapidities.

A parameterization of the HIJING generator (80 events) has been used for this analysis. The plots refer to 0.1-unit pseudo-rapidity intervals centred at  $\eta = 1.7$  (corresponding to the Si1 outer detector),  $\eta = 3.4$  (Si1 inner) and  $\eta = 5.0$  (Si3). The relative r.m.s. deviations on the reconstructed primary particle multiplicity are dominated by the statistics of the generated primary particles per event, and are inversely proportional to the square root of the number of particles falling in the small  $\eta$ -interval considered. Therefore, the relative r.m.s. deviations shown in Fig. 6.29 are considerably larger for low multiplicities. Of course, by choosing a somewhat larger  $\eta$ -binning (of the order of 0.5) one could reduce them to less than 10% even for peripheral events. It should anyway be noticed that in any case the average values of primary particles multiplicity, even with the small event sample used in this analysis, are reconstructed with good accuracy. Of course, the accuracy is better for central events due to larger statistics of primary particles. Finally, it should be noted that, since the production of secondaries per primary particle is approximately constant as a function of centrality, the primary to total ratio is also centrality independent.

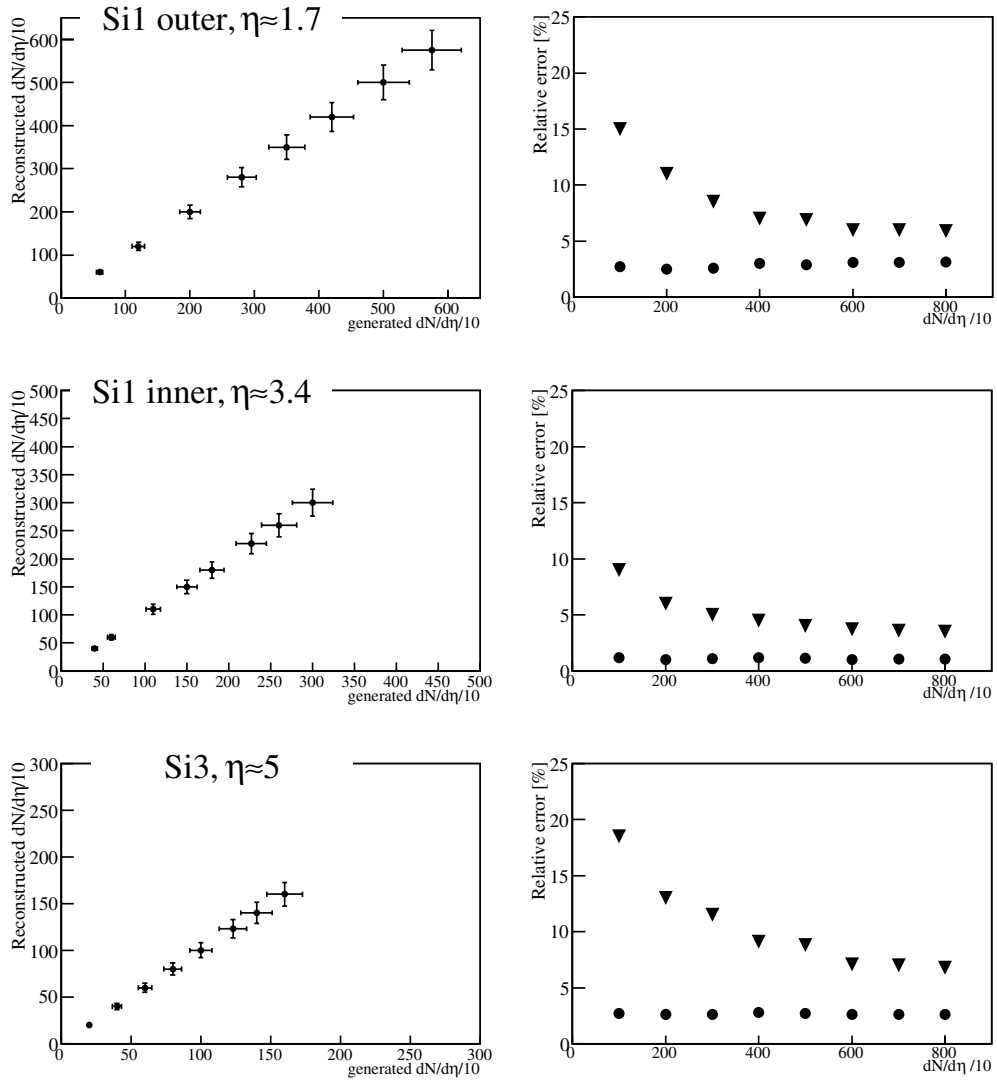


**Figure 6.29.** Left panels: reconstructed multiplicity ( $dN/d\eta$ ) from HIJING, using the Poisson method, as a function of the generated multiplicity for three different pseudo-rapidity values ( $\eta = 1.7$  (Si1 outer),  $\eta = 3.4$  (Si1 inner) and  $\eta = 5$  (Si3)). Right panels: relative r.m.s. deviations, for the total multiplicity, using the Poisson method (circles). Triangles show the relative r.m.s. deviations after correcting for the contribution of secondaries.

An example of a multiplicity distribution in the FMD acceptance, using all the FMD crowns, is shown in Fig. 6.30. It corresponds to a set of 80 central HIJING events ( $dN/d\eta = 6000$  for  $\eta = 0$ ). One should note that the rapidity coverage of the FMD overlaps with that of the ITS in the pseudo-rapidity intervals  $1.7 < \eta < 2$  and  $-2 < \eta < -1.7$ . As will be shown in next section this allows a measurement of the charged multiplicity over a continuous interval about 8  $\eta$ -units wide.

Finally, since the measured pseudo-rapidity distribution could be different from the one obtained by HIJING, the background correction coefficients of Fig. 6.28 should be considered

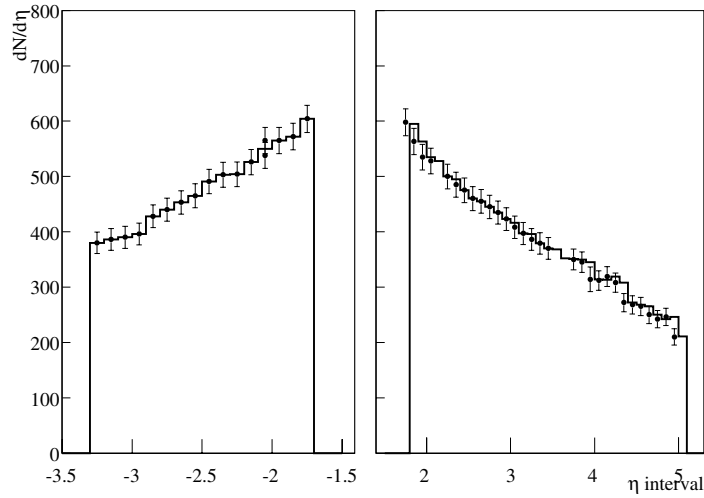


**Figure 6.30.** Reconstructed  $dN/d\eta$  distribution for 80 HIJING events ( $dN/d\eta = 6000$ ). The histogram represents the generated primary distribution, while the points correspond to the number of reconstructed primary particles.

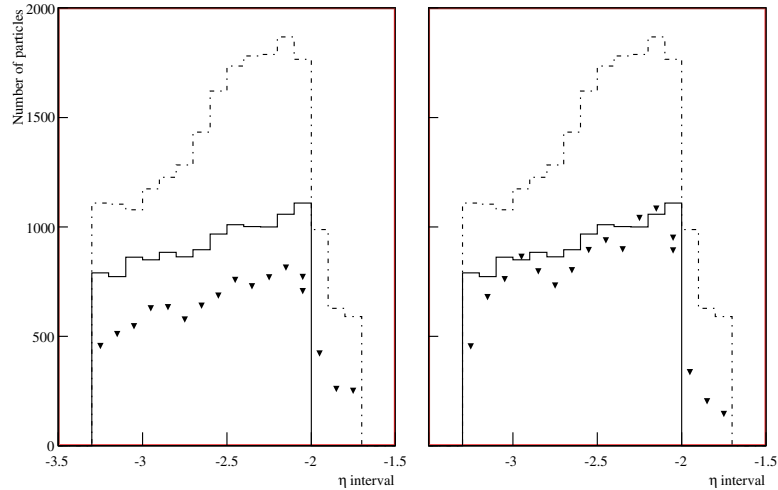


**Figure 6.31.** Result of the iterative procedure applied to a 'step-like' rapidity distribution. The continuous line histogram is the generated primary distribution, the dashed line histogram corresponds to the total number of hits in the detector (primary + secondary), while the triangles represent the reconstructed primary distribution. The figure shows the first two iterations.

as a first approximation. One can therefore develop an iterative method for a more accurate estimate of these coefficients. Basically, after applying the HIJING-calculated coefficients to the raw multiplicity distribution obtained from experimental data, one could use the corrected distribution as an input to the simulation. In this way a second set of correction factors can be calculated and so on, until a convergence towards stable values is reached. The reliability of this method has been tested by using simple, unphysical multiplicity distributions. In Fig. 6.31 and Fig. 6.32 one can observe a reasonable agreement between the generated and reconstructed distributions already after two steps in the iteration.

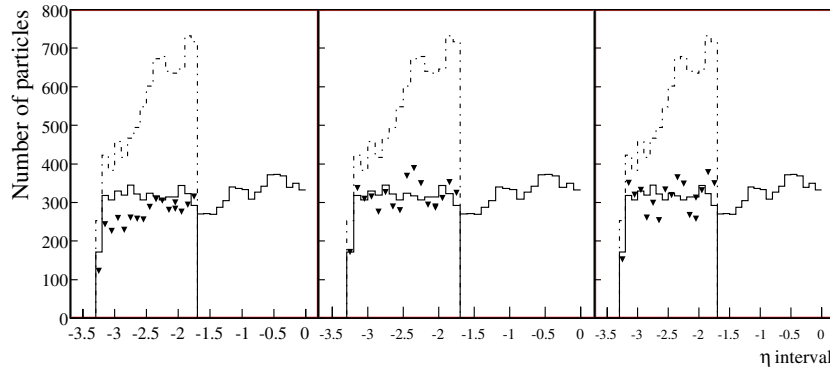


**Figure 6.32.** Result of the iterative procedure applied to a flat rapidity distribution. The continuous line histogram is the generated primary distribution, the dashed line histogram corresponds to the total number of hits in the detector (primary + secondary), while the triangles represent the reconstructed primary distribution. The figure shows the first three iterations

This method could be also used to reduce some systematic errors connected with critical zones of the detectors (e.g. overlapping regions) or with uncertainties in the description of the materials budget.

In summary, the forward multiplicity can be estimated in ALICE using the proposed FMD set-up which includes five Si-strip detectors. The pseudo-rapidity coverage will be  $1.6 < \eta < 3.4$  and  $-5 < \eta < -1.7$ , and we expect to reach an accuracy at the level of a few percent in the measurement.

**6.1.3.3. Pseudo-rapidity coverage in ALICE.** The study of the charged particle distribution over a wide  $\eta$  range plays an important role in the event characterization. While the central region is especially sensitive to the details of the hadroproduction mechanism, the study of the forward region is essential in order to really constrain the models and to investigate effects connected with the fragmentation of the projectile and the target. This issue has been recently studied at RHIC, where it has been shown [149] that the ‘limiting fragmentation’ region, where the pseudo-rapidity distribution becomes energy-independent, is larger than expected, extending more than two  $\eta$ -units away from beam rapidity.

In ALICE, thanks to the  $\eta$ -coverage of ITS and FMD one can measure the multiplicity distributions over about 8  $\eta$ -units. In Fig. 6.33, we show, for a single central HIJING event, the generated and reconstructed multiplicity distributions. For what concerns the central region, we show the results obtained with both the cluster counting and the tracklets method, described in Section 6.1.3.1, not corrected for acceptance effects. One can see that even for a single event the accuracy on the multiplicity determination, when using a bin width of 0.1  $\eta$ -units, is of the order of 7%. The few bins in the ITS acceptance region where one observes a clear underestimation of the multiplicity are simply due to the geometrical junctions of the ladders of the ITS (see Section 6.1.3.1).

**6.1.4. Multiplicity vs. centrality: a physics performance study.** In the previous sections, we have discussed several estimators of the event centrality and of the charged particle multiplicity in ALICE, and we have shown their properties in detail. Now we present the physics performance of the apparatus for a specific study concerning global variables, namely the centrality dependence of the charged multiplicity at mid-rapidity. For this study, about  $10^3$  Pb–Pb events were generated using HIJING, without vertex smearing. In order to have

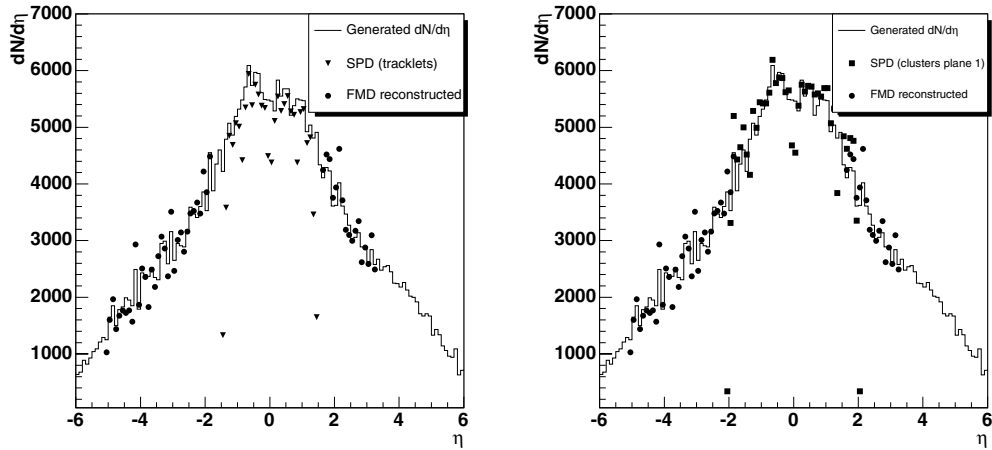


**Figure 6.33.** The reconstructed charged particle  $\eta$  distribution, in the ITS and FMD detectors, for a central HIJING event.

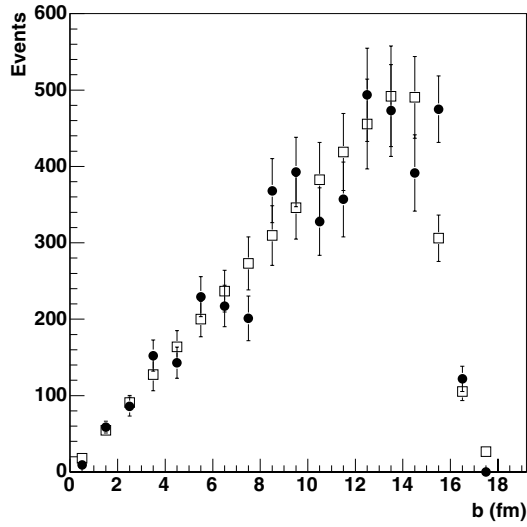


**Figure 6.34.** Generated (open symbols) and reconstructed (closed symbols) impact parameter distributions. The generation was performed using HIJING.

a significant statistics for central events, the generation was performed in various impact parameter classes, with approximately the same number of events per class. Then, the relative normalization between the various classes was computed, introducing appropriate weights in order to reproduce a minimum-bias event distribution.

The events were tracked through the detectors used for this study, namely the ITS and the ZDC, the digitization of the hits was performed, and finally the number of participants, the impact parameter, and the charged multiplicity in the pseudo-rapidity interval  $|\eta| < 0.5$  were reconstructed. The algorithms developed in the previous sections were used for the reconstruction. In particular, for the centrality variables, we adopted the so-called event-by-event method, described in Section 6.1.2.2, while, for the multiplicity, both cluster counting on the first pixel layer and the tracklet method were used. In Figs. 6.34, 6.35, and 6.36

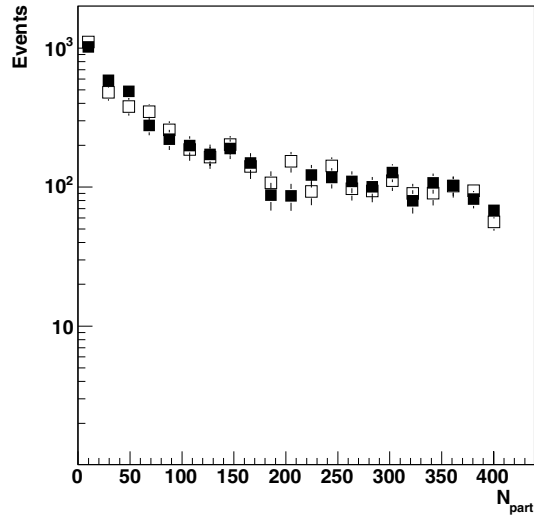


**Figure 6.35.** Generated (open symbols) and reconstructed (closed symbols) participant nucleon distributions. The generation was performed using HIJING.

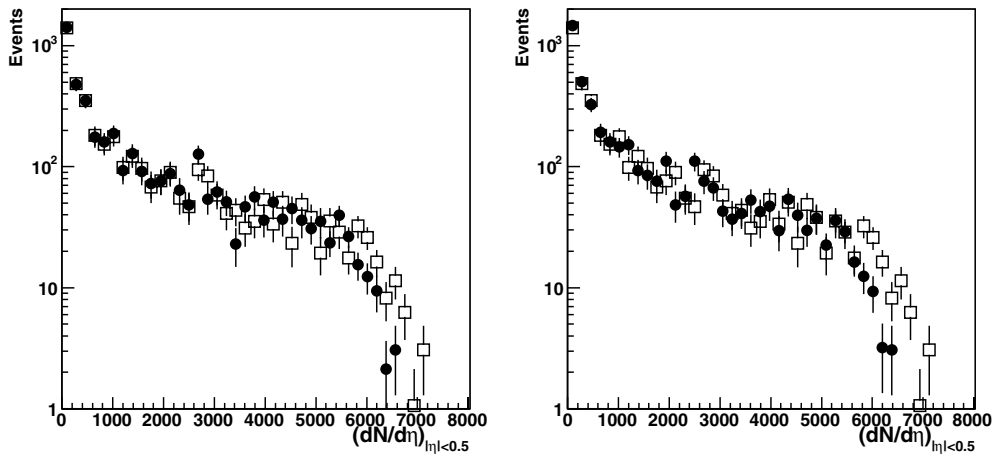


**Figure 6.36.** Generated (open symbols) and reconstructed (closed symbols) charged multiplicity at central rapidity ( $|\eta| < 0.5$ ). The generation was performed using HIJING. The left plot refers to the cluster counting method, the right plot to tracklets.

we show the comparison between the generated and reconstructed distributions for the impact parameter  $b$ , the number of participants  $N_{\text{part}}$  and the multiplicity at mid-rapidity  $dN/d\eta|_{|\eta|<0.5}$ , respectively.

We find that there is good compatibility between generated and reconstructed centrality variables. For multiplicity, an inefficiency of the adopted algorithms becomes visible for central events. The difference between reconstructed and generated multiplicity, as a function of the generated multiplicity, is shown in Fig. 6.37. We see, as already noted in Section 6.1.3.1 that both cluster counting and tracklet methods tend to underestimate the true multiplicity. However, the discrepancy is small, being not larger than 10%.

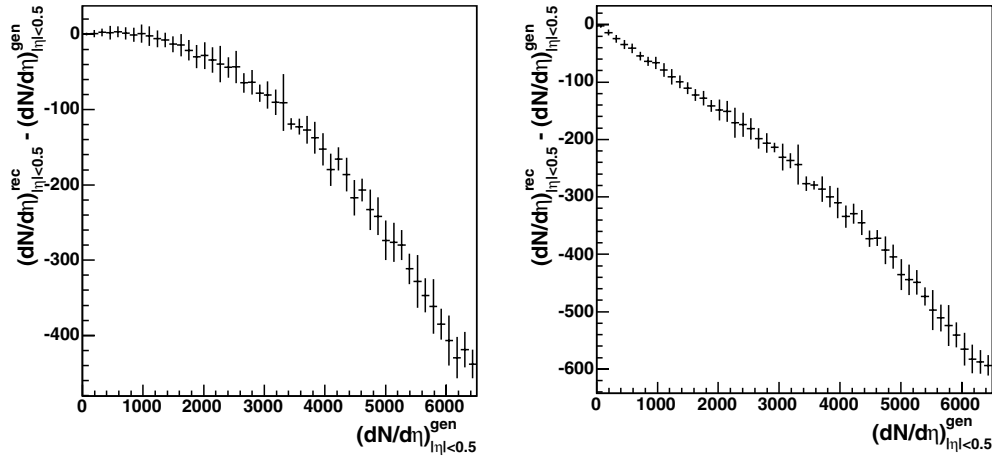


**Figure 6.37.** The difference between reconstructed and generated charged multiplicity at mid-rapidity. The left plot refers to cluster counting, the right plot to tracklets.

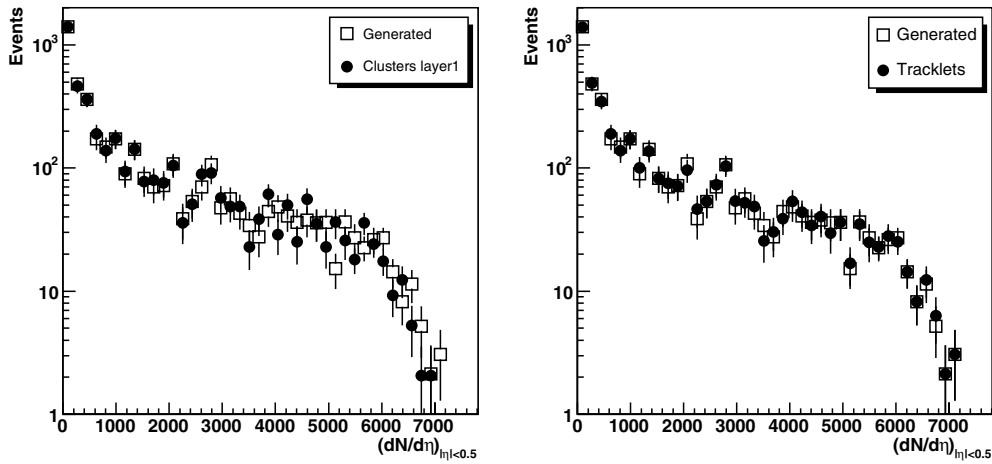


**Figure 6.38.** Generated (open symbols) and reconstructed (closed symbols) charged multiplicity at central rapidity ( $|\eta| < 0.5$ ). The generation was performed using HIJING. The left plot refers to the cluster counting method, the right plot to tracklets. The reconstructed spectra were corrected for the inefficiency of the methods.

Using the information of Fig. 6.37, we corrected the reconstructed multiplicity, event by event, for the average inefficiency of the two methods. In Fig. 6.38 we show the multiplicity distributions, after correction.

For the analysis of the centrality dependence of multiplicity we considered 10 centrality bins, defined through percentages of the Pb–Pb inelastic cross section. For the sake of comparison we used the same centrality binning adopted by PHOBOS for this kind of analysis, which spans from semiperipheral to very central events. We then calculated, for both the generated and reconstructed samples of events, the  $\langle N_{\text{part}} \rangle$  values corresponding to each centrality bin. In Fig. 6.39, we compare the (efficiency-corrected) reconstructed multiplicity with the generated one, as a function of  $\langle N_{\text{part}} \rangle$ . We find a good agreement, using either cluster counting or the tracklet method for the multiplicity reconstruction. The use of HIJING for the

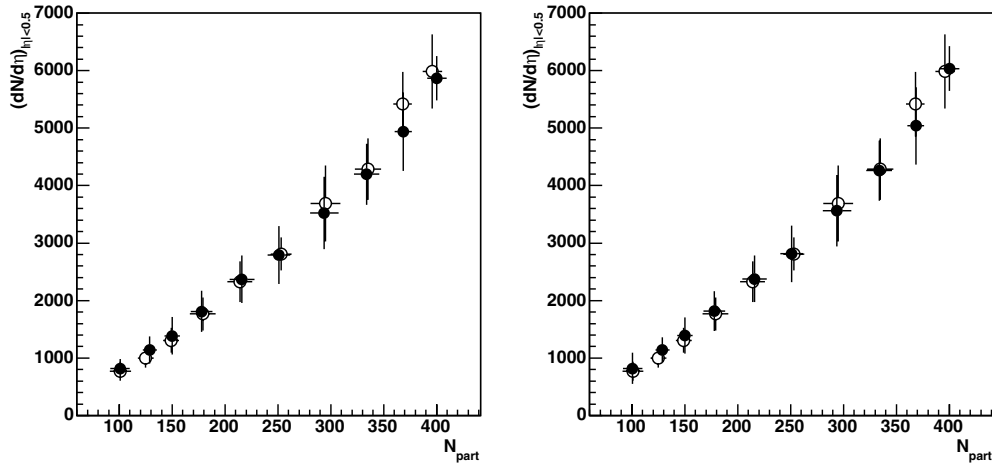


**Figure 6.39.** Comparison of generated (open symbols) and (efficiency-corrected) reconstructed multiplicity (closed symbols), as a function of  $N_{\text{part}}$ , for cluster counting (left) and tracklets (right).

event generation leads to a simulated production, at mid-rapidity, of about 28 charged particles per participant pair for very central events, a value about 7 times larger than the one measured by PHOBOS.

As we explained in Section 6.1.3, from the study of the correlation between multiplicity and centrality it is possible to extract information on the fraction of the total multiplicity due to hard scattering. Therefore, we fitted our results in the framework of the Kharzeev–Nardi [111] model (see Eq. (6.6)). In this way we can try to apply such a description to LHC energies, and, in particular, check if the values of the parameter  $x$  (see Eq. (6.6)) obtained with our reconstruction algorithms are compatible with that at the generation level. For the multiplicity per unit of pseudo-rapidity in pp collision we used the value  $n_{\text{pp}} = 5.0$ , which results from an extrapolation of the parametrization of  $p\bar{p}$  collider data:

$$n_{\text{pp}} = 2.5 - 0.25 \times \ln s + 0.023 \times \ln^2 s. \quad (6.7)$$

The average number of nucleon–nucleon collisions  $N_{\text{coll}}$  corresponding to each bin in  $N_{\text{part}}$  was calculated in the framework of the Glauber model. The only free parameter in the fit is therefore the quantity  $x$ . The results of the fits are presented in Fig. 6.40, for generated and reconstructed data points. The quality of the fits is good, i.e., the simple Kharzeev–Nardi approach is able to reproduce the essential features of the data at LHC energies. The  $x$  values obtained for reconstructed data are  $x = 0.60 \pm 0.03$  (cluster counting) and  $x = 0.57 \pm 0.03$  (tracklet method). The values are in very good agreement with the result of the fit to the generated variables, which yields  $x = 0.61 \pm 0.03$ .

These results show that the reconstruction algorithms developed for centrality and multiplicity can indeed be used to extract physics information from the data. The fraction  $F$  of the produced particles originating in hard processes, defined as

$$F = \frac{x \times n_{\text{pp}} \times N_{\text{coll}}}{dn/d\eta}, \quad (6.8)$$

turns out to be of the order of 80% for the most central Pb–Pb collisions, compared with  $F \sim 37\%$  at RHIC (at  $\sqrt{s} = 130$  GeV/nucleon). In Table 6.8 we present a summary of the results of this analysis.

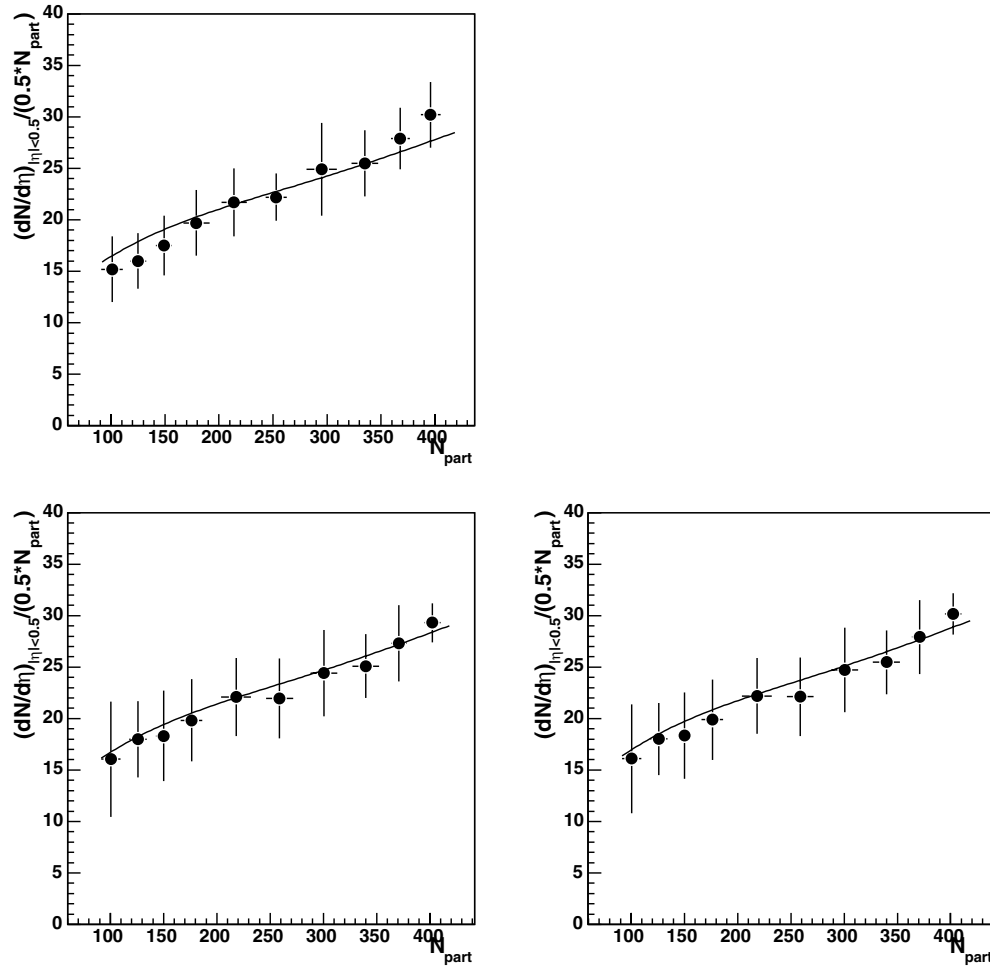


**Figure 6.40.** The results of the fit to the centrality dependence of multiplicity, in the Kharzeev–Nardi approach. The upper plot refers to the generated events, the lower plots to cluster counting (left) and tracklets (right).

**6.1.5. Global event properties in  $pp$  collisions.** In high energy proton–proton collisions most events involve low momentum transfer between incoming and outgoing particles. Therefore, the main feature of minimum bias events is the production of a large number of particles with small  $p_t$ . Because of its sensitivity to very low  $p_t$  (thanks to the low magnetic field and the small amount of material between the interaction region and the tracking devices) and its unique particle identification capabilities, ALICE can explore very effectively the properties of minimum bias events at  $\sqrt{s} = 14$  TeV, such as the distributions of charged tracks in multiplicity, pseudo-rapidity and transverse momentum, in the total sample of events and in any eventual subclass. The knowledge of these properties in a new energy domain is interesting in itself, for a detailed understanding of many topics of fundamental interest like the colour exchange properties or the contribution of low  $x$  to the  $p_t$  spectra, and also for clarifying problems connected with the discrepancies observed at lower energies in the multiplicity distributions. However, it is also an important input to understand the underlying event structures that will act as a background for the experiments searching for

**Table 6.8.** Summary of the results on the centrality dependence of multiplicity.

Cross section (%)	$\langle N_{\text{part}} \rangle_{\text{gen}}$	$\langle N_{\text{coll}} \rangle_{\text{gen}}$	$\langle N_{\text{part}} \rangle_{\text{rec}}$	$\langle N_{\text{coll}} \rangle_{\text{rec}}$
0–3	396	1675	401	1710
3–6	368	1494	370	1510
6–10	335	1295	338	1312
10–15	295	1075	300	1104
15–20	253	866	259	895
20–25	214	689	218	710
25–30	179	540	176	528
30–35	149	419	149	422
35–40	125	328	125	330
40–45	101	242	101	242

Cross section (%)	$dN/d\eta_{\eta < 0.5}$ (gen)	$dN/d\eta_{\eta < 0.5}$ (cluster)	$dN/d\eta_{\eta < 0.5}$ (tracklet)
0–3	$5983 \pm 644$	$5658 \pm 387$	$5499 \pm 392$
3–6	$5146 \pm 559$	$4888 \pm 681$	$4726 \pm 674$
6–10	$4278 \pm 534$	$4136 \pm 531$	$3976 \pm 526$
10–15	$3688 \pm 662$	$3579 \pm 630$	$3425 \pm 623$
15–20	$2810 \pm 287$	$2787 \pm 502$	$2647 \pm 490$
20–25	$2328 \pm 356$	$2372 \pm 413$	$2241 \pm 402$
25–30	$1769 \pm 287$	$1729 \pm 356$	$1622 \pm 347$
30–35	$1307 \pm 215$	$1361 \pm 329$	$1272 \pm 315$
35–40	$1002 \pm 167$	$1124 \pm 235$	$1047 \pm 220$
40–45	$771 \pm 162$	$804 \pm 162$	$747 \pm 269$

$x$	
Generated	$0.61 \pm 0.03$
Rec. clusters	$0.60 \pm 0.03$
Rec. tracklets	$0.57 \pm 0.03$

rare signals (as the Higgs or SUSY particles), and will provide reference data for comparison with heavy-ion data. The latter could be done via interpolation to  $\sqrt{s} = 5.5$  TeV (the centre-of-mass energy for Pb–Pb runs) between the Tevatron and the maximum LHC energy. However, this interpolation will be affected by rather large uncertainties, due to the poor predictive power of current event generators, that are generally ‘tuned’ to each successive energy, and to the differences in acceptance or in the particle identification capabilities between apparatus at different accelerating machines. Therefore it is obvious that, even if we shall focus in this section on pp collisions at  $\sqrt{s} = 14$  TeV, dedicated runs at the same energy as measured in heavy-ion collisions ( $\sqrt{s} = 5.5$  TeV) will be necessary to obtain a more reliable reference to understand the heavy-ion data, as it was shown very clearly by experiments at RHIC (i.e. to extract the nuclear suppression factors in jet quenching studies).

In this section we will present the ability of the ALICE detector to trigger and characterize the proton–proton collisions. The trigger uses the capabilities of the V0 and SPD detectors, while for the event properties we limit ourselves here to the measurements that can be performed with the ITS and TPC detectors. In order to separate effects of the trigger from those coming from the acceptance/resolution we consider a 100% efficient trigger in

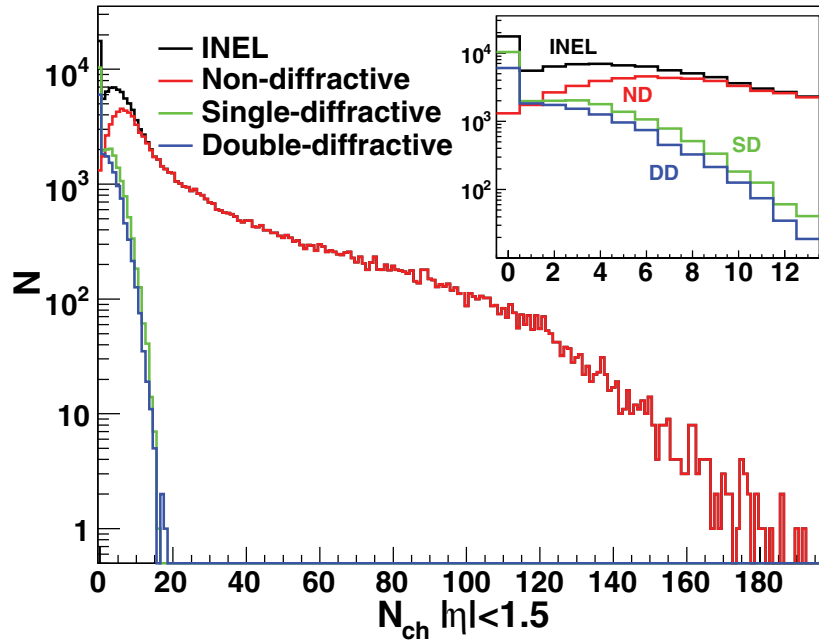


**Figure 6.41.** Charged particle multiplicity ( $|\eta| < 1.5$ ) from PYTHIA 6.214 for different process types. The insert shows the region of low multiplicities.

discussing the measurements of global event properties. This is a very good approximation since, as we will show in Section 6.1.5.1, very efficient minimum bias triggers can be defined.

Our study is based on a Monte Carlo simulation using the PYTHIA event generator [150], the simulation of the detector response (with a value  $B = 0.5$  T for the magnetic field), followed by the full reconstruction and tracking procedures. We used the version 6.214 of the PYTHIA code, with the set CTEQ5L of parton distribution functions (p.d.f.). The input parameters controlling the multiple parton collision scenario used by PYTHIA to model the low  $p_t$  interactions were set according to [151], where those parameters were tuned to reproduce a large set of collider data (see Section 4.3.1 of Volume I [3] for more details on the tuning of PYTHIA parameters). Figure 6.41 shows the generated multiplicity distribution of charged particles in proton–proton collisions according to PYTHIA for single and double diffraction as well as the non-diffractive inelastic contribution and the sum of all these processes.

All the simulations presented throughout this section are based on the analysis of a sample of 60 000 events. It was argued [152, 153] that  $\sim 10^5$  events would be indeed sufficient to discriminate between the predictions of most models on the global characteristics of inelastic interactions, such as multiplicity distributions and charged particle spectra in pseudo-rapidity and transverse momentum. However, since ALICE is foreseen to collect a large sample ( $10^9$ ) of pp events in the first year of LHC running, we provide also predictions for the largest statistics, in order to give an idea of the maximum reach for some observables (like  $p_t$  or multiplicity).

Finally, we discuss also the possibility to study the charged-particle multiplicity as a function of the energy effectively available for particle production, as estimated by means of the Zero-Degree Calorimeter (ZDC).

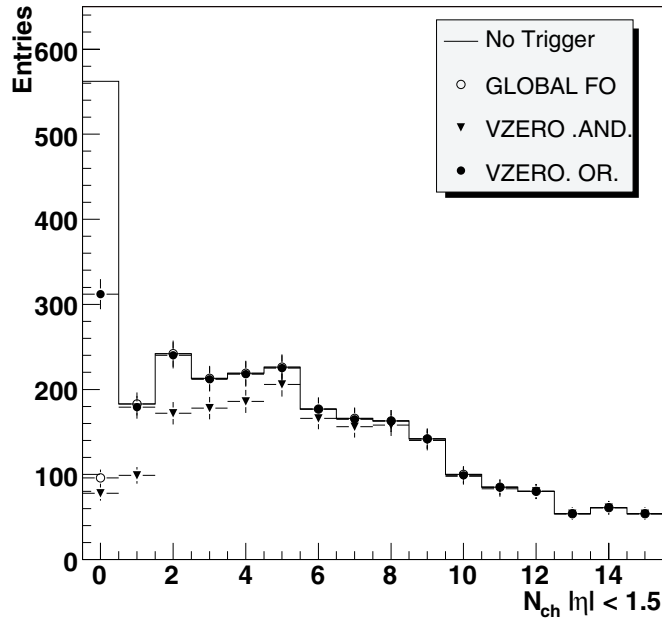


**Figure 6.42.** The multiplicity distribution of primary charged particles for events triggered by the GLOBAL.FO, VZERO.OR and VZERO.AND. triggers. Primary charged particles (generated) have been considered in  $|\eta| < 1.5$ .

*6.1.5.1. Minimum bias triggers in pp collisions.* The main tasks of the minimum bias (MB) trigger are to (i) select events from pp collisions with the highest possible efficiency and lowest possible bias and (ii) to reject events coming from collisions of the proton beam with the residual gas in the beam pipe (beam-background interactions). Here we investigate the capabilities of the V0 and Pixel Fast-OR trigger to define an optimal MB trigger. The full details of the study can be found in [154]. This section deals only with trigger issues. The issues related to the reconstruction of tracks to measure the multiplicity distribution and transverse momentum spectra are discussed in the following sections.

The V0 detector [123] is composed of two independent arrays of fast scintillator counters located along the beam pipe on each side of the nominal interaction point and at forward/backward rapidities. The V0 detector uses the time of hits produced by charged particles to distinguish and trigger events from pp or beam-background interactions. Two different trigger elements are built with the logical combination of the signals from counters on the two sides: VZERO.OR requires at least one hit in one counter on one side, while VZERO.AND requires at least one hit in one counter on both sides.

The basic building blocks of the Silicon Pixel Detector (SPD) [1] are ladders, consisting of a  $200\ \mu\text{m}$  thick silicon sensor bump-bonded to 5 front-end chips. The ladders are arranged in two concentric layers which cover the central pseudo-rapidity region. The first layer has 400 chips and the second 800. Each chip produces a trigger signal. These 1200 signals are logically combined to form the global fast-OR (GLOBAL.FO) trigger element. The GLOBAL.FO can not be identified with a specific bunch crossing, because the signal is integrated over 100 ns equivalent to 4 bunch crossings for the nominal LHC parameters.

Figure 6.42 shows the multiplicity distributions for primary charged particles ( $|\eta| < 1.5$ ) for the three trigger elements considered here.

Due to its pseudo-rapidity coverage the `GLOB.FO` is 100% efficient for events with one or more charged particles within  $|\eta| < 1.5$ . Even for the case of zero primary charged particles in the central rapidity region, it may occur that some secondary particles traverse the SPD and fire the `GLOB.FO` trigger.

The `VZERO.OR` is almost as efficient as the `GLOB.FO`, while the `VZERO.AND` is highly efficient at high multiplicities but is not as good at lower multiplicities. The entries at multiplicities zero are dominated by diffractive events. Since the `VZERO` counters cover relatively small angles, the `VZERO.OR` is very efficient in selecting single and double diffractive interactions.

The main background to MB events are beam–gas and beam–halo interactions. It has been shown that the structure of beam–halo events is similar to that of beam–gas events, the difference being that beam–halo events happen at greater distances to the nominal interaction point (more than 20 m) [155]. In order to study beam–gas and beam–halo events a sample of pA collisions, where  $A = \{O, H, C, He\}$ , has been simulated using the HIJING event generator. In this sample, events happening within 20 m from the nominal interaction point are identified as beam–gas events while events happening beyond are identified as beam–halo events.

The rate of beam–gas collisions is expected to be much smaller than the rate of beam–halo collisions, whose magnitude should be of the same order as proton–proton collisions. The trigger element `notBG` is defined by requiring no signal in either of the `V0` counters within the time windows corresponding to beam–background processes. It turns out that this trigger condition is very helpful to reject beam–background interactions without affecting the efficiency to trigger on proton–proton interactions.

Using logical combinations of the different trigger elements we propose three candidates for a MB trigger:

MB 1:	<code>(GLOB.FO)</code>	or	<code>(VZERO.OR)</code>	and	<code>(notBG)</code>
% MB 2:	<code>(GLOB.FO)</code>	and	<code>(VZERO.OR)</code>	and	<code>(notBG)</code>
% MB 3:	<code>(GLOB.FO)</code>	and	<code>(VZERO.AND)</code>	and	<code>(notBG)</code>

The first option (MB1) would be the preferred one if (i) the rate of beam–background collisions is not much higher than current estimates and (ii) if the integration over 100 ns of the signal from the `GLOB.FO` element is not a problem. The second trigger (MB2) is an option if one needs to assign each trigger to a specific bunch crossing. The third trigger (MB3) would be the least efficient for pp collisions, but has an excellent background rejection. The efficiencies for the different triggers and trigger elements are shown in Table 6.9. The trigger efficiencies as a function of the multiplicity of charged particles emitted within  $|\eta| < 1.5$  are shown in Fig. 6.43.

*6.1.5.2. Multiplicity and  $dN/d\eta$  reconstruction.* Measurements of the charged particle multiplicity distributions in pp collisions can be performed in a similar way to that already discussed for Pb–Pb interactions in Section 6.1.3.1. The multiplicity can be evaluated by the counting of either clusters or tracklets. The main differences in the pp case come from the following points:

- at low multiplicity the statistical fluctuations produced by the background are no longer negligible compared with the signal;
- the primary vertex position (that is an input to the tracklet calculation) is not always available, because the vertex reconstruction is not fully efficient in events with a low number of charged particles (see Section 5.1.1.4 of this document for details on this).

**Table 6.9.** Percentage of events tagged as pp or beam–gas/beam–halo events for combinations of Fast–OR and V0 trigger elements. Note that pp and beam–background have different rates as explained in the text. \*The MB3 trigger option rejected all simulated beam–background events.

Process	VZERO . AND	VZERO . OR	GLOB . F0	MB1	MB2	MB3
Non-Diff	97.8	99.9	99.1	99.9	99.1	96.9
Single-Diff	40.8	73.0	60.0	73.8	59.5	38.4
Double-Diff	46.8	86.2	69.6	87.8	68.7	45.6
All Inelastic	81.4	93.4	88.0	93.6	87.8	79.3
Beam Gas	–	–	–	7.7	2.0	0.0 *
Beam Halo	–	–	–	2.3	0.3	0.0 *

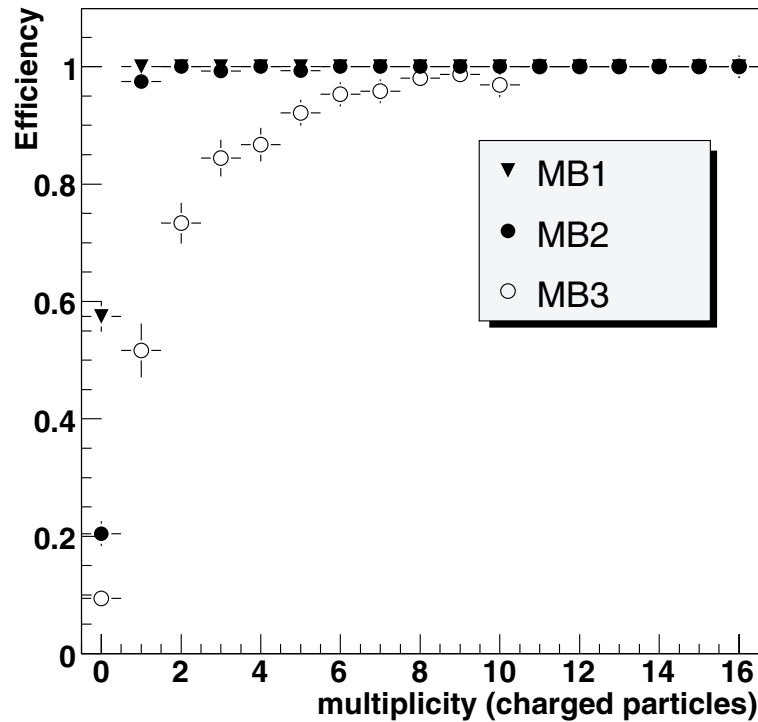


**Figure 6.43.** Efficiency of the different MB triggers as a function of the charged particle multiplicity in  $|\eta| < 1.5$ .

The cluster production is very sensitive to the background (noise, secondary interactions); on the other hand the tracklets can provide a measure which is largely independent on it. Similarly, the primary vertex position is a mandatory information for tracklets reconstruction; on the other hand the cluster multiplicity is not very sensitive to it. In this case however the pseudo-rapidity cannot be determined in a correct way.

In the following the results of the analysis of a sample of 60 000 fully-reconstructed pp events will be shown; the reconstructed vertex position was used when available.

Figure 6.44 shows the measured reconstructed multiplicity as a function of the true multiplicity. The multiplicity is evaluated in the full SPD acceptance for tracklets ( $|\eta| < 1.5$ , upper plot) and in the central unit of  $\eta$  (bottom plot).

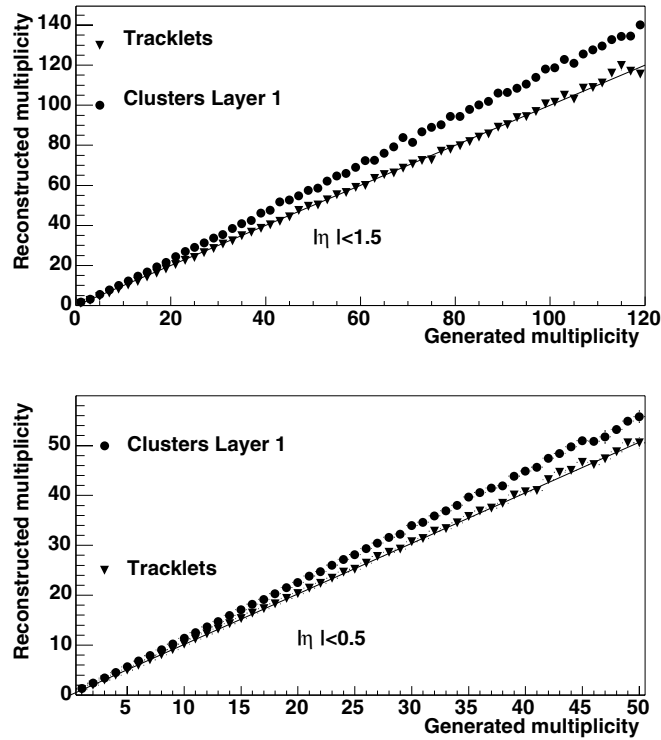


**Figure 6.44.** Correlation between generated and reconstructed multiplicity in the full SPD acceptance ( $|\eta| < 1.5$ , top) and in the central unit of  $\eta$  (bottom). The straight line corresponds to the ideal case of perfect reconstruction.

The difference between the generated and the reconstructed multiplicity can be fitted (in each multiplicity bin) with a gaussian distribution, whose  $\sigma$  is an estimate of the absolute error on the reconstructed multiplicity. Its value is shown for the tracklet method in Fig. 6.45 (top) as a function of the generated multiplicity (evaluated in  $|\eta| < 0.5$ ). In the same figure (bottom) it is shown that the relative error, evaluated by taking the ratio  $\sigma/\text{multiplicity}$ , becomes smaller and smaller with the increase of multiplicity (see also Fig. 6.25, right).

As can be seen from Fig. 6.44, the tracklet multiplicity is very close to the real one, whereas the clusters production is affected by the background and the noise. The ratios between reconstructed and generated multiplicities are shown in Fig. 6.46 (for clusters and tracklets) and in Fig. 6.47 (only for tracklets).

In Fig. 6.46 all the generated events are considered, and in this case a clear inefficiency of tracklets is shown at very low multiplicity as a consequence of the unavailability of the primary vertex position, whereas the clusters show some background.

In Fig. 6.47 only events with reconstructed primary vertex position are considered. In this case the ratio for the tracklets is close to 100% down to very low multiplicity. The higher tracklet efficiency compared to the Pb–Pb case is due to the fact that the low multiplicity allows to enlarge the fiducial window where clusters are associated to form a tracklet.

The generated and reconstructed (tracklets) multiplicity distributions in the full range  $|\eta| < 1.5$  are shown in Fig. 6.48, where only events with reconstructed vertex are considered. It can be seen that the reconstructed distribution is rather close to the generated one.

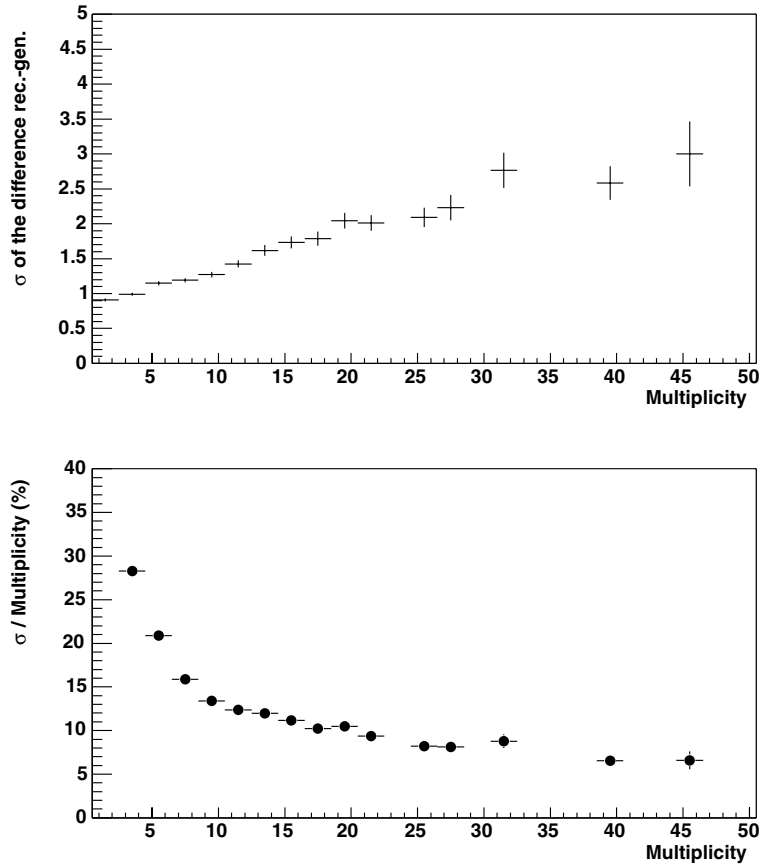


**Figure 6.45.** Absolute (top) and relative (bottom) error on the multiplicity reconstructed with the tracklet method, as a function of the generated multiplicity (in  $|\eta| < 0.5$ ).

The reconstructed  $dN/d\eta$  is shown in Fig. 6.49, for both clusters in layer 1 (top) and tracklets (bottom, full triangles).

Only events with well reconstructed vertex are selected. It can be seen that the reconstruction made with the clusters in the first layer shows a background which depends on the pseudo-rapidity, showing a clear increase with increasing  $|\eta|$ . On the other hand the pseudo-rapidity density from reconstructed tracklets is flat in the range  $|\eta| < 1$ , whereas outside this range the efficiency is smoothly decreasing. This effect depends on the spread of the longitudinal position of the primary vertex, and can be corrected for by taking into account the geometrical acceptance. This is shown in the same plot (open circles), where an event-by-event correction depending on  $z_v$  was applied. In this way an extended range of pseudo-rapidity ( $|\eta| < \approx 1.5$ ) can be explored, as already shown.

**6.1.5.3. Transverse momentum distributions.** Transverse momenta of charged particles are available from the tracking system (TPC and ITS) in the central pseudo-rapidity range  $|\eta| < 1.5$ , but with optimum momentum resolution within the range  $|\eta| < 0.9$ .

Figure 6.50 shows the comparison between the  $p_t$  spectrum of charged primary tracks reconstructed in TPC and ITS, and the corresponding spectrum of charged tracks generated

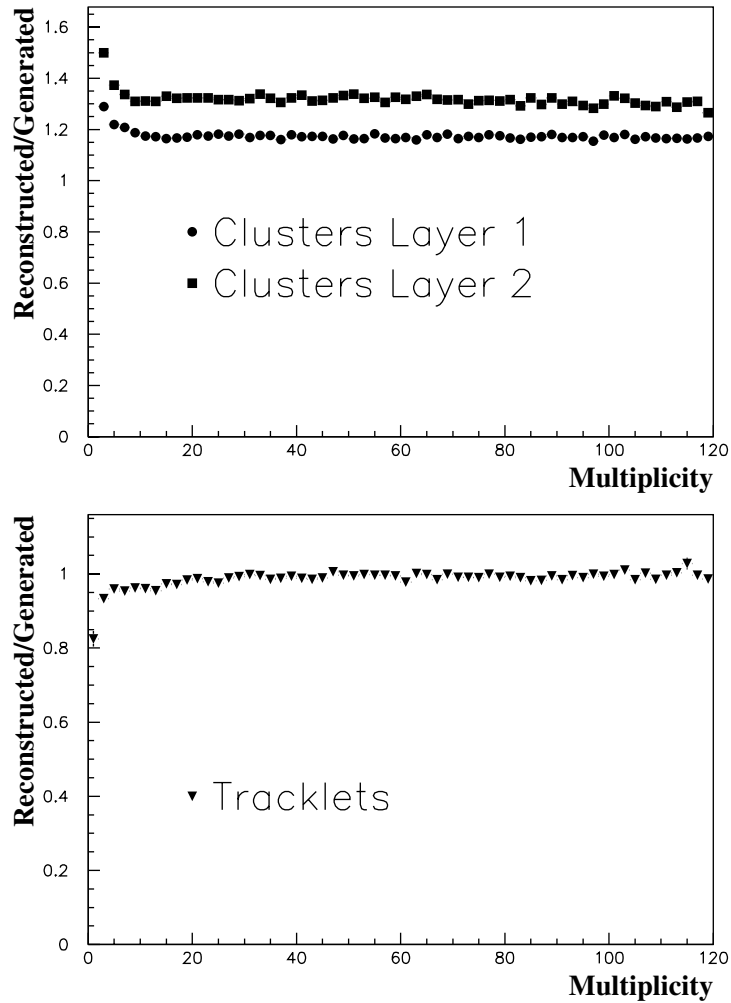


**Figure 6.46.** Ratio of the reconstructed and generated multiplicity, as determined by clusters (top) and tracklets (bottom) as a function of the generated multiplicity ( $|\eta| < 1.5$ ). All events are considered, also those with no determination of primary vertex position.

within the pseudo-rapidity range  $|\eta| < 0.9$ . The ratio between the two distributions is presented in Fig. 6.51.

The secondary tracks, not included in the above spectra, have a softer  $p_t$  distribution, while their number is approximately 2% of the total number of reconstructed charged tracks. However, when considering only the lowest  $p_t$  region, this fraction is larger (3.5 % for tracks with  $0.2 < p_t < 0.3$  GeV/ $c$ , and 13 % for  $p_t < 0.2$  GeV/ $c$ ).

The transverse momentum dependence of the  $p_t$  resolution at the magnetic field  $B = 0.5$  T is shown in Fig. 6.52. The values of the  $p_t$  resolution at high values of  $p_t$  were calculated by mixing PYTHIA events with additional high- $p_t$  tracks.

**6.1.5.4. Dependence of mean  $p_t$  on charged multiplicity.** The mean  $p_t$  of each event was calculated simply as the arithmetic mean of the  $p_t$  of all the reconstructed charged tracks. The distribution of the reconstructed  $\langle p_t \rangle$  for a sample of about 60 000 minimum bias

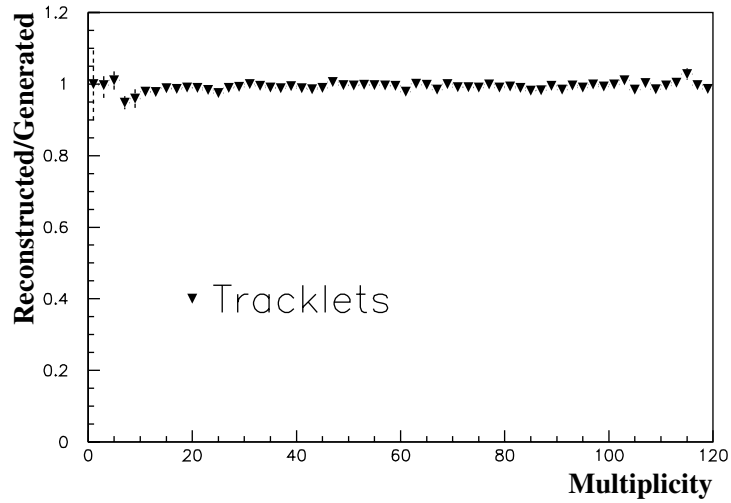


**Figure 6.47.** Tracklet efficiency as a function of the generated multiplicity ( $|\eta| < 1.5$ ). Only events with reconstructed primary vertex position are considered.

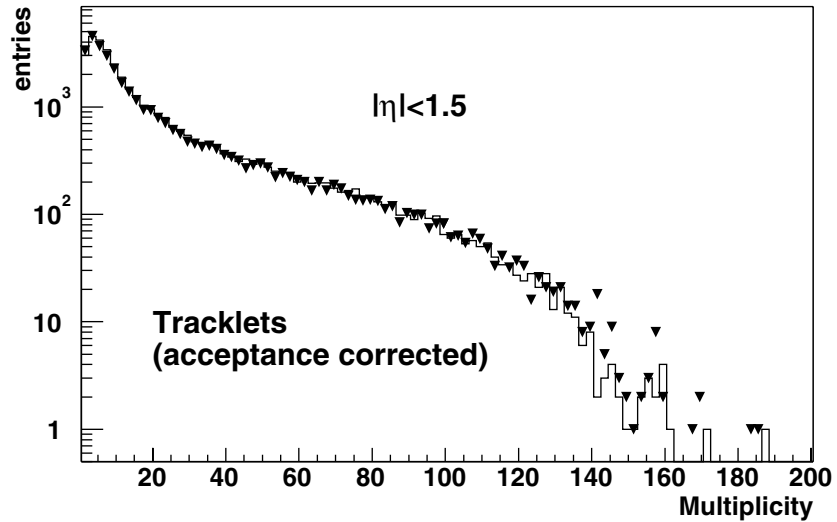


**Figure 6.48.** Generated (solid line) and reconstructed (full triangles) multiplicity distributions in the pseudo-rapidity range  $|\eta| < 1.5$ . Only events with reconstructed primary vertex position are considered.

events is shown in Fig. 6.53, superimposed to the original  $\langle p_t \rangle$  distribution of the generated events. Thus, it results from this plot that the  $\langle p_t \rangle$  for each event is reconstructed quite well. According to the model used for the simulation (PYTHIA 6.214), the expected  $\langle p_t \rangle$  is of the order of 0.6 GeV/c, a momentum where CMS is essentially blind and ATLAS is reaching its limit.

Values of average transverse momentum  $\langle p_t \rangle$  are presented in Fig. 6.54 as a function of charged multiplicity  $N_{ch}$  within the pseudo-rapidity range  $|\eta| < 0.9$ . The correlation is shown

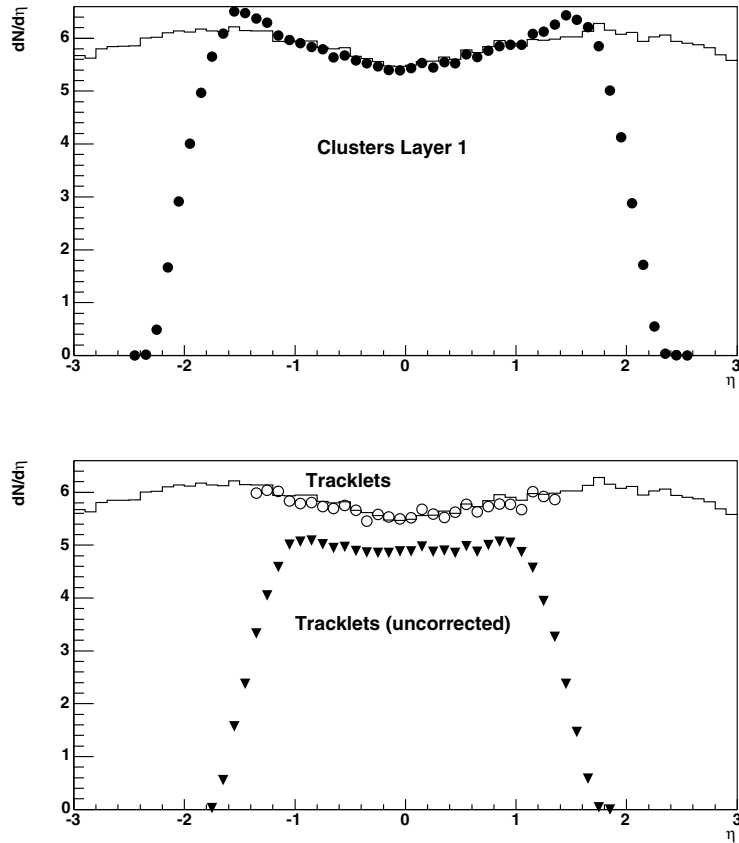


**Figure 6.49.** Generated and reconstructed pseudo-rapidity distributions. The reconstruction is performed with clusters in layer 1 (top, black circles), and tracklets with (open circles) and without (black triangles) geometrical corrections.

for the generated primary charged particles as a function of the true multiplicity, and for the reconstructed tracks as a function of the number of reconstructed tracklets. Also in this case there is a good agreement between the distribution obtained from the reconstructed and generated data.

The correlation between charged tracks  $\langle p_t \rangle$  and multiplicity is known since its first observation by UA1 [156], and it was successively studied at the ISR [157] and Tevatron [158, 159] energies. On the other hand, the increase of  $\langle p_t \rangle$  as a function of multiplicity was suggested by cosmic ray measurements [160]. This correlation between  $\langle p_t \rangle$  and multiplicity is generally attributed to the onset of gluon radiation, and explained in terms of the production of minijets [161]. Since these mechanisms should become dominating at large energies, this correlation is expected to disappear.

Another interesting subject for ALICE, due to its powerful PID system at low  $p_t$  is the correlation between  $\langle p_t \rangle$  and multiplicity studied separately for pions, kaons and proton/antiprotons. The data collected at Tevatron by the E735 experiment [158] indicate that the correlation has rather different behaviour for the three types of particles, especially as regards the proton/antiproton  $\langle p_t \rangle$ , that appears to saturate at high multiplicities. This is not yet understood in terms of the available hadronic models.

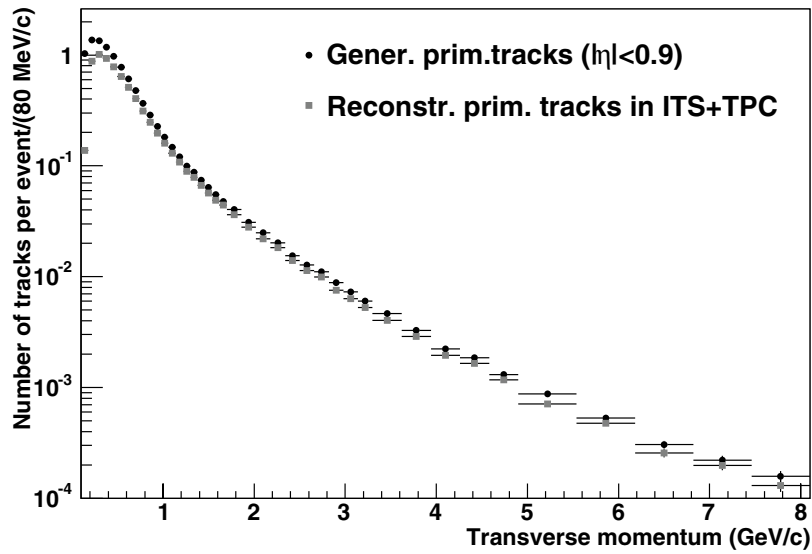


**Figure 6.50.** Transverse momentum spectrum of charged primary tracks generated within  $|\eta| < 0.9$ , compared with the one reconstructed by ITS and TPC (based on the analysis of 60 000 minimum bias events).

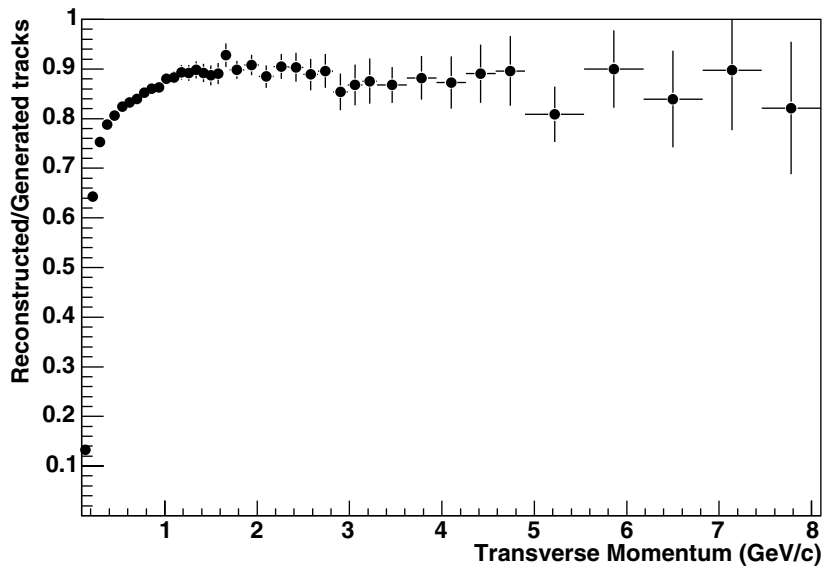


**Figure 6.51.** Ratio between the transverse momentum distributions of reconstructed and generated tracks, in the range  $|\eta| < 0.9$ . The tracks were reconstructed in ITS and TPC.

**6.1.5.5. The ALICE reach in  $p_t$  and multiplicity.** In the first years of running, the main limitation to the ALICE reach in  $p_t$  spectra will be due to statistics. The results presented in the last sections were drawn from the analysis of a Monte Carlo sample of 60 000 fully-reconstructed inelastic events. Then, in order to make predictions about the  $p_t$  limit that can be reached for higher event statistics, we generated with PYTHIA also a sample of  $10^9$  non-single-diffractive events (NSD) events. The integral number of tracks above a given  $p_t$  is

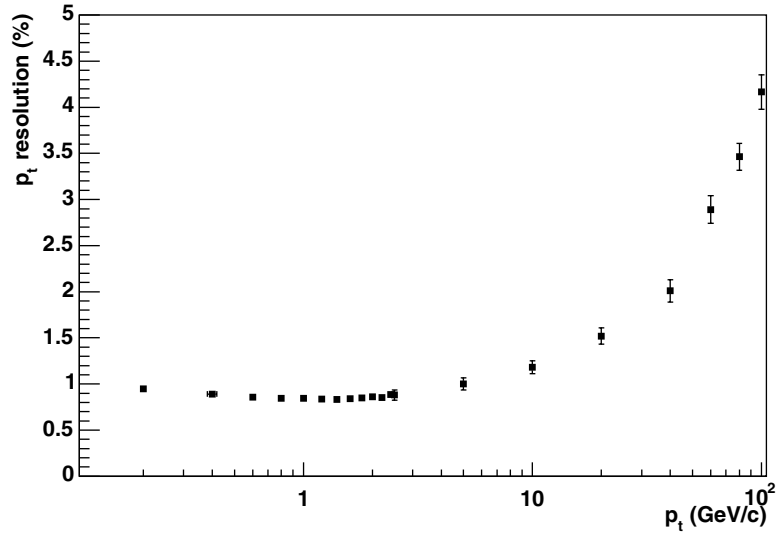


**Figure 6.52.** Transverse momentum resolution as a function of  $p_t$  for non-diffractive pp events. The magnetic field was taken at its nominal value  $B = 0.5$  T.

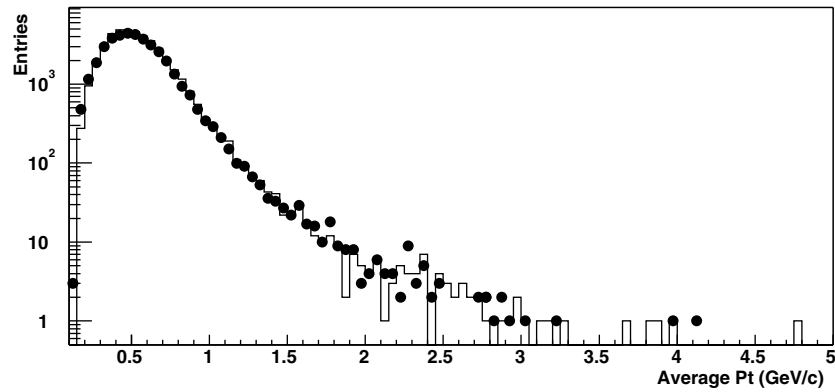


**Figure 6.53.** Average transverse momentum of charged tracks in minimum bias proton-proton events in ALICE ( $|\eta| < 0.9$ ). Reconstructed distribution (full circles) is compared to the one (solid line) obtained by calculating  $\langle p_t \rangle$  from the generated  $p_t$  values.

shown in Fig. 6.55 as a function of  $p_t$ , for several event sample sizes (from  $10^5$  to  $10^9$  NSD events). The horizontal line shows the  $p_t$  limit that can be reached, at different event statistics, to collect a sample of at least 100 tracks.

Concerning the multiplicity, in ALICE it will be measured in the region  $|\eta| < 1.5$  covered by the TPC (or even between  $-5.1$  to  $3.4$  units of pseudo-rapidity, when using also the FMD), but the high precision momentum measurement with the ITS, the TPC and the TRD, needed to identify particle type, will be available only in the pseudo-rapidity window  $|\eta| < 0.9$ . The estimated mean multiplicity in the TPC acceptance is about 11 particles out of about 75 charged particles produced on the average in an inelastic pp interaction in the full pseudo-rapidity interval. The first number is consistent with an expected charged particle density  $dN/d\eta \sim 6$  in the central region for all inelastic collisions (ND+SD+DD, following

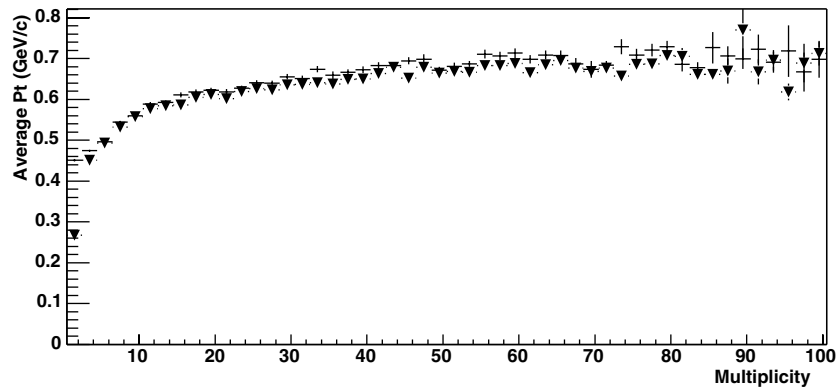


**Figure 6.54.** Average transverse momentum ( $\langle p_t \rangle$ ) as a function of charged track multiplicity in ALICE ( $|\eta| < 0.9$ ). Generated (solid line) and reconstructed (full triangles) values are superimposed.

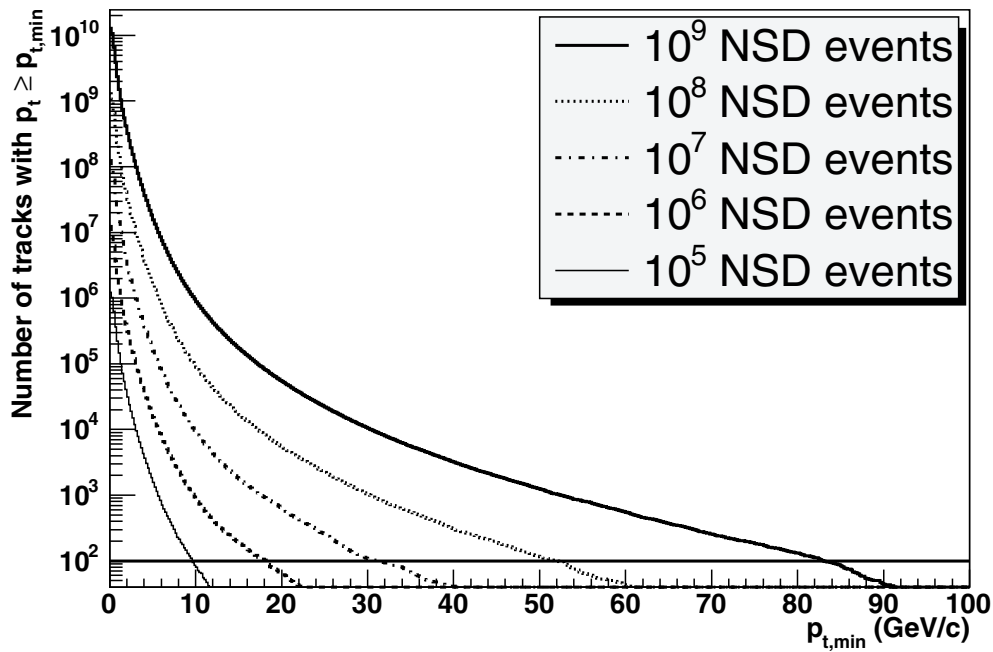


**Figure 6.55.** Number of charged tracks (within the range  $|\eta| < 0.9$ ) above a given  $p_t$  for different NSD pp events statistics. The horizontal line corresponds to 100 tracks. Its intercept with the  $p_t$  spectra obtained for various event statistics is a measure of the maximum  $p_t$  reached in each case.

the scheme of Fig. 6.41 on page 1525), while a density  $dN/d\eta \sim 7$  is expected for non-single diffractive interactions [151]).

In order to measure with reasonable statistics the highest multiplicity events, i.e. with multiplicity larger than few times the average, a large overall statistics is needed. In a similar way as it was done for the extrapolation of the  $p_t$  distribution, we made an estimate of the limits in multiplicity that can be reached with various numbers of events.

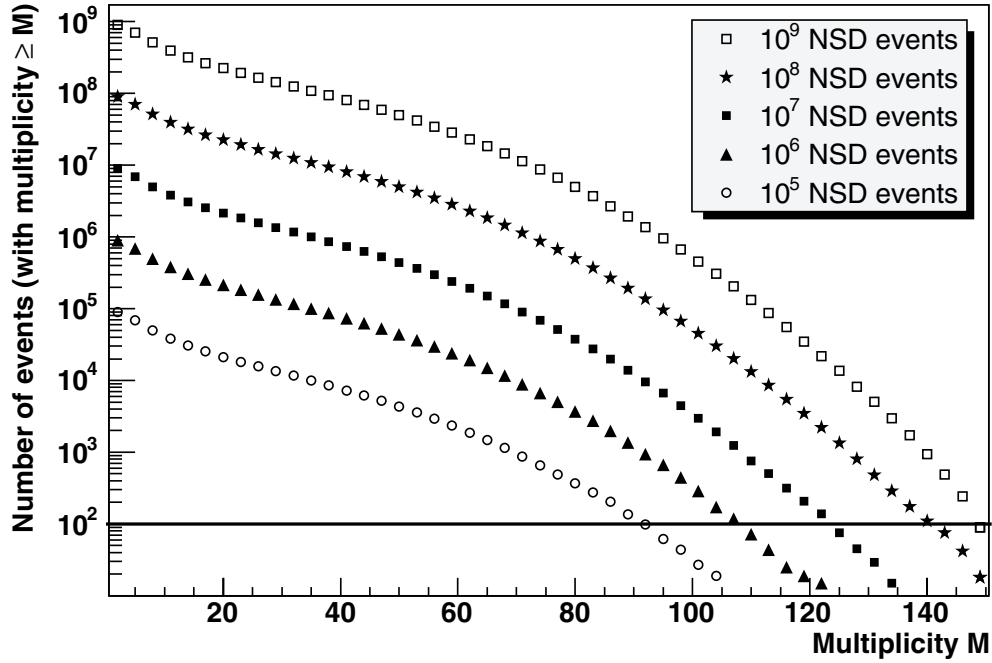


**Figure 6.56.** Number of events over a given multiplicity (measured in the pseudo-rapidity range  $|\eta| < 0.9$ ), for various statistics of minimum bias (NSD) pp events generated with PYTHIA 6.214. The intercepts with the horizontal line, corresponding to 100 events, gives a measure of the maximum multiplicity reached in each case.

The integral number of events above a given multiplicity is shown in Fig. 6.56 for several event sample sizes (from  $10^5$  to  $10^9$  NSD events). The horizontal line corresponds to 100 events. Its intercept with the integral multiplicity distributions gives therefore a rough estimate of the maximum multiplicity that can be reached in each case.

**6.1.5.6. Charged multiplicity and effective energy.** In this section we study the charged-particle multiplicity as a function of the energy effectively available for particle production. This kind of analysis requires a detector able to measure particles with large longitudinal momenta. ALICE has a good capability for such a measurement, owing to the presence of Zero-Degree Calorimeters (ZDC).

In fact, even though the ALICE ZDCs are optimized for Pb–Pb collisions, their energy resolution in the forward region is sufficient to make possible a pp data analysis in terms of the so-called ‘effective energy’ [162].

While the effective energy in  $e^+e^-$  collisions coincides with the total centre-of-mass energy, in  $pp(\bar{p})$  collisions it is usually assumed that, on average, it is half of  $\sqrt{s}$ , once the ‘leading effect’ has been taken into account. The leading effect is due to the quantum number flow from the initial to the final state. Hence, in  $pp(\bar{p})$ , it concerns the particles conserving the baryon number along the beam axis.

Therefore, the usual definition of the effective energy per event in a single hemisphere, for  $pp(\bar{p})$  collisions, is given by the expression

$$E_{\text{eff}} = \sqrt{s}/2 - E_{\text{lead}},$$

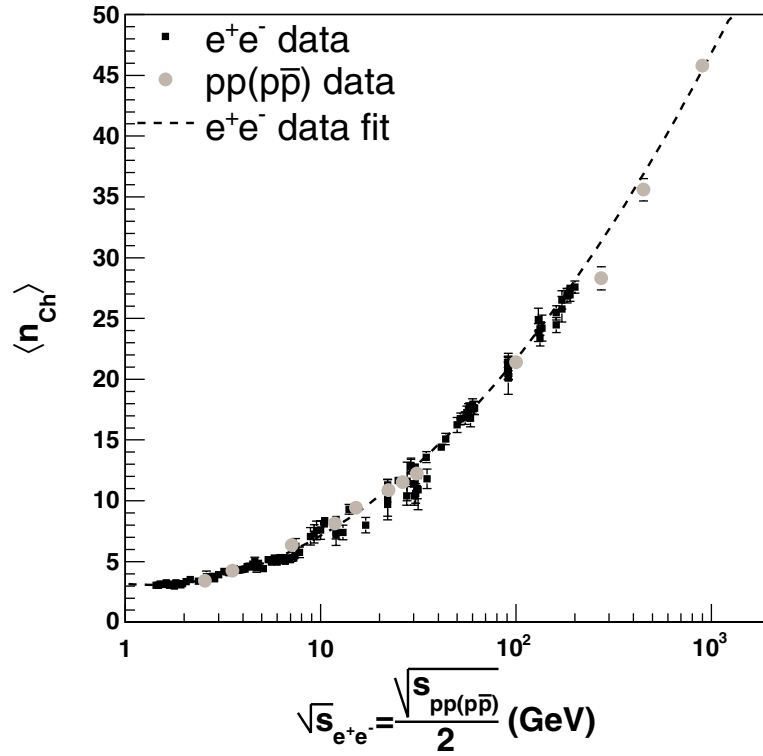


**Figure 6.57.** Compilation of existing experimental data on the mean charged multiplicity in  $e^+e^-$  and  $\text{pp}(\text{p}\bar{\text{p}})$  collisions at different centre-of-mass energies [162, 163]. The centre-of-mass energy in  $\text{pp}(\text{p}\bar{\text{p}})$  data is scaled by a factor  $\frac{1}{2}$ .

where  $E_{\text{lead}}$  is the energy carried by the outgoing leading particle in a given hemisphere. The role of the ZDCs will be to measure  $E_{\text{lead}}$  by detecting the leading particle in the forward region.

The mean charged multiplicity  $\langle N_{\text{ch}} \rangle$  in  $e^+e^-$  and hadron–hadron collisions, measured by previous experiments, with respect to the effective energy for particle production, is shown in Fig. 6.57, where one can notice that all the data fall on the same plotted curve, corresponding to a fit of the  $e^+e^-$  points, regardless of the interaction type.

It will be then very interesting to check if the universality features of Fig. 6.57 still hold at LHC energies.

As already detailed in Section 6.1.2.1, the ZDCs are placed at about 115 meters from the interaction point and are mainly designed to measure the number of participant nucleons in Pb–Pb collisions, through the separate measurements of protons (ZP detectors) and neutrons (ZN detectors). However, we have checked that they can also be used to measure leading particles in pp collisions in a wide range of energies. In particular, for charged particles measured in the ZP, the beam optics selects an energy interval between 2.2 TeV and 4.5 TeV, corresponding to a Feynman- $x$  range  $0.30 < x_{\text{F}} < 0.64$ , with the  $x_{\text{F}}$  defined as  $x_{\text{F}} = 2p_{\text{L}}/\sqrt{s}$ . For neutral particles the beam optics constraints are obviously not present, and the ZN accepts all particles emitted in a cone of 0.3 mrad around the beam direction.

The PYTHIA event generator was used to generate pp collisions, that were then used to perform a complete study of charged multiplicity and leading particle production. Figure 6.58 shows  $\langle N_{\text{ch}} \rangle$  as a function of  $E_{\text{eff}}$ , at generation level and after reconstruction. The good

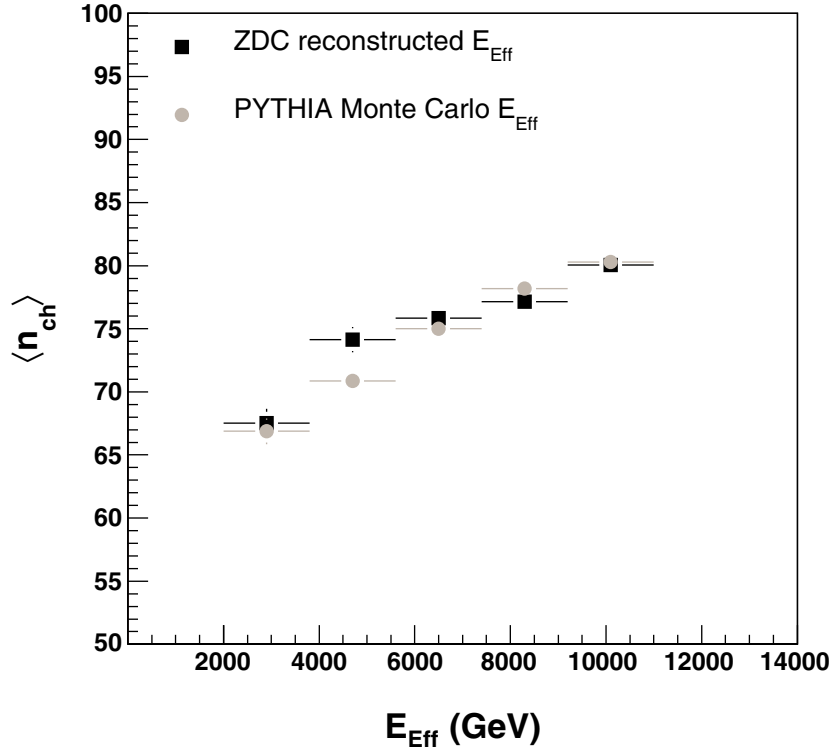


**Figure 6.58.** Correlation between mean charged multiplicity and mean effective energy in PYTHIA pp events, using the leading energy measurement of the ZDC calorimeter (squares). The dots are the same quantities estimated at the generator-level.

agreement confirms that an analysis of pp events in terms of the effective energy will indeed be possible.

The extension of the universal behaviour in hadron production to nucleus–nucleus collisions is a very interesting point. Indeed, there are already some experimental data (in particular from PHOBOS at RHIC [164]) that seem to be in good agreement with such a behaviour.

Assuming that this will be confirmed also at LHC, it is possible to derive a prediction for the mean charged multiplicity in Pb–Pb collisions at  $\sqrt{s} = 5.5$  TeV, based on an extrapolation from the  $e^+e^-$  fit. In this case, the mean total charged multiplicity, scaled with the number of participant nucleons, would turn out to be

$$\frac{2}{N_{\text{part}}} \langle N_{\text{ch}} \rangle = 72 \pm 2.$$

In the hypothesis of ‘limiting fragmentation’ it is then possible, using the RHIC data, to fix the shape of the pseudo-rapidity distribution [140, 149, 165] and derive the mean charged multiplicity at mid-rapidity in central Pb–Pb collisions at LHC. The result is

$$\frac{2}{N_{\text{part}}} \left\langle \frac{dN_{\text{ch}}}{d\eta} \right\rangle_{|\eta=0} = 5.3 \pm 0.4$$

corresponding to about  $1100 \pm 100$  charged tracks per unit rapidity.

**Table 6.10.** Classification of particles produced in hadron–nucleus collisions, with the approximate borders of the momentum range.

Name	$p$ (MeV/c)
black	$< 250$
grey	$> 250 < 1000$
shower	$> 1000$

This value is significantly lower than the predictions of well-known Monte Carlo generators (such as HIJING, for example) [166]. However, it should be remarked that other effects, in particular the jet quenching, could sizeably increase the multiplicity in the central region. Different types of quenching have been simulated in the Monte Carlo, and an increase up to a factor  $\sim 2$  was observed.

Even considering these additional effects, if the universality features will hold at LHC energies, this would anyway imply a rather small value for the charged multiplicity at mid-rapidity, implying not too severe background conditions in ALICE.

*6.1.6. Event centrality in pA collisions.* The study of pA interactions is a fundamental part of the ALICE physics programme. By studying pPb collisions it will be possible to estimate the importance of initial and final-state nuclear effects not directly connected with the creation of a hot medium. In this section we limit ourselves to a particular aspect of the study of pA interactions, namely the possibility of distinguishing central and peripheral events. This study has already been performed at fixed-target experiments, using as experimental technique the detection of slow target nucleons. We briefly present the basic physics concepts of this technique, and then the results of a simulation showing that it is possible also at a collider experiment to perform a centrality selection in pA.

*6.1.6.1. Centrality control of hadron–nucleus interactions by detection of slow nucleons.* The terminology of slow particles comes from pioneering emulsion work. The emitted slow particles are classified according to their grain density left in the detection material: ‘black’ or ‘grey’. They are called in a word ‘heavy’. The lighter coloured particles are emitted in the forward direction and called ‘shower’. These names can be converted to corresponding momentum ranges. A common choice is shown in Table 6.10.

Slow particles are believed to come from different production mechanisms. Such an idea emerged at fixed-target experiments, where two components have been identified:

- Fast, high-energy nucleons. These are prompt, pre-equilibrium particles, knocked out of the nucleus and are often called grey nucleons.
- Slow, low-energy nucleons. These are ‘equilibrated’ particles, from evaporation, decay, or fragmentation of the remnants of the original nucleus and are often called black nucleons.

The general observation is that the multiplicity of produced shower particles is correlated with the number of slow particles: for heavy (black) prongs one has a quasi linear dependence, while for grey ones a more curved relationship is observed (see examples in Fig. 6.59).

The features of the produced slow particles are highly energy independent, and they are found to be very similar in the fixed-target energy range. This applies to angular, momentum, and number distributions. However, it is unclear whether this behaviour still holds at LHC energies. The similarities at different energies suggest that the emission of slow particles is dictated by nuclear geometry, hence supporting the hypothesis of limiting fragmentation. The proper knowledge of the momentum distribution of the emitted particles is crucial for planning

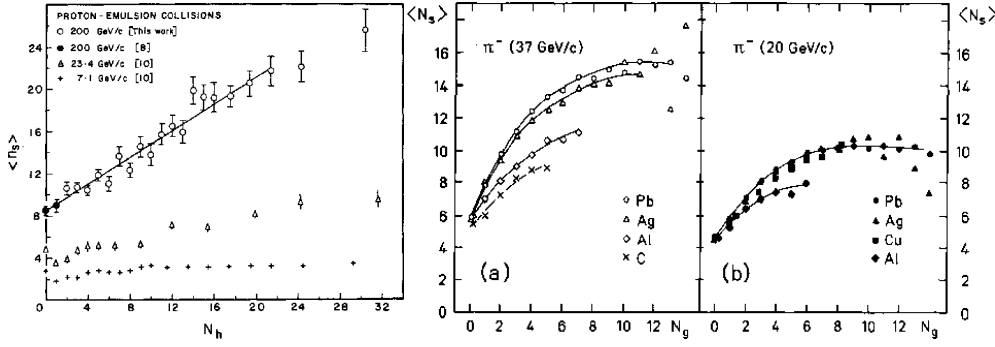


**Figure 6.59.** (a) Dependence of the mean number of fast particles ( $n_s$ ) on the number  $N_h$  of heavy particles at 200, 23.4 and 7.1 GeV/c, from Ref. [167]. The line represents the best linear fit of the data. (b) Dependence of the mean number ( $\langle N_s \rangle$ ) of fast particles on the number  $N_g$  of slow particles, from Ref. [168].

a measurement of slow particles at a collider experiment, because of the presence of a large Lorentz-boost.

Both black and grey components of slow nucleons can be described by independent statistical emission from a moving frame. This is rather surprising for the prompt grey component where such ‘equilibrated’ behaviour would not be expected *a priori*. The distributions may be parametrized in the form of a modified Maxwell–Boltzmann distribution: particles are emitted isotropically from a source moving with velocity  $\beta$ . The invariant cross-section can be written as

$$E \frac{d^3\sigma}{dp^3} \propto \exp(-E_{\text{kin}}/E_0), \quad (6.9)$$

where  $E_{\text{kin}}$  is the kinetic energy and  $E_0$  is the characteristic energy per particle, both in the moving system.

In a fixed-target environment, while the black nucleons are emitted from a stationary source, the grey nucleons come from a frame moving slowly in the direction of the beam particle. Reasonable values for the parameters of the Maxwell-Boltzmann distributions, for targets with atomic number close to that of Pb, are  $\beta_{\text{black}} = 0$ ,  $E_{0,\text{black}} \approx 5$  MeV and  $\beta_{\text{grey}} \approx 0.05$ ,  $E_{0,\text{grey}} \approx 50$  MeV. The values of  $\beta$  decrease with increasing  $A$ : for bigger nuclei the intranuclear cascade can develop more, yielding a more isotropic emission of particles.

In order to extract the number of nucleon–nucleon collisions in pA interactions from the multiplicity of grey particles, data are traditionally analysed in the framework of the Glauber model, using Woods–Saxon density distribution. The Glauber framework provides the distribution  $\pi(\nu)$  of the number of projectile collisions  $\nu$  in the nucleus, which has to be folded with a model giving the probability distribution of the number of grey protons  $P(N_g|\nu)$ . For the latter quantity a simple geometric model is used, where each collision of the incoming hadron in the nucleus corresponds to the same distribution of grey particles [169]. Successive collisions therefore give independent contributions, and for each collision the number of grey particles follows a normalized geometric distribution. From the assumption of independence, it follows that for  $\nu$  collisions  $P(N_g|\nu)$  is a negative binomial distribution. This also means that  $\overline{N_g} \propto \overline{\nu}$ .

A practical model has been proposed by the BNL-E910 experiment [170]. The main assumption is that for a given nucleus the mean number of grey particles  $\overline{N_g}$  is a second-order polynomial of the number of projectile collisions  $\nu$ . It is further assumed that the  $P(N_g|\nu)$

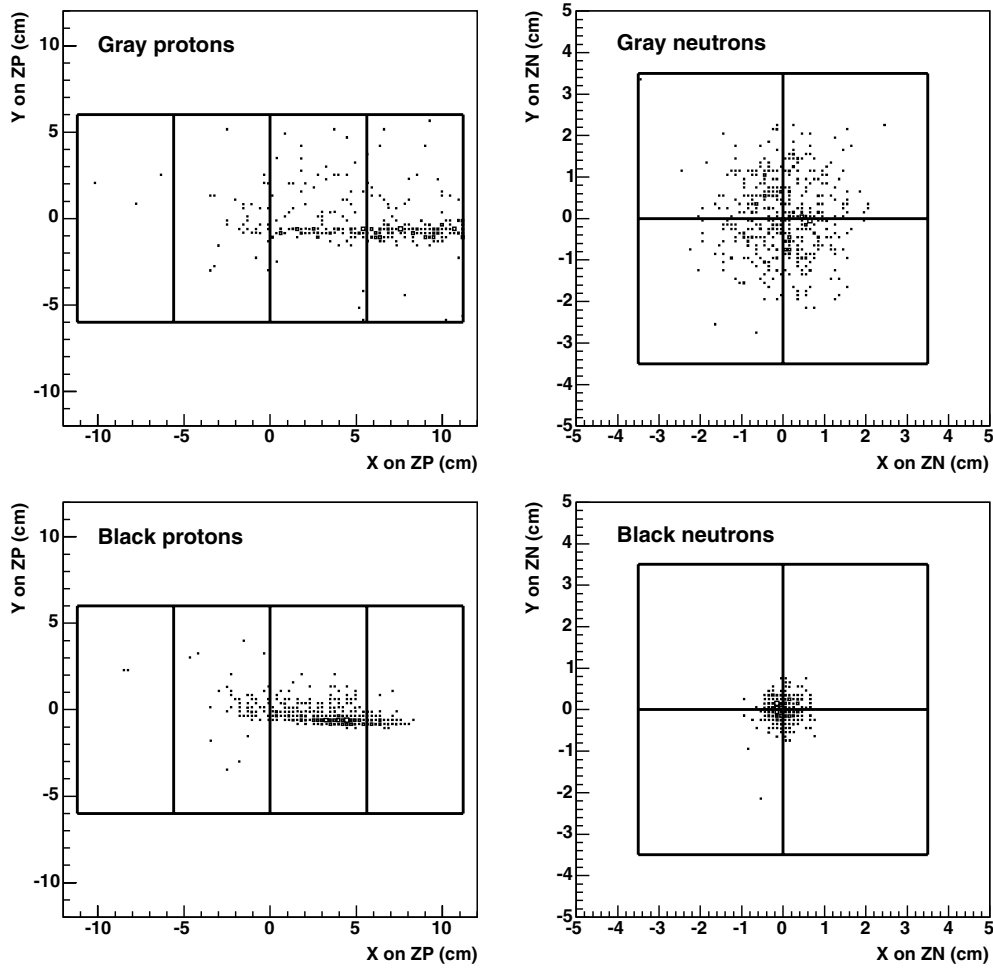


**Figure 6.60.** Impact point distributions of grey and black nucleons on the ZDCs. The solid lines indicate the neutron and proton ZDC front faces and their segmentation.

is binomial, and that each target proton can be emitted with probability  $p = \overline{N}_g(v)/Z$ , where  $Z$  is the atomic number of the target. The coefficients of the polynomial are derived from fits to the data, which show that the quadratic component is negligible and therefore a simple proportionality relation holds, as expected from the simpler geometric model.

Turning to black nucleon production, the processes involving the production of such particles are connected with excitation energies of the order of the nuclear binding energy. In recent years, observations pointed to the thermal nature of such processes: the remnant nucleus undergoes equilibration before break-up. Thus a thermodynamic or statistical interpretations should be appropriate.

One can assume that the average black nucleon multiplicity, connected to the target excitation, depends linearly on the number of projectile collisions. This can be deduced from the observation that  $\overline{N}_b$  is proportional to  $N_g$ . In other words, each collision provides independent and identical production of prompt grey nucleons with identical excitation of the nucleus, leading to the subsequent emission of black nucleons.

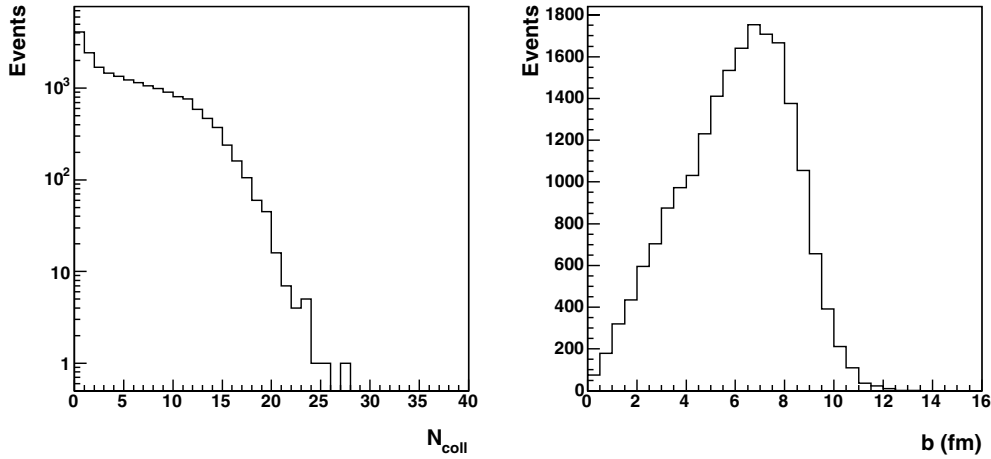


**Figure 6.61.** Distribution of the number of collisions (left) and of the impact parameter (right) in pPb collisions at the LHC, generated with HIJING.

Formally, the distributions of the number of black (or grey) particles can be expressed through the following binomial distributions:

$$P(N|\nu) = \binom{M}{N} p^N (1-p)^{M-N} \quad p = \bar{N}(\nu)/M, \quad (6.10)$$

where  $M$  is the maximum available black (or grey) protons (or neutrons) in the nucleus,  $p$  is the emission probability depending on  $\nu$ . Based on experimental results, the average numbers of black and grey nucleons in a minimum-bias hadron–nucleus collision are  $\bar{N}_b \approx 0.080A$  and  $\bar{N}_g \approx 1.2A^{1/3}$ . For centrality-selected collisions on a Pb target this amounts to  $\bar{N}_b(\nu) \approx 4\nu$  and  $\bar{N}_g(\nu) \approx 2\nu$  per collision. (Note that these values have been obtained from experiments where one has an elementary cross-section  $\sigma_{NN} = 30$  mb.)

The estimate of  $\bar{\nu}$  when detecting  $N$  slow nucleons is then given by the projection of the joint  $P(N|\nu)\pi(\nu)$  distribution.

Even if the model presented in this section reasonably reproduces the available data, alternative options can not be excluded at this stage. In particular, it was observed that the production of slow nucleons in hadron–nucleus collisions has a rather weak dependence on the projectile [171]. This observation may be understood assuming that the yield of slow nucleons is dominated by a single, large cascade, generated by the first hadron–nucleon collision. In this way, grey nucleon production would be proportional to the thickness of nuclear matter seen by the cascade, and therefore would rather measure the impact parameter of the collision. For more details on the issues presented in this section, see also Ref. [172].

**6.1.6.2. Detection of grey and black nucleons in the ALICE set-up.** At colliders the slow nucleons emitted in pA collisions are Lorentz-boosted and therefore the ideal detectors for their measurement are the Zero-Degree Calorimeters (ZDCs). Simulations have been performed to evaluate the ZDC response for the detection of slow nucleons and study the centrality determination in pA collisions [173].

A generator of slow nucleons has been implemented in AliRoot, based on the parametrization of experimental results discussed in the previous section (and illustrated in detail in Ref. [172]). Using this generator, samples of 5000 grey (black) neutrons (protons) were separately generated and transported through the experimental set-up till the ZDCs. The

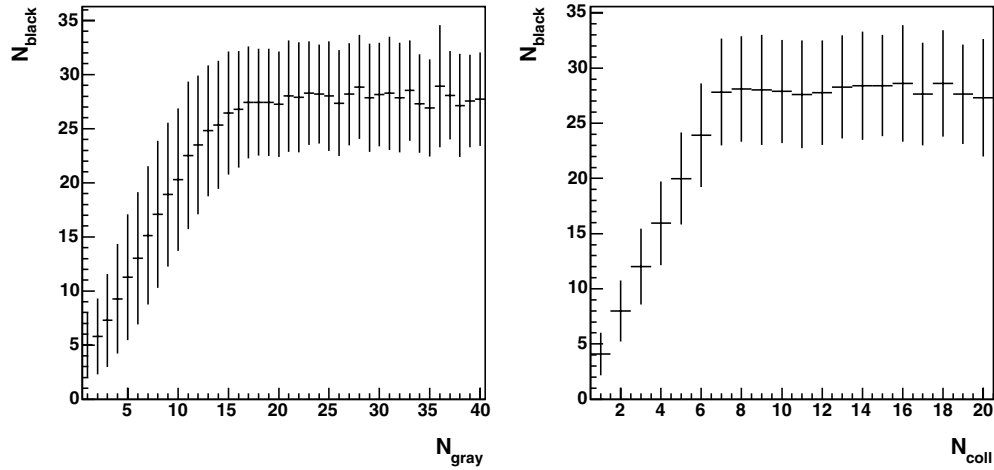


**Figure 6.62.** Saturation of the total number of black nucleons, as a function of  $N_{\text{grey}}$  (left) and  $N_{\text{coll}}$  (right).

distributions of the impact point over the detector front faces are shown in Fig. 6.60. The detectors have full acceptance, except for grey protons where a few per cent of particles is lost. Looking at the impact points it is clear that, even if the detectors are segmented, it is not possible to separate the contribution of black and grey nucleons.

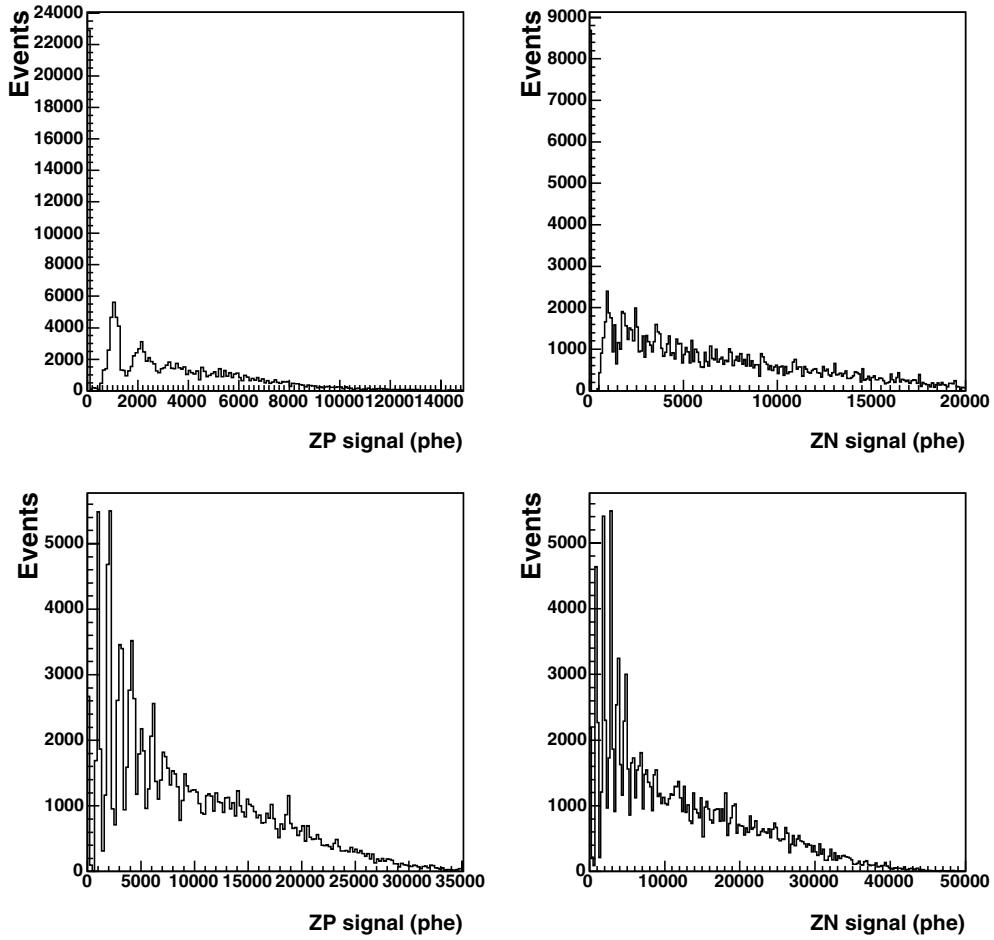
The distribution of the impact parameter and of the number of collisions in pPb interactions at LHC energy has been determined using HIJING as event generator (see Fig. 6.61). Then the number of slow nucleons per collision is extracted event by event from a binomial distribution, while their momentum is derived from a Maxwell–Boltzmann distribution, with the choice of parameters outlined in the previous section.

As discussed in Ref. [172], in experiments with emulsions, a saturation in the number of black particles was observed for a number of grey particles higher than seven. The experimental results refer to light nuclei (O and S) and in both cases the maximum value reached by  $N_{\text{black}}$  is about 12. For Pb nuclei no experimental data exist. Anyway, simple scaling arguments lead us to suppose that this saturation may occur at higher  $N_{\text{grey}}$  values. Supposing that the number of slow nucleons emitted in the interaction is proportional to the thickness of the target nucleus, one expects similar saturation values for O and S, as observed by experiments, while for Pb these values should be considerably larger. This simple estimate leads to a saturation value for Pb nuclei  $N_{\text{black}} \sim 28$ , corresponding to  $N_{\text{grey}} \sim 15$ . This saturation pattern is shown in the left plot of Fig. 6.62, while in the right panel the saturation effect is shown as a function of  $N_{\text{coll}}$ . Two sets of simulations were performed, without and with saturation effect.

The response of proton (ZP) and neutron (ZN) calorimeters is shown for black and grey nucleons in Fig. 6.63 for the case where no saturation is considered.

As discussed before, the measurable quantity in the ZDCs is the total energy deposited by grey and black neutrons in the ZN, and by grey and black protons in the ZP. The response of proton and neutron calorimeters is shown in Fig. 6.64 (without saturation effects) and Fig. 6.65 (with saturation effects).

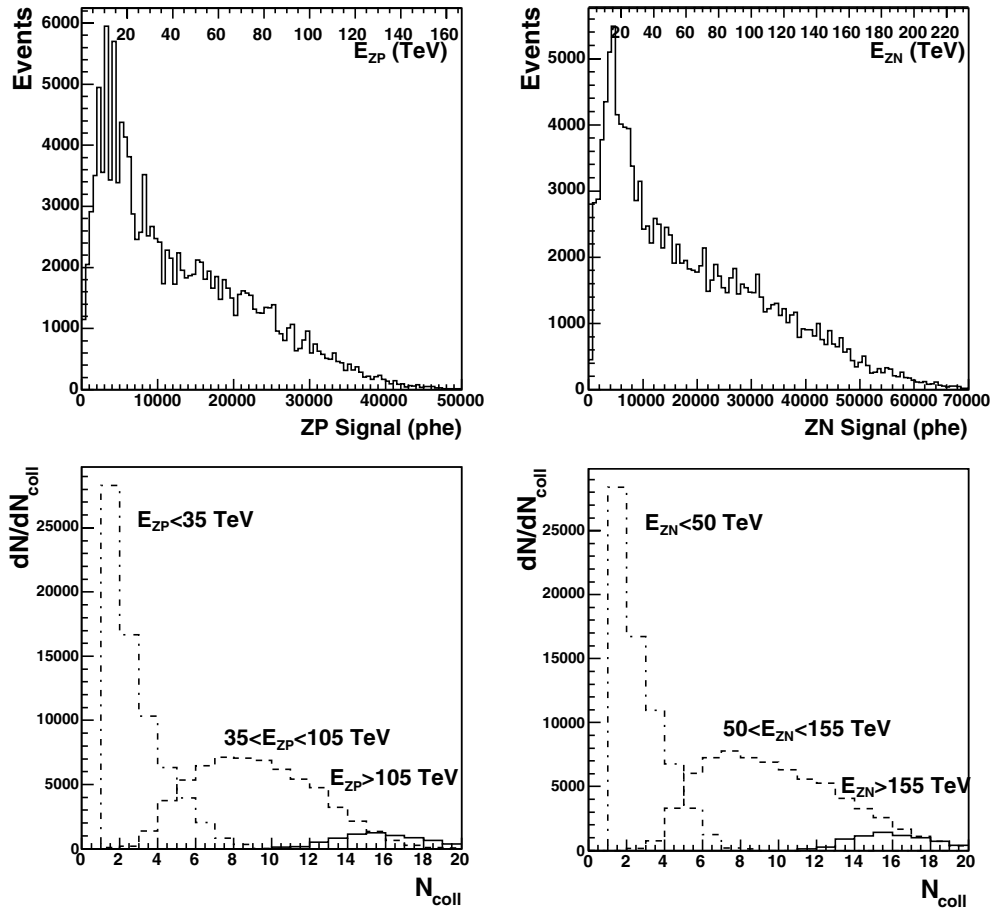
We evaluated the possibility of selecting the centrality in pA collisions by cutting the energy spectra in classes corresponding to well-defined fractions of the total pA cross-section. The distributions of the number of collisions corresponding to the defined bins is shown in



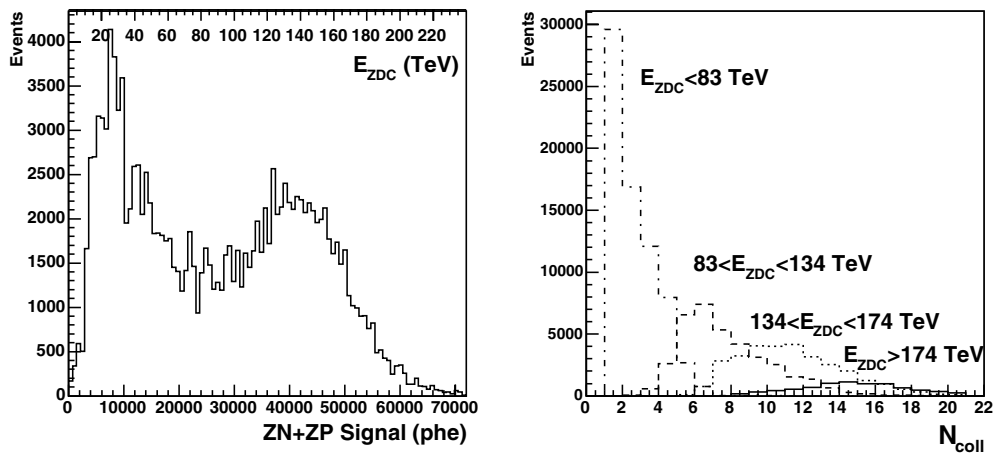
**Figure 6.63.** ZDC response (expressed in photoelectrons), separately for grey protons (top left), grey neutrons (top right), black protons (bottom left) and black neutrons (bottom right). Saturation effects have not been included.

Fig. 6.64. In this case, we have obtained the centrality classes by separately selecting slices in the  $E_{ZN}$  and  $E_{ZP}$  spectra. In Fig. 6.65 the bins have been defined on the sum of the two energy spectra, in order to partly compensate for the loss of resolution induced by the saturation. Tables 6.11 and 6.12 show the mean values and the r.m.s. of the  $N_{\text{coll}}$  distributions. Without saturation we see that, defining three centrality classes, the  $N_{\text{coll}}$  distributions are well separated. Obviously the saturation effect introduces a further smearing in the  $N_{\text{coll}}$  bins. The ZDC response begins to saturate for  $N_{\text{coll}} \geq 8$  and the distribution for the most central class has a slightly larger spread if compared with the corresponding one without saturation.

Finally, in the simulation described above, we have considered a uniform angular distribution for the emitted grey tracks. At least for proton-induced collisions on light ions (S and O), it was experimentally observed that such an emission is rather forward peaked [170, 174]. Therefore, we have investigated the effect of this anisotropy on our results by including in our simulation a parametrization of the measured angular distribution for grey



**Figure 6.64.** Upper:  $E_{ZP}$  and  $E_{ZN}$  spectra (expressed in photoelectrons), without saturation effect. Lower:  $N_{\text{coll}}$  bins corresponding to the  $E_{ZP}$  and  $E_{ZN}$  selections described in the text.



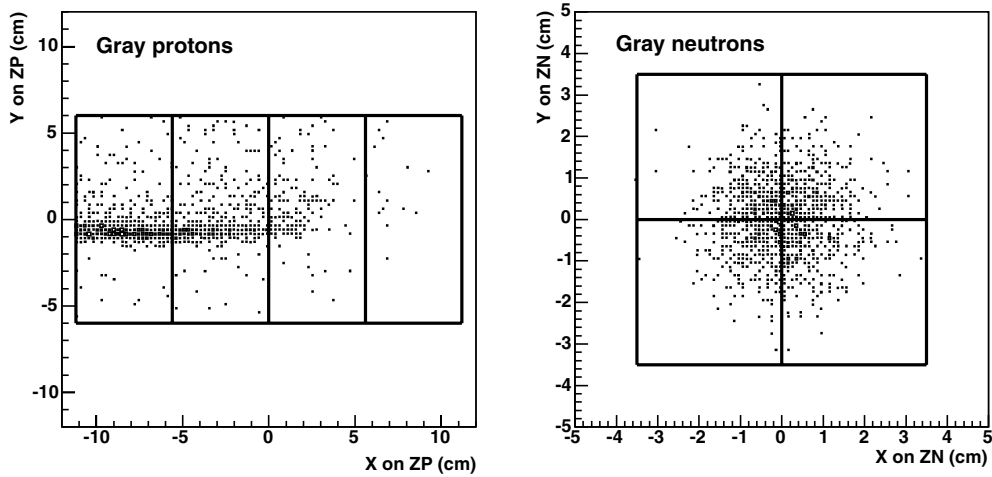
**Figure 6.65.** Left:  $E_{ZDC}$  ( $E_{ZP}+E_{ZN}$ ) spectrum, with saturation effect. Right:  $N_{\text{coll}}$  bins corresponding to the  $E_{ZDC}$  selection described in the text.

**Table 6.11.** Mean values (and r.m.s.) of  $N_{\text{coll}}$  distributions for three centrality bins defined on the  $E_{ZP}$  and  $E_{ZN}$  spectra separately. No saturation effects have been considered.

$\% \sigma_{\text{inel}}$	$\langle N_{\text{coll}} \rangle$ from ZP	$\langle N_{\text{coll}} \rangle$ from ZN
0–5	15.1 (2.1)	15.4 (1.9)
5–50	8.7 (3.1)	9.3 (3.5)
50–100	2.3 (1.5)	2.2 (1.3)

**Table 6.12.** Mean values (and r.m.s.) of  $N_{\text{coll}}$  distributions for four centrality bins defined on  $E_{ZP}+E_{ZN}$  spectra. Saturation effects have been considered.

$\% \sigma_{\text{inel}}$	$\overline{N}_{\text{coll}}$
0–5	14.2 (2.8)
5–25	10.8 (2.8)
25–50	7.2 (2.5)
50–100	2.1 (1.3)

**Figure 6.66.** Impact point distributions of grey tracks on the ZDCs. The grey track angular distribution has been obtained from the data of Refs. [170, 174].

tracks. It turns out that the effect on the  $E_{ZP}$  and  $E_{ZN}$  spectra is negligible, therefore the centrality selection is not directly affected. However, contrarily to what has been shown in Fig. 6.60 on page 1542, the grey protons now hit an area of the ZP front face different from that of black protons (see Fig. 6.66). This is essentially due to the rather different kinematical distributions for the two classes of particles, leading to a different effect of the beam-line optics on them. This result opens up the possibility of separating the contribution of the grey and black protons, thanks to the ZP segmentation. In this way the centrality selection might be performed directly on the energy distribution of grey protons, which are not affected by the saturation effect.

## 6.2. Particle production

### 6.2.1. Overview of current results

**6.2.1.1. Introduction.** Quantum Chromodynamics (QCD) predicts that strongly interacting matter undergoes a phase transition from a state of hadronic constituents to a plasma of unbound quarks and gluons (QGP) [175–178]. By colliding heavy ions at ultrarelativistic energies, one expects to create hadronic matter under conditions that are sufficient for deconfinement [175, 176, 179–183]. The partonic matter created in the ultrarelativistic collisions of heavy ions hadronizes into a large number of hadronic species. Through their yields, momentum distributions and correlations these particles carry information on the hadronisation process and also on characteristics of the matter created in the initial partonic state. A detailed study of these particles is therefore of importance for our understanding of the evolution of the system. This requires a broad coverage of different particle yields. Such a coverage will be realized in the ALICE detector.

At the very first part of the collision, the distribution of initially produced partons is far from being thermal, and the system needs time to reach equilibrium. Recently, it was shown [184] in the framework of perturbative QCD (pQCD) and kinetic theory that the partons should come into equilibrium within a few fm/c at RHIC and at LHC.

The energy density reached in heavy-ion collisions can be estimated using the Bjorken model [112] or by applying different saturation models [111, 185–190]. A detailed study shows that at the SPS the energy density inside the collision fireball already exceeds the critical value required for deconfinement ( $\sim 1.3 \text{ GeV}/\text{fm}^3$ ). At RHIC and LHC it is larger by more than an order of magnitude. Thus, the necessary conditions to create a partonic medium in a deconfined phase are satisfied from top SPS up to LHC energies.

At LHC energies, the fireball with its high multiplicity is expected to have a rather long life time (4–10 fm/c) and its volume might be much larger than that at RHIC ( $\approx 2 \times 10^4 \text{ fm}^3$ ). Based on this a large fraction of particles will come from a region in the  $T - \mu_B$  diagram above the phase transition line (see Fig. 6.67). Indeed, chemical freeze out<sup>6</sup> (where inelastic interactions cease) will govern the composition of the emitted hadrons. Elastic scattering can still occur until kinetic freeze out is reached. The measured momentum distribution of particle type might then tell us its history, from the hard collisions at the beginning until the soft part, indicating the temperature at the kinetic freeze out. Their distribution in space would then reflect the pressure created in the partonic phase.

The detector arrangement of ALICE, with its ability to identify particles up to high momenta, will allow us to obtain detailed information on their momentum distribution. Particles at low momenta are also measured, allowing us to extract the chemical composition.

We divide the particles emerging from the system into wide categories: (*i*) those particles hadronizing out of a system which is essentially in a chemical equilibrium, called the ‘soft part’, with  $p_t < 1\text{--}2 \text{ GeV}/c$ , and (*ii*) those coming from hard partonic interactions, called the ‘hard part’, with  $p_t > 5\text{--}6 \text{ GeV}/c$ . The ‘soft’ particles usually exhibit a thermal spectrum. ‘Hard’ particles originate from the non-equilibrated initial interactions. The intermediate region with  $2 < p_t < 5\text{--}6 \text{ GeV}/c$ , might be dominated by coalescence (see Section 6.2.1.10). ALICE will be able to measure particles with high precision, allowing for a study from the early phase through to the final hadronic freeze out. Further, it can be studied whether and how these sets of information are correlated.

<sup>6</sup> We use the word ‘chemical’ to describe cases referring to relative abundances of hadrons or partons.

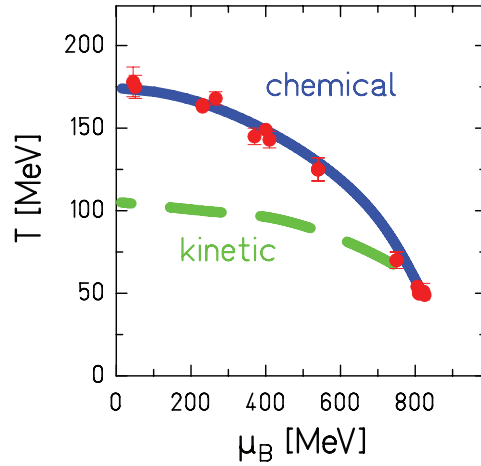


**Figure 6.67.** Compilation of chemical freeze out parameters at SIS [191–193], AGS [194], at the SPS at 40 A GeV [195–198] and 160 A GeV [194, 199, 200] and RHIC [201–203]. The full lines represent the phenomenological condition of chemical freeze out at fixed mean energy/particle  $\simeq 1.0$  GeV [204]. The dashed line indicates the temperatures where kinetic freeze out is observed [182, 183, 205–209].

Hadron multiplicities and their correlations are observables which can provide information on the nature, composition, and size of the medium from which they originate. Of particular interest is the extent to which the measured particle yields approach equilibrium. The appearance of the QGP, that is, a partonic medium being at (or close to) local thermal equilibrium, and its subsequent hadronisation during phase transition might drive the hadronic constituents towards chemical equilibrium [179–183, 210, 211].

The level of equilibrium of the secondaries in heavy-ion collisions was tested by analyzing particle abundances [181–183, 194–200, 204, 212–217] and their momentum spectra [207, 208, 215]. In the first case one establishes the chemical composition of the system, while in the second additional information on the dynamical evolution, e.g. collective flow, can be extracted. Of particular interest is the approach to strangeness equilibrium. For this purpose, it is useful to define the strangeness content, often called the Wroblewski factor [218, 219], defined as

$$\lambda_s \equiv 2 \frac{\langle s\bar{s} \rangle}{\langle u\bar{u} \rangle + \langle d\bar{d} \rangle}, \quad (6.11)$$

where the quantities in brackets refer to the number of quark-antiquark pairs. Ideally, one would like to pin down the  $s/u,d$  ratio at the hadronisation point before the hadronic decays take place. This is a difficult task because the secondary decays increase the number of  $u,d$  quarks significantly while the number of  $s$  quarks remains almost unaffected. Alternatively, one could study a well chosen particle ratio, e.g.  $K/\pi$ , but there is no ideal choice. Both aspects will be discussed later in detail.

In the following sections, experimental data on hadronic abundances obtained in ultrarelativistic heavy-ion collisions over a broad energy range are summarised starting from RHIC/BNL ( $\sqrt{s} = 200$  GeV, where  $\sqrt{s}$  is the centre-of-mass energy of the nucleon-nucleon system), SPS/CERN ( $\sqrt{s} \simeq 20$  GeV) down to AGS/BNL ( $\sqrt{s} \simeq 5$  GeV) and SIS/GSI ( $\sqrt{s} \simeq 2$  A GeV). Introducing transverse collective motion in addition to thermal motion, a brief survey of thermal freeze-out conditions is presented.

*6.2.1.2. Lattice gauge theory.* In ultrarelativistic heavy-ion collisions the value of  $\varepsilon_c$ , the critical energy density, characterises the necessary initial conditions in heavy-ion collisions to create a QGP, whereas the equation of state (EoS) is required as an input to describe the space–time evolution of the collision fireball. Both pieces of information can be obtained from first principles by formulating QCD on the lattice and performing numerical Monte Carlo simulations (see the first chapter of PPR Volume I [3]). The energy density obtained in Lattice Gauge Theory (LGT) exhibits the typical behaviour of a system with a phase transition [220]: an abrupt change within a very narrow temperature range around  $T_c$ . In the region below  $T_c$  the basic constituents of QCD, quarks and gluons, are confined within their hadrons. Above  $T_c$  the system appears in the QGP phase, where quarks and gluons can penetrate distances that exceed the typical size of hadrons substantially. The results of an improved perturbative expansion of the thermodynamical potential in continuum QCD [221] shows that, well above  $T_c$ , the EoS of QGP can be well described by a gas of massive quasi-particles, whose mass is temperature dependent. LGT predicts that in two and two+one flavour QCD a critical temperature  $T_c \sim 173 \pm 8$  MeV and a corresponding critical energy density  $\varepsilon_c = 0.3\text{--}1.3$  GeV/fm<sup>3</sup> are required for deconfinement [220].

*6.2.1.3. Thermal analysis.* The basic quantity required to verify the thermal composition of particles measured in heavy-ion collisions is the partition function  $Z(T, V)$ . In the Grand Canonical (GC) ensemble,

$$Z^{\text{GC}}(T, V, \mu_Q) \equiv \text{Tr}[e^{-\beta(H - \sum_i \mu_{Q_i} Q_i)}], \quad (6.12)$$

where  $H$  is the Hamiltonian of the system,  $Q_i$  are the conserved charges and  $\mu_{Q_i}$  are the chemical potentials that guarantee that the charges  $Q_i$  are conserved on average in the whole system;  $\beta = 1/T$  is the inverse temperature.

The Hamiltonian usually describes a non-interacting hadron resonance gas, which contains contributions from all mesons with masses below  $\sim 1.8$  GeV and baryons with masses below  $\sim 2$  GeV. In this mass range the hadronic spectrum is well established and the decay properties of resonances are known. This mass cut in the contribution to the partition function limits, however, the maximum temperature to  $T_{\text{max}} < 190$  MeV, up to which the model predictions can be trusted. For higher temperatures the contributions of heavier resonances must be taken into account.

The main motivation for using the Hamiltonian of a hadron resonance gas in the partition function is that it contains all relevant degrees of freedom for a confined, strongly interacting medium and implicitly includes interactions that result in resonance formation. Secondly, this model is consistent with the equation of state obtained from LGT below the critical temperature [222].

In a strongly interacting medium, one includes the conservation of electric charge, baryon number and strangeness. Thus, the partition function depends in general on five parameters. However, only three are independent, since the isospin asymmetry in the initial state fixes the charge-chemical potential and the condition of strangeness neutrality eliminates the strange-chemical potential. By using particle multiplicity ratios derived from the above partition the volume also drops out and we are thus left with only the temperature  $T$  and the baryo-chemical potential  $\mu_B$  as independent parameters.

Strangeness conservation in statistical models can be described in the grand-canonical (GC) ensemble only if the number of produced strange particles per event is much larger than one. In the opposite limit of ‘rare’ particle production (i.e. for multistrange baryons, which will be discussed later), strangeness conservation must be implemented locally, i.e. strangeness conservation per event. This canonical (C) description is relevant in the statistical

description of particle production at low incident energies, in high-energy hadron–hadron or  $e^+e^-$  collisions and in peripheral heavy-ion collisions. The exact conservation of quantum numbers, i.e. the canonical approach, is known to reduce severely the phase space available for particle production [223–227].

In order to illustrate canonical suppression, we consider  $K^-$  production via  $K^+K^-$  pairs. At high temperatures  $T$ , kaons are abundantly produced and the density of  $K^-$  can be described in the GC limit,

$$n_{K^-}^{\text{GC}} = (1/2\pi^2)m_{K^-}^2 T K_2(m_{K^-}/T) \quad (6.13)$$

with  $K_2$  the Bessel function.

In contrast, in the limit of low temperatures,  $K^-$  are rarely produced and in order to satisfy strangeness conservation, kaons must appear as pairs. The density of  $K^-$  then follows the C ensemble which can be written as  $n^{\text{C}} = n^{\text{GC}} F_s(V, T)$ . Here,  $F_s(V, T)$  is the canonical suppression factor, where  $F_s = I_1(x)/I_0(x)$  is a ratio of generalized Bessel functions, and the argument  $x = 2\sqrt{N_{s=1}N_{s=-1}}$  is proportional to the number of particles with  $s = 1$  and  $s = -1$ . Above top AGS energies the canonical description approaches the grand-canonical ensemble, for details see [191–193].

In the asymptotic limit for  $\langle K \rangle \ll 1$ , the canonical description shows a linear dependence of the correlation volume  $V_0$ :

$$n_{K^-}^{\text{C}} = [(1/2\pi^2)m_{K^-}^2 T K_2(m_{K^-}/T)] \times [V_0(1/2\pi^2)m_{K^+}^2 T K_2(m_{K^+}/T)]. \quad (6.14)$$

The first term coincides with the GC value, the second describes the phase-space suppression due to local strangeness conservation. The underlying physics of the correlation volume  $V_0$  is not fully settled (see later). It turns out that in low-energy heavy-ion collisions  $V_0$  scales with the number of participating nucleons and in pp collisions  $V_0$  can be approximated by the volume of a proton.

A detailed analysis of SPS data has shown [199] that choosing a temperature  $T = 168 \pm 4$  MeV and a baryon chemical potential  $\mu_{\text{B}} = 266 \pm 8$  MeV, a statistical model with only two parameters can indeed describe seventeen different particle multiplicity ratios with an accuracy of one to two standard deviations.

Recently, a more general equilibrium thermal model was proposed [228, 229]. This model describes not only strange but also light quarks off chemical equilibrium distributions. The fit to data at the SPS and RHIC has comparable or even lower  $\chi^2$  than that obtained in equilibrium models. It should be noted that as the strangeness undersaturation parameter  $\gamma_s$  increases the freeze-out temperature decreases as shown in a recent paper [230].

The equilibrium statistical model has also been applied to Au–Au collisions at the RHIC energies of  $\sqrt{s} = 130$  GeV and at 200 GeV [201, 231]. The measurements of the BRAHMS, PHENIX and STAR Collaborations for different particle multiplicity ratios are presented here to test chemical equilibration at RHIC at 200 GeV. Two fits were performed [232] including stable particle ratios from BRAHMS, PHENIX and STAR. Figure 6.68 shows that the data are well reproduced by the model within the experimental errors except for some of the resonances which are discussed in Section 6.2.1.7. In the first case (full line), a chemical freeze-out at  $T = 160.5 \pm 2$  MeV and  $\mu_{\text{B}} = 20 \pm 4$  MeV is obtained (close to the values of reference [233]) when the ratios  $\bar{p}/\pi^-$  and  $\phi/K^-$  of PHENIX are excluded. The second fit (dashed line) which includes these last two ratios led to both a lower temperature  $T = 155 \pm 2$  MeV (with  $\mu_{\text{B}} = 26 \pm 5$  MeV) and a higher  $\chi^2/\text{DOF}$ . Both temperatures are close to those previously found at SPS energies ( $T \sim 160$ – $170$  MeV). Such values for the temperature are to be expected since, in the limit of vanishing baryon density, the temperature should not exceed the critical value required for deconfinement. The substantial decrease of

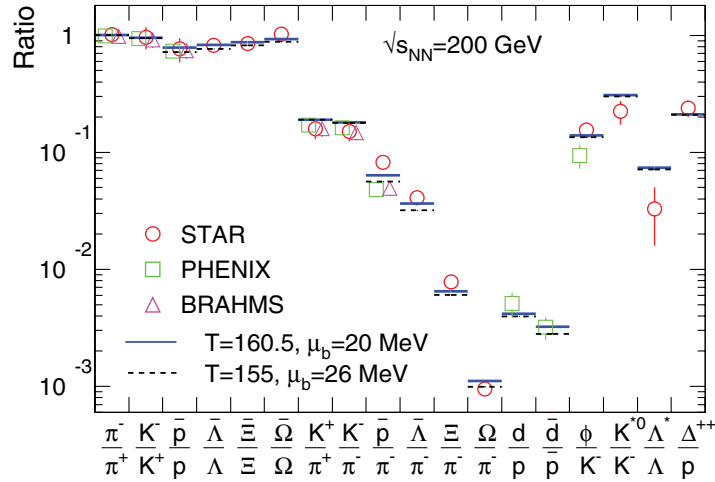


**Figure 6.68.** Comparison of the experimental data on different particle multiplicity ratios obtained at RHIC at  $\sqrt{s} = 200$  GeV with two thermal model fits [232]. The first fit includes stable particle ratios from BRAHMS, PHENIX and STAR except  $\bar{p}/\pi^-$  and  $\phi/K^-$  of PHENIX ( $T = 160.5 \pm 2$  MeV and  $\mu_B = 20 \pm 4$  MeV) whereas the second one also include these last two ratios ( $T = 155 \pm 2$  MeV,  $\mu_B = 26 \pm 5$  MeV).

the baryo-chemical potential from  $\mu_B \simeq 230$ – $270$  MeV at the SPS to  $\mu_B \simeq 25$  MeV at RHIC shows that we are dealing with a medium of low net-baryon density at LHC.

One could thus conclude that, with respect to the statistical operator formulated for an equilibrated hadron resonance gas, the experimental data at SPS and RHIC show a high degree of chemical equilibration. The question arises, whether this statistical operator provides a unique description of the data. As a possible alternative, the influence of in-medium effects on the chemical equilibrium description of particle yields at the SPS was studied [234]. The chemical freeze-out temperature extracted in the thermal analyses [194, 199] of experimental data in Pb–Pb collisions at the SPS and Au–Au at RHIC is remarkably close to the critical temperature  $T_c \simeq 173 \pm 8$  MeV obtained from lattice Monte Carlo simulations of QCD at vanishing baryon density [220].

**6.2.1.4. Multistrange baryons.** One of the earliest predictions made concerning strange-particle production is that it should be enhanced in nucleus-nucleus collisions, that is, that the yields for strange-particle species in ultrarelativistic nucleus–nucleus collisions should be higher than the corresponding yields at the same energy in nucleon–nucleon collisions [235–238]. There are two ways of arguing why this should take place. Both indicate that the state produced in heavy-ion collisions is different from that in pp collisions, and in both cases the time interval for the strangeness content to develop is important.

Firstly, hyperons are baryons containing one to three units of strangeness, and are not readily produced in nucleon–nucleon collisions at known energies. This can be explained in terms of: (i) the low cross sections for producing multistrange baryons, given that there are no strange initial state valence quarks and not much strangeness in the nucleon sea; (ii) the short time span for producing strangeness, which means final-state interactions will not have much effect.

Alternatively, in a nucleus–nucleus collision without deconfinement, it is argued that a similar situation should result, for although there is more opportunity for strangeness

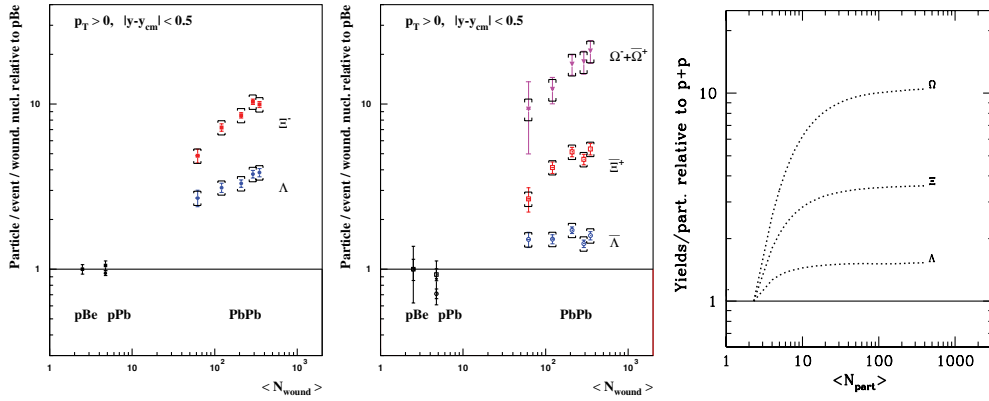


**Figure 6.69.** Left: Enhancement factors measured by the NA57 collaboration in pPb and Pb–Pb interactions relative to pBe interactions. The data correspond to 158 AGeV/c. Right: statistical model predictions [195, 243] for yield/participant in AA collisions at  $\sqrt{s} \simeq 130$  GeV, normalized to the corresponding value in pp collisions.

enhancement in final-state interactions, the short timescale for these to occur would still not allow full (GC) chemical equilibrium to develop. We may contrast this with the situation expected if deconfinement has occurred. Here the reactions leading to strangeness production are partonic; they have lower thresholds and higher cross sections, particularly if the strange quark mass reduces owing to the associated partial restoration of chiral symmetry. Strangeness production, up to GC equilibrium levels, is therefore expected to be achievable within the short time span available. These arguments lead us to expect that if deconfinement occurs, we should observe hadron abundances in accordance with GC chemical equilibrium, which implies we expect a large increase in strangeness yields with respect to systems where such partonic mechanisms are not available [237, 238].

Large strangeness enhancements are indeed observed [239–242], and thermal analysis shows that chemical equilibrium, describable with minimal corrections by a GC ensemble, is achieved from SPS energies upwards [199, 201]. Figure 6.69 shows the enhancement factors obtained for different hyperon species by the NA57 and WA97 experiments; the results are normalized to the pBe yields, and the corresponding enhancements calculated for pPb and different centrality classes for Pb–Pb, separated as a function of the number of ‘wounded nucleons’, i.e. the number of nucleons taking part in primary collisions. No enhancements are seen for pPb, but enhancements are seen in Pb–Pb. These increase with centrality, and are systematically larger according to the strangeness content of the particle, reaching a value of about 20 for  $\Omega$ s in the most central collisions. Very similar results, taking into account the drop in  $\mu_B$  between SPS and RHIC, have recently been reported by the STAR collaboration.

What is perhaps more surprising is that chemical equilibrium of a kind, albeit with lower strangeness, is also found in hadron–hadron and even  $e^+e^-$  collisions, where deconfinement cannot occur [244, 245]. Such systems are nowadays described in terms of canonical ensembles, appropriate where overall particle population sizes are big enough for thermodynamics to be applicable, but where strangeness conservation must be applied locally rather than globally [223–227, 246]. They are discussed in greater detail in Section 6.2.1.3. Qualitatively, current calculations, in terms of a gradual transition from canonical to grand canonical ensembles as the system size increases, reproduce the broad features of the observed enhancements, including their hierarchy in terms of strangeness content and the approximate

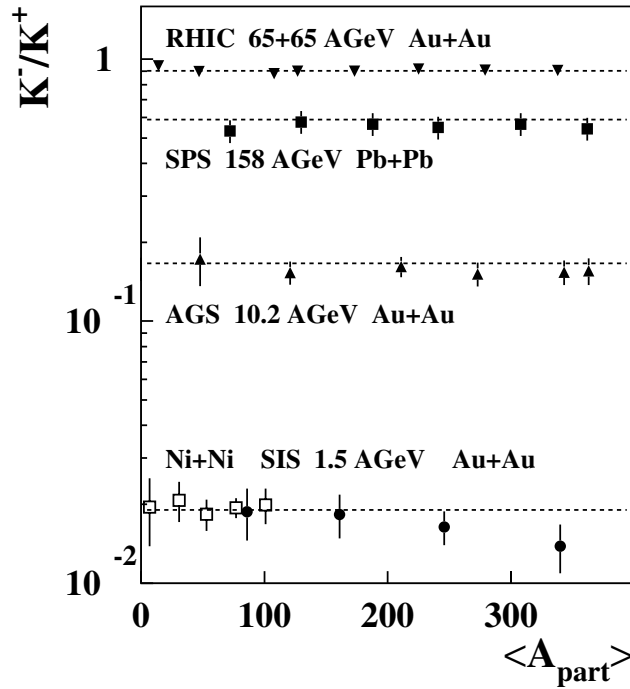


**Figure 6.70.** The  $K^-/K^+$  ratio appears to be constant as a function of centrality from SIS up to RHIC. Data are from the STAR, NA49, E866, and KaoS Collaborations. The dashed lines are statistical model results.

magnitudes in Pb–Pb. Detailed quantitative agreement has not yet been achieved in such a description. As an example, the right panel of Fig. 6.69 shows the results of a calculation for  $\sqrt{s} = 130$  GeV. Either way, we should bear in mind that even simple quark counting already leads to a bigger effect according to the strangeness content, and thus to the observed hierarchies between  $\Delta$ s,  $\Xi$ s and  $\Omega$ s [247]. What is made evident is that mechanisms exist which are available only to the heavy-ion system, and which allow it to satisfy GC equilibrium in a very short time. A careful investigation of available models has found that only models in which the system reaches or goes beyond  $T_C$  allow this [248–250].

At LHC, several new possibilities may emerge. It is likely that GC equilibrium remains, in which case a similar pattern to that seen at the SPS and RHIC would be found. In some non-equilibrium models, however, the ion–ion system may exceed the GC strangeness levels [230], leading to even greater enhancements. Alternatively, the pp system may itself become deconfined, at least for some multiplicity classes, and in this case the enhancement factor might drop.

This discussion indicates that the enhancement factor remains a useful way to compare strangeness production mechanisms in different systems at the same energy. It is well within the capabilities of ALICE to measure it.

**6.2.1.5. Energy dependence of strange-particle yields.** A compilation of the chemical freeze-out parameters determined from the measured particle yields in central AA collisions at SIS, AGS, SPS and RHIC energies has been shown in Fig. 6.67. The GSI/SIS results have the lowest freeze-out temperature and the highest baryon chemical potential. As the beam energy increases a clear shift towards higher  $T$  and lower  $\mu_B$  occurs. There is a common

feature to all these points, namely that the average energy per hadron is approximately 1 GeV. Chemical freeze-out in AA collisions is thus reached when the mean energy per particle drops below 1 GeV at all collision energies [204]. The above phenomenological freeze-out condition provides the relation between temperature and chemical potential at all collision energies. This relation, together with one particle ratio, e.g. the ratio of pions per participant, establishes the energy dependence of the two thermal parameters  $T$  and  $\mu_B$ . Consequently, predictions of particle excitation functions can be given in terms of this model.

The constancy of the  $K^-/K^+$  ratio with centrality together with the observation of a constant  $M_\pi/A_{\text{part}}$  gives a strong argument for the dominance of the strangeness-exchange channel in producing  $K^-$ . Both the application of the law-of-mass action [251] and transport-model calculations [252] gives a strong argument that the strangeness-exchange process is at or close to chemical equilibrium. The constancy of the ratio can also be explained by the volume dependence in the canonical description as the volume dependence just drops out when making the ratio  $K^-/K^+$ .

The measured  $K^+/\pi^+$  ratio [253] is a very rapidly rising function of collision energy from SIS up to top AGS energy. At higher energies it reaches a broad maximum between 20 and 40 AGeV and gradually decreases up to RHIC energy [254]. In microscopic transport models [255, 256] the increase of the kaon yield with collision energy is qualitatively expected as a result of a change in the production mechanism from associated production of  $K^+$  with strange baryons to direct  $K^+K^-$  pair production. However, hadronic cascade transport models do not provide a quantitative explanation of the experimental data in the whole energy range [257]. Mid-rapidity data exhibit the trends shown in the model calculations. This drop can only be reproduced using a statistical model of the early stage, as originally proposed by Gadzicki and Gorenstein [258, 259], or by the statistical model with further modifications, e.g. by introducing an additional strangeness undersaturation parameter  $\gamma_s \sim 0.75$  [194].

At low incident energies, results might contain contributions from the fragmentation region at forward/backward rapidity that do not belong to the fireball of interest. On the other hand, the use of mid-rapidity data, giving good agreement, is problematic as strangeness is not necessarily conserved in a limited phase-space area. At SPS energies, one has the choice between these two non-ideal situations. At high incident energies, due to boost invariance, this problem disappears.

The appearance of a maximum in the strange-to-non-strange particle-multiplicity ratios, already seen in  $K^+/\pi^+$ , is even more pronounced for strange baryon-to-non-strange meson ratios. Figure 6.71 shows the energy dependence of  $\Lambda/\pi^+$  and  $\Xi^-/\pi^+$ . There is a very pronounced maximum, especially in the  $\Lambda/\pi^+$ . The fast drop towards higher energies is related to the strong decrease of chemical potential together with only a moderate increase in associated temperature. The shift in maximum seen in the  $\Xi^-/\pi^+$  ratio is caused by the higher production threshold of  $\Xi^-$  and the higher strangeness content. The actual experimental data both for  $\Lambda/\pi^+$  and  $\Xi^-/\pi^+$  ratios shown in Fig. 6.71 follow the predictions of the statistical model.

The rather different behaviour of the various particle ratios shown in Fig. 6.71 gives evidence that any choice of a specific particle ratio is not very useful to characterise the strangeness content. Therefore, the use of the global strangeness content, the Wroblewski factor  $\lambda_s$  [218] defined earlier (Eq. (6.1)), is to be preferred. The solid line (marked ‘sum’) in Fig. 6.72 (right) shows  $\lambda_s$  as a function of  $\sqrt{s}$  as obtained from statistical-model calculations along the unified freeze-out curve [204] with energy-dependent parameters  $T$  and  $\mu_B$ . From Fig. 6.72 we conclude that around  $\sqrt{s} = 6$  GeV (30 AGeV laboratory energy) the relative strangeness content in heavy-ion collisions reaches a clear and well pronounced maximum. The Wroblewski factor decreases with increasing incident energies and reaches a limiting value of about 0.43. For details see Ref. [260].

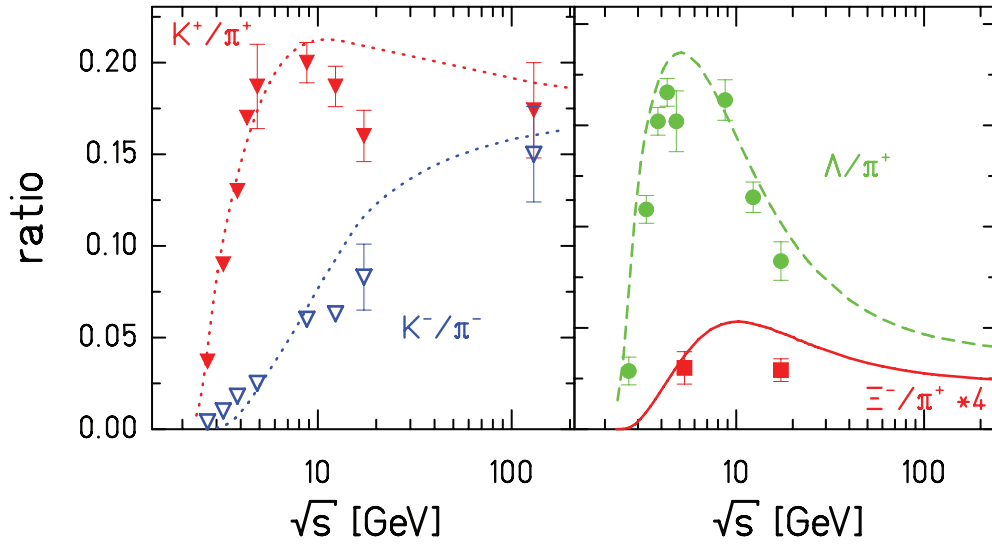


**Figure 6.71.** Various particle ratios involving strange/non-strange hadrons as a function of  $\sqrt{s}$ . Left for mesons and right for baryons. The lines exhibit the trends given by the statistical model calculated with the parameters along the unified freeze-out curve [204]. They describe well the behaviour of the ratios, which turns out to be quite different for the various species. Data at the SPS are fully integrated NA49 results.

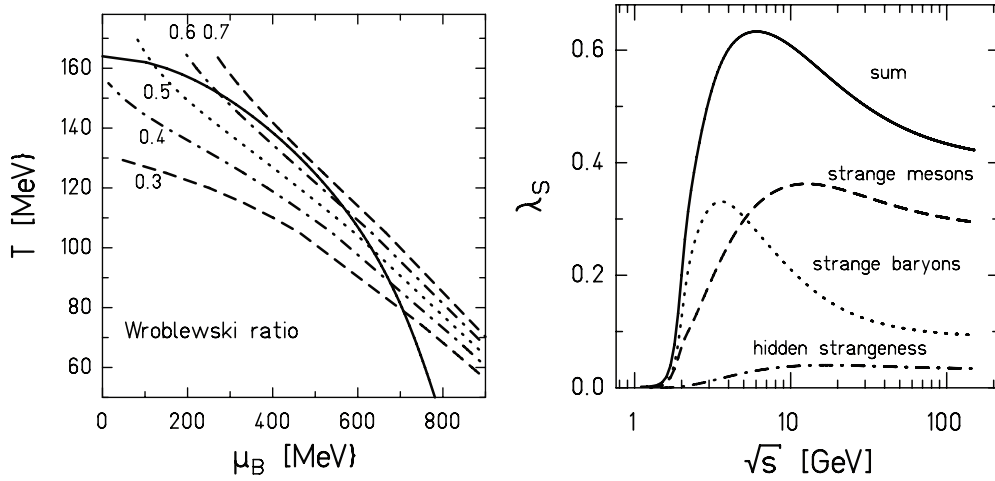


**Figure 6.72.** Left: Lines of constant Wroblewski factor  $\lambda_s$  in the  $T-\mu_B$  plane together with the freeze-out curve (dashed line) [204]. Right: Contributions to the Wroblewski factor (for definition see text) from strange baryons (dotted line), strange mesons (dashed line) and mesons with hidden strangeness (dash-dotted line). The sum of all contributions is given by the full line.

The appearance of the maximum can be traced to the specific dependence of  $\mu_B$  and  $T$  on the beam energy. Figure 6.72 (left) shows lines of constant  $\lambda_s$  in the  $T-\mu_B$  plane. As expected  $\lambda_s$  rises with increasing  $T$  for fixed  $\mu_B$ . Following the chemical freeze-out curve, shown as the solid line in Fig. 6.72, one can see that  $\lambda_s$  rises quickly from SIS to AGS energies, then reaches a maximum at  $\mu_B \approx 500$  MeV and  $T \approx 130$  MeV corresponding to  $\sqrt{s} = 6$  GeV. At

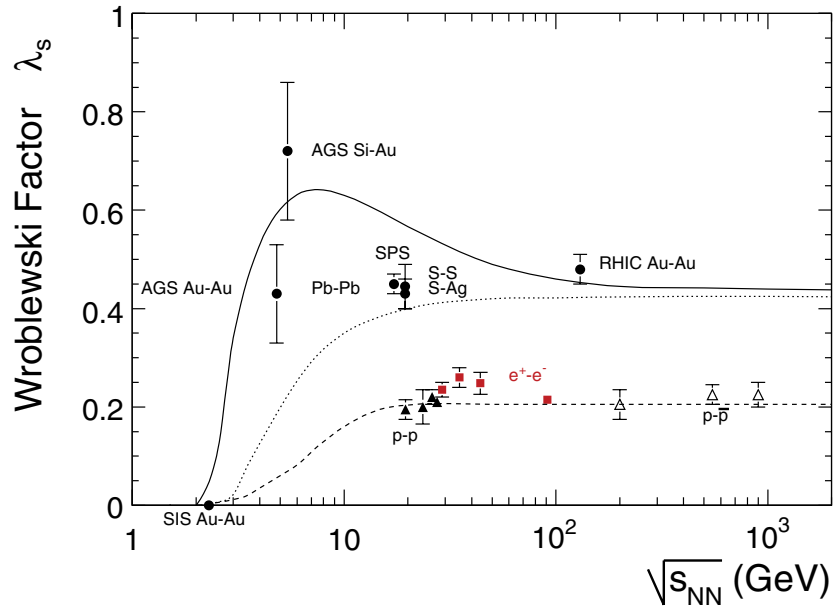


**Figure 6.73.** The Wroblewski factor  $\lambda_s$  as a function of  $\sqrt{s}$ . The thick solid has been calculated using the freeze-out values [204]. The dotted line reflects a calculation using the same  $T$  but keeping  $\mu_B = 0$ . This demonstrates that the maximum is caused by finite baryo-chemical potential. The dashed line has been calculated using a radius of 1.2 fm, keeping  $\mu_B = 0$  and taking the energy dependence of  $T$  as determined previously. All calculations are performed using strangeness saturation  $\gamma_s = 1$ .

higher incident energies the increase in  $T$  becomes negligible but  $\mu_B$  keeps on decreasing and as a consequence  $\lambda_s$  also decreases.

The importance of finite baryon density on the behaviour of  $\lambda_s$  is seen in Fig. 6.72 (right hand side), showing separately the contributions to  $\langle s\bar{s} \rangle$  coming from strange baryons, from strange mesons and from hidden strangeness, i.e. from hadrons like  $\phi$  and  $\eta'$ . As can be seen in Fig. 6.72 (right); the origin of the maximum in the Wroblewski ratio can be traced to the contribution of strange baryons. This channel dominates at low  $\sqrt{s}$  and loses importance at high incident energies. Even strange mesons exhibit a broad maximum. This is due to associated production of e.g. kaons together with hyperons.

For high incident energy,  $\lambda_s$  reaches a saturation value of about 0.43 in the hadron-gas approach, reflecting the situation  $T = 170$  MeV and  $\mu_B = 0$ . For an ideal QGP a value of  $\lambda_s$  of about 1 is expected at infinite temperature. However, recent lattice calculations demonstrate that due to the quark-mass difference of  $s$  and  $u, d$  in the QGP phase,  $\lambda_s$  also reaches  $0.45^{+0.02}_{-0.05}$  when approaching  $T_c$  (with  $\mu_B = 0$ ) [261]. This is a first hint as to why the observed strangeness reflects the value corresponding to an equilibrated hadron gas, since it is equal to that for a QGP at  $T_c$ .

**6.2.1.6. Strangeness production in  $pp$  collisions.** It has been demonstrated that the yields of hadrons emitted in  $e^+e^-$ ,  $pp$  and  $p\bar{p}$  collisions can also be well described by a statistical model [194] in a canonical formulation. From these studies the corresponding Wroblewski factor had been extracted and is given in Fig. 6.73. This figure also summarises the results from heavy-ion collisions.

In elementary collisions, often very few particle ratios are available. In order to extract the Wroblewski factor the population of high-lying resonances should also be known. These resonances decay into lighter particles (mainly pions) and dilute the experimentally observed strangeness content. This problem is the main drawback in using the Wroblewski factor as mentioned earlier. Usually their yield is unknown and it is taken from the model calculations. In the original work [219] analyzing elementary collisions feed-down was corrected on the basis of quark distributions in quark multiplets. In more recent analyses based on the statistical model [244, 245], it has been shown to yield a much better agreement with the data. This description implies a lower population of high-lying resonances and hence a smaller correction for their decay. As a result, Wroblewski factors based on [219] gave values which were too high, in contrast to those derived from the statistical model.

In pp collisions and in the energy range from the SPS up to RHIC a rather constant value of  $\lambda_s \sim 0.2$  was extracted from the data. The canonical model is able to describe these findings. This is demonstrated in Fig. 6.73 by the dashed line, which comes from a canonical description using a correlation volume of two protons. This correlation volume causes a strangeness reduction as compared to heavy-ion collisions, which have a  $\lambda_s$  around 0.43. The dotted line in Fig. 6.73 for the elementary processes does not exhibit a maximum, as the calculation was performed for  $\mu_B = 0$ . The maximum observed in the heavy-ion case is then caused by the finite  $\mu_B$ .

*6.2.1.7. Resonance production.* The production of short-lived resonances provides information about the later stages in the evolution of the hadronic system [237, 238]. Such particles decay with lifetimes of a few fm/c, comparable to the lifetime of the collision fireball itself. Owing to the typically large rescattering cross sections in the medium, the hadronic decays will be strongly influenced by final-state interactions. This results in deviations between expected thermal yields and those actually observed, as has been found in thermal fits to Au–Au data [262, 263]; the yields for long-lived particles are well described by a statistical model, while those for resonances are not. The worse agreement for resonances is clearly seen in Fig. 6.68, and is discussed in reference [233].

In addition to these effects, changes in line-shape for resonances are expected [264, 265] in heavy-ion collisions for two reasons: (i) the dense medium can induce significant collision broadening; (ii) shifts of both mass and width could be produced as a result of partial chiral symmetry restoration which is expected to lie close to deconfinement [266, 267]. In addition the resonance production has been argued to be useful to distinguish between different expansion and freeze-out scenarios [268].

Later in this section the capabilities of the ALICE experiment for studying the production of three resonances is discussed: the  $\rho^0(770)$ , the  $K^*(892)^0$  and the  $\phi(1020)$ . Each of these resonances is interesting in its own right.

The  $\rho^0$  is a broad resonance, with a width of 150 MeV, implying a lifetime of around 1.3 fm/c, which is short compared with the lifetime of the collision fireball.  $\rho^0$  decays from all stages of the collision can be seen in the leptonic decays of the  $\rho^0$ , since the decay products do not interact with the surrounding medium. In contrast, the pions formed in hadronic  $\rho^0$  decays will undergo final-state interactions. Therefore  $\rho^0$ s reconstructed in the hadronic channel will come from the last stages of the interaction. Nevertheless, distortions of the  $\rho^0$  line shape can occur as a result of in-medium effects [264, 265]. Such effects have been reported in both leptonic and hadronic decay modes.

$\phi$ -meson production is of interest for several reasons. Owing to its  $s\bar{s}$  valence quark content, it is expected to behave in a hadron gas as a non-strange particle. However, measurements [269] revealed a similarity of  $\phi$  production to that of strange particles. At LHC

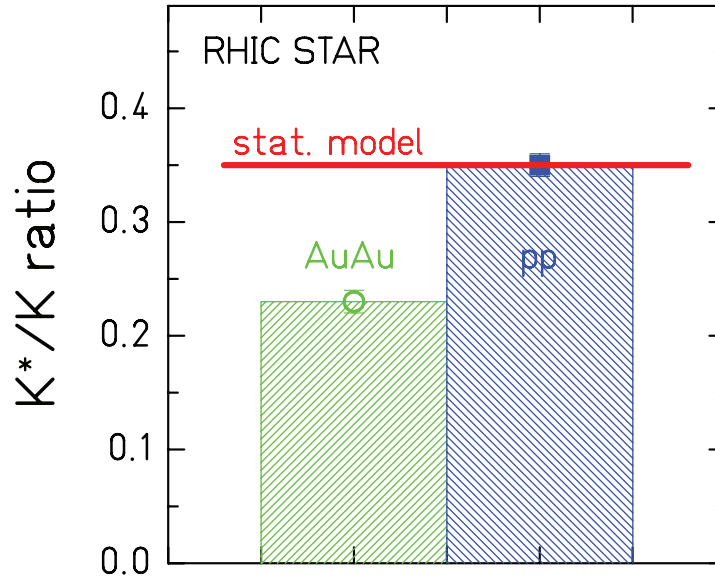


**Figure 6.74.** The measured ratios of  $K^*/K$  ratio for pp and central (10%) Au–Au collisions at  $\sqrt{s} = 200$  GeV from the STAR collaboration [262, 263]. The horizontal line gives the value of the statistical model [201].

with excellent statistics and high-quality data, it might be possible to extract the ‘effective’ strangeness content of the  $\phi$  meson. In addition, as in the case of the  $\rho^0$ , mass and width modifications for the  $\phi$  have been proposed, though as yet none has been observed. ALICE intends to study  $\phi$  production in both hadronic ( $K\bar{K}$ ) and leptonic ( $e^+e^-$ ) decay modes. The study below describes the  $K\bar{K}$  decay mode only.

Similar considerations apply to the  $K^*(892)^0$  as to the  $\phi(1020)$ . Owing to its strangeness content, the  $K^*(892)^0$  could also experience a strangeness enhancement. Recently, the STAR Collaboration has presented an interesting comparison of  $K^*/K$  ratio for pp and Au–Au collisions at RHIC ( $\sqrt{s} = 200$  GeV), as shown in Fig. 6.74 [262, 263].

While the results obtained in pp collisions agree roughly with statistical model predictions [201], the values for central Au–Au collisions are much lower indicating annihilation during thermal freeze-out.

Depending on the length of the time interval between chemical and kinetic freeze-out, the magnitude of the suppression factor of the measured resonance will change due to contributions from rescattering and recombination. A model using thermally produced particle yields at chemical freeze-out and an additional rescattering phase, including the life time of the resonance and the interaction of the decay products within the expanding fireball, can give an estimate of this time interval. Figure 6.75 shows that from two measured ratios  $K^*/K$  and  $\Lambda(1520)/\Lambda$ , where large rescattering is expected. Assuming a chemical freeze out at 160 MeV, a time interval  $\Delta\tau > 4$  fm/c has been obtained [270, 271].

#### 6.2.1.8. New opportunities at LHC with heavy-ion and pp collisions

*Heavy-ion collisions.* The collision fireball created in heavy-ion collisions at LHC is expected to be characterised by a rather long life time (4–10 fm/c) and an extended volume ( $2 \times 10^4$  fm<sup>3</sup>). If the systematics of particle production observed at SPS and at RHIC are preserved, then the particle yields will be determined by the values of  $T$  and  $\mu_B$ .

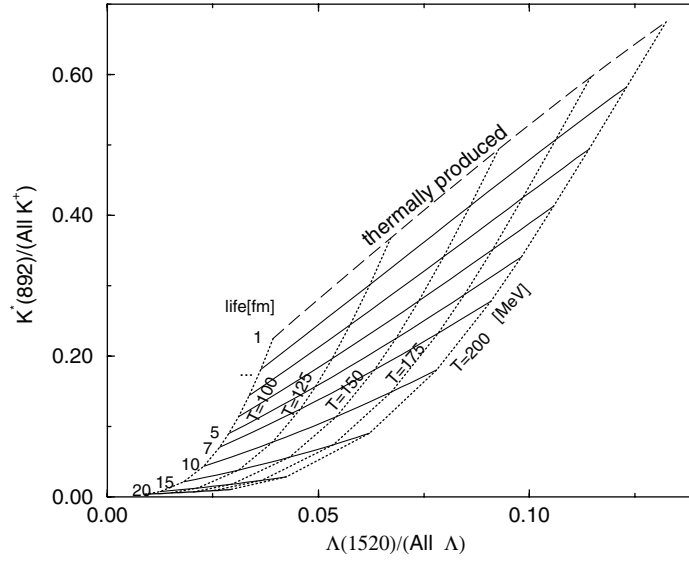


**Figure 6.75.** Dependence of the two ratios,  $K^*/K$  and  $\Lambda(1520)/\Lambda$ , on the freeze-out temperature and time interval between chemical and kinetic freeze out [270].

**Table 6.13.** Particle ratios in Pb–Pb collisions at freeze-out conditions expected at the LHC:  $T = (170 \pm 5)$  MeV and  $\mu_B = 1_{-1}^{+4}$  MeV in the case of the equilibrium model [201]. The given errors correspond to the variation in the thermal parameters. Additional, systematic uncertainties in the ratios of the right column arise from unknown decay modes. They are smaller than 1% in general, but reach 3% in the  $\Xi^-/\Lambda$  ratio and 7% in the  $p/\pi^-$  and the  $\Lambda/p$  ratios. In the case of the non equilibrium model [230] a lower temperature of  $T = 125$  MeV is assumed with chemical potential of  $\mu_B = 2.70$  MeV and  $\mu_S = 0.48$  MeV. The degree of light quark and strange quark equilibration are given by  $\gamma_s^H = 5$  and  $\gamma_q^H = 1.73$  respectively.

$\bar{h}/h$ ratio	eq. model	non. eq. model	mixed ratio	eq. model	non. eq. model
$\pi^+/\pi^-$	$0.9998_{-0.0010}^{+0.0002}$	0.9459	$K^+/\pi^+$	$0.180_{-0.001}^{+0.001}$	0.349
$K^+/K^-$	$1.002_{-0.002}^{+0.008}$	1.005	$K^-/\pi^-$	$0.179_{-0.001}^{+0.001}$	0.328
$\bar{p}/p$	$0.989_{-0.045}^{+0.011}$	0.960	$p/\pi^-$	$0.091_{-0.007}^{+0.009}$	0.037
$\bar{\Lambda}/\Lambda$	$0.992_{-0.036}^{+0.009}$	0.965	$\Lambda/p$	$0.473_{-0.006}^{+0.004}$	1.096
$\Xi^+/\Xi^-$	$0.994_{-0.026}^{+0.006}$	0.973	$\Xi^-/\Lambda$	$0.160_{-0.003}^{+0.002}$	0.432
$\bar{\Omega}^+/\Omega^-$	$0.997_{-0.015}^{+0.003}$	0.984	$\Omega^-/\Xi^-$	$0.186_{-0.009}^{+0.008}$	0.271

The temperature  $T$  will be hardly different from that obtained at RHIC,  $\mu_B$  will approach 0. Table 6.13 summarises the predictions for LHC based on  $T = (170 \pm 5)$  MeV and  $\mu_B = 1_{-1}^{+4}$  MeV for some particle ratios.

Resonances are also expected to be influenced in between chemical and kinetic freeze out, as mentioned in preceding section. The predictions of some ratios of resonances-to-stable particles are given in Table 6.14. Their yield will depend on their lifetime, which is also given.

The sensitivity of some particle ratios  $R$  to  $\mu_B$  and  $T$  are displayed in Fig. 6.76, demonstrating that  $\bar{p}/p$  is best suited to extract  $\mu_B$ . The chemical freeze-out temperature is obtained from particle ratios having a large mass difference. The ratio  $\Omega^-/\pi^-$  seems to be ideal. However, pions are dominantly produced from decays of higher resonances and, therefore, their mass plays a key role.

**Table 6.14.** Resonance to stable particle ratios in Pb–Pb collisions at freeze-out conditions expected at the LHC:  $T = (170 \pm 5)$  MeV and  $\mu_B = 1_{-1}^{+4}$  MeV. The given errors for the equilibrium model correspond to the variation in the thermal parameters. Additionally, systematic uncertainties arise from unknown decay modes. They are smaller than 1% in general, but reach 2% in the  $\phi/K^-$  ratio and 3.5% in the  $\rho^0(770)/\pi^-$  ratio. Resonance widths (taken from the PDG) are also indicated as well as non-equilibrium model ratios.

	Width (MeV)	Mixed Ratio	Eq. model [201]	Non. eq. model [230]
$\phi$	$4.26 \pm 0.05$	$\phi/K^-$	$0.138_{-0.004}^{+0.004}$	0.208
$\Lambda(1520)$	$15.6 \pm 1.0$	$\Lambda(1520)/\Lambda$	$0.090_{-0.003}^{+0.003}$	0.049
$K^*(892)^0$	$50.7 \pm 0.6$	$K^*(892)^0/K^-$	$0.323_{-0.009}^{+0.010}$	0.177
$\rho^0(770)$	$150.3 \pm 1.6$	$\rho^0(770)/\pi^-$	$0.127_{-0.002}^{+0.001}$	0.056

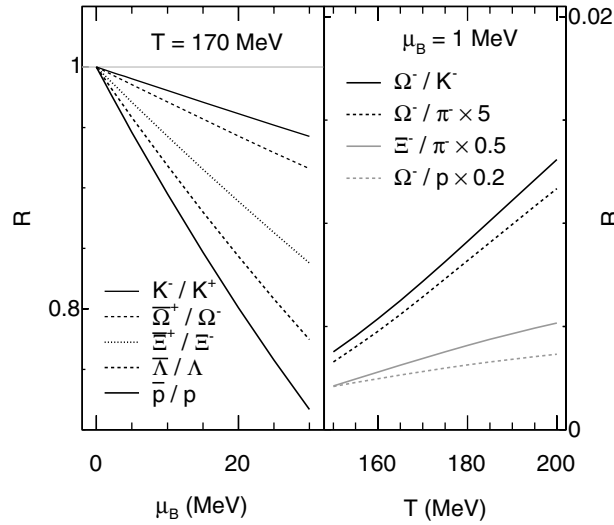


**Figure 6.76.** Left: Sensitivity of antiparticle to particle ratios on the baryon chemical potential  $\mu_B$  at a fixed freeze-out temperature  $T = 170$  MeV. It decreases with increasing strangeness content. Right: Sensitivity of ratios of particles with different masses on the decoupling temperature, calculated for a fixed  $\mu_B$  of 1 MeV. Both  $\Omega^-/K^-$  and  $\Omega^-/\pi^-$  are well suited to establish  $T$ .

Predictions for LHC in the non-equilibrium model have recently become available [230]. The value of  $\gamma_s$  for LHC energies is not known, but values much larger than 2 might be expected. A specific property of this approach is a decrease of the temperature  $T$  for increasing  $\gamma_s$ , as shown in the upper part of Fig. 6.77 (left). The particle ratios vary strongly with  $\gamma_s$  as shown in Fig. 6.77 for two ratios of strange-over-non-strange particles. This effect is even stronger when studying multi-strange particles [230]. It should be noted that for  $\gamma_s = 1$  lower values are obtained than for the equilibrium case (crosses). If, as expected by Rafelski, values of  $\gamma_s$  around 5–10 are reached at LHC energies, the particle ratios will differ strongly from the equilibrium situation.

However, at LHC a new situation will occur both in AA and in pp collisions. The dominance of jets and minijets will raise new questions since the final hadronic yields will originate from two different sources: a source reflecting the equilibrated (grand) canonical ensemble (soft physics) and on the other hand the fragmentation of jets which is sensitive to only a part of the volume (hard physics). Hence, the latter contribution will differ from the behaviour of an equilibrated ensemble.

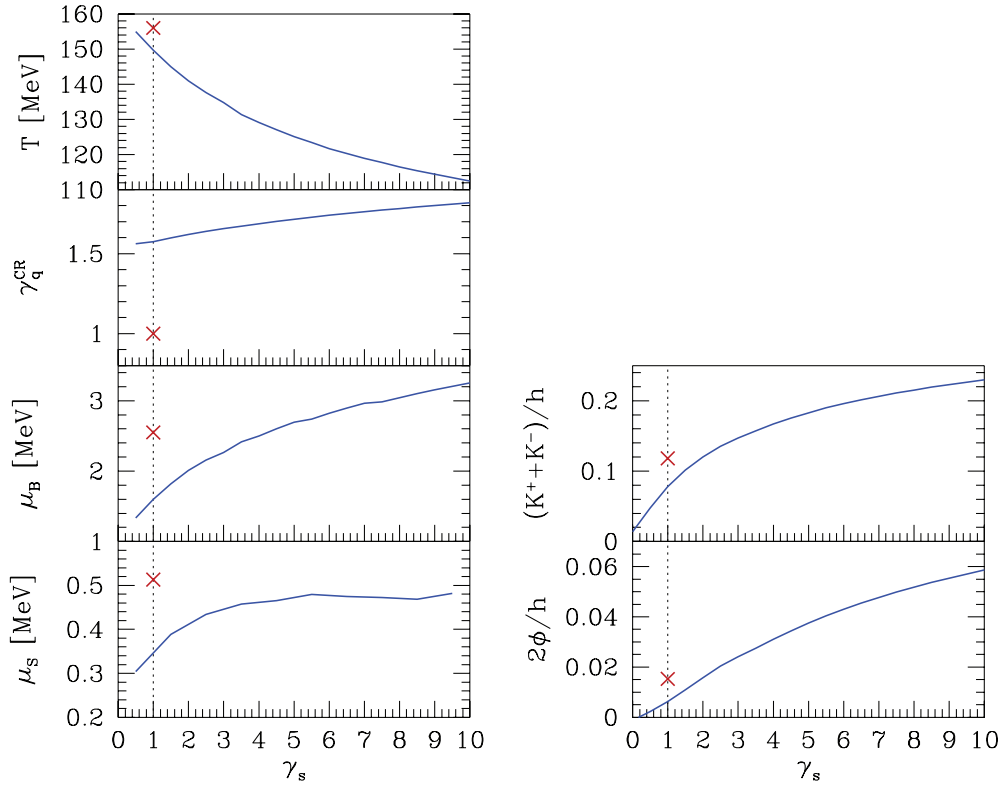


**Figure 6.77.** Left: The values of  $T$ ,  $\gamma_q^{\text{CR}}$ ,  $\mu_B$ , and  $\mu_s$  as a function of  $\gamma_s$  as obtained in the hadronisation model [230]. Right: Particle ratios of  $(K^+ + K^-)/h$  and  $2\phi/h$  as a function of  $\gamma_s$ . The crosses indicate chemical equilibrium model predictions. From [230].

In heavy-ion collisions where the jet fragmentation dominates, one might even expect a lowering of the strangeness content  $\lambda_s$  closer to that obtained in pp collisions as jet fragmentation leads to values around 0.3 for s/u,d [272]. Therefore, it will be important to test the validity of the statistical model.

Due to the large number of newly produced particles, a novel type of data analysis will be possible; a ‘chemical analysis’ of event classes might open a way to study the relation between soft and hard physics. Some examples are:

- The freeze-out condition can be extracted for single events. Thus, we obtain a whole distribution of  $T(i)$  and  $\mu_B(i)$  pairs. The width of this distribution can be compared to the statistical width to probe thermalisation. A 15% change in  $K^+/\pi^+$  correspond to a change of 1 MeV in  $T$ .
- The above mentioned procedure will furthermore allow us to characterise selected event classes, e.g. ‘high  $T$ ’ and ‘low  $T$ ’. Gating on these classes will allow us to disentangle different types of dynamic evolution in the  $T-\mu_B$  plane: early and late freeze-out.

*pp collisions.* From Fig. 6.73 one might conclude that the strangeness content in elementary collisions will hardly increase with incident energy. However, this is far from being clear. The number of produced particles in pp collisions will increase up to values similar to those observed in heavy-ion collisions at the SPS. Hence, the volume parameter in the canonical

description may have to be increased to account for the higher multiplicity. This will result in an increasing strangeness content. It is not clear whether the volume parameter should be related to the initial volume or to the final size of the system at hadronisation. In the extreme case, the observed strangeness content in pp collisions might also reach the saturation value of 0.43 for  $T_c$  and  $\mu_B = 0$  in the GC limit.

This effect of strangeness increase might be amplified when selecting events with high multiplicities. It has been observed by the UA1 Collaboration that the  $K^+/\pi^+$  ratio increases slightly with increasing  $\sqrt{s}$  [273]. ALICE will obtain sufficient statistics in pp to reach multiplicities 10 times the mean multiplicity. This study has gained special interest recently. Arguments for ‘deconfinement’ have been advocated in high-energy pp collisions [274]. Note that an alternative interpretation to the results, not connected to deconfinement has also been given [275]. The presence of jet events will allow for further very important studies. By triggering on events with one, two or more jets, a ‘chemical analysis’ of these collisions will be possible. A possible correlation between the initial and freeze-out phase might be extracted. This very new opportunity would allow us to study whether the occurrence of hard processes influences the distribution of the ‘soft physics’ part. Particularly interesting in this context is the behaviour of strange and multi-strange particles, e.g. the  $K/\pi$  or  $\Omega/\pi$  ratio in combination with extremely hard processes.

The measurement of higher resonances in pp will be important to obtain the respective population. This can be compared with what is found in heavy-ion studies, though in the latter case the yields are likely to be changed by the destruction of the resonances during the time between chemical and thermal freeze out (see the discussion of Fig. 6.74 above).

*6.2.1.9. Particle momentum distribution.* The agreement of the statistical model with most of the experimental data suggests that the collision fireball created in A–A collisions is thermal in nature. However, it does not explain how the system reached such a state; in particular, can the process be unambiguously related to interactions between its constituents, and are these partonic? As seen in Section 6.2.1.8, hadronic rescattering as well as an estimate between chemical and thermal freeze-out can be inferred from final resonance abundances and comparison with pure thermal model descriptions: apparently, at chemical freeze-out the density of the fireball is still high enough so hadrons undergo significant rescattering. But with increasing beam energy, it is expected that most of the reinteractions, which result in a thermodynamical pressure and lead to the collective expansion of the medium, occur at the partonic level. The overall collective motion, when integrated over the evolution of the system, can be studied via particle momentum spectra. In addition, using particles with low hadronic cross sections, one would like to quantify the partonic fraction.

The transverse component of the particle momentum spectra is often described using an inverse slope parameter: it characterises particle transverse spectra at first order, assuming that an exponential form describes the shape of the distribution properly. Therefore a system which undergoes partonic then hadronic transverse collective expansion should show particle momenta with three typical behaviours: (i) the inverse slope parameter must increase linearly with the rest mass of the particle; (ii) overall collective motion should increase with beam energy and consequently with developed pressure; (iii) particles with low hadronic cross sections may have a lower parameter than that from a simple extrapolation. We try here to define the main trend for particle momentum distributions from SIS to RHIC energies, and then to extrapolate to LHC energies.

The left panel of Fig. 6.78 shows the mass dependence of the inverse slope parameter for charged  $\pi$ , K and protons at SIS, SPS and RHIC. The collective transverse flow is not only seen in high-energy data but already at SIS. As already mentioned, the dependence of

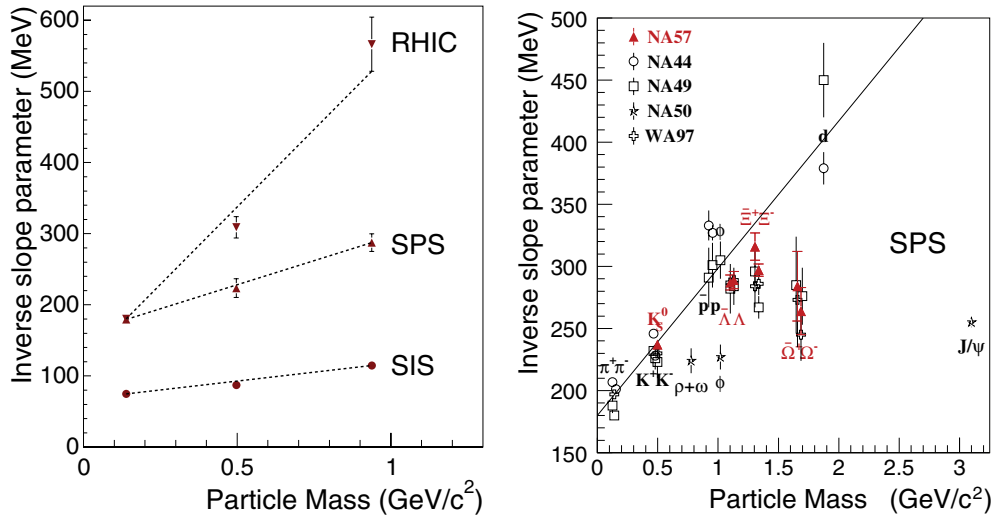


**Figure 6.78.** Left: Charged  $\pi$ , K and protons inverse slope parameters at the SIS, SPS and RHIC. Clear linearity is seen as a function of particle mass at rest. Right: Compilation of data at SPS energies where particles with low hadronic cross sections such as  $\Omega$  and  $J/\psi$  particle differ from simple linear extrapolation (see [208, 276–278]).

the inverse slope parameters of pion, kaon and proton is seen to be an increasing function of particle mass from SIS through SPS up to RHIC energies. If all particles decouple kinetically approximately at the same time, then hadronic  $m_t$  spectra could be characterised by only two parameters: average thermal freeze-out temperature ( $T_f$ ) and average flow velocity ( $\langle v_t \rangle$ ) [207]. Detailed analysis has shown that such a picture indeed works within currently available data at SPS for all particles with the exception of  $\Omega$  and  $J/\psi$  and possibly  $\phi$  [276]. These particles have inverse slope parameters that are significantly lower than expected from flow systematics as seen in the right panel of Fig. 6.78. The above discrepancy could indicate that these particles are decoupled earlier due to their very low rescattering cross section with the surrounding medium [278–280] at the hadronic stage.

At RHIC energies, the same picture was shown to be valid [281]. Moreover, important progress has been made by showing that particle  $p_t$  spectra are well described using the concepts of fast thermalisation and hydrodynamical evolution of the system. The left panel of Fig. 6.79 shows good agreement of the hydrodynamical model [282] with RHIC  $\pi^+$  and  $\bar{p}$  spectra measured in the low transverse momentum range for the most central data; the right panel corresponds to  $\bar{p}$  comparisons for several event centrality classes.

When fixing the equation of state, the decoupling energy density directly translates into kinetic freeze-out temperature ( $T_{fo}$ ). Hence, information related to thermal freeze-out can be extracted from hydrodynamical evolution models: these temperatures are remarkably constant at the AGS and SPS around 100–120 MeV but slightly higher at RHIC [282–285] with  $\langle T_{fo} \rangle \simeq 128$ –140 MeV. In this framework, centrality dependence is very important.

Models based on hydrodynamics [286, 287] can be used to estimate  $T_{fo}$  and the mean transverse velocity ( $\langle \beta_t \rangle$ ) simultaneously, and study their behaviour as a function of centrality. These models do not contain a full hydrodynamical description, but instead describe the shape of the  $m_t$  spectra as a function of the particle mass. They allow us to study the centrality and flavour dependence of the parameters  $T_{fo}$  and  $\langle \beta_t \rangle$  [233, 288]. For this purpose, the system is often modelled as an expanding source with a flow velocity profile that depends on the

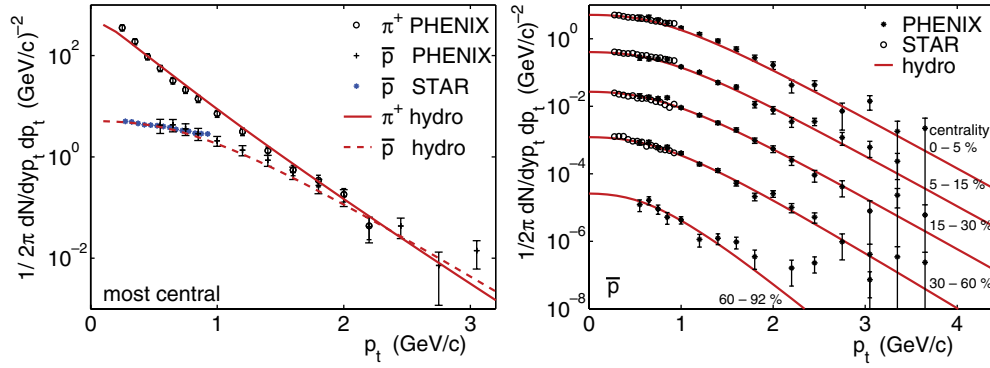


**Figure 6.79.** Particle spectra comparison of hydrodynamical calculations with RHIC data from PHENIX and STAR. Left panel:  $\pi^+$  and  $\bar{p}$  spectra for most central collisions. Right panel:  $\bar{p}$  spectra for different centrality samples [282].

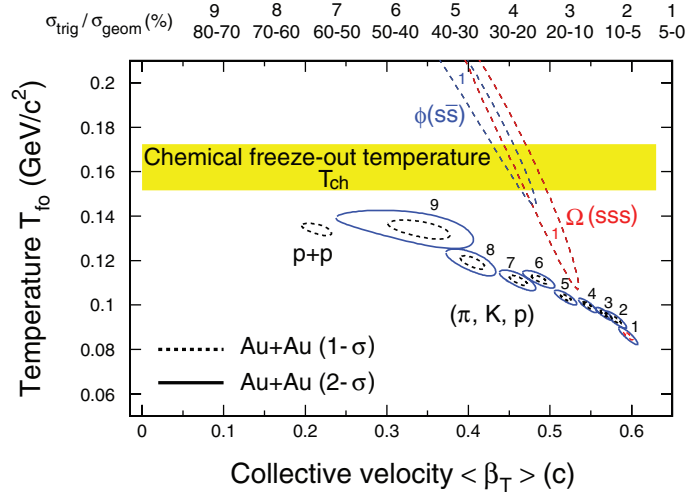


**Figure 6.80.** As presented in [233] (see references therein). The  $\chi^2$  contours extracted from thermal and radial flow fits (without allowance for resonance feed-down), for the copiously produced hadrons  $\pi$ , K and p and multi-strange hadrons  $\phi$  and  $\Omega$ . On the top of the plot, the numerical labels indicate the centrality selection. For  $\pi$ , K and p, 9 centrality bins (from top 5% to 70–80%) were used in  $\sqrt{s_{NN}} = 200$  GeV Au–Au collisions. The results from pp collisions are also shown. For  $\phi$  and  $\Omega$ , only the most central results [289] are presented. Dashed and solid lines are 1- $\sigma$  and 2- $\sigma$  contours, respectively.

maximum emission radius. Particle spectra are fitted independently according to their flavour content and information about a possible early hadronic decoupling (i.e. higher  $T_{fo}$  as well as a smaller  $\langle \beta_t \rangle$ ) is extracted. Figure 6.80 corresponds to  $\chi^2$  contour fits obtained with such a model in the  $T_{fo}$  vs  $\langle \beta_t \rangle$  estimated space. The behaviour of multi-strange hadrons produced in the most central collisions at top RHIC energies is compared with those for  $\pi$ , K and p together in 9 centrality bins. Although the uncertainties are large for multi-strange hadrons due to a lack of statistics (as shown by the rather large contours of  $\phi$  and  $\Omega$ ), and although  $\pi$ , K and p are not feed-down corrected here, the first noticeable characteristics of Fig. 6.80 are: (i) multi-strange particles and  $\pi$ , K and p have no overlap for contours for top central Au–Au

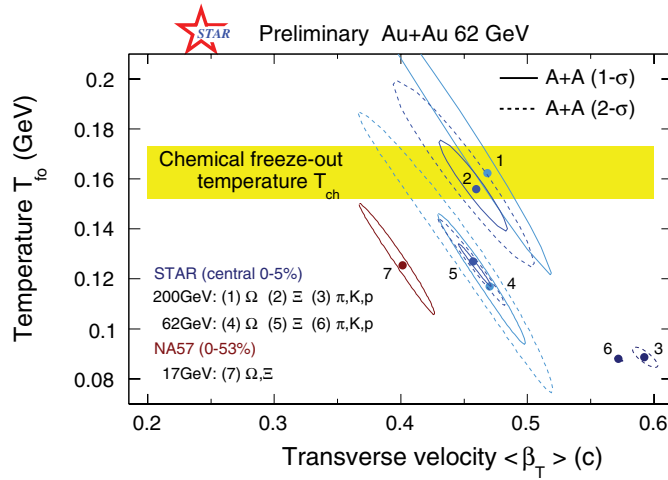


**Figure 6.81.** The  $\chi^2$  contours, extracted from thermal and radial flow fits (without allowance for resonance feed-down), for  $\pi$ , K and p and multi-strange baryons  $\Xi$  and  $\Omega$ . The data presented are for Au–Au collisions at the RHIC energies  $\sqrt{s_{NN}} = 200$  GeV and 62 GeV from the STAR experiment [289, 291, 292] and for 0–53% central Pb–Pb collisions at SPS energies of  $\sqrt{s_{NN}} = 17.3$  GeV from the NA57 experiment [290]. Minima of the fits are shown together with numerical labels which indicates the particle(s) and the beam energy. For  $\pi$ , K and p, only STAR data are shown for  $\sqrt{s_{NN}} = 62$  GeV and 200 GeV Au–Au collisions. The solid and dashed lines are 1- $\sigma$  and 2- $\sigma$  contours, respectively.

collisions; (ii) multi-strange particles have a  $T_{fo}$  parameter<sup>7</sup> minimum consistent with that for the chemical freeze-out temperature,  $T_{ch}$ , extracted from statistical thermal analysis, which also matches  $T_c$  of LGT, and (iii) the corresponding transverse velocity is  $\sim 2/3$  that of the  $\pi$ , K and p for the same central event sample. On the other hand, the evolution of the system between  $T_{ch}$  and  $T_{fo}$  is dominated by hadronic rescattering and would here be described by the cooling of the copiously produced particles ( $\pi$ , K and p), which acquire a stronger collective flow during this phase. This relates to the decrease of the  $T_{fo}$  parameter contour for  $\pi$ , K and p with increasing centrality whereas  $\langle \beta_t \rangle$  increases from  $\sim 0.35$  to  $\sim 0.6$ .

The multi-strange baryons do not feel the same cooling and therefore do not have the same time interval between chemical and thermal freeze-out. Consequently, by comparing both multi-strange hadron and  $\pi$ , K and p behaviour, at RHIC energies one would favour a scenario where a significant fraction of the transverse velocity is built at or prior to chemical freeze-out, so that even with a low hadronic cross section, produced particles have a strong collective motion. These main trends can be extrapolated to LHC energies by studying the beam energy dependence of the contours. Figure 6.81 shows together SPS and RHIC data from the NA57 [290] and STAR [289, 291, 292] experiments respectively for the multi-strange baryons  $\Xi$  and  $\Omega$ . From the evolution of the corresponding contours between top central Au–Au collisions at  $\sqrt{s_{NN}} = 62$  GeV to 200 GeV, it seems that the  $T_{fo}$  parameter increases rapidly up to temperatures consistent with chemical freeze-out, despite the large uncertainties due to statistics. However the evolution of the  $\langle \beta_t \rangle$  parameter for these particles is less pronounced and similar to the increase of lower mass particles  $\pi$ , K and p. In addition, it must be noted that no increase in the  $T_{fo}$  parameter is seen for  $\pi$ , K and p. This fact would

<sup>7</sup> This fit parameter is only an estimate of the physical kinetic freeze-out temperature and further studies must be performed to check that no systematic shift significantly biases its possible interpretation.

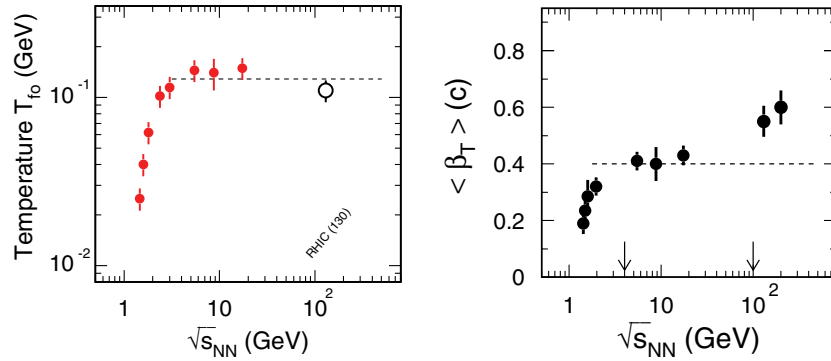


**Figure 6.82.** Excitation function of the kinetic freeze-out temperature parameter  $T_{f0}$  (left panel) and the average collective transverse flow velocity  $\langle \beta_t \rangle$  parameter (right panel) [202, 293].

suggest here again a different decoupling time between copiously produced particles and multi-strange baryons. Such a measurement at LHC energies could further test this hypothesis and help determining the systematics between the  $T_{f0}$  parameter and the thermal freeze-out for these hyperons. For this purpose, we note that obtaining the resonance spectra (see Sections 6.2.4, 6.2.6 and 6.2.5) is of great importance for the understanding of feed-down decay effects and systematics in such a picture.

Using the compilation [202, 293] of Figs. 6.82, one can observe the beam energy dependence over a larger scale for final-state particles corresponding mainly to  $\pi$ , K and p. At LHC energies the  $T_{f0}$  parameter may well have converged to a constant value; it would be very instructive to see if  $\langle \beta_t \rangle$  increases or starts to saturate.

Finally, we note that transverse flow is only one aspect, and that initial pressure also leads to other observables which are sensitive probes of collective motion and equilibration in heavy-ion collisions. One of these observables is the elliptic flow which is extensively discussed in Section 6.4.

#### 6.2.1.10. Dynamics in the soft and intermediate $p_t$ region

*Intermediate  $p_t$  region.* Soft particle production ( $p_t < 2$  GeV/ $c$ ) and the dynamics of the bulk matter can be well described by statistical models and hydrodynamics, as discussed in Section 6.2.1.3. However, one implication of fully thermal hadron distributions would be that most information is lost about the preceding deconfined phase and the details of the parton distribution functions. Fortunately, RHIC results have shown that some of this information may survive in the intermediate momentum region between soft phenomena ( $p_t < 2$  GeV/ $c$ ) and hard scattering ( $p_t > 6-8$  GeV/ $c$ ), described by perturbative QCD (pQCD). Anomalous proton/pion [294–297] and  $\Lambda/K_S^0$  ratios [298], as well as the momentum spectra relative to the reaction plane (elliptic flow) seem to carry information about the parton distributions in the early phases in this intermediate momentum region.

It is therefore essential to detect and identify mesons and baryons in this intermediate momentum region in order to obtain a detailed picture about the early collective state of the matter. Particle identification will be possible in ALICE (see Section 6.2.2) for most of the hadron species up to a  $p_t$  of at least 15 GeV/ $c$ , and here particle distributions should be governed by pQCD.

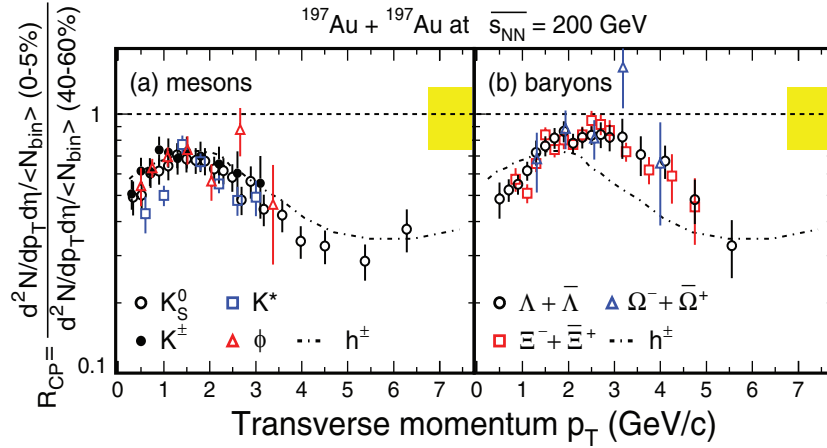


**Figure 6.83.** Binary scaled ratio  $R_{CP}$  of hadron yields for the 0–5% centrality (most central) bin divided by the 40–60% bin at RHIC for 200 GeV Au–Au collisions [233]. The spectra are normalised to the number of binary nucleon-nucleon collisions  $N_{bin}$  for each centrality range. Left and right panels show meson and baryon  $R_{CP}$  respectively. In each panel, the ratio corresponding to all charged hadrons is shown for reference.

Here we present some of the relevant results from RHIC, focusing on momentum spectra (i.e. the ratio of momentum spectra between central and peripheral collisions  $R_{CP}$ ) and baryon over meson ratios. Elliptic flow aspects will be discussed in Section 6.4.

*Nuclear modification factor.* Hadron production in the intermediate- $p_t$  region has been measured in Au–Au collisions at top RHIC energies. The extracted nuclear modification factors [299] display a different suppression pattern for mesons and baryons as shown in Fig. 6.83.

The data indicate a similar and strong modification factor for pions, kaons and  $\phi$ , independent of their large mass difference. For baryons the suppression is definitely much smaller; in fact between 1.5–3 GeV/ $c$  there seems to be no suppression at all for protons (not shown),  $\Lambda$ s and  $\Xi$ s. Since the proton and  $\phi$  have similar masses but different suppression, it can be claimed that the behaviour of these suppression patterns is not of ‘thermal’ origin, but instead depends on the quark content of the produced particles. This finding supports constituent quark coalescence/recombination models, which were invoked to explain the anomalous proton/pion ratio at RHIC energies [300–306]; however, there are a number of open issues with these models which need further clarification and confirmation.

The standard picture of hadron production at high  $p_t$  involves fragmentation of energetic partons described by factorised fragmentation functions in a pQCD-improved parton model. Fast partons propagate in the vacuum connected to each other via colour strings and finally hadronise via (string) fragmentation. This mechanism is not applicable at low or even intermediate- $p_t$ , especially in nucleus-nucleus reactions. In high-energy heavy-ion collisions, where many partons populate the phase space, multi-parton processes become important and potentially even dominant. In such conditions it may be most effective to create new hadrons from partons that are already present and close to each other. This process is called quark coalescence/recombination; it was first proposed for SPS energies in order to reproduce hadron yields [307–309] and spectra [310–312]. It seems to work even better at RHIC

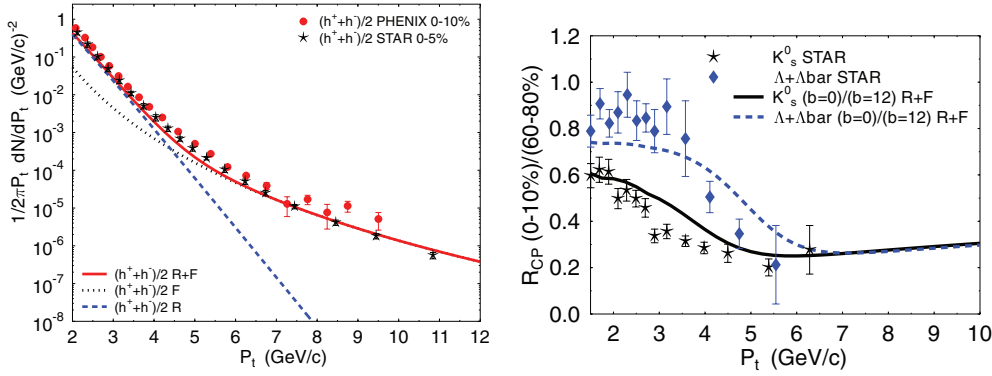


**Figure 6.84.** Left:  $p_t$  distribution predicted by a quark recombination+fragmentation model [316], compared to the inclusive charged hadron  $p_t$  spectra measured in Au–Au at 200 GeV by PHENIX and STAR for central collisions (R and F correspond to Recombination and Fragmentation contributions respectively). Right: Nuclear modification factor  $R_{CP}$  predicted by a quark recombination+fragmentation model [305, 306] for mesons ( $K_S^0$ ) and baryons ( $\Lambda$ ), compared to STAR data.

energies [313, 314]. Since the matter at SPS, RHIC and LHC energies may reach, after expansion, a similar pre-hadronisation state, where the strongly interacting quark matter may be described by a massive quasi-particle picture [315], quark-coalescence may actually work successfully over a very wide energy range.

For a quantitative analysis of the experimental data, one can follow two methods employing coalescence/recombination models. In the simplest case one assumes thermal soft hadron production and appropriate thermal spectra at  $p_t < 2$  GeV/c; then, neglecting quark mass effects, one calculates hadron spectra directly from quark recombination [303–306]. Another possibility is to consider quark coalescence down to the softest momenta, and treat the soft and intermediate hadron production jointly on the basis of quark coalescence [300–302, 310–312]. In the momentum region  $2 < p_t < 8$  GeV/c both methods yield similar results and the obtained coalescence yield must be added to the fragmentation yield from higher  $p_t$ . The left panel of Fig. 6.84 from Refs. [305, 306] displays this superposition for charged hadron spectra whereas the right panel displays  $R_{CP}$  distributions for neutral strange particles in RHIC collisions.

The interplay between fragmentation and recombination reproduces quite well the  $p_t$  spectrum of charged hadrons as well as pions and protons separately. The region below 4 GeV/c would be dominated by quark coalescence/recombination, the region above 6 GeV/c by parton fragmentation. In Au–Au collisions, parton energy loss effects were included in the fragmentation yields, thus reproducing the nuclear suppression observed in the data, which is an important effect in the fragmentation region (above 5 GeV/c). For lower  $p_t$  values, this suppression is counteracted by the recombination mechanism and a clear enhancement appears, as seen also in the experimental data. Recombination yields more baryons than mesons at a given hadron  $p_t$ , since the three quarks recombining into a baryon have a larger yield at  $p_t/3$  compared to quarks at  $p_t/2$ , which recombine to form the mesons [317].

**Baryon/meson ratio.** The behaviour of the anti-baryon/baryon ratios ( $\bar{B}/B$ ) as a function of  $p_t$  has been studied at RHIC energies [294–298], and differs from the predictions of pQCD-inspired models; these predicted a stronger decrease of the ratios (see e.g. Ref. [318]). For this reason one can conclude that perturbative effects are not dominant up to quite high transverse

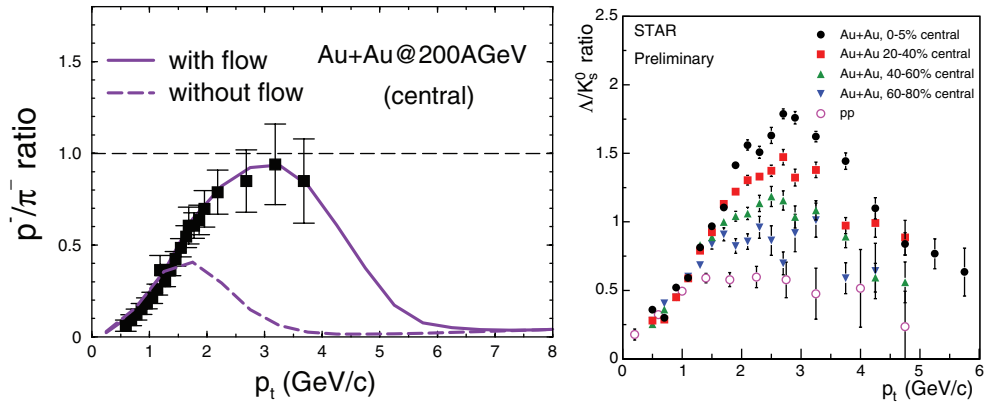


**Figure 6.85.** Left: Measured [294, 296, 297] and calculated [303, 304]  $\bar{p}/\pi$  ratio in central Au–Au collisions at  $\sqrt{s_{NN}} = 200$  GeV. Right: Measured  $\Lambda/K_S^0$  ratio for different centrality bins of Au–Au collisions and for pp collisions at  $\sqrt{s_{NN}} = 200$  GeV [298].

momenta ( $p_t \simeq 6$  GeV/c). Hadronization via coalescence in the intermediate  $p_t$  region is a possible scenario which could explain the measured  $R_{CP}$  as presented before. However, one can speculate whether this is not a more simple effect related to collective motion (i.e. transverse radial flow would ‘push’ spectra further for baryons than for mesons, depending on mass) or if instead this can only be explained by a more sophisticated mechanism, such as one involving gluonic baryon junctions [319, 320]. This can be further investigated using baryon/meson ratios and flavour dependence, shown in the left and right panels of Fig. 6.85 for the  $\bar{p}/\pi$  ratio in central Au–Au collisions and for the  $\Lambda/K_S^0$  ratio in several different centrality bins respectively.

In order to describe the  $\bar{p}/\pi$  ratio of the left panel of Fig. 6.85, the contribution of both coalescence and radial flow is needed, respectively, for the magnitude of the ratio and for the location of the turnover. In fact, if coalescence were the only mechanism, the proton/pion ratio would increase continuously with increasing  $p_t$ . However, a maximum can be seen clearly around 3 GeV/c. This is explained by the fact that pions have a significant fragmentation contribution above 3 GeV/c, whereas proton fragmentation appears much later due to the mass dependent transverse radial flow. The flavour and centrality dependences add more constraints to these models. The right panel of Fig. 6.85 shows the  $\Lambda/K_S^0$  ratio for pp collisions and Au–Au as a function of centrality at  $\sqrt{s} = 200$  GeV [298]. The radial flow contribution is expected to increase with centrality and lead to a  $p_t$  value for the turnover region that increases continuously with centrality. This is also true for calculations including baryon junctions [319, 320], whereas coalescence may not work for more peripheral collisions where the phase space is not populated enough. Therefore one can hope that, with sufficient statistics and precise measurements, it may be possible to distinguish between these models.

*Discussion and expectations at LHC energies.* Extrapolation to LHC energies [316] requires an estimate of radial flow and of quenching factors, both of which will affect hadron spectra. With quenching factors of order 10 at 10 GeV/c [321] and with flow presumably increasing, it is quite likely that the intermediate  $p_t$  region at LHC will extend to higher momenta than at RHIC. The left panel of Fig. 6.86 from Ref. [316] shows predictions for the recombination and fragmentation components of the  $\pi^0$  spectra assuming a freeze-out temperature of 175 MeV

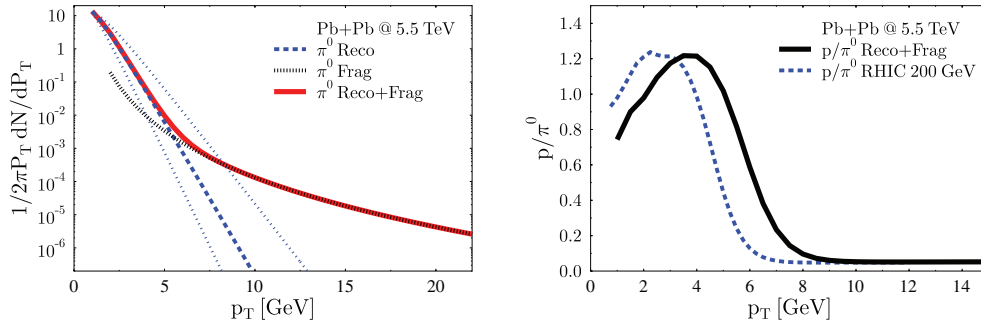


**Figure 6.86.** Left: Transverse momentum spectra of  $\pi^0$  for central Pb–Pb collisions with  $\sqrt{s} = 5.5$  TeV at mid-rapidity [316]. Fragmentation from pQCD (dotted), recombination (long dashed) and the sum of both (solid line) are shown. The parameters for the thermal parton phase are  $T = 175$  MeV and  $v_t = 0.75c$ . For pions recombination for different radial flow velocities  $0.65c$  and  $0.85c$  (lower and upper short dashed) are also shown. Right: The  $p/\pi^0$  ratio for Pb–Pb at LHC (solid) and for Au–Au at RHIC (dashed line) as predicted by a calculation using recombination and pQCD [316]. The baryon enhancement is pushed to higher  $p_t$  for LHC.

and a transverse radial flow of  $v_t = 0.75c$  (recombination components corresponding to  $v_t = 0.65c$  and  $v_t = 0.85c$  are also shown for comparison).

The turnover between the two regimes is shifted from 4 GeV/ $c$  (see left panel of Fig. 6.84 on page 1569) to 6 GeV/ $c$  for pions when going from RHIC to LHC energies and even further for protons [316], all well within the range of ALICE particle identification capabilities. The right panel of Fig. 6.86 shows the resulting prediction for the  $p/\pi^0$  ratio at LHC compared to RHIC.

## 6.2.2. Identified particle spectra

### 6.2.2.1. Particle identification ranges with ALICE.

Particle identification (PID) has proved to be invaluable for a number of observables at both SPS and RHIC and over a momentum range much larger than originally anticipated. Examples are the distinctive patterns observed for the mass and flavour dependence of radial and elliptic flow, or the anomalously large baryon to meson ratios measured in inclusive spectra out to several GeV at RHIC (see Section 6.2.1). Particle identification information is crucial in all these cases for a quantitative analysis and interpretation of the results.

The intermediate momentum region where particle ratios differ significantly between pp and heavy-ion collisions extends at RHIC out to 5–6 GeV/ $c$  and may well extend further at LHC. Particle identification in this transition region, where soft and hard processes compete, is crucial in order to disentangle different particle production mechanisms, e.g. constituent quark coalescence versus jet fragmentation.

At even higher momenta, it will be interesting to study both inclusive particle spectra and jet fragmentation with identified particles. Both observables are related to the energy loss of hard scattered partons in the surrounding hot and dense matter (‘jet quenching’). By identifying the leading hadron, one may be able to enrich the jet sample with either quark or gluon jets [322], which suffer different amounts of energy loss in matter owing to the different colour charges of the scattered parton. The hadron composition in the soft part of the jet fragmentation function may contain information about the interaction between the energy radiated into low momentum gluons and the surrounding matter. In summary, many physics analyses will be greatly improved or even rely on particle identification at intermediate and high  $p_t$ .

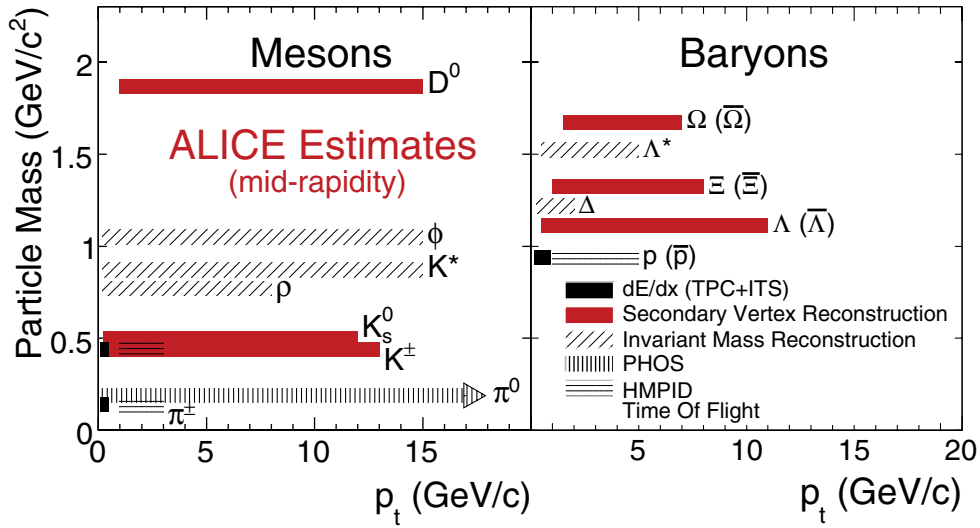


**Figure 6.87.** Transverse momentum ranges for particle identification at mid-rapidity using the main sub-detectors of the ALICE experiment. Each range is an estimate for 10 M most central events. Mesons and baryons  $p_t$  ranges are shown in the left panel and right panel respectively. Arrows are specified when the PID range exceeds that of the figure i.e. 20 GeV/c.

**Table 6.15.** The table shows the momentum range over which photons can be identified using the specified detector and technique. The rapidity region is also given.

Photon	Range ( GeV/c)	PID technique/sub-detector	Reference	Comments
direct $\gamma$	0.1–20	Stat. analysis (PHOS)	Section 6.9	mid-y

Estimated ranges for particle identification in ALICE at mid-rapidity are shown in Fig. 6.87. Each range is an estimate for 10 M most central events and corresponds to a particle identification technique using the main subdetectors of the experiment.

Details can be found in Tables 6.15, 6.16, 6.17 and 6.18. The list is not exhaustive and the ranges may vary depending on the model used for the simulation (e.g. no high- $p_t$  suppression was assumed). For technical aspects and dedicated analyses, see the ‘Reference’ column in these tables.

**6.2.2.2. Particle identification at large transverse momenta based on specific energy loss measurements in the TPC.** Specific ionization in the TPC provides an excellent way of identifying charged hadrons at high  $p_t$  with good efficiency and large acceptance, and compares well with the other particle identification techniques listed in Tables 6.16 and 6.17. Using the TPC we will be able to measure inclusive particle spectra for pions, kaons, and protons on a statistical basis and to identify individual tracks as pions or protons with reasonable efficiency and good purity up to momenta of at least 50 GeV/c. The upper limit will depend on the available statistics rather than instrumental limitations.

**Specific ionization at large transverse momenta in the ALICE TPC.** The mean energy loss  $\langle dE/dx \rangle$  of particles traversing the TPC detector gas is related to the velocity  $\beta$  of the particle by the Bethe–Bloch equation

$$\langle dE/dx \rangle = C_1/\beta^2 (\ln(C_2\beta^2\gamma^2) - \beta^2 + C_3), \quad (6.15)$$

**Table 6.16.** As for Table 6.15, but for mesons.

Meson	Range (GeV/c)	PID technique/sub-detector	Reference	Comments <sup>(1)</sup>
$\Upsilon''$	0–6	Inv. mass analysis	Section 6.6	$-4 < y < -2.5^{(2)}$
$\Upsilon'$	0–7	Inv. mass analysis	Section 6.6	$-4 < y < -2.5^{(2)}$
$\Upsilon$	0–13	Inv. mass analysis	Section 6.6	$-4 < y < -2.5^{(2)}$
$\psi'$	0–9	Inv. mass analysis	Section 6.6	$-4 < y < -2.5^{(2)}$
$J/\psi$	0–19	Inv. mass analysis	Section 6.6	$-4 < y < -2.5^{(2)}$
$D^0$	1–15	Secondary vertex reco.	Section 6.5.4	mid-y
$\phi$	0.2–15	Inv. mass reco.	Section 6.2.5	mid-y
$K^*$	0.2–15	Inv. mass reco.	Section 6.2.6	mid-y
$\rho^0$	0.2–8	Inv. mass reco.	Section 6.2.4	mid-y, hadronic decay
$K_S^0$	0.2–12	Secondary vertex reco.	Section 6.2.3.2	mid-y <sup>(3)</sup>
$K^\pm$	0.3–13	Secondary vertex reco.	Section 6.2.2.6	mid-y
$K^\pm$	0.1–0.5/5–50	$dE/dx$ (ITS+TPC/Rel. rise)	Section 5.4.1,2	mid-y <sup>(4)</sup>
$K^\pm$	1–3	HMPID	Section 5.4.5	mid-y <sup>(4)</sup>
$K^\pm$	0.35–2.5	Time Of Flight	Section 5.4.4	mid-y <sup>(4)</sup>
$\pi^0$	0–100	PHOS	Section 6.2.2.4	mid-y <sup>(4)</sup>
$\pi^\pm$	0.1–0.5/5–50	$dE/dx$ (ITS+TPC/Rel. rise)	Section 5.4.1,2	mid-y <sup>(4)</sup>
$\pi^\pm$	1–3	HMPID	Section 5.4.5	mid-y <sup>(4)</sup>
$\pi^\pm$	0.3–2.5	Time Of Flight	Section 5.4.4	mid-y <sup>(4)</sup>

<sup>(1)</sup> For all mesons no high- $p_t$  suppression was taken into account;

<sup>(2)</sup> Corresponds to  $4 \times 10^8$  central (10% most central) events recorded with the Muon Spectrometer;

<sup>(3)</sup> Corresponds to an exponential input distribution with an inverse slope of  $\sim 400$  MeV (see the  $\phi$  Section 6.2.5).

Estimations for power law or Levy spectrum shapes are under study;

<sup>(4)</sup> See Section 5.4.6 for combined PID and Sections 5.4.2,3 for PID technique in the relativistic rise.

**Table 6.17.** As for Table 6.15, but for baryons.

Baryon	Range (GeV/c)	PID technique/sub-detector	Reference	Comments <sup>(1)</sup>
$\Lambda_c$		Secondary vertex reco.	Under investigation	mid-y
$\Omega^\pm$	1.5–7	Secondary vertex reco.	Section 6.2.3.3	mid-y <sup>(2)</sup>
$\Lambda^*$	0.5–5	Inv. mass reco.	Extrapolation	mid-y
$\Xi^\pm$	1–8	Secondary vertex reco.	Section 6.2.3.3	mid-y <sup>(2)</sup>
$\Delta$	0.25–2	Inv. mass reco.	Extrapolation	mid-y
$\Lambda$	0.5–11	Secondary vertex reco.	Section 6.2.3.2	mid-y <sup>(2)</sup>
$p^\pm$	0.15–0.9/5–50	$dE/dx$ (ITS+TPC/Rel. rise)	Section 5.4.1,2	mid-y <sup>(3)</sup>
$p^\pm$	1–5	HMPID	Section 5.4.5	mid-y <sup>(3)</sup>
$p^\pm$	0.45–4	TOF	Section 5.4.4	mid-y <sup>(3)</sup>

<sup>(1)</sup> For all baryons no high- $p_t$  suppression has been taken into account;

<sup>(2)</sup> Optimization using the ITS are under study to allow us to reach lower limits;

<sup>(3)</sup> See Section 5.4.6 for combined PID and Sections 5.4.2,3 for PID technique in the relativistic rise.

**Table 6.18.** As for Table 6.15, but for nuclear fragments.

Nuclear fragments	Range (GeV/c)	PID technique/sub-detector	Reference	Comments
d, t, $^3\text{He}$ , $^4\text{He}$	0.5–10	$dE/dx$ (ITS+TPC)	Section 6.2.2.5	mid-y <sup>(1)</sup>

<sup>(1)</sup> This is an instrumental limit, the actual one depends on production cross section and  $p_t$  spectrum of each anti-nuclei.

with  $\gamma = 1/\sqrt{1 - \beta^2}$  and detector specific constants  $C_1$ ,  $C_2$ , and  $C_3$ . Since the mean energy loss depends on velocity rather than on momentum, combining momentum and  $\langle dE/dx \rangle$  information yields the particle mass, hence its identity.

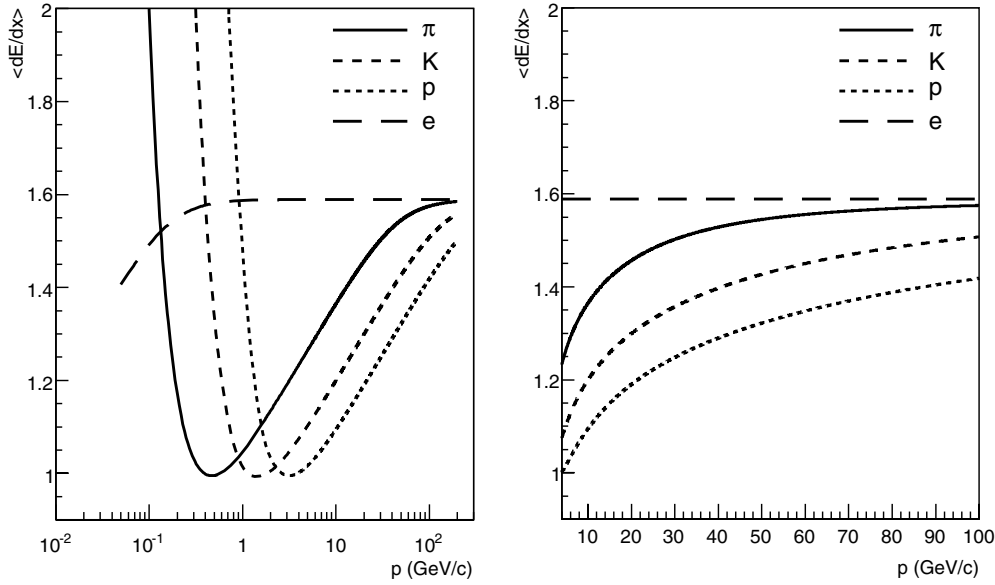


**Figure 6.88.** Momentum dependence of the mean energy loss  $\langle dE/dx \rangle$  for pions, kaons, protons, and electrons according to the parametrisation of equation 6.15 valid for the ALICE TPC. The mean energy loss is normalised to unity for minimum ionizing hadrons.

Figure 6.88 shows a parametrisation of equation 6.15 valid for the ALICE TPC. The mean energy loss for different particle species is well separated both below and above the minimum ionization region, which appears at  $3 < \beta\gamma < 4$ . Particle identification using energy loss information from both ITS and TPC at low momentum, in the non-relativistic region, is described in detail in Section 5.4.2 and 5.4.3.

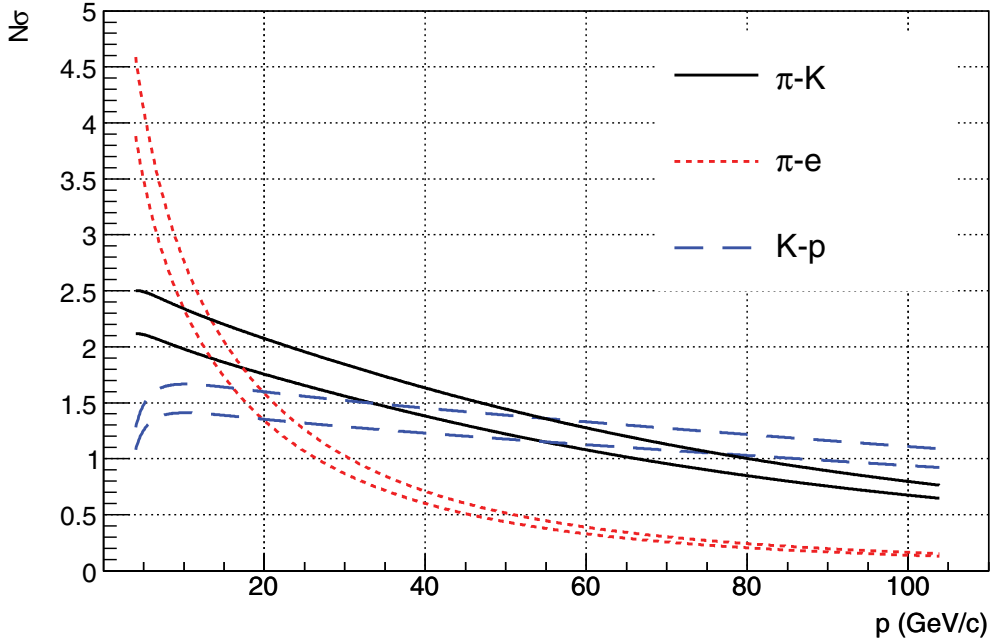
The TOF array and, with smaller acceptance, the HMPID can identify charged hadrons up to  $\beta\gamma \sim 5-6$ , where the energy loss curves cross each other and therefore the  $dE/dx$  information is ambiguous. In this section we focus on the relativistic region, i.e.  $\beta\gamma > 5-6$ ; which together with the other particle identification techniques used in ALICE provides continuous coverage for pions, kaons and protons from very low momentum up to at least 50 GeV/c.

The experimental procedure for the determination of  $dE/dx$  in the ALICE TPC is described in Section 5.1.3. The measured values of the energy loss at any given momentum follow a Gaussian distribution to a very good approximation, with a mean given by equation 6.15. The first moment of the distribution, the standard deviation ( $\sigma$ ), defines the separation power; it depends on detector design and on track properties, e.g. on the number of pads and on the number of measured points in the TPC.

The resolution, defined as the first moment divided by the mean value, was determined from detailed detector simulations to be 5.5% in situations at low multiplicity growing to 6.5% in high multiplicity environments. These results are experimentally confirmed by tests with a prototype of the ALICE TPC [323, 324].

The separation power between particles species A and B at a given momentum can be quantified by the difference of their mean energy loss values in units of  $\sigma$ :

$$N\sigma_{A,B} = \frac{\langle dE/dx \rangle_A - \langle dE/dx \rangle_B}{(\sigma_A + \sigma_B)/2}. \quad (6.16)$$



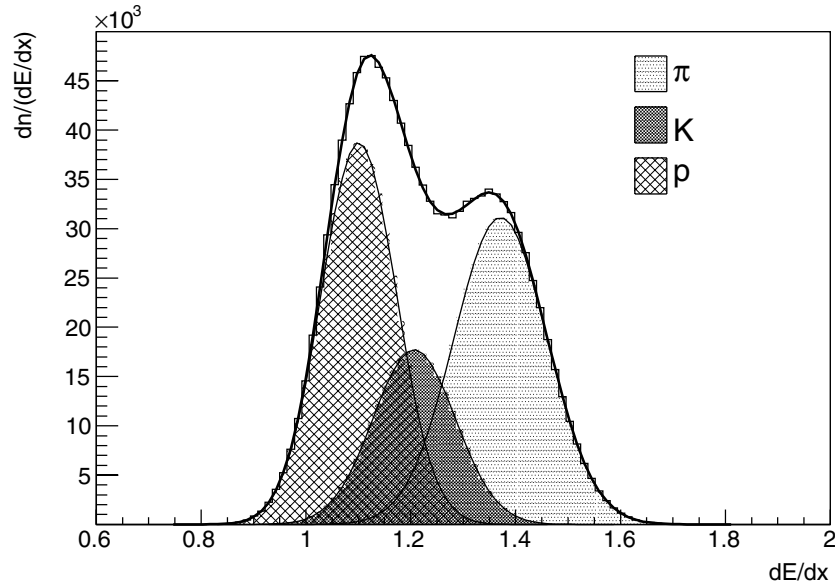
**Figure 6.89.** Momentum dependence of the separation between  $(dE/dx)$  values for three particle combinations in units of the energy loss resolution. The upper set of curves corresponds to 5.5% resolution the lower to 6.5% resolution.

Figure 6.89 shows the momentum dependence of  $N\sigma_{K-p}$ ,  $N\sigma_{\pi-K}$ , and  $N\sigma_{\pi-e}$ , using equation 6.15 for the mean energy loss and assuming a resolution of 6.5% (representative of central Pb–Pb collisions) or 5.5% (as expected in pp and peripheral Pb–Pb collisions).

The pion-electron separation was included to demonstrate the separation power available in addition to the TRD information for electron identification below 20 GeV/c. Both TOF and TRD information can be used to eliminate the electron contamination from the hadron spectrum in the cross-over region. At high multiplicities (6.5% resolution), the separation between pions and kaons drops from 2.1 at 5 GeV/c to 1.2 at 50 GeV/c; the kaon-proton separation shows in the same range a maximum of about 1.4 and drops to 1.2.

Given sufficient statistics, such a separation power is sufficient to identify hadrons on a statistical basis up to very high momenta [325]. However, it will require a good calibration of the TPC, excellent knowledge of the response function and good control of systematic errors. In ALICE we shall be able to measure the detector response (i.e. both position and width of the energy loss distribution) in real events by using high purity samples of particles identified with the other PID detectors (TOF, HMPID, TRD) in the appropriate momentum regions. Topological cuts (e.g.  $K_s^0 \rightarrow \pi^+\pi^-$ , photon conversions  $\gamma \rightarrow e^+e^-$ ) can be used to study the response function at high momentum. Charged and neutral kaon spectra are measured in addition via secondary vertices (see Sections 6.2.2.6 and 6.2.3.2), which will allow systematic comparisons between the independent methods.

*$p_t$  range of inclusive spectra of identified hadrons.* In order to reach reasonable statistics at high  $p_t$ , we have simulated the particle identification capabilities of the TPC in a parametrised fast Monte Carlo, using as input the mean energy loss (equation 6.15) and assuming a Gaussian energy loss resolution with a width of 6.5%. The statistics used in the examples given below corresponds to one year of running, i.e.  $10^7$  central Pb–Pb events.



**Figure 6.90.**  $dE/dx$  spectrum for pions, kaons and protons with  $p_t = 5.0 \text{ GeV}/c$  at midrapidity. Solid line indicates fit result, shaded areas correspond to contributions from individual hadrons. Total number of entries equals estimated hadron yield of  $10^7$  central Pb–Pb collisions.

Figure 6.90 shows an example of a  $dE/dx$  distribution of hadrons in a  $1 \text{ GeV}/c$  bin centred at  $p_t = 5 \text{ GeV}/c$ , integrated over the acceptance of the TPC. Particle ratios were chosen to be  $\pi : K = 2 : 1$  and  $\pi : p = 1 : 1$ , typical of RHIC measurements at intermediate  $p_t$  [295].

The solid line in Fig. 6.90 shows a fit to the  $dE/dx$  spectrum, with the sum of three Gaussian functions, representing the three hadron species. In the fitting procedure, the distances between mean values were fixed by the Bethe–Bloch relation and the resolution was assumed to be identical for all species. Hence five parameters needed to be optimised by the fitting algorithm: three normalisation constants (one for each species), the mean value of the pion peak and the common resolution.

The latter two parameters were allowed to vary, by 10% and 5%, respectively, around the expected value. Table 6.19 lists the result of the fit procedure along with the input values. To illustrate the importance of a detailed understanding of the detector response, the results using a less constrained fit with nine free parameters are also given in Table 6.19. If resolution, mean value, and normalisation constant of all three hadron contributions are treated as free fit parameters, the relative error increases significantly. In this range of intermediate momenta, pions and protons are well separated. Kaons are more difficult to identify, firstly because they are less abundant and secondly, because they are strongly contaminated by both, pions and protons.

Figure 6.91 shows a second example, corresponding to a one  $\text{GeV}/c$  bin around  $p_t = 50.0 \text{ GeV}/c$ . The total number of entries and resolution is chosen in the same way as in the above example. Ratios have been set to  $\pi : K = 3 : 1$  and  $\pi : p = 4 : 1$ , values which are typical for jet fragmentation at high  $p_t$ , as simulated by PYTHIA [150] for pp collisions.

Despite the fact that pions, kaons, and protons are less separated in this case, the input values can be recovered with reasonable precision as can be seen from the lower part of

**Table 6.19.** Comparing the input yields of the Monte Carlo study to yields retrieved from a 5- and 9-parameter fit. For details see text.

Momentum	Particle	Input number	Error of 5 parameter fit	Error of 9 parameter fit
5 GeV/c	$\pi$	5.86 M	0.05%	0.11%
5 GeV/c	K	2.93 M	0.15%	0.27%
5 GeV/c	p	5.86 M	0.08%	0.09%
50 GeV/c	$\pi$	4 377	3.8%	3.8%
50 GeV/c	K	1 461	9.1%	26%
50 GeV/c	p	1 087	7.3%	19%

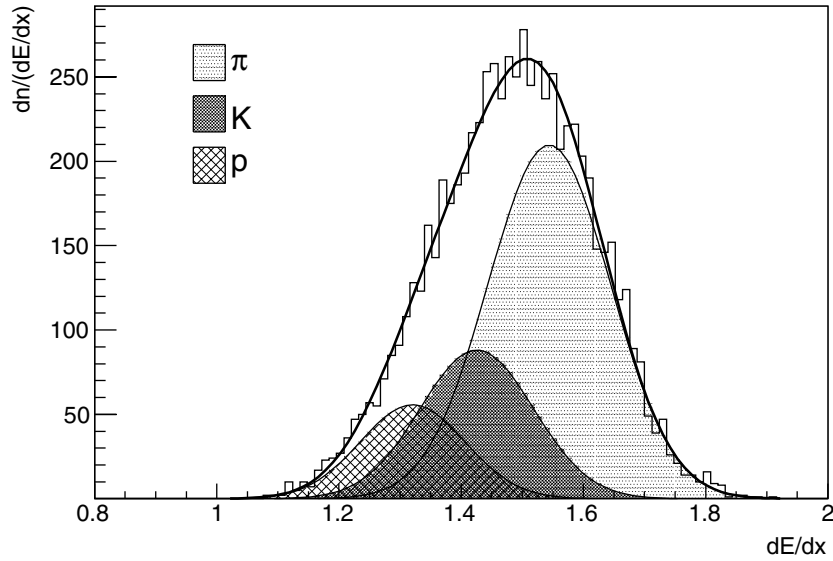
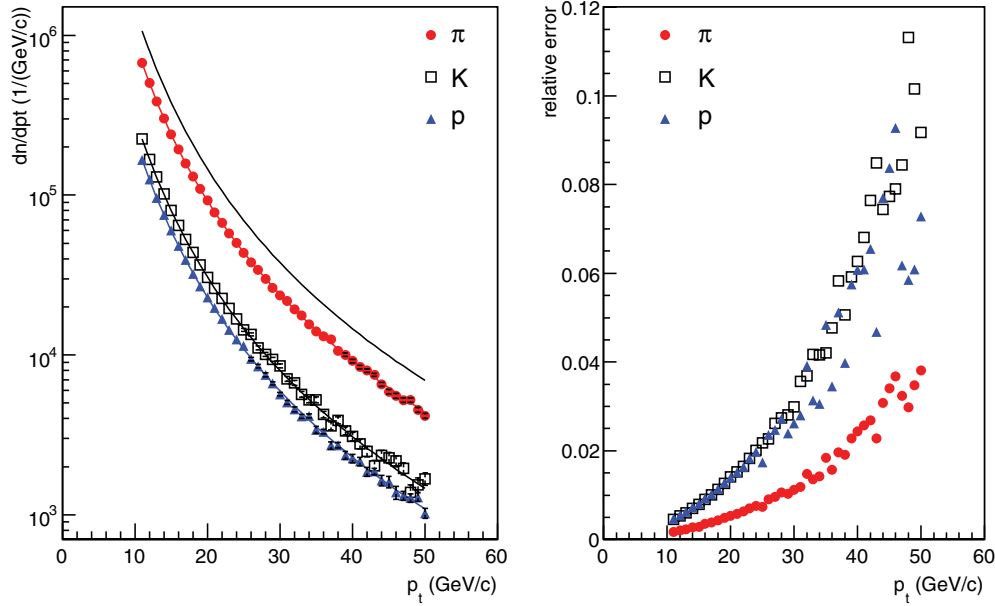
**Figure 6.91.**  $dE/dx$  spectrum of pions, kaons and protons with  $p_t = 50$  GeV/c at midrapidity. Solid line indicates fit result, shaded areas correspond to contributions from individual hadrons. Total number of entries equals estimated hadron yield of  $10^7$  central Pb–Pb collisions.

Table 6.19. Compared to an ideal situation, where the statistical error would be proportional to the square root of the number of particles, the unfolding procedure increases the uncertainty by a factor which varies between 1.2 (pions at low  $p_t$ ) and 10 (kaons at high  $p_t$ ).

The charged-particle spectrum, corresponding to  $10^7$  central Pb–Pb events, is shown in Fig. 6.92 between 10 and 50 GeV/c, assuming particle ratios  $\pi : K = 3 : 1$  and  $\pi : p = 4 : 1$ . Performing a five parameter fit as described above, the individual hadron yields have been determined in bins of one GeV/c. The error is given by the available statistics and reaches about 10% to 15% for kaons and protons at the highest  $p_t$ . It must be noted that no high- $p_t$  suppression was included for the determination of these hadron yields.

*Track-by-track particle identification at large transverse momentum.* Besides measuring inclusive spectra, where particles are identified on a statistical basis, a number of observables (e.g. leading particles in jets) require individual particle identification with good efficiency and purity. Given the TPC performance, this is possible for pions and protons in the complete



**Figure 6.92.** Left: expected total hadron yield (solid line), markers indicate yields of pions, kaons, and protons retrieved by five parameter fits to Monte Carlo  $dE/dx$  distributions (lines indicate input values). Right: error given by the fitting algorithm relative to the yield.

momentum range as discussed before, i.e. from 5 GeV/ $c$  to 50 GeV/ $c$ , where the upper end is likely to be given by statistics rather than instrumental limitations.

By applying a lower (upper) cut on the  $dE/dx$  distribution (see e.g. Fig. 6.90) for pions (protons), a reasonably pure sample of identified particles can be selected. The left hand side of Fig. 6.93 shows the dependence of the proton and kaon efficiencies as function of the pion efficiency when varying the  $dE/dx$  threshold. Closed and open symbols correspond to two different transverse momenta (5 and 50 GeV/ $c$ , respectively) assuming a resolution of 6.5%.

Examples of numerical values of the contamination are listed in Table 6.20. If in the lower transverse momentum case a minimum  $dE/dx$  value is chosen, which selects 90% of the pions, 2.8% of the total number of protons and 21% of the total number of kaons also meet the cut criterion. Assuming particle ratios  $\pi : K = 2 : 1$  and  $\pi : p = 1 : 1$ , the efficiencies correspond to a purity of 87%, where purity is defined as the ratio of correctly identified particles, to the total number of selected particles.

The choice of a maximum  $dE/dx$  value selects a proton sample. The relation between the proton efficiency and the contamination by pions and kaons is illustrated on the right hand side of Fig. 6.93. The lower part of Table 6.20 gives some numerical examples for this case as well. According to Fig. 6.89, the distance of the  $dE/dx$  values of kaons and protons in units of  $\sigma$  decreases only slightly with increasing transverse momentum. Hence the contamination of the proton sample by kaons is similar at low and at high transverse momentum.

**6.2.2.3. Pion and proton production in  $pp$  collisions.** Experimental results on  $\bar{p}/p$  and  $p/\pi$  ratios for  $\sqrt{s_{NN}} = 200$  GeV at RHIC were obtained up to a transverse momentum of at least 6.5 GeV/ $c$  [326, 327]. These measurements cannot be explained by pQCD-based models [318]. For Au–Au collisions the  $p/\pi$  ratio starts with the same value as in  $pp$  collisions at low  $p_t$  but increases up to a maximum around 2–3 GeV/ $c$  (see Section 6.2.1.10).

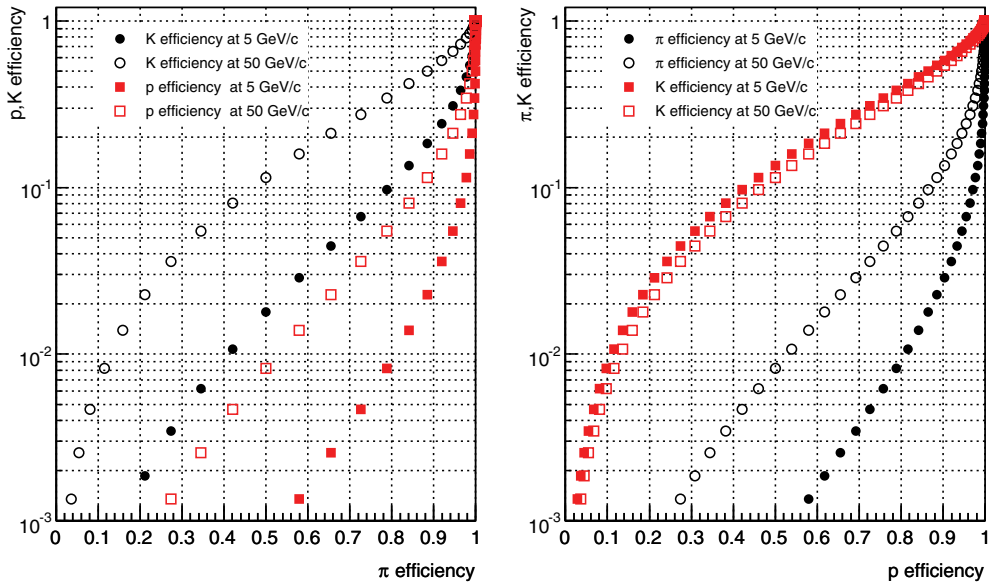


**Figure 6.93.** Left: proton and kaon efficiency as functions of the pion efficiency. Right: pion and kaon efficiency as functions of the proton efficiency. Open symbols correspond to  $p_t = 50 \text{ GeV}/c$ , closed symbols to  $p_t = 5 \text{ GeV}/c$ .

**Table 6.20.** Examples for individual track identification cuts. The purity has been calculated assuming the ratios  $\pi : K = 2 : 1$ ,  $\pi : p = 1 : 1$  at  $5.0 \text{ GeV}/c$ , and  $\pi : K = 3 : 1$ ,  $\pi : p = 4 : 1$  at  $50 \text{ GeV}/c$ .

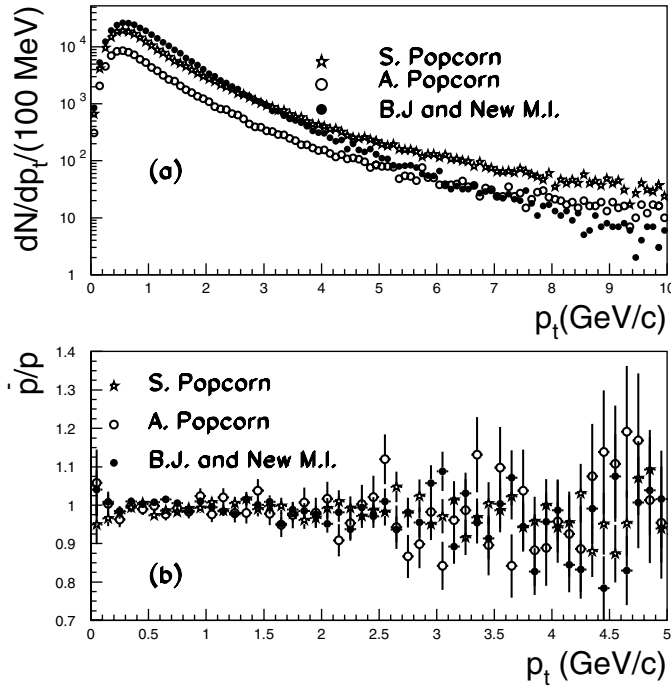
Momentum	pion efficiency	proton efficiency	kaon efficiency	pion purity
5.0 GeV/c	90%	2.8%	21%	87%
50 GeV/c	70%	3.1%	25%	88%

Momentum	proton efficiency	pion efficiency	kaon efficiency	proton purity
5.0 GeV/c	60%	1.6%	17%	86%
50 GeV/c	40%	0.4%	7.3%	78%

Moreover: (i) the ratio  $\bar{p}/p$  has been found to be virtually independent of the  $p_t$  of the particles [328], and is smaller than would be expected if only classical mechanisms of baryon stopping are invoked; (ii) the  $\bar{p}/p$  ratio measured in pp collisions is different from that obtained in Au–Au collisions at the same energy of  $\sqrt{s_{NN}} = 200 \text{ GeV}$ . For these reasons, baryon transfer and hadronisation into baryons still need to be investigated in both nucleon–nucleon and nucleus–nucleus collisions. The study of identical and mixed ratios at LHC energies will give further information about these mechanisms.

In this section we investigate the predictions of three different baryon production mechanisms (Simple Popcorn, Advanced Popcorn and ‘Baryon Junction with New Multiple Interaction’) as incorporated in the latest PYTHIA version [329] in pp collisions at 14 TeV in order to see the expected differences among them for some observables: the proton spectra, the multiplicity, and the  $\bar{p}/p$  and  $p/\pi$  ratios. For more details about the models and about this analysis, see [330].



**Figure 6.94.**  $p_t$  spectrum for antiprotons (a) and ratio for antiproton to proton (b) for three different models: Simple Popcorn, Advanced Popcorn and Baryon Junction with New Multiple Interaction.

*Proton production in pp collisions at 14 TeV.* We present simulations each of these three mechanisms in order to investigate their influence on certain experimental observables. The simulations at present do not take into account the feed-down of weak decays into protons and pions. For each case  $10^6$  events were generated.

*$\bar{p}/p$  ratio.* Fig. 6.94(a) shows the  $p_t$  spectra and the antiproton to proton ratio for Simple Popcorn compared to the Advanced Popcorn and ‘Baryon Junction with new Multiple Interaction’ models. The results indicate that the ratio is constant and very close to unity, see Fig 6.94(b). Qualitatively we observe that the Simple Popcorn algorithm produces more protons than the Advanced Popcorn, at any  $p_t$ . The  $\bar{p}/p$  ratio, integrated from a  $p_t$  of 300 MeV/c to 4 GeV/c, is identical for the three models. The Baryon Junction mechanism produces a different  $p_t$  spectrum from the other two at high  $p_t$ .

*$p/\pi$  ratio.* The systematics of baryon production are reflected in the ratio of proton to pion production. Fig. 6.95 shows the ratios obtained with the three models. The ratios are different both in full pseudorapidity and at central rapidity. Since the multiplicity distributions are different depending on the mechanism, see Fig. 6.96, we also show the predictions for different multiplicity bins. The results are given in Fig. 6.97(a) and Fig. 6.97(b) for the Advanced Popcorn and ‘Baryon Junction plus New Multiple Interaction’ mechanisms respectively. The simulations do not allow us to determine a clear trend with multiplicity, although significant differences are observed.

The results for the proton to pion ratio indicate a larger sensitivity to the proton production mechanism than in the case of the  $\bar{p}/p$  ratio. The present simulations show that with a million

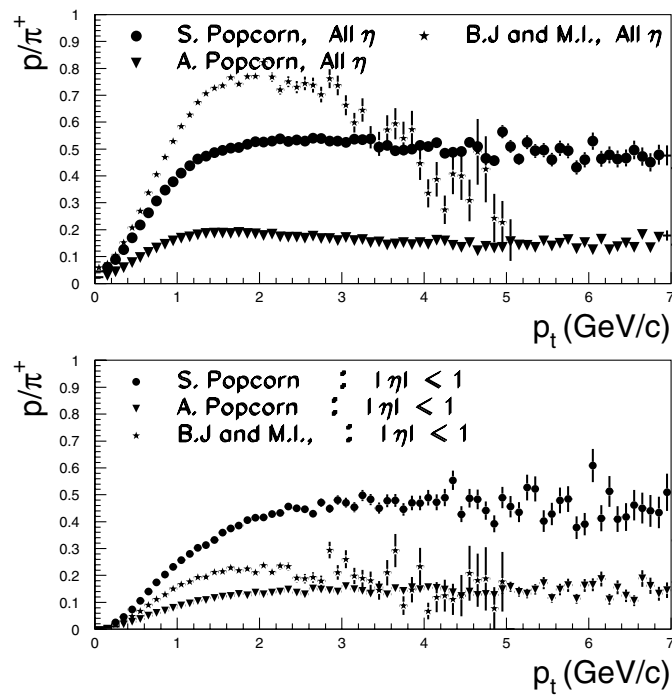


**Figure 6.95.** Proton to pion ratio as function of  $p_t$ , comparing the Simple Popcorn, Advanced Popcorn and ‘Baryon Junction with New Multiple Interaction’ mechanisms for production.

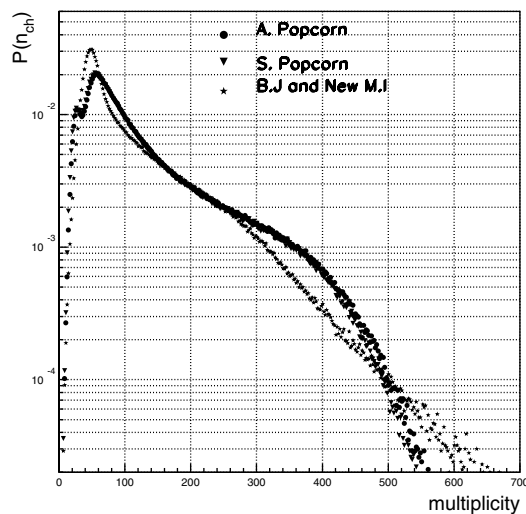


**Figure 6.96.** Charge multiplicity distributions for three different baryon production mechanisms in the whole pseudorapidity range.

pp minimum bias events it will be possible to extract spectra and ratios in the range where ALICE can provide particle identification, which would allow us to perform a study of the mechanisms of baryon production.

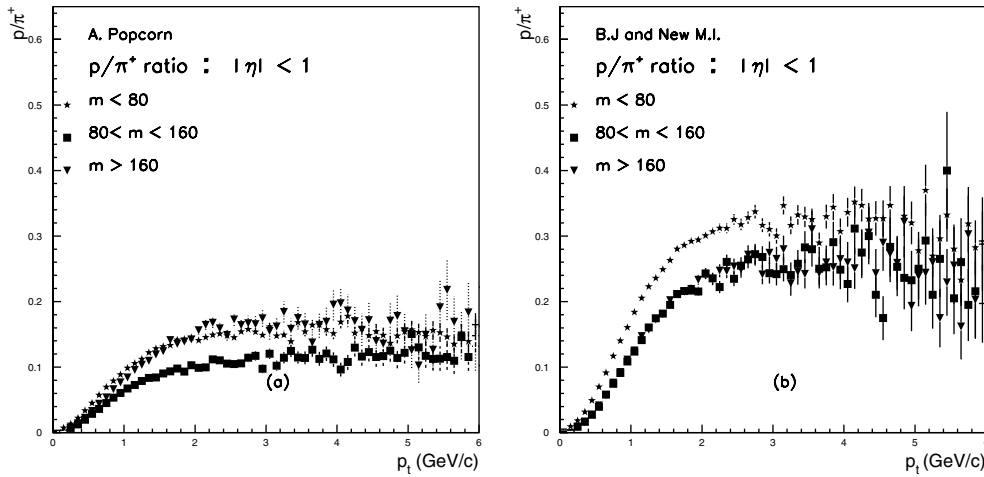


**Figure 6.97.** Proton to pion ratio for different multiplicity ranges,  $m$ , for (a) Advanced Popcorn and (b) Baryon Junction with New Multiple Interaction production mechanisms.

**6.2.2.4. Hadron and  $\pi^0$  transverse momentum spectra in central Pb–Pb collisions.** The study of  $p_t$  distributions is a very important tool in heavy-ion physics. Transverse momentum spectra in the region  $p_t \sim 1$  GeV/ $c$  provide valuable information on the details of the expansion process since they are very sensitive to radial flow effects and to the temperature of the expanding hadronic gas. Such studies will be carried out in ALICE by investigating the  $p_t$  distributions of identified particles. With the advent of heavy-ion colliders which can provide collisions with  $\sqrt{s} > 100$  GeV/nucleon, the region corresponding to  $p_t > 10$  GeV becomes accessible to experiments. At such energies it is possible to produce events where hard partonic collisions take place. These events can be experimentally tagged through the detection of jets of hadrons coming from the fragmentation of high- $p_t$  partons, in particular using the leading particles in the jets. Since hard scatterings occur well before any medium is formed in the collision, the high- $p_t$  partons probe the matter produced in the interaction. These partons are ‘quenched’ in a predictable way when they cross a deconfined medium, so that the measured  $p_t$  spectra are a possible signature of QGP formation.

In this section, we will try to evaluate the expected high- $p_t$  hadron yield in ALICE in the absence of any quenching effects. The investigation of various ‘quenching’ scenarios and of the possibility of discriminating between them will be addressed in another chapter of this document.

As a starting point, we use HIJING for event generation, without introducing in the generator any quenching effect. In more detail,  $10^4$  central events ( $b < 2$  fm) were generated, tracked and reconstructed in the ALICE set-up. We recall that the charged multiplicity at mid-rapidity for such a generator is of the order of 6000 particles per unit rapidity. The reconstruction of the tracks in the TPC was carried out through a parametrisation of Kalman filter tracking. This parametrisation was developed for physics performance studies involving the detection of hadronic  $D^0$  decays (see Section 6.5).

Figure 6.98 shows the reconstructed  $p_t$  spectrum of charged hadrons in the region  $10 < p_t < 50$  GeV/ $c$ , relative to a sample of  $10^7$  minimum bias events, a statistics roughly corresponding to one year of ALICE Pb–Pb data taking. The high  $p_t$  hadron yield for a centrality bin corresponding to the impact parameter region  $b_1 < b < b_2$  was obtained

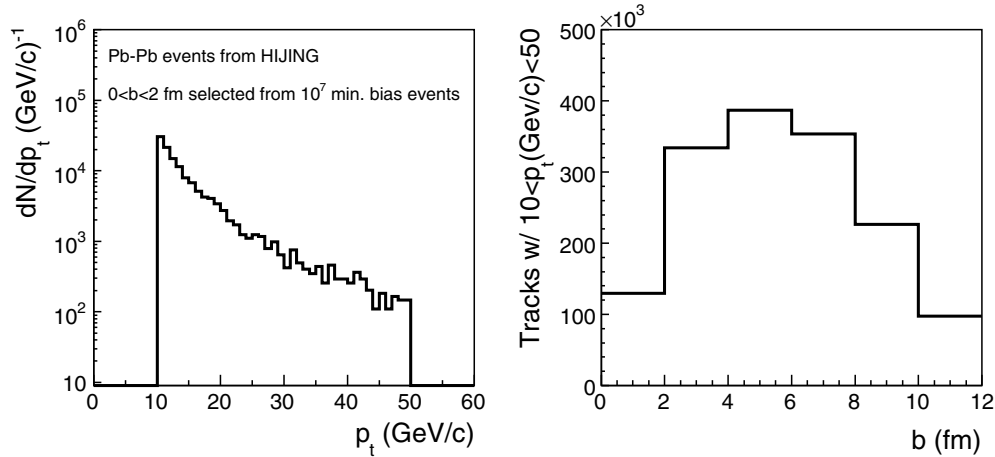


**Figure 6.98.** The high- $p_t$  hadron yield for Pb–Pb collisions. In the left plot, starting from a statistics of  $10^7$  minimum bias events, we show the high- $p_t$  charged hadron yield for the most central bin. On the right plot the integrated number of tracks in the  $p_t$  range  $10 < p_t < 50$  GeV/c for various centrality classes is presented.

by appropriately weighting the distribution obtained for central HIJING events with the probability  $P(b_1, b_2)$  of having an event in that centrality range. Furthermore, the high  $p_t$  yield, essentially due to hard scattering, was scaled proportionally to the average number of nucleon–nucleon collisions  $N_{\text{coll}}(b_1, b_2)$  for the various centrality bins. The quantities  $P(b_1, b_2)$  and  $N_{\text{coll}}(b_1, b_2)$  were calculated using the Glauber model, using as input parameters a Saxon–Woods density distribution for the Pb nuclei and the value  $\sigma_{\text{NN}}^{\text{inel}} = 57\text{mb}$  for the nucleon–nucleon inelastic cross section.

In Fig. 6.98 one can see the high- $p_t$  spectrum relative to the events in the range  $0 < b < 2$  fm, from an overall sample of  $10^7$  minimum bias events. In the same figure we also show the number of tracks in the  $p_t$  range  $10 < p_t < 50$  GeV/c for other centrality classes. All the quantities refer to a situation where no quenching effects were introduced.

The cut at  $p_t = 50$  GeV/c in Fig. 6.98 is due to the available generated statistics. One can get an idea of the statistics that can be expected at higher  $p_t$  by performing an extrapolation using a power-law function. In Fig. 6.99 we have extrapolated the charged hadron yield up to  $p_t = 100$  GeV/c, using the function  $f(p_t) = A/(p_t + p_0)^\alpha$ . For a sample of  $10^7$  minimum bias events, we find that, in the absence of quenching effects, we would have  $2.3 \times 10^3$  reconstructed tracks in the TPC with  $50 < p_t < 100$  GeV/c.

This estimate refers to a pure minimum bias trigger. The possible strategies being considered in order to enhance the selectivity of the trigger (HLT, central event selection at L1 with the ZDC) could significantly increase the statistics shown in Fig. 6.98.

Finally, high- $p_t$  physics can also be investigated in ALICE by detecting neutral particles. In particular, such a study can be performed with the PHOS. The prompt photon yield can be estimated from the simple parton model, which assumes no momentum dependence for the parton distributions and fragmentation functions. For prompt photon production, the power-law dependence of the cross section was derived by fitting a large number of data points with the function [331]:

$$\left( E \frac{d^3\sigma}{dp^3} \right)_{y=0} = A \frac{(\sqrt{s})^{n_1}}{p_t^{n_2}}, \quad (6.17)$$

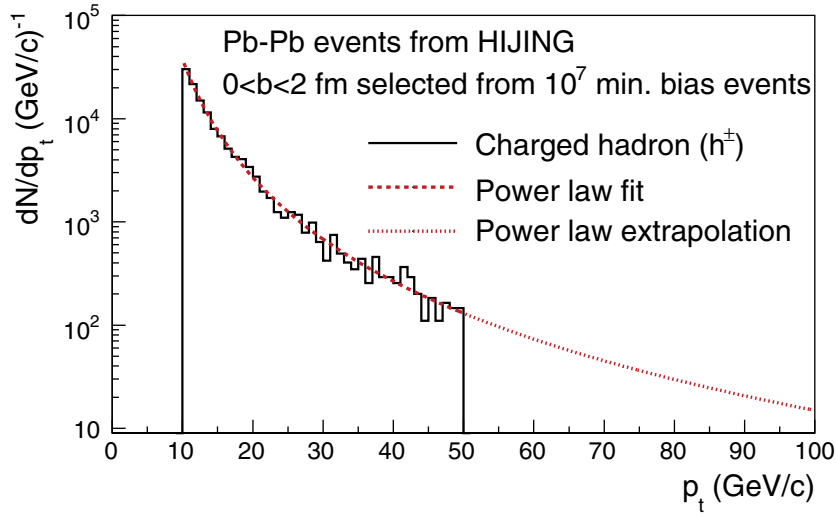


**Figure 6.99.** A possible extrapolation of the high- $p_t$  hadron yields for Pb–Pb collisions in the interval  $50 < p_t < 100$  GeV/ $c$ . The plot corresponds to the statistics expected for central events ( $0 < b < 2$  fm), starting from a sample of  $10^7$  minimum bias events.

where the cross section is in pb/GeV<sup>2</sup>,  $\sqrt{s}$  in GeV and  $p_t$  in GeV/ $c$ . The parameters are defined as

$$A = 6495, \quad n_1 = 1, \quad n_2 = 5.$$

The cross section for  $\pi^0$  production can be obtained from the parametrisation of cross sections measured at lower energy, by means of an extrapolation to LHC energies. The same functional form of Eq. 6.17 [332] was used, with parameter values

$$A = 7.89 \times 10^{-1}, \quad n_1 = 1.6744, \quad n_2 = 7.4515,$$

where the cross section is expressed in mb/GeV<sup>2</sup>.

These parametrisations of the photon and  $\pi^0$  production were used to estimate the detection rates of these particles in the PHOS detector. The evaluation of the efficiencies for photon and  $\pi^0$  detection is presented in Section 6.9 of the Physics Performance Report. The detection rates for one ALICE year ( $10^6$  s) for the most central Pb–Pb collisions are shown in Fig. 6.100. The photon detection rate (left plot) is shown for the PHOS standalone trigger without photon identification and with the selection of identified photons. The  $\pi^0$  yield is shown for the standard ALICE trigger as well as for the PHOS stand-alone trigger.

**6.2.2.5. Production of nuclei and anti-nuclei.** High phase space densities of nucleons and anti-nucleons will be achieved in central Pb–Pb collisions at the LHC. In this environment, nuclei and anti-nuclei can be formed through coalescence of nucleons and anti-nucleons at the late stages of the collision. Formation can of course occur also earlier, but, because of the low binding energy, light (anti-)nuclei are likely to dissociate if subjected to intense hadronic rescattering. The production of light nuclei and anti-nuclei at mid-rapidity is thus expected to reflect the conditions at or near freeze-out.

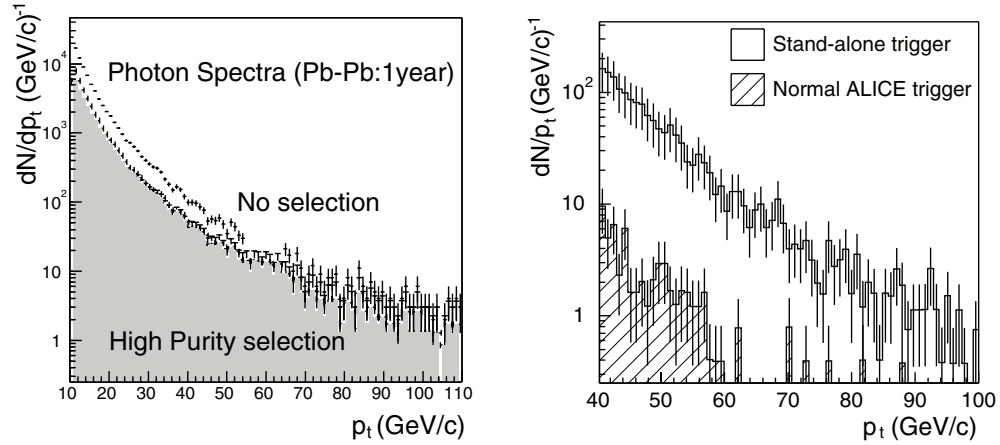


**Figure 6.100.** The photon (left) and  $\pi^0$  (right)  $p_t$  distributions expected for central Pb–Pb collisions during one ALICE year ( $10^6$  s).

The coalescence model relates the invariant yield of a nuclear fragment with mass number  $A$  to the invariant yield of protons and neutrons

$$E_A \frac{d^3 n_A}{d p_A^3} \Big|_{p_A = A p_p} = B_A \left( E_p \frac{d^3 n_p}{d p_p^3} \right)^A, \quad (6.18)$$

assuming that the proton and neutron yields are the same. Here,  $B_A$  is the coalescence parameter. For a static source, with a size much larger than the size of the nuclear fragment, it can be shown that  $B_A$  is determined by the volume,  $B_A \propto (1/V)^{A-1}$ .

The production of deuterons and anti-deuterons around mid-rapidity have been studied at RHIC. The STAR collaboration has measured anti-deuterons at  $\sqrt{s_{NN}} = 130$  GeV in the range  $0.5 \leq p_t \leq 0.8$  GeV/ $c$ , using the information on  $dE/dx$  from the TPC for identification [333]. STAR has also observed anti- ${}^3\text{He}$  using the same technique. The PHENIX collaboration has measured deuterons and anti-deuterons at  $\sqrt{s_{NN}} = 200$  GeV in the range  $1.1 \leq p_t \leq 4.3$  GeV/ $c$ , using the Time-of-Flight for identification [334]. ALICE could use both of these techniques, either separately or combined. The resolution in  $dE/dx$  and Time-of-Flight should be comparable or better than in STAR and PHENIX, respectively. Since the yield of deuterons and heavier nuclear fragments is relatively low, backgrounds from secondary interactions, e.g. in the beam-pipe, might be a challenge. The secondary fragments have a very steeply falling energy spectrum, however, so they are not expected to be a significant background above  $p_t > 1$  GeV/ $c$ .

The production of light nuclei and anti-nuclei at mid-rapidity has also been studied in heavy-ion interactions at the SPS [335] and AGS [336] energies.

The results at lower energies (RHIC and SPS) have shown that the assumption of a static source with a constant coalescence parameter,  $B_A$ , is an oversimplification. As expected,  $B_A$  decreases with increasing centrality of the collisions, reflecting the change in the size of the participant volume. However, even for a fixed centrality,  $B_A$  shows a clear increase with increasing transverse momentum; the results are (at least qualitatively) in agreement with the observed decrease in the HBT radius with  $p_t$ . This clearly complicates the direct determination of a source size from the coalescence analysis, but it also indicates that the yield of (anti-)nuclei probes other properties of the emitting source, e.g. its space-time evolution and collective transverse expansion.

Measurements of (anti-)deuterons and heavier nuclei provide an indirect way to measure the yield of (anti-)neutrons [334]. Assuming that coalescence is the correct formation mechanism, but allowing a non-constant  $B_A$  e.g. due to collective flow, the ratio of  $\bar{n}/n$  can be extracted from the measured  $\bar{d}/d$  and  $\bar{p}/p$  ratios. The ratios can be compared with predictions from thermal models.

In ALICE, light nuclear fragments (d,t,  $^3\text{He}$ ,  $^4\text{He}$ ) as well as their antiparticles can be identified via  $dE/dx$  and TOF up to very high momentum (10 to 20 GeV/c, depending on mass). Both thermal and coalescence models predict that the yield of these fragments scales approximately with a power of the fragment mass number with a ‘penalty factor’ of order 300 for each additional (anti-)nucleon. Using this scaling, we would expect to reconstruct in  $10^7$  central events about  $10^6$  deuterons, a few  $10^3$  tritium and  $^3\text{He}$  fragments and a small number  $^4\text{He}$  nuclei. Comparable but somewhat smaller numbers are expected for the respective anti-nuclei because of the larger interaction cross sections.

*6.2.2.6. Kaons identified via their kink topologies in pp and central Pb–Pb collisions.* The observed hadron spectra and correlations at RHIC reveal three transverse momentum ranges with distinct behaviour: a soft range ( $p_t \leq 1.5$  GeV/c) containing the remnants of the bulk collision, an intermediate range ( $1.5 \leq p_t \leq 6$  GeV/c) where hard processes coexist with the soft ones, and a hard-scattering range ( $p_t \geq 6$  GeV/c) providing partonic probes of the early stage of collision matter. The RHIC findings for each of these three ranges, some of them unexpected, raise a number of open questions (see for instance [233]) that will need to be addressed. The emerging picture shows that strange quark production in hot QCD is theoretically challenging, and experimental cross-checks requiring high statistics and precision data in a large- $p_t$  range are needed to fully explore the observed phenomena, and their connection to the properties of dense matter.

Recent theoretical studies [230, 337] suggest that at LHC strangeness may be further enhanced relative to RHIC given that at LHC we reach greater initial temperatures and more explosive flow. Being the lightest strange hadrons, kaons are expected to dominate the strange sector by virtue of canonical thermodynamics. Thus, with a significant kaon production at the LHC energies, owing to kaon’s high branching ratio to the muonic decay channel (branching 63.26%) and to the large angular acceptance of the central barrel of ALICE, the reconstruction of the kink topology is a key technique for identifying kaons over a momentum range much wider than that achieved by combining PID signals from different detectors (see Section 6.2.2.2 for this complementary technique).

The decay vertex is identified by selecting tracks of the same sign that are consistent with an origin at the decay of a kaon somewhere in the TPC. Selection cuts on geometry and kinematics are applied (at each step) to reduce the background due to random association of tracks. The  $K/\pi$  rejection is performed by cutting on the transverse charged daughter momentum calculated in the centre-of-mass system of the particle which decays. The kink-finding algorithm is discussed in Section 5.1.7.2.

One question that arises naturally is whether the identification range we achieve allows us to use kaons to get an insight into phenomena related to each of the three transverse momentum ranges mentioned above. Thus, in this section we aim to evaluate the expected yields and background contamination in pp and Pb–Pb collisions at LHC, as well as the range of the transverse momenta over which significant statistics of kaons identified via their decay topology will be available the first year of data taking at the LHC.

*Estimation of the kaon yields.* In order to evaluate the expected yields of kaons identified via their kink topology, we have to account for reconstruction efficiency, detector acceptance for the reconstruction chain, hadronic interactions and particle misidentification. All these

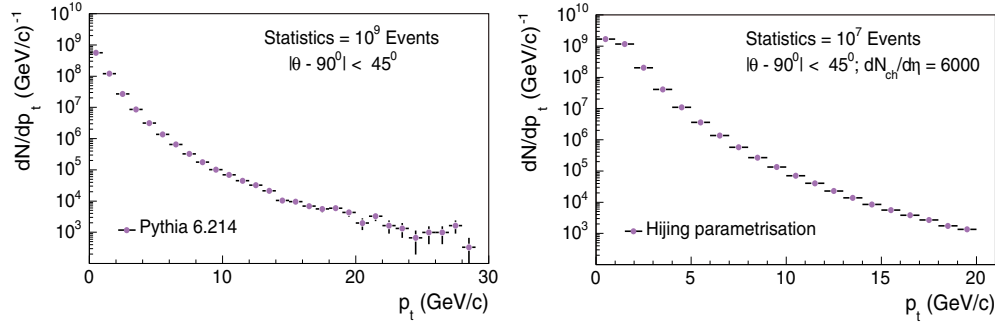


**Figure 6.101.** Left: PYTHIA 6.214 prediction for  $p_t$  distribution of charged kaons in  $10^9$  pp collisions at  $\sqrt{s} = 14$  TeV in the central barrel range. An overall event trigger efficiency of about 82% was taken into account. Right: HIJING parametrisation prediction for  $10^7$  central Pb–Pb collisions with  $dN_{\text{ch}}/d\eta = 6000$  at  $\sqrt{s} = 5.5$  TeV .

corrections not only depend on the transverse momentum, but also on rapidity, on the event multiplicity and track quality criteria. However, their functional dependence on  $p_t$  is the most important and we will obtain the inclusive spectrum of identified kaons via their kink topologies by convoluting the transverse momentum distribution predicted for kaon production at LHC, the acceptance profile and the reconstruction efficiency function. Thus, in each  $p_t$ -bin, the expected yield is given by:

$$N_{\text{K}}^{\text{rec}}(p_t) = N_{\text{K}}^{\text{prod}}(p_t) \times \text{ACC}(p_t) \times \text{EFF}(p_t) \quad (6.19)$$

where  $N_{\text{K}}^{\text{rec}}$  is the number of reconstructed kaons in the  $p_t$  bin,  $N_{\text{K}}^{\text{prod}}$  is the number of kaons produced, ACC is the acceptance of the reconstruction chain and EFF is the reconstruction efficiency.

*Kaon production at LHC and acceptance.* PYTHIA [150] version 6.214 with CTEQ5L as parton distribution functions, multiple interactions and default values that regulate the cut-off energy dependence was used to generate  $2.5 \times 10^6$  minimum-bias pp events at  $\sqrt{s} = 14$  TeV. The  $p_t$  distribution of kaons emerging from collisions as generated with PYTHIA in this configuration was extrapolated to one year of LHC pp data taking ( $10^9$  pp events). An overall event trigger efficiency of about 82% (see Section 3.15.2 of PPR Volume I [3]) was taken into account and a pseudo-rapidity ( $\eta$ ) cut,  $|\eta| < 0.9$ , corresponding to the TPC geometrical acceptance was applied. The extrapolated distribution is shown in the left panel of Fig. 6.101. The right panel of Fig. 6.101 shows the  $p_t$  distribution of kaons produced in  $10^7$  central Pb–Pb collisions at LHC energy, generated using a HIJING parametrisation model (for details, see [338] and Section 4.2 of PPR Volume I [3]). Here, we point out that the  $\eta$  distribution was scaled to a charged particle multiplicity of  $dN_{\text{ch}}/d\eta = 6000$  (expected to correspond to top central data at LHC) in the pseudo-rapidity interval  $|\eta| < 0.5$  and the kaon  $p_t$  distribution was obtained from the pion distribution by  $m_t$ -scaling. For Pb–Pb collisions, the event trigger efficiency is close to 100% (see PPR Volume I [3]). An  $\eta$  cut,  $|\eta| < 0.9$ , corresponding to the TPC geometrical acceptance was applied as well.

The acceptance for the reconstruction chain, see Fig. 6.102, is a product of several factors: geometrical acceptance, decay probability, the effect due to the fiducial volume restriction and tracks quality criteria. Hence, we calculate it in each  $p_t$  bin as the fraction of initially generated kaons resulting in ‘findable’ generated kinks (see Chapter 5 for definitions). In order to do this, we generated  $3.5 \times 10^6$  single particle events (50%  $\text{K}^+$ , 50%  $\text{K}^-$ ) with flat  $p_t$  and  $\eta$

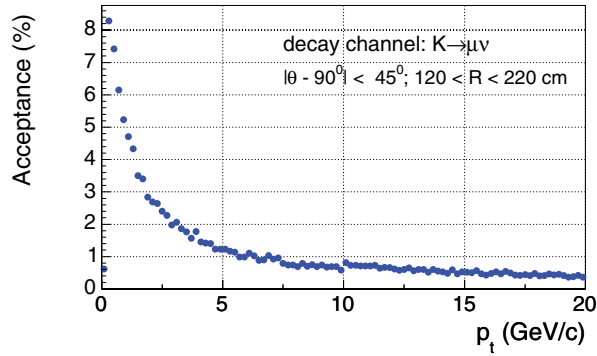


**Figure 6.102.** The  $p_t$ -dependence of the acceptance of the reconstruction chain for the  $K \rightarrow \mu\nu$  decays.

distributions, and transported them through the ALICE set-up using the GEANT transport code incorporated in the AliRoot framework. We recall that kaons have a  $c\tau$  of 371.3cm and we concentrate on the search for kinks inside the volume of the TPC. To maximize the acceptance, the fiducial region is extended as much as the track precision and tracking efficiency allow. Figure 5.55 of Chapter 5 shows that the fiducial volume cannot be extended much outside the  $R = 120\text{--}220$  cm range.

*Signal and background simulations.* The predicted kaon yields at the LHC and the acceptance of the reconstruction chain in the momentum range above a few  $\text{GeV}/c$ , see Figs. 6.101 and 6.102 respectively, have shown that the estimation of the background conditions, the efficiencies and the expected yields for reconstructed kaon decays would require the generation of a huge number of events to get results with reasonable statistics, and would therefore entail heavy use of computing resources. Hence, we performed this study making use of the event mixing technique, where pure signal events are embedded into background events at the level of summable digits (see Chapter 4 of PPR Volume I [3]). This choice is based on the assumption that the quality of the reconstruction and, implicitly, the background conditions depend crucially on the particle density and that the combinatorial background given by pairs of uncorrelated tracks dominates over other background sources. The mixing is done at the level of summable digits in order to incorporate the interference due to the detector response between the tracks.

We generated a number  $N$  of signal events each consisting of 500 kaons (50%  $K^+$  and 50%  $K^-$ ) in the TPC acceptance in intervals of  $0.5 \text{ GeV}/c$  covering a wide range in transverse momentum, with  $p_t$  following  $m_t$ -scaling and pseudo-rapidity distributions fixed by HIJING model parametrisations. The kaons were transported by GEANT through the detector set-up and forced to decay in the TPC fiducial volume ( $120 < R < 220$  cm) to the  $K \rightarrow \mu\nu$  decay channel. This was done to increase further the statistics of findable generated signals. In addition to these signal events we also generated  $M = 60$  HIJING background events. Next, using the ‘microscopic’ simulators for the TPC and the other two tracking detectors, ITS and TRD, the detector response up to the zero suppression level is simulated independently for both pure signal and for HIJING background events. Then, the event mixing is carried out in turn for combinations of each of the  $N$  signal events (500 kaons) with each of the  $M$  HIJING background events, the result being  $N \times M$  signal enriched events. Finally, the full reconstruction chain was applied to each of these signal enriched events and estimations of the reconstruction efficiencies and precision, and of the background which

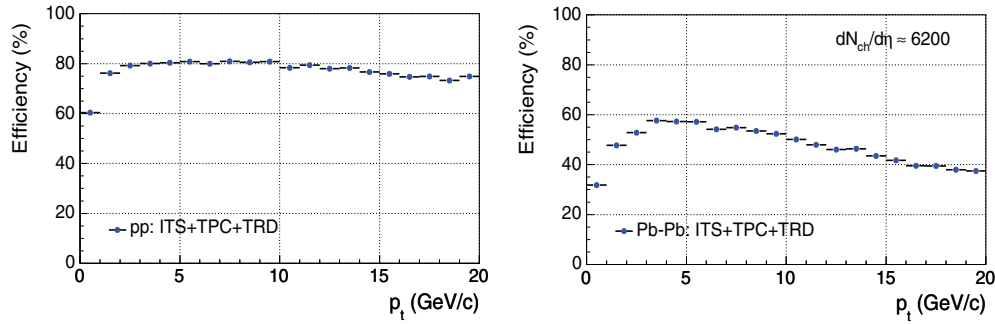


**Figure 6.103.** Left: Reconstruction efficiency as a function of  $p_t$  for pp multiplicities. Right: Reconstruction efficiency as a function of  $p_t$  for central Pb–Pb ( $b < 3$  fm) with  $dN_{ch}/d\eta \sim 6200$ .

might be expected, were obtained for different charged particle densities under different tracking detectors configurations: TPC stand-alone, ITS+TPC, and ITS+TPC+TRD.

Since the  $\pi \rightarrow \mu\nu$  decay ( $c\tau$  of 780.4 cm and branching ratio 99.98%) is the main competing source of kinks, and the estimation of pion contamination with reasonable confidence would also require a large number of events, especially in the hard  $p_t$  region, we have adopted the following strategy. We have fully simulated the central barrel, using samples of 3000 kaons and pions respectively, with  $p_t$  generated in intervals of 0.5 GeV/c spanning the 0.1–10 GeV/c range (in practice, we do not reconstruct pions with  $p_t$  above 10 GeV/c). The momentum and pseudo-rapidity distributions were fixed by HIJING model parametrisations and both pions and kaons were forced to decay uniformly in the TPC fiducial volume to the  $\mu\nu$  channel. This was done in order to achieve, both for kaons and pions, a uniform population of the fiducial volume of the TPC with decays. Then we build the distribution of the  $K/\pi$  ratio as a function of  $p_t$  and decay radius, which later will be used to perform a normalisation which takes into account the difference in the expected yields for kaons and pions, their different lifetimes and the exponential lifetime distribution for the decaying particle, and the difference in their branching ratios for the  $\mu\nu$  decay channel. After performing the selection cuts the pion contamination found was below 2%.

*Reconstruction efficiency, yields of reconstructed kaon decays and contamination.* In this section we will summarize the current results only for pp and central Pb–Pb ( $b < 3$  fm) event multiplicities when we use full combined tracking information (ITS+TPC+TRD). Some 60 central Pb–Pb ( $b < 3$  fm) background events at  $\sqrt{s} = 5.5$  TeV generated using the HIJING 1.36 generator with jet quenching and nuclear shadowing switched on, and a total of about 250 enriched signal events with a charged particle density  $dN_{ch}/d\eta \sim 6200$  at midrapidity have been considered for this study. The magnetic field was set to 0.5 T.

The reconstruction efficiency was evaluated as the fraction of the findable generated kaon decays that can be associated to reconstructed kaon decays. The left and right panels of Fig. 6.103 show the results for pp and central Pb–Pb multiplicities respectively, as a function of  $p_t$ . Compared to pp, there is a significant drop in the reconstruction efficiency for central Pb–Pb events due to cluster overlaps, which lead to lower tracking efficiencies for the two track segments associated to a kink and higher uncertainties for the track parameters. At high  $p_t$  ( $p_t > 10$  GeV/c) both efficiency functions decrease gradually with the increase of  $p_t$ . This behaviour is consistent with a decrease in the decay angle and consequently, with the fact that more kinks have decay angles which fall below the angular resolution of our detector. In addition, the parameters of small decay angle kinks are determined with less precision and

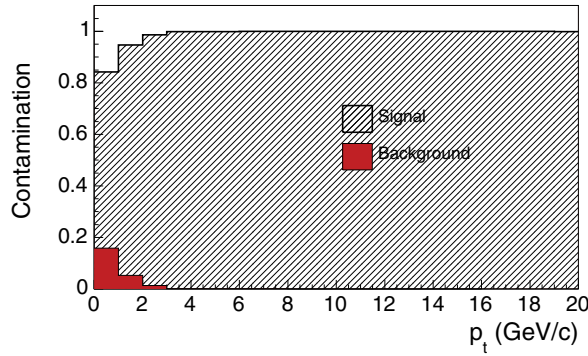


**Figure 6.104.** Background contamination (dark area) for central Pb–Pb ( $b < 3$  fm) with  $dN_{\text{ch}}/d\eta \sim 6200$ . The hashed area represents the reconstructed signal.

fewer candidates meet our quality selection criteria. One of the cuts introduced to reduce the background level is a  $p_t$ -dependent selection on the decay angle. Here, we require that the kink angle is not smaller than a certain critical angle parametrised in terms of the decay angle reconstruction error. The main selection parameters and their cut values are listed in Table 5.4 of Chapter 5. We note that the cuts have been optimised to minimize the level of background contamination while preserving the signal. The overall efficiencies for pp and central Pb–Pb events with a charged-particle density  $dN_{\text{ch}}/d\eta \sim 6000$  is about 77% and 47% respectively.

Considering the existing uncertainties in the prediction of the charged-particle density, we also calculated the efficiencies (not shown here) for central Pb–Pb events with different charged-particle densities. For  $dN_{\text{ch}}/d\eta = 4000$ , the overall efficiency is about 54%, while for  $dN_{\text{ch}}/d\eta = 2000$  is around 67%. As expected, the background contamination in these cases is lower.

The main source of contamination is background due to random association of tracks, mostly low- $p_t$  tracks, and to a much lesser extent track splitting, pion decays, and decays of kaons coming from secondary interactions. The level of background contamination in central Pb–Pb events is shown as a function of  $p_t$  in Fig. 6.104. In pp events the background is negligible (well below the 1% level).

The yields of reconstructed kaon decays as a function of  $p_t$  are obtained by convoluting the distributions shown in Figs. 6.101, 6.102 and 6.103, namely the predicted momentum distribution for kaons at LHC, the acceptance of the reconstruction chain and the efficiency. They are illustrated in Fig. 6.105.

Using the left panel of Fig. 6.105 we see that for a total sample of  $10^9$  pp events, usable statistics of kaons can be obtained up to  $p_t = 14$  GeV/ $c$ . For  $10^7$  central Pb–Pb events with  $dN_{\text{ch}}/d\eta = 6000$ , see right panel of Fig. 6.105, this range extends up to at least  $p_t = 13$  GeV/ $c$ .

The results depend strongly on factors which are poorly known, and it is possible that the shapes, notably the inverse slope parameters ( $T$ ), of the real spectra will differ from the ones we used in this simulation. The fit value for the exponential distribution slope parameter we have used for kaons was found to be  $T \approx 610$  MeV in the intermediate- $p_t$  region  $1 \leq p_t \leq 5$  GeV/ $c$  integrated over the whole pseudorapidity range of  $|\eta| < 8$ .

Statistically significant numbers of identified hyperons will be available up to transverse momenta dominated by hard scattering of partons from the incoming nuclei (see Sections 6.2.3 and 6.2.4). Owing to the access to a higher- $p_t$  range than that available to

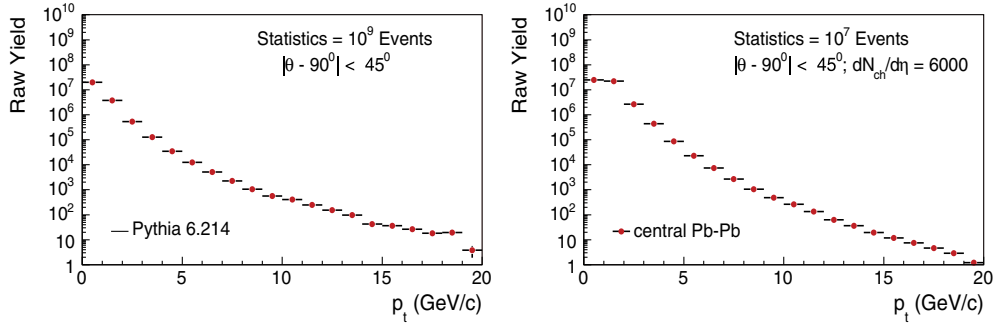


**Figure 6.105.** Left: Transverse momentum distribution of reconstructed Ks as expected for  $10^9$  pp events. Right: Transverse momentum distribution of reconstructed Ks as expected for  $10^7$  central Pb–Pb events.

the RHIC experiments, we will be able to investigate more definitively the quark scaling behaviour expected from coalescence models and the effects of the traversed matter on hard probes, i.e., the origin of the observed meson-baryon differences in flow and yield in the intermediate- $p_t$  region, and also whether jet quenching is an indicator of parton, and not hadron, energy loss. On the same footing, the broad- $p_t$  range we found to be statistically accessible in pp collisions will allow us not only to provide references for the heavy-ion collision data but also to gain insight into possible deconfinement in pp collisions and poorly understood properties (e.g. the mean transfer momentum) via the measured strangeness content (see Section 6.2.1.8).

Finally, we note that in the transverse momentum range  $0.1 \leq p_t \leq 3$  GeV/c, the kink reconstruction technique is complementary to the combined particle identification technique described in Section 5.4.6.

**6.2.3. Topological identification of strange and multi-strange particles.** At LHC energies, it is expected that a large number of particles containing strange valence quarks will be produced (see Section 6.2.1.3). In Section 5.1.7.1 reconstruction of the decay topology was presented as a key technique for strange-particle identification and hence the determination of yields and dynamical properties for these particles.

In this section we show that, for both Pb–Pb and pp events, the statistics of the first years of data taking (estimated to be  $10^7$  Pb–Pb events and  $10^9$  pp events at  $\sqrt{s_{NN}} = 5.5$  TeV) should allow us to determine the main characteristics of hyperon production at mid-rapidity with the ALICE detector. Note that the identification of hyperons is not limited by their momentum, thus allowing them to be useful probes far beyond the scope of soft physics.

The expected yields for Pb–Pb collisions and the corresponding transverse momentum ( $p_t$ ) spectra are presented for different hypotheses; the aim here is to evaluate the main analyses which will rely on this technique and consider the prospects for others which should be feasible in the short term. For example, anti-baryon/baryon ratios, mixed ratios and binary collision scaled centrality ratios ( $R_{CP}$ ), should be statistically significant up to transverse momenta dominated by hard scattering of partons from the incoming nuclei. Measurements in elementary collisions will not only establish references for the heavy-ion analyses at LHC but can in themselves bring significant insights to pp physics. For many observables the understanding of specific behaviour in A–A collisions can be understood only by comparison with data from lighter systems, and especially pp. For instance, it was by comparing with the yields in simple reactions (such as pp and pBe) that it was possible to observe strangeness

enhancement [239, 241] in the yields of strange and multi-strange hyperons at the top SPS energies. This effect was put forward as evidence for deconfinement [339] and remains an important probe of chemical equilibration for the created species in the medium (see Section 6.2.1). However, at LHC energies it is not obvious (i) how to define the correlated volume describing the system, i.e. the volume over which the particles created must satisfy local conservation of quantum numbers, as regards strange-particle production [243], and/or the scale ruling strange quark production [242]; (ii) whether there will still be significant differences between Pb–Pb and pp collisions. If it turns out that deconfinement occurs in pp collisions (see Section 6.2.1.6), strange production analyses could give the first indication of this.

One of the major results at RHIC has been the clear evidence of high transverse momentum suppression and jet quenching [340, 341]. The reconstruction of secondary vertices and strange particles may shed light on the flavour dependence of in-medium effects as well as jet suppression since no limit in momentum other than statistics is reached using this identification method. Corresponding analyses must be performed both for pp and Pb–Pb data before conclusions can be drawn.

In addition, understanding pp physics at LHC will require the study of all phenomena, including processes with large cross sections; ALICE can provide significant contributions and results in this sector as well. In many respects, strangeness studies can play an important role in the determination of the general properties of pp collisions. First of all, the mechanism for baryon production is poorly known at LHC. It has been proposed that the gluons could carry part of the baryon number [342, 343]; in this case, baryon stopping would extend to mid-rapidity. The measurement of the baryon asymmetry at mid-rapidity for the proton and  $\Lambda$  would clearly reveal this phenomenon. In Eqs. 6.20 and 6.21, the values given are the ones expected if this hypothesis [344] is true:

$$A_p = 2 \frac{p - \bar{p}}{p + \bar{p}} \approx 0.05, \quad (6.20)$$

$$A_\Lambda = 2 \frac{\Lambda - \bar{\Lambda}}{\Lambda + \bar{\Lambda}} \approx 0.3. \quad (6.21)$$

The mean transverse momentum ( $\langle p_t \rangle$ ) in pp collisions is also not well understood; when observed at RHIC as a function of the particle mass [345, 346], the  $\langle p_t \rangle$  for the heavy particles tends to approach the values obtained in Au–Au collisions. Although transverse radial flow increases the observed  $\langle p_t \rangle$  of particles in heavy-ion collisions, the reasons for similar values in pp collisions remain uncertain. Two other examples show that strangeness is a key tool for investigating the properties of pp collisions: (i) strange baryon production allows us to address the flavour dependence of the fragmentation functions [347, 348]; (ii) the feed-down correction of proton yields needs the measurement of the primary  $\Lambda$  yield which in turns requires the measurement of  $\Xi$ .

Studies of  $\Lambda$  and  $K_S^0$  and of  $\Xi^-$  and  $\Omega^-$  in Pb–Pb and pp collisions at mid-rapidity and with the ALICE detector are investigated in the following paragraphs, which summarize the information presented in several ALICE internal documents [349, 350]. The technical conditions corresponding to both the simulation and the topology reconstruction of strange particles are similar to those described in Section 5.1.7.1.

Firstly, we shall describe the simulated events: (i) for Pb–Pb, we use events generated with HIJING and the selection strategies are based on a compromise between efficiency and signal over background ratio (S/B); (ii) for pp events, more than 120 000 Monte Carlo events were generated with the PYTHIA event generator [150, 351]. We shall present in the next two subsections our best estimates of the expected efficiencies and reconstruction

**Table 6.21.** Number of hyperons embedded in central HIJING events and related inverse slope parameter (exponential distribution).

Particle	$\Lambda, \bar{\Lambda}$	$\Xi^-, \bar{\Xi}^+$	$\Omega^-, \bar{\Omega}^+$
Embedded in Central Pb–Pb	100	15	3
$T$ (MeV)	650	700	800

rates in Pb–Pb for neutral single strange particles ( $K_S^0, \Lambda$ ) and charged multi-strange ones ( $\Xi, \Omega$ ) respectively. In the subsequent pp subsections, the invariant mass distributions, the reconstruction rates as a function of  $p_t$ , and the  $p_t$  spectra for a typical year of LHC running are presented. Finally we shall discuss the assumptions used for these studies and the analyses which will be investigated.

*6.2.3.1. Simulation and selection strategies.* A sample of 300 HIJING [42, 67, 352–354] central events with  $dN_{ch}/dy = 4000$  (i.e. the most central 10% of collisions) are considered for Pb–Pb simulation studies. In order to estimate detection efficiencies for strange particles, we need to generate realistic global production rates for these particles and combinatorial background. Because the production rates of strange particles from HIJING are slightly low as compared to the ones measured at RHIC energies [281, 355, 356], strange and multi-strange particles are embedded in those events. The number of particles used corresponds to predictions for LHC energies from thermal models (see Sections 6.2.1.3 and 6.2.1.4) and extrapolations from RHIC and TEVATRON data [357]. The momentum distributions have been chosen according to  $m_t$ -scaling from pions [345] with characteristics shown in Table 6.21.

Definitions of the acceptance, efficiency and reconstruction rate of the hyperon reconstruction are explained below. The general notion of the acceptance corresponds to the probability for a given produced particle to be findable, or reconstructible. The acceptance depends on both the geometry and the physical properties of the detector. The definition of ‘findable’ is an extension of that given for a simple track (see Section 5.1.7.1) to a weakly decaying particle. Hence we call ‘findable’ a particle which decays inside a fiducial zone, and whose daughter tracks are all ‘findable’ for the weak decay channel we investigate. The decay channels considered in this section are:  $K_S^0 \rightarrow \pi^+\pi^-$ ,  $\Lambda \rightarrow p\pi^-$ ,  $\Xi^- \rightarrow \Lambda\pi^-$  and  $\Omega^- \rightarrow \Lambda K^-$  (with their antiparticles for hyperons).

The definition of acceptance (ACC) for a given particle  $X$  is the following:

$$ACC_X = \frac{\text{number of findable } X}{\text{number of generated } X}.$$

As a consequence, the acceptance for a given particle is limited by its decay branching ratio, namely 68.6%, 63.9%,  $99.9\% \times 63.9\%$  and  $67.8\% \times 63.9\%$  for  $K_S^0, \Lambda, \Xi^-$  and  $\Omega^-$  respectively. Similarly, we define the reconstruction efficiency (EFF) for a given particle  $X$  as:

$$EFF_X = \frac{\text{number of reconstructed } X}{\text{number of findable } X}.$$

This efficiency describes the tracker ability to reconstruct a findable particle for a given set of reconstruction cuts. Finally the reconstruction rate ( $\varepsilon_X$ ) of a given particle  $X$  is defined as the product of  $ACC_X$  and  $EFF_X$  (i.e. the probability to reconstruct a generated particle):

$$\varepsilon_X = ACC_X \times EFF_X = \frac{\text{number of reconstructed } X}{\text{number of generated } X}.$$

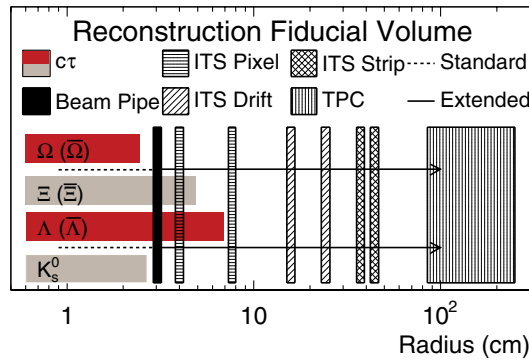


**Figure 6.106.** Fiducial volume for strange and multi-strange particles together with their  $c\tau$ . The extended radius reaches  $R = 100$  cm.

Using a magnetic field of 0.5 T for momentum determination, several reconstruction Pb–Pb strategies were evaluated differing on the size of the fiducial region and the corresponding track selections: the first consists in limiting the hyperon vertex reconstruction to the very narrow fiducial zone inside the beam-pipe (i.e. a cylindrical radius between 0.9 and 2.9 cm with respect to the beam direction) in order to benefit fully from the ITS resolution and reduce as much as possible the background from primary particle combinations and secondaries produced in the beam-pipe material. With this first approach, it is possible to obtain clean signals (with a S/B of the order of 10), for the  $K_S^0$  and  $\Lambda$ ; however the price to be paid is a small reconstruction rate for all strange particles. This is especially noticeable at high transverse momentum ( $p_t$ ) since the decay is likely to happen further away. This is a consequence both of the choice of a small fiducial volume and of the selection of only high quality tracks containing one cluster per ITS layer (i.e. 6 clusters). This is illustrated in Fig. 6.106 showing the extent of the reconstruction region together with the radius of the ITS layers and the  $c\tau$  of the hyperons (which would correspond to the mean decay length only with  $\beta\gamma = 1$ ).

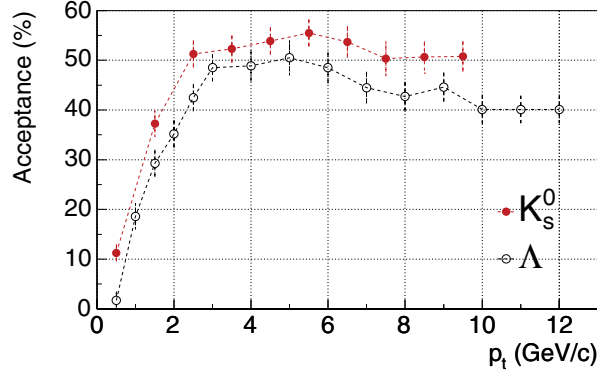
In order to increase the reconstruction rates in Pb–Pb, especially at high  $p_t$ , a second strategy was investigated. It consists of performing the  $V^0$  reconstruction with all the tracks available in the TPC and no further selection based on the number of ITS clusters. However the information given by the ITS for determining the vertex characteristics is used when available. In such a case, the reconstruction zone radius can be larger than that of the last ITS strip layer and extended up to the inner TPC radius. Although this limit could even be chosen further inside the TPC, the extended radius was set to  $R_{\max} = 100$  cm for this study.

The methods used for the reconstruction of strange particles in Pb–Pb events are also used for  $V^0$  vertices and cascade identification in pp events. The cut parameters are however relaxed in order to obtain the same signal to background ratio. One additional selection is made by requiring that a given track can be associated to one  $V^0$  and one cascade only. Thus, only the best candidate is kept when several  $V^0$  or cascades have a common track.

The reconstruction of secondary vertices relies on the reconstruction of the primary vertex. In contrast with Pb–Pb events, the primary vertex resolution in pp varies [358] over a wide range as a function of the multiplicity and can be considerably worse (see Section 5.1.1.4 on page 1320 and Fig. 5.5 on page 1319) than the value obtained in Pb–Pb collisions (see Fig. 5.6 on page 1321). The position of the pp collision is determined in 3 dimensions via the tracks reconstructed in the central tracker system (see Section 5.1.1.4 on page 1320). In

**Table 6.22.** pp events classes used for these analyses.

Events	Double diffractive	Single diffractive	Non diffractive	Total
Not selected	9 098	14 451	3 643	27 192
Selected (% triggered events)	9 386 (4.3%)	12 891 (5.1%)	101 681 (90.6%)	123 958

**Figure 6.107.** Acceptance of  $K_S^0$  and  $\Lambda$  particles as a function of  $p_t$  for a  $V^0$  vertex reconstruction zone extending up to a radius  $R = 100$  cm.

low multiplicity pp events, the small number of tracks found in the ITS and the TPC leads to a broadening of the vertex resolution. In the extreme case, the event cannot be reconstructed satisfactorily in the central part of the detector because the position of the primary vertex is not well determined. In this study, a selection is therefore made to remove those pp events prior to the analyses of the strange particles. The selected events are those where at least one SPD tracklet [359, 360] has been found. The accuracy of some reconstruction parameters depends on the primary vertex reconstruction. The broadening of the primary vertex resolution therefore leads to a decrease of the efficiency. However, relaxing the selection parameters both increases the efficiency and minimizes the sensitivity to the error on the primary vertex position. Although it was designed primarily for the reconstruction of Pb–Pb collisions, ALICE is also well able to deal with high multiplicity pp events. Thus, the efficiency is essentially increasing for such events.

We generated minimum bias pp collisions with PYTHIA 6.214 tuned for the LHC [361]. Table 6.22 contains the numbers of events divided in non diffractive, single and double diffractive processes. Approximately 82% of all generated events are selected for this study. However, the experimental event trigger would decrease this number. Assuming that a coincidence between both V0 detectors is required, the event trigger efficiency has been estimated to be 98% for non diffractive events, 50.7% for double diffractive events and 43.5% for single diffractive events. The corresponding proportion of the analysed event sample for each category when the trigger efficiency is taken into account is written in parentheses in Table 6.22.

**6.2.3.2. Single strange-particle identification in Pb–Pb collisions:  $\Lambda$  and  $K_S^0$ .** For  $\Lambda$  particles, the increase of the reconstruction zone results in a considerable rise with transverse momentum for the acceptance (up to 25% on the average when integrated over the whole  $p_t$  range). The gain is most noticeable at high  $p_t$  where a plateau at about 40–50% is reached with a slight decrease after 6 GeV/c, as illustrated in Fig. 6.107.

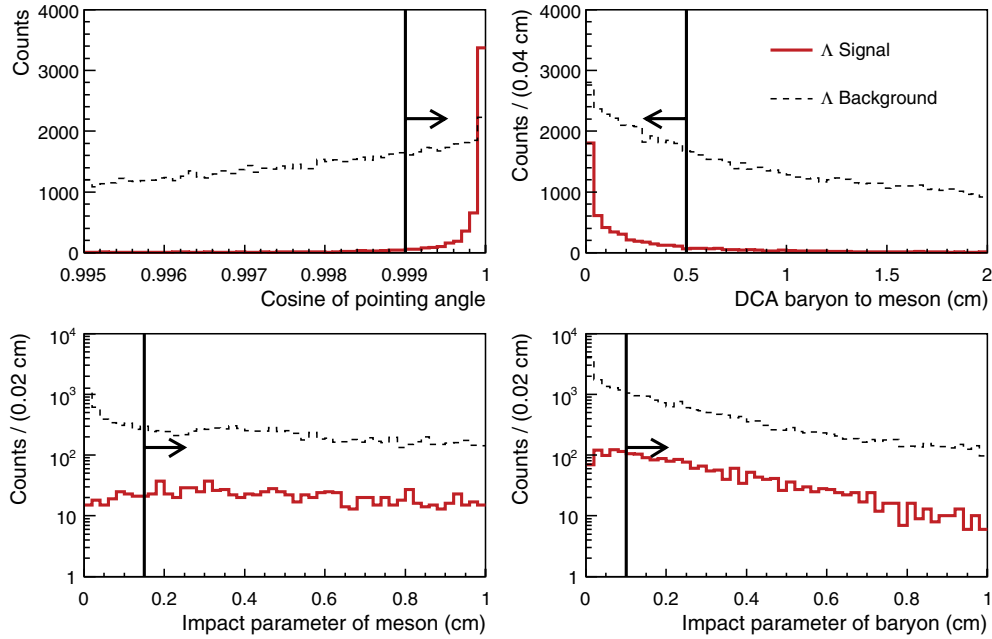


**Figure 6.108.** Distribution of the geometrical quantities for  $\Lambda$  signal (bold) and background (dashed) for: (i) the cosine of the pointing angle (upper left panel); (ii) the DCA between positive and negative tracks (upper right panel); (iii) impact parameters of the meson and baryon daughters of the  $\Lambda$  (respectively left and right lower panels). The areas kept by the geometrical selections are indicated by arrows.

Using this strategy, the secondary vertex parameters are determined, on average, with a smaller accuracy than in the case where daughter tracks contain 6 ITS clusters. Therefore, the geometrical selections on the  $V^0$  parameters (e.g. on the distance of closest approach between the positive and negative daughter tracks (DCA), see Fig. 5.49 on page 1363) must be loosened. The extended acceptance leads to a higher level of background. However, while keeping a high level of efficiency, the S/B can be improved by tightening the conditions on the track parameters (e.g. setting the minimum impact parameters of the daughters to higher values) and by having more stringent kinematical selections.

Figure 6.108 shows the distributions of geometrical quantities (corresponding respectively to  $\cos \Theta_p$ ,  $dca$ ,  $b_-$ , and  $b_+$  of Section 5.1.7.1 for  $\Lambda$  signal and  $\Lambda$  combinatorial background together with the set of selections used as reference for reconstruction (see ‘refcuts’ in Section 5.1.7.1). This set of selections is optimised so as to get a good compromise between signal efficiency and low level of background. The selections for  $\Lambda$  particles are described below:

- cosine of  $\Lambda$  pointing angle:  $\cos \Theta_p > 0.999$ ;
- distance of closest approach between  $\Lambda$  daughters:  $dca < 0.5$  cm;
- impact parameter in the transverse plane for the meson daughter of  $\Lambda$ :  $b_- > 0.15$  cm;
- impact parameter in the transverse plane for the baryon daughter of  $\Lambda$ :  $b_+ > 0.1$  cm.

Additional kinematical conditions were required to reduce the background further, namely a minimum transverse momentum value of 180 MeV/c for meson (i.e. pion) and 600 MeV/c for baryon (i.e. proton). The corresponding distributions are shown in Fig. 6.109.

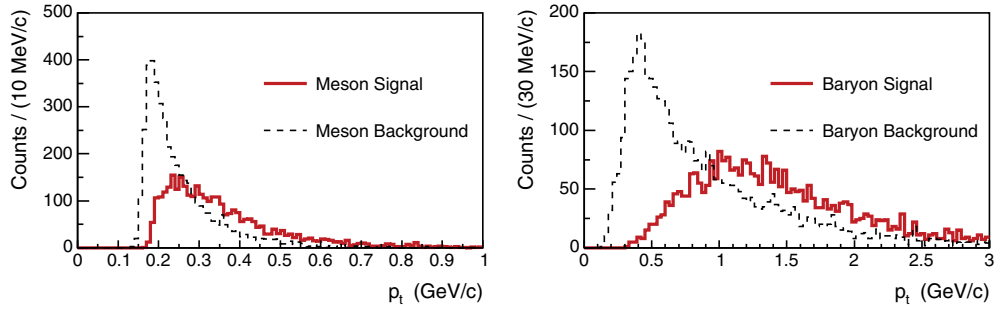


**Figure 6.109.** Transverse momentum distribution of the  $\Lambda$  daughters for signal (plain) and combinatorial background (dashed).

**Table 6.23.** Estimated production yields, mean acceptances, efficiencies, reconstruction yields and signal to background ratios for a reconstruction region restricted to  $0.9 < R < 100$  cm and reference selections.

Particle	Generated per event in $45^\circ < \theta < 135^\circ$	ACC [%]	EFF [%]	Reconstructed per event	S/B
$K_S^0$	264	15	58	23	1.5
$\Lambda^0$	100	25.5	43	11	1.5

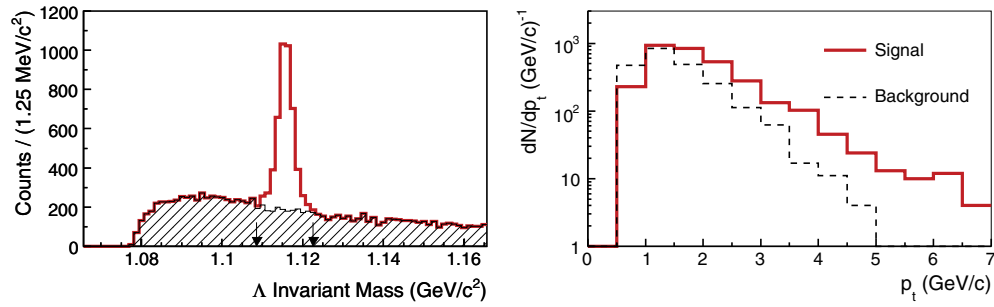


**Figure 6.110.**  $\Lambda$  invariant mass spectrum corresponding to the reference set of selections (see text) and obtained after reconstruction of 300 HIJING events (left panel). Signal (plain) and background (dashed) as a function of  $p_t$  for  $\Lambda$  reconstruction for the same 300 HIJING events.

Using this set of selections, an average efficiency of 43% and a  $\Lambda$  reconstruction rate of about 11 per event were obtained. These estimates rely both on the yields and on the related  $p_t$  distributions which are quoted in Table 6.21. The relevant information is gathered in Table 6.23 together with an integrated S/B of approximately 1.5. This is shown in the left panel of Fig. 6.110, which represents the  $\Lambda$  invariant mass distribution obtained with these conditions. In order to have an upper limit for the multiplicity dependence of these results, and given the uncertainty range on top track density prediction at LHC,  $\Lambda$  reconstruction has also been studied for  $dN_{ch}/dy = 6000$ . Using the reference selections quoted above, the corresponding average efficiency is found to be 38%.

The  $p_t$  distribution is shown in the right panel of Fig. 6.110 with a S/B larger than unity over the whole  $p_t$  range except below 1 GeV/c.

For  $K_S^0$  reconstruction, the global acceptance value is about 15%. We obtain an average efficiency of 58% which provides a reconstruction rate of 23 reconstructed  $K_S^0$  per event when

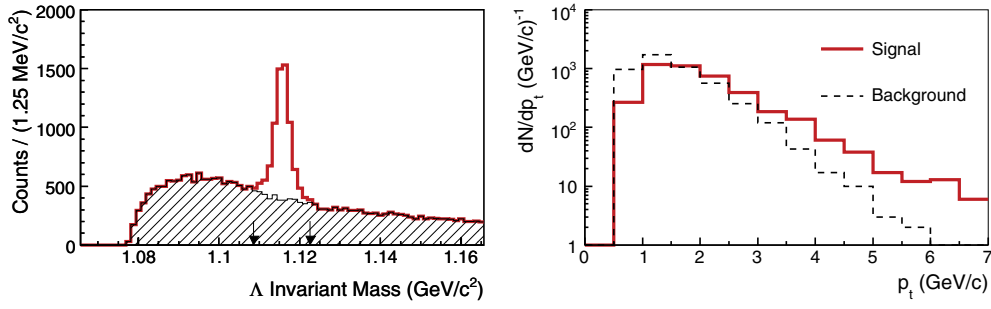


**Figure 6.111.** Left panel shows the  $\Lambda$  invariant mass spectrum, corresponding to the ‘loose’ set of selections and obtained for the reconstruction of 300 HIJING events. The right panel corresponds to the  $\Lambda$  signal (full histogram) and background (dashed) as a function of  $p_t$ , obtained for the reconstruction in 300 HIJING events with the same selections.

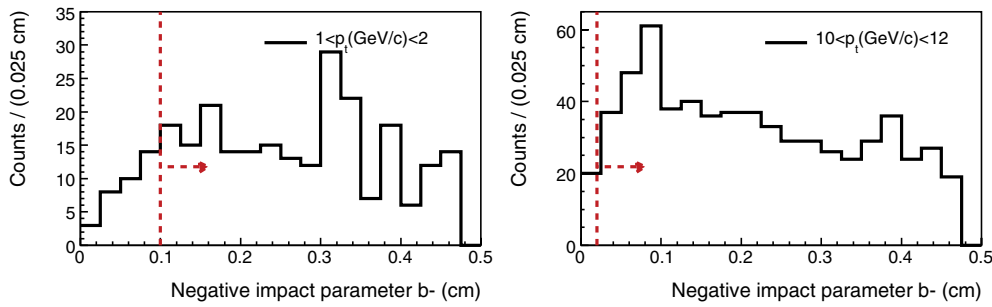


**Figure 6.112.** Comparison between the negative impact parameter ( $b_-$ ) distributions for two different momentum ranges:  $1 < p_t(\text{GeV}/c) < 2$  (left panel) and  $10 < p_t(\text{GeV}/c) < 12$  (right panel) with the corresponding selections (arrows) for  $\Lambda$  reconstruction.

using the selections:

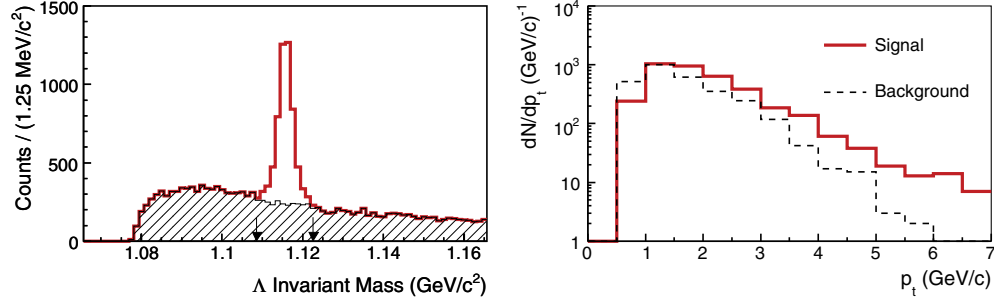
- cosine of  $K_S^0$  pointing angle:  $\cos \Theta_p > 0.998$ ;
- distance of closest approach between  $K_S^0$  daughters:  $dca < 0.5$  cm;
- impact parameter for the negative daughter of  $K_S^0$ :  $b_- > 0.07$  cm;
- impact parameter for the positive daughter of  $K_S^0$ :  $b_+ > 0.07$  cm.

For the  $\Lambda$  reconstruction, if we release the conditions on the daughter impact parameters (‘loosecuts’) in the following way:  $b_- > 0.1$  cm,  $b_+ > 0.05$  cm and increase the minimum  $dca$  to 1 cm, the efficiency goes up to 55.5% (more than 14 reconstructed  $\Lambda$  per event) but the global background level becomes higher ( $S/B=0.9$ ). This is shown in the left panel of Fig. 6.111. Nevertheless, as shown in this figure (right), the background is dominant essentially at low  $p_t$ . For  $p_t > 2$  GeV/c, the background clearly drops below the signal amplitude. Therefore, this set of selections can be used to increase the efficiency for  $\Lambda$  particles at intermediate and high  $p_t$ .

For any set of cuts, when  $p_t > 5$  GeV/c, the efficiency decreases slowly with increasing  $p_t$ . This is mainly due to the fact that the vertices are determined with less precision as the  $\Lambda$  decay position moves away from the main vertex. To prevent such a drop, selections must be loosened. Because the higher the  $p_t$  of the  $V^0$ , the smaller the impact parameters of the daughters, we choose to loosen the requirements on the minimum impact parameter with increasing  $p_t$ . This is illustrated in Fig. 6.112 where the impact parameter distributions of the

**Table 6.24.** Transverse momentum dependent selections for  $\Lambda$  reconstruction (see Fig. 6.113 and related caption for definitions).

$p_t$ range (GeV/c)	$\cos \Theta_P$	$dca$ (cm)	$b_-$ (cm)	$b_+$ (cm)
0–2.5	> 0.999	< 0.5	> 0.10	> 0.05
2.5–4.5	> 0.999	< 1.0	> 0.10	> 0.05
4.5–8	> 0.999	< 1.0	> 0.06	> 0.03
8–12	> 0.999	< 1.0	> 0.02	> 0.01

**Figure 6.113.**  $\Lambda$  invariant mass spectrum obtained with the  $p_t$ -dependent selection set (left panel). Corresponding signal (plain) and background (dashed) distributions as a function of  $p_t$  (right panel).

negative  $\Lambda$  daughters are compared for two different momentum ranges:  $1 < p_t$  (GeV/c)  $< 2$  and  $10 < p_t$  (GeV/c)  $< 12$  respectively.

Hence, according to these trends, a set of  $p_t$ -dependent selections was built up, allowing for an improvement of the efficiency at intermediate and high  $p_t$ , with which the background is kept at a low level ( $S/B > 1$ ) over the whole  $p_t$  range (except below 1 GeV/c). This set of  $p_t$ -dependent selections is defined for four  $p_t$  ranges, as shown in Table 6.24.

Compared to the reference selections (see Table 6.24), the efficiency integrated over the whole  $p_t$  range shows a substantial increase (50% instead of 43%), whereas the global S/B is only slightly reduced (from 1.4 to 1.2). The corresponding yield of reconstructed  $\Lambda$ s reaches 13 per event, to be compared with 11. These results are illustrated in Fig. 6.113.

The reconstruction efficiency profile resulting from the  $p_t$ -dependent selections is shown in Fig. 6.114 together with its product with the acceptance (see Fig. 6.107) which gives the reconstruction rate for  $\Lambda$  particles. The  $\Lambda$   $p_t$  spectra are shown in the left panel of Fig. 6.115 for two hypotheses. They define a likely interval for the expected spectra at LHC for central Pb–Pb collisions, with an upper and lower estimate depending on transverse radial flow for the  $\Lambda$  particle: the generated exponential spectra correspond respectively to inverse slopes of 800 MeV and 500 MeV. The convolutions of these spectra with the  $\Lambda$  reconstruction rate are shown in the right panel and provide an estimate of the inclusive spectrum at mid-rapidity. We conclude that for a total of  $10^7$  central events,  $\Lambda$  particles can be reconstructed up to at least  $p_t = 10$  GeV/c.

**6.2.3.3. Cascade particle identification in Pb–Pb collisions:  $\Xi$  and  $\Omega$ .** Assuming the inverse slope parameters presented in Table 6.21 on page 1593, the integrated acceptances for the reconstruction of  $\Xi$  and  $\Omega$  are  $\sim 9\%$  and  $\sim 6\%$  respectively. Their  $p_t$  dependence at mid-rapidity is shown in Fig. 6.116. The slight decrease for high- $p_t$  particles is due to the finite fiducial volume.

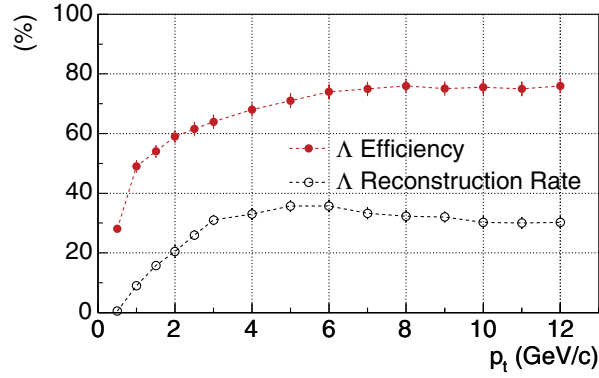


**Figure 6.114.** Efficiency and reconstruction rate as a function of transverse momentum for  $\Lambda$  particles, obtained with  $p_t$ -dependent selections for identification.

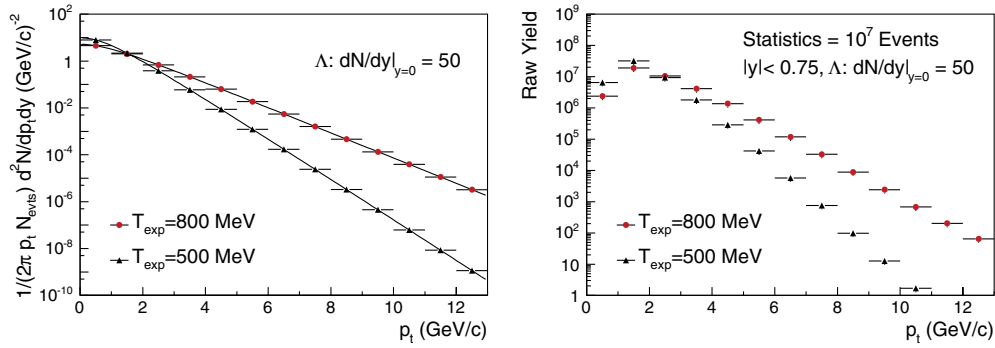


**Figure 6.115.** Left panel: Generated  $p_t$  spectra for  $\Lambda$  particles for two hypotheses of the inverse slope parameter (exponential functional form) and an estimated yield at mid-rapidity of 50. Errors are from the simulation statistics. Right panel: Reconstructed  $\Lambda$  (raw spectra) distributions corresponding to the convolution of inclusive  $p_t$  spectra with the reconstruction rate and for a total statistics of  $10^7$  central Pb–Pb events.

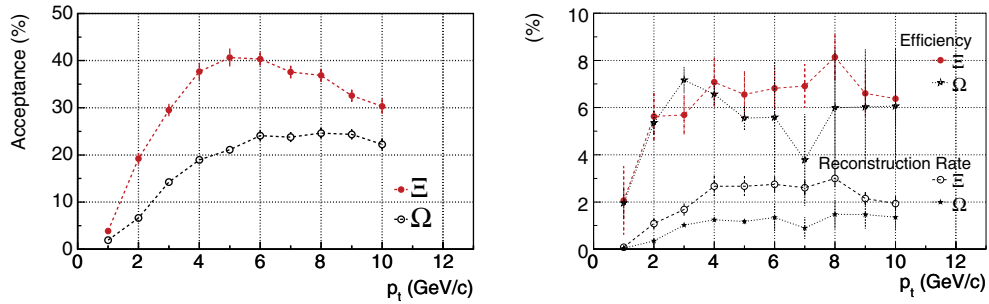


**Figure 6.116.** Left panel: Acceptance for  $\Xi$  and  $\Omega$  reconstruction as a function of  $p_t$ . Right panel: Efficiency and reconstruction rate as a function of transverse momentum for  $\Xi$  and  $\Omega$  particles obtained with quoted selections for identification (see text).

For the cascade (charged  $\Xi$  or  $\Omega$ ) identification in Pb–Pb environment, we need to reconstruct the three daughter tracks from the two successive weak decays, as shown in Colour Figure IV. We first select the likely secondary  $\Lambda$  from the  $V^0$  sample. The selection of the  $\Lambda$

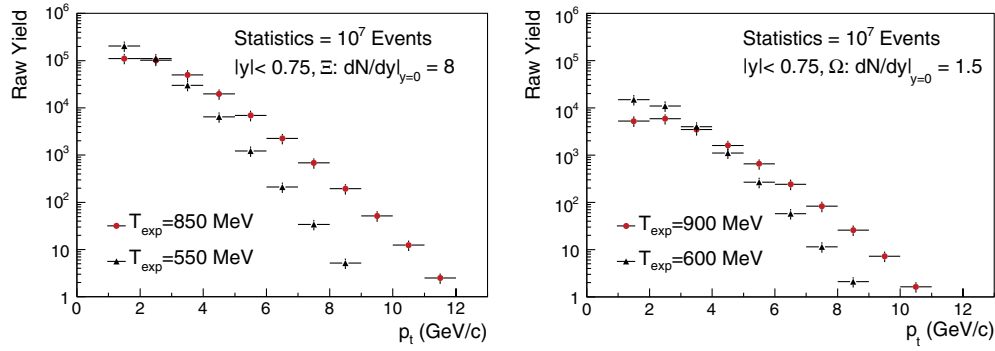


**Figure 6.117.** Estimate of reconstructed cascade distributions (raw spectra) corresponding to the convolution of inclusive  $p_t$  spectra with the reconstruction rate and for a total statistics of  $10^7$  central Pb–Pb events (Left and right panels:  $\Xi$  and  $\Omega$  particle respectively).

daughters is done using minimum values of impact parameter which are similar to those used for the primary  $\Lambda$ . However, the condition on the  $dca$  of the  $\Lambda$  daughter tracks is tightened in order to limit the combinatorial background. Further conditions are required for the  $\Lambda$  candidates, such as a minimum impact parameter to the primary vertex and an invariant mass range selection. The  $V^0$  pointing angle to the primary vertex, however, must be kept loose. The bachelor candidate must have a short  $dca$  to the  $\Lambda$  trajectory while its impact parameter has a minimum value for selecting a secondary particle. Finally, the reconstructed cascade must point back to the primary vertex. Therefore a maximum value for the cosine of its pointing angle is used. The following selections and values are the ones which were used for both  $\Xi$  and  $\Omega$  studies:

- impact parameter for the meson daughter of  $\Lambda$ :  $b_- > 0.2$  cm;
- impact parameter for the baryon daughter of  $\Lambda$ :  $b_+ > 0.06$  cm;
- distance of closest approach between  $\Lambda$  daughters:  $dca_{(-,+)} < 0.1$  cm;
- cosine of  $\Lambda$  pointing angle:  $\cos \Theta_{pV^0} > 0.995$ ;
- invariant mass window around the  $\Lambda$  mass:  $m_\Lambda \in [1115.68 \pm 5 \text{ MeV}/c^2]$ ;
- impact parameter for the  $\Lambda$ :  $b_\Lambda > 0.1$  cm;
- impact parameter for the bachelor daughter of cascade:  $b_b > 0.12$  cm;
- distance of closest approach between the bachelor and the  $\Lambda$  candidate:  $dca_{(\Lambda,b)} < 0.1$  cm;
- cosine of cascade pointing angle:  $\cos \Theta_{p\xi} > 0.9995$ .

The expected spectra for the  $\Xi$  and  $\Omega$  particles, using the efficiency and acceptance profiles of Fig. 6.116, and for two hypotheses for the inverse slope parameters, are shown in Fig. 6.117. Owing to the limited statistics for the simulated data, no further optimisation as a function of  $p_t$  has been considered so far. PID will significantly enhance the S/B, and will be used to separate the  $\Omega$  signal from the  $\Xi$  by identifying the decay daughter (kaon instead of pion). The  $\Xi$  and the  $\Omega$  invariant mass spectra obtained with such a set of selections are shown in the left and right panels of Fig. 6.118 respectively. The estimated reconstruction efficiency for the  $\Xi$  is close to 5% (6%) on average which yields a  $\Xi$  ( $\Omega$ ) reconstruction rate of 0.075/event (0.01/event).

**6.2.3.4. Single strange-particle identification in pp collisions:  $\Lambda$  and  $K_S^0$ .** For pp events, the reconstruction of secondary  $V^0$  vertices is studied with two different selection sets listed in Table 6.25. The first sample corresponds to the selection parameters employed for the event

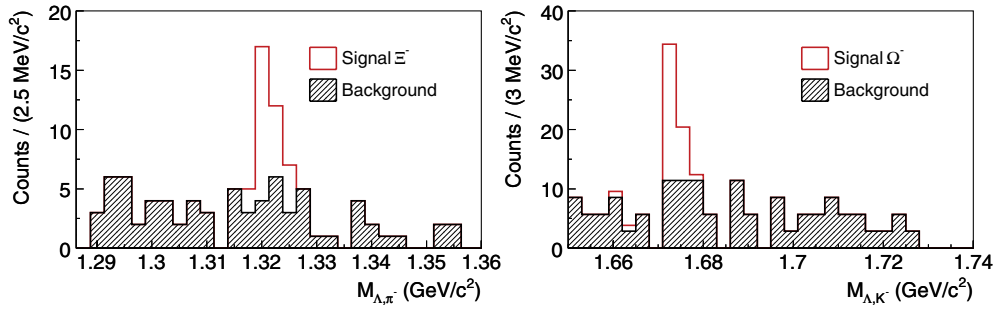


**Figure 6.118.** Left panel:  $\Xi^-$  invariant mass spectrum obtained with the reconstruction of 300 HIJING events. Right panel: For the  $\Omega^-$  particle a dedicated study was performed due to the low efficiency and requested 6000 events.

**Table 6.25.** Selection parameters for strangeness reconstruction in pp events.

Selections	$b_{-/+}$ min. ( $\mu\text{m}$ )	$\cos \Theta_P$ min.	daughter dca max. (cm)	decay length min. (cm)
loose	21	0.717	5.30	0.07
tight	115	0.994	3.46	0.34

reconstruction which is done prior to the analyses. At this level, the selections have to be as loose as possible in order to keep most of the secondary vertices with the background still at a reasonable level. They have been chosen to set the memory size of the array of  $V^0$  vertices in the Event Summary Data (ESD) files at approximately 1/15 of the size of the track array. For the second sample, tighter selections are applied, so the purity is improved and we obtain approximately the S/B values required for typical spectra and correlation analyses. The invariant mass distributions of  $\Lambda$  and  $K_S^0$  are presented in Fig. 6.119. The upper panel of Fig. 6.119 shows the signals and backgrounds for the first sample whereas the lower part shows the distributions from the second sample.

The total integrated reconstruction rate for both  $\Lambda + \bar{\Lambda}$  and  $K_S^0$  are presented on the left panel of Fig. 6.120 for the second selection set. The upper part of this panel shows the event distribution and the lower part the global reconstruction rates, both presented as a function of the charged track multiplicity. A clear drop in the reconstruction rates appears at low multiplicity while they remain almost constant after  $N_{\text{ch}} > 20$ . This decrease is mainly due to the softening of the momentum distribution of single strange particles in low multiplicity collisions. Indeed, as shown for the  $\Lambda$  on Fig. 6.121, the strange-particle correction factor increases gradually with  $p_t$  from 0 to 3 GeV/c and introduces a strong dependence between the momentum distribution and the global reconstruction rate. The effect of primary vertex resolution can be seen on the right panel of Fig. 6.120, where the intrinsic efficiency (computed by dividing the number of reconstructed secondary vertices by the number of vertices which can be found) is plotted as a function of the multiplicity. The efficiency is mainly constant for loose selections but starts to decrease for tight selection parameters and low multiplicity. This behaviour can be explained by the fact that the  $V^0$  reconstruction becomes more sensitive to the precision of the measurement of the primary vertex position when the selections are tightened. Although the effect is weak, it means that analyses of pp events therefore requires the separation of events into multiplicity classes. We plan to investigate this multiplicity dependence in detail, with high statistics. Nevertheless the reconstruction rate of  $\Lambda + \bar{\Lambda}$  as a function of  $p_t$  and for low ( $N_{\text{ch}} < 20$ ) and high ( $N_{\text{ch}} > 30$ )

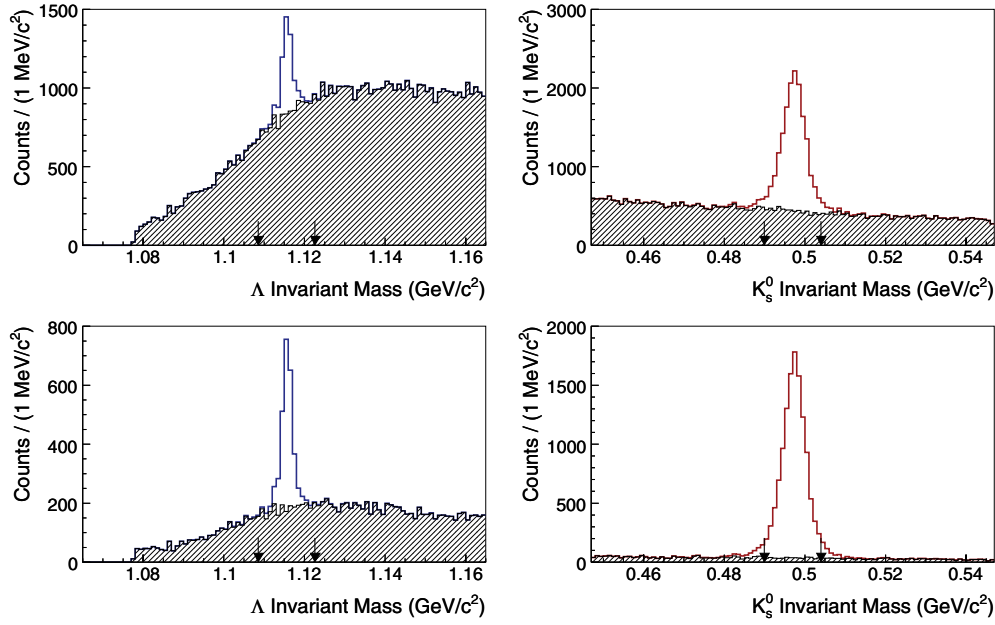


**Figure 6.119.** Invariant mass distributions of  $\Lambda$  and  $K_S^0$  reconstructed in pp events for both loose (upper panels) and tight selections (lower panels).

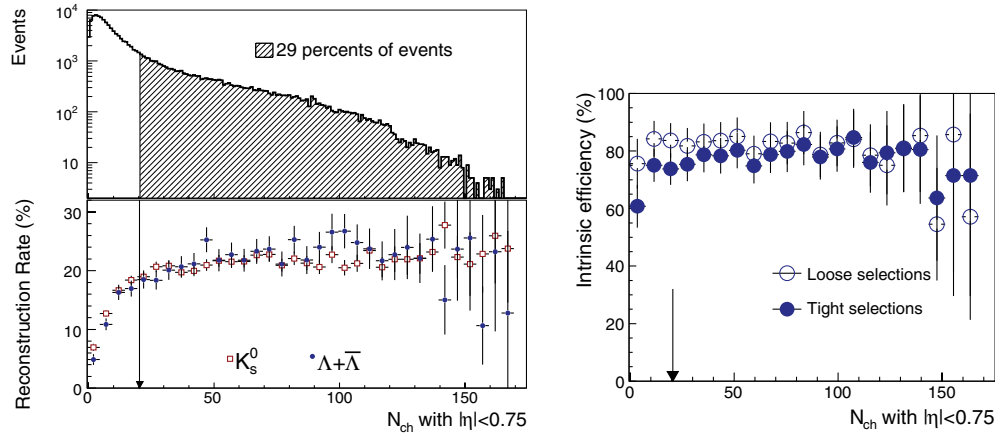


**Figure 6.120.** Left panel: event distribution and global reconstruction rate for  $\Lambda$  (open symbols) and  $K_S^0$  (full symbols) as a function of pp collision track multiplicity. Right panel: intrinsic efficiency of the  $V^0$  finding method as a function of the event multiplicity for the two sets of selections.

multiplicity events can still be calculated (see the right panel of Figure 6.121). No strong difference is found between the two distributions except a slightly lower reconstruction rate for low  $N_{ch}$ . Finally Fig. 6.122 shows an estimation of the raw  $\Lambda$  distribution versus  $p_t$  for one year of LHC pp runs (i.e.  $10^9$  events). This distribution is based on the  $\Lambda$  Monte Carlo production in PYTHIA minimum bias events which is fitted by an *ad hoc* function. The function is then corrected by the actual reconstruction rate of Fig. 6.121 and scaled by the expected number of events.

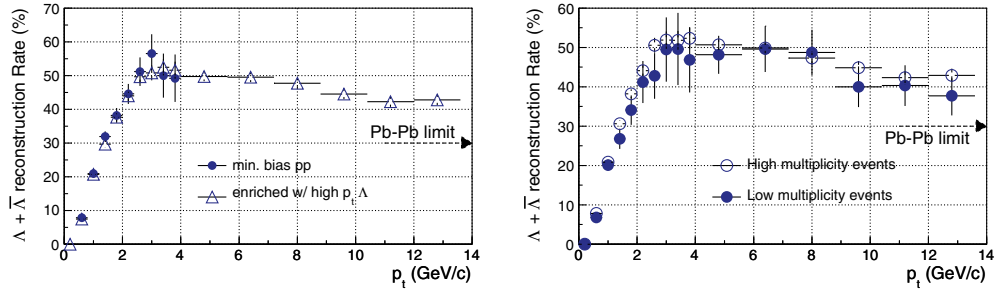


**Figure 6.121.** Reconstruction rate for  $\Lambda + \bar{\Lambda}$  as a function of  $p_t$ . Left panel: the reconstruction rate is calculated for minimum bias pp events (full symbol) and for minimum bias events enriched in high- $p_t$   $\Lambda$  and  $\bar{\Lambda}$  (open symbol). Right panel: the reconstruction rates for low (full symbol) and for high (open symbol) multiplicity pp events are presented.

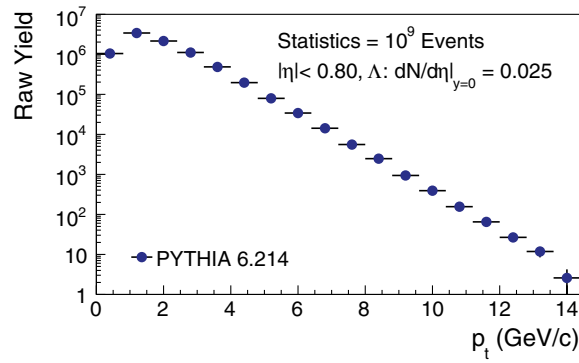


**Figure 6.122.** Distribution of reconstructed  $\Lambda$  as a function of  $p_t$  for  $10^9$  pp events at  $\sqrt{s} = 14$  TeV.

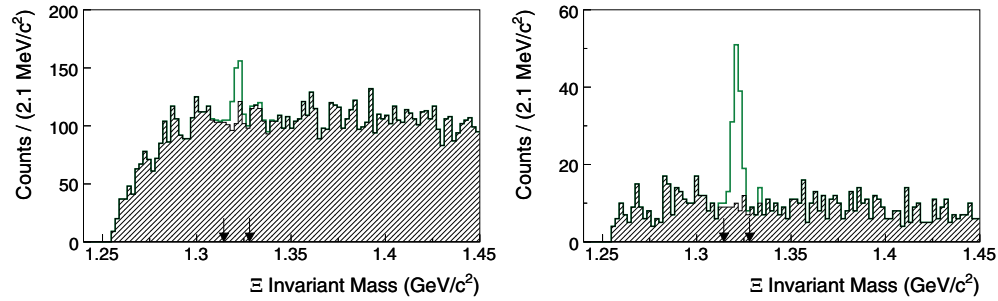


**Figure 6.123.** Invariant mass of  $\Xi^- + \Xi^+$  in pp events for loose (left panel) and tight (right panel) selections.

**6.2.3.5. Cascade particle identification in pp collisions:  $\Xi$  and  $\Omega$ .** The reconstruction of cascades has also been investigated using two sets of selections: one with loose selections and one with tighter parameters. A clear  $\Xi$  signal is obtained in the pp events as shown with the resulting invariant mass distributions of Fig. 6.123 with  $S/B \sim 0.3$  for loose selections (left panel) and  $S/B \sim 2.6$  for tight selections (right panel) respectively. The dependence on the cascade momentum is studied by generating pp enriched with high- $p_t$   $\Xi^-$  and  $\Xi^+$ .

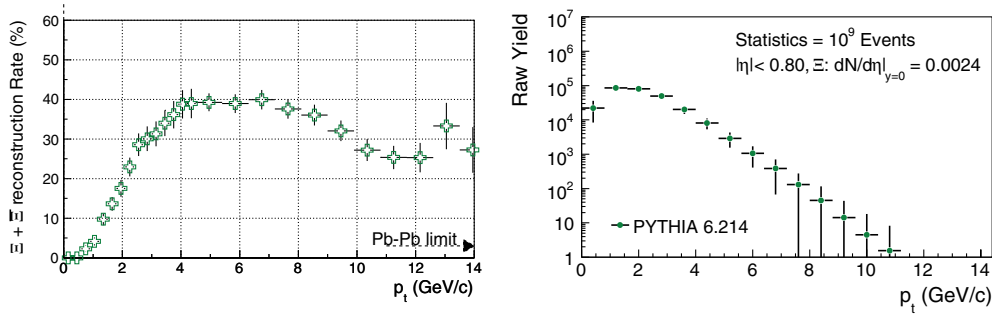


**Figure 6.124.** Left panel: Reconstruction rate of  $\Xi^- + \Xi^+$ . Right panel: Estimated numbers of reconstructed  $\Xi^-$  for  $10^9$  pp events at  $\sqrt{s} = 14$  TeV as a function of  $p_t$ .

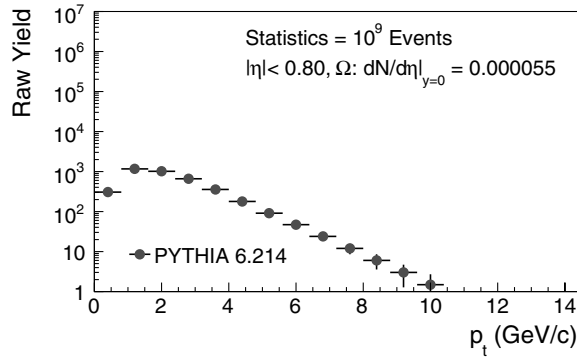


**Figure 6.125.** Distribution of reconstructed  $\Omega^-$  as a function of  $p_t$  for  $10^9$  pp events at  $\sqrt{s} = 14$  TeV.

The resulting reconstruction rate as a function of  $p_t$  and for the tight selection parameters is shown on the left panel of Fig. 6.124 while the corresponding estimation of the reconstructed cascades distribution versus  $p_t$  is presented on the right.

In the case of the  $\Omega$ , the reconstruction rate is estimated by scaling down the reconstruction rate of  $\Xi$  in pp collisions by the factor found for the decrease of this rate in Pb–Pb collisions. Using the  $p_t$  distribution of the Monte Carlo  $\Omega$  generated with PYTHIA, we consequently estimate the reconstructed  $p_t$  distribution shown in Fig. 6.125.

**6.2.3.6. Discussion.** The simulation shows that transverse mass spectra for weakly decaying single and multi-strange particles should be measurable up to  $\sim 10$  GeV/c in the first year of Pb–Pb data taking at the LHC. The range appears to be shorter for pp data. However, the events were generated with PYTHIA, which tends to underestimate the yields for strange particles. Our preliminary studies of efficiencies and of the signal-to-noise predict clean signals for the first years of data taking for both Pb–Pb and pp collisions. Not only will this allow us to obtain the production yields with good accuracy, which is necessary for the feed-down correction of lower mass particles, but it will be possible to investigate the shape of the spectra in detail. It is also possible that the shapes of the real spectra differ markedly from the simplified parametrisations which were used. For this reason, we have shown two inverse slope parameters per particle corresponding to lower and higher Pb–Pb estimates. A significant hard scattering contribution (depending on the coupling with a suppression) would

lead to a higher yield at intermediate and high  $p_t$ . On the other hand, hadronic decoupling of hyperons would give the opposite trend. In any case, we expect the statistics and the range of identification to be large enough for the investigation of different hadronisation scenarios (e.g. coalescence with baryon/meson spectra differences), transverse radial flow effects and nuclear modification factor studies [362, 363].

#### 6.2.4. Reconstruction of the $\rho^0$ signal

**6.2.4.1.  $\rho^0$  physics.** The  $\rho^0$  meson has a lifetime of 1.3 fm/c. This is comparable to the lifetime of the collision fireball and, for this reason, the  $\rho^0$  particle could provide a signal of the transition to the Quark–Gluon Plasma through the modifications of its properties in the medium [364].

It is useful to study two decay modes: the hadronic channel,  $\rho^0 \rightarrow \pi^+\pi^-$ , and the leptonic channel,  $\rho^0$  to  $e^+e^-$ . Measurements in the leptonic decay channel probe all stages of the system, as leptons have a low probability of subsequent interaction in the medium and therefore escape without rescattering. Therefore, study of the leptonic decay channel can provide information on the early stages of the fireball when the QGP is expected to be present. Large changes to the mass and shape of the  $\rho^0$  are expected under the high temperature and high energy density conditions of the early stages of the system [364]. Effects such as mass reductions [365], mass increases and  $\rho^0$  shape broadening have been proposed [364]. There is some evidence for a  $\rho^0$  mass reduction of around 300 MeV/c<sup>2</sup> as measured by the CERES collaboration in the  $e^+e^-$  decay channel [366]. This is manifested as an excess of dilepton pairs in the 400–500 MeV/c<sup>2</sup> mass range together with a lack of a  $\rho^0$  peak having the PDG values of mass and width.

Unlike leptons, hadrons have a high probability of rescattering in the medium. Therefore, pions from  $\rho^0$ s which decayed in the early stages will be rescattered, and the  $\rho^0$  will not be reconstructible. Additionally, final-state interactions will regenerate  $\rho^0$ s later in the fireball's evolution. As a result of this, the  $\rho^0$ s measured in the hadronic decay channel will represent conditions at the final stages of the system. Even under these conditions,  $\rho^0$  properties are expected to be modified by interactions with the medium [367], although to a smaller degree than in the earlier stages where temperature and density are much larger. For example, STAR has observed a possible reduction of the  $\rho^0$  mass in the hadronic channel [368].

In the following sections, we evaluate the current possibilities of reconstructing the  $\rho^0$  in the hadronic channel. We shall adopt the following outline: we first introduce the simulation method, then report the yield predictions on which we base our study. The signal extraction and fitting strategies are presented in the next two sections, and following this we show the signal over background ratio (S/B) and significance. Finally, we discuss the limitations of our study and draw conclusions. More details about this study can be found in Ref. [369].

**6.2.4.2. Simulation method.** The simulation of events is done in three steps:

- simulation of the physics of pp and heavy-ion collisions, and prediction of the particles generated in these collisions;
- simulation of the response of the ALICE detectors and reconstruction algorithms to these generated particles;
- selection of appropriate reconstructed tracks and reconstruction of resonances by performing invariant mass calculations on pairs of positive and negative tracks.

The physics of Pb–Pb events is simulated using the HIJING event generator [42, 370]. The output from this generator is then passed to the detector simulation.

The standard ALICE detector simulation uses GEANT to track particles through the apparatus, and simulate the response of the detectors for each such track. Because this process is too time-consuming to be used to generate the large number of events which is required for the analysis, a fast simulation method was developed. This method uses a parametrisation of track reconstruction efficiency, errors on momentum measurement and PID efficiency (see Section 5.1.3).

The detailed detector simulation and reconstruction, which uses a combination of ITS, TPC, TRD and TOF detectors, is applied to a sample of approximately 4000 events. Tracks from these events are divided into  $p_t$  and particle species bins. The reconstruction efficiency in each bin is calculated by finding the fraction of generated particles in this bin which are successfully reconstructed in the detailed simulation. A total of about  $3 \times 10^7$  tracks are included in this calculation. Appropriate efficiencies are computed for each bin for the particles  $\pi^+ + \pi^-$ ,  $K^+ + K^-$  and  $p + \bar{p}$ , and functions are fitted to these data to allow the calculation of efficiency for arbitrary  $p_t$ .

The resolution of track momentum measurements is calculated in a similar way. For each particle species and  $p_t$  bin, a table of measurement ‘errors’ is calculated from the detailed simulation, for  $p_x$ ,  $p_y$  and  $p_z$ .

The particle identification efficiency is also included in the fast simulation. The conditions for identifying a track as a pion are applied to the results from the detailed simulation, a table of the probability of a particle of given  $p_t$  and particle species being identified correctly is made, and this is subsequently used in the fast simulation.

For each input track to the fast simulation, the probability of successful reconstruction,  $P_{\text{rec}}$ , is obtained from the efficiency parametrisation above, together with the probability for the PID identifying the track as a pion,  $P_{\text{pid}}$ . The probabilities are taken from the appropriate  $p_t$  bin. A random number,  $R$ , from 0 to 1 is generated, and if  $R < P_{\text{rec}} P_{\text{pid}}$ , the track is stored in the output. Finally, for tracks which pass the previous criterion, momentum smearing is applied by randomly selecting ‘errors’ in  $p_x$ ,  $p_y$  and  $p_z$  from the appropriate  $p_t$  bin of the table described above and adding them to the input values of  $p_x$ ,  $p_y$  and  $p_z$ .

The output tracks from this fast simulation are passed to the resonance finding algorithm, which makes all combinations of positive and negative tracks and calculates the invariant mass of the candidate particle using a  $\pi^+ \pi^-$  hypothesis.

It must be noted this fast simulation does not include contributions from secondary tracks. Use of both the ITS and the TPC to calculate the impact parameter of tracks allows cuts to be done to remove most of them. The number of secondary tracks after these cuts is small compared to the number of primaries, at under 10%, and it is possible to reduce this further using impact parameter cuts.

Use of the fast simulation gives approximately a factor of 100 increase in generation speed. Systematic errors introduced by this method are below 10%, which is small compared to the reduction in statistical error achieved.

**6.2.4.3. HIJING predictions.** In this analysis, the output from HIJING was used directly. For central events, it predicts a multiplicity of 6000 charged primary tracks per unit of pseudorapidity in the central rapidity region, which is larger than most predictions 6.2.1.7.  $\rho/\pi$  ratios have been measured over a range of centre-of-mass energies of 8–200 MeV at various experiments and various collision systems, such as pp,  $e^+e^-$ ,  $\pi^-p$ ,  $K^+p$  and peripheral Au–Au [368]. The ratio is approximately constant in this region. Extrapolating to ALICE energies assuming a constant ratio gives a first-order approximation of the value, which may then be modified by in-medium effects. The predicted values at ALICE are 0.165 for peripheral Pb–Pb and 0.150 for central Pb–Pb, which compare to the measured value for

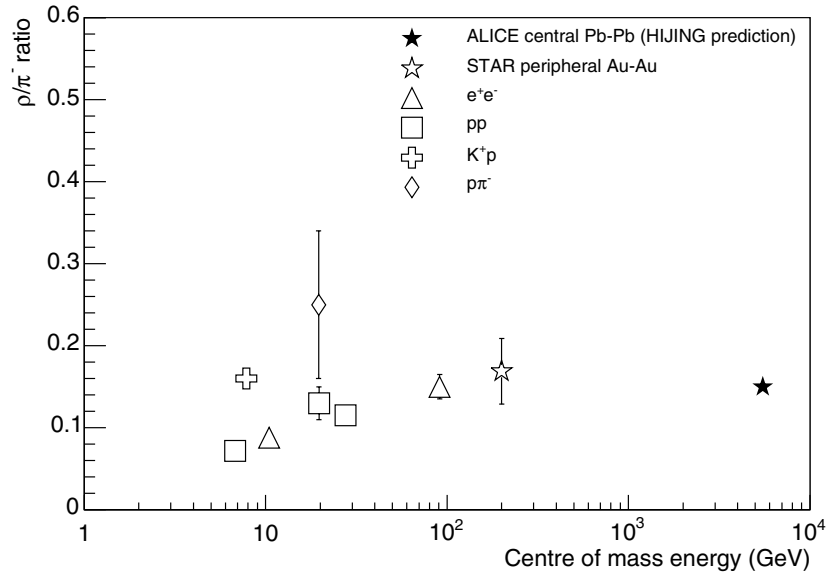


**Figure 6.126.** Ratio of  $\rho$  to  $\pi$  for various collision systems and energies, including HIJING's prediction for Pb–Pb at ALICE. The other systems are  $e^+e^-$  at 10.45 GeV [371] and 91 GeV [372], pp at 6.8 GeV [373], 19.7 GeV [374], 27.5 GeV [81] and 52.5 GeV [375],  $K^+p$  at 7.82 GeV [376],  $\pi^-\pi^+$  at 19.6 GeV [377] and peripheral Au–Au at 200 GeV [368].

peripheral Au–Au collisions at STAR of  $0.169 \pm 0.037$ . Figure 6.126 shows the comparison of these to the measured ratio at various experiments.

6.2.4.4.  $\rho^0$  signal extraction. The  $\pi^+\pi^-$  invariant mass spectrum is complicated, and consists of several contributions:

- the  $\rho^0$  mass peak;
- a very large combinatorial background from uncorrelated positive and negative tracks;
- the  $\omega \rightarrow \pi^+\pi^-\pi^0$  decay, with the invariant mass of the charged pion pairs forming a large, wide peak in the invariant mass spectrum;
- the  $\omega \rightarrow \pi^+\pi^-$  decay, forming a small peak at  $0.782 \text{ GeV}/c^2$ ;
- the  $\eta \rightarrow \pi^+\pi^-\pi^0$  and  $\eta' \rightarrow \pi^+\pi^-\eta$  decays, behaving in a similar way to the  $\omega \rightarrow \pi^+\pi^-\pi^0$  decay;
- the  $K^* \rightarrow K\pi$  decay, with the kaon misidentified as a pion;
- the  $\phi \rightarrow K^+K^-$  decay, with both kaons misidentified as pions.

Some of these are shown in Fig. 6.127. The  $K^*$  and  $\phi$  are removed using PID.

The combinatorial background is reduced by the ‘like-sign’ method, where the spectrum is created by making an invariant mass spectrum from pairs of particles of the same sign. This reproduces the contribution from uncorrelated  $\pi^+\pi^-$  pairs but not the contributions from resonance decays, as shown in Fig. 6.127.

It must be noted that without PID, the  $K^*$  would be an important problem: as the reflection of its invariant mass peak under a  $\pi^+\pi^-$  hypothesis lies under the  $\rho^0$  peak, it makes the fit to the  $\rho^0$  a challenging task. Therefore, measurement of  $\rho^0$  properties such as mass shifts and yields are subject to significant errors which will have to be evaluated. The ALICE PID is used to solve this problem, making it possible to reduce the contribution of  $K^*$  by a factor of

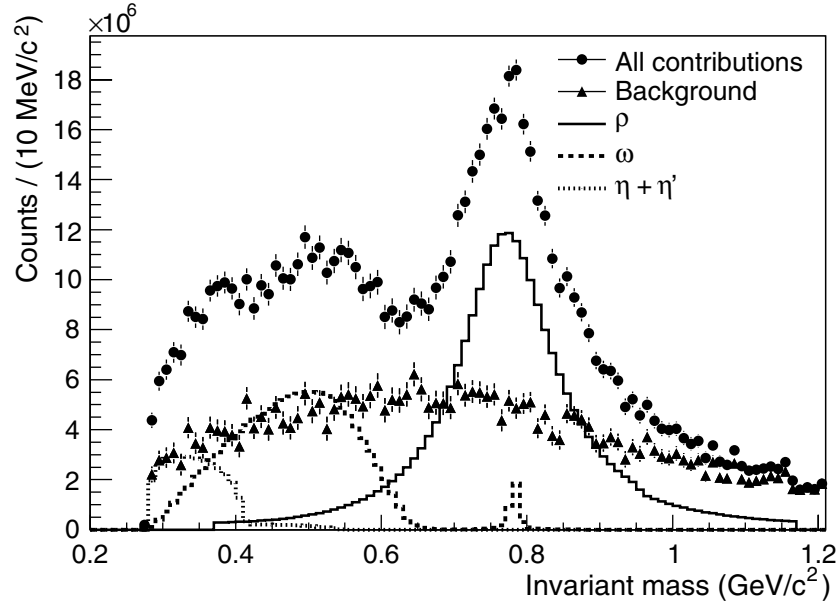


**Figure 6.127.** The  $\pi^+\pi^-$  invariant mass spectrum after like-sign background subtraction for  $10^6$  HIJING generated central Pb–Pb events, with contributions from  $\rho^0$ ,  $\omega$ ,  $\eta + \eta'$  and remaining combinatorial background indicated.

about 100, making it negligibly small compared to the  $\rho^0$  peak. As a  $\phi$  must have both of its decay tracks misidentified to be included in the  $\pi^+\pi^-$  spectrum, the use of PID eliminates most of the  $\phi$  contamination.

**6.2.4.5. Fitting.** After these subtractions and selections, the spectrum contains a residual combinatorial background, the  $\rho^0$ , the  $\omega$  and the  $\eta$  and  $\eta'$ . The  $\rho^0$  function used is the non-relativistic Breit–Wigner:

$$\frac{dN}{dm} = A \times \frac{\Gamma}{(m - \mu)^2 + \frac{1}{4}\Gamma^2}, \quad (6.22)$$

where  $m$  is the invariant mass of the resonance candidate,  $\mu$  is the central mass of the resonance Breit–Wigner and  $\Gamma$  is the width parameter of the resonance Breit–Wigner. The non-relativistic form of the Breit–Wigner corresponds to the one PYTHIA and HIJING use to decay hadrons [67, 150, 329]. A different form of the Breit–Wigner may have to be used for the real data.

A function containing a sum of the background, the  $\omega$  and the  $\rho^0$  Breit–Wigner is fitted to the data in the region  $0.55 < m < 1.2 \text{ GeV}/c^2$ . The background is modelled as a straight line in this mass range, and the shape of the  $\omega$  is obtained from a Monte Carlo simulation. For  $m < 0.55 \text{ GeV}/c^2$ , the background cannot be modelled as a straight line and contributions from  $\eta$  and  $\eta'$  are also present. Finally, it is required that the total number of  $\rho^0$  candidates in the fitted mass range is the same for both the fitted function as the actual histogram. This reduces the number of free parameters by one, and results in a more stable fit with better estimates of errors.

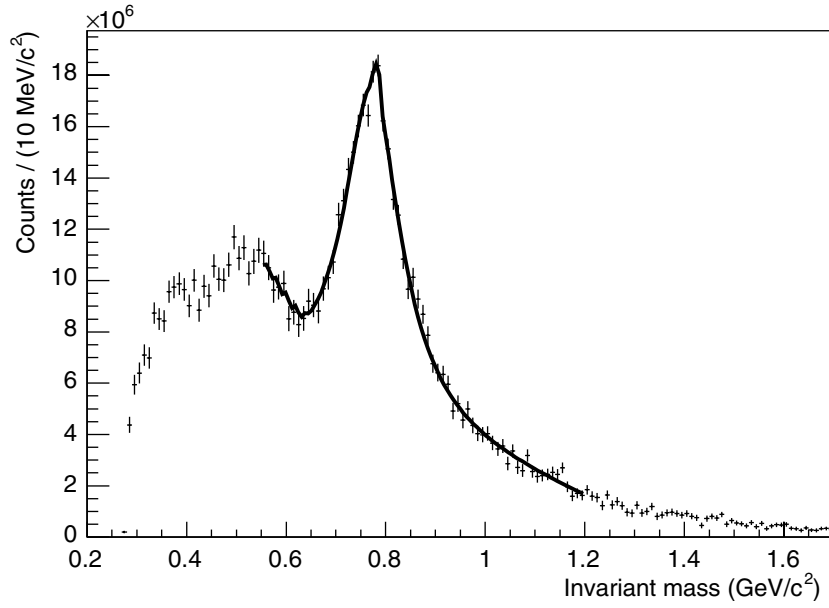


**Figure 6.128.** Fit of  $\rho^0$  Breit-Wigner,  $\omega$  and background to  $\pi^+\pi^-$  invariant mass spectrum after like-sign subtraction for  $10^6$  central Pb-Pb events. The fitted parameters are shown in Table 6.26.

**Table 6.26.** Comparison of the fit of the realistic  $\rho^0$  results to a fit of the  $\rho^0$  result with no background. The fit is performed for  $10^6$  HIJING central Pb-Pb events.

	Full fit	Fixed width fit	$\rho^0$ without background
Mass ( $\text{GeV}/c^2$ )	$0.771 \pm 0.001$	$0.772 \pm 0.001$	0.774
Width ( $\text{GeV}/c^2$ )	$0.162 \pm 0.008$	0.139 (fixed)	0.139
Number $\rho^0$ s	$(2.30^{+0.69}_{-0.47}) \times 10^8$	$(2.02 \pm 0.10) \times 10^8$	$1.97 \times 10^8$

Figure 6.128 shows the result of this fit applied to  $10^6$  central Pb-Pb events. The results of the fit are given in Table 6.26. The ‘ $\rho^0$  without background’ values for mass and width are the results of fits to the  $\rho^0$  mass spectrum which contains genuine  $\rho^0$ s only. The number of  $\rho^0$ s refers to those with masses in the range 0.630–0.930  $\text{GeV}/c^2$ , and is calculated by summing the bin contents in the ‘ $\rho^0$  without background’ case and integrating the fitted function in the fitted cases.

These results suggest that the  $\rho^0$  mass can be measured to a precision of 2–3  $\text{MeV}/c^2$ . However, it may be necessary to assign a larger systematic error as the  $\rho^0$  shape may be modified from that described by the fitted Breit-Wigner. The yield is also measured quite accurately, and the quoted errors are reasonable. Fixing the width allows the error in the yield measurement to be reduced, provided it is reasonable to assume that the width is not significantly changed from the accepted value.

Variation of detector efficiency with  $p_t$  distorts the  $\rho^0$  shape. This leads to the fitted width being smaller than would be expected (e.g. the Breit-Wigner fitted to the generated  $\rho^0$  sample has a width of 150  $\text{MeV}/c^2$ ) whereas the Breit-Wigner fitted to the reconstructed  $\rho^0$  sample has a width of 139  $\text{MeV}/c^2$ . This was not corrected for in this analysis, so the fit was done to the distorted  $\rho^0$ , resulting in a width which is different from the PDG value.

**Table 6.27.** Significance and S/B values for  $\rho^0$  in various  $p_t$  regions for  $10^6$  HIJING central Pb–Pb events. Significance is also shown for the expected central event sample of  $10^7$  events for 1 year of data taking at the LHC.

$p_t$ range	PID	Signal	Background	S/B	Significance	
					$10^6$ events	$10^7$ events
All	Yes	$1.97 \times 10^8$	$2.65 \times 10^{12}$	$7.43 \times 10^{-5}$	121	382
	No	$2.66 \times 10^8$	$4.11 \times 10^{12}$	$6.0 \times 10^{-5}$	127	402
Below 1 GeV/c	Yes	$1.78 \times 10^8$	$2.40 \times 10^{12}$	$7.42 \times 10^{-5}$	115	364
	No	$2.27 \times 10^8$	$3.74 \times 10^{12}$	$6.0 \times 10^{-5}$	117	369
1–2 GeV/c	Yes	$1.71 \times 10^7$	$2.42 \times 10^{11}$	$7.06 \times 10^{-5}$	34.8	110
	No	$3.35 \times 10^7$	$6.89 \times 10^{11}$	$4.86 \times 10^{-5}$	40.4	181
2–4 GeV/c	Yes	$2.15 \times 10^6$	$9.30 \times 10^9$	$2.31 \times 10^{-4}$	22.3	70.5
	No	$5.05 \times 10^6$	$3.50 \times 10^{10}$	$1.44 \times 10^{-4}$	27.0	85.4
Above 4 GeV/c	Yes	$2.16 \times 10^5$	$2.14 \times 10^8$	$1.0 \times 10^{-3}$	14.8	46.8
	No	$8.20 \times 10^5$	$1.27 \times 10^9$	$6.45 \times 10^{-4}$	23.0	72.7

Measurement of the  $\rho^0$  width is problematic. As can be seen in Table 6.26, the fit gives a width which is significantly larger than the correct value. This suggests that there is a source of systematic error which has not been considered. One possible cause is the assumption that the background can be described by a straight line. If this is not true under the  $\rho^0$  peak, the difference between the true background and the linear approximation may distort the  $\rho^0$  shape, appearing as a change of the width. As the exact form of the background for the real data will be unknown, a better approach may be to fix the width at a known value based on results from previous experiments, taking experimental resolution and distortions due to efficiency into account.

**6.2.4.6. S/B and signal significance.** The signal-to-background and signal significance ( $S/\sqrt{S+B}$ ) for  $\rho^0 \rightarrow \pi^+\pi^-$  in HIJING central Pb–Pb collisions are obtained for each studied  $p_t$  region. They are calculated for the region within  $150 \text{ MeV}/c^2$  of the fitted central value, i.e.  $0.630$  to  $0.930 \text{ GeV}/c^2$ . Results are shown in Table 6.27, with significance listed for both the sample of  $10^6$  events studied here and the expected  $10^7$  central events which will be available after one year of ALICE data collection. The predicted signal significances do not change much with event centrality.

The study of subsamples in selected  $p_t$  regions is complicated by the lower signal significance, equivalent to a factor of 10 reduction in statistics for the  $p_t$  region 1–2 GeV/c and a factor of 65 reduction for the region  $p_t > 4 \text{ GeV}/c$ . As the PID becomes less efficient at high  $p_t$ , it is possible to improve significance by either not using it at all or using less strict identification criteria. However, this may leave a significant contribution from  $K^* \rightarrow K\pi$ , which must either be fitted together with the  $\rho^0$ ,  $\omega$  and background or subtracted if the yield and shape are known from a dedicated  $K^*$  analysis. Additionally, as Table 6.28 shows, the statistical significance of the signal decreases as  $p_t$  increases, which will prevent yield measurements at high  $p_t$  even if the problem of  $K^*$  contamination can be solved.

**6.2.4.7. Effect of reduced signal.** The real data may differ significantly from the HIJING predictions. To investigate this, the  $\rho^0$  part of the  $\pi^+\pi^-$  spectrum was reduced by several fixed factors. The fitting procedure was used with a fixed width of  $140 \text{ MeV}/c^2$  to extract values of  $\rho^0$  mass and yield. The results are shown in Table 6.29. It is possible to obtain a fit even with the  $\rho^0$  signal reduced by a factor of four, albeit with somewhat larger errors. For a  $\rho^0$  contribution which is 25% of the predicted one, the error in the yield is 25%. Therefore,

**Table 6.28.** Significance and S/B values for  $\rho^0$  at high  $p_t$  based on a sample of 93 000 HIJING central Pb–Pb events. Significance is shown for  $10^7$  events.

$p_t$ range	PID	Signal	Background	S/B	Significance ( $10^7$ events)
4–6 GeV/ $c$	Yes	18010	$2.14 \times 10^7$	$8.41 \times 10^{-4}$	40.3
	No	63958	$1.17 \times 10^8$	$5.47 \times 10^{-4}$	61.3
6–8 GeV/ $c$	No	14383	$1.28 \times 10^7$	$1.12 \times 10^{-3}$	41.7
8–10 GeV/ $c$	No	3898	$2.01 \times 10^6$	$1.94 \times 10^{-3}$	28.4

**Table 6.29.** Mass and yield for reduced signal analysis and a comparison to the true values for  $\rho^0$  contributions of 50%, 25% and 10% of the predicted value for  $10^6$  HIJING central Pb–Pb events. The width is fixed at 140 MeV/ $c^2$ .

$\rho^0$ fraction	Fitted mass (GeV/ $c^2$ )	Fitted $N_{\rho^0}$	Correct $N_{\rho^0}$
50%	$0.771 \pm 0.002$	$10.8 \pm 0.8 \times 10^7$	$9.85 \times 10^7$
25%	$0.769 \pm 0.004$	$6.13^{+0.65}_{-0.57} \times 10^7$	$4.92 \times 10^7$
10%	$0.765 \pm 0.007$	$1.03 \pm 0.16 \times 10^6$	$1.97 \times 10^7$

the  $\rho^0$  signal should be measurable even if the  $\rho^0$  fraction is somewhat lower than predicted. However, as the case for the  $\rho^0$  signal reduced by a factor of 10 shows, a very low signal will not be measurable.

**6.2.4.8. Conclusions.** This Monte Carlo study suggests that the  $\rho^0$  signal should be measurable in central Pb–Pb collisions. It has been demonstrated that the yield can be measured to within 10%, and the central mass value with an error of 2–3 MeV/ $c^2$ . This suggests that any large mass shifts will be measurable. However, given the difficulty obtaining good fits, it will probably be necessary to assign larger systematic errors than are suggested above.

The largest errors are due to uncertainties in the HIJING predictions of multiplicity,  $\rho^0$  abundance,  $\rho^0$  mass etc. As a result, the signal significance may be much better or worse than indicated here, although the constant  $\rho^0$  to  $\pi^-$  ratio used here is a reasonable starting point. In the extreme case, it may not be possible to measure  $\rho^0$  in central Pb–Pb collisions. If it is assumed that the predictions are accurate, it should be possible to measure  $\rho^0$  yields and properties in various  $p_t$  regions, as the signal significance in the sub-regions for the full statistics is similar to or larger than the significance of the sample studied here. High  $p_t$  (e.g. over 4 GeV/ $c$ ) studies will require different PID selection criteria to those used for the full- $p_t$  study shown here, as the conventional ALICE PID begins to lose the capability to distinguish between  $\pi$  and K at about 2 GeV/ $c$ . The PID may be improved by using the relativistic rise phenomenon, which could allow  $\pi$  and K separation at much larger  $p_t$  (see Section 6.2.2.1). However this extended PID capability is still under study, and was not included in the simulation used for this analysis. Additionally, there is a further limit imposed by the decreased statistical significance which will make measurements of the  $\rho^0$  more difficult for  $p_t > 8$  GeV/ $c$ .

It must be noted that this study gives an indication of the statistical limits of the  $\rho^0$  measurement. As the S/B is very low, even very small systematic effects can have a large influence on the fit. The real  $\rho^0$  measurement may be subject to factors which are not taken into account by HIJING, such as changes of the  $\rho^0$  line shape, mass shifts of  $\rho^0$  and  $\omega$ , other resonance contributions such as  $f_0$  and other correlations between particles. It is possible that such factors may make a measurement more difficult than suggested by this study, even if the statistical significance of the signal is similar.

6.2.5. *Detection of  $\phi \rightarrow K^+K^-$ .* The  $\phi$  meson is of particular interest owing to its ( $s\bar{s}$ ) valence quark content, which makes the  $\phi$  a signature of strangeness production mechanisms from a possible early partonic phase [237, 378, 379]. An enhancement of  $\phi$  production in 3–10 times was proposed [380, 381] as a quark–gluon plasma signature, or alternatively as a result of the secondary collisions in the dense nuclear matter. Also a decrease of the  $\phi$  mass by up to 150 MeV [264, 265] and an increase of the  $\phi$  width by a factor of 2–3 [382, 383] have been predicted.

The  $\phi$  will be measured in ALICE [384] both in the lepton and kaon decay channels. The ratio of the decay widths in these two channels might be sensitive to changes in parton or kaon masses [383]. The recent SPS Pb–Pb and RHIC Au–Au results show that no significant change of the mass or width are observed at these energies [385–387]. However, a moderate rise of the slope parameter in the transverse spectra and an enhancement of the  $\phi/\pi$  ratio by a factor of 3 as compared to the minimum bias pp interactions were found [385, 388].

The main experimental problem in selecting the hadronic mode of  $\phi$  decays in heavy-ion collisions at the LHC energy is the very high combinatorial background. The HIJING event generator [42, 370] predicts about 1400 primary charged kaons in the pseudo-rapidity window  $-1 \leq \eta \leq 1$  and for central Pb–Pb events. This number is  $\sim 14$  times larger than the estimated number of kaons from  $\phi$  decays. It is clear that, in such conditions, very good particle identification and the best possible signal-to-background ratio (S/B) are required to measure the properties of this particle.

Preliminary results of the expected ( $K^+K^-$ ) mass spectrum of pairs and the detection capability of the decay  $\phi \rightarrow K^+K^-$  in ALICE were described in [389] (see also Section 11.4.3 in [384]). Different kinematic selections were studied in order to improve the S/B value and based on fast simulation. Here we present results obtained within the AliRoot framework [3]. Details on the detector efficiencies and track reconstruction algorithms can be found in Section 5.1.3. The simulation was performed for two different classes of events: in the full transverse momentum ( $p_t$ ) region and for particles with  $p_t > 1.5$  GeV/c (high  $p_t$  region). In the following sections, the current possibilities of  $\phi \rightarrow K^+K^-$  detection are evaluated. The following outline will be adopted: Firstly the simulation method will be introduced, then the simulation results in full and high  $p_t$  regions will be reported; next, the detection of a possible double peak structure in the  $\phi$  signal resulting from a phase transition to QGP will be studied [390]; finally the systematic uncertainties in the simulation will be discussed with respect to existing and forthcoming data. Most of the results which are presented here were published in [391, 392].

#### 6.2.5.1. Simulation method

*Full transverse momentum region.* A detailed simulation of the Inner Tracking System (ITS, [1]) and the Time Projection Chamber (TPC, [393]), were used for the tracking. The TPC and the Time of Flight (TOF, [394]) were used for kaon identification at the first step. The charged particle density ( $dN_{ch}/d\eta$  at  $\eta = 0$ ) is expected to be 6000 for Pb–Pb collisions at LHC energy with 10% of charged kaon production. These conditions were reproduced in order to generate about 250 HIJING [42, 370] events. They were transported through the ITS, TPC and TOF acceptance (in the full azimuthal angle ( $\varphi$ ) range and in the pseudo-rapidity ( $\eta$ ) range  $-1 \leq \eta \leq 1$ ). A magnetic field of 0.4 T was used. The full efficiency as a function of  $p_t$  and  $\eta$  has been extracted for charged kaons. We call the ‘full efficiency’ the ratio of the number of identified kaons to the generated ones. This means that the full efficiency takes into account the losses during the detection, tracking and PID.

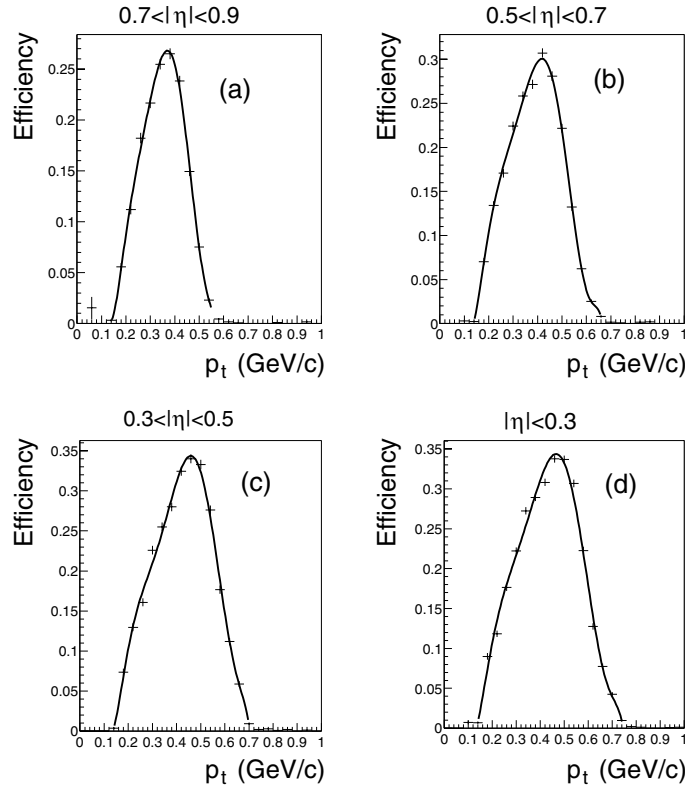


**Figure 6.129.** Full kaon efficiency (see text) as a function of  $p_t$  in the different pseudo-rapidity ( $\eta$ ) regions for the TPC. The curves are the results of polynomial fits.

Figure 6.129 shows the dependence of the full kaon efficiency on  $p_t$  in the different  $\eta$  regions for the TPC. The low efficiencies at lower momentum are mostly the result of kaon decays and tracking inefficiency, which in turn is a consequence of the short particle path inside the TPC resulting from the track curling in the magnetic field. The high- $p_t$  limit of the kaon selection is a consequence of the TPC PID limit since the signals from pions and kaons overlap one another in the momentum range of 0.6–0.7 GeV/ $c$  (see, for example, Fig. 11.18 in [384]). Figure 6.130 (a,b,c,d) shows the dependence of the full TOF efficiency for charged kaons on the  $p_t$  in different  $\eta$  regions (Fig. 6.129 a,b,c,d, respectively). It is seen from Figs. 6.129 and 6.130 that the maximum full efficiency does not exceed 40% in either the TPC or the TOF. Figures 6.129 and 6.130 show also that the kaon identification regions of the TPC and TOF overlap in the interval  $0.35 < p_t < 0.75$  GeV/ $c$ .

The  $p_t$  dependences of the angle and  $p_t$  resolutions were determined during the simulation. It was shown [391, 392] that for  $0.2 < p_t < 9.0$  GeV/ $c$ , the relative  $p_t$  resolution is between 1.0 and 2.0%, and the angular resolutions decrease from 5.0 to 0.3 mrad for both polar ( $\theta$ ) and azimuthal ( $\varphi$ ) angles.

The AliGenParam generator of AliRoot was used in the second fast simulation step. It can generate an arbitrary number of different type of particles with a uniform pseudo-rapidity distribution in the acceptance under study (i.e.  $-1 \leq \eta \leq 1$ ) and exponential  $p_t$  distribution (see below). The decays of the particles are performed using the PYTHIA generator [395]. To combine the generation both of charged kaons and of  $\phi \rightarrow K^+K^-$  decays,

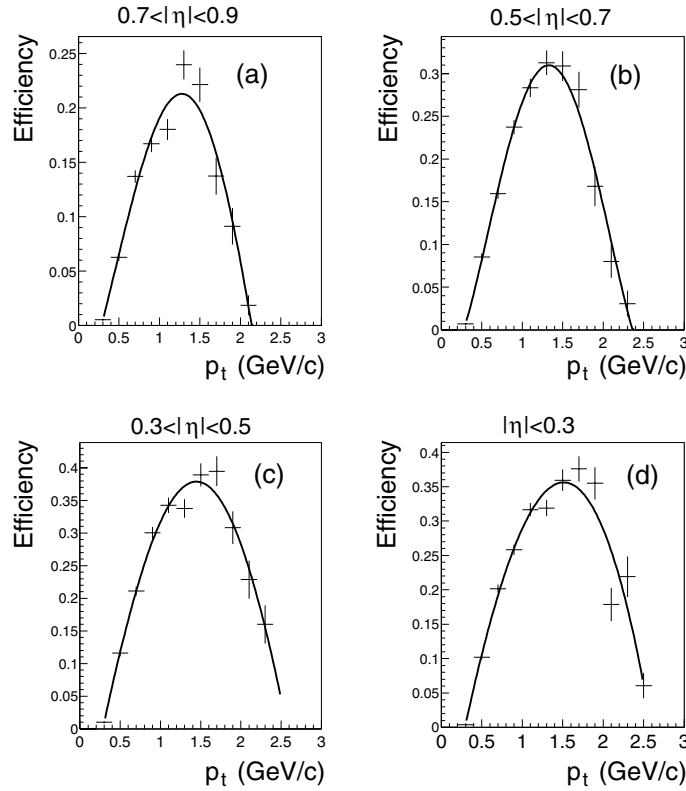


**Figure 6.130.** Full kaon efficiency (see text) as a function of  $p_t$  in the different pseudo-rapidity ( $\eta$ ) regions for the TOF. The curves are the results of polynomial fits.

the AliGenCocktail generator (also part of the AliRoot framework) was used, allowing us to combine any arbitrary number of particle types. The number of charged kaon and  $\phi$  decays in the acceptance was estimated from the charged pion multiplicity (i.e. 9000  $\pi^\pm$  taken from HIJING) using the particle ratios,  $K^-/\pi^- = 0.15 \pm 0.02$  and  $\phi/K^- = 0.15 \pm 0.03$  obtained from RHIC experimental data [396, 397]. As a result 1350 charged kaons and 50  $\phi \rightarrow K^+K^-$  decays were generated per event, on average, in the acceptance of the detectors.

The left panel of Fig. 6.131 shows the generated distribution of  $m_t - m_0$  for kaons and  $\phi$  mesons where  $m_t$  and  $m_0$  are the transverse and particle masses respectively. The lines are fit results by the function  $\exp(-(m_t - m_0)/T)$  with the  $T = 480$  MeV for  $\phi$  and  $T = 309$  and  $390$  MeV for the first and second slopes respectively of the distribution for kaons. We note that the values for  $T$  are higher than those obtained in experiments at the AGS ([398]), SPS ([385], [399]) and RHIC ([387], [396]) for central events, and this tendency corresponds to the rise of this parameter with energy, as seen in the right panel of Fig. 6.131.

Next, kaons were identified, taking into account the TPC and TOF efficiencies separately for each kaon, using the polynomial fits (the curves in Figs. 6.129 and 6.130). We note that we can increase the number of found  $\phi$ 's by 20% using different detectors for the identification of the two decay products. To obtain a more realistic signal-to-background ratio, a 15% contamination from pion and proton to kaon sample (see Sections 5.4.1, 5.4.2 and 5.4.4) was taken into account for the simple recalculation of the  $K^+K^-$  background.

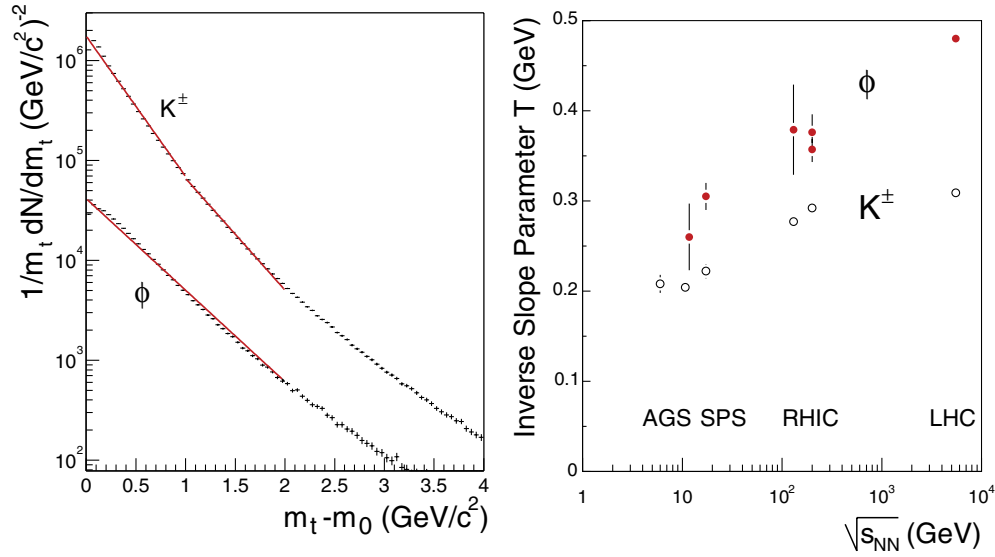


**Figure 6.131.** Left panel:  $m_t$  spectra for kaons and  $\phi$  obtained using the AliGenParam generator. The curves are the results of exponential fits. Right panel: Dependence of slope parameter  $T$  (see text) on energy in c.m.s per nucleon for  $\phi$  at  $(m_t - m_0) < 2 \text{ GeV}/c^2$  (full circles) and charged kaon at  $(m_t - m_0) < 1 \text{ GeV}/c^2$  (empty circles) production in different experiments (AGS, SPS and RHIC). The LHC points were obtained by simulation using the AliGenParam generator (see text).

The  $p_t$  and the angles of the  $K^+$  and  $K^-$  were smeared by Gaussian distributions with widths equal to their respective resolutions [391, 392]. Then new  $p_x$ ,  $p_y$ ,  $p_z$  components were applied to calculate the effective mass of the  $K^+K^-$  pairs.

*High transverse momentum region.* To study the detection of  $\phi$ -mesons and background ( $K^+K^-$ ) pairs in the high- $p_t$  region,  $p_t > 1.5 \text{ GeV}/c$  for each particle, a simulation was performed without any particle identification. The AliGenParam and AliGenCocktail generators were used to generate pions, kaons, protons, antiprotons and  $\phi$  resonances. We have taken for the full  $p_t$  region the numbers of  $\pi^\pm$ ,  $K^\pm$  and  $\phi$  decays presented in Section 6.2.1.7 and the numbers of protons and antiprotons from  $\bar{p}/\pi^-$  and  $\bar{p}/p$  ratios obtained in the STAR experiment [254, 400]. We determined the number of each particle type in the high- $p_t$  region ( $p_t > 1.5 \text{ GeV}/c$ ), and, as a result, 320 charged pions, 160 charged kaons, 200 protons and antiprotons and 18  $\phi \rightarrow K^+K^-$  decays were generated per event on the average. Again, the momentum components were smeared according to the relative  $p_t$  and angular resolution functions.

### 6.2.5.2. Results

*Full transverse momentum region.* An analysis of the  $K^+K^-$  effective mass spectra was carried out for different  $p_t$  bins of  $K^+K^-$  pairs using statistics of  $10^6$  cocktail generator events. Figure 6.132(a) shows the  $K^+K^-$  effective mass spectrum taken at  $p_t(K^+K^-) > 2.2 \text{ GeV}/c$ . The  $\phi$  signal is clearly seen above the combinatorial background obtained for  $K^+K^+$  pairs. Figure 6.132(b) shows the  $\phi$  signal found after subtraction of this combinatorial background. To extract the resonance width it is necessary to take into account the effective mass resolution. Figure 6.132(c) shows the distribution of the differences of the effective masses obtained with

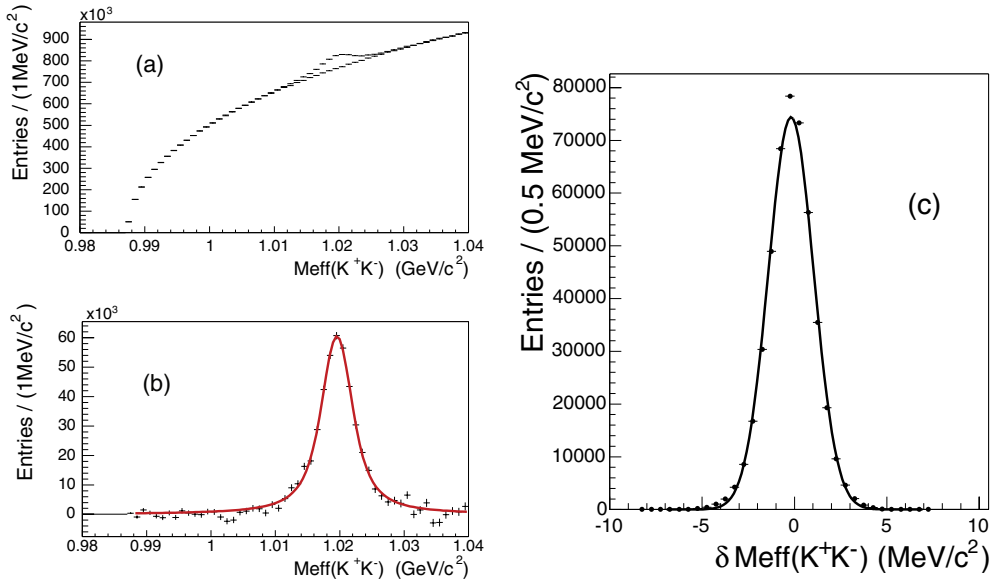


**Figure 6.132.** Panel (a): Spectrum of  $(K^+K^-)$  effective mass in  $(K^+K^-)$  pair transverse momentum region of  $\geq 2.2$  GeV/c. The  $(K^+K^+)$  background distribution is also shown. Panel (b): Signal of  $\phi$  meson after subtraction of the background. The curve is a Breit–Wigner fit result taking into account the effective mass resolution (see text). Panel (c): Effective mass resolution of  $(K^+K^-)$  for  $p_t(K^+K^-) > 2.2$  GeV/c. The curve is the fit result for a Gaussian function.

and without track momentum and angle smearing using the respective Gaussian functions. The curves are the Gaussian fit results with the parameter  $\sigma = 1.23$  MeV/c<sup>2</sup>. This  $\sigma$  value (the effective mass resolution) has been taken for a convolution of the Breit–Wigner and Gaussian functions used for the  $K^+K^-$  lineshape approximation. The result is shown in the effective mass region 0.99–1.04 GeV/c<sup>2</sup> by the curve in Fig. 6.132(b) with the mass and width of the  $\phi$  resonance  $1019.60 \pm 0.04$  MeV/c<sup>2</sup> and  $4.32 \pm 0.11$  MeV/c<sup>2</sup> respectively. One can see that these values are consistent with the PDG ones used in the generation code (i.e. 1019.5 MeV/c<sup>2</sup>).

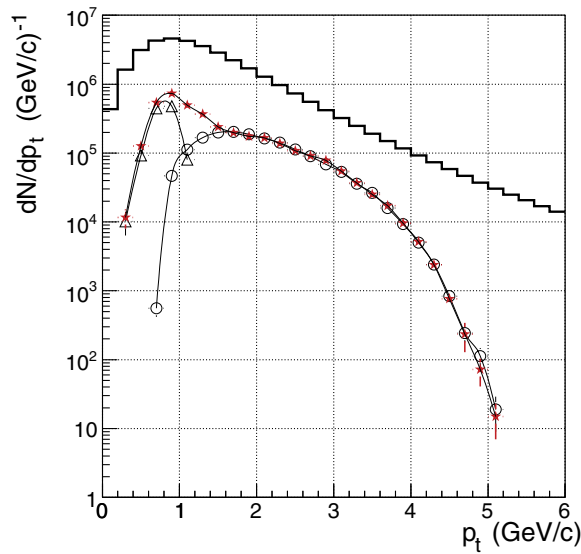
Table 6.30 presents the S/B and the significance ( $S/\sqrt{S+B}$ ) in the different  $p_t$  regions of the  $(K^+K^-)$  pairs. The signal (S) is presented as well. One can see that the S/B improves from 0.4% at the lowest  $p_t$  to 5.3% at the highest  $p_t$  and the significance is 108 for  $p_t > 2.2$  GeV/c.

Figure 6.133 shows the reconstructed  $\phi$  meson  $p_t$  spectrum: the yields (and the relative errors) in each  $p_t$  bin were determined by fitting background subtracted  $m_{\text{eff}}(K^+K^-)$  distributions (such as that shown in Fig. 6.132(b)) to a Breit–Wigner function convoluted with a Gaussian function plus a linear residual background in the mass range 0.99–1.05 MeV/c<sup>2</sup> [401]. Three spectra are shown separately for particle identification with the TPC alone, the TOF alone, and the combination of both detectors. For comparison, the generated  $p_t$  distribution for  $\phi$  mesons whose daughters are charged kaons in the range  $|90^\circ - \theta| \leq 45^\circ$  is also shown.

To estimate the efficiency in  $\phi \rightarrow K^+K^-$  detection, the correction factors were determined as the reconstructed to generated  $p_t$  spectrum ratio (i.e. correction factor) for  $\phi$  meson whose daughters are charged kaons in the range  $|90^\circ - \theta| \leq 45^\circ$ . Figure 6.134 shows the correction factors as a function of  $p_t$  by taking into account the TPC alone, the TOF alone and both detectors for kaon identification.

**Table 6.30.** Signal number (S), signal-to-background ratio (S/B) and significance ( $S/\sqrt{S+B}$ ) for the  $\phi$  in FWHM around the central mass bin in different  $p_t$  intervals for the  $(K^+K^-)$  pairs.

$p_t$ (GeV/c)	S	S/B	$S/\sqrt{B+S}$
$\leq 0.6$	63186	0.004	16
0.6–0.8	230339	0.005	34
0.8–1.0	322276	0.007	47
1.0–1.2	240668	0.009	46
1.2–1.4	159045	0.012	43
1.4–1.6	113491	0.015	41
1.6–1.8	87719	0.020	42
1.8–2.0	75912	0.024	42
2.0–2.2	66312	0.030	44
$> 2.2$	231067	0.053	108



**Figure 6.133.** Transverse momentum spectra of  $\phi \rightarrow K^+K^-$  signal after background subtraction. The triangle, circle and star markers refer to charged kaon identification with the TPC alone, the TOF alone and the combination of both detectors respectively. The solid lines are to guide the eye. The solid histogram refers to the Monte Carlo  $p_t$  spectrum for  $\phi$  meson.

*High transverse momentum region.* The results of an analysis in the high- $p_t$  region without particle identification are presented in Table 6.31 for  $10^6$  events (these statistics correspond to  $\sim 1.5 \times 10^7$  events in the full- $p_t$  region). The S/B value increases from 0.6% to 18% at the  $p_t(K^+K^-) \geq 7.5$  GeV/c. The significance is 46 at this maximum transverse momentum. Figure 6.135(a) shows the  $K^+K^-$  effective mass distribution for  $p_t(K^+K^-) > 7.5$  GeV/c and the  $K^+K^+$  background. Figure 6.135(b) shows the signal after background subtraction. The curve in Fig. 6.135(b) is the Breit–Wigner fit result in the effective mass region 0.99–1.04 GeV/ $c^2$  taking into account the effective mass resolution set equal to 1.7 MeV/ $c^2$  (again, a convolution of the Breit–Wigner and Gaussian functions was used). The fit parameters, the mean mass and width, are  $1019.56 \pm 0.09$  MeV/ $c^2$  and  $4.50 \pm 0.26$  MeV/ $c^2$ , respectively. These values are again close to the PDG ones which were used in the generation code.

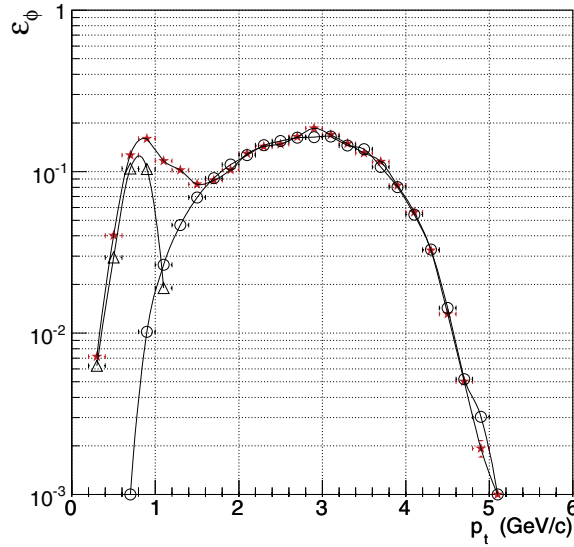


**Figure 6.134.** The ratios of reconstructed to generated  $p_t$  spectra (i.e. correction factors) for  $\phi \rightarrow K^+K^-$  signal. The triangle, circle and star markers refer to charged kaon identification with the TPC alone, the TOF alone and the combination of both detectors respectively. The solid lines are to guide the eye.

**Table 6.31.** The same as in Table 6.30 but for high  $p_t$  ( $K^+K^-$ ) pairs.

$p_t$ (GeV/c)	S	S/B	$S/\sqrt{S+B}$
3.0–3.5	131404	0.006	28
3.5–4.0	192692	0.009	42
4.0–4.5	137092	0.013	43
4.5–5.0	79061	0.020	39
5.0–5.5	46228	0.029	36
5.5–6.0	27563	0.041	33
6.0–6.5	18428	0.060	32
6.5–7.0	11339	0.085	30
7.0–7.5	7407	0.114	28
> 7.5	13659	0.182	46

The left panel of Fig. 6.136 shows the  $p_t$  distributions for the generated  $\phi \rightarrow K^+K^-$  (circles) and of the reconstructed  $\phi$  decays (triangles). The latter was obtained taking into account the tracking efficiency, the kaon decay probability and the geometrical efficiency to find both daughter kaons inside the range  $|90^\circ - \theta| \leq 45^\circ$ . One can see from Fig. 6.136 that the shapes of both distributions are very similar, i.e. the reconstruction efficiency does not depend on  $p_t$  in the high  $p_t$  region. This effect is also seen in the right panel of Fig. 6.136 where the ratio of the reconstructed to generated  $p_t$  spectra of  $\phi \rightarrow K^+K^-$  decays is shown. The last bin of the reconstructed  $p_t$  distribution contains  $\sim 100$  phi mesons, i.e. it represents the limit of the statistics to study the shape of the  $p_t$  spectrum.

**6.2.5.3. Search for a double peak structure in the  $\phi$  signal, a possible signature of phase transition to QGP.** To illustrate the capabilities of the ALICE detector, results are presented on the sensitivity to identify a double peak  $\phi$  signal, which has been suggested to be a possible

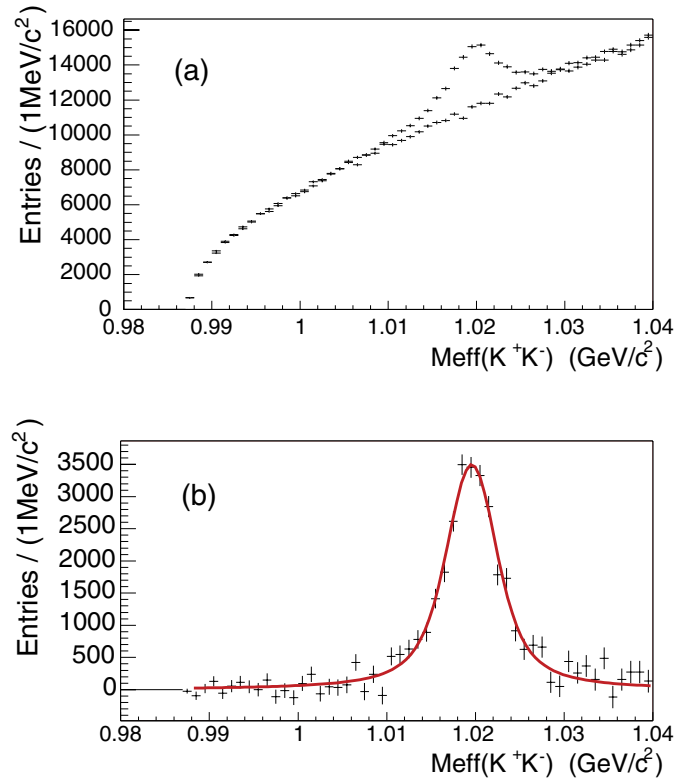


**Figure 6.135.** (a) Spectrum of  $(K^+K^-)$  effective mass at  $p_t(K^+K^-) > 7.5$  GeV/c obtained without particle identification. The  $(K^+K^+)$  background distribution is also shown. (b) Signal of  $\phi$  meson after subtraction of the background. The curve is a Breit-Wigner fit result taking into account the effective mass resolution(see text).

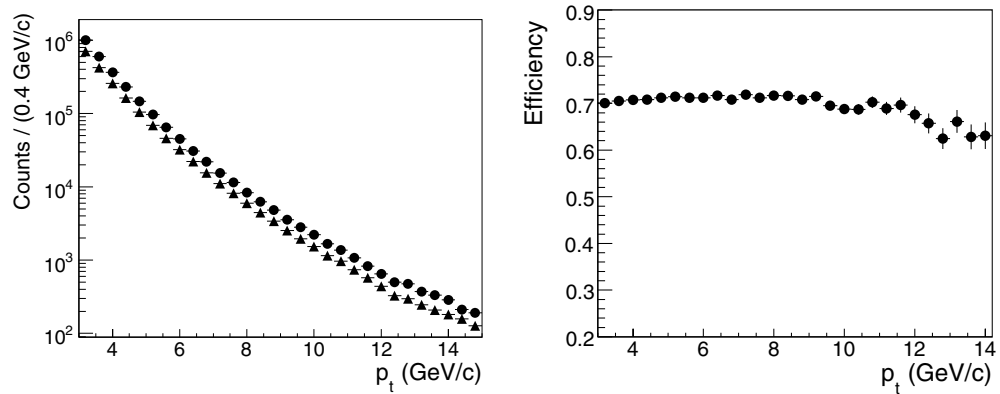


**Figure 6.136.** Left panel: Transverse momentum spectra of  $\phi \rightarrow K^+K^-$  signal for generated (circles) and reconstructed (triangles)  $\phi$  mesons in the high  $p_t$  region. Right panel: The ratios of reconstructed to generated  $p_t$  spectra (the reconstruction efficiency) for  $\phi \rightarrow K^+K^-$  signal in the high  $p_t$  region.

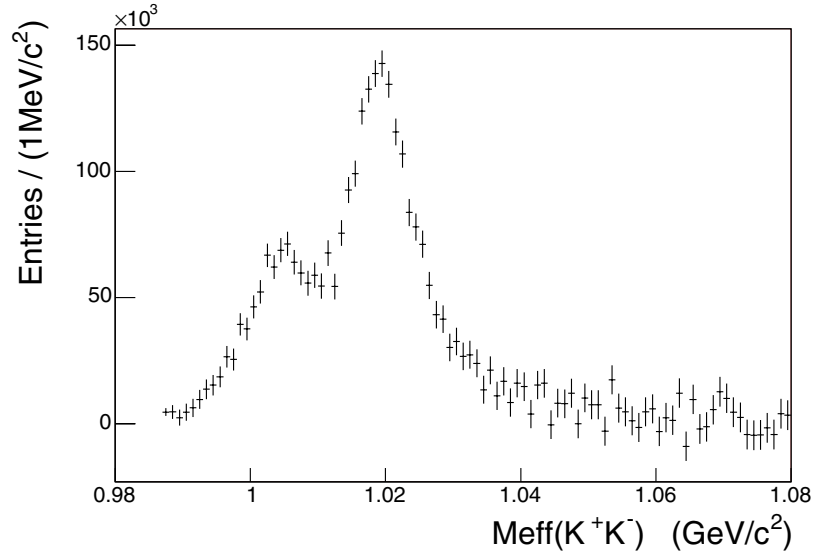


**Figure 6.137.** Double peak structure of the  $\phi$  meson signal simulating a possible phase transition induced effect (see text).

signature for the QCD phase transition to QGP [264, 265]. This effect could be due to the non-negligible duration time ( $\simeq 10$  fm/ $c$ ) of the plasma phase compared to the lifetime of the  $\phi$  in vacuum ( $\simeq 45$  fm/ $c$ ). In such a case the contribution to dilepton pairs from  $\phi$  decays at phase transition (mixed phase) becomes comparable to that from  $\phi$  decays at freeze-out. The mass of a  $\phi$  meson decaying in the mixed phase is expected to be lower than the nominal one as a result of partial restoration of chiral symmetry. The value of the shift, subject to considerable theoretical uncertainty, depends on various factors, among which is the value of the critical temperature [264, 265].

The simulation [390] was carried out by mixing the double component  $\phi$  meson signal with the kaon background. The  $\phi$  mass at the phase transition was taken to be  $1004$  MeV/ $c^2$ , i.e. between the KK threshold and the nominal  $\phi$  mass (the value at freeze-out). Kaon rescattering in the nuclear matter was taken into account by introducing a width  $\Gamma = 10$  MeV/ $c^2$  for both peaks, which is larger than the nominal value. An inverse slope parameter of  $T = 480$  MeV was used for the  $m_t$  spectrum of the freeze-out component following the AliGenParam generator results (Fig. 6.131, left panel). However, a much smaller value of 180 MeV was assumed for the mixed phase component, in view of the theoretical predictions for the temperature at the phase transition [264, 265]. Both peaks were assumed to be equally populated at the step before taking into account phase space effects. At the next step a factor  $\Psi(m)/\Psi(m^*)$  was introduced, where  $m^*$  is the nominal  $\phi$  mass value and  $\Psi(m)$  and  $\Psi(m^*)$  are the 2-body  $K^+K^-$  phase space factors, respectively, at  $\phi$  masses  $m$  and  $m^*$ .

Figure 6.137 shows the  $K^+K^-$  effective mass distribution for the signal after background subtraction. For a statistics of  $10^6$  events, the double peak structure is clearly visible. The lower mass peak is suppressed with respect to the freeze-out one; this is a consequence of the different phase space factors for the two peaks, combined with the PID efficiencies for the TPC and TOF detectors.

Figure 6.138 shows the two  $(m_t - m_{\text{eff}})$  distributions ( $m_{\text{eff}}$  is the effective mass of each  $K^+K^-$  pair) after background subtraction in each  $m_t - m_{\text{eff}}$  bin. The distributions refers to the

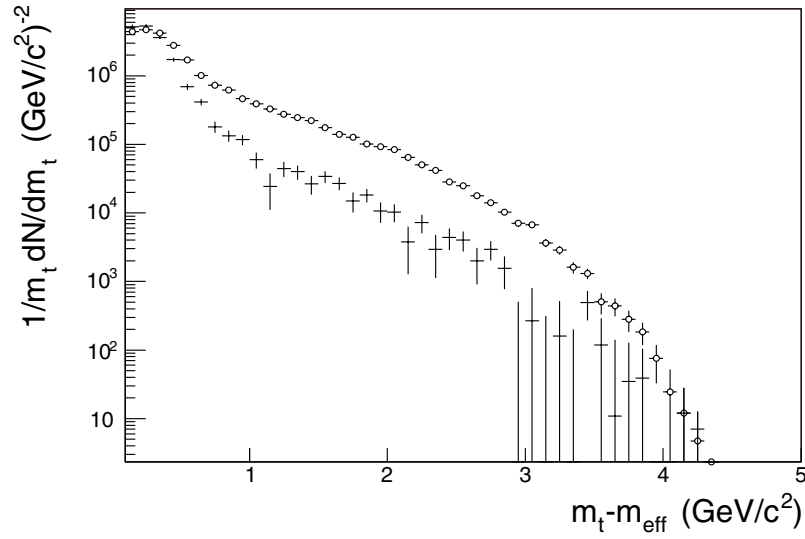


**Figure 6.138.**  $m_t$  spectra for the two peaks shown in Fig. 6.137. The open circles are for the higher mass signal in Fig. 6.137 and the crosses are for the lower mass one.

two effective mass regions: one corresponds to the mixed phase and the other to the freeze-out Breit–Wigner peak. Each region is selected within  $\pm\Gamma/2$  around the corresponding centre of the peaks. The  $(m_t - m_{\text{eff}})$  spectra are not corrected for detector  $K^+K^-$  transverse mass acceptance, to avoid the introduction of biases, as this correction maintains a dependence from the assumed input spectra. A difference in slope is clearly visible for the two distributions up to  $m_t - m_{\text{eff}} \simeq 1.5 \text{ GeV}/c^2$ , with a softer spectrum for the mixed phase peak. Above this value the shapes of the distributions become quite similar. The contamination under the lower mass peak from decays in the freeze-out component grows with  $m_t$ .

**6.2.5.4. Systematic uncertainty.** The S/B values obtained in the previous sections depend crucially on factors which are unknown or not well known at present. First of all, the prediction for the charged particle density,  $dN_{\text{ch}}/d\eta$  at  $\eta = 0$ , is between 1400 and 6800 depending on the model (see Section 11.2.2 in [384] and Section 1.3.1 in [3]), i.e. the particle multiplicities may be 3–4 times lower than that used in our simulation. As a consequence, the S/B value could increase by a factor of 3 or 4. On the other hand, the experimental trend suggests a rise in the  $K^-/\pi^-$  ratio [397] by a factor of 2 with 20–30% accuracy in the RHIC–LHC energy region. However, the  $\phi/K^-$  ratio depends very weakly on energy [402]. This means that the S/B value may be a factor of 2 lower. The other factor is the  $m_t(p_t)$  spectrum slope parameter for  $K^\pm$  and  $\phi$  mesons, known also with an accuracy of 30–40% (see Fig. 6.131 right panel). Lastly, it should be noted that the PID contamination to the kaon sample also depends from the particle multiplicity and may be lower by factor of 2.

As a result we believe that the obtained S/B is pessimistic and we can expect 1.5–2 larger values for more realistic particle multiplicities, yields and  $p_t$ -spectra.

## 6.2.6. Reconstruction of the $K^*(892)^0$ signal

**6.2.6.1. Introduction.** The study of resonances which have lifetimes comparable to that of the dense matter created in heavy-ion collisions at ultrarelativistic energies is an important

tool to get information on the collision dynamics. Modifications of the properties of such resonances and of their production rate may be expected when they are produced in a dense medium [364, 403]. The study of such resonances, compared to that of other particles produced in the collision, may also probe the role of the rescattering phase between chemical and kinetic freeze-out. Since these resonances may decay while still in the hot hadronic matter, rescattering of the daughter particles may take place, depending on the source size and lifetime, as well as on the parent transverse momentum. Finally, the combined investigation of resonances with strange quark content, such as the  $K^*(892)^0$  and  $\phi(1020)$  mesons, is also important due to the expected overall strangeness enhancement in heavy-ion collisions [378]. Moreover, they can serve as a tool to distinguish various hadronic expansion and freeze-out scenarios [268, 270].

The observation of such resonances is difficult in heavy-ion experiments, owing to the large background and to detector limitations. Among the most recent results, the NA49 Collaboration reported an experimental study of the  $\phi(1020)$ ,  $K^*(892)^0$  and  $\Lambda(1520)$  in Pb–Pb at  $\sqrt{s} = 17.2$  GeV through their hadronic decay channels [388]. Results on the production of  $K^*(892)^0$  and its antiparticle were reported by the STAR Collaboration in Au–Au central collisions at  $\sqrt{s} = 130$  GeV [262, 404] and 200 GeV [405, 406], where transverse mass spectra, yields and particle ratios were extracted from the data.

The reconstruction of such resonances in Pb–Pb collisions at LHC energies will be challenging due to the expected high multiplicity environment. Here a simulation study of the  $K^*(892)^0$  signal in Pb–Pb and pp collisions [407] is discussed. First results on this topic were published in [408]. The  $K^*(892)^0$  meson resonance and its antiparticle decay into  $K\pi$ , with a  $c\tau$  around 4 fm/c and full width  $\Gamma = (50.7 \pm 0.6)$  MeV. Their decay products may therefore be considered as coming from the primary vertex as far as the tracking is concerned. The selection of the  $K^*(892)^0$  decay channel into charged particle is performed by the invariant mass analysis.

In Section 6.2.6.2 we discuss the reconstruction procedure of the  $K^*(892)^0$  decay, and present results which were obtained in the pp collisions with both a perfect particle identification and with a realistic one. In Section 6.2.6.3 we report the results obtained for Pb–Pb collision at the LHC energies.

*6.2.6.2. Reconstruction of the  $K^*(892)^0$  signal in pp collisions.* For this study we generated and fully analyzed  $2 \times 10^5$  PYTHIA pp minimum bias events at  $\sqrt{s} = 14$  TeV, which represents  $\sim 10^{-7}$  of an estimated year of data-taking. A magnetic field of 0.4 T inside the ALICE magnet was chosen. Particles were considered over the whole solid angle and in the full momentum range. All ALICE subdetectors, together with the beam-pipe, were included in the simulation, and all physical processes were switched on in GEANT. The average  $K^*(892)^0$  multiplicity, as generated by PYTHIA, is of order 1.7 per event (i.e. 3.4 for both  $K^*(892)^0$  and its antiparticle), whereas the number of possible  $K^+\pi^-$  combinations is in the order of 70 per event. Several factors need to be taken into account in order to understand the actual number of  $K^*(892)^0$  candidates which are findable after the reconstruction process. The geometrical acceptance of the TPC ( $-0.9 \leq \eta \leq 0.9$ ), the branching ratio of the  $K^*(892)^0$  decay into  $K^+\pi^-$  and the tracking efficiency, especially for low momentum particles originating from the resonance decay and for the charged kaons which in turn decay inside the TPC volume, are all factors which strongly reduce the number of findable candidates, to about 0.02 per event. After tracking, the  $K^+\pi^-$  combinations are reduced to about 1.4 per event.

We first assumed a perfect knowledge of the particle identification. The effect of misidentifying the decay products will be discussed later. Under such conditions, the signal which could be obtained from a proper correlation of the true pairs is shown in the left panel

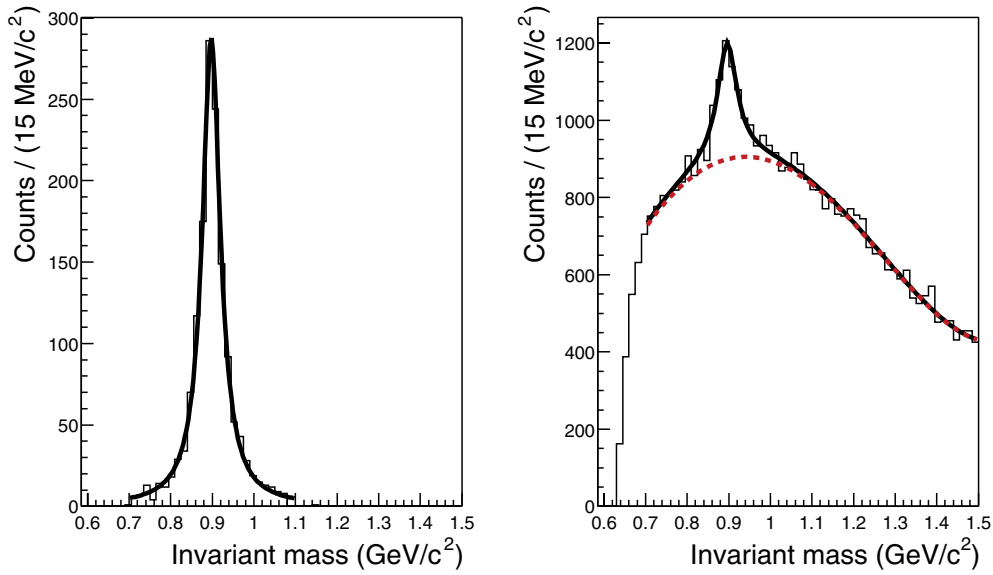


**Figure 6.139.** Invariant mass distribution of the true pairs originating from the  $K^*(892)^0$  and its antiparticle decay (left panel) and from all  $K\pi$  pairs (right panel) in the case of a perfect particle identification for  $2 \times 10^5$  PYTHIA pp collisions. The solid curves are the fits results. The dashed curve in the right part is the polynomial function representing the background.

of Fig. 6.139. Both  $K^*(892)^0$  and its antiparticle were included in the plot, by summing  $K^+\pi^-$  and  $K^-\pi^+$  pairs. A fit of this peak gives a centroid at  $897.6 \pm 0.9 \text{ MeV}/c^2$ , and a width of  $52.8 \pm 2.1 \text{ MeV}/c^2$ , which are compatible with the standard PDG values (mass =  $896.10 \pm 0.27 \text{ MeV}/c^2$ ,  $\Gamma = 50.7 \pm 0.6 \text{ MeV}/c^2$ ) [409].

The decay products from the  $K^*(892)^0$  are embedded in a sample of primary tracks, with a signal-to-background ratio  $S/B = 0.1$  within  $2\sigma$  with respect to the nominal  $K^*(892)^0$  invariant mass, and a significance  $S/\sqrt{S+B}$  equal to 18.0 for the actual number of events considered in the present analysis. A Breit–Wigner fit of the  $K\pi$  invariant mass distribution from the same event pair (Fig. 6.139, right panel) carried out with the sum of a polynomial and a Breit–Wigner shape, gives a centroid at  $896.3 \pm 2.6 \text{ MeV}/c^2$  and a width  $\Gamma = 57.2 \pm 8.6 \text{ MeV}/c^2$  for the  $K^*(892)^0$  peak, which are values still compatible with the nominal ones, although with a large error on the width.

These results show that with perfect particle identification, the  $K^*(892)^0$  signal may be extracted even with a limited number of events.

Two cases were considered as regards more realistic particle identification (PID). In the first, to maximize the number of tracks, PID information was required from at least one of the three detectors ITS, TPC and TOF; in the second case, to improve the performance, PID information was required in each of the three detectors.

A  $K^*(892)^0$  is classified as ‘findable’ if both its two daughters were tracked, and as ‘good’ if both the daughters were tracked and correctly identified. In the first case, the number of findable  $K^*(892)^0$  is 0.02/event. The number of good  $K^*(892)^0$  is 0.015/event. Therefore we have a signal to noise ratio  $S/B = 0.08$  within  $2\sigma$  with respect to the nominal  $K^*(892)^0$  invariant mass and a significance of 14. The invariant mass distribution for  $K^+\pi^-$  and  $K^-\pi^+$  combinations is shown in the left panel of Fig. 6.140.

The background was evaluated by the event-mixing technique and subtracted from the  $K\pi$  invariant mass distribution. Both  $K^+\pi^-$  and  $K^-\pi^+$  combinations were included.

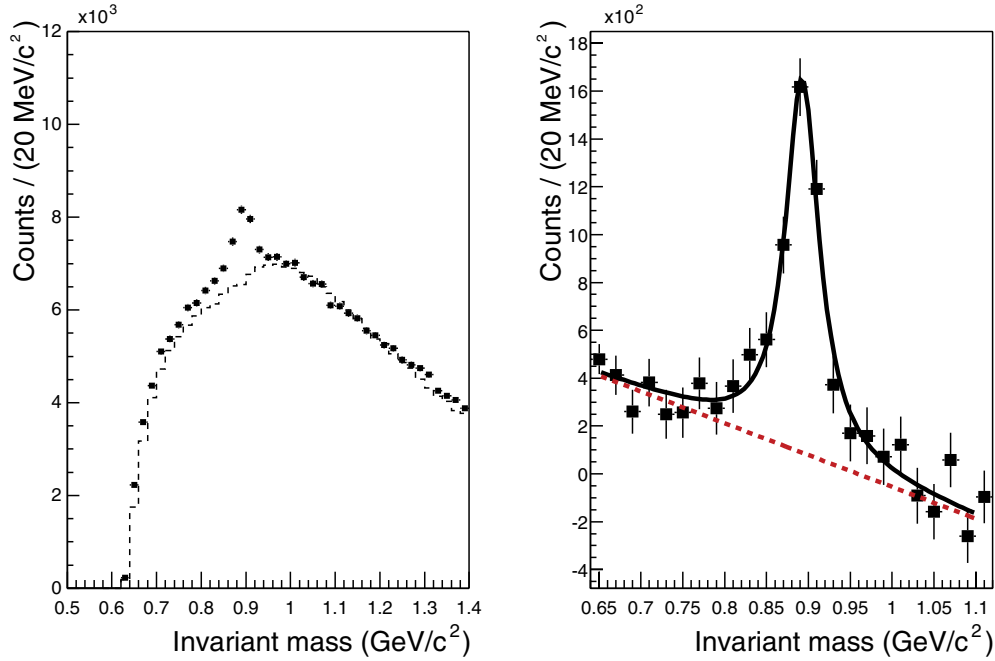


**Figure 6.140.** Left panel: invariant mass distribution of the  $K^+\pi^-$  and  $K^-\pi^+$  in the case of a realistic PID (i.e. case I in the text); the dashed line represents the combinatorial background obtained from the mixed-event method. The background spectrum is normalized to the entries with an invariant mass larger than  $1.1 \text{ GeV}/c^2$ . Right panel: signal spectrum obtained after the background subtraction. The solid curve is a Breit–Wigner fit to the spectrum whereas the dashed curve is the linear function representing the residual background.

The number of event pairs was chosen so as to have a negligible statistical error on the combinatorial spectrum. Since the multiplicity fluctuations in pp collisions may be relatively large, a more correct procedure would be to mix only events which have comparable multiplicities. However, using a Kolmogorov test, we checked that the two procedures give very similar combinatorial spectra when event pairs whose multiplicities differ not more than 5 units are considered. The normalisation factor of the combinatorial spectrum to the signal spectrum was calculated taking the ratio between the number of entries in the signal and in the mixed-event distributions for invariant masses greater than  $1.1 \text{ GeV}/c^2$ , since a minimal contribution from correlated  $K\pi$  pairs is expected at invariant mass greater than this value. The spectrum obtained after the background subtraction (see the right panel of Fig. 6.140) was fitted with a Breit–Wigner curve with a linear residual background. The fit gives a mass  $M = 892.6 \pm 2.1 \text{ MeV}/c^2$  and a width  $\Gamma = 49.2 \pm 6.0 \text{ MeV}/c^2$ .

To improve purity, although at the expense of efficiency, PID information can be demanded from each individual ITS, TPC and TOF detector resulting in a more regular behaviour of the PID efficiency as a function of the particle momenta. In this specific case we define as findable a  $K^*(892)^0$  for which the two daughters were tracked and PID information has been assigned. We determine the number of findable  $K^*(892)^0$  per event to be  $0.0027/\text{event}$ , and the number of good  $K^*(892)^0$  per event to be  $0.0026/\text{event}$ . Considering the interval of invariant mass  $0.8\text{--}1.0 \text{ GeV}/c^2$ , the signal-to-noise ratio is equal to 0.13 with a significance of 7.5. The invariant mass distribution for both  $K\pi$  combinations is shown in the left panel of Fig. 6.141. In this case also the background was evaluated by the event mixing technique and the combinatorial background has been normalized to the invariant

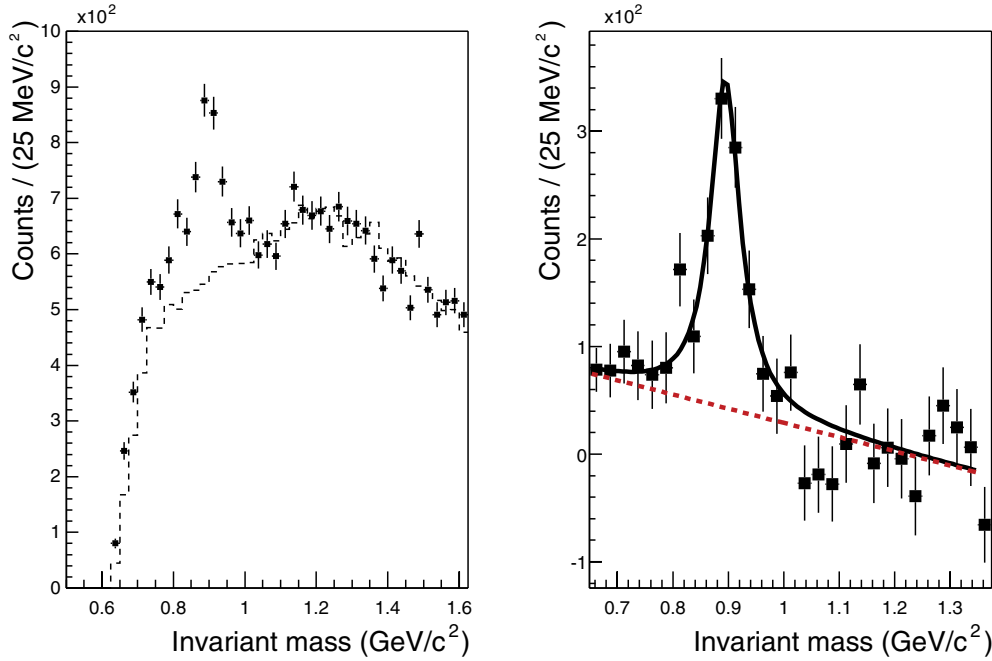


**Figure 6.141.** Left panel: invariant mass distribution of the  $K^+\pi^-$  and  $K^-\pi^+$ , in the case of realistic particle identification (i.e. case II in the text); the dashed line represents the combinatorial background obtained from the mixed-event method. The background spectrum is normalized to the events with an invariant mass larger than  $1.1 \text{ GeV}/c^2$ . Right panel: signal spectrum obtained after the background subtraction. The solid curve is the fit result. The dashed curve is the linear function representing the residual background.

mass spectrum at  $M > 1.1 \text{ GeV}/c^2$ . The resulting difference spectrum between the signal and the combinatorial spectrum is shown in the right panel of Fig. 6.141. The fit, i.e. a combination of a Breit-Wigner curve and a linear background, gives  $M = 894.5 \pm 4.0 \text{ MeV}/c^2$  and  $\Gamma = 66 \pm 13 \text{ MeV}/c^2$ .

We conclude that in the case of a realistic particle identification and with a number of 200 000 events, it is possible to extract values for the centroid and for the width compatible with the standard values.

**6.2.6.3. Reconstruction of the  $K^*(892)^0$  signal in Pb–Pb collisions.** As shown in Fig. 6.142, the number of  $K^*(892)^0$  generated in a Pb–Pb collision increases with the centre-of-mass energy and it is of order  $10^3$  per central event in the whole solid angle.

In order to study the visibility of the  $K^*(892)^0$  signal in Pb–Pb collisions, a sample of 3840 central HIJING events ( $b \leq 5 \text{ fm}$ ), was generated and fully reconstructed. The magnetic field was set to 0.5 T. The analysis was performed assuming perfect particle identification.

Table 6.32 shows the S/B, calculated within  $\pm 2\sigma$  and the significance obtained with the sample of events used for this study, calculated for different bins in the total transverse momentum  $p_t$  of the pair. For each bin, a significance estimate is made for  $10^7$  events, i.e. the estimated number of central events collected after 1 year of data taking.

The  $K^*(892)^0$  was identified by its hadronic decay channels of  $K^*(892)^0 \rightarrow K^+\pi^-$  and  $K^*(892)^0 \rightarrow K^-\pi^+$ . In the following, the terms  $K^*(892)^0$  stands for both  $K^*(892)^0$  and  $\overline{K^*(892)^0}$ . For this sample of events,  $\sim 2100$   $K^*(892)^0$  are generated in each event. After reconstruction, the number of findable  $K^*(892)^0$  per event is roughly 67, where a  $K^*(892)^0$  is

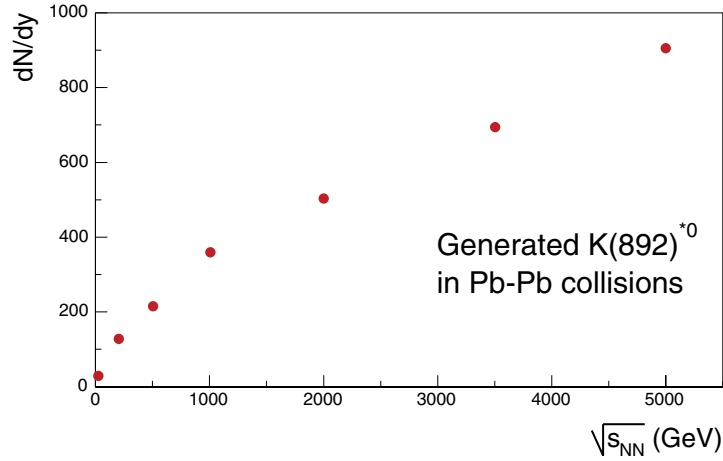


**Figure 6.142.** Number of  $K^*(892)^0$  generated for Pb–Pb collisions with  $b = 3$  fm as a function of the c.m. energy  $\sqrt{s_{NN}}$ .

**Table 6.32.** S/B (second column) and significance (third column) for different bins in total momentum  $p_t$  of  $K^*(892)^0$  in the case of perfect particle identification, for the about 3800 HIJING Pb–Pb events. Rightmost column reports the significance scaled by the expected number of central events collected after one year of data-taking ( $\simeq 10^7$  events).

$p_t$ bin (GeV/c)	S/B	$\frac{S}{\sqrt{S+B}}$ (I)	$\frac{S}{\sqrt{S+B}}$ (II)
0.0–1.0	$2.4 \times 10^{-4}$	6.5	331.6
1.0–2.0	$3.1 \times 10^{-4}$	4.0	201.4
2.0–3.0	$1.1 \times 10^{-3}$	2.8	145.4
3.0–4.0	$2.8 \times 10^{-3}$	2.3	118.0
4.0–5.0	$4.8 \times 10^{-3}$	1.9	98.4
5.0–6.0	$6.2 \times 10^{-3}$	1.4	72.0
6.0–7.0	$8.5 \times 10^{-3}$	1.2	60.1

considered findable if both its daughter particles were reconstructed. The findable  $K^*(892)^0$  are embedded in a large background with  $S/B(\pm 2\sigma) \simeq 10^{-4}$ .

The  $K^*(892)^0$  signal was reconstructed from the invariant mass of unlike-sign pion-kaon pairs. The  $K\pi$  invariant mass distribution is shown as full circles in left panel of Fig. 6.143. The combinatorial background was calculated by sampling the like-sign pairs ( $K_i^+\pi_i^+$  and  $K_i^-\pi_i^-$ ). Since the number of positive and negative particles may not be the same, to subtract correctly the subset of non correlated pairs in the unlike-sign  $K\pi$  distributions, the like-sign  $K\pi$  invariant mass ( $m$ ) distribution was calculated as:

$$N_{\text{like-sign}}(m) = 2 \times \sqrt{N_{K_i^+\pi_i^+}(m) \times N_{K_i^-\pi_i^-}(m)} \quad (6.23)$$

This procedure has already been used by the STAR Collaboration [405, 406]. The histogram shown in the left panel of Fig. 6.143 represents the like-sign distribution.

In order to get a better normalisation between the estimated background and the real one, the like-sign spectrum was multiplied by a polynomial function, resulting from a fit to the ratio of the unlike-sign spectrum over the like-sign spectrum in the invariant mass region outside the expected position of the resonance peak. A more complete description of this analysis can be found in [407].

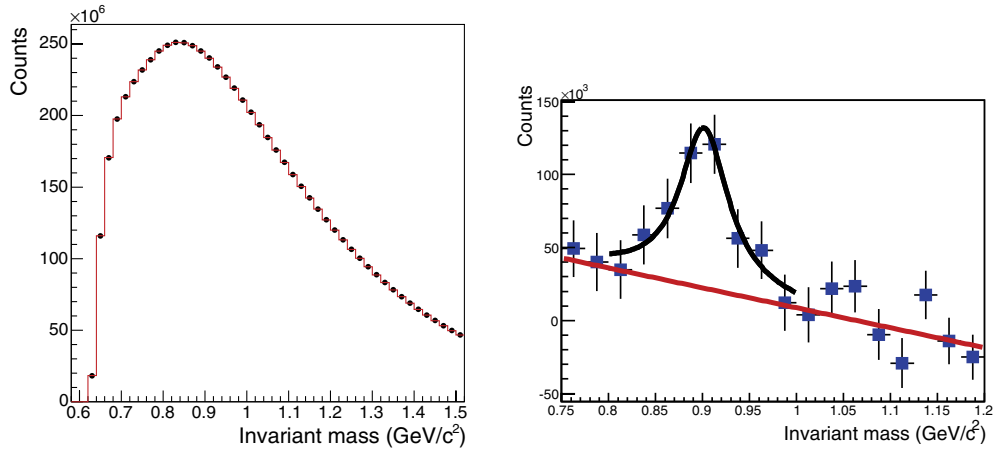


**Figure 6.143.** Left panel:  $K^*(892)^0$  invariant mass spectra of like-sign (histogram) and unlike-sign (full circles) pairs for the about 3800 Pb–Pb HIJING events. Right panel:  $K\pi$  invariant mass distributions after background subtraction. The curve represents the result of a fit by a Breit–Wigner with a linear background.

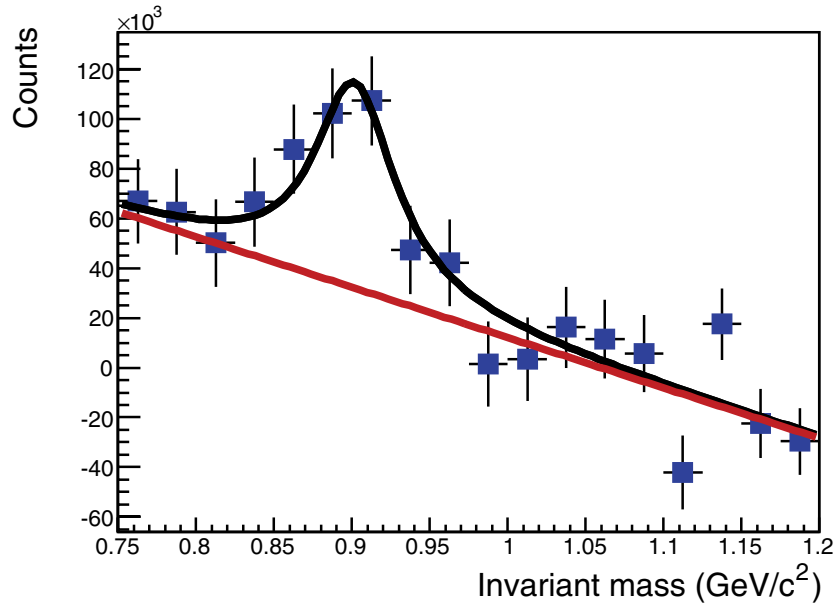


**Figure 6.144.** The  $K\pi$  invariant mass distributions after background subtraction, for the about 3800 events with perfect particle identification, in the total transverse momentum bin  $0.0 \leq p_t \leq 1.0 \text{ GeV}/c$ . The curve represents the result of a fit with a Breit–Wigner distribution on a linear background.

The like-sign background was subtracted from the unlike-sign  $K\pi$  invariant mass distributions. The result is shown in the right panel of Fig. 6.143, where the  $K^*(892)^0$  signal is now visible. Even when limiting the study to a bin in total transverse momentum  $p_t$ , it is possible to see the peak, as shown in Fig. 6.144. A fit of the  $K\pi$  effective mass spectrum using

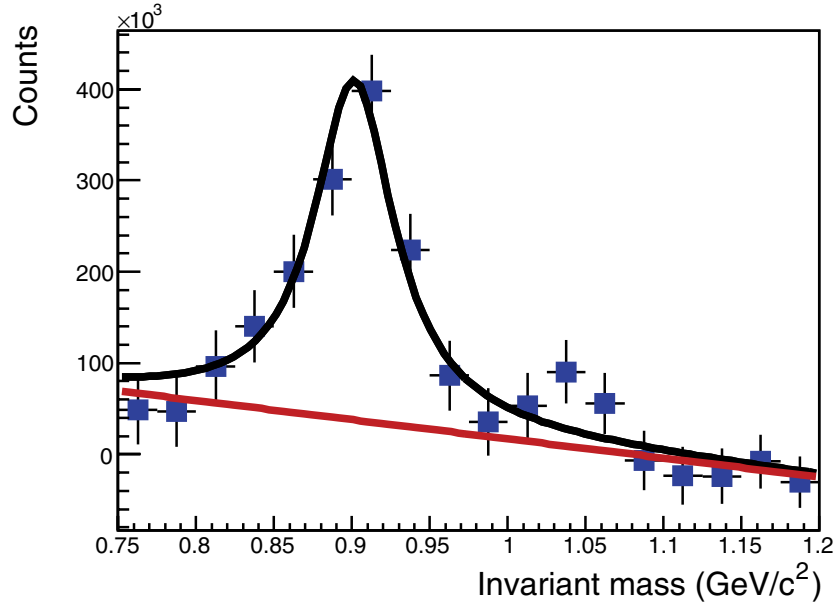


**Figure 6.145.** The  $K\pi$  invariant mass distributions after background subtraction, for 15 440 events with realistic particle identification. The curve represents the result of a fit by a Breit–Wigner distribution on a linear background.

a Breit–Wigner function and a linear background gives reasonable results for the centroid and the width of the resonance peak.

In order to evaluate the visibility of the peak in a more realistic scenario, another sample of 15 440 HIJING events fully reconstructed was used. In this case a realistic particle identification, based on the Bayesian weights calculated during the tracking procedure, was used. The same operations described above were performed on the like-sign distribution, before subtraction to the unlike-sign one. As shown in Fig. 6.145, the  $K^*(892)^0$  peak is also visible in this case. Even when limiting the study to a bin in total transverse momentum  $p_t$ , it is possible to see the peak, as shown in Fig. 6.146.

Taking into account the significance obtained with one year of data-taking, we can conclude that the  $K^*(892)^0$  signal can be detected for a transverse momentum range spanning between 0 and  $\sim 15$  GeV/ $c$ . In the case of a perfect PID, the global reconstruction efficiency (including geometrical acceptance, branching ratio and tracking efficiency) ranges from  $\sim 4\%$  for  $p_t \leq 1$  GeV/ $c$  to  $\sim 11\%$  for  $p_t = 6$  GeV/ $c$ . If a realistic particle identification is used, the efficiency has a maximum at about 4.5% for  $p_t = 1$  GeV/ $c$ , and decreases smoothly to 0.5% for  $p_t = 6$  GeV/ $c$ . It must also be noted that for  $p_t \geq 3$  GeV/ $c$ , it is possible to find the  $K^*(892)^0$  without requiring any PID information. Indeed, the  $K^*(892)^0$  peak is clearly visible after the subtraction of the background (estimated with the like-sign pairs) from the invariant mass spectrum of all unlike sign pairs with a total  $p_t$  larger than 3 GeV/ $c$ .

### 6.2.7. Search for strange dibaryons

**6.2.7.1. The  $H$ -dibaryon.** It has been suggested that a six quark bag bound state, (uuddss), could exist, because the colour magnetic forces are attractive and thus allow its ground state

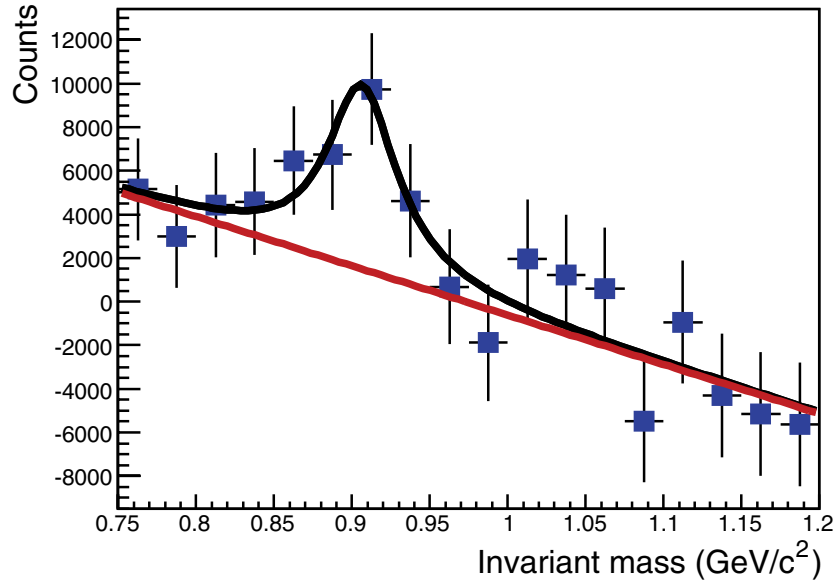


**Figure 6.146.** The  $K\pi$  invariant mass distributions after background subtraction, for 15 440 events with realistic particle identification, in the total transverse momentum bin  $2.0 \leq p_t \leq 3.0 \text{ GeV}/c$ . The curve represents the result of a fit with a Breit–Wigner distribution on a linear background.

to be below the strong decay threshold ( $M_{\Lambda\Lambda} = 2231 \text{ MeV}/c^2$ ) [410, 411]. The configuration with hypercharge  $Y = 0$  (charge = 0, spin = 0, isospin = 0 and  $S = -2$ ) is called an H-dibaryon ( $H^0$ ). According to these predictions, it should not be stable against weak hadronic decay and its most probable mass range should be  $2055\text{--}2231 \text{ MeV}/c^2$ . In this region, the  $H^0$  can decay to  $\Lambda n$  or  $\Sigma N$  ( $N = \text{nucleon}$ ) (if  $m_{H^0} > 2134 \text{ MeV}/c^2$ ) and  $\Lambda N\pi$  (if  $m_{H^0} > 2195 \text{ MeV}/c^2$ ). The lifetimes associated with these various decay modes are predicted to be in the interval  $10^{-10}\text{--}10^{-8} \text{ s}$ .

The  $H^0$  could also be a resonance (if  $m_{H^0} > 2231 \text{ MeV}/c^2$ ) decaying to  $\Lambda\Lambda$ ,  $\Xi N$  or  $\Sigma\Sigma$  [412]. It may be experimentally observed by analyzing the baryon–baryon continuum invariant mass spectrum.

**6.2.7.2. Strange hadronic dibaryons.** The hadronic counterpart to the  $H^0$  is the so-called dilambda  $(\Lambda\Lambda)_b$ , a bound state of two  $\Lambda$ s, with the same quantum numbers and the same decay channels as the  $H^0$ . Actually, many other dibaryon bound states might exist according to predictions using weak  $SU(3)$  symmetric contact interactions; these provide estimates of their corresponding weak hadronic decays and their lifetimes [413]. Production estimates for RHIC were also calculated by combining transport simulations with wave function coalescence using RQMD [414, 415]. Examples of such predicted dibaryons are the following:  $(\Sigma^+p)_b \rightarrow pp$ ,  $(\Xi^0p)_b \rightarrow \Lambda p$ ,  $(\Xi^0\Lambda)_b \rightarrow \Xi^- p$  or  $(\Xi^0\Xi^-)_b \rightarrow \Xi^- \Lambda$ .

With binding energies of a few MeV, their predicted decay lengths ( $c\tau$ ) are between 1 and 5 cm. The predicted yields per event vary from  $5 \times 10^{-3}$  dilambdas per unit of rapidity down to much smaller values if multi-strange hyperon combinations are considered:  $10^{-4}/\text{event}$  for  $(\Xi^0\Xi^-)_b$ .

Experimentally, these decay topologies can be identified with an appropriate tracking device. For instance in the case of  $(\Xi^0p)_b$  bound state, one has to find secondary  $\Lambda$  vertices

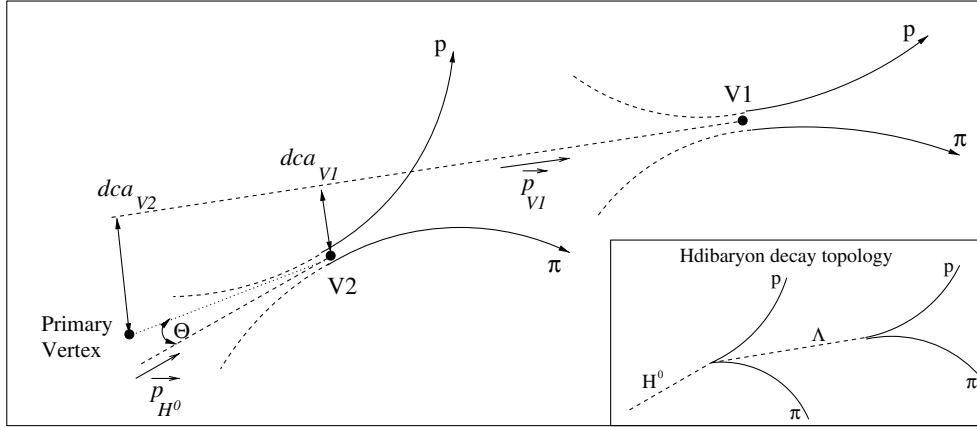


Figure 6.147.  $H^0 \rightarrow \Lambda p \pi^-$  reconstruction procedure.

associated with a proton track (bachelor). Such a procedure is comparable to the one applied to  $\Omega$  or  $\Xi$  decay reconstruction (see Section 5.1.7.1 on page 1362), the  $K^-$  or  $\pi^-$  bachelors being replaced by a proton.

**6.2.7.3. The search for strange dibaryons in the central barrel of ALICE.** In the following paragraphs, we shall study the capability of the central barrel of ALICE to identify the  $H^0$  particle or strange hadronic dibaryons. We first focus on weak decay modes via the topological identification method described in Section 6.2.3. Then it will be shown that mixed event technique can be used if the  $H^0$  is a resonance.

The identification of one of the  $H^0$  possible weak decay modes,  $H^0 \rightarrow \Sigma^- p \rightarrow n \pi^- p$ , is very challenging because of the huge multiplicity of Pb–Pb collisions at LHC energies and because of the very short  $\Sigma^-$  track and the undetected neutron. The second weak decay mode,  $H^0 \rightarrow \Lambda p \pi^- \rightarrow p \pi^- p \pi^-$ , can, however, be observed with the ALICE detector if its two successive weak decays are reconstructed. The hadronic dibaryon  $(\Xi^0 p)_b$  identification via a weak decay mode:  $(\Xi^0 p)_b \rightarrow \Lambda p$  will be studied as well. Finally, we shall report the analysis corresponding to an  $H^0$  strong decay mode, the  $H^0 \rightarrow \Lambda \Lambda$ .

**6.2.7.4. The  $H^0 \rightarrow \Lambda p \pi^-$  weak hadronic decay.** For the  $H^0$  properties, a lifetime of the same order of magnitude as for the  $\Lambda$  (i.e.  $\tau \sim 2 \times 10^{-10}$  s) and a mass of  $2210 \text{ MeV}/c^2$  were chosen. We note however that recent measurements of a double- $\Lambda$  hypernucleus suggest a weak attractive  $\Lambda \Lambda$  interaction and would mean slightly higher masses (just below  $m_{\Lambda \Lambda}$ ) [416]. The rapidity distribution is constant and limited to the mid-rapidity region ( $|y| < 1$ ). An exponential functional form was used for the transverse momentum distribution.

As a first step, we reconstruct all the secondary  $(p\pi^-)$  vertices ( $V^0$ ) candidates. Then we find the  $V^0$ - $V^0$  associations that could correspond to an  $H^0$  decay. The principle of the method is shown in Fig. 6.147. For each possible association between two  $(p\pi^-)$  vertices ( $V1, V2$ ), starting here with  $V1$ , we calculate the  $V1$  mother momentum ( $\mathbf{p}_{V1}$ ) and its invariant mass. It is kept if this mass is close to the  $\Lambda$  mass. Then we require that it points back to the  $V2$  vertex (selection on  $dca_{V1}$ ). Finally we calculate the  $V2$  mother momentum ( $\mathbf{p}_{V2}$ ), assuming that this vertex corresponds to a  $p\Lambda\pi^-$  emission. If the candidate points correctly back to the primary vertex (selection on the cosine of  $\Theta$ ), it is selected as an  $H^0$  candidate and its invariant mass is computed. By tagging all the proton and  $\pi^-$  tracks, we know which reconstructed  $H^0$

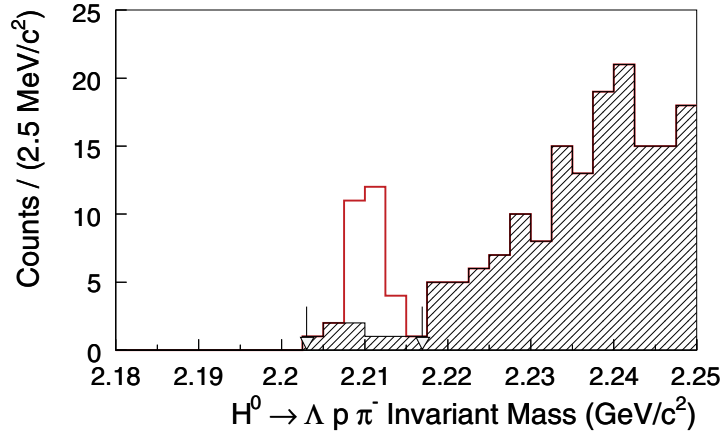


**Figure 6.148.**  $\Lambda p \pi^-$  invariant mass spectrum for  $H^0 \rightarrow \Lambda p \pi^-$  reconstruction in ALICE, for 135 000 simulated Pb–Pb central events at 5.5 TeV ( $dN_{\text{ch}}/dy = 4000$ ), assuming an average yield of 1  $H^0$  per event in the  $|y| < 1$  rapidity range.

are true (i.e. correspond to the Monte Carlo ones) and which are fake. From this study, we obtain the reconstruction efficiency as well as the combinatorial background level.

A dedicated simulation including  $H^0$  mixing with realistic HIJING events, detector digitisation and full event reconstruction (space point finding and tracking) was performed. This acceptance and efficiency study would require  $\sim 10^5$  events because of the expected low yield of  $H^0$ s per event (less than one). Therefore we first generated events containing only  $H^0$ s (several tens of thousands per event). Of this number, only a few  $H^0$ s were ‘good’ (a total of  $\sim 650$ ). According to the general definition used for cascade reconstruction, a ‘good’ generated  $H^0$  is a findable one, hence it is made of two ‘good’  $V^0$ s. The acceptance (ACC) of the  $H^0$  decay chain can then be defined as the ratio of the number of ‘good’ generated  $H^0$  to the number of generated ones. This acceptance factor was found to be 0.48%.

Then the  $H^0$  reconstruction efficiency (EFF), including the secondary track finding and  $V^0$  reconstruction efficiencies, was estimated using ‘signal enriched’ events, i.e. HIJING events with a particle density of  $dN_{\text{ch}}/dy = 4000$ , mixed with only the ‘good’  $H^0$ s selected in the previous step. The quantity EFF, defined as the ratio of the number of ‘good’ found  $H^0$ s (a total of 23) to the number of ‘good’ generated ones, is equal to 3.5%. The rate ( $\varepsilon$ ) of reconstructed  $H^0$ s is then given by the acceptance factor multiplied by the reconstruction efficiency

$$\varepsilon = \text{EFF} \times \text{ACC} = 1.7 \times 10^{-4}.$$

The extracted signal of 23 ‘good’ found  $H^0$ s would correspond to about  $23/\varepsilon = 135\,000$  events if we assume that the multiplicity of produced  $H^0$ s in the detector acceptance is one per event. The next step consists in evaluating the background level corresponding to this set of events. Here, we assume that wrong associations between a primary and a ‘signal’ track, coming either from a hyperon or from an  $H^0$ , constitute the dominant part of the background.

We generated  $N = 15$  HIJING events and  $M = 9000$  ‘purely signal’ events with the expected multiplicity of the ‘signal’ particles. Then we combine the tracks from each of the  $N$  HIJING events with each of the  $M$  signal events. After reconstructing  $N \times M$  such mixed track sets, we obtain a background statistically equivalent to  $N \times M$  ‘signal+HIJING’ events. The resulting background is shown in Fig. 6.148, together with the corresponding  $H^0$  signal. In the mass window around  $2210 \text{ MeV}/c^2$ , shown on the invariant mass spectrum, the background level is less than 10 counts.

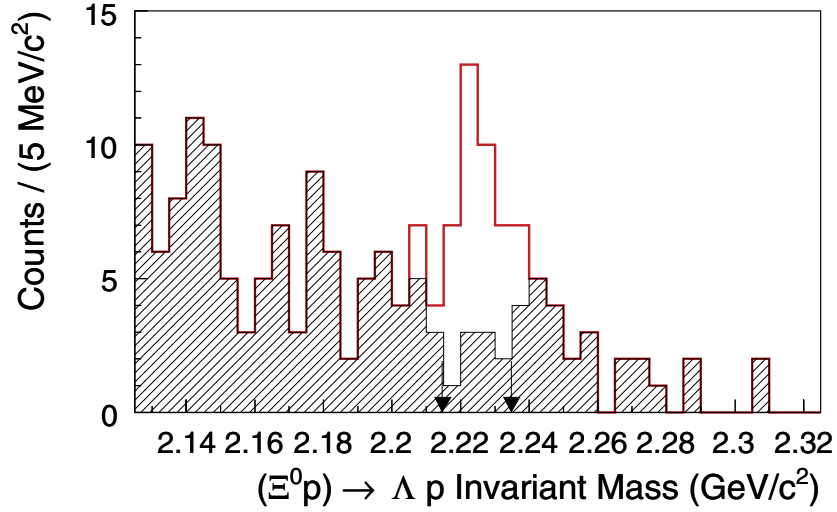


**Figure 6.149.**  $\Lambda p$  invariant mass spectrum for  $(\Xi^0 p)_b \rightarrow \Lambda p$  reconstruction in ALICE, for 58 000 Pb–Pb central events at 5.5 TeV ( $dN_{ch}/dy = 4000$ ), assuming an average yield of 1  $(\Xi^0 p)_b$  per event in the range  $|y| < 1$ .

The last step is to extrapolate this background to the full expected statistics,  $N_{\text{event}} \sim 10^7$  central events and hence deduce the detection sensitivity. We find that the observation of an  $H^0$  signal, above the background at a  $3\sigma$  confidence level, requires the reconstruction of  $n_{H^0} \simeq 80 H^0$ s.

The sensitivity ( $S_{H^0}$ ) is defined by this number divided by the total number of analyzed events and by the rate  $\varepsilon$ :

$$S_{H^0} = n_{H^0} / (\varepsilon \times N_{\text{event}}).$$

The sensitivity obtained is about  $5 \times 10^{-2} H^0/\text{event}$  over the two covered units of rapidity, hence  $dN_{H^0}/dy = 2.5 \times 10^{-2} H^0$  per event in this rapidity range [417].

**6.2.7.5. The  $(\Xi^0 p)_b \rightarrow \Lambda p$  weak hadronic decay.** For this study, we have chosen a  $(\Xi^0 p)_b$  lifetime of  $\tau = 2.6 \times 10^{-10}$  s and a mass of  $2225 \text{ MeV}/c^2$ . Such a mass corresponds to a binding energy of about 30 MeV.

The principle of the reconstruction algorithm for the  $(\Xi^0 p)_b$  is the same as for the  $\Xi$  decay to  $\Lambda\pi$  albeit the  $\pi$  is here being replaced by a proton. Then, applying the same procedure and definition as for  $H^0$  reconstruction, we found the following results: ACC = 0.57% and EFF = 9.64%, which gives us a rate of reconstructed  $(\Xi^0 p)_b$  of  $5.5 \times 10^{-4}$ .

The invariant mass distribution shown in Fig. 6.149 contains a signal of 32 ‘good’ found  $(\Xi^0 p)_b$ . It corresponds to about 60 000 events with a production rate of 1  $(\Xi^0 p)_b$  per event. The background under the peak is less than 20 counts. Extrapolated to  $10^7$  events, this result shows that the evidence of such a dibaryon needs a minimum number of 180 reconstructed  $(\Xi^0 p)_b$ , which requires in turn a minimum number of  $\sim 3.5 \times 10^{-2} (\Xi^0 p)_b$  produced per event in the region  $|y| < 1$ . We conclude that the production rate should be at least  $dN_{H^0}/dy = 1.7 \times 10^{-2} (\Xi^0 p)_b$  for this particle to be observed.

**6.2.7.6. The  $H^0 \rightarrow \Lambda\Lambda$  strong decay resonance.** In this section we describe the search for an H-dibaryon strong decay resonance in Pb–Pb collisions. The mode under consideration is

**Table 6.33.** Selections used for the  $\Lambda$  reconstruction (same variable definitions as in Section 6.2.3.2 on page 1596).

$b_-$	$b_+$	$dca$	$\cos \Theta_P$
0.15	0.10	0.10	0.9997

$H^0 \rightarrow \Lambda\Lambda$ . To predict the ability of the ALICE detector to identify such objects, we start by creating realistic background events. For this purpose, HIJING events with  $dN_{ch}/dy = 4000$  are generated and enriched with primary hyperons at mid-rapidity ( $|y| < 1$ ):

- $100\Lambda + 100\bar{\Lambda}$  ;
- $15\Xi^- + 15\bar{\Xi}^+$  .

The simulation of one year's statistics of data taking (i.e. the generation and full propagation of  $\sim 10^7$  of such events) is too time-consuming to be performed. Therefore we developed a fast simulation strategy which consists in generating 'fast' pseudo-realistic events, and then extrapolating the results to the full statistics of  $10^7$  events.

We generated 300 realistic events, each containing the aforementioned number of particles, and used the set of topological reconstruction selections for  $\Lambda$ s described in Table 6.33. The average number of reconstructed  $\Lambda$  candidates is 6.6 per event with a purity of 85% in the invariant mass window  $1115.7 \pm 5 \text{ MeV}/c^2$ .

The  $H^0$  reconstruction procedure is a simple algorithm which produces all the pairs of  $\Lambda$  candidates within an event. The strategy is therefore to generate lighter ('fast') events, each of them containing only  $\Lambda$  and  $H^0$  particles: after reconstruction with the given set of selections, we obtain the same number of  $\Lambda$ s in the defined mass window as for realistic events (i.e. 6.6 per event). In this way, we can create approximately the same conditions as for full real events: the number of correlations between  $2\Lambda$  candidates must be the same.

In the 'fast' event simulation, both  $\Lambda$ s and  $H^0$ s are generated according to an exponential  $p_t$  distribution. The chosen physical properties of the simulated  $H^0$  resonance are presented below:

- mass:  $m_{H^0} = 2252 \text{ MeV}/c^2$ ;
- branching ratio of  $H^0 \rightarrow \Lambda\Lambda$ : 100%;
- width:  $\Gamma_{H^0} = 13 \text{ MeV}/c^2$ .

A total of 10 000 events were generated, each containing 110  $\Lambda$ s and 5  $H^0$ s. We used those events to estimate both the  $H^0$  reconstruction rate (for signal) and the background level coming from primary  $\Lambda$  candidates. The average number of reconstructed primary  $\Lambda$ s per event is 6.7, which is close to the expected 6.6.

The  $H^0$  reconstruction rate obtained with the 'fast' events is  $7 \times 10^{-4}$ . The invariant mass spectra of the reconstructed Monte Carlo  $H^0$  are shown in Fig. 6.150 with (left panel) and without (right panel) the combinatorial background. It should be noted that the combinatorial background was computed without any contribution from the  $H^0$  daughter tracks. This is based on the assumption that the contribution of correlated background (for instance, the correlation between a  $\Lambda$  daughter from an  $H^0$  and a primary  $\Lambda$ ) is insignificant because of the low expected yields for the  $H^0$ . We obtain a signal which is hardly discernible from the background and this effect is obviously worse when the  $H^0$  width is large.

The values of the  $H^0$  reconstruction rate and background level obtained with 10 000 events can provide an estimate of the  $3\sigma$ -sensitivity for such a particle, as was done for weak decays. We define the significance as the ratio  $S/\sqrt{B}$  in the mass range  $2237\text{--}2267 \text{ MeV}/c^2$ ,

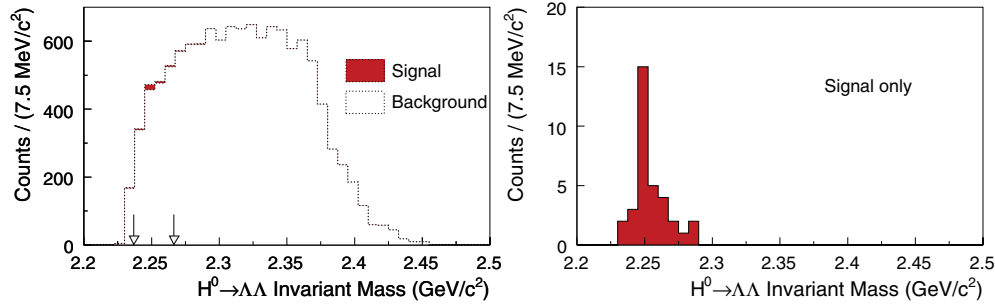


**Figure 6.150.** Left panel: Monte Carlo  $H^0$  and combinatorial background coming from non- $H^0$  daughters. Right panel: Monte Carlo  $H^0$  reconstructed mass.

where  $S$  is the number of signal counts, and  $B$  the number of background counts. Hence, to get a  $3\sigma$ -significance peak within a statistics of  $10^7$  central Pb–Pb events, the number of produced  $H^0$  in the interval  $-1 < y < 1$  and per event must be at least 0.74, or  $dN_{H^0}/dy = 0.37$  assuming a flat rapidity distribution.

### 6.3. Momentum correlations

**6.3.1. Introduction.** The space–time evolution of the system created in heavy-ion collisions is studied by analysing the momentum correlation of the emitted particles. This information complements the image of the collision geometry and its dynamics extracted from the analysis of different observables registered simultaneously.

Particle correlations in the kinematic region of small relative velocities arise mainly from two effects: quantum statistics (QS), for identical bosons or fermions; and final state interactions (FSI), Coulomb interaction for charged particles and strong interaction for all types of hadrons. Both effects depend on the distance between the particle emission points in space and time, and on their relative momentum. Therefore, the space–time evolution is reflected in particle correlations.

We start by briefly introducing the formalism of two-particle correlations, as a necessary tool for further considerations. The role of momentum correlations in interpreting the Quark–Gluon Plasma (QGP) signatures is reviewed, the most important results from experiments at lower energies are presented, and some predictions for LHC are then discussed. A dedicated software for the analysis of particle correlation in ALICE has been developed; after a brief introduction to the available tools for simulations and analysis, some specific features of the correlation effects in ALICE are discussed. The form of the measured correlation functions is strongly influenced by experimental effects such as detector acceptance, resolution, and efficiency. Because of the huge number of particle pairs that will be produced, the statistical uncertainties will be very small and, therefore, the reduction of systematic errors will be essential. The first results of simulations to study systematic effects are presented. We conclude with an overview of additional analysis topics that will be addressed in ALICE.

**6.3.2. Formalism of two-particle correlations.** The momentum correlation of particles, when used to study the space–time characteristics of the production processes, serves as a correlation femtoscope. For non-interacting identical particles, like photons, the correlations appear solely due to the effect of QS [418–420]. These QS correlations have an analogy in

astronomy, where the two-photon space–time correlations allow one to measure the angular radii of stars (HBT effect [421, 422]). The momentum QS correlation in particle physics was first observed as an enhanced production of pairs of identical pions with small opening angles in proton–antiproton annihilations. From this enhancement, Goldhaber *et al.* were able to extract the spatial extent of the particle emitting source (GGLP effect [418]).

The two-particle correlation function  $C(p_1, p_2)$  is defined as the ratio of the differential two-particle production cross section to a reference cross section which would be observed in the absence of the effects of QS and FSI. We assume that the correlation of two particles emitted with a small relative momentum is influenced by the effects of their mutual QS and FSI only, and that the momentum dependence of the one-particle emission probabilities is negligible when varying the particle four-momenta  $p_1$  and  $p_2$  by the amount characteristic for the correlation due to QS and FSI (*smoothness assumption* [207]). Clearly, the assumption that the Wigner function  $S(x, K)$  varies smoothly over phase-space volumes larger than the volume  $(2\pi\hbar)^3$  of an elementary phase-space cell, is well justified for heavy-ion collisions.

As already discussed in Volume 1 of this PPR [3], the two-particle correlation is defined as

$$C(\vec{p}_1, \vec{p}_2) = \frac{d^6 N}{dp_1^3 (dp_2^3)} \bigg/ \frac{d^3 N}{dp_1^3} \frac{d^3 N}{dp_2^3}. \quad (6.24)$$

Experimentally, it is obtained from the ratio:

$$C(\vec{q}, \vec{K}) = \frac{A(\vec{q}, \vec{K})}{B(\vec{q}, \vec{K})}, \quad (6.25)$$

normalized to unity at large  $\vec{q}$ , where  $\vec{q}$  is the relative momentum of the pair  $(\vec{p}_1 - \vec{p}_2)$  and  $\vec{K}$  is the average pair momentum  $(\vec{p}_1 + \vec{p}_2)/2$ . The numerator  $A(\vec{q}, \vec{K})$  is the distribution of the relative momentum for pairs of particles in the same events and represents the distribution of the two-particle probability for the relative momentum of each pair. The denominator  $B(\vec{q}, \vec{K})$  is the distribution for pairs of particles in different events and represents the product of single-particle probabilities.

In order to extract information from the measured correlation function about the space–time geometry of the source, one needs to choose a coordinate system in which to work. We have chosen the Cartesian or Pratt–Berstch (‘out-side-long’) parametrization [423–425], in which the relative momentum vector of the pair  $\vec{q}$  is decomposed into a longitudinal direction along the beam axis  $q_l$ , an outward direction parallel to the pair transverse direction  $q_o$ , and a sideward direction perpendicular to those two  $q_s$ ; see Fig. 6.151. Then, the emission function for identical particles is usually parameterized in terms of a Gaussian. In that case, for an azimuthally integrated analysis, and in the longitudinal comoving system (LCMS) reference frame in which the longitudinal component of the pair velocity vanishes, the correlation function takes the form [426]:

$$C(\vec{q}, \vec{K}) = 1 + \lambda \exp(-R_o^2(\vec{K})q_o^2 - R_s^2(\vec{K})q_s^2 - R_l^2(\vec{K})q_l^2). \quad (6.26)$$

The HBT parameters  $R_o$ ,  $R_s$ , and  $R_l$  contain information about the space–time extent of the particle emitting source in the out, side, and long direction. References [207, 427] give a detailed description of the relation between the HBT parameters and the space–time geometry of the final freeze-out stage.

Equation 6.26 applies only if the sole cause of correlation is quantum statistics. However, charged particles suffer long-range Coulomb interaction effects, and all hadrons interact through the strong interaction. These interactions will affect the correlation function and need to be taken into account in order to isolate the Bose–Einstein (Fermi–Dirac) interference effects; this will be discussed in Section 6.3.5.

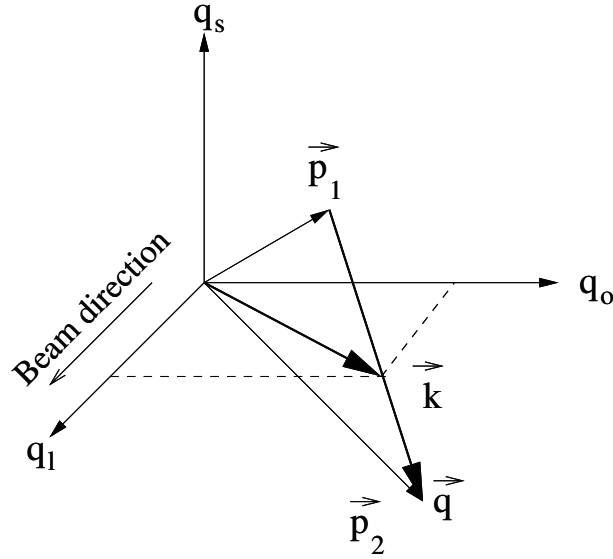


**Figure 6.151.** Cartesian or Pratt–Berstch (‘out-side-long’) parametrization of the relative momentum vector of the pair  $\vec{q}$ .

### 6.3.3. Momentum correlations in heavy-ion collisions

**6.3.3.1. Particle correlations for expanding systems.** One of the main goals of the LHC experiments with ultra-relativistic heavy ions is the study of the matter properties at very high temperatures and energy densities (see for example Ref. [428]). There is a direct connection between these properties and the character of the evolution of the system created in nuclear collisions. Therefore, the space–time structure of the system at the freeze-out stage is determined by the fundamental matter properties we are interested in. The interferometry parameters at this stage can be expressed through geometrical and thermodynamic characteristics of the system: its sizes and temperature, and via the system’s dynamical properties, such as a proper time of expansion and intensity of transverse flows [424, 425, 429–437].

The main feature of expanding sources is that the momentum spectrum of particles depends on the spatial coordinates of the emission point (so-called  $p$ – $x$  correlation). This dependence appears since the collective expansion velocity  $v$ , and therefore the resulting Doppler shift of the momentum spectrum, is different in both magnitude and direction for different parts of the expanding system. On account of the Doppler shift, only some relatively small part of the system, defined mainly by the gradient of collective velocities, contributes to the particle momentum spectra at any given  $p$ . Likewise, for two-particle spectra, the correlation function at a given total pair momentum  $P$  is dominated by the small part of the source which forms spectra in the vicinity of  $P/2$ .

For thermalized expanding systems, the sizes of the effective emission region in the vicinity of momentum  $p$  are associated directly with the system’s *lengths of homogeneity*  $l_j$  [433, 436] at the point  $x(p)$  corresponding to the maximum of the source distribution function  $f(x, p)$  at momentum  $p$ . The lengths of homogeneity express the sizes of the region in which the distribution function  $f(x, p)$  does not change much, e.g.,  $|f(x+l, p) - f(x, p)|/f(x, p) = 1/2$ . For Gaussian sources, the latter differential criterion make the HBT

parameters  $R_j$  to be equal to  $l_j$  (for  $j = 0, s, l$ ). These lengths contain the basic parameters of the evolution: proper time of the expansion, transverse radius, intensity of transverse flows, freeze-out temperature, etc. To extract these parameters one needs to measure the interferometry radii in different regions of rapidity and transverse momentum [429, 430, 437]. This is the basic idea of the interferometry analysis of expanding systems that are formed in A–A collisions.

*6.3.3.2. Role of HBT correlations in interpreting QGP signatures.* We briefly summarize below the main physics information which can be extracted from the analysis of momentum correlations in heavy-ion collisions.

*Probing the emitting source structure at decoupling.* Two-particle correlations, whether they are of QS origin [207] or caused by soft FSI [438, 439], probe the phase-space distribution of the emitting source at decoupling, i.e. the Wigner density of the emitted particles just after their last interactions with the surrounding medium. When combined with the single-particle momentum spectrum, which provides space-averaged information on the momentum–space distribution of the source, they give access to the space–time structure of the reaction zone at decoupling. More specifically, two-particle correlations measure the width of the distribution of the relative space–time distances between every two particles at the point where they are set free.

*Identifying traces left behind by the QGP.* Two-particle correlation measurements require high statistics and can thus, so far, only be performed with the more abundant hadron species such as pions, kaons, protons, and  $\Lambda$  hyperons. Because of their strong interactions, these particles are set free (i.e. their measured momenta and momentum correlations are fixed) very late in the collision, long after the QGP or any other previous state of matter created in the early collision stages has disappeared. Therefore, two-particle correlations do not carry any direct signature of the early stages. However, they are sensitive to the complete dynamical evolution from the first hard interactions to the final freeze-out; their power lies in identifying traces left behind by the early state, such as the geometric growth of the reaction zone and its collective expansion flow generated by the early pressure imprinted on the final state in the form of very specific space–momentum correlations at decoupling. By providing an accurate quantitative characterization of the phase-space distribution at freeze-out, correlation measurements strongly constrain the global evolution of the reaction zone including its early stages, thereby establishing the basis for an accurate interpretation of genuine QGP signatures.

*Testing the relations between collective expansion and thermal motion.* A crucial aspect of particle correlation measurements in heavy-ion collisions is the dependence of the width of the correlations on the momentum of the correlated pair (or triplet). This momentum dependence identifies space–momentum correlations in the emission function and is therefore sensitive to the collective dynamics of the collision fireball at freeze-out. For very rapidly expanding systems such as those expected in heavy-ion collisions at the LHC, the correlation radii are almost completely controlled by a competition between collective expansion (which tends to decrease the homogeneity lengths) and random thermal motion (which tends to increase the homogeneity lengths by smearing out collective velocity gradients). The actual global geometry of the source at freeze-out plays at most a minor role.

*Measuring the spatial deformations of the source.* Two-particle correlations can be measured as functions of six variables: the three components of the relative momentum  $\vec{q}$ , and the three components of the average momentum of the pair  $\vec{K}$ . The dependence on the azimuthal angle  $\Phi$  of the pair transverse momentum is interesting for non-central collisions

where it provides access to spatial deformations of the source in the transverse plane at freeze-out and to a possible tilt of the source relative to the beam axis [427, 440]. Such measurements of spatial deformation at freeze-out complement the study of azimuthal momentum–space asymmetries, such as elliptic flow, which are created early in the collision and thus are directly sensitive to the initial equation of state. By probing the influence of elliptic flow on the geometric shape of the reaction zone at freeze-out, the measurement of the shape at freeze-out provides strong constraints for the dynamical evolution of the reaction zone.

*Distinguishing between different models of the collision dynamics.* To fully exploit the constraining power of correlation measurements for the early, quark–gluon-dominated, collision dynamics one must perform a full three-dimensional correlation analysis in terms of the relative momentum  $\vec{q}$  as a function of the total momentum of the pair. Any averaging over one or several of these variables leads to space–time ambiguities and/or washes out information on the all-important space–momentum correlations which characterize a collectively expanding source. An accurate determination of the latter requires one to study the dependence of the correlation radii  $R_i$  on the pair momentum [207, 441–443] in sufficiently narrow bins; this explains the need for very large pair statistics. It has been shown at lower energies [207, 443] that such multi-dimensional correlation studies indeed provide the resolving power needed to distinguish between different models for the collision dynamics; they provide crucial help in establishing a global dynamical picture for the space–time evolution of the collision, on the basis of which the early signatures (such as hard probes, strangeness enhancement and elliptic flow) can be analysed in a quantitatively accurate way.

*6.3.3.3. Conclusions from experiments at AGS, SPS, and RHIC.* We briefly discuss here four ‘milestones’ of the field achieved at the lower energies of AGS, SPS, and RHIC as the HBT analysis entered its ‘era of precision’ [444] and upon which ALICE can build and expand.

*Excitation function.* A stringent test of our understanding of the space–time dynamics of nuclear collision, as well as the potential for discovery, is maximized via the study of the excitation function [445]. The first ‘milestone’ is therefore the systematic construction of such an excitation function (over almost 2 orders of magnitude in  $\sqrt{s}$ ) for central collisions between the heaviest nuclei. This is shown in Fig. 6.152 [446] for identical pion correlations at mid-rapidity and low  $K_t$ , where  $K_t$  is the magnitude of the transverse momentum vector of the pair and is defined as  $K_t = (\vec{p}_1 + \vec{p}_2)_t/2$ .

Hydrodynamic calculations [445] predicted that, in heavy-ion collisions at relativistic energies, the source would emit pions over a long time period resulting in a long lifetime of the source and, consequently, in a large  $R_o$  parameter and in a  $R_o/R_s$  ratio much larger than unity. However, as can be seen in Fig. 6.152, this predicted increase with energy is not observed up to RHIC energies. On the other hand, these hydrodynamic calculations are in good agreement with the experimental measurements of the momentum structure of the emitting source (particle spectra) and the elliptic flow at RHIC [282]. The fact that they fail to reproduce (at all energies) the space–time distribution at freeze-out as given by the HBT parameters is known as the ‘RHIC HBT puzzle’.

At the LHC we can extend this excitation function by another order of magnitude. Perhaps hydrodynamic concepts only *approximately* apply at RHIC (and so hydrodynamic models can describe  $v_2$ ), but break down in the space–time details; at the LHC, the underlying assumptions of hydrodynamic models may be better justified and may finally lead to a quantitative description of both momentum and coordinate space distributions in terms of hydrodynamic evolution. It is even conceivable, if unlikely, that the long-awaited QGP signal

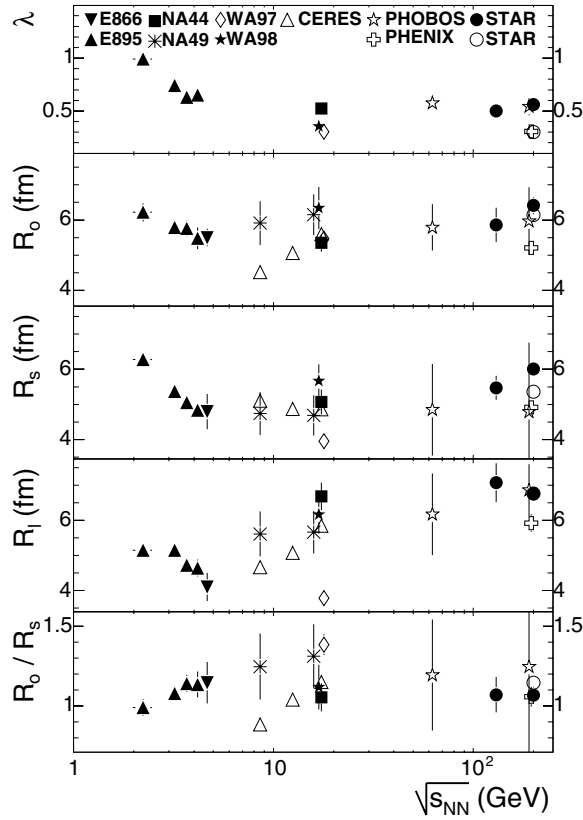


**Figure 6.152.** Energy dependence of identical pion HBT parameters for central Au–Au, Pb–Pb, and Au–Pb collisions at midrapidity and  $K_t \approx 0.2$  GeV/ $c$ . The SPS data, and the 200 GeV RHIC data, are slightly offset in  $\sqrt{s_{NN}}$  for clarity. Error bars on NA44, NA49, CERES, PHENIX, Phobos and STAR results include systematic uncertainties; error bars on other results are only statistical. Open symbols indicate that fitting was done according to an improved approach for taking Coulomb interaction into account [446].

of extended time-scales may appear only at LHC energies, helping to map out the phase transition as a function of energy.

*$p_t$  dependence.* At lower energies, the crucial interplay between coordinate- and momentum-space components of the dynamics has been studied with increasing sophistication. Once simply *assumed* from the shapes of the  $p_t$  distributions, the space-time structure of the radial flow is now readily probed directly by measuring homogeneity lengths as a function of the pair transverse mass  $m_t$  [443]. Extraction of such information is theoretically well-grounded for collisions with vanishing impact parameter ( $b = 0$ ). Figure 6.153 shows the dependence of the HBT parameters on  $m_t$  for the 5% of the most central collisions at  $\sqrt{s_{NN}} = 200$  GeV as measured by the STAR experiment [446]. The decrease on the transverse radii ( $R_o$  and  $R_s$ ) attributed to transverse flow is clearly seen in the data.

Remarkably, while the effects of radial flow are already present at very low AGS energies [447], they appear to saturate and remain constant as the energy is increased to the maximum AGS energy ( $E_{beam} \approx 10$  AGeV) and beyond [448]. However, the radial expansion

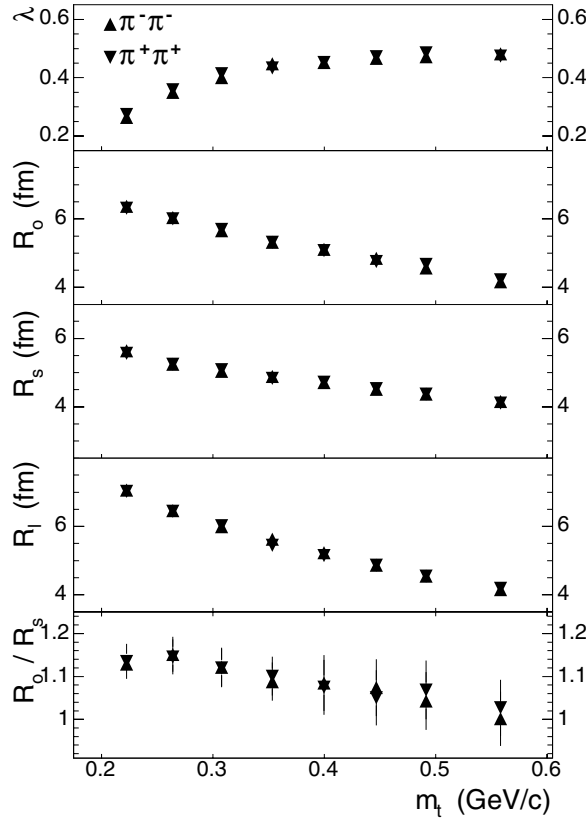


**Figure 6.153.** HBT parameters for the most central collisions for  $\pi^+\pi^+$  and  $\pi^-\pi^-$  correlation functions as measured by the STAR experiment [446].

velocity should rise again at the LHC [449] and verification of this prediction will be a crucial test for hydrodynamic models.

*$\Phi$  dependence.* To probe the space–time geometry of non-central collisions, one may simply apply the formalism employed for central collisions and observe that more peripheral collisions yield smaller transverse radii than central ones, as expected [446, 450–452]. This is a comforting test that HBT is indeed probing something related to geometry.

However, by developing and applying the more general formalism applicable to non-azimuthally-symmetric cases [427], one obtains qualitatively new information on the anisotropic shape of the source in full four dimensions, leading to important insights into the dynamics of anisotropic flow [440].

Experimentally, when correlating the transverse momentum of the pair  $K_t$  with the impact parameter vector, as determined from event-by-event flow analysis, one observes oscillations in the six HBT parameters (for a detailed description of the HBT parameters see Refs. [207, 426, 427]), as shown in Fig. 6.154 for 4 AGeV Au–Au collisions [453]. The second-order oscillations in the transverse radii  $R_o^2$ ,  $R_s^2$ , and  $R_{os}^2$  correspond directly to the ellipsoidal transverse shape of the emitting source (extended out-of-reaction-plane in this case). Meanwhile, the first-order oscillations in  $R_{ol}^2$  and  $R_{sl}^2$  carry information about the spatial tilt of the source away from the beam axis. At AGS energies, model comparisons at this

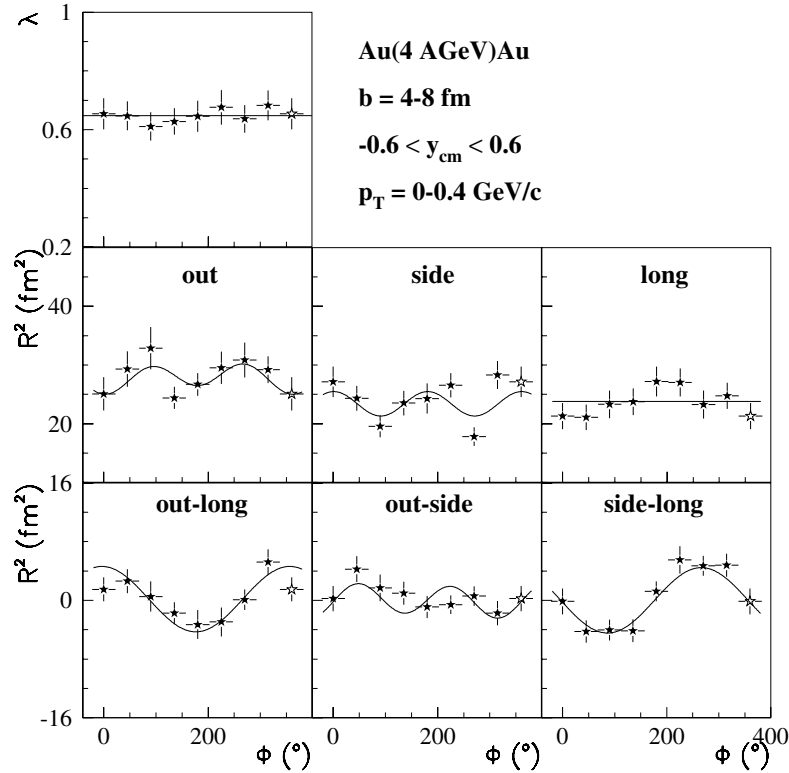


**Figure 6.154.** Stars show the E895 HBT parameters from 4 AGeV Au–Au collisions. The values at  $\Phi = 0^\circ$  are redisplayed as open stars at  $\Phi = 360^\circ$ . The line in the  $\lambda$  panel represents the average value of  $\lambda$ . Lines in the other panels represent a global fit to the HBT radii.

level of detail reveal important discrepancies in the space-momentum correlations leading to anisotropic flow [453].

At RHIC, the STAR Collaboration has performed a similar analysis [454]. The results from this analysis clearly show that the out-of-plane extended transverse shape is retained at freeze-out even at RHIC energies. This puts rather severe and important constraints on the evolution time-scale of the collision. (The evolution time-scale is to be distinguished from the freeze-out time-scale associated with  $R_o/R_s$  for example). So far, STAR could only measure the second-order reaction-plane (i.e. the plane containing  $\vec{b}$ , not the direction of  $\vec{b}$  itself); therefore any first-order oscillations, and the ‘tilt’ information associated with them, are inaccessible.

ALICE shares with STAR the unique ability to measure the reaction-plane event-by-event. Since the elliptical flow signal (from which the reaction-plane is determined) is expected to grow with energy, ALICE should be able to make precision measurements of the shape and the anisotropy of space-momentum correlations in non-central heavy-ion collisions at the highest energies. While this experimental ‘milestone’ has not been fully explored theoretically, it seems clear that the azimuthal dependence of two-particle correlations holds much promise for providing insights into the underlying physics of the collisions.

*New directions.* At the SPS and RHIC, the high multiplicity and abundance of previously rare particles has opened up entirely new and important areas of study. Besides

two-pion HBT, there are published results from the SPS for two-kaon HBT [455], and three-pion correlations [456]. The STAR Collaboration has also published results from a three-pion analysis [457]. The general conclusions which can be drawn from these more exotic measurements are that for kaons, the radius parameters tend to be smaller than for pions; and that three-pion measurements for S–Pb collisions indicate a coherent source component whereas Pb–Pb and Au–Au measurements tend to look, with large error bars, more like a chaotic source.

The STAR Collaboration has also published results from non-identical particle correlations such as  $\pi K$  [458], in which, by studying differences in the correlation function depending on which particle has the higher absolute momentum, one can discern space–time anisotropies in the emitting source. In a static (non-flowing) source model, this corresponds to discerning which particle species (on average) is emitted first. In a more realistic model including flow, it probes the details of the spatial flow field in ways previously inaccessible. There are also preliminary results on  $K_s^0 K_s^0$  correlations [459], which have no final-state Coulomb interactions and therefore allow a cleaner extraction of the QS signal at low relative momentum in the case of charged particles, on  $p\Lambda$  correlations [460], and on  $\pi \Xi$  correlations [461]. Given the high particle multiplicities at LHC and excellent particle identification (PID) capabilities, ALICE will extend the existing systematics to a large number of different hadron species.

**6.3.3.4. Predictions for the LHC.** In this Section, an estimate of the expected pion HBT parameters at LHC will be presented. This estimate is based on the observed systematics of pion freeze-out at lower energies and on predictions of the charged particle multiplicity  $dN_{ch}/d\eta$  in central Pb–Pb collisions at  $\sqrt{s_{NN}} = 5.5$  TeV.

The observed HBT parameters in central collisions of heavy nuclei at AGS, SPS, and RHIC have been found to be consistent with a constant mean free path  $\lambda_f$  of pions at freeze-out [462]:

$$\lambda_f = \frac{1}{\sigma \rho} = \frac{V_f}{\sigma N} = \frac{V_f}{\sigma_{\pi\pi} N_\pi + \sigma_{\pi N} N_N} \approx 1 \text{ fm}. \quad (6.27)$$

In this equation,  $\rho$  is the particle density at freeze-out and  $\sigma$  is the (thermal and isospin averaged) cross section of pions with the medium. The density  $\rho$  can be expressed by the ratio  $N/V_f$ , where  $V_f = (2\pi)^{3/2} R_s^2 R_l$  is the interferometric volume at freeze-out and  $N$  is the number of particles contained in it. For details see [462].

In the presence of different particle species in the medium, the product  $\sigma N$  has to be decomposed into the sum of the particle species  $N_i$  multiplied by the corresponding cross section of pions with these particles  $\sigma_{\pi i}$ . For simplicity, only the most abundant particle species pions and (anti-)nucleons are considered here. A compilation of  $\sigma N$  and  $V_f$  as a function of beam energy is shown in Fig. 6.155. It has been demonstrated that this universal behaviour is independent of the system size and valid even in pp and dAu collisions at RHIC [463].

For an extrapolation of recent measurements of  $V_f$  at RHIC to LHC energies, we assume that the universality of the mean free path at freeze-out holds also at LHC:

$$\lambda_{f,\text{RHIC}} = \lambda_{f,\text{LHC}}. \quad (6.28)$$

At collider energies ( $\mu_B \rightarrow 0$ ,  $T \rightarrow T_c$ ) the chemical composition is expected to change only very little, i.e. the ratio of pions to nucleons plus antinucleons can be considered as constant:

$$N_N = \text{const} \times N_\pi \rightarrow \lambda_{f,\text{ce}} = \frac{V_f}{N_\pi (\sigma_{\pi\pi} + \text{const} \times \sigma_{\pi N})}. \quad (6.29)$$

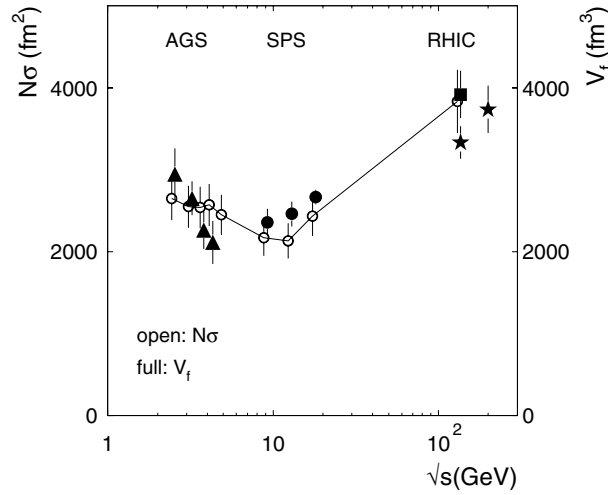


**Figure 6.155.** The interferometric freeze-out volume  $V_f$  and  $N\sigma$  (for  $K_t \approx 0.16$  GeV/ $c$ ) in central collisions of lead and gold nuclei as function of beam energy [462]. The data point for  $V_f$  at  $\sqrt{s_{NN}} = 200$  GeV was extracted from [446] and added to the original compilation.

Assuming that the number of pions  $N_\pi$  in the interferometric volume  $V_f$  is proportional to  $dN_{ch}/d\eta$  we obtain

$$\frac{V_{f,LHC}}{V_{f,RHIC}} \approx \frac{dN_{ch}/d\eta(LHC)}{dN_{ch}/d\eta(RHIC)} \rightarrow \rho_{LHC} \approx \rho_{RHIC}. \quad (6.30)$$

Obviously, the concept of a constant  $\lambda_f$  implies freeze-out at constant density, as long as the hadro-chemical composition of the medium does *not* change. This is approximately true for top SPS energies and above, and for different system sizes at fixed collision energy [464]. In this case, the HBT parameters scale with the charged particle multiplicity  $dN_{ch}/d\eta$ , as demonstrated in Fig. 6.156 (from [465]). However, if the hadro-chemical composition is taken into account, a consistent description of HBT parameters is achieved also at AGS energies by the assumption of constant  $\lambda_f$ .

In essence, the interferometric volume  $V_f$  is expected to scale with charged particle multiplicity between RHIC and LHC. For the one-dimensional HBT parameters, this results in an approximate scaling by  $(dN_{ch}/d\eta)^{1/3}$ . Predictions for  $dN_{ch}/d\eta$  at LHC vary between 1000 and 8000. Most recent estimates, however, seem to favour a value at the lower bound of this range. In this case, the mid-rapidity charged particle density would exceed the RHIC value by only a factor 1.5–2, and as a consequence, the HBT parameters would increase by no more than 15–25%. This is consistent with an extrapolation of the HBT parameters in Fig. 6.156.

**6.3.3.5. Predictions from a rescattering model.** Since it has been found that the predictions from a simple hadronic rescattering model agree rather well with flow and HBT measurements for Pb–Pb collisions at the SPS [466] and Au–Au collisions at RHIC [467], it is interesting to use this model to make similar predictions for Pb–Pb collisions at the LHC. Preliminary calculations for the LHC have been carried out with the rescattering model, the results from which are shown below. In performing LHC calculations, the following parameters were used in the code: (1) a collision impact parameter of  $b = 8$  fm, (2) an initial temperature parameter of 500 MeV, (3) a hadronization proper time for the initial system of 1 fm/ $c$ , (4) a  $dN/dy$  at midrapidity for central collisions for all particles of 4000, and (5) an initial rapidity width

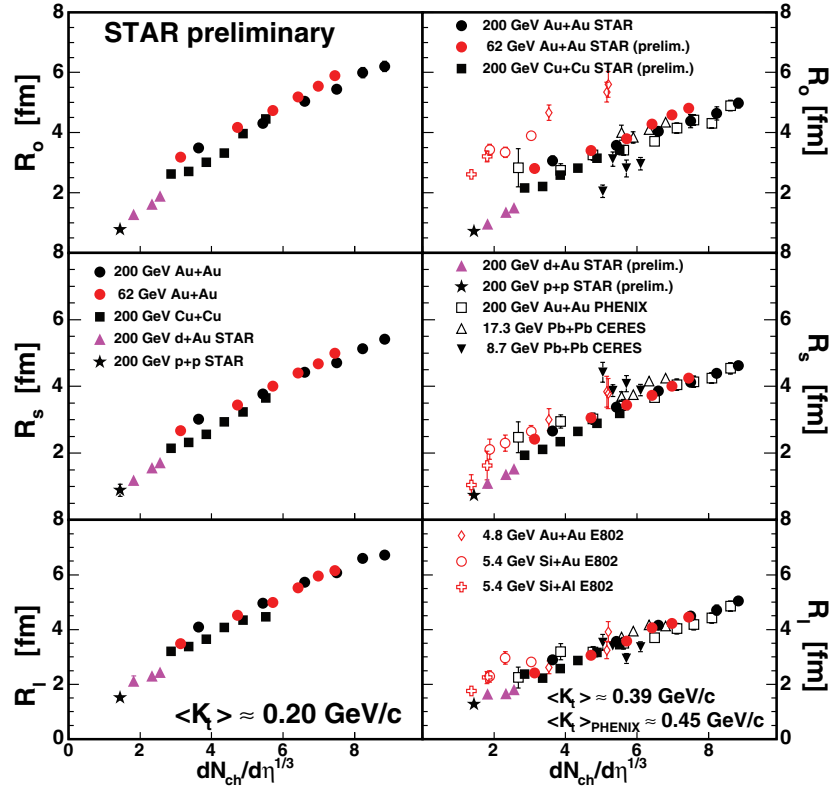
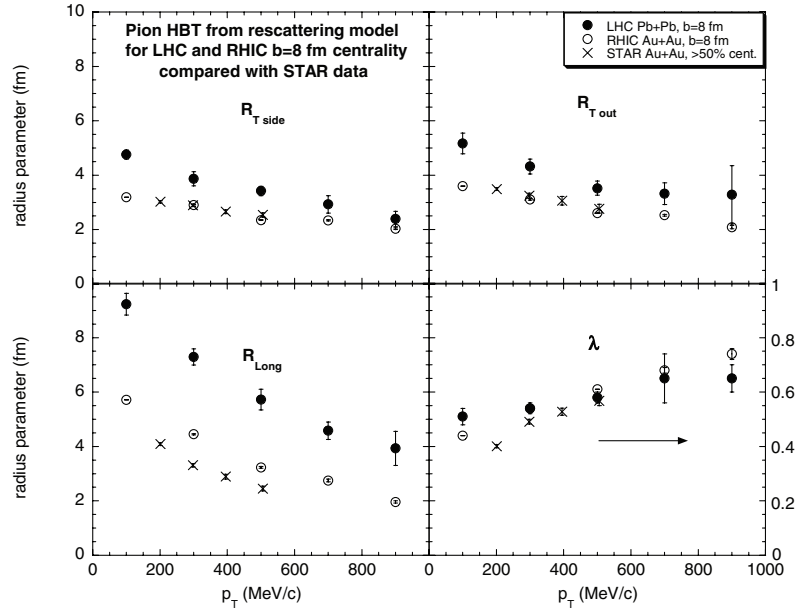


Figure 6.156. HBT parameters at different beam energies and collision systems as function of  $(dN_{ch}/d\eta)^{1/3}$  [465].

of 4.2. These parameters were judged to be reasonable guesses to simulate LHC Pb–Pb collisions. They at least satisfy the self-consistency check that summing over the energy of all particles in an event at the end of the calculation agrees with the input total energy of a LHC Pb–Pb collision with an impact parameter of  $b = 8$  fm. An impact parameter of  $b = 8$  fm was chosen for the present preliminary study both to obtain non-negligible elliptic flow values and for calculational convenience (even for this impact parameter the CPU time used by the code for each LHC Pb–Pb event was about 60 hours). For item (3) above, the hadronization proper time was taken to be the same as was used in the SPS and RHIC calculations. HBT results of these calculations are compared with similar calculations at  $b = 8$  fm centrality for RHIC Au–Au collisions and are shown in Fig. 6.157. These results are obtained at mid-rapidity, i.e.  $-2 < y < 2$ .

Figure 6.157 shows the pion HBT parameters vs.  $K_t$  for LHC Pb–Pb compared with RHIC Au–Au from the rescattering model and with RHIC Au–Au results at  $\sqrt{s_{NN}} = 200$  GeV for the 50–80% most central events [446]. HBT parameters are extracted by fitting the usual Gaussian 3D parameterization of the pion source [441, 442] to the 3D correlation function as calculated from the rescattering model. The transverse radius parameters,  $R_s$  and  $R_o$ , are seen to be somewhat larger and show a stronger  $K_t$  dependence for LHC as compared with RHIC. The longitudinal radius parameter,  $R_l$  is seen to be significantly larger for LHC as compared with RHIC, clearly reflecting that the pion freeze-out times at LHC are twice as long as at



**Figure 6.157.** Pion HBT predictions for LHC Pb–Pb compared with RHIC Au–Au for  $b = 8$  fm centrality collisions at mid-rapidity from the rescattering model. STAR results [446] correspond to a slightly larger average impact parameter.

RHIC according to the rescattering model. The lambda parameter is seen to increase with increasing  $K_t$  in the same way for both LHC and RHIC, reflected the reduced influence of long-lived resonances at the higher  $K_t$  values.

Summarizing the results of this preliminary study, it is predicted from the rescattering model that medium-peripheral ( $b = 8$  fm) LHC Pb–Pb collisions will produce larger HBT radii than the analogous RHIC Au–Au collisions, although the lambda parameter values will look the same.

**6.3.4. Software tools for the simulation of momentum correlations.** The huge number of particles ( $\sim 6000$  charged particles per rapidity unit at mid-rapidity in central events) [3] that will be created in heavy-ion collisions at LHC energies will generate a very dense pattern of hits in the detectors. Reconstruction defects, such as track splitting or track merging, strongly affect the measured correlation function at small relative momentum, where the HBT signal is found. Therefore, the study of the effects of these reconstruction defects on the correlation functions are necessary to estimate and reduce the systematic distortions, since the statistical uncertainties are expected to be negligible in most cases.

In this section, we introduce the software tools, available within the AliRoot framework, for simulating events with momentum correlations. These events are used to study the capabilities of the ALICE detection system in measuring different features of particle correlations. The results of this study are presented and discussed in Section 6.3.5.

**6.3.4.1. Simulation of two-particle correlation functions.** The simulation chain starts with the event generation, using in principle any of the commonly used generators (HIJING, RQMD, UrQMD or NEXUS/EPOS), which are based on different physics assumptions. However, with these generators, the user cannot directly control the momentum, angular,

or multiplicity distributions of the generated particles. Therefore, in order to study the dependence on these quantities, we also use a simple event generator in which the different event features can be directly tuned by the user. An example of such a generator is MEVSIM [468], described in Volume I of this PPR [3].

These event generators do not include the particle correlations arising from FSI effects and QS. In order to add the effects of particle correlations, we could use an ‘after-burner’, the HBT processor [469], which introduces two-particle correlations to the selected set of particles previously generated by any of the event generators. (More information about the principles and action of the HBT processor can also be found in Volume I of this PPR [3].) The HBT processor is an excellent tool to study the influence of different experimental factors on the shape of the two-particle correlation functions. However, it is not accurate enough to generate dynamic effects for different intervals of  $K_t$  and  $y$ . To study these cases we have applied the method of weights described in the next section.

*6.3.4.2. Quantum statistics and final-state-interaction weights.* As mentioned above, in some cases the correlation function needs to be constructed by calculating weights that take into account QS and FSI. Each pair of selected particles is attributed a weight which depends on the (unmeasurable) space–time coordinates of particle emission points and on the measured four-momenta of both particles. The correlation function is obtained as the ratio of the weighted to unweighted distributions, as a function of the particle relative momentum (expressed as  $q_{\text{inv}}$ ,  $\vec{q}$ , or its components out, side, and long).

The calculation of correlation functions with the method of weights consists of four main steps:

1. Generation of events, with or without the freeze-out coordinates of the emitted particles, depending on the model. In the latter case the coordinates are generated separately assuming some model of the space–time evolution, e.g. a Gaussian distribution of particle emission points.
2. Calculation of weights for all two-particle combinations. At this point one can also construct the ratio of weighted to unweighted generated distributions of the relative momentum. This correlation function does not contain any experimental effects and can be used as a reference.
3. Construction of the weighted distribution with pairs formed by reconstructed and identified tracks which are weighted according to the weights calculated in step 2. Experimental effects resulting from the reconstruction procedure may change the particle momenta and PID, and add or remove particles according to detector acceptance, track splitting and merging or other experimental effects. As a consequence:
  - (a) the momentum difference for which the weight is attributed may be different than the momentum difference for which the weight was calculated (because of the single particle momentum resolution);
  - (b) the number of reconstructed pairs in a given interval of the relative momentum may be different than the number of generated ones (because of two track reconstruction defects such as track splitting and merging).
4. Generation of the unweighted distribution in two different ways in order to be able to study the influence of different experimental factors on the shape of the correlation function:
  - (a) by forming pairs of particles from the same events, but without weights;
  - (b) by forming pairs of particles from different events.

In case (a) only the single-particle effects influence the shape of correlation function; in case (b) both, single and double particle experimental effects are taken into account.

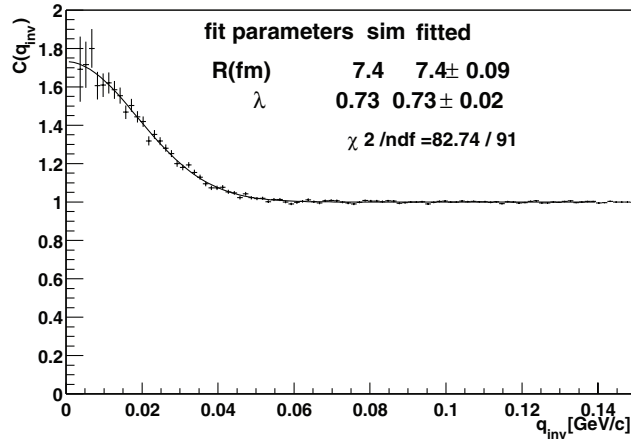


**Figure 6.158.** Correlation function simulated by the method of weights for pairs of positively charged pions.

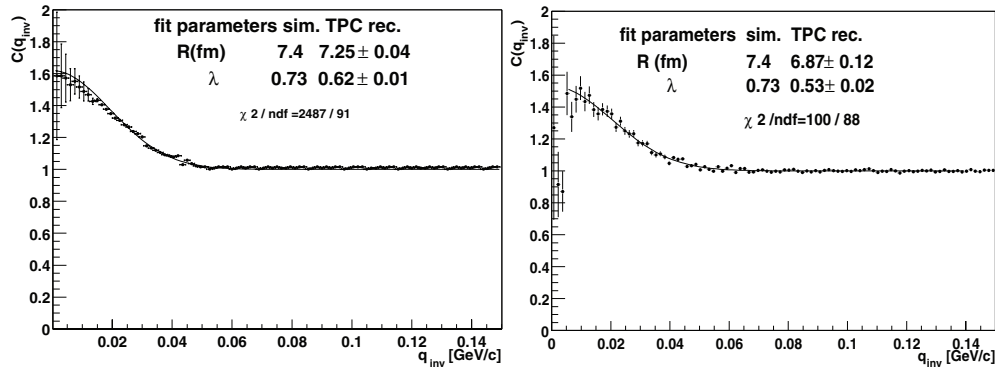


**Figure 6.159.** Correlation functions for pairs of tracks reconstructed in the TPC. The reference distribution was generated using particles taken from the same (left) and different (right) events (see text for details).

In this analysis, we have applied the weight method approach suggested by Lednicky and Lyuboshitz [470]. With this approach, the user may switch on/off different kinds of interactions: QS, strong or Coulomb FSI, or Coulomb interaction with the emitting source. This allows one to study the role of different effects on the final shape of the correlation function.

Figure 6.158 shows a one-dimensional correlation function calculated from generated (not reconstructed) events using the method of weights for the system of two positively charged pions emitted from a spherical Gaussian source with parameters  $R = 7.4$  fm and  $\lambda = 0.73$ . In this case only QS interaction was switched on. The parameters extracted from a Gaussian fit ( $f(q_{\text{inv}}) = 1 + \lambda \cdot \exp(-q_{\text{inv}}^2 R^2)$ , where  $q_{\text{inv}} = \sqrt{|\vec{q}|^2 - (q^0)^2}$ ) are in excellent agreement with the input parameters.

The influence of the single- and two-track reconstruction effects on the shape of correlation function is shown in Fig. 6.159. Both correlation functions were calculated from reconstructed and identified tracks in the TPC, using the method of weights and assuming the same system as above. In the left figure, the background was generated with particles taken from the same events (without weights). The changes on the shape of the correlation function can be seen, not only in the differences of the extracted parameters, but also in

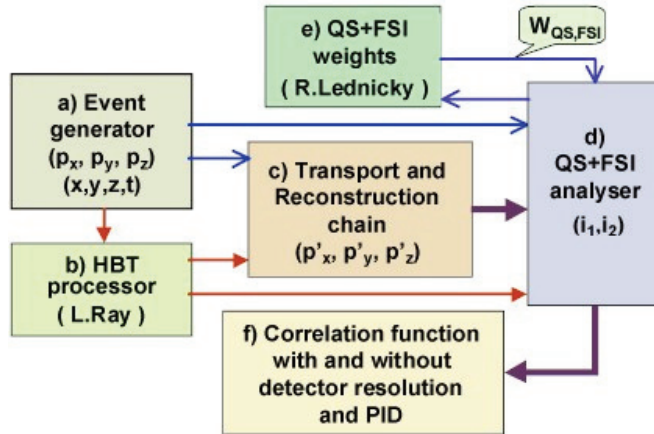


**Figure 6.160.** Schema of the simulation chain for analysis of two-particle correlations at ALICE.

the quality of the fit given by the value of  $\chi^2/\text{ndf}$ . In this correlation function two-particle reconstruction effects, such as merging, are not seen since they vanish when the ratio of the two distributions is taken. The generation of the background by mixing particles from different events (right) allows us to study the influence of two-track reconstruction defects on the shape of the correlation function. In the region of small relative momentum, one can observe a lack of pairs in the numerator due to the merging of tracks in the reconstruction process.

The method of weights can be used effectively for many combinations of two-particle systems and it is sensitive to the details of the experimental procedure.

**6.3.4.3. Simulation chain for the momentum correlation analysis.** As a summary, a scheme of the simulation chain for the particle correlation analysis in ALICE is shown in Fig. 6.160. The upper part of the figure and the arrows with the empty arrow-heads show the flow of data corresponding to the weight method for the correlation function calculation. The lower part shows the generation of events with correlations made by the HBT processor. Thick arrows indicate that the process is common for both methods. Each block is, in fact, a separate piece of software and can also be used independently in another AliRoot environment.

(a) Event generation. This block represents the generation of particles by any event generator. It gives a list of particles. Each particle is described by its mass, charge, and three-momentum components ( $p_x, p_y, p_z$ ). Some generators give also the freeze-out coordinates ( $x, y, z, t$ ).

(b) HBT processor. It changes the momenta of the particles producing events with particle correlations.

(c) Reconstruction. It simulates the reconstruction of the whole event in detail and attributes to each particle a PID index, the three components of the reconstructed momentum ( $p'_x, p'_y, p'_z$ ), and the index of the corresponding generated particle.

(d) Construction of the momentum distributions. The distributions for the construction of the correlation function are calculated. Different selection criteria of events, particles, and particle pairs may be applied by the user. All combinations of selected pairs ( $i_1, i_2$ ) are considered and the relative momentum vector for each pair is calculated in a given reference frame (such as LCMS). It is important to note that the background distribution is generated with pairs of particles taken from events with similar characteristics. This block is based on the HBT maker from the STAR experiment and will be used in the analysis of experimental data.

(e) QS+FSI weights. This block takes pair-by-pair all the combinations of reconstructed particles ( $i_1, i_2$ ) from block (d) together with the corresponding original momenta and freeze-out coordinates generated in block (a). The value of the weight is calculated for the generated momentum values and attributed to the reconstructed momenta. The influence of the possible experimental distortions is therefore taken into account.

(f) Correlation functions. This final block constructs the correlation function from the distributions calculated in previous steps, and plots it. This block will also be used in the analysis of experimental data.

The arrows that join blocks (a) and (b) with block (d) provide undistorted data to the correlation analysis. With these data we construct the reference correlation functions which will be used to study possible defects in the reconstruction process.

With these tools, we are able to generate events that will allow us to study:

1. the correlation function for different two-particle systems;
2. one-dimensional (as a function of  $q_{inv}$ ) and three-dimensional (as a function of  $q_o, q_s,$  and  $q_l$ ) correlation functions;
3. the number of events needed for different two-particle systems, with different cuts;
4. particular correlation effects such as flow;
5. reconstruction effects that may affect the correlation function;
6. FSI effects;
7. event-by-event correlations for different charged-particle multiplicities per unit of rapidity.

*6.3.5. Two-pion momentum correlation analysis.* In this section we present the results of the analysis of the data produced during phase 1 of the Physics Data Challenge 2004 (PDC04). More details on this analysis can be found in Refs. [471–473]. We use only the most central events (impact-parameter range from 0 to 2 fm) with an average multiplicity of the order of 6000 charged particles per unit of rapidity at mid-rapidity. In order to introduce the correlation effects we use the weighting method described in the previous section.

Unless otherwise stated, we take only tracks reconstructed with the central barrel detectors: ITS, TPC, TRD and TOF; and we consider only particles with a particle identification (PID) probability larger than 50%. In order to study distortions from the reconstruction, we can ignore the effects from FSI. However, a detailed study of strong and Coulomb FSI will be needed when analysing experimental data in order to extract the source properties.

The details of the analysis procedures are described for the case of two identical pions since they are the most abundant particles. Unless stated otherwise, the methodology for any other two-particle system is the same, and for these cases we discuss only the differences and the results. All the analysis tools used are available in the AliRoot framework. With the analysis presented here, we try to address possible reconstruction effects on the correlation function and give a detailed description of how the analysis of the experimental data will need to be done.

*6.3.5.1. Event selection for background mixing.* In order to form pairs for the reference distribution (denominator of the correlation function), the two tracks in the pair should come from events with very similar properties in order to avoid any kind of bias in the correlation function. To show the importance of mixing events with similar characteristics, Fig. 6.161(a) shows the 1D correlation function as a function of the polar angle between the two pions. We observe a structure caused by mixing events that have the primary vertex at different positions. This effect is related to the length of a pixel in the SPD and can be explained as follows (see Fig. 6.161(b)). The position of the point where the track crosses the detector is

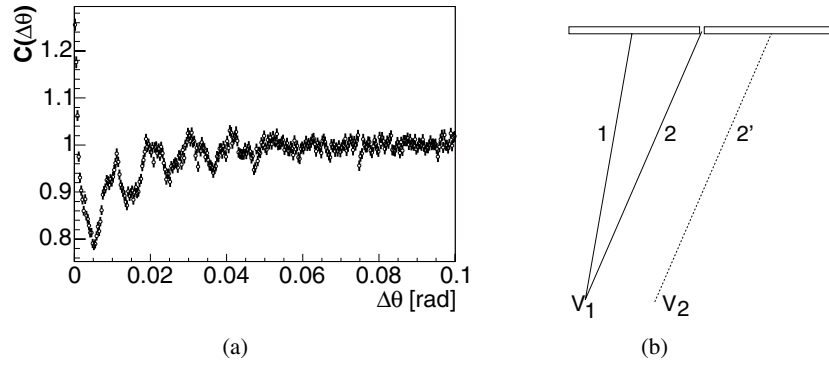


**Figure 6.161.** (a) Correlation function of the polar angle between two  $\pi^+$ . (b) Schema of the effect leading to the structure observed in (a). The rectangles represent the SPD pixels, the solid lines the tracks from an event with primary vertex position at  $V_1$ , and the dashed line the tracks from an event with primary vertex position at  $V_2$ . Pairs like 1–2 are relatively less efficiently reconstructed than pairs like 1–2'. See text for details.

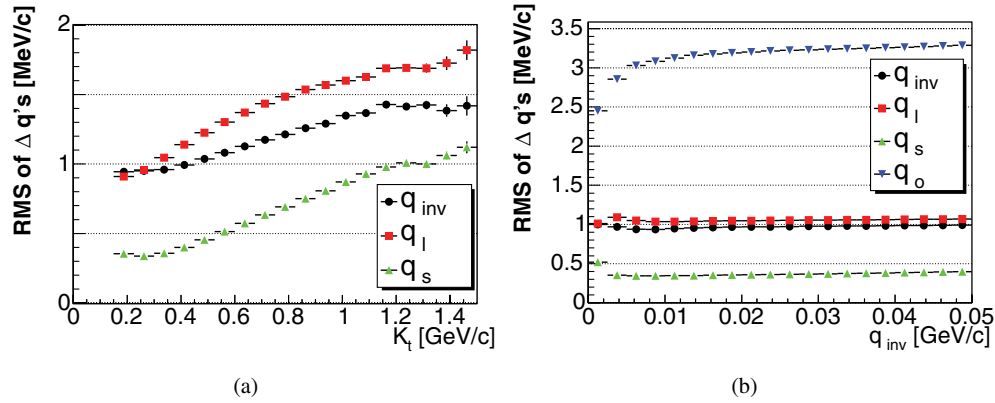


**Figure 6.162.** Resolution of  $q_{inv}$ ,  $q_o$ ,  $q_s$  and  $q_l$  vs. (a)  $K_t$  and (b)  $q_{inv}$ , for positive pions.

always assumed to be at the centre of a cluster. Since most of the clusters are composed of only one pixel, the reconstructed coordinates correspond always to the centre of the pixels. As a consequence, some values of  $q_l$  are more probable than others. Therefore, it is necessary to mix events with their  $z$  position of the primary vertex closer than half the width of a pixel, i.e.  $225 \mu\text{m}$ . In our analysis we group events according to the  $z$  vertex position, and only events falling into a single bin were mixed. The width of the bin is  $100 \mu\text{m}$  which allow us to remove the effect.

**6.3.5.2. Two-track resolution.** In this section we study the capability of our detector to reconstruct the relative momentum of a pion pair. To do that, we calculate the distribution of the difference between reconstructed and generated relative momentum and define the resolution of the pair relative momentum as the r.m.s. of a Gaussian fit to this distribution.

Figures 6.162, 6.163, 6.164 and 6.165 show the resolution for  $q_{inv}$ ,  $q_o$ ,  $q_s$  and  $q_l$  vs.  $K_t$  and  $q_{inv}$  for pions, kaons, and protons. The numerical values for the resolution of pions are given in Table 6.34(a). The resolution in  $q_o$  slightly improves for very small values of  $q_{inv}$ , while

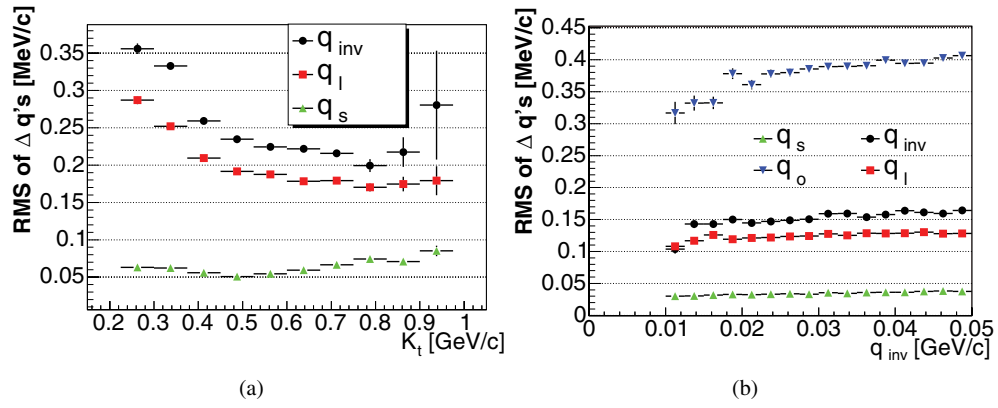


Figure 6.163. Resolution of  $q_{inv}$ ,  $q_o$ ,  $q_s$  and  $q_l$  vs. (a)  $K_t$  and (b)  $q_{inv}$ , for positive kaons.

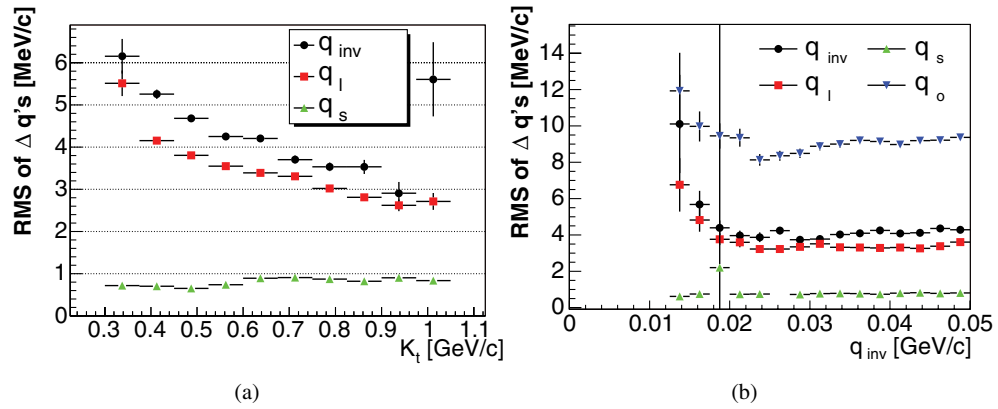


Figure 6.164. Resolution of  $q_{inv}$ ,  $q_o$ ,  $q_s$  and  $q_l$  vs. (a)  $K_t$  and (b)  $q_{inv}$ , for protons.

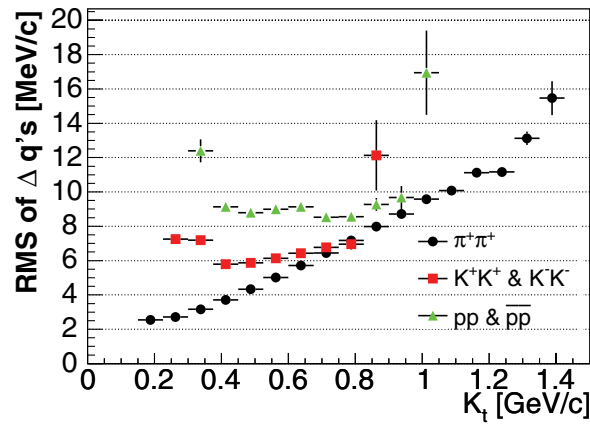
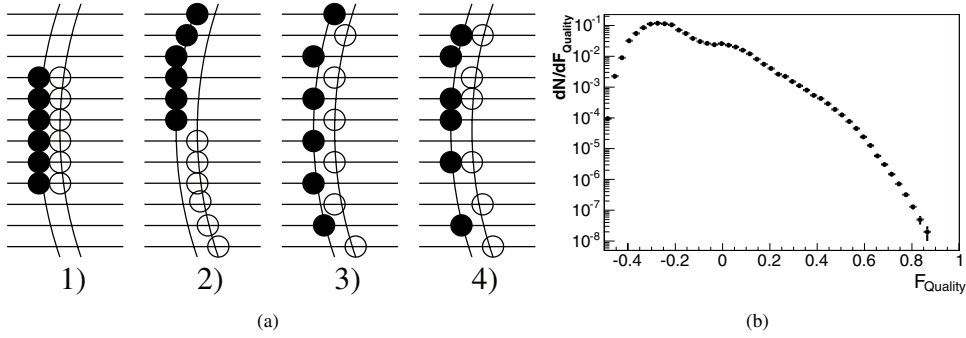


Figure 6.165.  $q_o$  resolution as a function of  $K_t$  for positive pions, charged kaons, and protons.

**Table 6.34.** (a) Resolution of the relative momentum  $q_{inv}$  and the three components of  $\vec{q}$  for the  $\pi^+\pi^+$  system. (b)  $2k^*$  resolution for different particle systems (see text).

(a)					(b)	
$K_t$ range	Resolution (r.m.s.) (MeV/c)				Particle system	$2k^*$ (MeV/c)
(MeV/c)	$q_{inv}$	$q_o$	$q_s$	$q_l$		
$100 < p_t < 300$	0.95	0.70	0.34	0.95	$\pi^+\pi^-$	1.0
$300 < p_t < 600$	0.99	0.62	0.40	0.12	$\pi^+K^+$	1.4
$p_t > 600$	0.17	0.33	0.62	0.42	$\pi^+K^-$	1.4
					$\pi^+p$	1.7
					$\pi^+\bar{p}$	1.7
					$K^+K^-$	2.6
					$K^+p$	3.6
					$K^+\bar{p}$	3.4
					$K^-p$	3.5
					$K^-\bar{p}$	3.4

**Figure 6.166.** (a) Four examples of clusters attributed to two tracks. Full circles are clusters assigned to one track and open circles are clusters assigned to the other one. (1)  $F_{Quality} = -0.5$ , (2) and (3)  $F_{Quality} = 1$ , and (4)  $F_{Quality} = 0.25$ . (b) Normalized distribution of  $F_{Quality}$ .

for the other components it does not depend on  $q_{inv}$ . The resolution of  $2k^*$  for non-identical systems is listed in Table 6.34(b).  $k^*$  is the magnitude of the three momentum of either particle in the pair rest frame.

**6.3.5.3. Track splitting.** A split track is a single particle reconstructed as two tracks. Split tracks may strongly modify the correlation function since they will create fake pairs at low relative momentum, where the HBT signal is located. To remove split tracks we have implemented and tested the anti-splitting cut developed by the STAR Collaboration [446]. For every pair, a quantity called *quality factor* is calculated as follows:

$$F_{Quality} = \frac{\sum_{n=1}^{N_{pad\ rows}} A(n)}{\sum N_{Clust}}, \quad (6.31)$$

where:

$$A(n) = \begin{cases} -1, & \text{if both tracks have a cluster on pad row } n \\ 0, & \text{if neither track has a cluster on pad row } n \\ 1, & \text{if only one track has a cluster on pad row } n, \end{cases} \quad (6.32)$$

where  $N_{pad\ rows}$  is the number of TPC pad rows and  $\sum N_{Clust}$  is the total number of clusters for both tracks. It can take values in the range  $(-0.5, 1)$ . A value close to 1 describes a pair of tracks that has a high probability of being formed by a split track. A value close to  $-0.5$  indicates that the two tracks are most likely two particles, see Fig. 6.166(a).

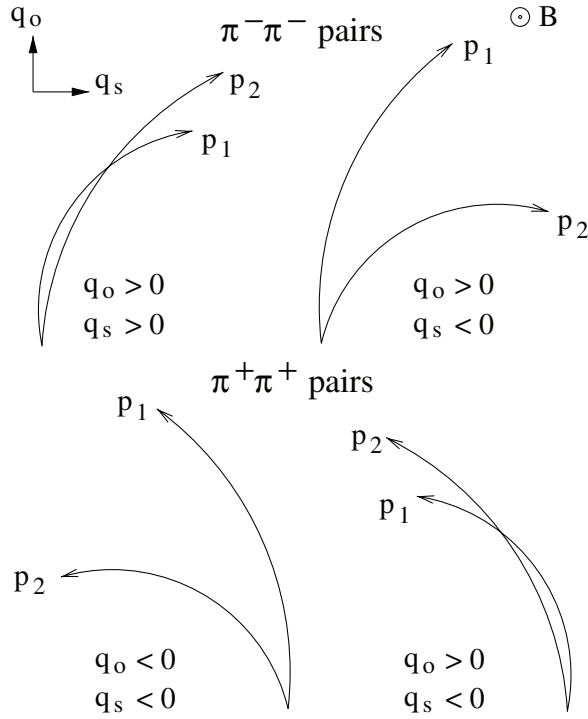


**Figure 6.167.** For negative pions, merging occurs more often for tracks with  $|q_o q_s| = q_o q_s$  than with  $|q_o q_s| \neq q_o q_s$ .

However, this cut is not needed in our case because the tracking software already performs a number of checks and removes all split tracks. In Fig. 6.166(b), the normalized distribution of  $F_{\text{Quality}}$  is shown. The STAR experiment rejects all pairs with a quality factor above 0.6. In our case the fraction of pairs above this values is smaller than 1%. We do not observe any artificial rise on the correlation function at small relative momentum when no cut is applied.

#### 6.3.5.4. Track merging

*Identical pions.* A merged track is the reconstruction of two close particles as a single track. As a consequence, in the HBT analysis, one observes a reduction in the number of pairs with small relative momentum.

In the analysis, the presence of merging can be detected with a non-zero value of the zero-th order Fourier coefficient, or  $R_{0s}$  parameter, when fitting the 3D correlation function for azimuthally symmetric events according to

$$C(q_o, q_s, q_l) = 1 + \lambda \exp(-q_o^2 R_o^2 - q_s^2 R_s^2 - q_l^2 R_l^2 - 2q_o q_s R_{os}^2). \quad (6.33)$$

Track merging introduces a deviation of  $R_{0s}$  from 0 caused by the preferential merging of track pairs with correlated transverse momenta  $q_o$  and  $q_s$  as shown in Fig. 6.167. In the case of negative pions and with the indicated orientation of the magnetic field, there is a higher degree of track merging when  $|q_o q_s| = q_o q_s$  than when  $|q_o q_s| \neq q_o q_s$ . For positive pions, or opposite direction of the field, the condition is reversed. Figure 6.167 (left panel) shows the 2D correlation function of  $q_o$  vs.  $q_s$ . One can clearly see the correlation between merging and the sign of  $q_o q_s$ .

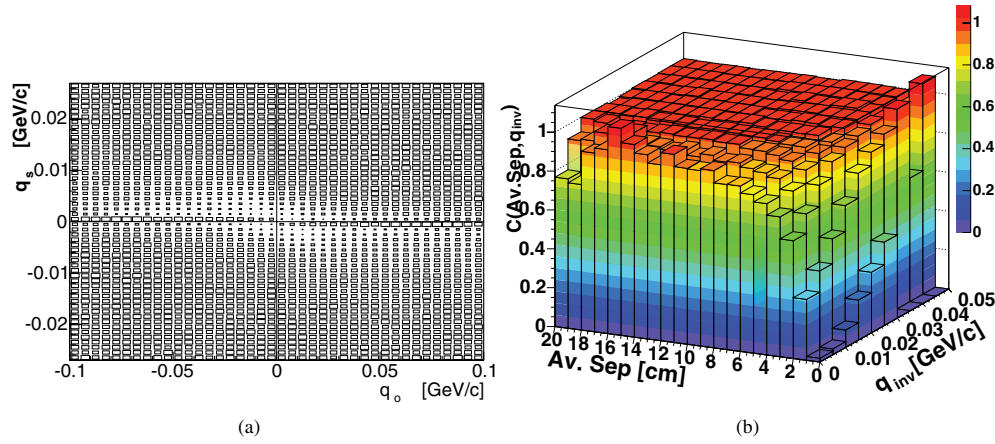


**Figure 6.168.** (a)  $q_0 q_s$  correlation function ( $q_1 < 20$  MeV). (b) Average separation in the TPC vs.  $q_{inv}$  correlation function for  $\pi^+\pi^+$  pairs and  $p_t < 500$  MeV. No correlation effect was introduced in the simulation.

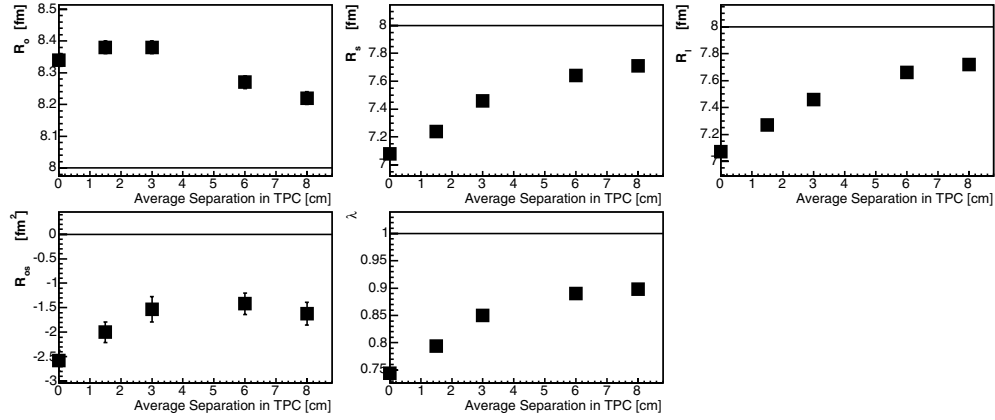
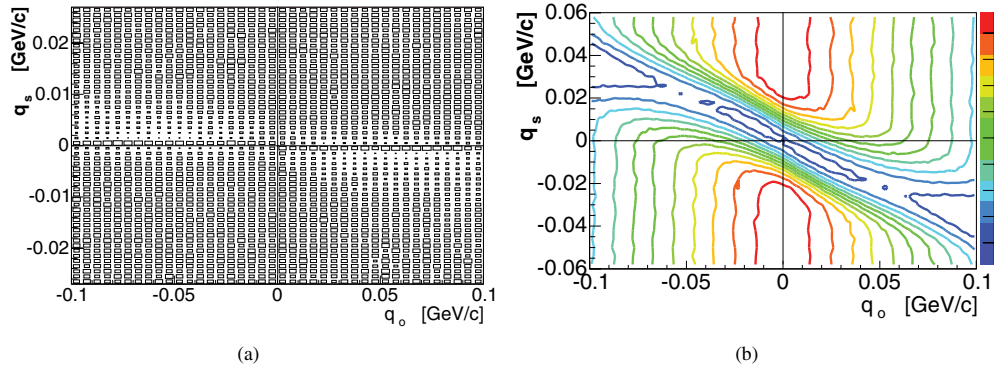


**Figure 6.169.** Extracted parameters as a function of the minimum required average separation in the TPC for all  $\pi^+\pi^+$  pairs entering the correlation function and  $p_t < 500$  MeV.

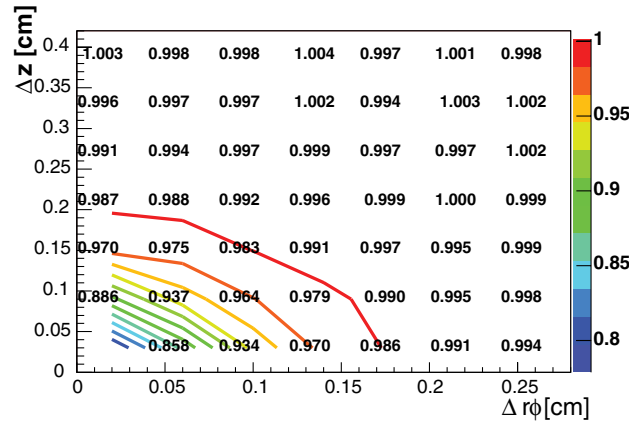
In order to remove the effects of merging, we calculate the average distance between the two tracks in every pair as they traverse the TPC and we reject those pairs (in numerator and denominator) with an average separation smaller than a given threshold. This average distance is calculated at 10 equidistant radii (every 15 cm), starting from the inner radius of the TPC (84.1 cm). In order to find the appropriate minimum value, the correlation function of  $q_{inv}$  vs. average separation is calculated. This correlation function is shown in the right panel of Fig. 6.168 where one can clearly see a lack of pairs at low  $q_{inv}$  and small average separation. In the events from which this correlation function was calculated, no QS correlations were introduced.

Figure 6.169 shows the values of the HBT parameters for different minimum average separation for all pairs entering the correlation function. It can be seen in  $R_{0s}$  that the cut reduces the effect of merging but does not remove it completely.

Figure 6.170 shows the  $q_0$  vs.  $q_s$  correlation function (left panel) and its denominator (right panel) with a minimum average separation of 6 cm for all pairs. While the effects of



**Figure 6.170.** (a)  $\pi^+\pi^+$   $q_o q_s$  correlation function and (b) its denominator for  $p_t < 500$  MeV. No correlation effect was simulated. Pairs of tracks with an average separation in the TPC below 6 cm were rejected.



**Figure 6.171.** Correlation function of the spatial separation at the innermost layer of the ITS when no antimerging-cut is applied. Lines represent the isolines. No correlation effect was introduced in the simulation.

merging are weaker than in Fig. 6.168, they are still prominent, caused by track reconstruction inefficiencies in the ITS.

In order to study merging in the ITS, we construct a 3D correlation function:  $q_{inv}$  vs. spatial track separation in  $z$  and  $r\phi$  at a given ITS layer. The 2D projection of this correlation function for the innermost layer is presented in Fig. 6.171. From this study we decided that, in addition to the antimerging-cut in the TPC, a minimum value for  $z$  and  $r\phi$  in the ITS was required. The best values for this cut are listed in Table 6.35.

After applying the cuts we verify that the correlation function is almost free from merging effects. For a simulated correlation function with parameters  $R_o = R_s = R_l = 8$  fm and  $\lambda = 1$ , the extracted parameters with a 3D fit to the reconstructed correlation function are  $R_o = 7.89 \pm 0.03$  fm,  $R_s = 7.87 \pm 0.02$  fm,  $R_l = 7.89 \pm 0.02$  fm,  $R_{os} = -0.50 \pm 0.23$  fm<sup>2</sup>,  $\lambda = 0.923 \pm 0.005$ , and  $\chi^2/\text{ndf} = 1.01$ , where the uncertainties are only statistical.

We also need to study how the extracted HBT parameters change with the anti-merging cut strength. We define the threshold values listed in Table 6.35(a) as the base, and change them by a multiplicative factor (0 means no cuts). The results are shown in Fig. 6.172. This

**Table 6.35.** Chosen values for the anti-merging cut in the ITS for (a)  $p_t < 500$  MeV and (b)  $p_t > 500$  MeV for  $\pi^+\pi^+$ . These cuts need to be applied in addition to the one applied in the TPC.

(a)			(b)		
Layer	$r\varphi$ (mm)	$z$ (mm)	Layer	$r\varphi$ (mm)	$z$ (mm)
1 (SPD1)	1.5	2	1 (SPD1 cut 1)	0.75	1
2 (SPD2)	3	3	1 (SPD1 cut 2)	0.45	3
3 (SDD1)	6	8	1 (SPD1 cut 3)	1.2	0.6
4 (SDD2)	12	12	2 (SPD2)	1.2	1.2
5 (SSD1)	15	15	3 (SDD1 cut 1)	1	8
6 (SSD2)	15	15	3 (SDD1 cut 2)	3	2
			4 (SDD2)	5	6
			5 (SSD1)	6	8
			6 (SSD2)	6	8

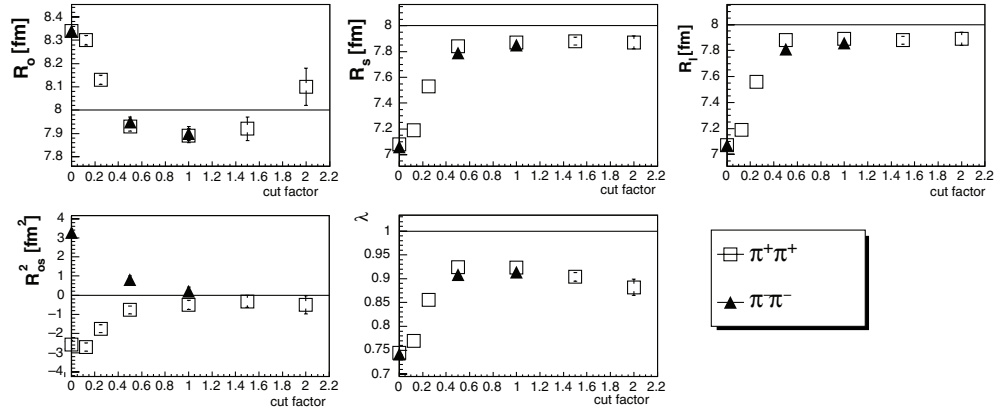
**Figure 6.172.** Extracted parameters as a function of the anti-merging cut strength for  $\pi^+\pi^+$ . Unity corresponds to the set of cuts in the ITS listed in Table 6.35(a) and the minimum average separation in the TPC equal to 6 cm.

figure indicates that these values are optimal because making them 50% weaker considerably increases  $q_{os}$ , and increasing them by about 50% significantly removes the signal, as seen in the increasing error of  $q_o$ . This figure also suggests that the discrepancies from the simulated values are caused by the resolution and imperfect PID effects, which will be discussed in the following subsection.

In order to estimate the systematic errors we study how the extracted parameters change when we modify by about 50%:

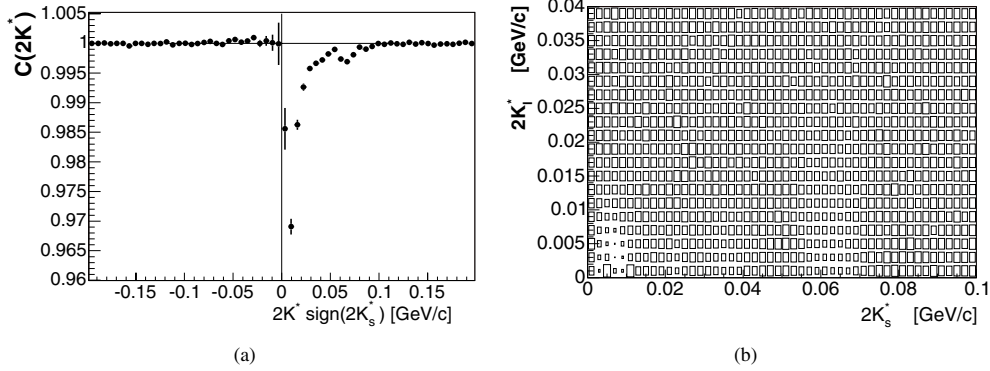
1. all threshold values;
2. only the values at the innermost layer of ITS (SPD1);
3. the minimum average separation required in the TPC;
4. the threshold values in the ITS only in the  $z$  direction;
5. the threshold values in the ITS only in the  $r\varphi$  direction.

None of them has a very strong influence on the obtained parameters. Their spread defines the systematic errors and the resulting values are listed in Table 6.36.

*Non-identical pions.* The merging effect should not be present for opposite-charge particle systems, because such particles are curved in opposite directions by the magnetic field. However, it may happen that their trajectories cross inside the detector which leads to a lower

**Table 6.36.** Systematic errors due to the antimergering cut for  $\pi^+\pi^+$ , defined as the spread of the parameters when varying all the cut thresholds up to 50%.

$p_t$ (MeV)	$R_o$ (fm)	$R_s$ (fm)	$R_l$ (fm)	$R_{os}^2$ (fm <sup>2</sup> )	$\lambda$
< 500	0.04	0.03	0.03	0.25	0.025
> 500	0.3	0.2	0.3	0.5	0.05

**Figure 6.173.** (a)  $2k^*$  and (b)  $2k_s^*2k_1^*$  (for  $2k_0^* > 0$ ) correlation functions for  $\pi^+\pi^-$  and  $p_t < 500$  MeV.**Table 6.37.** Chosen values for the anti-merging cut in the ITS for opposite-charged pions and  $p_t < 500$  MeV.

Layer	$r\varphi$ (mm)	$z$ (mm)
1 (SPD1)	1	1.5
2 (SPD2)	1	1.5
3 (SDD1)	8	5
4 (SDD2)	8	5
5 (SSD1)	20	20
6 (SSD2)	20	20

reconstruction efficiency for such tracks and, as a consequence, to an artificial correlation. Indeed, we observe such an effect.

In order to determine the level of merging for opposite-charged pairs, we calculate the  $2k^*$  correlation function for both, negative and positive  $2k_s^*$ , which should be identical because of symmetric constraints. Therefore, different shapes of these correlation functions would indicate that there is merging.

Fig. 6.173(a) shows these two correlation functions. The effects of merging can only be seen for pairs with  $2k^* > 0$ . The inefficiencies are related to the case when two tracks cross an ITS layer too close to each other. Each of the ‘dips’ in Fig. 6.173(b) is associated with merging at a given layer. The one at  $2k^* < 20$  MeV is due to the SPD, the next two to the SDD, and the last one to the SSD layer.

As in the  $\pi^+\pi^+$  case, we have decided to apply a cut based on the calculated track separation. In order to choose the threshold value, we construct the 3D correlation function  $2k_s^*$  vs. spatial track separation in  $z$  and  $r\varphi$  at a given ITS layer. Table 6.37 lists the best values for this cut.

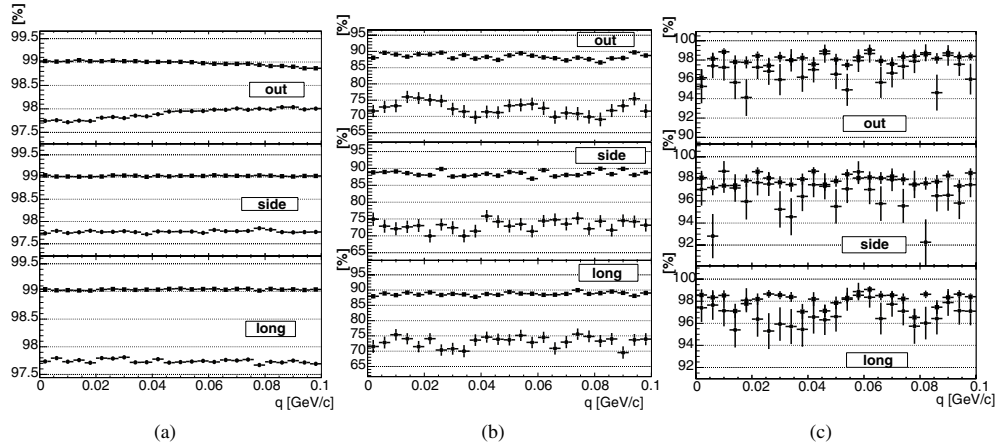


**Figure 6.174.** Pair probability (squares) and purity (circles) vs.  $q_0$ ,  $q_s$  and  $q_l$  for (a)  $\pi^+\pi^+$  (b)  $K^+K^+$  and (c)  $pp$ . The plots are constructed by projecting 3D histograms (absolute values of other variables  $< 20$  MeV).

**6.3.5.5. Pair purity.** The accuracy of the PID depends on the proximity of other tracks. Clusters can be shared between two tracks which decreases the quality of the  $dE/dx$  measurement and makes the PID determination more difficult and less efficient.

The pair purity is defined as the ratio of the number of pairs with both particles correctly identified to the number of all pairs. In the experimental data analysis, it cannot be directly calculated, however, it can be estimated from the product of the two-particle PID probabilities, which is further referred as the *pair probability*. Pair purity and pair probability for  $\pi^+\pi^+$ ,  $K^+K^+$  and  $pp$  systems as a function of  $q_0$ ,  $q_s$  and  $q_l$  are shown in Fig. 6.174. In almost all cases the PID purity does not depend on any of the  $q$  variables. The very slight dependence on  $q_0$  for the case of pions is the consequence of the uneven contribution of particles with different transverse momenta to each  $q_0$  bin. The purity decreases as the contribution of pions with large  $p_t$  increases. The anti-merging cut also modifies the contamination at small relative momentum. These effects are illustrated in Fig. 6.175, where the PID purity and pair probability are shown for two different ranges of  $p_t$ . However, it is important to notice that all these effects influence the purity of the numerator and of the denominator in exactly the same way.

In principle, the introduction of correlations by the weighting method could modify the performance of the reconstruction. In order to exclude this possibility, we generated 500 events using the HBT processor after-burner described in Section 6.3.4 and the efficiencies were indeed found to be compatible with the ones presented in Fig. 6.175.

**6.3.5.6. Coulomb interaction and fitting procedure for like-sign pairs.** As already discussed in Section 6.3.3, Eq. (6.26) applies only if the sole cause of correlation is quantum statistics. However, pions suffer long-range Coulomb interaction on their way from the source to the detector, which for like-sign (unlike-sign) particles causes a suppression (enhancement) of the measured correlation function at low  $q$ . These particles also feel the total electric charge of the source from which they are emitted. In addition there is also a strong interaction between the outgoing particles. These FSI will affect the correlation function and need to be taken into account in order to isolate the QS interference effects.

In the case of like-charged pions, the only case that will be discussed here, only Coulomb interaction between the outgoing particles plays an important role. The distortion arising from

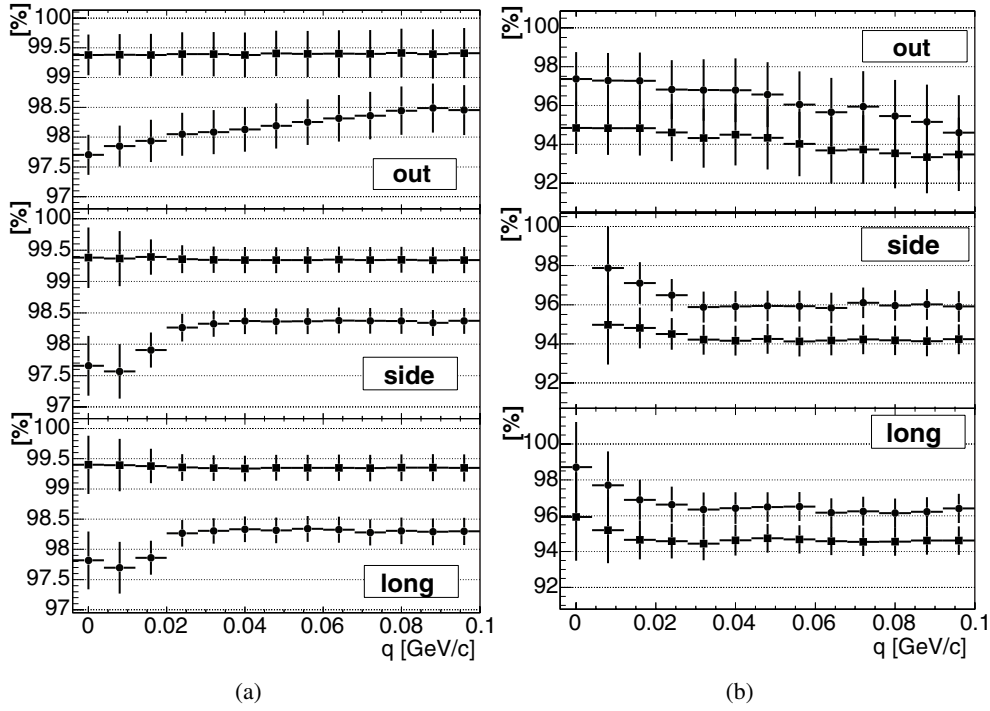


**Figure 6.175.** Pair probability (squares) and purity (circles) vs.  $q_0$ ,  $q_s$  and  $q_l$  for  $\pi^+\pi^+$  with  $p_t$ 's (a)  $< 500$  MeV and (b)  $> 500$  MeV. The plots are constructed by projecting 3D histograms (absolute values of the other variables  $< 20$  MeV). Anti-merging cuts were applied.

the strong interaction between these particles is negligible. A repulsive  $s$ -wave interaction exists for the  $I = 2$   $\pi\pi$  system. However, the range of the interaction is estimated to be  $\sim 0.2$  fm [474], and there are no doubly charged mesonic resonances that could decay into like-charged pions. For this reason the strong interaction will be ignored in this analysis. Also the interaction between the outgoing particles and the positively charged source was found to be very small and it decreases as the collision energy becomes ultrarelativistic [475, 476].

The mutual Coulomb interaction between the particles of a pair has to be taken into account when extracting the source parameters. Several methods exist, we describe here the one first suggested by Bowler [477] and Sinyukov [438]. The correlation function is fitted to

$$C(q_0, q_s, q_l) = (1 - \lambda) + \lambda K_{\text{coul}}(q_{\text{inv}})(1 + \exp(-q_0^2 R_0^2 - q_l^2 R_l^2 - q_s^2 R_s^2)), \quad (6.34)$$

where  $K_{\text{coul}}(q_{\text{inv}})$  is the squared Coulomb wave function integrated over the whole source [424, 477]. The values for this Coulomb factor have to be tabulated according to the source size and the particle mass. Assuming that  $\lambda$  is the fraction of primary pions, the first term on the right-hand side of Eq. (6.34) accounts for the pairs that do not interact and the second term for the ones that (Coulomb and Bose–Einstein) interact.

**6.3.5.7. Single-particle momentum-resolution correction.** The finite, single-particle momentum resolution induces a broadening of the correlation function and therefore an underestimation of the HBT parameters. To account for momentum resolution we have implemented the following correction procedure, which has been developed by the STAR Collaboration [446].

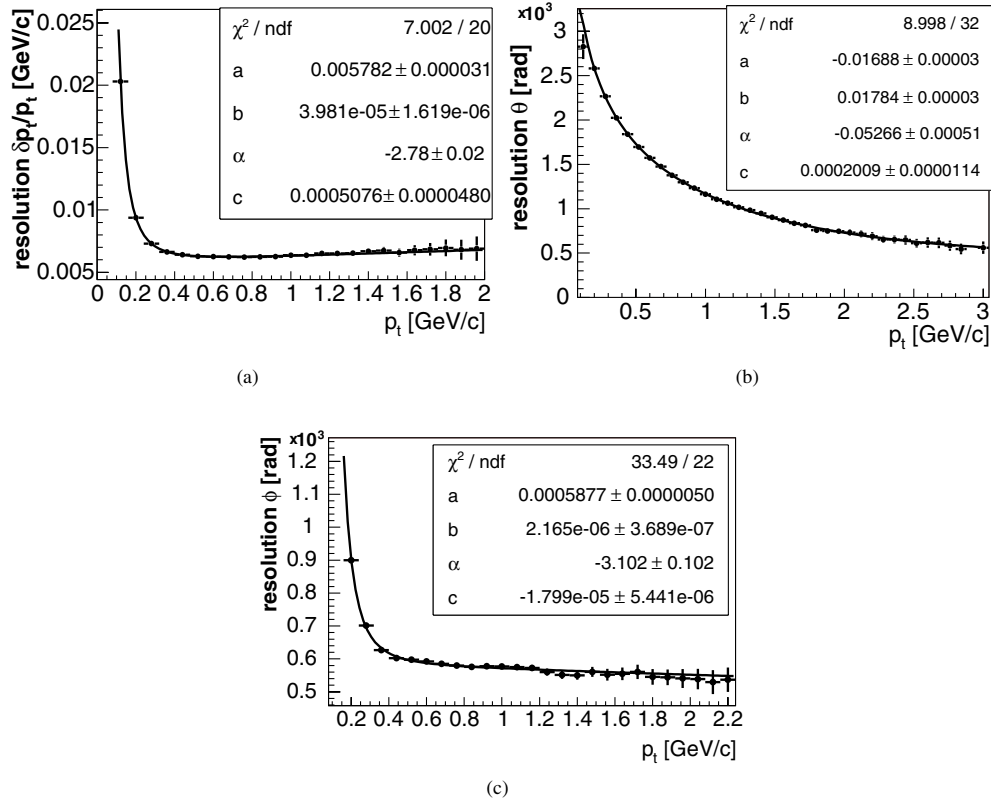


**Figure 6.176.** Single-particle momentum resolution in terms of (a)  $\delta p_t/p_t$ , (b)  $\delta\theta$ , and (c)  $\delta\phi$  as a function of the transverse momentum.

Each measured correlation function,  $C(q_{\text{meas}})$ , is multiplied by a correction factor given by  $C(q_{\text{ideal}})/C(q_{\text{smearred}})$ :

$$C(q) = C(q_{\text{meas}}) \frac{C(q_{\text{ideal}})}{C(q_{\text{smearred}})} = \frac{N(q_{\text{meas}})}{D(q_{\text{meas}})} \frac{N(q_{\text{ideal}})/D(q_{\text{ideal}})}{N(q_{\text{smearred}})/D(q_{\text{smearred}})}, \quad (6.35)$$

where  $C(q_{\text{ideal}})$  and  $C(q_{\text{smearred}})$  are formed as follows. Numerator and denominator of  $C(q_{\text{ideal}})$  are filled with pairs of pions coming from different events (i.e. with no correlation) but each pair entering the numerator is weighted according to some correlation model, a Gaussian in our case.  $C(q_{\text{smearred}})$  is filled in the same way but in this case the momentum of the particles in every pair has been smeared according to the resolution of the detector in terms of the transverse momentum ( $\delta p_t/p_t$ ), of the azimuthal angle of the particle ( $\delta\phi$ ), and of the angle between the particle and the beam axis ( $\delta\theta$ ). The resolution of these variables is shown in Fig. 6.176 as a function of  $p_t$ .

This correction procedure is iterative and converges quickly. The starting values of the parameters are obtained from the fit without correction. The change on the parameters extracted from the fit in consecutive iterations is shown in Tables 6.38 and 6.39.

The most affected parameter is  $R_0$ , especially at high momentum. This can be explained by the fact that this component depends linearly on the transverse momentum and its resolution gets worse with increasing  $p_t$ .

**Table 6.38.** Parameters obtained after resolution correction for different iterations, for  $p_t < 500$  MeV.

Iteration No.	$R_0$ (fm)	$R_s$ (fm)	$R_l$ (fm)	$R_{os}^2$ (fm <sup>2</sup> )	$\lambda$
0	$7.90 \pm 0.03$	$7.87 \pm 0.02$	$7.89 \pm 0.02$	$-0.51 \pm 0.23$	$0.923 \pm 0.005$
1	$8.03 \pm 0.06$	$7.88 \pm 0.05$	$7.90 \pm 0.05$	$-0.62 \pm 0.51$	$0.941 \pm 0.012$
2	$8.03 \pm 0.03$	$7.89 \pm 0.03$	$7.91 \pm 0.03$	$-0.63 \pm 0.27$	$0.942 \pm 0.006$

**Table 6.39.** Parameters obtained after resolution correction for different iterations, for  $p_t > 500$  MeV.

Iteration No.	$R_0$ (fm)	$R_s$ (fm)	$R_l$ (fm)	$R_{os}^2$ (fm <sup>2</sup> )	$\lambda$
0	$7.63 \pm 0.13$	$7.78 \pm 0.10$	$7.85 \pm 0.10$	$-0.42 \pm 0.85$	$0.891 \pm 0.024$
1	$7.98 \pm 0.16$	$7.75 \pm 0.12$	$7.85 \pm 0.12$	$-0.51 \pm 1.04$	$0.925 \pm 0.030$
2	$8.03 \pm 0.16$	$7.75 \pm 0.12$	$7.85 \pm 0.12$	$-0.52 \pm 1.05$	$0.928 \pm 0.030$
3	$8.03 \pm 0.16$	$7.75 \pm 0.12$	$7.85 \pm 0.12$	$-0.52 \pm 1.04$	$0.928 \pm 0.030$

**Table 6.40.** Parameters obtained before and after PID correction is applied,  $p_t < 500$  MeV.

	$R_0$ (fm)	$R_s$ (fm)	$R_l$ (fm)	$R_{os}^2$ (fm <sup>2</sup> )	$\lambda$
Low $p_t$ no corr.	$8.03 \pm 0.03$	$7.89 \pm 0.03$	$7.91 \pm 0.03$	$-0.63 \pm 0.27$	$0.942 \pm 0.006$
Low $p_t$ corrected	$8.03 \pm 0.03$	$7.89 \pm 0.03$	$7.91 \pm 0.03$	$-0.62 \pm 0.28$	$0.947 \pm 0.006$
High $p_t$ no corr.	$8.03 \pm 0.16$	$7.75 \pm 0.12$	$7.85 \pm 0.12$	$-0.52 \pm 1.04$	$0.928 \pm 0.030$
High $p_t$ corrected	$8.04 \pm 0.16$	$7.73 \pm 0.12$	$7.85 \pm 0.12$	$-0.54 \pm 1.08$	$0.958 \pm 0.032$

6.3.5.8. *Particle-identification correction.* The shape of the correlation function may also be influenced by incorrect particle identification. To account for this, the correlation function  $C(q)$  can be corrected in the following way,

$$C(q)_{\text{pid-corrected}} = \frac{C(q) - 1}{PID(q)} + 1, \quad (6.36)$$

where  $PID(q)$  is the PID purity function and is calculated by dividing the numerator of the correlation function, weighted pair by pair by the pair probability, by the numerator itself. This gives the average PID probability in each bin of a correlation function.

We find (see Table 6.40) that the correction has almost no influence on the reconstructed parameters, only the  $\lambda$  parameter increases by about 2%. The correction made with the real purity gives very similar results. It was also verified that the correlation function constructed with correctly identified pions only gives very similar results.

6.3.5.9. *Correlation functions.* All the procedures for cuts and corrections described in this Section are implemented in the AliRoot framework. We use them to calculate the  $\pi^+\pi^+$  and  $\pi^+\pi^-$  correlation functions for the most central events from the data produced during phase 1 of the PDC04. In this Section we present the results from this analysis. The input parameters for the simulation were  $R_0 = R_s = R_l = 8$  fm and  $\lambda = 1$ .

$\pi^+\pi^+$ . After applying all required cuts and corrections previously discussed, we obtain the  $\pi^+\pi^+$  correlation function from reconstructed events shown in Fig. 6.177 for  $p_t < 500$  MeV. For comparison, we have also included in the figure the correlation function calculated from generated events with no correlation effects introduced, the one calculated from generated events with correlation effects included, as well as the one calculated with reconstructed

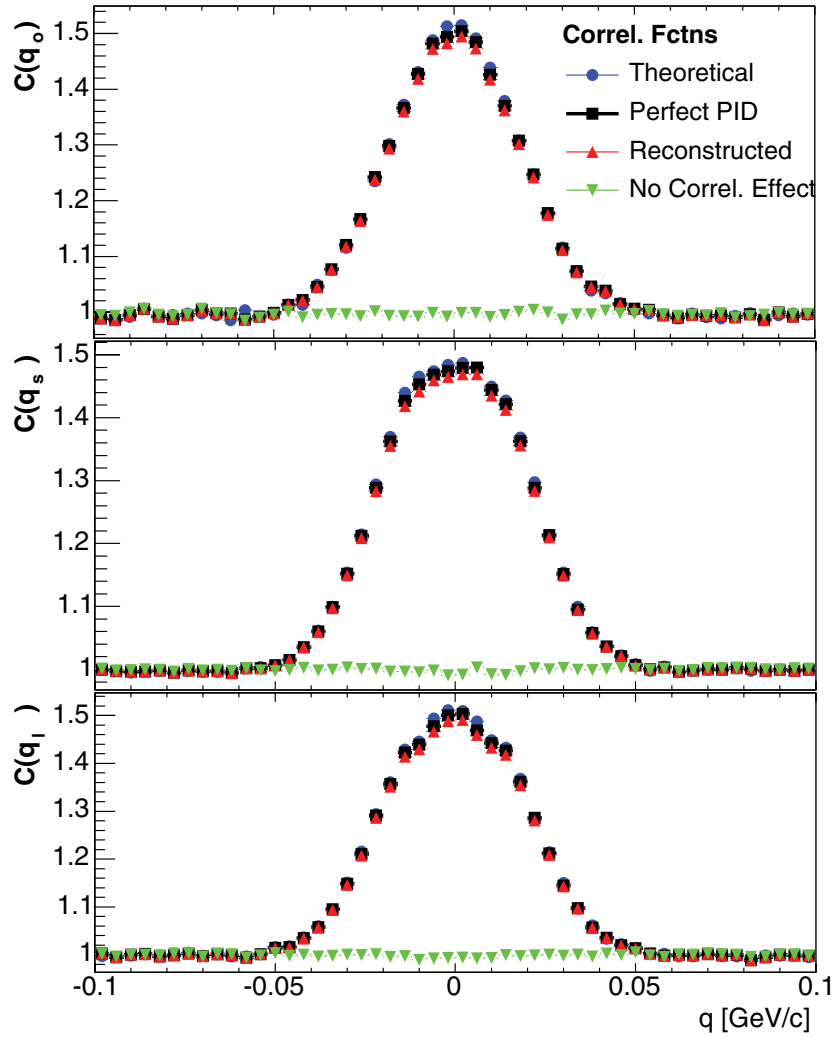


**Figure 6.177.** Projections of the 3D  $\pi^+\pi^+$  correlation function on  $q_0$  (top),  $q_s$  (centre), and  $q_1$  (bottom) for  $p_T < 500$  MeV. Up-pointing triangles represent the reconstructed correlation function, squares the one constructed with correctly identified particles, dots the one from the generated momenta and perfect PID, and down-pointing triangles the one without simulated Bose–Einstein effect.

particles but with perfect PID. One observes that the shape of the reconstructed correlation function is very close to the generated one, and that the PID impurities have a small influence. The extracted parameters are  $R_o = 8.03 \pm 0.03$  fm,  $R_s = 7.88 \pm 0.03$  fm,  $R_1 = 7.90 \pm 0.03$  fm and  $\lambda = 0.947 \pm 0.006$ , where the uncertainties are only statistical. The non-Gaussian shape, or flatness at  $q \sim 0$ , of the projections is produced by the anti-merging cut, which removes mostly pairs with small relative momentum.

For  $p_T > 500$  MeV, the extracted parameters are  $R_o = 8.14 \pm 0.23$  fm,  $R_s = 7.90 \pm 0.17$  fm,  $R_1 = 8.14 \pm 0.17$  fm and  $\lambda = 0.942 \pm 0.043$ . The remaining discrepancies of the reconstructed parameters are related to the resolution effects.

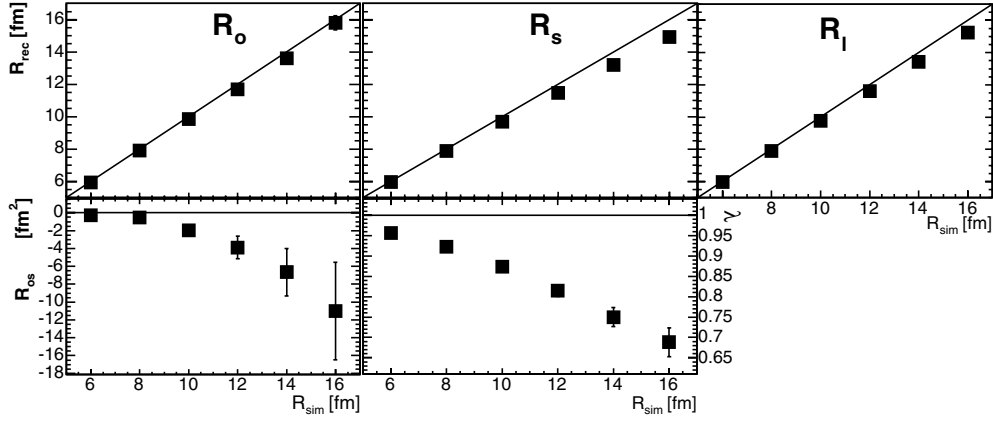


**Figure 6.178.** Extracted parameters as a function of the simulated parameters for  $\pi^+\pi^+$ ,  $p_T < 500$  MeV.

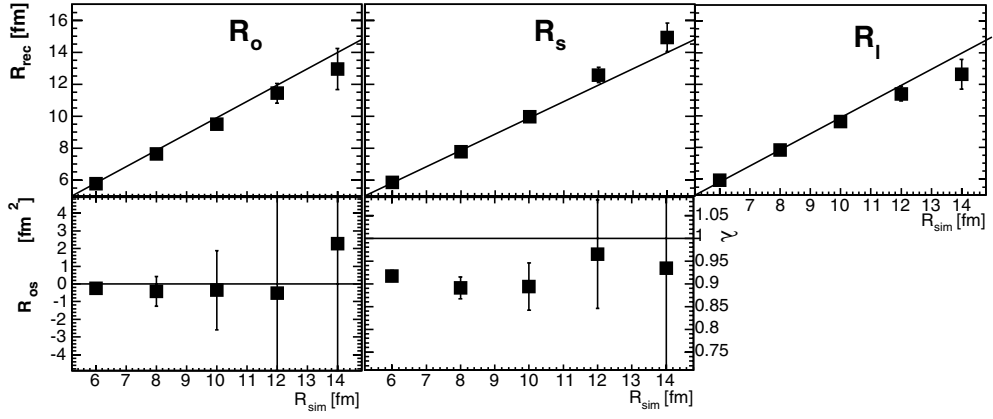


**Figure 6.179.** Extracted parameters as a function of the simulated parameters for  $\pi^+\pi^+$ ,  $p_T > 500$  MeV.

We have also checked that ALICE is able to reconstruct HBT parameters up to 15 fm (see Figs. 6.178 and 6.179). For higher values of the simulated parameters, the fits do not converge.

$\pi^+\pi^-$ . To study an example of non-identical correlation function, we have calculated the  $\pi^+\pi^-$  case using a simulated radius parameter of 8 fm and a simulated time shift of 5 fm. We do not expect to observe any time shift in the experimental data in this analysis. However, since the insufficient statistics does not allow us to study the pion-kaon nor the pion-proton system, we decided to study this unphysical example. To fit these correlation functions we use CorrFit [478], which provides a way to fit arbitrary non-identical two-particle correlation functions using the knowledge of the interaction between the two particles. The fitted function is shown in Fig. 6.180. The extracted parameters are  $R = 7.99 \pm 0.2$  fm and  $\Delta t = 4.3 \pm 0.2$  fm/c. The statistical errors can be extracted from the  $\chi^2/\text{ndf}$  map. The systematical uncertainties are derived from the change of the reconstructed parameters as one varies the threshold values of the cuts. We find them to be  $\sim 0.1$  and  $\sim 0.2$  fm for radius and time, respectively.

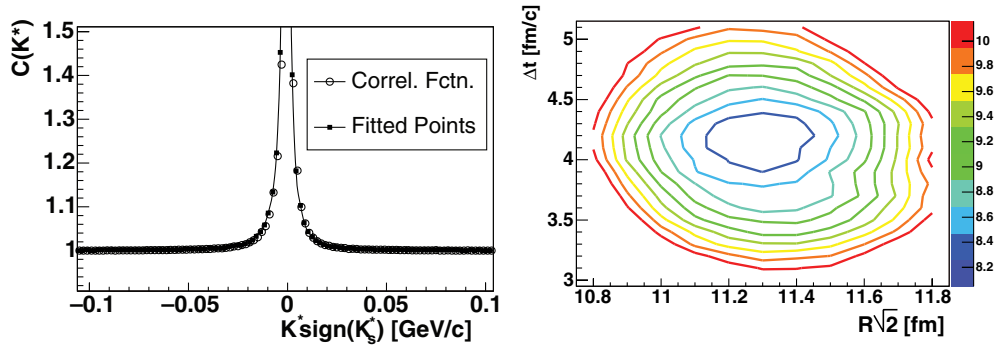


**Figure 6.180.** (a) Fitted  $\pi^+\pi^-$  correlation function and (b)  $\chi^2/\text{ndf}$  map of the fit.

**Table 6.41.** Expected resolution for each of the components of the momentum for the KK and pp systems.

	Resolution (r.m.s.) (MeV/c)			
	$q_{\text{inv}}$	$q_0$	$q_s$	$q_l$
$K^+ K^+$	4.2	9.5	0.5	2.3
$K_s^0 K_s^0$	4.0	7.8	3.9	3.4
pp	8.0	13.0	0.7	4.3

### 6.3.6. Other potential analyses and particular aspects of momentum correlation analyses

**6.3.6.1. Two-kaon and two-proton momentum correlations.** The limited number of available events has not allowed us to do a detailed analysis of the  $K^+K^+$  and proton-proton systems. Table 6.41 gives the expected resolution for each of the components of the momentum in those two systems as given in the ALICE Technical Proposal [33].

**6.3.6.2. Momentum correlations in proton-proton collisions.** The expected sizes in pp collisions are of the order of 1–2 fm. Therefore, the correlation function is much wider than the one from Pb–Pb reactions. This, together with the small track density, makes, in principle, the momentum correlation analysis easier in pp than in heavy-ion collisions. In order to study the capabilities of our detection system to do a momentum correlation analysis in pp collisions, we generated events with correlation parameters  $R = 1$  fm,  $\lambda = 1$  and no final-state interactions.

In pp collisions, other correlations than the ones due to QS and FSI are usually pronounced. One of the main correlations comes from the fact that a substantial fraction of the particles is produced inside jets. To minimize the effects of these particles, one usually uses a reference distribution constructed with opposite-sign pairs (i.e.  $\pi^+\pi^-$  in the case of  $\pi^+\pi^+$  correlations), or the Stavinskiy procedure [479]. Unfortunately, none of these methods completely removes the effects. The former one is influenced by resonance decays and by the Coulomb interaction; the latter one is effective only in the case of dijet events. However, these effects are more pronounced in the low-multiplicity events and at high momentum. In order to minimize the problem, we consider only events with at least five charged tracks reconstructed.

Figure 6.181 shows the projections of the 3D  $\pi^+\pi^+$  correlation function. The same anti-merging cuts as for the low-momentum pions in Pb–Pb collisions have been applied although the effects of merging are smaller than in heavy-ion collisions because of the smaller multiplicity. However, we observe that the event generator PYTHIA introduces new,

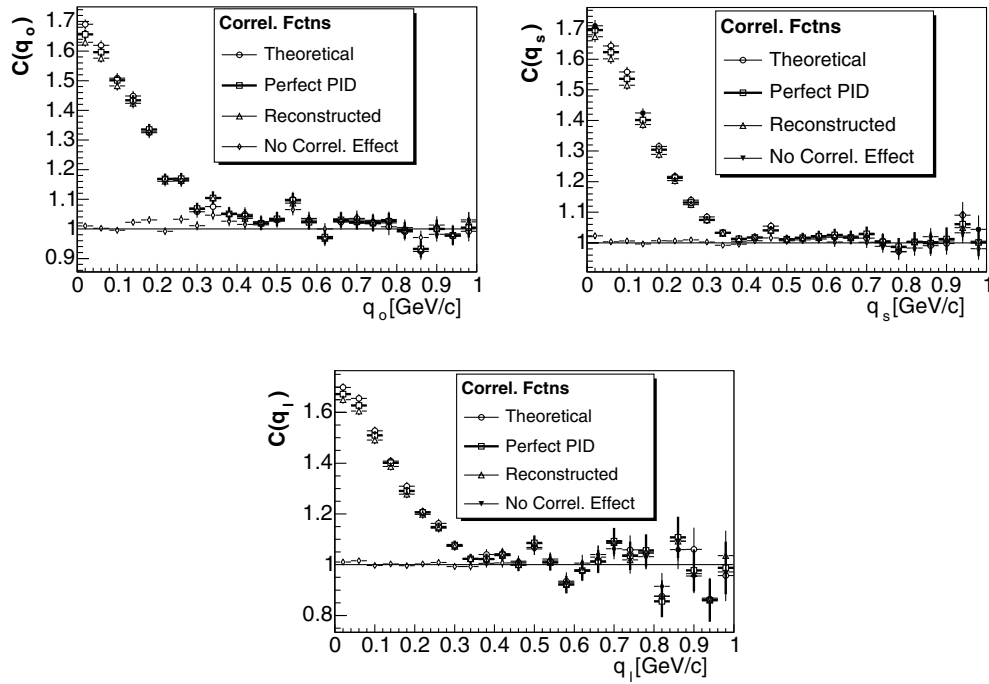


**Figure 6.181.** Projections of the  $\pi^+\pi^+$  correlation function in pp collisions for other components smaller than 100 MeV.

**Table 6.42.** Reconstructed  $\pi^+\pi^+$  radii in pp collisions. ‘Anti-merging corr.’ means anti-merging, PID and resolution corrected. ‘Corrected’ means that the non-QS correlations present in PYTHIA events were removed, see text for details.

	$R_o$ (fm)	$R_s$ (fm)	$R_l$ (fm)	$R_{os}$ (fm <sup>2</sup> )	$\lambda$
No cuts	$0.86 \pm 0.03$	$1.00 \pm 0.02$	$1.03 \pm 0.02$	$0.10 \pm 0.05$	$0.937 \pm 0.017$
Anti-merging	$0.90 \pm 0.03$	$0.98 \pm 0.02$	$1.00 \pm 0.02$	$0.07 \pm 0.05$	$0.943 \pm 0.019$
Anti-merging corr.	$0.89 \pm 0.07$	$0.96 \pm 0.05$	$0.99 \pm 0.04$	$0.08 \pm 0.12$	$0.949 \pm 0.050$
Corrected	$0.96 \pm 0.04$	$0.97 \pm 0.03$	$0.97 \pm 0.02$	$0.00 \pm 0.07$	$0.908 \pm 0.025$

non-QS correlations. In order to remove these correlations, we divide the distributions in the reconstructed correlation function by the ones from the simulated events without correlations. The extracted parameters are listed in Table 6.42. In order to account for the momentum resolution, the same correction procedure used in the Pb–Pb analysis has been applied here; however, it has no influence in the reconstructed parameters.

We have observed that, in general, the reconstructed parameters are not sensitive to changes in the different cut thresholds, thus implying that the systematic uncertainties from this source are small. However, the influence of Coulomb and strong FSI are larger than in heavy-ion reactions and need to be well understood.

**6.3.6.3. Single-event interferometry in heavy-ion collisions.** The analysis of correlation functions for single events is an important subject in order to understand fluctuations. This was practically impossible so far, including at RHIC, because of the lack of sufficient particle pairs in single events. Besides overall multiplicity, effective acceptance and the track reconstruction efficiency at small relative momentum are relevant for this analysis.

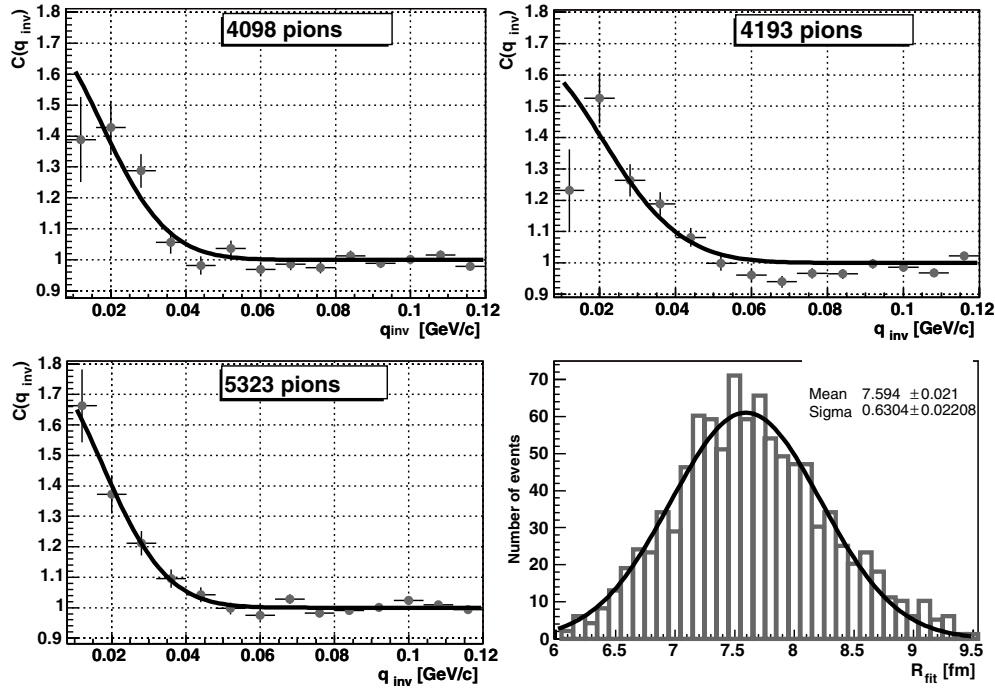


**Figure 6.182.** Examples of single-event correlation functions for different number of reconstructed pions. Bottom-right: the distribution of the reconstructed radii.

For a simulated Gaussian source with  $R = 8$  fm,  $\lambda = 1$  and using only tracks reconstructed in the TPC, we obtain the correlation functions for different number of reconstructed pions as shown in Fig. 6.182. Positive and negative pions have been added in order to increase statistics.

The distribution of the extracted parameter  $R$  is shown on the bottom-left panel. From a Gaussian fit to this distribution we get a mean of  $7.59 \pm 0.02$  fm and  $\sigma = 0.63 \pm 0.02$  fm. The systematic shift of the mean value can be explained by merging effects and detector resolution. The results indicate that single-event interferometry in ALICE may for the first time be sensitive enough to study source fluctuations.

**6.3.6.4. Direct-photon interferometry measurements with PHOS.** In contrast to hadrons, direct photons are emitted at all stages of the collision evolution, and they keep information even about the earliest and hottest stage of the collision. Therefore, measurement of Bose–Einstein correlations of direct photons gives the unique possibility to explore directly the space–time sizes and dynamics of the system in the first stages of the evolution.

Theoretical considerations of direct-photon correlations in heavy-ion collisions [480–484] predict that at LHC energies, direct photons emitted from the hadron gas contribute predominantly to the  $p_t$  region up to  $\sim 1\text{--}2$  GeV, photons emitted from the QGP phase contribute to the  $p_t$  region  $1\text{--}2 \lesssim p_t \lesssim 3\text{--}5$  GeV, and photons with larger transverse momentum come from the hard collisions in the pre-equilibrium phase. Therefore, by looking at different  $p_t$  regions, one gets information about different stages of the collision: pre-equilibrium, hot QGP phase, and cooler hadronic gas phase.

Besides providing information about the space–time dimensions of the collision region, the strength of the two-photon correlation can be used to obtain an independent estimate of

the yield of direct photons which can be compared to the results of the conventional statistical methods.

We investigate the possibility of measuring direct-photon correlations with the PHOS detector, and we estimate the accessible  $p_t$  region for such analysis. It was estimated [480–484], that direct photons are only a few per cent (5–20%, depending on  $p_t$ ) of the total photon yield in the interesting region of  $p_t$ , so that extraction of direct photon correlations is a very difficult task. One can expect the correlation strength to be on the level of  $10^{-3}$ – $10^{-2}$ , which requires detailed simulations of the detector response and of the possible physical background. Another important parameter is the width of the two-photon correlation. The HBT radius reaches 6 fm at small  $K_t \sim 100$  MeV and decreases down to 1–2 fm at  $K_t \sim 5$  GeV [480–484].

If the source size is of the order of 5 fm or larger, the two-photon correlation appears at  $q < 50$  MeV. If we consider photons with an energy of 1 GeV and above, then the opening angle between photons would be as small as  $q_{\text{inv}}/K_t \approx L_{12}/R$ , where  $q_{\text{inv}} \sim 50$  MeV,  $K_t \sim 1000$  MeV,  $L_{12}$  (distance between photons in the PHOS plane)  $\sim 20$  cm, and  $R$  (distance from interaction point to PHOS) = 460 cm. This implies that photons closer than 20 cm are important for the analysis. At such small distances, clusters can overlap and their position and energy may be modified in the process of unfolding.

In order to be able to unfold clusters they should be at a distance  $> 2.5$  cm (1 crystal unit) and the distance at which two clusters can be unfolded increases with the energy of the unfolded clusters. The first distance is defined by the requirement that two local maxima, which are seeds for unfolding procedure, are separated at least by one crystal unit. The second distance is defined by the size of the cluster, which increases logarithmically with the energy of the cluster. We find that the mean difference between the simulated and the measured relative distances is of the order of 1–2% for relative distances larger than 4–5 cm.

We also need to study the change on the energy of a cluster during the unfolding procedure. We are interested mainly in photons with similar momenta. No change is found in the energy of unfolded and well separated clusters down to relative distances  $L_{12} \approx 5$  cm, while for closer clusters the reconstructed energy appears to be slightly larger (0.5–1%) than that of well separated clusters. Therefore, one should not expect serious distortions on the two-photon correlation function at relative distances between photons in PHOS larger than 5 cm.

The next step is to estimate the resolution of the pair relative momentum as we did for pions. To do that, we simulate the response of the PHOS for various ranges of the photon-pair relative momentum, and for each  $K_t$  range we construct a two-dimensional histogram, simulated relative momentum vs. reconstructed one. We find a linear dependence of the mean of the simulated relative momentum with the mean of the reconstructed one. Figure 6.183 shows the resolution for  $q_{\text{inv}}$  and for  $q_0$ .

In both cases, we fit the dependence of the resolution on momentum to the functional form

$$\sigma = q \sqrt{a^2 + \frac{b^2}{q} + \frac{c^2}{q^2}}, \quad (6.37)$$

and the values of the parameters  $a$ ,  $b$ , and  $c$  are shown on Fig. 6.183. For the case of  $q_{\text{inv}}$ , the momentum resolution is as small as a few MeV for the interesting region of  $q_{\text{inv}}$ . The resolution of  $q_0$  is on the level of 10–15 MeV, comparable with the expected width of correlation function, which implies that the uncertainty on  $R_0$  will be larger.

Up to now we have considered only clusters generated by photons. However, in a real event, a lot of other particles reach the PHOS detector. Especially problematic are antineutrons

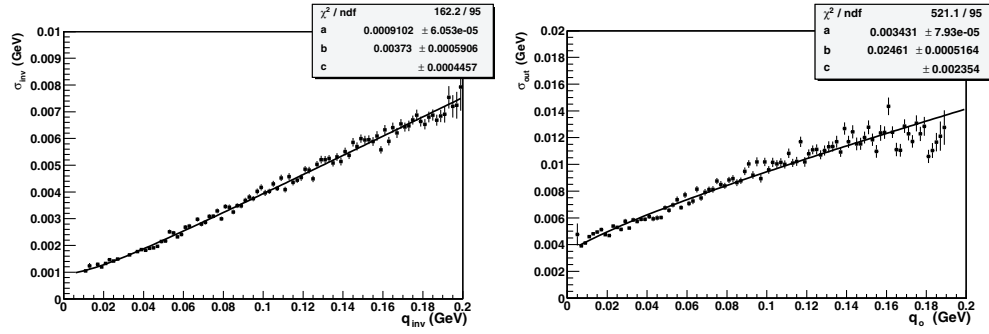


Figure 6.183. Relative resolution of  $q_{\text{inv}}$  (left) and of  $q_o$  (right).

and antiprotons because when they annihilate in the PHOS, they produce clusters of complicated shapes which could have several local maxima that could be unfolded during the reconstruction process and can produce several reconstructed particles. To simulate the response of the PHOS to neutrons, antineutrons, protons, and antiprotons we generate a set of events with one such particle per event with transverse momentum as predicted by HIJING 1.36 for central Pb–Pb collision at LHC. We then calculate the number of fake pairs per event, and we find that their contribution is 1–2 orders of magnitude smaller than that of direct photons.

In order to study how clusters coming from the photon conversion between the interaction point and the PHOS detector and how residual correlations from decays of heavier resonances affect the correlation function, we compare the measured and simulated correlation functions and find that they agree for  $q_{\text{inv}} > 15 \text{ MeV}$  at  $0.7 < K_t < 1 \text{ GeV}$  and for  $q_{\text{inv}} > 25 \text{ MeV}$  at  $1 < K_t < 2 \text{ GeV}$ . Therefore, these contributions should be accurately calculated.

In this analysis we have estimated the possibility of measuring Bose–Einstein correlations of direct photons in Pb–Pb collisions with the PHOS spectrometer. The distortions on the correlation function caused by the reconstruction procedure appear only at small relative momentum,  $q_{\text{inv}} < 0.02K_t$ , which is close to the physical limit of the PHOS, defined by the size of the crystal:  $q_{\text{inv}}^{\text{phys}} < 0.01K_t$ . The resolution of PHOS in measuring relative momentum is good for  $q_{\text{inv}}$ ,  $q_s$  and  $q_1$ , while for  $q_o$  it is comparable with the expected width of the correlation function. The distortion of the two-photon correlation function in a high multiplicity environment at small relative momentum increases only slightly with increasing multiplicity. We have therefore demonstrated the possibility of measuring two-photon correlation functions up to  $K_t \sim 3 \text{ GeV}$  in central Pb–Pb collisions.

*6.3.6.5. Influence of hard processes on particle correlations.* At LHC energies hard processes will give an important contribution to the overall particle spectrum produced in Pb–Pb collisions. They will affect not only the high-energy part of the spectra but also the soft part where the fragmentation products appear. Since the space–time evolution of jet hadronization will in general be different from the kinetic freeze-out of the soft hadrons, correlations introduced by jet fragments will influence the measured HBT parameters [485]. Correlations can arise from:

- pairs of particles from a single jet, which will reflect the dimension of the region where the jet fragmented;
- pairs of particles from different jets;
- pairs where both particles belong to the decoupling of the thermal fireball;
- pairs where one particle comes from the thermal fireball and the other one from jet fragmentation.

The correlation patterns will be sensitive to the relative importance of the various components listed above as well as to the details of the evolution of the system (e.g. jet quenching will result in a ‘doughnut’ type source of particles whose dimensions and detailed shape will reflect the intensity of the quenching and the energy repartition of the jets, since we know that higher energy jets hadronize further from the initial hard scattering than low-energy jets).

It has been shown in Ref. [485] that the correlation function may exhibit quite characteristic structures at large momentum differences beyond the main peak at  $q = 0$ . Therefore it will be important to extend the measurement and analysis of momentum correlations to large momentum differences.

Although the present calculations using a yield of 100 jets per event with total transverse energy greater than 5 GeV in the ALICE central barrel acceptance ( $|\eta| < 0.9$ ) show that the effect becomes visible only for particles above 1 GeV/ $c$ , the possible importance of the phenomena at lower transverse momenta cannot be excluded.

The radii measured in pp reactions exhibit no dependence on the collision energy. On the other hand, they strongly increase with the particle multiplicity [486, 487]. The observed behaviour may be related to the details of the hadronization of jets. We know that the point of hadronization of a jet and the point of the initial parton–parton hard scattering do not coincide. Numerical estimates for the time-scale of hadronization vary significantly [488–490], but owing to the Lorentz boost to the laboratory frame, they are proportional to the energy,  $L_{\text{hadr}} \sim O(1)E_t$  [491]. On the other hand, the energy spectrum of the emitted jets is correlated to the charged-particle multiplicity of the events. Hence, if we assume that the hadronization occurs at different distances from the initial hard scattering, depending on the energy of the jet, we can expect that this effect will result in a variation of the measured HBT parameters without implying the presence of a thermalized medium as in the heavy-ion description of the effect. A simple model [275] successfully reproduces the measured correlations assuming that:

1. The distribution of the hadronization points along the jet axis is Gaussian. Its mean and dispersion depend on the energy of emitted partons.
2. The distance between the hadronization point and the jet axis has a Gaussian distribution. Its dispersion is also proportional to the energy of the emitted partons. Moreover, it is a function of the position along the jet axis, so it is the largest at the point where the distribution along the jet has the maximum value.
3. The underlying event particles create a source with a three-dimensional Gaussian distribution centred around the point of collision.

The correlation function takes non-trivial shapes, which can be approximately fitted with a double Gaussian form. This behaviour is more pronounced as  $dN/d\eta$  increases, which is also observed in the experimental data.

The proposed model implies that this kind of measurement may offer insight on the space–time evolution of hadronization. One-dimensional analysis prohibits the drawing of any unambiguous conclusions within the model. However, the expected number of events in ALICE will offer the possibility to perform 3D analysis of the momentum correlations and hence collect more precise information.

**6.3.7. Conclusion.** The necessary software tools for the momentum correlation analysis in ALICE have been developed, and are integrated within the AliRoot framework.

We have presented a detailed analysis of the experimental effects on the correlation function. These effects need to be minimized in order to reduce the systematic uncertainties

of the final results, since the statistical errors will be very small in most cases. These effects are well understood and the appropriate tools to remove them have been developed and implemented.

The procedure for the two-pion correlation analysis in Pb–Pb collisions has been shown. This procedure will be the basis for most of the HBT analyses. We have also shown that ALICE is able to reconstruct pion HBT parameters up to 15 fm, about a factor of two larger than the predicted parameters for LHC energies.

We have given an overview of potential analyses that ALICE will be able to perform, some of which will be done for the first time, opening a window to study new aspects of momentum correlations and of the space–time evolution of the system.

#### 6.4. Flow

Flow is an ever-present phenomenon in nucleus–nucleus collisions, from low-energy fixed-target reactions below 100 A MeV at GANIL or MSU up to  $\sqrt{s_{NN}} = 200$  GeV collisions at RHIC, and is expected to be observed at the LHC. Flow is a *collective* expansion of bulk matter exhibiting various possible patterns: there can be an isotropic expansion as well as, in non-central collisions, a non-isotropic component. Note that the generic term ‘flow’ should be understood as a phenomenological description of the expansion, without any reference to a specific theoretical interpretation. In particular, the notion of flow does not necessarily imply any hydrodynamic behaviour, although the underlying physics is conveniently pictured in terms of pressure gradients. It is also important to realize that flow refers to a collective phenomenon which affects *all* (or almost all) particles in a given event. In that sense, it signals the presence of multiple interactions between the outgoing particles which contribute to the appearance of an overall pattern. This should be contrasted to nucleon–nucleon collisions where such effects are absent.

Depending on collision energy, flow does reflect different collective aspects of the interacting medium. At low energies, where relatively few new particles are created, flow effects are mostly caused by the nucleons from the incoming nuclei so that their theoretical interpretation relies on notions like the compressibility of nuclear matter or the competition between two-body interactions and mean field effects [492–494]. At high energies the number of newly created particles is so large that it is their behaviour which dominates the observable flow effects. The primordial nucleons are expected to make only minor contributions to the dynamical processes inside the reaction volume, in particular in the region near mid-rapidity.

The usual theoretical tools to describe flow in that regime are hydrodynamic or microscopic transport (cascade) approaches. Flow depends in the latter models on the interaction cross sections, be it partonic or hadronic. Hydrodynamics, on the other hand, is valid only when the mean free path of particles is much smaller than the system size and relies on a description of the system in terms of macroscopic quantities. This gives a handle on the equation of state of the flowing medium and, in particular, on the value of the sound velocity [495]. In both types of models it may be possible to deduce from a flow measurement whether it originates from partonic or hadronic matter or from the hadronization process [496–498].

In the following subsections we introduce the possible different patterns of collective flow (radial or anisotropic). We then present the various methods devised for the experimental measurement of anisotropic flow. Next, we briefly review the experimental results at SPS and RHIC energies. Finally, we present the experimental potential of the ALICE detector [499].

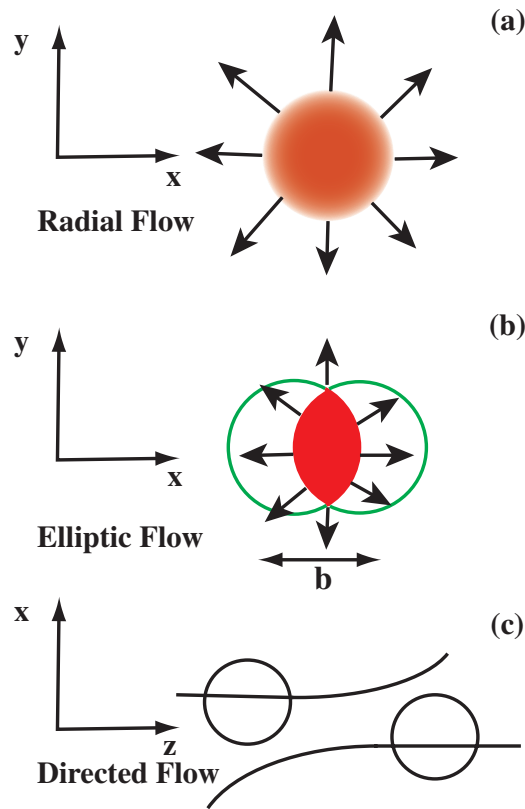


**Figure 6.184.** Illustration of the three most common flow phenomena.

**6.4.1. Radial flow.** In *central* collisions between spherical nuclei, the initial state is symmetric in azimuth (see Fig. 6.184(a)). This implies that the azimuthal distribution of the final state particles is isotropic as well. Under such conditions, any pressure gradient will cause an azimuthally symmetric collective flow of the outgoing particles which we call *radial flow*. The relevant observables to study such effects are the transverse momentum distributions of the various particle species. For a given particle type, the random thermal motion is superimposed onto the collective radial flow velocity which may or may not depend on space and time. Correspondingly, the invariant transverse-momentum distribution of a specific particle type depends on the temperature at freeze-out, the particle mass and the velocity profile in space–time [286, 500]. Furthermore, particles originating from resonance decays may follow different trends and thereby introduce modifications of the spectral shapes. The analysis of transverse momentum spectra in terms of temperature and transverse velocity is presented in Section 6.2.

**6.4.2. Anisotropic flow.** In the previous subsection we have discussed central nucleus–nucleus collisions. In this section, we focus on *non-central* collisions where the pressure gradients will, in general, not be azimuthally symmetric. The impact parameter  $\mathbf{b}$  defines a direction in the plane perpendicular to the beam, relative to which the net pressure gradients may be probed (Fig. 6.185). These pressure gradients establish a correlation between configuration and momentum space. The initial anisotropy in the transverse configuration space

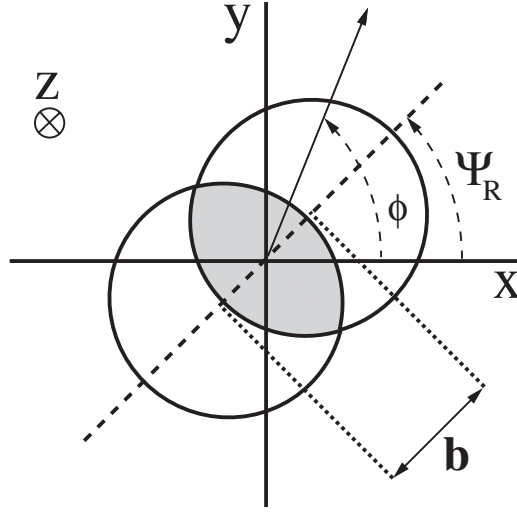


Figure 6.185. Definition of the coordinate system.

translates into an anisotropy of the transverse momentum distributions of outgoing particles, which is referred to as *anisotropic flow*. The anisotropic flow pattern depends on the collision energy, the phase-space region under consideration (rapidity, transverse momentum) and on the particle species.

The dominating flow pattern at low energies arises from a build-up of the pressure *between* the two nuclei. In such a case, the flow of the nucleons from the projectile nuclei must have its maximum in the reaction plane, the plane determined by the impact parameter and the beam axis. Furthermore, the flow of particles originating from one of the nuclei is equal in magnitude but opposite to the flow of particles from the other nucleus. This kind of collective motion is called *directed flow* (see Fig. 6.184(c)). In fixed-target experiments the directed flow of the projectile remnants is defined as positive. In collider experiments it is desirable to adopt an equally arbitrary (but consistent) convention that directed flow of *forward*-going nucleons is taken to be positive. Directed flow can be large at low energies but the velocity of the incoming nuclei at ultra-relativistic energies is such that most of the available energy flows in the longitudinal direction rather than in the transverse plane. As a result, the directed flow is significantly reduced at high energies.

At ultra-relativistic energies most of the particles are *produced* in the interaction volume and can exhibit additional flow patterns. The momentum tensor of these particles can be visualized in the transverse plane as an ellipse with the principal axis either parallel or perpendicular to the reaction plane (see Fig. 6.184(b)). The corresponding dominant flow pattern is called *elliptic flow*.

A convenient way of characterizing the various patterns of anisotropic flow is to use a Fourier expansion of the triple differential invariant distributions [501]:

$$E \frac{d^3 N}{d^3 \mathbf{p}} = \frac{1}{2\pi} \frac{d^2 N}{p_t dp_t dy} \left\{ 1 + 2 \sum_{n=1}^{+\infty} v_n(p_t, y) \cos[n(\varphi - \Psi_R)] \right\}, \quad (6.38)$$

where  $\varphi$  and  $\Psi_R$  are the particle and reaction-plane azimuths in the laboratory frame, respectively. The sine terms in such an expansion vanish due to reflection symmetry with

respect to the reaction plane. The Fourier coefficients in Eq. (6.38) are given by

$$v_n(p_t, y) = \langle \cos[n(\varphi - \Psi_R)] \rangle, \quad (6.39)$$

where the angular brackets denote an average over the particles in the  $(p_t, y)$  bin under study. These Fourier coefficients also depend on the particle type. With this parametrization, directed (elliptic) flow is quantified by the first (second) harmonic parameter  $v_1$  ( $v_2$ ). Flow analysis in ALICE should be able to yield, or at least set upper bounds on, the values of the next even coefficients  $v_4, v_6, v_8$ , in several windows of  $p_t$  and  $y$ . Various methods can be used to estimate the  $v_n$  coefficients, as described in the next subsection. In the following, we use azimuths measured in the laboratory frame instead of with respect to the reaction plane.

*6.4.3. Methods of anisotropic flow measurement.* The importance of obtaining accurate measurements of anisotropic flow has led to the development of a wealth of analysis methods, each of which has its advantages and limitations. In this subsection, we shall briefly review these methods. The first procedure includes an estimate, event-by-event, of the true reaction plane (the ‘event-plane’). The flow coefficients are determined by correlating the azimuths of the outgoing particles with that event-plane, Section 6.4.3.1. A less intuitive approach, which does not require any approximation of the reaction plane but allows a much easier handling of detector inefficiencies, is described in Section 6.4.3.2. Finally, we shall discuss two new methods that use a more contrived mathematical apparatus than the previous two but remedy some of the limitations of the two-particle correlation methods, Section 6.4.3.3. In Section 6.4.3.4 we present a short comparison of the methods.

Let us, however, first introduce an important distinction: throughout this Section we shall emphasize the difference between the actual flow *value*  $v_n$ , as would be obtained from an ideal measurement or a theoretical calculation, and flow *estimates* which are the outcomes of a given analysis procedure aiming at measuring  $v_n$ . These flow estimates will be denoted by  $v_n\{\dots\}$ , where the label between curly brackets stands for the specific method used to derive the estimate. We shall see in the following discussions that the different estimates of an identical flow value may differ from each other, as well as from the true  $v_n$ . This is either because of a bias from physical effects unrelated to anisotropic flow (‘non-flow effects’) or because of features of the flow signal itself. Improved understanding of these possible discrepancies between estimates and actual flow values represents an important progress made in the past few years; it is now clear that much can be learned from using different methods of measurement and comparing the results.

#### 6.4.3.1. Event-plane based methods of flow analysis

*Determination of the event plane.* Since anisotropic flow is a correlation between the direction of outgoing particles and the direction of the impact parameter in the event, as is expressed mathematically in Eq. (6.39), it seems most natural to study flow by reconstructing the reaction plane. Accordingly, the first methods developed proceed by first determining in each event an estimate of the reaction plane, the so-called *event plane*, whose azimuth we shall denote by  $\Phi_R$ . It should be noted that even in the most favorable case  $\Phi_R$  differs from the reaction-plane azimuth  $\Psi_R$ , the difference between both angles being only known on a statistical basis. For an apparatus with large azimuthal coverage the uncertainty on  $\Phi_R - \Psi_R$  depends not so much on the angular resolution of the apparatus as on the magnitude of the flow and on the number of the observed particles (and possibly their momenta, if measured). This means that experiments which do not measure the remnants of the nuclei or have their acceptance constrained to the central rapidity region may have difficulties

determining the event plane corresponding to directed flow, which is weak within their phase-space coverage. (Correspondingly, measuring  $v_1$  is a complicated task for such experiments.) In these conditions, it is still possible to determine a preferred direction in the event, namely the direction of the principal axes of the momentum-tensor ellipse, provided that the elliptic flow is sizable.

When a sizable amount of directed flow is present, a straightforward method for the determination of the event plane was devised by Danielewicz and Odnyc in 1985 for low-energy nuclear collisions [502]. Here the vector sum of all (or some selection of) the particles is computed separately in the forward and backward hemispheres, which gives experimental measures of the event-plane azimuth  $\Phi_R$ . The generalization to cases where only elliptic flow is present was introduced in Refs. [495, 503, 504] and further extended in Refs. [143, 505]. In this way one can define an *event flow vector*  $\mathbf{Q}_n$  for each harmonic  $n = 1, 2, \dots$  of the anisotropic flow

$$Q_x \equiv \sum_i w_i \cos(n\varphi_i) \equiv Q_n \cos(n\Phi_R), \quad (6.40)$$

$$Q_y \equiv \sum_i w_i \sin(n\varphi_i) \equiv Q_n \sin(n\Phi_R), \quad (6.41)$$

where the sums run over the particles used for the event-plane determination. The  $w_i$  are *weights* which are selected so as to ensure a maximum resolution [506] (see also Ref. [507]). The event-plane azimuthal angle  $\Phi_R$  can be derived modulo  $2\pi/n$  from Eqs. (6.40) and (6.41).

As long as the colliding nuclei are not polarized, any ensemble of events should have randomly distributed azimuthal angles of the reaction planes. This provides a useful check of detection and analysis biases: the reconstructed event planes (and also the inclusive particle distributions) must be randomly oriented in azimuth. A straightforward detector-induced bias is a non-uniform azimuthal coverage which can easily be corrected for as long as the non-uniformities are small. Procedures aiming at flattening the event-plane azimuthal distribution can be found in Refs. [139, 143]. This procedure corrects for acceptance and for possible track density effects (inefficiencies) if they do not depend on the reaction-plane angle.

*Correlating particle azimuths with the event plane: standard method.* The standard method [143, 505] correlates the azimuthal angles  $\varphi$  of the particles with an estimated event plane to obtain the coefficients of a Fourier expansion Eq. (6.38) in the plane transverse to the beam. Technically, one computes the average  $\langle \cos[p(\varphi - \Phi_R)] \rangle$  over the particles (possibly of a given type and with definite transverse momenta and rapidities) in all events. Here  $\Phi_R$  has been determined, separately for each event, from Eqs. (6.40) and (6.41). To avoid trivial autocorrelations one usually excludes the particle whose flow one wants to study from the event flow vector definition;  $\Phi_R$  might thus (slightly) vary within a given event.

The flow estimates are computed by dividing the average obtained above by a number that accounts for the so-called *event-plane resolution*, that is, for the statistical difference between the event and reaction planes,

$$v_p\{\text{EP}_n\} = \frac{\langle \cos[p(\varphi - \Phi_R)] \rangle}{\langle \cos[p(\Phi_R - \Psi_R)] \rangle}. \quad (6.42)$$

Procedures to derive the resolution from experimental data are given in Refs. [143, 505]. In the most common procedure each event is randomly divided into two statistically equivalent sub-events, each of which are assumed to retain the same flow properties as the whole event.

It should be noted that the harmonic  $p$  in Eq. (6.42) may be different from  $n$  in Eqs. (6.40) and (6.41), with the restriction that  $p$  be a multiple of  $n$ . At ultra-relativistic energies in particular, the most easily measured event plane is that of the second harmonic ( $n = 2$ ) which allows one to obtain the elliptic flow estimate  $v_2\{\text{EP}_2\}$ , as well as estimates of the higher even harmonics  $v_4\{\text{EP}_2\}$ ,  $v_6\{\text{EP}_2\}$  . . . . If the first-harmonic event plane is determined, it becomes possible to obtain  $v_1\{\text{EP}_1\}$  together with independent measurements of elliptic flow and the higher harmonics  $v_2\{\text{EP}_1\}$ ,  $v_4\{\text{EP}_1\}$  and so on. However, the event-plane resolution in the denominator of Eq. (6.42) becomes less and less accurate as the relative-harmonic order  $n$  increases [505].

It should be realized that the procedure described above for analyzing anisotropic flow relies on the assumption that flow is the only, or at least the dominant, source of correlation in azimuth between particles [502]. Obviously there exist other physical sources of correlations caused by, for instance, global momentum conservation, quantum interference between identical particles, kinematic correlations between the daughters of a decaying particle and correlations between particles belonging to a same (mini)jet. The possible bias from these non-flow effects was evidenced at SPS energies in Refs. [508, 509] and at RHIC energies in Ref. [510]. An exact procedure to correct for the effect of global momentum conservation, which affects only the measurement of directed flow, is given in Ref. [511] and is used in an analysis of NA49 data. There is however no rigorous way to safeguard this method against all other possible sources of non-flow effects. As it stands, the influence of these non-flow contributions should be included, as best as possible, in the systematic error.

**6.4.3.2. Pair correlation-function method.** Besides the methods based on an event-plane determination described above, it has long been known that anisotropic flow can also be measured *without* first estimating the azimuth of the reaction plane [512]. The underlying idea is that, since all particles are correlated to the reaction plane, they are also indirectly correlated to each other. One may thus write

$$\begin{aligned}
 \langle \cos[n(\varphi_1 - \varphi_2)] \rangle &= \langle \cos[n(\varphi_1 - \Psi_R + \Psi_R - \varphi_2)] \rangle \\
 &= \langle \cos[n(\varphi_1 - \Psi_R)] \cos[n(\varphi_2 - \Psi_R)] \rangle \\
 &\quad + \langle \sin[n(\varphi_1 - \Psi_R)] \sin[n(\varphi_2 - \Psi_R)] \rangle \\
 &\approx \langle \cos[n(\varphi_1 - \Psi_R)] \rangle \langle \cos[n(\varphi_2 - \Psi_R)] \rangle \\
 &= v_n(p_{t1}, y_1) v_n(p_{t2}, y_2),
 \end{aligned} \tag{6.43}$$

where the angular brackets denote averages over the particles. In passing from the second to the third line we assumed that *all* (or at least most) two-particle correlations between the particles 1 and 2 are due to anisotropic flow. Symmetry with respect to the reaction plane allows us to discard the sine terms.

Equation (6.43) is the key to a method for measuring the flow coefficient  $v_n$ . Letting first both particles 1 and 2 run over the whole detector acceptance gives an estimate of the average

$$\langle v_n \rangle^2 \equiv \langle \cos[n(\varphi_1 - \varphi_2)] \rangle,$$

which we shall call *integrated flow*. Once the estimate of  $\langle v_n \rangle$  has been determined, the second step is to restrict particle 2 to a small  $(p_t, y)$  bin (and to a given particle type) while still letting particle 1 run over the whole phase space. In that case Eq. (6.43) reads

$$\langle \cos[n(\varphi_1 - \varphi_2)] \rangle = \langle v_n \rangle v_n(p_t, y)$$

so that we obtain the Fourier coefficient  $v_n(p_t, y)$ .

In practice, the procedure is to construct two-particle correlators similar to those used in interferometry studies of short-range correlations. One thus counts particle pairs within a given  $\Delta\varphi$  bin, both for pairs of particles belonging to a same event and for pairs of particles from different events. Taking the ratio gives

$$C_2(\varphi_1 - \varphi_2) \equiv \frac{N_{\text{pairs}}(\varphi_1 - \varphi_2)}{N_{\text{mixed}}(\varphi_1 - \varphi_2)}. \quad (6.44)$$

The correlator  $C_2(\varphi_1 - \varphi_2)$  is an even function of the relative angle and the coefficients of its expansion in a Fourier series are precisely the two-particle averages in the left-hand side of Eq. (6.43):

$$C_2(\varphi_1 - \varphi_2) = 1 + 2 \sum_{n=1}^{+\infty} \langle \cos[n(\varphi_1 - \varphi_2)] \rangle \cos[n(\varphi_1 - \varphi_2)]. \quad (6.45)$$

Thus, by fitting the first few terms of a Fourier expansion to the measured two-particle correlator, one actually obtains the two-particle averages  $\langle \cos(n(\varphi_1 - \varphi_2)) \rangle$  from which the integrated flow  $\langle v_n \rangle$  and  $v_n(p_t, y)$  can be estimated.

The advantage of this procedure is that the mixed event sample automatically corrects for the detector anisotropies, even when these are strong [513]. In this respect, the correlation-function method is much more robust than event-plane based approaches. On the other hand, in this method each harmonic of the azimuthal distributions is determined independently without taking into account that they are related to each other by the reaction plane. In the event plane method this provides useful consistency checks which are absent here.

Finally, we remark that the statistical uncertainties and those arising from non-flow effects are the same in the event-plane methods and in the correlation-function approach, the reason being that all these methods ultimately rely on two-particle azimuthal correlations.

**6.4.3.3. Flow analysis with cumulants and with Lee–Yang zeroes.** The sensitivity to non-flow effects in the methods of analysis described above motivated the development of new methods which make use of the fact that anisotropic flow correlates *all* particles in the event. This is in contrast to non-flow effects which typically induce few-particle correlations only. It was therefore proposed to measure flow with the help of *multi-particle* azimuthal correlations by performing a *cumulant* expansion [507, 514, 515] where the collective source of correlation can be disentangled from the others. Note that global momentum conservation, even though it involves all particles, behaves as non-flow in this cumulant expansion [516]. For instance, at the level of four-particle correlations, one can remove in a systematic way all non-flow two- and three-particle correlations, irrespective of their origin, thus keeping only the correlation due to collective flow plus some systematic uncertainty arising from genuine non-flow *four*-particle correlations. The six-particle cumulant will even be more dominated by flow since non-flow correlations of six-particles are expected to be more scarce. Since cumulants of multi-particle azimuthal correlations of increasing order are less and less biased by non-flow effects, it is desirable to perform the expansion to the largest possible order. Extending the cumulant method to infinite order yields the Lee–Yang zero method [57, 518]. The multi-particle methods are described in detail below.

*Cumulant method of flow analysis.* The actual cumulant approach proceeds in two successive steps. First, a study of  $2k$ -particle correlations ( $k \geq 1$ ) between all possible  $k$ -tuples of particles in the whole detector acceptance allows to build a cumulant, which we denote by  $c_n\{2k\}$ . Each such cumulant yields an estimate of ‘integrated flow’, the latter being defined

here as the average over events

$$V_n \equiv \left\langle \sum_j w_j \cos[n(\varphi_j - \Psi_R)] \right\rangle,$$

where the sum runs over all particles detected in each event. This is a detector-dependent quantity, representing an average weighted ‘total flow’ of particles in each event: if all events had the same multiplicity  $M$  and all particles the same flow  $v_n$ , then in the case unit weights were used,  $V_n$  would equal  $M v_n$ . (The integrated flow thus defined is actually the average over events of the projection over the reaction plane of the event flow vector  $\mathbf{Q}_n$ , see Eqs. (6.40) and (6.41).) To identify the various estimates of integrated flow derived from different cumulants, we denote them by  $V_n\{2k\}$ :

$$V_n\{2\}^2 = c_n\{2\}, \quad V_n\{4\}^4 = -c_n\{4\}, \quad V_n\{6\}^6 = \frac{c_n\{6\}}{4}, \quad V_n\{8\}^8 = \frac{-c_n\{8\}}{33}, \dots \quad (6.46)$$

Next, given an estimate of the integrated flow  $V_n$ , one can measure an estimate of flow in any harmonic  $p = mn$ , where  $m$  is an integer  $\geq 1$ . Thus, the study of  $(2k' + m + 1)$ -particle azimuthal correlations between a particle (of a given type) in a given  $(p_t, y)$  bin and  $2k' + m$  arbitrary particles in the whole detector yields an estimate of  $v_p(p_t, y)$ , denoted by  $v_p\{2k' + m + 1\}(p_t, y)$ , through the construction of cumulants  $d_p\{2k' + m + 1\}$  [514]. For instance, one can build a four-particle cumulant  $d_n\{4\}$ , which yields a flow estimate  $v_n\{4\} \equiv -d_n\{4\}/V_n\{4\}^3$ , where the four-particle estimate of integrated flow is used in the denominator although any other one could have been used as well. Note that the estimate  $v_p\{2\}$ , determined with two-particle correlations, is *a priori* consistent with the value given by the two-particle methods of the previous two subsections.

In practice, the most appropriate way to implement this method is to build a generating function [514]:

$$G_n(z) = \left\langle \prod_{j=1}^M [1 + w_j (z e^{-in\varphi_j} + z^* e^{in\varphi_j})] \right\rangle, \quad (6.47)$$

where the angular brackets denote an average over events,  $z$  is a complex variable and  $z^*$  its complex conjugate. The cumulants we want to measure are in fact the coefficients of the successive powers of  $|z|^{2k}$  in a series expansion of the logarithm of  $G_n$ . After computing the function for a set of points in the complex plane around the origin  $z = 0$ , one can merely take the logarithm at each of these points and interpolate the successive derivatives of  $\ln G_n$ , to obtain the cumulants  $c_n\{2k\}$  which, in turn, yield estimates of integrated flow  $V_n$ . The derivation of the cumulants for measuring  $v_p$  is also conveniently done through a generating-function formalism.

An advantage of using this formalism is that the generating functions automatically involve all possible particle  $k$ -tuples when building the  $k$ -particle cumulants: one thus minimizes the statistical uncertainty on the flow estimates, which is the main limitation of the method (see below). Moreover, the formalism automatically removes spurious non-flow correlations arising from detector inefficiencies (i.e. non-physical correlations), which are tedious to deal with in any other implementation of the method. Finally, the computation of a single generating function gives access to all cumulants at once and thus to different independent flow estimates. This gives an important cross check of the analysis. (Note, however, that extracting higher and higher order cumulants is admittedly tedious and requires more and more interpolation points.)

Let us mention another method, which also makes use of cumulants, although with a much more specialized scope than the one we just discussed, since it was devised with the

single purpose of making measurements of directed flow  $v_1$  at ultra-relativistic energies [515]. It relies on a study of *three*-particle correlations (and is thus free of the bias from two-particle non-flow effects) which involve both  $v_1$  and  $v_2$ :

$$\langle \cos(\varphi_1 + \varphi_2 - 2\varphi_3) \rangle \simeq (v_1)^2 v_2, \quad (6.48)$$

where  $\varphi_1$ ,  $\varphi_2$ , and  $\varphi_3$  denote the azimuths of three particles belonging to the same event. The brackets denote an average over triplets of particles in a given event and then over events. Measuring the three-particle average given above (or, better, the corresponding cumulant, using a generating-function formalism [515]) and using a previously derived estimate of  $v_2$ , an estimate of directed flow is obtained, denoted by  $v_1\{3\}$ . As shown in Ref. [515], this method of  $v_1$  extraction is especially well suited to SPS, RHIC and LHC energies where we are in the situation that  $v_2$  is large (and thus well measured) and  $v_1$  is (expected to be) small and not well measured by two-particle methods or cumulants. Indeed, in this way the first measurement of directed flow was obtained at RHIC by the STAR Collaboration [138].

Finally, in both methods, the effect of detector anisotropies is to modify the relations between cumulants and flow. For example, the four-particle cumulant and the corresponding flow estimate should no longer be related by  $v_n\{4\} = -d_n\{4\}/V_n^3$ , but by  $v_n\{4\} = -\alpha d_n\{4\}/V_n^3$  where  $\alpha$  is some (detector-dependent) coefficient which can be either computed analytically or determined from Monte Carlo simulations.

*Analysis of anisotropic flow with Lee–Yang zeroes.* Let us consider a generating function, closely related to that introduced above,

$$G^\theta(r) \equiv \left\langle \prod_{j=1}^M [1 + ir w_j \cos(n(\varphi_j - \theta))] \right\rangle, \quad (6.49)$$

where  $r$  is a real positive variable,  $0 \leq \theta < \pi/n$  an angle and the  $w_j$  are the same weights as in Eq. 6.47. The product runs over all particles in an event and the average denoted by the angular brackets is over events. To see the relevance of this function, assume first that there is no collective effect so that the system actually consists of independent subsystems. The product can then be factorized into a product over these subsystems (which we assume to be equivalent), to obtain, after averaging,

$$G^\theta(r) = [G_{\text{sub}}(r)]^N,$$

where  $N$  is some number proportional to the multiplicity  $M$ . It follows (i) that the zeroes of  $G^\theta$  are the same as those of the subsystem function  $G_{\text{sub}}$  and (ii) that the positions of the zeroes of  $G^\theta$  are independent of the system size (multiplicity). On the other hand, in the presence of collective flow, the generating function can no longer be factorized and one can show [517] that the positions of its zeroes (that closest to the origin in particular) change when the multiplicity increases. In other words, the behaviour of the zeroes reflects the presence or absence of collective flow in the system.

This is in close similarity to the behaviour of the zeroes of the grand partition function in statistical physics. It was shown by Lee and Yang [519, 520] that in the vicinity of a phase transition, which induces long-range collective effects in the system, the zeroes of the partition function vary with the system size, coming closer to the origin as the size increases. Far away from transitions, on the other hand, the position of the zeroes does not depend on the size of the system provided that collective effects are absent.

The position of the first zero of  $G^\theta$  is thus directly related to the presence (and magnitude) of anisotropic flow in the system. Referring the reader to Ref. [518] for further details, let us just briefly lay-out the method for measuring flow with Lee–Yang zeroes. The first step is to

compute  $G^\theta(r)$ , Eq. (6.49) for various values of  $\theta$ , and  $r$ , so as to find for each  $\theta$  the first minimum  $r_0^\theta$  of the modulus  $|G^\theta|$ . This first minimum (which is a good approximation of the first zero) then yields an estimate of the integrated flow  $V_n$  defined above, through

$$V_n^\theta\{\infty\} \equiv \frac{j_{01}}{r_0^\theta}, \quad (6.50)$$

where  $j_{01} = 2.40483$ . The estimate  $V_n^\theta\{\infty\}$  is then used to obtain estimates  $v_n^\theta\{\infty\}$ ,  $v_{mn}^\theta\{\infty\}$  of the anisotropic flow coefficient  $v_n(p_t, y)$  and of the higher harmonics  $v_{mn}(p_t, y)$ , through the computation of a function at  $r_0^\theta$ . Note that using several values of  $\theta$  allows one to derive several flow estimates for a given harmonic, which provides a useful cross-check.

#### 6.4.3.4. Method comparison

*Statistical and systematic uncertainties.* In general, the size of the statistical errors depends on the number of events, the average multiplicity and the magnitude of the flow. This is characterized by the resolution parameter  $\chi$ , which is roughly equal to  $v_n$  multiplied by the square root of the average event multiplicity. For the differences between the various methods a detailed comparison can be found in Ref. [517]. For the large values of  $\chi$  that can be expected at LHC energies, the uncertainties on flow estimates from four-, six-particle cumulants and from Lee–Yang zeroes are the same.

It is impossible to give a complete list of the possible systematic uncertainties which can enter in the determination of the reaction plane and the measurement of the anisotropic flow. We will therefore discuss a few found to be significant at RHIC energies and which might become even more important at the LHC.

Non-flow correlations, e.g. from jets, affect the determination of flow. The introduced bias on  $v_2$  is larger for two-particle methods (including the standard event-plane method) than for the multi-particle methods. To illustrate this we have generated 20000 events with  $500 \pm 20$  particles per event, distributed with a RHIC-inspired  $v_2(p_t)$ . A mock-up non-flow correlation was introduced by emitting 25%, 50%, 75% or 100% of the particles in pairs (resp. quadruplets) where both (all four) particles of the pair (quadruplet) get the same transverse momentum and azimuth. Figure 6.186(a) shows that in the case of no non-flow correlations all the methods, including the ones based on two-particles, reproduce the generated flow. With non-flow contributions included, these two-particle correlation methods fail to reproduce the generated flow as shown in Fig 6.186(b). While the non-flow contribution in these generated events is constant as function of transverse momentum the difference between the true  $v_2$  and the reconstructed  $v_2\{2\}$  becomes  $p_t$  dependent. The higher order cumulants and the Lee–Yang zeroes do, also in this case, reproduce the generated flow. Table 6.43 shows the reconstructed average flow values for the simulations with various non-flow contributions. As expected, the two-particle estimates  $v_2\{2\}$  differ from the generated input  $v_2$  while  $v_2\{4\}$ ,  $v_2\{6\}$  and  $v_2\{\infty\}$  are in much better agreement.

Closely related to non-flow correlations are those from track merging and splitting due to the granularity of the detector. This introduces a two-particle correlation which does not affect higher order cumulants or the Lee–Yang zero analysis.

It was realized that yet another phenomenon can induce discrepancies between flow estimates from different methods, namely flow fluctuations. Such fluctuations may arise either from impact parameter variations within an experimental centrality bin or from fluctuations in the flow signal itself at fixed impact parameter. Such fluctuations will induce a shift of the flow estimates with respect to the true flow value and this shift differs from method to method. For instance, estimates of  $v_n$  from two-particle methods will be (slightly) larger (in absolute value) than  $v_n$  itself, while the fourth-order cumulant estimate  $v_n\{4\}$  will be smaller [521].

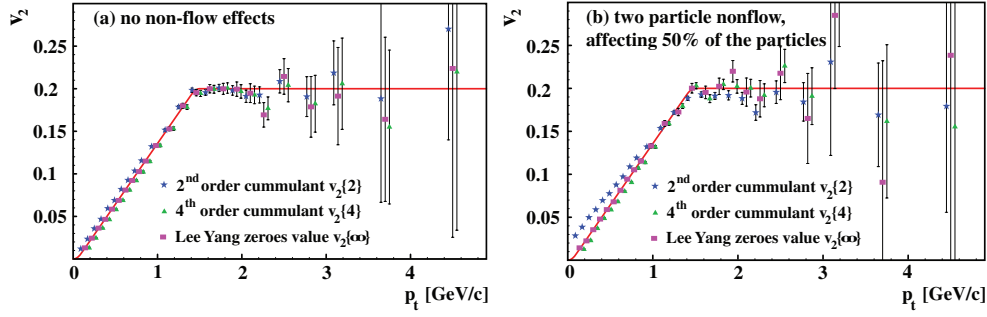


**Figure 6.186.**  $v_2(p_t)$  reconstructed with different methods (cumulants of two- and four-particle correlations and Lee–Yang zeroes): (a) in the absence of non-flow effects and (b) when 50% of the particles are emitted in pairs. The solid line represents the simulated  $v_2(p_t)$ .

**Table 6.43.** Values of the average elliptic flow reconstructed with different methods of analysis (cumulants of two-, four- and six-particle correlations, and Lee–Yang zeroes), for an input value  $v_2 = 0.0653$ .

non-flow effects	$v_2\{2\}$	$v_2\{4\}$	$v_2\{6\}$	$v_2\{\infty\}$
none	$0.0653 \pm 0.0002$	$0.0654 \pm 0.0002$	$0.0652 \pm 0.0002$	$0.0654 \pm 0.0002$
25% pair-wise	$0.0712 \pm 0.0002$	$0.0656 \pm 0.0002$	$0.0655 \pm 0.0002$	$0.0656 \pm 0.0003$
50% pair-wise	$0.0748 \pm 0.0002$	$0.0656 \pm 0.0003$	$0.0656 \pm 0.0002$	$0.0658 \pm 0.0003$
75% pair-wise	$0.0772 \pm 0.0002$	$0.0670 \pm 0.0002$	$0.0657 \pm 0.0002$	$0.0659 \pm 0.0004$
100% pair-wise	$0.0793 \pm 0.0002$	$0.0658 \pm 0.0002$	$0.0653 \pm 0.0003$	$0.0654 \pm 0.0004$
100% quadruplets	$0.1013 \pm 0.0002$	$0.0667 \pm 0.0005$	$0.0660 \pm 0.0006$	$0.0674 \pm 0.0013$

Figures 6.187(a) and (b) show the elliptic flow  $v_2$  of charged particles as measured at RHIC by the STAR Collaboration in  $\sqrt{s_{NN}} = 130$  GeV collisions, both as a function of transverse momentum and of centrality. The second-order cumulant is the true two-particle correlation which is maximally affected by non-flow effects. It coincides to a large extent with the results from the conventional event-plane based method. However, the cumulant to fourth-order is significantly lower. Following the previous discussions, this could be due to substantial non-flow contributions, but also to significant fluctuations of  $v_2$ . However, it is clear that the difference between the standard method and the fourth-order cumulant is non-negligible (about 15%). Differences of somewhat different relative magnitude have also been observed at lower energies [139, 522, 523].

As we already have remarked in Section 6.4.2 it is important, for a good understanding of the systematic errors, to measure flow with the various available techniques. Only then a reliable comparison to theory can be made.

**6.4.4. Results on flow from lower energies.** Anisotropic flow has been measured from GANIL/MSU up to RHIC energies [137, 138, 205, 362, 492, 493, 513, 524–541]. At RHIC, the anisotropic flow coefficients  $v_1$ – $v_8$  have been measured in detail as a function of rapidity, transverse momentum and particle species. This subsection will give a short summary and current interpretation of these results.

**6.4.4.1. Directed flow.** Directed flow is the first harmonic  $v_1$  of the Fourier expansion of the azimuthal particle distribution. At AGS and SPS energies it is an almost linear function of

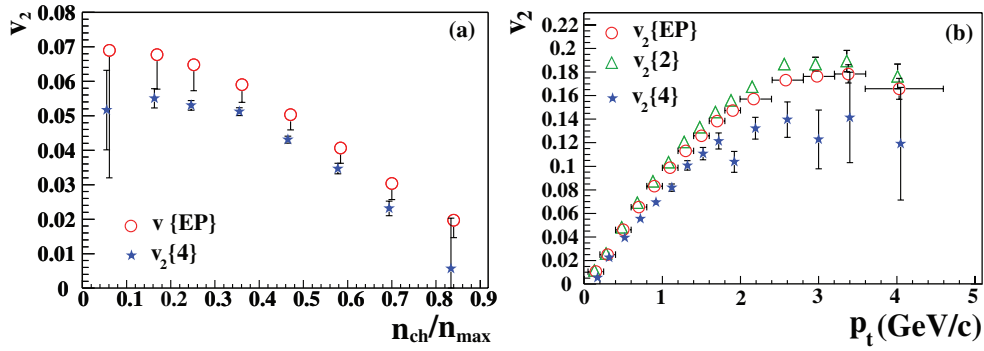


**Figure 6.187.** (a) Charged particle elliptic flow as a function of centrality as measured by STAR. The circles show the conventional  $v_2$  with the estimated systematic uncertainty due to non-flow and the stars show the fourth-order cumulant  $v_2$ . (b) STAR elliptic flow versus transverse momentum (minimum bias) from the conventional method (circles), from the second-order cumulant method (triangles), and from the fourth-order cumulant method (stars).

rapidity so that at these energies the slope  $dv_1(y)/dy$  at mid-rapidity is often used to quantify the strength of directed flow.

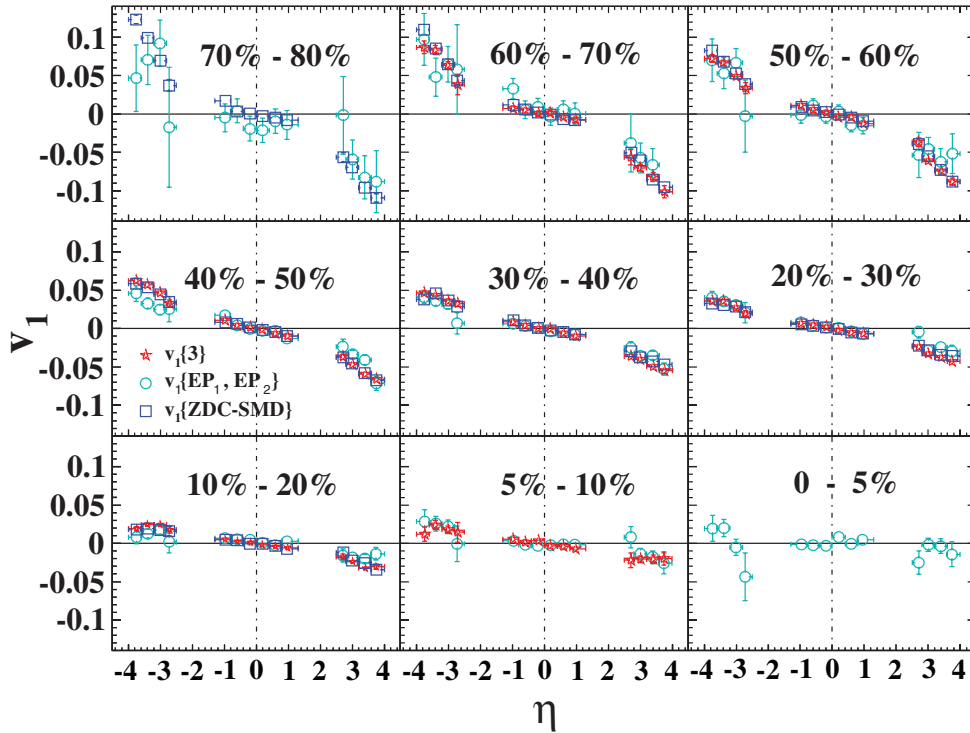
At higher energies this linear dependence is expected to break-down; at mid-rapidity the directed flow is predicted to be very small and it is possible that the slope at mid-rapidity has a sign opposite to that in the beam rapidity region. This so-called ‘wiggle’, whereby the directed flow changes sign three times outside the beam fragmentation region, is very sensitive to the equation of state [542–545]. Using a hydrodynamic approach it is observed in Refs. [543, 545] that this wiggle structure only appears under the assumption of a QGP equation of state, thus becoming a signature of the QGP phase transition.

Figure 6.188 shows the charged particle directed flow measured at RHIC for 9 different centralities in Au–Au collisions at  $\sqrt{s_{NN}} = 62$  GeV [541]. These measurements show that the directed flow observed at mid-rapidity is very small for all centralities, as predicted. The wiggle structure, however, is not observed.

With detectors which only cover mid-rapidity it becomes practically impossible to measure directed flow due to its small magnitude. At RHIC energies, however, use is made of the fact that the elliptic flow is large (as shown in the next section) to determine directed flow as described in the methods section (see Eq (6.48)). The open circles in Fig. 6.188 use elliptic flow from the reaction plane method while the stars use elliptic flow from  $v_2\{4\}$ . It was not possible to determine  $v_2\{4\}$  for the most central and most peripheral datasets. Directed flow is large at beam rapidity so that the reaction plane can be determined with a segmented forward calorimeter (the ZDC–SMD). Measurements of  $v_1$  using this approach are shown by the open squares in Fig. 6.188.

Comparing the results from the three methods shows that they agree within errors and that the measurements obtained with the ZDC–SMD have the smallest statistical uncertainties, in particular for the more peripheral collisions. Provided that directed flow at beam rapidities is also sizeable at the LHC it is expected that segmented zero-degree calorimetry in ALICE can be used to determine the reaction plane (see Section 6.1).

**6.4.4.2. Elliptic flow.** One of the most exciting first results from RHIC was the observation of strong elliptic flow in Au–Au collisions at  $\sqrt{s_{NN}} = 130$  GeV [534]. Generally speaking, large values of elliptic flow are considered to be signs of hydrodynamic behaviour as was first



**Figure 6.188.** Directed flow  $v_1$  of charged particles in Au–Au collisions at  $\sqrt{s_{NN}} = 62$  GeV as function of pseudorapidity and centrality [541]). Different symbols indicate different methods (see text).

put forward by Ollitrault [495]. In hydrodynamics the elliptic flow originates from a larger pressure gradient in the direction of the reaction plane than perpendicular to it. Of course, hydrodynamics is an idealization which assumes a zero mean free path and complete local thermalization after a small thermalization time  $\tau_0$ . Cascade models are another approach which can describe the development of anisotropic flow, see e.g. Ref. [546]. Such models give anisotropic flow values which are always smaller than those from hydrodynamic models.

*Elliptic flow versus collision energy.* Figure 6.189 shows the measured elliptic flow value as a function of beam energy [533, 547–552]. A clear increase in the magnitude of  $v_2$  is observed. Hadron cascade model calculations do not, for this centrality, generate  $v_2 > 0.02$  even at the highest beam energy. It follows that the measured elliptic flow above AGS energies is under-predicted by hadron cascade models like RQMD [553], for example. This shows that the effective equation of state of a hadron cascade is too soft. One reason for this might be that the rescattering between hadrons is too much delayed by their formation time [554]. This already shows that interactions *early* in the high density phase are important since elliptic flow has its origin in the amount of rescattering and the eccentricity of the collision zone. The latter is maximal at the time of overlap of the colliding nuclei. Expansion of the source, pressure driven or free streaming, will diminish this eccentricity because the driving force for elliptic flow disappears as the source becomes spherically symmetric (‘self quenching’). All this leads to the conclusion that elliptic flow is one of the signatures of the early phase of the collision [546, 555].

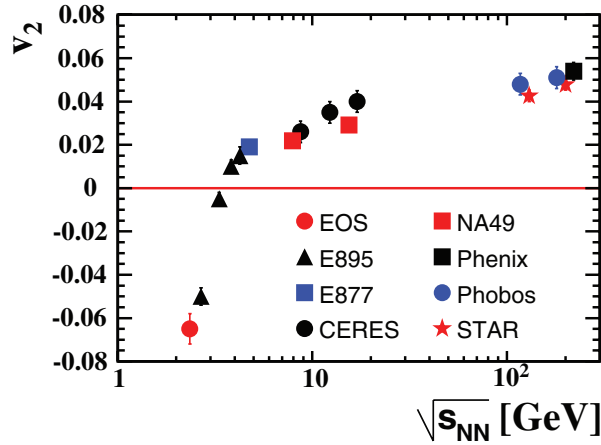


Figure 6.189. Elliptic flow as a function of  $\sqrt{s_{NN}}$ , from AGS to the highest RHIC energies.

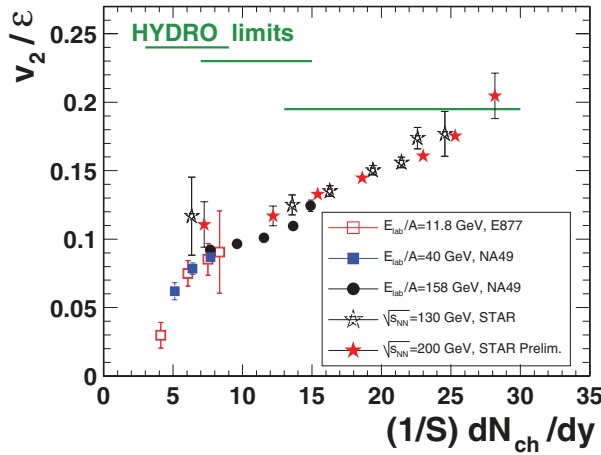


Figure 6.190. Elliptic flow divided by the initial eccentricity of the collision as a function of the multiplicity density.

Parton cascade models are not constrained by large formation times and calculations show that they are able to describe the large values of elliptic flow observed at RHIC [556–558]. This also holds for mixed mode models like QGSM [559]. However, the parton cascade models need, in order to describe the data, parton–parton cross sections which are an order of magnitude larger than calculated in pQCD although the required interaction cross sections can be significantly reduced when a coalescence mechanism is assumed for particle production.

It is observed that the measured elliptic flow values at RHIC energies are consistent with those from hydrodynamical model calculations [561]. So far this has been the strongest indication that the system created at RHIC approaches local thermal equilibrium.

Figure 6.190 shows the measured value of  $v_2$  divided by the spatial eccentricity  $\epsilon$  of the collision as a function of the multiplicity density. The spatial eccentricity is defined by

$$\epsilon = \frac{\langle y^2 - x^2 \rangle}{\langle y^2 + x^2 \rangle},$$

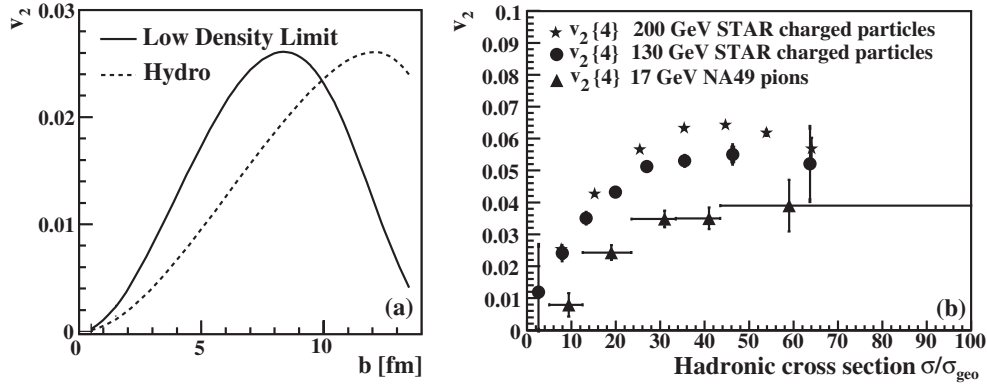


**Figure 6.191.** (a) Elliptic flow versus centrality from the low density limit (full curve) or hydrodynamics (dashed curve). Figure adapted from Ref. [549]. (b) Elliptic flow as function of centrality from NA49 at the SPS and at two RHIC energies from STAR [539].

where  $x$  and  $y$  are the spatial coordinates in the plane perpendicular to the collision axis. The brackets  $\langle \rangle$  denote an average weighted with the initial density. The quantity  $S = \pi \sqrt{\langle x^2 \rangle \langle y^2 \rangle}$  is a measure of the initial transverse size of the collision region. The measured values of  $v_2/\varepsilon$  fall approximately on a single curve, independent of beam energy or impact parameter. This curve shows an approximately linear increase from AGS to the highest RHIC energy. Ideal hydrodynamical model calculations, whose elliptic flow predictions rather well matched the measurements at the highest RHIC energies, show a markedly different behaviour. In hydrodynamics,  $v_2/\varepsilon$  is approximately constant as a function of centrality even though the magnitude does depend on the velocity of sound in the fluid (and thus on the different contributions from the different phases and the phase transition). The lines in the figure (so-called Hydro limits) show this constant behaviour in several energy intervals including the highest RHIC energy. The disagreement between the data and hydrodynamical calculations at lower energies is interpreted as a sign of incomplete thermalization. Indeed, models that assume a mean free path of the same order as the size of the system (the so-called low density limit) show a monotonic dependence of  $v_2/\varepsilon$  versus  $(1/S)dN/dy$  as seen in the data. One of the important questions to answer is whether this linear dependence continues into the LHC energy regime [562].

*Elliptic flow versus centrality.* Elliptic flow has its origin in the amount of rescattering and the eccentricity of the collision zone. The amount of rescattering is expected to increase with increasing centrality, while the eccentricity decreases. This combination of trends dominates the centrality dependence of elliptic flow.

Figure 6.191(a) indeed shows this characteristic dependence of elliptic flow versus centrality for both the low density and hydrodynamical limit. It is seen that the low density limit compared to hydrodynamics has the maximum elliptic flow at a smaller impact parameter [549, 560]. Figure 6.191(b) shows the measured centrality dependence of  $v_2\{4\}$  at the SPS and RHIC. It is clear that the SPS data do not constrain the position of the maximum so that these results cannot disentangle between the hydro and low density limits. At RHIC energies the maximum is found to lie in-between the low density limit and hydrodynamics [561].

*Elliptic flow versus rapidity.* It is known that particle production in the fragmentation region (i.e. close to the beam rapidity) exhibits universal scaling when plotted as a function of

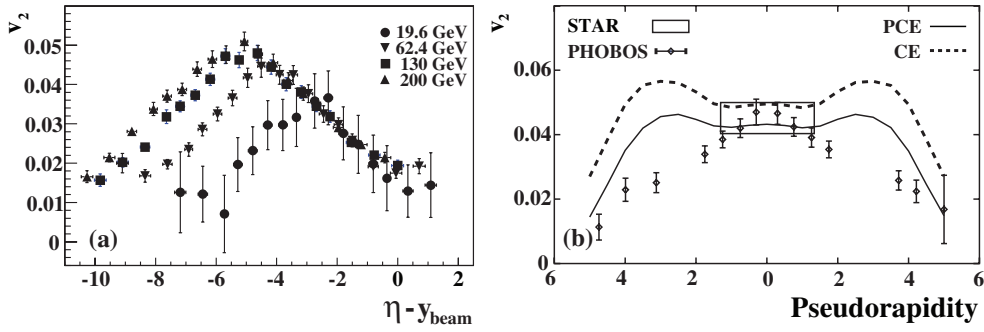


**Figure 6.192.** Left: Elliptic flow versus pseudorapidity [563]. Right: Elliptic flow versus pseudorapidity from PHOBOS [532] and STAR compared to ideal hydro calculations [564, 565].

$y - y_{\text{beam}}$  (or  $\eta - y_{\text{beam}}$ ). This observation is known as limiting fragmentation. The PHOBOS collaboration at RHIC has shown that this scaling extends over a large region of rapidity at collision energies ranging from  $\sqrt{s_{\text{NN}}} = 19.6$  GeV to 200 GeV [149]. In Fig. 6.190 we showed that the integrated elliptic flow, for a fixed centrality, is proportional to the particle production  $dN/dy$ .

Figure 6.192 (left) shows the integrated elliptic flow of charged particles for the beam energies from  $\sqrt{s_{\text{NN}}} = 19.6$  GeV to 200 GeV [563] as function of  $\eta - y_{\text{beam}}$ . This figure reveals that, similar to particle production, the integrated elliptic flow also exhibits scaling versus  $\eta - y_{\text{beam}}$ . Ideal hydrodynamical calculations predict a much broader plateau in  $v_2$  as function of rapidity as shown in Fig. 6.192 (right) [564, 565]. It follows that the agreement of the elliptic flow at RHIC with ideal hydro calculations only holds at mid-rapidity. The full and dashed curves in Fig. 6.192 (right) are results from calculations using full Chemical Equilibrium (CE) or Partial Chemical Equilibrium (PCE) in the hadron phase, respectively. While this affects the magnitude of the flow, it does not change the rapidity dependence. A description using hydrodynamics until chemical freeze-out followed by a hadron cascade until kinetic freeze-out does produce a similar dependence as observed in the data [566–568].

*Elliptic flow versus transverse momentum.* Elliptic flow as a function of transverse momentum is sensitive to the evolution and freeze-out conditions of the created system. For charged particles, shown in Fig. 6.193, the elliptic flow increases almost linearly as function of  $p_t$  reaching values of about 0.15 at large  $p_t$ . At low transverse momenta, the dependence is well described by hydrodynamics as shown by the full line in Fig. 6.193. However, above 1 GeV/c the observed dependence starts to deviate from ideal hydrodynamics. The position of the onset of the deviation from ideal hydrodynamics and its magnitude are thought to constrain the shear viscosity of the fluid [569]. At high- $p_t$  the observed elliptic flow might be related to parton energy loss in the medium [553, 570, 571] and may thus provide a constraint on the initial gluon density. The dashed lines in Fig. 6.193 show predictions based on energy-loss calculations in a static medium [572]; in an expanding medium the inferred gluon densities will be different.

Figure 6.194 shows  $v_2$  for identified particles as function of transverse momentum. At low  $p_t$  the elliptic flow depends on the mass of the particle with  $v_2$  at a fixed  $p_t$  decreasing with increasing mass. This dependence is expected in a scenario where all the particles have a common radial flow velocity [573, 574] as shown by the full curves in Fig. 6.194 from ideal hydrodynamics. A more detailed comparison, for different equations of state, is shown in Fig. 6.195 and will be discussed later. In ideal hydrodynamics the mass ordering in  $v_2$  persists

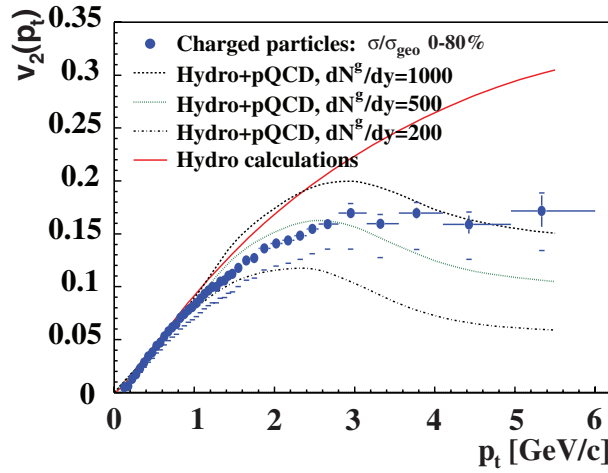


**Figure 6.193.** Elliptic flow versus transverse momentum for charged particles [538]. The solid line is a hydro model calculations and the dashed lines show hydro+pQCD calculations for various gluon densities [572].

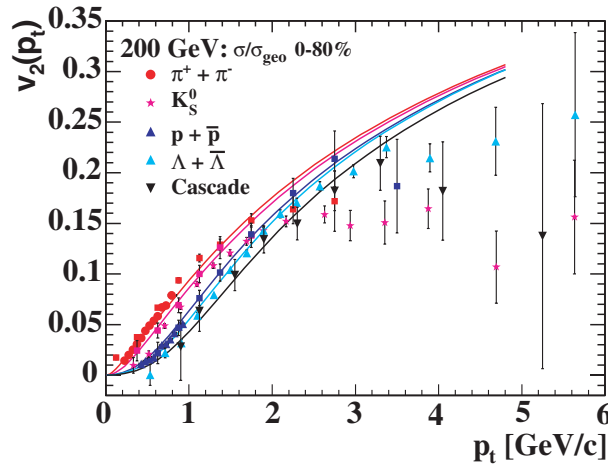


**Figure 6.194.** Elliptic flow versus transverse momentum for various particle species [530, 540]. The solid lines are ideal hydrodynamical model calculations for these particle species [216].

up to large  $p_t$ , although less pronounced because the  $v_2$  of the different particles start to approach each other. It is seen that at higher  $p_t$  the measurements start to deviate significantly from hydrodynamics for all particle species, and that the observed  $v_2$  of the heavier baryons is larger than that of the lighter mesons. This mass dependence is the reverse of the behaviour observed at low  $p_t$ . This is not expected in hydrodynamics and is also not expected if the  $v_2$  is caused by parton energy loss (in the latter case there would, to first order, be no particle type dependence). An elegant explanation of the unexpected particle type dependence and magnitude of  $v_2$  at large  $p_t$  is provided by the coalescence picture [317, 575].

The elliptic flow of the different mass particles at low- $p_t$  can be characterized rather well by a common set of four parameters: the temperature, the mean radial flow velocity,

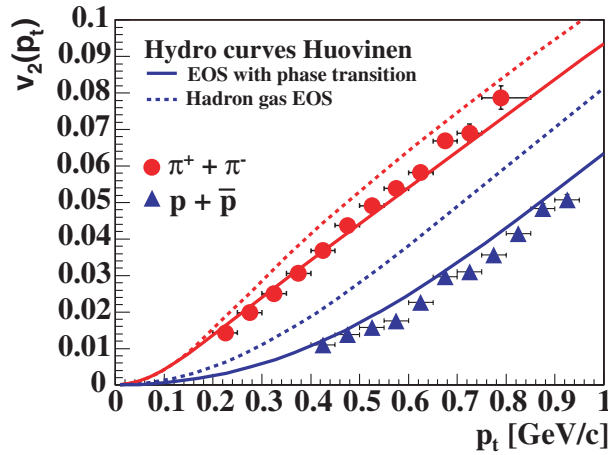


**Figure 6.195.** Elliptic flow for pions and protons + antiprotons versus transverse momentum. The lines are hydro model calculations. The full line is a calculation with an equation of state incorporating a phase transition, the dashed line is without phase transition.

the azimuthal dependence of the radial flow velocity and the source deformation [205]. In hydrodynamics, these parameters are not independent since they are related by the equation of state. While the kinetic freeze-out temperature and radial flow are constrained by the  $p_T$ -spectra of particles with different mass, the elliptic flow is sensitive to the equation of state in ideal hydrodynamics [216, 566, 567, 576].

Figure 6.195 shows the hydrodynamical model predictions of  $v_2(p_T)$  for pions and (anti-) protons for two equations of state: the full curves are for an EOS which incorporates the effect of a phase transition from a QGP to a hadron gas, the dashed curves are for a hadronic EOS without phase transition. The hydro calculations clearly predict the observed behaviour rather well with a better description of the measurements provided by the EOS incorporating a phase transition. For the pions the effect of a phase transition is less pronounced compared to the protons. The lighter (heavier) particles are more (less) affected by the temperature thus less (more) sensitive to the collective flow velocity. Therefore, low  $p_T$  measurements of particles containing heavy quarks, like the D-mesons which are abundant at LHC energies, would be very sensitive to the equation of state and to the phase transition.

The coalescence picture [304, 306, 317, 575, 577–581] which provides a possible explanation for the unexpected particle type dependence and magnitude of  $v_2$  at intermediate  $p_T$  assumes elliptic flow on the constituent quark level. In this description the elliptic flow of the most common mesons and baryons should scale with the number of constituent quarks ( $n_q$ ), provided there is no difference in flow between the u, d and s quarks near hadronization. Figure 6.196 [582] shows the  $n_q$ -scaled elliptic flow versus the  $n_q$ -scaled transverse momentum for various mesons and baryons. Above  $p_T/n_q = 1$  GeV/c such scaling is indeed observed.

**6.4.4.3. Higher harmonics.** Higher harmonics of the momentum anisotropy are expected to be small [583, 584]. More recently it was realized that at higher  $p_T$  they may become significant and that they are sensitive to the initial conditions [585]. It was shown that they depend on the equation of state [586] and in Ref. [562, 587] it is argued that  $v_4(p_T) = v_2^2(p_T)/2$  for ideal fluid behaviour. The measured  $p_T$ -integrated  $v_4$  and  $v_6$  as function of centrality are shown in Fig. 6.197. For comparison,  $v_2$  is shown in the same figure. The integrated  $v_4$  is an

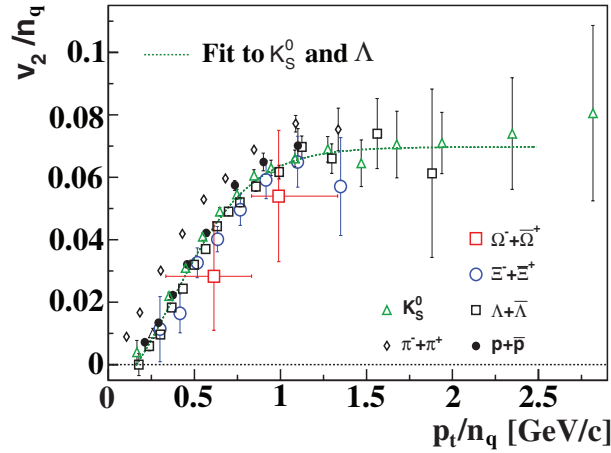


**Figure 6.196.** The elliptic flow per constituent quark versus the transverse momentum per constituent quark. The line is a parametrization of the  $K_S^0$  and  $\Lambda$  elliptic flow, from Ref. [582].

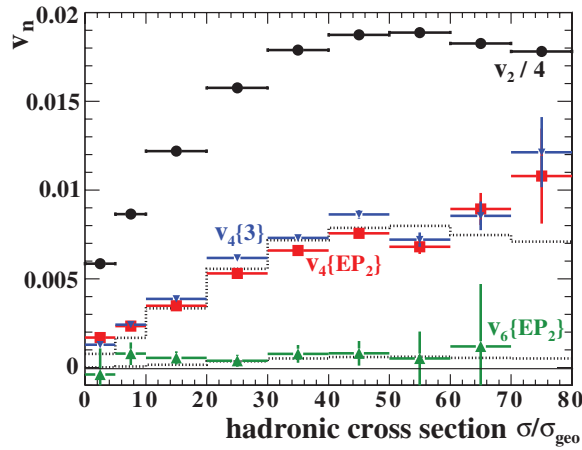


**Figure 6.197.**  $v_2\{EP\}$ ,  $v_4\{EP\}$  and  $v_6\{EP\}$  versus centrality [138]. The dotted histograms are  $1.4 \cdot v_2^{n/2}$ , where  $n$  is the corresponding harmonic. For  $v_4$  also the cumulant values  $v_4\{3\}$  are shown (triangles).

order of magnitude smaller than  $v_2$ , as expected. The higher harmonics  $v_6$  and  $v_8$  (not shown) are consistent with zero and only upper limits can be given. Figure 6.198 shows  $v_4$  and  $v_6$  as function of  $p_t$ . Indeed, as predicted,  $v_4$  becomes significant at higher  $p_t$ . Both Figs. 6.197 and 6.198 show as dotted lines and dotted histograms the dependence of the higher harmonics as calculated from the relation  $v_n \propto v_2^{n/2}$ . Both the  $p_t$  and centrality dependence for  $v_4$  as well as for  $v_6$  follow this scaling remarkably well. The proportionality between  $v_2^2$  and  $v_4$  is found to be larger than unity which is in disagreement with the value 0.5 expected for ideal fluid behaviour. Measuring the relation between  $v_2$  and the higher harmonics is of interest at the LHC because it provides a test of ideal hydrodynamic behaviour [562].

**6.4.5. Flow measurements in ALICE.** Experience from RHIC shows that among the first physics results that become available are measurements of azimuthal correlations relative to

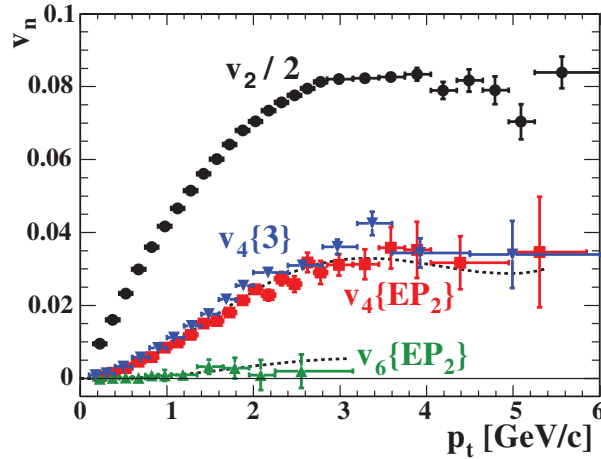


**Figure 6.198.**  $v_2\{\text{EP}\}$ ,  $v_4\{\text{EP}\}$  and  $v_6\{\text{EP}\}$  as a function of transverse momentum [138]. The lines are  $1.2 \cdot v_2^{n/2}$ , where  $n$  is the corresponding harmonic. For  $v_4$  also the cumulant values  $v_4\{3\}$  are shown (triangles).

the reaction plane. To give an indication of the relevance of such measurements we show in Fig. 6.199 model calculations of  $v_2/\varepsilon$  as function of the centre-of-mass energy  $\sqrt{s_{\text{NN}}}$  [568, 589]. Using colour glass condensate (CGC) estimates for the initial condition the flow is calculated from ideal hydrodynamics up to the kinematic freeze-out temperature of 100 MeV (full squares and upper curve). More realistic estimates are obtained by assuming hydrodynamics up to the chemical freeze-out temperature of 169 MeV followed by a hadron cascade description of the final phase (full circles). The contribution from the QGP phase (i.e. hydrodynamics up to 169 MeV) is shown by the triangles (and lower curve) in the figure. It is seen from Fig. 6.199 that at LHC energies the contribution from the QGP phase is much larger than at RHIC or SPS, and that, as a consequence, there is less uncertainty due to the detailed modeling of the hadronic phase. Theoretical calculations such as these or those in Ref. [588], as well as straight-forward extrapolations from lower energies based on particle multiplicities predict flow values of about 5–10% at the LHC. If the flow values and multiplicities at the LHC are indeed that large then the flow measurement should be relatively easy. It must be realized, however, that non-flow contributions to the azimuthal correlations like those from (mini) jets are expected to be much larger at the LHC than at RHIC and may tend to obscure the flow signal.

In the flow analysis at the LHC, it is important to have various independent estimates from different regions of phase space as argued in Section 6.4.3. The various sub-systems of the ALICE detector are well suited to this task. In the following section, the expected resolution of the event plane and elliptic flow determinations with the ALICE sub-systems are discussed. In the simulations presented here, the particle multiplicity and magnitude of the flow were varied over a wide range.

*TPC flow analysis chain.* The TPC flow analysis chain is implemented in AliRoot and contains routines which generate events with anisotropic flow, simulate the detector response, reconstruct the signal and, finally, perform the analysis of the obtained resolutions as a function of the simulation parameters.

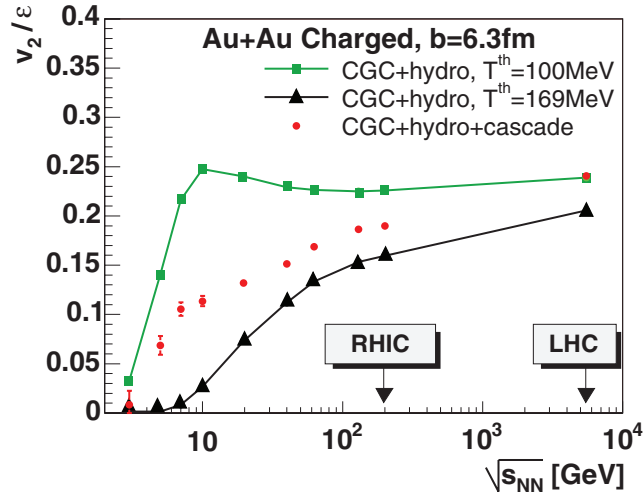


**Figure 6.199.** Theoretical predictions of  $v_2/\epsilon$  versus collision energy using colour glass condensate estimates for the initial conditions [568]. Ideal hydrodynamic expansion up to kinetic freeze-out (squares) or chemical freeze-out (triangles) is assumed. The full circles are results using a hadronic cascade model to describe the final phase after chemical freeze-out.

Events with azimuthal anisotropy are generated by GeVSim [590], which provides several options including particle generation from parametrized distributions as a function of transverse momentum and rapidity. These parametrizations are based on results from RHIC as presented in Section 6.4.4. Furthermore, it is possible to add azimuthal correlations to events generated by microscopic event generators (like HIJING) by the Flow Afterburner, see Chapter 4 of PPR Volume I [3]. The generated events are processed either through the full detector simulation and reconstruction chain or, for large statistics studies, through a fast simulation with parameterized resolutions.

The reconstruction and analysis of the signal are performed by an extension of the analysis package developed by NA49 and STAR [143, 591]. This package implements the sub-event method [143] and the cumulant method [514] as described in Section 6.4.3.3 and is designed such that identical analysis can be performed both on the generated tracks (before and after particle transport through the detector) and on the reconstructed tracks.

*Flow measurements in the TPC.* The high-statistics studies presented below were performed employing fast simulations. The fast simulation was checked by comparing the results to those from an analysis of a limited number of fully simulated and reconstructed events. The reaction plane and elliptic flow resolution were studied as a function of the event multiplicity and magnitude of  $v_2$ . The multiplicity of tracks available for analysis was varied in the range 200–5000 and the elliptic flow  $v_2$  in the range 0.04–0.10, covering the RHIC measurements as well as the expectations for the LHC.

The performance of the sub-event method was studied from a generated sample of 400 events with a multiplicity of 1000 and a  $v_2$  value of 0.06. The corresponding event plane was randomly oriented in azimuth. The difference between the generated event-plane angle and the result from the sub-event method is shown in Fig. 6.200. The r.m.s. of the distribution is found to be 11.4 degrees. In the analysis of real data the resolution is estimated from the difference in orientation of event planes determined from sub-events. Each of the sub-events contains half of the tracks of the original event so that the resolution of the event plane reconstruction

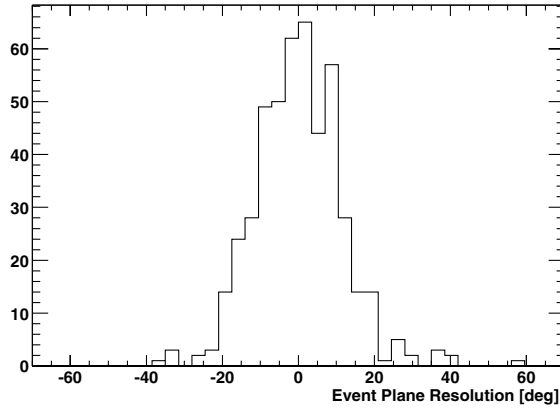


**Figure 6.200.** Difference between generated and reconstructed event plane angle for events with 1000 tracks and  $v_2 = 0.06$ .

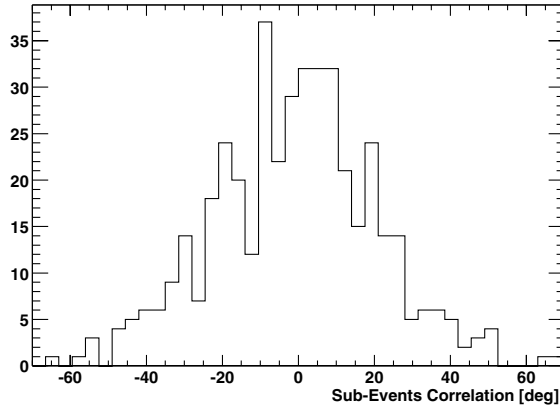


**Figure 6.201.** Difference between the orientation of the event planes of two sub-events for events with 1000 tracks and  $v_2 = 0.06$ .

is reduced by a factor of  $\sqrt{2}$ . The subtraction of the two measured angles results in another factor of  $\sqrt{2}$  as can be seen from the distribution plotted in Fig. 6.201 which is roughly two times broader than the one in Fig. 6.200.

The variation of the event plane resolution with the magnitude of  $v_2$  is plotted in Fig 6.202. For 1000 particles per event it varies between  $6^\circ$  and  $30^\circ$  for elliptic flow magnitudes between 0.1 and 0.02. The dependence of the event plane resolution on both multiplicity and flow magnitude is displayed in Fig. 6.203.

We conclude from these studies that the resolution in the event-plane angle is better than  $8^\circ$  as long as the particle multiplicity is larger than 1000 per event and the flow magnitude larger than 0.06.

More detailed information is obtained by studying the detector response on elliptic flow as function of rapidity, transverse momentum and particle type. We restrict our study to the particle type and  $p_t$  dependence because the TPC acceptance covers only two units in rapidity where elliptic flow is not expected to change significantly. Figure 6.204 shows  $v_2$  as a function of  $p_t$  from the analysis of 100 events with particle multiplicity 2000. The result reproduces well the generated transverse momentum dependence shown by the full curve in the figure. As

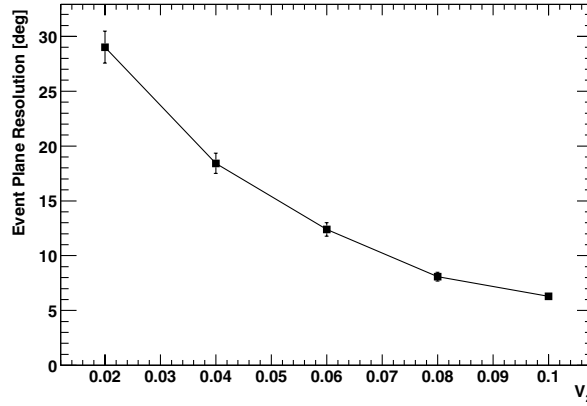


**Figure 6.202.** Event plane resolution as function of magnitude of elliptic flow for events with 1000 tracks.

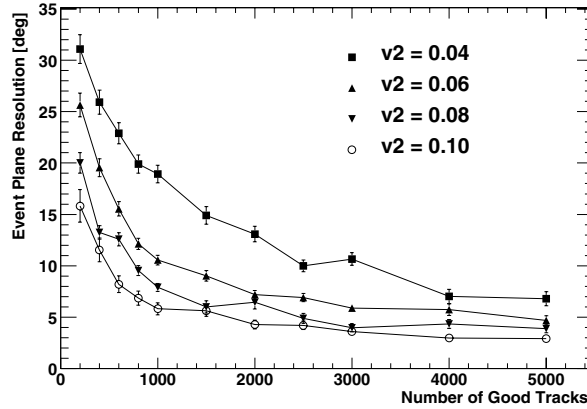


**Figure 6.203.** Dependence of the event plane resolution on multiplicity and flow magnitude.

an example of the performance for identified particles we show in Fig. 6.205 the reconstructed  $p_t$  dependence of  $v_2$  for Kaons compared to the input signal (full curve).

*Azimuthal anisotropy measurement with the PMD.* The determination of the anisotropy parameters in different rapidity regions enables a reconstruction of 3-dimensional event shapes of the emitted particles. The Photon Multiplicity Detector (PMD) is designed to measure the spatial distribution of photons in the forward region  $2.3 \leq \eta \leq 3.5$ , enabling a determination of the anisotropy within this range. The photons in the PMD originate predominantly from  $\pi^0$  decay. The decay introduces non-flow correlations and also dilutes the anisotropy present in the pions by randomizing the direction of the emitted photons. Using a fast simulation, the kinematic distributions were generated using ALICE parametrizations for  $dN/d\eta$  varying between 250 and 5000 at  $\eta = 0$ . This corresponds to a range of photon multiplicity varying between 100 and 2000 in the region  $2.5 \leq \eta \leq 3.5$  of the PMD. The simulations have been done for different scenarios corresponding to a constant flow and a  $p_t$  dependent flow which were taken to be the same for neutral and charged pions. The flow was introduced by choosing a random  $\Psi_r$  for each event and changing the uniformly generated

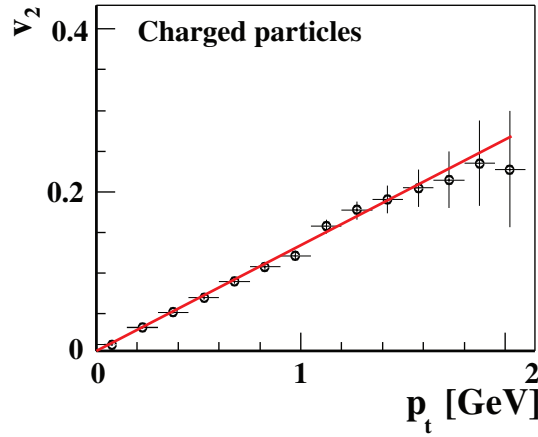


**Figure 6.204.** Elliptic flow  $v_2$  as function of transverse momentum as determined from 100 generated events.

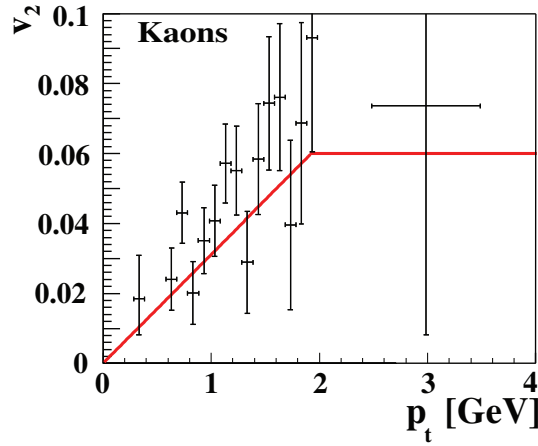


**Figure 6.205.** Elliptic flow  $v_2$  as function of transverse momentum for Kaons from the full reconstruction of 2000 generated events.

azimuthal angle of each particle in that event by  $\Delta\Phi$  where

$$\Delta\Phi = -\sum \frac{2v_n}{n} \sin n(\varphi - \Psi_r). \quad (6.51)$$

Pions were generated, with various combinations of multiplicity and constant flow, and the neutral pions were allowed to decay. The ratio of flow observed in decay photons to flow in the parent pions is seen to scale with the experimentally measurable anisotropy parameter  $\chi$ . This parameter  $\chi$  can be obtained by studying the correlation between the event plane angles of two sub-events. For a given magnitude of flow,  $\chi$  increases with the measured multiplicity [143]. This scaling can be parametrized by [592]

$$\frac{v(\gamma)}{v^{in}(\pi^0)} = \frac{a}{(\chi - b)^2} + c \quad (6.52)$$

and is shown, for elliptic flow, in Fig. 6.206. The values of the constants  $(a, b, c)$  depend weakly on the parametrization of the kinematic distributions and on the acceptance region

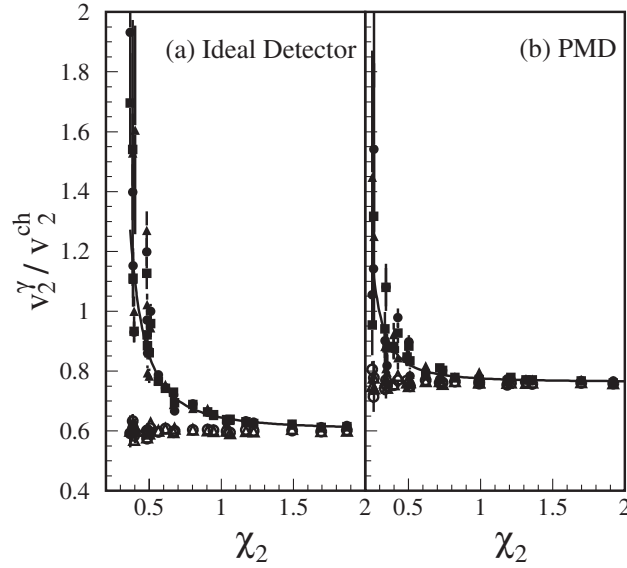


**Figure 6.206.** Ratio of elliptic flow in photons to that in charged pions as function of anisotropy parameter  $\chi$  (see text) as measured in (a) an ideal detector (b) PMD. The filled (open) symbols are results using the reconstructed (generated) event plane. Circles, squares and triangles represent the values of the ratio when the incident particle fall on the detector unscattered, after moderate scattering and after large scattering respectively. The data are plotted for  $v_n = 0.01, 0.03$  and  $0.05$  and are shown by the *same* symbol for all values of flow and multiplicity. The full curve shows a fit to Eq. 6.52.

used for analysis, and are obtained using simulations. These also depend upon the details of the analysis method which affect the magnitude of non-flow correlations present in the photon sample. By construction, the pions do not have any non-flow correlation in this simulation.

The hits in the PMD arise from both photons and charged hadrons, causing formation of clusters. The photons in these clusters are isolated using appropriate discrimination algorithms. The rapidity dependence of the efficiency can be parametrized as (see the ALICE ATDR [593])

$$\varepsilon = 0.65 - 0.3(\eta - 2.5).$$

The purity of the detected sample is about 60% throughout the range of acceptance of the PMD. These values were assumed to be constant for all multiplicities. The azimuthal distribution of these photons reflect the anisotropy present in the parent  $\pi^0$ s and are affected by charged-particle contamination. Multiple scattering in the upstream material is incorporated into the fast simulation by a Gaussian smearing of the rapidity and azimuth. Moderate scattering is represented by  $\sigma_{\delta\eta} = 0.07$ ,  $\sigma_{\delta\varphi} = 7^\circ$  and large scattering is represented by twice these values.

The ratio photon to parent pion flow in the PMD scales as would be the case for an ideal detector. The values of the constants for the two cases are shown in Table 6.44. The differences are due to charged particle contamination of the photon sample in the PMD. The results for the ratio of the anisotropies, including scattering due to upstream material, are also shown in Fig 6.206 and follow the same behaviour as they do without multiple scattering. For a more realistic study, inspired by RHIC results, we have used a  $p_t$  dependent  $v_2$  parametrized as

$$v_2 = a + bp_t$$

**Table 6.44.** Values of constants obtained in the scaling relation for photons measured in an ideal detector and in PMD.

Photons measured in	$a$	$b$	$c$
Ideal Detector	0.0285	0.161	0.604
PMD	0.0099	0.0926	0.763

**Table 6.45.** Charged-particle density  $dN/d\eta$  at mid rapidity, The corresponding multiplicity in the PMD acceptance and the slope parameter  $b$  used in the simulations as described in the text.

$dN/d\eta(y=0)$	PMD multiplicity	$b$ [ $\text{GeV}^{-1}$ ]
250	102	0.2
500	203	0.18
1000	407	0.16
1500	610	0.14
2000	814	0.12
3000	1221	0.10
4000	1629	0.08
5000	2035	0.06

up to  $p_t = 2.0$  GeV. At larger  $p_t$ ,  $v_2$  has been taken as a constant. The value of  $a$  was chosen to be zero, unless otherwise stated and the values of  $b$  are shown in Table 6.45 for the different multiplicities. In Fig. 6.207 we show the  $v_2$  ratio of photons to that of the generated pions for different values of the particle density  $dN/d\eta$  as for an ideal detector and as measured in the PMD. This figure also shows results from simulations where the value of  $a$  was set to 0.01 for  $dN/d\eta > 2000$  and from simulations where multiple scattering in the upstream material was included. Note that here the choice of  $v_2$  and multiplicity restricts the value of  $\chi$  to larger than 0.8 so that the strong variation in  $v_2^\gamma/v_2^{\text{charged}}$  as shown in Fig. 6.206 is not observed.

The PMD is capable of recording data at a much higher rate than the TPC, and can provide an event plane which allows the study of anisotropic particle emission in other detectors for different rapidities and particle types [594]. The event plane angle from the PMD is required and how, on average, it differs from the reaction plane angle (see Eq. 6.42). The average difference between the reaction plane angle and the event plane angle is expressed by a Resolution Correction Factor (RCF), obtained from the correlation between two sub-events. The RCF may include contributions due to non-flow, and detector effects. To estimate the magnitude of these contributions we therefore, in simulations, compare the reconstructed RCF to the generated RCF. Since the contribution from multiple scattering is assumed to be the same for the photons and charged pions, the reconstructed RCF over generated RCF for photons is divided by the same ratio for charged pions. Figure 6.208 shows this double ratio for (a) an ideal detector and (b) the PMD. At lower multiplicities, the non-flow contribution introduced by the neutral pion decay affects the reconstructed RCF for both the ideal detector and the PMD. Due to charged-particle contamination in the photon sample the PMD is less affected by this.

The study shows that in addition to obtaining the flow values of photons and neutral pions using the PMD, the present design of the PMD can provide a good estimate of the event plane which can be used to study anisotropic emission of particles from another detector sub system, in another acceptance region (see for example the section on quarkonia in this PPR).

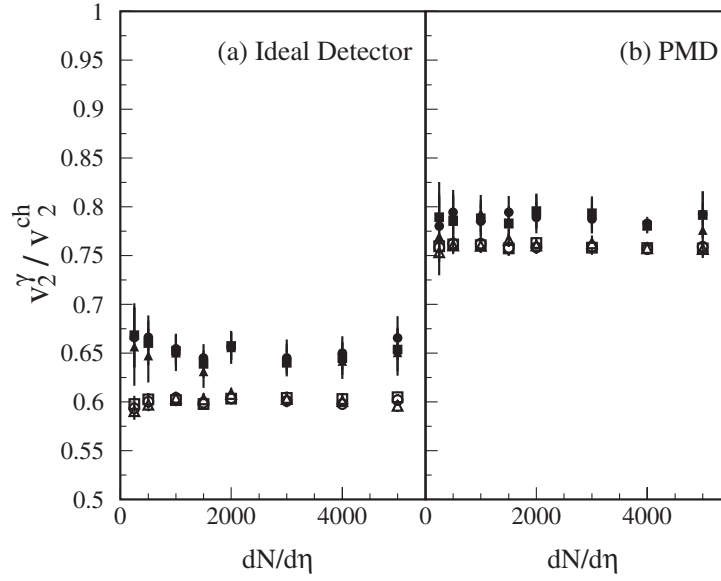


**Figure 6.207.** Ratio of elliptic flow in photons to that in charged pions as a function of  $dN/d\eta$  (see text) as measured in (a) an ideal detector (b) PMD. The full (open) symbols are results using the reconstructed (generated) event plane. Circles, squares and triangles represent the values of the ratio when the incident particles fall on the detector unscattered, after moderate scattering and after large scattering respectively. The *same* symbol is used for all values of multiplicity.

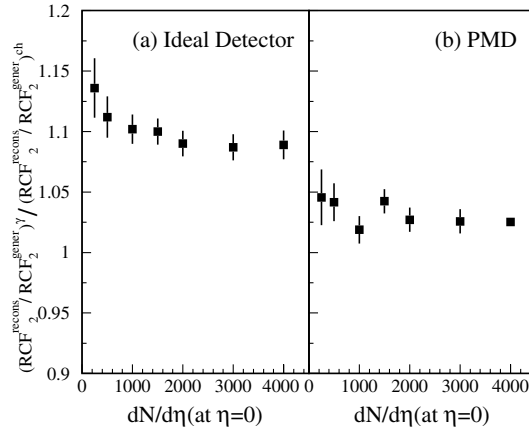


**Figure 6.208.** Ratio of reconstructed and generated values of RCF (see text) for photons scaled with the corresponding values for charged particles as a function of  $dN/d\eta$  at  $\eta = 0$  for: (a) an ideal detector; (b) PMD.

*Azimuthal anisotropy measurement with the SPD.* The Silicon Pixel Detector (SPD) can reconstruct the azimuthal angle  $\varphi$  of the charged particles in the central region of pseudorapidity with high precision. The azimuthal anisotropy can then be measured by reconstruction of the  $dN/d\varphi$  distribution or by a determination of the transverse sphericity tensor [495]. In both cases the weights of the particles should be set equal to unity because the transverse momentum cannot be determined by the SPD alone. On the other hand, the

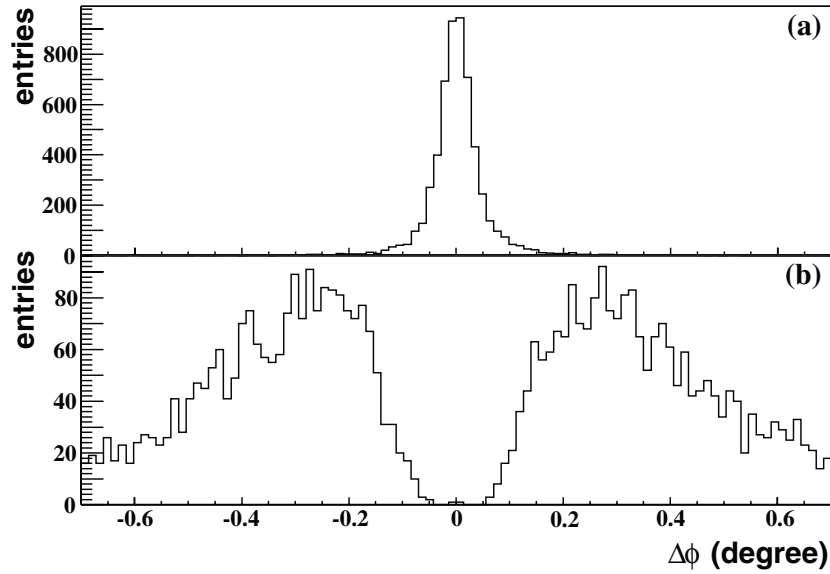


**Figure 6.209.** Distribution of the difference between generated and reconstructed azimuthal angle  $\varphi$ . (a) The magnetic field is switched off. (b) The magnetic field is switched on.

high efficiency of the multiplicity determination and the larger acceptance with respect to the TPC (up to  $|\eta| < 2$  for the first layer) allow for a good measurement at low multiplicity where the determination of the intrinsic anisotropy is more difficult due to statistical fluctuations.

For this analysis several events were generated with different values of the multiplicity and anisotropy and tracked through the ALICE apparatus with the standard magnetic field both switched on and off. The  $\varphi$  angles of the tracks were reconstructed with the SPD by using either the clusters in both layers or the tracklets, which are defined by the association of clusters from both layers with a straight line to the main vertex (see Section 6.1). The pseudorapidity acceptance is  $\eta < 2$  for the first layer and  $\eta < 1.4$  for the second layer and for the tracklets.

Figs. 6.209(a) and (b) show the distributions of the differences between generated and reconstructed  $\varphi$  in the first pixel layer with the magnetic field off and on, respectively. In the first case, a resolution of about 0.06 degree is achieved, whereas a clear separation between positive and negative particles is shown in the second case. The systematic shift due to the magnetic field is about 0.3 degree and the full spread of the residual distribution is about 0.4 degree.

The effect of the detector resolution on the reconstruction of  $dN/d\varphi$  can be seen in Fig. 6.210, where the generated distribution ( $dN/d\eta = 3000$ , magnetic field off) is compared with the distributions obtained with the clusters in layer 1 (top), layer 2 (centre) and with the tracklets (bottom). In all cases, the shape of the generated distribution is well reproduced, although some background is clearly present in the second layer.

The effect of the magnetic field can be seen in Fig. 6.211, where a small inefficiency on the tracklets distribution is visible. In this case, an additional high  $p_t$  selection can be applied by shrinking the fiducial window where clusters are associated. This allows one to perform a separate analysis for high and low  $p_t$  particles, at least in principle.

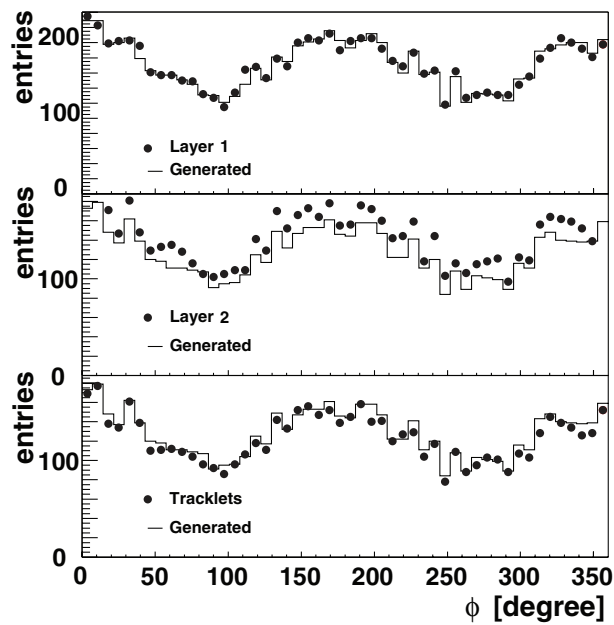


**Figure 6.210.** Generated and reconstructed  $dN/d\phi$  distributions. The reconstruction has been done with clusters in layer 1 (top), layer 2 (centre) and with tracklets (bottom). The magnetic field is switched off.

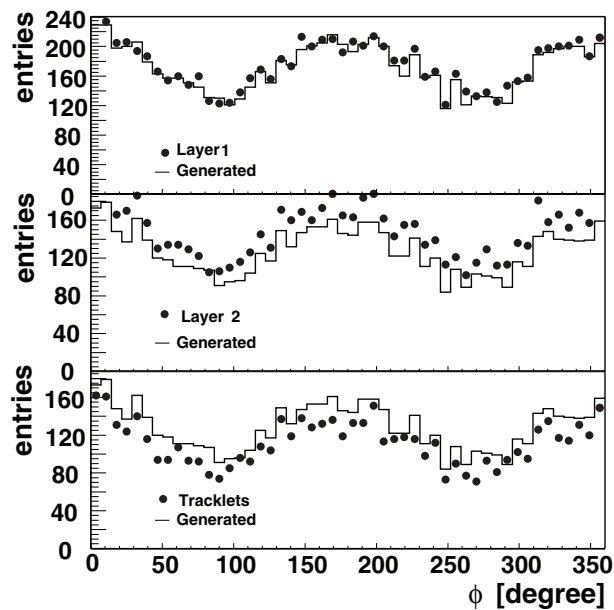


**Figure 6.211.** Generated and reconstructed  $dN/d\phi$  distributions. The reconstruction has been done with clusters in layer 1 (top), layer 2 (centre) and with tracklets (bottom). The magnetic field is switched on.

**Table 6.46.** Generated and reconstructed anisotropy parameters from a fit to the azimuthal distribution  $dN/d\varphi$ .

$dN/d\eta$	Generated		Clusters Layer 1		Tracklets	
	$v_2$	$\Psi_2$ [degree]	$v_2$	$\Psi_2$ [degree]	$v_2$	$\Psi_2$ [degree]
1400	0.05	0	$0.07 \pm 0.01$	$4 \pm 1$	$0.07 \pm 0.01$	$5 \pm 2$
2800	0.05	0	$0.06 \pm 0.01$	$2 \pm 4$	$0.06 \pm 0.01$	$0 \pm 4$
5500	0.05	0	$0.059 \pm 0.006$	$-2 \pm 3$	$0.058 \pm 0.006$	$-5 \pm 3$
1400	0.10	0	$0.12 \pm 0.01$	$0.5 \pm 3$	$0.12 \pm 0.01$	$-1 \pm 3$
2800	0.10	0	$0.12 \pm 0.01$	$-0.6 \pm 2$	$0.12 \pm 0.01$	$-1 \pm 2$
2800 (no field)	0.10	0	$0.115 \pm 0.009$	$0.2 \pm 2$	$0.115 \pm 0.009$	$-0.3 \pm 2$
5500	0.10	0	$0.102 \pm 0.006$	$-1 \pm 2$	$0.103 \pm 0.007$	$-3 \pm 2$

**Table 6.47.** Anisotropy parameters from diagonalization of the transverse sphericity tensor.

$dN/d\eta$	Generated		Clusters Layer 1		Tracklets	
	$v_2$	$\Psi_2$ [degree]	$v_2$	$\Psi_2$ [degree]	$v_2$	$\Psi_2$ [degree]
1400	0.05	0	$0.06 \pm 0.01$	$-2.5 \pm 4$	$0.07 \pm 0.01$	$-7 \pm 4$
2800	0.05	0	$0.06 \pm 0.01$	$2 \pm 3$	$0.06 \pm 0.01$	$-0.3 \pm 3$
5500	0.05	0	$0.058 \pm 0.005$	$-2 \pm 3$	$0.058 \pm 0.005$	$-8 \pm 3$
1400	0.10	0	$0.11 \pm 0.01$	$0.4 \pm 3$	$0.12 \pm 0.01$	$-1 \pm 3$
2800	0.10	0	$0.114 \pm 0.009$	$-2.4 \pm 2$	$0.115 \pm 0.009$	$-1 \pm 2$
2800 (no field)	0.10	0	$0.113 \pm 0.009$	$0.4 \pm 2$	$0.114 \pm 0.009$	$-0.9 \pm 2$
5500	0.10	0	$0.101 \pm 0.006$	$-3 \pm 2$	$0.104 \pm 0.007$	$-3 \pm 2$

As an example of the reconstruction capability we list in Tables 6.46 and 6.47 the generated and reconstructed  $v_2$  and  $\Psi_2$  for several events generated with different values of the multiplicity and anisotropy. The determination of  $v_2$  and  $\Psi_2$  has been carried out with clusters and tracklets as discussed above. In Table 6.46 the anisotropy parameters were determined from a fit of the distributions to the following expression:

$$\frac{dN}{d\varphi} \propto \frac{1}{2\pi} + 2v_2 \cos[2(\varphi - \Psi_2)].$$

It can be seen that the reconstructed  $v_2$  are systematically larger than those generated and that the differences become smaller with increasing multiplicity or  $v_2$ , as expected. No significant differences were found between the tracklet and cluster methods. Also, no large improvements are observed when comparing the two cases with magnetic field off and on. This confirms that the magnetic field has a small effect on the SPD reconstruction.

The results of an independent determination obtained by the diagonalization of the transverse sphericity tensor are given in Table 6.47. In this case the ratio  $\varepsilon = (f_2 - f_1)/(f_2 + f_1)$  between the two eigenvalues is equal to  $v_2$  ( $f_2 > f_1$ ) while the rotation of the reference system yields  $\Psi_2$ . Clearly, the reconstructed  $v_2$  are slightly lower than the corresponding values in Table 6.46, the behaviour being essentially the same. Again, no significant differences are visible between tracklets and clusters and between events with the magnetic field on and off.

**6.4.6. Summary.** The anisotropic flow measurements with the ALICE detector, for a very wide range of possible particle multiplicities and magnitudes of the elliptic flow, can be done for ultra-relativistic heavy-ion collisions with unprecedented accuracy. The determination of the event plane will benefit from the possibility of having independent flow estimates from the different subsystems of ALICE and from the different methods of analysis. It is clear that the comparison of these estimates is crucial for the interpretation of the observed anisotropic flow. These high accuracy anisotropic flow measurements are, as at RHIC, expected to be very important in understanding the dynamics of the heavy-ion collisions at the LHC and constrain the underlying equation of state.

## **6.5. Event-by-event physics**

**6.5.1. Introduction.** It is expected that the hot and dense system created in heavy-ion collisions at ultra-relativistic energies and its evolution in time will show very characteristic behaviour of QGP phase transition, which may vary dramatically from one event to the other. Such interesting behaviour can be studied by the measurement and subsequent analysis of various observables in every single event. Thus event-by-event measurements and the study of various physically observable quantities offer the best possibility for studying the QGP phase transition and the nature of the QGP matter. Because of the production of large number of particles in each event in heavy-ion collisions at SPS, RHIC, and LHC energies it has become possible to make precision event-by-event measurements and study fluctuations of various measured quantities for given event classes. The fluctuation measures provide possible ways to study variations in physical quantities from event to event. The performance of ALICE for event-by-event measurements may be found in Ref. [595].

Fluctuations of thermodynamic quantities such as temperature and entropy have been proposed to give evidence for the existence of QGP phase transition and also provide direct insight into the properties of the system created in high energy heavy-ion collisions [596–602]. Large fluctuations in energy density due to droplet formation are expected if the phase transition is of first order. A second-order phase transition may lead to divergence in specific heat and increase the fluctuation of energy density due to long range correlations in the system. It is predicted that near a critical point, i.e., a second-order phase transition, fluctuations will be strongly enhanced [598]. Present lattice computations (see the next section for details) reveal that the QCD critical point could be at reasonably small chemical potential [603] but still be too high for the LHC to reach. The situation becomes different with the production of jets and minijets at LHC energies. Characterisation of jets and their interaction with the medium will be quite crucial to understand the phase transition and physical characteristics of QGP [604, 605]. Formation of disoriented chiral condensates (DCC) [606–610], which is a consequence of chiral phase transition, would lead to large fluctuations in the ratio of neutral to charged pions.

The rapid development of the field of event-by-event physics in recent years is directly related to the progress in the field of high-energy nucleus–nucleus collisions. Recent detector technologies and availability of high beam energies along with experiments containing large acceptance detectors allow the detection of a large fraction of thousands of particles produced in each collision at SPS, RHIC, and LHC energies. Active study of event-by-event fluctuations in heavy-ion collisions was initiated by experiments at the SPS [611–626]. These studies include fluctuations in multiplicity of charged-particles and photons, kaon to pion ratio, net charge, mean transverse momentum and formation of DCC domains. These along with results from more sophisticated analysis methods are now available from RHIC

experiments [627–638]. The experimental procedures, statistical tools, and theoretical models are constantly challenged by the requirements of event-by-event study.

The regime of event-by-event physics spans from understanding the bulk properties of matter to high  $p_t$  particles including jets. The ALICE experiment has the unique capability to track the majority of the particles produced in heavy-ion collisions, and measure relevant quantities needed for event-by-event physics. In this section, the methodology for event-by-event physics and fluctuations and the performance of the ALICE detector in terms of these measurements are discussed. The next subsection deals with predictions from lattice calculations, followed by a brief discussion of the physics of correlations and fluctuations. The measurement capabilities of ALICE are discussed after that. The remainder of the section contains discussions on temperature and  $\langle p_t \rangle$  fluctuations, multiplicity and strangeness fluctuations, fluctuations of conserved quantities, net charge fluctuations, balance functions, fluctuations in azimuthal anisotropy, disoriented chiral condensates, the importance of jets and minijet production in fluctuation studies and finally long-range dynamical correlations of various observables measured in separated rapidity intervals.

*6.5.2. Lattice predictions.* Lattice QCD is the theoretical tool of choice for computing the fluctuations of conserved quantities such as charge and energy. Other quantities, such as strangeness, which are conserved by the strong interactions, but not by the weak, are practically conserved within the lifetime of the fireball. Lattice QCD is able to provide a prediction for the fluctuations of such quantities as well. Two regimes of baryon chemical potential,  $\mu_B$ , and temperature,  $T$ , are of interest—the intermediate chemical potential regime,  $\mu_B \simeq T$ , close to the critical point of QCD, and the small chemical potential regime,  $\mu_B \ll T$ , the condition which will prevail at the LHC energies. The two cases are discussed below.

*6.5.2.1. The QCD critical end point.* The lattice QCD explorations around the QCD critical point have started following the prediction of a critical end point of QCD [598]. This lattice calculations were performed using several methods, such as reweighting method [639–641], analytic continuation from imaginary chemical potential [642, 643], and a Taylor series expansion [644–646]. These computations are performed in lattice QCD with two flavours of light dynamical quarks. Three important parameters in these computations are:

- The physical volume of the lattice: the volume,  $V$ , must be sufficiently large in units of the pion’s Compton wavelength. In practice, it was found that, in units with  $\hbar = c = 1$ , one must select  $m_\pi V^{1/3} > 5$ .
- The quark mass: the quark mass is measured in terms of the ratio of pion mass to the mass of  $\rho_x$ ,  $m_\pi/m_\rho$ . In order to get realistic physics, one must have  $m_\pi/m_\rho \ll 0.5$ , and the actual physical value is  $m_\pi/m_\rho = 0.18$ .
- The lattice spacing: the lattice spacing should be extrapolated to zero to get to the continuum limit. In practice, one may be able to tolerate a finite lattice spacing as long as the ratio  $m_\pi/m_\rho$  is realistic.

None of the computations performed so far could satisfy all of the three conditions, in particular all computations work at rather coarse lattice spacings of the order of 0.25 fm. In Ref. [639], the ratio  $m_\pi/m_\rho$  is realistic but  $m_\pi V^{1/3} \approx 3$ . In [645]  $m_\pi V^{1/3} \approx 15$ , but  $m_\pi/m_\rho \approx 0.7$ . In Ref. [646] calculations were performed for a range of volumes,  $m_\pi V^{1/3} = 3$ –10, and extrapolations were made to infinite volume at a quark mass of  $m_\pi/m_\rho \approx 0.3$ . This is also the quark mass value used in [639, 643]. A strong dependence of the position of the critical end point on the volume has been observed as seen in Fig. 6.212. As a result, the best estimate at

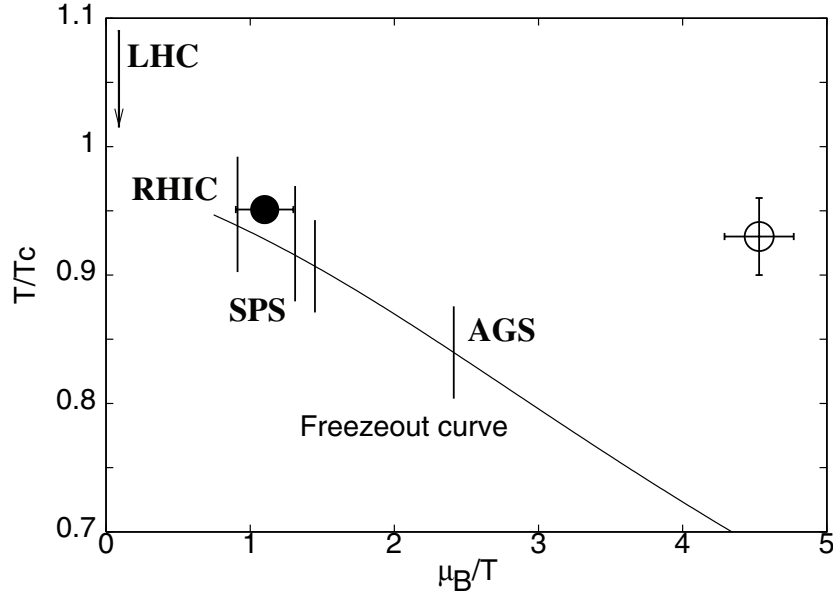


**Figure 6.212.** Estimates of the critical end point of QCD overlaid on a freeze-out curve [647]. The open and filled circles are estimates for the critical end point from Refs. [639] and [646], respectively, computed for quark mass such that  $m_\pi/m_\rho \approx 0.3$ . For realistic quark mass, the critical chemical potential corresponding to the critical end point is expected to decrease.

present comes out to be  $\mu^E/T^E \approx 1$  with  $T^E/T_c \approx 0.95$  [646]. This is likely to decrease as the quark mass is reduced to more realistic values.

The chemical potential at LHC energies will be quite small, however, the analysis of particles emitted at forward and backward rapidities (but not the fragmentation region) will be of interest, as presumably they are emitted at larger chemical potential compared to the particles at central rapidities.

**6.5.2.2. Thermodynamic fluctuations at small chemical potential.** The best established results for fluctuations of conserved quantities come from lattice computations of the quark number susceptibilities [648]. Lattice results are also available for the baryon number susceptibility,  $\chi_B$ , the susceptibility of the third component of isospin,  $\chi_3$ , and strangeness,  $\chi_s$ , which are defined as

$$\chi_B = \left. \frac{\partial^2 P}{\partial \mu_B^2} \right|_{\mu_3, \mu_s, T, V}, \quad \chi_3 = \left. \frac{\partial^2 P}{\partial \mu_3^2} \right|_{\mu_B, \mu_s, T, V}, \quad \chi_s = \left. \frac{\partial^2 P}{\partial \mu_s^2} \right|_{\mu_B, \mu_3, T, V}, \quad (6.53)$$

where  $P$  is the pressure,  $T$  the temperature,  $\mu_B$ ,  $\mu_3$  and  $\mu_s$  the chemical potentials associated with baryon number, isospin, and strangeness, respectively. Results in the continuum limit come from quenched QCD computations [644]. Comparison of quenched results with those in dynamical 2 flavour [646, 649] and 2+1 flavour [650] QCD at similar lattice spacing shows that, in the high temperature phase for  $T \geq 1.5T_c$ , there is a 5–10% effect due to unquenching. In the high temperature phase of QCD, above  $1.5T_c$ , there is good agreement of these lattice results with weak coupling theory [651–653]. Figure 6.213 shows the behaviour of the baryon chemical potential with temperature for 2 flavour QCD in the continuum limit.

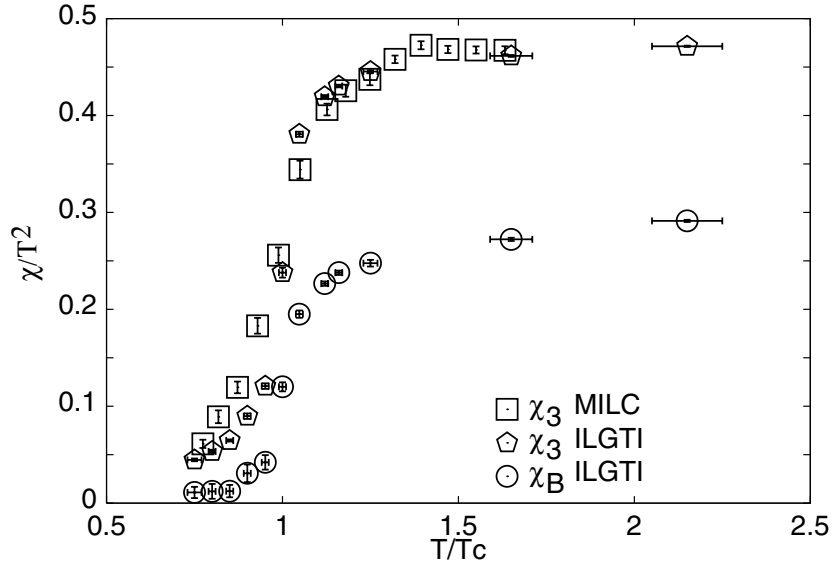


**Figure 6.213.** Estimates of  $\chi_3/T^2$  and  $\chi_B/T^2$  in the continuum limit of two flavour QCD. A scaling factor obtained from the quenched computation of [644] has been applied to the data of Ref. [646] indicated as ILGTI. Values obtained at lattice spacing  $1/8T$  with a different way of putting quarks on the lattice [650] are shown as MILC.

The susceptibilities, being variances and covariances of quantum numbers, also throw light on the degrees of freedom in the hot phase of QCD [654, 655]. Lattice computations show that this is indeed the case, and the conclusion is independent of quark masses as long as they are substantially smaller than the charm quark [655].

Non-linear quark number susceptibilities (NLS) are higher derivatives of the pressure with respect to chemical potentials [644]. The ratios of the fourth and second order NLS are also sensitive to the presence of valence quarks (as was shown by a computation in quenched QCD [644], and in two flavour QCD both with heavy pions  $m_\pi/m_\rho = 0.7$  [656] as well as with lighter pions  $m_\pi/m_\rho = 0.3$  [657]). These signals indicate that quarks are definitely the flavour carriers for  $T \geq 1.25T_c$ . However the higher (fourth) order NLS seem to feature interesting structure very close to  $T_c$  as shown in Fig. 6.214 [656, 657]. While the origin of the structure is under discussion [657, 658], it will be possible to make precise measurement of higher order moments in ALICE. Net charge fluctuations as well as fluctuations in terms of the fourth and higher order cumulants can be measured in various collision geometries (event centralities) as well as different cuts in transverse momenta of charged-particles.

Concerning fluctuations in the total energy of a canonical ensemble, or the temperature of a microcanonical ensemble, the appropriate quantity to measure is the specific heat, defined as

$$c_v = \left. \frac{\partial \varepsilon}{\partial T} \right|_{\mu_B, \mu_3, \mu_s, \nu}, \quad (6.54)$$

where  $\varepsilon$  is the energy density and  $T$  the temperature. This has been studied recently on the lattice in quenched QCD [646] and the result is shown in Fig. 6.215. Strong temperature dependence is observed, which is consistent with predictions of a conformal theory, given by  $c_v/T^3 = 4\varepsilon/T^4$  (for  $T > 2T_c$ ). However, it increases as the temperature drops towards  $T_c$ .

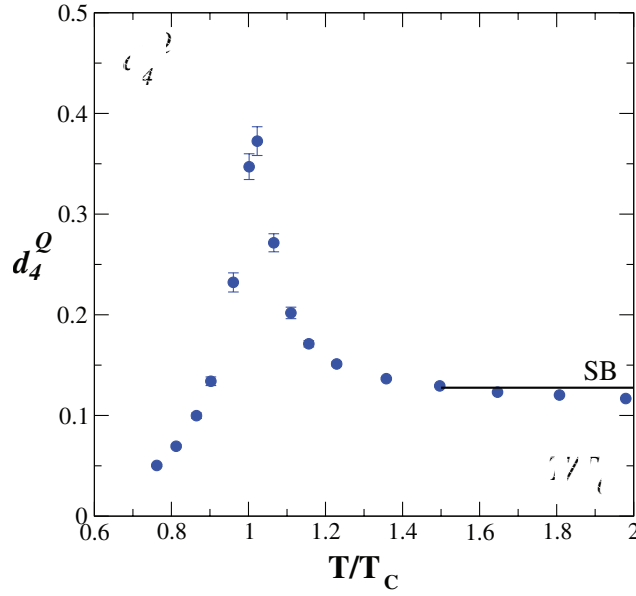


**Figure 6.214.** Fourth order cumulant of charge fluctuations showing a peak structure around  $T = T_c$ , taken from Ref. [656]. Similar structures are also seen for fourth order cumulant of quark and isospin number fluctuations [656, 657].

Below  $T_c$  the specific heat is lower. If a reliable extraction of the specific heat can be made through event-by-event fluctuations, the rapid change with  $T$  makes it a good candidate for a thermometer.

**6.5.3. Correlations and fluctuations.** The challenge of event-by-event studies is that, beyond the fluctuations linked to the details of the phase transition, there are a number of other fluctuations which will appear. The observed fluctuations will have contributions from statistical fluctuations and those from dynamical origin. Contributions having dynamical origin comprise of (a) fluctuations which do not change event-to-event, e.g., those from Bose-Einstein (BE) correlations, resonance decays, etc. and (b) the fluctuations which have a new physics origin and may vary from event-to-event. The fluctuations impact different observables in different manner and act on different scales. For example, the energy and momentum conservation correlate all particles in the collision and thus can influence fluctuations at large scales. On the other hand, short-range correlations due to quantum statistics obeyed by fermions and bosons result in suppression (fermions) or enhancement (bosons) of fluctuations at small scales.

The present results at the SPS and RHIC indicate that statistical models of strong interactions reproduce surprisingly well the energy dependence of entropy and strangeness production [259] and the hadronization process [244, 245, 659], resulting in a correct description of hadron yield systematics (see Section 6.2). However, the interpretation of the data within statistical models is under discussion. It is difficult to apply QCD for the interpretation of the experimental results since most of the effects connected to the transition to QGP are in the domain of soft processes for which experimentally testable predictions of QCD are not available. Attempts to build phenomenological, QCD-inspired, models have not been very successful so far. Conclusive interpretation of the data within these models

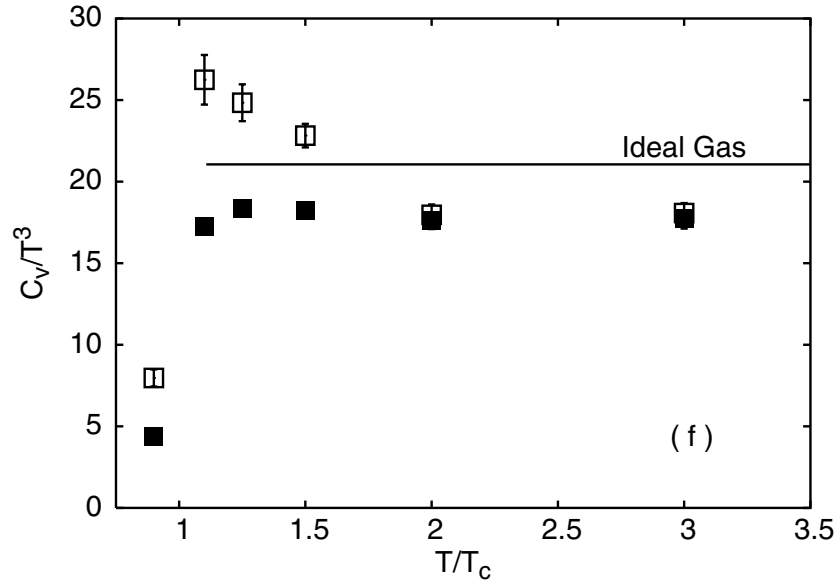


**Figure 6.215.** Continuum results for  $c_v/T^3$  (open boxes) and  $4\epsilon/T^4$  (filled boxes) from the lattice computation of Ref. [646]. Values corresponding to the ideal gas situation are also indicated (straight line).

seems to be impossible since one cannot estimate the uncertainties due to the approximations introduced.

Thus, the questions concerning the interpretation of heavy-ion results unavoidably lead to the more fundamental questions about our understanding of strong interactions and the validity of various frameworks. In particular, further tests on limits of the application of the statistical models are needed. Within this context the study of event-by-event fluctuations plays a special role as it allows for independent tests of competing approaches.

It has been suggested that the processes following QGP hadronization like hadronic rescattering [660] and resonance decays may almost completely wipe out fluctuations originally developed in the QGP phase. Thus the propagation of fluctuation from initial stages of collision to the freeze-out has to be considered before making any conclusions about the fluctuations from QGP and non-QGP stages [661].

There are numerous well-established physical sources of event-by-event fluctuations in high-energy nucleus–nucleus collisions:

- geometrical (impact parameter, number of participants, detector acceptance) [621, 662, 663];
- energy, momentum, charge conservations [664, 665];
- anisotropic flow [666];
- Bose-Einstein correlations [667, 668];
- resonance and string decays [664, 669, 670];
- jets and minijets [604, 605, 671];
- quantum statistics [669];
- temperature fluctuations [672, 673].

Many exotic (still not observed and/or identified) phenomena may also occur and significantly impact the observed fluctuations. Among them are:

- formation of DCC [606–610];
- colour collective phenomena [674, 675];
- frozen statistical QGP fluctuations [676, 677];
- formation of colour ropes [678].

Dedicated analysis methods and statistical tools are well established in order to study the majority of the standard processes listed above (geometrical fluctuations, quantum statistics, Coulomb interactions, resonance production, anisotropic flow). Their impact on event-by-event fluctuations can therefore be estimated based on the experimental results and thus they serve as a background above which other effects are sought.

Depending on the nature of QGP phase transition, there will be large density fluctuations leading to droplet formation and hot spots. These will give rise to large rapidity and multiplicity fluctuations of produced particles and have distinct effects on the space time extent of the source [667, 668]. The Bose-Einstein correlation measurement of particle pairs give handle on the space-time extent of the system. Up until now it has become impossible to measure the space-time correlations on an event-by-event. As a result of the production of large number of particle pairs in heavy-ion collisions at LHC energy, one can do single event interferometry in ALICE. As discussed in Section 6.3 the correlation measurements in ALICE will be sensitive enough to study source fluctuations on an event-by-event basis. Measurement of HBT radii at different rapidity windows and multiplicity bins will be possible in ALICE.

Of special interest at LHC energies is the study of jet and minijet production in nucleus–nucleus collisions. Since the jet/minijet production cross section measured in  $pp(\bar{p})$  interactions strongly increases with energy, one expects that copious jet/minijet production may be a dominant feature of heavy-ion collisions at the LHC. Standard methods developed for the jet search in elementary interactions do not work well in the case of heavy-ion collisions on account of the very high background of soft hadrons. Direct jet identification is possible only at the very high  $p_t$  range. On the other hand, hadrons originating from a jet are correlated in momentum space, and therefore jet production should lead to an increase of fluctuations. Consequently, the study of event-by-event fluctuations may yield important information on jet/minijet production not accessible by direct methods because of the high background. Copious jet/minijet production and consequently large fluctuations may, however, shadow fluctuations caused by other processes of interest. It is therefore clear that the relation between jet/minijet production and search for event-by-event fluctuations needs careful study.

Formation of DCC is a direct consequence of the chiral symmetry restoration at high temperatures and densities. This gives rise to anomalous fluctuations in the ratio of neutral to charged pions. At the SPS, both WA98 and NA49 experiments searched for the formation of DCC. The WA98 collaboration made an extensive study for the formation of DCC in global as well as localized domains in phase space. Based on DCC simulation models upper limits on the production of DCC have been estimated [613, 622, 624, 625]. Several methods to search for DCC have been proposed in the literature. The sensitivity of these methods will be discussed later in the section.

A copious production of partons, mainly gluons, due to hard and semi-hard processes, is expected in heavy-ion collisions at the LHC. During the early stages of collision the system is on average locally colourless, but random fluctuations can break the neutrality. Since the system is initially far from equilibrium, specific colour fluctuations can exponentially grow in time and then noticeably influence the evolution of the system. The very existence of

such fluctuations would be a clear manifestation of the quark–gluon plasma where the colour forces act well beyond the confinement scale. The colour plasma instabilities can indeed occur due to the strongly elongated parton momentum distribution [674, 675]. These instabilities, in particular the filamentation instability, generate collective transverse flow in heavy-ion collisions. The occurrence of the filamentation breaks the azimuthal symmetry of the system. The azimuthal orientation of the wave vector will change from one collision to another, while the instability growth will lead to the energy transport along this vector. Consequently, one expects significant variation of the transverse energy as a function of the azimuthal angle. This expectation is qualitatively different from that based on the parton cascade simulations [679], where the fluctuations are strongly damped due to the large number of uncorrelated partons. On account of the collective character of the filamentation instability, the azimuthal symmetry will be presumably broken by a flow of a large number of particles with relatively small transverse momentum. One expects the generation of the collective transverse motion as a result of the anisotropic pressure gradient [495, 680]. The flow is of hydrodynamic nature, and, in contrast to the colour instability driven transport, it is strongly correlated with the orientation of the collision plane. The collective flow can be studied by means of various methods. The fluctuation measure  $\Phi$  [662] may be used for this purpose which has been proven to be very sensitive to the collective effects [666, 671].

Fluctuations in physical quantities that arise out of hydrodynamic predictions can discern whether the fluid is perfect or not perfect. A dissipation in a non-perfect fluid is related to the fluctuations of these physical quantities [666]. In this context, it has been proposed to study elliptic flow and higher harmonics on an event-by-event basis [666]. Fluctuation in elliptic flow is argued to be sensitive to the following physical effects: (a) filamentation instability initiated due to the strong momentum anisotropy of the partonic system, and the generation and subsequent explosions of the topological clusters and (b) multiplicity fluctuations. Fluctuation of elliptic flow can be explored in detail in the ALICE experiment.

Additional valuable information on the collision dynamics, specifically on the string fusion and percolation phenomenon, may be obtained in the event-by-event studies of the correlations between various observables measured in separated rapidity intervals (long range correlations). These can be studied in different rapidity intervals for multiplicity correlations,  $\langle p_t \rangle$  correlations and multiplicity- $\langle p_t \rangle$  correlations. Model-independent detailed experimental information on long-range correlations between such observables as charge, net charge, strangeness, multiplicity and mean transverse momentum of specific type particles could be a new powerful tool to discriminate theoretical reaction mechanisms.

The ALICE experiment is well equipped to address all these issues. Event-by-event fluctuations of the measured quantities can be studied in ALICE using specific analysis methods sensitive to phase transition, deconfinement and chiral symmetry restoration. Various aspects of these will be discussed in the rest of the section.

*6.5.4. Event-by-event measurements in ALICE.* ALICE is a multi-purpose experiment with highly sensitive detectors surrounding the interaction point. The experiment is designed for event-by-event measurement of several of the observables. The information about a collision or an event is the collision geometry is provided by the ZDC and multiplicity detectors as discussed in the section on event characterisation in Section 6.1. The central detectors ( $-0.9 < \eta < 0.9$ ) with their good particle identification capabilities provide momentum measurement for each particle species in every event. The forward detectors extend the coverage of charged-particles and photons. Charged-particle multiplicity in the central region is given by a combination of ITS, TPC, and TOF. A combination of these three detectors provides momenta information and particle identification of hadrons as discussed in the

section on particle production. The charged-particle multiplicity measurement in ITS can be obtained to  $\eta = \pm 1.8$  and the FMD extends these measurements from up to  $\eta = \pm 5.09$ . In the central rapidity region PHOS with a limited coverage provides photon multiplicity and photon momenta whereas PMD is designed for multiplicity of photons in the high particle density region of forward rapidity ( $2.3 < \eta < 3.5$ ). A combination of information from these detectors provides excellent opportunity to study event-by-event physics and fluctuation at LHC energies.

*6.5.5. Centrality selection for fluctuation studies.* The characteristics of the phase transition are supposed to be different with differing collision energy and also for different centralities. It is important to have proper control over centrality for the majority of the analysis. Centrality is normally characterised by the impact parameter of the collision or the number of participating nucleons ( $N_{\text{part}}$ ). As it is not possible to measure either  $b$  or  $N_{\text{part}}$  directly, estimations of these quantities are based on calorimetric and multiplicity measurements. As described in section 6.1, in ALICE it is possible to determine the centrality quite precisely in every event by using the forward energy from ZDC and multiplicity of produced particles from multiplicity detectors such as ITS, FMD, etc. From these one extracts the impact parameter or the number of participants in a model dependent way. This is needed in order connect any measured quantity with theoretical calculations and to compare them with measurements from other experiments.

The importance of proper centrality selection for fluctuation studies can be understood in terms of a simple participant model [596, 621, 681]. The number of produced particles ( $N$ ) in a collision depends on the centrality of the collision expressed in terms of  $N_{\text{part}}$  and the number of collisions suffered by each particle. Mathematically this can be expressed as

$$N = \sum_{i=1}^{N_{\text{part}}} n_i, \quad (6.55)$$

where  $n_i$  is the number of particles produced in the detector acceptance by the  $i$ -th participant. On an average, the mean value of  $n_i$  is the ratio of the average multiplicity in the detector coverage to the average number of participants, i.e.,  $\langle n \rangle = \langle N \rangle / \langle N_{\text{part}} \rangle$ . Thus the fluctuation in particle multiplicity is directly related to the fluctuations in ( $N_{\text{part}}$ ). In order to infer any dynamical fluctuation arising from various physics processes one has to make sure that the fluctuations in  $N_{\text{part}}$  are minimal.

For a variable,  $X$ , whose distribution is Gaussian, the relative fluctuation,  $\omega_X$ , may be expressed as

$$\omega_X = \frac{\sigma_X^2}{\langle X \rangle}, \quad (6.56)$$

where  $\sigma_X^2$  is the variance of the distribution and  $\langle X \rangle$  denotes the mean value. Multiplicity fluctuations and fluctuations in  $N_{\text{part}}$  can be obtained using this formula.

Fluctuations in  $N_{\text{part}}$  have been addressed at the SPS by the WA98 experiment [621] where the centrality selections were made by using the mid-rapidity calorimeter and the zero-degree calorimeter.  $N_{\text{part}}$  values are calculated using the VENUS event generator [682] and the WA98 simulation framework.

Figure 6.216 shows the mean, sigma,  $\chi^2/ndf$  fit value of the Gaussian distribution and extracted fluctuation for the number of participants for narrow centrality bins such as 0–2%, 2–4%, 4–6%, ..., 50–52% for the WA98 experimental set-up [621]. The fluctuations in  $N_{\text{part}}$  remain around unity for most of the centrality bins. On the other hand, for broad centrality

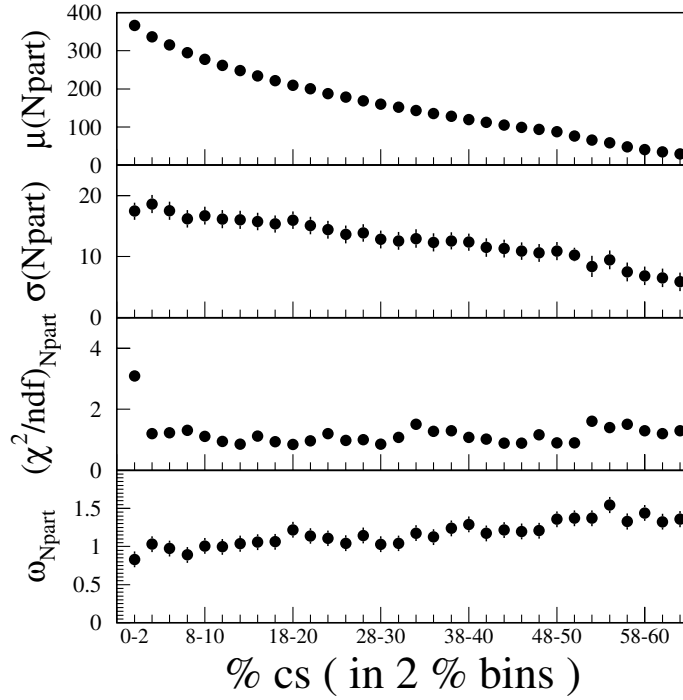


**Figure 6.216.** Variation of  $\mu$ ,  $\sigma$ , and  $\chi^2/ndf$  for the distribution of the number of participants as a function of centrality in case of Pb-Pb collisions at SPS energies are shown in top three panels. The fluctuation in the number of participants, shown in the bottom panel, remain minimal and close to unity for narrow bins in centrality.

bins these fluctuations are much larger and bias the fluctuation study. This suggests narrow cross section slices in the centrality bins are necessary to study any kind of fluctuations and minimize the influence of impact parameter fluctuations.

In ALICE attempts will be made to study fluctuations in narrow bins of centrality which will be obtained in combining information from ZDC and multiplicity detectors.

**6.5.6. Temperature fluctuations.** The concept of temperature plays a key role in the description of relativistic heavy-ion collisions because the matter produced at early stages of the collision achieves, at least to some extent, local thermodynamic equilibrium. Although the thermodynamic interpretation of temperature is a subject on ongoing debate, the main point of interest would be to find out whether there is a unique temperature of the system at freeze-out or whether the temperature fluctuates from one collision to another [672, 673]. The ALICE experiment is capable of high-precision measurements of the event-by-event temperature fluctuations.

**6.5.6.1. Methods of study.** The temperature can be inferred from the experimental data in several ways. In particular, one analyses the  $p_t$  distribution which is usually taken in the form

$$\frac{1}{p_t} \frac{dN}{dp_t} \propto \exp\left(-\frac{m_t}{T}\right), \quad (6.57)$$

where  $m_t \equiv \sqrt{m^2 + p_t^2}$  with  $m$  being the particle mass;  $T$  is the *effective* temperature which, as commonly accepted, see for example Ref. [683], combines the genuine temperature  $\mathcal{T}$  and transverse flow velocity  $u$  according to the approximate relation  $T = \mathcal{T} \sqrt{(1+u)/(1-u)}$  [684]. Obviously, the fluctuations of  $\mathcal{T}$  and  $u$  both contribute to that of  $T$ .

The temperature fluctuations influence the shape of the  $p_t$  distribution. As shown in Ref. [685], the  $T$  fluctuations in the exponential formula (6.57) lead in a natural way to the power-law like form, known as the Lévy distribution. Indeed, averaging the exponential formula over the fluctuations of  $1/T$  which follow the gamma distribution, one gets

$$\frac{1}{p_t} \frac{dN}{dp_t} \propto \left[ 1 - (1-q) \frac{m_t}{T_0} \right]^{\frac{1}{1-q}}, \quad (6.58)$$

where  $1/T_0 \equiv \langle 1/T \rangle$ . The parameter  $q$  is the entropic index or non-extensivity parameter in Tsallis statistics [686], which is connected to the size of the fluctuations. Namely,

$$q - 1 = \frac{\langle 1/T^2 \rangle - \langle 1/T \rangle^2}{\langle 1/T \rangle^2} \simeq \frac{\langle T^2 \rangle - \langle T \rangle^2}{\langle T \rangle^2}, \quad (6.59)$$

where the second approximate equality holds for sufficiently small fluctuations. When  $q = 1$  there are no temperature fluctuations and the exponential formula is restored.

The Lévy type (6.58) distribution has been observed in inclusive processes [687]. The source of such a behaviour is unknown. An event-by-event analysis of the data will help in understanding this because of the fact that when  $T$  fluctuates from event to event, the  $p_t$  distribution in a single event differs from the  $p_t$  distribution averaged over many events. In particular, if the single-event  $p_t$  distribution is given by the exponential formula (6.57) the averaged one is that of Lévy (6.58). As shown in Ref. [688], a very large multiplicity of the central Pb–Pb collisions allows one to observe the difference for  $q - 1$  as small as 0.05.

Fluctuations in temperature may be studied more quantitatively by using a method proposed and developed in Ref. [689]. The temperature variance can be found by measuring the event's transverse mass defined as

$$\mu_T = \frac{1}{N} \sum_{i=1}^N m_T^i, \quad (6.60)$$

where  $N$  denotes the event's multiplicity and  $m_T^i$  is the transverse mass of  $i$ -th particle. If the single particle  $p_t$  distribution is of the form given in Eq. 6.57, then the event's temperature can also be expressed in terms of  $\mu_T$ . By measuring  $\mu_T$  on an event-by-event basis one can get the fluctuation in temperature as the variance, defined as,  $\langle T^2 \rangle - \langle T \rangle^2$ . However, the statistical fluctuations due to the finite event multiplicity have to be subtracted from the result. The variance of  $T$  because of statistical fluctuations has been estimated in terms of a simple simulation [689] to see how well the subtraction procedure works. It appears that for event multiplicity  $N$  as small as 10 the value of  $q > 1.05$  can be unambiguously observed provided the single-particle  $p_t$  distribution is indeed described by Eq. (6.57).

The temperature fluctuations can also be observed by analysing the event-by-event  $p_t$  fluctuations by means of the  $\Phi$  measure [662]. The  $\Phi$  measure is defined by introducing a single-particle variable  $z = x - \bar{x}$  with the over-line denoting average over a single particle inclusive distribution. The event variable  $Z$ , which is a multi-particle analogue of  $z$ , is defined as  $Z = \sum_{i=1}^N (x_i - \bar{x})$ , where the summation runs over particles from a given event. Finally, the  $\Phi$  measure is defined as

$$\Phi = \sqrt{\frac{\langle Z^2 \rangle}{\langle N \rangle}} - \sqrt{z^2}. \quad (6.61)$$

Following this procedure,  $\Phi_{p_t}$  for fluctuating  $T$  was computed in [689]. If  $P_{(T)}(p_t)$  denotes the single-particle transverse momentum distribution in events with temperature  $T$  which is assumed to be independent of the event multiplicity,  $N$ , then, the inclusive transverse momentum distribution turns out to be

$$P_{\text{incl}}(p_t) = \int_0^{\infty} dT \mathcal{P}(T) P_{(T)}(p_t), \quad (6.62)$$

where  $\mathcal{P}(T)$  describes the temperature fluctuations. The  $N$  particle transverse momentum distribution in the events of multiplicity  $N$  is assumed to be the  $N$  product of  $P_{(T)}(p_t)$  weighted by the multiplicity and temperature distributions. One finds

$$\begin{aligned} \langle Z^2 \rangle &= \sum_N \mathcal{P}_N \int_0^{\infty} dT \mathcal{P}(T) \int_0^{\infty} dp_T^1 P_{(T)}(p_T^1) \dots \int_0^{\infty} dp_T^N P_{(T)}(p_T^N) \\ &\quad \times \left( p_t^1 + \dots + p_t^N - N \bar{p}_t \right)^2, \end{aligned}$$

where  $\mathcal{P}_N$  is the multiplicity distribution. In the limit  $m = 0$ , the  $p_t$  distribution (6.57) acquires a simple exponential form and one easily computes  $\overline{z^2}$  and  $\langle Z^2 \rangle$ . Assuming additionally that the  $N$  and  $T$  fluctuations are small, one gets a very simple result:

$$\Phi(p_t) = \sqrt{2} \langle N \rangle \frac{\langle T^2 \rangle - \langle T \rangle^2}{\langle T \rangle} = \sqrt{2} \langle N \rangle \langle T \rangle (q - 1). \quad (6.63)$$

Thus,  $\Phi$  has a linear dependence on the variance of the temperature. The results for the  $\Phi$  measure is presented in the following subsection.

These three methods of studying temperature fluctuations can be explored for an unambiguous answer about the event-by-event temperature fluctuations.

**6.5.6.2. Temperature fluctuation study in ALICE.** It is expected that large number of particles will be produced in central Pb–Pb collisions at LHC energies. This will permit to have  $p_t$  distributions of identified particles in every event. Presently this is studied using AliRoot simulation framework starting with events generated by using HIJING [636] generator for impact parameters between 0–5 fm. The combined particle identification algorithm as described in the performance section of this document is used to get tracks and particle-id for pions, kaons, and protons. Using these results multiplicity and  $p_t$  distribution of reconstructed tracks and identified particles are studied. Figure 6.217 shows the normalised  $p_t$  distribution of identified pions for (a) 3250 events and (b) one typical event. The solid lines are exponential fits to the data. The inverse slope parameters, which give estimates of the temperature, have been extracted from both the spectra. The slope parameters with the error bar (only from fitting) have been indicated in the figure.

The slope parameters obtained from single events as in Fig. 6.217(b) for a large number of generated events are plotted in Fig. 6.218. This distribution can be studied to get information about temperature fluctuations. The nature and amount of fluctuation in the data have to be studied by comparing the data distributions to generated mixed events sample and information from event generators. The temperature fluctuation extracted from the slopes of fitted  $p_t$  distributions provides complimentary information to those obtained from other methods.

**6.5.7.  $\langle p_t \rangle$  fluctuations.** The mean transverse momentum of emitted particles in an event is related to the temperature of the colliding system. So the event-by-event fluctuations

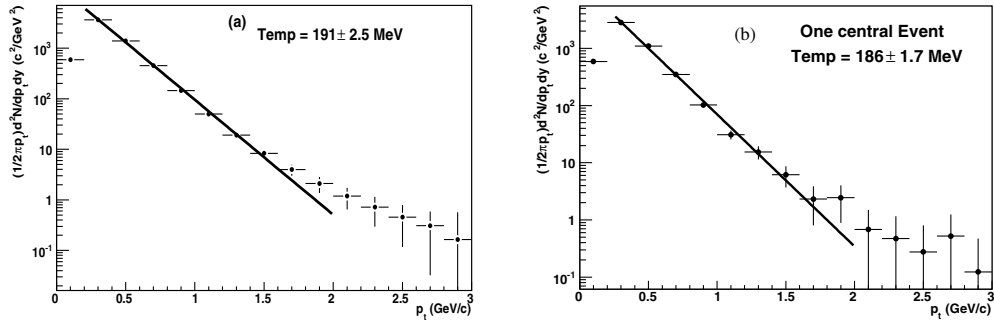


**Figure 6.217.** Normalised  $p_t$  distribution of pions for (a) 3250 events and (b) a single event for central Pb–Pb collisions at  $\sqrt{s_{\text{NN}}} = 5.5$  TeV. The solid lines are exponential fits to the data points (fits are made within the  $p_t$  range of 0.2 GeV/c to 2.0 GeV/c).

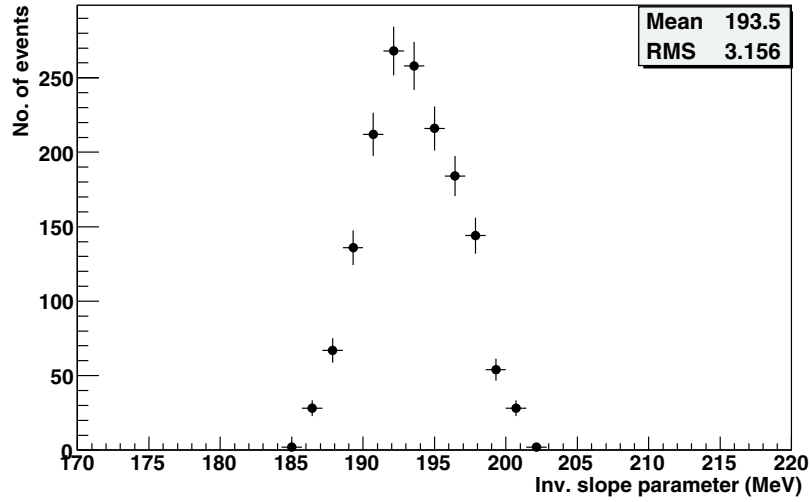


**Figure 6.218.** Inverse slope parameters of the  $p_t$  distribution of pions obtained for single events for central Pb–Pb collisions at  $\sqrt{s_{\text{NN}}} = 5.5$  TeV. The mean value turns out to be 193.5 MeV with an r.m.s. of 3.2 MeV (fits are made within the  $p_t$  range of 0.2 GeV/c to 2.0 GeV/c).

of average  $p_t$  will be sensitive to the temperature fluctuations predicted for QCD phase transitions. The dependence of the  $\langle p_t \rangle$  and its fluctuation is predicted to exhibit thermal equilibrium [690].

The fluctuations in  $\langle p_t \rangle$  have been measured by NA49, CERES, STAR and PHENIX experiments. The NA49 experiment was the first to report Gaussian behaviour of the event-by-event mean  $p_t$  for central events in Pb–Pb collisions at  $\sqrt{s_{\text{NN}}} = 17.2$  GeV as shown in the left panel of Fig. 6.219 [612, 613]. Analysis of the mean and sigma of the distribution indicated that the measured fluctuations are consistent with the expectation derived within statistical models of particle production when effects due to quantum statistics, Coulomb interaction, and resonance decays are taken into account [669, 681].

Systematic, quantitative study of event-by-event fluctuations is made using the  $\Phi$  measure of fluctuations [662] or closely related measures [691]. The  $\Phi$  measure allows us to remove the influence of ‘unwanted’ volume fluctuations (due to variations in the impact parameter

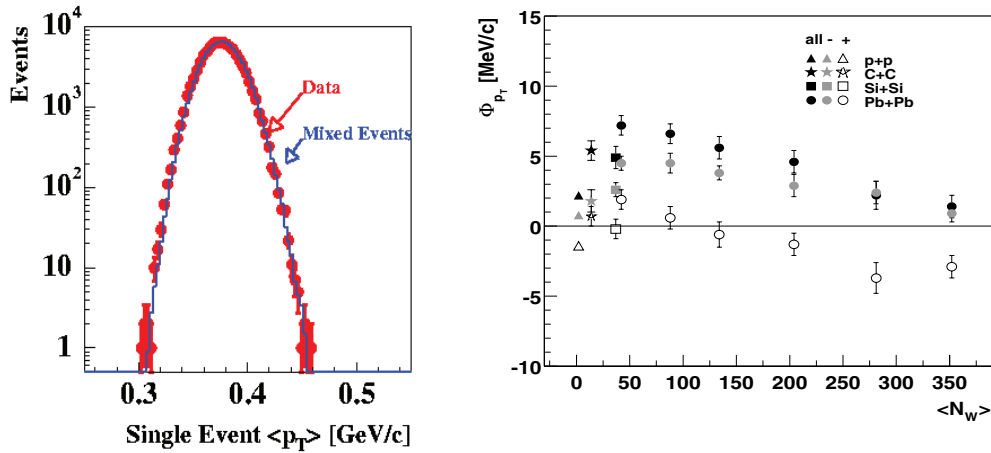


**Figure 6.219.** The left panel shows the event-by-event fluctuations of the mean transverse momentum for central Pb–Pb collisions at  $\sqrt{s_{NN}} = 17.2$  GeV as measured by NA49. The solid line indicates results from mixed events. The right panel gives the dependence of  $\Phi_{p_t}$  on the number of wounded nucleons for nucleus–nucleus collisions and inelastic pp interactions at  $\sqrt{s_{NN}} = 17.2$  GeV. The results indicate significant non-statistical fluctuations for light nuclei as well as peripheral Pb–Pb collisions [612].

of the collision resulting in turn in variations in the number of nucleons participating in the collision). It may be noted that the value of  $\Phi_{p_t}$  for uncorrelated particle production is equal to zero. The values of  $\Phi_{p_t}$  (the measure of transverse momentum fluctuations) obtained for all inelastic pp interactions and nucleus–nucleus (from C–C to central Pb–Pb) collisions at  $\sqrt{s_{NN}} = 17.2$  GeV are shown in the right panel of Fig. 6.219 as a function of the mean number of wounded nucleons [612] at forward rapidities ( $4.0 < y < 5.5$ ). The results indicate significant non-statistical fluctuations of transverse momentum for light nuclei and peripheral Pb–Pb collisions. Similar results have been reported by PHENIX at RHIC [627, 628]. For central Pb–Pb (Au–Au) collisions significant non-statistical  $p_t$  fluctuations are reported at mid-rapidity by STAR [631, 632] and CERES [626] experiments.

In ALICE, it will be possible to study fluctuations of mean transverse momentum for identified particles for different colliding systems and system centralities. Using the AliRoot simulated events discussed earlier, mean  $p_t$  distributions for identified pions, kaons and protons are obtained for a sample of 3250 events with  $b < 5$  fm for Pb–Pb collisions at  $\sqrt{s_{NN}} = 5.5$  TeV. The distributions are shown in Fig. 6.220. The mean values of  $\langle p_t \rangle$  come out to be 488.7 MeV, 581.2 MeV and 746.5 MeV with r.m.s. values of 7.2 MeV, 19.5 MeV and 25.5 MeV for pions, kaons and protons, respectively. These distributions will be studied in detail along with the mixed events for different fluctuation measures. The values of  $\langle p_t \rangle$  and their fluctuations are sensitive to QGP phase transition [597–602]. It would be essential to have these values from ALICE and see how these compare to the existing experimental data [692, 693] and theoretical calculations.

**6.5.8. Multiplicity fluctuations.** Multiplicity of produced particles is an important quantity to characterise the evolving system in a heavy-ion collision. Fluctuation of particle multiplicity from event to event may provide a distinct signal of the QGP phase transition. Several methods have been proposed to study event-by-event multiplicity fluctuations. A few of these methods are discussed here.

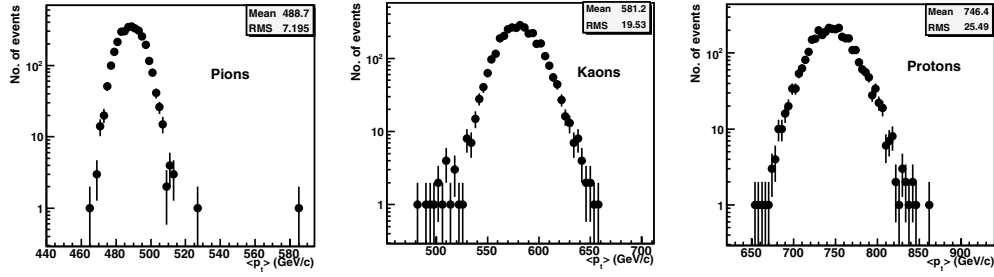


**Figure 6.220.** Distributions of the mean transverse momenta for identified pions, kaons and protons in central Pb–Pb collisions at  $\sqrt{s_{NN}} = 5.5$  TeV.

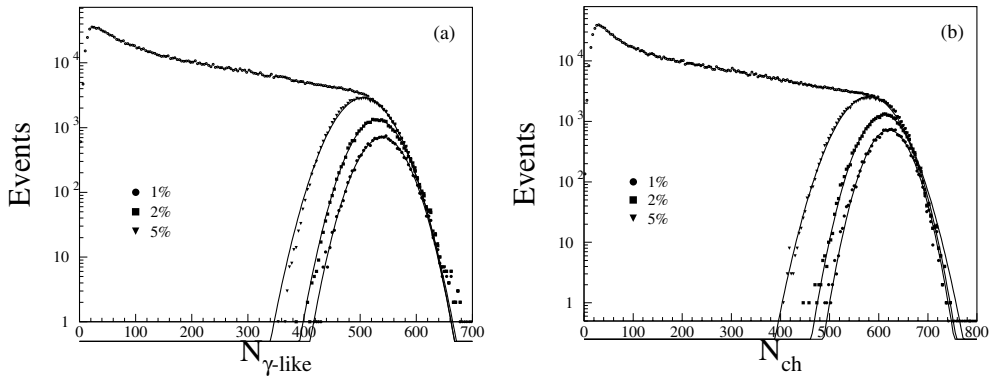


**Figure 6.221.** Minimum bias multiplicity distributions of photons and charged-particles for Pb–Pb reactions at  $\sqrt{s_{NN}} = 17.2$  GeV as measured by the WA98 experiment [621]. The distributions for the top 1%, 2% and 5% most central events are shown and fitted by Gaussian distributions.

Since the multiplicity distributions for narrow bins in centrality can be described by Gaussian distributions, the SPS experiments WA98 [621] and NA49 [615] used the normalised variance to quantify multiplicity fluctuations. In a simple participant model the multiplicity of produced particles may be expressed as given in Eq. 6.55. The fluctuations in multiplicity may be studied by a simple expression as given in Eq. 6.56. Figure 6.221 shows the minimum bias multiplicity distributions for charged-particles and photons in Pb–Pb collisions at  $\sqrt{s_{NN}} = 17.2$  GeV [621]. The multiplicity distributions for the top 1%, 2%, and 5% most central events are shown and fitted by Gaussian distributions. Multiplicity fluctuations of charged-particles and photons at various centrality bins going from central collisions at the left to peripheral at the right are shown in Fig. 6.222. The results are compared to calculations of participant model and VENUS calculations. The experimental data are found to agree reasonably well with results obtained from a simple participant model that takes into account impact parameter fluctuations. Recent NA49 results NA49 (see Fig. 6.223) show deviations from HIJING calculations [619]. The behaviour of the scaled variance is similar for positively and negatively charged-particles.

Multiplicity fluctuations can be studied using the ALICE experimental set-up. Charged-particle multiplicity distribution for central events in ALICE has been simulated in the AliRoot framework. This is shown in Fig. 6.224. For studying multiplicity fluctuation in detail,

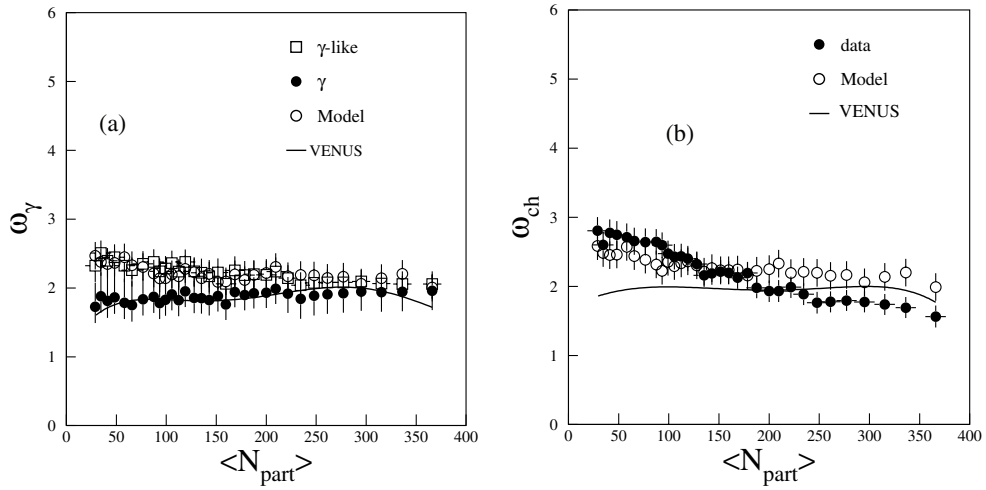


**Figure 6.222.** Multiplicity fluctuations of photons and charged-particles as a function of number of participants for Pb–Pb collisions at  $\sqrt{s_{\text{NN}}} = 17.2$  GeV from the WA98 experiment [621]. Data from the experiment are compared to calculations using the participant model and those from the VENUS event generator.

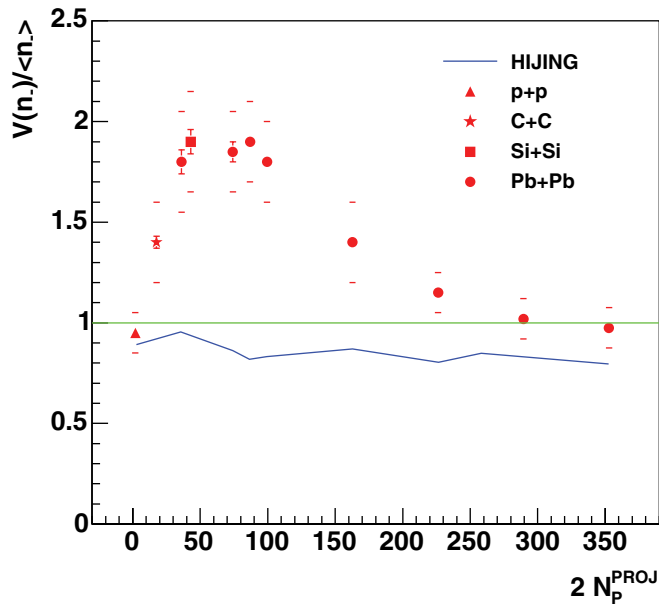


**Figure 6.223.** The scaled variance of multiplicity distributions for negatively charged hadrons on the number of projectile participants measured in various reactions at  $\sqrt{s_{\text{NN}}} = 17.2$  GeV by the NA49 experiment [619]. Results obtained within the string-hadronic model HIJING are shown by the solid line.

these distributions will be made for various centrality and  $p_t$  bins, and compared to results from mixed events as well as participant and other model predictions in order to make any conclusion about the presence or absence of fluctuations.

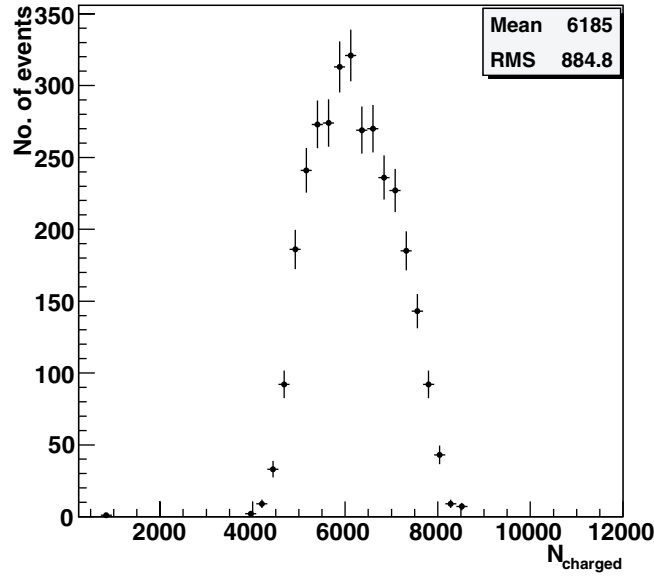


**Figure 6.224.** The event-by-event multiplicity distribution of charged-particles for simulated Pb–Pb events at  $\sqrt{s_{NN}} = 5.5$  TeV.

*6.5.9. Fluctuations in particle ratio and strangeness.* Early theoretical investigations [236, 694] have suggested that in case of large differences in free enthalpy of the hadronic and the QGP phases, a marked overheating-supercooling fluctuation might set in at temperatures around the critical temperature  $T_c$ , which is reflected in the broadening of the event-by-event ratio of kaon to pion yields. Recent calculations also suggest that the fluctuation patterns of event-by-event observables may be altered in the vicinity of the QCD phase boundary and especially in the vicinity of the tricritical point. It is suggested that strangeness fluctuations, especially fluctuations in  $K/\pi$  ratio, are sensitive to QCD phase transitions.

Both the NA49 experiment at SPS and STAR experiment at RHIC have studied event-wise kaon to pion ratio in detail. Both the experiments are well suited for event-by-event measurement of particle ratios. Recent analysis of event-by-event  $[K^+ + K^-]/[\pi^+ + \pi^-]$  and  $[p + \bar{p}]/[\pi^+ + \pi^-]$  have been performed for Pb–Pb collisions at fixed beam energies of 20, 30, 40, 80 and 158 A GeV by the NA49 collaboration [695]. At all five available beam energies the 3.5% most central Pb–Pb collisions were selected based on projectile spectator energy. The distributions of the particle ratios of kaons to pions and protons to pions at 20, 40 and 158 A GeV are shown in Figs. 6.225 and 6.226 [695, 696], respectively. The contribution due to finite number fluctuations in the particle multiplicities and effects of detector resolution are estimated using the mixed event technique. The mixed events are then subjected to the same fitting procedure as the real events.

For each data set, an estimation of the dynamical fluctuations may be made from the widths of the distribution of particle ratios in real data compared to those of the corresponding mixed events. This is denoted by

$$\sigma_{\text{dyn}} = \text{sign}(\sigma_{\text{data}}^2 - \sigma_{\text{mixed}}^2) \sqrt{|\sigma_{\text{data}}^2 - \sigma_{\text{mixed}}^2|}. \quad (6.64)$$

Left and right panels of Fig. 6.227 show the energy dependence of the event-wise dynamical fluctuations in the ratios  $(K^+ + K^-)/(\pi^+ + \pi^-)$  and  $[p + \bar{p}]/[\pi^+ + \pi^-]$ , respectively

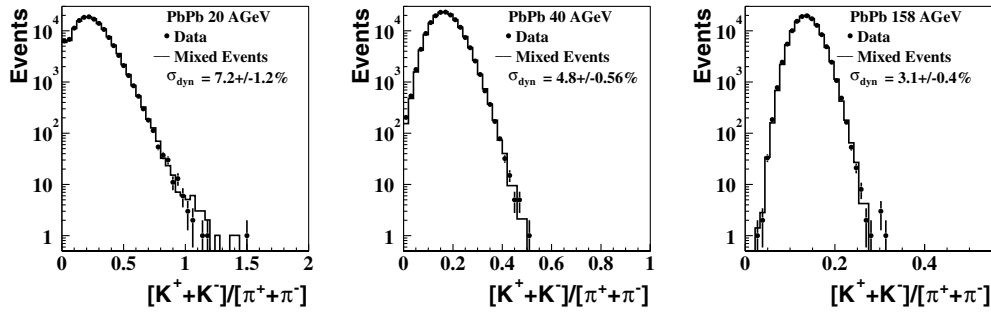


**Figure 6.225.** Distributions of the event-by-event  $[K^+ + K^-]/[\pi^+ + \pi^-]$  ratios for data (points) and mixed events (histograms) for central (top 3.5%) Pb–Pb collisions at 20, 40, 158 AGeV [695].

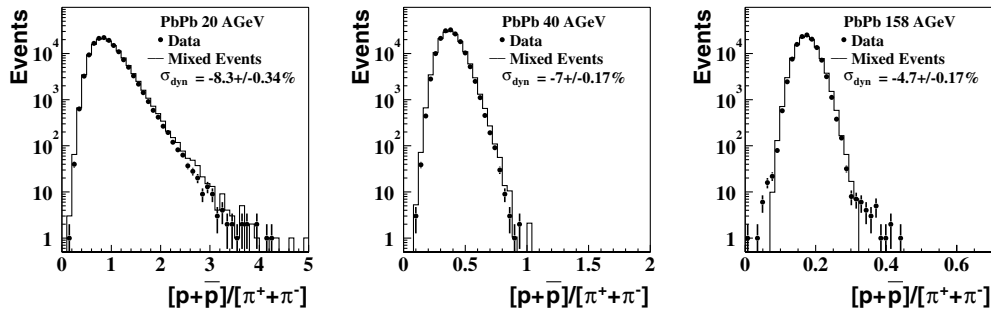


**Figure 6.226.** Distributions of the event-by-event  $[p + \bar{p}]/[\pi^+ + \pi^-]$  ratios for data (points) and mixed events (histograms) for central (top 3.5%) Pb–Pb collisions at 20, 40, 158 AGeV [695].

[695, 696]. Fluctuations of the  $K/\pi$  ratio are positive and decrease with beam energy. The distributions of the  $[p + \bar{p}]/\pi$  ratio shows that the width in case of the data is smaller than those of the mixed events. This gives rise to negative dynamical fluctuations which can be understood by considering resonance decays for pions and protons. The magnitude of the negative fluctuation signal in the  $[p + \bar{p}]/\pi$  channel may be related to the relative contribution of resonance decay products in the final state of the collision.

The data have been compared to the UrQMD model [697]. In this model, by construction, no fluctuations due to a potential phase transition are present, while resonance decays are included as well as effects of correlated particle production due to quantum number and energy–momentum conservation laws. The energy dependence of the event-by-event  $[p + \bar{p}]/\pi$  ratio in UrQMD closely matches the energy dependence observed in the data, as shown in Fig. 6.227. This lends further support to interpreting the negative fluctuation signal resulting from resonance decays. With fluctuations of the event wise  $K/\pi$  ratio, the energy dependence of the signal cannot be reproduced in the cascade model. Since the relative contribution of resonances changes dramatically with incident beam energy, one concludes that in the  $K/\pi$  ratio resonances do not give a significant contribution to the fluctuation signal. The finite fluctuation signal in the UrQMD model can be attributed to correlated particle production due to conservation laws.

The STAR experiment at RHIC has also performed a relevant study on the event wise fluctuations of the  $K/\pi$  ratio for Au–Au collisions at  $\sqrt{s_{NN}} = 62.4$  GeV and  $\sqrt{s_{NN}} = 200$  GeV [634]. Figure 6.228(a) shows the distribution of  $K/\pi$  ratio for the top 5% central Au–Au collisions at 200 GeV. The distributions from real and mixed events are superimposed

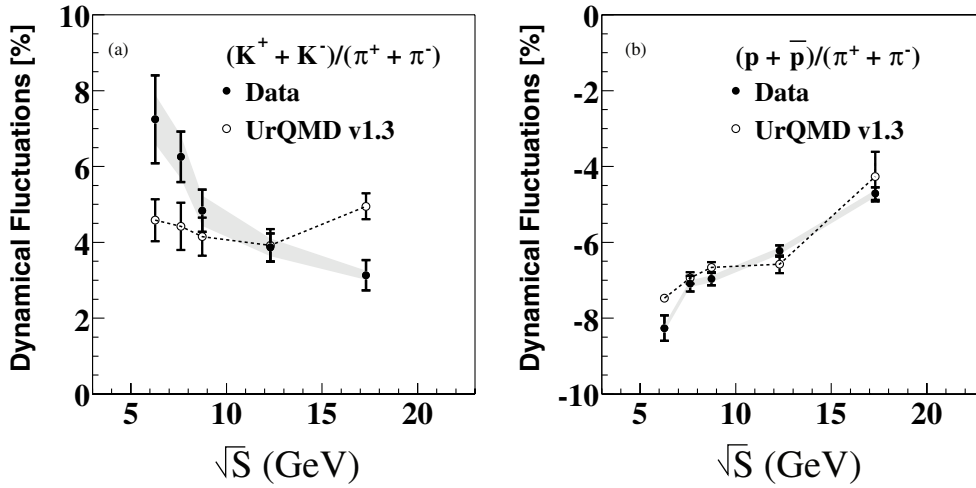


**Figure 6.227.** Energy dependence of the event-by-event fluctuation signal of (a) the  $[K^+ + K^-]/[\pi^+ + \pi^-]$  ratio, and (b) the ratio of  $[p + \bar{p}]/[\pi^+ + \pi^-]$ . The systematic errors of the measurements are shown as grey bands.

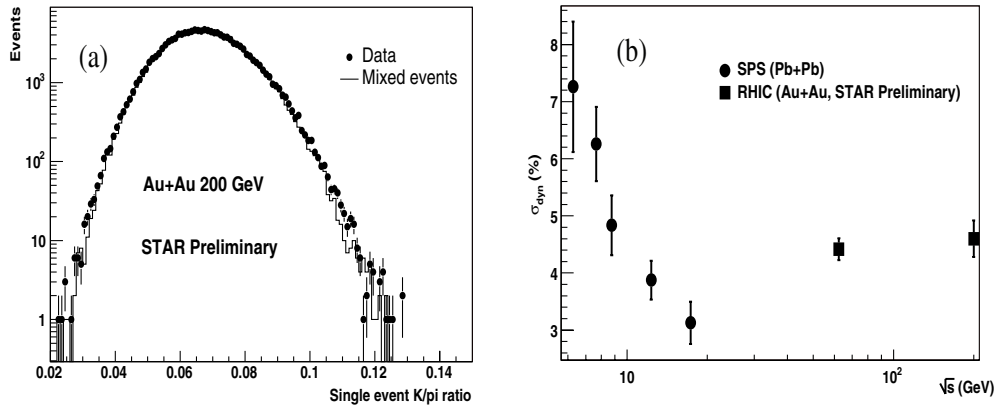


**Figure 6.228.** (a) Distribution of  $K/\pi$  ratio from data and mixed events from Au–Au at 200 GeV. The calculated dynamical fluctuation comes out to be  $\sigma_{\text{dyn}} = 4.6 \pm 0.038\%$ . (b) Excitation function for  $\sigma_{\text{dyn}}$  compiled from AGS to RHIC energies.

to help comparing the widths of the distributions. The STAR experiment also measured the  $K^+/\pi^+$  and  $K^-/\pi^-$  ratios and obtained the corresponding measures of dynamical fluctuations:  $\sigma_{\text{dyn}} = 3.06 \pm 0.88\%$  and  $\sigma_{\text{dyn}} = 3.61 \pm 0.67\%$  respectively.

In Fig. 6.228(b) the energy dependence (excitation function) of  $\sigma_{\text{dyn}}$  is plotted [634] from AGS to RHIC energies. One observes that the observed dynamical fluctuations take their maximum value for the lowest SPS energy and then decreases towards the highest SPS energy [695, 696]. The measured dynamical fluctuations increase as one goes to RHIC energies.

Fluctuations in particle ratio and strangeness can be carefully studied in ALICE. Using the simulated events as discussed earlier, ratio of kaons to pions and protons to pions are

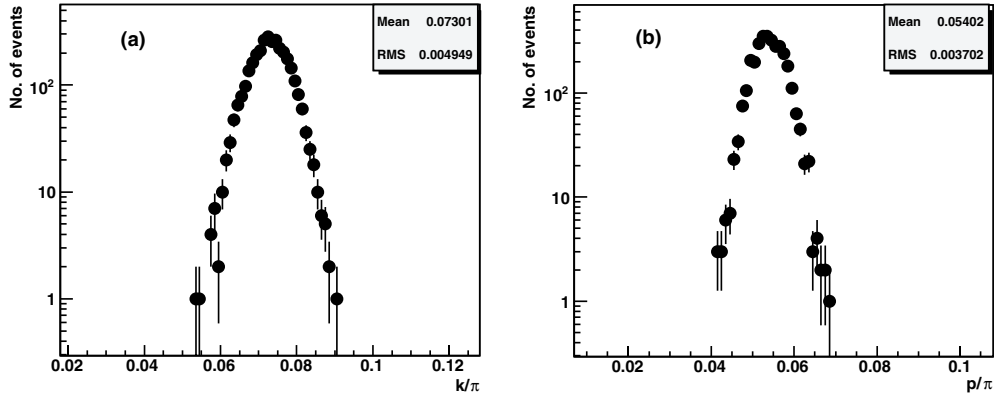


**Figure 6.229.** Ratios of event-by-event (a) kaons to pions and (b) protons to pions in simulated central Pb–Pb events at  $\sqrt{s_{\text{NN}}} = 5.5$  TeV within the ALICE acceptance for central detectors ( $0.9 < \eta < 0.9$ ).

plotted in Fig. 6.229 for central rapidity ( $-0.9 < \eta < 0.9$ ). The  $K/\pi$  ratio has a mean of 0.073 and r.m.s. of 0.005 whereas the ratio of  $p/\pi$  has a mean of 0.054 with a r.m.s. value of 0.004. These distributions will be investigated in detail using data from experiment, mixed events and generated events.

*6.5.10. Fluctuations of conserved quantities.* The major advantage [676, 677] of studying fluctuations of conserved quantities is that their relaxation time in a thermal system is much slower than that of non-conserved quantities, since there is no process which can generate conserved quantum numbers from the vacuum or via particle collisions. A detailed discussion of the relaxation time of fluctuation of conserved quantities is provided in Ref. [660]. As a consequence, the fluctuation of conserved charges such as net electric charge or baryon number may provide information from deep inside the system created in these collisions, where possibly a system with different degrees of freedom existed.

In addition, the fluctuations of baryon number and charge are sensitive to the fractional charge to baryon number carried by the quarks in the QGP, and may provide therefore an important signature for the existence of a deconfined phase as discussed in detail below. Of course, global charge conservation leads to vanishing fluctuations once the entire system is considered. Appropriate corrections have to be applied while considering only a fraction of the produced particles.

Fluctuation in electric charge can be simply expressed by

$$\langle (\delta Q)^2 \rangle = \langle Q^2 \rangle - \langle Q \rangle^2, \quad (6.65)$$

where  $Q$  is the net charge measured in the acceptance. For a system of several particle species  $i$  with charges  $q_i$  and multiplicities  $n_i$ , one writes

$$Q = \sum_i q_i n_i, \quad \langle Q \rangle = \sum_i q_i \langle n_i \rangle,$$

$$\text{and} \quad \langle (\delta Q)^2 \rangle = \sum_i (q_i)^2 \langle n_i \rangle + \sum_{i,k} c_{ik}^{(2)} \langle n_i \rangle \langle n_k \rangle q_i q_k, \quad (6.66)$$

where  $c_{i,k}^{(2)}$  are the normalised two-particle correlation functions given by:

$$c_{ii}^{(2)} = \frac{\langle n_i(n_i - 1) \rangle}{\langle n_i \rangle^2} - 1, \quad (6.67)$$

$$c_{ik}^{(2)} = \frac{\langle n_i n_k \rangle}{\langle n_i \rangle \langle n_k \rangle} - 1 \quad \text{if } i \neq k. \quad (6.68)$$

Correlations introduced by particle interactions, such as resonances affect the fluctuations [698–701]. The fluctuation measures may also be used to measure particle correlations in these systems. If, on the other hand, the particles are uncorrelated, the second term of Eq. (6.66) vanishes.

In a thermal system the charge fluctuations are given by the charge susceptibility:

$$VT\chi_Q = -T \frac{\partial^2 F}{\partial \mu_Q^2}, \quad (6.69)$$

which for a macroscopic system measures the response to external electric fields. In the case of a free uncorrelated pion gas the charge fluctuations are then

$$\langle (\delta Q)^2 \rangle_{\pi\text{-gas}} = \langle N_+ \rangle + \langle N_- \rangle = \langle N_{\text{ch}} \rangle, \quad (6.70)$$

where  $N_{\text{ch}}$  is the total number of charged-particles. For a QGP, on the other hand, assuming uncorrelated quarks and gluons, one obtains

$$\langle (\delta Q)^2 \rangle_{\text{QGP}} = q_u^2 \langle N_u + N_{\bar{u}} \rangle + q_d^2 \langle N_d + N_{\bar{d}} \rangle = \frac{5}{18} \langle N_q \rangle, \quad (6.71)$$

where  $N_q$  is the total number of quarks in the system. The contribution of heavy quarks can be neglected assuming their yield is suppressed.

Note that in the case of QGP formation, the charge fluctuations depend on the square of the fractional charge of the quarks. In order to expose the dependence on the fractional charge, one should divide the charge fluctuations by the number of particles or the entropy carried by the system. A good measure for the entropy is the number of charged-particles in the final state and thus the observable

$$\frac{\langle (\delta Q)^2 \rangle}{\langle N_{\text{ch}} \rangle} \quad (6.72)$$

should be sensitive to the fractional charges of the QGP. Indeed, using  $N_{\text{ch}} \simeq N_q + N_g$  (which follows from the assumption of entropy conservation), where  $N_g$  is the number of gluons (for detailed discussion see Ref. [677]) one obtains

$$\frac{\langle (\delta Q)^2 \rangle}{\langle N_{\text{ch}} \rangle}_{\text{QGP}} \simeq 0.2 \quad (6.73)$$

and

$$\frac{\langle (\delta Q)^2 \rangle}{\langle N_{\text{ch}} \rangle}_{\pi\text{-gas}} = 1 \quad (6.74)$$

for the pion gas. Correcting for quantum statistics and taking hadronic resonances into account, which introduce correlation terms (see Eq. 6.66), for the hadron gas one gets

$$\frac{\langle (\delta Q)^2 \rangle}{\langle N_{\text{ch}} \rangle}_{\text{hadron-gas}} \simeq 0.75. \quad (6.75)$$

On the quark–gluon plasma side, one can consult Lattice QCD calculations, available for the charge fluctuations as well as for the entropy as discussed earlier. In this case one finds [677]

$$\frac{\langle(\delta Q)^2\rangle}{\langle N_{\text{ch}}\rangle_{\text{QGP}}} \simeq 0.25 - 0.4, \quad (6.76)$$

where the uncertainty is due to the way in which entropy is related to the number of charged-particles (see Refs. [676, 677]).

To access this observable in the experiment it is not sufficient to simply measure the charge fluctuations and the number of charged-particles separately. As can be seen from Eq. 6.66 the magnitude of the charge fluctuations scales with the number of charged-particles in the system, i.e. it scales with the system size. Therefore fluctuations of the system size, or impact parameter fluctuations, which are present even if centrality cuts are applied, will contribute to the charge fluctuations. Of physical interest, however, are the charge fluctuations due to density fluctuations. Thus, the effect of volume fluctuations has to be removed by an appropriate choice of observables.

It has been shown in Ref. [664] that the  $\Phi_q$  measure is less sensitive to the biasing effects than the originally proposed  $\tilde{D}$  measure. Both are sensitive to the hypothetical suppression of fluctuations in charge particles due to QGP creation. Similar information may also be obtained by measuring balance functions described later in this section.

*6.5.10.1. Net charge fluctuations.* Recent suggestions [676, 677] that event-by-event fluctuations of electric charge in high-energy A–A collisions may provide information on the state of matter at the early stage of the collision triggered corresponding experimental studies. The first results [612, 629–631] indicate that the net electric charge fluctuations are governed by the conservation of electric charge [664, 665, 702] and that additional contributions, if any, are small. Event-by-event fluctuations of the electric charge are expected to be suppressed as a consequence of deconfinement [676, 677]. Estimates of the magnitude of the charge fluctuations indicate that they are much smaller in a quark–gluon plasma than in hadron gas.

Different measures for studying charge fluctuations are applied by the experiments NA49, PHENIX and STAR. One of them is the  $\Delta\Phi_q$  which is used by the NA49 experiment and is defined as:  $\Delta\Phi_q = \Phi_q - \Phi_{q,\text{GCC}}$ .  $\Phi_q$  is the established measure  $\Phi$  of the event-by-event fluctuations [662, 664] and  $\Phi_{q,\text{GCC}}$  is the value of  $\Phi_q$  corresponding to a scenario where particles are correlated only by global charge conservation and is given by [664]  $\Phi_{q,\text{GCC}} = \sqrt{1-P} - 1$  where  $P = \langle N_{\text{ch}} \rangle / \langle N_{\text{ch}} \rangle_{\text{tot}}$ , with  $\langle N_{\text{ch}} \rangle$  and  $\langle N_{\text{ch}} \rangle_{\text{tot}}$  being the mean charged-particle multiplicity in the detector acceptance and in the full phase space respectively.

In Fig. 6.230 the  $\Phi_q$  and  $\Delta\Phi_q$  values are plotted as a function of  $\langle N_{\text{ch}} \rangle / \langle N_{\text{ch}} \rangle_{\text{tot}}$  for central Pb–Pb collisions at 20–158 A GeV [616]. The main trend observed in the data is a monotonic decrease with increasing fraction of accepted particles. This is approximately reproduced by introducing global charge conservation as the only source of correlations. One can notice from Fig. 6.230(b) that the measured  $\Delta\Phi_q$  values are close to zero as expected for a gas of pions correlated only by global charge conservation [665]. The results of a model which incorporates intermediate resonances [616, 664] show that the decay of the  $\rho$  meson may increase the initial QGP charge fluctuations to  $\Delta\Phi_q \approx 0$  and thereby completely masking a possible QGP signal at SPS energies.

At RHIC, both PHENIX and STAR experiments have studied net charge fluctuations for Au–Au interactions at  $\sqrt{s_{\text{NN}}} = 130$  GeV. In the PHENIX experiment, the fluctuations were studied in the variable,  $Q = n_+ - n_-$  [629] with a variance

$$V(Q) = \langle Q^2 \rangle - \langle Q \rangle^2 = n_{\text{ch}}. \quad (6.77)$$

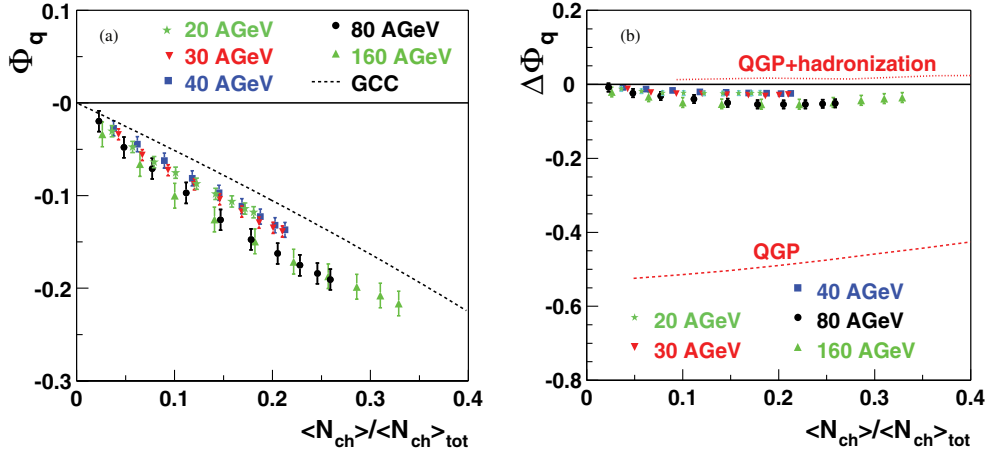


**Figure 6.230.** The dependence of (a)  $\Phi_q$  and (b)  $\Delta\Phi_q$  on the fraction of accepted particles for central Pb–Pb collisions at 20–158 AGeV. In (a) the dashed line shows the dependence expected for the case where the only source of particle correlations is the global charge conservation. In (b) the prediction for the ideal QGP is indicated by the dashed curve (QGP), whereas the prediction for the QGP including hadronization and resonance decay is shown by the dotted curve (QGP + hadronization)

The experimental data behave in an almost stochastic matter, and there is a reasonable agreement between data and RQMD calculations, including the effects of global charge conservation and neutral hadronic resonances decays. Furthermore, the data show no centrality dependence [629].

The STAR experiment has discussed the fluctuations as the difference of the number of positive and negative particles in a fixed rapidity range, defined as [691]

$$\nu_{+-} = \left\langle \left( \frac{N_+}{\langle N_+ \rangle} - \frac{N_-}{\langle N_- \rangle} \right)^2 \right\rangle. \quad (6.78)$$

The dynamical fluctuations are defined as  $\nu_{+-,\text{dyn}} = \nu_{+-} - \nu_{+-,\text{stat}}$ , where

$$\nu_{+-,\text{stat}} = \frac{1}{\langle N_+ \rangle} + \frac{1}{\langle N_- \rangle}. \quad (6.79)$$

The dynamical fluctuations of the 5% most central collisions are obtained as [630]

$$\nu_{+-,\text{dyn}} = -0.00236 \pm 0.00006(\text{stat}) \pm 0.00012(\text{syst}).$$

This was compared to results from PHENIX [629] by modifying the expression of  $\nu(Q)$  in order to take acceptance effects into account [691]:

$$\nu_{+-,\text{stat}} = \frac{4}{N_+ + N_-} \cdot (\nu(Q) - 1), \quad (6.80)$$

which gives

$$\nu_{+-,\text{dyn}} = -0.0018 \pm 0.0004(\text{stat}) \pm 0.0009(\text{syst})$$

in agreement with the value measured by the STAR collaboration for the 11% central collisions. A comparison of the STAR measurements with thermal models [677, 704] indicates fluctuations at a level that might be expected if the Au–Au system behaved like a resonance gas. Although the size of the fluctuations is larger than expected for a quark–gluon gas,

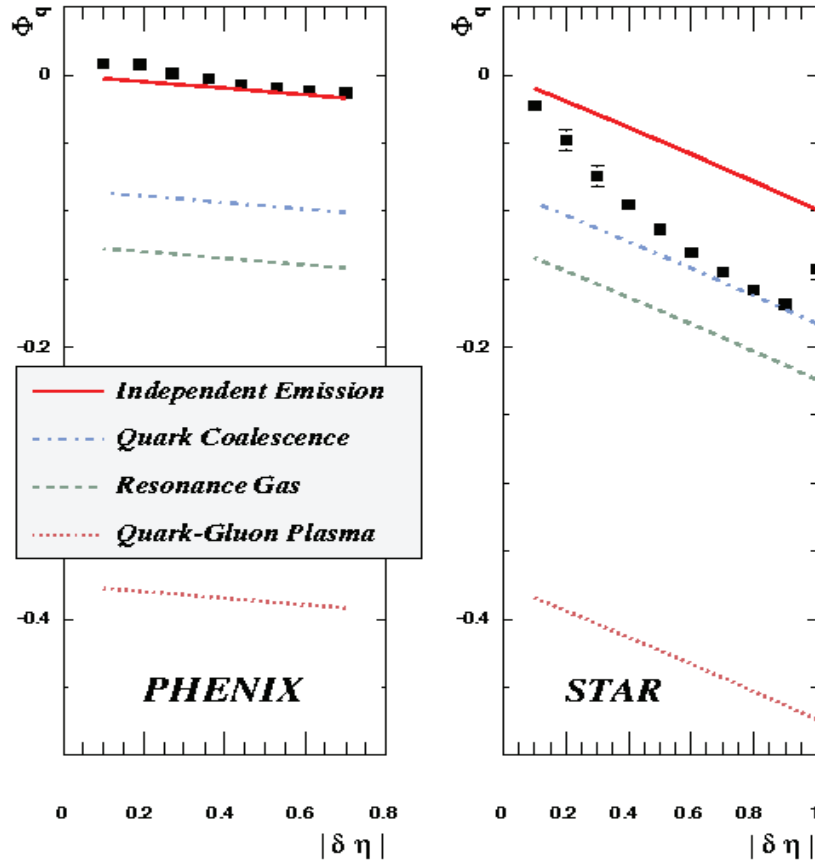


**Figure 6.231.** Results for charge fluctuation calculations [703] obtained for PHENIX [629] and STAR [630] experiments for Au–Au collisions at  $\sqrt{s_{NN}} = 130$  GeV.

limitations of the model used [630] prevent a conclusion on the existence or non-existence of a quark–gluon plasma phase based on the above results.

Figure 6.231 gives a compilation of net charge fluctuation results from PHENIX and STAR experiment [703] for Au–Au collisions at  $\sqrt{s_{NN}} = 130$  GeV in terms of  $\Phi_q$  variable. Superimposed on the plots are curves representing the predictions for independent particle emission, quark coalescence, resonance gas and QGP after correcting for acceptances of the detectors. The results are closer to independent particle emission and the resonance gas scenarios.

**6.5.11. Balance functions.** The Balance Functions (BF), introduced by Bass, Danielewicz and Pratt [705] provides an important measure of correlations. It measures the correlation of the oppositely charged-particles produced during a heavy-ion collision, and its width can be related to the time of hadronization. The BF is derived from the charge correlation function that was used to study the hadronization of jets in pp collisions at the ISR [706] and  $e^+e^-$  annihilations at PETRA [707, 708]. The first results on the BF were obtained for Au–Au collisions by the STAR collaboration at RHIC [636].

The motivation for studying the BF comes from the idea that hadrons are produced locally as oppositely charged-particle pairs. Particles of such a pair are separated in rapidity due to

the initial momentum difference and secondary interactions with other particles. Particles of a pair created earlier are separated further in rapidity because of the expected large initial momentum difference and the long lasting rescattering phase. On the other hand, oppositely charged-particle pairs that were created later are correlated within a smaller interval  $\Delta y$  of the relative rapidity. Our aim is to measure the degree of this separation of the balancing charges and to find possible indications for delayed hadronization.

The BF can be studied as a function of several parameters in order to gain insight about different physics mechanisms. The BF can be studied as a function of the relative pseudorapidity difference for all charged-particles, and can be written as  $B(\Delta\eta)$  [617, 636]. In addition, there is the possibility to study the BF for different particle species. For example, one can analyse the correlations between oppositely charged pions, kaons (and thus extend the method to a strange-anti strange correlation study) or even protons (extension to baryon-antibaryon study) [633]. By performing this study, one could gain insight about the possible different mechanisms that are important in the creation process for these species. Furthermore the BF can be studied as a function of the azimuthal angle  $\phi$  as proposed in [709] and thus translate the correlation function into a measure of transverse flow. By doing that one will be able to quantify the transverse flow for different particle species (pions, kaons, protons) by analysing the  $B(\Delta\phi)$  for identified oppositely charged-particles. Finally, the BF can be studied as a function of the invariant relative momentum  $Q_{\text{inv}}$  [710]. This variable is suggested to yield a clearer insight for interpreting the physics of the balancing charges as well as providing a better illumination of the distorting effects.

In order to examine the  $\eta$  correlation of charged-particles the BF is defined as a difference of the correlation function of oppositely charged-particles and the correlation function of like-charge particles normalised to the total number of particles. The general definition of the BF reads [705]

$$B(P_2|P_1) = \frac{1}{2} \left[ \frac{N(b, P_2|a, P_1) - N(a, P_2|a, P_1)}{N(a, P_1)} + \frac{N(a, P_2|b, P_1) - N(b, P_2|b, P_1)}{N(b, P_1)} \right], \quad (6.81)$$

where  $a$  and  $b$  could be different kinds of particles, whereas  $P_1$  and  $P_2$  could be intervals in pseudorapidity. For example  $a$  could refer to all negative particles and  $b$  to all positive particles. Alternatively  $P_2$  could be an interval of the relative pseudorapidity  $\Delta\eta = |\eta_b - \eta_a|$  of the oppositely charged-particles, whereas  $P_1$  could be the interval of the pseudorapidity of the produced particles that is covered by the detector. In the numerator,  $N(b, P_2|a, P_1)$  represents a conditional probability of observing a particle of type  $b$  in bin  $P_2$  given the existence of a particle of type  $a$  in bin  $P_1$ . The terms  $N(b, P_2|a, P_1)$ ,  $N(a, P_2|a, P_1)$ ,  $N(a, P_2|b, P_1)$ , and  $N(b, P_2|b, P_1)$  are calculated using pairs from each event and the resulting values are summed over all events. For example, the term  $N(b, P_2|a, P_1)$  is calculated by counting all possible combinations of a positive particle in  $P_2$  and a negative particle in  $P_1$  in an event and summing the number of combinations over all events. The other three terms are calculated analogously. The terms  $N(a, P_1)$  and  $N(b, P_1)$  are the total number of negative and positive particles, respectively, that are within the pseudorapidity interval  $P_1$ , summed over all events.

In this case,  $a$  and  $b$  are the negative and positive particles, respectively, that are within the pseudorapidity interval  $P_1$  and have a pseudorapidity difference  $\Delta\eta$ . Thus, with this formulation, the definition of the BF takes the following form:

$$B(\Delta\eta) = \frac{1}{2} \left[ \frac{N_{+-}(\Delta\eta) - N_{--}(\Delta\eta)}{N_-} + \frac{N_{-+}(\Delta\eta) - N_{++}(\Delta\eta)}{N_+} \right]. \quad (6.82)$$

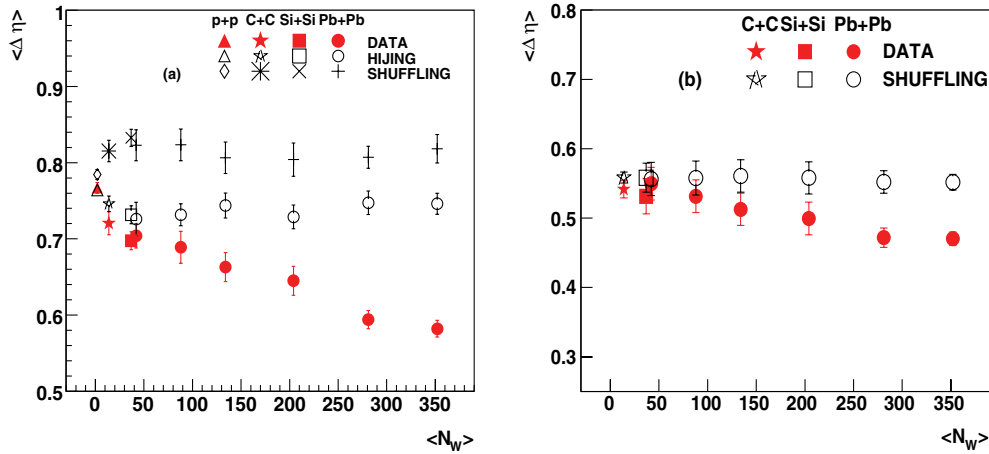


**Figure 6.232.** The dependence of the width of Balance Function on the number of wounded nucleons for pp, C–C, Si–Si and Pb–Pb collisions at (a)  $\sqrt{s_{NN}} = 17.2$  GeV, and (b)  $\sqrt{s_{NN}} = 8.8$  GeV, as measured by the NA49 experiment, shown for different cases.

The most interesting property of the BF is its width. Early stage hadronization is expected to result in a broad BF, while late stage hadronization leads to a narrower distribution [705]. The width of the BF can be characterised by the weighted average  $\langle \Delta \eta \rangle$ :

$$\langle \Delta \eta \rangle = \frac{\sum_{i=0}^k (B_i \cdot \Delta \eta_i)}{\sum_{i=0}^k B_i}, \quad (6.83)$$

where  $i$  is the bin number of the BF histogram.

In the following, the corresponding results from both SPS (NA49) and RHIC (STAR) experiments are discussed and reference will be made to the most established theories that provide both qualitative and quantitative interpretation to these results. Finally, extension of the method to LHC energies will be presented.

**6.5.11.1. System size and centrality dependence.** The recent results that are included in this section come from the analysis of pp, C–C, Si–Si, and Pb–Pb collisions at  $\sqrt{s_{NN}} = 17.2$  GeV and  $\sqrt{s_{NN}} = 8.8$  GeV (NA49–SPS) [617] and the corresponding analysis of Au–Au collisions at  $\sqrt{s_{NN}} = 130$  GeV (STAR–RHIC) [636]. The conditions and details concerning the analysis procedure are described in [617, 636]. The BF for each centrality class was also calculated for mixed events produced with the shuffling mechanism to estimate the maximum possible value of the width of the BF while retaining the constraint of charge conservation [617, 636].

In order to further investigate the origin of the system size and centrality dependence of the BF, the HIJING event generator was used to generate A+A collisions for the highest SPS and the corresponding RHIC energy. Fig. 6.232(a) shows the dependence of the width  $\langle \Delta \eta \rangle$  of the BF on the mean number of wounded nucleons  $\langle N_W \rangle$  for the highest SPS energy. The results for pp, C–C and Si–Si collisions are also included. The width decreases monotonically with  $\langle N_W \rangle$ . On the other hand, the width of the BF from both HIJING and shuffled data does not show any clear dependence on centrality [617]. Fig. 6.232(b) shows the dependence of the width  $\langle \Delta \eta \rangle$  of the BF on the mean number of wounded nucleons  $\langle N_W \rangle$  for the lower SPS energy ( $\sqrt{s_{NN}} = 8.8$  GeV). The width decreases monotonically with  $\langle N_W \rangle$  also for this energy. On the other hand, the width of the BF from shuffled data does not show any clear dependence on centrality.

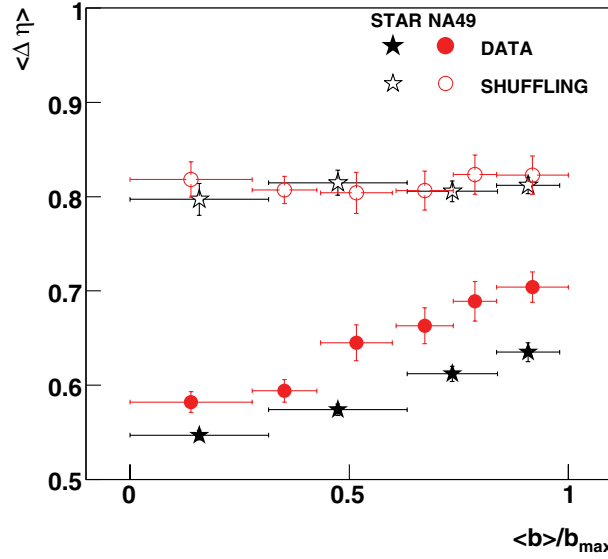


**Figure 6.233.** The dependence of the width of BF on the normalised impact parameter  $b/b_{\max}$ , as measured by NA49 for Pb–Pb collisions at  $\sqrt{s_{\text{NN}}} = 17.2$  GeV and by STAR for Au–Au collisions at  $\sqrt{s_{\text{NN}}} = 130$  GeV.

The results from the analysis performed for Au–Au collisions at  $\sqrt{s_{\text{NN}}} = 130$  GeV by the STAR collaboration at RHIC [636] are plotted in Fig. 6.233. The width of the BF decreases from peripheral to central collisions by  $17 \pm 3\%$  for the NA49 data, whereas for the higher energy STAR data the corresponding decrease is of the order of  $14 \pm 2\%$  [617]. It needs to be mentioned that there should be no direct comparison between the actual values of the widths for the two experiments since first of all the BF is studied in different pseudorapidity intervals and the analysis procedure (event and track quality cuts) is not identical. Thus, the proposed way to compare the two effects is simply by studying the slope.

**6.5.11.2. Pseudorapidity dependence.** An attempt has been made to study the centrality dependence of the width of BF in different pseudorapidity intervals for both energies in the NA49 set-up. This was done in order to test the theory upon which the BF is based [705], and which describes the hadronization process mainly as the creation of oppositely charged-particles at the same location in space-time. In order to perform this study, the pseudorapidity interval that was analysed was shifted towards the forward region. In particular, the intervals are  $3.3 \leq \Delta\eta \leq 4.7$  and  $4.0 \leq \Delta\eta \leq 5.4$  for  $\sqrt{s_{\text{NN}}} = 8.8$  and  $\sqrt{s_{\text{NN}}} = 17.2$  GeV, respectively, while the previous ones were  $1.8 \leq \Delta\eta \leq 3.2$  and  $2.5 \leq \Delta\eta \leq 3.9$ .

Figure 6.234 shows the dependence of the width  $\langle \Delta\eta \rangle$  of the BF on the mean number of wounded nucleons  $\langle N_W \rangle$  for the  $\sqrt{s_{\text{NN}}} = 17.2$  GeV (left plot) and for the  $\sqrt{s_{\text{NN}}} = 8.8$  GeV (right plot) in this forward region. The width of the BF for all data samples (real, shuffled and HIJING data) does not show any clear dependence on centrality.

The main conclusion from this study is that the effect is located in the mid-rapidity region. This can be explained if one takes into account the fact that the width of the BF is a measure of correlations. Thus there may be an excess of correlation in the mid-rapidity region compared to the forward one.

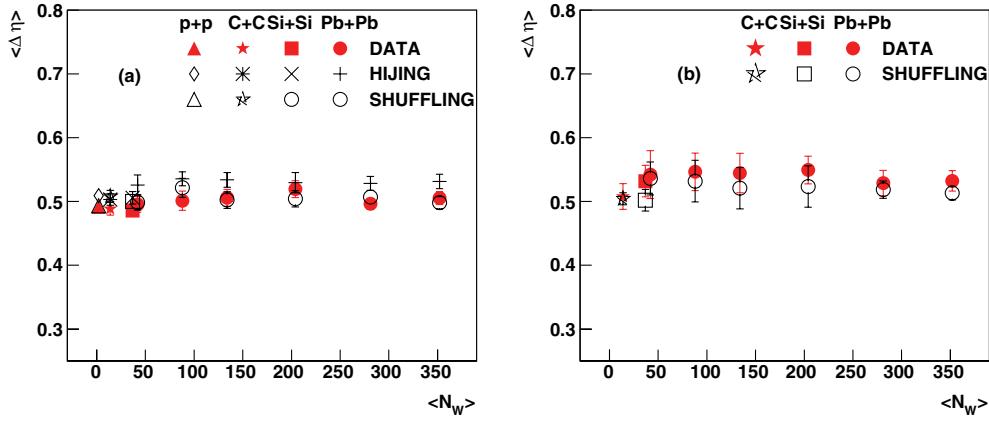


**Figure 6.234.** The dependence of the widths of BF on the number of wounded nucleons for pp, C–C, Si–Si and Pb–Pb collisions at  $\sqrt{s_{NN}} = 17.2$  GeV (left plot) and  $\sqrt{s_{NN}} = 8.8$  GeV (right plot) in the forward pseudorapidity region as measured by the NA49 collaboration [620].

**6.5.11.3. Balance function for pions and kaons.** An attempt to study the centrality dependence of the BF for identified pions and kaons has been performed by the STAR collaboration [633]. This investigation was motivated by the principles of the BF described in [705], which in particular suggest that the width of the distribution of heavier particles is narrower than the one for lighter particles. Charged kaons and pions produced in Au–Au collisions at  $\sqrt{s_{NN}} = 200$  GeV and at pp collisions at  $\sqrt{s} = 200$  GeV were identified and used in order to examine the possible centrality dependence for each particle family. The conclusions extracted from this analysis were that the BF for kaons are narrower than the ones for pions at all centrality classes. This confirms the original expectations. Furthermore, BFs for pions are narrower for central Au–Au collisions than in peripheral Au–Au collisions [633], whereas there is no evidence of such centrality dependence for BF of kaons. The fact that the BFs for kaons does not narrow with centrality may indicate a different hadronization process for kaons than for pions.

**6.5.11.4. Energy dependence.** The energy dependence of the BF was studied within the NA49 detector acceptance. The most central Pb–Pb events were analysed throughout the whole SPS energy range. These data samples are passed once again through the shuffling mechanism so that one can estimate the largest value of the width for each energy. The pseudorapidity interval analysed for each energy was limited to the same range. In order to quantify the decrease of the width for different energies, the normalised parameter  $W$  is calculated as

$$W = \frac{100 \cdot (\langle \Delta \eta \rangle_{\text{shuffled}} - \langle \Delta \eta \rangle_{\text{data}})}{\langle \Delta \eta \rangle_{\text{shuffled}}}. \quad (6.84)$$

The left panel of Fig. 6.235 shows the dependence of this parameter on the  $\sqrt{s_{NN}}$  [620]. As far as the data is concerned, after the use of acceptance filter, one notices a first indication of an energy dependence. The normalised parameter  $W$  takes a small value for the central Pb–Pb collisions at  $\sqrt{s_{NN}} = 6.3$  GeV. Then takes a somehow constant value for the intermediate SPS energies and finally rises as towards top SPS energy of  $\sqrt{s_{NN}} = 17.2$  GeV. In addition, two model comparisons are made in order to further investigate this energy dependence. The UrQMD and the Hadron-String Dynamics (HSD) transport approach [711] are two

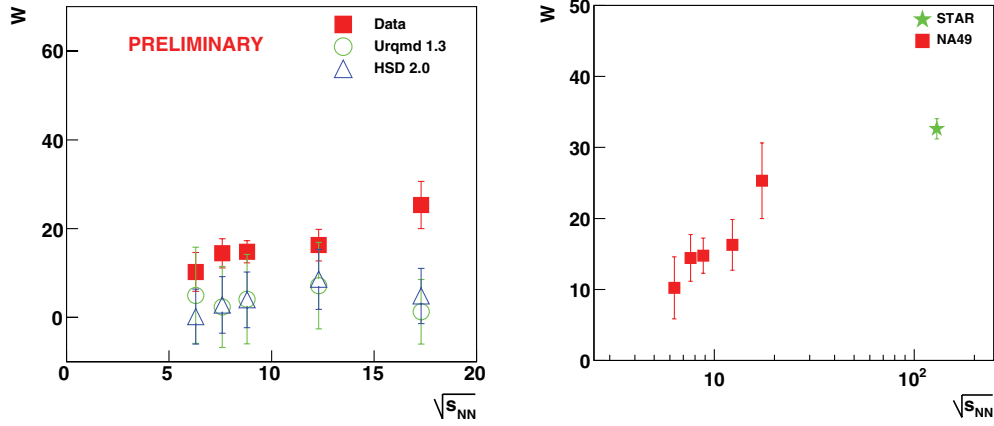


**Figure 6.235.** The dependence of the normalised parameter  $W$  on the  $\sqrt{s_{NN}}$  for central Pb–Pb collisions in the SPS energy range after applying the acceptance filter (left plot). Comparisons with models are also shown. The right panel shows the  $W$  parameter from NA49 as well as from the STAR experiment for Au–Au collisions at  $\sqrt{s_{NN}} = 200$  GeV.

microscopic models used to simulate (ultra)relativistic heavy-ion collisions in the energy range from Bevalac and SIS up to AGS, SPS and RHIC. The points from the corresponding analysis of both UrQMD and HSD generated events throughout the whole SPS energy range can also be seen in Fig. 6.235. By studying these plots one notices no sign of energy dependence of the  $W$  parameter from the models [620].

The NA49 data for the  $W$  parameter is plotted along with the data from STAR in the right panel of Fig. 6.235. This shows the dependence of the  $W$  parameter on the  $\sqrt{s_{NN}}$  for a large range of energy. The increase of the  $W$  parameter from SPS to RHIC energy is significant and the results for ALICE will be interesting to understand the nature of QGP phase transition.

**6.5.11.5. Interpretation of the results.** The measured narrowing of the BF is qualitatively consistent with the delayed hadronization scenario [636, 705] of an initially deconfined phase. Several model calculations have been published which provide a more quantitative description [698, 713, 714]. In particular, within models based on statistical hadronization and hydrodynamic expansion the width of the BF was found to decrease with increasing transverse collective velocity of the matter at freeze-out [713, 714] and thus with the collision centrality. However, a quantitative description of the STAR data was possible only when the condition of global charge conservation (a single fireball model) [713, 714] was substituted by a stronger condition of charge conservation in sub volumes (a multi-fireball model) [712]. The quark coalescence model was applied to the hadronization of the deconfined phase in [698]. When including radial flow, good agreement with the STAR measurements was obtained also in this model calculation.

The influence of the decay of resonances on the width of the BF was estimated using the HIJING event generator. One finds that the BF width increases by about 4% when  $\rho^0$ -meson decays are switched off. In the model, the fraction of pions coming from  $\rho^0$  decays (about 19%) is approximately independent of centrality [617]. Therefore, the effect of  $\rho^0$  decay can not explain the strong system size and centrality dependence of the width of the BF that is observed in experimental data.

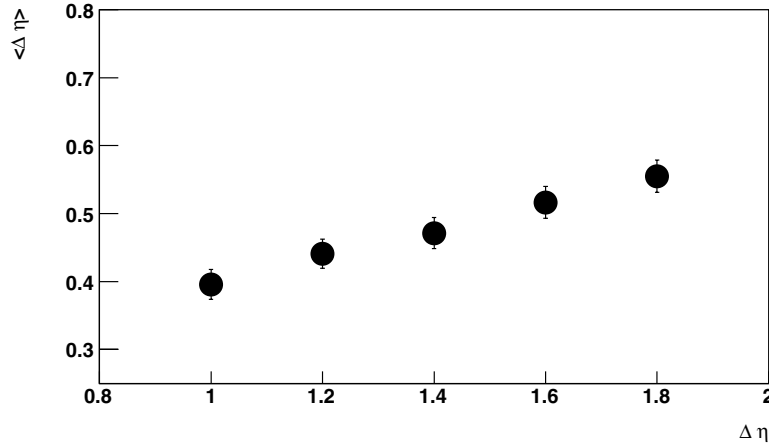


**Figure 6.236.** The dependence of the BF width on the pseudorapidity interval analysed for simulated pp events at c.m. energy of 14 TeV.

**6.5.11.6. Balance function in ALICE.** The method of BF has been extended to LHC energies in terms of the ALICE experimental set-up. Results of analysis performed on reconstructed pp and Pb–Pb simulated data are discussed here.

*Proton–proton interactions.* The BF was studied for  $6 \times 10^4$  simulated pp events at  $\sqrt{s} = 14$  TeV events that have passed through the whole reconstruction chain of ALICE as a function of the relative pseudorapidity interval  $\Delta\eta$ . This study is done using the PYTHIA generator.

The dependence of the width of the BF distribution on  $\Delta\eta$ , the range of the analysed pseudorapidity window from half a unit up to 0.9 around mid-rapidity with a step of 0.1, is shown in Fig. 6.236. This dependence is shown for different runs as well as for the whole data sample. A linear dependence of the width is observed, which is something already seen in both SPS and RHIC energies. Thus, in order to directly compare the actual values of the width with the corresponding values from RHIC, one should analyse the maximum phase space interval provided by the detector’s acceptance. The errors shown in Fig. 6.236 correspond to the statistical ones.

Furthermore, a detailed study was performed in order to estimate the contribution of the systematic errors on the calculated width. In order to do that event and track level quality cuts were varied, and the corresponding width for each distribution was calculated. In Fig. 6.237(a) one sees the dependence of the width of the BF on the range of the cut on  $z$  coordinate of the primary vertex. The systematic error that was estimated as the average of the biggest and the smallest value was of the order of the statistical error or even less. The other two plots of Fig. 6.237(b) and (c) show the dependence of the width on the distance of the track’s closest approach to the primary vertex in the  $r$  direction (in Fig. 6.237(b)) and on the corresponding distance on the  $z$ -coordinate (Fig. 6.237(c)). The stability here is better and the estimated systematic errors are even smaller than the previous one.

In addition, the whole data sample was analysed with the BF in the whole pseudorapidity and transverse momentum space provided by the detectors ( $|\eta| < 1.0$ ) in order to establish the dependence on the multiplicity which might exist. Fig. 6.238(a) shows the width of the BF distribution as a function of the mean multiplicity. One can notice that such a dependence on multiplicity is not apparent.

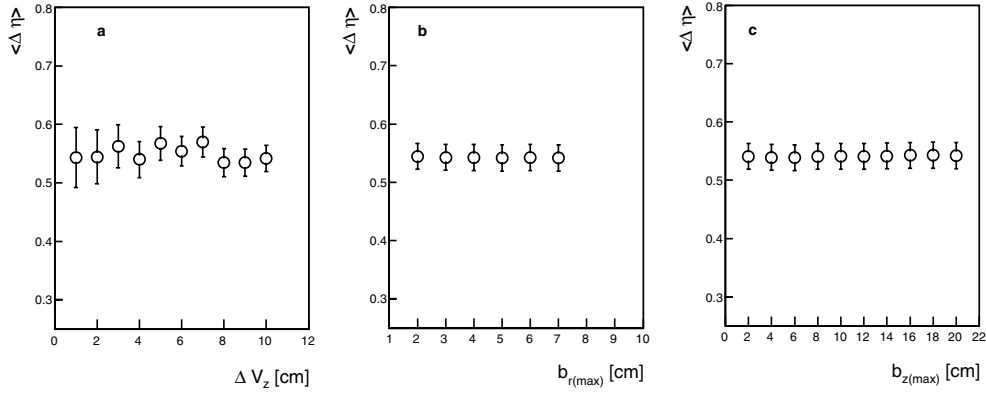


**Figure 6.237.** The dependence of the width of the BF on the range of the cuts for different parameters: (a) on the range of the cut on  $z$ -coordinate of the primary vertex, (b) on the distance of the track's closest approach to the primary vertex in the radial direction, and (c) on the corresponding distance along the  $z$ -coordinate.

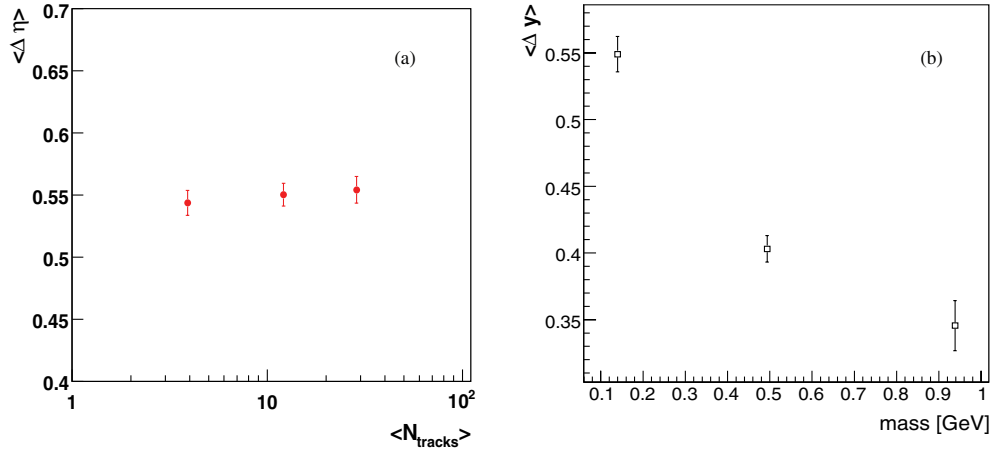


**Figure 6.238.** The dependence of the width of the BF for pp collisions at 14 TeV on (a) the mean multiplicity, (b) the mass of the analysed oppositely charged-particle pairs ( $\pi^\pm$ ,  $K^\pm$  and  $p$ - $\bar{p}$ ).

Moreover, the BF was studied in the whole rapidity space for oppositely charged identified particles such as:  $\pi^\pm$  pairs,  $K^\pm$  pairs and  $p$ - $\bar{p}$  pairs. Fig. 6.238(b) summarizes the corresponding results. The width  $\langle \Delta y \rangle$  gets narrower with increasing mass of the analysed particle. This effect has already been shown by the STAR collaboration [633], and was even proposed in [705] as a method to investigate the possible different mechanisms that are important in the production of the different particle species. The ratios of the calculated widths for all particle species are

$$\frac{\langle \Delta y \rangle_\pi}{\langle \Delta y \rangle_K} = 1.362 \pm 0.047, \quad \frac{\langle \Delta y \rangle_\pi}{\langle \Delta y \rangle_p} = 1.589 \pm 0.095, \quad \frac{\langle \Delta y \rangle_K}{\langle \Delta y \rangle_p} = 1.167 \pm 0.070.$$

The corresponding value obtained in [633] from pp collisions at  $\sqrt{s} = 200$  GeV is

$$\frac{\langle \Delta y \rangle_\pi}{\langle \Delta y \rangle_K} \approx 1.31.$$

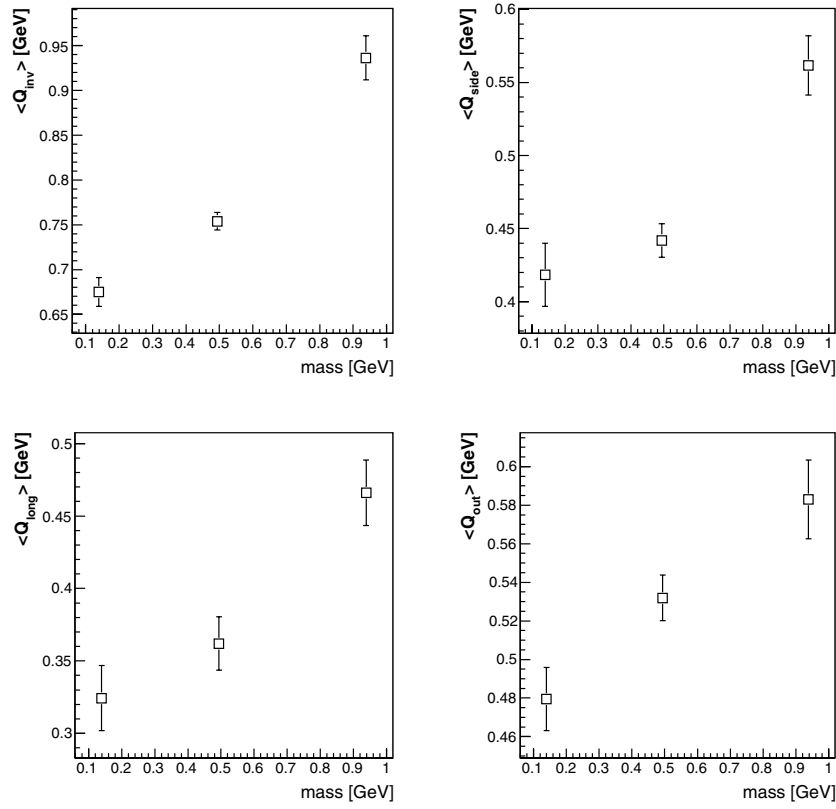


**Figure 6.239.** The dependence of the width of the BF measured in all different components of  $Q$  ( $Q_{inv}$  top left,  $Q_{side}$  top right,  $Q_{long}$  bottom left and  $Q_{out}$  bottom right) on the mass of the analysed oppositely charged-particle pairs ( $\pi^\pm$ ,  $K^\pm$  and  $p-\bar{p}$ ) for pp collisions at 14 TeV.

Finally, the method is extended to study the BF as a function of the two particles relative momentum  $Q_i$  as proposed in [710]. As is proposed, studying the BF in these observables yields a clearer insight for interpreting the physics of the balancing charges as well as providing a better illumination of the distorting effects [710]. The BF has been studied for different particle species as a function of  $Q_{inv}$  the two particle invariant momentum, of  $Q_{long}$  which is the projection of  $q$  along the beam axis, of  $Q_{out}$  which is the corresponding projection along the outward direction (defined by the pair's transverse momentum) and of  $Q_{side}$  which is the projection of  $q$  along the sideways direction (perpendicular to the pair's transverse momentum and to the beam axis). Figure 6.239 summarizes the main results: the corresponding width ( $\langle Q_{inv} \rangle$ ,  $\langle Q_{side} \rangle$ ,  $\langle Q_{long} \rangle$  and  $\langle Q_{out} \rangle$ ) increases with increasing particle mass.

*Pb–Pb collisions.* The method of BF was also used to analyse centrality selected Pb–Pb reconstructed events. These events correspond to the two extreme centrality classes of ALICE:

- The most central Pb–Pb collisions that correspond to an impact parameter range  $0 < b < 5$  fm.
- The most peripheral Pb–Pb collisions with an impact parameter range  $b > 15$  fm.

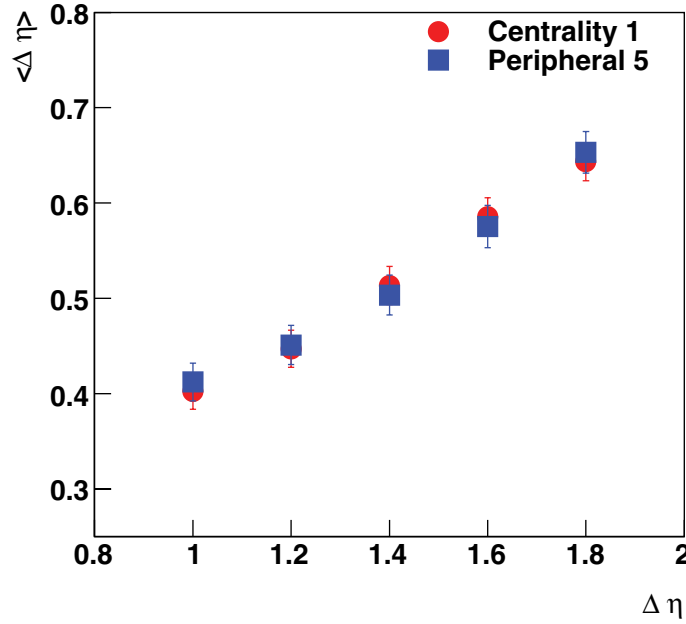


**Figure 6.240.** The dependence of the width on the pseudorapidity interval analysed for the most central and the most peripheral Pb–Pb collisions at  $\sqrt{s_{\text{NN}}} = 5.5$  TeV.

These events were also passed through the shuffling mechanism in order to extract an estimation for the biggest possible width for each centrality class. Analysis of additional Pb–Pb events is possible in order to extract a final results. Preliminary results are presented here.

The dependence of the width of the distribution on the range of the analysed pseudorapidity window starting from half a unit up to 0.9 around mid-rapidity with a step of 0.1 is shown in Fig. 6.240. One notices once again the linearity in the behaviour of the width. Figure 6.241 shows the width of the BF distributions as a function of the normalised impact parameter ratio  $b/b_{\text{max}}$  for the most central and the most peripheral Pb–Pb collisions. This picture is consistent for a non QGP hadronization phase because of the lack of the centrality dependence.

*6.5.12. Fluctuations in azimuthal anisotropy.* Fluctuation in elliptic flow and higher harmonics give proper insight to the explosive system produced in heavy-ion collisions at the LHC energy [666]. These have been studied in the context of results from the STAR experiment at RHIC [521, 540]. Event-by-event fluctuation in  $v_2$  of photons measured by the PMD at the forward rapidity in ALICE have been investigated earlier [103, 715]. In the central rapidity region of ALICE it may be possible to measure flow on an event-by-event basis using the large coverage of TPC. This has been simulated by taking the charged-particle rapidity density at  $\eta = 0$  to be between 100 to 5000. For each multiplicity class, the events have been generated for a constant flow for each event as well as varying flow within a given range. Flow was introduced by modifying the azimuthal angle ( $\phi$ ) of each particle by an amount  $\Delta\Phi$  such that

$$\Delta\Phi = - \sum_i \frac{2v_n}{n} \sin n(\phi_i - \Psi_r), \quad (6.85)$$

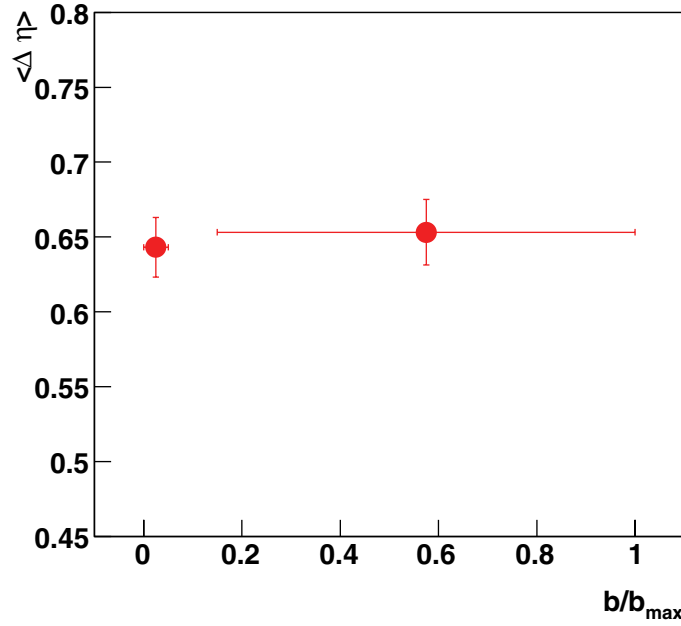


**Figure 6.241.** The dependence of the width on the normalised impact parameter ratio  $b/b_{\max}$  for Pb–Pb collisions at  $\sqrt{s_{\text{NN}}} = 5.5$  TeV.

where  $\Psi_i$  is chosen randomly, once for each event,  $i$  runs over all particles and  $n = 2$  in case of elliptic flow.

The generated data were analysed by dividing each event into two sub-events of equal multiplicity, separated by a small rapidity interval, and  $v'_a$  is obtained as  $\langle \cos 2(\phi_a - \psi_b) \rangle$ , where the  $\phi_a$  are the azimuthal angles of particles in sub-event  $a$  and  $\psi_b$  is the event plane obtained using particles in sub-event  $b$ , and the average is over all particles.  $v'_b$  is obtained in a similar manner. Then,  $v_2$  can be expressed as

$$v_2 = \sqrt{\frac{v'_a \cdot v'_b}{\cos 2(\psi_a - \psi_b)}} \quad (6.86)$$

and is termed  $v_2^{\text{out}}$ , while the injected flow is termed  $v_2^{\text{in}}$ . Figure 6.242 shows the  $v_2^{\text{out}}$  distribution reconstructed on an event-by-event basis for a given multiplicity class, with two choices for  $v_2^{\text{in}}$ , namely constant  $v_2^{\text{in}} = 0.05$  and fluctuating  $v_2^{\text{in}}$ . For some very low flow values, the geometric mean is replaced by the arithmetic mean. In this way  $v_2$  is obtained for each event and is termed as  $v_2^{\text{out}}$ .

By taking the quadratic difference of the total r.m.s. (as for dotted line) and the r.m.s. intrinsic to the method (as for solid line), one can ascertain the presence of event-by-event fluctuations of  $v_2$  in the data sample. This quadratic difference has been plotted as a function of multiplicity in Fig. 6.243. As the multiplicity increases, the quadratic difference reaches the input value of 0.017. This validates the estimates of  $v_2$  for each event.

**6.5.13. Disoriented chiral condensates.** The QCD phase transition is predicted to be accompanied by chiral symmetry restoration at high temperatures and densities. One of the most interesting consequences of chiral transition is the formation of a chiral condensate in an extended domain, such that the direction of the condensate is misaligned from that of the true

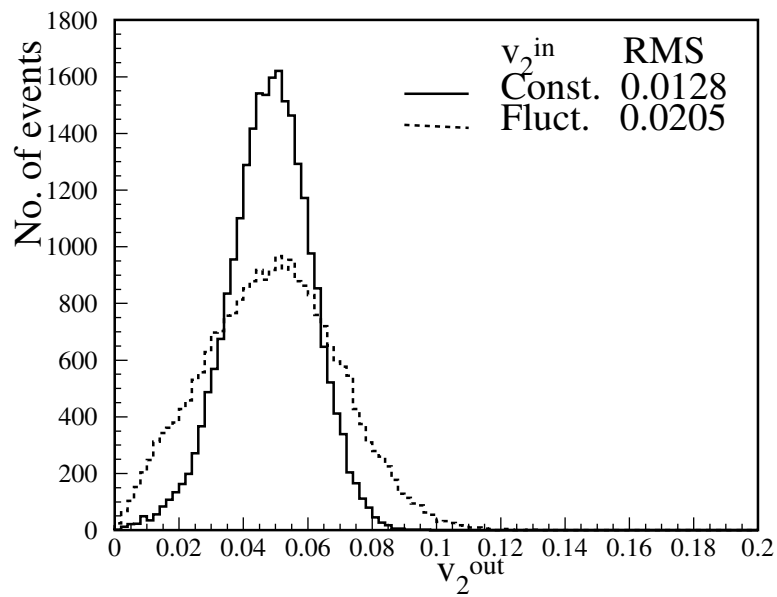


**Figure 6.242.** The results for  $dN/d\eta_{\text{max}} = 2000$ . Solid lines correspond to  $v_2^{\text{in}} = 0.05$  for each event and dotted lines correspond to  $v_2^{\text{in}}$  chosen randomly from a Gaussian distribution peaked at 0.05 with a width of 0.017.

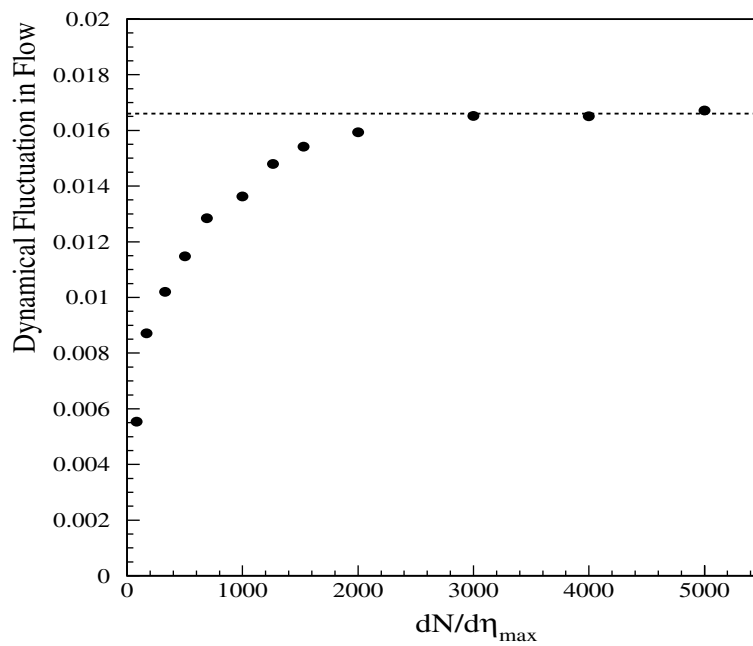


**Figure 6.243.** The r.m.s. of the distribution corresponding to constant  $v_2^{\text{in}}$  is subtracted quadratically from the r.m.s. of the distribution corresponding to fluctuating  $v_2^{\text{in}}$  and shown for different multiplicities. The dotted line shows the r.m.s. of the fluctuation introduced.

vacuum. This phenomenon is termed as the disoriented chiral condensates (DCC) [606–609]. The formation of DCC results in an excess of low momentum pions in a single direction in isospin space giving rise to large imbalances in the production of charged to neutral pions. This is studied in terms of the distribution of neutral pion fraction,  $f$ , given by

$$f = \frac{N_{\pi^0}}{N_{\pi}}, \quad (6.87)$$

where  $N_{\pi^0}$  and  $N_{\pi}$  are the number of neutral pions and total pions, respectively. The pions in a normal event would follow a binomial form with a mean of  $1/3$ , whereas within a domain of DCC the probability of pion fraction would follow a binomial distribution pattern such as

$$P(f) = \frac{1}{2\sqrt{f}}.$$

DCC is a metastable state which results from the cooling down of the high-temperature chiral symmetric phase of quark–gluon plasma. Such a state appears in both linear and non-linear  $\sigma$ -models which are simplified versions of the full chiral effective theory. The condensate may have a large isospin vector oriented in any direction in isospace, and thus it may be a source of secondary pions with any isospin configuration. A DCC state may occupy the full available phase space or only a part of it, and thus it may constitute a source of all secondary pions or only of small fraction of them. Some theoretical models [716–719] predict ‘DCC domains’ of sizes 3–4 fm in radius, emitting 50–200 pions. Such a source may be situated in any kinematic region of the expanding source, and the pion emission pattern might be statistical or coherent. If the pion emission from DCC is indeed coherent, the pions will be collimated in a limited region of phase space and will have small relative transverse momenta. In this case one would expect to find ‘jet-like’ structures with high isospin imbalance. In view of these it seems plausible to search for DCC in various phase space regions. A recent review of theoretical and experimental aspects of DCC maybe found in Ref. [610].

The formation of DCC was hypothesized in the context of explaining observed abnormal events from cosmic ray experiments [160, 720] which had either excess of charged-particles compared to neutrals (called centauro events) or excess of neutrals with respect to charged-particles (anti-centauro events). A dedicated experiment, MiniMax, was set up at the Tevatron at Fermilab to study  $p + \bar{p}$  collisions at  $\sqrt{s} = 1.8$  TeV [721]. MiniMax was composed of 24 MWPCs with a removable lead gamma converter, and a segmented electro-magnetic calorimeter behind it. The detector had a very small angular acceptance: a cone with axis at  $\eta = 4.1$ , with half-angle 0.65. No evidence for DCC was found at a few per cent level.

A thorough DCC search in Pb–Pb collisions at  $\sqrt{s_{NN}} = 17.2$  GeV was performed by the WA98 Collaboration at CERN [622–625]. This was based on a systematic study of photon and charged-particle multiplicity correlation using the data from a preshower photon multiplicity detector (PMD) and a silicon pad multiplicity detector (SPMD) for charged-particles. No DCC signal was observed and the upper limit for DCC production at 90% CL was established as a function of the fraction of DCC pions among all pions produced. A DCC search was carried out by the NA49 experiment [722] for semi-central Pb–Pb collisions at  $\sqrt{s_{NN}} = 17.2$  GeV. The ratio of electro-magnetic to hadronic transverse energy,  $E_T^{EM}/E_T^{HAD}$ , was calculated for each event using the radially and azimuthally segmented cylindrical calorimeter. The distribution of this ratio was found compatible with that predicted by the VENUS model, with the mean value close to 0.3. The tails donot show the presence of any anomalous events. The results of DCC search in Au–Au collisions at c.m. energy up to  $\sqrt{s_{NN}} = 200$  GeV is expected from experiments at RHIC.

Many powerful techniques have now been developed for DCC search. A review of these along with the sensitiveness of ALICE detector is discussed in the following.

*6.5.13.1. Signatures of DCC formation.* A large number of signatures have been proposed as a consequence of the DCC formation in heavy-ion collisions. A short list of important signatures is given below:

- Fluctuation in neutral pion fraction,  $f$ :  
the event-by-event fluctuation in the neutral pion fraction is the most basic signature of DCC formation. This study is equivalent to studying the fluctuation in the number of charged-particles and photons. This study can be carried out in the full phase space or in smaller  $\eta - \phi$  domains where DCC formation might give rise to distinct patterns of the emission of pions [723, 724].
- Kaon correlations:  
formation of DCC give rise to enhanced correlations of  $K^+ K^-$  and  $K_s^0 K^\pm$  [725, 726].
- Baryon abundances:  
formation of many small DCC domains may give rise to enhanced production of baryons, particularly,  $\Omega$  and  $\bar{\Omega}$  [727–729].
- HBT correlations:  
DCC formation will affect the two-particle HBT correlations of identified pions [726].
- Direct photons:  
search for non-equilibrium photons in the direct photon measurements has been proposed a potential test of the formation of DCC [730].

Most of these signatures have been proposed for use in the ALICE experiment for the search of DCC. The analyses so far are based on the fluctuations in neutral to charged-particle measurements. Various analysis methods, which are sensitive to details of DCC formation, have been developed. The experimental observation of DCC depends on various factors, such as the probability of DCC occurrence, the number of possible DCC domains in an event, size of the domains, number of pions emitted from the domains, and the interaction of pions with the rest of the system. The sensitiveness of ALICE detectors for DCC search has been studied by simulation.

*6.5.13.2. DCC measurements in ALICE.* The ALICE detector makes it possible to search for DCC by comparing the emission of charged and neutral pions in two distinct regions of phase space as discussed below:

- Central rapidity region: combination of PHOS and TPC within a common coverage of  $-0.12 < \eta < 0.12$ ,  $\Delta\phi = 100^\circ$  may be used. In this region, photon measurements are made by PHOS whereas charged pions will be measured by the TPC. The expected number of photons in this region is about 500 for central Pb–Pb events with a similar number for charged-particles.
- Intermediate rapidity region: combination of PMD and FMD within common coverage of  $2.3 < \eta < 3.5$ ,  $\Delta\phi = 360^\circ$  will be used. PMD is a preshower detector with good space resolution and the photon detection efficiency is about 70%. The FMD measures charged-particles multiplicity. The expected number of photons in the PMD acceptance is about 4000 for central Pb–Pb events with about similar number for charged-particles. Due to this large multiplicity, a search for DCC in finer  $\eta$ - $\phi$  bins will be possible. A description of DCC measurements in this region may be found in [103, 715].

The two sets of detector combinations can also be used to isolate events with large fluctuations in the relative number of charged-particles to photons. These can be further investigated to infer any signal of DCC.

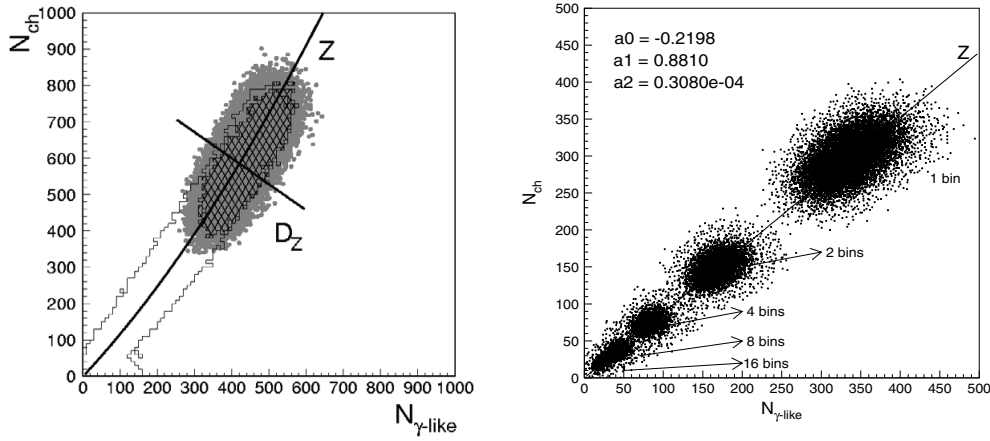


**Figure 6.244.** Left panel shows scatter plots of the  $N_\gamma$  and  $N_{ch}$  distributions for the global study (full available phase space of charged-particle and photon detectors in the WA98 experiment) and the right panel shows similar distributions for local study for 1, 2, 4, 8, and 16 bins in azimuthal angle for a common coverage of the detectors. The correlation axes are shown by the solid curves.

**6.5.13.3. Simulation of DCC events.** The effect of non-statistical DCC-like fluctuations has been studied within the framework of a simple model in which the output of the parametrised HIJING event generator has been modified by using an algorithm similar to that of refs. [731–733]. Within a domain size given in terms of its extent in  $\eta$  and  $\phi$ , the identity of the charged pions to neutral pions is changed following the neutral pion distribution given in Eq. (6.87). The neutral pions are allowed to decay. The parameters of the model are the following:

- domain size in terms of  $\Delta\eta$  and  $\Delta\phi$ ,
- production of additional pions,
- percentage of events of DCC-type.

The simulated events are used to study the sensitiveness of DCC detection in the experimental set-up.

**6.5.13.4.  $N_\gamma$ – $N_{ch}$  correlation.** In a given set of normal events  $N_\gamma$  and  $N_{ch}$  are correlated. The presence of events with DCC would show up as deviations from the general correlation. This correlation can be studied in the full detector coverage for global fluctuations or within a subset of the coverage for localized fluctuations. Inference on the presence of non-statistical fluctuation may be made from the distance of the data points in the correlation plots to a common correlation axis.

Correlations of  $N_\gamma$ – $N_{ch}$ , measured by the WA98 experiments [622, 624, 625] for SPS energies, are shown in Fig. 6.244. The left panel shows a scatter plot of  $N_\gamma$  and  $N_{ch}$  distributions in the full available phase space of the detectors and the right panel shows a superimposition of the  $N_\gamma$  and  $N_{ch}$  distributions where the available phase space is divided into smaller segments of 2, 4, 8, and 16 bins. The solid lines in both cases show correlation axes ( $Z$ ).

The distribution of the closest distance of the data points to the correlation axes represent the relative fluctuations of charged-particles to photons. The resulting distribution is quantified in terms of the scaled variable  $S_z = D_z/\sigma(D_z)$  where  $D_z$  is the distance of a point in the

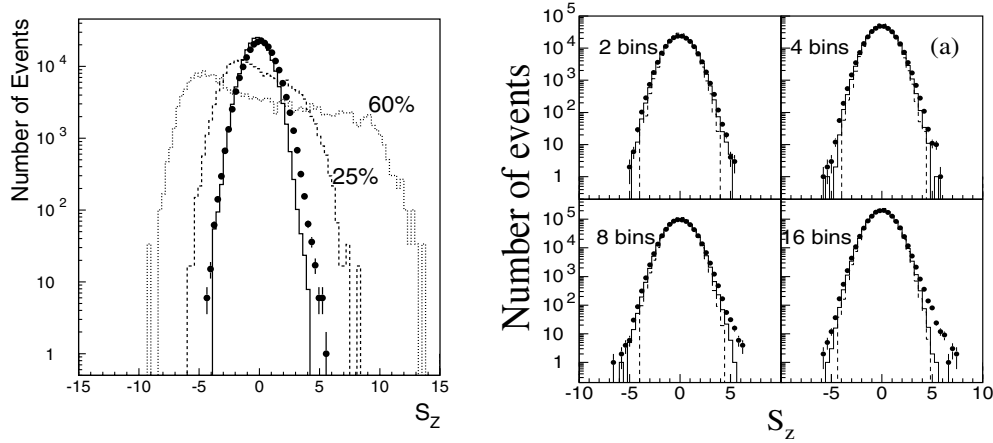


**Figure 6.245.**  $S_z$  distributions for the global and local cases. In the left panel the solid points are experimental data and the solid histogram corresponds to the mixed events. DCC simulated events, where 25% and 60% pions are of DCC origin, are superimposed in the figure. In the right panel the experimental data (solid points), mixed event (solid histogram) and GEANT simulated events (dashed histogram) are shown for different bin sizes.

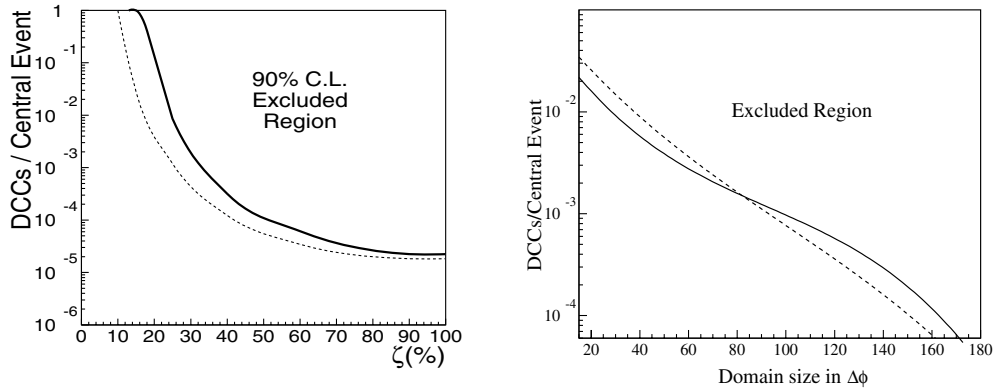


**Figure 6.246.** 90% C.L. upper limits on DCC production per central event for the global and local studies from the WA98 experimental data [622, 624, 625]. The horizontal axis in the left figure gives a fraction of pions which are assumed to be of DCC origin whereas the horizontal axis on the right figure gives the DCC domain size in azimuthal angle.

$N_\gamma - N_{ch}$  plane to the correlation axis, and  $\sigma(D_z)$  is the dispersion of the  $D_z$  distribution for ‘normal’ events.

The  $S_z$  distributions for the global case and for two bins in localized cases are shown in Fig. 6.245. The r.m.s. deviations of the experimental data distributions are then compared to those of the mixed events and simulated events. Since the r.m.s. deviations of the experimental data and the derived mixed events are close to each other, upper limits on the predictions of DCC are set by comparing these results to DCC simulated events with various input parameters. The upper limit on global DCC is shown in the left panel of Fig. 6.246 and for smaller domains of DCC is shown in the right panel of Fig. 6.246.

In the ALICE experiment the correlation of the number of photons in PHOS and the number of charged-particles in TPC in the common coverage and the correlation of number of

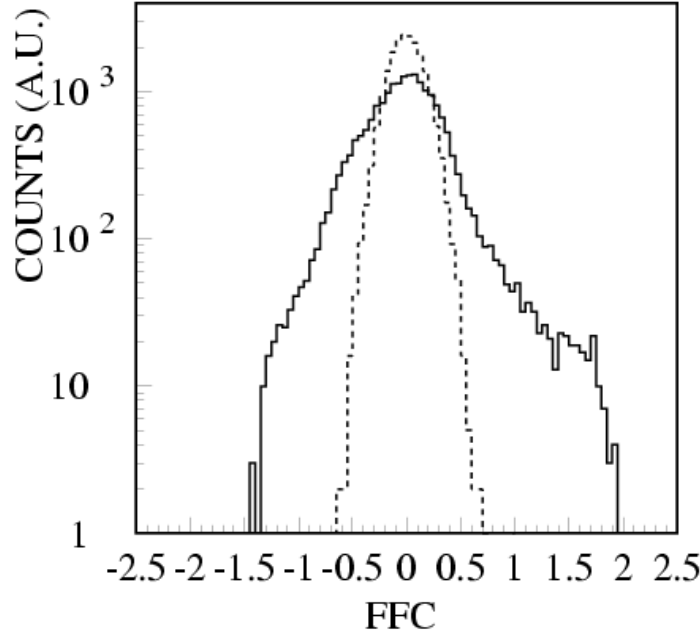


**Figure 6.247.** FFC distribution for simulated generic events (dotted line) and pure DCC-like events (solid line).

photons in PMD and number of charged-particles in FMD can be studied. Further correlation studies in smaller domains in  $\eta - \phi$  in the forward rapidity region can be made to look for possible signatures of DCC formation.

*6.5.13.5. Discrete wavelet technique.* Discrete Wavelet Technique (DWT) has been proved to be quite successful in many fields of research to analyse and identify fluctuations at various distance scales [734]. This technique has been suitably adopted to search for bin-to-bin fluctuations in charged-particles and photons. The analysis has been carried out by making  $2^j$  bins in the azimuthal angle where  $j$  is the resolution scale. The output of the DWT analysis consists of a set of Father Function Coefficients (FFCs) at each scale,  $j$ . The distribution of FFC's for normal events is Gaussian whereas the presence of DCC-like fluctuations makes the distribution wider and non-Gaussian. Inference about the presence of DCC can be made by studying the width of FFC distributions. Figure 6.247 shows FFC distributions for normal and DCC-like events where the increase in the width for DCC events can be seen. The correlation method described previously gives anomalous fluctuation within a given window in  $\eta - \phi$  whereas the DWT method has the added advantage that it is quite powerful for studying bin-to-bin fluctuation and can give the exact dimension of the bin in  $\eta - \phi$  which has larger fluctuation compared to other bins. The effect of DCC using the DWT method may be quantified using a strength parameter  $\zeta$ , defined as [732]

$$\zeta = \frac{\sqrt{(s_X^2 - s_N^2)}}{s_N}, \quad (6.88)$$

where  $s_N$  is the r.m.s. deviations of the FFC distribution for normal events and  $s_X$  is the r.m.s. deviation for DCC events.

Using the DWT technique, the WA98 collaboration has made extensive study for the search of DCC [624, 625]. DWT technique can be easily applied to the ALICE data. The forward rapidity region will be particularly suitable for the DWT study where the available phase space can be divided into large number of bins.

*6.5.13.6. Power spectrum analysis.* The power spectrum technique [735–737] can be applied to study event-by-event fluctuation over limited  $\phi$  regions. In this approach, one computes the fraction  $f = N_\gamma/N_{\text{ch}}$  for a certain window, e.g. a window in azimuthal angle  $\phi$ , and this window is then displaced by a small amount,  $f$  is recalculated, etc. The power spectrum is the square of the Fourier transform of the  $(f(\phi) - f_o(\phi))$  distribution where  $f_o(\phi)$  is the distribution for ‘normal’ events. It shows a characteristic pattern, with narrow peaks indicating local fluctuations in the original distribution [103]. The capability of the method was investigated by generating a set of 5000 events with a multiplicity of 4000 particles in the common coverage of both FMD and PMD. The power spectrum generated from these events is compared to events with the presence of DCC domains within a domain size of  $\delta\eta = 0.1$  and  $\delta\phi = 40^\circ$ . With a proper selection criteria it was possible to select DCC events with 60% efficiency. This method will be very useful to identify exotic events corresponding possibly to DCC formation.

*6.5.13.7. ‘Robust’ variables.* The analysis method used by the Minimax experiment at Fermilab is named as ‘robust’ variables [721]. This analysis uses the ratios of factorial moments

$$R_{i,1} = \frac{F_{i,1}}{F_{i+1,0}}, \quad (6.89)$$

where

$$F_i = \frac{\langle N(N-1)\dots(N-i+1) \rangle}{\langle N \rangle^i} \quad (6.90)$$

and

$$F_{i,j} = \frac{\langle N_{\text{ch}}(N_{\text{ch}}-1)\dots(N_{\text{ch}}-i+1)N_\gamma(N_\gamma-1)\dots(N_\gamma-j+1) \rangle}{\langle N_{\text{ch}} \rangle^i \langle N_\gamma \rangle^j}. \quad (6.91)$$

The variables  $R$  have been named ‘robust variables’ because the detection efficiencies, often difficult to estimate (especially for photons) cancel out and thus do not influence the results.

The analysis can be done inclusively or event-by-event for high multiplicity events in ALICE. For ‘normal’ events (statistical uncorrelated emission)  $R_{i,1} = 1$ , while for DCC  $R_{i,1} = 1/(i+1)$ , a remarkable difference for all  $i \geq 1$ . Results of a DCC simulation using this technique is shown in Fig. 6.248.

*6.5.13.8. Event-shape analysis.* This method combines the wavelet technique and flow analysis [731]. It is based on the realization that localized DCC formation is expected to lead to an event shape anisotropy which is out of phase for charged-particles and photons. The flow direction is found separately for charged-particles and photons and compared. For a DCC component a difference between the two directions might be expected. The results of the second-order Fourier analysis is shown in Fig. 6.249 for the difference in flow angle of photons and charged-particles. The presence of DCC leads to an anti-correlation of flow angles in the two detectors peaking at  $90^\circ$ . This will be a very powerful method to study DCC formation in the high multiplicity environment of ALICE.

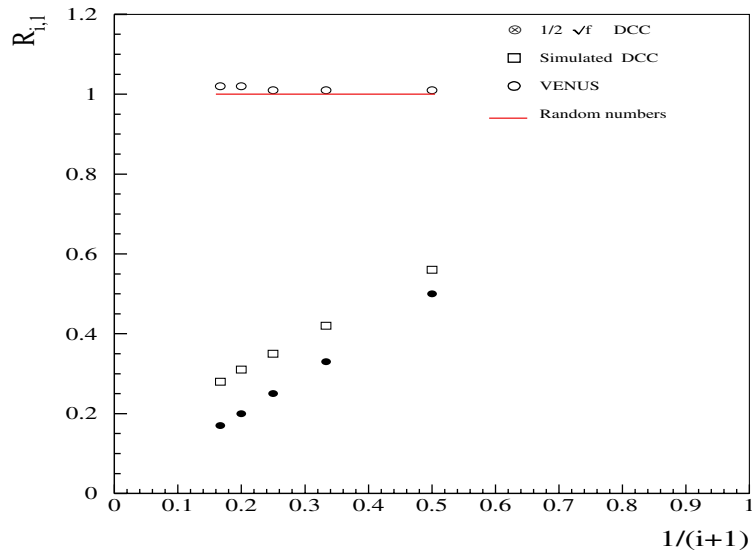


**Figure 6.248.** Results of DCC analysis using ‘robust’ variables. Normal events using VENUS event generator do not show any correlation whereas pure DCC events follow  $R_{i,1} = 1/(i+1)$  behaviour. The simulated events with detector effects follow a behaviour similar to that of pure DCC events.

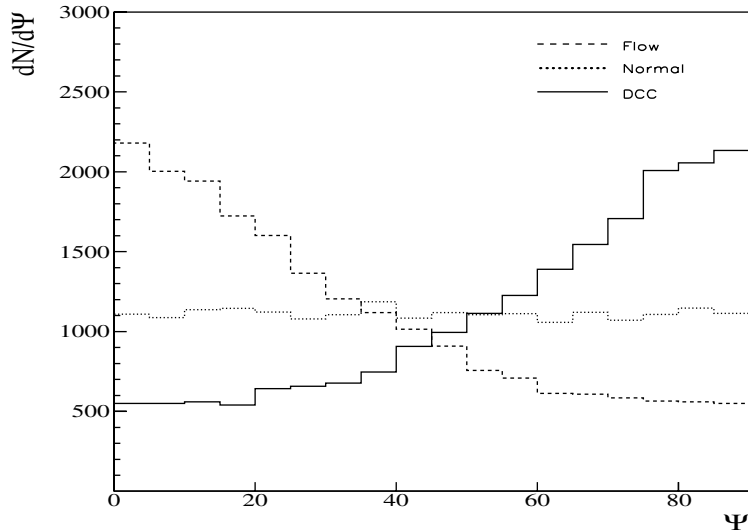


**Figure 6.249.** Difference in flow angle distribution for charged-particles and photons is plotted for three cases: (a) normal events, (b) events with flow, and, (c) events with DCC. Characteristic differences between three types of events are seen.

**6.5.13.9. Sliding window method.** The Sliding Window Method (SWM) has been developed to search for patches, on an event- by-event basis, having unusual fluctuations in the neutral pion fraction ( $f$ ) which may arise due to the formation of DCC. In this method one chooses a window in azimuthal plane of size  $\Delta\phi$ , in the common coverage of charged-particle and photon detectors and calculates the neutral pion fraction  $f$ . The entire azimuthal range of

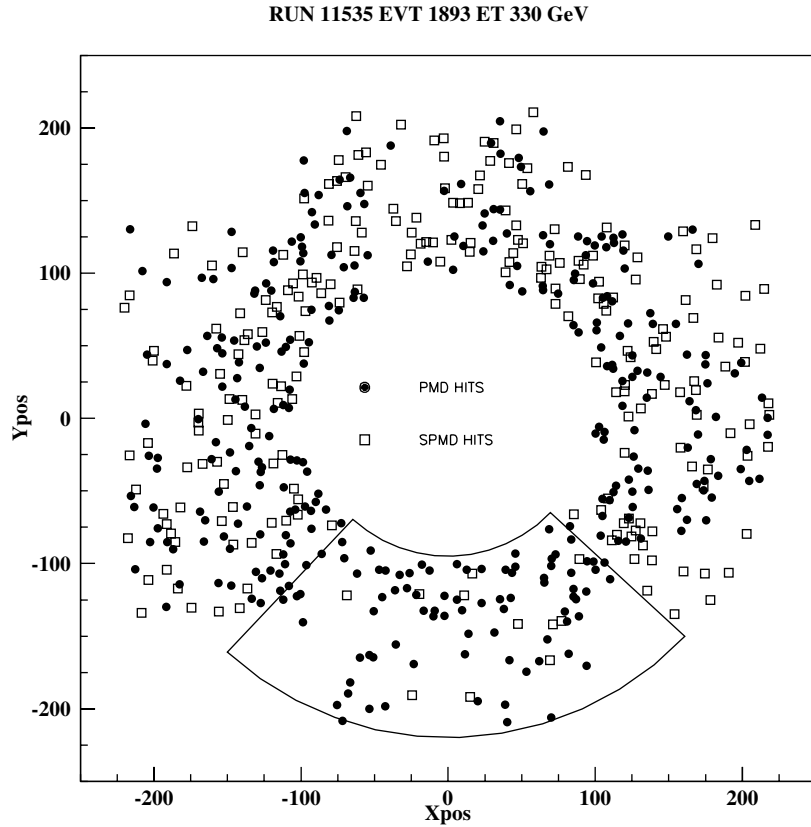


**Figure 6.250.** Photon (PMD) and charged-particle (SPMD) hits in an azimuthal plane in the WA98 experimental set-up [738]. The marked  $90^\circ$  patch corresponds to  $f_{\max} = 0.77$ .

common coverage is scanned by continuously sliding the window, i.e. shifting each time by a small amount,  $\delta\phi$ , to search for a patch having the neutral fraction,  $f$ , several standard deviations away from the mean value of the generic  $f$  distribution. This method utilises the full advantage of azimuthal resolution of the detectors.

The SWM can be used to search for the anti-Centauro and Centauro events by looking for the maximum and minimum  $f$  values in an event by continuously sliding the patch depending upon the detector resolutions. It is found that  $f_{\max}$  and  $f_{\min}$  distributions for generic events for a given window size are Gaussians whereas for simulated DCC-like events these distributions extend well beyond those of the generic events. This method allows the direct observation of patches having large  $f$  values.

The SWM has been applied to the analysis of data in the WA98 experiment which had a photon multiplicity detector and a charged-particle multiplicity detector overlapping fully in azimuth over 0.5 unit of pseudorapidity [738]. The azimuthal scanned was performed by sliding the window by  $\delta\phi = 2^\circ$ . The percentage of events having exotic patches in the top 10% central events, with  $f$  value beyond  $4.5\sigma$  of the generic  $f$  distribution, is found to be  $0.39 \pm 0.016$ , as compared to  $0.081 \pm 0.007$  in the mixed events and  $0.013 \pm 0.008$  in the Geant simulated VENUS events. One such event is displayed in Fig 6.250 which shows the photon hits ( $\bullet$ ) and charged-particle hits ( $\square$ ) within the common coverage of both the detectors. The patch with the highest  $f = 0.77$  is also marked; it contains 84 photon hits as compared to

only 12 charged-particle hits. This demonstrates the power of the method to search for exotic patches in a given  $\eta - \phi$  phase space and can be easily applied to data from ALICE.

*6.5.14. Fluctuations in intermediate and high  $p_t$  sector and jets.* Presence of jets and mini-jets affect the event-by-event fluctuations. This is to be understood in detail for: (a) to make any inference about the event-by-event fluctuations, and (b) to understand the effect of jets passing through the medium. This may allow to test various models of jet production in the region not accessible to the standard method of jet analysis. In this subsection results are presented based on simulations concerning jet production on event-by-event fluctuations of  $p_t$  and  $E_t$ .

*6.5.14.1. Fluctuations in  $p_t$ .* In order to study exclusively the effect of jet production, a simple model of central Pb–Pb collisions at the LHC was developed. Two independent sources of particle production were assumed: the ‘soft’ component models production of particles at low transverse momenta, whereas the ‘hard’ component simulates particles originating from jets. The ‘soft’ component was simulated assuming independent production of charged hadrons. The azimuthal angle distributions were assumed to be uniform. The transverse momentum spectrum was generated according to a ‘thermal’ distribution:

$$\frac{1}{p_t} \frac{dn}{dp_t} = C \times \exp\left(-\frac{m_t}{T}\right), \quad (6.92)$$

where  $T = 190 \text{ MeV}$  is an inverse slope parameter, and  $C$  is an arbitrary normalisation parameter. The rapidity density distribution of the ‘soft’ component was taken to be Gaussian with a mean of 6000 and standard deviation of  $\sigma = 1000$ . For each event, in addition to ‘soft’ component, a ‘hard’ component jet production was generated. The  $p_t$  spectrum of jets produced in central Pb–Pb collisions at  $\sqrt{s_{\text{NN}}} = 5.5 \text{ TeV}$  was calculated by scaling the corresponding  $p_t$  spectrum obtained for pp interactions at 5.5 TeV using PYTHIA (version 6.1) with the standard (2 jet-events, LO calculations and no initial and no final state radiation) parameters. The scaling factor for the spectrum normalised to mean multiplicity was calculated following the pQCD-based rule  $\langle \text{jet} \rangle \sim \langle N_W \rangle^{4/3}$ , where  $\langle N_W \rangle$  is the mean number of wounded nucleons.

The resulting jet  $p_t$ -spectrum is presented in Fig. 6.251. The multiplicity distribution of jets was assumed to be Poissonian. The jet fragmentation properties were introduced by a parametrisation of the appropriate distributions generated within PYTHIA.

Events generated within the ALIROOT framework and passed through the ALICE TPC fast simulation chain, which allows for a proper introduction of the detector acceptances. For the final analysis of fluctuations, only tracks measurable (long enough for reconstruction) in the ALICE TPC were selected and the  $\Phi_{p_t}$  fluctuation measure was calculated for them.

The observed transverse momentum fluctuations depend on the acceptance selected for the study. In order to investigate this effect a rectangular acceptance window is defined in azimuthal angle  $\phi$  and pseudorapidity  $\eta$ , in addition to the geometrical TPC acceptance. The size of the window

$$L_{\eta,\phi} = \sqrt{\Delta\eta^2 + \Delta\phi^2} \quad (6.93)$$

was varied by scaling  $\Delta\eta$  and  $\Delta\phi$  by the same factor. In this procedure, it is assumed that  $\Delta\eta/\Delta\phi = 2/(2 \cdot \pi) \approx 0.32$ .

The dependence of  $\Phi_{p_t}$  on  $L_{\eta,\phi}$  is shown in Fig. 6.252(a) for two cases: ‘soft’ component only and ‘soft’ + ‘hard’ components, as defined above. In the case of the ‘soft’ component, independently of the size of the acceptance window, the value of  $\Phi_{p_t}$  was equal to zero.

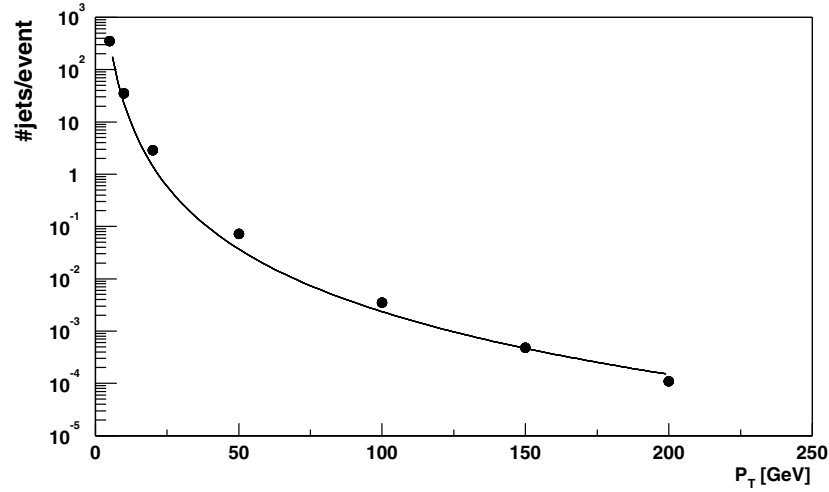


**Figure 6.251.** Transverse momentum spectrum of jets in central Pb–Pb collisions at  $\sqrt{s_{NN}} = 5.5$  TeV assumed in the simulation. The solid line is drawn to guide the eye.

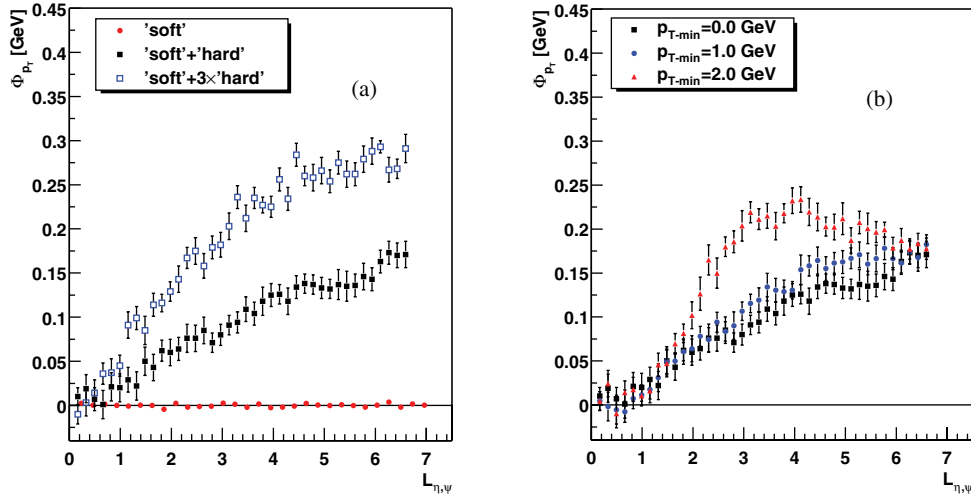


**Figure 6.252.** (a) The dependence of  $\Phi_{p_t}$  on the acceptance for ‘soft’ component (dots), ‘hard’ + ‘soft’ component (squares) and the contribution of hard component increased by a factor of 3 (open squares). (b) The dependence of  $\Phi_{p_t}$  on the acceptance for ‘hard’ + ‘soft’ component model without (squares) and with low  $p_t$  cut at 1.0 GeV/c (dots) or 2.0 GeV/c (triangles).

This result was expected because of the assumption of uncorrelated particle production in the ‘soft’ component model. However, in the ‘soft’+ ‘hard’ case large non-zero values of  $\Phi_{p_t}$  were obtained. The strong event-by-event fluctuations result from the correlated particle production in the ‘hard’ component. The  $\Phi_{p_t}$  increases with the size of the acceptance window  $L_{\eta,\phi}$ . In order to understand this dependence it is useful to consider two asymptotic regions. For very small acceptance ( $L_{\eta,\phi} \rightarrow 0$ ) at most one particle from a jet is accepted and thus the correlation of particles within a jet is not seen,  $\Phi_{p_t} \rightarrow 0$ . For very large acceptances all particles from a jet are accepted and a positive value of  $\Phi_{p_t}$  is measured. With increasing acceptance one increases proportionally the number of accepted jet- and ‘soft’-hadrons. The

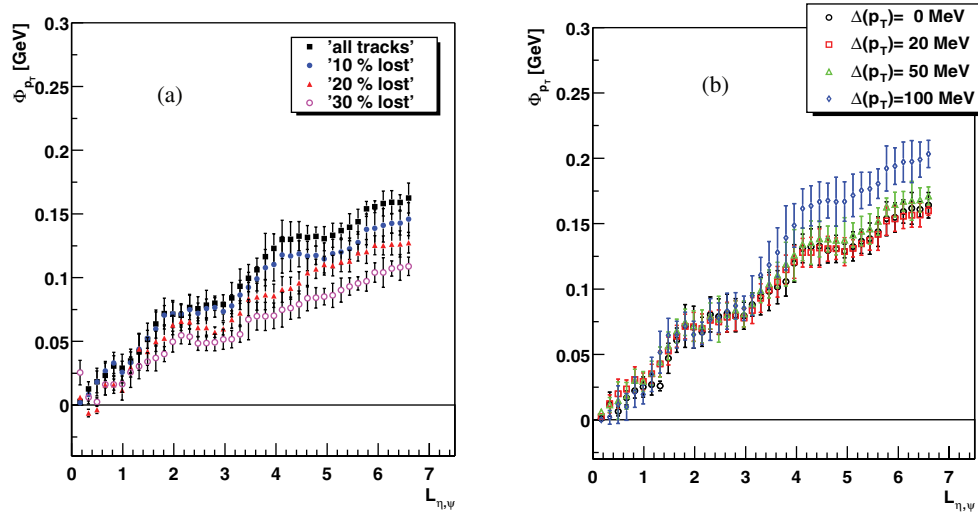


**Figure 6.253.** (a) The dependence of  $\Phi_{p_t}$  on the acceptance for ‘hard’ + ‘soft’ component calculations including possible effect of random track losses due to reconstruction inefficiencies. (b) The dependence of  $\Phi_{p_t}$  on the acceptance for ‘hard’ + ‘soft’ component model including possible effects of limited two track resolution modeled by lower cut on transverse momentum difference of two tracks.

value of  $\Phi_{p_t}$  should be independent of the acceptance because of the ‘intensive’ property of the  $\Phi$  measure. The expected saturation of  $\Phi_{p_t}$  for large acceptance is, however, not observed in Fig. 6.252(a). This is probably because the ALICE TPC acceptance in pseudorapidity is too small. Finally, in order to illustrate the sensitivity of the  $p_t$  fluctuations on the ratio between ‘hard’ and ‘soft’ components, the expected jet multiplicity is increased by a factor of 3; the results are shown as open symbols in Fig. 6.252(a).

Since the fraction of particles originating from the ‘hard’ component increases with increasing  $p_t$  one expects an increase of  $\Phi_{p_t}$  when a low  $p_t$  cut is applied to select particles for the analysis. In fact this is seen in Fig. 6.252(b) where the results without  $p_t$  cut (squares) and with a low  $p_t$  cut at 1.0 GeV/c (dots) and 2.0 GeV/c (triangles) are plotted. The results for 2 GeV/c cut suggest an early onset of saturation of  $\Phi_{p_t}$  with  $L_{\eta,\phi}$  which may be due to the narrowing of the jet extension in  $L_{\eta,\phi}$  after increasing the low  $p_t$  cut.

In the previous study only the geometrical acceptance of ALICE TPC was taken into account. The influence of detection inefficiency is discussed here. First, one considers the effect of random track losses due to tracking and fitting. In Fig. 6.253(a) the standard results obtained assuming a perfect detection and the result that includes random losses of 10% are compared. The difference is small in comparison to the expected effect due to the presence of jets. Losses of tracks that are close in the detector space (effect of the two-track resolution) are simulated. One assumption made here is that tracks that have a neighbour track with  $\Delta p_t = |p_{t1} - p_{t2}| < \text{cut MeV}/c$  are lost. The results obtained including the effect of the finite two-track resolution are shown in Fig. 6.253(b). The bias is small in comparison to the expected effect due to presence of jets.

The expected jet production in central Pb–Pb collisions at  $\sqrt{s_{NN}} = 5.5$  TeV should lead to large event-by-event fluctuations of mean transverse momentum. This may allow one to test various models of jet production in the jet  $p_t$  region not accessible to the standard methods of jet detection. On the other hand, fluctuations due to jet production should be taken into account when considering the detection of fluctuations due to other processes.

The influence of random detection inefficiencies as well as two-track resolution was estimated to be small for  $p_t$  fluctuations as expected for unquenched jet production.

**6.5.14.2. Azimuthal fluctuations in  $E_t$ .** In this subsection results from an event-by-event azimuthal asymmetry in the transverse energy flow induced by the minijet dynamics [739] is discussed. The underlying idea is that the presence of new physics brought in by semihard degrees of freedom should manifest itself through reasonably well-defined changes in the inelasticity pattern that can be measured experimentally, depending on the relative weight of minijet and soft hadronic contributions to the inelastic cross section. Let us stress, that in order to reproduce an experimentally observed transverse energy spectrum, the description of minijet dynamics should go beyond the lowest-order elastic scattering and include, in particular, initial and final state radiation (see, for example, Ref. [740]) as included into the HIJING Monte Carlo event generator. HIJING allows one to study the effects due to the presence of semi-hard degrees of freedom at the early stages of high-energy collision in a simple setting, where the only nontrivial effects distinguishing the nuclear collision from an incoherent superposition of nucleon-nucleon ones are jet quenching, i.e. energy losses experienced by partons traversing the surrounding debris created in nuclear collision, and accounting for nuclear effects in the parton structure functions. Effects of rescattering and possible evolution of the initially produced parton system towards equilibrium are not included in this consideration.

To quantify the event-by-event asymmetry of transverse energy flow, one can study, as proposed in Ref. [741], the difference between the transverse energy deposited in some rapidity window  $y_{\min} < y_i < y_{\max}$ , and in two oppositely azimuthally oriented sectors with an angular opening  $\delta\varphi$  each. The idea of using this quantity as a measure of the presence of semi-hard dynamics comes from the expectation that perturbative transverse energy production mechanisms have a built-in tendency of creating an event-by-event azimuthal asymmetry *in a fixed rapidity window*. For example, the partonic transverse energy flow occurring through binary parton collisions becomes, with increasing collision energy, more and more azimuthally unbalanced, because one of the two scattered partons just misses the rapidity window in question [741]. In the limit of high energies even the binary parton scattering at central rapidities as such becomes azimuthally unbalanced because of the growing contribution of primordial transverse momentum to particle production [742]. In contrast, one expects the soft transverse energy production mechanisms, e.g. string decays, to be more azimuthally balanced *locally in rapidity* on an event-by-event basis because of the small momentum transfer involved.

By denoting the transverse energy going into the ‘upper’ and ‘lower’ cones in a given event by  $E_t^\uparrow(\delta\varphi)$  and  $E_t^\downarrow(\delta\varphi)$ , respectively, the asymmetry in transverse energy production in a given event is thus described by  $\delta E_t(\delta\varphi)$ :

$$\delta E_t(\delta\varphi) = E_t^\uparrow(\delta\varphi) - E_t^\downarrow(\delta\varphi). \quad (6.94)$$

An ensemble of collisions is characterised by an event-by-event probability distribution

$$P(\delta E_t|\delta\varphi) = \frac{d w(\delta E_t(\delta\varphi))}{d \delta E_t(\delta\varphi)}. \quad (6.95)$$

This distribution was calculated in Ref. [739] in the HIJING model for central Au–Au collisions at RHIC energy  $\sqrt{s_{\text{NN}}} = 200$  GeV and central Pb–Pb collisions at LHC energy  $\sqrt{s_{\text{NN}}} = 5.5$  TeV for  $\delta\varphi = \pi$  and in central rapidity interval  $-0.5 < y < 0.5$ . The distributions  $P(\delta E_t|\pi)$  were calculated *both* at partonic level and at the level of final hadrons with semi-hard interactions and quenching on and off. This allowed one to separate the contribution of minijets as described by HIJING from the background of soft processes. The resulting

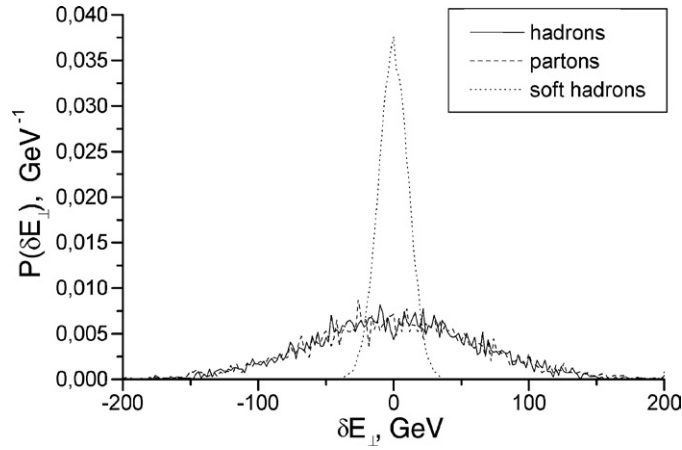


**Figure 6.254.** Probability distribution for azimuthal transverse energy imbalance in the unit rapidity window for Pb–Pb collisions at LHC energy  $\sqrt{s_{NN}} = 5.5$  TeV and  $p_0 = 2$  GeV with quenching on.

**Table 6.48.** Values of the standard deviation  $\sqrt{\langle \delta E_t^2 \rangle}$  characterising the widths of the of the probability distributions for different energies and assumptions.

A–A	$\sqrt{s}$ (GeV)	$p_0$ (GeV)	Asymmetry	$\sqrt{\langle \delta E^2 \rangle}$ (GeV)
Au–Au	200	2	hadrons (quenching on)	16
			hadrons (quenching off)	17
			partons	18
			soft hadrons	7
			hadrons (quenching on)	61
Pb–Pb	5500	2	hadrons (quenching off)	71
			partons	65
			soft hadrons	15
			hadrons (quenching on)	69
Pb–Pb	5500	4	partons	76
			soft hadrons	16

distributions for the LHC are shown in Fig. 6.254 with quenching turned on and the chosen value of the minijet’s infrared cutoff  $p_0 = 2$  GeV.

The numerical values of the standard deviation  $\sqrt{\langle \delta E_t^2 \rangle}$  characterising the widths of the corresponding probability distributions are shown in the Table 6.48, where for completeness standard deviations for the cases of quenching turned off and with a larger value for the infrared cutoff  $p_0 = 4$  GeV are also reported.

The magnitude of the azimuthal asymmetry is essentially determined by the relative yield of the semihard (minijet) contribution. Switching off minijets, and thus restricting oneself to purely soft mechanisms, leads to a substantial narrowing of the asymmetry distribution; by the factor of 2.3 at RHIC and by the factor 4.1 at LHC energy (these values correspond to the case of quenching turned on). Quite remarkably, the parton and final (hadronic) distributions of  $\delta E_t$  in both cases practically coincide indicating that the contribution to transverse energy due to hadronization of the primordial parton system is, to a high accuracy, additive and symmetric

in azimuthal angle and thus cancels out. The transverse energy flow imbalance Eq. (6.94) is a sensitive indicator of the presence of primordial semi-hard parton dynamics that can be studied in calorimetric measurements in central detectors at the LHC.

As mentioned earlier, rescattering of produced partons, which is essential for possible evolution of the primordial partons towards equilibration, was not taken into account in the above consideration. In fact one expects parton rescattering to destroy at least some of the initial asymmetry of the transverse energy flow, making its measurement even more interesting.

*6.5.15. Long-range correlations.* Soft and semihard parts of the multi-particle production in pp collisions at high energy are successfully described in terms of colour strings stretched between the projectile and target [743–747]. The hadronization of these strings produces the observed hadrons. In the case of nuclear collision, the number of strings grows with the growing energy and the number of nucleons of colliding nuclei, and one has to take into account the interaction between strings in the form of their fusion and/or percolation [749].

In the case of colour string fusion, a new string is formed which may have higher colour charge at its ends, corresponding to the sum of the initial colour charges of fusing strings. Thus heavy flavour is produced more efficiently in the process of this new string fragmentation. Fusion process results in the reduction of total multiplicity of charged-particles, growth of transverse momentum and increase of strange-particle yields [751, 752], that was confirmed later [753, 754] in comparison with RHIC data.

Around percolation threshold [755, 756, 864], strong fluctuations in the number of strings with a given colour should appear. As a result one may expect large fluctuations in values of different observables from one event to another. The characteristic and unique feature of the string fusion (percolation) phenomenon is that these fluctuations will manifest themselves as the long-range correlations between observables obtained in an event-by-event analysis in separate rapidity windows.

The possible experimental observation of the string percolation phenomenon as an intermediate process, leading to the QGP formation, is extremely interesting. Therefore, the long-range correlations were proposed as the main tool to study the mentioned phenomenon [670, 757, 758, 761–764].

The benefit of studies of correlations between the variables in two windows sufficiently separated in rapidity has the possibility of eliminating short-range correlations, arising due to other processes such as resonance decays. Besides, it is also possible to discriminate correlations originating from the string fusion and those from multiple jet formation. This can be done by choosing different sizes of rapidity bins and making proper transverse momentum cuts. The additional variables like net charge and strangeness could be used to discriminate existing theoretical scenarios bringing a deeper insight to string fusion and percolation mechanism [753, 754, 764].

*6.5.15.1. Observables.* The long-range correlation studies are made between observables in two different and significantly separated rapidity intervals  $\Delta y_F$  and  $\Delta y_B$ , which are conventionally referred as forward ( $F$ ) and backward ( $B$ ) rapidity windows. Within these two windows correlations between two main dynamical variables, the multiplicity of charged-particles ( $n$ ) and the mean transverse momenta ( $p_t$ ) in the given event (6.96) are used:

$$p_t \equiv \frac{1}{n} \sum_{i=1}^n |\mathbf{p}_{ti}|, \quad \text{where } y_i \in \Delta y; \quad i = 1, \dots, n. \quad (6.96)$$

Three main types of long-range correlations can be studied within the two rapidity windows: (a)  $n$ - $n$ , the correlation between multiplicities of charged-particles, (b)  $p_t$ - $p_t$ , the correlation between values of mean transverse momenta [760] and (c)  $p_t$ - $n$ , the correlation between mean transverse momenta in one rapidity interval and the multiplicity of charged-particles in another interval.

Usually, to describe these correlations numerically the average values  $\langle B \rangle_F$  of one dynamical variable  $B$  in the backward rapidity window  $\Delta y_B$ , as a function of another dynamical variable  $F$  in the forward rapidity window  $\Delta y_F$  are studied. Here  $\langle \dots \rangle_F$  denotes averaging over the events with a fixed value of the variable  $F$  in the forward rapidity window. Averaging over events, denoted by  $\langle \dots \rangle$ , is also used.

As a result, one arrives at a correlation function:  $\langle B \rangle_F = f(F)$ . In the majority of cases one can use linear parametrisation for this function, known as linear regression. For the  $n$ - $n$  correlation in this case one gets:

$$\langle n_B \rangle_{n_F} = a + \beta_{nn} \cdot n_F. \quad (6.97)$$

Here the coefficient  $\beta_{nn}$  characterises the strength of the  $n$ - $n$  correlation,  $n_B$ ,  $n_F$  are the multiplicities of the charged-particles, produced in the *given event* in the backward ( $\Delta y_B$ ) and forward ( $\Delta y_F$ ) rapidity windows.

In case of  $p_t$ - $p_t$  and  $p_t$ - $n$  correlation the corresponding correlation coefficients  $\beta_{p_t p_t}$  and  $\beta_{p_t n}$  can be defined in a similar manner. One must realize that these correlation coefficients depend on the absolute mean values of the observables  $\langle F \rangle$  and  $\langle B \rangle$  in the forward and backward windows and that the correlation coefficient  $\beta_{p_t n}$  has the dimension of GeV/c.

It is more natural to define the correlation coefficient as the response of  $\langle B \rangle_F$  on the variations of the variable  $F$  in the vicinity of its average value  $\langle F \rangle$ . It is also useful to go to *the relative variables*, i.e. to measure a deviation of  $F$  from its average value in units of  $\langle F \rangle$ , and similarly for  $B$ . This can reduce the possible influence of experimental bias such as detection efficiency, background, etc. So it is reasonable to define a correlation coefficient  $b_{B-F}$  for a correlation between observables  $B$  and  $F$  in backward and forward rapidity windows in the following way:

$$b_{B-F} \equiv \frac{\langle F \rangle}{\langle B \rangle} \left. \frac{d\langle B \rangle_F}{dF} \right|_{F=\langle F \rangle} \quad \text{or} \quad b_{p_t-n} \equiv \frac{\langle n_F \rangle}{\langle p_{tB} \rangle} \left. \frac{d\langle p_{tB} \rangle_{n_F}}{dn_F} \right|_{n_F=\langle n_F \rangle} \quad (6.98)$$

as an example for  $p_t$ - $n$  correlations. Here the  $p_{tB}$ ,  $p_{tF}$  are the mean transverse momentum of the charged-particles, produced in the *given event* (6.96) correspondingly in the backward ( $\Delta y_B$ ) and forward ( $\Delta y_F$ ) rapidity windows.

It is clear that these relative dimensionless coefficients are simply connected with absolute correlation coefficients defined above:

$$b_{n-n} = \frac{\langle n_F \rangle}{\langle n_B \rangle} \beta_{nn}, \quad b_{p_t-p_t} = \frac{\langle p_{tF} \rangle}{\langle p_{tB} \rangle} \beta_{p_t p_t}, \quad b_{p_t-n} = \frac{\langle n_F \rangle}{\langle p_{tB} \rangle} \beta_{p_t n}. \quad (6.99)$$

These studies can be made in different azimuthal windows and by introducing additional cuts on the transverse momentum of the particles in these rapidity intervals. It can be useful for discrimination of the correlations originating due to the string fusion phenomenon from other effects such as jets, space phase boundaries or elliptic flow.

Preliminary results for Pb-Pb collisions at  $\sqrt{s_{NN}} = 17.2$  GeV [764] from the NA49 experiment indicate the existence of  $n$ - $n$  and  $p_t$ - $n$  long-range correlations both for minimum bias data and for different classes of collision centrality. In particular, the new effect of

*negative long-range correlation* and the transition to *positive one* is observed under the condition of using a narrow window in the event selection on the number of participants.

*6.5.15.2. Extending from SPS to RHIC to LHC energies.* A microscopic explanation of the phenomena of long-range correlations observed at SPS energies and predictions for RHIC and LHC were obtained in the framework of a String Fusion Model (SFM) [757–760, 763–765]. The SFM is based on a specific assumption of the interaction of overlapping strings (quark–gluon string fusion) and it takes into account the changes of the mean values of the observables in the case of overlap.

SFM Monte Carlo calculations of the correlations are done both at fixed values of the impact parameter [759, 765] and taking its fluctuation into account [763]. The calculations with a narrowly selected number of nucleons-participants of the collision were also performed [764]. Predictions for the observation of long-range correlation at RHIC and ALICE at the LHC are done based on the results of comparison of theoretical SFM description of the experimental NA49 data on long-range correlations.

The results of SFM calculations [763] of the  $b_{p_t-p_t}$  correlation coefficient as a function of the impact parameter  $b$  for three Pb–Pb collision energies  $\sqrt{s_{NN}} = 17, 130, \text{ and } 5500 \text{ GeV}$  are presented in Fig. 6.255. In these calculations the forward rapidity interval was chosen to be 0.5 units and within the central ALICE acceptance. Black and open circles and squares in Fig. 6.255 represent different approaches (see [763] for the details). Results show the considerable growth of the  $p_t-p_t$  correlation coefficient in transfer from the SPS to the LHC energies. The results of SFM MC calculations for the  $p_t-p_t$  correlation function  $\langle p_{tB} \rangle_{p_{tF}} = f(p_{tF})$  are also presented in this figure [763]. A drastic change of the shape of this correlation function with energy is observed.

*6.5.15.3. Long-range correlation studies at ALICE.* ALICE installation provides charged-particle multiplicity information in a wide rapidity range up to  $\eta = 5.09$ . Precise  $p_t$  measurements and detailed particle composition data are provided event-by-event in the central rapidity window up to  $\eta = 0.9$ . Therefore, studies of long-range correlations in ALICE will be done using the information obtained from the ITS, TPC and the TOF detectors in combination with event-by-event multiplicity from the SPD and the FMD detectors.

It is important to start the long-range correlation investigations in ALICE from the pp collisions, which will form the base for pA and A–A collisions. In particular, scanning the impact parameter space for the Pb–Pb collisions using the ZDC data gives the possibility to change the density of the overlapping strings by moving from the most peripheral to the central collisions [670]. Therefore, the onset of the critical fluctuations relevant to the string fusion and/or percolation phenomenon could be obtained in ALICE from the observation of the behaviour of the long-range correlation coefficients vs. event centrality. These will provide the important information on the early stages of the QGP formation.

*6.5.16. Summary.* To summarize, the capability of the ALICE experiment in terms of making detailed event-by-event measurements has been discussed in order to address the issue of the nature of QGP phase transition. Recent findings from the lattice calculations at small chemical potentials have been discussed. These calculations have revealed that interesting fluctuation patterns will prevail for heavy-ion collisions at LHC energies. The issue of correlations and fluctuations and the complexity in interpreting the results because of several competing processes has been addressed. The importance of controlling centrality in fluctuation studies is discussed. In ALICE, fluctuations in temperature can be estimated from the event-by-event measurement of the slope of  $p_t$  distribution of identified hadrons

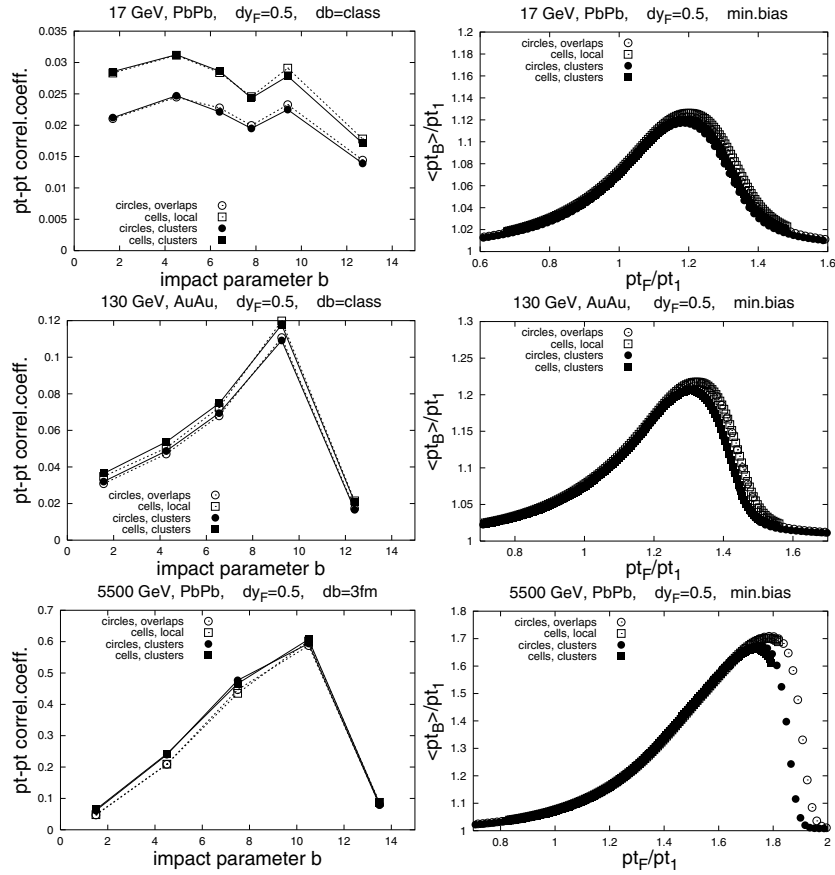


**Figure 6.255.** Left panel: String Fusion Model(SFM) MC calculations [763] of the  $b_{p_t-p_t}$  long-range correlation coefficient as a function of the impact parameter  $b$  for three Pb–Pb collision energies:  $\sqrt{s_{NN}} = 17, 130$  and  $5500$  GeV. Right panel: Corresponding  $p_t-p_t$  correlation functions  $\langle p_{tB} \rangle_{p_{tF}} = f(p_{tF})$ , presented in units of  $p_{t1} \equiv \bar{p}$  which is the average transverse momentum of particles produced from a decay of one string.

in addition to those from the fluctuations in  $\langle p_t \rangle$ . Fluctuation measurements in particle multiplicity, strangeness, net charge and the ratio of particles can be performed with high accuracy. The method of studying fluctuations through balance functions has been explored in ALICE environment. Possibilities of event-by-event measurements of source sizes and azimuthal asymmetry parameters are discussed. The capability of ALICE in terms of measurement of the formation of disoriented chiral condensate has been discussed. An attempt has been made to understand the event-by-event fluctuations in the presence of jets and minijets. This is important in order to make any inference about the nature of event-by-event fluctuations as well as to understand the effect of jets passing through the high density medium created in heavy-ion collisions. It has been shown that information about the collision dynamics, especially on the string fusion and percolation phenomenon can be obtained from the study of long-range correlations. Extraction of long-range correlation coefficients for different colliding systems and centralities will help to understand critical fluctuations relevant to the string fusion and percolation phenomena.

## 6.6. Charm and beauty

This section is organized as follows.

The physics motivations for the study of heavy-flavour production in pp, pA and AA collisions at the Large Hadron Collider (LHC), already introduced in the first chapter of PPR Volume I (Section 1.3.8) [3], are discussed in Section 6.6.1. Section 6.6.2 is a short summary of the present experimental measurements of open charm and beauty production in hadronic collisions. In Section 6.6.3 we describe the assumptions we made for the heavy-quark production cross sections and kinematical distributions at LHC energies.

We then present simulation results on the ALICE capability for open-heavy-flavour physics<sup>8</sup>. We assume the following data samples:  $10^7$  central (5%) Pb–Pb events for one month of data taking at nominal luminosity  $\mathcal{L}_{\text{Pb–Pb}} = 5 \times 10^{26} \text{ cm}^{-2}\text{s}^{-1}$ ;  $10^9$  minimum-bias pp events for eight months at  $\mathcal{L}_{\text{pp (ALICE)}} = 5 \times 10^{30} \text{ cm}^{-2}\text{s}^{-1}$ ;  $10^8$  minimum-bias pPb events for one month at  $\mathcal{L}_{\text{pPb}} = 10^{29} \text{ cm}^{-2}\text{s}^{-1}$ . In Section 6.6.4 we show the feasibility for the reconstruction of charm particles, in Pb–Pb, pp and pPb collisions, using as a benchmark the  $D^0 \rightarrow K^- \pi^+$  decay channel. Some physics perspectives based on this measurement are then discussed: we evaluate the sensitivity for the study of the in-medium energy loss of charm quarks in Pb–Pb collisions (Section 6.6.5) and for the comparison to theoretical calculations on charm production in pp collisions (Section 6.6.6). The measurements of open beauty production via semi-electronic decays in the ALICE central barrel and via semi-muonic decays in the forward muon spectrometer are described in Sections 6.6.7 and 6.6.8, respectively. Finally, in Section 6.6.9, we shortly outline the activities currently in progress in the heavy-flavour sector, as well as the main directions for future developments.

*6.6.1. Physics motivations.* The measurement of open charm and open beauty production allows one to investigate the mechanisms of heavy-quark production, propagation and, at low momenta, hadronisation in the hot and dense medium formed in high-energy nucleus–nucleus collisions. The open charm and open beauty cross sections are also needed as a reference to measure the effect of the transition to a deconfined phase on the production of quarkonia. In fact, since at LHC energies heavy quarks are mainly produced through gluon–gluon fusion processes ( $gg \rightarrow Q\bar{Q}$ ), the Drell–Yan process ( $q\bar{q} \rightarrow \ell^+\ell^-$ ) does not provide an adequate reference, besides having a very small cross section at these energies; a direct measurement of the D and B mesons yields would provide a natural normalization for charmonia and bottomonia production. Finally, the measurement of B meson production is necessary in order to estimate the contribution of secondary  $J/\psi$  (from  $B \rightarrow J/\psi + X$ ) to the total  $J/\psi$  yield.

The measurement of charm and beauty production in proton–proton and proton–nucleus collisions, besides providing the necessary baseline for the study of medium effects in nucleus–nucleus collisions, is of great interest *per se*, as a test of both perturbative and non-perturbative sectors of QCD in a new energy domain.

*6.6.1.1. Accessible  $x$  range with heavy quarks in ALICE.* The LHC will allow us to probe the parton distribution functions of the nucleon and, in the case of pA and AA collisions, also their modifications in the nucleus, down to unprecedentedly low values of the momentum fraction (Bjorken  $x$ ). Here, we compare the regimes in  $x$  corresponding to the production of a  $c\bar{c}$  pair at SPS, RHIC and LHC energy and we estimate the  $x$  range that can be accessed with ALICE as far as heavy-flavour production is concerned. Charm and beauty production

<sup>8</sup> On account of the rapid evolution and optimization of the cluster/track reconstruction and particle identification algorithms, most of the studies presented here were obtained with former and, in some cases, slightly less-well performing versions of these algorithms, with respect to the state-of-the-art ones described in Chapter 5. Therefore, as far as detector performance is concerned, the following results should be considered as a ‘conservative’ case.

**Table 6.49.** Bjorken  $x$  values corresponding to charm and beauty production at central rapidity and  $p_t \rightarrow 0$  at SPS, RHIC and LHC energies.

Machine	SPS	RHIC	LHC	LHC
System	Pb–Pb	Au–Au	Pb–Pb	pp
$\sqrt{s_{\text{NN}}}$	17 GeV	200 GeV	5.5 TeV	14 TeV
$c\bar{c}$	$x \simeq 10^{-1}$	$x \simeq 10^{-2}$	$x \simeq 4 \times 10^{-4}$	$x \simeq 2 \times 10^{-4}$
$b\bar{b}$	–	–	$x \simeq 2 \times 10^{-3}$	$x \simeq 6 \times 10^{-4}$

cross sections at the LHC are significantly affected by parton dynamics in the small- $x$  region, as we will discuss in the following sections. Therefore, the measurement of heavy-flavour production should provide valuable information on the parton densities (see Section 6.6.1.3).

We consider the simple case of the production of a heavy-quark pair  $Q\bar{Q}$  through the leading-order pair-creation process  $gg \rightarrow Q\bar{Q}$  in the collision of two nuclei ( $A_1, Z_1$ ) and ( $A_2, Z_2$ ). The  $x$  range actually probed depends on the value of the centre-of-mass (c.m.s.) energy per nucleon pair  $\sqrt{s_{\text{NN}}}$ , on the invariant mass  $M_{Q\bar{Q}}$  of the  $Q\bar{Q}$  pair produced in the hard scattering and on its rapidity  $y_{Q\bar{Q}}$ . If the intrinsic transverse momentum of the parton in the nucleon is neglected, the four-momenta of the two incoming gluons are  $(x_1, 0, 0, x_1) \cdot (Z_1/A_1) \sqrt{s_{\text{pp}}}/2$  and  $(x_2, 0, 0, -x_2) \cdot (Z_2/A_2) \sqrt{s_{\text{pp}}}/2$ , where  $x_1$  and  $x_2$  are the momentum fractions carried by the gluons, and  $\sqrt{s_{\text{pp}}}$  is the c.m.s. energy for pp collisions (14 TeV at the LHC). The square of the invariant mass of the  $Q\bar{Q}$  pair is given by

$$M_{Q\bar{Q}}^2 = \hat{s} = x_1 x_2 s_{\text{NN}} = x_1 \frac{Z_1}{A_1} x_2 \frac{Z_2}{A_2} s_{\text{pp}}, \quad (6.100)$$

and its longitudinal rapidity in the laboratory is

$$y_{Q\bar{Q}} = \frac{1}{2} \ln \left[ \frac{E + p_z}{E - p_z} \right] = \frac{1}{2} \ln \left[ \frac{x_1}{x_2} \cdot \frac{Z_1 A_2}{Z_2 A_1} \right]. \quad (6.101)$$

From these two relations we can derive the dependence of  $x_1$  and  $x_2$  on colliding system,  $M_{Q\bar{Q}}$  and  $y_{Q\bar{Q}}$ :

$$x_1 = \frac{A_1}{Z_1} \cdot \frac{M_{Q\bar{Q}}}{\sqrt{s_{\text{pp}}}} \exp(+y_{Q\bar{Q}}) \quad x_2 = \frac{A_2}{Z_2} \cdot \frac{M_{Q\bar{Q}}}{\sqrt{s_{\text{pp}}}} \exp(-y_{Q\bar{Q}}), \quad (6.102)$$

which simplifies to

$$x_1 = \frac{M_{Q\bar{Q}}}{\sqrt{s_{\text{NN}}}} \exp(+y_{Q\bar{Q}}), \quad x_2 = \frac{M_{Q\bar{Q}}}{\sqrt{s_{\text{NN}}}} \exp(-y_{Q\bar{Q}}), \quad (6.103)$$

for a symmetric colliding system ( $A_1 = A_2, Z_1 = Z_2$ ).

At central rapidities we have  $x_1 \simeq x_2$  and their magnitude is determined by the ratio of the pair invariant mass to the c.m.s. energy. For production at threshold ( $M_{c\bar{c}} = 2m_c \simeq 2.4$  GeV,  $M_{b\bar{b}} = 2m_b \simeq 9$  GeV) we obtain the values reported in Table 6.49. The  $x$  regime relevant for charm production at the LHC ( $\sim 10^{-4}$ ) is about 2 orders of magnitude lower than at RHIC and 3 orders of magnitude lower than at the SPS.

Because of its lower mass, charm allows one to probe lower  $x$  values than beauty. The capability to measure charm and beauty particles in the forward (or backward) rapidity region ( $|y| \simeq 4$ ) gives access to  $x$  regimes about 2 orders of magnitude lower, down to  $x \sim 10^{-6}$ .

In Fig. 6.256 we show the regions of the  $(x_1, x_2)$  plane covered for charm and beauty by the ALICE acceptance, at 5.5 TeV (the planned Pb–Pb c.m.s. energy) and at 14 TeV (the planned pp c.m.s. energy). In this plane the points with equal invariant mass lie on hyperbolae ( $x_1 = M_{Q\bar{Q}}^2 / (x_2 s_{\text{NN}})$ ), straight lines in the log–log scale: we show those corresponding to the

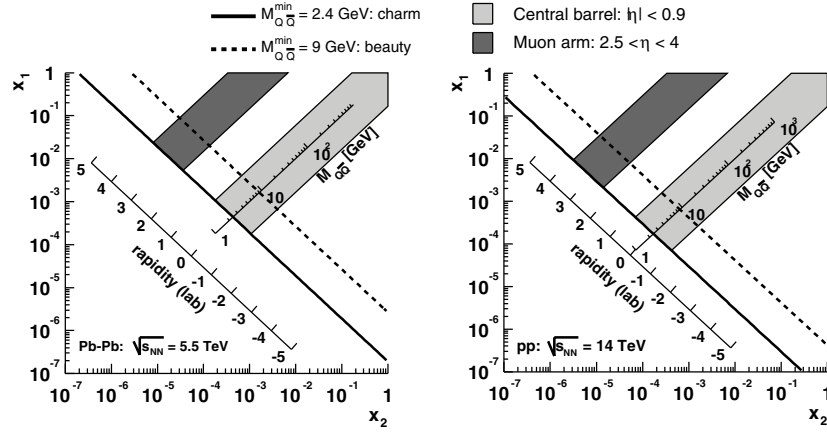


**Figure 6.256.** ALICE acceptance in the  $(x_1, x_2)$  plane for heavy flavours in Pb–Pb at 5.5 TeV (left) and in pp at 14 TeV (right). The figure is explained in detail in the text.

production of  $c\bar{c}$  and  $b\bar{b}$  pairs at the threshold; the points with constant rapidity lie on straight lines ( $x_1 = x_2 \exp(+2y_{Q\bar{Q}})$ ). The shadowed regions show the acceptance of the ALICE barrel, covering the pseudorapidity range  $|\eta| < 0.9$ , and of the muon arm<sup>9</sup>,  $-4 < \eta < -2.5$ .

In the case of asymmetric collisions<sup>10</sup>, e.g. pPb and Pb–p, we have a rapidity shift: the centre of mass moves with a longitudinal rapidity

$$y_{\text{c.m.}} = \frac{1}{2} \ln \left( \frac{Z_1 A_2}{Z_2 A_1} \right), \quad (6.104)$$

obtained from equation (6.101) for  $x_1 = x_2$ . The rapidity window covered by the experiment is consequently shifted by

$$\Delta y = y_{\text{c.m.}}, \quad (6.105)$$

corresponding to +0.47 (–0.47) for pPb (Pb–p) collisions. Therefore, running with both pPb and Pb–p will allow the largest interval in  $x$  to be covered. The c.m.s. energy in this case is 8.8 TeV. Figure 6.257 shows the acceptances for pPb and Pb–p, while in Fig. 6.258 the coverages in pp, Pb–Pb, pPb and Pb–p are compared for charm (left) and beauty (right).

These figures are meant to give only an approximate idea of the regimes accessible with ALICE; the simple relations for the leading-order case were used, the ALICE rapidity acceptance cuts were applied to the rapidity of the  $Q\bar{Q}$  pair, and not to that of the particles actually detected. In addition, no minimum  $p_t$  cuts were accounted for: such cuts will increase the minimum accessible value of  $M_{Q\bar{Q}}$ , thus increasing also the minimum accessible  $x$ . These approximations, however, are not too drastic, since there is a very strong correlation in rapidity between the initial  $Q\bar{Q}$  pair and the heavy-flavour particles it produces and the minimum accessible  $p_t$  for D and B mesons in ALICE is expected to be of order 1–2 GeV/ $c$ .

**6.6.1.2. Heavy-quark production in nucleus–nucleus collisions at high energy.** Heavy quarks are produced in the early stage of the collision in primary partonic scatterings with

<sup>9</sup> In the figures the acceptance of the muon arm is shown as  $2.5 < \eta < 4$ ; because of a recent change in the definition of the ALICE global coordinate system, the acceptance reads now  $-4 < \eta < -2.5$ .

<sup>10</sup> When we write pPb, we mean that the proton moves with  $p_z > 0$ ; when we write Pb–p, we mean that the proton moves with  $p_z < 0$ .

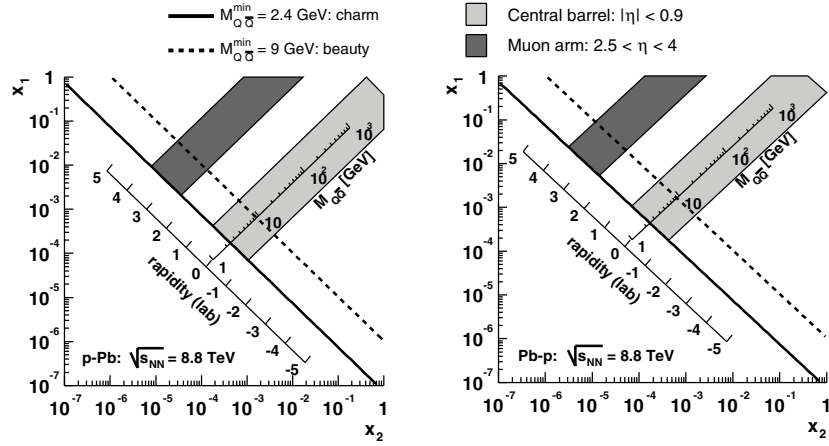


**Figure 6.257.** ALICE acceptance in the  $(x_1, x_2)$  plane for heavy flavours at 8.8 TeV in pPb (left) and in Pb-p (right).

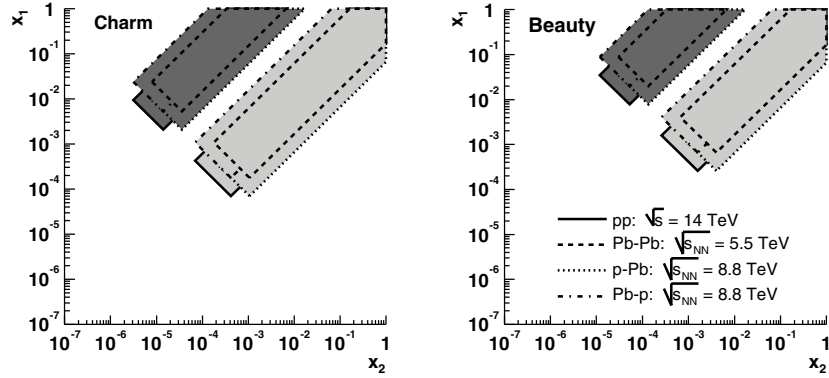


**Figure 6.258.** ALICE acceptance in the  $(x_1, x_2)$  plane for charm (left) and beauty (right) at 5.5, 8.8 and 14 TeV.

large virtuality  $Q$  and, thus, on temporal and spatial scales,  $\Delta\tau \sim \Delta r \sim 1/Q$ , which are sufficiently small for the production to be unaffected by the properties of the medium, in the case of nucleus–nucleus collisions. In fact, the minimum virtuality  $Q_{\min} = 2m_Q$  in the production of a  $Q\bar{Q}$  pair implies a space-time scale of  $\sim 1/(2m_Q) \simeq 1/2.4 \text{ GeV}^{-1} \simeq 0.1 \text{ fm}$  (for charm), to be compared to the expected lifetime of the QGP phase at the LHC,  $>10 \text{ fm}$ . Thus, the initially-produced heavy quarks experience the full collision history.

We assume that, given the large virtualities that characterise the production of heavy quarks, the baseline cross section in nucleon–nucleon collisions can be calculated in the framework of collinear factorisation and perturbative QCD (pQCD). The general lines followed for the cross section calculations in proton–proton collisions were described in Section 1.3.8 of PPR Volume I [3] and the results and theoretical uncertainties at LHC energies are reported in Section 6.6.3. Here, we write the schematic expression for the single-inclusive

differential cross section for the production of a heavy-flavour hadron  $H_Q$ :

$$\begin{aligned} d\sigma^{\text{NN}\rightarrow H_Q X}(\sqrt{s_{\text{NN}}}, m_Q, \mu_{\text{F}}^2, \mu_{\text{R}}^2) &= \sum_{i,j=q,\bar{q},g} f_i(x_1, \mu_{\text{F}}^2) \otimes f_j(x_2, \mu_{\text{F}}^2) \otimes d\hat{\sigma}^{ij\rightarrow Q(\bar{Q})^{(k)}} \\ &\times (\alpha_s(\mu_{\text{R}}^2), \mu_{\text{F}}^2, m_Q, x_1 x_2 s_{\text{NN}}) \otimes D_Q^{H_Q}(z, \mu_{\text{F}}^2), \end{aligned} \quad (6.106)$$

where the partonic  $d\hat{\sigma}^{ij\rightarrow Q(\bar{Q})^{(k)}}$  is calculable as a power series in the strong coupling  $\alpha_s$ , which depends on the renormalisation scale  $\mu_{\text{R}}$ ; currently, calculations are performed up to next-to-leading order (NLO),  $\mathcal{O}(\alpha_s^3)$ . The nucleon Parton Distribution Function (PDF) for the parton of type  $i$  at momentum fraction  $x_1$  and factorisation scale  $\mu_{\text{F}}$ , which can be interpreted as the virtuality  $Q$  of the hard process, is denoted by  $f_i(x_1, \mu_{\text{F}}^2)$ . The fragmentation function  $D_Q^{H_Q}(z, \mu_{\text{F}}^2)$ , also dependent on the factorisation scale, parametrizes the probability for the heavy quark  $Q$  to fragment into a hadron  $H_Q$  with momentum fraction  $z = p_{H_Q}/p_Q$ .

For hard processes, in the absence of nuclear and medium effects, a nucleus–nucleus (or p–nucleus) collision would behave as a superposition of independent NN collisions. The charm and beauty differential yields would then scale from pp to AA (or pA) proportionally to the number  $N_{\text{coll}}$  of inelastic NN collisions (binary scaling):

$$d^2 N_{\text{AA(pA)}}^{H_Q}/dp_t dy = N_{\text{coll}} \times d^2 N_{\text{pp}}^{H_Q}/dp_t dy. \quad (6.107)$$

The number of binary collisions can be computed on the basis of the Glauber model of heavy-ion collisions [766, 767], (see Section 6.6.3.2). Several effects can determine the breakdown of binary scaling. They are usually divided into two classes:

- **Initial-state effects**, such as nuclear shadowing, the modification of the parton distribution functions in the nucleus due to gluon recombination at small  $x$  (see Section 1.5.2 of PPR Volume I [3]). Initial-state effects can, at least in principle, be studied comparing proton–proton and proton–nucleus collisions, as we briefly discuss in Section 6.6.13. In the same section we show that, indeed, at LHC energy gluon recombination may occur even in pp collisions and affect the charm production cross section.
- **Final-state effects**, due to the interaction of the produced partons with the medium formed in the collision. Partonic energy loss in the medium would be an example of such an effect. It is expected to depend on the properties of the medium (gluon density, temperature and volume) and should, therefore, provide information on such properties. Charm and beauty quarks are qualitatively different probes with respect to light partons, since, on QCD grounds, the in-medium energy loss of massive partons is expected to be different from that of ‘massless’ partons (light quarks and gluons) [768–771], as discussed in Section 6.6.1.4. Therefore, a comparative study of the attenuation of massless and massive probes allows one to test the consistency of the interpretation of quenching effects as due to energy loss in a deconfined medium and to investigate the properties (density) of such a medium. For heavy quarks with moderate momenta ( $p_t \lesssim 10 \text{ GeV}/c$ ), hadronisation may predominantly occur inside the medium via the mechanism of coalescence with other quarks present in the system, rather than via fragmentation in the vacuum outside the medium. As we briefly discuss in Section 6.6.1.5, the study of this effect may allow the degree of thermal equilibration of the partonic system formed in the collision to be assessed.

Note that, for heavy quarks, given the large intrinsic virtuality of their production processes, pQCD allows one to perform the energy extrapolations needed to compare pp, pA and AA collisions (having different  $\sqrt{s_{\text{NN}}}$  values) in order to disentangle initial- and final-state effects. This is discussed in Section 6.6.3.1.

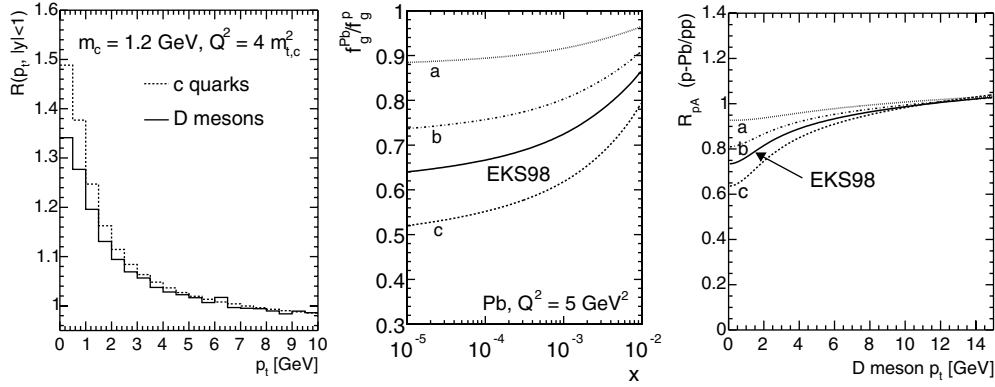


**Figure 6.259.** Left: enhancement due to non-linear gluon evolution for c quarks and D mesons in pp collisions at  $\sqrt{s} = 14$  TeV [774]. Centre: four different scenarios for the modification of the gluon PDF in a Pb nucleus at  $Q^2 = 5 \text{ GeV}^2 \simeq 4 m_c^2$ . Right: corresponding  $R_{pA}^D$  in pPb at  $\sqrt{s_{NN}} = 8.8$  TeV.

**6.6.1.3. Probing initial-state gluon densities in a new energy domain with heavy quarks.** In the kinematic range relevant for  $Q\bar{Q}$  production, assessed in Section 6.6.1.1, the density of low- $x$  gluons in the two colliding hadrons will be close to saturation of the available phase-space, so as to already produce significant gluon-recombination effects ( $gg \rightarrow g$ ) in the case of pp collisions. These effects can be accounted for in the PDF  $Q^2$ -evolution equations by adding to the standard linear DGLAP term a negative non-linear (quadratic) term (see Ref. [772] and references therein):

$$\partial f_g(x, Q^2)/\partial \log Q^2 = [\text{DGLAP term of } \mathcal{O}(f_g)] - [\text{term of } \mathcal{O}(f_g^2)]. \quad (6.108)$$

The non-linear term, currently calculated only at LO, ‘slows down’ the  $Q^2$  evolution at given  $x$ . It has been shown [772] that, for  $x \lesssim 10^{-2}$ , it allows a higher gluon density at small  $Q^2$  ( $\lesssim 10 \text{ GeV}^2$ ), with respect to that obtained with DGLAP terms only, and can maintain at the same time a good fit of the proton structure function data from HERA. A higher gluon PDF would imply an enhancement, w.r.t. to DGLAP-based calculations, of  $c\bar{c}$  production at low  $p_t$  at LHC energy [773]. Figure 6.259 (left) shows, as a function of  $p_t$ , the enhancement at the c quark and at the D meson level, for  $m_c = 1.2 \text{ GeV}$  and  $\mu_F^2 = \mu_R^2 = Q^2 = 4 m_{t,c}^2 \equiv 4(m_c^2 + p_t^2)$  [774]. Here, hadronisation of heavy quarks is performed using the string fragmentation model implemented in PYTHIA [150]. The enhancement is expected to survive fragmentation and is about 30% for D meson  $p_t \rightarrow 0$ , even in this ‘pessimistic’ case where relatively-large  $Q^2$  values are considered (it should be noted, however, that this is a LO result and the effect might be smaller at NLO). In Section 6.6.6.2 we show how the enhancement increases in a more ‘optimistic’ case, corresponding to smaller values of  $\mu_F$  and  $\mu_R$ , and we outline a possible strategy to detect the enhancement in pp collisions at the LHC with ALICE. Also other approaches [775–777] for the inclusion of recombination in gluon evolution, based on the BK  $x$ -evolution equation, lead to potentially observable effects on the charm and beauty production cross sections in pp collisions at the LHC [778].

In the case of proton–nucleus and nucleus–nucleus collisions, when large-A nuclei are involved, the high density of gluons at small  $x$  and small  $Q^2$  induces a suppression of the PDFs. The effect, indicated as nuclear shadowing, is usually parametrized in terms of the modification of the parton distribution functions of the nucleon in the nucleus,  $f_i^A(x, Q^2)$ ,

with respect to those of the free nucleon,  $f_i^N(x, Q^2)$ :

$$R_i^A(x, Q^2) = \frac{f_i^A(x, Q^2)}{f_i^N(x, Q^2)}, \quad (6.109)$$

where  $i = q_v, q_{\text{sea}}, g$  for valence quarks, sea quarks, and gluons.

A direct consequence of shadowing is the reduction of hard-scattering cross sections in the phase-space region characterised by small- $x$  incoming partons, hence, at mid-rapidity, low transverse momentum outgoing partons. As an example, the EKS98 parametrisation [779] of the PDF's nuclear modification, shown in Fig. 6.259 (centre) for  $Q^2 = 5 \text{ GeV}^2$ , predicts a reduction of the charm (beauty) cross section at NLO of about 35% (20%) in Pb–Pb at 5.5 TeV and 15% (10%) in pPb at 8.8 TeV (see Section 6.6.3.2). However, because of the lack of experimental data for  $x \lesssim 0.005$ , there is a significant uncertainty on the strength of shadowing in this  $x$  region and some models predict a much larger suppression than EKS98 (see Section 1.5.2 of PPR Volume I [3] or Ref. [780] for a review). The comparison of  $Q\bar{Q}$  production in pp and pPb collisions (where final-state effects are not expected to be present) is regarded as a sensitive tool to probe nuclear PDFs at LHC energy. The ratio of invariant-mass spectra of dileptons from heavy-quark decays in pPb and pp collisions would measure the nuclear modification  $R_g^{\text{Pb}}$  [780]. Another promising observable in this respect is the nuclear modification factor of the D meson  $p_t$  distribution, defined as

$$R_{\text{pA(AA)}}^{\text{D}}(p_t, \eta) = \frac{1}{\langle N_{\text{coll}} \rangle} \times \frac{d^2 N_{\text{pA(AA)}}^{\text{D}}/dp_t d\eta}{d^2 N_{\text{pp}}^{\text{D}}/dp_t d\eta}. \quad (6.110)$$

In Fig. 6.259 (right) we show the sensitivity of  $R_{\text{pPb}}^{\text{D}}$  to different shadowing scenarios, obtained by varying the modification of the PDFs in the Pb nucleus (displayed, for gluons, by the curves labeled ‘a’, ‘b’, ‘c’ and ‘EKS98’ in the central panel of the same figure).

The use of nuclear-modified parton distributions functions allows high-density effects at small  $x$  to be accounted for within the framework of perturbative QCD collinear factorisation. However, factorisation is expected to break down when the gluon phase-space becomes saturated. In these conditions, partons in the nuclear wave function at small  $x$  would act coherently, not independently as assumed with factorisation, and, in the limit, they may form a Colour Glass Condensate (CGC), as discussed in Section 1.2.4 of PPR Volume I [3]. The relevant parameter in the CGC is the so-called saturation scale  $Q_s^2(x)$ , determined by the parton density per unit transverse area, and thus growing with the nuclear mass number  $A$  as  $Q_s^2 \sim A/R_A^2 \sim A^{1/3}$ , at fixed  $x$ . For a Pb nucleus probed at LHC energy, the estimated saturation scale at  $x \sim 10^{-4}$ – $10^{-5}$  is  $Q_s^2 \sim 2$ – $3 \text{ GeV}^2$ . It has been argued [781] that charm-quark production in the kinematic domain corresponding to transverse masses smaller than the saturation scale,  $m_{t,c} \lesssim Q_s \sim 1.5$ – $2 \text{ GeV}$  would be strongly affected by the presence of the CGC. In particular, since the mean intrinsic transverse momentum  $k_t$  of partons in the CGC is of order  $Q_s$ , rather than of order  $\Lambda_{\text{QCD}} \sim 0.2 \text{ GeV}$  as assumed in collinear factorisation, the fact that  $Q_s \gg \Lambda_{\text{QCD}}$  would lead to significantly harder transverse momentum distributions for charm quarks in pPb collisions than in pp collisions. In addition, the centrality dependence of the production yields would follow  $\sqrt{N_{\text{part}}}$  rather than  $N_{\text{coll}}$  scaling [781]. Since robust predictions are not yet available, for the ALICE performance studies presented in this chapter, we did not include these saturation effects in the estimate of the baseline heavy-quark production cross sections, relying instead on the standard collinear factorisation approach.

Heavy-flavour production in proton–nucleus collisions is also suggested as a probe for multipartonic interaction events, in which more than one hard partonic interaction takes place within the same hadronic collision (see Section 1.5.3 of PPR Volume I [3]). In the case of proton–nucleus collisions, these events can be of two types, normal or

anomalous multipartonic events, depending whether one or more nucleons in the nucleus are involved [782, 783]. The probability for multiparton scatterings and the normal-to-anomalous ratio depend on the many-body parton distributions, which contain much more information on the hadron structure than the single-body parton distributions usually considered in pQCD (the standard PDFs). They are related to the parton correlations generated by the underlying strong interaction dynamics. Hence, multipartonic interactions are a promising tool to investigate the three-dimensional partonic structure functions [782, 783]. The first measurement of double-parton events was performed in  $p\bar{p}$  collisions at the Tevatron, selecting final states with three jets and a photon [784]. Calculations for the LHC energy predict a significant cross section for final states with four jets, even in the case of charm and beauty heavy-flavour jets. In particular, the cross section for two  $c\bar{c}$  pairs produced via a double-parton event is expected to be up to 10% of the total  $c\bar{c}$  production cross section [785], and much larger than the  $c\bar{c}$   $c\bar{c}$  cross section in a single-parton event. Therefore, the observation of a  $DD$  or  $D\bar{D}$  pair in the same event would be a clear signal for  $c\bar{c}$   $c\bar{c}$  production in a double-parton collision. Experimentally, one could look for events with a fully-reconstructed  $D(\bar{D})$  meson and a high- $p_t$   $\ell^+(\ell^-)$  lepton, or a same-sign high- $p_t$  lepton pair<sup>11</sup>  $\ell^\pm\ell^\pm$ . Since normal and anomalous double-parton cross sections are predicted to have different  $A$  dependences, measurements with different nuclei would allow one to study their relative weight and investigate the interactions between partons in the hadron structure.

*6.6.1.4. Parton energy loss for heavy quarks in nucleus–nucleus collisions.* While traversing the dense matter produced in nucleus–nucleus collisions, the initially-produced hard partons lose energy, mainly on account of multiple scatterings and medium-induced gluon radiation, and become quenched. An intense theoretical activity has developed around the subject [786–790]. We summarize here the general lines of the model proposed by R. Baier, Yu. L. Dokshitzer, A. H. Mueller, S. Peigné and D. Schiff [787, 788] (BDMPS).

In a simplified picture, an energetic parton produced in a hard collision undergoes, along its path in the dense medium, multiple scatterings in a Brownian-like motion with mean free path  $\lambda$ , which decreases as the medium density increases. In this multiple scattering process, the gluons in the parton wave function pick up transverse momentum  $k_t$  with respect to its direction and they may eventually ‘decohere’ and be radiated.

The scale of the energy loss is set by the characteristic energy of the radiated gluons, which depends on  $L$  and on the properties of the medium:

$$\omega_c = \hat{q} L^2/2, \quad (6.111)$$

where  $\hat{q}$  is the transport coefficient of the medium, defined as the average transverse momentum squared transferred to the projectile per unit path length,  $\hat{q} = \langle k_t^2 \rangle_{\text{medium}}/\lambda$  [791].

In the case of a static medium, the distribution of the energy  $\omega$  of the radiated gluons (for  $\omega \ll \omega_c$ ) is of the form:

$$\omega \frac{dI}{d\omega} \simeq \frac{2\alpha_s C_R}{\pi} \sqrt{\frac{\omega_c}{2\omega}}, \quad (6.112)$$

where  $C_R$  is the QCD coupling factor (Casimir factor), equal to 4/3 for quark–gluon coupling and to 3 for gluon–gluon coupling. The integral of the energy distribution up to  $\omega_c$  estimates the average energy loss of the parton:

$$\langle \Delta E \rangle = \int_0^{\omega_c} \omega \frac{dI}{d\omega} d\omega \propto \alpha_s C_R \omega_c \propto \alpha_s C_R \hat{q} L^2. \quad (6.113)$$

<sup>11</sup> These final states can also originate from standard  $b\bar{b}$  production and decay events (e.g.  $b \rightarrow \ell^-$  and  $\bar{b} \rightarrow \bar{c} \rightarrow \ell^-$ ). However, this ‘background’ can be calculated and subtracted, once inclusive beauty production is measured.

The average energy loss is: proportional to  $\alpha_s C_R$  and, thus, larger by a factor  $9/4 = 2.25$  for gluons than for quarks; proportional to the transport coefficient of the medium; proportional to  $L^2$ ; independent of the initial parton energy  $E$ . It is a general feature of all parton energy loss calculations [786–794] that the gluon energy distribution (6.112) does not depend on  $E$ . Depending on how the kinematic bounds are taken into account, the resulting  $\Delta E$  is then independent [787, 788] or logarithmically dependent on  $E$  [792–794]. However, there is always an intrinsic dependence of the radiated energy on the initial energy, determined by the fact that the former cannot be larger than the latter,  $\Delta E \leq E$ . As discussed in Ref. [795], this effectively results in reducing the difference between quark and gluon average energy losses and in changing the  $L$  dependence from quadratic to approximately linear. Moreover, since a consistent theoretical treatment of the finite-energy constraint is at present lacking in the BDMPS framework, approximations have to be adopted, thus introducing uncertainties in the results [795, 796].

The transport coefficient is proportional to the density of the scattering centres and to the typical momentum transfer in gluon scattering off these centres. A review of the estimates for the value of the transport coefficient in media of different densities can be found in Ref. [797]: the estimate is  $\hat{q}_{\text{cold}} \simeq 0.05 \text{ GeV}^2 \text{ fm}$  for cold nuclear matter and, for a QGP formed at the LHC with energy density  $\varepsilon \sim 50\text{--}100 \text{ GeV}/\text{fm}^3$ ,  $\hat{q}$  may be as large as  $100 \text{ GeV}^2/\text{fm}$ .

The medium-induced energy loss of heavy quarks was first studied in Refs. [798, 799]. Subsequently, in Ref. [768] it was argued that for heavy quarks, because of their large mass, the radiative energy loss should be lower than for light quarks. The predicted consequence of this effect was an enhancement of the ratio of D mesons to pions (or light-flavoured hadrons in general) at moderately-large ( $5\text{--}10 \text{ GeV}/c$ ) transverse momenta, with respect to that observed in the absence of energy loss.

Heavy quarks with moderate energy, i.e.  $m/E \gg 0$ , propagate with a velocity  $\beta = \sqrt{1 - (m/E)^2}$  significantly smaller than the velocity of light,  $\beta = 1$ . As a consequence, in the vacuum, gluon radiation at angles  $\Theta$  smaller than the ratio of their mass to their energy  $\Theta_0 = m/E$  is suppressed<sup>12</sup> [800]. The relatively depopulated cone around the heavy-quark direction with  $\Theta < \Theta_0$  is called the ‘dead cone’.

In Ref. [768] the dead-cone effect is assumed to characterise also in-medium gluon radiation, and the energy distribution of the radiated gluons (6.112), for heavy quarks, is estimated to be suppressed by a factor

$$\omega \frac{dI}{d\omega} \Big|_{\text{Heavy}} / \omega \frac{dI}{d\omega} \Big|_{\text{Light}} = \left[ 1 + \frac{\Theta_0^2}{\Theta^2} \right]^{-2} = \left[ 1 + \left( \frac{m}{E} \right)^2 \sqrt{\frac{\omega^3}{\hat{q}}} \right]^{-2} \equiv F_{\text{H/L}}(m/E, \hat{q}, \omega), \quad (6.114)$$

where the expression for the characteristic gluon emission angle [768]  $\Theta \simeq (\hat{q}/\omega^3)^{1/4}$  has been used. The dead-cone suppression factor  $F_{\text{H/L}}$  in Eq. (6.114) increases (less suppression) as the heavy-quark energy  $E$  increases (the mass becomes negligible) and it decreases at large  $\omega$ , indicating that the high-energy part of the gluon radiation spectrum is drastically suppressed by the dead-cone effect.

A detailed calculation of the radiated-gluon energy distribution  $\omega dI/d\omega$  in the case of massive partons [769] confirms the qualitative feature of lower energy loss for heavy quarks, although the effect is found to be quantitatively smaller than that derived with the dead-cone approximation of Ref. [768]. A comparison of the results obtained in the two cases for the D meson suppression in central Pb–Pb collisions at the LHC can be found in Ref. [801]. Calculation results published in Ref. [802] and based on the BDMPS formalism (modified for

<sup>12</sup> A term  $(\Theta^2 + \Theta_0^2)^{-2}$  governs the angular dependence of the propagator of the gluon-radiation process  $Q \rightarrow Qg$ .

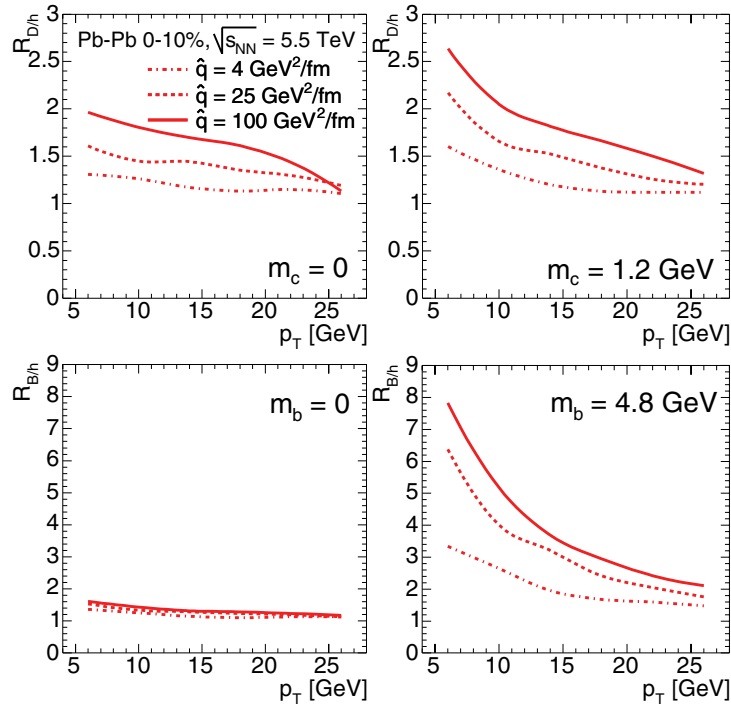


**Figure 6.260.** Heavy-to-light ratios, Eq. (6.115), for D mesons (upper plots) and B mesons (lower plots) for the case of a realistic heavy quark mass (plots on the right) and for a case study in which the quark-mass dependence of parton energy loss is neglected (plots on the left). From Ref. [802].

massive partons according to Ref. [769]) and on a Glauber-model description of the collision geometry, indicate the *heavy-to-light ratios* at the LHC as promising new observables to test the partonic mechanism expected to underlie jet quenching. The heavy-to-light ratios for D and B mesons,  $R_{D/h}$  and  $R_{B/h}$ , are defined as the ratio of the nuclear modification factors of the heavy-flavoured mesons to that of light-flavoured hadrons ( $h$ ):

$$R_{D(B)/h}(p_t) = R_{AA}^{D(B)}(p_t) / R_{AA}^h(p_t) = \frac{d^2 N_{AA}^{D(B)} / dp_t dy}{d^2 N_{pp}^{D(B)} / dp_t dy} \bigg/ \frac{d^2 N_{AA}^h / dp_t dy}{d^2 N_{pp}^h / dp_t dy}. \quad (6.115)$$

Heavy-to-light ratios are suggested to be sensitive to the colour-charge and to the mass dependence of medium-induced parton energy loss [802], as illustrated in Fig. 6.260 where  $R_{D/h}(p_t)$  and  $R_{B/h}(p_t)$  are shown, without and with the effect of the  $c$  and  $b$  masses, for the transport coefficient range  $\hat{q} = 25\text{--}100 \text{ GeV}^2/\text{fm}$ , expected for central Pb–Pb collisions at the LHC on the basis of the  $R_{AA}^h$  values measured at RHIC [340, 803] (the curves for the much lower value  $\hat{q} = 4 \text{ GeV}^2/\text{fm}$  are reported as well for comparison).

- For D mesons (see upper panels of Fig. 6.260 for  $m_c = 0, 1.2 \text{ GeV}$ ) the effect of the charm mass is expected to be small and limited to the range  $p_t < 10 \text{ GeV}/c$ , where initial-state effects, like shadowing, or final-state effects other than parton energy loss, like in-medium hadronisation, may prevent a clear analysis of heavy-to-light ratios. For higher transverse momentum ( $10 \lesssim p_t \lesssim 20 \text{ GeV}/c$ ), charm quarks would behave essentially like massless quarks. However, since at LHC energy light-flavoured hadron yields are dominated by gluon parents,  $R_{D/h}$  would be enhanced with respect to unity as a consequence of the larger

colour charge (reflected in the Casimir factor  $C_R$ ) of gluons relative to quarks. Therefore,  $R_{D/h}$  would be a sensitive probe of the colour-charge dependence of parton energy loss.

- For B mesons (see lower panels of Fig. 6.260 for  $m_b = 0, 4.8$  GeV), in contrast, the heavy-to-light ratio would be strongly enhanced due to the large b mass even in the range  $10 \lesssim p_t \lesssim 20$  GeV/c, thus providing a sensitive test of the mass dependence of parton energy loss.

These predictions for the heavy-flavour meson nuclear modification factors  $R_{AA}^{D,B}$ , published in Ref. [802], are taken as a reference to estimate the ALICE sensitivity to the quenching of charm particles. The results of this study are presented in Section 6.6.5.

#### 6.6.1.5. Azimuthal dependence of heavy-flavour production in nucleus–nucleus collisions.

The azimuthal anisotropy of particle production in non-central events is regarded as a powerful tool to study the early stage of nucleus–nucleus collisions (see Section 1.3.2 of PPR Volume I [3] and Section 6.4). The spatial anisotropy of the almond-shaped nuclear overlap region in the initial stage is expected to be transferred into momentum anisotropy in the final state. The azimuthal anisotropy is defined by

$$\frac{dN}{d\varphi} = N_0 \left\{ 1 + \sum_i 2v_i \cos(i(\varphi - \Psi_{R.P.})) \right\}, \quad (6.116)$$

where  $N_0$  is a normalization constant,  $\varphi$  is the azimuthal angle of particles, and  $\Psi_{R.P.}$  is the direction of the collision impact parameter (reaction plane) in a given event. The parameter  $v_2$ , the second harmonic coefficient of the Fourier expansion of the azimuthal distribution, is called elliptic flow and it is expected to be sensitive to the early pressure.

The  $p_t$  dependence of  $v_2$  has been measured for identified hadrons at RHIC up to  $p_t \simeq 4\text{--}6$  GeV/c [205, 362, 530, 536]. It is found that  $v_2$  scales as a function of  $p_t$  according to the number of constituent quarks, namely  $v_2/n$  as a function of  $p_t/n$  is universal, where  $n$  is the number of constituent quarks, i.e. 2 (3) for mesons (baryons). This scaling behaviour is consistent with the prediction of the quark coalescence model for hadronisation [304, 305, 575, 804], in which mesons (baryons) at intermediate  $2 \lesssim p_t \lesssim 5$  GeV/c would be formed by coalescence of 2 (3) quarks or antiquarks from the partonic medium that are close in phase-space (velocity), rather than by parton fragmentation. The  $n$ -scaling of  $v_2$  suggests that elliptic flow develops in the partonic phase for hadrons made of light quarks.

A non-zero  $v_2$  also for heavy quarks would support partonic level thermalisation and very high density at the early stage of the collision. A recent measurement of the  $v_2$  of electrons from heavy-flavour (mainly charm) decays by the PHENIX Collaboration [805], that we will further discuss in Section 6.6.2, and preliminary measurements by the STAR Collaboration [806], compared to theoretical predictions [807], favour a scenario in which the charm quark has a similar  $v_2$  to lighter quarks. At the LHC, the large cross section for heavy-quark production will allow the direct measurement of charm and beauty mesons  $v_2$ , not only in the intermediate  $p_t$  region up to 8–10 GeV/c, where the parton coalescence mechanism is expected to be relevant, but possibly also at higher momenta, where hadronisation should take place via fragmentation out of the medium. The high- $p_t$  hard partons (or heavy quarks) should not thermalize in the medium and, thus, they should not acquire the large elliptic flow induced by collective pressure effects. Their azimuthal anisotropy in non-central collisions should instead be mainly determined by the path-length dependence of QCD energy loss in the geometrically-asymmetric dense medium.

In summary, depending on the considered momentum range, the measurement of the D and B mesons azimuthal anisotropy  $v_2$  probes (a) the degree of thermalisation of charm and

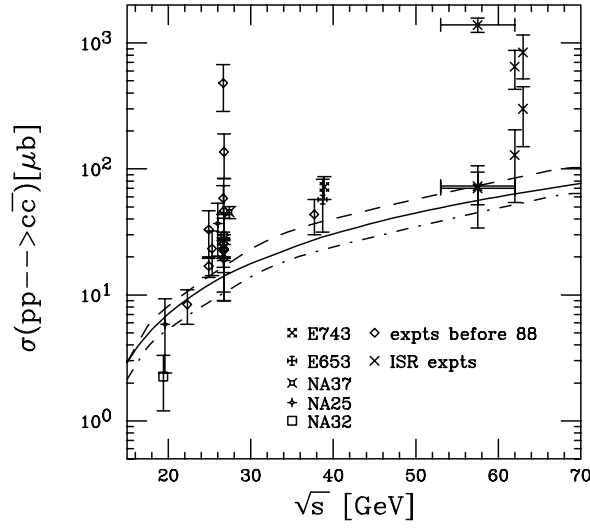


**Figure 6.261.** Total charm production cross section from pp and pA measurements compared to NLO calculations [808] using MRSD- (solid), MRST HO (dashed) and MRST LO (dot-dashed) parton distributions.

beauty quarks in the expanding medium, at low and intermediate momenta ( $\lesssim 10 \text{ GeV}/c$ ); (b) the in-medium path-length dependence of heavy-quark energy loss in the almond-shaped partonic system, at higher momenta ( $\gtrsim 10 \text{ GeV}/c$ ).

## 6.6.2. Current experimental results on heavy-quark hadroproduction

**6.6.2.1. Proton–proton and proton–nucleus collisions.** The existing data on the total charm production cross section in pp and pA collisions up to ISR energies,  $\sqrt{s} \simeq 63 \text{ GeV}$ , are roughly reproduced by NLO pQCD calculation results (scaled by the number of binary nucleon–nucleon collisions, in the pA case). This is illustrated in Fig. 6.261, where the data, normalized to one binary collision, are compared [808] to theoretical results obtained with the HVQMNR program by Mangano, Nason and Ridolfi [809], using the following values for the heavy-quark masses ( $m_c, m_b$ ) and for the factorisation and renormalisation scales ( $\mu_F, \mu_R$ ):

$$m_c = 1.2 \text{ GeV} \quad \mu_F = \mu_R = 2 \mu_0 \quad \text{for charm,} \quad (6.117)$$

$$m_b = 4.75 \text{ GeV} \quad \mu_F = \mu_R = \mu_0 \quad \text{for beauty,} \quad (6.118)$$

where  $\mu_0 \equiv \sqrt{(p_{t,Q}^2 + p_{t,\bar{Q}}^2)/2 + m_Q^2}$  is approximately equal to the transverse mass of the produced heavy quarks. For the estimation of the baseline  $Q\bar{Q}$  production cross sections and single-inclusive  $p_t$  distributions in pp collisions at LHC energies, we use the HVQMNR program with these parameter values (see Section 6.6.3).

For RHIC (pp and dAu at  $\sqrt{s_{NN}} = 200 \text{ GeV}$ ) and for the Tevatron ( $p\bar{p}$  at  $\sqrt{s} = 1.96 \text{ TeV}$ ), the best description of the  $p_t$ -differential cross sections has been obtained within the FONLL (fixed order next-to-leading log) theoretical framework [810], which coincides with the fixed order (NLO) HVQMNR calculation in the low- $p_t$  region while being more accurate at high

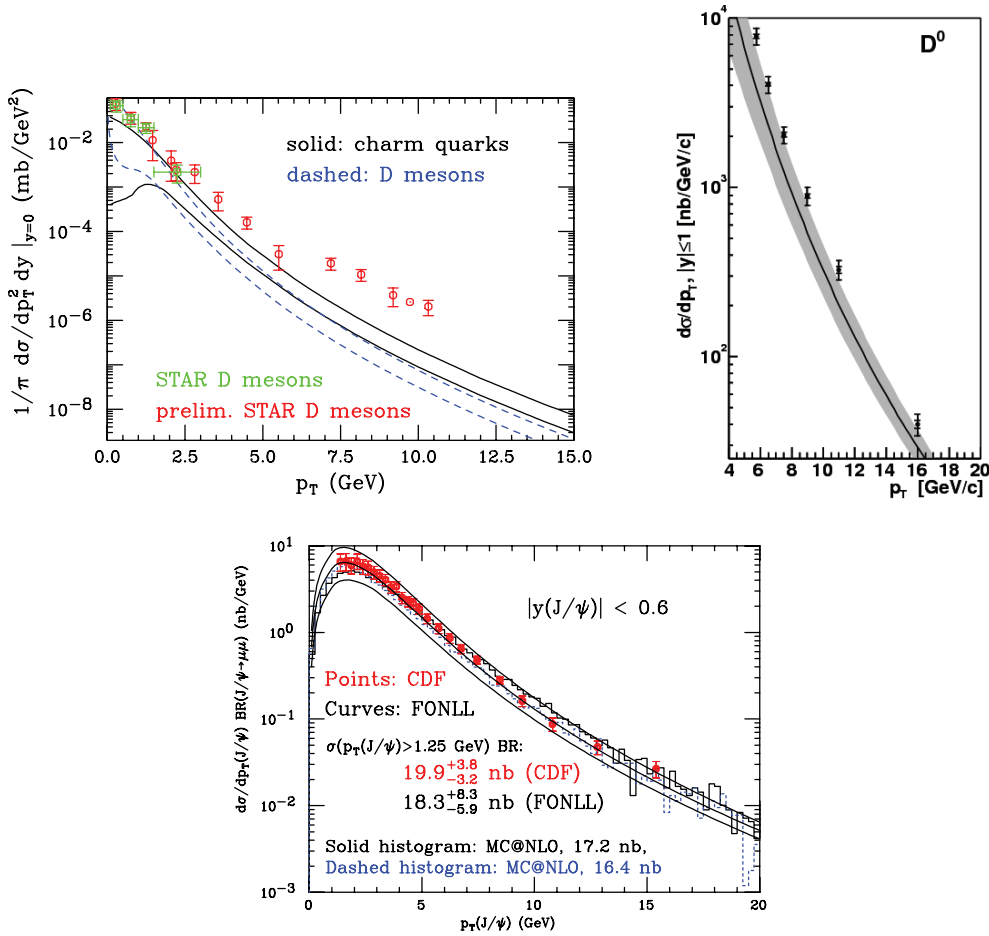


**Figure 6.262.** D-meson production measurements from the STAR experiment in dAu collisions at  $\sqrt{s_{NN}} = 200$  GeV [811, 812] (top left) and from the CDF experiment in  $p\bar{p}$  collisions at  $\sqrt{s} = 1.96$  TeV [815] (top right) compared to FONLL calculations [813, 815]. Beauty production measurements from the CDF experiment ( $p\bar{p}$  at  $\sqrt{s} = 1.96$  TeV) [810] compared to FONLL and MC@NLO [816] calculations (bottom).

$p_t$  where terms beyond next-to-leading order are partially accounted for in a next-to-leading-log resummation. Charm production is slightly underpredicted by the theory at both c.m.s. energies, as shown by the comparison of D meson  $p_t$ -differential cross sections at RHIC [811, 812]<sup>13</sup> and Tevatron [815] to FONLL predictions in Fig. 6.262 (upper panels) [813, 815]. In contrast, beauty production at the Tevatron is fairly well described by the calculation results (see comparison for the  $p_t$  distribution of  $J/\psi$  from B decays in the lower panel of Fig. 6.262 [810]).

**6.6.2.2. Heavy-ion collisions.** The currently available data on open charm production in ultra-relativistic nucleus–nucleus collisions do not allow us to draw firm conclusions yet. At SPS energy,  $\sqrt{s_{NN}} = 17.3$  GeV, the dimuon enhancement in the invariant-mass region

<sup>13</sup> Similar results are found for the comparison [813] to data on single electrons from heavy-flavour decays in pp collisions at RHIC [811, 812, 814].

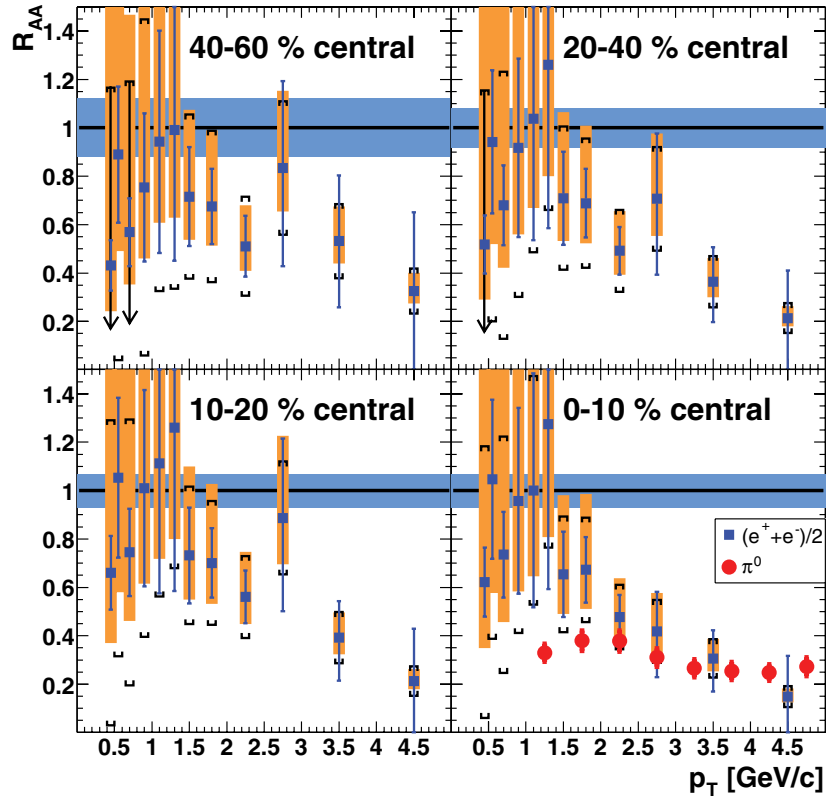


**Figure 6.263.** Heavy-quark decay electron nuclear modification factor  $R_{AA}$  in different Au–Au centrality classes at  $\sqrt{s_{NN}} = 200$  GeV, as measured by the PHENIX Collaboration [821]. The point-by-point shaded error bars represent the systematic uncertainties coming from the pp normalization.

between 1 and 3 GeV, measured by the NA50 experiment [817] in central Pb–Pb collisions, was suggested as a possible indication for enhanced open charm production. However, preliminary data from the NA60 experiment [818], which is equipped with silicon-pixel vertex detectors, do confirm the observation of a dimuon excess, but seem to rule out charm enhancement as the origin of the excess [819]. At RHIC energy,  $\sqrt{s_{NN}} = 200$  GeV, single electrons from heavy-flavour decays (mainly D and B mesons) are found to have a large suppression for  $p_T \gtrsim 2$  GeV/c in Au–Au relative to binary-scaled pp collisions (PHENIX [820, 821] and STAR preliminary [327]). The nuclear modification factor values are similar to those measured for light-flavour hadrons, and comparison with theory calculations will clarify whether such a large suppression can be reconciled with the prediction of smaller energy loss of massive partons. The PHENIX and STAR Collaborations have as well measured the azimuthal anisotropy of heavy-flavour electrons [805, 806]. In the following, we shortly describe the  $R_{AA}$  and  $v_2$  measurements that have been published by PHENIX [805, 821].

The PHENIX experiment at RHIC obtained an indirect estimate of heavy-flavour production in pp and Au–Au collisions at  $\sqrt{s_{NN}} = 200$  GeV from the measurement of single electrons at central rapidity ( $|\eta| < 0.35$ ) [820]. The expected sources of electrons are (1) Dalitz and dielectron decays of light mesons, (2) photon conversions, (3) kaon semi-electronic decays, and (4) semi-electronic decays of D mesons (and of B mesons for electron

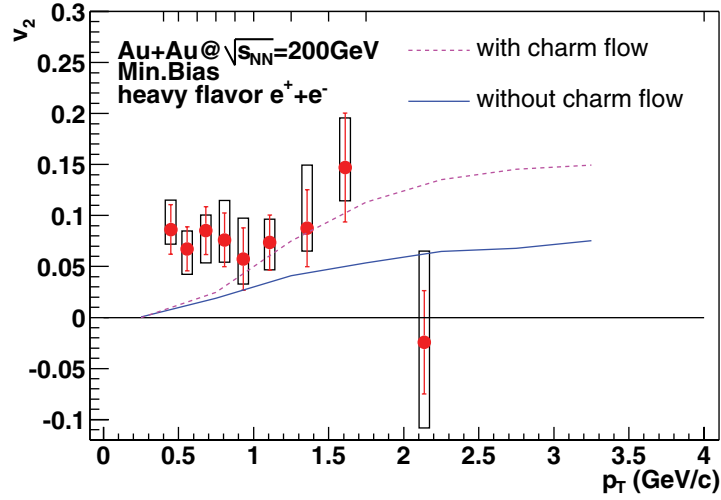


**Figure 6.264.** The elliptic flow coefficient  $v_2$  for electrons from heavy-flavour decays measured by PHENIX in Au–Au collisions at  $\sqrt{s_{NN}} = 200$  GeV [805], compared to theoretical calculations from Ref. [807].

$p_t \gtrsim 4$  GeV/c [813]). Contributions (1) and (3) were estimated using a simulation tuned to reproduce the  $\pi^\pm$  and  $\pi^0$  measurements by PHENIX and subtracted. The contribution of photon conversions (2) was directly estimated in a special run with an additional converter layer and subtracted. In central Au–Au collisions at RHIC, high- $p_t$  hadrons are observed to be significantly suppressed relative to binary scaling from pp collisions ( $R_{AA} \simeq 0.2$ – $0.3$  for  $p_t \gtrsim 5$  GeV/c) [340, 803]. A similarly-large suppression has recently been measured by the PHENIX Collaboration also in the  $R_{AA}$  of single electrons from heavy-quark decays for  $p_t \gtrsim 2$  GeV/c, as shown in Fig. 6.263 from Ref. [821] (similar results have been reported by the STAR Collaboration [327]). Theoretical calculations of in-medium energy loss predict comparable  $R_{AA}$  suppression for high- $p_t$  charm-decay electrons and for light-flavoured hadrons (see Section 6.6.1.4). However, the perturbative QCD calculations implemented in FONLL predict beauty decays to contribute significantly to the heavy-flavour electron spectrum at RHIC energy for  $p_t \gtrsim 4$  GeV/c [813]. When this beauty component is included, the calculated electron  $R_{AA}$  values become larger [822, 823], but still compatible with data within the experimental and theoretical uncertainties. In particular, the relative importance of the charm and beauty components has a significant perturbative uncertainty, which could be removed by a precise direct measurement of the D meson  $p_t$ -differential production cross section at RHIC.

The PHENIX experiment has measured the elliptic flow coefficient  $v_2$  (see Section 6.6.1.5) of electrons from heavy-flavour decays in minimum-bias Au–Au collisions at  $\sqrt{s_{NN}} = 200$  GeV [805]. The measurement is obtained by subtracting, from the inclusive electron  $v_2$ , the  $v_2$  of electrons from non-heavy-flavour sources, such as photon conversions and Dalitz decays of light neutral mesons. In the covered range  $0.4 < p_t < 2$  GeV/c, the heavy-flavour electron  $v_2$  is found to be non-zero with a 90% confidence level. The data are compared to results of two model calculations [807], in the framework of hadronisation via coalescence, that assume different scenarios: either no reinteraction of the initially produced charm quarks (in this case  $v_{2,c} = 0$  and the  $v_2$  of the D meson is only due to that of the u or d quark it contains) or complete thermalisation with the bulk matter ( $v_{2,c} \approx v_{2,u,d}$  and

**Table 6.50.** NLO calculation [809] for the total  $c\bar{c}$  and  $b\bar{b}$  cross sections in pp collisions at 5.5, 8.8 and 14 TeV, using the MRST HO and CTEQ 5M1 parton distribution functions.

$\sqrt{s}$	$\sigma_{pp}^{c\bar{c}}[\text{mb}]$			$\sigma_{pp}^{b\bar{b}}[\text{mb}]$		
	5.5 TeV	8.8 TeV	14 TeV	5.5 TeV	8.8 TeV	14 TeV
MRST HO	5.9	8.2	10.3	0.19	0.28	0.46
CTEQ 5M1	7.4	9.4	12.1	0.22	0.31	0.55
Average	6.6	8.8	11.2	0.21	0.30	0.51

$v_{2,D} \approx v_{2,c} + v_{2,u,d}$ ). Both of these calculations are consistent, within errors, with the measured heavy-flavour electron  $v_2$ . Preliminary results [806] from the STAR experiment reaching up to  $p_t \simeq 3 \text{ GeV}/c$  favour the scenario of  $v_{2,c} \approx v_{2,u,d}$  (upper curve in Fig. 6.264). Higher statistics data that will be available in the near future are expected to allow an unambiguous statement on this issue.

**6.6.3. Charm and beauty production at the LHC.** In Section 6.6.3.1 we report the most recent results (and the uncertainties) of the next-to-leading order pQCD calculations for the cross sections in proton–proton collisions at LHC energies. These results are extrapolated to Pb–Pb and pPb collisions in Section 6.6.3.2, taking into account the predicted nuclear modification of the parton distribution functions. The heavy-quark kinematic distributions as predicted by NLO pQCD are reported in Section 6.6.3.3. We tuned the PYTHIA event generator in order to reproduce such results for the c and b single-inclusive transverse momentum distributions (Section 6.6.3.4). Finally, we report the expected yields and transverse momentum distributions for D and B mesons (Section 6.6.3.5).

**6.6.3.1. Cross sections in nucleon–nucleon collisions.** The results for LHC energies ( $\sqrt{s} = 5.5, 8.8$  and 14 TeV) are reported in Table 6.50. These values are obtained using the NLO pQCD calculation implemented in the HVQMNR program [809] with the two sets of parton distribution functions MRST HO [824] and CTEQ 5M1 [825]. The difference due to the choice of the parton distribution functions is relatively small ( $\simeq 20\text{--}25\%$ ). We chose to use as a baseline the average, also reported in Table 6.50, of the values obtained with these two sets of PDFs.

The dependence on the PDF set represents only a part of the uncertainty on the theoretical estimate. Using as a guideline the prescription described in Ref. [813], we performed an evaluation of the theoretical uncertainties on the single-inclusive  $p_t$ -differential cross sections for c and b quarks by varying the  $m_c$  ( $m_b$ ),  $\mu_F$  and  $\mu_R$  parameters in the ranges  $1.3 < m_c < 1.7 \text{ GeV}$ ,  $4.5 < m_b < 5.0 \text{ GeV}$ ,  $0.5 < \mu_F/\mu_0 < 2$  and  $0.5 < \mu_R/\mu_0 < 2$ , with  $\mu_0 \simeq m_{t,Q}$  as defined in Section 6.6.2.1<sup>14</sup>. The two scales  $\mu_F$  and  $\mu_R$  are varied independently with the constraint  $0.5 < \mu_F/\mu_R < 2$ . The uncertainty bands shown in Fig. 6.265 are the envelope of the resulting cross sections. The contribution due to the mass uncertainty, shown separately, is significantly smaller than that due to the variation of the scales. The total uncertainties span an approximately  $p_t$ -independent factor of about 2–3 for  $p_t \gtrsim 5 \text{ GeV}/c$ , while they become larger at lower transverse momenta where the scales,  $\mu_F$  and  $\mu_R$ , and the momentum fractions,  $x_1$  and  $x_2$ , are small and the scale-dependence of the PDFs is large.

<sup>14</sup> We use central parameter values as in Ref. [813], namely  $m_c = 1.5 \text{ GeV}$ ,  $m_b = 4.75 \text{ GeV}$  and  $\mu_F = \mu_R = \mu_0$ . Note that, for charm, they are slightly different with respect to those we use to define our baseline cross section (see Eq. (6.117)).

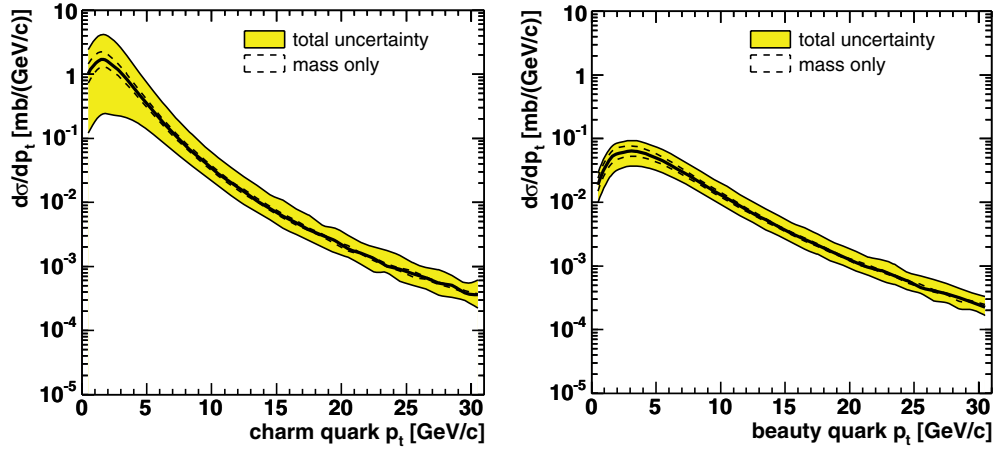


**Figure 6.265.** Evaluation of the theoretical uncertainty on the single-inclusive c and b quark  $p_t$ -differential cross sections at  $\sqrt{s} = 14$  TeV. Calculations are performed using the HVQMNR program [809]. No rapidity selection is applied.

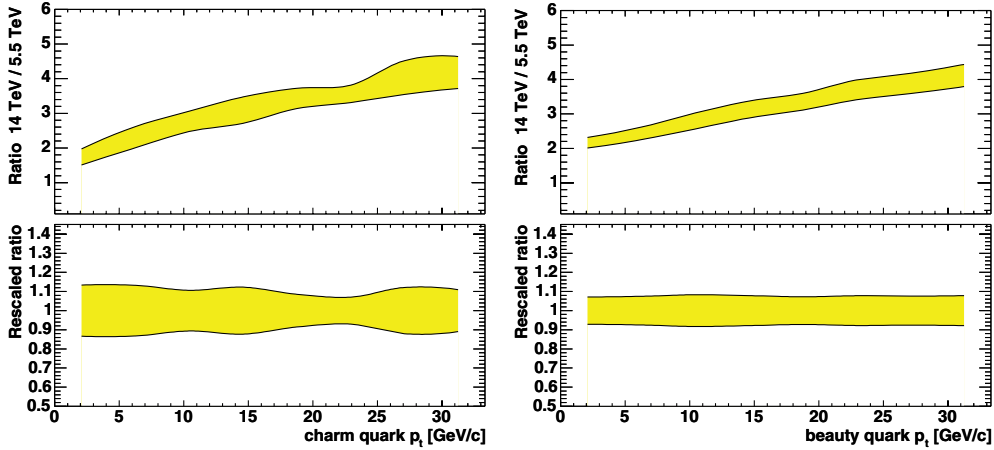


**Figure 6.266.** The theoretical uncertainty on the ratio of single-inclusive heavy-quark  $p_t$ -differential cross sections at  $\sqrt{s} = 14$  TeV and at  $\sqrt{s} = 5.5$  TeV (upper panels, charm on the left and beauty on the right). In the lower panels, the same band is normalized to unity, i.e. divided by its central value, in order to quantify its relative width. Calculations are performed using the HVQMNR program [809]. No rapidity selection is applied. The oscillations observed for charm are caused by statistical fluctuations in the calculation results.

Figure 6.266 shows the corresponding theoretical uncertainty band for the ratio of the single-inclusive heavy-quark cross sections at  $\sqrt{s} = 14$  TeV and  $\sqrt{s} = 5.5$  TeV. Despite the large spread in the absolute cross sections at a given energy, the ratio is much less dependent on the choice of the parameters. In particular, we observe no dependence at all on the value of the heavy-quark mass  $m_Q$  and on the value of the renormalisation scale  $\mu_R$ . The uncertainty on the ratio is solely determined by the variation of the factorisation scale  $\mu_F$ ; this is due to the fact that, for the same heavy-quark  $p_t$ , different Bjorken  $x$  ranges are probed at 5.5 and at 14 TeV, and changing the factorisation scale affects the  $x$  dependence

of the PDFs. These results indicate that a pQCD-based extrapolation can be used to compare the cross sections measured in Pb–Pb collisions at  $\sqrt{s_{\text{NN}}} = 5.5$  TeV with those measured in pPb at  $\sqrt{s_{\text{NN}}} = 8.8$  TeV and in pp at  $\sqrt{s} = 14$  TeV. The systematic error introduced by the extrapolation is of about 12% for charm and 8% for beauty, as shown in the lower panels of Fig. 6.266.

*Yields in proton–proton collisions at  $\sqrt{s} = 14$  TeV.* Using the proton–proton inelastic cross section  $\sigma_{\text{pp}}^{\text{inel}} = 70$  mb at 14 TeV [3] and the average heavy-flavour cross sections in the last row of Table 6.50, we calculate the yields for the production of  $Q\bar{Q}$  pairs as

$$N_{\text{pp}}^{Q\bar{Q}} = \sigma_{\text{pp}}^{Q\bar{Q}} / \sigma_{\text{pp}}^{\text{inel}}. \quad (6.119)$$

We obtain the central values of 0.16  $c\bar{c}$  pairs and 0.0072  $b\bar{b}$  pairs per event.

*6.6.3.2. Extrapolation to heavy-ion collisions.* In this section we derive the extrapolation of the cross sections and yields to central Pb–Pb collisions and to pPb collisions.

*Nucleus–nucleus collisions.* If no nuclear effects are taken into account, a nucleus–nucleus collision can be considered, for hard processes, as a superposition of *independent* nucleon–nucleon (NN) collisions. Thus, the cross section for such processes in heavy-ion collisions can be calculated using a simple geometrical extrapolation from pp collisions, i.e. assuming that the hard cross section scales from pp to nucleus–nucleus collisions proportionally to the number of inelastic nucleon–nucleon collisions (binary scaling).

Nuclear effects—such as nuclear shadowing, broadening of the parton intrinsic transverse momentum ( $k_t$ ) in the nucleon, in-medium parton energy loss, as well as possible enhancements due to additional production in the medium—can modify this geometrical scaling from pp to nucleus–nucleus collisions. Such effects are, indeed, what we want to measure. We chose to include in the simulation only nuclear shadowing and broadening of the intrinsic  $k_t$ , since they are well established effects. While the broadening of the intrinsic  $k_t$  affects only the kinematic distributions of the produced heavy quarks, shadowing modifies also the total hard cross section. Nuclear shadowing can be accounted for by recalculating the hard cross section in elementary nucleon–nucleon collisions with nuclear-modified parton distribution functions and extrapolating to the nucleus–nucleus case.

In the following, the extrapolation, based on the Glauber model [766, 767], is derived in the general case of the collision of two nuclei with mass numbers  $A$  and  $B$ , and numerical examples are given for the specific case of Pb–Pb reactions at  $\sqrt{s_{\text{NN}}} = 5.5$  TeV.

We are interested in the cross section for a set of events in a given centrality range, defined by the trigger settings. The centrality selection is assumed to correspond to a cut on the impact parameter  $b$  of the collision:  $0 \leq b < b_c$ . The sample of events defined by this cut contains a fraction of the total number of inelastic collisions, i.e. of the total inelastic cross section, given by

$$F(b_c) = \int_0^{b_c} db \frac{d\sigma_{\text{AB}}^{\text{inel}}}{db} / \int_0^{\infty} db \frac{d\sigma_{\text{AB}}^{\text{inel}}}{db}. \quad (6.120)$$

The definition of the centrality in terms of integrated inelastic cross section is more appropriate, since the cross section is directly measured, while the estimate of the impact parameter depends on the model used to describe the geometry of the collision.

In the following, we consider two options for the centrality selection, corresponding to 5% and 10% of the total inelastic cross section. The values of  $b_c$  that give these selections are 3.5 fm and 5 fm, respectively.

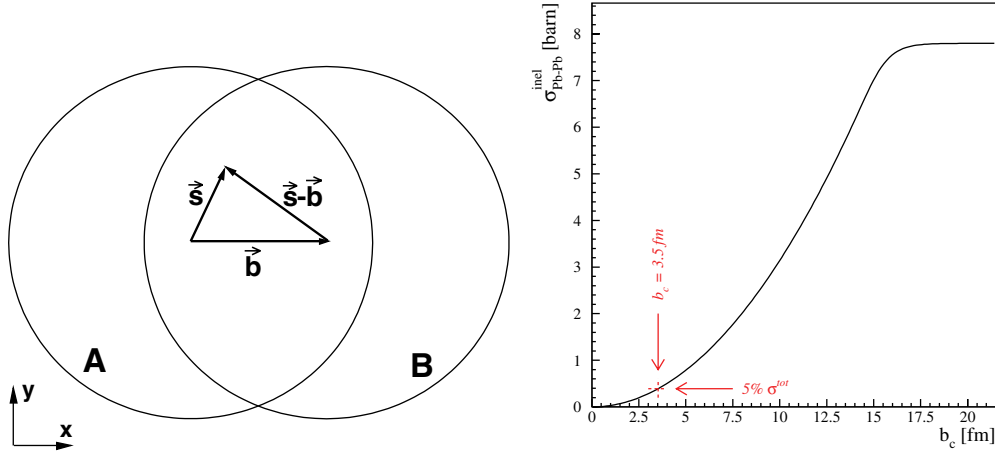


**Figure 6.267.** Left: collision geometry in the plane transverse to the beam line. Right: inelastic Pb–Pb cross section as a function of the impact parameter cut  $b < b_c$ ; for clarity, here and in Fig. 6.268, only the value corresponding to 5% of the total inelastic cross section is explicitly indicated.

The inelastic cross section corresponding to a given centrality selection is found by integrating the interaction probability up to impact parameter  $b_c$ :

$$\sigma_{AB}^{\text{inel}}(b_c) = \int_0^{b_c} db \frac{d\sigma_{AB}^{\text{inel}}}{db} = 2\pi \int_0^{b_c} b db \{1 - [1 - \sigma_{NN} T_{AB}(b)]^{AB}\}. \quad (6.121)$$

For the numerical examples, we used the value  $\sigma_{NN} = 60$  mb for the nucleon–nucleon inelastic cross section at 5.5 TeV [409]. The total thickness function  $T_{AB}$

$$T_{AB}(b) = \int d^2s T_A(\vec{s}) T_B(\vec{s} - \vec{b}) \quad (6.122)$$

(vectors defined as in Fig. 6.267, left) is expressed in terms of the thickness function of the nucleus  $T_i(\vec{s}) = \int dz \rho_i(z, \vec{s})$  for  $i = A, B$ , where  $\rho_i$  is the Woods–Saxon nuclear density profile [128]—the thickness function is normalized to unity:  $\int d^2s T_i(\vec{s}) = 1$ . In Fig. 6.267 (right) the inelastic cross section (6.121) is shown as a function of  $b_c$ .

The average number of inelastic collisions for a given impact parameter  $b$  is

$$\sigma_{NN} \cdot AB T_{AB}(b). \quad (6.123)$$

By replacing the inelastic nucleon–nucleon cross section  $\sigma_{NN}$  with the elementary cross section for a given hard process  $\sigma_{NN}^{\text{hard}}$ , we obtain the average number of inelastic collisions that yield the considered hard process:

$$\sigma_{NN}^{\text{hard}} \cdot AB T_{AB}(b), \quad (6.124)$$

and the cross section for hard processes for  $0 \leq b < b_c$ :

$$\sigma_{AB}^{\text{hard}}(b_c) = \sigma_{NN}^{\text{hard}} \cdot 2\pi \int_0^{b_c} b db AB T_{AB}(b). \quad (6.125)$$

For minimum-bias collisions ( $b_c = +\infty$ ), we have

$$\sigma_{AB}^{\text{hard}} = \sigma_{NN}^{\text{hard}} AB. \quad (6.126)$$

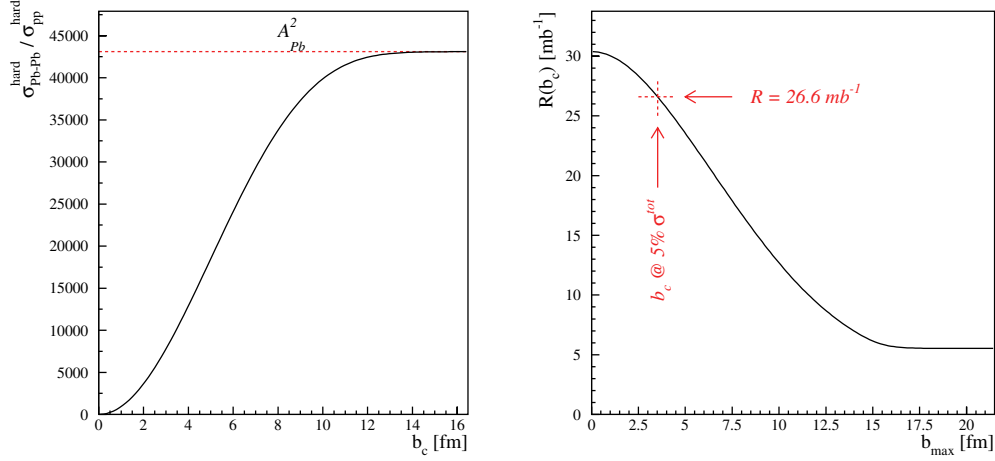


**Figure 6.268.** Left: cross section for a hard process in Pb–Pb collisions relative to that in nucleon–nucleon collisions as a function of the impact parameter cut  $b < b_c$ . Right: yield of the hard process in Pb–Pb collisions relative to that in nucleon–nucleon collisions as a function of the impact parameter cut  $b < b_c$  (right).

The ratio of the hard cross section in nucleus–nucleus collisions, with a centrality cut  $b < b_c$ , relative to the cross section in nucleon–nucleon interactions is (see Fig. 6.268, left)

$$f^{\text{hard}}(b_c) = \frac{\sigma_{\text{AB}}^{\text{hard}}(b_c)}{\sigma_{\text{NN}}^{\text{hard}}} = 2\pi \int_0^{b_c} b db \text{AB} T_{\text{AB}}(b). \quad (6.127)$$

The number (yield) of hard processes per triggered event is

$$N_{\text{AB}}^{\text{hard}}(b_c) = \frac{\sigma_{\text{AB}}^{\text{hard}}(b_c)}{\sigma_{\text{AB}}^{\text{inel}}(b_c)} = \mathcal{R}(b_c) \cdot \sigma_{\text{NN}}^{\text{hard}} \quad (6.128)$$

where (Fig. 6.268, right)

$$\mathcal{R}(b_c) = \frac{\int_0^{b_c} b db \text{AB} T_{\text{AB}}(b)}{\int_0^{b_c} b db \{1 - [1 - \sigma_{\text{NN}} T_{\text{AB}}(b)]^{\text{AB}}\}}. \quad (6.129)$$

For a 5% (10%) centrality cut in Pb–Pb collisions, the yield  $N_{\text{AB}}^{\text{hard}}$  is obtained by multiplying the elementary cross sections by 26.6 (23.7)  $\text{mb}^{-1}$ .

*Cross sections and yields in Pb–Pb collisions at  $\sqrt{s_{\text{NN}}} = 5.5$  TeV.* We used the EKS98 parametrisation [779] of nuclear shadowing (see Section 6.6.1.3). The shadowing factor  $R_g^{\text{Pb}}$  for gluons in a  $^{208}\text{Pb}$  nucleus has been shown in the central panel of Fig. 6.259. The centrality dependence of the shadowing is weak for collisions in the considered centrality range (up to 10% of  $\sigma^{\text{inel}}$ ) [826] and is neglected here. The reduction of the cross section due to shadowing amounts to about 35% for  $c\bar{c}$  pairs and to about 15% for  $b\bar{b}$  pairs (as seen in Section 6.6.1.1, beauty production corresponds to larger values of  $x$ , less affected by the shadowing suppression). In Section 6.6.3.3 we will discuss how nuclear shadowing is expected to modify the heavy-quark kinematical distributions.

**Table 6.51.** Total cross sections and yields for charm and beauty production in NN and Pb–Pb collisions at  $\sqrt{s_{\text{NN}}} = 5.5$  TeV. The effect of shadowing is shown as the ratio  $C_{\text{shad}}$  of the cross section calculated with and without the modification of the parton distribution functions. For the Pb–Pb case we report results for two centrality ranges: 5% and 10% of the total inelastic cross section.

		Charm	Beauty
$\sigma_{\text{NN}}^{Q\bar{Q}}$ [mb]	w/o shadowing	6.64	0.21
	w/shadowing	4.32	0.18
$C_{\text{shad}}$		0.65	0.84
$\sigma_{\text{Pb–Pb}}^{Q\bar{Q}}$ [b]	5% $\sigma^{\text{inel}}$	45.0	1.79
	10% $\sigma^{\text{inel}}$	81.0	3.38
$N_{\text{Pb–Pb}}^{Q\bar{Q}}$	5% $\sigma^{\text{inel}}$	115	4.56
	10% $\sigma^{\text{inel}}$	102	4.06

Table 6.51 reports the charm and beauty total cross sections and yields per NN collision (with and without shadowing) at  $\sqrt{s_{\text{NN}}} = 5.5$  TeV, as calculated with the HVQMNR program, and the extrapolated values for Pb–Pb collisions. The values shown correspond to the average of the results obtained with MRST HO and CTEQ 5M1 parton distribution functions. For the Pb–Pb case we used two centrality ranges: 5% and 10% of the total inelastic cross section. The ratio  $N_{\text{Pb–Pb}}^{Q\bar{Q}}(5\%\sigma^{\text{inel}})/N_{\text{Pb–Pb}}^{Q\bar{Q}}(10\%\sigma^{\text{inel}})$  is about 1.12.

*Proton–nucleus collisions.* For the extrapolation to proton–nucleus collisions we use the same method described for the case of nucleus–nucleus collisions. We consider minimum-bias collisions (with no centrality selection<sup>15</sup>), and we use  $B = 1$  and  $T_B(\vec{s}) = \delta(\vec{s})$  for the proton, assumed to be point-like. The total cross section for hard processes (6.125) becomes

$$\sigma_{\text{pA}}^{\text{hard}} = \sigma_{\text{NN}}^{\text{hard}} \cdot 2\pi \int_0^\infty b db A T_A(b) = A \sigma_{\text{NN}}^{\text{hard}}. \quad (6.130)$$

The number of hard processes per minimum-bias pA collision is

$$N_{\text{pA}}^{\text{hard}} = A \sigma_{\text{NN}}^{\text{hard}} / \sigma_{\text{pA}}^{\text{inel}}. \quad (6.131)$$

*Cross sections and yields in pPb collisions at  $\sqrt{s_{\text{NN}}} = 8.8$  TeV.* Using  $A = 208$  and  $\sigma_{\text{pPb}}^{\text{inel}} = 1.9$  barn [3], the yield of  $Q\bar{Q}$  pairs per minimum-bias collision is

$$N_{\text{pPb}}^{Q\bar{Q}} = \sigma_{\text{NN}}^{Q\bar{Q}} \cdot 0.109 \text{ mb}^{-1}. \quad (6.132)$$

As for the Pb–Pb case, the effect of nuclear shadowing was accounted for by using the EKS98 parametrisation [779]. Clearly, the effect is lower for pPb, since one of the colliding nuclei is a proton: the reduction of the cross sections due to nuclear shadowing is about 20% for charm and about 10% for beauty. The cross sections and yields for charm and beauty production in NN (with and without shadowing) and minimum-bias pPb collisions at

<sup>15</sup> It has recently been shown that the sample of minimum-bias pPb collisions can be subdivided in at least three centrality classes using the ALICE Zero Degree Calorimeter (Section 6.1.6). However, for the estimate of the heavy-quark production yields, as well as for the open charm detection performance study presented in Section 6.6.4.6, we considered minimum-bias pPb collisions.

**Table 6.52.** Total cross sections and yields for charm and beauty production in NN and pPb collisions at  $\sqrt{s_{\text{NN}}} = 8.8$  TeV. The effect of shadowing is shown as the ratio  $C_{\text{shad}}$  of the cross section calculated with and without the modification of the parton distribution functions.

		Charm	Beauty
$\sigma_{\text{NN}}^{Q\bar{Q}}$ [mb]	w/o shadowing	8.80	0.30
	w/ shadowing	7.16	0.27
$C_{\text{shad}}$		0.80	0.90
$\sigma_{\text{pPb}}^{Q\bar{Q}}$ [b]		1.49	0.056
$N_{\text{pPb}}^{Q\bar{Q}}$		0.78	0.029

**Table 6.53.** Summary table of the production yields and of the average magnitude of nuclear shadowing in pp, pPb, and Pb–Pb collisions.

System Centrality $\sqrt{s_{\text{NN}}}$	Charm			Beauty		
	pp	pPb	Pb–Pb	pp	pPb	Pb–Pb
	min.-bias 14 TeV	min.-bias 8.8 TeV	centr. (5%) 5.5 TeV	min.-bias 14 TeV	min.-bias 8.8 TeV	centr. (5%) 5.5 TeV
$N^{Q\bar{Q}}$	0.16	0.78	115	0.0072	0.029	4.56
$C_{\text{shad}}$	1	0.80	0.65	1	0.90	0.84

$\sqrt{s_{\text{NN}}} = 8.8$  TeV are reported in Table 6.52. The values shown correspond to the average of the results obtained with the MRST HO and CTEQ 5M1 parton distribution functions.

A summary of the production yields and of the average magnitude of nuclear shadowing in the three considered colliding systems is presented in Table 6.53.

**6.6.3.3. Heavy-quark kinematical distributions.** Figures 6.269 and 6.270 present the transverse momentum and rapidity distributions, obtained using the NLO pQCD program HVQMNR, for c and b quarks, respectively. The distributions for Pb–Pb and pPb are normalized to the cross section per nucleon–nucleon collision.

We used the CTEQ 4M [827] set of PDFs. We verified that the results given by this set lie in between the ones obtained with the more recent CTEQ 5 and MRST sets for all the relevant kinematical quantities [828]. For the other parameters the values specified in Section 6.6.3.1 were used:  $m_c = 1.2$  GeV,  $\mu_R = \mu_F = 2\mu_0$  for charm and  $m_b = 4.75$  GeV,  $\mu_R = \mu_F = \mu_0$  for beauty. Nuclear shadowing is included via the EKS98 parametrisation [779]. The parton intrinsic  $k_t$  is sampled from a Gaussian distribution with mean 0 and  $\sigma (= \sqrt{\langle k_t^2 \rangle})$  equal to 1, 1.16, 1.30 GeV/c for charm production in pp, pPb and Pb–Pb, respectively, and equal to 1, 1.60, 2.04 GeV/c for beauty production in pp, pPb and Pb–Pb, respectively. These values are taken from Ref. [808]. The same parameters are used also in the calculations shown in the next section. In the case of pPb events the rapidity distribution in the centre-of-mass frame is plotted; the rapidity distribution in the laboratory frame would be shifted by  $\Delta y = 0.47$ .

The comparison of the  $p_t$  distributions for pp and Pb–Pb (and for pp and pPb) at the same centre-of-mass energy shows that nuclear shadowing affects heavy-quark production only for relatively low transverse momenta ( $p_t < 5\text{--}6$  GeV/c with EKS98), where the  $Q\bar{Q}$  pairs are produced by low- $x$  gluons. This is clearly seen in the ratios of the distributions, reported in the insets. The value for the upper limit,  $\approx 5$  GeV/c, of the  $p_t$ -region affected by

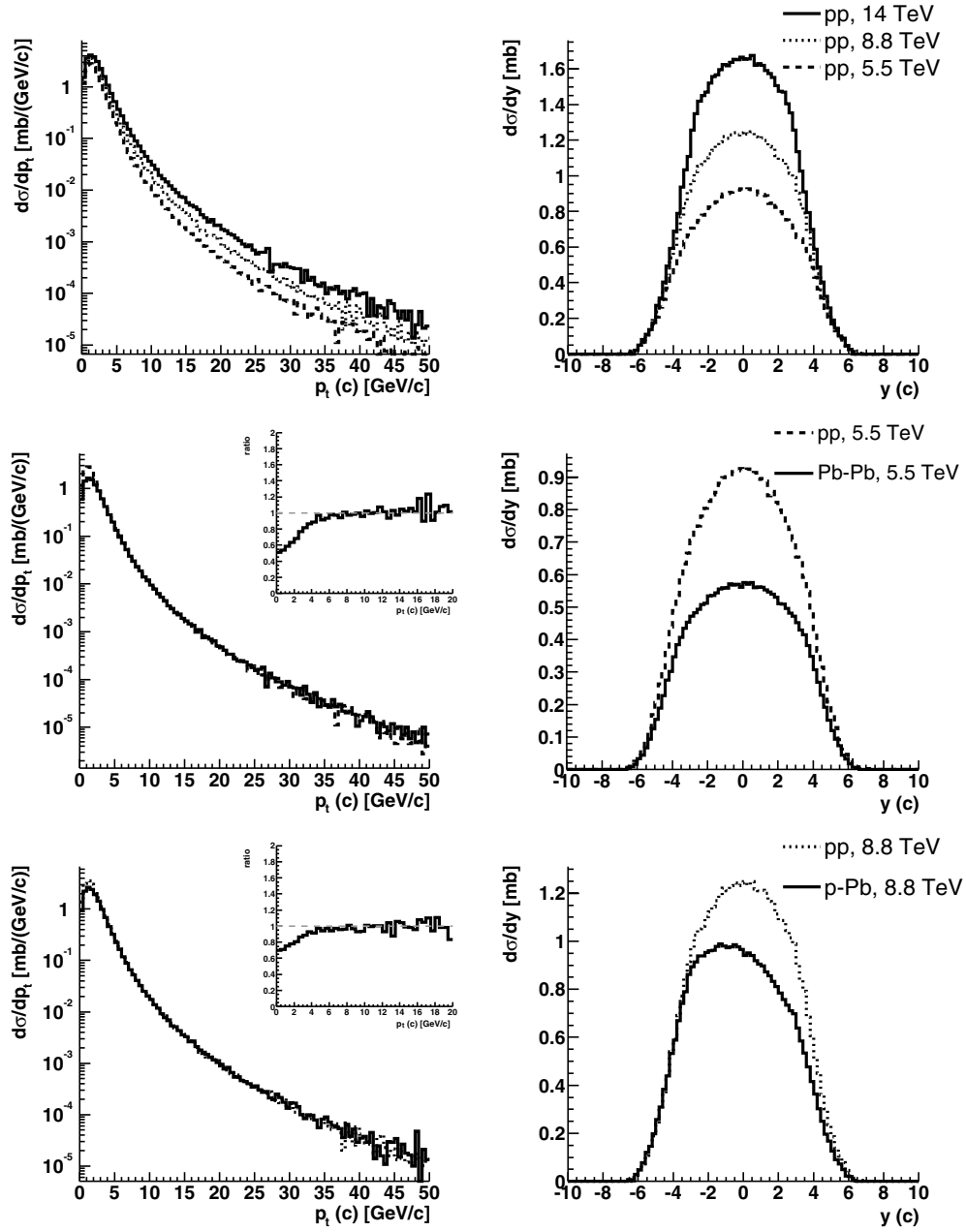


**Figure 6.269.** Inclusive  $c$  quark  $p_T$  and rapidity distributions obtained from the HVQMNR program. The distributions for Pb–Pb and pPb are normalized to the cross sections per nucleon–nucleon collision and they include the effects of nuclear shadowing and intrinsic  $k_T$  broadening.

the shadowing in Pb–Pb collisions can be cross-checked with the following simple estimate: for the back-to-back production of a  $c\bar{c}$  pair at central rapidity, with transverse momenta  $p_t^c = p_t^{\bar{c}} = 5 \text{ GeV}/c$ , we have  $Q \simeq 2 p_t = 10 \text{ GeV}$  and  $x \simeq Q/\sqrt{s_{NN}} = 10/5500 \simeq 2 \times 10^{-3}$ ; for these values of  $x$  and  $Q$ , the EKS98 parametrisation gives  $R_g^{\text{Pb}}$  (defined in Eq. (6.109))

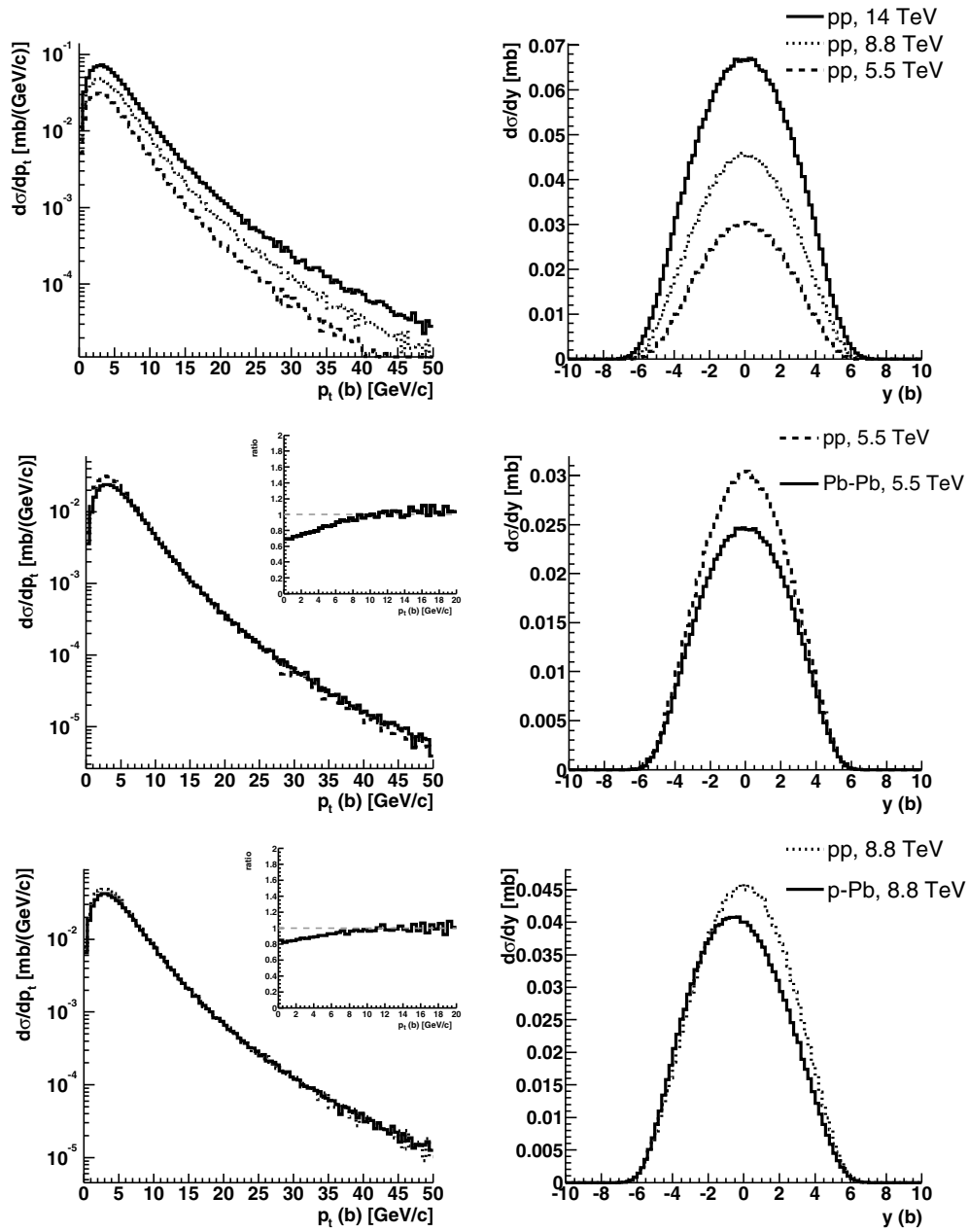


**Figure 6.270.** Inclusive  $b$  quark  $p_t$  and rapidity distributions obtained from the HVQMNR program. The distributions for Pb–Pb and pPb are normalized to the cross sections per nucleon–nucleon collision and they include the effects of nuclear shadowing and intrinsic  $k_t$  broadening.

$\simeq 90\%$ . This suppression is already quite small and it is partially compensated by the  $k_t$  broadening.

A relevant feature of  $Q\bar{Q}$  production in pPb collisions is a depletion in the forward region (where the proton goes) of the rapidity distributions. This effect is due to the shadowing

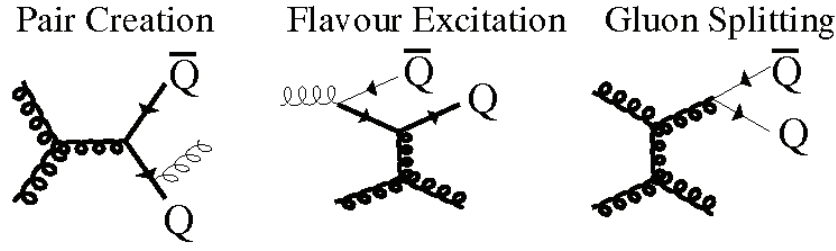


**Figure 6.271.** Some of the PYTHIA processes defined as pair creation, flavour excitation and gluon splitting. The thick lines correspond to the hard process, the thin ones to the initial- or final-state parton shower.

which is biased toward forward rapidities, where the smallest  $x$  values in the Pb nucleus are probed.

Note that the width of the rapidity distributions is expected to increase with increasing  $\sqrt{s}$  (see Eq. (6.103)). This is not observed in the plotted results on account of a feature of the parametrisations of the parton distribution functions: most of them, including CTEQ 4, are valid only down to  $x = 10^{-5}$ ; below this value the behaviour depends on the implementation of the specific parametrisation but has no physical meaning [for example, for CTEQ 4 the gluon density  $g(x)$  is kept constant at  $g(10^{-5})$ ]. The rapidity range in which the evolution of the parton distribution functions is reliable depends on the c.m.s. energy; for charm production at  $\sqrt{s} = 5.5$  TeV (14 TeV) this range is found to be  $|y| < 4.3$  ( $|y| < 3.4$ ), using equation (6.103) with  $x_1 > 10^{-5}$  and  $x_2 > 10^{-5}$ . This feature is not present in the latest CTEQ set of PDFs, CTEQ 6 [829], which are parametrized down to  $x = 10^{-6}$ .

**6.6.3.4. Heavy-quark production in Monte Carlo event generators.** The program used for the NLO calculations reported in the previous sections is not well suited to be included in a simulation since it is not an event generator and it does not provide parton kinematics, but only inclusive distributions. On the other hand, widely used event generators, like PYTHIA [150] and HERWIG [830], are exact only at leading order, when only the *pair creation* processes,  $q\bar{q} \rightarrow Q\bar{Q}$  and  $g\bar{g} \rightarrow Q\bar{Q}$  (see Fig. 6.271), are included. Higher-order contributions are included in these generators in the parton shower approach (see, for example, Ref. [831]). This model is not exact at next-to-leading order, but it reproduces some aspects of the multiple-parton-emission phenomenon. In the following we will concentrate on the PYTHIA event generator; the version we have used is PYTHIA 6.150.

In PYTHIA, the processes giving rise to contributions above leading order, like (see Fig. 6.271) *flavour excitation*,  $qQ \rightarrow qQ$  and  $gQ \rightarrow gQ$ , and *gluon splitting*,  $g \rightarrow Q\bar{Q}$ , are calculated using a massless matrix element. As a consequence the cross sections for these processes diverge as  $p_t^{\text{hard}}$  vanishes<sup>16</sup>. These divergences are regularized by putting a lower cut-off on  $p_t^{\text{hard}}$ . The value of the minimum  $p_t^{\text{hard}}$  cut has a large influence on the heavy-flavour cross section at low  $p_t$ , a region of prime interest for ALICE physics. Our approach was, therefore, to tune the PYTHIA parameters in order to reproduce as well as possible the NLO predictions (HVQMNR). We used PYTHIA with the option MSEL = 1 that allows the different processes to be switched on one by one (see Ref. [832] for more details). The main parameter we tuned is the lower  $p_t^{\text{hard}}$  limit. In this procedure we compared, between

<sup>16</sup>  $p_t^{\text{hard}}$  is defined as the transverse momentum of the outgoing quarks in the rest frame of the hard interaction.

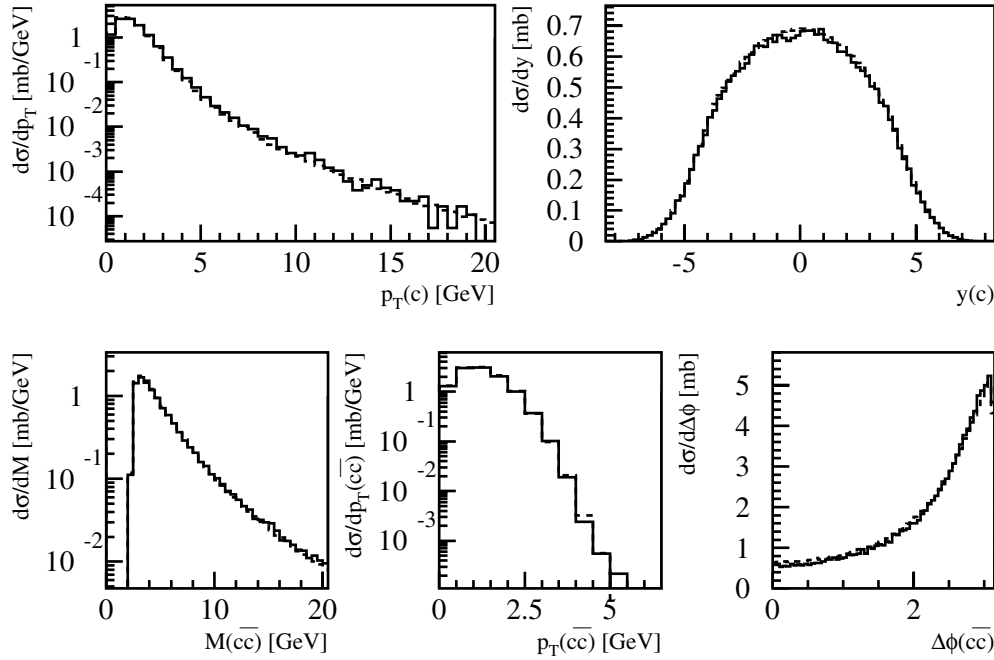


**Figure 6.272.** Comparison between PYTHIA results (solid histograms) for the LO process  $gg \rightarrow c\bar{c}$ , without parton shower, and corresponding HVQMNR prediction (dashed histograms). The centre-of-mass energy is  $\sqrt{s} = 5.5$  TeV.

PYTHIA and HVQMNR, the following distributions of the bare quarks:

- inclusive  $p_t$  and rapidity distributions of the quark (antiquark);
- invariant mass  $M_{Q\bar{Q}}$  of the pair;
- $p_t$  of the pair, defined as the projection on the plane normal to the beam axis of the  $Q\bar{Q}$  total momentum;
- angle  $\Delta\phi$  between the quark and the antiquark in the plane normal to the beam axis.

In the simulations for Pb–Pb collisions at  $\sqrt{s_{NN}} = 5.5$  TeV the parton distribution functions used are the CTEQ4, modified for nuclear shadowing using the EKS98 [779] parametrisation.

Before presenting the results of the tuning of PYTHIA to reproduce the pQCD results at NLO, we show that, with the same input parameters, PYTHIA and the pQCD calculation in HVQMNR give exactly the same kinematical distributions for the LO process  $gg \rightarrow Q\bar{Q}$ . The comparison is reported in Fig. 6.272 for  $c\bar{c}$  production in pp collisions at  $\sqrt{s} = 5.5$  TeV; the normalization is set to the value of the cross section obtained for proton–proton without shadowing (first row of Table 6.51 on page 1773) and the PYTHIA results are scaled to this number.

The results of the tuning to pQCD at NLO are shown in Figs. 6.273 and 6.274, where the distributions from PYTHIA and the NLO calculation are compared. In this case the overall normalization is set to the value of the cross sections obtained for proton–proton with shadowing (second row of Table 6.51 on page 1773). Despite the fundamental differences between the two models, the agreement is relatively good. However, significant discrepancies are present, especially in the  $\Delta\phi$  distribution for  $c\bar{c}$  pairs.

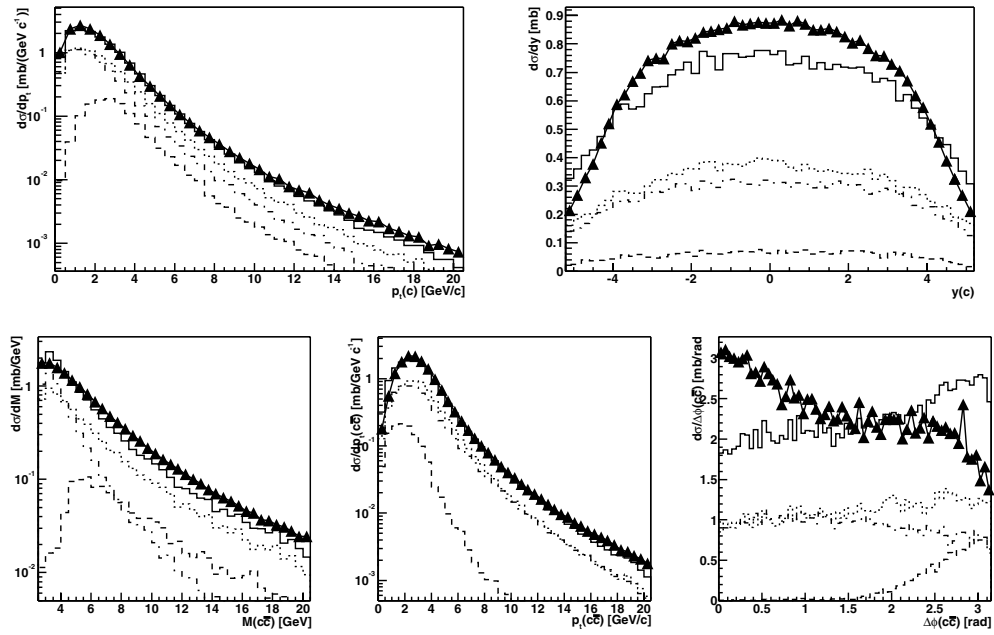


**Figure 6.273.** Comparison between charm production in Pb–Pb collisions at  $\sqrt{s_{NN}} = 5.5$  TeV in the HVQMNR NLO calculation and in PYTHIA with parameters tuned as described in the text. The triangles show the NLO calculation, the solid histogram corresponds to the PYTHIA total production. The individual PYTHIA contributions are pair production (dashed), flavour excitation (dotted) and gluon splitting (dot-dashed).

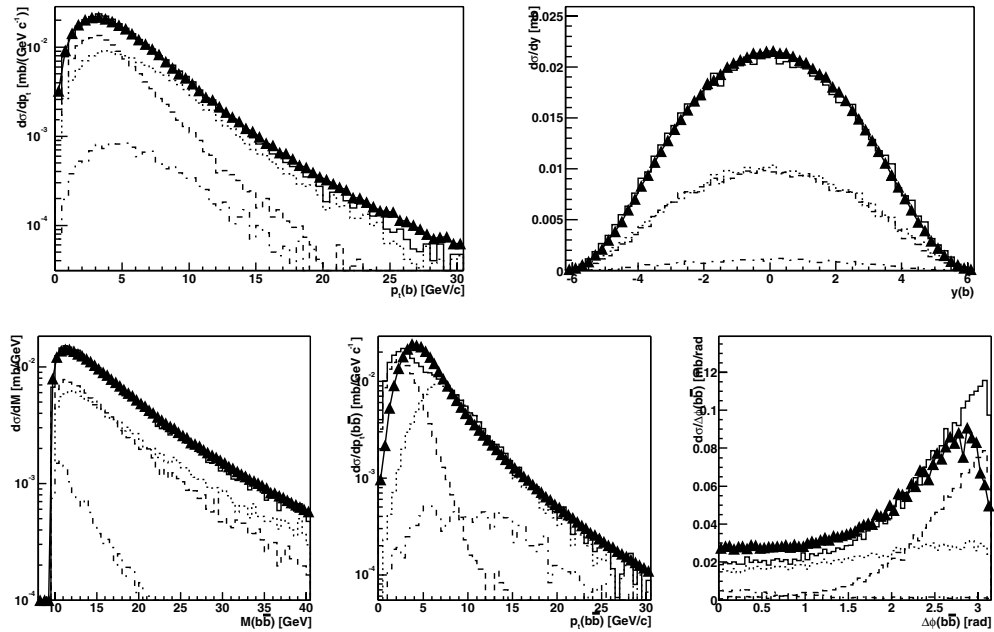


**Figure 6.274.** Equivalent of Fig. 6.273 for beauty production.

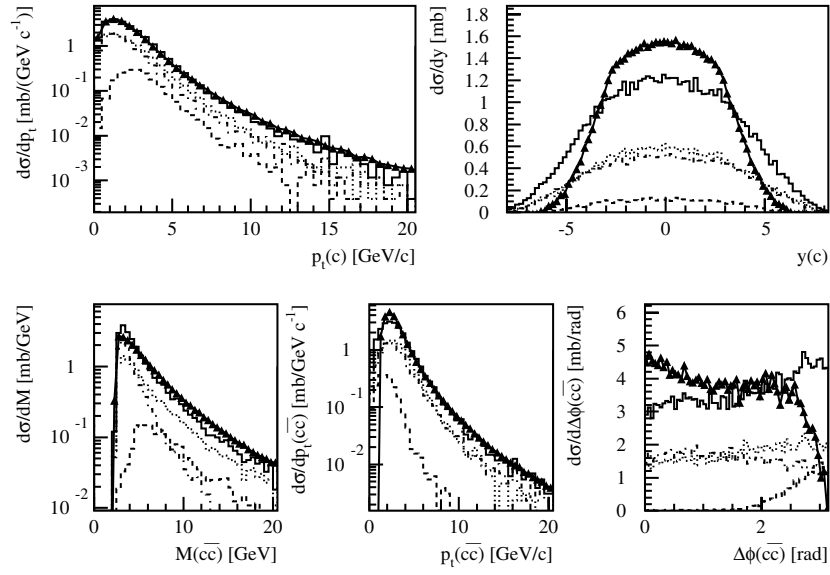


**Figure 6.275.** Comparison between charm production in pp collisions at  $\sqrt{s} = 5.5$  TeV in the HVQMNR NLO calculation and in PYTHIA with parameters tuned as described in the text. The triangles show the NLO calculation, the solid histogram corresponds to the PYTHIA total production. The individual PYTHIA contributions are pair production (dashed), flavour excitation (dotted) and gluon splitting (dot-dashed).

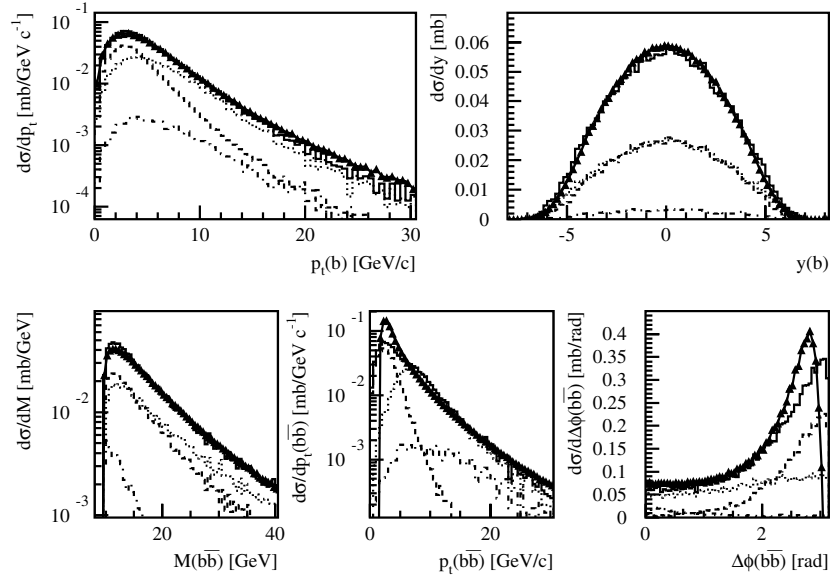


**Figure 6.276.** Equivalent of Fig. 6.275 for beauty production.

A similar tuning of the PYTHIA event generator was done also for the production of charm and beauty in pp collisions at  $\sqrt{s} = 14$  TeV. The same set of parton distribution functions (CTEQ4) was used, without the modification for nuclear shadowing. Results are shown in Figs. 6.275 and 6.276. The largest difference with respect to the results obtained

**Table 6.54.** PYTHIA parameters used for the generation of charm and beauty quarks in pp collisions at 14 TeV, pPb collisions at 8.8 TeV, and Pb–Pb collisions at 5.5 TeV. All non-specified parameters are left to PYTHIA 6.150 defaults [150].

Description	Parameter	Charm	Beauty
Process types	MSEL	1	1
Quark mass [GeV]	PMAS(4/5,1)	1.2	4.75
Minimum $p_t^{\text{hard}}$ [GeV/c]	CKIN(3)	2.1	2.75
CTEQ4L	MSTP(51)	4032	4032
Proton PDF	MSTP(52)	2	2
Switch off multiple interactions	MSTP(81)	0	0
	PARP(81)	0	0
	PARP(82)	0	0
Initial/Final parton shower on	MSTP(61)	1	1
2 <sup>nd</sup> order $\alpha_s$	MSTP(71)	1	1
	MSTP(2)	2	2
QCD scales for hard scattering and parton shower	MSTP(32)	2	2
	PARP(34)	1	1
	PARP(67)	1	1
	PARP(71)	4	1
Intrinsic $k_t$ from Gaussian distr. $\sigma$ [GeV/c]	MSTP(91)	1	1
	PARP(91)	1.00 (pp) 1.16 (pPb) 1.30 (Pb–Pb)	1.00 (pp) 1.60 (pPb) 2.04 (Pb–Pb)
Upper cut-off (at $5\sigma$ ) [GeV/c]	PARP(93)	5.00 (pp)	5.00 (pp)
		5.81 (pPb)	8.02 (pPb)
		6.52 (Pb–Pb)	10.17 (Pb–Pb)

for the Pb–Pb case is a worse description of the rapidity distribution of charm quarks, a consequence of the aforementioned limitation in the  $x$  coverage of the employed set of PDFs. The values of the PYTHIA parameters [150] obtained from the tuning are reported in Table 6.54 [832].

We also investigated heavy-quark production in HERWIG, observing an unphysical behaviour in the final kinematical distributions of heavy quarks produced in *flavour excitation* topologies (for details see Ref. [828]). We note, however, that HERWIG has recently been coupled to a perturbative QCD calculation in the MC@NLO event generator [816], which provides NLO accuracy without need for further tuning.

**6.6.3.5. Hadron yields and distributions.** For the hadronisation of heavy quarks we use the default Lund string fragmentation model [831] included in PYTHIA via the JETSET package. Note that, since the quark  $p_t$  distributions given by our PYTHIA tuning match in shape the NLO ones, rigorously, also the hardness of the fragmentation should have been retuned; we neglect this effect, considered also the significant uncertainty in the knowledge of heavy flavour hadron production at the LHC. The total yield and the rapidity density  $dN/dy$  in the central region for hadrons with open charm and beauty in Pb–Pb at 5.5 TeV (5%  $\sigma^{\text{inel}}$  centrality selection), pp at 14 TeV and pPb at 8.8 TeV are summarized in Tables 6.55, 6.56 and 6.57, respectively. The rapidity densities are calculated in  $-1 < y_{\text{lab}} < 1$ , corresponding

**Table 6.55.** Total yield, average rapidity density for  $|y| < 1$ , and relative abundance, for hadrons with charm and beauty in Pb–Pb collisions at  $\sqrt{s_{\text{NN}}} = 5.5$  TeV. The values reported correspond to a centrality selection of 5%  $\sigma^{\text{inel}}$ .

Particle	Yield	$\langle dN/dy \rangle_{ y_{\text{lab}}  < 1}$	Rel. Abund.	Particle	Yield	$\langle dN/dy \rangle_{ y_{\text{lab}}  < 1}$	Rel. Abund.
$D^0 + \bar{D}^0$	140.8	13.7	61%	$B^0 + \bar{B}^0$	3.65	0.535	40%
$D^+ + D^-$	44.6	4.12	19%	$B^+ + B^-$	3.65	0.521	40%
$D_s^+ + D_s^-$	26.8	2.52	12%	$B_s^0 + \bar{B}_s^0$	1.06	0.159	6%
$\Lambda_c^+ + \bar{\Lambda}_c^-$	17.9	2.03	8%	$\Lambda_b^0 + \bar{\Lambda}_b^0$	0.67	0.097	4%

**Table 6.56.** Total yield, average rapidity density for  $|y| < 1$ , and relative abundance, for hadrons with charm and beauty in pp collisions at  $\sqrt{s} = 14$  TeV.

Particle	Yield	$\langle dN/dy \rangle_{ y_{\text{lab}}  < 1}$	Rel. Abund.	Particle	Yield	$\langle dN/dy \rangle_{ y_{\text{lab}}  < 1}$	Rel. Abund.
$D^0 + \bar{D}^0$	0.1908	0.0196	61%	$B^0 + \bar{B}^0$	0.00577	0.00084	40%
$D^+ + D^-$	0.0587	0.0058	19%	$B^+ + B^-$	0.00576	0.00083	40%
$D_s^+ + D_s^-$	0.0362	0.0038	12%	$B_s^0 + \bar{B}_s^0$	0.00168	0.00025	6%
$\Lambda_c^+ + \bar{\Lambda}_c^-$	0.0223	0.0026	8%	$\Lambda_b^0 + \bar{\Lambda}_b^0$	0.00106	0.00016	4%

**Table 6.57.** Total yield, average rapidity density for  $|y_{\text{lab}}| < 1$ , and relative abundance, for hadrons with charm and beauty in pPb collisions at  $\sqrt{s_{\text{NN}}} = 8.8$  TeV.

Particle	Yield	$\langle dN/dy \rangle_{ y_{\text{lab}}  < 1}$	Rel. Abund.	Particle	Yield	$\langle dN/dy \rangle_{ y_{\text{lab}}  < 1}$	Rel. Abund.
$D^0 + \bar{D}^0$	0.926	0.096	61%	$B^0 + \bar{B}^0$	0.0221	0.0030	40%
$D^+ + D^-$	0.293	0.030	19%	$B^+ + B^-$	0.0221	0.0030	40%
$D_s^+ + D_s^-$	0.176	0.018	12%	$B_s^0 + \bar{B}_s^0$	0.0064	0.0009	6%
$\Lambda_c^+ + \bar{\Lambda}_c^-$	0.118	0.012	8%	$\Lambda_b^0 + \bar{\Lambda}_b^0$	0.0041	0.0005	4%

to  $-1.47 < y_{\text{c.m.s.}} < 0.53$  for pPb and  $-0.53 < y_{\text{c.m.s.}} < 1.47$  for Pb–p. No dependence of the relative hadron abundances on the centre-of-mass energy is observed.

It is interesting to notice the large ratio of the neutral-to-charged D meson yields:  $N(D^0)/N(D^+) \simeq 3.1$ . In PYTHIA, charm quarks are assumed to fragment to D (spin singlets:  $J = 0$ ) and  $D^*$  (spin triplets:  $J = 1$ ) mesons according to the number of available spin states; therefore,  $N(D^0) : N(D^+) : N(D^{*0}) : N(D^{*+}) = 1 : 1 : 3 : 3$ . Then, the resonances  $D^*$  are decayed to D mesons according to the branching ratios. The difference between neutral and charged D mesons arises here: owing to the slightly larger ( $\approx 4$  MeV) mass of the  $D^+$ , the  $D^{*+}$  decays preferably to  $D^0$  and the  $D^{*0}$  decays exclusively to  $D^0$ . We have [409]

$$\begin{aligned}
 \frac{N(D^0)}{N(D^+)} &= \frac{N(D_{\text{primary}}^0) + N(D^{*+}) \times BR(D^{*+} \rightarrow D^0) + N(D^{*0}) \times BR(D^{*0} \rightarrow D^0)}{N(D_{\text{primary}}^+) + N(D^{*+}) \times BR(D^{*+} \rightarrow D^+) + N(D^{*0}) \times BR(D^{*0} \rightarrow D^+)} \\
 &= \frac{1 + 3 \times 0.68 + 3 \times 1}{1 + 3 \times 0.32 + 3 \times 0} \\
 &= 3.08.
 \end{aligned} \tag{6.133}$$

We chose to use the relative abundances given by PYTHIA, although, experimentally, the fraction  $D^0/D^+$  was found to be lower than 3. The value measured in  $e^+e^-$  collisions at LEP by the ALEPH Collaboration is  $\approx 2.4$  [833]. This would reduce by about 6% the expected yield for the  $D^0$  mesons.

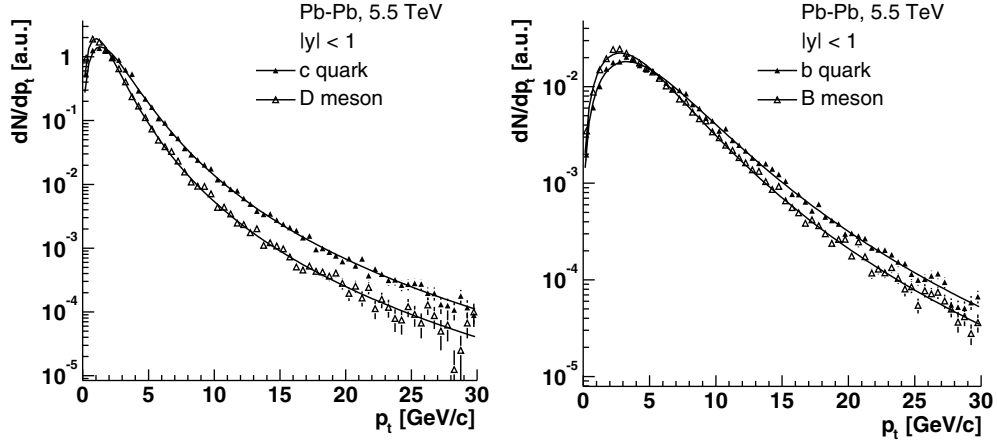


**Figure 6.277.** Transverse-momentum distributions at mid-rapidity for heavy quarks and mesons in Pb–Pb at 5.5 TeV. The distributions are normalized to the same integral in order to compare their shapes.

**Table 6.58.** Parameters derived from the fit of the  $p_t$  distributions of D and B mesons to the expression (6.134) and average value of  $p_t$  for these particles.

Particle	System	$\sqrt{s_{NN}}$ [TeV]	$p_t^0$ [GeV/c]	$n$	$\langle p_t \rangle$ [GeV/c]
D ( $ y_{lab}  < 1$ )	pp	14	2.04	2.65	1.85
	pPb	8.8	2.09	2.72	1.83
	Pb–Pb	5.5	2.12	2.78	1.81
D ( $2.5 <  y_{lab}  < 4$ )	pp	14	2.18	3.04	1.67
	pPb	8.8	2.22	3.11	1.66
	Pb–Pb	5.5	2.25	3.17	1.64
B ( $ y_{lab}  < 1$ )	pp	14	6.04	2.88	4.90
	pPb	8.8	6.08	2.90	4.89
	Pb–Pb	5.5	6.14	2.93	4.89
B ( $2.5 <  y_{lab}  < 4$ )	pp	14	6.45	3.54	4.24
	pPb	8.8	6.49	3.56	4.24
	Pb–Pb	5.5	6.53	3.59	4.24

Figure 6.277 presents the transverse-momentum distributions at mid-rapidity ( $|y| < 1$ ) for c quarks and D mesons (left panel) and for b quarks and B mesons (right panel), in Pb–Pb at 5.5 TeV. For  $p_t > 0$  and  $|y| < 1$ , we have, on average,  $p_t^D \simeq 0.75 p_t^c$  and  $p_t^B \simeq 0.85 p_t^b$ . The shape of the transverse momentum distributions for D and B mesons was fitted to the following expression:

$$\frac{1}{p_t} \frac{dN}{dp_t} \propto \left[ 1 + \left( \frac{p_t}{p_t^0} \right)^2 \right]^{-n}. \quad (6.134)$$

The  $p_t$  distributions were studied also for pp at 14 TeV and for pPb at 8.8 TeV. The results of the fits are reported in Table 6.58, together with the average  $p_t$  of D and B mesons in the different conditions. The average  $p_t$  does not depend strongly on the colliding system and on the energy in the centre of mass. On the other hand, we remark that  $\langle p_t \rangle$  is larger by  $\approx 10\%$  at mid-rapidity than in the forward region ( $2.5 < |y| < 4$ ). These two regions correspond to the acceptance of the ALICE detector: barrel,  $|\eta| < 0.9$ , and forward muon arm,  $-4 < \eta < -2.5$ .

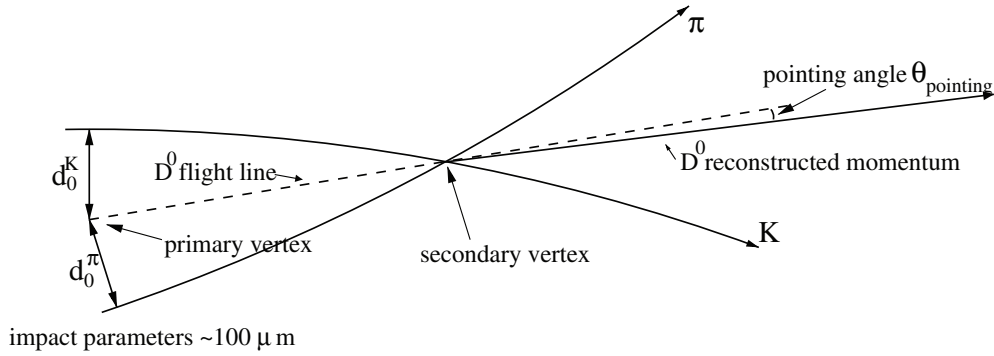


**Figure 6.278.** Schematic representation of the  $D^0 \rightarrow K^- \pi^+$  decay with the impact parameters ( $d_0$ ) and the pointing angle ( $\theta_{\text{pointing}}$ ).

**6.6.4. Charm reconstruction in the  $D^0 \rightarrow K^- \pi^+$  channel.** The feasibility study for the reconstruction of  $D^0$  mesons in the  $K^- \pi^+$  decay channel in central Pb–Pb collisions [53, 834] is presented in detail in Sections 6.6.4.1–6.6.4.4. The same study was repeated also for the case of pp [53] and pPb collisions [835]; the aspects which are specific to these cases and the results are reported in Sections 6.6.4.5 and 6.6.4.6. The extrapolated results for different values of the magnetic field in the ALICE barrel are reported in Section 6.6.4.7. Statistical and systematic uncertainties on the measurement of the  $D^0$  production cross section are discussed in Section 6.6.4.8.

**6.6.4.1. Detection strategy.** The lowest-mass charm hadron states,  $D^0$  and  $D^+$  (and antiparticles), can decay only through weak processes and they have proper decay lengths of few hundred microns ( $c\tau = (123.0 \pm 0.4) \mu\text{m}$  for the  $D^0$  and  $c\tau = (311.8 \pm 2.1) \mu\text{m}$  for the  $D^+$  [409]). Therefore, the distance between the interaction point (primary vertex) and their decay point (secondary vertex) is measurable. The selection of a suitable decay channel, which involves only charged-particle products, allows the direct identification of the charm states by computing the invariant mass of fully reconstructed topologies originating from secondary vertices.

In this analysis we follow the general lines for the detection strategy of open charm in the hadronic channels defined in the ALICE ITS Technical Design Report [1]. We consider as a benchmark the process  $D^0 \rightarrow K^- \pi^+$  (and  $\bar{D}^0 \rightarrow K^+ \pi^-$ ); the branching ratio for this channel is  $(3.83 \pm 0.09)\%$  [409]. Colour Figure V shows the event display picture of a  $D^0 \rightarrow K^- \pi^+$  decay in the ALICE Silicon Pixel Detector.

A sketch of the decay is shown in Fig. 6.278. The main feature of this topology is the presence of two tracks displaced from the primary vertex and compatible with originating from a common point. The variable that allows one to evaluate the displacement of a track is the impact parameter, defined as the distance of closest approach of the track to the primary vertex. We indicate as  $d_0$  the projection of the impact parameter on the bending plane ( $r\phi$ ), normal to the field, and beam, direction. The decay products of  $D^0$  mesons have typical  $r\phi$  impact parameters ranging from about  $50 \mu\text{m}$ , for  $p_t^{D^0} \simeq 0.5 \text{ GeV}/c$ , to about  $120 \mu\text{m}$ , for  $p_t^{D^0} > 5 \text{ GeV}/c$ .

The impact parameter resolution depends mainly on the thickness and radius of the beam-pipe and on the position, spatial resolution, and material thickness of the inner detector layers. In ALICE, the beam-pipe, built in beryllium, has a thickness of  $0.8 \text{ mm}$  ( $0.3\%$  of  $X_0$ ) and

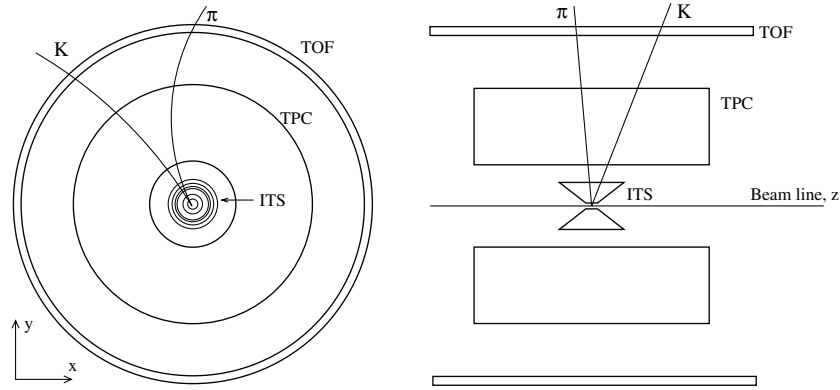


**Figure 6.279.** Schematic view of the detectors employed for the reconstruction of  $D^0 \rightarrow K^- \pi^+$  decays.

a radius of 3 cm. The Inner Tracking System is composed of two layers of Silicon Pixel Detectors (SPD), two layers of Silicon Drift Detectors (SDD), and two layers of Silicon Strip Detectors (SSD) (see Chapter 3 of PPR Volume I [3]). Each of the six layers has a thickness of about 1% of  $X_0$ . The two most important detectors for the measurement of the impact parameter are the two layers of silicon pixels. For  $p_t \simeq 1 \text{ GeV}/c$ , they allow a resolution of about  $60 \mu\text{m}$  to be achieved for the impact parameter projection in the bending plane, as we will detail in the next section. This precision is necessary in order to reduce the combinatorial background by selecting a few displaced tracks out of the large number of primary vertex tracks, thus enabling us to restrict the invariant-mass analysis to decay topologies well separated from the primary vertex.

In addition to the ITS, the other ALICE detectors employed for the detection of hadronic charm decays are the Time Projection Chamber [3, 393] (tracking and momentum measurements) and the Time Of Flight [3, 394] (particle identification). Also the Transition Radiation Detector [3, 836] will provide useful information for track reconstruction, but for the moment it is not included in this simulation. A schematic view of the detectors employed in this analysis is shown in Fig. 6.279.

#### 6.6.4.2. Simulation and reconstruction

*Background and signal generation.* The background events and the signal of open charm mesons were generated and analysed separately.

The background to the charm signal is mainly given by combinations of primary tracks that undergo scatterings in the material of the beam-pipe and of the innermost detector layer and appear as large impact parameter tracks. Other background sources are given by tracks with large impact parameter coming from the decay of hyperons and  $K_S^0$ , tracks from undetected charm decays and from  $\bar{p}$  and  $\bar{n}$  annihilations in the beam-pipe and in the innermost SPD layer.

The background events were generated using the HIJING [42, 67] event generator, activating the option to include nuclear shadowing and quenching effects. The collision impact parameter  $b$  was sampled according to the geometrical cross section dependence  $d\sigma^{\text{inel}}/db \propto b$  and the condition  $b < 2 \text{ fm}$  was applied in order to generate central collisions. The resulting charged-particle rapidity density is  $dN_{\text{ch}}/dy \simeq 6000$ , at mid-rapidity. Our background sample consists of  $2 \times 10^4$  such events that were generated in 1000 subsamples of 20 events each, the events of a subsample having the same values for the impact parameter  $b$  and for the

three coordinates of the primary vertex. Since the background for the  $D^0 \rightarrow K^- \pi^+$  channel is combinatorial, 400 equivalent events were obtained out of each subsample by combining each positive track of the subsample with all negative tracks of the subsample. In this way,  $4 \times 10^5$  equivalent events were obtained, increasing the background statistics by a factor 20.

At LHC energies, the ratio of the production cross sections for beauty and for charm is of the order of 5% (see Section 6.6.3). Considering also that the average inclusive branching ratio of B mesons to  $D^0$  is  $\simeq 65\%$  [409], we conclude that a significant fraction of all produced  $D^0$  particles comes from b quarks ( $b \rightarrow B \rightarrow D^0$ ). The ratio ( $D^0$  from b)/( $D^0$  from c) can be calculated as

$$\begin{aligned} \frac{dN(b \rightarrow B \rightarrow D^0)/dy}{dN(c \rightarrow D^0)/dy} &= \frac{dN(b \rightarrow B^0, B^+)/dy \times BR(B^0, B^+ \rightarrow D^0)}{dN(c \rightarrow D^0)/dy} \\ &= \begin{cases} 0.049 & \text{for Pb-Pb at } \sqrt{s_{NN}} = 5.5 \text{ TeV} \\ 0.054 & \text{for pp at } \sqrt{s} = 14 \text{ TeV.} \end{cases} \end{aligned}$$

where the rapidity densities are taken from Tables 6.55 and 6.56. This ‘B contribution’ was included in the study presented here, since it is important to understand how the ratio of secondary (from b) to primary (from c)  $D^0$  is affected by the selection cuts that we apply. After the selections this contribution has to be corrected for by subtracting, in bins of transverse momentum, the estimated number of secondary  $D^0$ 's. As we will discuss in Section 6.6.4.8, the uncertainty on this number, which is proportional to the uncertainty on the beauty cross section and to the fraction of secondary  $D^0$ , is one of the main contributions to the final systematic error. It is, therefore, essential to keep this fraction under control and, possibly, low. This is also motivated by the fact that, since the  $p_t$  distribution of b quarks is harder than that of c quarks and the selections will naturally tend to be more efficient for larger momenta, we expect the fraction of secondary  $D^0$ 's to increase after the selection cuts.

The signal was generated using PYTHIA, tuned to reproduce the  $p_t$  distribution of charm and beauty quarks given by the NLO calculations by Mangano, Nason and Ridolfi, as explained in Section 6.6.3.4. Many  $D^0/\bar{D}^0$  mesons, with decay forced into a charged  $K\pi$  pair, were superimposed in special ‘signal events’. The number of  $D^0$ 's per event (13 000 in  $|y| < 2$ ) was tuned in order to have the same track multiplicity as in a central HIJING event. In this way, the  $D^0$  decay products are reconstructed with the same efficiency as if they were produced in a central Pb–Pb collision. Indeed, it was verified that the different momentum and impact parameter distributions of these ‘signal events’ with respect to central HIJING events do not affect significantly the reconstruction efficiency (more details are given in the next section).

A total of 1000 such ‘signal events’ were generated with primary  $D^0$  particles. Using our present rate estimate for central collisions<sup>17</sup> with  $b < 3.5$  fm (from Table 6.55) and a branching ratio of 3.8%, such a number of  $D^0 \rightarrow K^- \pi^+$  decays corresponds to  $\simeq 6.1 \times 10^6$  central Pb–Pb events. In addition, we have generated 49 similar events with secondary  $D^0$ 's from the decay of B mesons. In this case we set PYTHIA in order to reproduce the NLO pQCD results for the  $p_t$  distribution of b quarks. We did not transport through the detector the other decay products of the b quarks and of the B mesons, but only the kaons and pions from the  $D^0$  decays. Figure 6.280 shows the  $p_t$  distributions for primary and secondary  $D^0$  mesons: as expected the latter have a harder spectrum.

<sup>17</sup> The impact parameter range used for the generation of the background events is  $b < 2$  fm, while it is  $b < 3.5$  fm (5% most central collisions) for the estimate of the charm production rate. This choice is due to technical reasons; however, it is a conservative one, since  $b < 2$  fm gives a larger multiplicity for background tracks than  $b < 3.5$  fm.

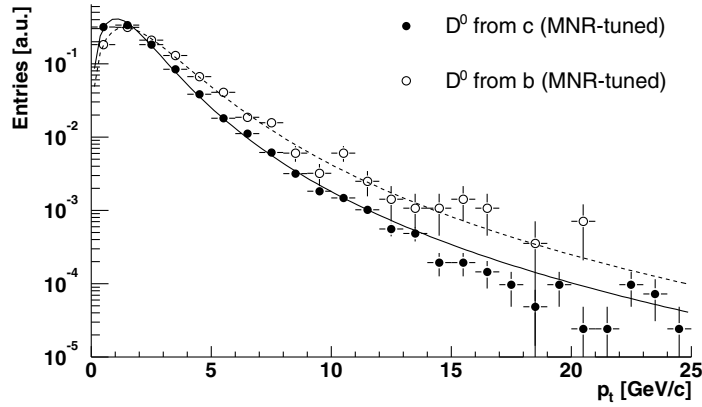


**Figure 6.280.** Transverse momentum distributions for primary and secondary (from B meson decays)  $D^0$  mesons, in Pb–Pb collisions at 5.5 TeV.

All the results presented here are scaled to  $10^7$  central Pb–Pb events, expected to be collected in the one-month heavy-ion run of one LHC year.

For both signal and background events, the  $z$  position of the primary vertex was sampled from a Gaussian distribution ( $\sigma = 5.3$  cm) with a cut at  $\pm 1\sigma$ . This corresponds to the expected width of the fiducial interaction region. We assumed that the beam is centred at  $(0, 0)$  in the  $(x, y)$  plane.

*Detector simulation and event reconstruction.* The simulation was performed within the ALICE object-oriented framework, AliRoot [837]. The value of the magnetic field used in the simulation was  $B = 0.4$  T, which is close to the maximum value that can be provided by the ALICE magnet. This kind of physics studies yields better performance with relatively large values of the magnetic field, since (a) the invariant mass resolution is better with larger fields and (b) the acceptance at very low track  $p_t$  ( $< 500$  MeV/ $c$ ) is not crucial. The extrapolation of the results for lower values of the magnetic field is straightforward and will be discussed in Section 6.6.4.7.

The combinatorial background for charm detection in hadronic decay channels is very large (e.g. for  $D^0 \rightarrow K^- \pi^+$  we have  $S/B \sim 10^{-6}$  in the mass range  $M_{D^0} \pm 3\sigma$ , before selections) and to extract the charm signal with good significance one has to apply cuts strong enough to reduce the background by 6–7 orders of magnitude. As a consequence, a large number of events is required in the analysis. This makes the simulation of the whole ALICE detector very expensive in terms of CPU time and disk space. Therefore we used a fast simulation technique. Each particle is transported through the apparatus; however, the track is followed only up to the entrance of the TPC, where its position and momentum on the first pad row are stored. The reconstructed track parameters at the entrance of the TPC are then estimated from the generated quantities at the first pad row using the parametrized response of the TPC tracking, as described in Ref. [838]. This parametrisation describes accurately the resolutions of the track parameters, their correlations, and the tracking efficiency in the TPC as obtained from the TPC Kalman filter. It also accounts for efficiency losses due to in-flight decays. Computing time and mass storage are in this way reduced by about a factor 35, because TPC digits are not created. Using this approach, however, the tracking efficiency is slightly underestimated since about 12% of the tracks traverse the dead area between the first pad rows of two adjacent TPC sectors. These tracks may still be reconstructed if they enter

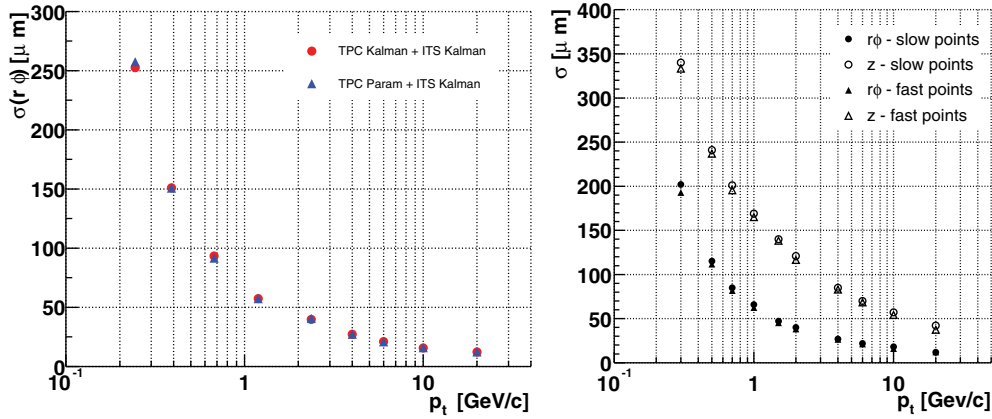


**Figure 6.281.** Comparison between standard reconstruction, TPC Kalman + ITS Kalman, and fast reconstruction, TPC Param + ITS Kalman, for the  $r\phi$  impact-parameter resolution as a function of  $p_t$  (left-hand panel). Comparison between fast and detailed (slow) ITS response for the  $r\phi$  and  $z$  impact-parameter resolutions (right-hand panel).

the TPC at a larger radius, but they are lost from the point of view of the parametrisation since they lack the information on the generated track parameters stored in the first TPC pad row.

For the beam-pipe and the ITS detectors, which are instrumental in determining the impact parameter of the tracks and the position of the secondary vertex, the crucial quantities required to extract the charm signal, we instead use a detailed description of the geometry. The transport of the charged particles in the materials, performed by the GEANT3 package, takes into account the complete theory of multiple Coulomb scattering. Pattern recognition and track fitting in the ITS were performed, exactly as in the complete simulation, with the standard Kalman filter algorithm, which uses the TPC tracks as seeds for the tracking in the ITS (see Chapter 5).

Fig. 6.281 (left-hand panel) shows the resolution on the bending-plane projection ( $r\phi$ ) of the impact parameter as a function of  $p_t$  for pion tracks reconstructed in the TPC and in the ITS with points in all six layers. The resolution is of  $\simeq 60 \mu\text{m}$  for  $p_t = 1 \text{ GeV}/c$ , the average transverse momentum of the  $D^0$  decay products. As shown in the figure, the  $d_0$  resolution does not change if we use the parametrized response of the TPC.

In order to further reduce the CPU time and storage space, the position resolution of the ITS detectors was also parametrized. The comparison between the fast and the detailed ITS responses is shown in Fig. 6.281 (right-hand panel) for the  $r\phi$  and  $z$  impact parameter resolutions.

The  $z$  position of the primary vertex was estimated for each event using a method based on the correlation of the points in the two pixel layers as described in Chapter 5 and Refs. [4, 5]. The obtained resolution is  $\sigma_z \simeq 5.5 (7.0) \mu\text{m}$  for  $dN_{\text{ch}}/dy \simeq 6000 (3000)$ . In the bending plane, the position of the centre of the Pb beams will be stable for a given machine fill (a few hours). Thus, it will be measured very precisely averaging over many events, and the uncertainty on the position of the interaction vertex will be given by the transverse size of the beam ( $\sigma_x = \sigma_y \simeq 15 \mu\text{m}$ ). We applied a smearing to take into account this uncertainty, which is, however, negligible with respect to the track position resolution.

The reconstruction in the ITS was performed with a three-steps procedure:

- (a) at first, the tracks are found using a strong constraint on the primary vertex position, in order to maximize the tracking efficiency;

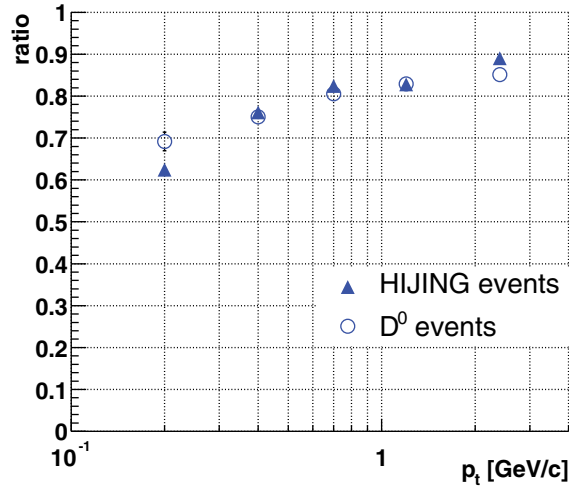


**Figure 6.282.** ITS tracking efficiency, defined as the ratio of the number of tracks reconstructed in the ITS to the number of tracks reconstructed in the TPC, as a function of  $p_t$  for central HIJING events and for ‘signal events’ containing only  $D^0/\bar{D}^0$ , decaying in  $K\pi$ , with the same track multiplicity as a central HIJING event.

- (b) these tracks are then re-fitted releasing the vertex constraint, in order not to bias the determination of the impact parameter; clusters associated to reconstructed tracks are removed;
- (c) a second pass of track finding is done, without any vertex constraint, to search for tracks originating from decays far from the primary vertex (mainly hyperons and  $K_S^0$  decays).

The tracks considered in this analysis are required to have at least five points in the ITS, including the points from both pixel layers. This allows the statistics, w.r.t. requiring always six points, to be increased without deteriorating the impact parameter resolution, as shown in Ref. [32].

We estimated a loss of  $\approx 10\%$  of the tracks due to the dead channels in the ITS. We did not correct for this effect since it roughly compensates the efficiency loss due to the incorrect treatment of the TPC dead regions in the parametrisation.

The reconstruction was done exactly in the same way for background and signal. Figure 6.282 demonstrates that the tracking efficiency in the ITS for the ‘signal events’ is the same as for the background events.

*Particle identification.* In the momentum range of interest for low- $p_t$  charm selection ( $p \simeq 0.5\text{--}2\text{ GeV}/c$ ) the particle-identification capability of ALICE is determined mainly by the TOF detector. Figure 6.283 presents a scatter plot of the measured momenta versus the estimated masses for the particles produced in central Pb–Pb collisions generated with HIJING. The figure, from the TOF TDR [394], is obtained for  $B = 0.4\text{ T}$  assuming an overall time resolution<sup>18</sup> of 150 ps. The association of the time-of-flight and, hence, of the mass to a specific reconstructed track is obtained by means of a matching algorithm that propagates the track from the outer radius of the TPC to the TOF detector and matches it with one of the  $\approx 3 \times 3\text{ cm}^2$  pads of the detector [394]. Tracks matched with a non-active region of the

<sup>18</sup> Since the TOF TDR, the design of the Multigap Resistive Plate Chambers has been improved and an overall time resolution of  $\approx 120\text{ ps}$  can now be achieved. The analysis presented here uses the slightly worse resolution that was expected at the time of the TOF TDR.

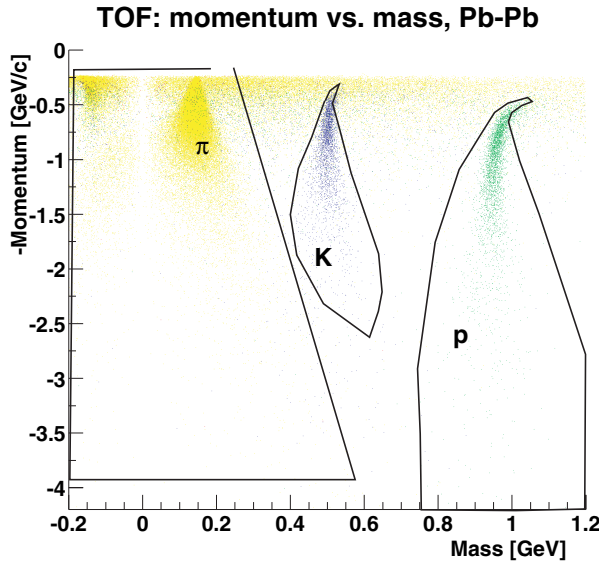


**Figure 6.283.** Momentum versus mass calculated from TOF for a sample of HIJING Pb–Pb events. The lines correspond to the chosen graphical cuts relative to the selection of pions, kaons, and protons. (Negative values of the mass are assigned when, owing to wrong matching of the TOF signal with a reconstructed track, a velocity larger than the velocity of light is calculated.)

detector or with a non-fired or multifired<sup>19</sup> pad are not assigned a mass. The TRD, which lies between the TPC and the TOF, should provide a ‘bridge’ between the two detectors and improve the matching procedure. Since the extension of track reconstruction to the TRD was still under development, Fig. 6.283 was obtained from a simulation that does not include the material of the TRD. On the other hand, it would be unjustified to consider the TRD just as a layer of inactive material.

For  $0.5 < p < 2\text{--}2.5$  GeV/c there is a good mass separation for pions, kaons and protons. For lower momenta the matching tends to fail because of multiple scattering and energy loss, while for  $p > 2\text{--}2.5$  GeV/c the separation vanishes, especially between pions and kaons, as they become relativistic.

The association of the particle type to a track (tagging) is obtained by applying cuts on the momentum-versus-mass plane. The values of these cuts determine the identification efficiency and the contamination of the sample. The identification efficiency for a particle type  $i$  is defined as the ratio of the number of tracks of type  $i$  correctly tagged as  $i$  to the total number of tracks of type  $i$ ; the contamination is defined as the ratio of the number of tracks incorrectly tagged as  $i$  to the total number of tracks tagged as  $i$ . The optimal level of contamination and efficiency depends on the physics measurement under study.

We divide our set of reconstructed tracks into four samples: those identified as pions ( $\pi_{\text{tag}}$ ), as kaons ( $K_{\text{tag}}$ ), as protons ( $p_{\text{tag}}$ ), and non-identified ( $?_{\text{tag}}$ ). A  $D^0 \rightarrow K^- \pi^+$  decay for which both the pion and the kaon tracks are reconstructed corresponds to a pair of tracks of opposite charge ( $-$ ,  $+$ ). According to their PID, the pair can fall in one of the following samples:

**Sample A:** ( $K_{\text{tag}}, \pi_{\text{tag}}$ ) + ( $K_{\text{tag}}, ?_{\text{tag}}$ ); the kaon is identified while the other track can be identified as pion or non-identified.

<sup>19</sup> A pad is non-fired if it does not have hits; it is single-fired if it has only one hit; it is multifired if it has more than one hit.

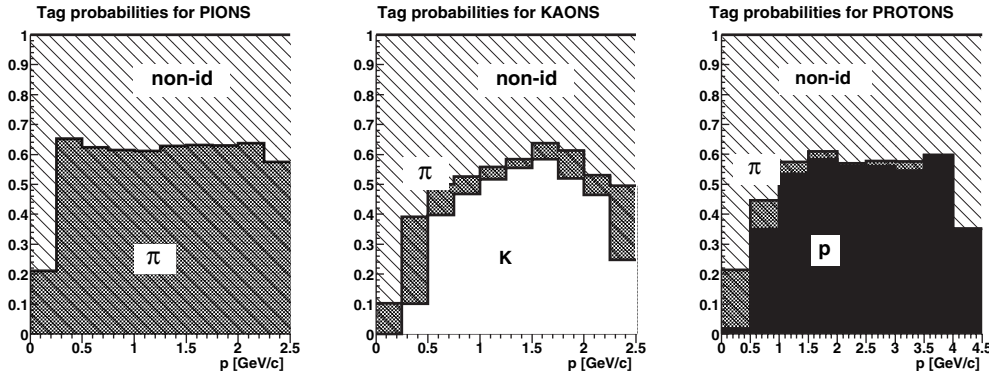


**Figure 6.284.** PID tag probabilities for reconstructed pions, kaons, and protons in Pb-Pb collisions with the TOF detector.

**Sample B:** ( $?_{\text{tag}}, \pi_{\text{tag}}$ ); only the positive track is identified as pion.

**Sample C:** ( $?_{\text{tag}}, ?_{\text{tag}}$ ); both tracks are not identified; in this sample each pair is counted twice: once as a  $D^0$  candidate and once as a  $\bar{D}^0$  candidate.

**Sample D:** All other combinations, such as ( $\pi_{\text{tag}}, \pi_{\text{tag}}$ ); these pairs are rejected.

If the pion from a  $D^0$  decay is correctly identified, but the kaon is misidentified as a pion, the candidate falls in sample D and is lost. Therefore, for open charm detection, the PID strategy has to be optimised in order to minimize the number of kaons tagged as pions, while tagging correctly a large fraction of the pions.

On the basis of this guideline the PID tags were defined as follows:

- any track not matched with a single-fired TOF pad is tagged as  $?_{\text{tag}}$ ;
- tracks matched with a single-fired TOF pad are tagged according to the graphical cuts shown in Fig. 6.283; if a track falls outside all graphical cuts it is tagged as  $?_{\text{tag}}$ .

The graphical cuts were optimised in order to minimize the probability to tag a kaon as a pion, i.e. to minimize the loss of signal.

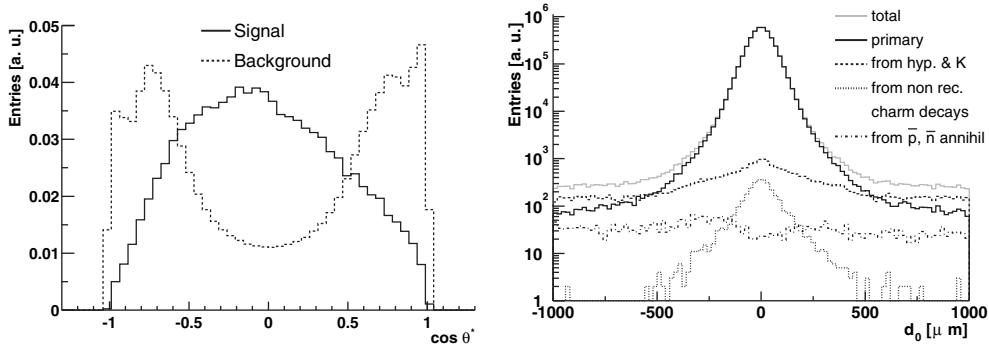
In this way, for every particle type, we can compute the probabilities to be tagged as pion, kaon, proton, or non-identified. These probabilities are shown in Fig. 6.284 as a function of the total momentum. We give an example of how these figures should be read: for a reconstructed track (in TPC and ITS), known from the simulation to be a kaon, with  $p = 1 \text{ GeV}/c$ , the probability to be tagged as kaon is 45%, the probability to be tagged as pion is 8% and the probability to be tagged as non-identified is the remaining 47% (see central panel).

In our study the TOF detector was not included in the simulation of all the events and the three samples A, B, and C were populated with  $D^0$  candidates according to the tabulated probabilities from the figure, both for the signal and for the background. The PID information was used for  $p < 2 \text{ GeV}/c$  for pions and kaons and for  $p < 4 \text{ GeV}/c$  for protons; for larger momenta all tracks were tagged as  $?_{\text{tag}}$  (non-id). The fraction of signal lost because the kaon is tagged as a pion is 10%.

**6.6.4.3. Analysis.** Figure 6.278 shows a sketch of the  $D^0 \rightarrow K^- \pi^+$  decay. For each  $D^0$  candidate (opposite-charge tracks pair) the position of the decay vertex is computed by a minimization of the distance in space between the two helices representing the particle

**Table 6.59.** Initial values of S/B in the invariant mass range  $M_{D^0} \pm 3\sigma$ , before selection.

Sample	S/event	B/event	S/B
A	0.054	$2.5 \times 10^3$	$2.16 \times 10^{-5}$
B	0.041	$1.4 \times 10^4$	$2.98 \times 10^{-6}$
C	0.031	$1.2 \times 10^4$	$2.69 \times 10^{-6}$
Total	0.126	$2.8 \times 10^4$	$4.53 \times 10^{-6}$

**Figure 6.285.** Left: distribution of  $\cos \theta^*$  for the  $D^0$  signal (solid line) and for the background (dashed line). The histograms are normalized to the same integral. Right: impact parameter distribution for pions coming from the different background sources. The analysis cut  $p_t > 800 \text{ MeV}/c$  is applied in both panels.

trajectories. The momentum of the  $D^0$  candidate is calculated as the sum of the momenta of the kaon and of the pion at the position of closest approach between the two tracks. The average  $D^0$  invariant mass resolution is  $12 \text{ MeV}$  for  $B = 0.4 \text{ T}$ .

In Table 6.59 we present the signal-to-background ratios for the three samples A, B, and C in the invariant mass range  $|M_{K\pi} - M_{D^0}| < 3\sigma$ , before any other selection. Owing to the small fraction of kaons in the background, sample A (kaon identification required) shows the highest S/B ratio ( $\sim 2 \times 10^{-5}$ ). However, Fig. 6.284 (central panel) shows that the identification probability decreases rapidly for kaons with momentum larger than  $1.5 \text{ GeV}/c$ ; therefore, for  $D^0$  momenta larger than  $\sim 2\text{--}3 \text{ GeV}/c$ , the fraction of signal that populates sample A becomes marginal. For this reason, we consider as our standard sample the sum of the three samples A, B, and C (called ‘Total’ in Table 6.59); this corresponds to the rejection of  $(\pi_{\text{tag}}, \pi_{\text{tag}})$  and  $(K_{\text{tag}}, K_{\text{tag}})$  pairs. In the low- $p_t$  region, it would perhaps be convenient to restrict the PID selection to sample A only.

Several selection cuts are applied in order to increase the S/B ratio to the level needed to extract the signal. Their definition is presented in the following paragraphs.

Pairs for which the distance of closest approach,  $dca$ , between the tracks is larger than  $dca_{\text{max}}$  ( $300\text{--}400 \mu\text{m}$ , depending on the transverse momentum of the  $D^0$  candidate) are rejected.

Since the transverse momentum distributions for the signal are harder than those for the background, it is convenient to apply a cut on the minimum  $p_t$  for K and  $\pi$  ( $p_t > 800 \text{ MeV}/c$ ).

In the reference frame of the decaying  $D^0$ , we define  $\theta^*$  as the angle between the pion momentum and the  $D^0$  flight line. As shown in Fig. 6.285 (left-hand panel), the background accumulates at  $\cos \theta^* = \pm 1$ . The distribution for the signal is not uniform because of the other applied cuts, in particular the cut on the minimum  $p_t$  of the pion and of the kaon.

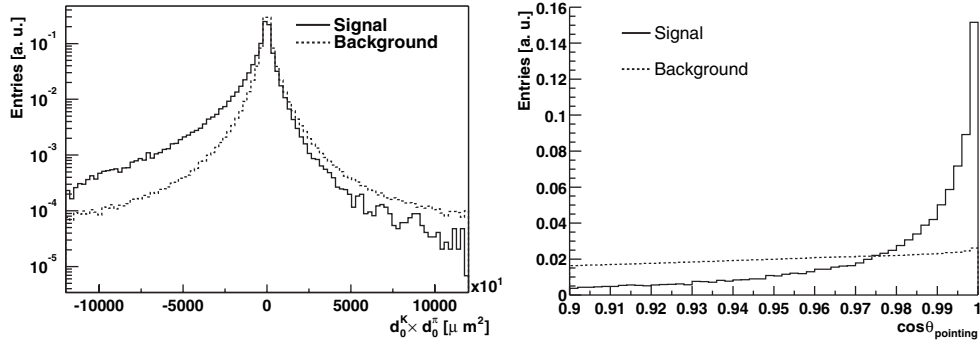


**Figure 6.286.** Left: product of the pion and kaon  $r\phi$  impact parameters for signal and background combinations. Right: cosine of the pointing angle for signal and background combinations. Signal and background distributions are normalized to the same integral.

The slight asymmetry reflects the different masses of the kaon and the pion. Only pairs with  $\cos\theta < cth_{\text{max}} (\simeq 0.6)$  are kept.

With these cuts the signal-to-background ratio increases by a factor  $\sim 100$ . Further improvement can be obtained by applying a displaced-vertex identification procedure based on the track impact-parameters and on the requirement that the reconstructed  $D^0$  points back to the primary vertex.

We consider only the impact parameter projection on the transverse plane,  $d_0(r\phi)$ , simply indicated as  $d_0$  in the following, since it is measured much more precisely than that along the  $z$  direction (see right-hand panel of Fig. 6.281). The impact parameter distribution for the different background sources is shown in Fig. 6.285 (right-hand panel). For large impact parameters ( $|d_0| > 500 \mu\text{m}$ ) the dominant background comes from the decay of hyperons and kaons. The upper cut on  $|d_0| < 500 \mu\text{m}$  gives an efficient rejection of this background contribution.

The projection of the tracks on the bending plane ( $r\phi$ ) allows us to define a sign for the impact parameter. This sign is positive or negative according to the position of the track projection with respect to the primary vertex (the orientation is given by the direction of the track momentum). The tracks of opposite charge originating from a  $D^0$  decaying far from the primary vertex will then have impact parameters of opposite signs and large in absolute value. A very appropriate variable for selection is the product of the two  $r\phi$  impact parameters. For true decays this quantity should tend to be negative and large in absolute value. In Fig. 6.286 (left-hand panel) we plot the distribution of the product of impact parameters for signal and background, normalized to the same integral. The cut  $d_0^K \times d_0^\pi < -40000 \mu\text{m}^2$  improves the S/B ratio by a factor  $\simeq 10$ .

The condition for the  $D^0$  to point back to the primary vertex is imposed by a cut on the angle between the momentum vector of the  $D^0$  candidate and the line connecting the primary and the secondary vertex (pointing angle  $\theta_{\text{pointing}}$ ). The cosine of  $\theta_{\text{pointing}}$  peaks at +1 for the signal, and is almost uniformly distributed for the background, as shown in Fig. 6.286 (right-hand panel). Requiring to have  $\cos\theta_{\text{pointing}} > 0.98$  would also give, by itself, a background rejection of about one order of magnitude.

A much larger rejection factor can be obtained by combining these two cuts. In fact, if the secondary vertex is well separated from the primary one, the impact parameters are large and the pointing angle is small, since the  $D^0$  flight direction is measured with a better resolution. Therefore, the two variables are strongly correlated in the signal, while this correlation is

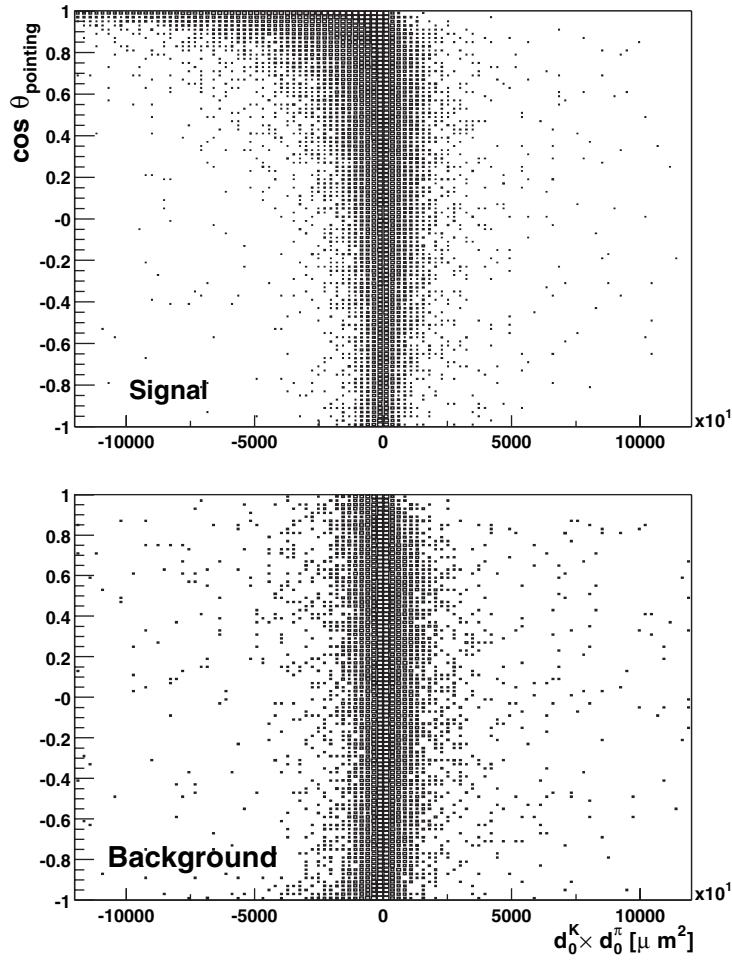


**Figure 6.287.** Cosine of the pointing angle versus product of the impact parameters for signal and background combinations.

absent in the background. This can be seen in Fig. 6.287, which shows the bidimensional plot of  $\cos \theta_{\text{pointing}}$  versus the product of impact parameters. The improvement in the signal-to-background ratio obtained by applying the combined cut is about a factor  $10^3$ .

Each cut was studied in order to maximize the statistical significance  $S/\sqrt{S+B}$ , calculated for  $10^7$  central Pb–Pb events. Also, the optimization of the cuts was done separately for the following bins in the  $p_t$  of the  $D^0$ :  $1 < p_t < 2 \text{ GeV}/c$ ,  $2 < p_t < 3 \text{ GeV}/c$ ,  $3 < p_t < 5 \text{ GeV}/c$ ,  $p_t > 5 \text{ GeV}/c$ . The optimization procedure consists in varying one cut at a time, while the others are kept constant, and selecting the value of the cut which maximizes the significance. As an example, Fig. 6.288 shows the tuning of the  $d_0^K \times d_0^\pi$  cut for the different  $p_t$  bins. The significance is plotted as a function of the value of the cut. For larger momenta the maximum of the significance is found at higher values of the cut, since the impact parameter resolution improves as  $p_t$  increases.

In Table 6.60 the final values of the cuts are reported. The most sensitive cut is that on the product of the impact parameters, since it selects the tail of the distribution in order to exploit

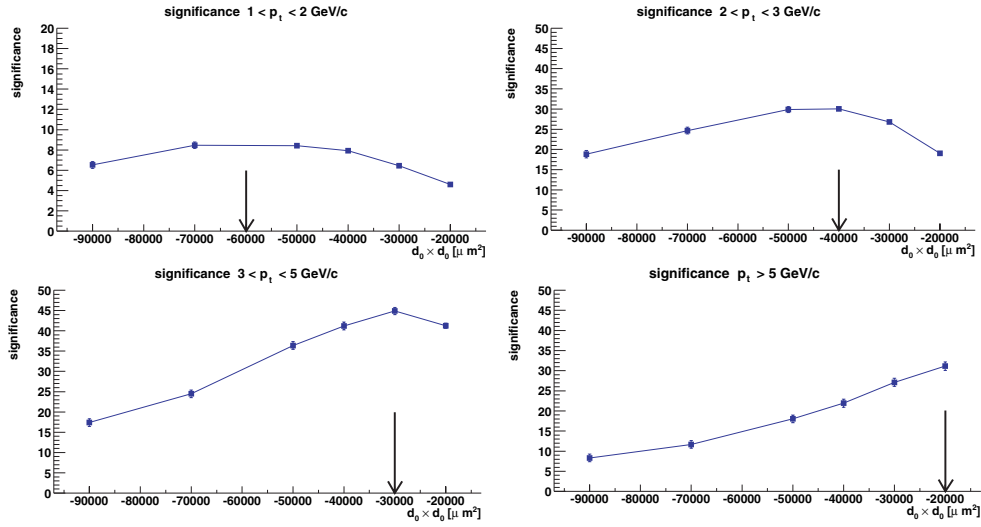


**Figure 6.288.** Tuning of the  $d_0^K \times d_0^\pi$  cut for the different  $p_t^{D^0}$  bins. The arrows mark the values chosen for the cut.

**Table 6.60.** Final value of the cuts in the different  $p_t$  bins.

Cut name	$1 < p_t < 2 \text{ GeV}/c$	$2 < p_t < 3 \text{ GeV}/c$	$3 < p_t < 5 \text{ GeV}/c$	$p_t > 5 \text{ GeV}/c$
Distance of closest approach ( $dca$ )	$< 400 \mu\text{m}$	$< 300 \mu\text{m}$	$< 300 \mu\text{m}$	$< 300 \mu\text{m}$
Decay angle $ \cos\theta^* $	$< 0.6$	$< 0.6$	$< 0.6$	$< 0.6$
$K, \pi p_t$	$> 800 \text{ MeV}/c$	$> 800 \text{ MeV}/c$	$> 800 \text{ MeV}/c$	$> 800 \text{ MeV}/c$
$K, \pi  d_0 $	$< 700 \mu\text{m}$	$< 500 \mu\text{m}$	$< 500 \mu\text{m}$	$< 500 \mu\text{m}$
$d_0^K \times d_0^\pi$	$< -60000 \mu\text{m}^2$	$< -40000 \mu\text{m}^2$	$< -30000 \mu\text{m}^2$	$< -20000 \mu\text{m}^2$
Pointing angle $\cos\theta_{\text{pointing}}$	$> 0.95$	$> 0.98$	$> 0.98$	$> 0.98$

the different shapes of signal and background (as shown in the left-hand panel of Fig. 6.286). Figure 6.289 shows the bidimensional plot of  $d_0^K \times d_0^\pi$  versus  $p_t^{D^0}$  for the signal candidates, after all other cuts have been applied, as reported in Table 6.60. The distribution becomes very narrow at high  $p_t$  as a consequence of the strong  $p_t$  dependence of the impact parameter resolution. The step-like cut obtained by the tuning procedure described before is shown. From the shape of the distribution it is clear that using this step-like cut would determine the loss of most of the signal for  $p_t > 8\text{--}10 \text{ GeV}/c$ ; this high- $p_t$  region is extremely important for the parton energy loss studies, as we shall see in Section 6.6.5. It is, therefore, mandatory to have a ‘really’  $p_t$ -dependent cut, for  $p_t > 2 \text{ GeV}/c$ , such as that indicated by the line in the figure.

**6.6.4.4. Results for central Pb–Pb collisions at  $\sqrt{s_{\text{NN}}} = 5.5 \text{ TeV}$ .** Figure 6.290 shows the invariant mass distribution for the sum of samples A, B, and C after selection, corresponding to  $10^7$  events.

In Table 6.61 the values for S/event, B/event and S/B, in the invariant mass range  $|M_{K\pi} - M_{D^0}| < 1\sigma$ , are presented. In the same table, we report also the statistical significance  $S/\sqrt{S+B}$  for  $10^7$  central Pb–Pb events and the relative error  $\sigma_S/S$  on the estimation of the number S of detected  $D^0$  mesons. This relative error is  $\sqrt{S+B}/S$ , i.e. the inverse of the significance.

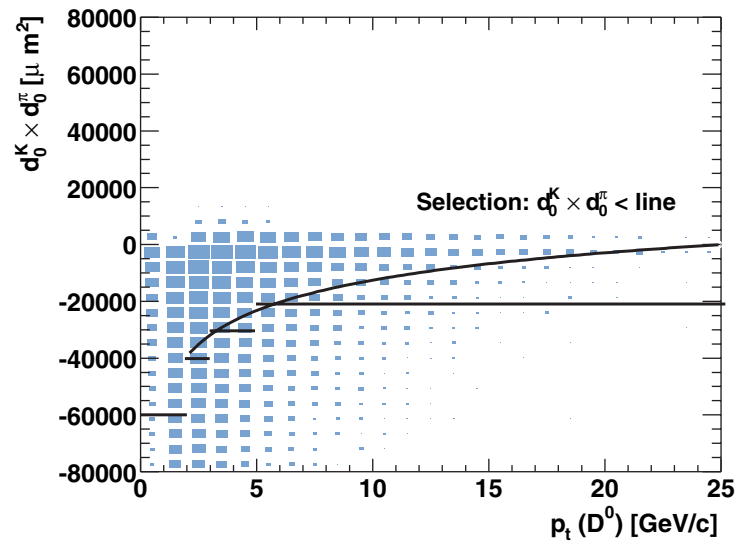


Figure 6.289. Product of the impact parameters as a function of the  $D^0$   $p_t$  for signal candidates. The step-like cut obtained by the cut-tuning procedure is shown. The line starting from 2 GeV/c represents the smooth cut chosen in order to avoid the loss of signal at high  $p_t$ .

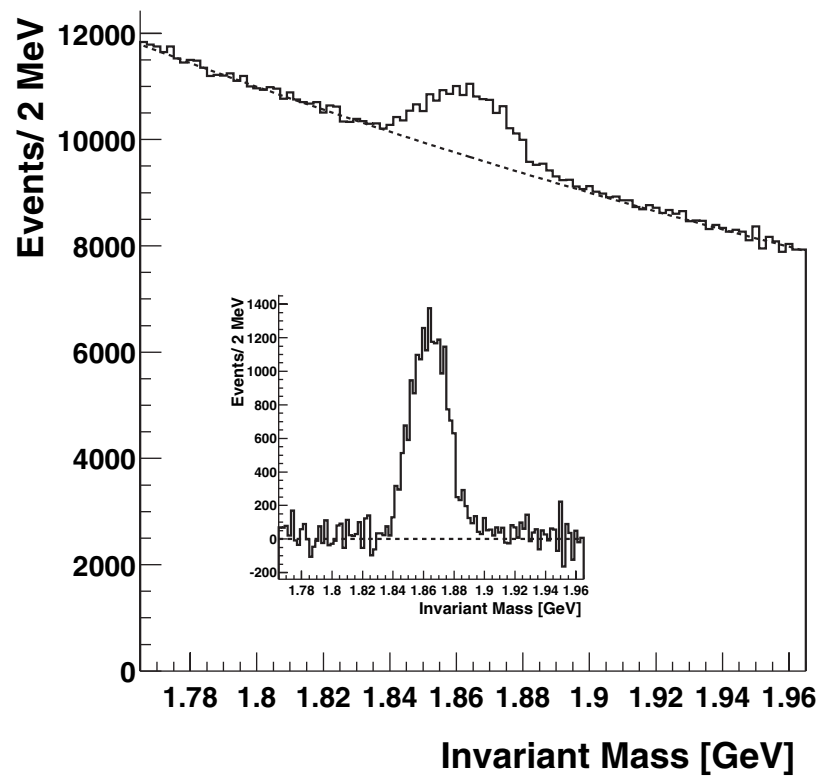
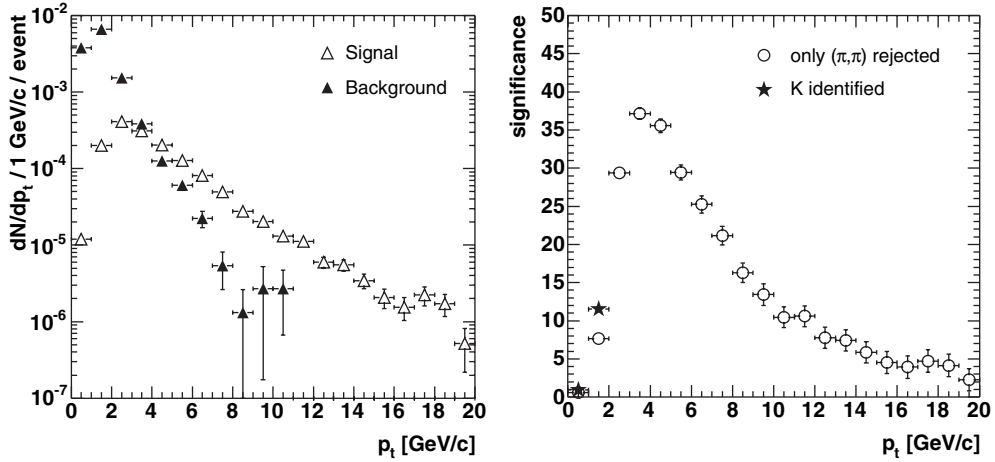


Figure 6.290.  $K\pi$  invariant mass distribution for  $10^7$  events. The same distribution after background subtraction is shown in the inset.

**Table 6.61.** Final values of S/B and  $\sqrt{S+B}$  for  $10^7$  Pb–Pb events.

Sample	S/event	B/event	S/B	$S/\sqrt{S+B}$ ( $10^7$ events)	$\sigma_S/S$
A	$4.4 \times 10^{-4}$	$1.4 \times 10^{-3}$	32%	33	3%
B	$4.3 \times 10^{-4}$	$5.2 \times 10^{-3}$	8%	8	13%
C	$4.6 \times 10^{-4}$	$5.0 \times 10^{-3}$	9%	9	11%
Total	$1.3 \times 10^{-3}$	$1.16 \times 10^{-2}$	11%	37	3%



**Figure 6.291.** Transverse momentum distribution for the signal and for the background after selection (left); the normalization corresponds to one central Pb–Pb event. Corresponding significance for  $10^7$  events as a function of  $p_t$  (right). The full markers show the significance obtained for  $p_t < 2$  GeV/c requiring the identification of the kaon in the Time of Flight.

Considering the sum of the three samples A, B, and C, the  $p_t$ -integrated significance is 37. Figure 6.291 shows the  $p_t$  distribution of the signal and of the background absolutely normalized and the significance as a function of  $p_t$ , in bins of 1 GeV/c. With  $10^7$  events the significance is larger than 10 up to about 12 GeV/c of  $p_t$ . For  $p_t > 4$  GeV/c, the S/B ratio grows but the significance decreases because of the decrease of the signal statistics.

Concerning the distribution of the signal in the three PID classes: sample A covers the low- $p_t$  region, where the kaon can be efficiently identified in the TOF detector; samples B and C, even if their integrated significances are quite low, are essential to cover the high- $p_t$  region above 5 GeV/c.

In general, it is convenient to merge the three samples, which essentially corresponds to rejecting only  $(\pi_{\text{tag}}, \pi_{\text{tag}})$  pairs<sup>20</sup> using the TOF information. However, this strategy gives the quite marginal significance of 8 in the bin  $1 < p_t < 2$  GeV/c. Since for  $p_t < 2$  GeV/c sample A contains most of the signal and only a small fraction of the background, considering only candidates with the kaon identified (sample A) yields a significance of 12 in  $1 < p_t < 2$  GeV/c (as shown by the star markers in the right-hand panel of Fig. 6.291). For this reason, we consider only sample A for candidates with  $p_t < 2$  GeV/c. Figure 6.292 shows the invariant mass distribution for this sample in  $1 < p_t < 2$  GeV/c; even for this low- $p_t$  bin, the signal is well visible over the background.

<sup>20</sup>  $K_{\text{tag}}, K_{\text{tag}}$  pairs and pairs with an identified pion are a small fraction of the total background.

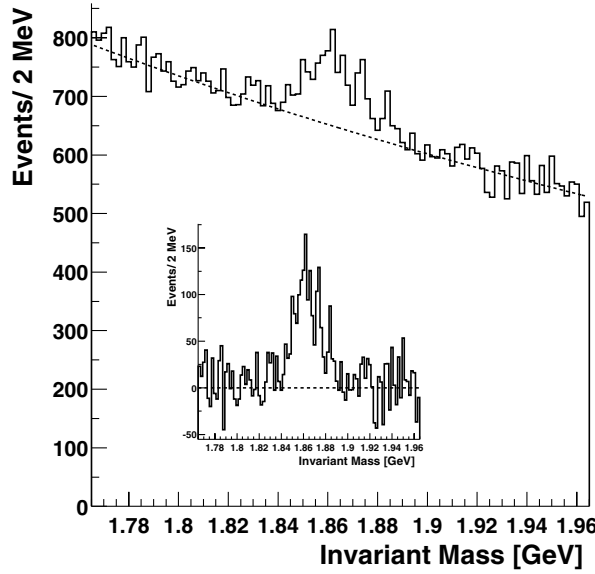


**Figure 6.292.**  $K\pi$  invariant mass distribution in the bin  $1 < p_t < 2 \text{ GeV}/c$  for the sample of candidates with kaon identified in the Time of Flight ( $10^7$  events).

**Table 6.62.** ‘History’ of the  $D^0/D^0$  signal in Pb–Pb events.

Step	S/event
Total produced ( $4\pi$ )	141
Decaying to $K^\mp\pi^\pm$	5.4
With K and $\pi$ in $ \eta  < 0.9$	0.5
With K and $\pi$ reconstructed	0.14
After $(\pi_{\text{tag}}, \pi_{\text{tag}})$ rejection	0.13
After selection cuts (including $\pm 1\sigma$ mass cut)	0.0013

With the choice of parameters we have used for the generation of the signal, the fraction of the transverse momentum distribution for which we have sensitivity ( $p_t > 1 \text{ GeV}/c$ ) corresponds to about 70% of the total  $D^0$  production cross section, at mid-rapidity.

The cuts applied so far, including also the  $\pm 1\sigma$  cut on the invariant mass, reduce the background by a factor  $4 \times 10^{-7}$  and select  $\simeq 1\%$  of the signal we had after track reconstruction. In Table 6.62 we summarize the ‘history’ of the signal, showing the effects of acceptance, reconstruction efficiency, and selection efficiency. These effects are illustrated as a function of transverse momentum and rapidity in Fig. 6.293.

*Results scaled to a lower-multiplicity scenario.* The present analysis assumes a charged-particle rapidity density  $dN_{\text{ch}}/dy = 6000$  at mid-rapidity for the underlying events. According to recent extrapolations of the RHIC data, the multiplicity is more likely to be of the order of  $dN_{\text{ch}}/dy = 3000$  (Section 1.3.1 of PPR Volume I [3]). We have therefore estimated how the results on signal-to-background ratio and significance scale in this scenario.

If  $dN_{\text{ch}}/dy$  decreases, the number of background pairs decreases as  $(dN_{\text{ch}}/dy)^2$ . Therefore,  $S/B$  is proportional to  $(dN_{\text{ch}}/dy)^{-2}$ . The significance is proportional to  $(dN_{\text{ch}}/dy)^{-1}$  if  $S \ll B$ , so that  $S/\sqrt{S+B} \simeq S/\sqrt{B}$ . This condition holds for our  $p_t$ -integrated significance, since we have  $S \simeq B/10$ ; for the  $p_t$ -dependent significance such a scaling can

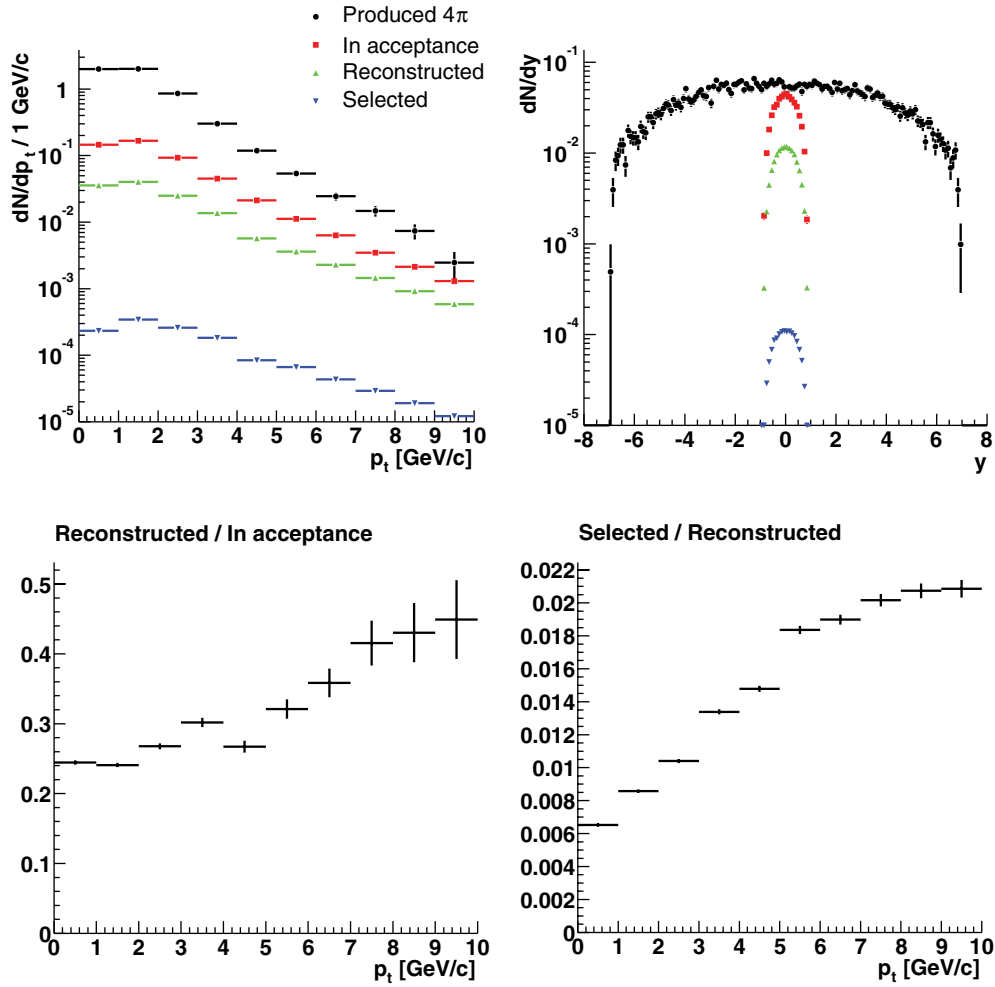


**Figure 6.293.** Upper row: transverse momentum and rapidity distributions for the  $D^0 \rightarrow K^- \pi^+$  signal produced per event, with  $K$  and  $\pi$  in the acceptance of the barrel ( $|\eta| < 0.9$ ), reconstructed, and selected. Lower row: reconstruction and selection efficiencies as a function of  $p_t$ .

be applied only up to  $p_t \simeq 3 \text{ GeV}/c$ , as, for larger transverse momenta, the significance is dominated by the statistics of the signal,  $S/\sqrt{S+B} \simeq \sqrt{S}$ .

The  $p_t$ -integrated results scaled to  $dN_{\text{ch}}/dy = 3000$ , according to the proportionalities mentioned above<sup>21</sup> are  $S/B \simeq 44\%$  and  $S/\sqrt{S+B} \simeq 74$  ( $10^7$  events). In addition, with a lower multiplicity the tracking efficiency would presumably improve and a further improvement can be expected from a refinement of the cuts.

*Feed-down from beauty decays.* In Section 6.6.4.2 we pointed out that, for Pb–Pb collisions at  $\sqrt{s_{\text{NN}}} = 5.5 \text{ TeV}$ , about 5% of all the produced  $D^0$  mesons are expected to come from the decay of  $B$  mesons. After the described selection cuts, the ratio of secondary-to-primary  $D^0$  mesons increases to  $\simeq 12\%$ . Such a result does not match the expectation that the pointing

<sup>21</sup> The production rate is not rescaled because it is not clear how it is correlated with the total multiplicity and because we have used the average of the values given by the different PDFs, which is already a conservative estimate.

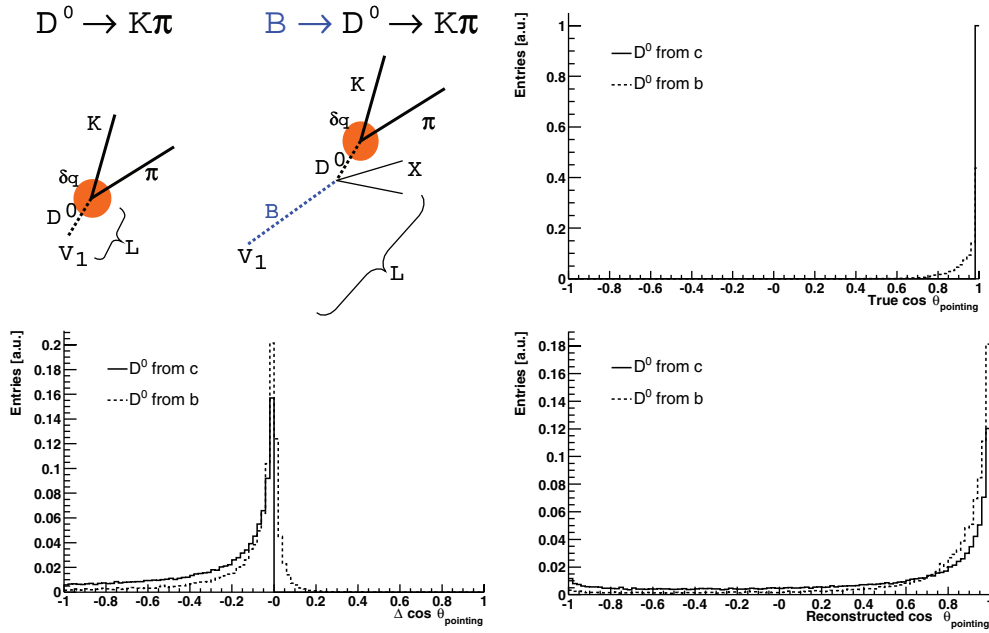


**Figure 6.294.** Sketch of the decay topologies of primary and secondary  $D^0$  mesons (top-left panel). The shaded circle represents the uncertainty  $\delta q \sim 50 \mu\text{m}$  on the reconstructed position of the secondary vertex (see text). Comparison between primary (from c) and secondary (from b)  $D^0$  mesons for true distribution of  $\cos \theta_{\text{pointing}}$  (top-right panel), resolution on  $\cos \theta_{\text{pointing}}$  (bottom-left panel), and reconstructed distribution of  $\cos \theta_{\text{pointing}}$  (bottom-right panel). The cut  $2 < p_t < 3 \text{ GeV}/c$  is applied in order to compare the two signals at the same  $p_t$ .

requirement should suppress the  $D^0$ 's from beauty, as they point to the decay vertex of the B meson and not to the primary vertex. In the following we clarify this issue by analysing how the main selections affect secondary  $D^0$  particles.

- **Pointing angle:** this cut has the effect of *enhancing* the fraction of secondary  $D^0$ 's. In fact, in the decay  $B \rightarrow D^0 + X$ , the  $D^0$  takes most of the momentum of the B meson and, thus, it approximately follows its flight line. Figure 6.294 (top-right panel) shows that the 'true' distribution of  $\cos \theta_{\text{pointing}}$  (generator level) for secondary  $D^0$  mesons is accumulated in the region  $\cos \theta_{\text{pointing}} > 0.9$ . Moreover, the resolution on this variable is better in the case of secondary  $D^0$  particles (Fig. 6.294, bottom-left panel, for  $2 < p_t < 3 \text{ GeV}/c$ ). This is explained by the sketch in Fig. 6.294: at the same value of  $p_t$  the resolution  $\delta q$  on the position of the secondary vertex is the same for primary and secondary  $D^0$  particles, but the resolution on the pointing angle is proportional to  $\delta q/L$ , where  $L$  is the distance of the secondary vertex from the interaction point, which is larger for  $D^0$  from B decays. As a consequence, the reconstructed distribution of  $\cos \theta_{\text{pointing}}$  is more accumulated at 1 for secondary than for primary  $D^0$  particles (Fig. 6.294, bottom-right panel).
- **Product of the impact parameters:** the tracks from the decay  $B \rightarrow D^0 \rightarrow K^- \pi^+$  have larger impact parameters than those from  $D^0 \rightarrow K^- \pi^+$  and the selection  $d_0^K \times d_0^\pi < -40000 \mu\text{m}^2$  *enhances* the fraction of the former in the final sample (Fig. 6.295, left-hand panel).
- **Upper cut on  $d_0$ :** the analysis cut  $|d_0| < 500 \mu\text{m}$ , introduced to reject the background from strange-particle decays, is effective also to *reduce* by  $\simeq 30\%$  the fraction of  $D^0$  from B mesons.

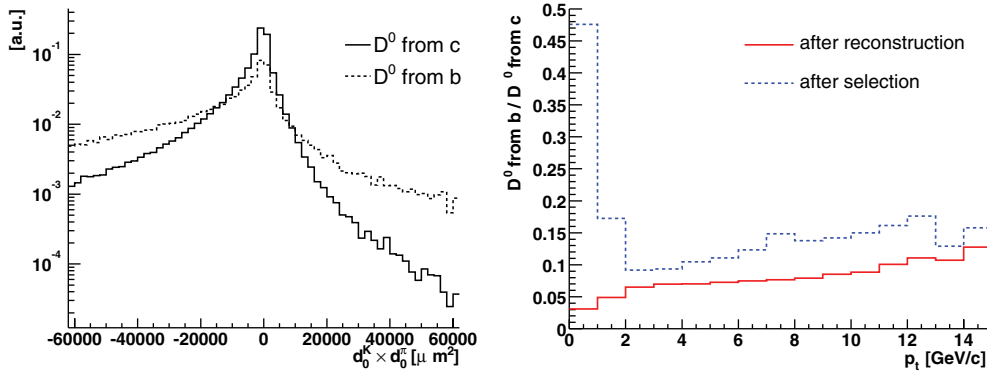


**Figure 6.295.** Distributions of the product of the impact parameters for primary and secondary  $D^0$  mesons, normalized to the same integral (left-hand panel). Ratio of secondary-to-primary  $D^0$  mesons after track reconstruction and after selections, as a function of  $p_T$  (right-hand panel).

The ratio  $(D^0 \text{ from b})/(D^0 \text{ from c})$  is reported in Fig. 6.295 (right-hand panel) as a function of  $p_T$ , after track reconstruction and after selections. The ratio grows with  $p_T$  on account of the harder spectrum of the  $D^0$ 's from beauty. The increase in the fraction of secondary  $D^0$ 's after selections is very large at low  $p_T$  where tighter displaced vertex requirements have to be applied in order to reject the combinatorial background.

**6.6.4.5. Feasibility study in pp collisions at  $\sqrt{S} = 14$  TeV.** In order to estimate the expected performance for the detection of  $D^0 \rightarrow K^- \pi^+$  decays in pp events, we conducted a study following the same general lines as that for the Pb–Pb case. In particular, the same selection strategy was adopted, with cuts on the product of impact parameters and on the pointing angle.

One may expect the significance of the extracted signal to be much higher in pp than in Pb–Pb because the initial S/B ratio is much higher. The S/B ratio is proportional to  $N^{cc}/(dN_{ch}/dy)^2$ ; the charm production yield is lower by a factor about 700 in pp with respect to Pb–Pb (see Table 6.53), but the multiplicity of the background event is lower by a factor 1000 ( $\langle dN_{ch}/dy \rangle \simeq 6$  in pp at 14 TeV with PYTHIA); therefore, the initial S/B is larger by a factor  $\simeq 1500$  in pp collisions. In addition, the detector performance will be better in the very-low-multiplicity environment of pp collisions.

However, the track impact parameter resolution in the bending plane will be worse than in Pb–Pb, because of the larger uncertainty in the position of the primary vertex. As discussed in Sections 2.3 and 2.5 of PPR Volume I [3], for the pp runs the nominal luminosity of  $5 \times 10^{32} \text{ cm}^{-2} \text{ s}^{-1}$ , at the ALICE intersection point, will have to be reduced to  $< 3 \times 10^{30} \text{ cm}^{-2} \text{ s}^{-1}$ , in order to limit the pile-up in the TPC and in the Silicon Drift Detector (SDD). Such a reduction can be achieved in two ways: either by increasing the value of  $\beta^*$  or by displacing the two beams in the transverse plane to collide the tails of the particle distributions. If the first option is chosen, the transverse size of the interaction ‘diamond’ might be broadened up to  $\simeq 150 \mu\text{m}$ . If the second option is necessary, the beams might be displaced to a distance of  $\simeq 4\text{--}5\sigma_{x,y}^{\text{bunch}}$  and the collisions would occur in the tails at  $4\text{--}5\sigma$  from the centre of the beams: these tails will likely be non-Gaussian and the size of the interaction ‘diamond’ may be even larger than  $150 \mu\text{m}$ . It will, therefore, be necessary to reconstruct event-by-event the position of the primary vertex using the tracks. The algorithm developed for this purpose allows a resolution of  $\simeq 60 \mu\text{m}$  for the two coordinates in the bending plane (see Chapter 5 and Ref. [8]). This worsens the  $r\varphi$  impact parameter resolution

by 50% for  $p_t = 1 \text{ GeV}/c$  (from  $60 \mu\text{m}$  to  $90 \mu\text{m}$ ) and by almost 100% for  $p_t = 10 \text{ GeV}/c$ . The disadvantage for the selection of heavy-flavour displaced vertices is clear.

In the following, along with the results for the realistic scenario (indicated as ‘vertex reconstructed’), we present the results for a scenario of perfect knowledge of the vertex position (‘vertex known’). This is done in order to have a situation (‘vertex known’) more directly comparable to the Pb–Pb one and to quantify and understand the weight of the larger uncertainty on the vertex position.

*Background and signal generation.* The magnetic field was set to the same value as for Pb–Pb, 0.4 T. The same settings were also used for the generation of the position of the interaction vertex.

Proton–proton minimum-bias events at a centre-of-mass energy  $\sqrt{s} = 14 \text{ TeV}$  were generated using PYTHIA, as described in Section 4.3.1 of PPR Volume I [3], excluding diffractive events. The average charged-particle rapidity density was  $\langle dN_{\text{ch}}/dy \rangle = 6$ . A total of  $8.5 \times 10^6$  events were used. These events correspond to  $12.1 \times 10^6$  minimum-bias events using  $\sigma_{\text{pp}}^{\text{non-diffr.}}/\sigma_{\text{pp}}^{\text{inel}} = 0.7$  from PYTHIA.

For the generation of the  $D^0$  signal we did not use the same method as in the Pb–Pb case, i.e., generating many  $D^0 \rightarrow K^- \pi^+$  decays in special signal events. In the case of pp collisions, it is essential to have the signal with ‘its own pp event’. In fact, the primary vertex has to be reconstructed event-by-event using the tracks; therefore, the signal events must be pp events with charm.

In order to have a more realistic description of the underlying event, we were forced to generate standard pp events with PYTHIA, with the same settings as for the generation of the background, selecting ‘*a posteriori*’ events that contained a  $D^0$  in  $|y| < 1$  (the decay in the  $K\pi$  channel was forced). The part of these  $D^0$  mesons coming from beauty feed-down was weighted in order to match the correct ratio secondary/primary (Section 6.6.4.2)<sup>22</sup>. We simulated  $2 \times 10^6$  such events, corresponding to  $1.7 \times 10^9$  pp minimum-bias events, using the yields in Table 6.56.

All the results are given for  $10^9$  pp minimum-bias events, corresponding to a run of about eight months.

*Event reconstruction and particle identification.* Track reconstruction was performed in the same way as for the Pb–Pb case, using the parametrisation of the tracking response in the TPC, with a pp-specific tuning, and the Kalman filter in the ITS, where at least five clusters (two in the pixel layers) were required.

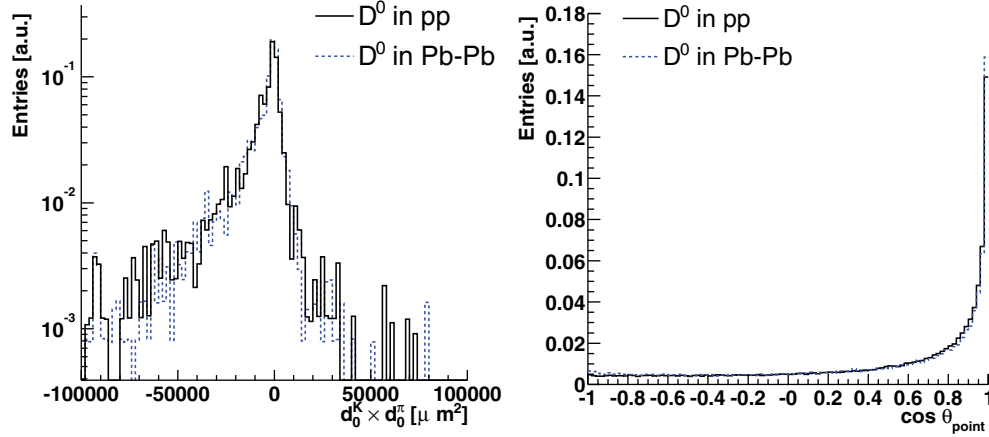
After the tracking, the interaction vertex position was determined by means of the reconstructed tracks, as described in Chapter 5 and in Ref. [8]. In order not to bias the measurement of the impact parameters of the two  $D^0$  decay tracks, for each  $D^0$  candidate the vertex was reconstructed excluding the two tracks belonging to the candidate.

In the low-multiplicity environment of proton–proton collisions, particle identification in the Time of Flight is more efficient, because the probability to match the tracks incorrectly with the TOF pads is much lower. By optimizing for pp collisions the graphical cuts applied on the TOF momentum-versus-mass plane, we succeeded in reducing to 2% the fraction of  $D^0$  signal lost because of mis-tagging of the charged kaon as a pion (this loss is about 10% in Pb–Pb).

<sup>22</sup> The drawback of this method is that the produced  $D^0$  mesons have to be reweighted according to their  $p_t$  in order to reproduce the distributions given by the NLO pQCD calculations. In fact, the settings of PYTHIA necessary to reproduce these distributions cannot be used to generate standard pp events. The  $D^0$  mesons produced in  $c\bar{c}$  and in  $b\bar{b}$  events were reweighted separately, in order to take into account their different  $p_t$  spectra.

**Table 6.63.** Initial statistics for signal and background (in  $M_{D^0} \pm 3\sigma$ ), for pp and Pb–Pb. Sample A + B + C. The ratio Pb–Pb/pp is also reported.

	S/event	B/event	S/B
pp	$2.4 \times 10^{-4}$	$1.1 \times 10^{-1}$	$2.3 \times 10^{-3}$
Pb–Pb	$1.3 \times 10^{-1}$	$2.8 \times 10^4$	$4.5 \times 10^{-6}$
Ratio Pb–Pb/pp	520	$2.6 \times 10^5$	$2 \times 10^{-3}$

**Figure 6.296.** Distribution of the product of impact parameters (left) and of the cosine of the pointing angle (right) for  $D^0$  mesons in Pb–Pb and pp (case ‘vertex known’) events.

*Analysis and results.* The statistics for signal and background after track reconstruction are reported in Table 6.63. Where not otherwise specified, here and in the following we consider the sum of the three samples A, B, and C, as defined in Section 6.6.4.2. Only a  $\pm 3\sigma$  cut on the invariant mass is applied (the invariant mass resolution for the  $D^0$  is 10% better in pp than in Pb–Pb, due to the improved momentum resolution). In the table, along with the values for pp, the corresponding values for Pb–Pb and the ratio between the two are quoted, for comparison. The initial signal-to-background ratio is much larger (about three orders of magnitude) in pp than in Pb–Pb. This is due to the fact that, when going from pp to Pb–Pb, the background, which is combinatorial, increases much more than the signal.

In the following, selection criteria and results are shown first for the case ‘primary vertex known’, and then for the more realistic case ‘primary vertex reconstructed’.

*Scenario 1: ‘primary vertex known’.* In this scenario we assume that the  $(x, y)$  position of the interaction point is known as precisely as in the case of Pb–Pb collisions. The position along  $z$  is measured using the reconstructed tracks with a resolution of  $\sim 100 \mu\text{m}$ . We remark that this might be the case if the machine luminosity is below the nominal value so that beam defocussing or displacements are not necessary at the ALICE interaction point.

In Fig. 6.296 we report the distributions of the two main variables for the selection,  $d_0^K \times d_0^\pi$  and  $\cos\theta_{\text{pointing}}$ , for the signal in Pb–Pb and in pp. Both distributions have a similar shape in the two cases. This is not surprising for the product of the impact parameters, since it is shown in Chapter 5 and Ref. [32] that the track position resolution is the same for Pb–Pb and pp events and we are assuming the same resolution on the primary vertex in the bending plane. In the case of the pointing angle one may expect the resolution in pp to be spoiled by

**Table 6.64.** Final value of the cuts in the different  $p_t$  bins for pp (case ‘vertex reconstructed’).

Cut name	$p_t < 1 \text{ GeV}/c$	$1 < p_t < 2 \text{ GeV}/c$	$2 < p_t < 3 \text{ GeV}/c$	$3 < p_t < 5 \text{ GeV}/c$	$p_t > 5 \text{ GeV}/c$
$dca$	$< 400 \mu\text{m}$	$< 300 \mu\text{m}$	$< 200 \mu\text{m}$	$< 200 \mu\text{m}$	$< 200 \mu\text{m}$
$ \cos\theta^* $	$< 0.8$	$< 0.8$	$< 0.8$	$< 0.8$	$< 0.8$
$K, \pi p_t$	$> 500 \text{ MeV}/c$	$> 600 \text{ MeV}/c$	$> 700 \text{ MeV}/c$	$> 700 \text{ MeV}/c$	$> 700 \text{ MeV}/c$
$K, \pi  d_0 $	$< 500 \mu\text{m}$	$< 500 \mu\text{m}$	$< 500 \mu\text{m}$	$< 500 \mu\text{m}$	$< 500 \mu\text{m}$
$d_0^K \times d_0^\pi$	$< -20000 \mu\text{m}^2$	$< -20000 \mu\text{m}^2$	$< -20000 \mu\text{m}^2$	$< -10000 \mu\text{m}^2$	$< -5000 \mu\text{m}^2$
$\cos\theta_{\text{pointing}}$	$> 0.5$	$> 0.6$	$> 0.8$	$> 0.8$	$> 0.8$

**Table 6.65.** Final values of S/B and significance for pp and Pb–Pb.

System	S/event	B/event	S/B	$S/\sqrt{S+B}$	$\sigma_S/S$
pp ( $10^9$ events) vertex known	$2.1 \times 10^{-5}$	$4.1 \times 10^{-5}$	50%	84	1%
pp ( $10^9$ events) vertex reconstructed	$1.5 \times 10^{-5}$	$12.4 \times 10^{-5}$	12%	39	3%
Pb–Pb ( $10^7$ events)	$1.3 \times 10^{-3}$	$1.16 \times 10^{-2}$	11%	37	3%

the fact that the  $z$  position of the primary vertex is known with a resolution of  $100 \mu\text{m}$ , with respect to  $6 \mu\text{m}$  in Pb–Pb. However, this difference does not significantly affect the pointing angle resolution, since the dominant contribution to it comes from the position resolution of the secondary vertex, which is of  $\sim 70 \times 70 \times 120 \mu\text{m}^3$  in the three perpendicular directions for a  $D^0$  with  $p_t \simeq 2 \text{ GeV}/c$ .

The cuts were tuned in order to maximize the significance, in different  $p_t$  bins. The numerical values are omitted here for brevity. We remark, however, that, as a consequence of the better initial S/B ratio, the cuts on impact parameters and pointing angle are much less tight than in the Pb–Pb case. In addition, the cut on the maximum absolute value of  $d_0$  is not necessary. As in Pb–Pb, a smooth  $p_t$ -dependent cut for the product of the impact parameters was used.

The final statistics are shown in the first row of Table 6.65: the integrated S/B ratio is 50% and the significance for  $10^9$  pp minimum-bias events is 84. The lower  $p_t$  limit is  $\simeq 0$ , with a significance of 17 for  $0 < p_t < 1 \text{ GeV}/c$  if the K identification in the TOF is required.

*Scenario 2: ‘primary vertex reconstructed’.* We now consider the scenario in which the information on the vertex position in the transverse plane given by the position and size of the proton beams is very poor ( $\sim 150 \mu\text{m}$ ). Since this uncertainty is larger than the track position resolution given by the pixels and the mean impact parameter of the decay products of  $D^0$  mesons is  $\sim 100 \mu\text{m}$ , it is clear that, without a primary vertex reconstruction, it is impossible to separate the decay vertex from the interaction point. Figure 6.297 shows the distribution of the product of impact parameters in the three cases ‘vertex known’ (labeled  $\sigma(\text{vtx}) = 15 \mu\text{m}$ ), ‘vertex unknown’ (labeled  $\sigma(\text{vtx}) = 150 \mu\text{m}$ ) and ‘vertex reconstructed’ (labeled vtx reconstructed); two  $p_t$  bins are considered:  $1\text{--}2 \text{ GeV}/c$  (left) and  $5\text{--}7 \text{ GeV}/c$  (right). In the case ‘vertex unknown’, at low  $p_t$  the distributions of signal and background have exactly the same shape and even at high  $p_t$ , where the effect of multiple scattering is negligible, the difference is very tiny. After the reconstruction of the vertex using the method specifically developed for this purpose, described in Chapter 5 and Ref. [8], we obtain the distributions reported in the lower panels of the figure. Now a cut at  $d_0^K \times d_0^\pi < -20000 \mu\text{m}^2$  allows the S/B ratio to be improved even at very low  $p_t$ .

All the cuts were re-optimised and are shown in Table 6.65. The cut  $|d_0| < 500 \mu\text{m}$ , already used in Pb–Pb, was reintroduced in order to reduce the feed-down from B meson

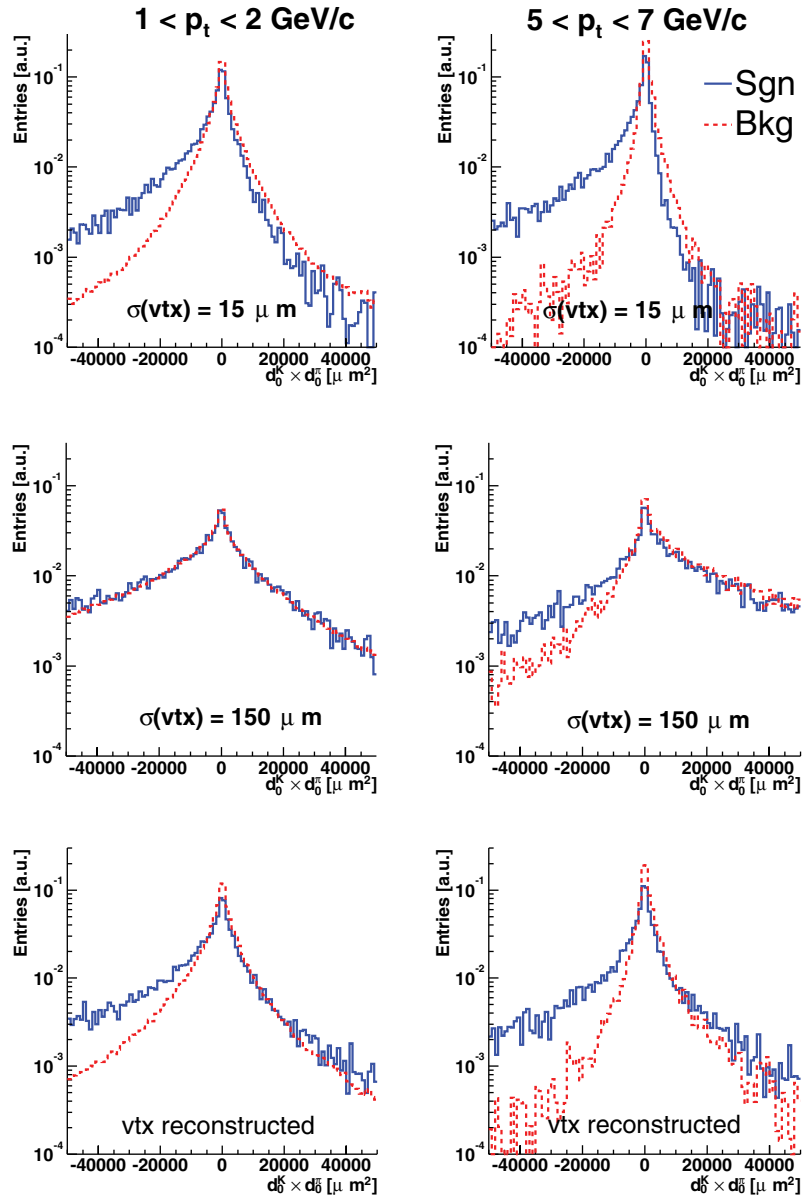


**Figure 6.297.** Distribution of the product of impact parameters for ‘vertex known’ (top), ‘vertex unknown’ (centre) and ‘vertex reconstructed’ (bottom).

decays. The final statistics for the realistic scenario with interaction vertex reconstruction are given in Table 6.65.

The larger uncertainty on the position of the interaction point in the case ‘vertex reconstructed’ obviously has a dramatic effect on the performance for the detection of  $D^0 \rightarrow K^- \pi^+$  decays: the background increases by a factor about 4 and, consequently, the S/B ratio and the significance go down by factors 4 and 2, respectively, relative to the case with small and well-defined interaction region. The additional cut on  $|d_0|$  reduces the signal

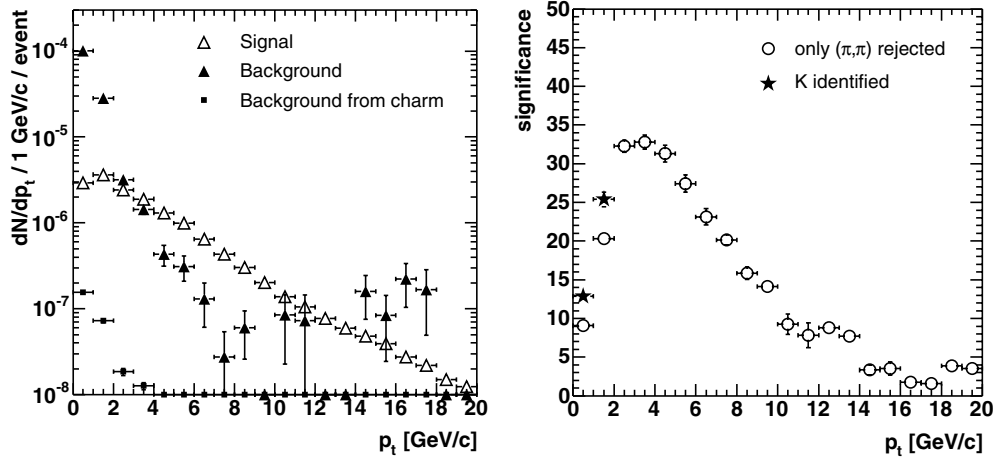


**Figure 6.298.** Transverse-momentum distribution for the signal and for the background after selection (left); the normalization corresponds to one pp minimum-bias event. Corresponding significance for  $10^9$  events as a function of  $p_t$  (right). The full markers show the significance obtained for  $p_t < 2 \text{ GeV/c}$  requiring the identification of the charged kaon in the Time of Flight.

by 25% but it is necessary to bring the ratio ( $D^0$  from b)/( $D^0$  from c) from 16% to 11%, after selections.

In Fig. 6.298 (left) we report the transverse-momentum distributions for signal and background. The background with a track from charm, also shown, is negligible. The right-hand panel of the same figure reports the significance as a function of  $p_t$ : the method developed for the vertex reconstruction allows one to maintain the capability of ALICE to measure charm mesons down to essentially 0 in  $p_t$ : the significance is 14 for  $0 < p_t < 1 \text{ GeV/c}$  if the charged kaon identification in the TOF is required. For larger transverse momenta, the significances are very close to those obtained in the Pb–Pb case.

The cuts applied, including a  $\pm 1\sigma$  cut on the invariant mass, select 6% of the signal.

**6.6.4.6. Feasibility study in pPb collisions at  $\sqrt{s_{NN}} = 8.8 \text{ TeV}$ .** The case of minimum-bias pPb events is similar to that of pp events in the scenario ‘primary vertex known’. Here again we used the simple approach of adapting the strategy developed for Pb–Pb collisions. The average charged multiplicity per unit of rapidity is taken to be  $\langle dN_{ch}/dy \rangle \simeq 18$  (as given by the HIJING event generator), i.e. only a factor about three larger than that expected for pp events at  $\sqrt{s} = 14 \text{ TeV}$ . Therefore, the detector performance (track reconstruction and particle identification) is taken to be the same as in pp events. During the proton–nucleus runs, the interaction ‘diamond’ at the ALICE intersection point will have transverse dimensions of  $\sigma_x = \sigma_y \simeq 15 \mu\text{m}$ . Therefore, the position of its centre will be precisely measured by averaging over all events in a given machine fill, and the uncertainty on the event-by-event primary vertex position will be determined by the beam spread. The three coordinates of the primary vertex can be determined for each event from the reconstructed tracks using the same algorithm as for pp events. The average resolutions were found to be  $\approx 45 \mu\text{m}$  for  $x$  and  $y$ , and  $\approx 65 \mu\text{m}$  for  $z$ , for a sample of minimum-bias pPb events generated with HIJING.

The simulation study was performed using again a magnetic field of 0.4 T. Signal and background events were generated separately, as in the Pb–Pb and pp cases.  $10^6$  signal events, each containing 25  $D^0/\overline{D^0}$  particles in  $|y| < 1$  and forced to decay in the  $K^\mp \pi^\pm$  channel, were

**Table 6.66.** Initial statistics for signal and background (in  $M_{D^0} \pm 3\sigma$ ) for pPb. Sample A + B + C.

S/event	B/event	S/B
$1.1 \times 10^{-3}$	$6.3 \times 10^{-1}$	$1.7 \times 10^{-3}$

**Table 6.67.** Final values of S/B and significance for pp, pPb and Pb–Pb.

System	S/event	B/event	S/B	$S/\sqrt{S+B}$	$\sigma_S/S$
pp ( $10^9$ events) vertex reconstructed	$1.5 \times 10^{-5}$	$12.4 \times 10^{-5}$	12%	39	3%
pPb ( $10^8$ events)	$2.4 \times 10^{-4}$	$5.4 \times 10^{-3}$	4%	32	3%
Pb–Pb ( $10^7$ events)	$1.3 \times 10^{-3}$	$1.16 \times 10^{-2}$	11%	37	3%

generated with PYTHIA. The detector occupancy for these events is the same as for a typical pPb event generated with HIJING. We used  $2 \times 10^6$  background events.

The response of track reconstruction in the TPC was parametrized, as well as the particle identification probabilities in the TOF detector. In both cases, the same parameters as for pp events were used. The geometry of the beam-pipe and of the six ITS layers was fully simulated, and the parametrized tracks from the TPC were prolonged in the ITS using the Kalman filter, with the usual requirement of at least fine clusters (two in the pixel layers) per track.

The initial statistics for signal and background after track reconstruction are reported in Table 6.66.

The final values of the cuts, tuned as a function of the  $D^0$  transverse momentum in order to maximize the statistical significance, are basically the same as for the pp case (see Table 6.64). A dedicated study of the correlation between the topological cuts and the PID-based selection has demonstrated that, for  $p_t \lesssim 1 \text{ GeV}/c$ , requiring the charged kaon identification in the TOF (candidates in sample A), before applying any topological cut, allows most of the background and only a small fraction of the signal to be rejected. This strategy yields a large significance, that further topological cuts do not improve much. In future studies we plan to test it also for pp and Pb–Pb events. In Table 6.67 we show the final  $p_t$ -integrated statistics, signal-to-background, and the significance corresponding to  $10^8$  minimum-bias events that we expect to collect in a one-month pPb run at the LHC.

*6.6.4.7. Dependence of the results on the value of the magnetic field.* The width of the  $D^0$  invariant mass peak is roughly proportional to the momentum resolution and, consequently, the integral B of the background under the peak is also proportional to it. Since the momentum resolution is proportional to  $1/B$  [409] (we use here the notation  $B$  for the magnetic field to distinguish it from the background B), the extrapolation of the results to  $B = 0.2 \text{ T}$  is straightforward: the background would be larger by a factor 2.

The S/B ratio would be lower by a factor 2:  $\simeq 6\%$  for Pb–Pb and pp, and  $\simeq 2\%$  for pPb. The  $p_t$ -integrated significance ( $\simeq S/\sqrt{B}$ ) would be lower by a factor  $\sqrt{2}$ :  $\simeq 30$  for Pb–Pb and pp,  $\simeq 24$  for pPb. The low- $p_t$  limit would not be much affected: a significance of 10 for the bin 1–2 GeV/ $c$  in Pb–Pb and for the bin 0–1 GeV/ $c$  in pp gives a statistical error of 10%, which may still be acceptable. At high- $p_t$  the significance does not depend on the magnetic field, since the background is negligible. However, the worse  $p_t$  resolution might increase the systematic uncertainties in the determination of the shape of the  $D^0$   $p_t$ -differential cross section.

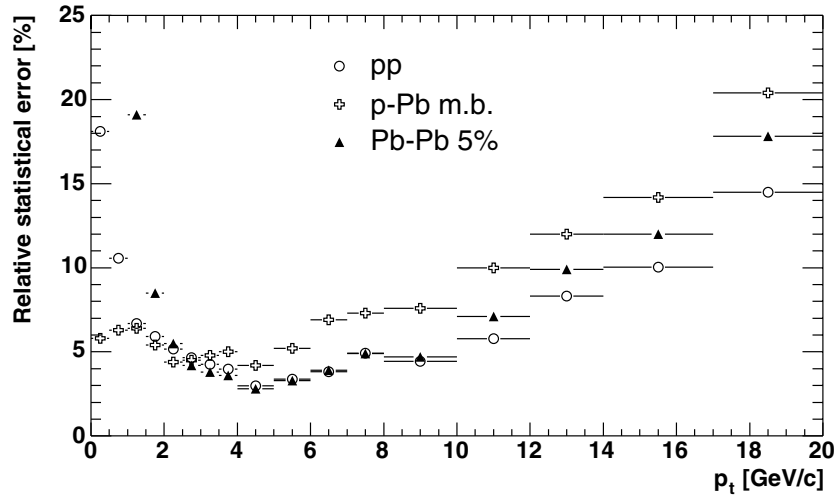


**Figure 6.299.** Relative statistical errors on the  $D^0$   $p_t$  distribution for  $10^9$  pp events,  $10^8$  minimum-bias pPb events and  $10^7$  central Pb–Pb events. In Pb–Pb, for  $p_t < 1$  GeV/ $c$  the error is larger than 50%; these first two bins are not considered in the following analyses.

#### 6.6.4.8. Uncertainties on the $D^0$ cross section measurement

*Statistical uncertainties.* The relative statistical error,  $\sigma_S/S$ , on the number of reconstructed  $D^0$  candidates, in a given  $p_t$ -bin and for a given number of events, is equal to the inverse,  $\sqrt{S+B}/S$ , of the statistical significance, as long as the statistical error on the estimated background  $B$  is small relative to that on the  $S+B$  sum in the  $D^0$  invariant mass region (this is, for example, the case if the background is estimated from a fit on large side-bands of the invariant mass distribution, e.g.  $4\sigma < |M - M_{D^0}| < 10\sigma$ ).

We fitted the reconstructed  $p_t$  distributions for signal and background, presented in Figs. 6.291 and 6.298 for the Pb–Pb and pp cases, to remove the large fluctuations at high  $p_t$  due to the limited statistics of the background in the simulations. We then optimised the  $p_t$ -binning in order to have a significance larger than 5, i.e. statistical error lower than 20%, up to 20 GeV/ $c$ .

Figure 6.299 shows the relative statistical errors  $\sigma_S/S$  for Pb–Pb ( $10^7$  central events), pp ( $10^9$  events), and pPb ( $10^8$  minimum-bias events) collisions. We have  $\sigma_S/S < 15$ –20% up to  $p_t \simeq 20$  GeV/ $c$ .

*Systematic uncertainties.* The number  $S$  of selected signal  $D^0$ , estimated from the fit, will have to be corrected for efficiency and acceptance in order to obtain the total and  $p_t$ -differential yields, or the cross sections, for  $D^0$  production per event. A number of corrections are applied and, in principle, each of them introduces a systematic error. A correction consists, essentially, in multiplying  $S$  by a certain factor:  $S(\text{corrected}) = C \times S(\text{non-corrected})$ ; the systematic error introduced is  $\delta C \times S(\text{non-corrected})$ , where  $\delta C$  is the error on the correction factor  $C$ . In Table 6.68 we list the main corrections and the expected systematic errors that are introduced.

The corrections for tracking and PID efficiency and for acceptance will be calculated by embedding of Monte Carlo signal candidates in real events, at the level of detector raw data. The non-perfect description in the simulation of the geometry and of the physics processes

**Table 6.68.** Main corrections and related systematic errors.

Correction	Systematic error
1) Extrapolation from TOF PID to perfect PID	Matching and PID efficiencies and contaminations in the TOF
2) Feed-down from beauty	Uncertainty on $b\bar{b}$ production at LHC
3) Reconstruction efficiency	Tracking efficiencies and resolutions
4) Acceptance	Geometrical detector acceptance
5) From $D^0 \rightarrow K^- \pi^+$ to $D^0 \rightarrow X$	Error on branching ratio $D^0 \rightarrow K^- \pi^+$
6) Cross section normalization	Pb–Pb: error on centrality selection and number of binary collisions pp: error on inelastic cross section

that determine the detector response introduces systematic uncertainties (entries 1, 3 and 4 in Table 6.68). These uncertainties can, for instance, be estimated by investigating the stability of the results for different sets of selection cuts. It is reasonable to assume that they will initially amount to about 10%. However, we remark that experience from other experiments shows that this kind of systematic error can be reduced after a few years of running as the understanding of the detector response improves.

The error on the branching ratio of the  $D^0$  to the  $K^- \pi^+$  channel (entry 5 in Table 6.68) is quite small, 2.4% [409], and it is essentially negligible with respect to the errors from other sources. It is included for completeness.

After the selections, the number of primary  $D^0$  particles will be determined as  $N^{c \rightarrow D^0} = N^{D^0} - N^{b \rightarrow B \rightarrow D^0}$ , where  $N^{D^0}$  is the total number of selected  $D^0$  particles and  $N^{b \rightarrow B \rightarrow D^0}$  is the amount of feed-down from beauty that will be estimated via Monte Carlo. The systematic error introduced by this correction is equal to the error on the estimated number of  $D^0$  mesons from beauty that pass the selection cuts,  $N^{b \rightarrow B \rightarrow D^0}$ . The relative error on  $N^{b \rightarrow B \rightarrow D^0}$  is essentially equal to the relative error on the  $b\bar{b}$  production cross section,  $\sigma^{b\bar{b}}$ , at LHC energy and, thus, the relative error on  $N^{c \rightarrow D^0}$  is equal to the relative error on  $\sigma^{b\bar{b}}$  multiplied by the ratio of secondary-to-primary  $D^0$ 's, after selections. Such ratio, as obtained with the present baseline on charm and beauty production, has been shown in Fig. 6.259, for Pb–Pb, and it amounts to about 10% on average. It is very similar also for pp and pPb. At present, the  $b\bar{b}$  cross section at LHC energies is estimated by pQCD calculations at NLO with a very large theoretical uncertainty,  $\simeq 80\%$ , as we have reported in Section 6.6.3. We assume here this large relative error. This is an overestimate, since B meson production will be measured by ALICE, in the semi-leptonic decay channels (see Sections 6.6.7 and 6.6.8), and also by ATLAS and CMS. However, it is not yet clear how precise these measurements can be, especially at low  $p_t$ . Multiplying the two factors, 10% (ratio of selected secondary-to-primary  $D^0$ ) and 80% (relative uncertainty on  $\sigma^{b\bar{b}}$ ), we obtain an average relative error arising from the correction for beauty feed-down of about 8%. Recently, the CDF Collaboration has directly estimated the fraction of primary  $D^0$ 's using the distance of the reconstructed  $D^0$  flight line to the interaction vertex as a variable to separate primary and secondary  $D^0$ 's [815]. This technique allows them to correct for the feed-down with a systematic error as low as 3–5%. A study on the possibility of using the same technique in ALICE is currently being carried out.

In proton–proton collisions, the cross section for  $D^0$  production, which is necessary for example for the comparison with pQCD calculations, can be determined by multiplying the estimated number  $N_{pp}^{D^0}$  of (primary)  $D^0$ 's produced per inelastic event by the inelastic pp cross section at  $\sqrt{s} = 14$  TeV:

$$\sigma_{pp}^{D^0} = N_{pp}^{D^0} \times \sigma_{pp}^{\text{inel}}. \quad (6.135)$$

**Table 6.69.** Expected relative uncertainties for the measurement of  $d\sigma_{\text{NN}}^{\text{D}^0}/dy$  in  $|y| < 1$  and  $p_t > p_t^{\text{min}}$ .

System	Pb–Pb $p_t^{\text{min}} = 1 \text{ GeV}/c$	pp $p_t^{\text{min}} = 0.5 \text{ GeV}/c$	pPb $p_t^{\text{min}} = 0.5 \text{ GeV}/c$
<b>Statistical error</b>	<b>7%</b>	<b>3%</b>	<b>2%</b>
<b>Systematic error</b>	<b>17%</b>	<b>14%</b>	<b>16%</b>
Correction for b feed-down	9%	8%	8%
Monte Carlo corrections	10%	10%	10%
Branching ratio	2%	2%	2%
Cross section normalization	9%	5%	9%

The pp cross section will be measured at the LHC by the TOTEM experiment [839] with an expected precision of about 5%. Therefore, the normalization of  $\text{D}^0$  production to pp inelastic collisions will contribute a systematic error of  $\simeq 5\%$ , of course independent of  $p_t$ .

In the case of central nucleus–nucleus collisions, the  $\text{D}^0$  production cross section per binary NN collision can be obtained as

$$\sigma_{\text{NN}}^{\text{D}^0} = N_{\text{AA}}^{\text{D}^0} / R(b_c), \quad (6.136)$$

where  $R(b_c)$ , defined in Eq. (6.129), is essentially the average number of binary NN collisions in a AA collision with impact parameter  $b < b_c$ , divided by the inelastic NN cross section. Two sources contribute to the error on  $R(b_c)$ :

1. Error on the centrality selection, i.e., on the determination of the upper limit  $b_c$  ( $\simeq 3.5$  fm) in impact parameter for the class of most central Pb–Pb collisions (5% of the total cross section). The impact parameter is measured in ALICE by means of the Zero Degree Calorimeters, which are expected to provide a relative precision  $\delta b/b \simeq 30\%$  for  $b < 3\text{--}4$  fm (Section 6.1). The upper limit will be, therefore, determined as  $b_c = (3.5 \pm 1.0)$  fm, which gives  $R(b_c) = (27 \pm 2) \text{ mb}^{-1}$  (from Fig. 6.266, right panel). The relative error on  $R(b_c)$  and on  $\sigma_{\text{NN}}^{\text{D}^0}$  from this source is then  $2/27 \simeq 8\%$ .
2. Uncertainty on the parameters of the Woods–Saxon nuclear density profile. These uncertainties are of order 5% [128].

Combining these two contributions we obtain an overall normalization error of about 9% for central Pb–Pb collisions. For this document, we assume the same normalization error of 9% also for pPb collisions.

The total systematic error, obtained as a quadratic sum of the single contributions, amounts to 16–17% for the Pb–Pb and pPb cases and 14–15% for the pp case. However, we remark that (a) some of the systematic errors do not affect the shape of the  $p_t$  distributions (uncertainty on branching ratio and normalization errors) and (b) many of them are common to Pb–Pb and pp and will cancel in the ratio (correction for b feed-down, branching ratio, uncertainty on NN cross section and, partially, Monte Carlo corrections, e.g. acceptance).

*Errors on  $d^2\sigma^{\text{D}^0}/dp_t dy$  and  $d\sigma^{\text{D}^0}/dy$ .* Figure 6.300 presents the distributions of  $d^2\sigma_{\text{NN}}^{\text{D}^0}/dp_t dy$  in  $|y| < 1$  with the estimated statistical (inner) and quadratic sum of statistical and  $p_t$ -dependent systematic (outer) error bars. A normalization error of 9% for Pb–Pb, 9% for pPb, and 5% for pp is not included in the error bars, as it will not affect the shape of the transverse-momentum distribution.

The expected relative uncertainties for the measurement of the  $\text{D}^0$  production cross section per unit of rapidity, integrated over  $p_t > p_t^{\text{min}} = 1 \text{ GeV}/c$  for Pb–Pb and  $p_t > p_t^{\text{min}} = 0.5 \text{ GeV}/c$  for pp and pPb, are reported in Table 6.69. The statistical uncertainty was obtained

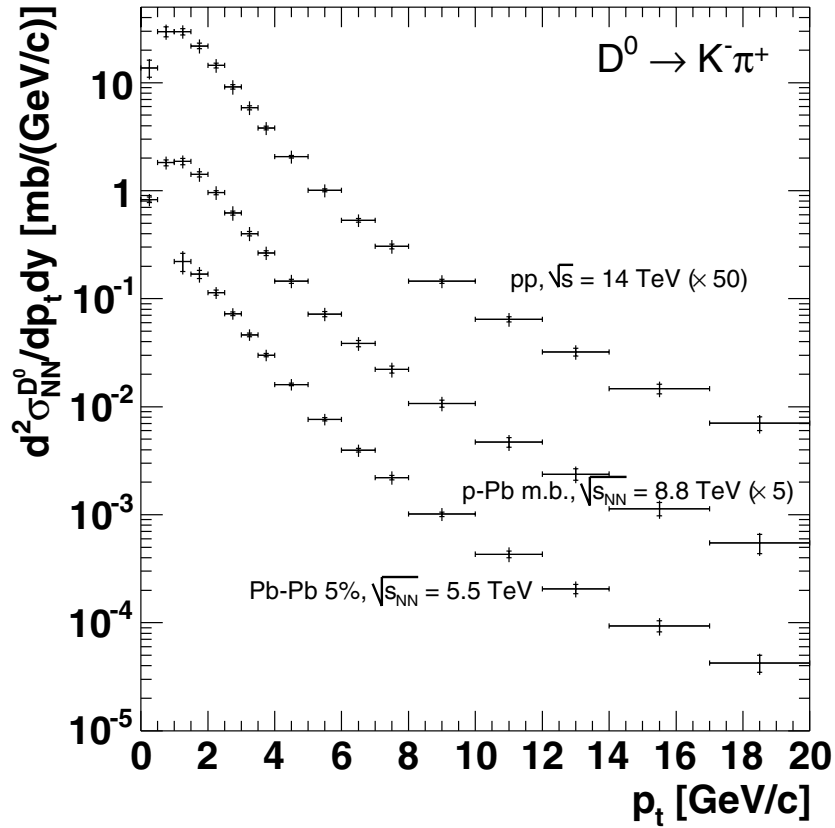


**Figure 6.300.**  $p_t$ -differential cross section per nucleon–nucleon collision for  $D^0$  production, as it can be measured with  $10^7$  central Pb–Pb events, corresponding to one month of data-taking,  $10^8$  minimum-bias pPb events, corresponding to one month of data-taking, and  $10^9$  pp minimum-bias events, corresponding to eight months of data-taking. Statistical (inner bars) and quadratic sum of statistical and  $p_t$ -dependent systematic errors (outer bars) are shown. A normalization error of 9% for Pb–Pb, 9% for pPb, and 5% for pp is not shown.

as a quadratic sum of the statistical errors of the  $p_t$ -bins for  $p_t > p_t^{\min}$ . The single contributions to the systematic uncertainty were obtained as a linear sum over the  $p_t$ -bins and they were then added in quadrature to get the total systematic uncertainty.

Concerning the pp result, we remark that, with statistical and systematic errors of 3% and 14%, and  $p_t^{\min} = 0.5$  GeV/ $c$ , the reconstruction of  $D^0 \rightarrow K^- \pi^+$  decays in ALICE will probably provide the most precise measurement of the total charm production cross section at LHC energy. For comparison, the CDF Collaboration has recently measured  $D^0$  production in  $p\bar{p}$  collisions at the Tevatron,  $\sqrt{s} = 1.96$  TeV, with similar uncertainties, 1.5% statistical and 11% systematic, but with a much higher low- $p_t$  cut-off,  $p_t^{\min} = 5.5$  GeV/ $c$  [815].

**6.6.5. Perspectives for the study of charm quenching.** In this section we investigate the possibility of using the exclusive reconstruction of  $D^0 \rightarrow K^- \pi^+$  decays to perform a comparative study of the quenching of charm quarks and massless partons. Such study could be carried out by measuring:

- the nuclear modification factor of D mesons as a function of transverse momentum,  $R_{AA}^D(p_t)$ , defined in Eq. (6.110);

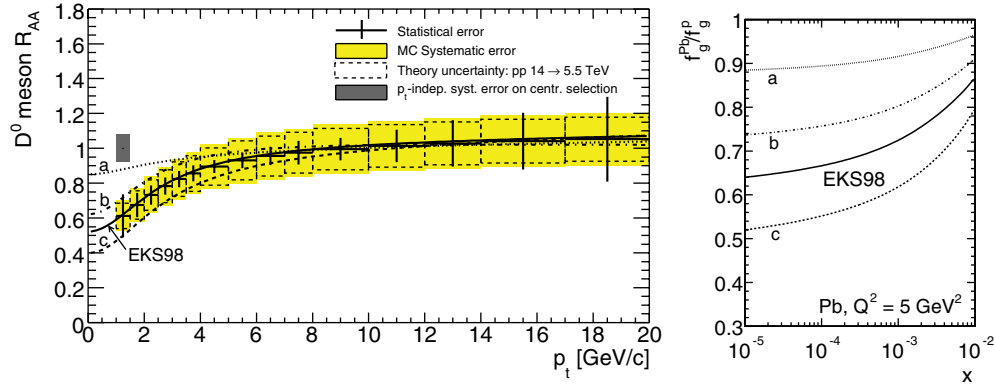


**Figure 6.301.** The  $R_{AA}$  of  $D^0$  mesons, without energy loss (left-hand panel). Different nuclear modifications of the gluon PDF (right-hand panel) —the valence and sea quark PDFs were also changed accordingly.

- the heavy-to-light ratio,  $R_{D/h}(p_t)$ , defined in Eq. (6.115) as the ratio of the nuclear modification factors of D mesons and of charged light-flavoured hadrons.

This study was originally described in Refs. [53, 840]. Here we update those results, using the most recent theoretical predictions for the effect of parton energy loss on the observables  $R_{AA}^D$  and  $R_{D/h}$  [802].

The expected performance for the measurement of the nuclear modification factor for  $D^0$  mesons is reported in Fig. 6.301 (left-hand panel). Only nuclear shadowing and parton intrinsic transverse-momentum broadening are included (no energy loss). The reported statistical (bars) and systematic (shaded areas) errors are obtained combining the errors for Pb–Pb and pp collisions and assuming that the contributions due to cross section normalization, feed-down from beauty decays and, partially, acceptance/efficiency corrections will cancel out in the ratio. The uncertainty of about 12% introduced in the extrapolation of the pp results from 14 TeV to 5.5 TeV by pQCD, as shown in Fig. 6.266, is also reported.

The effect of shadowing, included via the EKS98 parametrisation [779], is visible as a suppression of  $R_{AA}$  at low transverse momenta, corresponding to small Bjorken  $x$ . As estimated in Section 6.6.3.3, the effect is negligible for  $p_t > 6\text{--}7\text{ GeV}/c$ . Since there is significant uncertainty on the magnitude of shadowing in the low- $x$  region, we studied the effect of such uncertainty on  $R_{AA}$  by varying the nuclear modification of parton distribution functions. In Fig. 6.301 (right-hand panel) we show different modifications of the gluon PDF in a Pb nucleus at the scale  $Q^2 = 5\text{ GeV}^2 \simeq (2m_c)^2$ —the valence and sea quark PDFs were changed accordingly—and the resulting  $R_{AA}$  (curves in the left-hand panel). Also in the case of shadowing 50% stronger than in EKS98 (curve labelled ‘c’), we find  $R_{AA} > 0.93$  for  $p_t > 7\text{ GeV}/c$ . Under these assumptions, for  $p_t > 7\text{ GeV}/c$  only parton energy loss is expected to affect the nuclear modification factor of D mesons.

Figure 6.302 presents the predicted [802] nuclear modification factor without ( $\hat{q} = 0$ ) and with energy loss (the bands correspond to the range  $25 < \hat{q} < 100\text{ GeV}^2/\text{fm}$ ). The effect of the charm mass on energy loss is included for the thick-line band ( $m_c = 1.2\text{ GeV}$ ) and not included for the thin-line band ( $m_c = 0$ ). The small difference between the two bands indicates that, with respect to energy loss, charm behaves essentially as a massless quark. The rapid increase of  $R_{AA}$  as  $p_t \rightarrow 0$  is due to the fact that, in the calculation adopted in Ref. [802], the charm quarks that lose most of their initial energy in the medium are assumed to thermalize and give a component with a steeply falling spectrum at low  $p_t$ .

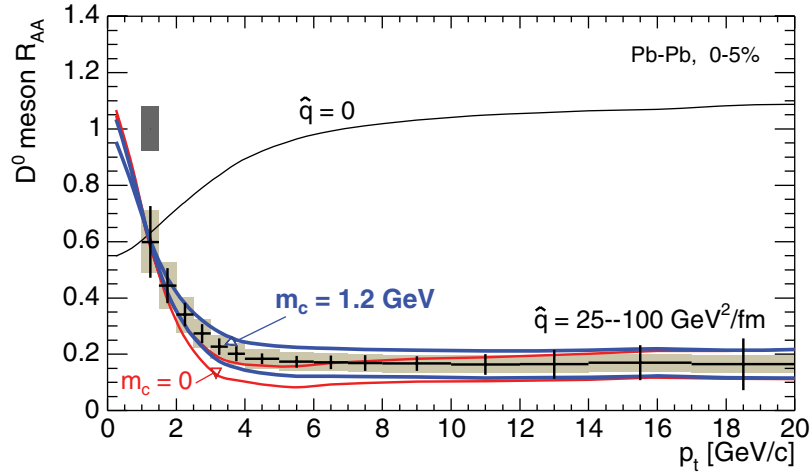


**Figure 6.302.** Nuclear modification factor for  $D^0$  mesons with shadowing, intrinsic  $k_t$  broadening and parton energy loss. The two bands represent theoretical predictions with and without the effect of the charm mass in the energy loss for the medium transport coefficient range = 25–100  $\text{GeV}^2/\text{fm}$  [802]. Errors corresponding to the centre of the prediction band for  $m_c = 1.2 \text{ GeV}$  are shown: bars = statistical, shaded area = systematic. The normalization error is shown by the box at  $R_{AA} = 1$ .

The estimated uncertainties for the measurement of this observable are reported here for the case *with* energy loss. The bars represent the statistical errors, while the shaded areas represent the quadratic sum of the systematic error from Monte Carlo corrections and that from the  $\sqrt{s}$  extrapolation of the pp measurement from 14 TeV to 5.5 TeV. Owing to the predicted suppression of about a factor 5 for  $p_t \gtrsim 5 \text{ GeV}/c$ , the relative statistical errors in Pb–Pb are larger by more than a factor 2, with respect to the case of no suppression, and they become the dominant contribution to the statistical error on  $R_{AA}^D$ .

As discussed in Section 6.6.1.4, the comparison of the high- $p_t$  suppression of charm-quark-originated mesons and gluon-originated hadrons may be the tool best suited to single out the predicted colour-charge dependence of QCD energy loss. The ALICE sensitivity to the heavy-to-light ratio  $R_{D/h}$  in the range  $5 < p_t < 20 \text{ GeV}/c$  is presented in Fig. 6.303. As for the case of  $R_{AA}^D$ , the two bands correspond to including or not including the effect of the c-quark mass for a medium transport coefficient in the range 25–100  $\text{GeV}^2/\text{fm}$ . For  $10 < p_t < 20 \text{ GeV}/c$ , the two bands coincide and predict  $R_{D/h} \approx 1.5$ , i.e., about 50% smaller suppression for D mesons relative to light-flavoured hadrons.

Many of the systematic uncertainties on  $R_{D/h}$  cancel out (centrality selection and, partially, acceptance/efficiency corrections and energy extrapolation by pQCD) since  $R_{D/h}$  is essentially a double ratio (Pb–Pb/Pb–Pb)/(pp/pp). The residual systematic error is estimated to be of about 15%. We assumed the statistical error on  $R_{AA}^h$  to be negligible with respect to that on  $R_{AA}^D$  for  $p_t < 20 \text{ GeV}/c$ . The resulting statistical errors on  $R_{D/h}$  are quite large for  $p_t \gtrsim 15 \text{ GeV}/c$ . However, at lower momenta, the measurement of the compatibility (or incompatibility) of  $R_{D/h}$  with unity appears to be feasible.

### 6.6.6. Testing QCD with charm production in pp collisions

**6.6.6.1. Sensitivity in the comparison to perturbative QCD calculations.** In Section 6.6.3 we have shown that the results of perturbative QCD calculations for  $c\bar{c}$  (and  $b\bar{b}$ ) production at the

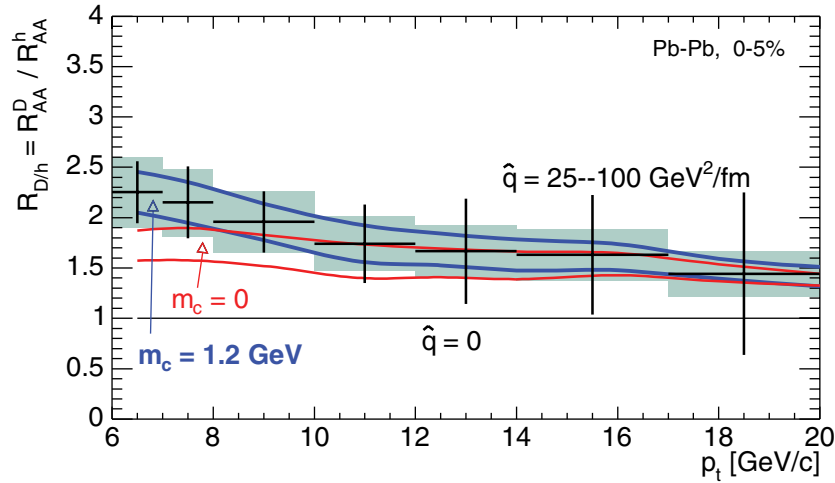


**Figure 6.303.** Ratio of the nuclear modification factors for  $D^0$  mesons and for charged hadrons. Errors corresponding to the centre of the prediction band for  $m_c = 1.2$  GeV are shown: bars = statistical, shaded area = systematic.

LHC are strongly dependent on the choice of the heavy-quark masses and of the factorisation and renormalisation scales,  $\mu_F$  and  $\mu_R$ . We compare the sensitivity of ALICE for the measurement of the total and  $p_t$ -differential cross section for  $D^0$  production in pp collisions at  $\sqrt{s} = 14$  TeV to this theoretical uncertainty. We used the HVQMNR program [809] to calculate the cross sections for different sets of parameters. The  $p_t$  distributions for D mesons were obtained from those for c quarks using a parametrisation of the  $c \rightarrow D$  fragmentation function extracted from  $c\bar{c}$  events generated with PYTHIA.

Figure 6.304 shows the comparison for  $d\sigma^{D^0}/dy$ , integrated for  $p_t > 0.5$  GeV/c. Statistical (narrower) and systematic (broader) error bands are reported separately; the latter include all normalization errors. The error bars are hereafter applied to the value obtained with the set of parameters used in our simulations ('default parameters'):  $m_c = 1.2$  GeV,  $\mu_F = \mu_R = 2\mu_0 = 2\sqrt{(p_{t,c}^2 + p_{t,\bar{c}}^2)/2 + m_c^2}$  and PDF set = CTEQ4M. The comparison for the  $p_t$ -differential cross section is presented in Fig. 6.305 along with the ratio 'data/theory' ('default parameters/theory parameters') which allows a better comparison of the different  $p_t$ -shapes obtained by changing the input 'theory parameters' and an illustration of the expected sensitivity of the ALICE measurement. The estimated experimental errors are much smaller than the theoretical uncertainty band. We note that the data cover the region at low transverse momentum where the accuracy of the pQCD calculation becomes poorer and where novel effects, determined by the high partonic density of the initial state at LHC energies, may play an important role (see next section).

**6.6.6.2. A tentative strategy for tackling non-linear effects in gluon evolution.** We outline a possible approach [774] for the detection of an enhancement of charm production at low  $p_t$ , with respect to standard pQCD predictions, obtained when adding a non-linear term to the DGLAP parton evolution equations. The non-linear term would account for recombination effects in the saturated gluon densities (see Section 6.6.1.3).

1.2, 2, 2, MRST HO  
 1.2, 2, 2, CTEQ 4M  
 1.2, 2, 2, CTEQ 5M  
 1.5, 2, 2, CTEQ 5M  
 1.2, 2, 1, CTEQ 5M  
 1.5, 2, 1, CTEQ 5M  
 1.8, 2, 1, CTEQ 5M

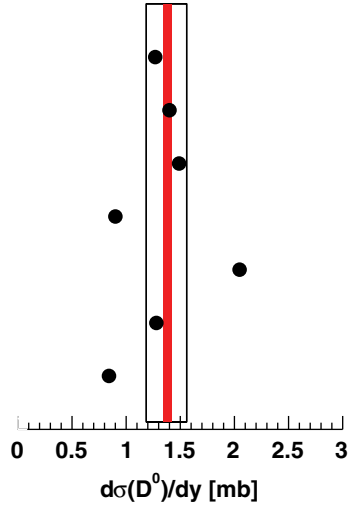


**Figure 6.304.** ALICE sensitivity on  $d\sigma^{D^0}/dy$  integrated for  $p_t > 0.5 \text{ GeV}/c$ , in pp at 14 TeV, compared to the pQCD predictions obtained with different sets of the input parameters  $m_c$  [GeV],  $\mu_F/\mu_0$ ,  $\mu_R/\mu_0$  and PDF set ( $\mu_0$  is defined in the text). The narrower band represents the statistical error, the broader band the systematic error, including all normalization errors.

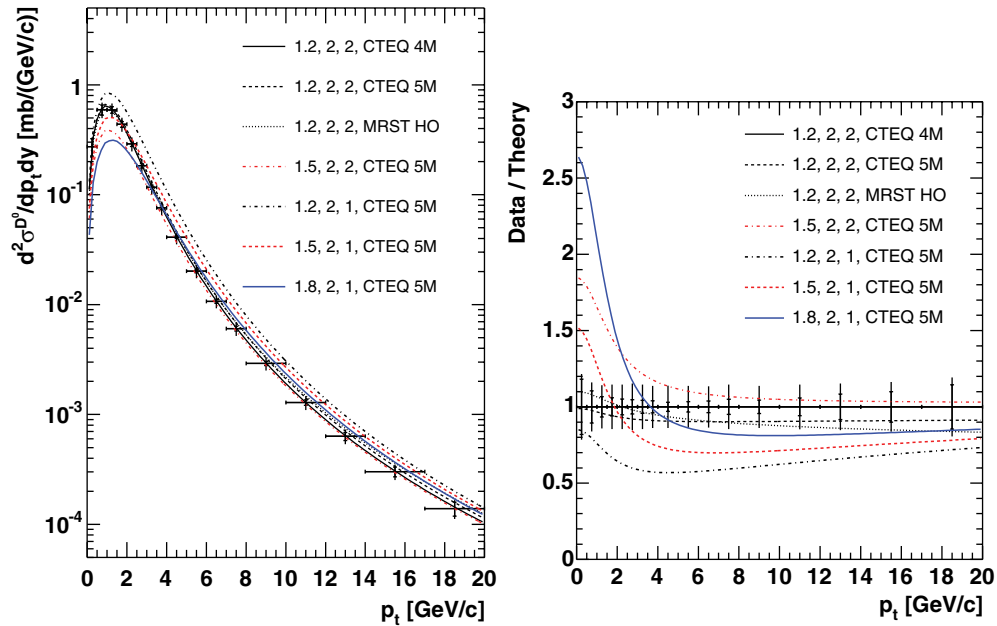


**Figure 6.305.** ALICE sensitivity on  $d^2\sigma^{D^0}/dp_t dy$ , in pp at 14 TeV, compared to the pQCD predictions obtained with different sets of the input parameters  $m_c$  [GeV],  $\mu_F/\mu_0$ ,  $\mu_R/\mu_0$  and PDF set ( $\mu_0$  is defined in the text). The inner bars represent the statistical error, the outer bars the quadratic sum of statistical and  $p_t$ -dependent systematic errors. A normalization error of 5% is not shown. The panel on the right shows the corresponding 'data/theory' plot.

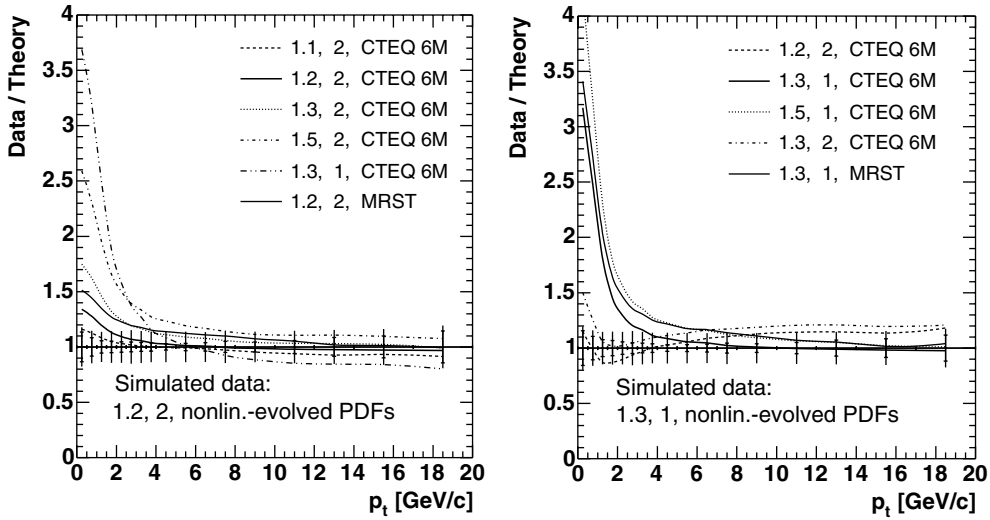


**Figure 6.306.** Ratios of simulated ALICE  $D^0$  data to pQCD curves (parameters:  $m_c$  [GeV],  $Q/\mu_0$  ( $\mu_R = \mu_F = Q$ ), PDF set); the data contain the enhancement due to non-linear gluon evolution while the theory curves do not (adapted from Ref. [774]).

The idea is to study to what extent the ‘signature’—enhancement only at low  $p_t$ —can be mimicked by NLO pQCD cross sections calculated with linearly-evolved PDFs and different combinations of parameters ( $m_c$ ,  $\mu_F$  and  $\mu_R$ ). We consider, as a function of  $p_t$ , the ‘data/theory’ ratio of the simulated data, including the enhancement, to NLO calculations using a range of  $m_c$  and  $Q/\mu_0$  ( $\mu_F = \mu_R = Q$ ) along with parametrized PYTHIA fragmentation. Thus, given the measured  $D^0$   $p_t$  distribution, one tries to reproduce this result with NLO calculations employing recent linearly-evolved PDFs and tuning  $m_c$  and  $Q/\mu_0$ . Note that these parameters are not really free but are bounded by the range  $1.2 \lesssim m_c \lesssim 1.8$  GeV and  $1 \lesssim Q/\mu_0 \lesssim 2$  in order to maintain an acceptable description of low-energy data [808]. The data/theory plots are shown in Fig. 6.306 (adapted from Ref. [774]). The points with the statistical errors (inner bars) and quadratic sum of statistical and  $p_t$ -dependent systematic errors (outer bars) correspond to the data divided by themselves. The 5% normalization error, not shown, is essentially negligible with respect to the other systematic contributions. The data include the enhancement as obtained with two sets of parameters: on the left  $m_c = 1.2$  GeV and  $Q/\mu_0 = 2$ , corresponding to the ‘pessimistic’ case also shown in Fig. 6.259 (left), with an enhancement of 30% for  $p_t \rightarrow 0$ , here shown by the thick solid line; on the right  $m_c = 1.3$  GeV and  $Q/\mu_0 = 1$ , giving, because of the lower value of  $Q$ , a much larger enhancement of a factor about 3 for  $p_t \rightarrow 0$ , shown by the thick solid line. In the ‘optimistic’ case, on the right, the effect is very large and no set of parameters can reproduce it with linearly-evolved PDFs. In the ‘pessimistic’ case, on the left, one observes that the enhancement can be mimicked with linearly-evolved PDFs provided a very small value of the charm mass, e.g.  $m_c = 1.1$  GeV, is used. If the effect is that small, the accuracy of the measurement and the intrinsic uncertainty of pQCD calculations will probably not allow a firm conclusion to be drawn.

### 6.6.7. Beauty detection in Pb–Pb collisions in the semi-electronic decay channels

**6.6.7.1. Detection strategy.** The wide coverage of ALICE for electron identification, with the Transition Radiation Detector (TRD) and the Time Projection Chamber (TPC), allows us

to study the production of open beauty by measuring the decays of beauty hadrons (mostly B mesons) with an electron in the final state [841]. These decays have a ‘global’ branching ratio of  $\approx 21\%$ :  $\approx 11\%$  for direct semi-electronic decays,  $B \rightarrow e\nu_e + X$ , and  $\approx 10\%$  for semi-electronic decays via a charm hadron,  $B \rightarrow D(\rightarrow e\nu_e + X) + X'$  [409]. The expected numbers of beauty hadrons and beauty-decay electrons in a central Pb–Pb collision ( $5\% \sigma^{\text{inel}}$ ) at  $\sqrt{s_{\text{NN}}} = 5.5$  TeV are about 9.0 and 1.9, respectively, of which about 1/4 within the ALICE central barrel acceptance  $|\eta| < 0.9$  (see Table 6.55).

The main sources of background electrons are: (a) decays of primary D mesons, which have a branching ratio of  $\approx 10\%$  in the semi-electronic channels [409], and have an expected production yield larger by a factor about 20 with respect to B mesons (see Table 6.55); (b) decays of light mesons (mainly  $\rho$ ,  $\omega$ , K); (c) conversions of photons in the beam-pipe or in the inner layers of the Inner Tracking System (ITS); and (d) pions identified as electrons.

The strategy for beauty detection in the semi-electronic decay channels, based on concepts discussed in the TRD Technical Proposal [842], relies on:

1. **Electron identification.** A combined TPC–TRD particle identification procedure is employed.
2. **Impact parameter cut.** Since beauty mesons have mean proper decay lengths of  $\simeq 500 \mu\text{m}$  [409], their decay electrons are characterised by large impact parameters with respect to the interaction vertex. Therefore, a cut on the minimum value of  $d_0$  (impact parameter projection on the transverse plane) allows us to reject a large part of the electrons from the sources (b) and (c), as well as primary pions misidentified as electrons. Electrons from charm decays, although the  $c\tau$  values for D’s are somewhat smaller than for B’s, still can have rather large impact parameters, so that we do not expect a good rejection efficiency for source (a) by applying the  $d_0$  cut alone.
3. **Transverse momentum cut.** Electrons from charm decays can be further rejected by means of a cut on their transverse momentum  $p_t$ , since, due to the larger mass of the b quark, electrons from B meson decays have a harder  $p_t$  distribution with respect to those coming from D mesons.

We first evaluate the signal-to-total ratio,  $S/(S+B)$ , that measures the signal purity, and the integrated signal statistics corresponding to a sample of  $10^7$  central Pb–Pb events (one month data-taking at ALICE), in Section 6.6.7.4. Then, we estimate statistical and systematic uncertainties on the reconstruction of the  $p_t$  distribution of electrons from B decays (Section 6.6.7.5). Finally, in Section 6.6.7.6, we show how such measurement can be converted to a measurement of the integral B meson production cross section  $d\sigma^{\text{B}}(p_t > p_t^{\text{min}})/dy$  as a function of  $p_t^{\text{min}}$ .

The study is based on a detailed simulation of the signal and background sources, while for the detector response we partly rely on parametrisations, as explained in the next section. A charged-particle rapidity density  $dN_{\text{ch}}/dy = 6000$  for central Pb–Pb collisions is assumed.

**6.6.7.2. Simulation.** The heavy-flavour signals and the background events were generated and analysed separately, as done for the study of the reconstruction of  $D^0 \rightarrow K^- \pi^+$  decays (see Section 6.6.4).

The assumed yields for electrons from B and D meson decays in central Pb–Pb collisions ( $5\% \sigma^{\text{inel}}$ ) at  $\sqrt{s_{\text{NN}}} = 5.5$  TeV, obtained combining the production yields reported in Table 6.55 on page 1782 and the branching ratios, are 1.9 (including  $B \rightarrow e$  and  $B \rightarrow D \rightarrow e$ ) and 19 per event, respectively. The two sources of electrons from heavy-flavour decays were generated in special events, in which the multiplicity was tuned in order to have a similar track reconstruction efficiency as in Pb–Pb events with  $dN_{\text{ch}}/dy = 6000$  (as done for the

$D^0$  study). We used PYTHIA [150] with parameters tuned in order to reproduce the  $c$ - and  $b$ -quark  $p_t$  distributions from NLO pQCD (see Table 6.54 on page 1781). In particular, we used the QCD process-selection option MSEL=1, a minimum  $p_t^{\text{hard}}$  of 2.75 GeV/ $c$ , and the CTEQ4L [827] set of parton distribution functions with EKS98 nuclear modification [779]. The total generated statistics of electrons from beauty and charm is  $1.3 \times 10^7$  and  $1.5 \times 10^8$ , respectively. For the background, we used the same sample of events as for the  $D^0$  study:  $2 \times 10^4$  central Pb–Pb collisions ( $b < 2$  fm) generated with HIJING [42, 67]. The multiplicity of electrons for such events, including decays and photon conversions up to the innermost Silicon Pixel Detector (SPD) layer ( $r \simeq 4$  cm)<sup>23</sup>, is  $\sim 1000$  per event. The magnetic field was set to  $B = 0.4$  T.

Event reconstruction was performed as described in Section 6.6.4.2, using a parametrized response of the tracking in the TPC and the standard Kalman filter tracking in the ITS, in order to have a realistic simulation of the performance for the impact parameter measurement. Tracks were required to have a point in each of the six ITS layers. The probability for prolongation in the TRD of a track reconstructed in the TPC and in the ITS was assumed to be 75% for transverse momenta larger than 1 GeV/ $c$  (see Section 5.1.6).

**6.6.7.3. Electron identification.** Electrons in the transverse-momentum range of interest for heavy-flavour physics (above 1 GeV/ $c$ ) can be identified using information from the TRD and the TPC. Fig. 6.307 (left-hand panel), from the TRD Technical Design Report [836], shows the expected performance values for the electron-tagging probability for pions ( $\pi_{\text{eff}} =$  probability to tag a pion as an electron) versus the electron-tagging probability for electrons ( $e_{\text{eff}} =$  probability to correctly identify an electron), for different values of the charged-particle rapidity density. For  $dN_{\text{ch}}/dy = 6000$ , we observe that, for an efficiency of electron identification  $e_{\text{eff}}^{\text{TRD}} \simeq 0.90$ , a contamination from pions  $\pi_{\text{eff}}^{\text{TRD}} \sim 10^{-2}$  is expected. These are the values used for the present study. Test-beam results [61, 843], shown in Fig. 6.307 (right-hand panel), agree with these estimates and show that the efficiency remains approximately constant in the momentum range 1–6 GeV/ $c$ , which contains most of the statistics of electrons from B. The contamination from charged kaons and protons is expected to be negligible [844].

Electrons can be further separated from heavier particles by their specific energy loss  $dE/dx$  in the TPC. The  $dE/dx$ -versus-momentum distribution resulting from the simulation of a sample of HIJING events enriched in electrons is presented in the left-hand panel of Fig. 6.308. The two bands corresponding to electrons and pions (and muons) are well separated at low momenta, where electrons are already in the relativistic rise regime while pions and muons are not. The separation decreases at higher momenta, as all particles reach the Fermi plateau. If the TPC energy loss is analysed only for tracks tagged as electrons in the TRD, the contamination from charged kaons and protons can be neglected. The right-hand panel of Fig. 6.308 shows the effect of the simple cut indicated by the black lines on the  $dE/dx$ -versus-momentum plot. The cut fixes the efficiency for electrons to  $e_{\text{eff}}^{\text{TPC}} \simeq 0.90$  over the entire momentum range shown in the figure. The electron-tagging probability for pions remains at the level  $\pi_{\text{eff}}^{\text{TPC}} \sim 10^{-2}$  up to a momentum of 2–3 GeV/ $c$ ; it then increases as the electron/pion separation in the TPC gets worse, exceeding 0.60 around  $p = 15$  GeV/ $c$ . We parametrized  $\pi_{\text{eff}}^{\text{TPC}}$  and  $e_{\text{eff}}^{\text{TPC}}$  from Fig. 6.308 (right) and included them in our analysis.

**6.6.7.4. Analysis.** Our strategy relies on exploiting the different shapes of the  $p_t$  and impact parameter distributions for electrons from beauty, from charm, and for the different background contributions. These distributions are shown in Fig. 6.309 with the cut

<sup>23</sup> Electrons from conversions that happen at larger radii will, in general, not be reconstructed if a point in the inner SPD layer is required.

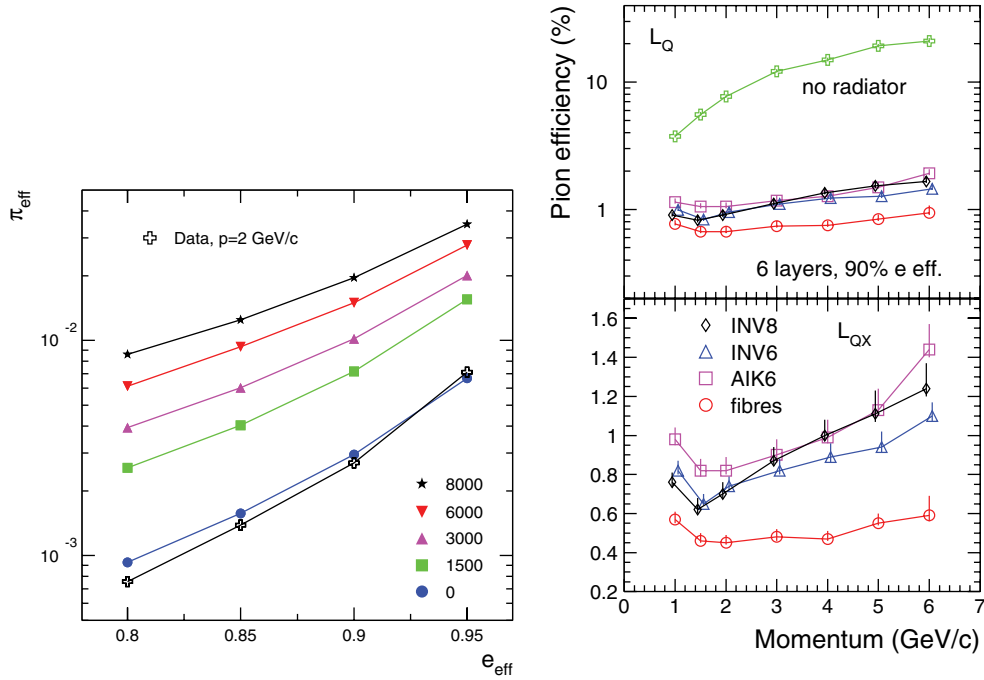


**Figure 6.307.** Electron identification in the TRD. Left: electron-tagging probability for pions,  $\pi_{\text{eff}}$ , versus electron-tagging probability for electrons,  $e_{\text{eff}}$ , at  $p = 2$  GeV/c, extrapolated to different values of  $dN_{\text{ch}}/dy$  [836]. Right: test-beam results on  $\pi_{\text{eff}}$  as a function of the momentum when  $e_{\text{eff}} = 0.90$  is required [61, 843]. The different markers represent different radiator types and the top and bottom graphs show the results for two different PID algorithms (see Refs. [61, 843]).

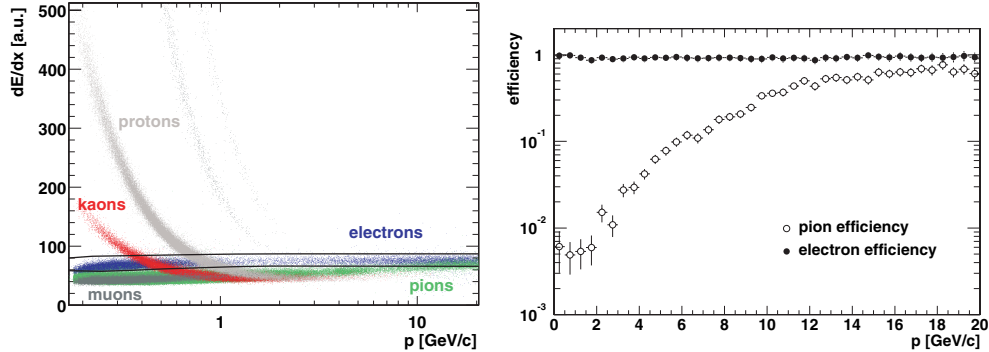


**Figure 6.308.** Electron identification in the TPC. Left: specific energy loss ( $dE/dx$ ) in the TPC as a function of the momentum. Right: efficiency for correct electron identification and pion contamination as a function of the momentum, obtained with the cut indicated in the left-hand panel.

$p_t > 1$  GeV/c. We have also included the distributions for charged pions, a fraction of which will be tagged as electrons. As expected, electrons from beauty have the hardest  $p_t$  distribution and the broadest  $d_0$  distribution, due to the large mass and mean decay length of B mesons. Electrons from  $B \rightarrow D \rightarrow e$  decays (not singled out in the figure) dominate the beauty electron spectrum for  $p_t < 1$  GeV/c, but, having a steep  $p_t$  distribution, for higher transverse momenta they rapidly decrease to about 1/10 of the total beauty electron yield.

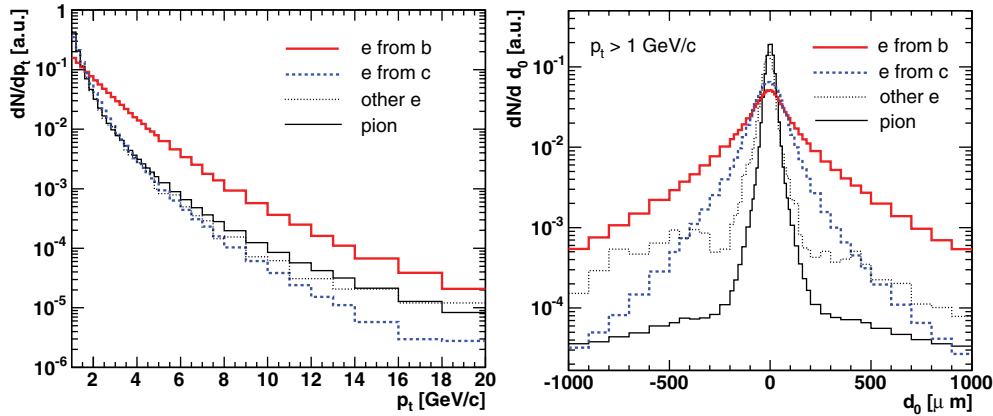


**Figure 6.309.** Comparison of transverse momentum (left) and impact parameter projection in the transverse plane (right) for electrons from beauty, from charm, from light mesons and conversions, and for pions. The cut  $p_t > 1 \text{ GeV}/c$  is applied and the distributions are normalized to the same integral.

The pion  $p_t$  distribution becomes harder than those of electrons from charm and from beauty for transverse momenta beyond 3–4  $\text{GeV}/c$  and 8–10  $\text{GeV}/c$ , respectively. This is due to the fact that, for semi-electronic heavy-flavoured meson decays, the average ratio (electron  $p_t$ )/(meson  $p_t$ ) decreases with increasing  $p_t$ . At high  $p_t$ , where the masses of  $c$  and  $b$  quarks become negligible, the  $\pi$ ,  $D$  and  $B$  distributions have comparable slopes, but the electrons from  $D$  and  $B$  decays have softer distributions.

A cut  $|d_0| > 100\text{--}200 \mu\text{m}$  is very effective in rejecting electrons from conversions and light-meson decays, as well as misidentified pions. The  $d_0$  distributions for these particles present large tails due to decays of long-lived strange particles and to tracks suffering large-angle scatterings in the materials. To remove these large- $|d_0|$  background tracks we also apply an upper cut  $|d_0| < 600 \mu\text{m}$ .

The  $d_0$  distribution for background electrons presents an asymmetry toward negative values, caused by electrons from photon conversions in the detector materials. Given the procedure that we use to give a sign to the impact parameter and the topology of the  $\gamma$ -conversion process, electrons from this source tend to have  $d_0 < 0$ .

As discussed above, a combined TRD–TPC electron identification technique is adopted. In Fig. 6.310 we show the impact parameter (absolute value) distributions of identified electrons from beauty and from charm, identified background electrons and charged pions tagged as electrons. The cut  $p_t > 1 \text{ GeV}/c$  is applied. The two panels correspond to: no electron identification, i.e. all particles tagged as electrons, (left) and combined TRD–TPC identification (right). Without identification, charged pions dominate the electron sample over the whole range. The filter provided by the TPC and the TRD globally reduces the pion contamination by a factor  $10^{-4}$ , of which about  $10^{-2}$  from the TRD and  $10^{-2}$  from the TPC.

We determined the optimal conditions for the selection of a beauty sample by studying the signal purity, defined as the ratio  $S/(S+B)$  (where  $S$  includes all electrons coming from beauty hadrons and  $B$  includes light-hadron decays, conversions, misidentified pions and charm-originated electrons), for different thresholds in  $p_t$  and  $|d_0|$  (as explained above, an upper limit of  $600 \mu\text{m}$  for the latter has also been set). Figure 6.311 (left-hand panel) shows the  $S/(S+B)$  ratio as a function of the impact parameter threshold for three  $p_t$  thresholds (1, 2 and 3  $\text{GeV}/c$ ), the lowest being fixed by the minimum  $p_t$  required for electron

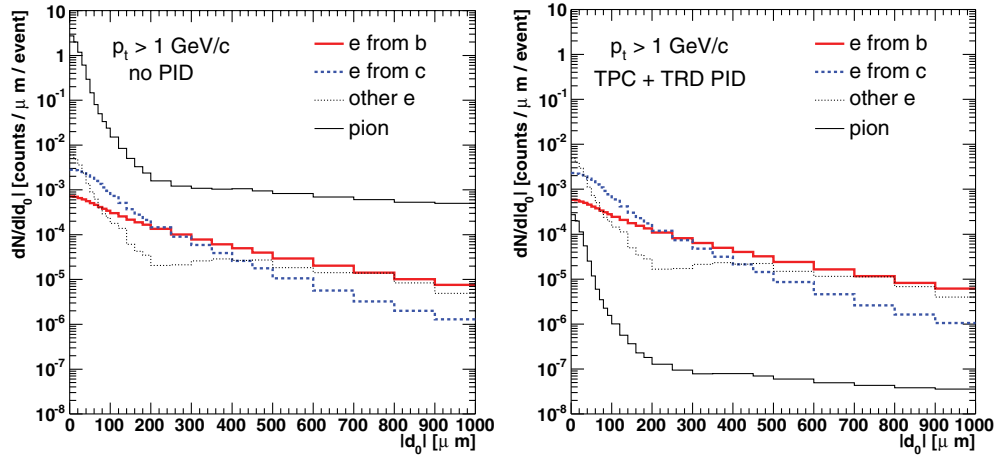


**Figure 6.310.** Distribution of the absolute value  $|d_0|$  of the impact parameter for identified electrons from beauty decays, from charm decays, identified electrons from the background and pions tagged as electrons. Left: no electron identification (all particles tagged as electrons). Right: combined TPC–TRD identification. The cut  $p_t > 1 \text{ GeV}/c$  is applied.

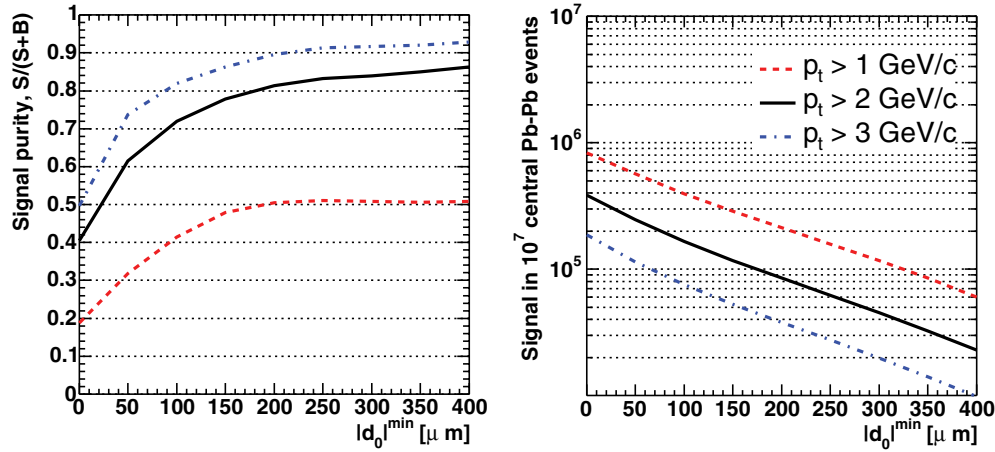


**Figure 6.311.** Left:  $S/(S+B)$  ratio of reconstructed electron tracks as a function of the  $|d_0|$  threshold and for three values of the  $p_t$  threshold. The background includes charm decays, other electron sources and misidentified pions. Right: statistics of electrons from B decays in  $10^7$  central Pb–Pb events. The cut  $|d_0| < |d_0|^{\max} = 600 \mu\text{m}$  is applied for both panels.

identification in the TRD. As an example, the cuts  $p_t > 2 \text{ GeV}/c$  and  $200 < |d_0| < 600 \mu\text{m}$  yield a sample of electrons from B meson decays with a purity  $S/(S+B)$  of 80% (see left-hand panel of Fig. 6.311). Even with the lowest  $p_t$  threshold (1 GeV/c), a sample with a purity of  $\simeq 50\%$  is achievable. In this case a further optimization is possible, e.g. by applying separate cuts on the positive and negative sides of the impact parameter distribution, so as to reject more efficiently the electrons from conversions.

The right-hand panel of Fig. 6.311 shows, as a function of the  $|d_0|$  threshold and for three values of the  $p_t$  threshold, the number of beauty decay electrons that we expect to select in

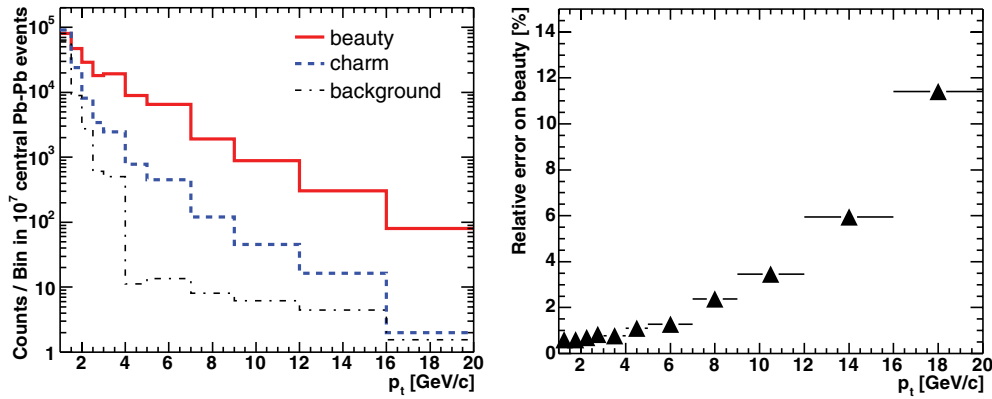


**Figure 6.312.** Left: expected statistics (counts/ $p_t$ -bin) in  $10^7$  central Pb–Pb events for electrons from beauty, from charm and for the background (misidentified pions or electrons from other sources). Right:  $p_t$  dependence of the relative statistical error on the yield of electrons from beauty.

$10^7$  central Pb–Pb events, corresponding to a one-month run of ALICE. For  $p_t > 2$  GeV/ $c$  and  $200 < |d_0| < 600$   $\mu\text{m}$  we obtain a statistics  $S \simeq 8 \times 10^4$ .

*6.6.7.5. Measurement of the  $p_t$  distribution of electrons from B decays.* Figure 6.312 (left) shows the yields as a function of the transverse momentum for electrons from beauty decays, electrons from charm decays, and background (misidentified pions or electrons from other sources), as expected in  $10^7$  central Pb–Pb collisions. The impact parameter cut  $200 < |d_0| < 600$   $\mu\text{m}$  is applied.

The background component, which dominates at the lowest  $p_t$  limit for electron identification ( $\approx 1$  GeV/ $c$ ), decreases steeply for increasing  $p_t$  and becomes negligible ( $< 2\%$ ) for  $p_t \gtrsim 4$  GeV/ $c$ . This contribution to the distribution of electron-tagged particles can be estimated, and subtracted, with high precision from Monte Carlo simulations tuned to reproduce the measured  $p_t$  distributions of charged pions, that may be misidentified as electrons, and of light mesons that decay to electrons.

The ratio of electrons from charm to electrons from beauty is about one at  $p_t \sim 1$ – $2$  GeV/ $c$ , then it decreases, though remaining non-negligible up very large transverse momentum, 5% at  $p_t \approx 13$  GeV/ $c$ . Our current strategy is to estimate and subtract this component on the basis of the D-meson production cross section measured via  $D^0 \rightarrow K^- \pi^+$  reconstruction. In the following discussion on systematic errors, we describe with more details this procedure and estimate the resulting systematic uncertainty.

*Statistical uncertainties.* The yields reported in the left-hand panel of Fig. 6.312 allow us to calculate the expected statistical errors associated to the  $p_t$  distribution of electrons from beauty, obtained after subtraction of the background and charm components. For the  $i$ -th  $p_t$  bin, that contains  $N_i^{\text{e,beauty}}$  electrons from beauty,  $N_i^{\text{e,charm}}$  electrons from charm and  $N_i^{\text{e,bkg}}$  background particles, the relative statistical error on the signal  $S_i = N_i^{\text{e,beauty}}$  is

$$\sigma_{S_i}/S_i = \sqrt{N_i^{\text{e,beauty}} + N_i^{\text{e,charm}} + N_i^{\text{e,bkg}}} / N_i^{\text{e,beauty}}. \quad (6.137)$$

The relative statistical errors are shown in the right-hand panel of Fig. 6.312. Increasing the size of the bins toward higher momentum, these errors can be kept smaller than 12% up to  $p_t \approx 18$  GeV/ $c$ .

*Systematic uncertainties.* The main systematic uncertainties on the measured  $p_t$ -differential cross section of electrons from B meson decays are expected to be the following:

- Error introduced in the Monte Carlo corrections for detector acceptance, track reconstruction and electron identification efficiencies, and selection efficiency (impact parameter cuts). This error is assumed to be about 10% over the entire covered  $p_t$  range. However, it is, in principle, dependent on the electron momentum and its evaluation will be addressed in future dedicated studies.
- Error on the normalization to one nucleon–nucleon collision of the cross section measured in Pb–Pb collisions in a given centrality range. This error was discussed in the context of  $D^0$  reconstruction (Section 6.6.4.8). It is due to the definition of the centrality range and the uncertainty on the Woods–Saxon parameters that describe the density profile of the Pb nucleus, which add up to about 8%, and to the expected 5% uncertainty on the nucleon–nucleon inelastic cross section at  $\sqrt{s_{NN}} = 5.5$  TeV. The total normalization error is, thus, about 9%.
- Error due to the uncertainties on the background and on the charm decay electron contributions to be subtracted from the spectrum. The former is assumed to be negligible. The latter is estimated below.

The reconstruction of  $D^0 \rightarrow K^- \pi^+$  decays will provide a measurement of the  $D^0$ -meson  $p_t$  distribution. The statistical and systematic uncertainties on this measurement were studied in detail, as reported in Section 6.6.4. Statistical errors are of the order of 5% on average and increase to about 20% at small transverse momentum,  $\simeq 1$  GeV/ $c$ , and to about 10% at large transverse momentum,  $\simeq 14$  GeV/ $c$ . Systematic uncertainties due to Monte Carlo corrections are approximately  $p_t$ -independent and of the order of 10%. We assume the production cross section of all charm hadrons ( $H_c \equiv D^0, D^+, D_s^+, \Lambda_c^+$ ) to be proportional to that of  $D^0$  mesons, and we use the relation  $d^2\sigma^{H_c}/dp_t dy = (1.70 \pm 0.07) \times d^2\sigma^{D^0}/dp_t dy$ . The proportionality factor is the average between the value measured by the ALEPH Collaboration at LEP [833] and that extracted from the PYTHIA [150] event generator (see Table 6.55), and the 4% systematic error is obtained from the comparison of the two values. Such error is basically negligible with respect to the quoted 10% systematic error on the  $D^0$  cross section itself. The  $D^0$  cross section normalization error is not considered for the purpose of charm subtraction from the total electron spectrum, since we assume the  $D^0 \rightarrow K^- \pi^+$  and single-electron analysis to be performed on the same sample of events and with the same centrality class(es).

The  $p_t$  distribution  $dN^{e,\text{charm}}/dp_t$  of electrons from charm decays to be subtracted from the measured electron spectrum is obtained by filtering through the detector simulation and analysis cuts (electron identification and  $|d_0|$  window)  $H_c \rightarrow e + X$  decays generated with PYTHIA and reweighted so as to match the  $d^2N^{H_c}/dp_t dy$  yield inferred as described above. The  $\approx 10\%$  systematic error on  $d^2N^{H_c}/dp_t dy$  converts to an equal error on  $dN^{e,\text{charm}}/dp_t$ . The statistical errors on  $d^2N^{D^0}/dp_t dy$  convert to a  $p_t$ -dependent systematic error on  $dN^{e,\text{charm}}/dp_t$ . This error can be estimated by a Monte Carlo method: the measured  $d^2N^{D^0}/dp_t dy$  is fit to a given expression, e.g.

$$\frac{1}{p_t} \frac{d^2N^{D^0}}{dp_t dy} = A \left[ 1 + \left( \frac{p_t}{p_t^0} \right)^2 \right]^{-n}, \quad (6.138)$$

to be used to reweight the PYTHIA  $H_c \rightarrow e + X$  input; then, each measured point is randomly smeared according to a Gaussian with RMS given by the statistical error, and the fit is repeated, thus giving a different PYTHIA input. This smear–fit–reweight procedure is

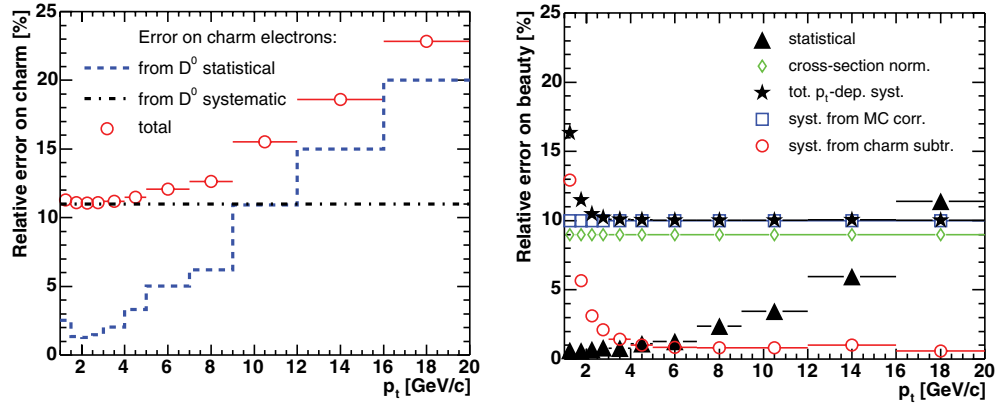


**Figure 6.313.** Left: relative error on charm-decay electrons as a function of  $p_t$ , estimated by propagating to the electron level the statistical and systematic errors on the measurement of the  $D^0$  production cross section in the  $D^0 \rightarrow K^- \pi^+$  channel. Right: summary of all error contribution for the measurement of the  $p_t$ -differential cross section of electrons from beauty decays.

iterated several times and the resulting spread in the  $dN^{e,\text{charm}}/dp_t$  distribution is taken as the systematic error due to the statistically-limited knowledge of the  $D^0$  production cross section.

We cross-checked this procedure using an analytic error propagation from the  $H_c$  to the electron  $p_t$  distribution: relying on PYTHIA, the content of each bin  $i$  in the  $dN^{e,\text{charm}}/dp_t$  distribution is written as the sum of contributions from charm hadrons in the different  $p_t$  bins,  $j = 1, \dots, n$ , used for the  $D^0$  measurement,  $N_i^{e,\text{charm}} = \sum_{j=1}^n N_{i,j}^{e,\text{charm}}$ ; the relative error on  $N_{i,j}^{e,\text{charm}}$  is assumed to be that of the  $j$ -th bin of the measured  $d^2N^{D^0}/dp_t dy$  and the resulting error on  $N_i^{e,\text{charm}}$  is obtained by a quadratic error propagation. The results given by the two methods agree within 20%.

Figure 6.313 (left) shows the relative uncertainties on the charm-decay electron  $p_t$  distribution: the uncertainties coming from the systematic and statistical errors on  $d^2N^{H_c}/dp_t dy$ , and their quadratic sum. The relative systematic error introduced on the beauty electron  $p_t$  distribution by the charm electron subtraction is shown by the open circles in the right-hand panel of Fig. 6.313, where all error contributions are summarized. In particular, the closed triangles represent the statistical errors, the closed stars represent the total  $p_t$ -dependent systematic error (quadratic sum of error from MC corrections and error from charm subtraction), and the open diamonds represent the  $p_t$ -independent systematic error from the cross section normalization.

The production cross section of electrons from B decays is shown in Fig. 6.314, with the estimated statistical errors (inner bars) and the quadratic sum of statistical and  $p_t$ -dependent systematic errors (outer bars). The 9% cross section normalization error is not shown.

**6.6.7.6. Extraction of the B-level cross section.** In this Section we test a method to extract a minimum- $p_t$ -differential cross section at the B meson level from the decay-electron level  $p_t$ -differential cross section. The method, developed by the UA1 Collaboration [845, 846] and being considered in ALICE also for beauty detection in the semi-muonic decay channels (see Section 6.6.8 and Ref. [847]), is based on Monte Carlo and it relies on the fact that the B meson decay kinematics, measured and studied in several experiments (see e.g. [848] for a review), is well understood.

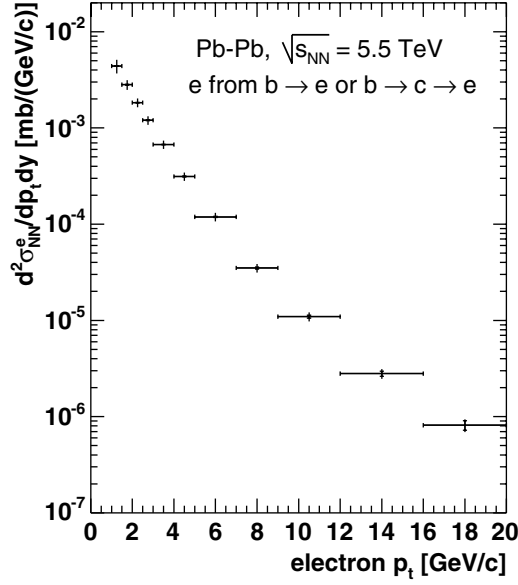


**Figure 6.314.** Double-differential cross section per nucleon–nucleon collision for electrons from B decays as a function of  $p_t$ , as it can be measured with  $10^7$  central Pb–Pb events, corresponding to one month of data-taking. Statistical errors (inner bars) and quadratic sum of statistical and  $p_t$ -dependent systematic errors (outer bars) are shown. A normalization error of 9% is not shown.

The B meson cross section per unit of rapidity at mid-rapidity with  $p_t^B > p_t^{\min}$  is obtained from a scaling of the electron-level cross section measured within a given electron parameter space  $\Phi^e$ :

$$\begin{aligned} \frac{d\sigma^B}{dy}(p_t^B > p_t^{\min}) &= \sigma^{e,\text{beauty}}(\Phi^e) \Big|_{\text{meas.}} \times \frac{\frac{d\sigma^B}{dy}(p_t^B > p_t^{\min})}{\sigma^B(\Phi^e)} \Big|_{\text{MC}} \quad (6.139) \\ &= \sigma^{e,\text{beauty}}(\Phi^e) \Big|_{\text{meas.}} \times \mathcal{F}_{e \rightarrow B}, \end{aligned}$$

where the Monte Carlo scaling factor  $\mathcal{F}_{e \rightarrow B}$  is the ratio of the B cross section per unit of rapidity at mid-rapidity with  $p_t^B > p_t^{\min}$  to the cross section for B mesons decaying to a final state containing an electron within the parameter space  $\Phi^e$ . The electron parameter space is, in our case, defined by a transverse momentum range, a pseudorapidity range, and an impact parameter range,  $\Phi^e \equiv \{\Delta p_t, \Delta \eta, \Delta d_0\}$ . This means that  $\sigma^{e,\text{beauty}}(\Phi^e) \Big|_{\text{meas.}}$  is not corrected for the impact parameter selection; this correction is included in  $\mathcal{F}_{e \rightarrow B}$ . In the following, we use, for  $\Delta p_t$ , the bins introduced in Fig. 6.313, for  $\Delta \eta$ , the range  $|\eta| < 0.9$ , and for  $\Delta d_0$ , the range  $200 < |d_0| < 600 \mu\text{m}$ . For given  $\Phi^e$ ,  $\mathcal{F}_{e \rightarrow B}$  depends on the choice of  $p_t^{\min}$ . Note that also the correction for the average  $B \rightarrow e + X$  branching ratio is encoded in  $\mathcal{F}_{e \rightarrow B}$ .

The correction factor  $\mathcal{F}_{e \rightarrow B}$  contains two different sources of systematic error: (a) the uncertainty on the semi-electronic decay branching ratio and (b) the dependence of  $\mathcal{F}_{e \rightarrow B}$  on the shape used in the MC simulation for the B meson  $p_t$  distribution. Also, the error on the correction for the  $d_0$  selection efficiency is, in principle, carried by  $\mathcal{F}_{e \rightarrow B}$ ; however, in the scope of the present discussion, we consider it decoupled from  $\mathcal{F}_{e \rightarrow B}$  and we account for it in the 10% systematic error due to MC corrections at the electron level.

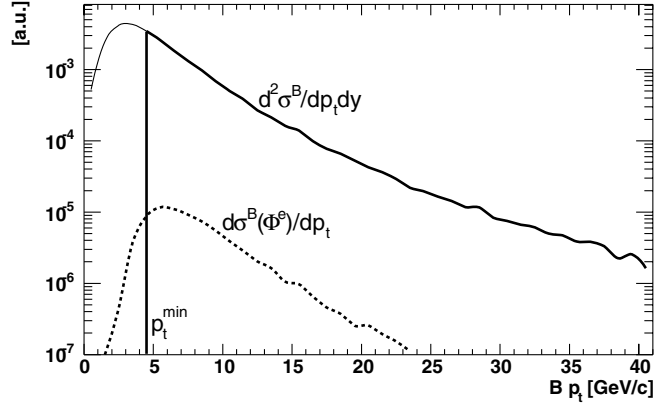


**Figure 6.315.** Determination of the Monte Carlo scaling factor  $\mathcal{F}_{e \rightarrow B}$ , Eq. (6.139), to obtain the B-level cross section above a minimum  $p_t$  from the measured electron-level cross section within a given parameter space  $\Phi^e$ .

The relative uncertainty on the branching ratio is about 3% and, thus, negligible with respect to the systematic contributions present already at the electron level, shown in the left-hand panel of Fig. 6.313. Concerning the error due to the MC shape of the B  $p_t$  distribution, in the following we study the dependence of the correction factor  $\mathcal{F}_{e \rightarrow B}$  on this shape. We find that, for any given  $\Phi^e$  (or better electron  $p_t$  bin), there is a value of the B meson  $p_t^{\min}$  which minimizes the correction dependence on the shape used in the simulation and that, at this minimum, the dependence is rather small. Thus, it is possible to apply the correction with a negligible additional systematic uncertainty, relative to the systematic uncertainty already present at the electron level.

We used  $B \rightarrow e + X$  and  $B \rightarrow D \rightarrow e + X$  decays generated with PYTHIA. Figure 6.315 shows an example of determination of the correction factor  $\mathcal{F}_{e \rightarrow B}$ . The solid-line distribution is  $d^2\sigma^B/dp_t dy$  and the dashed-line distribution is  $d\sigma^B(\Phi^e)/dp_t$  for  $3 < p_t^e < 4$  GeV/c.  $\mathcal{F}_{e \rightarrow B}$  is the ratio of the integral of the former above  $p_t^{\min}$  to the total integral of the latter.

The HVQMNR program [809] for NLO pQCD calculations was employed to modify the  $p_t$  shape of  $d^2\sigma^B/dp_t dy$  by varying: (a) the value of the b-quark mass and of the factorisation and renormalisation scales, (b) the nuclear modification of the parton distribution functions, as in the right-hand panel of Fig. 6.301, and (c) the shape of the  $b \rightarrow B$  fragmentation function (for the purpose of this study, the Peterson parametrisation [849] was used and  $\varepsilon_b$  was varied in the range 0.003–0.012). Each HVQMNR result was used to reweight the PYTHIA events, such that the B  $p_t$  distribution from PYTHIA matched that from HVQMNR; then, the function  $\mathcal{F}_{e \rightarrow B}(p_t^{\min})$  was calculated scanning a wide range in  $p_t^{\min}$ . Figure 6.316 (left) shows the explored range of variation of  $d^2\sigma^B/dp_t dy$ . The resulting band of systematic error on the value of  $\mathcal{F}_{e \rightarrow B}$ , for some selected electron  $p_t$  bins, is plotted in the panels on the right-hand side of Fig. 6.316. The quenching-induced modification of the B  $p_t$  distribution predicted by the model used for the charm energy loss study (Section 6.6.5) was considered as well, and is shown by the thicker lines in the plots. For any electron  $p_t$  bin above 2 GeV/c, there is an optimal value of  $p_t^{\min}$  for which the dependence of  $\mathcal{F}_{e \rightarrow B}$  on the shape of the B  $p_t$  distribution used in the simulation becomes at most 5%. The optimal value of  $p_t^{\min}$  typically selects about 80–90% of the B mesons that give an electron in  $\Phi^e$ , i.e.  $\sigma^B(\Phi^e; p_t^B > p_t^{\min})/\sigma^B(\Phi^e) \simeq 0.8$ –0.9. For electron transverse momenta smaller than 2 GeV/c the correlation between the electron and the B meson transverse momenta is poor and large uncertainties would be introduced in the extraction of a B-level cross section.

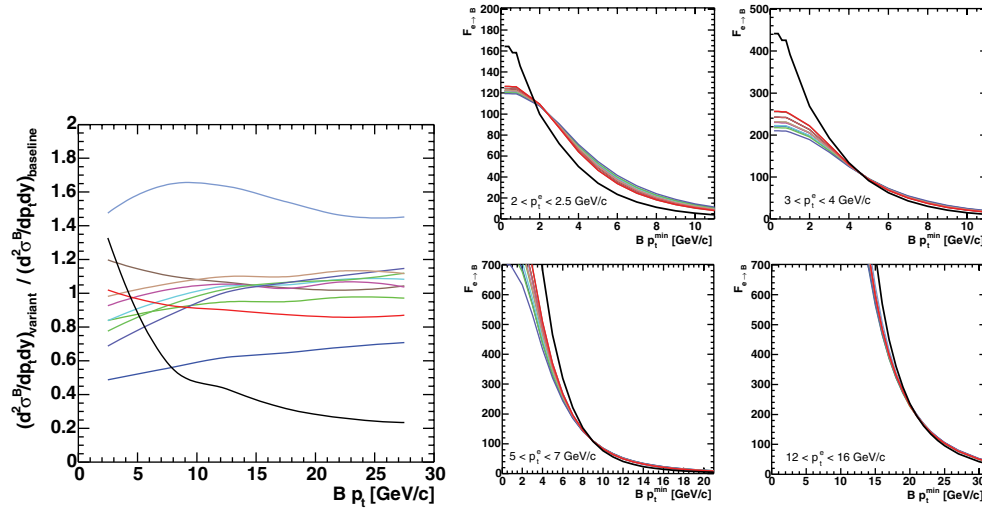


**Figure 6.316.** The different shapes of the B meson  $p_t$  distribution used in the Monte Carlo simulation (left) and the corresponding dependence of the scaling factor  $\mathcal{F}_{e \rightarrow B}$  on the value of  $p_t^{\min}$  (right).

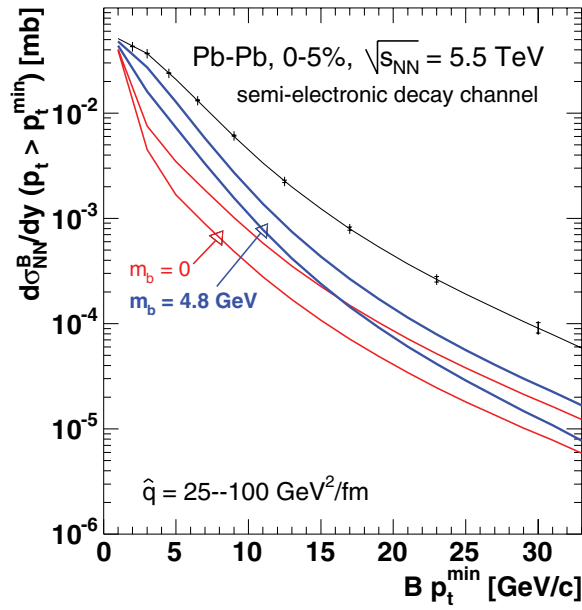


**Figure 6.317.** Minimum- $p_t$ -differential production cross section per nucleon–nucleon collision for B mesons, as it can be measured with  $10^7$  central Pb–Pb events, corresponding to one month of data-taking. Statistical errors (inner bars) and quadratic sum of statistical and  $p_t$ -dependent systematic errors (outer bars) are shown. A normalization error of 9% is not shown.

Figure 6.317 shows the expected ALICE performance for the measurement of the  $p_t^{\min}$ -differential cross section of B mesons,  $d\sigma^B(p_t > p_t^{\min})/dy$  vs.  $p_t^{\min}$  at  $y=0$ . The points correspond to the electron  $p_t$  bins in the range  $2 < p_t^e < 20 \text{ GeV}/c$  from Fig. 6.314. The

errors are (in percentage) equal to those of the electron-level cross section. The additional systematic error carried by  $\mathcal{F}_{e \rightarrow B}$  is smaller than 5% and, thus, negligible with respect to the other systematic uncertainties. A systematic error of 9% due to the normalization of the yield measured in Pb–Pb collisions to a cross section per nucleon–nucleon collision is not shown. For illustration, we report the two bands showing the predicted effect of parton energy loss on the  $p_t^{\text{min}}$ -differential B cross section. In contrast with the case of D mesons (Fig. 6.302), there is a significant reduction of the suppression when the b-quark mass is taken into account in the energy loss calculation. The study, currently in progress, of the ALICE performance for beauty production measurement in pp collisions will allow us to evaluate the sensitivity on the nuclear modification factor  $R_{AA}^B$ .

*6.6.8. Beauty detection in Pb–Pb collisions with the ALICE muon spectrometer.* The ALICE forward muon arm, described in Section 3.12 of PPR Volume I [3], covers in acceptance the region  $-4 < \eta < -2.5$  and it will allow us to detect muons from beauty decays [847]. While single-inclusive differential cross section measurements will provide large statistics and a wide coverage in transverse momentum, as only one muon has to enter the acceptance, the capability to measure both muons from the  $b\bar{b}$  pair decay offers additional information to test QCD predictions. In fact, the dimuon correlations in azimuthal angle, transverse momentum and rapidity are sensitive to relevant features of the  $b\bar{b}$  production process, like the relative importance of leading-order and higher-order topologies. In Fig. 6.318, we show the rapidity correlation between muons originating from  $Q\bar{Q}$  decays. In panels (b) and (d), rapidity difference distributions between the two decay muons, when one of them is in the spectrometer geometrical acceptance, are presented, for charm and beauty decays respectively. The correlation is stronger for beauty decays with a standard deviation of about 1.5 units (2 units for charm). Such strong rapidity correlation makes the muon spectrometer well-suited for  $b\bar{b}$  measurements, since if a b quark is detected in the forward region there is a high probability that the  $\bar{b}$  is also forward (the  $b\bar{b}$  acceptance is detailed in the next section).

*6.6.8.1. Detector effects.* Acceptance, detection efficiencies and resolution of the muon arm were included in this study using a parametrisation based on a full GEANT 3.21 simulation of the detector response (see Section 6.7.2.1).

The muon geometrical acceptance ( $A_{\text{geom}}$ ) was computed by applying simple pseudo-rapidity cuts corresponding to the geometric aperture of the spectrometer ( $-4 < \eta < -2.5$ ). The muon tracking implements a maximum-likelihood-expectation-maximization (MLEM) cluster finder and a Kalman filter track fitting [850]. Muon tracks with  $p_t > 1.5 \text{ GeV}/c$  have a relative  $p_t$  resolution better than 2% and a reconstruction efficiency  $\varepsilon_{\text{track}}$  of about 90% for trackable tracks (fraction  $A_{\text{track}}$  of the tracks emitted in the spectrometer opening angle giving hits in 1 chamber, out of 2, in each tracking station 1–3, 3 chambers, out of 4, in stations 4–5 and 3 chambers, out of 4, in trigger stations). Reconstruction efficiencies for single and dimuons are summarized in Table 6.70.

In central Pb–Pb collisions, about eight low transverse momentum muons from  $\pi/K$  decays are expected to be emitted per event in the spectrometer angular aperture. To reduce the trigger probability to a reasonable level, a muon trigger signal is issued only if a track has a transverse momentum above a predefined threshold. Although trigger levels have been optimised for quarkonia measurements, in this analysis we show that the low trigger transverse momentum cut-off of  $1 \text{ GeV}/c$  is enough to have a significant measurement of

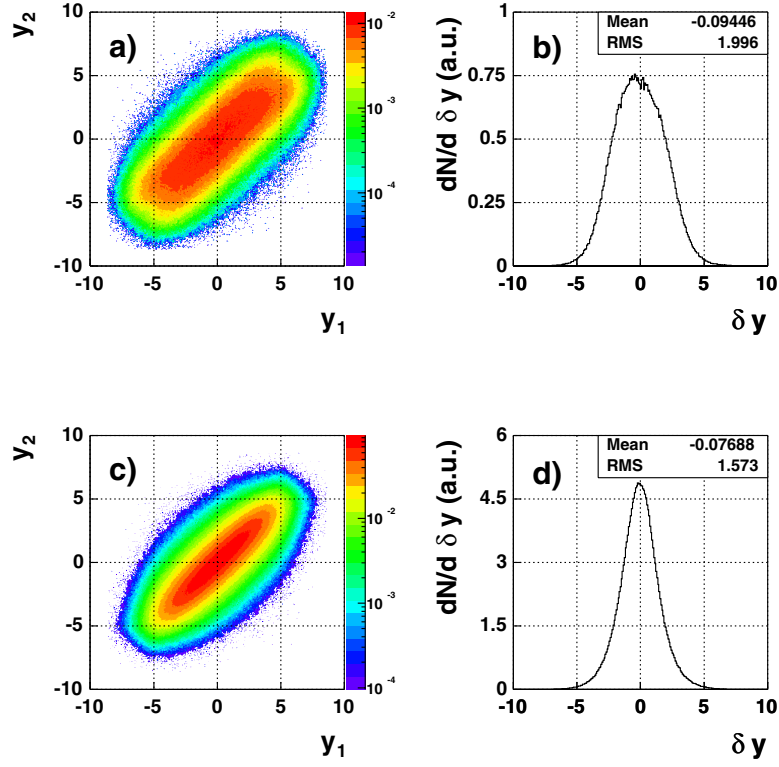


**Figure 6.318.** Dimuon rapidity correlation for (a) charm and (c) beauty decays. Rapidity difference distributions when one muon is in the muon arm acceptance for (b) charm and (d) beauty.

**Table 6.70.** Muon arm detection efficiency breakdown for single muons and dimuons from charm and beauty decays.  $A_{\text{geom}}$  stands for the muon arm geometrical acceptance,  $A_{\text{track}}$  for the fraction of trackable tracks, while  $\epsilon_{\text{track}}$  is the tracking efficiency,  $\epsilon_{\text{trig}}^{p_t > 1 \text{ GeV}/c}$  the low- $p_t$  trigger efficiency, and  $\epsilon_{\text{trig}}^{p_t > 2 \text{ GeV}/c}$  the high- $p_t$  trigger efficiency.

	$c\bar{c}$			$b\bar{b}$			
	$\mu^+$	$\mu^-$	$\mu^+\mu^-$	$\mu^+$	$\mu^-$	$\mu^+\mu^-$	$\mu^\pm\mu^\pm$
$A_{\text{geom}}$	0.130	0.127	0.035	0.122	0.122	0.050	0.031
$A_{\text{track}}$	0.422	0.420	0.191	0.756	0.757	0.465	0.515
$\epsilon_{\text{track}}$	0.271	0.270	0.080	0.622	0.624	0.287	0.339
$\epsilon_{\text{trig}}^{p_t > 1 \text{ GeV}/c}$	0.130	0.133	0.021	0.530	0.540	0.171	0.233
$\epsilon_{\text{trig}}^{p_t > 2 \text{ GeV}/c}$	0.040	0.042	0.003	0.285	0.293	0.043	0.067

open beauty in the dimuon channel using  $\mu^+\mu^-$  pairs distributed over a wide mass range. An additional analysis cut at  $1.5 \text{ GeV}/c$  is then applied to remove the low transverse momentum region, where the trigger efficiency drops rapidly. Low- $p_t$  ( $1 \text{ GeV}/c$ ) and high- $p_t$  ( $2 \text{ GeV}/c$ ) trigger cut efficiencies,  $\epsilon_{\text{trig}}^{p_t > 1 \text{ GeV}/c}$  and  $\epsilon_{\text{trig}}^{p_t > 2 \text{ GeV}/c}$ , for single muons and dimuons are given in Table 6.70. Beauty decays produce muons with larger  $p_t$  as compared to charm, resulting in higher single-muon efficiencies.

**Table 6.71.** Global efficiencies for single muons and opposite-sign muon pairs entering the spectrometer acceptance.

$p_t^\mu$ (GeV/c)	$\varepsilon$
1.5–2.0	0.794
2.0–2.5	0.834
2.5–3.0	0.852
3.0–4.0	0.872
4.0–5.0	0.869
5.0–6.0	0.867
6.0–9.0	0.876
9.0–12.0	0.877
12.0–15.0	0.872
15.0–20.0	0.869

$M_{\mu^+\mu^-}$ (GeV)	$\varepsilon(p_t^\mu > 1.5 \text{ GeV}/c)$
0–5	0.636
5–20	0.723

Combining the previously described efficiencies and applying the analysis cut  $p_t^\mu > 1.5 \text{ GeV}/c$ , we obtain the global efficiencies presented in Table 6.71 for single muons and muon pairs from heavy-quark decays. The analysis cut of  $1.5 \text{ GeV}/c$  yields a significantly larger global efficiency with respect to that expected with the low- $p_t$  trigger cut at  $1 \text{ GeV}/c$  (see Table 6.70).

#### 6.6.8.2. Muon sources

*Heavy-quark decays.* Semi-muonic decays of heavy quarks have essentially the same branching ratios as semi-electronic decays (given in Section 6.6.7.1). We recall that, for beauty, in addition to the direct semi-muonic decay  $B \rightarrow \mu \nu_\mu + X$ , second generation muons can also originate from cascade decays  $B \rightarrow D(\rightarrow \mu \nu_\mu + X) + X'$ . As a consequence, while charm semi-muonic decays can only contribute to the opposite-sign dimuon sample, beauty decays through cascade chains produce both same-sign and opposite-sign dimuons:

$$\begin{aligned}
 B^+ &\rightarrow \bar{D}^0 \mu_1^+ \nu_\mu \\
 &\quad \searrow \mu_2^- X' \\
 \bar{B}^0 &\rightarrow D^+ \mu_3^- \bar{\nu}_\mu \\
 &\quad \searrow \mu_4^+ X'' .
 \end{aligned}$$

The possible pairs are: a combination of muons ( $\mu_1\mu_2$  and  $\mu_3\mu_4$ ) from a single B meson<sup>24</sup> (referred to as  $BD_{\text{same}}$ ), two muons ( $\mu_1\mu_3$ ) from primary B decays ( $BB_{\text{diff}}$ ), two muons ( $\mu_2\mu_4$ ) from secondary decays ( $DD_{\text{diff}}$ ) feed-down from beauty to the open charm production<sup>25</sup>, and a primary muon from one B and a secondary muon from the other B ( $\mu_1\mu_4$  and  $\mu_2\mu_3$  or  $BD_{\text{diff}}$ ). Moreover, mixing in the  $B^0-\bar{B}^0$  system can change b into  $\bar{b}$  or vice-versa, producing same-sign correlated  $BB_{\text{diff}}$  and  $DD_{\text{diff}}$  muon pairs (for a detailed discussion, see Ref. [847]).

<sup>24</sup> Always opposite-sign.

<sup>25</sup> Both same- and opposite-sign.

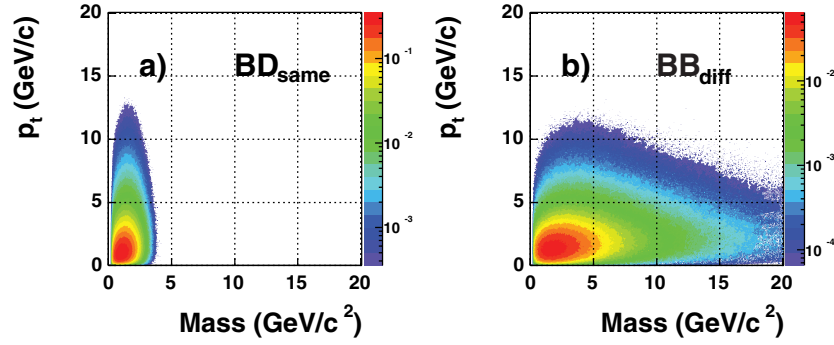


**Figure 6.319.** Beauty decay configurations: a) configuration of large transverse momentum and low mass muon pairs from the semi-leptonic chain decay of a single heavy b quark ( $BD_{\text{same}}$ ); b) dimuon events produced from semi-leptonic decay of both b quarks made of large mass and large transverse momentum muons.

An opposite-sign muon pair from a b-chain decay has an upper limit on its invariant mass  $M_{\mu^+\mu^-}$ , fixed by the initial b quark mass. Thus, beauty decays can be divided into two main topologically-distinct contributions: b-chain decays into low-mass and high transverse momentum dimuons (Fig. 6.319a) and muon pairs where the two muons originate from different quarks emitted at large angles, resulting in large invariant masses (Fig. 6.319b).

*Decays of pions and kaons.* An important source of background originates from charged kaon and pion decays. In order to evaluate this contribution, we have simulated events containing primary  $\pi^\pm$ ,  $K^\pm$  with  $\eta$  and  $p_t$  distributions as extracted from central Pb–Pb events generated with HIJING [42, 67] (with shadowing and jet quenching). The multiplicity was normalized such that  $dN_{\text{ch}}/d\eta|_{\eta=0} = 8000$ ; as already seen in Section 6.6.4.4, this is a conservative assumption. The produced mesons were subsequently decayed to muons with the JETSET package [851]. The  $p_t$  and rapidity distributions for the decay muons are shown in Fig. 6.320. Due to the long lifetime ( $c\tau \simeq 4\text{--}8\text{ m}$ ) and an additional Lorentz boost, most of the  $\pi^\pm$  and  $K^\pm$  are absorbed by the front absorber before decaying. However, the charged pions and kaons that decay to muons before entering the absorber yield dimuon pairs, in which one muon is from a heavy-flavour meson and the other from a light-flavour one. This combinatorial background is fairly large and it has to be subtracted.

*Resulting single-muon cocktail per central collision.* Figure 6.321 shows the number of muons, integrated above the transverse momentum  $p_t^{\text{min}}$ , detected per central Pb–Pb event ( $5\% \sigma^{\text{inel}}$ ) in the spectrometer ( $-4 < \eta^\mu < -2.5$ ) when the low trigger cut,  $p_t > 1\text{ GeV}/c$ , is applied. Charm and  $\pi/K$  decay muons dominate below  $p_t \sim 1.5\text{ GeV}/c$ , while beauty dominates for higher transverse momenta.

As one can see in Fig. 6.321, a large sample of beauty events can be collected using an inclusive muon trigger. Single-muon trigger rates are nevertheless limited by the DAQ bandwidth, which is about 1 kHz for dimuon events in Pb–Pb collisions. In the following, we assume that the 400 Hz of 5% most central Pb–Pb collisions are entirely recorded. Considering  $10^6\text{ s}$  of data taking in one month, a sample of  $4 \times 10^8$  central Pb–Pb events can be collected by the muon arm DAQ. The results of the study presented here can be easily rescaled to lower statistics scenarios.

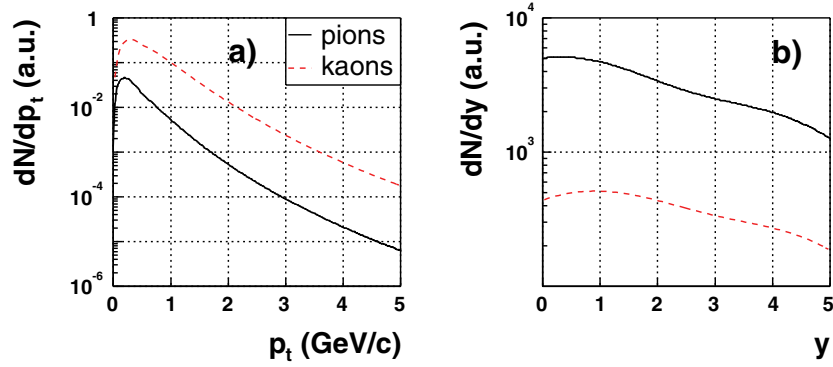


Figure 6.320. Transverse momentum (a) and rapidity (b) distributions for muons originating from decays in flight of charged kaons and pions.

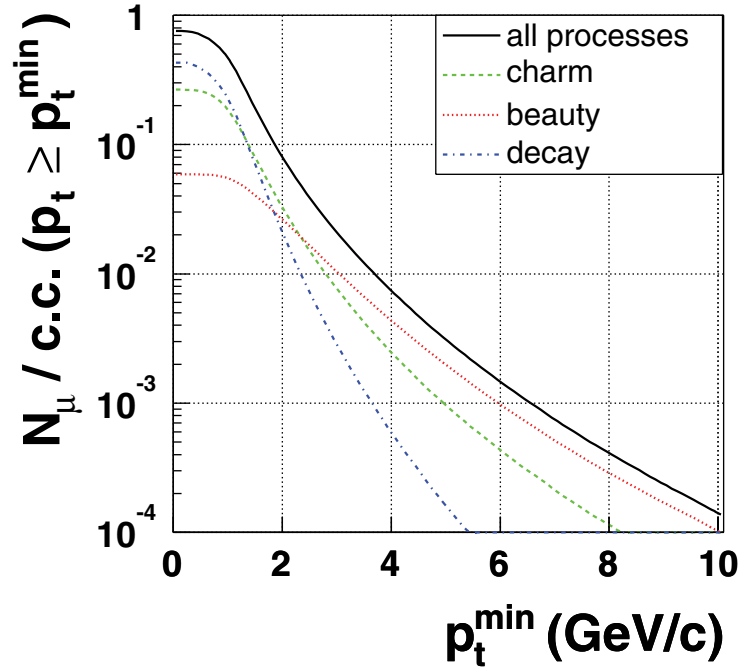


Figure 6.321. Number of muons with  $p_t \geq p_t^{\min}$  per central Pb–Pb collision (5% most central) detected in the muon spectrometer, including the low trigger cut  $p_t > 1$  GeV/c.

6.6.8.3. *Measurement of beauty production from muon data.* In the following, we detail the method to measure the inclusive beauty-hadron production cross section. Three muon data sets are used for this measurement:

- low-mass dimuons,  $M_{\mu^+\mu^-} < 5$  GeV, mainly coming from b-chain decays ( $\text{BD}_{\text{same}}$ );
- high-mass dimuons,  $5 < M_{\mu^+\mu^-} < 20$  GeV, mainly coming from  $b\bar{b} \rightarrow \mu^+\mu^-$ , each muon coming from a different quark in the pair ( $\text{BB}_{\text{diff}}$ );
- inclusive single muons.

The analysis, similar to that adopted by other experiments in the past (see e.g. Ref. [845, 846]), is subdivided in three steps:

1. maximization of the beauty signal component in the data sets;
2. evaluation of the signal content in the data sets and measurement of the muon level cross section from the number of  $B \rightarrow \mu$  events observed for each data set;
3. from muon-level cross sections, extraction of B-level cross sections for the data sets, each set covering a specific B meson  $p_t$  region.

*Muon signal selection.* The usual technique for background subtraction consists in estimating the uncorrelated background in the opposite-sign pairs sample from the measured distribution of same-sign pairs. Whereas this method has been successfully applied in dilepton physics at SPS energies [817, 852, 853], its applicability at the LHC is questionable because the same-sign sample contains a sizable fraction of leptons from B meson decays (correlated lepton pairs from chain decays and  $B^0-\bar{B}^0$  oscillations). The same-sign subtraction removes from the opposite-sign dilepton spectrum not only the uncorrelated component but also a fraction of the correlated signal. This would bias the estimation of the heavy-quark signal yield. The problem can be overcome by using a different method for background subtraction; namely, event mixing. With this procedure one estimates and subtracts the combinatorial opposite-sign background in each  $M_{\mu^+\mu^-}$  bin,  $N_{\mu^+\mu^-}^{\text{final}} = N_{\mu^+\mu^-} - N_{\mu^+\mu^-}^{\text{mixed}}$ . The statistical error on  $N_{\mu^+\mu^-}^{\text{final}}$  is  $\sqrt{N_{\mu^+\mu^-} + (\text{err}(N_{\mu^+\mu^-}^{\text{mixed}}))^2}$ ; here we assume that  $\text{err}(N_{\mu^+\mu^-}^{\text{mixed}})$  is negligible (this is true if the statistics of the mixed sample is larger than that of combinatorics), so that the error on  $N_{\mu^+\mu^-}^{\text{final}}$  is  $\sqrt{N_{\mu^+\mu^-}}$ , i.e. the statistical fluctuations of the final mass spectrum are numerically the same of the total spectrum. In addition, we assume that the background can be subtracted without any systematic bias. This corresponds to an optimistic case; a precise determination of possible systematic uncertainties related to the background subtraction with the event-mixing technique will have to be determined by means of full simulations. In particular, the definition of the classes of events to be used for mixing as well as the two-track resolution of the apparatus, which are known as potential sources of biases, must be investigated in detail.

At large transverse momentum, charm and beauty are produced with similar rates, but the harder beauty fragmentation results in a harder transverse momentum spectrum for its decay muons. Therefore, applying a muon  $p_t$  cut enriches the selected muon samples in  $b\bar{b}$  relative to  $c\bar{c}$  decays. This can be observed in Fig. 6.322 where signal statistics, signal purity and significance for charm and beauty decay muons are shown as a function of a  $p_t$  threshold on single muons. In our analysis we apply a conservative  $p_t$  threshold of 1.5 GeV/c to define a clean sample of muons from beauty decay. This value selects a large-statistics beauty signal with good signal-to-background ratio and significance. Note that, at the expense of a reduced signal statistics, a cleaner sample of muons from beauty decay could be obtained with a  $p_t$  threshold of 2 GeV/c.

A similar transverse momentum threshold of 1.5 GeV/c can be applied to the dimuon data samples. As shown in Fig. 6.323, the beauty signal purity,  $f_{b\bar{b}} = N_{b\bar{b}}/(N_{b\bar{b}} + N_{c\bar{c}})$ , reaches 80% of the correlated heavy-quark data in both the low-mass and high-mass regions. Note that increasing the transverse momentum threshold to values as high as 3 GeV/c enhances the beauty fraction by 10% only, while drastically reducing the available statistics. Therefore, a  $p_t$  threshold larger than 1.5 GeV/c is not mandatory for beauty analysis, though it could reduce the combinatorial background.

In summary, we apply the condition  $p_t^\mu > 1.5$  GeV/c for all three data sets.

*Evaluation of the beauty-signal fraction and of the muon-level cross sections.* The ALICE forward muon spectrometer is not equipped to discriminate b-decay muons from the

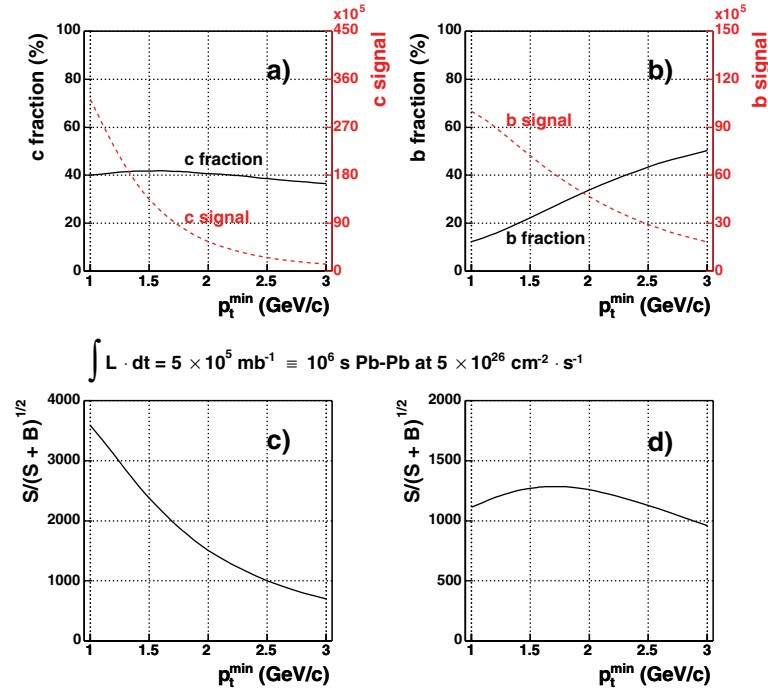


**Figure 6.322.** Signal statistics (dashed line, right scale), signal purity (solid line, left scale), and significance for charm (a and c) and beauty (b and d) decay muons.

background on the basis of their displacement from the collision vertex. The fraction of beauty signal is, instead, determined from a simultaneous analysis of the dimuon mass spectra and of the single-muon  $p_t$  distribution, after applying a cut on the minimum muon transverse momentum. As seen in the previous paragraph, the cut  $p_t^\mu > 1.5 \text{ GeV}/c$  is sufficient to maximize the beauty signal significance over the entire dimuon mass range. In order to evaluate the relative abundances of the beauty and charm signals, we perform a combined fit of the low-mass and high-mass dimuon mass spectra and of the single muons distribution. We use the beauty and charm mass and  $p_t$  shapes obtained from PYTHIA (with the tuning described in Section 6.6.3.4), with the amplitudes  $\mathcal{A}_{\text{beauty}}$  and  $\mathcal{A}_{\text{charm}}$  as fit parameters. Indeed, there is only one free parameter in the fit (namely, the ratio  $\mathcal{A}_{\text{charm}}/\mathcal{A}_{\text{beauty}}$ ). In fact, since the background-subtracted mass distributions are the sum of the charm and beauty signals, the amplitudes  $\mathcal{A}_{\text{charm}}$  and  $\mathcal{A}_{\text{beauty}}$  cannot be varied independently. This is true for the single muons as well, since the third component,  $\pi/K$  decays, is assumed to be known from measurements of  $\pi/K$  production in the ALICE central barrel (in Section 6.6.8.4 we provide an estimate of the systematic error due to the uncertainty in the normalization of the the decay component).

Figure 6.324 shows the opposite-sign dimuon mass spectra before (top panels) and after (bottom panels) the subtraction of the combinatorial background. Since the background is assumed to be subtracted using mixed events, the absolute statistical errors after subtraction are those of the total, unsubtracted, spectra. The result of the fit is also shown (bottom panels). In the high-mass region, where the beauty and charm components have similar shapes, the amplitude of the latter has been fixed to the value fitted in the low-mass region, where the shapes are different.

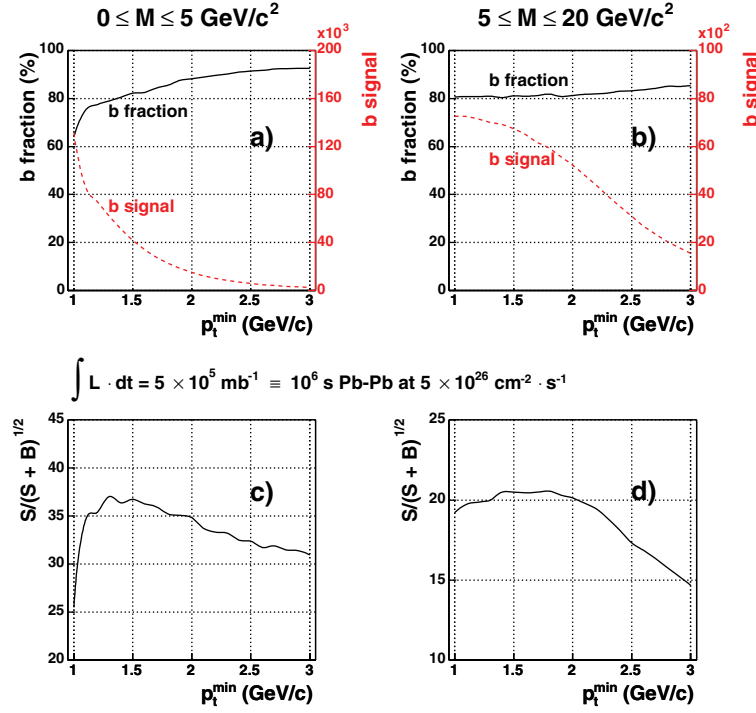


**Figure 6.323.** Signal statistics (dashed line, right scale), signal purity (solid line, left scale), and significance for opposite-sign muon pairs from beauty decays in the low-mass region (a and c) and high-mass region (b and d).

The inclusive muon  $p_t$  distribution in the range 1.5–20 GeV/c is shown in Fig. 6.325. The  $p_t$ -integrated beauty fraction resulting from the fit is about 0.223, while the main contributions come from charm and  $\pi/K$  decays that have large yields at low  $p_t$ .

The signal statistics  $N_{b\bar{b}}$  and  $N_b$  for one month of data-taking are given in Tables 6.72 and 6.73. The relative statistical errors are calculated as  $f_{b\bar{b}}\sqrt{N_{\mu^+\mu^-}}/N_{b\bar{b}}$  for dimuons and  $(N_b/N_\mu)\sqrt{N_\mu}/N_b$  for single muons.

After having determined, from the fitted  $b$  and  $b\bar{b}$  fractions, the number of beauty events in the three data samples, these numbers can be converted into cross sections by dividing by the integrated luminosity and by the global efficiencies  $\varepsilon$  (given in Table 6.71):

$$\sigma^\mu = \frac{N_b(N_{b\bar{b}})}{\int \mathcal{L} dt} \times \frac{1}{\varepsilon}, \quad (6.140)$$

where  $N_b$  ( $N_{b\bar{b}}$ ) is the number of beauty events, as extracted from the fit, in a given single-muon  $p_t$  bin or in the low- (high-) mass region for dimuons.

*Extraction of the B-level cross section.* The Monte Carlo based method described in Section 6.6.7.6 can be employed to extract, from the muon-level cross section, a cross section for B mesons in  $-4 < y < -2.5$  as a function of  $p_t^{\min}$ . The two dimuon samples, low-mass and high-mass, give two measurement points for  $p_t^{\min} = 2.05$  GeV/c and 2.85 GeV/c, respectively. The  $p_t$ -binned single muons in the range 1.5–20 GeV/c provide several measurements in the B meson  $p_t^{\min}$  range 1.25–22 GeV/c. The resulting  $\sigma^B(p_t > p_t^{\min})|_{-4 < y < -2.5}$  vs.  $p_t^{\min}$ , per nucleon–nucleon collision, is shown in Fig. 6.326.

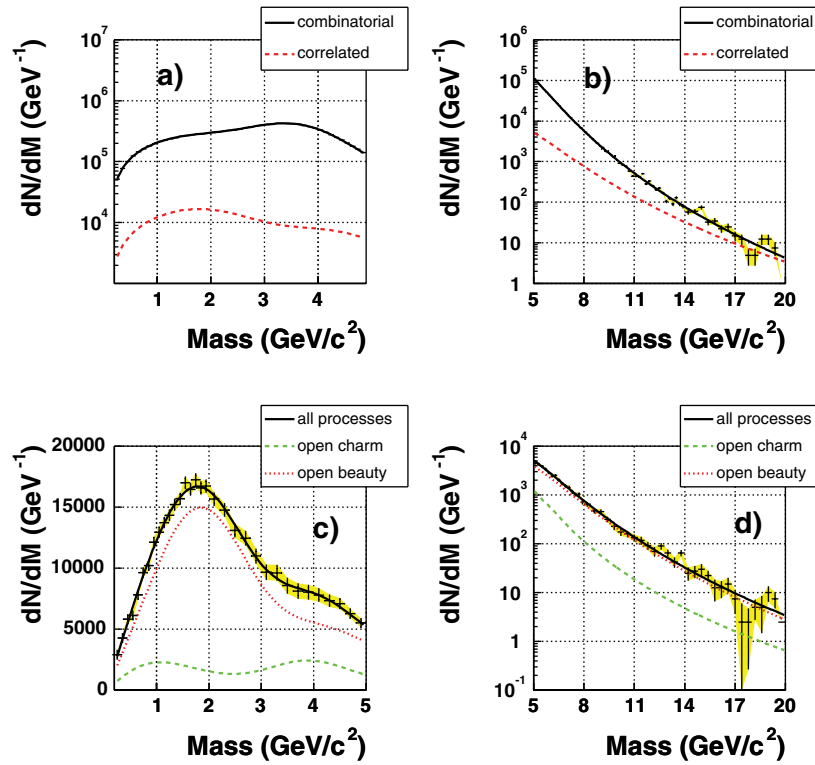


**Figure 6.324.** Invariant mass distributions of  $\mu^+\mu^-$  pairs produced in 5% most central Pb–Pb collisions at 5.5 TeV in the low-mass (left panels) and high-mass regions (right panels). A  $p_t^\mu > 1.5$  GeV/c cut was applied. Statistics corresponds to one month of data taking ( $10^6$  s). Top panels show the contribution of the combinatorial background (solid line) including the correlated signal (dotted line) made of a muon pair originating from the decay of the same initial heavy-quark pair. Background-subtracted mass spectra are presented in bottom panels. Charm and beauty signals are shown separately.

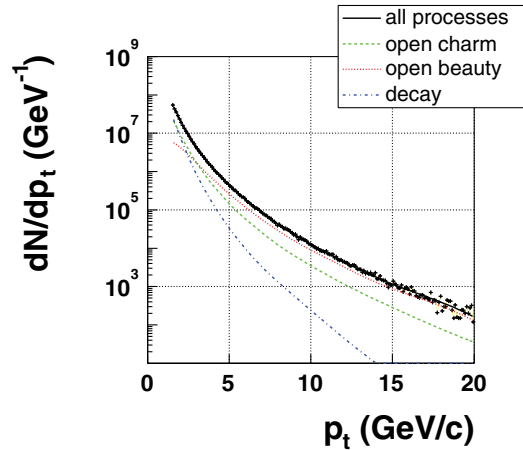


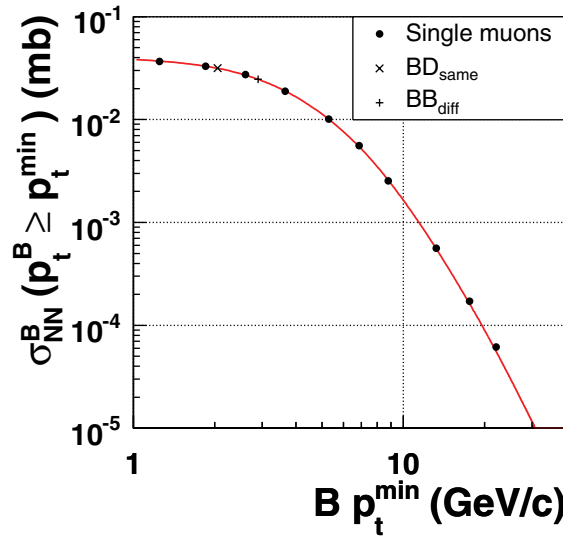
**Figure 6.325.** Inclusive muon transverse momentum distribution in 5% most central Pb–Pb collisions at 5.5 TeV. Statistics corresponds to one month of data taking ( $10^6$  s).

**Table 6.72.** Fitted dimuon beauty fractions in the low- and high-mass regions, and corresponding beauty statistics and statistical errors.

$M_{\mu^+\mu^-}$ (GeV)	$f_{b\bar{b}}$	$N_{b\bar{b}}$	Relative statistical error
0.3–5	0.835	41 461	1.91%
5–20	0.822	6 983	1.86%

**Table 6.73.** Beauty statistics as a function of  $p_t^\mu$  in the inclusive single-muon data set.

$p_t^\mu$ (GeV/c)	$N_b$	Relative statistical error
1.5–2.0	2 245 770	0.03%
2.0–2.5	1 516 447	0.04%
2.5–3.0	956 174	0.06%
3.0–4.0	951 659	0.07%
4.0–5.0	370 545	0.13%
5.0–6.0	155 667	0.20%
6.0–9.0	124 640	0.23%
9.0–12.0	19 910	0.60%
12.0–15.0	4 759	1.26%
15.0–20.0	1 875	2.06%

**Figure 6.326.** Minimum- $p_t$ -differential production cross section per nucleon–nucleon collision for B mesons with  $-4 < y < -2.5$  in 5% most central Pb–Pb collisions, as extracted from low-mass ( $BD_{\text{same}}$ ) and high-mass dimuons ( $BB_{\text{diff}}$ ), and from single muons. One month of data taking is assumed. Statistical errors (very small) are shown. Also shown (solid line) the input cross section used in our simulation.

**6.6.8.4. Estimation of the main systematic uncertainties.** Systematic uncertainties enter both the calculation of the muon-level cross sections  $\sigma^\mu$  and of the conversion factor  $\mathcal{F}_{\mu \rightarrow B}$  for the extraction of the B-level cross section (see Eq. (6.139)). Here, we only discuss the systematic uncertainties on the b-decay single-muon cross sections (the study of the systematic errors for

**Table 6.74.** Systematic errors on b-decay muons in the single-muon data set.

$p_t^\mu$ (GeV/c)	fit procedure	detector effects	total $p_t$ -dep.	$\pi/K$ decay	cross section normalization	total $p_t$ -indep.
1.5–2.0	4%	10%	11%			
2.0–2.5	4%	10%	11%			
2.5–3.0	3%	10%	10%			
3.0–4.0	3%	10%	10%			
4.0–5.0	2%	10%	10%	4%	9%	10%
5.0–6.0	2%	10%	10%			
6.0–9.0	3%	10%	10%			
9.0–12.0	4%	10%	11%			
12.0–15.0	8%	10%	13%			
15.0–20.0	12%	10%	16%			

dimuons is still under study). The main error sources are expected to be the following:

- Error introduced in the corrections for detector acceptance and efficiency. As done for the  $D^0 \rightarrow K^- \pi^+$  and  $B \rightarrow e$  cases, for present analysis we assume this error to be 10%; its precise evaluation will be addressed in future studies.
- Error due to the estimation of the  $\pi/K$  decay component in single-muon sample. By varying the normalization of this component by  $\pm 10\%$ , we estimated a systematic error of 4% on the amplitude of the beauty signal.
- Error introduced by the fit used to quantify the beauty fraction in the single-muon sample. We estimated this contribution by changing the shape of the beauty signal used in the fit, according to different choices of the parameters used in the pQCD calculation of  $b\bar{b}$  production and of the strength of nuclear shadowing. The resulting error, shown in Table 6.74, increases from about  $\pm 4\%$  at low  $p_t^\mu$  to about  $\pm 12\%$  for  $p_t^\mu > 15$  GeV/c.
- Error on the normalization to one nucleon–nucleon collision of the cross section measured in nucleus–nucleon collisions in a given centrality range. As discussed in Section 6.6.4.8 this error is estimated to be of about 9% for central Pb–Pb collisions (5%  $\sigma^{\text{inel}}$ ).

The estimated systematic errors, summarized in Table 6.74, were propagated to the minimum- $p_t$ -differential B meson production cross section per nucleon–nucleon collision, shown in Fig. 6.327. As discussed in Section 6.6.7.6, the additional systematic error introduced by the factor  $\mathcal{F}_{\mu \rightarrow B}$  is expected to be smaller than 5% and, thus, negligible with respect to the other systematic uncertainties.

*6.6.9. Outlook: ongoing studies and future directions.* In this section, we shortly describe some of the most relevant currently ongoing studies related to the detection of heavy-flavour particles:

- reconstruction of hadronic decays of charged charm mesons ( $D^+ \rightarrow K^- \pi^+ \pi^+$ );
- optimization of the selection of charm mesons using a pattern classification method;
- possible reconstruction of beauty decay vertices;
- charm detection at large rapidity using muons;
- detection of electron–muon coincidences;
- measurement of secondary  $J/\psi$ 's from B meson decays;
- beauty production measurement via multi-muon coincidences;
- detection of high- $p_t$  muons from W boson decays (which can be used as a medium-insensitive reference to study nuclear modifications to QCD probes).

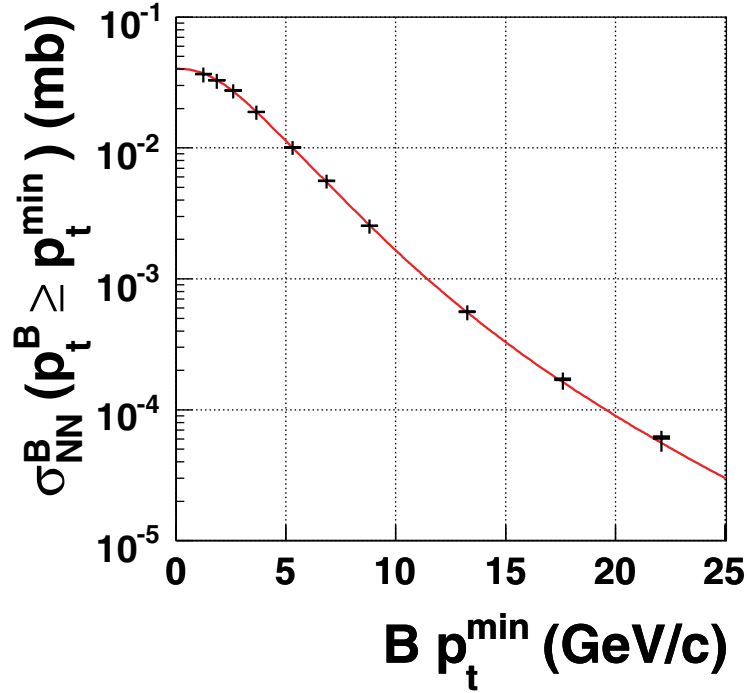


**Figure 6.327.** Minimum- $p_t$ -differential production cross section per nucleon–nucleon collision for B mesons with  $-4 < y < -2.5$  in central Pb–Pb collisions, as extracted from the single-muon data set. One month of data taking is assumed. Statistical errors (inner bars) and  $p_t$ -dependent systematic errors (outer bars) are shown. A normalization error of 10% is not shown.

**6.6.9.1.  $D^+$  hadronic decays.** A feasibility study for the reconstruction of charged D mesons produced in Pb–Pb and pp collisions is presently in progress.

The estimated number of  $D^+$  mesons in a 5% central event is  $\simeq 4$  in  $|y| < 1$  (see Table 6.55 on page 1782), about 1% of which come from beauty meson decays. With respect to the benchmark channel  $D^0 \rightarrow K^- \pi^+$ , discussed in Section 6.6.4,  $D^+$  mesons have a longer average decay length ( $c\tau \simeq 312 \mu\text{m}$ , compared to  $123 \mu\text{m}$  for the  $D^0$ ) and the decay channel  $D^+ \rightarrow K^- \pi^+ \pi^+$ , which is the most promising from an experimental point of view, has a larger branching ratio with respect to  $D^0 \rightarrow K^- \pi^+$  (9.2% compared to 3.8%). On the other hand, the combinatorial background for this three-body channel is significantly larger and, in addition, the average transverse momentum of the decay products is smaller ( $\simeq 0.7 \text{ GeV}/c$  compared to  $\simeq 1 \text{ GeV}/c$ ).

The selection strategy for this decay is now under study and it is rather similar to that used for  $D^0 \rightarrow K^- \pi^+$ . It is based on two sets of cuts, before and after the secondary vertex reconstruction. Since the number of all possible combinations of three tracks in a background event is of the order of  $10^{10}$ , a first set of cuts on the single tracks is needed before attempting to reconstruct the vertices. The selection can be done on the track impact parameter, on the transverse momentum and on the particle identification information. Tracks are then grouped requiring a correct combination of signs with an additional requirement on the invariant mass and passed to the vertexing algorithm. The algorithm currently under development is based on the method used to find the primary vertex in pp collisions; it finds

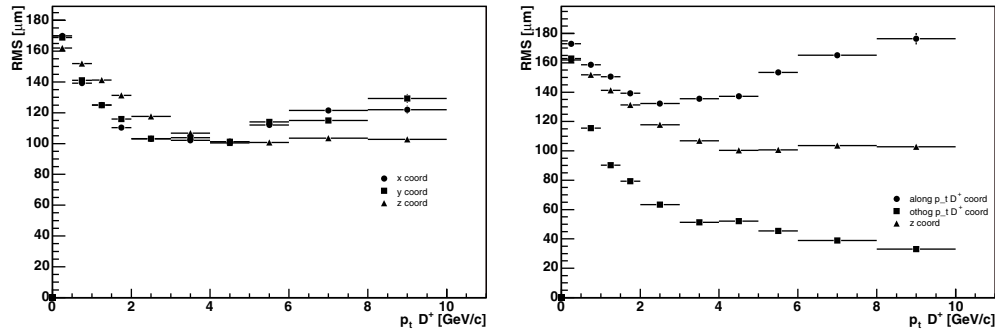


**Figure 6.328.** Left: resolution on the three coordinates ( $x$ ,  $y$ ,  $z$ ) of the position of the  $D^+$  decay vertex, as a function of the transverse momentum of the  $D^+$ . Right: the same resolution but on the three coordinates ( $x'$ ,  $y'$ ,  $z$ ), where ( $x'$ ,  $y'$ ) are directed respectively along and orthogonal to the  $D^+$  flight direction in the transverse plane.

the point of minimum distance in space to the three decay tracks approximated as straight lines. Figure 6.328 shows the expected resolution on the position of the  $D^+$  secondary vertex. A second selection is applied on the candidate vertices. The most promising cuts to be used are: the dispersion of the vertices (i.e. the sum of the squares of the distances of the secondary vertex from the three tracks), the cosine of the pointing angle between the  $D^+$  flight direction and momentum, and the separation of the secondary vertex from the interaction point.

*6.6.9.2. Perspectives for improving the  $D$  meson selection performance using a pattern classification method for cut-tuning.* The study of heavy-flavour particles suffer from their low production rate and from the dominant combinatorial background. We are studying the possibility to improve the signal/background discrimination, with respect to the approach presented in Section 6.6.4, by the use of a pattern classification method. These methods are meant to optimise the selection cuts such that they best select the signal and reject the background. Many of them also transform the  $n$ -dimensional space of the cut variables to a one-dimensional space, and hence reduce the cut-tuning process to finding the optimum of a function of only one variable. They therefore provide optimised selection cuts very rapidly.

Linear Discriminant Analysis (LDA) is one such method, which has the advantages of being simple and of having few parameters to be tuned. Its basic version consists in applying a cut along a linear combination of the variables, rather than on each of these variables separately. A better discrimination between signal and background is reached, and only one cut value, instead of  $n$ , has to be varied for the cut-tuning. The basic LDA method has been successfully adapted to the low signal-to-background ratio environments of the topological reconstruction of particles decaying weakly in heavy-ion collisions. Details about the method can be found in Ref. [854]. Preliminary studies for the  $D^0 \rightarrow K^- \pi^+$  channel show that a higher significance is obtained with LDA, while only little time has been dedicated to its cut-tuning.

LDA can also be used for the topological reconstruction of  $D^+$ ,  $D_s^+$  or  $\Lambda_c^+$  particles, as well as for the multi-strange baryons  $\Xi^-$  and  $\Omega^-$ . Improvements could also be obtained in specific areas such as low or high transverse momenta, where even the strange baryons are not easily observed with significant statistics.

*6.6.9.3. Reconstruction of beauty decay vertices.* The study of the ALICE performance for beauty detection in the central barrel presented here relies on the measurement of single electron tracks displaced from the primary vertex. A strategy based on the reconstruction of beauty decay vertices is currently under study. The knowledge of the vertex geometry provides additional information on the momentum of the parent particle and further constraints to be used for background rejection.

*6.6.9.4. Measurement of charm production in the muon spectrometer.* In this chapter we have discussed the ALICE capability for the measurement of beauty production in central Pb–Pb collisions via the detection of semi-muonic decays in the muon arm. A measurement of open charm in the muon arm would also be of primary importance, both in its own right, and as a reference to understand possible modifications of  $J/\psi$  production. While open beauty dimuons will dominate the high-mass high- $p_t$  region, charm dimuons will mostly be produced in the low-mass low- $p_t$  region where we also expect a large combinatorial background, making charm detection a more complicated business. A dedicated detection strategy is currently under investigation. The main challenge will be to maximize the charm signal-to-background ratio isolating the optimal phase space window with an appropriate set of kinematic cuts.

*6.6.9.5. Charm and beauty detection via  $e$ – $\mu$  coincidences.* The  $c\bar{c}$  and  $b\bar{b}$  production cross sections could be measured in ALICE from unlike-sign electron–muon pairs where the electron is identified in the central barrel ( $|\eta| < 0.9$ ) and the muon is detected in the forward muon spectrometer ( $-4 < \eta < -2.5$ ). The  $e$ – $\mu$  channel is the only leptonic channel that gives a direct access to the correlated component of the  $c\bar{c}$  and  $b\bar{b}$  pairs. Indeed, in contrast to  $e^+e^-$  and  $\mu^+\mu^-$  channels, neither a resonance, nor direct dilepton production, nor thermal production can produce correlated  $e$ – $\mu$  pairs. Within ALICE, the  $e$ – $\mu$  channel has the additional advantage that the rapidity distribution of the corresponding signal extends from  $y_{Q\bar{Q}} \simeq -1$  to  $y_{Q\bar{Q}} \simeq -3$ , therefore bridging the acceptances of the central and the forward parts of the detector [799]. Electron–muon coincidences have already been successfully measured in pp collisions at  $\sqrt{s} = 60$  GeV [855] and in proton–nucleon collisions at  $\sqrt{s} = 29$  GeV [856]. Fast simulation studies indicate that it should be possible to measure the correlated  $e$ – $\mu$  signal in ALICE after appropriate background subtraction [857].

*6.6.9.6. Measurement of  $J/\psi$ 's from B meson decays.* B mesons decay into  $J/\psi$  mesons with a branching ratio of about 1%. Since B mesons are produced by a factor of 5 more abundantly than  $J/\psi$  mesons, and since direct  $J/\psi$  production might be further suppressed by QGP effects, secondary  $J/\psi$  mesons are conceivably contributing a large fraction to the observable  $J/\psi$  signal (see also Section 6.7).

The interest for developing a procedure to measure the production of secondary  $J/\psi$ 's is clearly two-fold. First, they will provide a sensitive measurement of the B meson production cross section, complementary to the measurements described in Sections 6.6.7 and 6.6.8, that use the semi-leptonic decay channel —  $B \rightarrow J/\psi + X$  has become the standard decay channel to study beauty production in  $p\bar{p}$  collisions at the Tevatron. Second, the identification and reconstruction of secondary  $J/\psi$  mesons is essential to investigate medium effects on primary charmonia. This is particularly important for the  $p_t$  dependence of the  $J/\psi$  signal, since  $J/\psi$ 's from B meson decays exhibit a much harder transverse momentum spectrum than the primary one. At large transverse momentum the ratio of primary to secondary  $J/\psi$ 's may grow as large

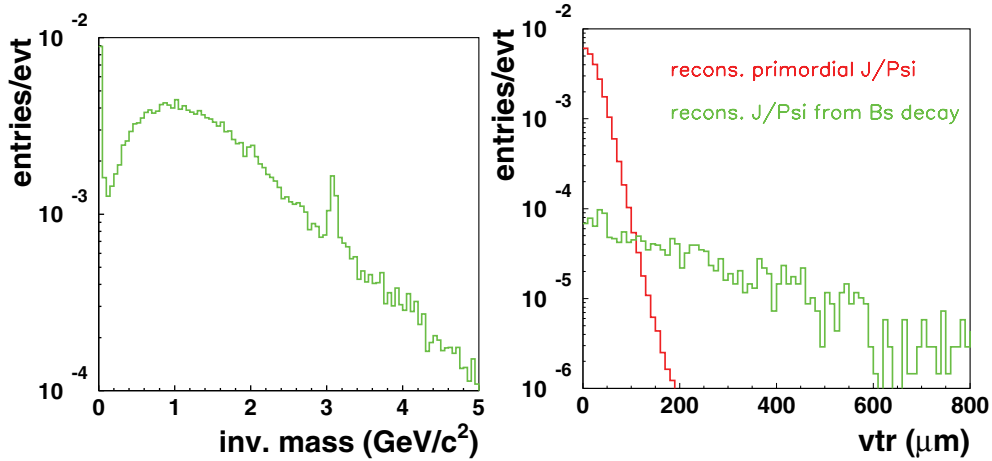


**Figure 6.329.** Invariant mass distribution of pairs with displaced vertices (left panel) and distance to primary vertex dependence of the  $J/\psi$  signal (right panel).

as  $1/l$ . A trustworthy physics interpretation of the measured  $J/\psi$  production can clearly only be given once the secondary contribution is quantitatively known.

The impact parameter measurement with the ITS and the particle identification by the TPC/TRD allow us to reconstruct the vertex of all  $e^+e^-$  pairs. In Fig. 6.329 we present the results of a fast simulation study with simple acceptance cuts and parametrized track reconstruction resolutions. Gating on large transverse impact parameter,  $|d_0|$ , enhances the fraction of electrons from B meson decays and results in the  $e^+e^-$  invariant mass spectrum shown in the left-hand panel of Fig. 6.329. A peak of secondary  $J/\psi$ 's is clearly visible with a signal-to-background ratio of 3/1. Selecting pairs near the  $J/\psi$  mass peak gives rise to the  $e^+e^-$  secondary-vertex displacement distribution shown in the right-hand panel of Fig. 6.329. An exponential distribution is observed and will allow us to experimentally establish the secondary  $J/\psi$  yield. Dedicated simulation studies, currently in progress, will allow us to prepare an analysis procedure along the lines briefly discussed here, and to assess the performance that can be reached.

**6.6.9.7. Beauty production measurement via multi-muon coincidences.** The ALICE muon spectrometer identifies and measures muons in the kinematic region  $-4 < \eta < -2.5$  and  $p_t > 1$  GeV/c. In addition to single-muons and dimuons (Section 6.6.8), multi-muons—three- and four-muons—are a promising signature that can be exploited for the study of beauty production.

In the low and intermediate transverse momentum region, beauty decays are the dominant source of correlated 3(4)-muon events. In these events, at least one beauty hadron from a  $b\bar{b}$  pair produced in the initial hard interaction decays through a chain decay  $b \rightarrow c(\rightarrow \mu + X) + \mu + X'$  and the other one, or two, muons come from the semi-muonic decay of its partner. The third muon tag can also be used to identify  $J/\psi$ 's produced in B decays. In this case, the beauty hadron recoiling against the  $J/\psi$  reconstructed in the dimuon channel decays semi-muonically.

This method works best for pp collisions, in which the contribution from uncorrelated muons is small. The third muon tag reduces the statistics by a factor of five due to the branching ratio and by another factor of five accounting for the acceptance of the third muon.

Preliminary studies for pp collisions show that  $J/\psi$ 's from B decays can be identified with a signal-to-background ratio of  $S/B \approx 3$  and a significance of  $S/\sqrt{S+B} = 80$  for one year of running. Beauty hadrons with almost zero transverse momentum can be identified. For central Pb–Pb collisions we expect of the order of one muon with  $p_t > 1 \text{ GeV}/c$  per event leading to a large rate of uncorrelated muon pairs. Under these conditions, the  $S/B$  ratio drops to about  $3 \times 10^{-3}$  and the significance for one year of running is as small as 1.5. Further studies will show to which extent the method can be used in lower multiplicity collisions, as Ar–Ar and peripheral Pb–Pb.

**6.6.9.8. W production at the LHC studied in the muon decay channel.** The high amount of centre-of-mass energy available at the LHC will allow W bosons to be produced with fairly large yields. These bosons have a decay branching ratio  $BR(W \rightarrow \mu\nu_\mu) \approx 10.6\%$  into muons [409], which can be detected by the muon spectrometer of ALICE. In pp collisions, W boson decay muons detected in the forward muon spectrometer will allow us to probe quark parton distribution functions in the low Bjorken- $x$  range,  $x \sim 10^{-4}$ – $10^{-3}$ , for large  $Q^2 \sim M_W^2$ . In pA collisions, the production cross section may be sensitive to the nuclear modification of quark distribution functions. In AA collisions, being weakly-interacting probes, W bosons will not interact with the surrounding medium, hence they could provide a reference for observing medium-induced effects on other probes, like energy loss of high- $p_t$  b quarks.

Perturbative QCD calculations at NLO predict the W production cross section in the muonic decay channel to be  $BR(W \rightarrow \mu\nu_\mu) \times \sigma_W \simeq 20.9 \text{ nb}$  in pp collisions at  $\sqrt{s} = 14 \text{ TeV}$  [858] and  $\simeq 280 \mu\text{b}$  in Pb–Pb collisions at 5.5 TeV [859]. In a nominal pp run (about  $10^9$  events), more than  $5 \times 10^5$  W bosons decaying into muons will be produced in ALICE, yielding  $\simeq 8.7 \times 10^4$  muons in the muon spectrometer acceptance. Those muons will populate the high- $p_t$  part of the single muon spectra, above  $25 \text{ GeV}/c$ . The other main muon contribution in this high- $p_t$  region comes from semi-leptonic decays of beauty and charm mesons. For example, in pp collisions at  $\sqrt{s} = 14 \text{ TeV}$ , W boson decays are expected to yield about 70% of muons at  $p_t \simeq 40 \text{ GeV}/c$ , the remaining 30% being mainly B decays.

Studies on the detection efficiency for such high- $p_t$  muons and on dedicated trigger strategies are currently in progress.

## 6.7. Quarkonia production

**6.7.1. General considerations.** The study of quarkonia production in heavy ion collisions represents one of the most powerful methods to probe the nature of the medium the fireball is made of. In fact, as discussed in the theoretical overview on ALICE physics (see PPR Volume I [3], Section 1.3.8), heavy quarkonia are sensitive to the collision dynamics at both short and long timescales, and are expected to be sensitive to plasma formation.

These reasons represent a strong motivation for experimental studies of quarkonia production, which have been (and are being) carried out both at SPS and RHIC energies. The results obtained so far have provided relevant contributions to form a coherent picture of the conditions achieved in the collisions.

The most complete set of data available at present is the one collected by the NA38/NA50 experiment at CERN SPS [860]. In this experiment, the charmonia ( $J/\psi$  and  $\psi'$ ) are detected via their  $\mu^+\mu^-$  decay by a magnetic spectrometer with acceptance covering the c.m. rapidity interval  $0 < y_{\text{cm}} < 1$ . Measurements have been carried out with different colliding systems and energies, from O–U and S–U (NA38), with a projectile energy of 200 GeV per nucleon,

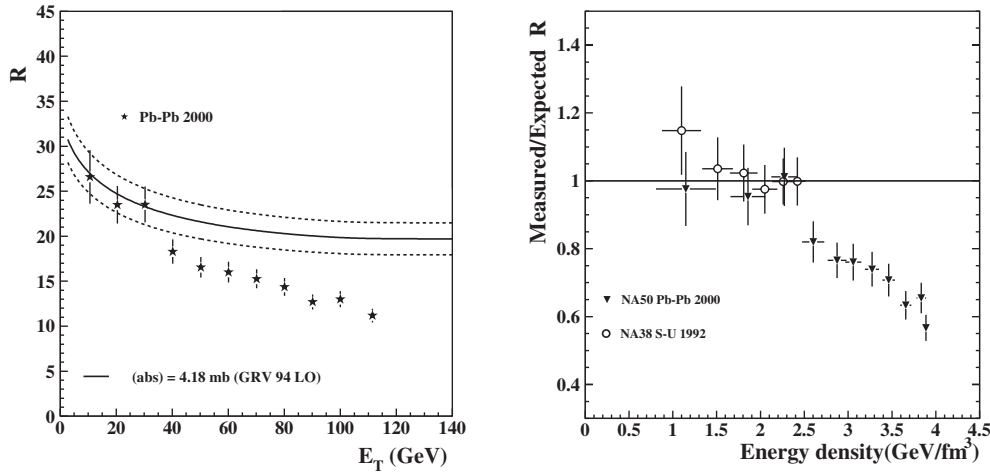


**Figure 6.330.** Left:  $J/\psi$  to Drell-Yan ratio  $R$  (defined as  $R = B_{\mu\mu}\sigma_{J/\psi}/\sigma_{\text{DY}}$ ) as a function of  $E_T$  [860]. The solid curve represents the  $J/\psi$  suppression due to ordinary nuclear absorption. Right: measured  $J/\psi$  to DY ratio  $R$  normalized to the one expected in case of nuclear absorption as a function of the energy density.

to Pb–Pb (NA50) with a projectile energy of 158 GeV per nucleon. Moreover, besides nucleus–nucleus collisions, proton–proton and p–nucleus interactions (with proton energy as high as 450 GeV) have been studied in detail. It is important to stress that the latter measurements have been of crucial importance for the interpretation of nucleus–nucleus data, as it is discussed below. At SPS energies, the Drell-Yan yield (DY) can be experimentally measured since it dominates the dimuon spectrum for masses above  $4 \text{ GeV}/c^2$  and therefore has been used to normalize the charmonia yields. However, it is worth noting that the statistics achievable for the DY process is poorer than the  $J/\psi$  one: this means that the error bars for the  $J/\psi$  to DY ratio are dominated by the DY statistics.

The NA38/NA50 data collected with proton, Oxygen and Sulphur beams on several targets show that the  $J/\psi$  yield is suppressed with respect to the DY one. Namely, the  $J/\psi$  to DY ratio shows an exponential behaviour when plotted as a function of mean length of nuclear matter crossed by the  $c\bar{c}$  pair (the so-called  $L$  variable). This ‘normal’ suppression is interpreted in terms of nuclear absorption of the  $c\bar{c}$  pair prior to  $J/\psi$  formation.

The extrapolation to the Pb–Pb system of the normal suppression pattern observed with lighter systems represents the baseline to which the Pb–Pb data can be compared. These data are shown in the left panel of Fig. 6.330, where the  $J/\psi$  to DY ratio is plotted as a function of the neutral transverse energy  $E_T$  measured by the NA50 electromagnetic calorimeter over the rapidity interval  $1.1 < y_{\text{lab}} < 2.3$ . As seen in this figure, while the low  $E_T$  data are consistent with the normal suppression mechanism (solid curve), a departure from nuclear absorption occurs above  $E_T \sim 40 \text{ GeV}$  (corresponding to an impact parameter of about 8 fm), where the data indicate a more pronounced suppression of the  $J/\psi$  (the so-called anomalous suppression).

The deviation from genuine nuclear absorption is even more clearly visible in the right panel of Fig. 6.330, where the ratio between the measured  $J/\psi$  to DY ratio and the one expected to arise from nuclear absorption is plotted as a function of the energy density  $\varepsilon$ . The use of this variable allows plotting in the same figure the data points measured for different colliding systems. For nucleus–nucleus collisions, the energy density is obtained from the

measured neutral transverse energy according to Bjorken's model, while for p–nucleus data  $\varepsilon$  is estimated by means of the RQMD cascade model (more details can be found in Ref. [861]). From this figure it can be seen that the ratio is close to one for light systems and for peripheral Pb–Pb collisions, while for more central Pb–Pb interactions ( $\varepsilon > 2.3 \text{ GeV fm}^{-3}$ ) it becomes smaller than one, showing a monotonic decrease as a function of  $\varepsilon$ . The existence of an anomalous suppression mechanism is also confirmed by the analysis [860] carried out by using as a centrality estimator the zero-degree energy (measured by the NA50 Zero-Degree Calorimeter [862]) and the charged particle multiplicity (measured by the silicon multiplicity detector [863]).

The data indicate that the departure from the normal absorption curve is setting in over a rather narrow range of centrality values. This feature turns out to be in line with the suppression pattern expected in case of deconfinement [864]. In this scenario, the 'anomalous' suppression is interpreted as the melting of  $\chi_c$  mesons, responsible for a sizeable fraction (20 ÷ 40%) of the detected  $J/\psi$  via their radiative decay. Models alternative to deconfinement have been proposed as well; most of them are based on the idea that the anomalous  $J/\psi$  suppression is due to its breakup by interaction with comoving hadrons [865, 866].

Recently, lighter systems have been investigated at SPS: data on charmonium production have been collected in indium–indium reactions by the NA60 Collaboration during Autumn, 2003. The NA60 apparatus [867] complements the muon spectrometer and the zero-degree calorimeter previously used by NA50 with a completely redesigned target area, which includes a vertex telescope made of 11 logical planes of radiation-hard pixel detectors placed immediately downstream of the target and a cryogenic radiation-hard silicon beam tracker. Preliminary results [868] on the  $J/\psi$  yield as a function of the number of participants  $N_{\text{part}}$  reveal the presence of an anomalous suppression pattern similar to the one induced by a percolation phase transition [869]: however, the model fails to reproduce the onset of such suppression ( $N_{\text{part}} = 90$  in the data, to be compared with  $N_{\text{part}} = 140$  in the model).

Where higher c.m. energies are available (RHIC and LHC), the study of charmonia is subject to significant differences with respect to the SPS energies. In addition to prompt charmonia produced directly via hard scattering, secondary charmonia can be produced according to different mechanisms which might result in an enhancement instead of a suppression of charmonium states. Secondary charmonium production can occur both as a consequence of QGP formation (kinetic recombination [870] and statistical hadronization [871–873] models) and during the hadronic phase (bottom decay [409] and  $D\bar{D}$  annihilation [874, 875]).

The experiment best suited for the study of quarkonia production at RHIC is PHENIX, which has the capability of detecting charmonium both in the dielectron ( $-0.35 < \eta < 0.35$ ) and in the dimuon ( $-2.2 < \eta < -1.2$  and  $1.2 < \eta < 2.4$ ) channels. The most recent data [876] exhibit a factor three suppression for most central Au–Au collisions at  $\sqrt{s} = 200 \text{ GeV}$ . Comparison with theoretical models suggests that, if on the one hand cold nuclear absorption is not sufficient to reproduce the observed suppression, on the other hand recombination/regeneration models seem to be needed in order not to overestimate the suppression when extrapolating from CERN experiments. Unfortunately, the statistics of the present Au–Au data sample is not sufficient to strongly discriminate between the production models cited above.

At LHC, the much higher energy offers the possibility of measuring with 'significant' statistics the bottomonium yields thus providing an additional probe for QGP studies. In fact, since the  $\Upsilon(1S)$  dissolves only significantly above the critical temperature [877], at a value which should not be reached at RHIC, the spectroscopy of the  $\Upsilon$  family at

LHC energies should reveal a unique set of information on the characteristics of the QGP [878].

However, new problems arise in the study of charmonium production at LHC. First of all, in the dense medium produced in a heavy ion reaction, energy loss of heavy quarks might substantially modify the spectra of the decay particles (see [879] and references therein): this implies that the study of onium production must be combined to the study of open heavy flavours. Moreover, the choice of the reference process for the normalization of the quarkonia signal is not obvious (see Section 6.7.1.4), and the fraction of  $J/\psi$  originated from B decay has to be taken into account. Finally, the quarkonium signals will be sitting on top of a complex combinatorial background, mainly coming from open charm and open bottom decay [880].

It is therefore obvious that a meaningful understanding of the QGP requires to perform systematic investigations. Indeed, the signals have to be measured:

- as a function of centrality (to identify suppression/enhancement patterns);
- as a function of the size of the colliding system (to disentangle normal and anomalous suppression);
- for all onium species (because their different survival probabilities probe the temperature of the system);
- as a function of  $p_t$  (to disentangle QGP models);
- together with open charm and open bottom (as discussed above);
- with good vertex resolution (to distinguish between prompt and secondary charmonia);
- versus the reaction plane (to unravel Glauber and comover absorption);
- together with other QGP signals.

This physics program should be achievable with the ALICE detector. Quarkonium states will be identified in the dielectron and the dimuon channels respectively in the central and in the forward region [881]. Open charm and bottom will be measured in the hadronic and semi-leptonic decay channels of heavy mesons.

*6.7.1.1. Quarkonia detection in ALICE.* Heavy quarkonia will be detected in ALICE both in the dielectron (at midrapidity) and in the dimuon channel (in the forward region). The key detectors for this study are the Transition Radiation Detector (TRD), which allows to identify electrons among the particles tracked by the Inner Tracking System (ITS) and the Time Projection Chamber (TPC), and the Forward Muon Spectrometer. The characteristics of these detectors relevant for heavy quarkonia measurements are summarized in Table 6.75; more details can be found in Sections 3.6 and 3.11 of PPR Volume I [3] and references therein. The two different sets of equipment will allow a comprehensive and detailed investigations on heavy quarkonia production thanks to their complementary performance and capabilities, briefly outlined here.

*Rapidity and  $x$  range.* It is important noting that, in the global ALICE coordinate system (outlined in Section 5.1) the  $z$  axis is oriented in the direction opposite to the one of the Muon Spectrometer. This means that the Muon Spectrometer lies at negative  $z$  values. However, for the sake of readability, in this chapter the orientation of the  $z$  axis is reverted. Therefore, in this reference system, the angular acceptance of the Muon Spectrometer is  $2^\circ < \theta < 9^\circ$ , and the corresponding rapidities are positive.

The rapidity acceptances of the TRD and of the Muon Spectrometer are given in Table 6.75. The acceptances seat at the centre and at the edge (respectively) of the rapidity plateau characteristic of quarkonia production (see Section 6.7.1.2). The combined

**Table 6.75.** Acceptance coverage for dileptons in the ALICE experiment. The  $x$  ranges are given for Pb–Pb at  $\sqrt{s} = 5.5$  TeV per nucleon pair.

	State	$y$ range	$x$ range	min. $p_t$ (triggerable)	Prompt vs. sec. $J/\psi$
Electron	$J/\psi$	$-0.9 \leq y \leq 0.9$	$2.3 \times 10^{-4} \leq x_{1,2} \leq 1.4 \times 10^{-3}$	5 GeV/ $c$	Yes
	$\Upsilon$	$-0.9 \leq y \leq 0.9$	$7.0 \times 10^{-4} \leq x_{1,2} \leq 4.2 \times 10^{-3}$	0	
Muon	$J/\psi$	$2.5 \leq y < 4.0$	$7.0 \times 10^{-3} \leq x_1 \leq 3.1 \times 10^{-2}$ $1.0 \times 10^{-5} \leq x_2 \leq 4.6 \times 10^{-5}$	0	No
	$\Upsilon$	$2.5 \leq y < 4.0$	$2.1 \times 10^{-2} \leq x_1 \leq 9.3 \times 10^{-2}$ $3.1 \times 10^{-5} \leq x_2 \leq 1.4 \times 10^{-4}$	0	

measurements at central and forward rapidities allow the study of the rapidity dependence of the enhancement/suppression patterns of heavy quarkonia production, providing a deeper understanding of the underlying physics mechanisms. The rapidity windows covered by the two detectors correspond to different  $x$  ranges, where  $x$  is the fraction of the nucleon momentum carried by the interacting parton. These ranges were computed for Pb–Pb collisions at  $\sqrt{s} = 5.5$  TeV per nucleon pair (for details see [828]) and are listed in Table 6.75: we use the convention of indicating with  $x_1$  ( $x_2$ ) the  $x$  variable relative to the beam particle moving in the direction of the Muon Spectrometer (opposite to the Muon Spectrometer, i.e. towards the Photon Multiplicity Detector). While the TRD covers the region  $x \sim 10^{-3}$ , the forward acceptance of the Muon Spectrometer makes  $x$  values as small as  $10^{-5}$  accessible to this detector. This means that ALICE will be able to measure quarkonia production in two complementary regions of  $x$ , providing an additional insight to PDFs and their modifications in nuclei.

*Transverse momentum range.* Both the TRD and the Muon Spectrometer are equipped with a trigger system to select events of interest containing, for instance, a lepton pair from quarkonia decay amongst all possible background sources. Since most of the background is due to leptons of low transverse momentum, a  $p_t$  cut is applied at the trigger level to each individual electron (muon) detected in the TRD (Muon Spectrometer). The relatively high value of the  $p_t$  trigger cut (3 GeV/ $c$ ) applied to single electrons prevents the detection of charmonia with transverse momentum lower than 5 GeV/ $c$  in the TRD if events are taken with the TRD-L1 trigger condition. In the case of central Pb–Pb events, the online trigger is not effective, due to the high multiplicity of background tracks, so that in this case the acceptance extends to  $p_t = 0$ . The trigger, however, will be important in the case of low multiplicity events (e.g. pp), especially for the measurement of the  $\Upsilon$ -family.

For the Muon Spectrometer, the modest  $p_t$  cut of 1 GeV/ $c$  (2 GeV/ $c$ ) applied to single muons allows charmonia (bottomonia) detection down to zero transverse momentum.

*Prompt and secondary  $J/\psi$ .* The excellent vertexing capabilities of the ALICE barrel detectors can be used in conjunction with electron identification in the TRD to discriminate prompt from secondary  $J/\psi$  originating from B decay. The latter are in fact produced at large distances from the primary vertex and can therefore be selected by identifying  $e^+e^-$  pairs with displaced vertex. Since the ITS does not cover the forward rapidity region, this method cannot be applied to the  $J/\psi$  detected in the Muon Spectrometer. In this case, the yield of prompt  $J/\psi$ 's can be determined only indirectly, by subtracting from the measured yield the one expected from B decay. The latter can be inferred from the open beauty measurements carried out with the Muon Spectrometer and reported in Chapter 6.6.

**Table 6.76.** Inclusive lepton pair cross sections as obtained from CEM (see text) for pp and minimum bias Pb–Pb collisions. All cross sections are in  $\mu\text{b}$ .

System	$\sqrt{s}$ (TeV)	$\sigma_{J/\psi}$	$\sigma_{\psi'}$	$\sigma_{\Upsilon}$	$\sigma_{\Upsilon'}$	$\sigma_{\Upsilon''}$
pp	14	3.18	0.057	0.028	0.0069	0.0041
pp	5.5	1.83	0.033	0.012	0.0030	0.0018
Pb–Pb	5.5	48930	879	420	109	61

### 6.7.1.2. Simulation inputs

*Heavy quarkonia.* Extrapolations from measured  $J/\psi$  and  $\Upsilon$  production cross sections to LHC energies have been performed using the Colour Evaporation Model (CEM) [882]. In this model the transition of a  $q\bar{q}$  pair into a colour singlet quarkonium state is performed by soft interactions at the QCD energy scale ( $\mathcal{O}(\Lambda_{\text{QCD}})$ ). The production cross section is calculated as a product of the  $q\bar{q}$  cross section and a transition probability which is specific to each state but independent of the energy. It can be computed from measured production cross sections and branching ratios. The obtained cross sections are the sum of direct production and feed-down from higher-mass resonances below the  $D\bar{D}$  and  $B\bar{B}$  thresholds. The  $q\bar{q}$  production cross section depends on the chosen parton density function (PDF), the heavy quark mass ( $m_q$ ) and the factorization scale ( $\mu$ ).

For bottomonium production, the pp cross sections used in the studies presented here are obtained with the MRST HO PDF,  $m_b = 4.5 \text{ GeV}/c^2$  and  $\mu = 2m_b$  [828]. With this choice of the parameters, the CEM predictions turn out to be in agreement with the experimental data at Tevatron energies, allowing a safe extrapolation to LHC energies.

The situation for charmonium production is rather different. In fact, the CEM predictions with the same PDF (and with  $m_c = 1.2 \text{ GeV}/c^2$  and  $\mu = 2m_c$  [828]), while being in reasonable agreement with total cross section data up to  $\sqrt{s} \approx 100 \text{ GeV}$ , turn out to be smaller than the recent midrapidity data at Tevatron by about a factor of two (we note that varying the CEM input parameters cross sections up to 20% higher and 30% lower can be obtained). Therefore, the charmonium cross sections used in this study represent a very conservative choice and the rates and yields presented in the following have to be regarded as a rather pessimistic estimate. The resulting inclusive lepton pair cross sections for pp collisions used are listed in Table 6.76. These cross sections include feed-down from resonances of higher mass and the branching ratios in the dilepton channel. (We note that, since quarkonia branching ratios in the  $e^+e^-$  and  $\mu^+\mu^-$  channels are almost identical, these cross sections will be used both for dielectron and dimuon studies.)

In addition to prompt  $J/\psi$  and  $\psi'$ , also those from B decay are taken into account. These cross sections (both at 5.5 and 14 TeV) have been obtained from the open beauty cross section (see Section 6.6) using the  $B \rightarrow J/\psi$  and  $B \rightarrow \psi'$  branching ratios.

For A–A collisions, binary scaling ( $\times A^2$ ) of the corresponding pp cross section is performed and EKS98 nuclear modifications (shadowing) of the parton distribution functions are taken into account [828]. The resulting inclusive lepton pair cross sections for Pb–Pb collisions are shown in Table 6.76.

The rapidity and transverse momentum distributions for prompt production of the different quarkonia states have been respectively obtained as a parameterization of the CEM predictions and by extrapolating to LHC energies the  $J/\psi$  [883, 884] and  $\Upsilon$  [885]  $p_t$  distributions measured (at midrapidity) by the CDF experiment at  $\sqrt{s} \sim 2 \text{ TeV}$ . The extrapolation of the  $p_t$  distribution consists of three steps. First of all, the CDF  $p_t$  distributions for  $\Upsilon$ 's and prompt  $J/\psi$ 's are fitted with the function  $f(p_t) = cp_t/(1 + (p_t/A)^2)^n$ . Then,

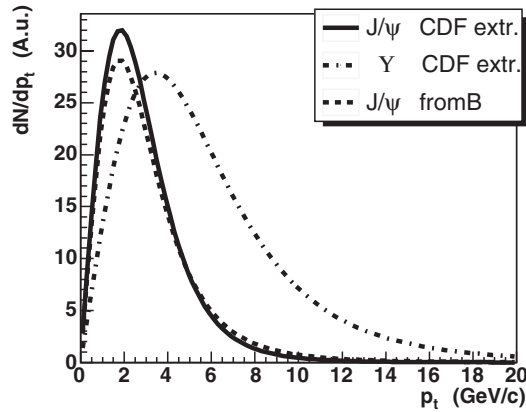


**Figure 6.331.** Transverse momentum distributions for  $J/\psi$  (prompt and from B decay) and  $\Upsilon$  in Pb–Pb collisions at  $\sqrt{s} = 5.5$  TeV per nucleon pair. The relative normalization of the different curves is arbitrary.

the resulting function is extrapolated to LHC energies according to the  $\sqrt{s}$  dependence of  $\langle p_t^2 \rangle$  predicted by the CEM [780]. Finally, the  $p_t$  dependence of shadowing is taken into account [828] to obtain the transverse momentum distributions for Pb–Pb collisions. These distributions are shown in Fig. 6.331. For the  $J/\psi$ 's from B decay, PYTHIA has been used to compute the rapidity and transverse momentum spectra. The latter is displayed in Fig. 6.331 (dashed line).

*Open charm and beauty cross sections.* In order to simulate correlated and uncorrelated dimuon and dielectron pairs from semileptonic beauty and charm hadrons we use the heavy flavour MC production and cross sections described in Section 6.6. The decays are performed using PYTHIA.

*Muons from kaon and pion decays.* An important source of uncorrelated dimuon background in the low-mass region comes from charged pion and kaon decays. The pseudo-rapidity and transverse momentum distributions of these particles have been generated using HIJING [42], as described in Section 6.6. The decay-in-flight has been simulated assuming a decay length of 1.3 m, which corresponds to the distance from the absorber to the interaction region plus one nuclear interaction length in carbon. A small fraction of muons with  $\eta > 3.8$  does not enter the absorber through the front-face but through the beam pipe inside the absorber. For these a corresponding longer decay length is assumed.

Muons can be produced also after the first hadronic interaction in the absorber (secondary  $\pi/K$  decays). However, these muons have substantially lower transverse momenta and are in general not pointing to the interaction vertex. Their contribution has been estimated to be  $< 10\%$  for a  $1 \text{ GeV}/c$  transverse momentum cut and  $2\sigma$  vertex pointing cut [886]. The vertex cut helps also to reduce the number of muons (with  $p_t \geq 1 \text{ GeV}/c$ ) from primary  $\pi/K$  decays by about 30 per cent.

*Electron background from misidentified hadrons.* The dielectron invariant mass spectra contain, in the lower mass region, a substantial background that results from charged pions and kaons, misidentified as electrons. To include this background in the simulations a realistic parameterization of the underlying hadronic event has to be provided. For this purpose, the parametrized HIJING event generator [42] is used, whose event multiplicity is adjusted to the

corresponding event centrality. An additional source of background is represented by electrons and positrons from the conversion of photons from  $\pi^0$  decays. However, initial investigations, using fully simulated and reconstructed events, showed that they contribute only marginally to the tracks reconstructed as main vertex tracks, due to the employed cut on the impact parameter at the main vertex. Therefore, this contribution is neglected in the study presented here, but might need to be re-evaluated in more detail in view of further studies.

*6.7.1.3. Centrality measurements.* The experimental work carried out at the SPS and RHIC has shown that a study of quarkonia yields as a function of the centrality (or as a function of variables related to the centrality) is necessary to understand the suppression pattern of heavy quarkonia in heavy-ion collisions. In addition, at LHC energies the suppression from QGP might be hidden (at least for the  $J/\psi$ ) by the enhancement due to the different mechanisms previously discussed. A careful analysis of the quarkonia yields as a function of centrality is therefore crucial to disentangle the different effects.

It is worth noting that QGP formation is expected to lead to sizeable modifications of the quarkonia yields as a function of the centrality (i.e. the effects to be observed should not be small). For the  $J/\psi$ , already at SPS energies the yield is reduced by about 40% in central collisions Pb–Pb due to the ‘anomalous’ suppression mechanism (see Fig. 6.330); at RHIC, preliminary PHENIX results show that the suppression in central Au–Au collisions with respect to pp data can be as large as a factor 3. At LHC, thanks to the higher temperatures and energy densities reached in the collision, prompt  $J/\psi$ ’s are expected to be almost fully suppressed in central collisions. Also the  $J/\psi$  enhancement due to kinetic recombination [870] or statistical hadronization [871, 873] is expected to be large. In fact, with respect to the scenarii without any suppression, charmonium yields at least two or three times larger are predicted by both models for central Pb–Pb collisions [828]. For the  $\Upsilon$ , the amount of suppression predicted by QGP-inspired calculations is more sensitive to the specific choice of the input parameters. However, Section 6.7.2.5 illustrates that, for dissociation temperatures of the order of 500 MeV,  $\Upsilon$  production in central Pb–Pb collisions turns out to be sizeably suppressed. The situation can be different if much higher dissociation temperatures are considered. In this case [887], only  $\Upsilon$ ’s coming from  $\Upsilon'$  and  $\Upsilon''$  decays are expected to be suppressed. On the other hand, recombination-regeneration mechanisms should play a minor role for the  $\Upsilon$  family [888].

For the dimuon channel, the centrality studies (both for  $\Upsilon$  and  $J/\psi$  families) have been carried out by using the information provided by the Zero-Degree Calorimeters (ZDC) [889]. The resolution of the ZDC system (see Section 6.1) allows the establishment of up to 10 centrality classes for Pb–Pb collisions. In fact, a significantly larger number of bins would lead to a bin width comparable to (or even smaller than) the experimental resolution on the centrality variable, implying that a large fraction of the events assigned to a given centrality bin actually belongs to another bin. One of the relevant consequences is that (potential) threshold-like behaviours in the quarkonia yields are, at least to some extent, smeared out.

The constraints on the maximum number of bins for the centrality study imposed by the ZDCs are not severe for the  $\Upsilon$  family since, in any case, a much higher number of bins cannot be envisaged because of the limited statistics expected (see Section 6.7.2.4). The situation is different for the  $J/\psi$ , where a much more abundant statistics will be achieved. In this case, more centrality bins can be foreseen, however implying a lower purity of each centrality class.

*6.7.1.4. Signal normalization.* The normalization of the signals is a crucial issue when using heavy quarkonia to probe the QGP. Conceivably, in order to extract relevant information on the survival probability of a given quarkonia species in the QGP, the measured yield of

this species must be compared to a reference signal which is not affected by a modification of the nature of the medium. As discussed in Section 6.7.1, at SPS energies, the reference signal for  $J/\psi$  production studies is the high mass dilepton continuum which is assumed to originate exclusively from the Drell-Yan process. Such a normalization is not conceivable at LHC energies because the Drell-Yan signal is predicted to be entirely drowned into dileptons from semi-leptonic decay of open charm and open beauty [890] even when assuming energy loss of heavy quarks [799, 891]. Drell-Yan might anyway be not well adapted for quarkonia normalization purposes at the LHC because of different shadowing of the quark and the gluon structure functions [826, 892]. As suggested in [893], the CMS collaboration plans to use the  $Z^0$  boson as a reference signal against the  $\Upsilon$  production in heavy ion collisions [894]. Moreover, as already discussed in Section 6.6, W bosons can be detected in ALICE Muon Spectrometer and could serve as a reference. These normalizations may however not be very suitable because of the different production mechanisms and the large difference in mass between the  $\Upsilon$  and the vector bosons W and  $Z^0$ , which probably implies a different influence of the nuclear effects [859, 893]. In addition, the performance of the Muon Spectrometer for  $Z^0$  detection still has to be investigated with detailed simulation studies.

Another type of normalization consists in using the open charm (bottom) cross section as the reference signal for charm (bottom) bound states. This provides the most natural normalization since both signals arise from the same production mechanism. One should mention that the use of open charm (bottom) as a reference signal for studying the properties of the QGP via charmonium (bottomonium) suppression should be done carefully. Indeed, charm thermal production cross section could be dramatically enhanced in a QGP with a relatively high temperature [895–897]. Then, shadowing and/or quenching effects might change the momentum distribution of heavy quarks (charm quarks may lose up to 40% of their energy when propagating in the QGP at the LHC [898]). Recent data [899] show that indeed a sizeable suppression of high  $p_t$  heavy quarks already occurs at RHIC energies in central Au–Au collisions. The reference signal could therefore be sensitive, like the  $J/\psi$  ( $\Upsilon$ ) yield, to the characteristics of the QGP. Such a correlation between signal and reference would obviously bias the interpretations. We stress that, in addition to the possible use of open charm (bottom) for normalization purposes, a systematic comparison of the yields of open and hidden charm (bottom) as a function of centrality is essential to disentangle prompt and secondarily produced quarkonia.

An alternative approach is represented by the minimum-bias method, which has been extensively used by the NA50 Collaboration [900, 901]. The starting point is represented by the measured differential distribution  $d\sigma_p/dc$ , where  $\sigma_p$  is the production cross section of a given quarkonium state (integrated over the detector acceptance) and  $c$  is any centrality variable. The distribution  $d\sigma_p/dc$  can be written as  $Y_p(c) \times d\sigma_{inc}/dc$ , where the inclusive distribution  $d\sigma_{inc}/dc$  carries the probability that the collision occurs at a given centrality and  $Y_p(c)$  is the number (yield) of quarkonia produced per nucleus–nucleus collision at this centrality. This yield can be determined if the inclusive distribution is measured:

$$Y_p(c) = \frac{d\sigma_p}{dc} \bigg/ \frac{d\sigma_{inc}}{dc}.$$

This basic physical quantity can be presented as a function of the impact parameter (estimated from the centrality variable), allowing a direct comparison with any theoretical model. For instance, with heavy quarkonia production via hard scattering,  $Y_p$  is expected to scale as the number of nucleon–nucleon collisions. It is important to underline that this method can be applied not only to heavy quarkonia, but also to any other process of interest in the continuum part of the dilepton spectrum. Finally, we note that one possible drawback of this method,

using the centrality distribution of the inclusive cross section, is the need to control the centrality dependence of the efficiency for dimuon or dielectron measurements, which adds some systematic uncertainty to the results.

The method of normalizing quarkonia yields to a different reference process is of course useful (for instance, most of systematic errors cancel out), but not mandatory. In fact, a different approach is adopted by the PHENIX collaboration, which decided to compare  $J/\psi$  data in A–A collisions to pp ones.

Such a comparison is carried out with the  $R_{AA}$  ratio, which can be written as

$$R_{AA}(c) = \frac{\sigma_{\text{inel}}^{\text{pp}}}{\sigma_{J/\psi}^{\text{pp}}} \cdot \frac{N_{J/\psi}^{\text{AA}}(c)}{N_{\text{binary}}(c)},$$

where  $\sigma_{\text{inel}}^{\text{pp}}$  and  $\sigma_{J/\psi}^{\text{pp}}$  are the inelastic cross section and the measured cross section for  $J/\psi$  production in pp collisions, respectively;  $N_{J/\psi}^{\text{AA}}(c)$  is the measured number of  $J/\psi$ 's per A–A collision at centrality  $c$  and  $N_{\text{binary}}(c)$  is the number of binary collisions for the same centrality.

If no nuclear effect (shadowing) and suppression/enhancement mechanism are present, one expects  $R_{AA}(c) = 1$  for all centralities. Values that are larger (smaller) than one indicate that shadowing and suppression (enhancement) are the dominant processes. pA or dA data are useful to disentangle cold nuclear matter effects (shadowing and normal absorption) from suppression/enhancement due to the medium produced in the heavy ion collision.

It is interesting to note that the choice made by the PHENIX Collaboration is to take data for pp, dA and A–A collision at the same nucleon–nucleon c.m. energy (200 GeV). This is indeed the optimum situation for two reasons. The first one is that, since the energy is the same for all the collision systems,  $R_{AA}$  ratios can be directly computed without any energy scaling of the measured cross sections (which represents a potential source of systematic errors). The second one is represented by the fact that dA collisions offer the advantage of a smaller rapidity shift compared to pA. This means that (for the same N–N c.m. energy) the  $x$  region explored in pp and A–A is much closer to the dA than to the pA one, allowing a more direct comparison of the data for the different systems.

Finally, we note that the option of presenting quarkonia yields without any normalization has been recently adopted by the NA60 Collaboration. This choice, driven by the limited statistics of the reference process (Drell-Yan) is interesting (by computing ratios, a part of the information is no longer available), but it requires a very careful examination of systematic errors.

**6.7.2. Quarkonia detection in the dimuon channel: Pb–Pb collisions.** A study of the Physics performance of the ALICE Muon Spectrometer in the field of heavy quarkonia detection has been carried out in the ‘fast simulation’ approach. The simulation tool is discussed in this section and the simulation results are presented.

**6.7.2.1. Simulation techniques.** The evaluation of the detector response to resonance decays and to processes in the continuum of the invariant mass spectrum requires a huge amount of computing time. This is particularly true for the second group of processes and in the presence of background. The collection of adequate statistics is not affordable with the computing facilities available today. To bypass this limitation, an alternative approach has been chosen. This ‘fast simulation’ method consists of two main components: one is aimed at reproducing the spectrometer response to single muons, the second one at simulating the muon continuum. Both issues are briefly discussed below.

The fast simulation of the Muon Spectrometer is based on the parametrization of the response of the whole detector at the single muon level. Given a muon of momentum  $p$

generated at the interaction point at polar and azimuthal angles  $\theta$  and  $\varphi$ , the fast simulation applies the smearing of the apparatus and gives the reconstructed  $p'$ ,  $\theta'$  and  $\varphi'$  together with the detection probability  $p_{\text{det}}$  for that muon. This last term is the product of three factors giving the probability for that muon to satisfy the acceptance ( $p_{\text{acc}}$ ), reconstruction ( $p_{\text{rec}}$ ) and trigger ( $p_{\text{trig}}$ ) requirements.

The acceptance probability ( $p_{\text{acc}}$ ), the reconstruction efficiency ( $p_{\text{rec}}$ ) and the smearing functions have been calculated and parametrized in a three-dimensional grid of  $10 \times 10 \times 10$  cells, with  $0 < p < 200 \text{ GeV}/c$ ,  $2^\circ < \theta < 9^\circ$  and  $-180^\circ < \varphi < 180^\circ$ . To evaluate these quantities, for each cell a number of positive, single muon tracks were generated and then reconstructed (the number of reconstructed events in each cell ranges from 1000 to 10000, depending on detector acceptance). The acceptance (i.e. 'traceable track') requirement is fulfilled when the track crosses the active regions of at least three trigger chambers, three tracking chambers of stations 4 and 5 and one out of two chambers for each of first three tracking stations. The reconstruction has been carried out with a fast method where the estimation of the impact point of the track on the tracking chambers is performed using a parametrization of the residual distributions (obtained by means of the full simulation). The latter has been checked to be consistent with the residual distributions measured in beam-tests of the tracking chamber prototypes. This approach allows one to speed up the computation, especially in the presence of background hits on the chambers due to particles generated in interactions of primaries with the hadron absorber and the beam shielding.

Then, the kinematical parameters of the reconstructed track  $p'$ ,  $\theta'$  and  $\varphi'$  have been compared with those generated, and the differences  $\Delta p$ ,  $\Delta\theta$  and  $\Delta\varphi$  were evaluated. Their distributions have been fitted; the former with an asymmetric function to account for asymmetric energy-loss fluctuations in the front absorber (Landau tail), the other two with Gaussian functions.

Then, for each cell the fit parameters (which contain the apparatus smearing), as well as the acceptance and reconstruction probabilities ( $p_{\text{acc}}$  and  $p_{\text{rec}}$ ) have been stored in a table.

To take into account the evolution of background with the centrality of the collision, the calculations have been performed with different background levels: no background (BKG 0), half (BKG 0.5) and nominal (BKG 1) background (the latter includes a safety factor of two with respect to the background level predicted by HIJING [42] for Pb–Pb central collisions). In the presence of background an additional Gaussian component was added to the function used to fit the  $\Delta p$  distributions, to account for the deterioration of the resolution due to the background. The negatively charged muons were treated using the same parameters and applying the transformation  $\varphi \rightarrow -\varphi$ . For momenta above  $200 \text{ GeV}/c$  the parameters have been extrapolated.

The last factor, i.e. the trigger probability ( $p_{\text{trig}}$ ) has been evaluated after the factorization of the detector acceptance (that is the basic requirement for the validation of the events). The spectrometer phase space has been divided into  $20 \times 10$  cells in the range  $-90^\circ \leq \varphi \leq 90^\circ$  and  $2^\circ \leq \theta \leq 9^\circ$ . The low and high trigger  $p_t$  cuts correspond to a transverse momentum of 1 and 2  $\text{GeV}/c$  and will be used for  $J/\psi$  and  $\Upsilon$  selection, respectively. Due to the granularity of the trigger detector and to the trigger algorithm, the  $p_t$  cut is not sharp: the trigger probability has then been studied as a function of  $p_t$ , in the range  $0 \leq p_t \leq 10 \text{ GeV}/c$ . The trigger response for single  $\mu^+$  has been computed while the response to single  $\mu^-$  was obtained with symmetry arguments (as well as the trigger probability for muons generated in the other half-plane).

*Fast muon continuum simulation.* Uncorrelated muon pairs represent an important part of the dimuon continuum. At low masses and transverse momenta they actually dominate. The kinematics of these pairs is determined by the kinematics of the individual muons, i.e.  $p_t$ ,

**Table 6.77.** Trigger, tracking and overall efficiency for  $\Upsilon$  and  $J/\psi$  as a function of the background level (defined in the text) as obtained from the fast simulation. For comparison, the values obtained with the full simulation are also reported in parentheses.

		BKG 0	BKG 0.5	BKG 1
$\Upsilon$	$\varepsilon_{\text{trig}}(\%)$	92 (92)	91 (91)	92 (91)
	$\varepsilon_{\text{track}}(\%)$	92 (97)	90 (94)	86 (91)
	$\varepsilon_{\text{all}}(\%)$	85 (89)	82 (86)	79 (83)
$J/\psi$	$\varepsilon_{\text{trig}}(\%)$	74 (72)	77 (76)	83 (83)
	$\varepsilon_{\text{track}}(\%)$	86 (92)	84 (90)	79 (84)
	$\varepsilon_{\text{all}}(\%)$	64 (67)	64 (69)	66 (70)

$\eta$  and  $\phi$ . Obtaining the uncorrelated continuum from real events in which all muon sources appear with frequencies proportional to their production cross section is difficult to achieve. The steeply falling  $p_{\text{T}}$ -spectra would require prohibitively long computing times to simulate the high mass part of the spectrum.

Instead, we use a fast simulation technique in which muons are generated according to flat  $p_{\text{T}}$ -distributions. Pseudo-events are constructed using many muons, typically  $10^6$ – $10^8$ , each muon carrying a weight proportional to its production probability per event. The statistical weight of a muon pair is proportional to the product of the statistical weights of the two muons. Combinations are formed between all muons of the pseudo-event. It can be shown that this procedure is equivalent to a detailed simulation in the case of event-by-event fluctuations of the number of muons proportional to the square-root of the mean-value. This condition is fulfilled if independence between the sources can be assumed, i.e. Gaussian or Poisson distribution of the number of muons per event.

*6.7.2.2. Key results from the fast simulation.* The simulation results presented in this document have been obtained with the nominal field of the dipole magnet, equal to 0.7 T [3]. The fast simulation was tested comparing, for different background levels, the results for the  $J/\psi$  and  $\Upsilon$  resonances with those obtained with the full procedure. No significant discrepancy was found. The trigger efficiency ( $\varepsilon_{\text{trig}}$ ) and the reconstruction efficiency in the tracking system ( $\varepsilon_{\text{track}}$ ) for  $J/\psi$  and  $\Upsilon$  obtained with the fast simulation at different background levels are shown in Table 6.77, where they are compared with the corresponding values given by the full simulation procedure. The efficiencies were computed by using as normalization a sample of events in which the acceptance requirements (traceable track conditions, see Section 6.7.2.1) are fulfilled by both the decay muons. The overall efficiency ( $\varepsilon_{\text{all}}$ ), taking into account both trigger and track reconstruction, is also shown in the same table.

Invariant mass spectra for a sample of  $J/\psi$  and  $\Upsilon$  resonances obtained with the fast simulation are shown in Fig. 6.332. The distributions have been fitted with a Gaussian in the region around the peak. The resulting mass resolutions for different background levels are summarized in Table 6.78.

*6.7.2.3.  $J/\psi$  and  $\Upsilon$  acceptance.* The fast simulation has been used to evaluate the acceptance of the Muon Spectrometer for heavy quarkonia. The acceptance has been computed by generating the resonances according to the phase space distributions described in Section 6.7.1.2 and by applying the acceptance requirements on single muons (traceable track condition) described in Section 6.7.2.1. It is worth noting that by imposing this condition, among other effects, the cutoff on muon momentum (about 4 GeV/ $c$ ) due to the front absorber and to the muon filter is taken into account.

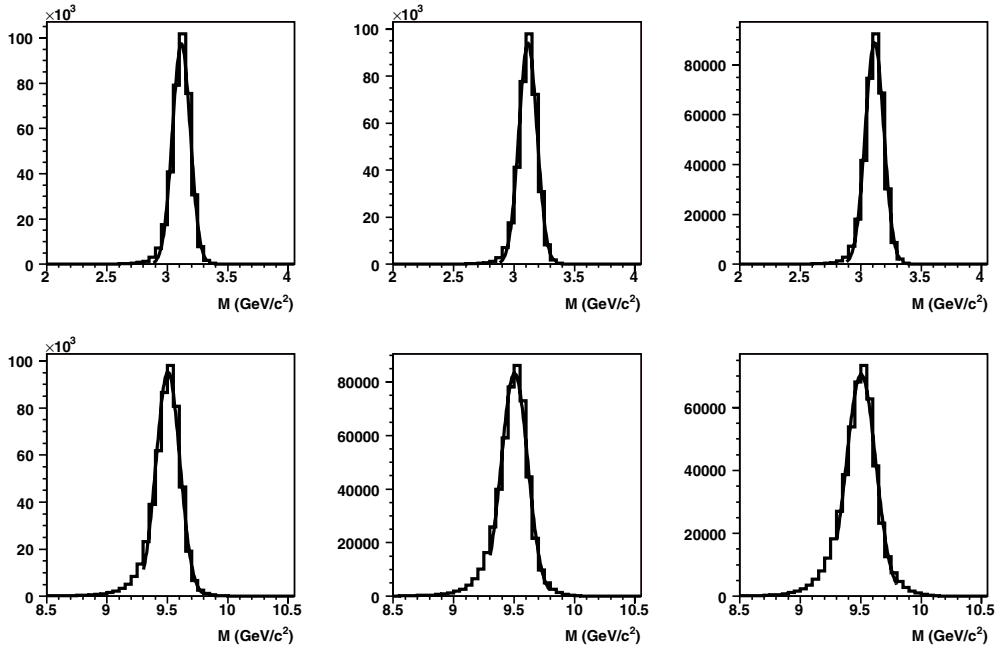


**Figure 6.332.** Invariant mass spectra obtained with the fast simulation for the  $J/\psi$  (upper row) and the  $\Upsilon$  (lower row) with no background (left), half the nominal (centre) and nominal background (right).

**Table 6.78.** Mass resolution from fast simulation for  $\Upsilon$  and  $J/\psi$  as a function of the background level (defined in the text). For comparison, the values obtained with the full simulation are also reported in parenthesis.

		BKG 0	BKG 0.5	BKG 1
$\Upsilon$	$\sigma$ (MeV)	97 (99 $\pm$ 2)	108 (109 $\pm$ 2)	120 (115 $\pm$ 2)
$J/\psi$	$\sigma$ (MeV)	75 (72 $\pm$ 2)	76 (74 $\pm$ 2)	77 (70 $\pm$ 2)

The acceptances (defined as the ratio  $n_{\text{acc}}(p_t, y)/n_{\text{gen}}(p_t, y)$ ) between the number of accepted and generated quarkonia at given  $p_t$  and  $y$  for  $J/\psi$  and  $\Upsilon$  are shown in the left panels of Fig. 6.333. The  $\Upsilon$  acceptance is almost uniform in  $p_t$  in the whole rapidity range  $2.5 < y < 4.0$ , while the one for the  $J/\psi$  is significantly higher at large transverse momenta.

The rapidity (transverse momentum) dependence of the acceptances for  $J/\psi$  and  $\Upsilon$  is also visible in the central (right) panels of the same figure, where the acceptances ‘integrated’ over  $p_t$  ( $y$ ) are shown. These were computed as the ratios  $n_{\text{acc}}(y)/n_{\text{gen}}(y)$  ( $n_{\text{acc}}(p_t)/n_{\text{gen}}(p_t)$ ) between the number of accepted and generated quarkonia at given  $y$  ( $p_t$ ). Together with these acceptances, the corresponding ones obtained after applying the low (high)  $p_t$  cut for  $J/\psi$  ( $\Upsilon$ ) also give an idea of the effects due to the trigger. As it can be seen, the trigger effects are almost negligible for the  $\Upsilon$ , but not for the  $J/\psi$ .

Finally, the acceptances for  $J/\psi$  and  $\Upsilon$  have been ‘integrated’ over  $y$  and  $p_t$  to get the absolute (i.e. normalized to the full phase space) acceptance of the spectrometer. These quantities were computed as the ratios between the number of accepted and generated resonances over the full phase space (we note that the results for the ‘integrated’ acceptances

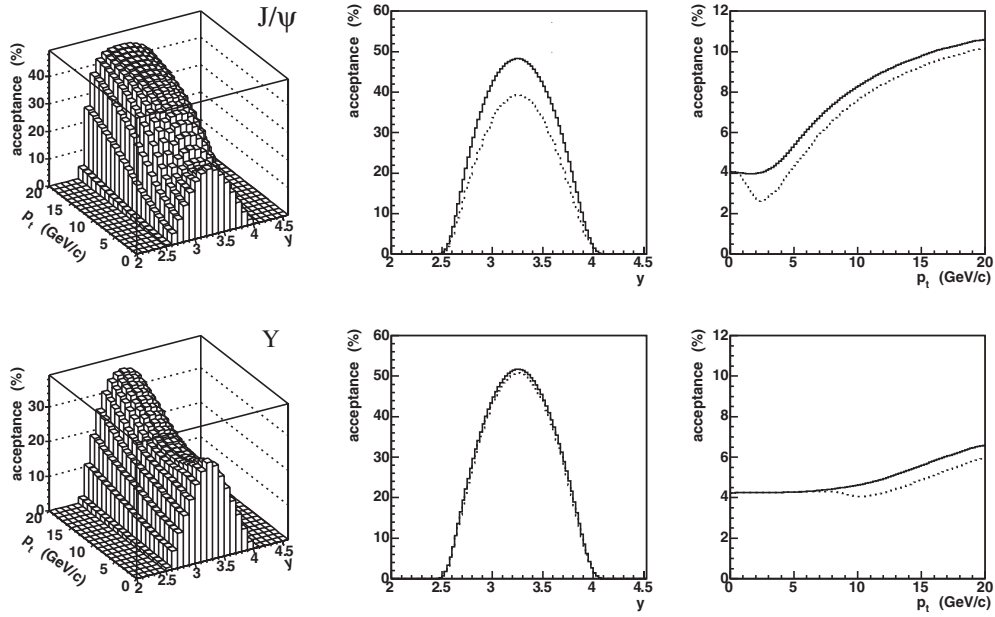


**Figure 6.333.** Acceptance for  $J/\psi$  (up) and  $\Upsilon$  (bottom). The left panels show the acceptance as a function of rapidity and transverse momentum. The middle (right) panels show the acceptances as a function of rapidity (transverse momentum). To give an idea of the effect of the trigger, on the middle and right panels the acceptances are shown without (solid histograms) and with (dashed histograms) a sharp cut on the transverse momentum of single muons of 1 GeV/c (2 GeV/c) for  $J/\psi$  ( $\Upsilon$ ).

**Table 6.79.** Integrated absolute (normalized to the full phase space) acceptance (in %) for  $J/\psi$  and  $\Upsilon$ .

	$J/\psi$	$\Upsilon$
Integrated acceptance (%)	4.46	4.41

are to some extent sensitive to the quarkonia  $y$  and  $p_t$  distributions used as input). The absolute acceptances are listed in Table 6.79.

**6.7.2.4. Expected yields.** In this section, the quarkonia yields expected in an ALICE Pb–Pb data taking period (i.e.  $10^6$ s running time at a luminosity of  $5 \times 10^{26} \text{ cm}^{-2} \text{ s}^{-1}$ ) are presented. The yields are obtained without assuming any suppression or enhancement. Therefore, they have to be taken simply as a general guideline. In the next section, the study of a specific suppression scenario will be addressed to illustrate in more detail the physics potential of the ALICE Muon Spectrometer.

This section is divided in two parts. In the first one, the quarkonia yields will be studied as a function of the collision centrality. In the second one, the study of the transverse momentum dependence of quarkonia yields will be presented, as an example, for a given centrality bin.

**Centrality dependence.** In this study, dimuon invariant mass spectra have been generated for five centrality classes (Section 6.7.1.3). For each class, the upper and lower values of the impact parameter, as well as the corresponding number of participant nucleons are shown in Table 6.80. The fractions of the total ( $f_{\text{tot}}$ ) and hard ( $f_{\text{hard}}$ ) cross sections corresponding to each centrality class are also displayed in the same table. The smearing due to the ZDC

**Table 6.80.** Main characteristics of the five centrality classes for Pb–Pb collisions.

Centrality class	c1	c2	c3	c4	c5
$b$ (fm)	0–3	3–6	6–9	9–12	$b > 12$
$N_{\text{part}}$	414–375	375–276	276–152	152–54	54–0
$\langle b^{\text{smear}} \rangle$ (fm)	1.92	4.65	7.6	10.6	14.3
$\langle N_{\text{part}}^{\text{smear}} \rangle$	385	297	177	70	8
$f_{\text{tot}}$ (%)	3.6	11.0	18.0	25.4	42.0
$f_{\text{tot}}^{\text{smear}}$ (%)	4.4	11.1	18.0	25.3	41.2
$f_{\text{hard}}$ (%)	18.0	37.8	30.7	11.9	1.6
$f_{\text{hard}}^{\text{smear}}$ (%)	20.6	35.6	28.7	12.6	2.5
Background level	1.0	0.8	0.5	0.2	0.03

**Table 6.81.** Shadowing factors at zero impact parameter.

	$c\bar{c}$	$b\bar{b}$	$J/\psi$	$\psi'$	$\Upsilon$	$\Upsilon'$	$\Upsilon''$
$C_{\text{sh}}(0)$	0.65	0.84	0.60	0.60	0.76	0.76	0.76

impact parameter resolution has been taken into account. The resulting mean values of the impact parameter ( $\langle b^{\text{smear}} \rangle$ ) and of the number of participant nucleons ( $\langle N_{\text{part}}^{\text{smear}} \rangle$ ) are shown in the same table for the different centrality classes, together with the fractions of the total ( $f_{\text{tot}}^{\text{smear}}$ ) and hard ( $f_{\text{hard}}^{\text{smear}}$ ) cross sections.

The inputs used for this study are those discussed in Section 6.7.1.2. As already mentioned in that section, binary scaling of the pp cross sections (for quarkonia,  $c\bar{c}$  and  $b\bar{b}$  production) is performed to obtain the cross section for each Pb–Pb centrality class. For this purpose, the Glauber model is used. According to Ref. [826, 892], the impact parameter dependence of the shadowing factor  $C_{\text{sh}}(b)$  is parametrized as  $C_{\text{sh}}(b) = C_{\text{sh}}(0) + (1 - C_{\text{sh}}(0))(b/16\text{fm})^4$ , resulting in an almost flat behaviour up to  $b \sim 10$  fm, followed by a rapid increase to 1 for larger impact parameters. The values of  $C_{\text{sh}}(0)$  (shadowing coefficient at zero impact parameter) for the open heavy flavours and heavy quarkonia are summarized in Table 6.81 (for  $\pi/K$  mesons  $C_{\text{sh}}(0) = 0.65$  is used). These values of  $C_{\text{sh}}(b)$  lead to shadowing factors averaged over the collision centrality in line with those from EKS98 parametrization (see PPR Volume I [3], Section 1.3.8).

The calculations presented here are performed within the fast simulation framework described in Section 6.7.2.1. For the most central collisions, i.e. for the 1st centrality class, the (nominal) background level (BKG 1) is used. The background levels for the other centrality classes are scaled down proportionally to the corresponding hadron multiplicity (given by HIJING) and are listed in Table 6.80. The ‘high’ and ‘low’ trigger cuts (see 6.7.2.1) on muon transverse momenta are applied to the  $\Upsilon$  and  $J/\psi$  mass regions, respectively. To suppress the dimuon background in the  $\psi$  mass region, an additional sharp cut  $p_{\text{t}} > 1$  GeV/ $c$  on the transverse momentum of each muon is applied.

The expected quarkonia signal and background yields, as well as the corresponding signal to background ratios and significances for the five Pb–Pb centrality classes c1–c5 (see Table 6.80) are presented in Table 6.82. The results of the calculation are referred to a data taking period of  $10^6$ s with a luminosity of  $5 \times 10^{26} \text{ cm}^{-2} \text{ s}^{-1}$  and correspond to the interval of  $M \pm 2\sigma$ , where  $M$  and  $\sigma$  are the parameters of the function used to fit the resonance mass peak (see below). Table 6.82 indicates that in one year of Pb–Pb data taking enough statistics will be collected to measure the centrality dependence of  $J/\psi$  and  $\Upsilon$  production. For the  $J/\psi$ ,

**Table 6.82.** Expected quarkonia signal (S) and background (B) yields (in units of  $10^3$ ) for five centrality classes c1–c5. The numbers in the parentheses represent the  $J/\psi$  and  $\psi'$  contributions from B decay. The yields correspond to an interval of  $\pm 2\sigma$  around the resonance mass. Signal-to-background ratios and significances are also listed. All yields are for a  $10^6$  s running time and a Pb–Pb luminosity of  $5 \times 10^{26} \text{ cm}^{-2} \text{ s}^{-1}$ .

State	Centrality	S [ $\times 10^3$ ]	B [ $\times 10^3$ ]	S/B	S/ $\sqrt{S+B}$
$J/\psi$	c1	130 (22)	680	0.20	150
	c2	230 (38)	860	0.27	220
	c3	200 (32)	410	0.48	250
	c4	95 (15)	88	1.08	220
	c5	21.7 (3.2)	6.9	3.13	130
$\psi'$	c1	3.7 (1.4)	300	0.01	6.7
	c2	6.5 (2.4)	385	0.02	11
	c3	5.5 (2.0)	190	0.03	13
	c4	2.6 (0.9)	42	0.06	12
	c5	0.59 (0.20)	3.4	0.17	9.3
$\Upsilon$	c1	1.3	0.8	1.7	29
	c2	2.4	1.0	2.3	41
	c3	2.0	0.55	3.6	39
	c4	0.93	0.15	6.1	28
	c5	0.20	0.022	9.1	14
$\Upsilon'$	c1	0.35	0.54	0.65	12
	c2	0.62	0.67	0.92	17
	c3	0.52	0.38	1.4	17
	c4	0.24	0.11	2.2	13
	c5	0.054	0.016	3.5	6.4
$\Upsilon''$	c1	0.20	0.42	0.48	8.1
	c2	0.35	0.55	0.64	12
	c3	0.30	0.30	0.99	12
	c4	0.14	0.088	1.6	9.2
	c5	0.030	0.014	2.2	4.6

despite the huge background, which accounts for the modest S/B ratios for the most central classes, the large signal leads to significances always larger than 100 for all the five centrality bins. For the  $\Upsilon$ , the signal is about two orders of magnitude smaller than the one of the  $J/\psi$ , but since the background is almost three orders of magnitude smaller, significances of the order of 30 are achieved. Similar significances can also be achieved for bottomonium states of higher mass by summing up the statistics collected in two or three Pb–Pb data taking periods. For the  $\psi'$ , the situation is worse, since the signal is of the same order of magnitude of the  $\Upsilon$  one, but the background is only a factor of two smaller than the one below the  $J/\psi$  peak.

The unlike-sign dimuon mass spectra for the three centrality classes c1, c3 and c5 are displayed as an example in Fig. 6.334. As it can be seen in the left panels, the ratio between the  $J/\psi$  signal and the underlying background becomes larger when increasing the impact parameter. This is due to the combinatorial nature of the background in the  $J/\psi$  mass region. The situation is somewhat different for the high-mass region of Fig. 6.334 (right panels): with respect to the  $J/\psi$ , the signal-to-background ratio for the  $\Upsilon$  family shows a weaker dependence on the centrality (see also Table 6.82). This is due to the fact that in the high mass region the correlated contribution to the continuum becomes relevant: with the only exception

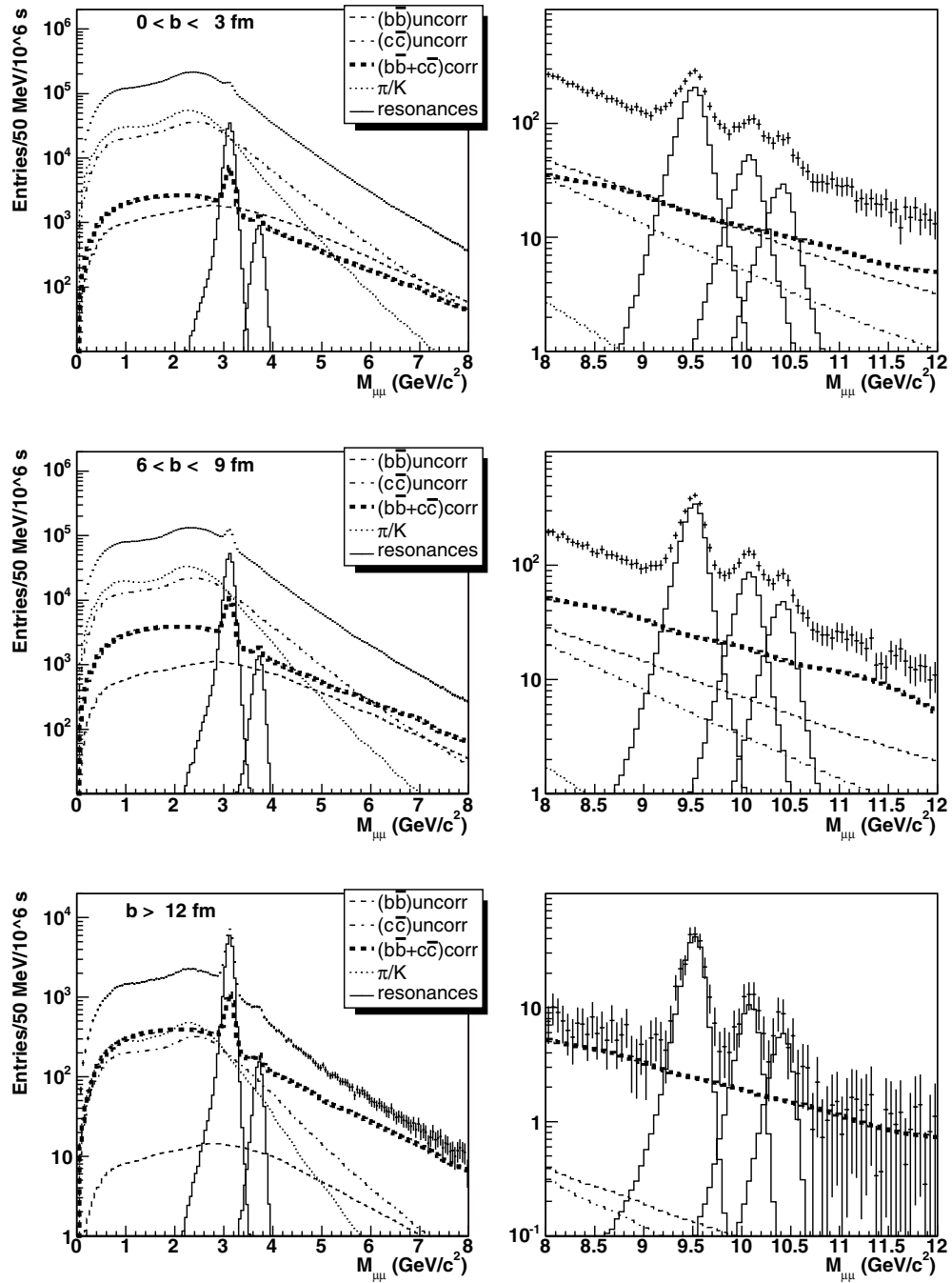


**Figure 6.334.** Unlike-sign dimuon mass spectra for the three Pb–Pb centrality classes c1, c3 and c5 for a running time of  $10^6$  s and a luminosity of  $5 \times 10^{26} \text{ cm}^{-2} \text{ s}^{-1}$ . Left and right panels represent the mass spectra in the  $J/\psi$  and in the  $\Upsilon$  family mass region, respectively. The different contributions to the dimuon mass spectrum (both muons come from the indicated source) are shown separately, while the points on top represent the total number of dimuons (including pairs with muons originated from different sources). The lines representing the different contributions do not include statistical fluctuations; these are shown only for the total number of muons.

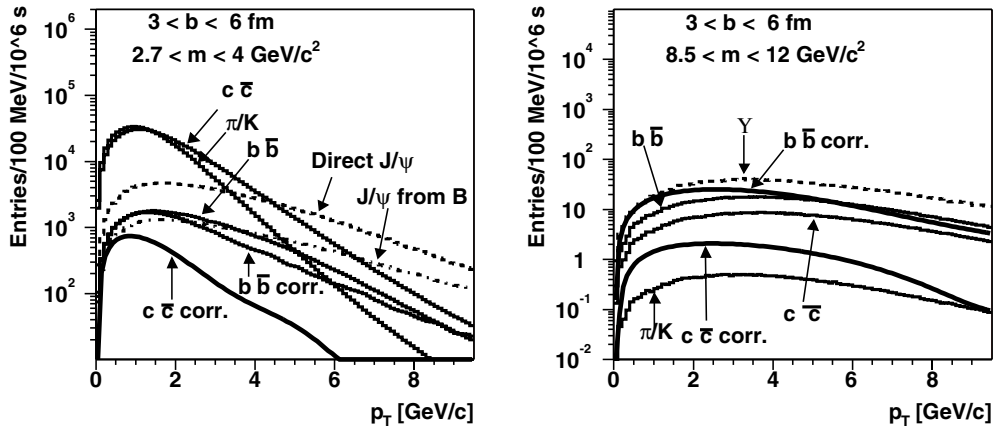


**Figure 6.335.**  $p_t$  distribution of the processes contributing to the dimuon mass spectrum in the muon arm acceptance (with trigger low  $p_t$  cut). On the left and right panels the  $p_t$  distributions for charmonium ( $2\text{--}5\text{ GeV}/c^2$ ) and bottomonium ( $8\text{--}11\text{ GeV}/c^2$ ) mass regions are displayed, respectively.

of the most central class, the background is dominated by muon pairs from bottom decay. (It is worth noting explicitly that, due to the  $p_t$  cut, the charm correlated component is several times less than the bottom one).

*$p_t$  dependence.* An analysis of heavy quarkonia production as a function of the transverse momentum for a given centrality class is presented in this section. As an example, the analysis was carried out for the second centrality interval ( $3 \leq b \leq 6$  fm, see above). The  $p_t$  distributions for the different processes used as input for this study are plotted in Fig. 6.335. Generated events were subjected to the fast simulation algorithm and selected according to the same analysis cuts described in discussing the centrality analysis.

The invariant mass spectra corresponding to  $10^6$  s of data taking at a luminosity of  $5 \times 10^{26} \text{ cm}^{-2} \text{ s}^{-1}$  were computed for different bins of the muon pair transverse momentum. Some of these spectra are shown in Fig. 6.336.

The signal, background, their ratio and the significance were calculated for each  $p_t$  bin and are listed in Table 6.83. For the  $J/\psi$ , thanks to the high statistics, significances of the order of 100 can be achieved for all the  $p_t$  bins considered in this analysis. Nevertheless, a progressive worsening of the signal to background ratio occurs when moving towards low  $p_t$ . This is due to the fact that, as it can be seen in Fig. 6.335, the  $J/\psi$ 's  $p_t$  distribution has a much harder tail than the ones of the different muon sources contributing to the continuum in the charmonium mass region. The situation for the  $\Upsilon$  is rather different. The significances are obviously smaller than the ones for the  $J/\psi$ , but the signal to background ratio is larger than one and is almost constant as a function of  $p_t$ . This is due to the similar slopes shown by the  $p_t$  distributions of the  $\Upsilon$  and of the muon sources contributing to the continuum in the bottomonium mass region (see Fig. 6.335).

The results presented in this section indicate that the statistics collected in one Pb–Pb data taking period is adequate to measure the  $p_t$  dependence of the  $J/\psi$  yield. For the  $\Upsilon$  family the statistics is obviously smaller; nevertheless a detailed measurement of the  $p_t$  dependence (and of quantities such as the  $\Upsilon$  to  $\Upsilon'$  ratio [878, 902], see below) can be performed by summing up the statistics of the first two centrality classes (c1 and c2) and/or the statistics collected in two or three Pb–Pb data taking periods.

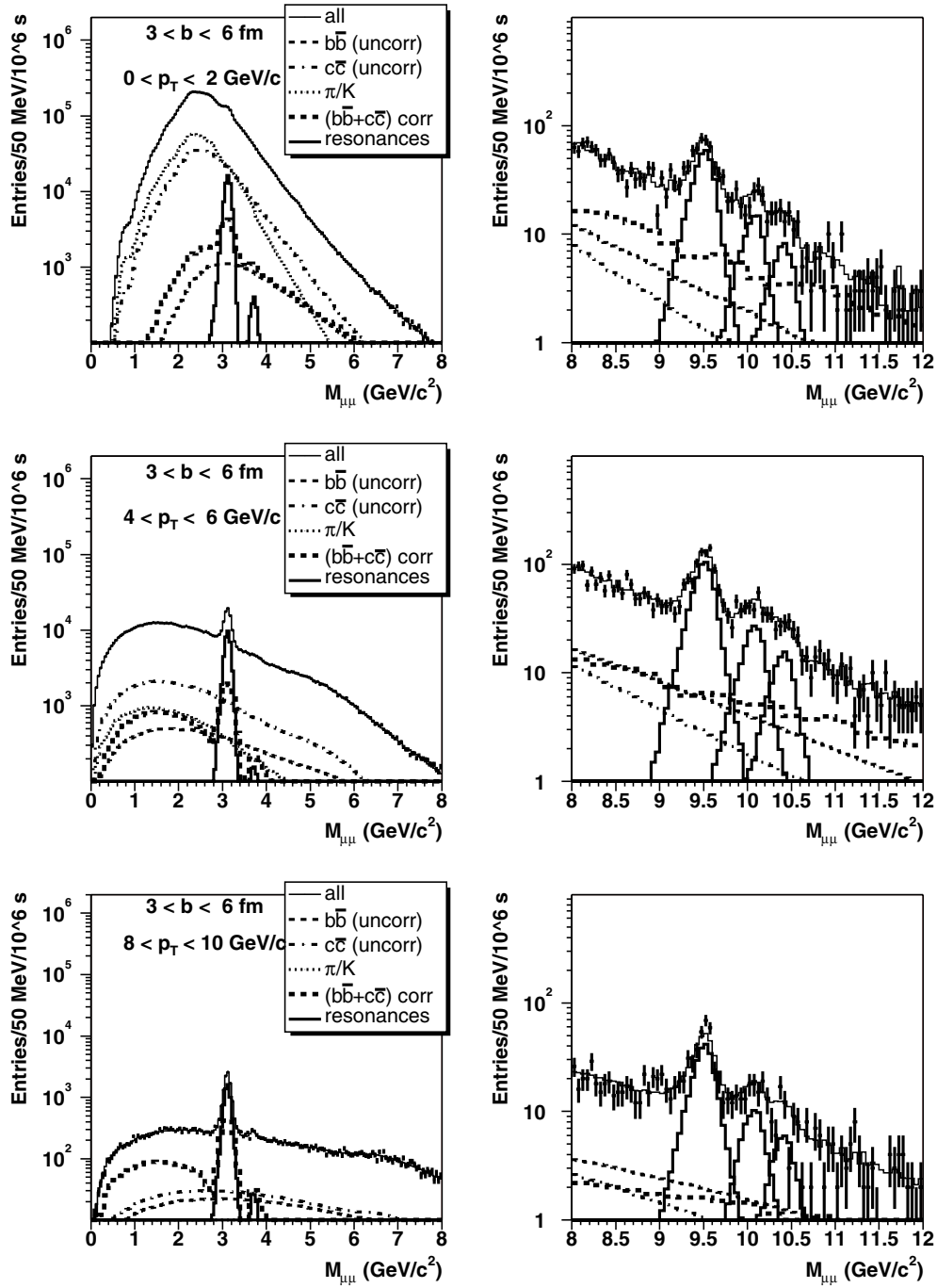


**Figure 6.336.** Unlike-sign dimuon mass spectra for different  $p_t$  intervals. The plots refer to the second centrality class (see text). On the left panel the events satisfy the trigger selection with the low  $p_t$  cut and for both muons the software cut  $p_t > 1 \text{ GeV}/c$  is applied. On the right panel the trigger high  $p_t$  cut is applied.

**Table 6.83.** Expected quarkonia signal and background yields (in units of  $10^3$ ) for five  $p_t$  bins in the second centrality class (see text). The numbers correspond to an interval of  $\pm 2\sigma$  around the resonance mass. Signal-to-background ratios and significances are also listed. All yields are for a  $10^6$  s running time and a Pb–Pb luminosity of  $5 \times 10^{26} \text{ cm}^{-2} \text{ s}^{-1}$ .

State	$p_t$ range (GeV/ $c$ )	S ( $\times 10^3$ )	B ( $\times 10^3$ )	S/B	S/ $\sqrt{S+B}$
J/ $\psi$	0–2	75	680	0.11	87
	2–4	77	230	0.34	140
	4–6	45	41	1.1	150
	6–8	20	7.3	2.7	120
	8–10	8.0	1.5	5.3	82
$\psi'$	0–2	2.4	250	0.0097	2.9
	2–4	2.3	140	0.016	3.6
	4–6	1.0	27	0.038	3.7
	6–8	0.47	5.9	0.079	3.2
	8–10	0.19	1.3	0.15	2.5
$\Upsilon$	0–2	0.33	0.18	1.8	15
	2–4	0.69	0.35	1.9	21
	4–6	0.60	0.31	1.9	20
	6–8	0.40	0.21	1.9	16
	8–10	0.24	0.11	2.1	13
$\Upsilon'$	0–2	0.087	0.12	0.73	6.1
	2–4	0.18	0.23	0.79	8.9
	4–6	0.16	0.21	0.76	8.3
	6–8	0.11	0.14	0.77	6.8
	8–10	0.063	0.086	0.73	5.1
$\Upsilon''$	0–2	0.048	0.086	0.55	4.1
	2–4	0.10	0.18	0.57	6.1
	4–6	0.091	0.16	0.56	5.7
	6–8	0.059	0.11	0.52	4.5
	8–10	0.036	0.068	0.54	3.5

**6.7.2.5. Suppression studies.** In the following, we consider only the correlated background assuming that the uncorrelated component can be subtracted with appropriate techniques, such as event-mixing. Therefore, the statistical error of the ‘full’ spectrum is assigned to the remaining spectrum. The corresponding invariant mass distributions for the centrality classes c1, c3 and c5 are shown in Fig. 6.337.

To extract the quarkonia signals from the dimuon mass spectra a fitting procedure was applied. Resonances are parametrized by a modified Landau function convoluted with a Gaussian one, while the underlying correlated background is fitted with an exponential. Typical fits (both in the J/ $\psi$  and  $\Upsilon$  mass regions) are displayed in Fig. 6.338.

The quarkonia rates presented so far do not include any suppression or enhancement mechanisms. The first mechanism which is expected to play a role is the one due to nuclear absorption of prompt quarkonium states (obviously, charmonia from bottom decay are not affected). Indeed, there are large uncertainties on the values of the absorption cross sections at LHC energies. If on the one hand theoretical calculations [828] predict cross sections as large as  $\sigma_{abs} = 10.3 \pm 1.0 \text{ mb}$  and  $\sigma_{abs} = 4.6 \pm 0.9 \text{ mb}$  for charmonium and bottomonium states, respectively, on the other recent PHENIX data indicate a much smaller charmonium absorption. Therefore, to have two extreme options, quarkonia yields have been calculated both with the cross sections from [828] and with no absorption (i.e. with cross sections equal

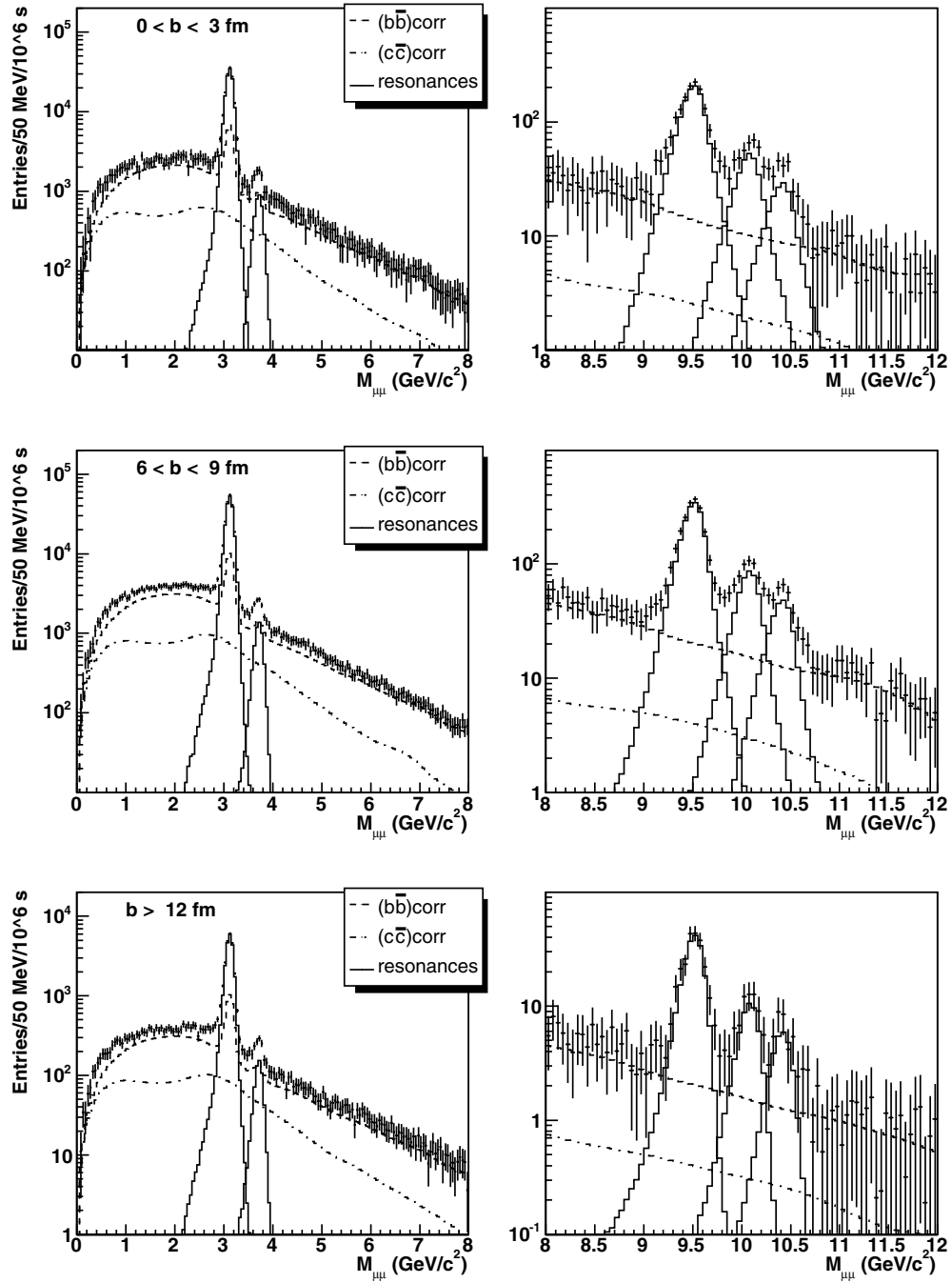
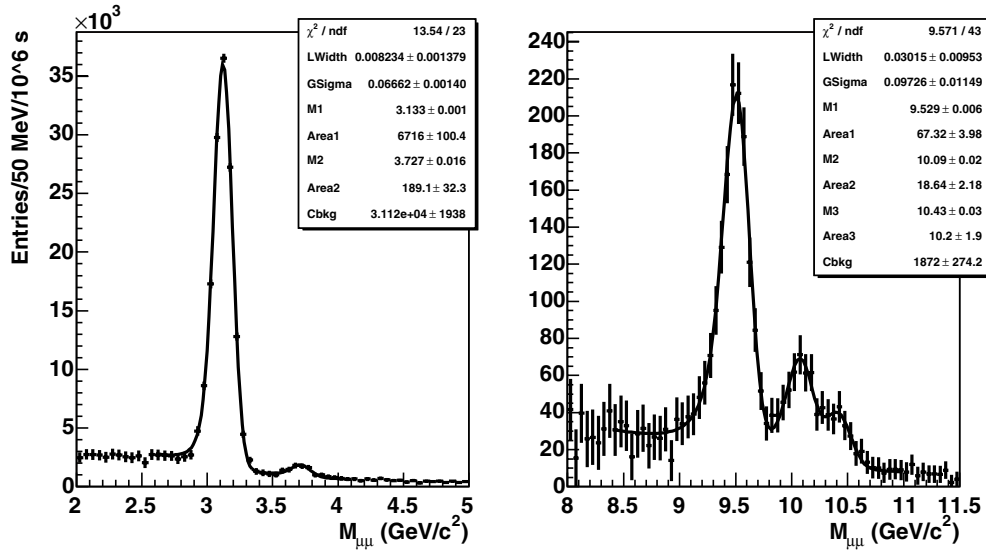


Figure 6.337. Same as in Fig. 6.334 but when the uncorrelated background is subtracted.

to zero). For the first option, the survival probabilities for different centrality classes are given in Table 6.84.

For each centrality class, the invariant mass distribution with nuclear absorption was deduced from the one without absorption by applying the central values of the quarkonia



**Figure 6.338.** Fit of the dimuon spectra for the 1st centrality class in the  $J/\psi$  (left) and  $\Upsilon$  (right) mass regions. The solid lines are the results of the fits with a function described in the text.

**Table 6.84.** Quarkonia survival probabilities caused by the nuclear absorption.

$b$ (fm)	0–3	3–6	6–9	9–12	$b > 12$
$J/\psi$	$0.249^{+0.030}_{-0.025}$	$0.263^{+0.030}_{-0.026}$	$0.308^{+0.031}_{-0.028}$	$0.422^{+0.032}_{-0.030}$	$0.691^{+0.023}_{-0.022}$
$\Upsilon$	$0.501^{+0.067}_{-0.057}$	$0.517^{+0.066}_{-0.057}$	$0.562^{+0.063}_{-0.055}$	$0.662^{+0.053}_{-0.048}$	$0.841^{+0.028}_{-0.027}$

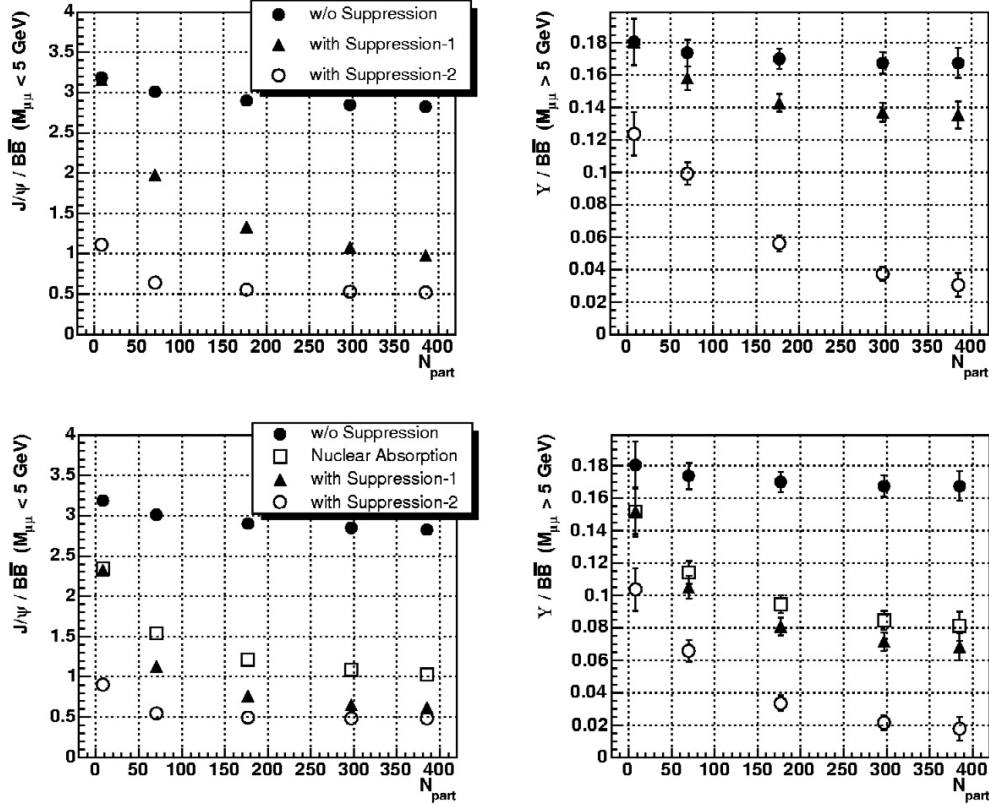
survival probability of Table 6.84. The corresponding charmonium and bottomonium yields were evaluated by applying to the resulting mass distributions the fitting procedure discussed above. When nuclear absorption is taken into account, the signal to background ratio becomes worse, in particular for central collisions. This is a consequence of the fact that for these collisions the survival probability is smaller. It is worth noting also that, without nuclear absorption effects, the contribution of  $J/\psi$  from B decay is about 16% of the total  $J/\psi$  yields while with the absorption this fraction increases and reaches 44% in the first and 22% in the fifth centrality bin. We also note that, when nuclear absorption is taken into account, the error bars resulting from the invariant mass fit are large for  $\psi'$ , in particular for the most central classes.

As discussed in Section 6.7.1.4, the quarkonia signal normalization is a crucial issue. One of the possibilities is the normalization to beauty production, which can be measured with the Muon Spectrometer (see Section 6.6). For instance, one can respectively normalize the  $J/\psi$  and  $\Upsilon$  rates to the low-mass and high-mass dimuons originating from correlated  $B\bar{B}$  pair decays. The corresponding unlike-sign dimuon rates from beauty for a Pb–Pb data taking period of  $10^6$  s and luminosity of  $5 \times 10^{26} \text{ cm}^{-2} \text{ s}^{-1}$  are listed in Table 6.85 for the different centrality classes.

The ratios of the resonance rates over those for beauty are plotted in Fig. 6.339 as a function of the number of participant nucleons (both without and with the resonance nuclear absorption).

**Table 6.85.** Correlated unlike-sign dimuon rates from beauty production in Pb–Pb collisions versus centrality.

Centrality class	c1	c2	c3	c4	c5
$M_{\mu\mu} < 5$ GeV	47568	83767	69589	32208	6918
$M_{\mu\mu} > 5$ GeV	8035	14125	11796	5442	1171

**Figure 6.339.** Resonance over beauty ratios for  $J/\psi$  (left) and  $\Upsilon$  (right) as a function of the number of participants. The solid circles stand for the case without any suppression. In the top figures the effects of quarkonia suppression due to two different QGP scenario (suppression 1 and 2, see text) are shown. The bottom figures show the analogous case obtained by taking into account the effects of nuclear absorption together with the QGP ones. The effects of nuclear absorption alone (open squares) are also shown.

The second effect included in this study is resonance suppression by QGP due to colour screening [903]. We assume that in Pb–Pb collisions at 5.5 TeV (even for the peripheral events) an equilibrated QGP is formed with proper formation time  $\tau_0(r)$  and initial temperature  $T_0(r)$  ( $r$  is the transverse coordinate). The plasma expands along the collision axis according to Bjorken’s hydrodynamic scaling and cools isentropically:  $\tau T(\tau)^3 = \tau_0 T_0^3$  [112].

The QGP formation time and initial temperature, their  $r$  and centrality dependence are taken from [187, 904] (pQCD and final-state saturation approach). For instance, the values (averaged over the transverse plane) for the most central collisions are:  $\tau_0 = 0.093$  fm/c,  $T_0 = 1.19$  GeV.

**Table 6.86.** Values of the parameters for the different quarkonium states used as input for the suppression studies.

Resonance	$J/\psi$	$\psi'$	$\chi_c$	$\Upsilon$	$\Upsilon'$	$\Upsilon''$	$\chi_b$	$\chi'_b$
$\tau_F$ , fm/c	0.89	1.5	2.0	0.76	1.9	1.9	2.6	2.6
$T_D/T_c$ [909]	1.7	1.1	1.13	4.0	1.4	1.14	1.6	1.16
$T_D/T_c$ [908]	1.21	1	1	2.9	1.06	1	1.07	1

We adopt the ‘threshold suppression’ model (see [905] and [878]), which states that if the QGP temperature at the resonance formation point is higher than some value  $T_D$  (called screening or dissociation temperature, specific for each quarkonium state) the resonance will be suppressed, otherwise it will survive and escape the QGP. The resonance formation times  $\tau_F$ , taken from [906], are listed in Table 6.86.

For the resonance dissociation temperature we adopt the latest results obtained within the approach based on lattice QCD and potential model [907–909] using quenched or unquenched QCD data on  $q\bar{q}$  pair free energy at temperatures above the critical deconfinement temperature  $T_c$ . Authors of Ref. [907, 908] and [909] utilize different definitions of the  $q\bar{q}$  potential and as a result obtain different sets of  $T_D/T_c$  ratios using the same QCD parameters. To have two extreme suppression scenarii we consider one  $T_D/T_c$  set from Ref. [909] (corresponding to quenched QCD with  $T_c = 270$  MeV) and another set from Ref. [908] (corresponding to unquenched QCD with  $T_c = 190$  MeV) giving small and large suppression, respectively. Note that within the present QGP model for Pb–Pb collisions at 5.5 TeV the prompt  $\Upsilon$  does not melt even in most central collisions when considering the first option, while in the second case the prompt  $\Upsilon$  is strongly suppressed (about five, four and two times for the first, second and third centrality classes, respectively). Both sets of  $T_D/T_c$  are shown in Table 6.86, expecting that the realistic case is somewhere in between (since the dissociation temperatures for  $\Upsilon''$  and  $\chi'_b$  are missing in Ref. [908], we assume that they melt at  $T_c$ ). In the following we will refer to these two extreme suppression options as ‘Suppression-1’ and ‘Suppression-2’, corresponding to  $T_D$  from [909] and [908], respectively.

Using these inputs and adding the nuclear absorption, the resonance survival probabilities are computed as a function of  $p_t$  and collision centrality. We note that a significant contribution to  $J/\psi$ ,  $\Upsilon$  and  $\Upsilon'$  yields comes from the decay of higher-mass resonances (feed-down, see Ref. [828]). Since, in general, the latter have smaller survival probabilities, this contribution varies with centrality and  $p_t$ . Such an effect is taken into account in our calculations (details are given in Ref. [910]). These probabilities, summed with weights proportional to the resonance production cross sections [828] and decay branching ratios, are folded with the corresponding non-suppressed dimuon mass spectra for the given  $p_t$  and centrality (see details in [910]).

Quarkonia yields are extracted by applying the fitting procedure discussed above. The resulting yields ( $10^6$  s data taking) for  $J/\psi$  and  $\Upsilon$  normalized to opposite-sign dimuons from beauty decays are shown in Fig. 6.339 as a function of centrality. We assume that  $B$  hadrons do not undergo suppression in nuclear matter and by QGP. The corresponding ratios between resonances are shown in Fig. 6.340. As it can be seen in Fig. 6.339, the error bars for the  $J/\psi$  to open beauty ratio are small enough to distinguish between different suppression scenarios. This statement also holds for the  $\Upsilon$  to open beauty ratio. This is not the case for the ratios between  $\psi'$  and  $J/\psi$  (see Fig. 6.340) because of the large fitting errors for  $\psi'$ .

*6.7.2.6. Possibility of measuring azimuthal anisotropy in  $J/\psi$  absorption.* As suggested in [911, 912], the measurement of  $J/\psi$  azimuthal anisotropy will provide additional

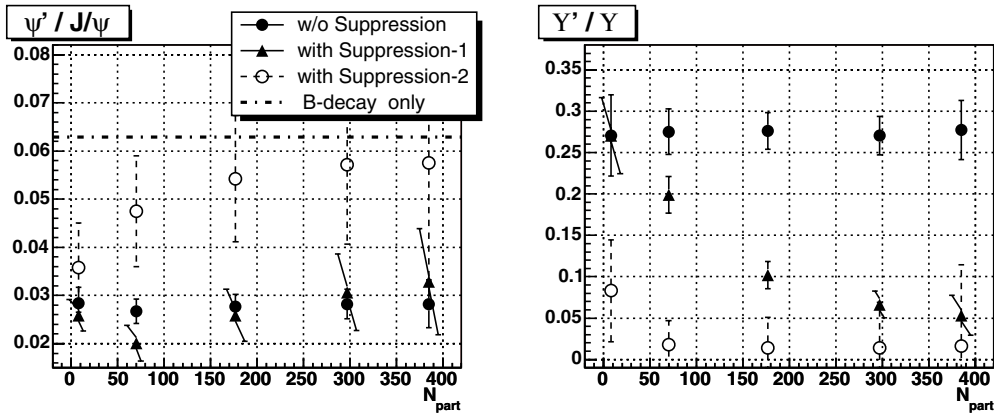


**Figure 6.340.**  $\psi'$  over  $J/\psi$  (left) and  $\Upsilon'$  over  $\Upsilon$  (right) ratios as a function of the number of participants. Three options are presented: without suppression (full circles), with Suppression-1 (triangles) and with Suppression-2 (open circles). In the left panel a fourth option is shown (dashed-dotted line) with total suppression of prompt  $\psi'$  and  $J/\psi$  (in this case, their ratio is determined only by beauty decay).

information on the  $J/\psi$  suppression mechanism such as direct absorption on participating nucleons, comover absorption or QGP formation.

The possibility of measuring this anisotropy is investigated in the framework of a fast simulation. The azimuthal distribution of the  $J/\psi$ 's detected in the Muon Spectrometer can be studied with respect to the event plane provided by the Photon Multiplicity Detector. The large coverage of the PMD (1.2 units in  $\eta$ ) minimizes the effects of non-flow correlations due to neutral pion decay and the effect of scattering of incident particles, thereby providing a good estimate of the event plane. The limited efficiency and purity of the data contribute to less than 5% systematic error on the event plane correction due to finite particle multiplicities at the multiplicities envisaged at LHC and considered in the present simulation.

The invariant mass spectra of like sign muons is reconstructed in different azimuthal regions with respect to the event plane. To investigate any anisotropy in the background spectra, the invariant mass distributions of the like sign muons is obtained with respect to the event plane. The yield in the region around the resonance mass peak is analysed to look for any possible anisotropy that may be remnant from the pion and kaon decay. The background spectrum is found to be azimuthally symmetric. The invariant mass spectra in different azimuthal regions is shown in Fig. 6.341 and the  $J/\psi$  yield is then analysed to extract the anisotropy components that describe the azimuthal distribution.

The precision of observation of anisotropy in  $J/\psi$  emission depends on several factors, e.g. background and its subtraction in the invariant mass spectra, increase in background due to charm and beauty decays, track reconstruction efficiency for muons in the Muon Spectrometer, the resulting mass resolution of the resonance, the  $J/\psi$  production cross section and the physical anisotropy present in resonance emission. A systematic study of variation in these parameters suggests that the significance of the data (and hence the number of events required) follows a simple relation with the anisotropy values to be studied and the associated precision, and is shown in Fig. 6.342. The fitted curve is  $\text{Significance} = 0.7/v_2 \times f$  where  $v_2$  is the value of anisotropy to be probed and  $f$  is the fractional error. A given set of values of these parameters determines the S/B ratio. The set of parameters and the relation for significance can be translated into the number of events required to enable such a determination.

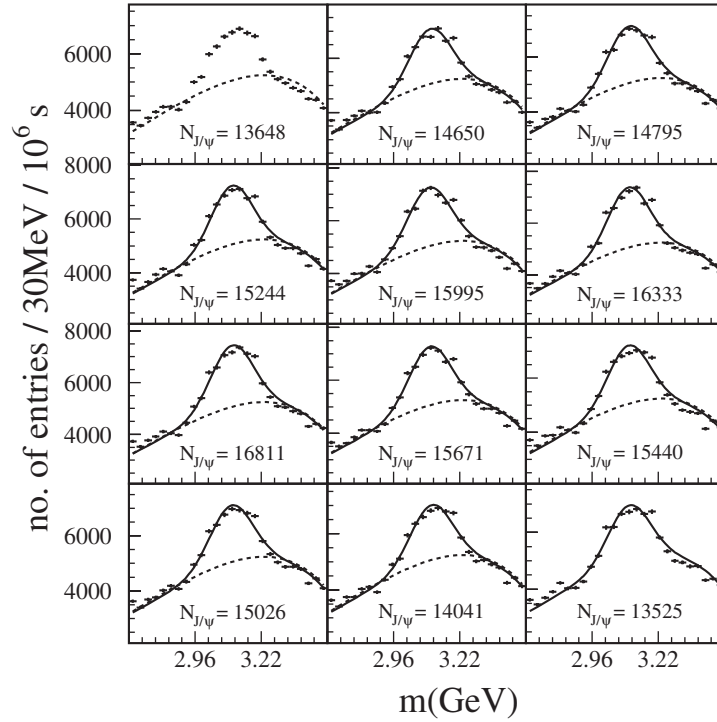


**Figure 6.341.** The signal and the background spectra in twelve azimuthal bins (see text) for  $\langle n_{\mu} \rangle = 5.8$  and an 85% track reconstruction efficiency. The  $J/\psi$  yield from the various bins is used for further analysis to determine the anisotropy parameters. The S/B and the significance for the whole sample (centrality class c2) is 0.27 and 194 respectively.

The contribution to measured  $J/\psi$  yield due to feed-down from higher mass resonances,  $p_t$  dependence of anisotropy and possible anisotropy in background due to jet quenching will all contribute to the observed anisotropy. Their effects have to be estimated.

### 6.7.3. Quarkonia detection in the dimuon channel: pp collisions

**6.7.3.1. Introduction.** The study of quarkonia production in pp collisions presents a twofold interest. On one hand, pp measurements (together with pA ones) represent a baseline for heavy-ion data. On the other, they have an intrinsic interest since they are expected to shed light on the production mechanisms by testing the existing theoretical models in an unexplored energy regime. In this respect, (according to the experience from Tevatron studies in  $p\bar{p}$  collisions) the relevant observables are quarkonia cross sections and  $p_t$  distributions. In addition, as already pointed out in Section 6.7.1.1, these measurements allow access to PDFs at very small  $x$ .

The results of simulations studies of the physics performance for quarkonia detection at  $\sqrt{s} = 14$  TeV in pp collisions are presented in this section. Similar studies at  $\sqrt{s} = 5.5$  TeV have been undertaken only recently and the final results are not yet available. Therefore, only a raw estimate of the expected quarkonia yields is given. However, we note that pp data at  $\sqrt{s} = 5.5$  TeV are interesting since they can be directly compared to Pb–Pb ones without any energy scaling. This scaling, needed for pp data at 14 TeV has to be performed by taking

Cent.Class	c2	c2	c2	c2	c2	c3	c3
J/ $\psi$ / event	0.011	0.011	0.011	0.015	0.007	0.0054	0.0054
Efficiency	0.085	0.075	0.085	0.085	0.085	0.085	0.075
Mass Resoln.	90	90	120	90	90	90	90
$v_2 = 0.05$	●	■	▲	▼	○	★	☆
$v_2 = 0.025$	□	△	+	◇	⊕	*	

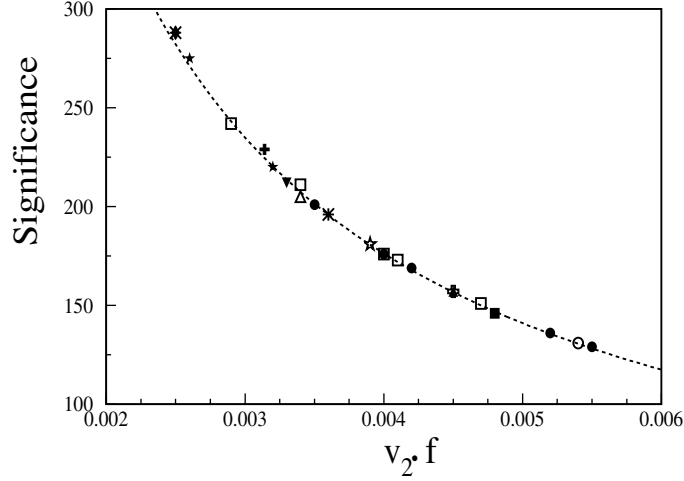


**Figure 6.342.** Significance as a function of  $v_2 \times f$  where  $v_2$  is the anisotropy to be probed with a fractional error  $f$ . The fitted curve corresponds to the minimum significance required.

**Table 6.87.** Acceptance coverage for J/ $\psi$  in the Muon Spectrometer for different colliding systems.

J/ $\psi$	$x_1$ range	$x_2$ range
pp 14 TeV	$2.7 \times 10^{-3} \leq x_1 \leq 1.2 \times 10^{-2}$	$4.1 \times 10^{-6} \leq x_2 \leq 1.8 \times 10^{-5}$
pPb 8.8 TeV	$2.7 \times 10^{-3} \leq x_1 \leq 1.2 \times 10^{-2}$	$1.0 \times 10^{-5} \leq x_2 \leq 4.6 \times 10^{-5}$
Pb-p 8.8 TeV	$6.8 \times 10^{-3} \leq x_1 \leq 3.1 \times 10^{-2}$	$4.1 \times 10^{-6} \leq x_2 \leq 1.8 \times 10^{-5}$
dPb 6.2 TeV	$5.4 \times 10^{-3} \leq x_1 \leq 2.4 \times 10^{-2}$	$1.0 \times 10^{-5} \leq x_2 \leq 4.6 \times 10^{-5}$
Pb-d 6.2 TeV	$6.8 \times 10^{-3} \leq x_1 \leq 3.1 \times 10^{-2}$	$8.1 \times 10^{-6} \leq x_2 \leq 3.6 \times 10^{-5}$

**Table 6.88.** Acceptance coverage for  $\Upsilon$  in the Muon Spectrometer for different colliding systems.

$\Upsilon$	$x_1$ range	$x_2$ range
pp 14 TeV	$8.2 \times 10^{-3} \leq x_1 \leq 3.7 \times 10^{-2}$	$1.2 \times 10^{-5} \leq x_2 \leq 5.5 \times 10^{-5}$
pPb 8.8 TeV	$8.2 \times 10^{-3} \leq x_1 \leq 3.7 \times 10^{-2}$	$3.1 \times 10^{-5} \leq x_2 \leq 1.4 \times 10^{-4}$
Pb-p 8.8 TeV	$2.1 \times 10^{-2} \leq x_1 \leq 9.4 \times 10^{-2}$	$1.2 \times 10^{-5} \leq x_2 \leq 5.5 \times 10^{-5}$
dPb 6.2 TeV	$1.6 \times 10^{-2} \leq x_1 \leq 7.4 \times 10^{-2}$	$3.1 \times 10^{-5} \leq x_2 \leq 1.4 \times 10^{-4}$
Pb-d 6.2 TeV	$2.1 \times 10^{-2} \leq x_1 \leq 9.4 \times 10^{-2}$	$2.5 \times 10^{-5} \leq x_2 \leq 1.1 \times 10^{-4}$

into account the evolution of the gluon distribution functions from the  $x$  region covered by the Muon Spectrometer at 14 TeV to the one at 5.5 TeV. As seen comparing Table 6.87 and Table 6.88 with Table 6.75, these  $x$  regions are only partially overlapped (we use the convention of first indicating the particle moving towards the Muon Spectrometer).

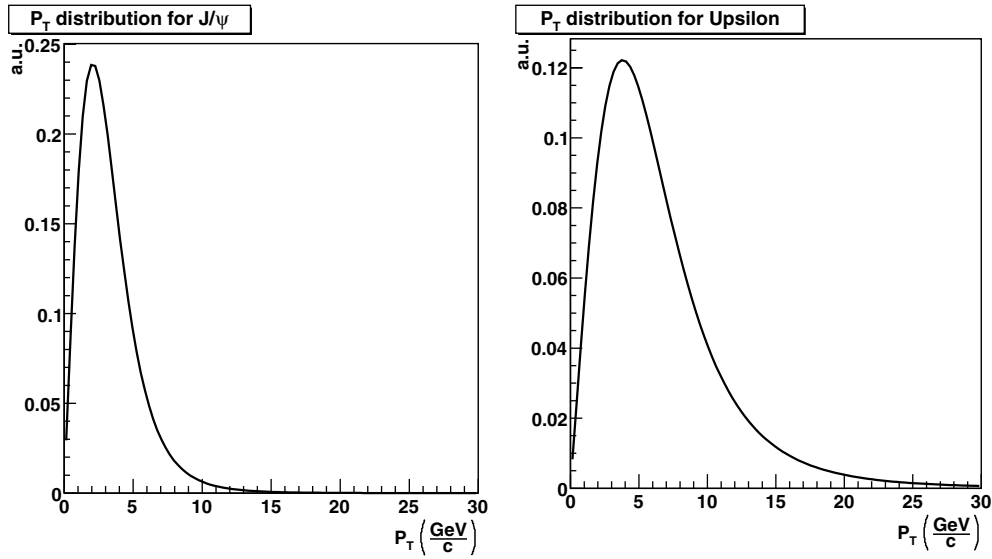


**Figure 6.343.** Transverse momentum distribution of  $J/\psi$  (left) and of  $\Upsilon$  (right) in pp collisions at  $\sqrt{s} = 14$  TeV.

**6.7.3.2. Simulation inputs and methods.** The simulation inputs for pp collisions at  $\sqrt{s} = 14$  TeV have been determined according to the same method used for Pb–Pb studies and outlined in Section 6.7.1.2.

The input cross sections for heavy quarkonia production in pp collisions at  $\sqrt{s} = 14$  TeV are those quoted in Table 6.76. In addition to prompt  $J/\psi$  and  $\psi'$ , also those from B decay are taken into account. The rapidity distributions for (prompt) production of the different quarkonia states are a parametrization of CEM predictions (with MRST-HO PDFs), while the  $p_t$  distributions (see Fig. 6.343) are obtained by extrapolating to LHC energies those measured by the CDF experiment. The extrapolation method is described in Section 6.7.1.2.

The invariant mass continuum from semileptonic decay of beauty and charm hadrons were simulated by means of PYTHIA. The input cross sections at  $\sqrt{s} = 14$  TeV are those given in Chapter 6.6.

The studies concerning the dimuon channel have been carried out by means of the fast simulation method outlined in Section 6.7.2.1. The multiplicity for pp collisions is much smaller with respect to the one expected in Pb–Pb. Therefore, the simulation of the Muon Spectrometer was carried out without including any degradation of the tracking and trigger chamber response due to the presence of background. In this situation, the trigger and tracking efficiencies as well as the invariant mass resolutions for  $J/\psi$  and  $\Upsilon$  are very close to the ones quoted for background level BKG 0 in Tables 6.77 and 6.78, respectively.

The fast simulation was used to evaluate the acceptance of the Muon Spectrometer for heavy quarkonia detection in pp collisions at  $\sqrt{s} = 14$  TeV. The resulting integrated absolute acceptances normalized to the whole phase space (see Section 6.7.2.3 for definitions) are given in Table 6.89. It is worth noting that the integrated acceptance is to some extent dependent from the rapidity and transverse momentum distributions used as input (i.e. slightly different values of acceptance are obtained if different input distributions are used). The rapidity and transverse momentum dependence of the acceptances for  $J/\psi$  and  $\Upsilon$  were calculated as well. Their shapes turn out to be very close to the one obtained for Pb–Pb collisions and shown in Fig. 6.333.

**Table 6.89.** Integrated absolute (normalized to the full phase space) acceptance (in %) for  $J/\psi$  and  $\Upsilon$  for pp collisions at  $\sqrt{s} = 14$  TeV .

Particle type	$J/\psi$	$\Upsilon$
Integrated acceptance (%)	4.24	4.42

*6.7.3.3. Expected yields at  $\sqrt{s} = 14$  TeV.* As reported in Volume I of the Physics Performance Report [3], ALICE pp data taking at  $\sqrt{s} = 14$  TeV will be carried out at a luminosity of  $5 \times 10^{30} \text{ cm}^{-2} \text{ s}^{-1}$ . The yields of heavy quarkonia detected in one year of pp data taking (assumed to be equivalent to an effective running time of  $10^7$  s) are presented in this section. Together with the overall statistics, also the analysis of  $J/\psi$  and  $\Upsilon$  production as a function of the transverse momentum and rapidity is discussed.

Indeed, only the correlated contribution to the unlike-sign dimuon mass continuum is taken into account in this study, while the uncorrelated one is not included yet. However, according to previous studies [913], the latter contribution is expected to be modest and should not affect in a dramatic way the results presented here.

*Overall statistics.* The opposite-sign dimuon invariant mass distributions corresponding to a data taking period of  $10^7$  s at  $\mathcal{L} = 5 \times 10^{30} \text{ cm}^{-2} \text{ s}^{-1}$  are shown in Fig. 6.344 both for the  $J/\psi$  and  $\Upsilon$  regions. As seen, all charmonium and bottomonium states are clearly resolved. The number of detected  $J/\psi$  is of the order of five millions, while the statistics expected for  $\Upsilon$  is about two orders of magnitude smaller. The yields for all quarkonia states are summarized in Table 6.90, where the corresponding signal to (correlated) background ratios and significances are also given.

*$p_t$  distributions.* The simulation study of the transverse momentum distributions for  $J/\psi$  and  $\Upsilon$  was carried out according to the following method. The transverse momentum of the detected opposite sign muon pairs was computed and the overall sample of events was divided in several bins. For each  $p_t$  bin, the corresponding dimuon invariant mass distribution was produced. From each of these distribution, the  $J/\psi$  and  $\Upsilon$  signal was extracted by fitting the invariant mass spectrum. For quarkonia a Gaussian function was used for the central part of the peak and two more Gaussians with variable width were added to describe the tails. The correlated continuum was parametrized according to the procedure described in [914]. Then, the raw number of detected resonances was corrected for the acceptance (which, as already mentioned, is not flat as a function of  $p_t$ ) to obtain the differential cross section  $d\sigma/dp_t$  (normalized to the rapidity interval  $2.5 < y < 4.0$  covered by the Muon Spectrometer). The results in Fig. 6.345 show that the statistical error bars on the measured differential cross section are small (in particular for the  $J/\psi$ ) due to the high expected statistics.

*Rapidity distributions.* The simulation study of the rapidity distributions for  $J/\psi$  and  $\Upsilon$  was carried out with the same procedure for transverse momentum distributions. The results are shown in Fig. 6.346.

*6.7.3.4. Expected yields at  $\sqrt{s} = 5.5$  TeV.* As mentioned above, at this energy detailed simulation studies have not been performed yet. Nevertheless, a first estimate of the expected quarkonia yields can be given by scaling the results obtained for Pb–Pb collisions at the same c.m. energy. For Pb–Pb collisions, the total yield expected in a  $10^6$  s data taking period can be deduced from Table 6.82 by summing up the yields for the different centrality classes. The total yields are then divided by the corresponding shadowing factors (assumed to be constant over centrality) from Table 6.81 and scaled to pp with  $A^2$  ( $A$  being the atomic number of

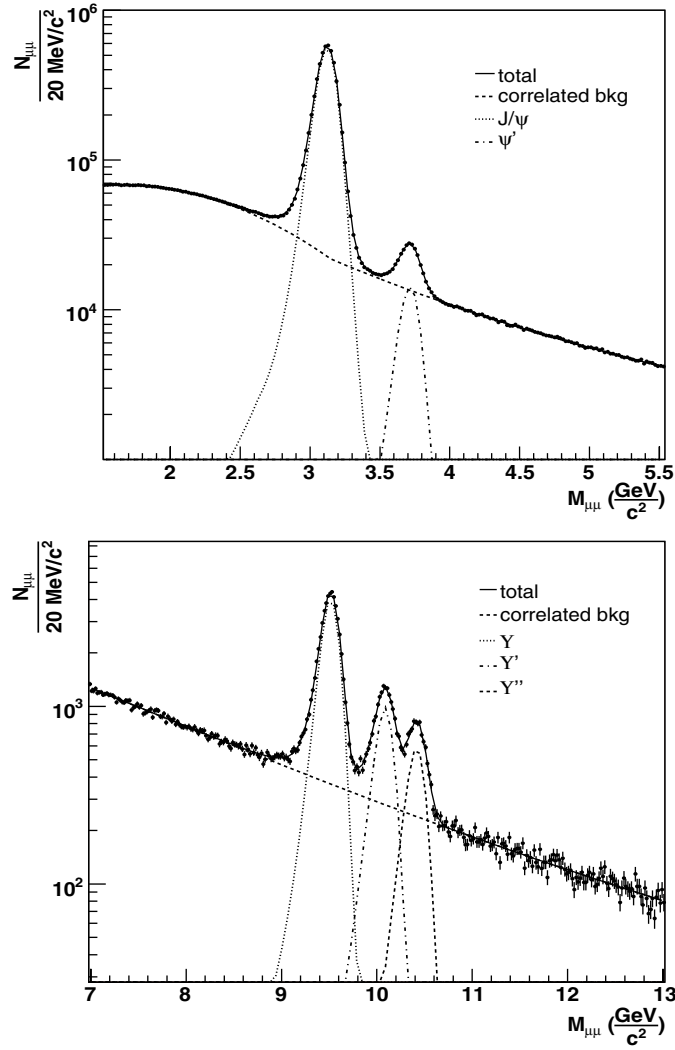


**Figure 6.344.** Unlike-sign dimuon mass spectra for a running time of  $10^7$  s at pp luminosity of  $5 \times 10^{30} \text{ cm}^{-2} \text{ s}^{-1}$  and  $\sqrt{s} = 14 \text{ TeV}$  (only the correlated background is taken into account). The  $J/\psi$  and  $\Upsilon$  mass regions are shown in the top and bottom panels, respectively.

**Table 6.90.** Expected quarkonia signal and background yields (in units of  $10^3$ ). The numbers refer to an interval corresponding to twice the FWHM around the resonance mass peak. Signal to background ratios and significances are also listed. All yields are for a  $10^7$  s running time and a pp luminosity of  $5 \times 10^{30} \text{ cm}^{-2} \text{ s}^{-1}$ .

State	$B(\times 10^3)$	$S(\times 10^3)$	S/B	$S/\sqrt{S+B}$
$J/\psi$	370	4670	12.6	2081
$\psi'$	220	122	0.55	209
$\Upsilon$	7.7	44.7	5.8	195
$\Upsilon'$	6.1	11.4	1.9	86
$\Upsilon''$	5.4	6.9	1.3	62

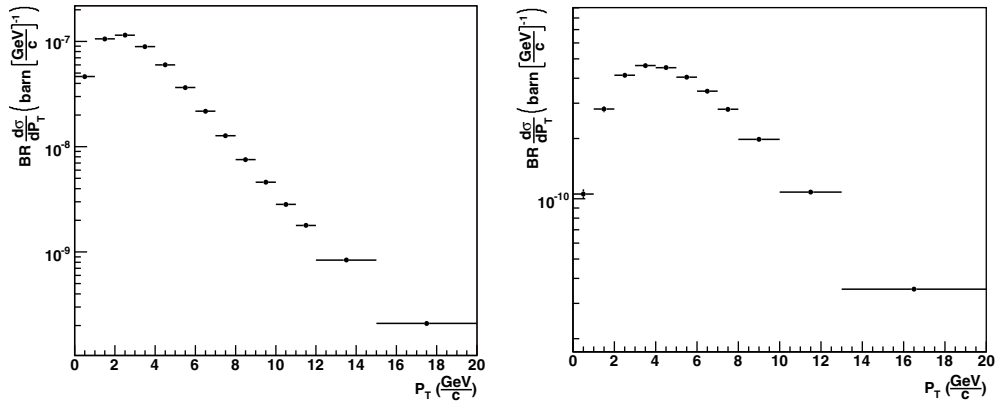


**Figure 6.345.**  $d\sigma/dp_T$  for  $J/\psi$  (left) and  $\Upsilon$  (right) measured in a data taking time of  $10^7$  s at pp luminosity of  $5 \times 10^{30} \text{ cm}^{-2} \text{ s}^{-1}$ . The cross section is referred to the rapidity window  $2.5 < y < 4$  covered by the Muon Spectrometer.

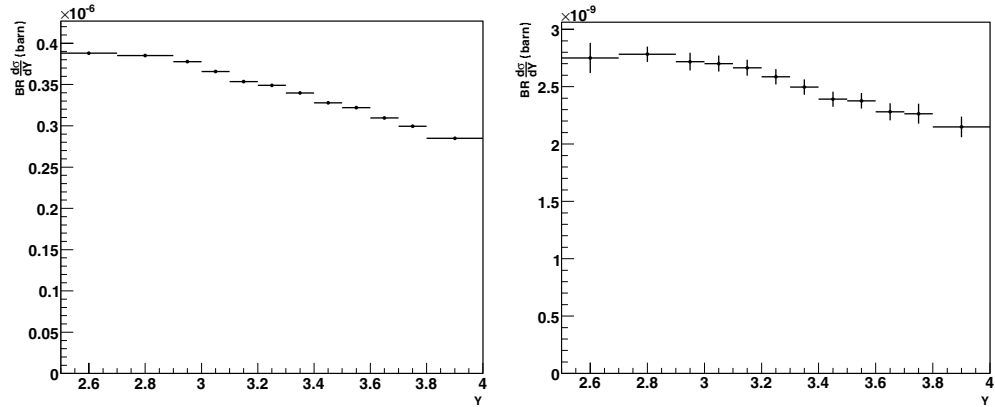


**Figure 6.346.**  $d\sigma/dy$  for  $J/\psi$  (left) and  $\Upsilon$  (right) measured in a data taking time of  $10^7$  s at pp luminosity of  $5 \times 10^{30} \text{ cm}^{-2} \text{ s}^{-1}$ .

lead). Finally, the scaled yields are multiplied by the ratio between pp and Pb–Pb luminosities (equal to  $5 \times 10^{30} \text{ cm}^{-2} \text{ s}^{-1}$  and  $5 \times 10^{26} \text{ cm}^{-2} \text{ s}^{-1}$ , respectively [3]). The resulting yields for  $10^6$  s pp data taking at 5.5 TeV are of the order of  $2.4 \times 10^5$  and  $2 \times 10^3$  for  $J/\psi$  and  $\Upsilon$ , respectively.

**6.7.4. Quarkonia detection in the dimuon channel: pA collisions.** A detailed simulation of p–nucleus (and deuteron–nucleus) collisions is at present under way. The purpose of those simulations is to compare the quarkonia yield for the different options: pPb, Pb–p, dPb and Pb–d (as already stated, the first particle is the one moving towards the Muon Spectrometer). Preliminary simulation results indicate that in a data taking period of  $10^6$  s at luminosity of  $1.1 \times 10^{29} \text{ cm}^{-2} \text{ s}^{-1}$  the number of detected  $J/\psi$  ( $\Upsilon$ ) is of the order of  $1.5 \times 10^6$  ( $1.5 \times 10^4$ ) for pPb collisions at  $\sqrt{s} = 8.8$  TeV. The quarkonia yields expected for Pb–p collisions are of the same order of magnitude, although slightly smaller as a consequence of the rapidity shift. The quarkonia yields expected for dPb and Pb–d collisions in a data taking period of  $10^6$  s at luminosity of  $8.1 \times 10^{28} \text{ cm}^{-2} \text{ s}^{-1}$  are close to those for pPb collisions. As well

as the yields, the comparison of the  $x_1$  and  $x_2$  regions covered by the Muon Spectrometer for the different collision-system options is another relevant point (we use to denote with  $x_1$  the  $x$ -variable corresponding to the first particle, i.e. the one moving towards the Muon Spectrometer). These regions are listed in Tables 6.87 and 6.88 for the top collision energies (8.8 TeV for pPb, 6.2 TeV for dPb).

Since one of the main motivation of p–nucleus data taking is to get information on nuclear shadowing (expected to be more pronounced at small  $x$ ), it should be interesting to take data with configurations which allow the exploration of the same  $x_2$  region as Pb–Pb ( $x_2$  is much smaller than  $x_1$ , see Tables 6.87 and 6.88). This happens both in pPb and dPb. In addition, for dPb, the  $x_1$  region is almost the same as in Pb–Pb: therefore, these two options (and in particular the second one) look very suitable for use as a reference for Pb–Pb.

Quarkonia yields for pPb and Pb–p collisions at  $\sqrt{s} = 5.5$  TeV have been estimated according to the method outlined in Section 6.7.3.4 and by taking into account the corrections due to the rapidity shift. The yields turn out to be about 30% smaller than those at  $\sqrt{s} = 8.8$  TeV. Similar calculations have been performed for dPb and Pb–d collisions. The yields at  $\sqrt{s} = 5.5$  TeV are smaller than those at  $\sqrt{s} = 6.2$  TeV by 10% at most. This fact suggest that dPb collisions at  $\sqrt{s} = 5.5$  TeV are also suitable to be used as a reference for Pb–Pb (we note that  $x_1$  and  $x_2$  are almost the same for both colliding systems). Finally, it is worth pointing out that the possibility of dividing the pPb (or dPb) data sample in centrality classes is very interesting, since it provides more detailed information on quarkonia nuclear absorption compared to the one provided by data integrated over centrality.

*6.7.5. Quarkonia detection in the dielectron channel: Pb–Pb collisions.* The measurement of electron pairs in the central barrel of ALICE is complementary to the dimuon channel discussed above. First, this extends quarkonia measurements from the forward rapidity region to the mid-rapidity region which is expected to be baryon free. Then, this enables the study of the correlation of quarkonia signals with photons and hadrons emitted (and identified) in a common rapidity region. Furthermore, the vertex capabilities of the ITS will allow to measure and separate secondary  $J/\psi$  from bottom decays. This not only leads to a direct measurement of the B meson production cross-section (Section 6.6), but also permits a distinction between primary and secondary  $J/\psi$ .

The centrepiece for dielectron physics is the Transition Radiation Detector (TRD) which provides electron identification for momenta larger than 1 GeV/ $c$  and an electron trigger for momenta larger than 3 GeV/ $c$  (see Chapters 4 and 5). Since the trigger on single electrons (TRD-L1) is not effective for central Pb–Pb collisions, due to the high track multiplicity, it is not applied in the simulations shown below. However, for reactions with lower multiplicities, such as peripheral Pb–Pb, Ar–Ar, and pp, the  $\Upsilon$ -measurement will greatly benefit from the use of the online trigger. The results shown in this section are based on the inclusive lepton pair cross-sections for  $J/\psi$  and  $\Upsilon$  discussed in Section 6.7.1.2 and summarized in Table 6.76. Additionally, nuclear shadowing of 60% was included, corresponding to the  $x$ -range accessible to the central barrel. The resulting yields were scaled by the appropriate number of binary collisions, in order to derive the numbers for Pb–Pb reactions. No additional suppression or enhancement mechanism was included. Therefore, these simulations provide a benchmark for all physics scenarios conceivable in A–A collisions.

*6.7.5.1. Simulation techniques.* Similar as in the case of the dimuon measurement, the evaluation of the physics performance cannot be carried out with a detailed simulation of the detector response, due to the statistics required and the prohibitively lengthy computing time required to generate them. Instead, the approach of a ‘fast simulation’ was employed.

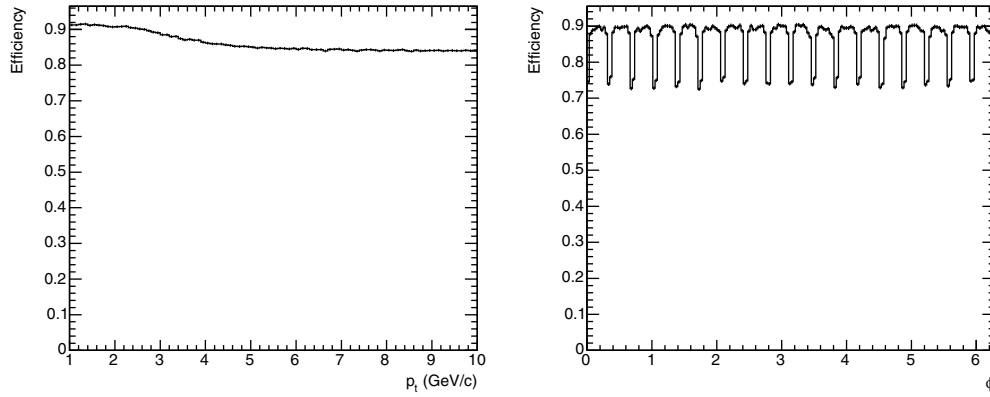


**Figure 6.347.** The reconstruction efficiency for single electrons as a function of  $p_t$  (integrated over  $\phi$  and  $\theta$ , left panel) and  $\phi$  (integrated over  $p_t$  and  $\theta$ , right panel). Please note that this efficiency also includes the effects of the detectors' dead areas and that the online trigger threshold is not included.

This means that the response of the ALICE central barrel to electrons was investigated in detail and, based on this analysis, a parametrization of this response was constructed. This allows the generation of dielectron spectra under different physics conditions with a reasonable computing effort. The different components of this fast simulation are described in the following.

*Evaluation of the response of the ALICE central barrel to electrons.* In order to investigate the performance of the ALICE central barrel detectors (ITS, TPC, and TRD) in reconstructing electrons, a detailed simulation was performed [915]. As an input to these simulations the HIJING event generator [42], tuned to different mid-rapidity densities of charged particles, was used. In these HIJING events, that provide the proper event background, electrons uniformly distributed in the  $p_t$ -range 1–10 GeV/ $c$  were embedded. The number of embedded electrons was kept low, in order not to significantly influence the occupancy in the TRD. These events were treated with the detailed simulation and digitization chain of the AliRoot simulation program. The simulated events were then reconstructed with the standard tracking software for the ALICE central barrel detectors. Only tracks assigned to the main interaction vertex were considered in order to reduce the background from photon conversion to a minimum. By comparing the results to the generated input electrons, the efficiency and momentum resolution were derived. All simulations were done for a magnetic field of  $B = 0.5$  T.

*Efficiency for single electrons.* Figure 6.347 shows the efficiency of reconstructing an electron as a function of  $p_t$  and azimuthal angle  $\phi$ . Efficiency in this context is a convolution of the acceptance, i.e. the probability that an electron passes through the sensitive area of the detector, and the efficiency of the reconstruction algorithm. The drop of the efficiency between  $p_t = 3$ –5 GeV/ $c$  is caused by the fact that tracks with higher  $p_t$  have a higher probability of remaining inside the dead areas of the detector than tracks with lower  $p_t$ , which are more strongly curved. The effect of the dead areas is even more pronounced in the  $\phi$ -dependence of the efficiency which clearly reflects the 18 sectors of TRD and TPC. The single electron efficiency that is folded into the fast simulation procedure has been evaluated in a 3-dimensional binning of  $p_t$ ,  $\phi$ , and  $\theta$ , as well as for the charged particle multiplicity densities  $dN_{ch}/d\eta = 3000$  and  $dN_{ch}/d\eta = 6000$ .

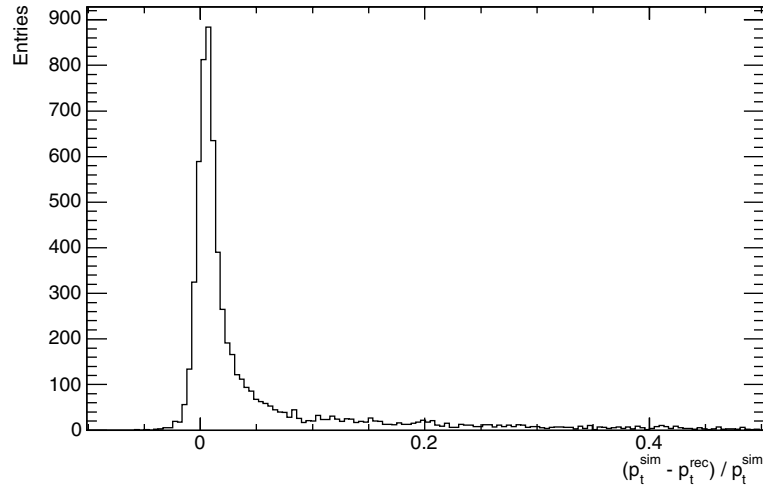


**Figure 6.348.** The difference between the simulated and reconstructed transverse momentum of electrons in a given  $p_t$  and  $\varphi$  bin. The asymmetric tail caused by bremsstrahlung is clearly visible.

*Momentum resolution for single electrons.* Due to the effect of bremsstrahlung, an electron can suffer, with a relatively high probability, a large energy loss beyond the normal energy loss of a charged particle. This causes an asymmetric tail of the momentum distribution of a reconstructed track as demonstrated in Fig. 6.348. In order to include this effect in the fast simulation approach, this  $p_t$ -broadening was parametrized in different bins of  $p_t$  by a convolution of a Gaussian and a Landau curve. The parameters of these fits were tabulated as a function of  $p_t$  and then used in the fast simulation environment.

*Electron identification.* The electrons are identified by combining the information from the TRD and the TPC. For the study presented the same parametrization of the pion suppression was employed as described in Section 6.6. For the TRD, an electron-tagging probability for pions of  $\pi_{\text{eff}}^{\text{TRD}} = 10^{-2}$  at a given electron efficiency of  $e_{\text{eff}}^{\text{TRD}} = 0.9$  is assumed. This takes into account an expected deterioration of the TRD performance in the high multiplicity environment at  $dN_{\text{ch}}/d\eta = 6000$ . While the TRD performance is assumed to be independent of momentum in the relevant momentum range, the electron identification capabilities of the TPC, based on the measurement of the specific energy loss  $dE/dx$ , depend strongly on  $p$  (see Section 6.6). In the currently used parametrization,  $\pi_{\text{eff}}^{\text{TPC}} = 10^{-2}$  for  $p < 2-3 \text{ GeV}/c$  and gets quickly worse above  $3 \text{ GeV}/c$ . The electron efficiency is also fixed at  $e_{\text{eff}}^{\text{TPC}} = 0.9$ . Therefore, the combined efficiency to properly detect an electron is  $e_{\text{eff}}^{\text{COMB}} = 0.81$ .

*Generation of dielectron spectra.* To all electron and positron candidates, whose momentum was smeared according to the parametrization of the momentum resolution and which survived the efficiency and particle identification criteria, a cut at  $p_t > 1 \text{ GeV}/c$  was applied. No TRD-L1 trigger condition was used in this simulations. From the remaining candidates unlike-sign pairs were constructed and the distribution of their invariant mass histogrammed.

*Input to the simulations.* The main background source for high mass dielectrons is caused by misidentified pions and by electrons from semi-leptonic D- and B-decays. A

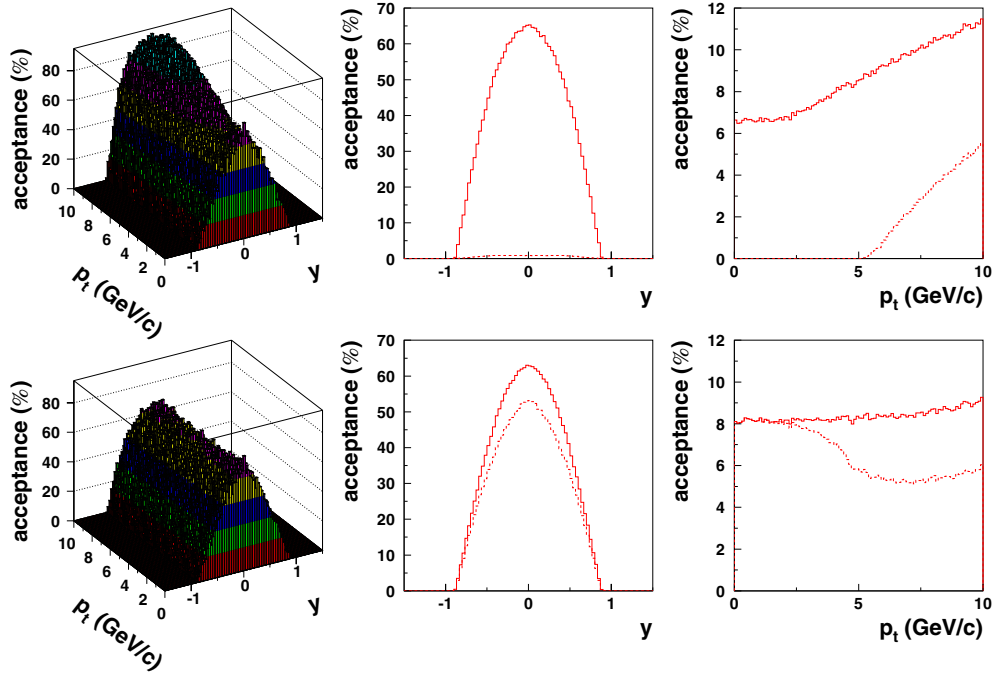


**Figure 6.349.** Geometrical acceptance for  $J/\psi$  (up) and  $\Upsilon$  (bottom). The left panels show the geometrical acceptance versus rapidity and transverse momentum. The middle and right panels show the acceptance as a function of rapidity and transverse momentum, respectively. On the middle and right panels the acceptance is shown without (solid histograms) and with (dashed histograms) the trigger cut on single electron  $p_t$ .

realistic simulation has therefore to include all these possible contributions. The members of the quarkonia families were generated using the parametrization and rates described in Section 6.7.1.2. These signals were then merged with electrons and positrons from D- and B-hadrons, which were generated using the same rates and distributions as described in Section 6.6. Additionally, a hadronic background, provided by the parametrized HIJING event generator was added to the input. The multiplicity of the HIJING background was adjusted so that it results in  $dN_{\text{ch}}/d\eta = 3000$ , as well as  $dN_{\text{ch}}/d\eta = 6000$ , in the case of central Pb–Pb events.

**6.7.5.2.  $J/\psi$  and  $\Upsilon$  acceptance.** The geometrical  $J/\psi$  and  $\Upsilon$  acceptances in the dielectron channel were evaluated with same inputs and similar techniques as for the dimuon channel (see Section 6.7.2.3). The TRD-L1 trigger condition was simulated by requiring a sharp  $p_t$  threshold of 3 GeV/ $c$  on both decay electrons. The results are displayed in Fig. 6.349.

For  $\Upsilon$  a small dip is clearly seen developing at  $p_t \sim 6$  GeV/ $c$ . This is due to the fact that low  $p_t$   $\Upsilon$  mesons decay by emitting  $e^+e^-$  pairs where both leptons have a  $p_t$  above 3 GeV/ $c$  and hence pass the trigger condition. The decay of intermediate  $p_t$   $\Upsilon$  mesons, of  $p_t \sim 6$  GeV/ $c$ , can be asymmetric in the laboratory reference frame with one of the decay particles having  $p_t$  less than 3 GeV/ $c$ ; therefore those  $\Upsilon$  are lost due to the L1 trigger condition.

The trigger cut on the  $p_t$  of  $e^+e^-$  has a much stronger effect on the  $J/\psi$  distribution since the mass difference of the  $J/\psi$  is much smaller than that of the  $\Upsilon$ ; hence the decays of low

**Table 6.91.** Geometrical acceptance for the detection of  $\Upsilon$  and  $J/\psi$  in the TRD. They are given for different  $y$  and  $p_t$  range of the parent particles, with and without the L1 trigger  $p_t$  cut on the  $e^+e^-$  pair ( $p_t > 3 \text{ GeV}/c$ ).

Parent particle	$p_t$ of $e^+e^-$ (L1 trigger)	$y$ and $p_t$ of $J/\psi$ and $\Upsilon$	TRD accept. (%)
$\Upsilon$	no cut	$ y  < 1.0$ , all $p_t$	26.6
	no cut	$ y  < 0.5$ , $p_t < 3 \text{ GeV}/c$	42.4
	$p_t > 3 \text{ GeV}/c$	$ y  < 1.0$ , all $p_t$	24.0
	$p_t > 3 \text{ GeV}/c$	$ y  < 0.5$ , $p_t < 3 \text{ GeV}/c$	41.7
$J/\psi$	no cut	$ y  < 1.0$ , all $p_t$	29.5
	no cut	$ y  < 0.5$ , $p_t < 6 \text{ GeV}/c$	62.8
	$p_t > 3 \text{ GeV}/c$	$ y  < 1.0$ , all $p_t$	1.4
	$p_t > 3 \text{ GeV}/c$	$ y  < 0.5$ , $p_t < 6 \text{ GeV}/c$	16.3

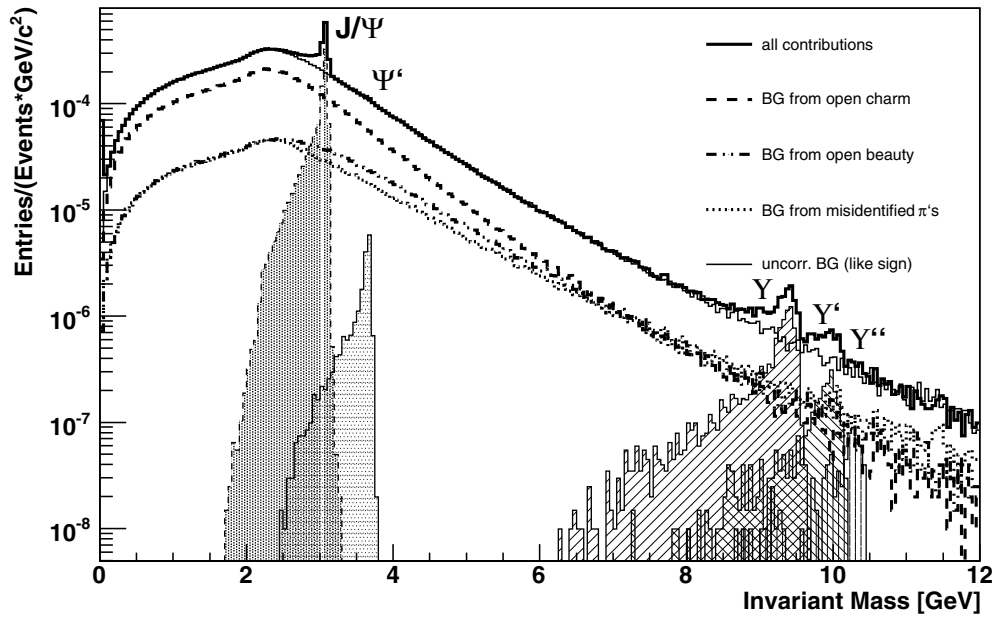


**Figure 6.350.** The invariant mass distribution of electron pairs for  $2 \times 10^8$  central Pb-Pb collisions. The sum of all contributions (black solid line) is shown, as well as the background contributions from open charm and open beauty and misidentified pions. The total uncorrelated background was constructed with the like sign technique.

$p_t$   $J/\psi$  produce  $e^+e^-$  pairs that do not make it through the  $p_t$  threshold of  $3 \text{ GeV}/c$  of the trigger. It is only at rather large  $p_t$  that the  $J/\psi$  decay kinematics allow both the  $e^+e^-$  to have  $p_t > 3 \text{ GeV}/c$ . This results in no  $J/\psi$  acceptance below a  $p_t$  of  $\sim 5.2 \text{ GeV}/c$  under the L1 trigger condition.

The geometrical acceptances for  $\Upsilon$  and  $J/\psi$  integrated over the rapidity range  $-1.0 < y < 1.0$  are summarized in Table 6.91. They are tabulated with the L1 trigger condition on their decay particles and for different  $p_t$  range of the  $J/\psi$  and  $\Upsilon$ .

**6.7.5.3. Dielectron spectra in central Pb-Pb collisions.** Figure 6.350 shows the expected invariant mass distribution of dielectrons for  $2 \times 10^8$  recorded Pb-Pb events (10% most

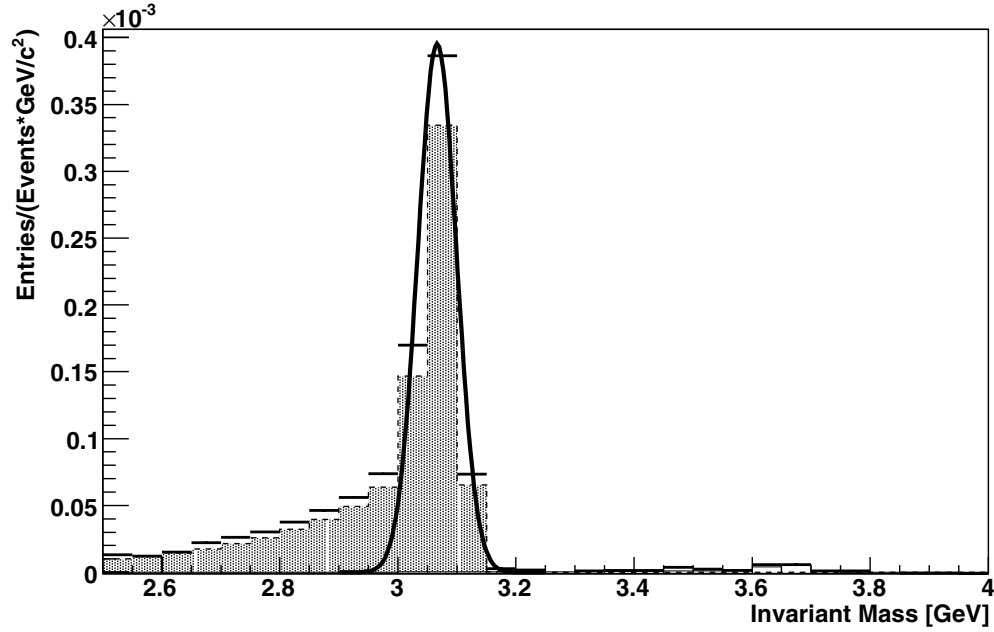


**Figure 6.351.** The invariant mass distribution of electron pairs for  $2 \times 10^8$  central Pb–Pb collisions in the  $J/\psi$  mass region after subtraction of the combinatorial background (symbols). The signal was fitted by a Gaussian (solid line). The dashed histogram represents the expected signal shape without combinatorial background.

central, without TRD-L1 trigger condition). Clear signals for the  $J/\psi$  and  $\Upsilon$  can be observed on top of the uncorrelated background. As one source for the background semi-leptonic decays of open charm and beauty contribute up to high mass regions (dashed and dashed–dotted lines in Fig. 6.350). However, even in the  $\Upsilon$ -mass region, the background from misidentified pions is still of the same order of magnitude.

However, due to the expected suppression of high- $p_t$  hadrons in central Pb–Pb collisions, this contribution is likely to be lower in real data. Therefore, this simulation represents a conservative estimate of the performance in this mass region.

As seen in Fig. 6.351, the  $J/\psi$  can be nicely reconstructed in this environment. Even though the background is not negligible, the  $\Upsilon$  can also be reconstructed with a good significance (see Fig. 6.352). The expected signals, the signal to background ratios, as well as the significances are summarized in Table 6.92, corresponding to a running time of  $10^6$  s at a luminosity of  $5 \times 10^{26} \text{ cm}^{-2} \text{ s}^{-1}$ , assuming an effective readout rate for the central barrel of 200 Hz.

The reconstructed peaks were fitted by a Gaussian to derive the resolution in the invariant mass. For the  $J/\psi$  it is found to be  $\sigma_m = 33 \text{ MeV}/c^2$  and in the  $\Upsilon$  mass region it is  $\sigma_m \approx 90 \text{ MeV}/c^2$ . However, as Fig. 6.351 demonstrates, the reconstructed line shape of the  $J/\psi$  is expected to be clearly asymmetric due to the influence of the bremsstrahlung on the electron reconstruction.

By integrating the invariant mass spectra in a mass window of  $\pm 1.5\sigma$  around the  $J/\psi$  mass the signal, the signal to background ratio, as well as the significance  $SGN = S/\sqrt{S+B}$  can be determined as a function of the  $p_t$  of the  $J/\psi$ . The result is summarized in Figs. 6.353 and 6.354. The analysis shows that a significant  $J/\psi$  signal can be

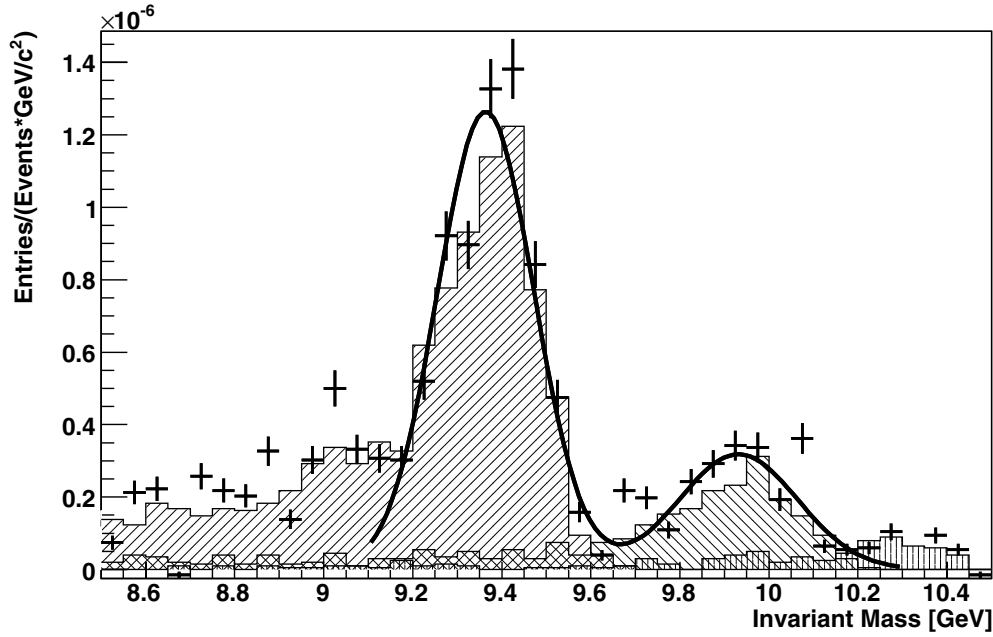


**Figure 6.352.** The invariant mass distribution of electron pairs for  $2 \times 10^8$  central Pb–Pb collisions in the  $\Upsilon$  mass region after subtraction of the combinatorial background (symbols). The signal was fitted by a Gaussian (solid line). The histograms represent the expected signal shapes without combinatorial background.

**Table 6.92.** Expected signal rates (S), background (B), signal-to-background ratios and significance for charmonium and bottomonium states, integrated over the full acceptance for  $dN_{\text{ch}}/d\eta = 3000$ . The numbers correspond to an interval of  $\pm 1.5\sigma$  around the resonance mass. The rates and ratios are given for 10% most central events, assuming  $10^6$  s running time and a Pb–Pb luminosity of  $5 \times 10^{26} \text{ cm}^{-2} \text{ s}^{-1}$  (corresponding to  $2 \times 10^8$  collected events).

State	S ( $\times 10^3$ )	B ( $\times 10^3$ )	S/B	$S/\sqrt{S+B}$
$J/\psi$	121.1	88.2	1.4	265
$\Upsilon$	1.3	0.8	1.6	28
$\Upsilon'$	0.46	0.8	0.6	13

reconstructed up to  $p_t = 10 \text{ GeV}/c^2$ , even in an environment of  $dN_{\text{ch}}/d\eta = 6000$ . However, in this case the signal/background ratio is clearly worse in the high- $p_t$  region than for  $dN_{\text{ch}}/d\eta = 3000$ .

**6.7.5.4. Expected yields for pp at  $\sqrt{s} = 5.5 \text{ TeV}$ .** For the pp case a detailed simulation has not yet been performed. Nevertheless, a first estimate of the expected quarkonia yields can be given by scaling the results obtained for Pb–Pb collisions at the same c.m. energy. For Pb–Pb collisions, the total yield expected in a  $10^6$  s data taking period can be deduced from Table 6.92. The total yields are then divided by the corresponding shadowing factor and scaled to pp by dividing by number of binary collisions. Finally, the scaled yields are multiplied by the different readout rates for the central barrel detectors. Assuming that the TRD L1 trigger

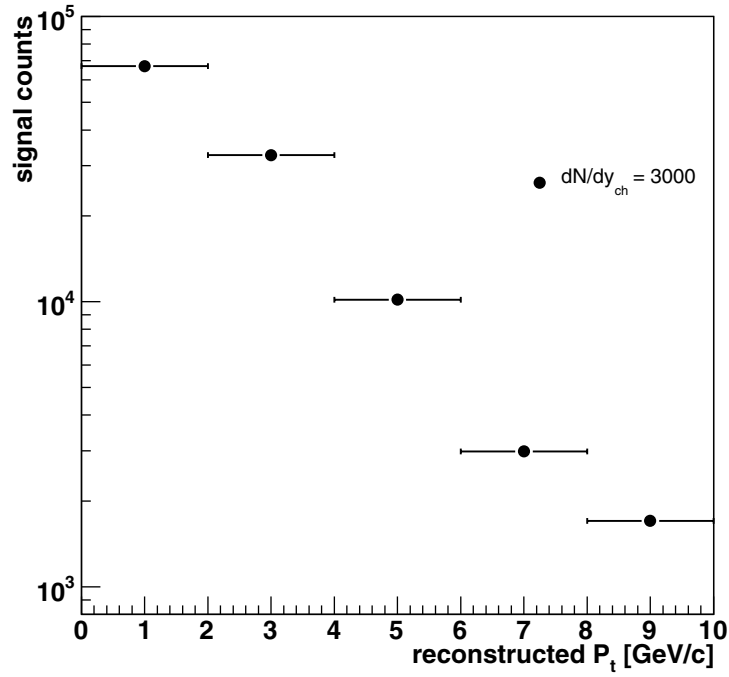


**Figure 6.353.** The reconstructed  $J/\psi$  events within  $\pm 1.5\sigma$  from the peak for  $2 \times 10^8$  central Pb–Pb events as a function of  $p_t$  for  $dN_{ch}/d\eta = 3000$ .

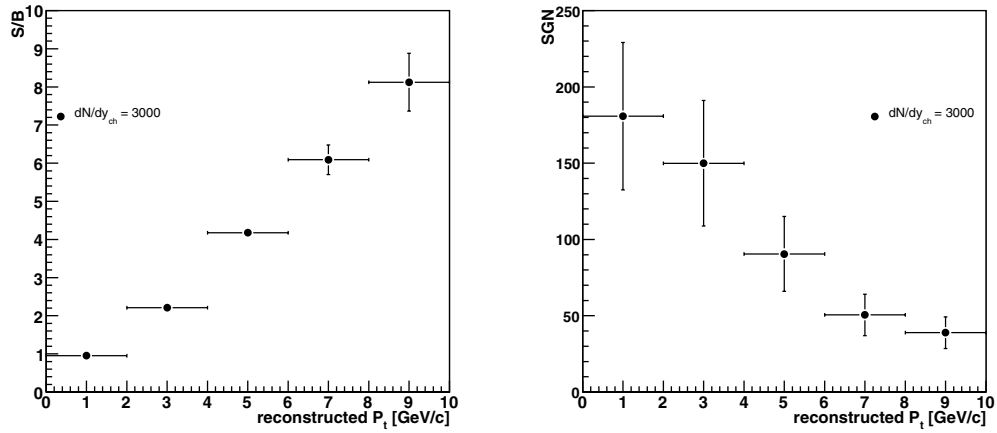


**Figure 6.354.** The signal to background ratio (left) and the corresponding significance (right) of the reconstructed  $J/\psi$  for  $2 \times 10^8$  central Pb–Pb events as a function of  $p_t$  for  $dN_{ch}/d\eta = 3000$ .

is capable of inspecting  $\approx 30\%$  of the pp interaction rate at a luminosity of  $5 \times 10^{30} \text{ cm}^{-2} \text{ s}^{-1}$  a yield can be estimated for  $10^6$  s running time at 5.5 TeV. For the  $J/\psi$  this is in the order of  $7.0 \times 10^5$  and for the  $\Upsilon$  it is  $0.6 \times 10^3$ .

## 6.8. Jet physics

*6.8.1. Introduction.* Jets are defined in QCD as cascades of consecutive emissions of partons initiated by partons from an initial hard scattering. The partons produce the observed hadrons due to confinement. Parton showering and the subsequent hadronisation are broadly known as parton fragmentation. Di-jets were discovered in 1975 in  $e^+e^-$  collisions [916] and detailed studies of their structure showed that the transverse momenta relative to the jet axis of particles associated to the jet are small compared to the jet momenta. The collimation increases with increasing jet energy. The observation of three coplanar jets [917] has provided the first experimental evidence for the existence of the gluon. In the following years a huge amount of data on multi-particle production in QCD jets has been collected at  $e^+e^-$ ,  $e^-p$  and hadron colliders which allowed many important tests of both perturbative and non-perturbative aspects of QCD.

High-energy nucleus–nucleus collisions allow us to change the scene of parton fragmentation from vacuum to a QCD medium, the quark–gluon plasma (QGP), and to study the properties of this medium through modifications of the jet-structure. High- $p_t$  partons produced in the initial stage of a nucleus–nucleus collision are expected to undergo multiple interactions inside the collision region prior to hadronisation. Hereby, the energy of the partons is reduced through collisional energy loss [918–920] and medium-induced gluon radiation [42, 786, 921], the latter being the dominant mechanism in a QGP. This so-called jet quenching has been suggested to behave very differently in cold nuclear matter and in QGP, and has been postulated as a tool to probe the properties of this new state of matter. This is the main motivation for studying jets as well as high- $p_t$  particle spectra and particle correlations in heavy-ion collisions.

First evidence of parton energy loss has been observed at RHIC from the suppression of high- $p_t$  particles studying the nuclear modification factor,  $R_{AA}$ , [922, 923] and the suppression of back-to-back correlations [924].

As compared to jet physics at RHIC, there are two fundamentally new features in central Pb–Pb collisions at the LHC: The multi-jet production per event is not restricted to the minijet region  $E_t < 2$  GeV but extends to about 20 GeV and jet rates are high at energies at which jets can be distinguished from the background energy of the underlying event. Hence, event-by-event reconstruction of jets with reasonable energy resolution will be possible.

As compared to studies of the nuclear modification factor  $R_{AA}$ , a much higher sensitivity to the medium properties is expected from studies of modifications of the structure of reconstructed jets, i.e. the manifestation of the partonic energy loss in a decrease of the number of particles carrying a high fraction,  $z$ , of the jet energy and the appearance of radiated energy via an increase of the number of low-energy particles with low  $z$  values. In addition, a broadening of the distribution of jet-particle momenta perpendicular to the jet axis,  $j_t$ , directly related to the colour density of the medium is expected [925]. The main limitation of inclusive high- $p_t$  particle studies is the fact that for extreme quenching scenarios one observes particle emission predominantly from the surface [926]. Full reconstruction of jets is potentially free of such a bias, allowing detailed study of the induced radiation patterns. It is our task to quantify to which extent jet reconstruction is possible in heavy-ion collisions and what are the possible remaining experimental biases.

As opposed to jet analysis at hadron colliders, the large background from the underlying events (see, for example, Colour Figure VI) imposes limitations to the reconstruction performance. In a typical cone of size  $R_c = \sqrt{\Delta\eta^2 + \Delta\phi^2} < 1$  we expect up to 2 TeV of energy from the underlying event. As a consequence, smaller cone sizes have to be used in heavy-ion collisions. In our physics performance studies, we will mainly address the question of what are

the resulting intrinsic limitations on the jet reconstruction efficiency and jet energy resolution and what are the influences on the jet-structure measurements. Additional limitations are imposed by the experimental set-up and have to be evaluated. Measuring charged jets using ALICE central barrel tracking is possible but severely limits the jet energy resolution to the amount of charged to neutral fluctuations ( $\simeq 30\%$ ) [927].

As demonstrated in the previous chapters, in the central barrel part of the experiment  $|\eta| < 0.9$ , ALICE will measure event-by-event the inclusive distribution and correlation of a wide range of flavour identified particles, whose momenta and masses are of the order of the typical energy scales involved ( $T \simeq \Lambda_{\text{QCD}} \simeq 200 \text{ MeV}$ ). In addition, tracking and particle identification capabilities reach far into the transverse momentum region in which particle production is dominated by hard processes. At  $p_t = 100 \text{ GeV}/c$ , the momentum resolution is still better than 10%, sufficient to analyse jets up to  $E_t = 200 \text{ GeV}$ .

As shown by the STAR experiment at RHIC [928], the combination of a TPC tracking system with an electromagnetic calorimeter is functionally equivalent to full electromagnetic plus hadronic calorimetry in a heavy-ion collision environment. Based on this concept an Electromagnetic Calorimeter (EMCal) has been proposed [929]. EMCal covers the region  $|\eta| < 0.7$ ,  $60^\circ < \varphi < 180^\circ$  and has a design energy resolution of  $\Delta E/E = 10\%/\sqrt{E}$ . The calorimeter will improve the jet energy resolution and adds trigger capabilities. Although the EMCal was not yet approved during the time of writing this document, we will discuss the possible improvement of jet reconstruction as compared to charged-jet reconstruction.

High- $p_t$  capabilities are needed for jet identification and reconstruction. However, the strength of ALICE consists in the possibility of combining these with low- $p_t$  tracking and PID capabilities to observe modifications of the jet-structure observables over a wide range of momenta and particle species [930]. Measurements in Pb–Pb collisions will be benchmarked against pp and pA. In the present document, we restrict the evaluation of the physics performance for jet reconstruction and jet-structure analysis to central Pb–Pb collisions, which are the most demanding concerning the background conditions. The results presented were obtained using a conservative assumption about the central charged multiplicity of  $dN_{\text{ch}}/d\eta = 5000$ .

Discussing jet reconstruction in heavy-ion collisions, we are entering mainly unexplored territories as the optimisation of reconstruction and analysis techniques is awaiting data. We are starting to outline the first boundaries based on present knowledge and predictions of jet production cross sections (Section 6.8.2), jet fragmentation and its modification in a dense medium (Sections 6.8.3 and 6.8.4) and the properties of background from low- $p_t$  particles (Section 6.8.5). This allows us to draw our first conclusions on intrinsic limitations of jet reconstruction in an heavy-ion collision environment (Section 6.8.6). We present analysis results obtained with fast and full simulation using a cone-type jet reconstruction algorithm optimised for the heavy-ion environment (Section 6.8.7) and discuss possible improvements using EMCal (Section 6.8.8).

As jet reconstruction will be restricted to relatively high-energy jets, approximately  $E_t > 30\text{--}40 \text{ GeV}$ , leading particle correlation studies play an important role in the low- $E_t$  region. A case study for the LHC applying typical transverse momentum cuts used at RHIC is presented in the last section.

**6.8.2. Jet production rates at the LHC.** Jet cross sections calculated in the framework of collinear factorised perturbative QCD at NLO have been successfully confronted with experimental data in hadron–hadron collisions [927]. Monte Carlo codes have become available [931–933] and have been adapted to include isospin effects and modifications of the nucleon parton distribution function inside nuclei. Using these codes, benchmark calculations

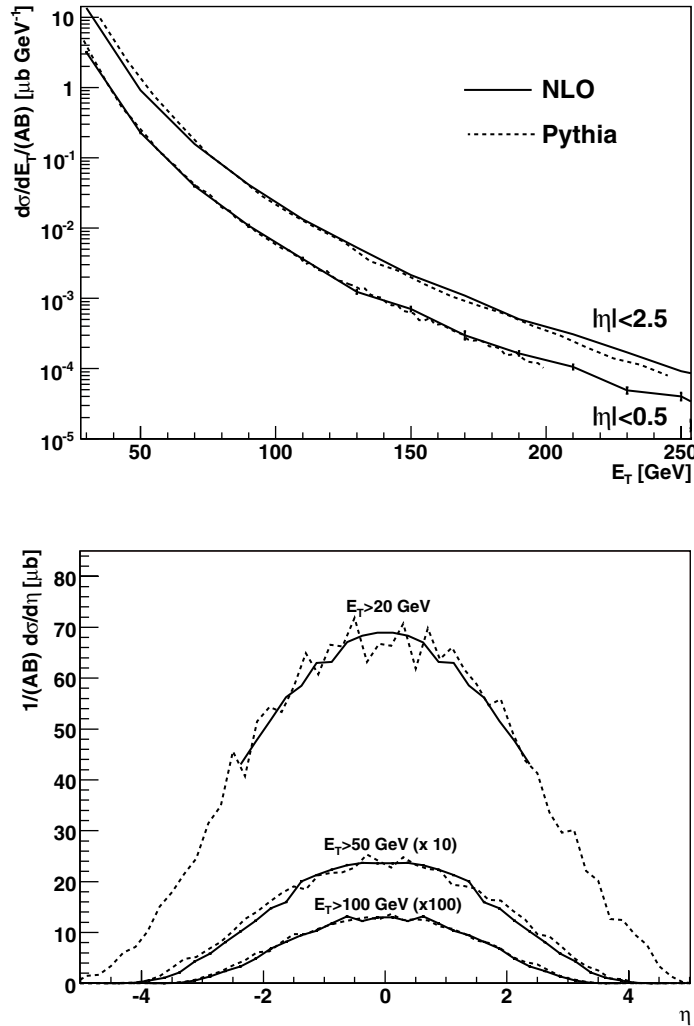


**Figure 6.355.** Jet cross section in Pb–Pb collisions at the LHC per binary collision ( $AB = 208^2$ ) versus transverse energy of the jet for  $|\eta| < 2.5$  and  $|\eta| < 0.5$  (upper) and versus pseudorapidity of the jet for  $E_T > 20, 50$  and  $100$  GeV (lower). The NLO calculations from Ref. [797] (solid lines) are compared to those obtained with PYTHIA 6.214 (dashed lines).

for jet spectra in nucleus–nucleus collisions at the LHC have been performed and have been presented in [797].

In Fig. 6.355, we show the differential jet cross section for Pb–Pb collisions at  $\sqrt{s_{NN}} = 5.5$  TeV versus transverse energy of the jet for  $|\eta| < 2.5$  and  $|\eta| < 0.5$  and versus the pseudorapidity of the jet for  $E_T > 20, 50$  and  $100$  GeV. The results of the NLO calculations from Ref. [797, 934] are compared to those obtained for pp collisions simulated with PYTHIA 6.214 [935–937] scaled up by a  $k$ -factor,  $k = 1.7$ . The NLO calculations have been performed with MRST98 [824] parton distribution functions modified using EKS98 [938]. The factorisation scale is equal to the renormalisation scale  $\mu = \mu_F = \mu_R = E_T/2$ . Jets are reconstructed using the  $k_t$ -clustering algorithm with  $D = 1$ . For the PYTHIA based calculation, jets have been reconstructed using the PYTHIA–PYCELL cone-algorithm on the

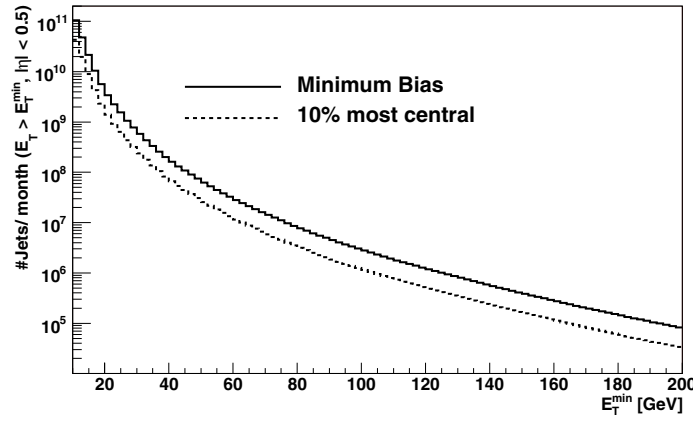


**Figure 6.356.** Number of jets with  $E_t > E_t^{\min}$  and  $|\eta| < 0.5$  produced in Pb–Pb collisions at  $\sqrt{s_{\text{NN}}} = 5.5$  TeV in one effective month of running ( $10^6$  s). The minimum bias rate (solid line) is compared to the rate in the 10% most central collisions (dashed line).

**Table 6.93.** Number of jets with  $E_t > E_t^{\min}$  produced in one month of Pb–Pb running within the central barrel ( $|\eta| < 0.5$ ) and within the EMCal acceptance ( $|\eta| < 0.3$  and  $83^\circ < \varphi < 157^\circ$ ). The acceptance limits assume that a cone size of  $R_c = 0.4$  is used for jet reconstruction.

$E_t^{\min}$ [GeV]	TPC fiducial region	EMCal fiducial region
20	$2.0 \times 10^9$	$2.4 \times 10^8$
50	$4.8 \times 10^7$	$5.8 \times 10^6$
100	$2.6 \times 10^6$	$3.1 \times 10^5$
150	$4.0 \times 10^5$	$4.8 \times 10^4$
200	$1.0 \times 10^5$	$1.2 \times 10^4$
250	$2.5 \times 10^4$	$3.0 \times 10^3$

final state particle level with cone-size  $R_c = 1$ . The two spectra agree within 20%. Taking into account that the uncertainty of the NLO calculation is 2% for the lowest and 15% for the highest  $E_t$  bins we consider the agreement sufficiently good to justify the usage of PYTHIA for the generation of the physics events as input for full detector simulation and fast simulation. For  $E_t > 20$  GeV, 17% of the produced jets are in the ALICE fiducial region  $|\eta| < 0.5$ . A fraction of 8.6% of the accepted jet events contain back-to-back di-jets defined as events having a second accepted jet with at least 90% of the minimum transverse energy required for the leading jet. For  $E_t > 100$  GeV, the single jet acceptance rises to 26% and the di-jet acceptance to 13.5%. Note that the size of the fiducial region is determined by the assumption that jets are reconstructed using a cone-size  $R_c = 0.4$  and requiring that the jet-cone is fully contained within the detector acceptance. As we will show later, this cone-size is close to the optimal cone size in a heavy-ion environment. The lowering of the jet-reconstruction efficiency due to the reduced cone-size has not been taken into account in the cross section and rate calculations.

From the expected average LHC Pb–Pb luminosity of  $5 \times 10^{26} \text{ cm}^{-2} \text{ s}^{-1}$  we calculate the number of jets produced per effective month of running ( $10^6$  s) within the fiducial region  $|\eta| < 0.5$  for charged jet reconstructed using ALICE central barrel tracking (ITS + TPC) and  $|\eta| < 0.3$ ,  $83^\circ < \varphi < 157^\circ$  for jet reconstruction with central barrel tracking and Electromagnetic Calorimetry (EMCal). The results are presented in Fig. 6.356 and Table 6.93.

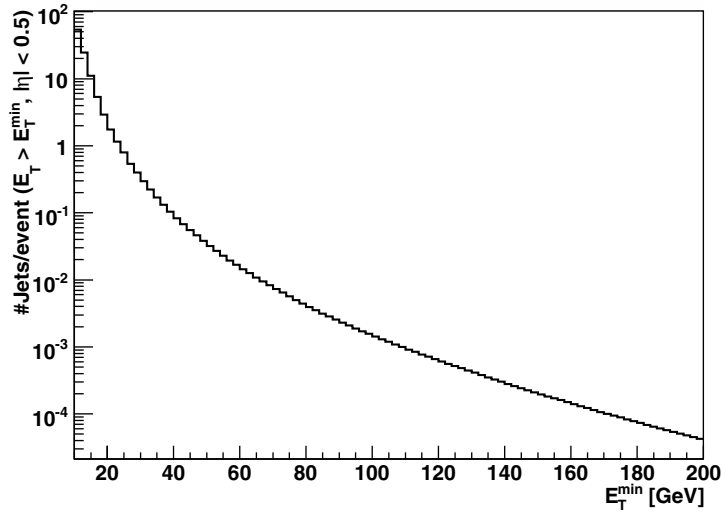


**Figure 6.357.** Average number of jets with  $E_t > E_t^{\min}$  and  $|\eta| < 0.5$  per event in the 10% most central Pb–Pb collisions.

Rates in minimum bias collisions are compared to those in the 10% most central collisions. The latter have been obtained by scaling with the average number of binary collisions for impact parameter  $b < 5$  fm.

ALICE will study the whole spectrum of jet production ranging from minijets,  $E_t > 2$  GeV, to high- $E_t$  jets of several hundred GeV. Experimental considerations delineate four distinct energy regions, which are discussed here for the 10% most central Pb–Pb collisions at  $\sqrt{s_{NN}} = 5.5$  TeV. In the region  $E_t < 20$  GeV several jets overlap in one event within the ALICE acceptance (Fig. 6.357). This means that jet identification in the traditional sense is not possible and their presence is revealed via studies of particle correlations. For  $E_t < 100$  GeV the jet rate  $> 1$  Hz is high enough so that, even with a read-out rate limited by the TPC to 20–40 Hz, an event sample of  $\mathcal{O}(10^4)$  jets can be collected in one effective month of running ( $10^6$  s). For  $E_t > 100$  GeV triggering will be necessary to collect jet enriched data. Considering that for a fragmentation function analysis of the order of  $10^4$  jet events are needed, the statistics limit is reached at about 250 GeV.

**6.8.3. Jet quenching at the LHC.** We will not cover the complete status of predictions for jet-structure modifications at the LHC here. For recent reviews of this subject see Ref. [797]. Instead, we will concentrate on general results that guide us in the performance studies presented in the following sections.

**6.8.3.1. The BDMPS model.** Mainly results obtained within the BDMPS [788] framework will be discussed. The reason is that based on these calculations, Monte Carlo tools have become available which can be used to estimate the expected jet-structure changes. Some of the Monte Carlo results will be discussed in the following section complementing the discussion in the present section.

A more detailed description of the BDMPS model can be found in Section 6.6.1.4. In short, in the BDMPS model of medium-induced partonic energy loss the medium is characterised by the transport coefficient  $\hat{q}$ . Physically,  $\hat{q}$  is the average squared transverse momentum transferred from the medium to a hard parton per unit path length

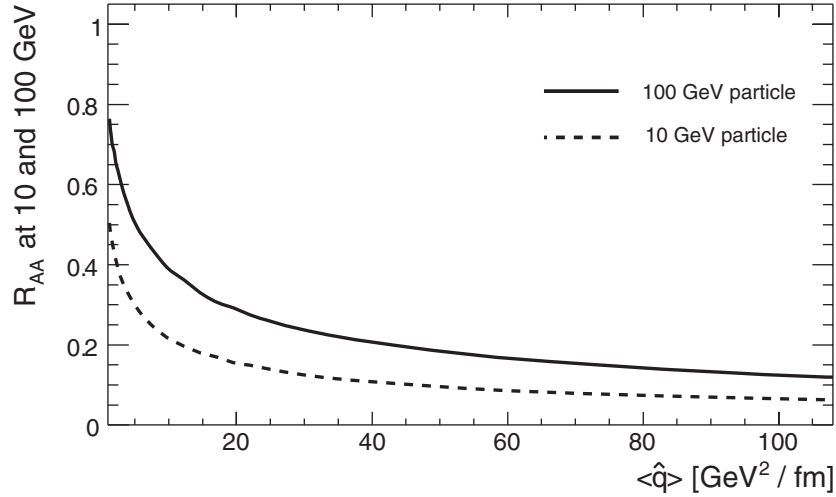


**Figure 6.358.**  $R_{AA}$  as a function of the average transport coefficient,  $\langle \hat{q} \rangle$ , for 10 and 100 GeV/c hadrons in the 10% most central Pb–Pb collisions at  $\sqrt{s_{NN}} = 5.5$  TeV as predicted by the Parton Quenching Model (PQM). Figure taken from Ref. [939].

( $[\hat{q}] = \text{GeV}^2/\text{fm}$ ). Transverse momentum broadening is characterised by  $\langle k_{\perp}^2 \rangle \sim \hat{q} L_{\text{med}}$ , where  $L_{\text{med}}$  is the in-medium path length. The energy loss is determined by  $\Delta E = \alpha_s C_R \omega_c \propto L^2$ , where  $\omega_c = \frac{1}{2} \hat{q} L^2$  is the characteristic energy scale of the radiated gluons. The loss is proportional to the strong coupling constant  $\alpha_s$  and to the Casimir factor  $C_R$  and hence by a factor 2.25 larger for gluons than for quarks. The inclusive energy distribution of medium-induced gluon radiation depends only on  $\omega_c$  and a dimensionless parameter  $R = \omega_c L_{\text{med}}$ .

The transport coefficient is proportional to the density of the scattering centres and to the average momentum transfer in gluon scattering off these centres. For cold nuclear matter the transport coefficient is small,  $\hat{q}_{\text{cold}} \simeq 0.05 \text{ GeV}^2/\text{fm}$ , whereas for a QGP formed at the LHC,  $\hat{q}$  may be as large as  $100 \text{ GeV}^2/\text{fm}$  [797].

**6.8.3.2. The nuclear modification factor.** One way to quantify the effect of the medium on the parton fragmentation is via the nuclear modification factor,

$$R_{AA}(p_t, \eta; b) = \frac{1}{\langle N_{\text{coll}}(b) \rangle} \frac{d^2 N_{AB}^{\text{hard}}/dp_t d\eta}{d^2 N_{pp}^{\text{hard}}/dp_t d\eta}, \quad (6.141)$$

where  $d^2 N_{AB}^{\text{hard}}/dp_t d\eta$  are the yields measured in A–A (pp) collisions. It measures the deviation of nucleus–nucleus (A–A) collisions from a superposition of  $\langle N_{\text{coll}}(b) \rangle$  independent nucleon–nucleon collisions. It has been demonstrated that as a consequence of the steeply falling parton  $p_t$ -spectrum and the emission of jets from the surface of the reaction volume,  $R_{AA}(p_t)$  is almost flat for high transverse momenta as observed at RHIC [795, 796, 939]. Its absolute size is not very sensitive to the transport parameter  $\hat{q}$  of the medium. Model calculations show that this situation is expected to persist at LHC energies (Fig. 6.358). A higher sensitivity to the medium parameters can be obtained from the jet-structure observables discussed in the following section.

**6.8.3.3. Jet-structure observables.** Experimentally, jets in pp-collisions are defined as an excess of transverse energy over the background of the underlying event within a typical cone

radius of  $R_c = 1.0$  in the  $\eta - \varphi$  plane.  $R_c$  defines the geometrical size of a jet. In heavy-ion collisions at the LHC the total (charged + neutral) energy,  $E_b$ , from the underlying event in a cone  $R_c = 1$  is expected to be 1.9 TeV assuming a central charged multiplicity of  $dN/d\eta = 5000$  and a mean transverse momentum of  $0.5 \text{ GeV}/c$ . This is one order of magnitude higher than the highest jet energies we want to measure. More importantly, this energy fluctuates by  $\Delta E_b = 36 \text{ GeV}$  rendering jet identification in large cones impossible. However jet energy is collimated and, hence, the situation changes dramatically for smaller cone sizes. Typically, 80% of the jet energy is inside a cone of  $R_c = 0.3$ , whereas the background energy scales proportional to  $R_c^2$  and its fluctuations proportional to  $R_c$  reducing them to  $E_b = 170 \text{ GeV}$  and  $\Delta E_b = 12 \text{ GeV}$ , respectively. Hence, the first question to answer experimentally is to what extent the collimated nature of the jets persists in heavy-ion collisions and if it can be used for their identification. On the one hand, a change of the jet shape is an interesting measurement by itself, as it can be related to the properties of the medium. On the other hand, any significant change will have also an influence on the jet reconstruction efficiency and energy resolution.

Jet shapes are described by the distribution of the average fraction of energy in a sub-cone of radius  $R$ :

$$\Psi(R) = \frac{1}{N_{\text{jet}}} \sum_{\text{jets}} \frac{p_t(0, R)}{p_t(0, R_c)}. \quad (6.142)$$

Intuitively, it is clear that a lowering of the momenta parallel to the jet axis and an increase of the mean momentum transverse to the jet axis leads to an increase of the jet size. Calculations performed for a relatively modest transport coefficient of  $\hat{q} L_{\text{med}} \simeq (2 \text{ GeV})^2$  (Fig. 6.359) show that the energy inside a cone of  $R_c = 0.3$  is reduced by only  $\sim 5\%$  for a jet of  $E_t = 50 \text{ GeV}$  and by  $\sim 3\%$  for a  $100 \text{ GeV}$  jet [925]. Whereas these differences are difficult to measure, the increase of the mean  $j_t$  and in particular the increase of the tail of the distribution is already significant (Fig. 6.360).

The same model has been used to extrapolate the range of transport coefficients consistent with RHIC data to the LHC, and values up to two orders of magnitude higher than those used for the model calculation shown above have been obtained [795]. Under these assumptions, partonic energy losses would saturate ( $\Delta E_t = E_t$ ) even for the highest observable jet energies and only jets coming from the surface directed outward would be observed. The model of partonic energy loss reduces to a pure absorption model which can be quantified by a corresponding  $R_{AA}^{\text{jet}}(E_t)$ .

Considering the range of possible scenarios one has to be prepared to perform the following measurements to understand the modification of the transverse jet-structure:

- Measure  $R_{AA}^{\text{jet}}(E_t)$  for different cone sizes to see whether the observed production rate is consistent with saturated energy loss or not.
- Measure the inclusive energy distribution around the jet axis, the jet shape, as a function of the reconstructed energy.
- Measure the  $j_t$  distribution as a function of the reconstructed energy.

Whereas the transverse structure is expected to have a relatively weak dependence on the jet energy (see, for example, Fig. 6.365 on page 1894 of the following section) the longitudinal structure of the jet, the fragmentation function,  $(1/N_{\text{jet}})dN/dz$  with  $z = p^{\text{hadron}}/E_t^{\text{jet}}$ , needs the jet energy  $E_t^{\text{jet}}$  as a scale. An unbiased measurement is only possible if the measured mean cone energy can be scaled to the parton energy. In particular, a systematic underestimation of the parton energy leads to a shift of  $z$  toward higher values canceling partially the effect of the energy loss. This again needs a good understanding of the transverse jet-structure and good efficiency and acceptance down to very low momenta.

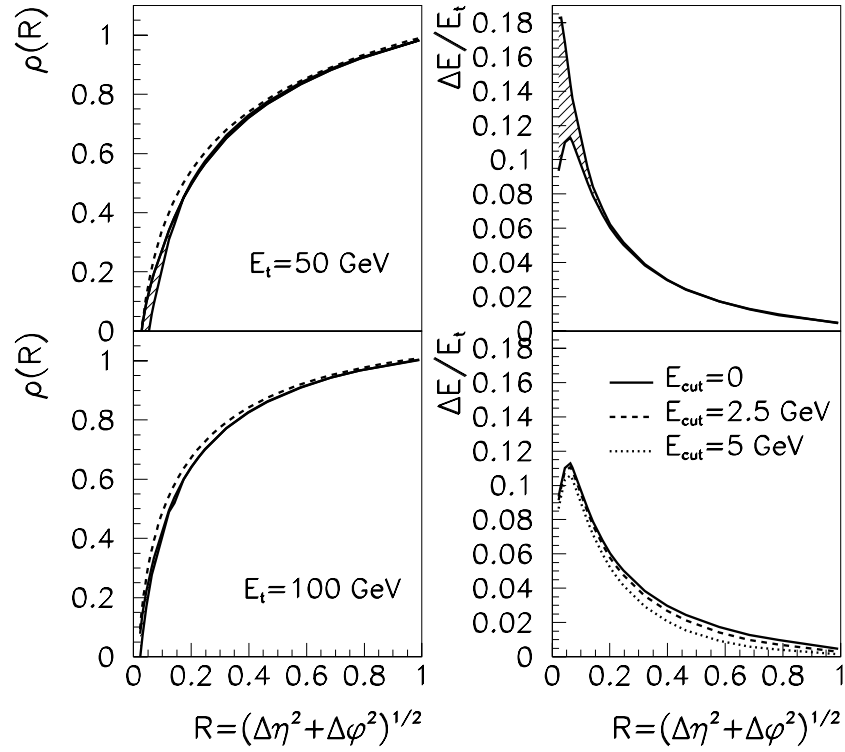


**Figure 6.359.** Left: The jet shape  $\rho(R)$ , defined as the average fraction of energy in a subcone of radius  $R$ , for 50 GeV (upper) and 100 GeV (lower) quark-lead jets which fragment in the vacuum (dashed curve) or in a dense QCD medium (solid curve) characterised by  $\omega_c = 62$  GeV and  $\omega_c L = 2000$ . Right: The corresponding average medium-induced energy loss  $\Delta E$  for jets of  $E_t = 100$  GeV outside a jet cone  $R$  radiated away by gluons (upper). Shaded regions indicate theoretical uncertainties. The lower panel shows the corresponding distributions for radiated gluons of energy larger than  $E_{cut}$ . Figure taken from Ref. [925]. Note that a notation for the jet shape variable different from the text has been used, i.e.  $\rho(R) = \Psi(R)$ .

An attractive method to obtain an unbiased measurement of the parton energy is to tag jets with prompt photons emitted in a direction opposite to the jet direction. The dominant processes for such events are  $q + q \rightarrow \gamma + g$  (Compton) and  $q + \bar{q} \rightarrow \gamma + g$  (annihilation). On the one hand, this coincidence technique will help localise the jets and on the other hand the measured photon energy is equal to that of the parton before energy loss. Performance studies for  $\gamma$ -jet correlations are presented in Section 6.9.

Medium-induced partonic energy loss through gluon radiation decreases the energy of the leading particle and produces extra particles from the fragmentation of the radiated gluons. Hence, one expects a decrease of the number of particles carrying a high fraction  $z$  of the jet energy and an increase of the number of particles with low  $z$ . Since  $z$  spans typically three to four orders of magnitude using the variable  $\xi = \ln(1/z)$  is a convenient way to represent the fragmentation function. The particular shape of the distribution  $dN/d\xi$  (Fig. 6.361) is called hump-backed plateau. Its calculation and comparison to data represent a standard test of the interplay between probabilistic parton splitting and quantum coherence in QCD. Medium-induced partonic energy loss distorts the shape of the plateau in a characteristic way (Fig. 6.361) [941].

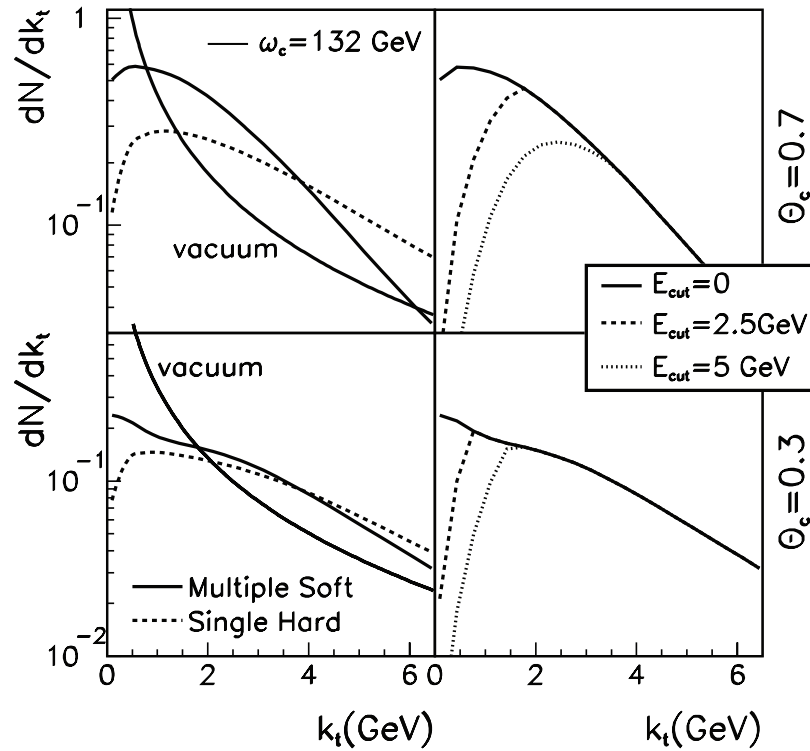


**Figure 6.360.**  $j_t$ -broadening calculated using the BDMPS formalism. Comparison of the vacuum and medium-induced parts of the gluon multiplicity distributions inside a cone size  $R_c = \theta_c$ , measured as a function of  $j_t$  with respect to the jet-axis. Removing gluons with energy smaller than  $E_{cut}$  from the distribution (dashed and dotted lines) does not effect the high- $j_t$  tails. Note that a notation different from the text has been used in the figure, i.e.  $k_t = j_t$ . Figure taken from Ref. [925].

**6.8.4. Monte Carlo production.** The simulation of jet production in heavy-ion collisions at the LHC is confronted by two challenges. First, there exists no full Monte Carlo algorithm for parton energy loss based on solid theoretical justifications, and secondly, simulation of jet production at high  $E_t$  would demand prohibitively long runs to simulate a number of events that is commensurable with the expected number of detected events in the experiment. As already outlined in Volume I of the ALICE Physics Performance Report [3], our general strategy for the Monte Carlo simulation of hard and rare processes in Pb–Pb collisions at the LHC consists in simulating hard processes in pp collisions and embedding them in the underlying event of the Pb–Pb collisions simulated using the HIJING v1.36 [42, 67] event generator.

The pp generators have to be adapted to simulate initial and final state modifications due to the nuclear environment. Initial state effects are taken into account by the modification of the parton density function inside the nucleon, for example using the EKS98 parametrisations [779, 938]. It has been shown that the influence on the transverse jet energy and pseudorapidity spectrum are small ( $< 3\%$ ) for production of jets with  $E_t > 20$  GeV [797]. Final state effects in high- $E_t$  jet production in heavy-ion collisions at the LHC are expected to be dominated by the energy loss through medium-induced gluon radiation. While no state of the art event generator exists to simulate these effects, various phenomenological

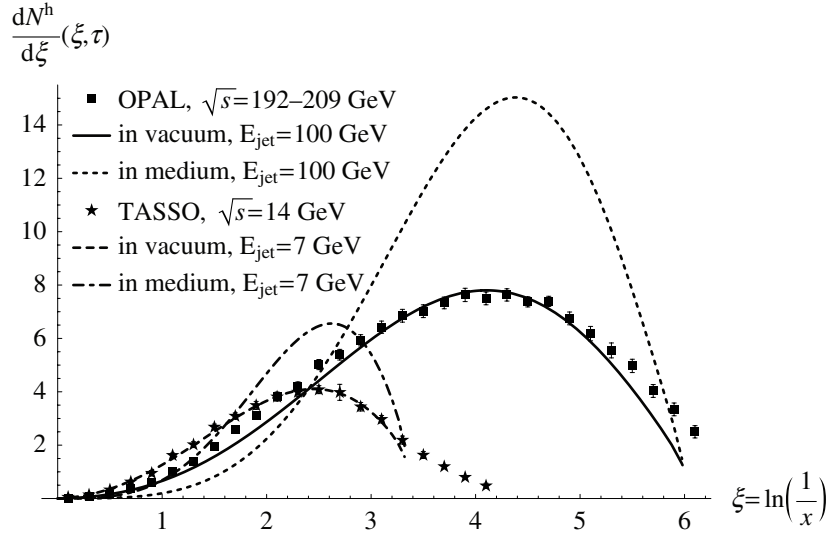


**Figure 6.361.** The single inclusive hadron distribution as a function of  $\xi = \ln(E_{\text{jet}}/p^{\text{hadron}})$ . Data taken from  $e^+e^-$  collision experiments TASSO and OPAL. Lines through data obtained from Modified Leading Logarithmic Approximation (MLLA) results. Dashed and dashed-dotted curves labeled ‘in-medium’ are calculated using the model describe in Ref. [941]. Figure taken from Ref. [941].

approaches can still yield valuable insight. CMS (PYQUENCH [942]) and ALICE (with AliPythia::Quench as part of the AliRoot simulation framework [930, 943]) have started efforts to use the PYTHIA event generator with afterburners acting on the final state partons as a simplified model for medium-induced gluon radiation.

**6.8.4.1. Simulation of jet production with PYTHIA.** High- $p_t$  parton production was simulated using the PYTHIA event generator in pp mode with CTEQ5L [825] parton distribution functions. Depending on whether the jet quenching effect is simulated or not, the partonic system after final state gluon radiation, is subsequently hadronised or first passed through an afterburner as described in the next section. After event generation, jets are reconstructed at the final state particle level using the PYCELL routine of PYTHIA with a cone radius  $R_c = 1$ . If at least one jet with  $E_t > 10$  GeV is found within the fiducial region  $|\eta_{\text{jet}}| < 0.5$ , the event is recorded. Since the production cross section varies by about five orders of magnitude in the range  $E_t = 20\text{--}200$  GeV, the events have been simulated in 13 bins  $[p_t^{\text{hard}}(i) \dots p_t^{\text{hard}}(i+1)]$  with  $p_t^{\text{hard}}(i+1)/p_t^{\text{hard}}(i) = 1.2$  from 20 to 180 GeV. Here,  $p_t^{\text{hard}}$  is the transverse momentum of the partons in the rest frame of the hard interaction. Within one bin the production cross section varies approximately by a factor of three.

The agreement of single inclusive jet production spectra as a function of  $E_t^{\text{jet}}$  and  $\eta_{\text{jet}}$  with NLO calculations has already been demonstrated in Section 6.8.2. However, more important for our physics performance studies is the correct simulation of the phase-space distribution of particles associated with the jet: jet fragmentation and jet shape. On the one hand, they represent the reference for measuring the modification of the jet-structure due to medium-induced gluon radiation and on the other hand, they determine the influence of our cuts on jet cone size and transverse momentum on the jet reconstruction efficiency and the resolution. During the past years, experiments have collected an impressive amount of information about multi-particle production in hadronic jets. Fragmentation studies are sensitive to both

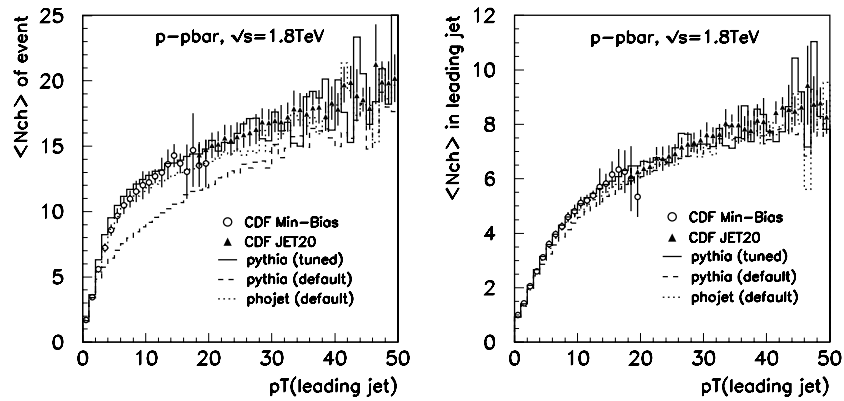


**Figure 6.362.** Comparisons of PYTHIA and PHOJET predictions with CDF data for the average number of charged particles in an event (left plot) and in the leading jet (right plot) as a function of the transverse momentum of the leading charged jets. Figure taken from Ref. [944].

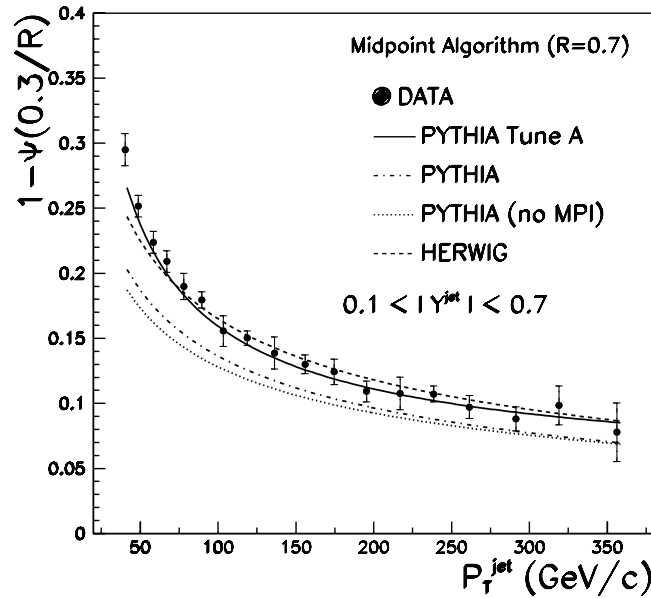


**Figure 6.363.** The average fraction of jet transverse energy outside a cone  $R = 0.3$ , which is notated  $1 - \Psi(0.3/R)$ , as a function of the transverse momentum of the jet with  $0.1 < |y^{\text{jet}}| < 0.7$  as measured by the CDF collaboration. The prediction of PYTHIA-Tune A (solid line), PYTHIA (dashed-dotted line) and HERWIG (dashed line) are shown for comparison. Figure taken from Ref. [945].

multi-gluon emission from the primary final state partons and to the proton remnants. They provide an important test of underlying event and fragmentation models in Monte Carlo programs and have been used to tune the parameters of these models.

In particular, PYTHIA was tuned to reproduce the charged-particle multiplicity [944] (Fig. 6.362), jet shapes [945] (Fig. 6.363) and momentum distributions [946] (Fig. 6.364) over a wide range of jet energies (PYTHIA Tune-A [947]). The tuning includes enhanced

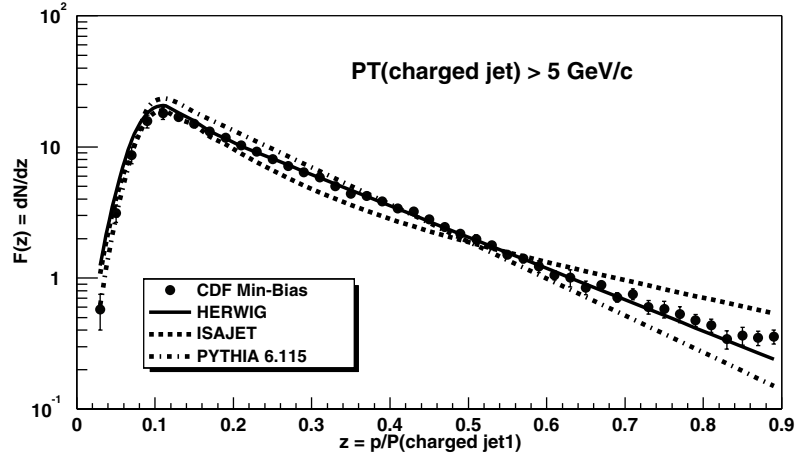


**Figure 6.364.** Momentum distribution of charged particles ( $p_t > 0.5 \text{ GeV}/c$ ,  $|\eta| < 1$ ) within the leading charged jet as measured by the CDF collaboration. The points are the charged number density,  $F(z) = dN_{\text{chg}}/dz$ , where  $z = p/p^{\text{jet}}$  is the ratio of the charged-particle momentum to the charged jet momentum. The predictions of HERWIG, ISAJET and PYTHIA are shown for comparison. Figure taken from Ref. [946].

contributions from initial state gluon radiation and secondary parton interactions between remnants, and leads to a satisfactory description of the present data. Using the tuning obtained from pp data at  $\sqrt{s} = 1800 \text{ GeV}$  for  $\sqrt{s_{\text{NN}}} = 5500 \text{ GeV}$  should introduce only small systematics because the  $\sqrt{s}$  dependence of the fragmentation is expected to be small. For example, we compare the jet shapes as obtained from our PYTHIA production with the parametrisation provided by the D0 collaboration [948] (Fig. 6.365).

**6.8.4.2. Simulation of in-medium energy loss by gluon radiation.** Partonic energy loss through medium-induced gluon radiation has been implemented as an afterburner acting on the partonic event generated by PYTHIA. The procedure is the following:

1. Generate the jet production point  $(x, y)$  in the transverse overlap region of the two nuclei and its direction of flight in the transverse plane with respect to the reaction plane. The density of production points  $\rho_{\text{coll}}(x, y)$  is taken proportional to the product of the transverse nuclear densities  $T_{A,B}$

$$\rho_{\text{coll}}(x, y; b) = T_A(r_1, b)T_B(r_2, b), \quad (6.143)$$

where  $r_1(x, y)$  and  $r_2(x, y)$  are radial coordinates in the nuclei A and B, respectively, and the transverse density is obtained by averaging the Wood-Saxon nuclear profile  $\rho_{\text{WS}}(x, y, z)$  over the beam direction  $z$ :

$$T_{A,B}(x, y) = \int dz \rho_{\text{WS}}(x, y, z). \quad (6.144)$$

2. The determination of the energy loss parameters  $R$  and  $\omega_c$  is performed as in the Parton Quenching Model (PQM) [795]. A local transport coefficient along the path of the parton, parametrised by the path-length  $s$ , starting at the production point  $(x_0, y_0)$  in direction  $(t_x, t_y)$  is defined as

$$\hat{q}(s; b) = k \times \rho_{\text{coll}}(x_0 + st_x, y_0 + st_y; b), \quad (6.145)$$

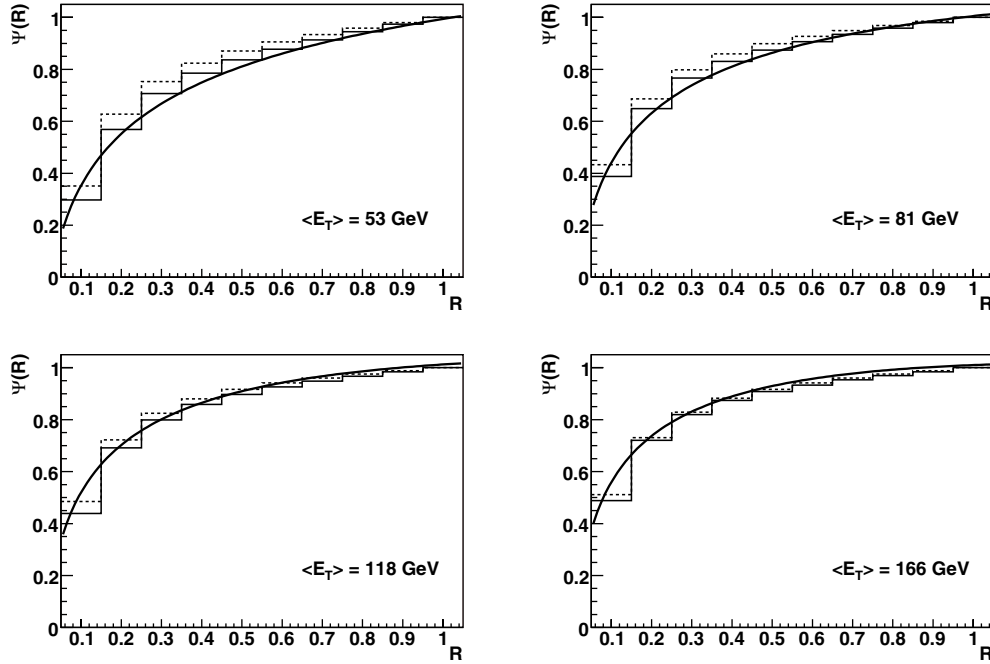


**Figure 6.365.** Jet shapes as simulated with PYTHIA (histograms) are compared with the D0 parametrisation (continuous curves) [948]. The dotted histograms are results using standard PYTHIA and the solid ones have been obtained with PYTHIA Tune-A.

where  $k$  is a free parameter that sets the scale of the transport coefficient. The parameters  $R$  and  $\omega_c$  determine the energy loss distribution  $P(\Delta E, R, \omega_c)$  [791, 949] and are calculated from

$$I_n = \int_0^{\infty} s^n \hat{q}(s; b) ds \quad (6.146)$$

$$\omega_c = I_1 \quad (6.147)$$

$$R = 2I_1^2/I_0. \quad (6.148)$$

3. For each parton  $p_i$  of energy  $E_i$  emerging from the hard  $2 \rightarrow 2$  process, we generate randomly the total energy loss  $\Delta E$  using the probability density function  $P_{q,g}(\Delta E, E_i, R, \omega_c)$ . Then for all final state partons  $p_f$  of the parton shower induced by  $p_i$ , we reduce the energy component parallel to  $p_i$  by a factor  $z = 1 - \Delta E/E_i$  keeping the transverse component constant. Total energy and momentum, up to the scale of the mass of the partons, are conserved by putting additional independently fragmenting gluons on the PYTHIA stack. The number of additional gluons  $N_g$  is calculated from  $N_g = 1/z$ . This insures that none of the radiated gluons has a momentum larger than the leading parton remnant<sup>26</sup>.
4. The event is hadronised using PYTHIA.

<sup>26</sup> In an earlier version of the code, which was used for the data challenge, the maximum number of gluons has been limited to 5. This limitation has been removed to study large  $\langle \hat{q} \rangle$  values [950].

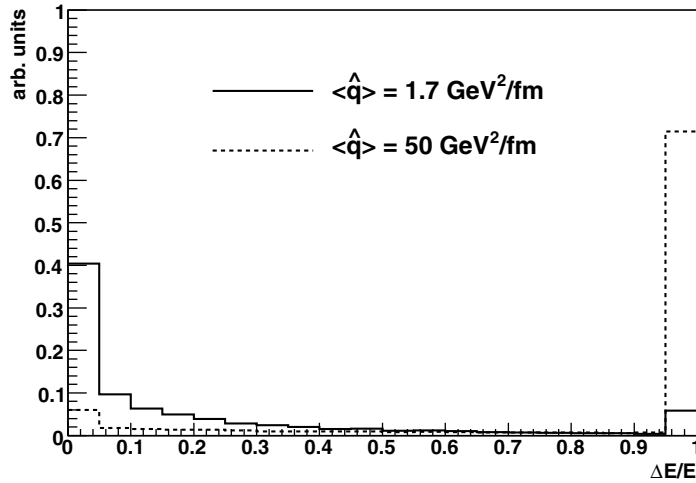


**Figure 6.366.** The energy loss distribution for 100 GeV jets produces in pp collisions at  $\sqrt{s} = 5.5$  TeV obtained using the PQM model for two values of  $\langle \hat{q} \rangle$ : 1.7 GeV<sup>2</sup>/fm (solid line) and 50 GeV<sup>2</sup>/fm (dashed line).

Fig. 6.366 shows the energy loss distribution for 100 GeV partons obtained using the PQM model for two values of  $\langle \hat{q} \rangle$ : 1.7 GeV<sup>2</sup>/fm and 50 GeV<sup>2</sup>/fm. The lower value corresponds to a mean energy loss of 20 GeV which is the same energy loss as used for the calculation of the jet-shape shown in Fig. 6.359. However, the latter has been obtained assuming a constant in-medium path-length.

As illustrated in Figs. 6.367 and 6.368, the toy model reproduces at least qualitatively some important features of theory predictions: a small broadening of the jet shape and the deformation of the hump-backed plateau. Also shown in Fig. 6.367 is the distribution of energy contained in low-momentum particles. As can be seen, even a relatively small transport coefficient leads to sizable increase of energy carried by low-momentum charged particles. From the experimental point of view, it is important to measure these particles in order to avoid a systematic underestimation of the parton energy.

The model does not include the increase of particles with high transverse momentum perpendicular to the jet axis, which results from the  $p_t$ -kick received by the leading particles. However, the radiated gluons produce extra particles at low  $j_t$  (Fig. 6.369).

One can only speculate about what will happen for very large values of  $\langle \hat{q} \rangle$ , i.e. if the critical gluon energy is much higher than the energy of the radiating parton. In particular, one cannot expect that the theory still gives self-consistent results. As can be seen from Fig. 6.366, a large fraction of partons suffer a complete energy loss and all the energy is in the radiated gluons. It is plausible that this leads to a sizable change of the jet size and thus, to a suppression of the jet rate measurable as the nuclear modification factor for jets,  $R_{AA}^{\text{jet}}(E_t)$  [940]. In this case, as for leading particles, a surface bias has to be taken into account (Fig. 6.370).

**6.8.4.3. Full event simulation and reconstruction.** Full event simulation and reconstruction is performed within the AliRoot framework developed within the ALICE Offline project. In short, the primary event is generated using external event generators: PYTHIA for jets and HIJING for the underlying events. Final state and undecayed long-lived particles are passed to the transport code (GEANT3 [951]) which simulates the trajectory of particles, their decays, as well as their interactions with the detector materials and generates the hit data representing

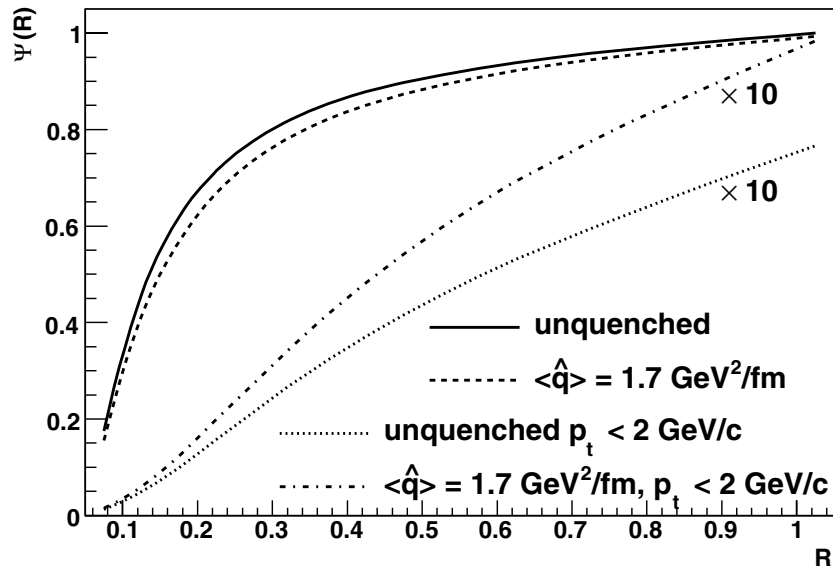


**Figure 6.367.** The jet shape  $\Psi(R)$  for 100 GeV jets without in-medium energy loss (solid line) is compared with the result of AliPythia::Quench using  $\langle\hat{q}\rangle = 1.7 \text{ GeV}^2/\text{fm}$  (dashed line). Also shown are the corresponding distributions obtained from charged particles with  $p_t < 2 \text{ GeV}/c$ .

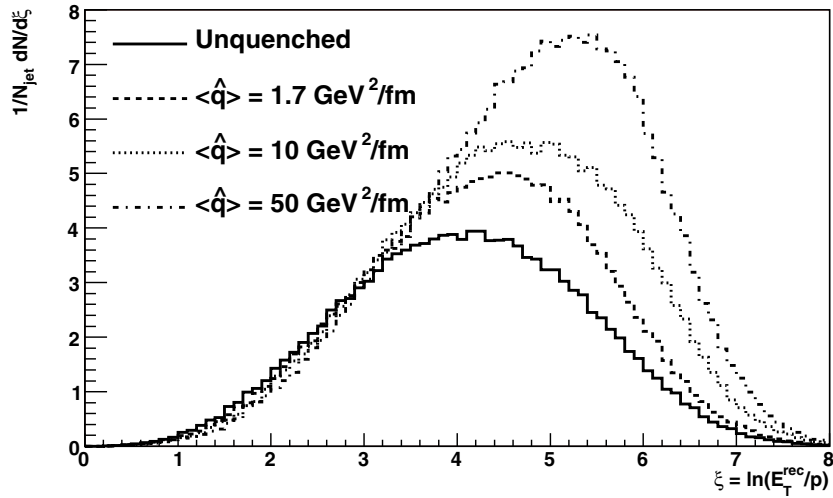


**Figure 6.368.** The hump-backed plateau  $1/N_{\text{jet}} dN/d\xi$  for charged particles inside a jet-cone  $R = 1$  of jets with  $E_t = 100 \text{ GeV}$  without in-medium energy loss (solid line) is compared with the result of AliPythia::Quench using  $\langle\hat{q}\rangle = 1.7 \text{ GeV}^2/\text{fm}$  (dashed),  $\langle\hat{q}\rangle = 10 \text{ GeV}^2/\text{fm}$  (dotted) and  $\langle\hat{q}\rangle = 50 \text{ GeV}^2/\text{fm}$  (dashed-dotted).

the detector response. The hit data is used to generate in a digitization process simulated raw data (digits). In order to be able to merge signal and underlying events, ‘summable digits’, are produced in an intermediate step. These are essentially digits before noise is added and

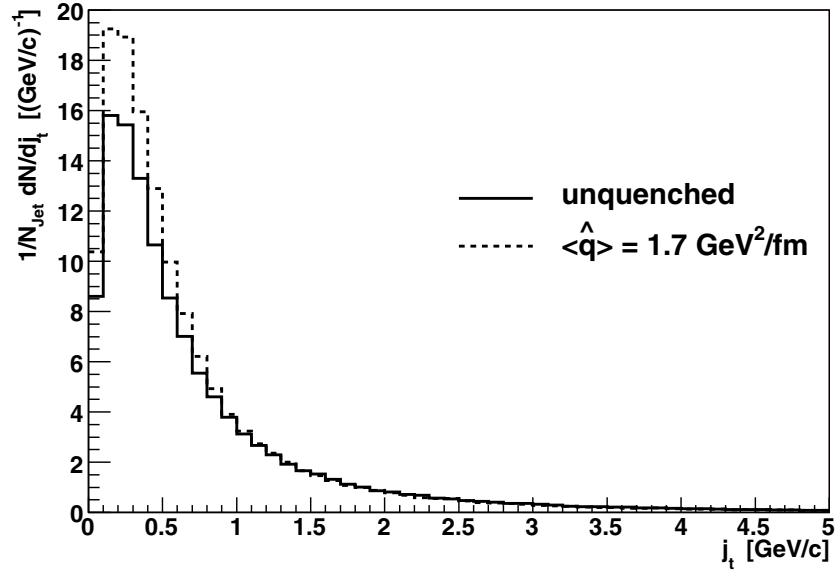


**Figure 6.369.** The momentum distribution perpendicular to the jet axis  $1/N_{\text{jet}}dN/dj_t$  for charged particles inside a jet-cone  $R = 1$  of jets with  $E_t = 100$  GeV without in-medium energy loss (solid line) is compared with the result of AliPythia::Quench using  $\langle \hat{q} \rangle = 1.7 \text{ GeV}^2/\text{fm}$  (dashed line).

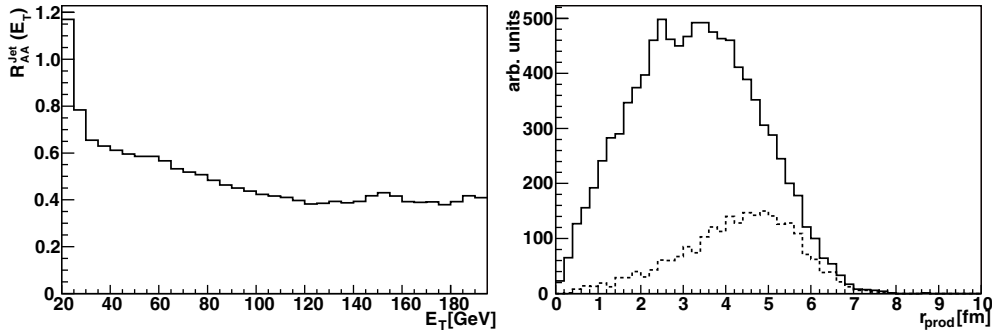


**Figure 6.370.** Left: The nuclear modification factor for jets  $R_{AA}^{\text{jet}}$  calculated for  $\langle \hat{q} \rangle = 50 \text{ GeV}^2/\text{fm}$  and using a jet-cone size of  $R = 1$ . Right: The production point of 100 GeV partons which result in reconstructed jets of the same energy using  $R_c = 1$  for no quenching (solid line) and for  $\langle \hat{q} \rangle = 50 \text{ GeV}^2/\text{fm}$  (dashed line).

before zero-suppression is applied. In this way, each subset of five jet events were merged with the same background event resulting in a final statistics which is five times higher than the number of generated background events. Subsequently, the merged events are digitized and passed to the AliRoot reconstruction algorithm to produce the Event Summary Data (ESD) used for analysis.

Two event samples have been produced, one containing unquenched and one containing quenched jets. Each event sample covers 13  $p_t^{\text{hard}}$ -bins as described above. Since we have equalised the statistics over a wide  $E_t$ -range the final statistics is almost constant (3000 events) for a  $E_t^{\text{min}}$ -cut between 50 GeV and 150 GeV. For  $E_t^{\text{min}} = 100$  GeV this corresponds approximately to the number of jets on tape for a few days of untriggered running.

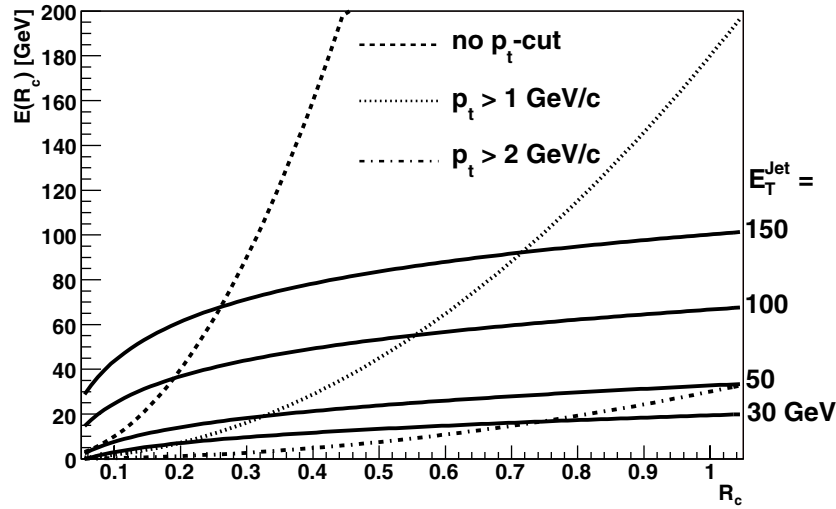


**Figure 6.371.** Charged jet energy within a cone of radius  $R_c$  (full lines) compared to the energy of the underlying event for different transverse momentum thresholds (dashed lines). The background energy has been calculated using HIJING quenched with  $b < 5$  fm.

**6.8.4.4. Fast simulation.** Due to computing time requirements, full event simulation is statistics limited. Furthermore, only a limited parameter-space for quenching scenarios can be covered. It will be clear from the discussions in the following sections that jet reconstruction is not very much influenced by the details of the detector acceptance and resolution but rather by the high multiplicity and, in case of charged jet reconstruction, by the charged-to-neutral fluctuations. This is an ideal case to employ fast simulations in which the acceptance and resolution are parametrised and applied directly to the particles of the primary event.

For the barrel tracking TPC + ITS we use the following fast simulation procedure:

1. Select charged particles within the TPC acceptance,  $|\eta| < 0.9$ .
2. Apply detector acceptance filter by setting the acceptance in the  $2^\circ$   $\varphi$ -region between read-out chambers to zero.
3. Apply tracking efficiency filter: 99% tracking efficiency for high- $p_t$  particles ( $p_t > 500$  MeV/c) and  $(99 - 67 \times (0.5 - p_t))\%$  for ( $p_t < 500$  MeV/c).
4. Apply momentum smearing:  $\Delta p = 0.01 p \sqrt{0.75^2 + 0.08^2 p^2}$ . The momentum resolution  $\Delta p/p$  is 8% at 100 GeV.

For the EMCal response, energy from all neutral particles within the acceptance  $|\eta| < 0.5$  and  $60^\circ < \varphi < 180^\circ$ , except neutrons and  $K_L^0$ , is taken into account and added to the energy from charged particles. This represents a simplification of the actual response. In reality, neutral hadrons deposit about 25% of their energy.

### 6.8.5. Characteristics of the background from the underlying event

**6.8.5.1. Background for jet reconstruction.** The main limitation for jet reconstruction in heavy-ion collisions results from the amount of background energy from the underlying event inside the jet cone and the fluctuation of this energy. Figure 6.371 compares the background energy from charged particles within a cone of size  $R_c$  to the energy from jets of different sizes  $R_c$ . The background energy that varies proportional to  $R_c^2$  has been calculated for

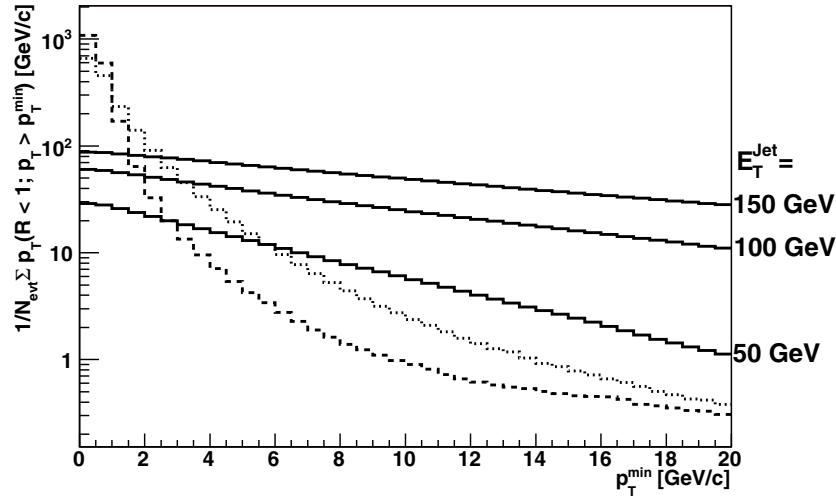


**Figure 6.372.** The background energy in a cone of  $R_c = 1$  for charged particles above a transverse momentum threshold  $p_T^{\min}$  is compared to the corresponding signal energy for jets of  $E_t = 50, 100$  and  $150$  GeV (solid lines). The background energy was calculated using HIJING simulations for the 10% most central Pb–Pb collisions with quenching (dashed line) and without quenching (dotted line).

transverse momentum thresholds from 0 to 2 GeV/ $c$ . For cone sizes used for jet reconstruction at hadron colliders  $R_c = 0.7$  to 1, the background energy exceeds the jet energy even for the highest jet energies considered here. The background can be reduced either by reducing the cone size or by applying a transverse momentum cut or both. These cuts reduce, to a much lesser extent, the signal energy (Fig. 6.372).

Of even higher importance are the background fluctuations. Event-by-event jet reconstruction is only possible if the signal energy is much higher than the background fluctuations. To reconstruct the jet energy the background energy has to be estimated and subtracted from the cone energy. There are three contributions to the background fluctuations:

1. Fluctuations caused by event-by-event variations of the impact parameter for a given centrality class. These fluctuations are proportional to the total energy inside the cone and hence proportional to  $R_c^2$ . The energy variations are correlated between different regions in the  $\eta - \varphi$  plane. Thus, they can be reduced by estimating the background energy within the cone from the energy or particle multiplicity outside the cone.
2. Poissonian fluctuations of uncorrelated particles. The r.m.s.,  $\Delta E_{\text{bg}}$ , of these fluctuations is given by:

$$\Delta E_{\text{bg}} = \sqrt{N} \sqrt{\langle p_t \rangle^2 + \sigma_{p_t}^2}, \quad (6.149)$$

where  $N$  is the mean number of particles within the cone,  $\langle p_t \rangle$  the mean transverse momentum, and  $\sigma_{p_t}$  the r.m.s. of the transverse momentum spectrum. These fluctuations are proportional to  $R_c$ .

3. Since the dominant source of medium and high- $p_t$  particles are jets, not all particles are uncorrelated. This leads to fluctuations which are higher than the lower limit given by the Poissonian fluctuation of  $N$  uncorrelated particles.

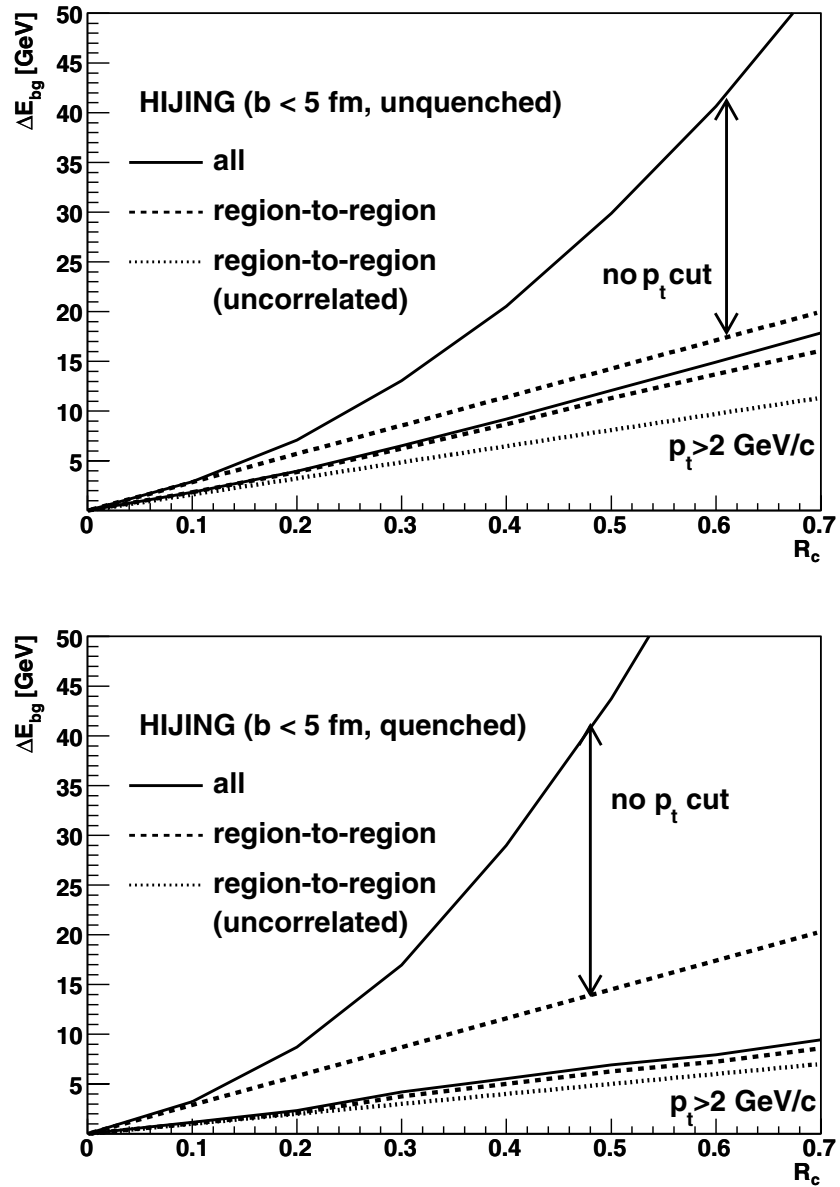


**Figure 6.373.** Different contributions to the background fluctuations as a function of the cone size  $R_c$  for the 10% most central Pb–Pb collisions simulated with HIJING unquenched (upper) and quenched (lower).

In Fig. 6.373 we plot the background fluctuations as a function of the cone size for HIJING unquenched and quenched. The total, including the impact parameter fluctuations, can in principle be reduced by optimising the background estimation techniques (see next section) down to the level of region-to-region fluctuations, i.e. fluctuations of energy in a cone of given size for different cone directions in the same event class of equal central multiplicity.

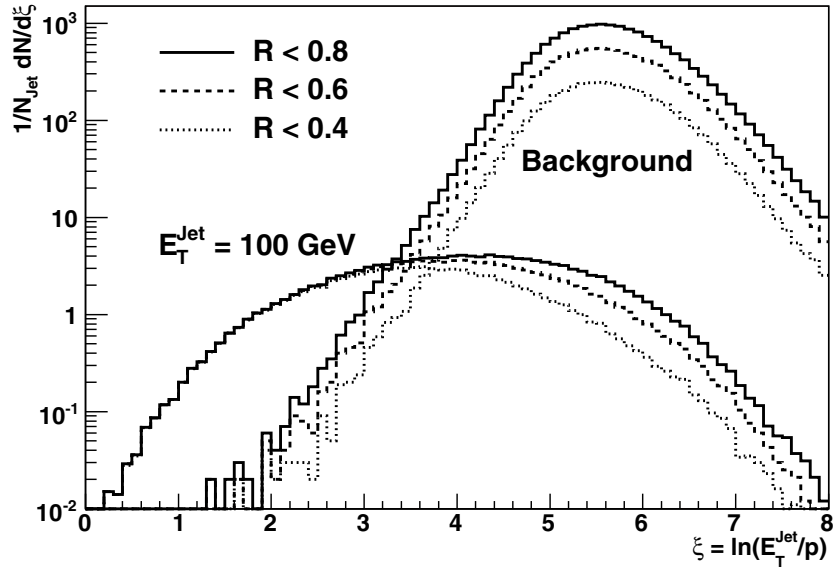


**Figure 6.374.** The hump-backed plateau for 100 GeV jets compared to the contribution from the background of the underlying event for different sub-cone sizes  $R$ .

Region-to-region fluctuations as they are caused by uncorrelated particles (Poissonian limit) are shown for comparison. Without transverse momentum threshold, the region-to-region fluctuations coincide with the Poissonian limit; the bulk of low- $p_t$  particles is uncorrelated. However, for a  $p_t$ -threshold of 2 GeV/ $c$  there is a clear difference (about 30%) between the observed region-to-region energy fluctuations and the Poissonian limit caused by correlated particle production. As expected, in HIJING unquenched the correlations are more important than in HIJING quenched. Furthermore, since for a large  $p_t$  threshold the cone energy is largely reduced, the impact parameter fluctuations are not important.

**6.8.5.2. Background for jet-structure observables.** As demonstrated in the previous section, small cone radii  $R_c = 0.3\text{--}0.4$  and a transverse momentum threshold  $p_t^{\min} = 1\text{--}2$  GeV/ $c$  are needed to identify and reconstruct jets in central Pb–Pb collisions at the LHC. For jet-structure analysis, these restrictions do not apply. Whereas the remnants of the leading particles lie inside the reconstruction cone, particles produced by medium-induced gluon radiation are expected to be observable at transverse momenta, which are small compared to the jet energy and also partially outside the cone used for reconstruction. In this section, we show which signal-to-background ratios can be expected in these regions.

**Hump-backed plateau.** For 100 GeV jets in the region  $\xi < 4$  corresponding to  $p_t > 1.8$  GeV/ $c$ , the leading particle remnants can be observed with a S/B  $> 0.1$  (Fig. 6.374). Due to the scaling with jet energy this corresponds to  $\xi < 3.3$  and  $\xi < 4.7$  for 50 GeV and 200 GeV jets, respectively. As shown in the previous section, particles from medium-induced gluon radiation are expected to show up predominantly in the region  $4 < \xi < 5$ . In this region, for 100 GeV jets the S/B is in the order of  $10^{-2}$ .

**Momentum transverse to jet axis.** The  $j_t$ -distribution for jets has the property that its shape can be measured in any sub-cone region around the jet axis (Fig. 6.375). On the contrary,

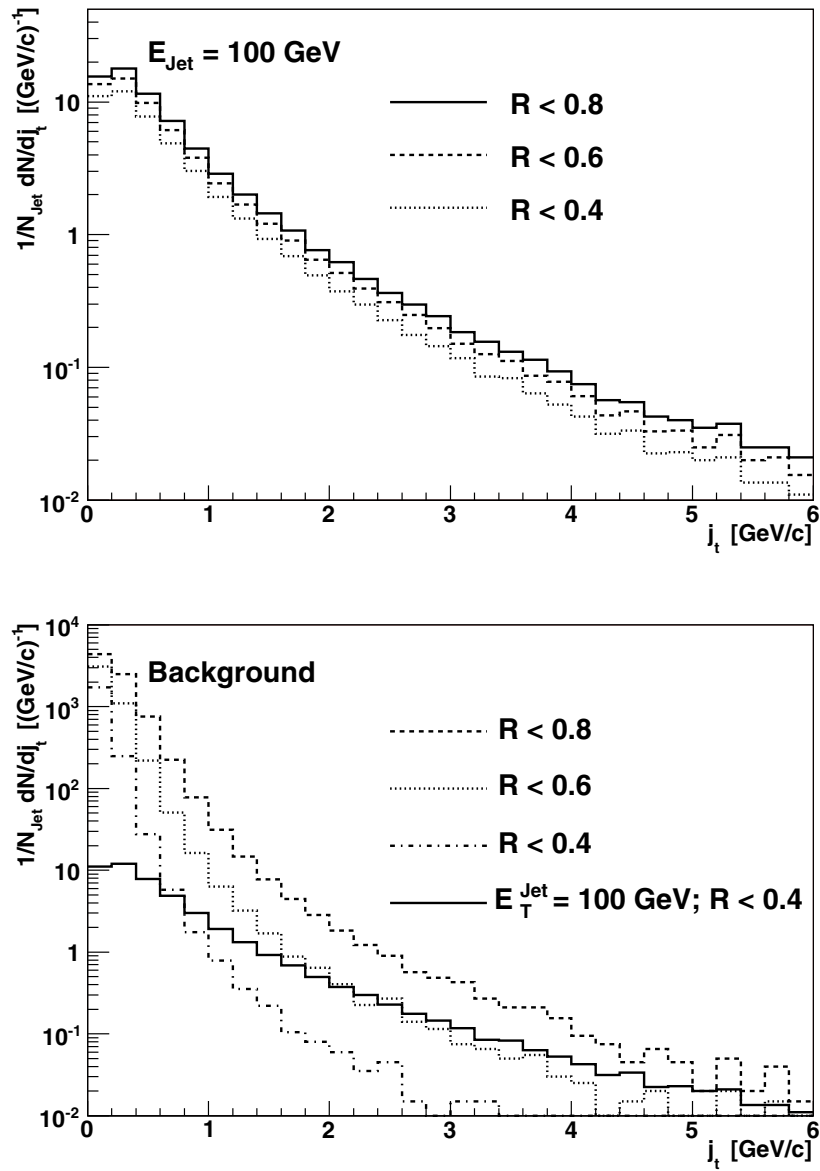


**Figure 6.375.** The distribution of momenta transverse to the jet-direction,  $(1/N_{\text{jet}})dN/dj_t$ , for particles inside 100 GeV jets for different sub-cone sizes  $R$  (upper) and for particles from the background of the underlying event for different sub-cone sizes  $R$  (lower). For comparison with the background distributions, the signal is shown for a sub-cone size of  $R = 0.4$ .

uncorrelated particles from the underlying event need a large angle with respect to the jet axis in order to have a large momentum perpendicular to the jet axis. Hence, measuring the  $j_t$ -distribution within a small radius preserves most of the signal, and reduces significantly the background. Only for  $j_t < 300 \text{ MeV}/c$  the background largely dominates decreasing the S/B ratio to  $10^{-2}$ .

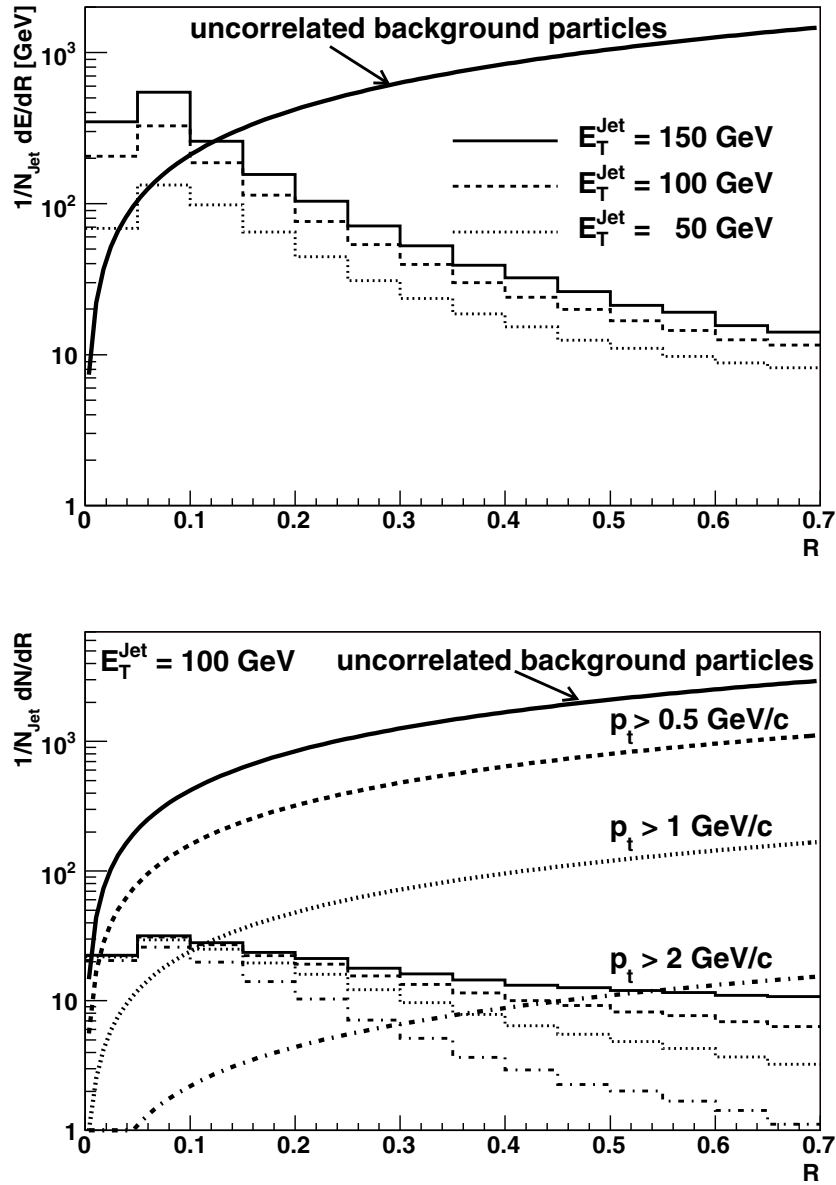


**Figure 6.376.** The jet energy distribution  $(1/N_{\text{jet}})dE/dR$  (upper) and the charged number density  $(1/N_{\text{jet}})dN/dR$  (lower) averaged over rings  $R \dots R+dR$  around the jet axis is compared to the corresponding distribution of energy from uncorrelated particles.

*Jet-shape.* In Fig. 6.376 (upper panel), we compare the distribution  $(1/N_{\text{jet}})dE/dR$  averaged over rings  $R, \dots, R+dR$  around the jet axis to the corresponding distribution of energy from uncorrelated particles. No transverse momentum threshold was applied. Observing energy of the order of a few GeV radiated outside a cone of  $R = 0.4$  is a challenge. Whereas close to  $R = 0.4$  the S/B ratio is about  $10^{-1}$ , it decreases rapidly to  $10^{-2}$  for the largest radii. Since for jets  $R$  and  $p_t$  are correlated ( $R \times p_t \simeq \langle j_t \rangle$ ) applying a transverse momentum will lead

to a sizable reduction of the signal at large  $R$  (Fig. 6.376 (lower panel)). On the contrary, it is clear that very good low-momentum capabilities are needed to study the jet shape observable.

### 6.8.6. Jet reconstruction in central Pb–Pb collisions

**6.8.6.1. Jet finder algorithm for heavy-ion collisions.** Jet-finding techniques for QCD studies are well established for pp, ep and  $e^+e^-$  collisions. Due to the presence of a high background from the underlying event these algorithms will not work without modification for the study of jets in heavy-ion collisions. For this purpose a jet finder (HIJA) based on the UA1 cone-type algorithm [952] was developed [953, 954]. In this algorithm, the jet is defined as a group of particles in a cone of fixed radius in the plane defined by the azimuth ( $\phi$ ) and pseudorapidity ( $\eta$ ). Since the time the UA1 algorithm was developed, there have been several refinements to make it more suitable for the comparison to next-to-leading order perturbative QCD calculations. These are of no importance for the study of jets in heavy-ion collisions, as the uncertainties are dominated by effects due to the underlying event.

In the case of ALICE, input to HIJA is an energy grid in the  $(\eta, \phi)$ -plane filled by a combination of charged-track transverse momenta ( $p_t$ ) and, if present, transverse energies ( $E_t^{\text{cell}} = E \sin \theta$ , where  $E$  is the total energy of the calorimeter cell and  $\theta$  is the polar angle of the cell) measured by the electromagnetic calorimeter. In order to reduce the contribution from uncorrelated background particles, the contribution from charged tracks with  $p_t < p_t^{\text{cut}}$  is excluded from the grid. Typically, we use  $p_t^{\text{cut}} = 2 \text{ GeV}/c$ , which rejects 98% of the background energy.

Neutral energy is only measured in the calorimeter while charged hadronic energy is registered in the tracking detectors and in the calorimeter. To correct for the double counting of energy, the estimated energy deposited by charged hadrons in the calorimeter is subtracted on a track-by-track basis using a parametrised energy deposition  $E_t^{\text{HC}}(\eta, p_t)$ .

**6.8.6.2. Jet finder.** The algorithm consists of the following steps:

- (1) Estimate the average background energy per grid cell  $E_t^{\text{bg}}$  from all grid cells.
- (2) Sort cells in decreasing cell energy  $E_t^i$ .
- (3) For at least 2 iterations, and until the change in  $E_t^{\text{bg}}$  between two successive iterations is smaller than a set threshold:
  - (a) Clear the jets list.
  - (b) Flag all cells outside a jet.
  - (c) Execute the jet-finding loop for each cell, starting with the highest cell energy. If  $E_t^i - E_t^{\text{bg}} > E_t^{\text{seed}}$ , where  $E_t^{\text{seed}}$  is a chosen threshold cell energy, and if the cell is flagged as being not inside a jet, treat it as a jet-seed candidate and execute the following steps:
    - (i) Set the jet-cone centroid to be the centre of the jet seed cell  $(\eta^C, \phi^C) = (\eta^i, \phi^i)$ .
    - (ii) Using all cells with  $\sqrt{(\eta^i - \eta^C)^2 + (\phi^i - \phi^C)^2} < R_c$  of the initial centroid, calculate the new energy weighted centroid to be the new initial centroid. Repeat the centroid calculation iteration until the difference between two subsequent centroids shifts by less than one cell.
    - (iii) Store the centroid as a jet candidate and flag all cells within the cone as inside a jet.

- (d) Recalculate the background energy  $E_t^{\text{bg}}$  using a background calculation routine (described later).
- (e) For each jet candidate, calculate the energy by summing the energies of the cells in the cone and subtracting the background. A jet has been found, if the jet energy is greater than  $E_t^{\text{cone}}$ , the minimum allowed cone energy.

Note that in the following we use  $E_t^{\text{cone}}$  for the energy inside the jet cone and  $E_t^{\text{rec}}$  for the reconstructed energy, i.e. the cone energy divided by the mean fraction of the generated jet energy inside the cone.

**6.8.6.3. Background subtraction.** Precise estimation of the background energy contribution inside the jet cone is necessary for accurate reconstruction of the jet energy. Systematic under- or overestimation of the background energy has to be avoided and the variance of the difference between true and reconstructed energy has to be reduced to a minimum.

The simplest approach, called here the statistical method, is to calculate an average background energy obtained from  $N$  jet-free events for different centrality classes. The best estimate of the background contribution is obtained by scaling this energy with the ratio  $K$  between the area of the jet cone and the total area of the  $\eta - \varphi$ -plane:

$$E_{\text{bg}}^{\text{stat}} = K \times \left\langle \sum_{p_t > p_t^{\text{th}}} p_t \right\rangle_N .$$

As shown in Fig. 6.373 on page 1900, this approach is limited by impact parameter fluctuations. In order to minimize this effect, event-by-event estimation methods were developed. The event-by-event methods rely on the assumption that the background energy is uncorrelated with the jet and therefore the background energy inside the jet cone is proportional to the background energy outside the cone. Two methods have been investigated; the cone- and ratio-methods. A detailed comparison of the methods for ALICE including EMCal has been presented in [954]. It uses a full simulation of the calorimeter and a fast simulation of the charged particle tracking. Here, we present the results obtained for charged particles only with full simulation and reconstruction of central Pb–Pb collisions.

In the cone method the background energy contribution inside the jet cone is calculated summing the energy in all the grid cells outside the cone of an identified jet and scaling with the ratio between jet cone area and total area, taking into account the  $dE/d\eta$  distribution.

$$E_{\text{bg}}^{\text{cone}} = K \times \sum_{p_t > p_t^{\text{th}}, R > R_c} p_t .$$

The ratio method consists of finding the ratio,  $F(p_t^{\text{min}}) = E_{\text{bg}}^{\text{cuts}} / E_{\text{bg}}^{\text{nocuts}}$ , by calculating the average of the total energy in the grid with a  $p_t$ -cut divided by the grid energy without a  $p_t$ -cut. Event-by-event the background energy is estimated by multiplying the background energy of the event without  $p_t$ -cut with  $F(p_t^{\text{min}})$ :

$$E_{\text{bg}}^{\text{ratio}} = F \times K \times \sum_{R > R_c} p_t$$

with

$$F(p_t^{\text{min}}) = \frac{\left\langle \sum_{p_t > p_t^{\text{th}}} p_t \right\rangle_N}{\left\langle \sum p_t \right\rangle_N} .$$

The error on the estimated cone energy, which is the r.m.s. of the difference between the estimated and the true cone energy, has been studied for the jet reconstruction algorithm

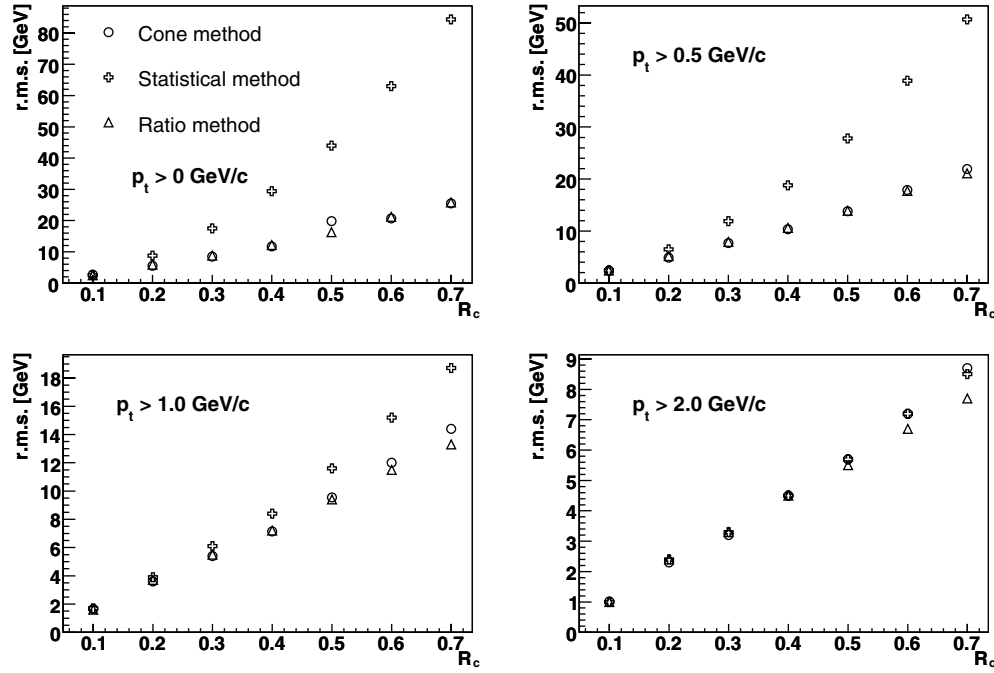


**Figure 6.377.** R.m.s. of the difference between the actual summed background energy within varying cone radii ( $R_c$ ) and the background energy calculated using the statistical, cone and ratio method, respectively. Results for four different transverse momentum thresholds for the charged particles (0, 0.5, 1.0, 2.0 GeV/c) are presented.

parameters, cone size  $R_c$  and transverse momentum threshold  $p_t^{\text{th}}$ . For this study we used 5000 central HIJING events (charged hadron multiplicity  $dN_{ch}/d\eta = 5000$ ) transported through the full ALICE set-up and reconstructed with the standard reconstruction algorithms. On an event-by-event basis, we select a cone pointing in a random direction within the ALICE charged-particle ( $\eta$ ,  $\varphi$ ) acceptance reduced to a fiducial area ensuring that the entire cone is contained in the acceptance. The cone energy,  $E_c$ , is calculated by adding the transverse momenta, above a minimum threshold value, of all reconstructed charged hadrons. The difference,  $\Delta E$ , between this value and the value obtained from the three different background estimation methods is calculated:

$$\Delta E^{(\text{stat, cone, ratio})}(R, p_t^{\text{th}}) = E_c(R, p_t^{\text{th}}) - E_{\text{bg}}^{(\text{stat, cone, ratio})}(R, p_t^{\text{th}}).$$

In Fig. 6.377 we show the r.m.s. of  $\Delta E$  as a function of the cone size for four different charged particle thresholds, 0, 0.5, 1.0 and 2.0 GeV/c. In general, with the ratio method the smallest r.m.s. values are obtained. However, for small cone sizes, the differences between the cone and the ratio method are not relevant. For a cone size  $R_c = 0.4$ , applying a  $p_t$  cut of 1 GeV/c (2 GeV/c), reduces the r.m.s. from 12 GeV to 7.0 GeV (4.5 GeV).

**6.8.6.4. Intrinsic jet reconstruction performance.** As described in the previous section, fluctuations of the reconstructed jet energy due to the background energy inside the jet cone can be reduced by applying appropriate cuts on the cone size and transverse momenta of jet particles. However this leads to a reduction of the reconstructed energy, which by itself causes fluctuations of the reconstructed jet energy, the out-of-cone or signal fluctuations.

*6.8.6.5. Importance of fluctuations: bias induced by the production spectrum.* Due to the steeply falling jet-production spectrum as a function of increasing  $E_t$ , fluctuations from an energy of the produced jet  $E_t^{\text{prod}}$  to a higher than average reconstructed energy  $E_t^{\text{rec}}$  are much more probable than the inverse. This causes effects that have been discussed in detail in the context of the RHIC particle correlation results. To give an example, for leading particle analysis the reconstructed jet energy is proportional to the transverse momentum of the leading particle. For a fixed jet energy, it carries on the average about 17% of the energy. For a fixed reconstructed energy interval, we have to consider contributions from lower energy jets that have a harder than average longitudinal fragmentation and higher energy jets with a softer than average fragmentation. The former are more important due to their higher production rate. As a consequence of this bias, the average energy fraction carried by leading particles is  $\simeq 60\%$ .

Other reconstruction and analysis cuts, will lead to similar bias due to the combined effect of fluctuations of the fragmentation function and the steeply falling production spectrum. For examples:

- The cut on the jet cone-size enhances more collimated jets.
- Reconstructing jets from charged particles only enhances jets with a larger than average charged particle fraction.

However, more important are fluctuations directly related to the physics of energy loss in partonic matter since they lead to a lower than average energy loss in the observed jet sample. They are related to:

- The jet production point and direction of flight. Production points closer to the surface of the interaction volume and directed outward are preferred.
- The energy loss distribution has a finite probability of none or only small energy loss. The distribution will be biased toward smaller energy losses.

In principle, the production spectrum induced bias can be eliminated by considering fully reconstructed jets. To what extent the bias can be reduced in central Pb–Pb collisions at the LHC for which reduced jet cone sizes are needed for reconstruction is one of the central questions for the jet physics performance evaluation, and is addressed in the following sections.

*6.8.6.6. Resolution for monochromatic jets.* To get a basic understanding of the signal fluctuations for jets reconstructed under typical LHC conditions, i.e. reduced cone size, transverse momentum cuts, we first discuss the resolution function for monochromatic jets. Since the underlying physical process is a parton shower with gluon radiation we have to distinguish relatively small Gaussian fluctuations around a mean value from rare ‘catastrophic’ events in which at least one relatively hard gluon has been radiated outside the jet cone. These fluctuations lead to a low energy tail. Another type of fluctuation can occur due to limited detector acceptance. In this case in a fraction of events proportional to the inefficiency, one or several of the leading jet particles are not reconstructed and do not contribute to the cone energy. Again these fluctuations lead to low energy tails.

The features described above are illustrated in Fig. 6.378 which shows the spectra of cone energies for mono-energetic jets of 100 GeV generated by PYTHIA for different cuts and idealised detector configurations. Jets were reconstructed using the PYCELL algorithm of PYTHIA with a cone size of  $R_c = 0.4$ . As explained above, the limited cone size alone leads already to a low-energy tail. This tail is enhanced if detector effects are included. The charged particle plus EMCal configuration is almost blind to neutrons and  $K_L^0$  increasing

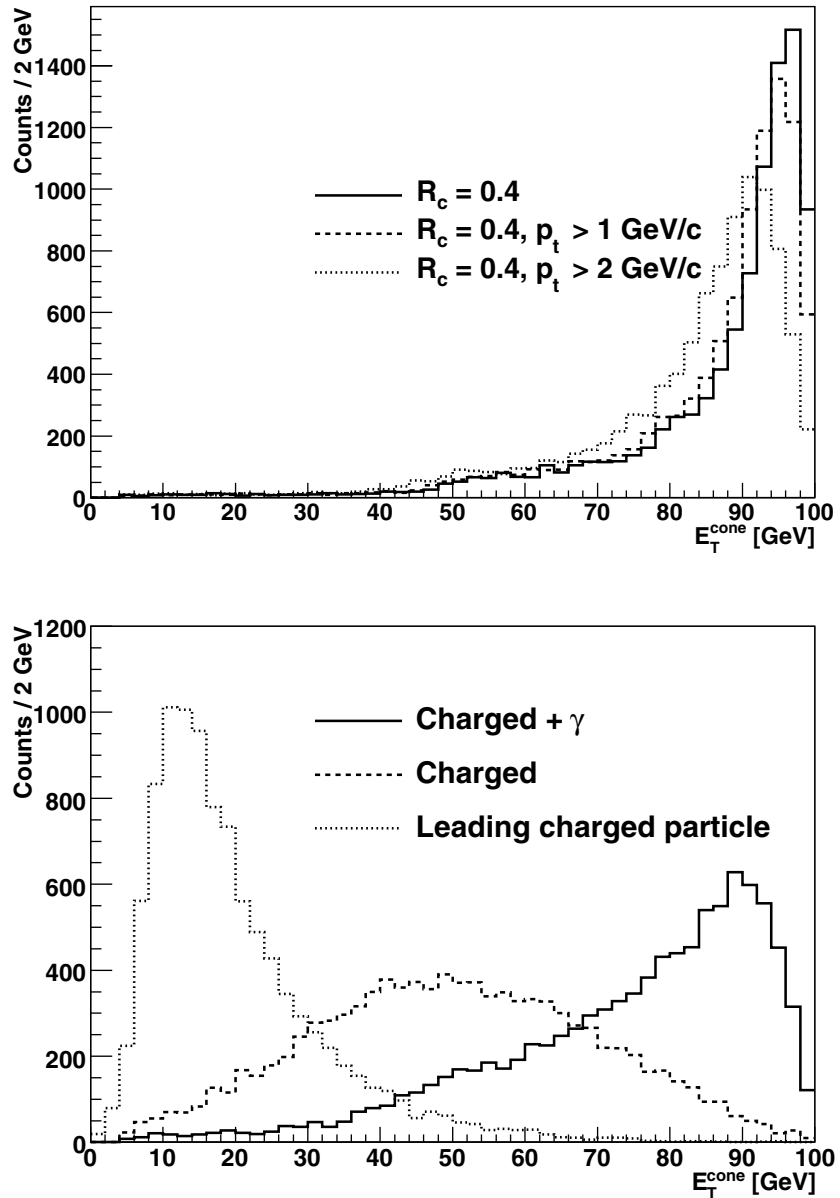


**Figure 6.378.** Spectra of reconstructed energy for a generated jet energy of 100 GeV for different cuts (upper) and for different detector configurations (lower). A cone size of  $R_c = 0.4$  has been used. Counts are for 10000 input jets.

the population of the tail by more than a factor of two. The charged jet reconstruction is completely dominated by the charged to neutral fluctuations which result in an almost Gaussian response function with a mean value at about half the input energy and a  $\Delta E_t/E_t$  of 40%.

Assuming an ideal detector and applying a  $p_t$ -cut of 2 GeV/c we expect a cone energy of 88 GeV with central Gaussian fluctuations of 10%. It is important to note that within a

**Table 6.94.** Intrinsic jet energy resolution, cone energy and reconstruction efficiency for different jet energies and cuts.

$E_{\text{jet}}$	r.m.s. [GeV]	$E_t^{\text{cone}}/E_t^{\text{jet}}$
$R_c = 0.4$		
50 GeV	7.4	0.80
100 GeV	14.1	0.85
200 GeV	32.0	0.88
$R_c = 0.4, p_t > 1 \text{ GeV}/c$		
50 GeV	7.5	0.77
100 GeV	14.6	0.84
200 GeV	32.0	0.87
$R_c = 0.4, p_t > 2 \text{ GeV}/c$		
50 GeV	8.4	0.69
100 GeV	14.8	0.80
200 GeV	32.2	0.85
$R_c = 0.4, p_t > 2 \text{ GeV}/c$ Ideal charged-particle measurement and ideal electromagnetic calorimetry		
50 GeV	9.4	0.63
100 GeV	17.4	0.74
200 GeV	36.6	0.77
$R_c = 0.4, p_t > 2 \text{ GeV}/c$ Ideal charged-particle measurement only		
50 GeV	9.0	0.43
100 GeV	18.4	0.48
200 GeV	38.0	0.51

$1\sigma$  fluctuation of the energy the jet production cross section varies by almost a factor of two. Hence, a meaningful evaluation of the jet energy resolution and reconstruction efficiency cannot be performed without taking into account the production spectrum as discussed in the next section. In particular, jets in the low energy tail of the resolution function are ‘buried’ below lower energetic jets with much higher production cross section and, hence, the amount of jets in these tails is a measure of the reconstruction inefficiency.

To be more quantitative, Table 6.94 summarises for jet energies of 50, 100 and 150 GeV, the fraction of energy inside the jet-cone and the resolution for different jet reconstruction cuts and idealised detector configurations. The resolution is defined as the r.m.s. of the cone energy distribution. This definition is by no means unique; it is rather an indication of the quality of jet reconstruction for different cuts and detector configurations.

Figure 6.379 shows for jets with  $E_t = 100 \text{ GeV}$  the variation of the cone energy and resolution with cone size and  $p_t$ -cuts. Complete calorimetry is assumed, i.e. we consider here the limiting resolution without considering detector effects. In order to illustrate the influence of the background fluctuations they have been added to the signal fluctuation for the case  $p_t > 1 \text{ GeV}/c$ . As can be seen, cone sizes in the range  $0.3 < R_c < 0.5$  result in optimal limiting resolution of  $\Delta E_t/E_t \simeq 22\%$ . This of course depends on the actual particle multiplicity and has to be optimised once data become available.

The resolution of charged jets is dominated by the charged-to-neutral fluctuations. To optimise the charged jet identification efficiency the signal energy has to be much larger than the background fluctuations  $\Delta E_t^{\text{bg}}$ . Requiring  $E_t > 3 \Delta E_t^{\text{bg}}$  for  $E_t > 30 \text{ GeV}$  implies again cone sizes in the range  $0.3 < R_c < 0.5$  and transverse momentum thresholds of  $1\text{--}2 \text{ GeV}/c$ .

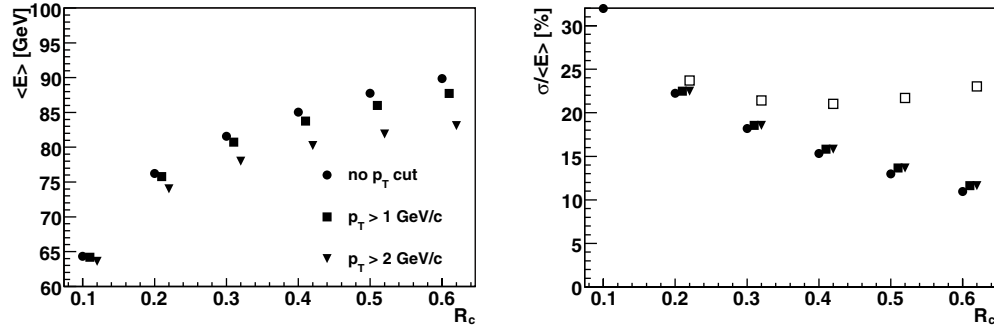


**Figure 6.379.** Cone energy (left) and energy resolution (right) for  $E_t = 100$  GeV jets as a function of the cone size used for reconstruction and for different  $p_t$  cuts: no cut (circles),  $p_t > 1$  GeV/c (full squares),  $p_t > 2$  GeV/c (triangles). In order to illustrate the influence of the background fluctuations they have been added to the signal fluctuation for the case  $p_t > 1$  GeV (open squares).

6.8.6.7. *Production rate weighted resolution functions.* The spectrum of reconstructed energy  $dN/dE_t^{\text{rec}}$  is related to the production spectrum  $dN/dE_t$  by

$$\frac{dN}{dE_t^{\text{rec}}}(E_t^{\text{rec}}) = \int_0^{\infty} dE_t' \frac{dN}{dE_t'}(E_t') w(E_t^{\text{rec}}, E_t'),$$

where  $w(E_t^{\text{rec}}, E_t')$  is the conditional probability that a jet of energy  $E_t'$  has reconstructed energy  $E_t^{\text{rec}}$ . The approximate power-law shape of the production spectrum is almost unmodified by a Gaussian resolution with constant relative width  $\sigma_{E_t}/E_t$ . Hence, in general the production spectrum can be obtained from the measured cone-energy spectrum through deconvolution. However, for jet shape analysis we are interested in the contributions to a sample of constant reconstructed energy and, hence, for a fixed energy  $E_t^{\text{rec}}$  or  $E_t^{\text{conc}}$  in the distribution

$$\frac{dN}{dE_t} = \frac{dN}{dE_t}(E_t) w(E_t^{\text{rec}}, E_t).$$

As discussed above, the steeply falling production spectrum favours contributions from jet energies with  $E_t < E_t^{\text{rec}}$  and, hence, mainly the high-energy tail of the resolution function  $w(E_t^{\text{rec}}, E_t)$  is important for the input cocktail. For example, for a power-law production spectrum  $\sim 1/E_t^n$  and a Gaussian resolution function with constant relative width  $w = \sigma_{E_t}/E_t$  the most probable energy  $E_t^0$  contributing to the reconstructed energy  $E_t$  is  $E_t/0.5(1 + \sqrt{1 + 4w^2(n+1)})$ . For charged jets with an intrinsic resolution limit of  $w = 0.4$ , the shift amounts to a factor of 1.64, for ideal jet reconstruction with  $R_c = 0.4$  and  $p_t > 2$  GeV/c, this factor is reduced to 1.03. Using these factors and the mean reconstructed energies from Table , bins of cone energies can be chosen so that the input spectrum is centred around a chosen energy  $E_t^0$ . Figures 6.380 and 6.381 illustrate this for  $E_t^0 = 100$  GeV and for different experimental set-ups and for charged jet reconstruction with  $E_t^0 = 50, 100$  and 150 GeV, respectively.

*Parton energy selectivity.* The parton-energy selectivity obtained for a given cone energy bin can be expressed by the range of parton energy which contains 90% of the events. Table 6.95 shows these ranges for various most probable parton energies  $E_t^0$  and experimental set-ups. Even for the charged jet energy resolution of  $\Delta E/E = 40\%$  one still obtains a reasonable selectivity on the parton energy. It is improved by including electromagnetic calorimetry.

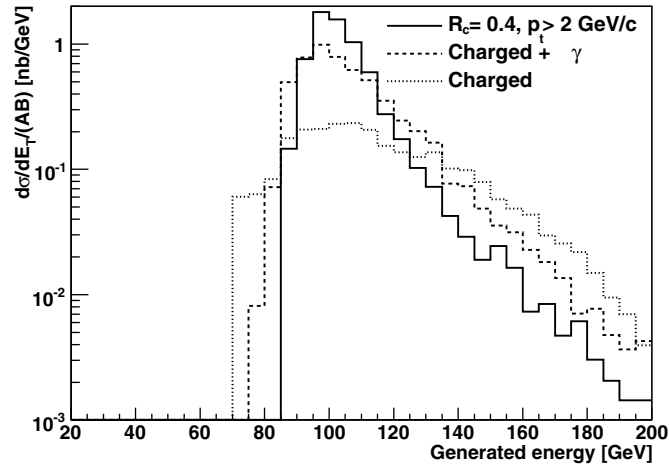


**Figure 6.380.** Spectrum of generated energies selected by fixed ranges of energies of jets reconstructed with different experimental set-ups. The bins of reconstructed energy are chosen so that the generated energy peaks at  $E_t^0 = 100$  GeV.

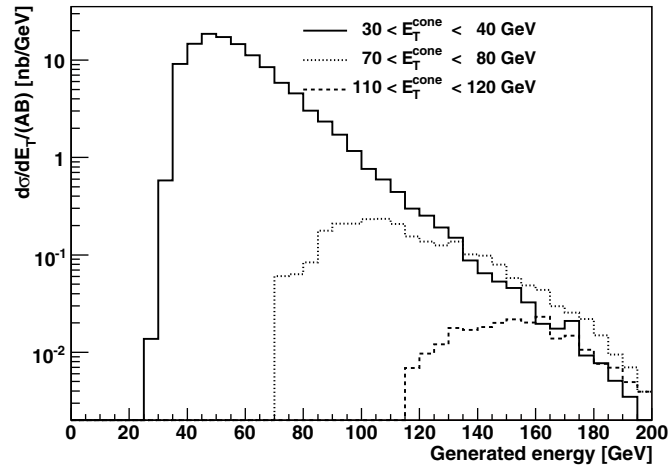


**Figure 6.381.** Spectrum of generated energies selected by fixed ranges of energies of charged jets. The bins of reconstructed energy are chosen so that the generated energy peak at  $E_t^0 = 50, 100$  and  $150$  GeV.

**Table 6.95.** The range of  $E_t$  containing 90% of the selected produced jets for different detector configurations for  $R_c = 0.4$  and  $p_t > 2$  GeV/ $c$ .

$E_t^0$ [GeV]	$E_t^{\min} - E_t^{\max}(90\%)$ [GeV]			
	Leading Particles	TPC	TPC+EMCal	Ideal calorimetry
50	25–85	30–75	40–70	40–60
100	60–140	70–145	75–125	85–112
150	90–180	110–175	130–170	135–160

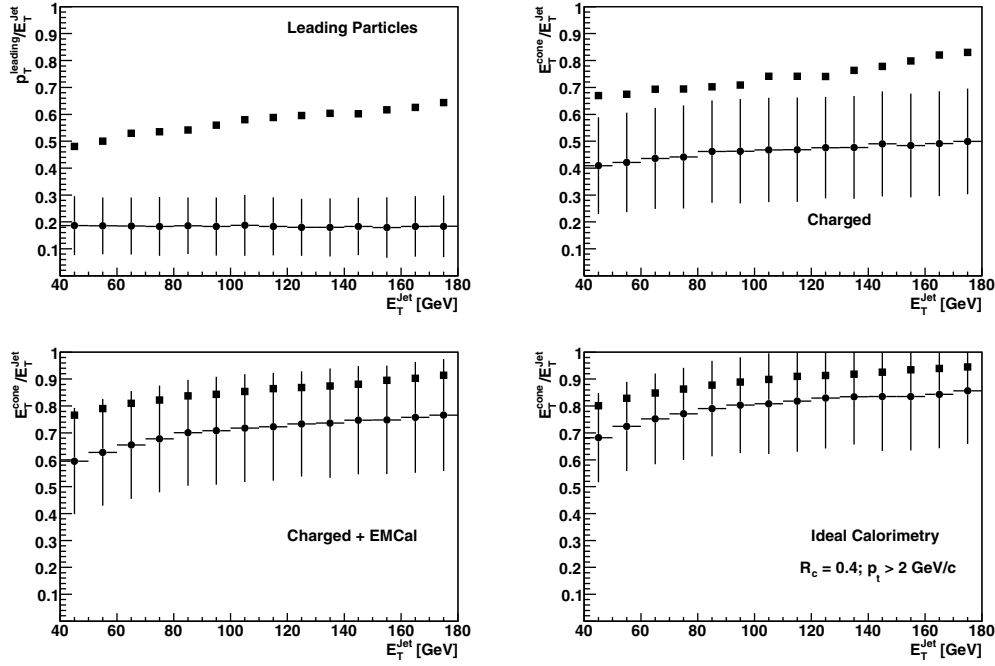


**Figure 6.382.** The ratio between cone energy and generated energy,  $E_t^{\text{cone}}/E_t^{\text{jet}}$ , as a function of the generated energy (circles), for which the r.m.s. values are shown as error bars, and as a function of the reconstructed energy (squares). The former is equivalent to the ratio obtained from monochromatic jets whereas the latter contains the bias induced by the input spectrum. Note that for leading particles  $E_t^{\text{cone}} = p_t^{\text{leading}}$ .

*Production spectrum bias.* Another way to quantify the expected selectivity is to use the ratios between reconstructed energy of the jet and parton energies and compare monochromatic jets with jets from a realistic input spectrum (Fig. 6.382). As explained above, for leading particles the ratio is 17% for monochromatic jets and increases to 58% due to the production spectrum bias. This bias can be decreased by using reconstructed charged jets and further reduced using electromagnetic calorimetry plus charged particles. In the latter case, 73% of the energy of a monochromatic jet can be reconstructed. The production spectrum bias increases this only by a factor of 1.2, which is a significant improvement with respect to the factor 3.4 expected for leading particle analysis.

*Selection efficiency.* Another important aspect is the fraction of partons above a given energy which can be selected by cutting on the reconstructed energy. Let us consider the case  $E_t^{\text{parton}} > 100 \text{ GeV}$  and jet reconstruction with  $R_c = 0, 4$  and  $p_t > 2 \text{ GeV}$ . Cutting  $E_t^{\text{cone}} > 88 \text{ GeV}$  ( $> 70 \text{ GeV}$ ,  $> 85 \text{ GeV}$ ) selects jet samples which contain 85% of partons with  $E_t > 100 \text{ GeV}$  assuming full calorimetry, charged jet reconstruction and charged jets + EMCal, respectively. The selection efficiency is 75% for the ideal case and 30% (67%) for charged jet reconstruction (charged jets + EMCal). Selecting high- $p_t$  partons by cutting on the leading particle transverse momentum is very inefficient. For the same purity as considered above the selection efficiency is only 6%.

**6.8.6.8. Angular resolution.** The angular resolution of a reconstructed jet is defined as the r.m.s. of the distribution of the differences between reconstructed and generated  $\varphi$  and  $\eta$  of

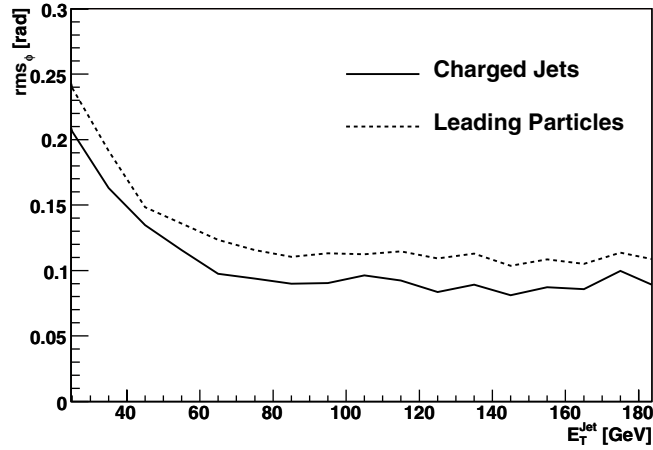


**Figure 6.383.** Angular resolution of the reconstructed jet direction as a function of the energy of the generated jets.

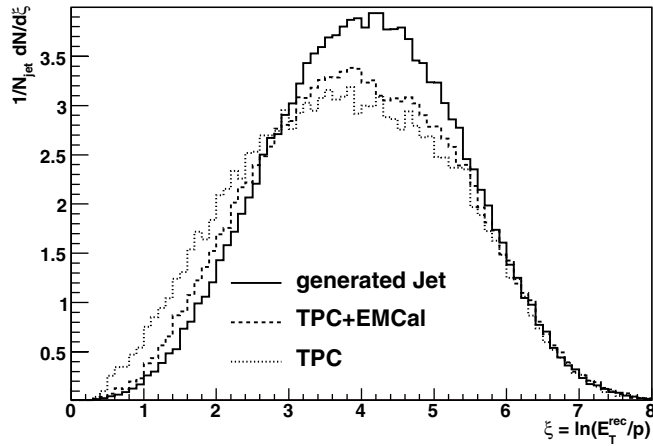


**Figure 6.384.** The hump-back plateau of generated jets with  $E_t > 100$  GeV is compared to the ones obtained with reconstructed charged jets ( $E_t^{\text{cone}} > 70$  GeV) and with charged + electromagnetic calorimetry ( $E_t^{\text{cone}} > 80$  GeV). Charged particles from a cone  $R < 0.8$  around the jet axis are used.

the jet axis. Figure 6.383 shows the angular resolution expected for charged jet reconstruction as a function of the energy of the generated jet. It is compared to the resolution obtained using direction of the leading particle as the best estimate of the jet direction. The resolution is 90 mrad for jet energies  $> 60$  GeV and degrades to about 200 mrad for  $E_t = 20$  GeV. Compared to leading particles, charged jet reconstruction improves the resolution by  $\simeq 20\%$ .

**6.8.6.9. Resolution and jet structure observables.** Since the reconstructed energy and its fluctuations are strongly correlated to the longitudinal and transverse fragmentation, a discussion of the influence of the resolution on the measurement of the hump-backed plateau and the  $j_t$ -spectra is mandatory. In this section, we present results obtained from fast simulations as described in Section 6.8.4.

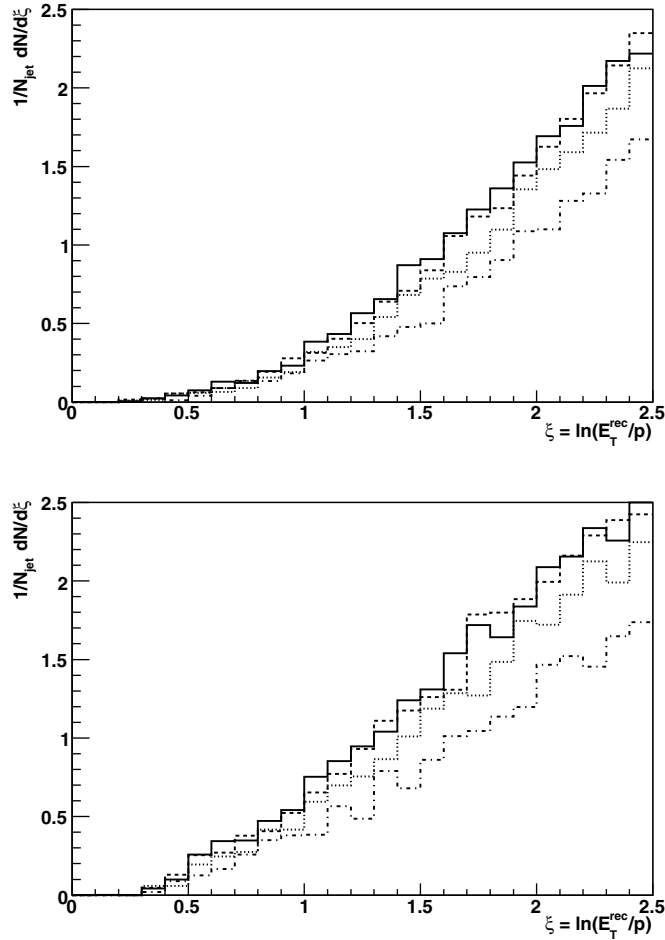


**Figure 6.385.** The leading particle fragmentation region for different transport coefficients: unquenched (solid line),  $\langle \hat{q} \rangle = 1.7 \text{ GeV}^2/\text{fm}$  (dashed line),  $\langle \hat{q} \rangle = 10 \text{ GeV}^2/\text{fm}$  (dotted) and  $\langle \hat{q} \rangle = 50 \text{ GeV}^2/\text{fm}$  (dashed-dotted). Jets are reconstructed using charged-particle information (upper) with  $E_t^{\text{cone}} > 70 \text{ GeV}$  and charged particles + electromagnetic calorimetry (lower) with  $E_t^{\text{cone}} > 80 \text{ GeV}$ .

*Hump-backed plateau.* In Fig. 6.384 we compare the hump-back plateau of generated jets with  $E_t > 100 \text{ GeV}$  to the ones obtained with charged jets ( $E_t^{\text{cone}} > 70 \text{ GeV}$ ) and with charged + electromagnetic calorimetry ( $E_t^{\text{cone}} > 80 \text{ GeV}$ ). The lowering of the plateau is due to the reduced acceptance, whereas the observed broadening is caused by the limited resolution. The broadening is mainly located in the leading particle fragmentation region and consequently it will depend on the strength of the partonic energy loss. This is shown in the curves of Fig. 6.385 which compare for both detector configurations the leading particle fragmentation region for different average transport coefficients  $\langle \hat{q} \rangle$ . For both detector configurations we observe, as expected, that the partonic energy loss depletes the low- $\xi$  region and this depletion increases with increasing  $\langle \hat{q} \rangle$ . Since  $\xi$  depends directly on the amount of reconstructed energy and its fluctuations, the depletion can be partially masked by a systematic underestimation of the reconstructed energy and the bias toward jets with a harder than average fragmentation. This effect is lower for the TPC + EMCAL configurations since the energy resolution is higher

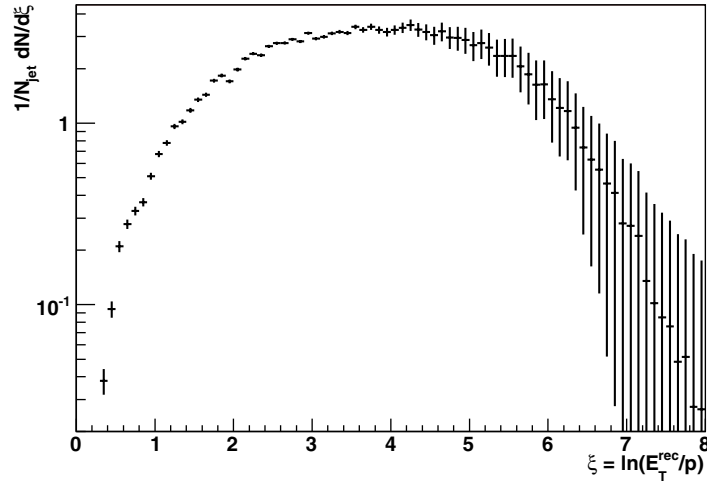


**Figure 6.386.** Expected statistical error for the hump-backed plateau measured from charged jets with  $E_t^{\text{cone}} > 70$  GeV assuming a statistics of 10000 jets.

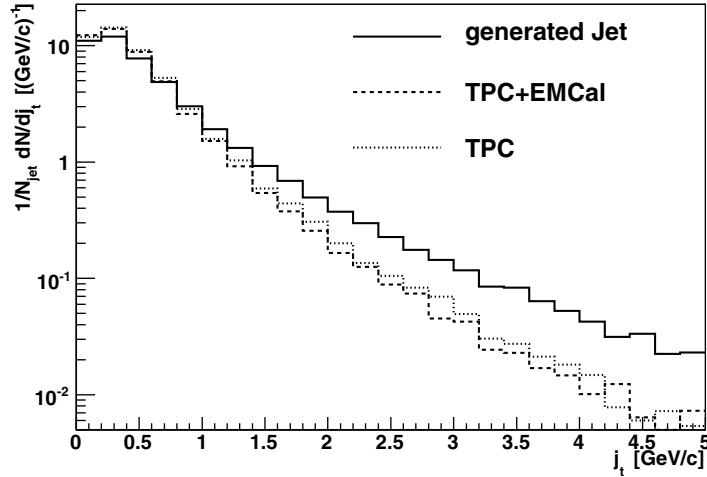


**Figure 6.387.** The unbiased  $j_t$  spectrum from the generated jets (solid line) is compared to the reconstructed spectrum for charged jets (dotted) and charged + EMCal (dashed).

and on average more energy will be collected. With charged jet reconstruction alone it will be challenging to be sensitive to the effect of very small  $\langle \hat{q} \rangle$  values. However, for  $\langle \hat{q} \rangle > 2$  GeV<sup>2</sup>/fm the depletion of the low- $\xi$  region is clearly visible.

As already shown in Fig. 6.374 the high- $\xi$  region is dominated by particles from the underlying event. Fast simulation allows us to combine the effects of the background and the resolution broadening and to estimate the statistical error. The result is shown in Fig. 6.386 for charged jet measurements with  $E_t^{\text{cone}} > 70$  GeV assuming a statistics of 10000 jets. As concerns the systematic error from the background subtraction, it has to be controlled to much better than 1% in order to reach  $\xi > 5$ . Note, however, that the background has been estimated using rather pessimistic assumptions about the central charged particle multiplicity.

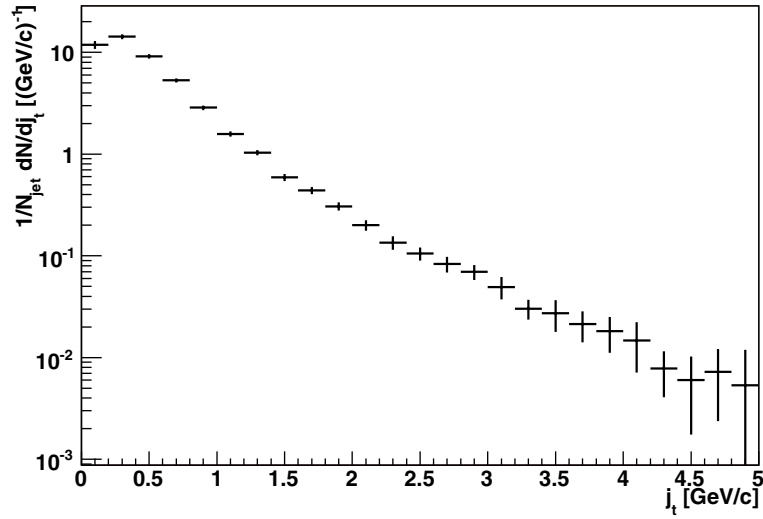


**Figure 6.388.** Expected statistical error for the  $j_t$ -spectrum measured from charged jets with  $E_t^{\text{cone}} > 70$  GeV assuming a statistics of 10000 jets.

Depending on the actual size of the systematic error we should be able to reach into the region above  $\xi = 4$  where the largest sensitivity to the transport parameter  $\hat{q}$  is expected.

*Momentum transverse to jet axis.* In Fig. 6.387 we compare the unbiased  $j_t$ -spectrum from the generated jets (solid line) to the reconstructed spectrum for charged jets (dotted) and charged+EMCal (dashed). The observed softening of the spectrum is a consequence of the limited angular resolution and the bias toward more collimated jets that suppresses the high- $j_t$  tail.

As shown in Fig. 6.375, the low- $j_t$  region is dominated by particles from the underlying event. Fast simulation allows us to combine the effects of the background and the softening of the  $j_t$ -spectrum and estimate the statistical error. The result is shown in Fig. 6.388 for charged jet measurements with  $E_t^{\text{cone}} > 70$  GeV assuming a statistics of 10000 jets. As concerns the systematic error from the background subtraction, it has to be controlled to much better than 1% in order to reach  $j_t < 200$  MeV/ $c$ .

*6.8.7. Jet-analysis results from full simulation.* Up to now, we have discussed separately the expected background and signal fluctuations and concluded that charged jet reconstruction should be possible in central Pb–Pb collisions at the LHC using a reduced cone size  $R_c = 0.4$  and a transverse momentum threshold of 2 GeV/ $c$ . In order to provide a proof of principle, this section presents the results obtained by the ALICE Jet Data Challenge. As described in Section 6.8.4 jets with  $20 < E_t < 200$  GeV were embedded into HIJING events and passed through the full detector simulation and reconstruction chain. Jets were reconstructed using charged particles reconstructed in the central barrel.

*6.8.7.1. Energy resolution and spectra.* In Fig. 6.389 we compare distributions of reconstructed energies for fixed generated energies  $E_t^{\text{gen}} = 50, 100$  and 150 GeV to the distributions obtained from the fast simulation using background free PYTHIA generated jets. As expected the energy resolution  $\Delta E_t/E_t$  is about 50%. For the lowest energy, 50 GeV, a high-energy tail caused by the background energy fluctuations is observed.

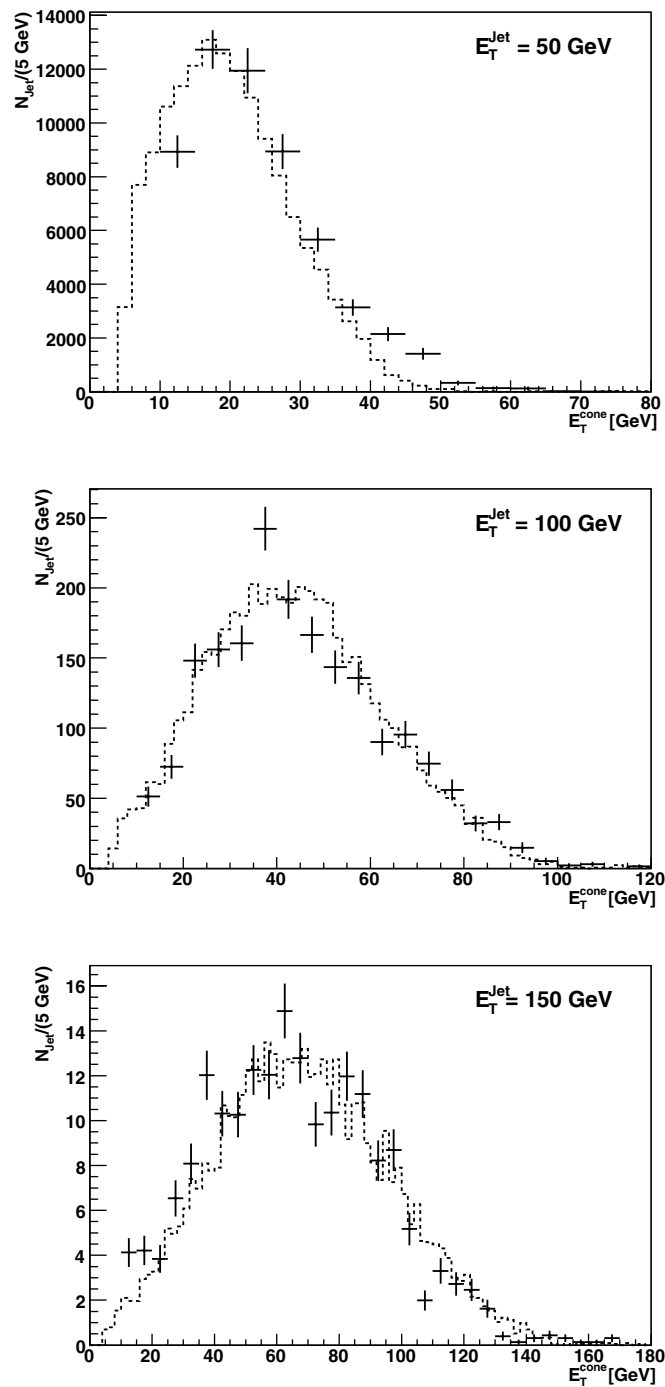


**Figure 6.389.** The distributions of reconstructed transverse cone energy for fixed generated energies from full detector simulation including the background from the underlying event (symbols) are compared to the line shape obtained from background-free fast simulation (dashed line).

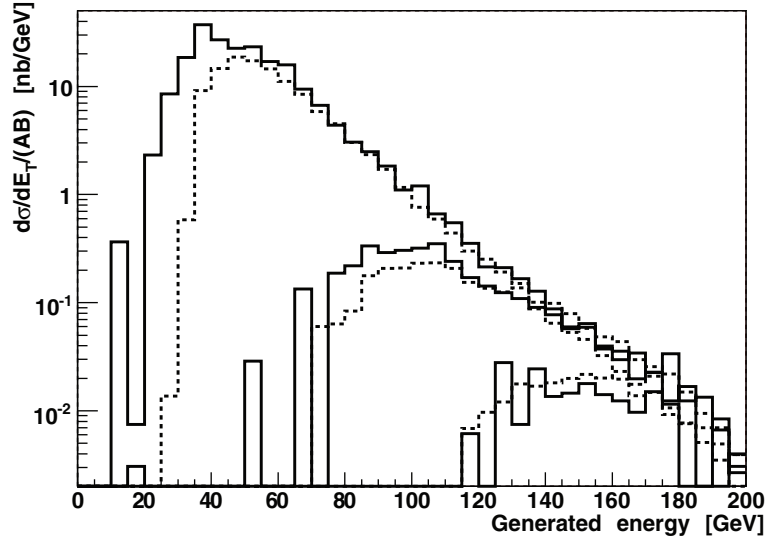


**Figure 6.390.** The distribution of generated energy for fixed bins of reconstructed energy ( $E_t^{\text{rec}} = 30\text{--}40$ ,  $70\text{--}80$  and  $110\text{--}120$  GeV). The bins were chosen so that the spectra are centred around  $E_t^{\text{gen}} = 50$ ,  $100$  and  $150$  GeV. The distributions obtained for full detector simulation (solid lines) are compared to those obtained from background-free fast simulation (dashed lines).

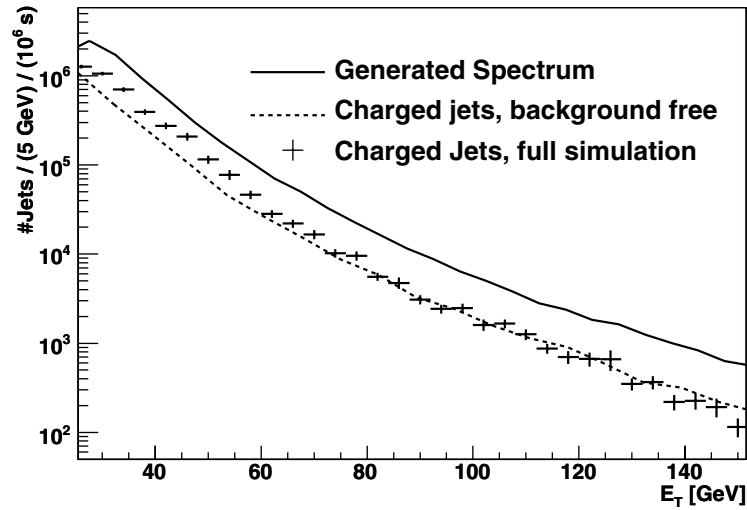


**Figure 6.391.** The reconstructed jet-energy spectrum for central Pb–Pb collisions using charged tracks in a cone  $R_c = 0.4$  is compared to the input spectrum (solid line) and the reconstructed jet-spectrum obtained using background-free fast simulation. The spectra are normalised to the untriggered yield for one effective month of running ( $10^6$  s), i.e.  $10^7$  central events.

In order to verify which part of the input spectrum contributes to different bins of reconstructed energy we plot in Fig. 6.390 the distribution of generated energy for fixed bins of reconstructed energy ( $E_t^{\text{rec}} = 30\text{--}40$ ,  $70\text{--}80$  and  $110\text{--}120$  GeV). The bins were chosen so that the spectra are centred around  $E_t^{\text{gen}} = 50$ ,  $100$  and  $150$  GeV. The distributions from the full simulation are compared to the expectations from the background-free fast simulation.

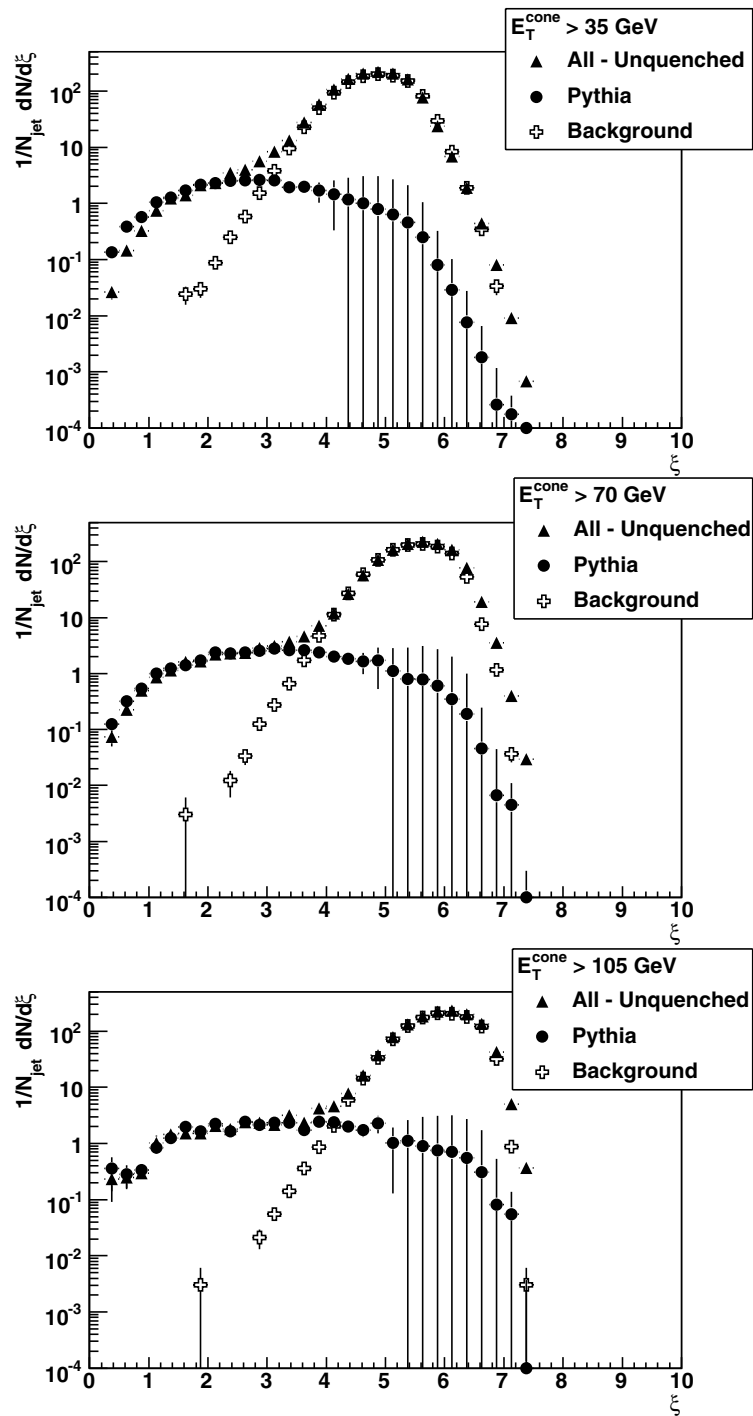


**Figure 6.392.** The reconstructed hump-backed plateau for three different ranges of reconstructed energy:  $E_T^{\text{cone}} > 35 \text{ GeV}$  (upper),  $E_T^{\text{cone}} > 70 \text{ GeV}$  (middle) and  $E_T^{\text{cone}} > 105 \text{ GeV}$  (lower). Only particles within  $R < 0.4$  enter the spectrum. The spectra are compared to the corresponding results for background free events and an estimation of the background distribution.

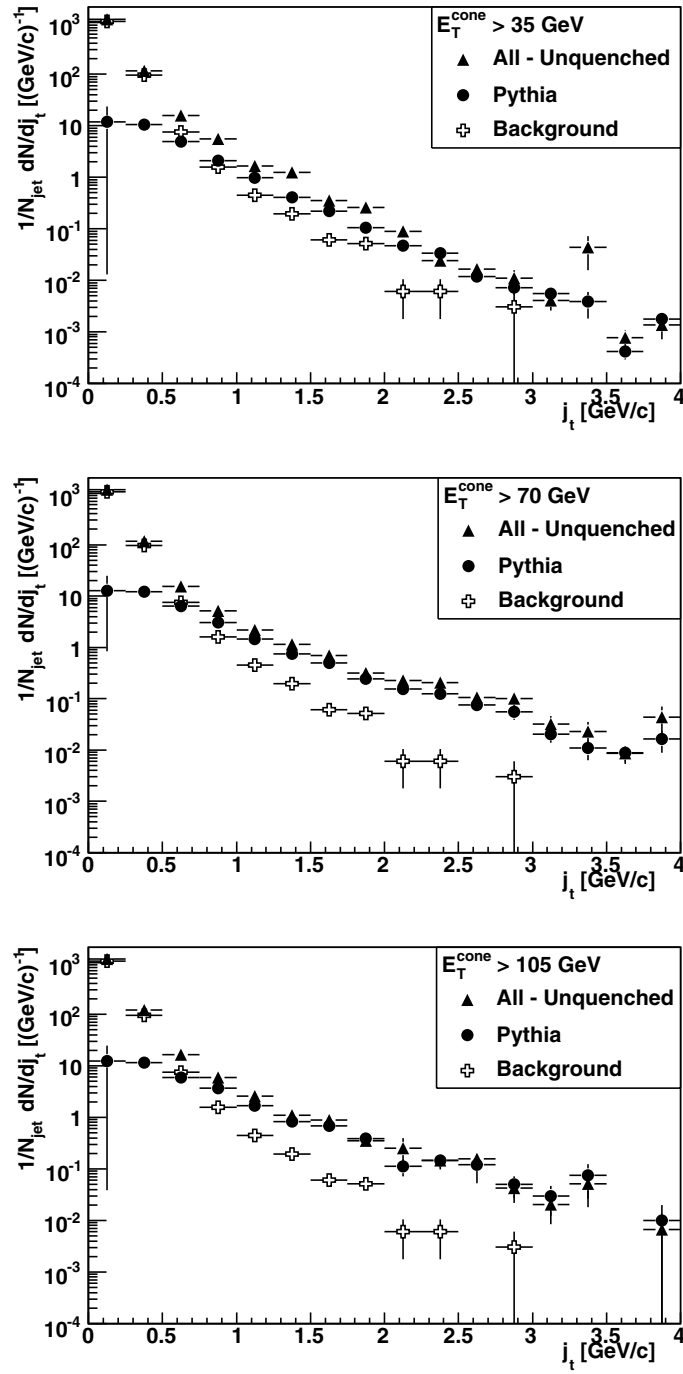


**Figure 6.393.** The reconstructed  $j_t$ -spectrum for three different ranges of reconstructed energy:  $E_T^{\text{cone}} > 35$  GeV (upper),  $E_T^{\text{cone}} > 70$  GeV (middle) and  $E_T^{\text{cone}} > 105$  GeV (lower). Only particles within  $R < 0.4$  enter the spectrum. The spectra are compared to the corresponding results for background free events and an estimation of the background distribution.

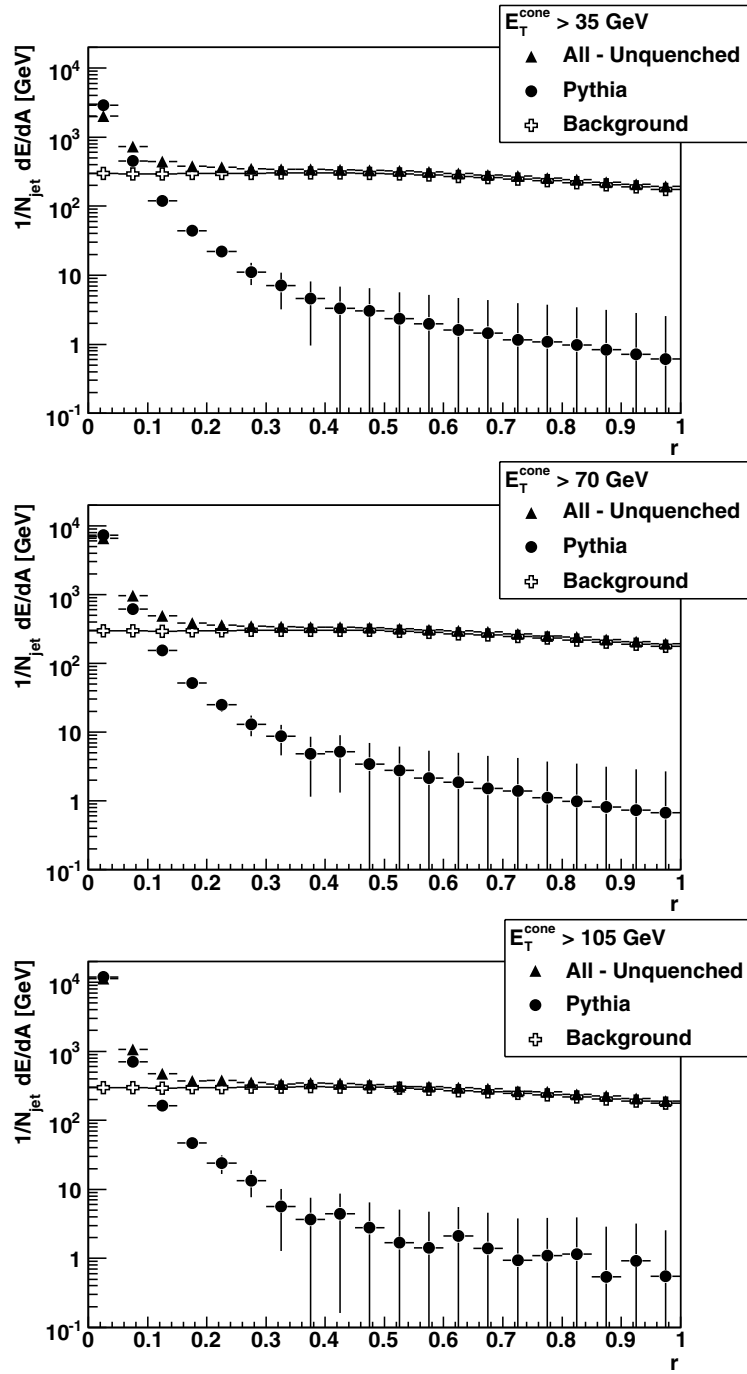


**Figure 6.394.** The reconstructed distribution of charged energy averaged over rings  $R \dots R + \Delta R$  around the jet-axis normalised to the area  $A$  of the ring for three different ranges of reconstructed energy:  $E_T^{\text{cone}} > 35$  GeV (upper),  $E_T^{\text{cone}} > 70$  GeV (middle) and  $E_T^{\text{cone}} > 105$  GeV (lower). The spectra are compared to the corresponding results for background free events and an estimation of the background distribution.

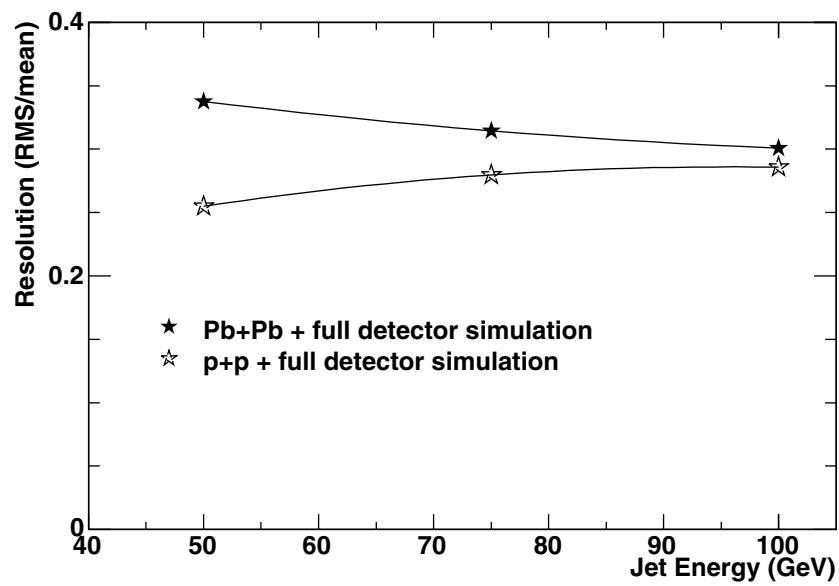


**Figure 6.395.** Jet-energy resolution as a function of the generated jet energy for jets embedded in central Pb–Pb collisions simulated with HIJING compared to the background free case and for an ideal detector only applying the jet reconstruction cuts ( $R_c = 0.3$ ,  $p_t > 2 \text{ GeV}/c$ ). Jets reconstructed combining energy from charged particles and neutral energy measured with the EMCal. Figure taken from Ref. [954].

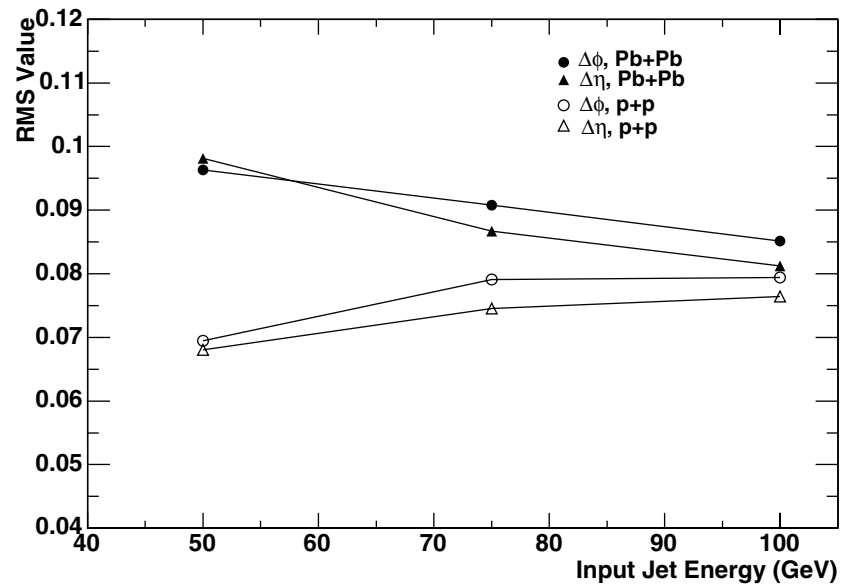


**Figure 6.396.** R.m.s. distributions of the differences between generated and reconstructed jet directions,  $\Delta\eta$  and  $\Delta\phi$ , as a function of the generated jet energy for jets embedded in central Pb–Pb collisions simulated with HIJING (black symbols) compared to the background free case (open symbols). Jets have been reconstructed combining energy from charged particles and neutral energy measured with the EMCal. Figure taken from Ref. [953].

Due to the background fluctuations, jets with generated energy lower than expected for the background-free scenario can enter the event samples. As expected, this effect is strongest for the lower energy bins.

Finally we show in Fig. 6.391 the reconstructed transverse energy spectrum normalised to the expected jet-yield in the 10% most central Pb–Pb collisions for one effective month of running ( $10^6$  s), i.e. in  $10^7$  central events. The error bars do not correspond to the expected statistics but to the statistics of the Monte Carlo samples. The presence of the background from the underlying event distorts the spectrum for  $E_t < 50$  GeV.

*6.8.7.2. Jet-structure observables.* In Figs. 6.392, 6.393 and 6.394 we demonstrate for three bins of reconstructed energy that jet-structure observables can be extracted from the sample of reconstructed jets (see [955] for details). The typical jet-characteristics: particles carrying a large fraction of the jet energy (low  $\xi$ ), the high- $j_t$ -tail and the excess of energy close to the jet axis are clearly visible, and agree with the corresponding spectra obtained from background-free events.

### 6.8.8. Level 1 jet triggering with the ALICE EMCal

*6.8.8.1. General considerations.* In this section we discuss Level 1 jet triggering for heavy-ion collisions, which utilises the ALICE Electromagnetic Calorimeter [956]. The EMCal is a sampling calorimeter comprising  $\sim 13\,000$  towers within acceptance  $0 < \Delta\varphi < 2\pi/3$ ,  $|\Delta\eta| < 0.7$ , with nominal energy resolution  $\sigma_E/E \sim 10\%/\sqrt{E}$ . Figures 6.395 and 6.396 show the expected EMCal performance in terms of jet energy and angular resolution.

Jet yields in the EMCal acceptance are large for a nominal Pb–Pb run:  $10^7$  per year ( $= 10^6$  seconds) for  $E_t > 50$  GeV and  $4 \times 10^5$  per year for  $E_t > 100$  GeV. The Pb–Pb minimum bias interaction rate is 4–8 kHz but such events can be recorded by ALICE only at  $\sim 100$  Hz. In order to achieve a jet rate to tape of  $\sim 10$  Hz, an overall rejection of 400–800 is therefore needed from the jet trigger. Required trigger rejection factors are larger for lighter collision systems, which have higher interaction rates.

The EMCal will utilise the same front-end electronics as the PHOS, and thus will provide  $\gamma$ ,  $\pi^0$  and electrons triggers. Leading particles triggers yield jet enriched data and can be considered to be a jet trigger of a sort. However, a 10 Hz  $\pi^0$  trigger rate requires a threshold  $p_t \sim 20$  GeV/ $c$ , which selects jets over a very broad energy range, and the resulting jet sample will be dominated by relatively low  $E_t$  jets that fragment hard. A more refined selection of high- $E_t$  jets requires a jet trigger which sums energy over a finite area of phase space.

The EMCal will provide a jet trigger on the Level 1 (L1) time scale of  $\sim 6$   $\mu$ s. Since the EMCal is primarily sensitive to electromagnetic energy, the optimal jet trigger will utilise the High Level Trigger (HLT) and require L1 rejection by the EMCal only sufficient to match the HLT input bandwidth, estimated to be about a factor 10 rejection for Pb–Pb. The HLT can then carry out more precise jet identification utilising both the EMCal data and charged tracks from the TPC, providing the remaining event rejection based on full jet reconstruction.

Table 6.96 shows the potential gain of the EMCal L1 trigger based on simple geometric and rate considerations, comparing rates to tape of EMCal-triggered observables and equivalent observables using only charged tracks in the TPC and simple interaction (‘minimum bias’) triggers. The EMCal acceptance is  $\sim 25\%$  of the TPC acceptance, though for jet triggers of finite extent in phase space (i.e. a square ‘jet patch’  $\Delta\eta \times \Delta\varphi = s \times s$ , with length of the side  $s$ ) the effective acceptance of the EMCal relative to that of the TPC will be smaller.

**Table 6.96.** EMCal trigger enhancement factor for various collision systems, comparing rate to tape of hard processes utilising an EMCal jet patch trigger and simple interaction triggers. The observable in both cases occupies a square patch in phase space of size  $\Delta E_t a \times \Delta\varphi = s \times s$ .

	$L_{\max}$ ( $\text{cm}^{-2} \text{s}^{-1}$ )	Interaction rate	Max rate to tape	EMCal enhancement ( $\Delta\eta \times \Delta\varphi = s \times s$ )		
				$\pi^0$ Trigger	0.4	0.8
Pb–Pb	$1.0 \times 10^{27}$	8 kHz	100 Hz	14	10	6
Ar–Ar	$0.6 \times 10^{29}$	130 kHz	500 Hz	44	31	21
O–O	$2.0 \times 10^{29}$	220 kHz	500 Hz	75	53	35
pp	$5.0 \times 10^{30}$	200 kHz	500 Hz	68	48	32

Table 6.96 shows the expected maximum luminosity for various collision systems at the beginning of a fill (when the trigger will be most effective), the corresponding minimum-bias interaction rate, and the maximum rate to tape due to ALICE taping bandwidth and TPC gating limitations. The three rightmost columns show the relative enhancement due to the EMCal trigger over equivalent measurements using the TPC only, for observables having negligible phase space area (e.g.  $\pi^0$  in EMCal vs. charged pions in TPC) and for jets of trigger patch size  $0.4 \times 0.4$  and  $0.8 \times 0.8$ . We assume 80% lifetime and 80% trigger efficiency. The loss in luminosity due to past/future protection is not accounted for (see [956] for details).

For the  $\pi^0$  trigger the enhancement is large relative to untriggered charged pion measurements, while for finite jet patches the enhancement is smaller than for  $\pi^0$  by up to a factor two. It should be noted however, that charged jets are substantially less complete than full jet measurements incorporating the EMCal. Thus even limited enhancement factors are valuable since the resulting measurement is much more robust.

**6.8.8.2. L1 trigger response to jets.** The L1 trigger response is studied using PYTHIA-generated jet events, with the heavy-ion event background modeled by HIJING. The EMCal response used here is a simple parametrisation, with photons and electrons depositing 100% of their energy, and hadrons depositing 25% of their energy. Charged-particle trajectories are bent by the 0.5 T field. Shower shape and energy resolution are not accounted for.

The L1 jet-trigger algorithm sweeps a square patch of dimensions  $\Delta\eta \times \Delta\varphi$  over the EMCal and finds the location of the patch with the highest integrated EMCal energy ( $E_t^{\max}$ ). Three patch sizes are considered here:  $\Delta\eta \times \Delta\varphi = (0.14 \times 0.14)$ ,  $(0.21 \times 0.21)$ , and  $(0.35 \times 0.35)$ , which appear to span the optimum size for the trigger patch (see below). Figure 6.397 shows the distribution of jet-trigger cross section in pp collisions (PYTHIA) for the  $0.21 \times 0.21$  patch and various lower bounds on  $E_t^{\max}$ . Cutting harder than  $E_t^{\max} > 10$  GeV evidently generates significant trigger biases beyond  $E_t^{\text{jet}} \sim 100$  GeV.

Figure 6.398 shows the  $E_t^{\max}$  cross section (jet patch  $0.21 \times 0.21$ ) for otherwise unbiased central ( $b = 0\text{--}2$  fm) and peripheral ( $b = 8\text{--}10$  fm) Pb–Pb collisions and for the same events with 50–60 GeV jets superimposed. Cross sections are calculated by taking into account the jet cross section from PYTHIA and the equivalent number of binary collisions for each event class. The filled area in each figure shows 80% of the jet yield, i.e. its lower bound indicates the  $E_t^{\max}$  cut necessary for 80% jet efficiency. Background fluctuations are seen to be significant relative to the intrinsic fluctuations of the jet, both for central and for peripheral collisions. The overall level of background is seen to be strongly centrality-dependent, as expected, meaning

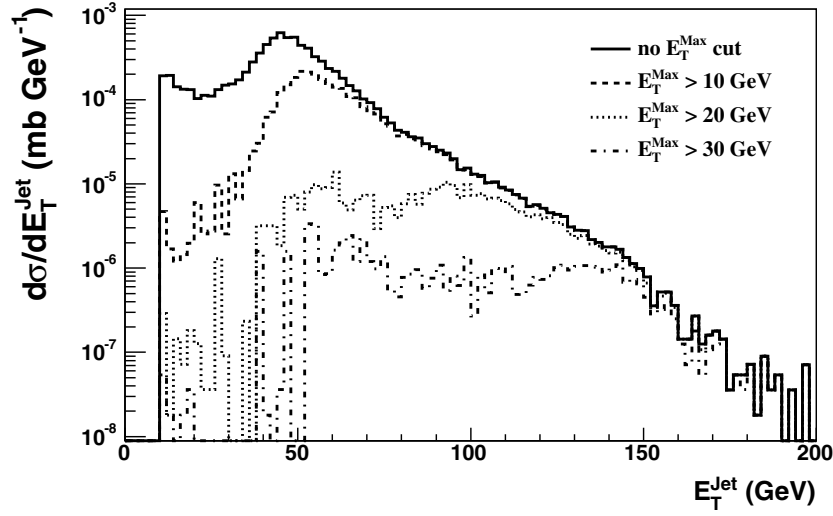


**Figure 6.397.** PYTHIA: trigger bias for various cuts on  $E_t^{\max}$ ; jet patch  $0.21 \times 0.21$ . Features at  $E_t < 50$  GeV are due to thresholds in event generation and should be disregarded.

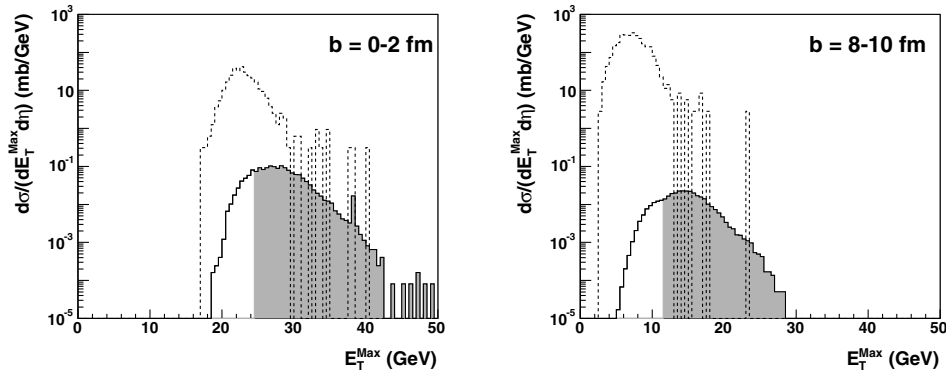


**Figure 6.398.** PYTHIA+HIJING for central and peripheral collisions, jet patch  $0.21 \times 0.21$ :  $E_t^{\max}$  differential cross section for background (dash-dot) and for background plus 50–60 GeV jets (solid). Filled area shows 80% of embedded jet yield.

that the  $E_t^{\max}$  threshold must vary with centrality (by a factor two in this calculation) for centrality-independent jet trigger efficiency.

This choice of thresholds also reduces the L1 output data rate by a factor 10, roughly the factor needed to match the HLT input bandwidth. While this model is probably missing essential aspects of the real physics and its results should not be taken quantitatively, it supports the qualitative conclusion that the required L1 rejection can be achieved while retaining reasonable efficiency for jets at intermediate  $E_t \sim 50$  GeV. The requirement for centrality dependent threshold is also qualitative and generic, stemming from the large phase space area integrated by any jet patch trigger. The capability to apply a centrality-dependent threshold is an essential requirement of the jet trigger hardware.

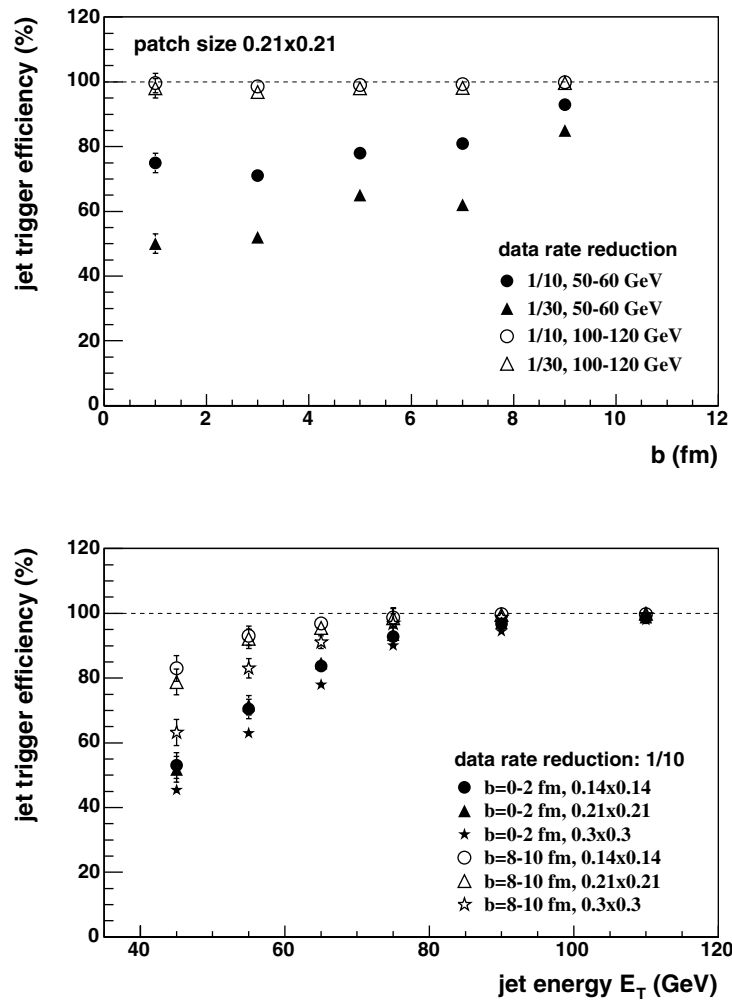


**Figure 6.399.** PYTHIA+HIJING. Upper: jet-trigger efficiency as a function of impact parameter for two jet energies, for a  $0.21 \times 0.21$  patch with data rate reduction of 1/10 and 1/30. Lower: jet-trigger efficiency vs. energy for 1/10 reduction in data rate, for various patch sizes and central and peripheral collisions.

A broader view of the trigger response to jets is seen in Fig. 6.399, where the trigger efficiency is studied for fixed L1 data rate reduction<sup>27</sup>. The upper panel shows jet trigger efficiency vs. centrality for the  $0.21 \times 0.21$  patch. For 100 GeV jets the efficiency is arbitrarily good, whereas for 50–60 GeV jets it varies strongly with data reduction factor and has a weak centrality dependence. The lower panel shows efficiency vs. jet  $E_T$  for data rate reduction 1/10 for various patch sizes. It can be seen that the  $0.3 \times 0.3$  patch has poorer efficiency for moderate energy  $E_T < 70$  GeV jets, indicating the faster growth in background relative to signal for increasing jet patch size in this region. Evidently the  $0.21 \times 0.21$  patch is closer to optimal for this model of signal and background, though this optimisation has not been studied in detail.

<sup>27</sup> Data-rate reduction in units of GB/s is used to define the trigger thresholds rather than event rejection, since the HLT input bandwidth is data rate limited.

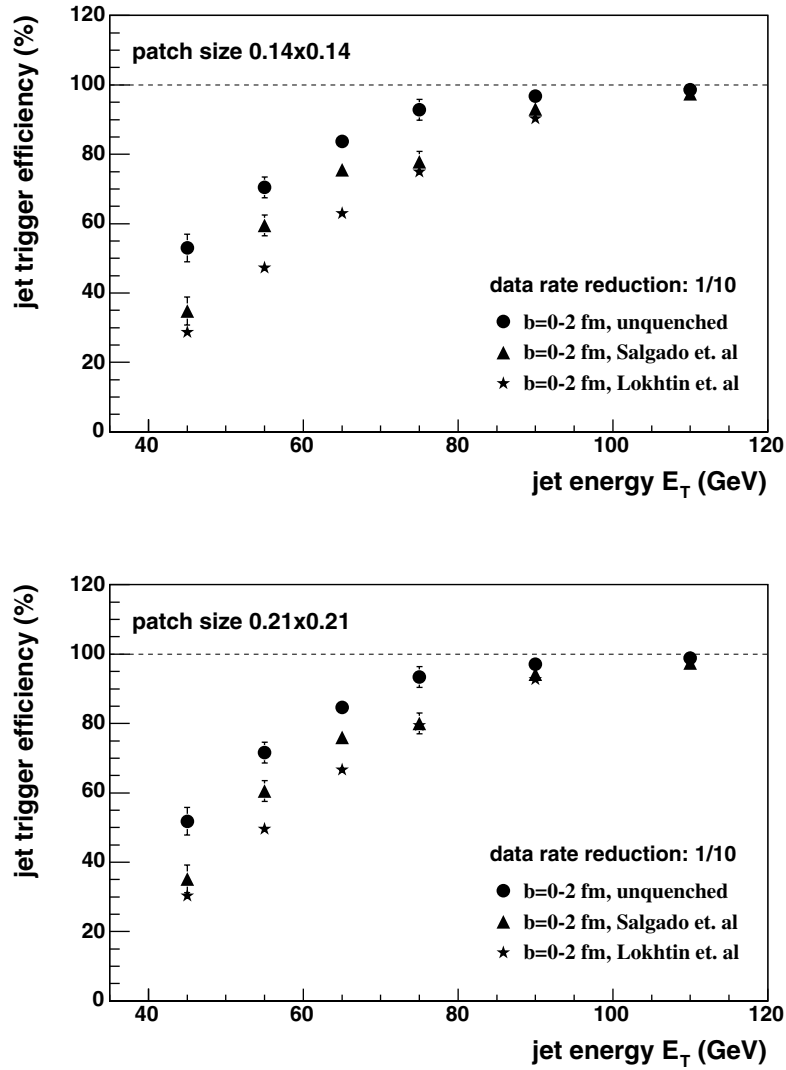


**Figure 6.400.** PYTHIA+HIJING+quenching: trigger efficiency vs. jet energy for central collisions for different jet quenching models and trigger patch sizes.

Finally, we assess the effects of jet quenching on the trigger efficiency using the Parton Quenching Model the ALICE afterburner described in Section 6.8.4.2. and the event generator PYQUEN [942]. Figure 6.400 shows trigger efficiency vs. jet energy for central collisions, for the various fragmentation models and for different trigger patch sizes. The quenching models introduce large and model-dependent reductions in efficiency up to  $E_t \sim 100$  GeV, though with no large distinction between the  $0.14 \times 0.14$  and  $0.21 \times 0.21$  patches. PYQUEN is known to generate very broad fragmentation, generating correspondingly low trigger efficiencies relative to AliPythia::Quench. The response of the  $0.3 \times 0.3$  patch (not shown) is uniformly worse than that of the smaller patches. The quenching models used in Fig. 6.400 are somewhat simplistic, with modification of the angular distribution of jet fragments that is not well motivated theoretically, and the figure should be regarded as

only a qualitative indication that quenching could have significant influence on the trigger efficiencies.

**6.8.8.3. Discussion.** While there are significant uncertainties in the physics underlying the models of signal and background used in this trigger study, some qualitative conclusions about L1 jet-trigger performance and hardware design can be drawn:

- The L1 rejection needed to match the HLT input bandwidth can likely be achieved while maintaining reasonable jet-trigger efficiency over a broad energy range.
- Uniform jet-trigger efficiency as a function of centrality in nuclear collisions requires a centrality-dependent trigger threshold. The centrality measurement should be supplied by an independent, azimuthally uniform device (the latter to avoid biases due to orientation of the reaction plane). The V0 detector is the appropriate detector for this in ALICE, providing a signal proportional to multiplicity [957] on the required L1 timescale.
- Flexibility in jet-trigger patch size: patch size is driven larger by the requirement of unbiased triggering in light of presently unknown and potentially large quenching effects, but is limited from above by increasing background for larger patch size. Optimisation will only be possible once data become available, but prudent hardware design should accommodate a range of patch sizes.

**6.8.9. Leading particle correlations.** For the first time in heavy-ion collisions, event-by-event jet reconstruction will be possible at LHC. As outlined in the previous sections, this will allow for a detailed study of medium-induced modifications of the jet fragmentation, providing a sensitive probe to investigate the properties of the QGP produced at LHC.

On the other hand, most of our present knowledge about jet modification in heavy-ion collisions at SPS and RHIC [522, 803, 922–924, 959] is based on *statistical* methods. These methods employ azimuthal correlations between a high- $p_t$  leading hadron (the trigger particle) and other particles from the same event, selected in a lower  $p_t$  range (the *associated* particles). In pp and dAu collisions, a clear di-jet pattern emerges, manifested by a positive correlation around  $\Delta\phi \simeq 0$  (the *near side*) and  $\Delta\phi \simeq \pi$  (the *away side*). In contrast to these findings, a significant suppression of moderate  $p_t$  associated particles on the away-side has been observed in central Au–Au collisions, interpreted as a consequence of medium-induced energy loss of the leading parton in the dense partonic matter at RHIC.

While event-by-event jet reconstruction at LHC will be feasible for jet energies  $E_t > 40$  GeV and jet fragments of  $p_t > 2$  GeV/c, leading hadron-correlation studies are in principle possible down to very low transverse momenta, in particular of associated particles, allowing the investigation of the transfer of radiated energy to the bulk medium. Such studies have been performed at RHIC, demonstrating that significant away-side correlations with a leading hadron persist at transverse momenta as low as 150 MeV/c [541].

Leading hadron-correlation studies at medium and low  $p_t$  are generally hampered by a huge background of uncorrelated soft particles and eventually limited by the signal-to-background ratio. At LHC, the situation is very different from that of lower beam energies: The larger cross section for large- $Q^2$  processes enhances the yield of leading hadrons at a given trigger  $p_t$ , thereby increasing the signal. For the same reason, the amount of uncorrelated particles in the range of associated  $p_t$  will also increase compared to lower beam energies, giving rise to an increased combinatorial background. In this section, we investigate the feasibility of leading hadron-correlation studies in Pb–Pb collisions in the central barrel of the ALICE detector. Additional complications, due to the asymmetry of the combinatorial background imposed by elliptic flow in non-central events, are neglected because we focus on rather central events only.

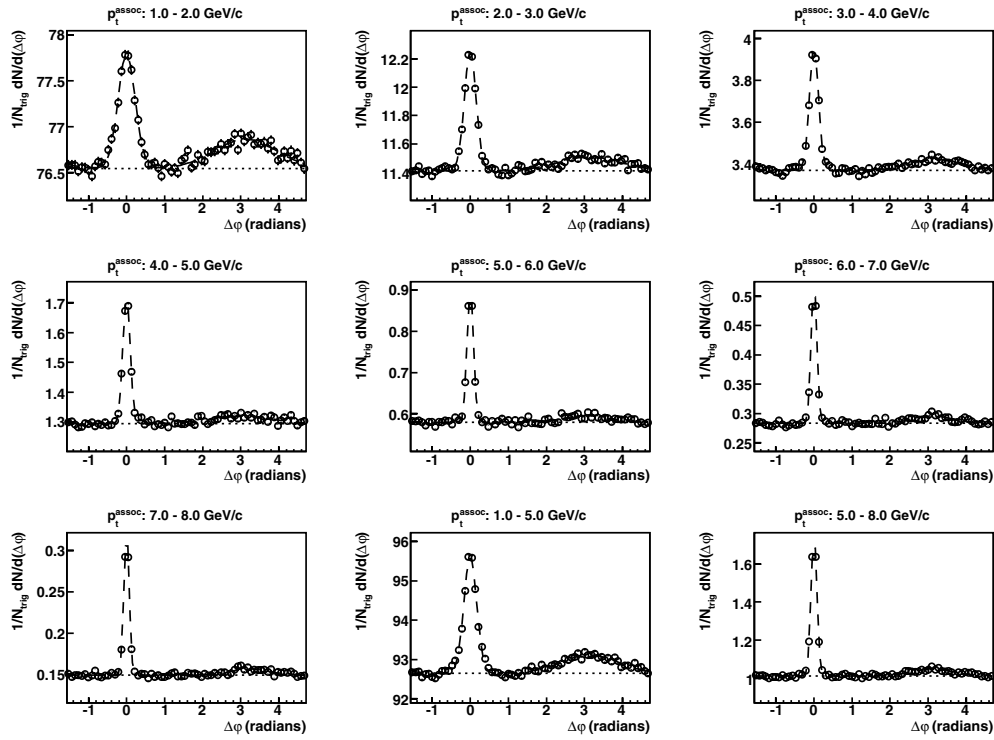


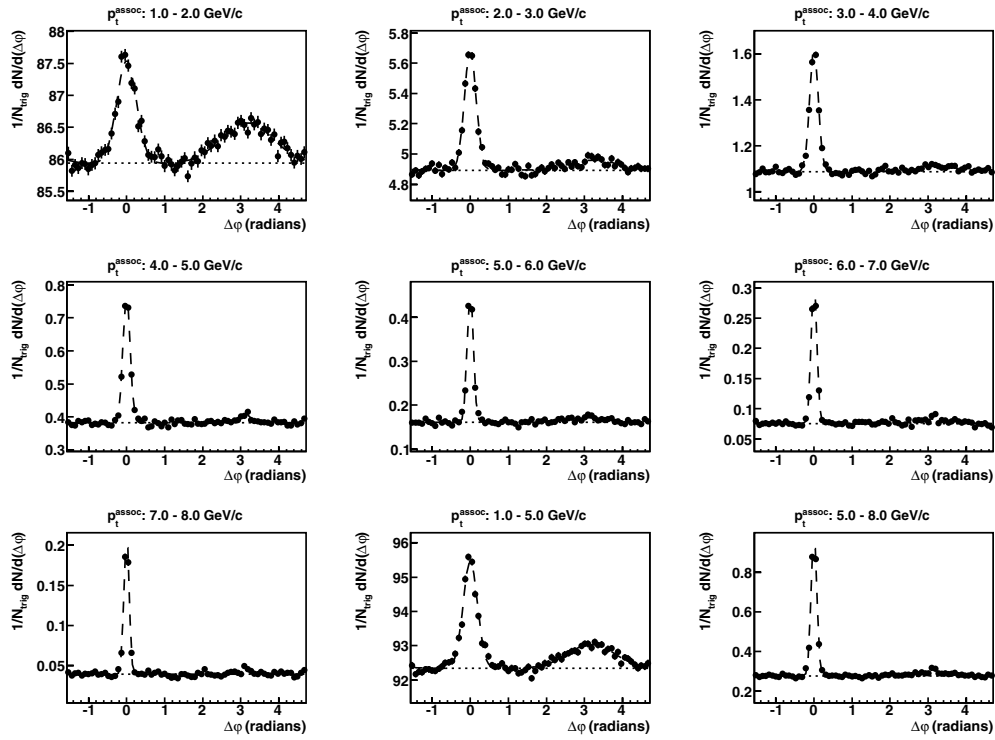
**Figure 6.401.** Leading hadron azimuthal correlations in unquenched central Pb–Pb HIJING events at  $\sqrt{s_{NN}} = 5.5$  TeV. For  $8 \text{ GeV}/c < p_t^{\text{trig}} < 15 \text{ GeV}/c$ , different ranges of  $p_t^{\text{assoc}}$  are shown.

For the present investigation [958], 10% most central Pb–Pb collisions simulated with HIJING  $\sqrt{s_{NN}} = 5.5$  TeV have been studied. The HIJING events have been processed with the fast simulation tool described above. We compare the results of HIJING event samples in quenched and unquenched modes. For each sample,  $4 \times 10^5$  events have been generated.

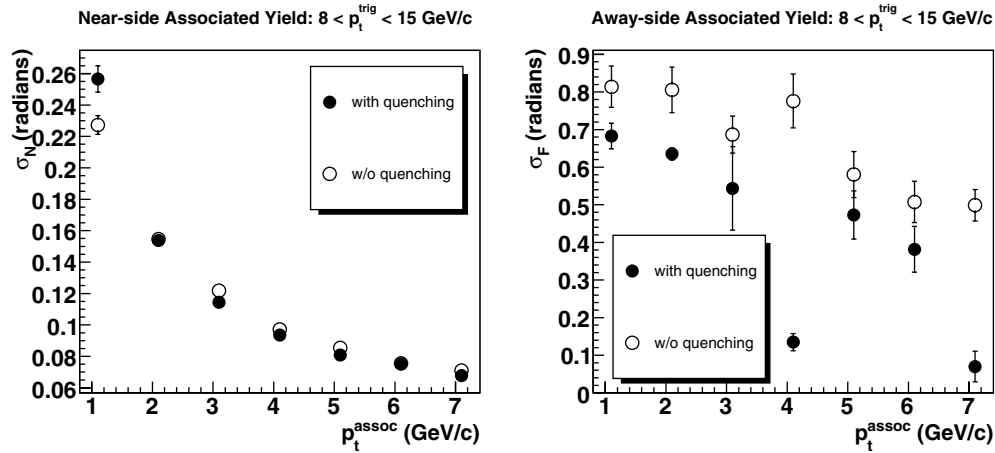
Charged trigger particles with transverse momentum  $8 \text{ GeV}/c < p_t^{\text{trig}} < 15 \text{ GeV}/c$  have been selected in the acceptance of the ALICE central barrel  $|\eta| < 0.9$ . Pairs are created with associated particles in the same acceptance and in a lower  $p_t$ -range and plotted as a function of their azimuthal separation  $\Delta\varphi$ . In this range of  $p_t^{\text{trig}}$ , we detected a trigger particle in about 30% of the quenched events and in about 70% of the unquenched events. The choice of this range of  $p_t^{\text{trig}}$  allows a comparison with recent results from RHIC for which the same  $p_t^{\text{trig}}$  had been chosen [960].

Figure 6.401 shows examples of leading hadron azimuthal correlations in unquenched events for  $8 \text{ GeV}/c < p_t^{\text{trig}} < 15 \text{ GeV}/c$  and different ranges of the transverse momenta,  $p_t^{\text{assoc}}$ , of associated particles. The number of associated tracks is normalised to the number of triggers  $N_{\text{trig}}$  (the *conditional yield*). A clear near-side jet topology can be observed in all cases, while only a shallow indication of an away-side structure is visible within the present statistics. This is consistent with the expectation that only a small fraction of the jets belongs to di-jet events in the acceptance. Similar distributions for quenched events are shown in Fig. 6.402.

The azimuthal correlations have been fitted by a constant plus two Gaussians at  $\Delta\varphi = 0$  and  $\Delta\varphi = \pi$ , respectively. In general, this leads to a very good description of the measured



**Figure 6.402.** Leading hadron azimuthal correlations in quenched central Pb–Pb HIJING events at  $\sqrt{s_{NN}} = 5.5$  TeV. For  $8 \text{ GeV}/c < p_t^{\text{trig}} < 15 \text{ GeV}/c$ , different ranges of  $p_t^{\text{assoc}}$  are shown.



**Figure 6.403.** Gaussian width of near- and away-side peak in quenched and unquenched HIJING events as function of  $p_t^{\text{assoc}}$  for  $8 \text{ GeV}/c < p_t^{\text{trig}} < 15 \text{ GeV}/c$ .

distributions. In a few cases, however, a successful fit of the away-side structure could not be performed within the present statistics.

With increasing  $p_t^{\text{assoc}}$ , the width of the near-side peak is significantly reduced, as demonstrated in Fig. 6.403. The away-side peak is substantially broader and shows only a

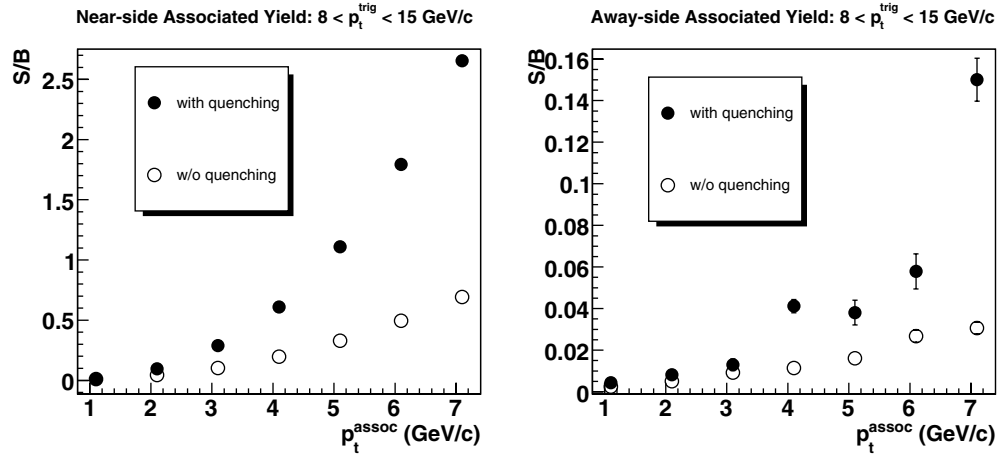


**Figure 6.404.** Near and away-side signal-to-background ratio  $S/B$  in quenched and unquenched HIJING events as function of  $p_t^{\text{assoc}}$  for  $8 \text{ GeV}/c < p_t^{\text{trig}} < 15 \text{ GeV}/c$ .

little  $p_t^{\text{assoc}}$  dependence. We note that this finding is in contrast to preliminary results from central Au–Au collisions at RHIC, where a significant narrowing of the away-side peak at high  $p_t^{\text{assoc}}$  was observed [960].

In all cases, a considerable amount of combinatorial background is observed, even at the highest selection of  $p_t^{\text{assoc}}$ . The signal-to-background ratio  $S/B$  has been determined in  $\pm 2\sigma$  windows around the peaks, using the fit results for  $\sigma$  and the integral. The dependence on  $p_t^{\text{assoc}}$  of  $S/B$  at the near- and away-side is shown in Fig. 6.404.

As expected,  $S/B$  improves with increasing  $p_t^{\text{assoc}}$ . In the quenched scenario, this improvement is much more pronounced than in the unquenched events, reflecting the softer  $p_t$  spectrum of the background in the quenched events.

The observed signal-to-background ratios are in contrast to preliminary results from central Au–Au collisions at RHIC, presented by STAR. At these energies and for the same choice of  $p_t^{\text{trig}}$ , the signal-to-background ratio at the near-side is close to unity for  $3 < p_t^{\text{assoc}} < 4 \text{ GeV}/c$ . At  $p_t^{\text{assoc}} > 6 \text{ GeV}/c$ , the STAR measurement is essentially free of combinatorial background [960]. This is explained by the much softer background spectrum at RHIC energies.

The significance  $S/\sqrt{S+B}$  of the present study has been extrapolated to  $10^7$  events, corresponding to one year of ALICE running (Fig. 6.405). The  $p_t^{\text{assoc}}$  dependence of  $S/\sqrt{S+B}$  reflects the interplay between  $S/B$  and the fragmentation function. On the near-side, highest significance can be achieved at intermediate  $p_t^{\text{assoc}}$ , while the significance on the away-side shows a monotonic decrease with  $p_t^{\text{assoc}}$ . We note, however, that the results of the present study rely strongly on the details of final-state interactions implemented in HIJING.

The measurement of the associated yield at fixed  $p_t^{\text{trig}}$  and in bins of  $p_t^{\text{assoc}}$  allows the determination of the hadron-triggered fragmentation function  $dN/dz_t$ , with  $z_t = p_t^{\text{assoc}}/p_t^{\text{trig}}$ . This quantity is related to the parton fragmentation function, however, without exact knowledge of the energy of the scattered parton. For a given range of  $z_t$ , the number of associated particles per trigger has been determined from the  $\Delta\phi$  distributions. The integrals of the Gaussian peaks at  $\Delta\phi = 0$  and  $\Delta\phi = \pi$  in a  $\pm 2\sigma$  window have been extracted from the fit results. The combinatorial background in the same window was subtracted using the result for the constant term in the fit function. The near and away-side hadron-triggered

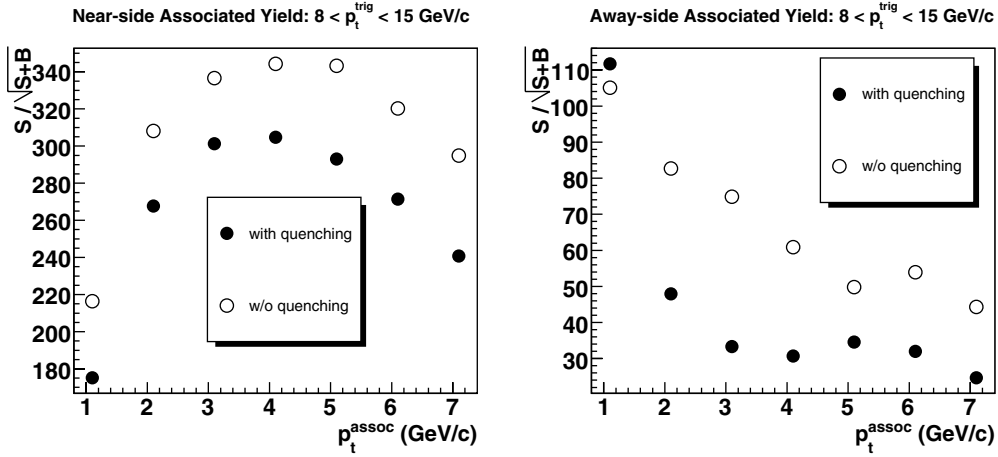


**Figure 6.405.** Near and away-side significance  $S/\sqrt{S+B}$  in quenched and unquenched HIJING events as function of  $p_t^{\text{assoc}}$  for  $8 \text{ GeV}/c < p_t^{\text{trig}} < 15 \text{ GeV}/c$ .

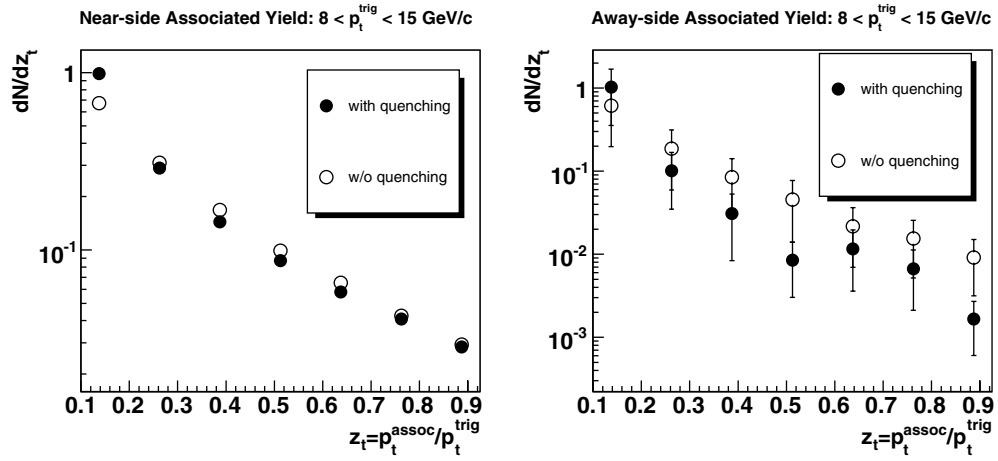


**Figure 6.406.** Near- and away-side leading-hadron fragmentation function  $dN/dz_t$  for  $8 \text{ GeV}/c < p_t^{\text{trig}} < 15 \text{ GeV}/c$  in quenched and unquenched HIJING events.

fragmentation functions for the quenched and unquenched scenario are shown in Fig. 6.406. Despite the rather high level of combinatorial background, a significant measurement of  $dN/dz_t$  for this range of  $p_t^{\text{trig}}$  can be performed down to  $p_t^{\text{assoc}} \simeq 1 \text{ GeV}/c$ . On the near-side, this constitutes a dramatic improvement compared to the situation at RHIC which is due to the much larger cross section for trigger particles at LHC. For a similar measurement on the away-side,  $10^7$  events will be sufficient, however, once again strongly depend on the underlying physical scenario.

Additional information about jet modification in the dense medium can be obtained by a measurement of the transverse momentum distribution of associated particles with respect to the direction of the trigger particle. For this study, we employ the measure  $j_t = p^{\text{assoc}} \times \sin(\alpha)$ , with  $\alpha$  the angle between trigger and associated particle. The resulting distribution  $dN/dj_t$  is shown in the left panel of Fig. 6.407. To account for combinatorial background, the same

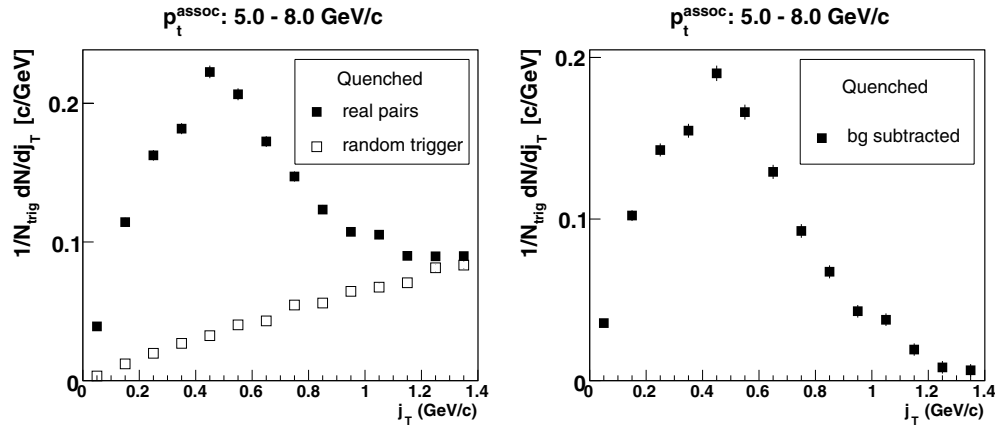


**Figure 6.407.** Transverse momentum distribution  $dN/dj_t$  of associated particles with respect to the trigger direction. Left panel: Real-event and mixed-event (random trigger) distributions. Right panel: After mixed-event subtraction.

distribution has been accumulated for trigger particles which have been embedded into a different event. Subtraction of the two spectra yields a very significant measurement of  $dN/dj_t$  within the present statistics, as demonstrated in the right panel of Fig. 6.407.

**6.8.10. Conclusions.** Studying jet quenching phenomena is a powerful tool to access properties of the hot and dense medium produced in nucleus–nucleus collisions. The highest sensitivity to the medium properties is expected from studies of modifications of the structure of reconstructed jets, i.e. the manifestation of the partonic energy loss in a decrease of the number of particles carrying a high fraction,  $z$ , of the jet energy and the appearance of radiated energy via an increase of the number of low-energy particles with low  $z$  values. In addition, a broadening of the distribution of jet-particle momenta perpendicular to the jet axis,  $j_t$ , directly related to the colour density of the medium is expected. Ideally, the analysis is performed on a sample of reconstructed jets with unbiased fragmentation functions.

In central Pb–Pb collisions at the LHC, jet rates are expected to be high at energies at which they can be reconstructed over the background of the underlying event. For the nominal annual integrated luminosity for Pb–Pb collisions at  $\sqrt{s_{NN}} = 5.5$  TeV of  $0.5 \text{ nb}^{-1}$ ,  $\simeq 4.8 \times 10^7$  ( $2.6 \times 10^6$ ,  $1 \times 10^5$ ) jets with  $E_t > 50$  GeV ( $E_t > 100$  GeV,  $E_t > 200$  GeV) are produced within the ALICE acceptance. This will allow us to map out the energy dependence of jet fragmentation modifications over a very wide kinematic range, up to  $E_t \simeq 250$  GeV. This is important, since the magnitude of the effects is expected to vary only logarithmically with energy. Furthermore, jet reconstruction will reduce significantly the bias on the parton fragmentation inherent to leading particle studies.

However, jet reconstruction at the LHC has to cope with the large background from the underlying event. Studies using the HIJING event generator with a pessimistic central charged-particle multiplicity of  $dN_{ch}/d\eta \simeq 5000$  suggest that jet reconstruction is limited to cone sizes in the range  $0.3 < R_c < 0.5$ . In addition a transverse momentum cut in the range  $1 \text{ GeV}/c < p_t < 2 \text{ GeV}/c$  has to be applied to reduce the background. As a consequence, even for full calorimetry, the energy resolution is limited to  $\Delta E_t/E_t \simeq 20\%$ .

In its present design, ALICE can only study charged jets, limiting the resolution to 40–50%. Nevertheless, at high  $E_t$  charged jet reconstruction is much superior to studying high- $p_t$  parton fragmentation using leading particles. For a parton of 100 GeV, the fraction of charged energy inside a cone of  $R_c = 0.4$  is  $\simeq 2.5$  times higher than the average fraction of energy carried by the leading particle. Cutting on the charged jet energy instead of the leading particle transverse momentum in order to select high- $p_t$  partons above a given transverse momentum is for the same purity more efficient. For example, requiring a purity of 85% the efficiency increases from 6% for leading particles to 30% using charged jets. Furthermore, we have shown that the bias toward a harder fragmentation, which depletes the multiplicity of sub-leading high-momentum hadrons, although still present for charged jets, can be largely reduced.

Background from the underlying event plays also an important role in the study of the jet structure. Whereas the high- $p_t$  and high- $j_t$  regions of the leading parton remnants are essentially background free, the spectra of particles originating from the radiated gluons have to be extracted mostly from kinematic regions, where background dominates the signal ( $S/B = 10^{-1} - 10^{-2}$ ). In this domain the low- $p_t$  tracking capabilities of ALICE are essential.

To demonstrate our charged jet reconstruction capabilities, we have run a Jet Data Challenge, in which jets with energies in the range from 20 to 200 GeV have been embedded into HIJING events and passed through the full detector simulation and reconstruction chain. The reconstructed energy spectrum and jet structure observables have been compared to the expectation from background-free jet samples. Only for cone energies below  $\simeq 40$  GeV fake jets produced as the sum of energy of real jets and background energy influence the quality of the reconstruction. Further studies will be needed to develop precise background subtraction techniques.

As shown by the RHIC experiments, in the low jet  $E_t$  region, jet structure modifications can be studied by analysing inclusive spectra of identified particles and particle correlations. These studies need excellent low- $p_t$  and PID capabilities. ALICE is well prepared to extend these studies to heavy ion collisions at the LHC.

The proposed electromagnetic calorimeter for ALICE, will improve the jet energy resolution, increase the selection efficiency and further reduce the bias on the jet fragmentation. Furthermore, it adds the jet trigger capabilities which are needed to record jet enriched data at high  $E_t$ . The low and high transverse momentum tracking capabilities combined with electromagnetic calorimetry represent an ideal tool for jet structure modification studies at the LHC over a wide kinematic region of jet and associated particle momenta.

### 6.9. Photons

The measurement of direct photons [961], defined as photons that do not originate from the decay of other particles, mainly serves a two-fold interest:

- the study of *prompt photons* production to learn about hard processes in the dense QGP medium;
- the understanding of the thermal properties of the early phase of the reaction from *thermal photons*.

While their identification is very difficult, especially at low transverse momentum, because of the large background from decay photons, direct photons have very little interaction with the surrounding medium and are therefore not altered by rescattering during the later moments of the collision. They provide therefore a very interesting probe and convey unique

and unperturbed information on the earliest stages of the collision. The assessment of direct photon measurements requires a thorough understanding of both the experimental challenges (photon and neutral meson identification) and the theoretical expectations.

One can distinguish two regions of interest in the direct-photon spectrum.

- In the high  $p_t$  domain ( $p_t > 10$  GeV/ $c$ ), prompt photons are produced in QCD hard-scattering processes. Medium effects in heavy-ion collisions are probed by studying photon–hadron and photon–photon correlations or photon tagged jets. The results obtained in heavy-ion collisions are then compared with the results in pp scattering.
- In the low  $p_t$  domain ( $p_t < 10$  GeV/ $c$ ), the thermal production adds to the prompt photon spectrum. Disentangling the various contributions to the low  $p_t$  domain requires the control of the absolute magnitude (cross sections convoluted with the collision dynamics) of each production mechanism. This is an ambitious challenge.

*6.9.1. Direct high- $p_t$  photons.* Prompt photons are produced in hard-parton collisions during the pre-equilibrium stage of the heavy-ion collision. They dominate the photon spectrum at  $p_t$  larger than 10 GeV/ $c$ . The production cross sections are obtained from the basic processes (annihilation, Compton scattering, and bremsstrahlung) by a convolution with the parton density distribution in the nucleus.

Medium effects in A–A collisions modify the vacuum production cross sections of prompt photons as measured in pp collisions: nuclear shadowing and in-medium parton energy loss lead to a suppression of the yield [962], whereas the intrinsic transverse momentum distribution of the partons [963, 964] and medium-induced photon radiation from quark jets [965] enhance the yield. To study medium effects in A–A collisions and disentangle nuclear effects present in the entrance channel of the collision from effects due to the medium created in the collision, it is mandatory to understand *a priori* the photon production in pp and pA collisions. Experimental results obtained from these collisions at SPS energies cannot all be described by perturbative QCD (pQCD) calculations in a consistent way [966]. Agreement appears to be better at higher energies, where e.g. data from Tevatron experiments on pp collisions and first results from RHIC are available.

*6.9.1.1. Production rates.* The photon production cross section in nucleus–nucleus collisions is derived following the factorisation theorem in pQCD. It depends on the elementary process cross sections described by a hard scattering between two initial partons convoluted with the parton density distributions in the nucleus and, in the case of the bremsstrahlung mechanism, on the fragmentation function of the scattered partons. A detailed review of the evolution of the various distributions and parameters involved in next-to-leading (NLO) pQCD calculations, in particular, the proper choices of the different renormalisation, factorisation and fragmentation scales involved can be found in [967] and other references therein. The parton density distribution in the nucleus is obtained from the density distribution in the nucleon modified by nuclear shadowing, which suppresses by about 30% the prompt photon production cross section in pA and A–A collisions. The amount of suppression can vary with the choice of the parametrisation of the density distribution by as much as 40% at high  $p_t$ . For the calculation discussed later, the parametrisation of Eskola *et al* (EKS98) [968, 969] is used. The medium created in nucleus–nucleus collisions will further modify the production cross section, in particular for bremsstrahlung photons, because the hard scattered partons experience secondary scatterings and induced radiation thus losing part of their energy before fragmenting. This effect is implemented in the cross section calculation through a modified fragmentation function, as discussed in Chapter 6.8. In addition, the production cross section of direct prompt photons is further reduced by the Landau–Pomeranchuk–Migdal (LPM)

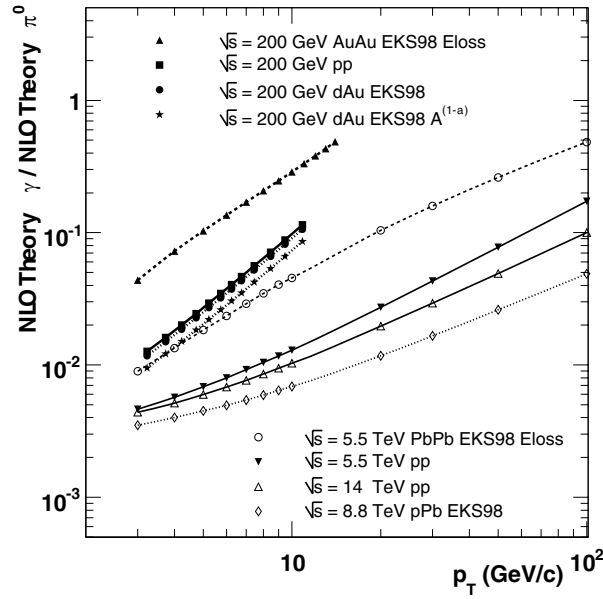


**Figure 6.408.** NLO QCD predictions [967] for the production ratio  $\gamma_{\text{prompt}}/\pi^0$  in pp, pA and AA collisions at 200 GeV and 5.5 TeV. The calculations for the photon production were performed using CTEQ5M BFG and for the  $\pi^0$  CTEQ5M KKP with  $M = \mu = M_F = p_t$ . The Au–Au ratio at  $\sqrt{s_{\text{NN}}} = 200$  GeV and the Pb–Pb ratio at  $\sqrt{s_{\text{NN}}} = 5.5$  TeV are modified by thermal effects at the lower  $p_t$  end of the spectrum and are predicted to be higher than shown.

effect, i.e. fast-moving hard-scattered quarks traversing the medium emit fewer photons than predicted by bremsstrahlung theory. Nuclear effects, shadowing, LPM and parton energy loss, reduce the cross section for prompt photon production by an order of magnitude at small  $p_t$  ( $p_t \sim 3$  GeV/ $c$ ) and by about a factor 7 at large  $p_t$  ( $p_t \sim 15$  GeV/ $c$ ). This reduction is very sensitive to the in-medium energy loss parameters. The cross section for photons produced in the annihilation or Compton scattering process is obviously not modified by the effect of this medium.

Predictions of production rates at LHC, obtained from calculations performed at next-to-leading order, still suffer from rather large uncertainties. These uncertainties are associated with e.g. the choice of renormalisation, factorisation and fragmentation scales [966, 970] (of the order of 30%). Furthermore, in the new kinematic regime involving small  $x_t = p_t/\sqrt{s_{\text{NN}}}$  values, the NLO calculations may be insufficient and resummed calculations may be required [971, 972]. Finally, processes are not constrained by existing data, such as bremsstrahlung production and its modification in the medium and thus carry large uncertainties.

**6.9.1.2. High- $p_t$  photon spectra.** The high- $p_t$  photon spectrum for Pb–Pb collisions at LHC was calculated from the photon and neutral pion production rates predicted by NLO pQCD calculations [967]. These calculations were performed with CTEQ5M [973] and/or CTEQ6M [974] parton distribution functions, and the KKP fragmentation functions [975] for  $\pi^0$ . The partons to photon fragmentation functions were taken as the BFG set II functions [976]. The calculated ratios of prompt direct photon to  $\pi^0$  are summarized in Fig. 6.408 for various entrance channels at RHIC and LHC energies. The calculations for

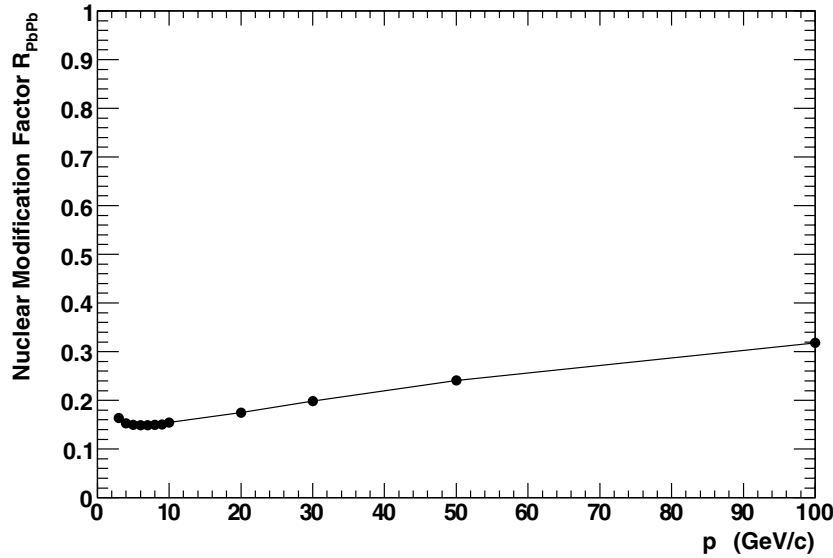


**Figure 6.409.** Nuclear modification factor for the 5% most central Pb–Pb collisions at  $\sqrt{s_{NN}} = 5.5$  TeV with respect to the pp system. It was obtained with the corresponding cross sections computed in NLO pQCD approximation developed in [967]. The black dots symbolize the  $p_t$  values where the computations were performed.

nucleus–nucleus collisions (5% most central collisions) include the jet quenching effect with the  $p_t$  dependence of the nuclear modification factor [967] shown in Fig. 6.409.

The decay-photon spectrum was calculated taking into account  $\pi^0$  decay photons<sup>28</sup> and approximating the ratio of the decay photon spectrum with the source  $\pi^0$  spectrum, as:

$$R_{\gamma_{\text{decay}}/\pi^0} = \frac{2}{n-1}, \quad (6.150)$$

where  $n$  is the exponent of the  $\pi^0$  spectrum described as a power law,  $d\sigma_{\pi^0}/dp_t \sim p_t^{-n}$ .

The ratio  $\gamma_{\text{All}}/\gamma_{\text{Bkgd}}$  of all the photons to the decay photons is commonly used to extract the excess of direct photons. This ratio was calculated [967] for Pb–Pb collisions at LHC energies by adding to the NLO pQCD computed cross sections the results expected from the emission from a hot quark–gluon plasma expanding according to the hydrodynamic model. A significant direct photon excess is predicted at high- $p_t$  values (Fig. 6.410), 10% at 10 GeV/ $c$  and 60% at 50 GeV/ $c$ . Within this  $p_t$  range, as we shall see later, sufficient statistics can be accumulated with ALICE during one heavy-ion run.

**6.9.1.3. Experimental method.** Photons will be detected by the photon spectrometer PHOS [977] which is able to measure with high precision their 4-momenta, only in a limited acceptance [978]. The identification power of prompt photons is limited by the background created by decay photons (mainly,  $\pi^0 \rightarrow \gamma + \gamma$ ). The identification of prompt photons in ALICE is optimal for photons with energy larger than 20 GeV. Below this value, decay and prompt photons cannot be efficiently distinguished on an event-by-event basis.

Two different procedures to select prompt photons among inclusive photons have been studied: the Shower Shape Analysis (SSA) [978], and the Isolation Cut Method (ICM). The former identifies photons by analysing the shape of the shower in PHOS, and the latter tags

<sup>28</sup> Neutral pions amount to about 80–85 % of all decay photons for  $p_t < 100$  GeV/ $c$ .

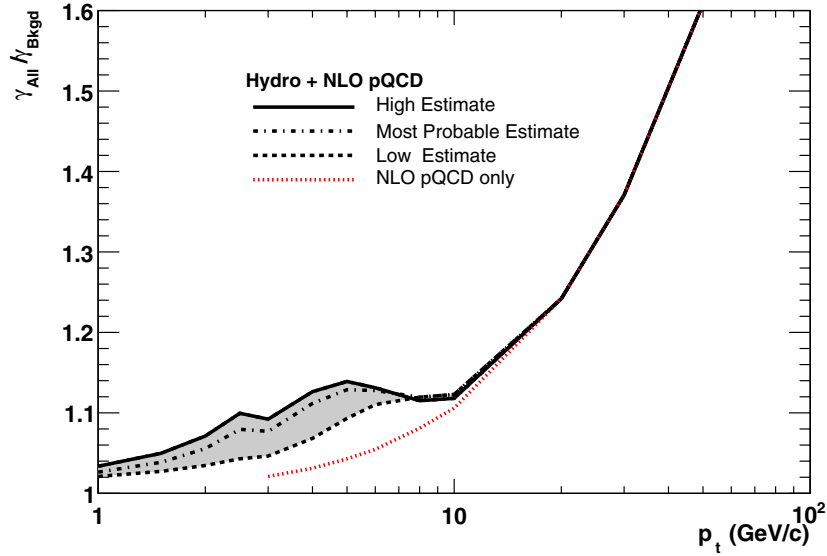


**Figure 6.410.** Ratio of all (NLO pQCD+Hydro) photons over all decay (NLO QCD+Hydro) photons as a function of  $p_t$ , calculated for the 5% most central Pb–Pb collisions at  $\sqrt{s_{NN}} = 5.5$  TeV. Predictions for primary production of prompt photons (NLO QCD) are given by the dotted line. From Ref. [967].

and identifies a photon as prompt if it appears isolated, i.e., without charged particles emitted in the same direction.

*Shower shape analysis.* The shower generated in the PHOS calorimeter by a particle can be characterized by several parameters which define the shower topology (see Section 5.5.1). They are taken as the length of the principal axes of the shower surface,  $\lambda_0$  and  $\lambda_1$ , the shower lateral dispersion, the core energy, the sphericity defined as  $(\lambda_0 - \lambda_1)/(\lambda_0 + \lambda_1)$ , the maximal energy fraction deposited in one crystal and the shower multiplicity. These parameters are found to be correlated to a large extent. To optimize the number of parameters conveying the maximal information about the shower topology, a principal component analysis is performed in which these seven parameters are transformed into seven new parameters obtained as the eigenvectors of the covariance matrix and minimizing correlations. A sufficiently precise description of the shower topology is obtained with the two most significant parameters, corresponding to the largest eigenvalues. The values of the two principal components corresponding to photon showers have a Gaussian distribution. Low, medium and high purity level photons are defined by cutting at three, two and one standard deviations, respectively, in these Gaussian distributions. For medium purity level, the prompt photon identification efficiency is about 85% for pp collisions and about 75% for Pb–Pb collisions. The contamination from misidentified neutral pions<sup>29</sup> ranges from 0% at  $E_\gamma = 40$  GeV to 40% at  $E_\gamma = 100$  GeV and the contamination from misidentified charged hadrons and neutrons ranges from 5% at  $E_\gamma = 20$  GeV to 15% at  $E_\gamma = 100$  GeV. The remaining contamination thus contributes at the same level as the prompt photon signal. Requiring higher purity photons, the rejection improves at the cost of an important identification efficiency reduction. To improve the situation, additional identification procedures are required.

<sup>29</sup> The decay photons of energetic  $\pi^0$ , above 40 GeV/c, have a small opening angle and generate a single cluster.

*Isolation cut.* Since prompt photons are produced in parton collisions<sup>30</sup> in which the final state photon and parton are emitted back-to-back, there is no hadron from the parton jet flying in the same direction as the photon. However, the underlying event generated by the heavy-ion collision may perturb this ideal topology. Two isolation algorithms are considered [980]. They are both searching for hadrons inside a cone centred around the direction  $(\eta_0, \varphi_0)$  of high- $p_t$  photon candidates ( $p_t > 20 \text{ GeV}/c$ ) identified by the SSA method. The cone radius is given by

$$R = \sqrt{(\varphi_0 - \varphi)^2 + (\eta_0 - \eta)^2}. \quad (6.151)$$

For prompt photons in pp collisions, there is almost no particle inside cones with  $R < 0.5$ , independently of the energy of the prompt photon but for  $\pi^0$  there is a clear dependence of the multiplicity inside the cone with the  $\pi^0$ 's energy. Thus, applying  $p_t$  cuts to the particles in a cone around a photon candidate helps to distinguish between prompt photons and  $\pi^0$ . Following this idea, two different selection criteria are considered to decide if a photon candidate is isolated and can be tagged as a prompt photon:

1. no hadron with  $p_t$  above a given threshold  $p_t^{\text{th1}}$  is found in the cone;
2. the sum,  $\Sigma_{p_t}$ , of the transverse momentum of all hadrons inside the cone is smaller than a given threshold  $p_t^{\text{th2}}$ .

The following optimal parameters for the prompt photon identification were deduced:

- in the case of pp collisions, a prompt photon identification probability of 100% and a  $\pi^0$  misidentification probability of 3% is obtained with  $R = 0.2$  and  $p_t^{\text{th2}} = 0.7 \text{ GeV}/c$ ;
- in the case of Pb–Pb collisions, a prompt photon identification probability of 50% and a  $\pi^0$  misidentification probability of 7% is obtained with  $R = 0.2$  and  $p_t^{\text{th1}} = 2 \text{ GeV}/c$ .

*Background and systematic errors.* The main source of background to the prompt-photon spectrum at high  $p_t$  is due to  $\pi^0$  which at  $p_t > 40 \text{ GeV}/c$  produce single clusters in PHOS. The ratio of the prompt photon and  $\pi^0$  spectra in pp collisions was taken from the NLO pQCD calculations shown in Fig. 6.408 on page 1936.

Systematic errors of the prompt photon spectrum measurements are due to several factors:

- cross section normalisation, is cancelled out in the cross section ratio, but is needed for the absolute cross section measurements;
- energy resolution and calibration uncertainties, at  $p_t = 50 \text{ GeV}/c$  the accuracy of the PHOS energy scale is  $\Delta p_t/p_t = 0.5\%$  which leads to a cross section uncertainty of 2%;
- background suppression of decay photons at lower  $p_t < 40 \text{ GeV}/c$  and  $\pi^0$  contamination at  $p_t > 40 \text{ GeV}/c$ , this uncertainty is estimated to be 8% at  $p_t = 50 \text{ GeV}/c$  in pp collisions and is expected to be small in Pb–Pb collisions due to jet quenching;
- systematic error due to reconstruction and identification efficiencies estimated to be 1%.

*Expected performance.* The statistics that can be accumulated in one standard year of running at LHC are calculated as:

$$\frac{dN}{dp_t} = \frac{d\sigma}{dp_t} \times \mathcal{L} \times \tau, \quad (6.152)$$

where  $\mathcal{L}$  and  $\tau$  are the luminosity and the experiment running time reported in Table 6.97. The cross section for pp collisions,  $\sigma_{\text{pp}}$ , is obtained from PYTHIA and the one for Pb–Pb

<sup>30</sup> This is not true for next-to-leading order processes like bremsstrahlung. However, PYTHIA predicts that such processes are suppressed compared to  $\pi^0$  production. This statement might have to be revised considering recent studies [979], which suggest that at high  $p_t$  the bremsstrahlung could be a competitive process ( $p_t < 50 \text{ GeV}/c$ ).

**Table 6.97.** Beam luminosity and running time for the ALICE experiment during a standard year of running at the LHC.

Collision	$\mathcal{L}$ (cm <sup>-2</sup> s <sup>-1</sup> )	$\tau$ (s)
pp	$3\text{--}5 \times 10^{30}$	$10^7$
Pb–Pb	$0.5 \times 10^{27}$	$10^6$

**Table 6.98.** Centrality factor and values of the nuclear overlap function for Pb–Pb collisions needed in Eq. (6.153), given for different collision centralities. Values of the nuclear overlap function are taken from Appendix I of [967].

Centrality (%)	$f_C$	$\langle T_{AA} \rangle_C$ (mb <sup>-1</sup> )
5	0.05	26.0
10	0.10	23.2
minimum bias	1.00	5.58

collisions,  $\sigma_{AA}$  is obtained by scaling  $\sigma_{pp}$  with the ‘binary scaling’ equation (nuclear effects are ignored):

$$\left( \frac{d^2\sigma_{AA}}{dp_t dy} \right)_C = \langle T_{AA} \rangle_C \times \sigma_{AA}^{\text{geo}} \times f_C \times \frac{d^2\sigma_{pp}}{dp_t dy}, \quad (6.153)$$

where  $\langle T_{AA} \rangle_C$  is the mean nuclear overlap function for the appropriate centrality class C,  $f_C$  the centrality factor and  $\sigma_{AA}^{\text{geo}} = 7745$  mb the geometrical cross section as postulated in Eq. (133) of [967] for  $\sqrt{s_{NN}} = 5.5$  TeV. The appropriate parameter values are listed in Table 6.98.

The production of prompt photons was calculated in leading order of the Standard Model, including Compton and annihilation processes ( $\gamma$ -jet events). These processes were simulated by the event generator PYTHIA 6.203 [981] in pp collisions at  $\sqrt{s} = 5.5$  TeV. The default parton distribution function, GRV 94L [982], was used. Events were generated in the energy range  $20 < p_t < 100$  GeV/c. In order to enrich the sample with events detected in PHOS, the event generation was restricted to the prompt photon pseudorapidity  $|\eta_\gamma| < 0.2$  and the azimuthal aperture to  $200^\circ < \varphi_\gamma < 340^\circ$ . Events with two jets in the final state (jet-jet events) are the most significant source of background. They were simulated by hard QCD  $2 \rightarrow 2$  processes in the leading pQCD order. These processes contribute to the background as hard fragmentation  $\pi^0$  mesons. Their decay photons may be detected in PHOS as a single electromagnetic shower and, hence, mimic prompt photons. To simulate a continuous  $p_t$ -spectrum of  $\pi^0$  mesons from 20 to 100 GeV/c, hard QCD processes were generated in the  $p_t$  range from 30 to 300 GeV/c. The generation of hard QCD processes was restricted to  $|y_{\text{parton}}| < 0.2$  and to  $|\eta_{\text{jet}}| < 0.15$ , without any azimuthal angle limitation. This more severe restriction in rapidity than in the  $\gamma$ -jet case is required to enrich events with detectable  $\pi^0$  mesons.

Pb–Pb collisions were simulated by merging pp collisions, generated by PYTHIA, with heavy-ion events produced by the HIJING 1.36 [983] event generator for Pb–Pb collisions at  $\sqrt{s_{NN}} = 5.5$  TeV and impact parameter  $b < 2$  fm. A Monte Carlo simulation was performed only for the transport of particles in the PHOS. To minimize computing time, a fast reconstruction method was applied for particles detected in the TPC and the EMCal. The EMCal response was assumed, in first approximation, to be the same as that for PHOS.

The spectra of photons detected in PHOS and identified with the SSA for pp and minimum bias Pb–Pb collisions at  $\sqrt{s_{NN}} = 5.5$  TeV are shown in Fig. 6.411. The contribution of wrongly identified  $\pi^0$  dominates the spectra over the entire  $p_t$  range. The ICM dramatically reduces this contribution to a level well below the true prompt photon signal (Fig. 6.412).

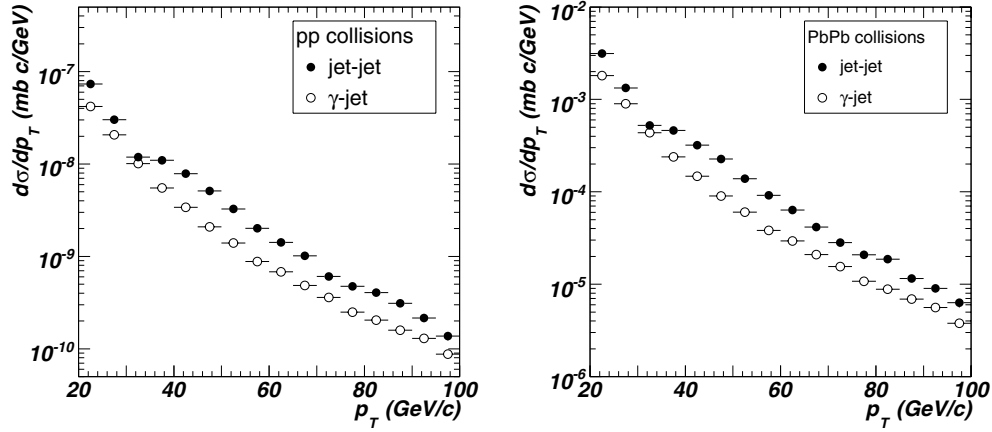


**Figure 6.411.** Spectra of prompt photons ( $\gamma$ -jet events ( $\circ$ ) and  $\gamma$ -like (single and overlapped photons from jet-jet events ( $\bullet$ )) detected in PHOS, for pp (left) and minimum bias Pb-Pb collisions (right) collisions at  $\sqrt{s_{\text{NN}}} = 5.5$  TeV .

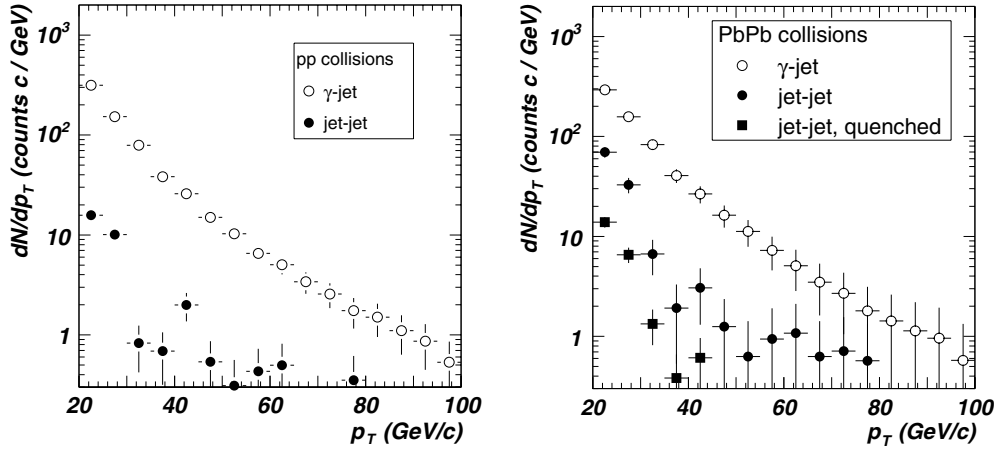


**Figure 6.412.** Spectra of prompt photons identified in ALICE during a LHC running year with statistical errors by medium purity SSA and, in the Pb-Pb case, ICM ( $R = 0.2$ ,  $p_t^{\text{th}} = 2$  GeV/ $c$ ) methods for jet-jet ( $\bullet$ ) and  $\gamma$ -jet events ( $\circ$ ) for pp (left) and Pb-Pb (right) collisions at  $\sqrt{s_{\text{NN}}} = 5.5$  TeV . For Pb-Pb collision, a quenching factor of 5 for jet-jet events is considered ( $\blacksquare$ ).

The total identified (with SSA and ICM) prompt photon spectrum  $N_{\gamma}^{\text{id}}$  is obtained by adding the identified prompt photon spectrum from  $\gamma$ -jet events and the remaining contribution of wrongly identified  $\pi^0$  from jet-jet events. It is then corrected for the various PID efficiencies: let  $N_{\gamma}$  be the original prompt photon spectrum,  $N_{\pi^0}$  the original  $\pi^0$  spectrum,  $N_h$  the original hadron spectrum,  $\varepsilon_i^{\text{id}}$  the identification probability of the particle  $i$  as a photon by SSA and  $\varepsilon_i^{\text{ic}}$  the identification probability of particle  $i$  as prompt photon by ICM, where  $i$  can be a photon, a one-cluster  $\pi^0$  or any other hadron:

$$N_{\gamma}^{\text{id}} = N_{\gamma} \varepsilon_{\gamma}^{\text{id}} \varepsilon_{\gamma}^{\text{ic}} + N_{\pi^0} \varepsilon_{\pi^0}^{\text{id}} \varepsilon_{\pi^0}^{\text{ic}} + N_h \varepsilon_h^{\text{id}} \varepsilon_h^{\text{ic}} = \zeta N_{\gamma}. \quad (6.154)$$

The correction factor  $\zeta$  is calculated for the different identification criteria (purity levels, cone sizes and  $p_t$  thresholds). The PID systematic error around the average value is calculated as the dispersion of the corrected spectra obtained for the different identification criteria. The PID

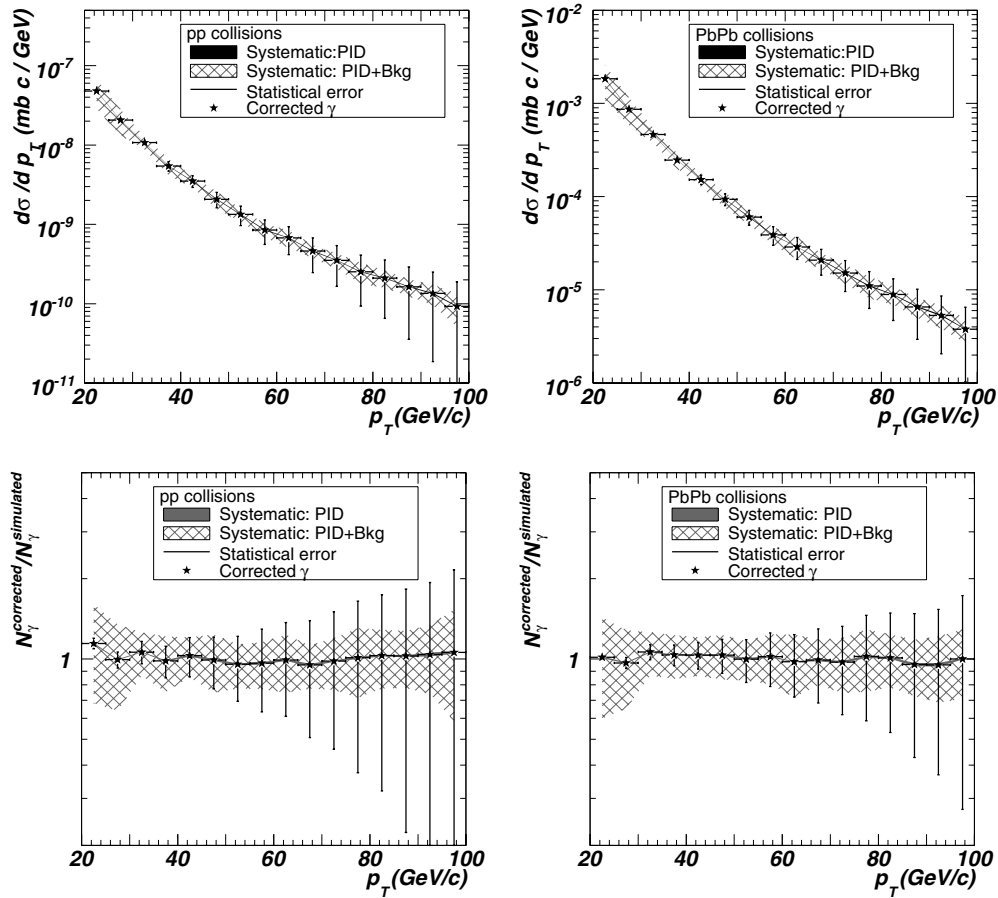


**Figure 6.413.** Upper plots: Simulated final prompt photon spectrum measured in ALICE during a LHC running year with statistical and systematic errors in pp and Pb–Pb collisions. Lower plots: Ratio of the corrected prompt photon spectrum to the original simulated spectrum in pp (left) and Pb–Pb (right) collisions.

systematic error is added quadratically to the error from the background in order to obtain the total systematic error. The statistical error is calculated from the photon statistics as  $\sqrt{N_\gamma^{\text{id}}}$ .

The final spectra of identified photons and the comparison with the original spectra are shown in Fig. 6.413. Similar spectra are obtained for Pb–Pb collisions by assuming that hadrons are quenched by a factor 5 (see Fig. 6.409), significantly reducing the systematic error.

These estimates indicate that with PHOS the photon spectrum both in pp and Pb–Pb collisions can be measured with the statistics of one standard year up to about 80–100  $\text{GeV}/c$  with a systematic error of the order of 20%.

Experimentally the fraction of decay photons present in the identified (by the shower shape analysis) prompt-photon spectrum can be estimated by analysing the photon-charged particles azimuthal correlation. The correlation functions were constructed from PYTHIA generated events. For decay photons, they exhibit a near side (ns) ( $|\theta_\gamma - \theta_{\text{hadron}}| = 0$ ) far side (fs) ( $|\theta_\gamma - \theta_{\text{hadron}}| = \pi$ ) two peak structure characteristic of jets (Fig. 6.414 right). For direct prompt photons only the far-side structure is present (Fig. 6.414 left). The fraction

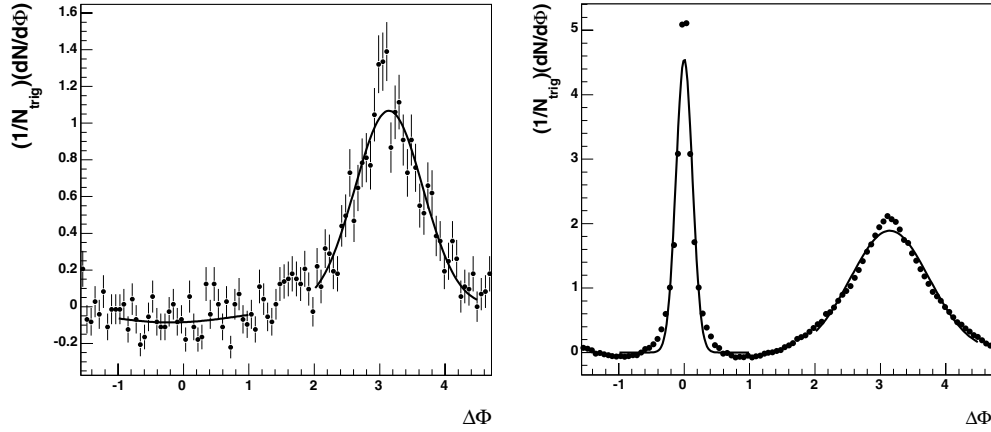


**Figure 6.414.** Azimuthal correlation for prompt photon (left) and  $\pi^0$  (right) events in pp collision at LHC energy. Photons with the highest  $p_t$  in the event are taken as trigger particles and charged particles with  $p_t > 1$  GeV/c as associated particles. The solid lines represent gaussian fits to the peak and linear fits to the background.

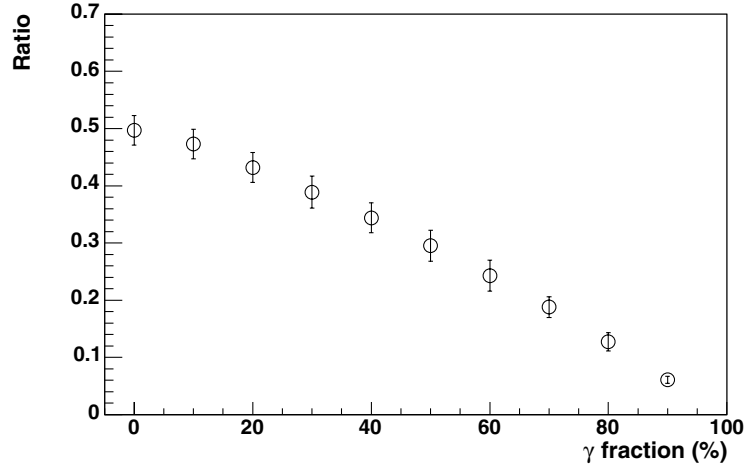


**Figure 6.415.** Ratio of near to far angle yields for various  $\gamma$  fractions in the event samples where correlation functions for direct-photon events are mixed with correlation functions of  $\pi^0$  leading particle events.

of  $\pi^0$  contamination can then be deduced from the ratio of the far side ( $R_{fs}$ ) and near side ( $R_{ns}$ ) correlation peak areas. The method is calibrated by mixing the simulated correlation function of direct prompt photon ( $\gamma$ -jet events) and  $\pi^0$  (jet-jet events) in given proportion. The resulting calibration curve of the ratio  $R_{fs}/R_{ns}$  is shown in Fig. 6.415 as a function of the fraction of prompt photons.

The method was tested in the heavy-ion environment by mixing PYTHIA  $\gamma$ -jet and jet-jet events in the proportion predicted by NLO pQCD calculation. Selecting photons in the energy range of 25 to 75 GeV and the threshold on the  $p_t$  of associated charged hadrons, either 2 or 4 GeV/c, the fraction of prompt photons to  $\pi^0$  can be estimated rather well (Fig. 6.416).

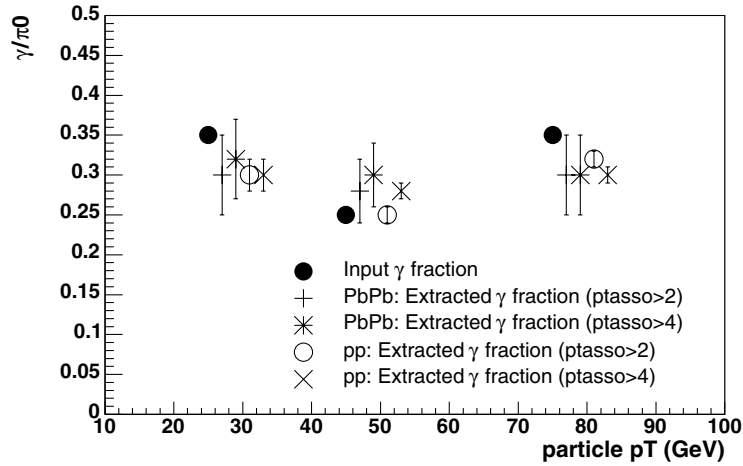


**Figure 6.416.** Extracted  $\gamma/\pi^0$  from correlation measurement. The full circle represents the input  $\gamma/\pi^0$ . Other symbols represent extracted  $\gamma/\pi^0$  values for pp and Pb–Pb cases. Results for associated  $p_t$  ( $p_{tasso}$ )  $> 2$  and  $4$  GeV/c are shown.

**6.9.2. Direct low- $p_t$  photons.** We consider here the photon spectrum in the  $p_t$  domain below a few GeV/c. The theoretical predictions for direct thermal photon spectra in relativistic heavy-ion collisions are based on two step calculations. First, the photon production rates from an equilibrated QGP and hadron gas are calculated. Second, these rates are convoluted with a model for the space–time evolution of the fireball.

**6.9.2.1. Production rates.** Several sources of thermal photons populating the low- $p_t$  part of the direct photon spectrum were identified. They include the early radiation from the equilibrated QGP, the later radiation of the hot hadron gas and the radiation induced by jets traversing the medium.

**Thermal rates from the QGP.** The thermal emission of real, energetic photons from the fireball created in relativistic heavy-ion collisions has been suggested as a promising signature for the QGP formation [984–991]. The production rates of these photons have been evaluated using perturbative QCD. To the lowest order, photons from the QGP are produced from quarks with gluon emission (quark–antiquark annihilation) or gluon absorption (Compton scattering). The production rate can be calculated from the imaginary part of the photon polarisation tensor at finite temperature [992]. An analytical result for the energetic photon production rate, assuming  $E \gg T$ , can be derived [993, 994] to the lowest order in  $\alpha_s$ :

$$\frac{dN}{d^4x d^3p} = a\alpha\alpha_s \ln \frac{0.23E}{\alpha_s T} e^{-E/T} \frac{T^2}{E}, \quad (6.155)$$

where  $\alpha$  is the electromagnetic coupling constant,  $a = 0.0281$  for  $N_F = 2$  thermalized quark flavours and  $a = 0.0338$  for  $N_F = 3$ , respectively. Additional diagrams, corresponding to bremsstrahlung and annihilation with scattering, contribute [995] to the same order  $\alpha\alpha_s$ . The bremsstrahlung contribution, assuming  $E \gg T$ , is given by

$$\frac{dN}{d^4x d^3p} = b\alpha\alpha_s e^{-E/T} \frac{T^2}{E}, \quad (6.156)$$

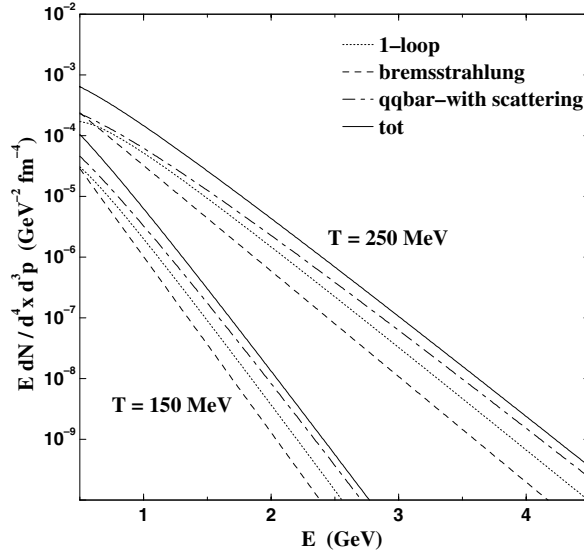


**Figure 6.417.** Hard thermal photon rates in the QGP calculated [996] for two fixed temperatures. The  $\alpha_s(T)$  parametrisation of Ref. [1004] is applied.

where  $b = 0.0219$  for  $N_F = 2$  and  $b = 0.0281$  for  $N_F = 3$  [996]. The annihilation with scattering leads to

$$\frac{dN}{d^4x d^3p} = c\alpha\alpha_s e^{-E/T} T, \quad (6.157)$$

where  $c = 0.0105$  for  $N_F = 2$  and  $c = 0.0135$  for  $N_F = 3$  [996]. The last contribution dominates for energetic photons ( $E \sim 2$  GeV) for realistic values of  $\alpha_s$  as shown in Fig. 6.417. The Landau–Pomeranchuk–Migdal effect reduces the rate of these last two processes by less than 30% in the  $p_t$  range of interest [997].

The extrapolation of a perturbative result to realistic values of the coupling constant  $\alpha_s = 0.3$ – $0.7$  is still doubtful. Therefore, it is desirable to have non-perturbative information on the photon rate. Preliminary lattice QCD calculations were performed for soft-virtual photons but they seem to be incomplete as the photon spectrum does not exhibit the expected bremsstrahlung spectrum (modified by the LPM effect) [998].

Furthermore, non-equilibrium effects are assumed to be important at RHIC and LHC energies. They were ignored here, for estimates see e.g. Refs. [999–1003].

*Thermal rates from the hadron gas.* The production of thermal photons from a hadron gas was considered using effective theories for hadronic interactions. The dominant reaction for photon energies above 1 GeV is  $\pi\rho \rightarrow \pi\gamma$  [993], in particular through the  $a_1$  resonance [1005–1007]. Further important contributions come from  $\pi\pi \rightarrow \rho\gamma$ , and from the decay of the thermal  $\omega$  meson,  $\omega \rightarrow \pi^0\gamma$  [993, 1008]. As a simple estimate, the following expression can be used for the sum of these contributions [996]

$$\frac{dN}{d^4x d^3p} \simeq 4.8T^{2.15} e^{-1/(1.35ET)^{0.77}} e^{-E/T}. \quad (6.158)$$

In Fig. 6.418 the thermal photon rate from the QGP (6.155) to (6.157) and the hadron gas (6.158) at the same temperature are compared. Note that the rates are in approximate agreement at  $T = 150$  MeV, but not at 200 MeV, due to a different temperature dependence.

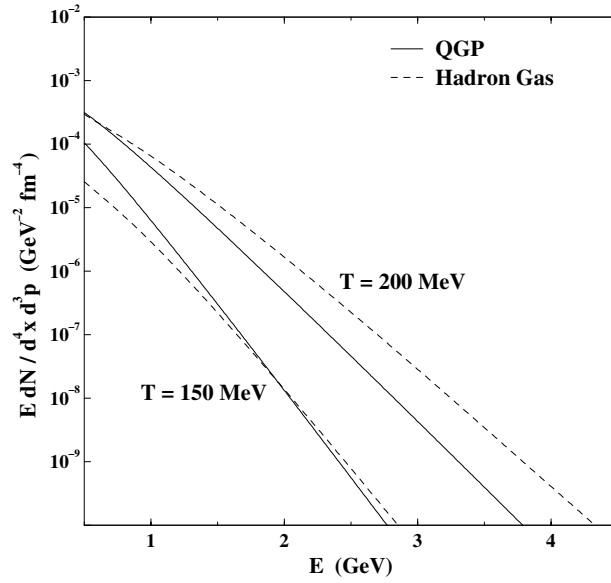


**Figure 6.418.** Comparison of the photon production rate from the QGP and the hadron gas at  $T = 150$  and  $200$  MeV ( $N_F = 2$ ).

As in the case of the QGP, the hadron gas rate is affected by uncertainties which come from various sources, which are probably as large as those from the QGP, e.g.:

- uncertainties in the form of the effective Lagrangians and their parameters;
- medium effects in the cross sections, such as dropping meson masses close to the critical temperature;
- effects from non-zero baryon density.

It is possible that the photon rates from the QGP and the hadron gas are similar in the relevant temperature regime, which is sometimes associated with the quark–hadron duality hypothesis [1009, 1010]. However, even in this case the QGP might be distinguishable from the hadron gas in the photon spectrum because of a different space–time evolution of the two phases as discussed below.

*Medium-induced photons from jets.* The multiple scatterings incurred by hard quarks and gluons in the medium induce the emission of soft gluons as well as soft photons. The contribution of the medium-induced photon bremsstrahlung at RHIC and LHC energy was calculated [1011] within a path-integral picture for the parton energy loss mechanism [1012, 1013]. The enhancement of the photon production is particularly important in the moderate energy range, below 20 GeV both at RHIC and at LHC. This enhancement of photon production in A–A collisions with respect to pp collisions at LHC energies is predicted [1011] to be as high as 50% at  $p_t \simeq 5$  GeV/c.

A similar calculation of medium-induced photon bremsstrahlung was also carried out recently by Turbide *et al* [1014] within the framework developed by Arnold, Moore and Yaffe [1015]. This calculation should, however, be valid only for relatively soft partons, with momenta of order  $T \lesssim p_t \lesssim T/g_s$  ( $g_s$  being the strong coupling constant) and neglects the possible finite size effects considered by Zakharov [1011–1013].

*6.9.2.2. Low- $p_t$  photon spectra.* Predictions for low- $p_t$  photon spectra, observed in heavy-ion experiments, follow from convoluting the rates with the space–time evolution of the fireball. For this purpose, hydrodynamical models including a phase transition, are used [1016]. These models describe the evolution of the fireball after a local equilibrium has been achieved. They assume an ideal fluid by neglecting dissipation. Under this simplifying assumption, the hydrodynamical equations can be solved using Equations Of State (EOS) for the two phases and the initial conditions such as initial time and temperature as input. In simple models, only a one-dimensional longitudinal or radial expansion is considered, whereas more sophisticated models describe the expansion in two or three dimensions. The final results depend strongly on the input parameters, such as the initial conditions which can be restricted by the hadron spectra [1017]. Alternatively, estimates of the initial conditions from partonic transport models [1018, 1019] could be used. It is also important to adopt a realistic EOS, especially for the hadron gas. For instance, an oversimplified EOS, e.g. a massless pion gas, leads to a strong first-order transition and hence to a very long-living mixed phase. Furthermore, transverse expansion and flow can lead to a flat photon spectrum even from late stages of the fireball. In addition, the high- $p_t$  tails of the spectra above 2 GeV/ $c$  depend on assumptions about the density profile of the fireball [1020]. Finally, the deviation from a chemically equilibrated QGP, which could be important at RHIC and LHC [999], must be taken into account [1021].

So far, a systematic and comprehensive hydrodynamical calculation of photon spectra from SPS to LHC energies, including the most recent rates, a realistic EOS, a reasonable procedure to fix the initial conditions, transverse expansion, and non-chemical equilibrium, is missing.

*Comparison with spectra at SPS.* Comparison of various calculations with the WA98 data [1022] lead to different conclusions. Some calculations [1024, 1025] favour a QGP contribution to explain the data. They start from very high initial temperature ( $T_0 = 335$  MeV) and very small initial time ( $\tau_0 = 0.2$  fm/ $c$ ). Using more realistic initial conditions ( $T_0 = 190$  MeV,  $\tau_0 = 1$  fm/ $c$ ) the data are underestimated, even if prompt photons are added [1026]. They conclude that owing to the uncertainties in the rates and the hydrodynamical parameters a definite conclusion is not possible at SPS energies. Other calculations [1010, 1023, 1027] can describe the data equally well with or without phase transition (see Fig. 6.419). These calculations do not take into account effects of a non-vanishing baryon density, which could suppress the contribution from the QGP because of a reduction of the initial temperature [1002] and enhance the photon rate from nucleons and other baryons [1028].

The WA98 Collaboration extended the  $p_t$  coverage of their direct photon measurements (Fig. 6.420) with low- $p_t$  results obtained via photon interferometry [1029]. The extracted radii are consistent with emission of these photons from a hadron gas phase; the correlation strength is used to extract the yield of direct photons in two intervals at low  $p_t$ . Calculations including prompt photons and thermal contributions from the QGP and the hadron phase using state-of-the-art rates are also shown [1030]. While they yield a reasonable description of the direct photon spectrum at high  $p_t$ , the calculations cannot account for the yield at low  $p_t$ .

*Predictions for RHIC and LHC.* The direct photon spectra [1031] measured by the PHENIX experiment at RHIC (Fig. 6.421) show good agreement at high  $p_t$  with predictions of pQCD calculations [970] scaled by the number of collisions. The predictions for the thermal photon spectra for RHIC and LHC indicate that the thermal QGP contribution is measurable in a narrow  $p_t$  domain of the direct-photon spectrum. However, these predictions suffer from large uncertainties coming from the unknown initial conditions. 1 + 1-dimensional hydrodynamical

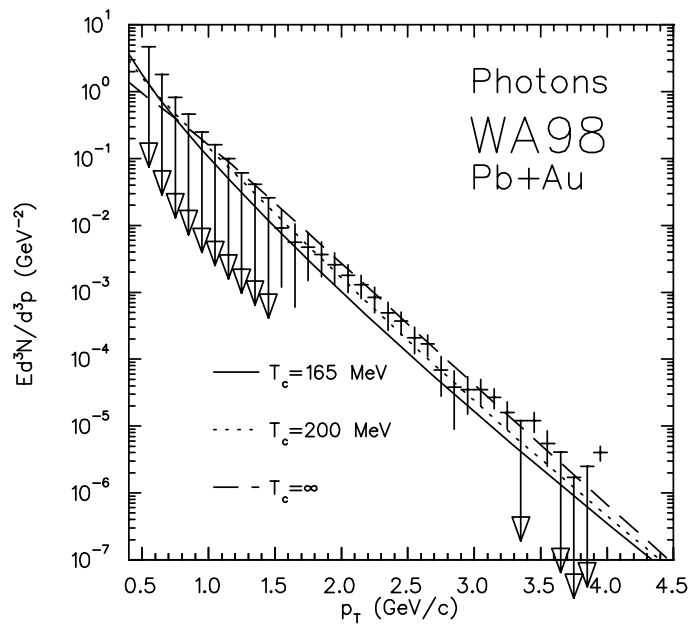


**Figure 6.419.** The photon spectrum calculated for different critical temperatures compared to WA98 data [1023].

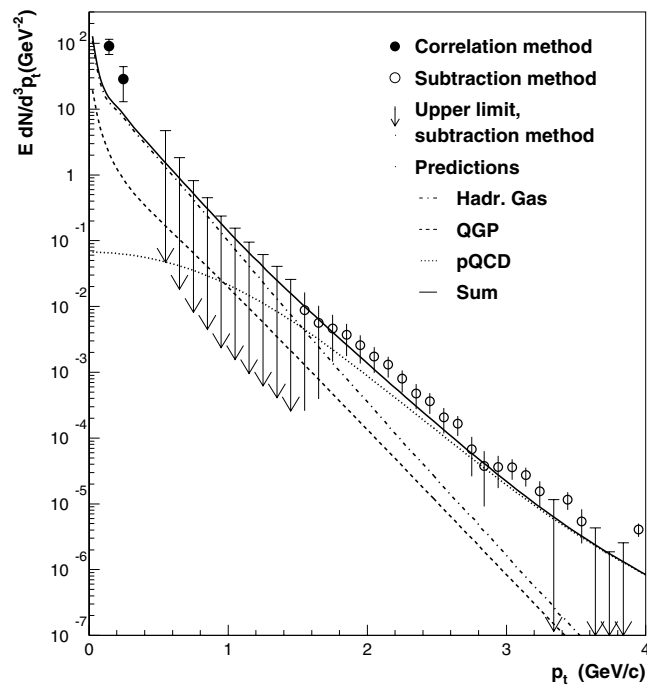


**Figure 6.420.** The photon spectrum for central Pb–Pb collisions at the SPS including recent interferometry results from WA98 [1029]. For comparison, results from a recent calculation [1030] are included.

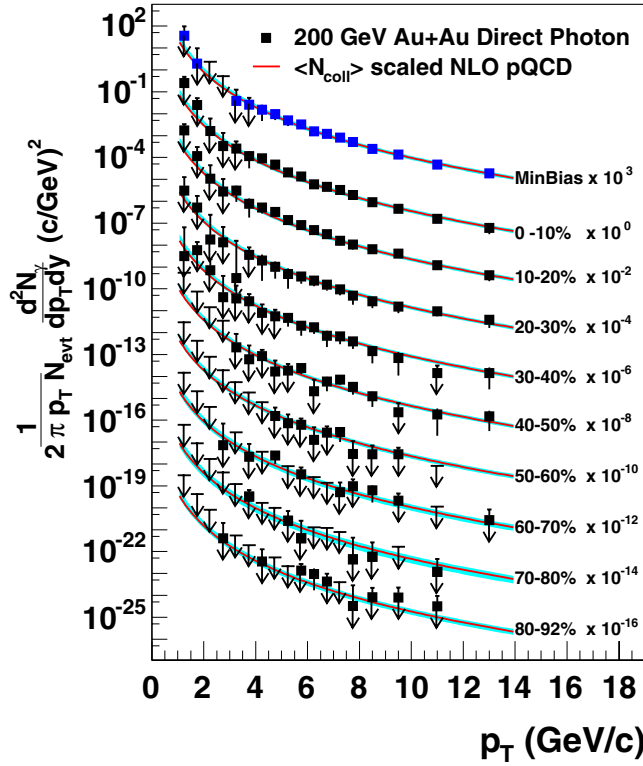


Figure 6.421. Direct photon spectra for different centralities in Au–Au collisions at RHIC [1031].

models [996] show a dominance of the QGP contribution over the hadron gas one for  $p_t > 3$  GeV/c (RHIC) and  $p_t > 2$  GeV/c (LHC), respectively.

Taking into account a transverse expansion, the strong flow in the late stages of the fireball reduces the slope of the photon spectrum from the hadron gas. But at LHC, the QGP contribution remains larger than the hadronic one in a  $p_t$  domain,  $p_t < 2\text{--}5$  GeV/c [1025, 1026, 1030, 1032], depending on the details of the calculation (see, for example, Fig. 6.422 and Fig. 6.423). Above these momenta the sum of the photons from the thermal hadron gas, enhanced by flow, and of the prompt photons dominates the photon production.

In evaluating the strength of the direct photon signal, the size of the background from decays of pions and other mesons has a non-negligible uncertainty, as hadron spectra are even more difficult to predict.

The observation of photons at the LHC should benefit from the jet quenching effect which should suppress direct photons from bremsstrahlung and the high- $p_t$  yield of decay photons. This has been investigated in [1033], where it is shown that at  $p_t = 5$  GeV/c bremsstrahlung photons and neutral pions are similarly suppressed. Hence, the unaltered thermal production becomes more easily observable. The predicted [1030, 1033] magnitude of the signal-to-background ratio for direct photons at LHC at  $p_t = 5$  GeV/c is

$$\frac{N_\gamma^{\text{thermal}}}{N_\gamma^{\text{total}}} \approx 10 - 25\%,$$

decreasing for lower transverse momenta.

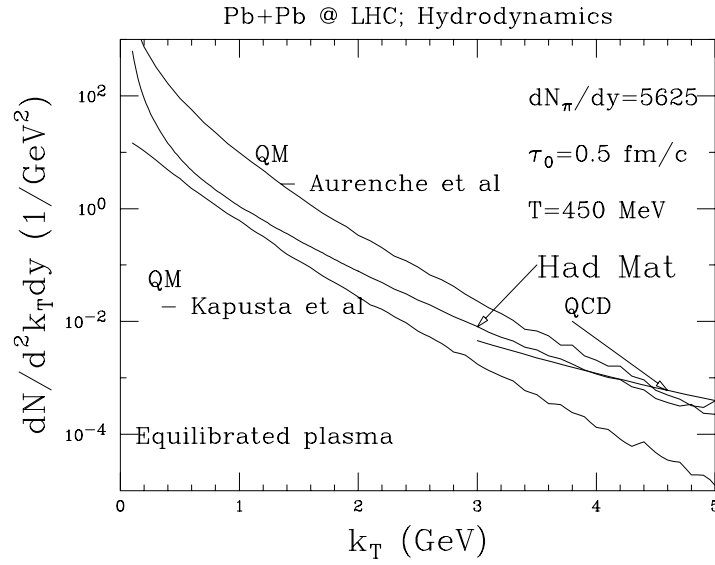


**Figure 6.422.** Prediction [1026] for the photon production in central Pb–Pb collisions at  $\sqrt{s_{NN}} = 5.5 \text{ TeV}$ . Contributions from the hadronic matter (in mixed phase and hadronic phase) and the quark matter (in QGP phase and the mixed phase) are shown.

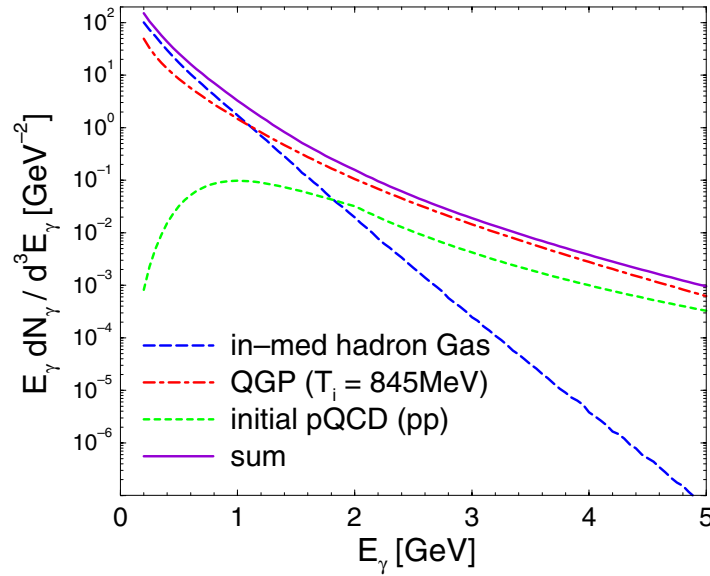


**Figure 6.423.** Predicted [1030] photon spectrum from various thermal sources in central Pb–Pb collisions at  $\sqrt{s_{NN}} = 5.5 \text{ TeV}$  at central rapidity ( $-0.5 < y < 0.5$ ). The charged particle rapidity density is taken to be 3000.

*Current theoretical status.* The calculation of direct photon spectra in relativistic heavy-ion collisions relies so far on the perturbative estimate of the photon production rates from the QGP and the hadron gas and their convolution with the space–time evolution of the fireball within hydrodynamical models. The main uncertainty in the computation of the thermal QGP rate comes from the complexity of thermal effects in QCD. The estimate of the rate from the

hadron gas depends on assumptions about the thermalized hadron species and their interactions and the role of medium effects. It is estimated that the predicted rates are correct within a factor of 2–5. In particular at LHC, where the initial temperature is large (the effective  $\alpha_s$  is reduced compared to SPS and RHIC) and where the baryon density at mid-rapidity is small, the estimates of the rates from the QGP as well as from the hadron gas should be more reliable.

The predictive power of hydrodynamical calculations depends mainly on uncertainties from the initial conditions and assumptions about the EOS of the hadron gas. A deviation from a chemically equilibrated QGP at RHIC and LHC may play a significant role. A systematic investigation, taking into account all these aspects, is still missing. A transport approach, treating the distribution functions and the particle production self-consistently and describing the entire evolution of the fireball from the cold nuclei to freeze-out would be desirable.

*6.9.2.3. Experimental method.* The major detector involved in the measurements of low- $p_t$  direct photons is PHOS with the complementing detectors (Charged Particle Veto, CPV and/or preshower) as discussed in Section 5.5.1. In the high-multiplicity environment of heavy-ion collisions at the LHC, the individual identification of direct photons is extremely difficult. Low- $p_t$  direct photons are therefore extracted on a statistical basis as was done successfully for the first time by the WA98 Collaboration in Pb–Pb collisions at the SPS [1034]. The same method was also applied successfully in Au–Au collisions at RHIC [1031].

*Statistical methods.* To obtain the direct photon spectrum the following steps are performed:

1. The raw photon spectrum is accumulated after application of the photon identification criteria (such as transverse shower size) to the showers observed in the detector.
2. The raw photon spectrum is then corrected for:
  - (a) contamination by charged particles,
  - (b) conversions, and
  - (c) contamination by neutral hadrons.
3. A correction for the identification efficiency is applied. This includes all effects of the detector response such as distortions by shower overlap, dead and bad modules, and energy resolution.
4. The spectrum is corrected for geometrical acceptance.

Neutral pions are reconstructed via their  $\gamma\gamma$  decay mode (98.8% branching ratio). A similar procedure to that for the photon measurements is followed:

1. Invariant-mass spectra are accumulated for all photon pairs for each pair  $p_t$  bin.
2. The photon-pair combinatorial background is estimated by event-mixing and then subtracted from the real-pair spectra.
3. The yield in the  $\pi^0$  mass peak is extracted to obtain the raw neutral pion  $p_t$  spectra.
4. These are then corrected:
  - (a) for conversions,
  - (b) for the  $\pi^0$  identification efficiency, and
  - (c) for geometrical acceptance.

An analogous procedure is followed to extract spectra of  $\eta$  mesons and possibly heavier hadrons having radiative decays.

The final measured inclusive photon spectra is then compared to the calculated background photon spectra to extract the photon excess beyond that from long-lived radiative decays. The background calculation is based on the measured  $\pi^0$  spectra and those of the  $\eta$

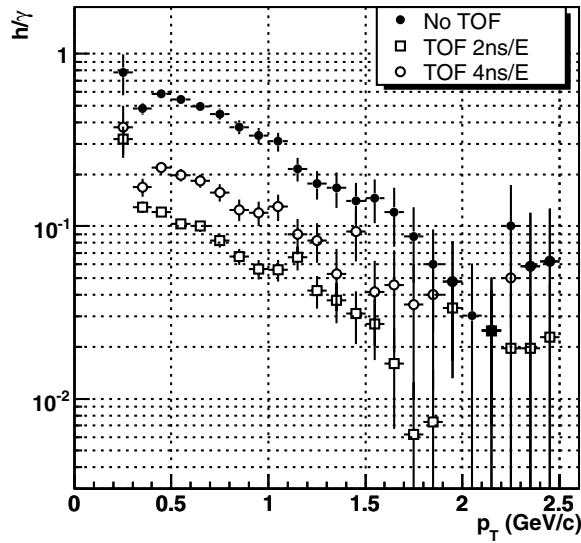


**Figure 6.424.** Ratio of misidentified hadrons to measured photons as a function of  $p_t$  for different time-of-flight selections for particle identification.

and heavier hadrons, as far as possible. The spectra of those hadrons not directly measured is taken from the combined information available from theory and earlier measurements at lower energies. Measurements in other detectors of the ALICE experiment help to better constrain the yields of all contributing hadrons.

*Sources of systematic error and uncertainty.* The expected performance relies heavily on the particle identification capabilities of the PHOS detector. Once inclusive photons, neutral pions and  $\eta$  mesons are identified with sufficient accuracy, the identification of direct photons implicitly follows.

The sources of systematic error of the standard extraction method can be divided in three categories:

1. errors on the inclusive photon measurement;
2. errors on the inclusive neutral hadron measurement;
3. errors on the theoretical assumptions entering the background calculations.

The dominant sources of the systematic error are the detection efficiencies for both inclusive photons and neutral mesons, the contamination of the measured inclusive photons from charged hadrons, anti-neutrons and non-vertex background, the neutral meson yield extraction and the statistical error of the  $\eta$  measurement.

The contamination from misidentified charged hadrons and (anti-)neutrons was estimated from simulations of the detector response and HIJING generated events. Figure 6.424 shows the ratio of hadrons misidentified as photons to the correctly measured photons as a function of measured transverse momentum. Results were obtained with different photon identification cuts, i.e. either making no use of the TOF information in PHOS (solid points), or including the TOF signal and assuming two different values of the TOF performance (open points). When using the TOF signal the contamination from hadrons is below 5% for  $p_t > 1.5$  GeV/c and decreases with increasing  $p_t$ . Even a 50% uncertainty of the hadron yield would thus lead to an uncertainty on the photon yield of less than 2.5%.

**Table 6.99.** Expected systematic uncertainties (%) on the direct photon measurement for two values of the photon transverse momentum.

	$p_t = 1.5 \text{ GeV}/c$	$p_t = 5 \text{ GeV}/c$
$\gamma$ detection	3	3
$\pi^0$ detection	5	5
$\eta$ detection	3	3
Hadron contamination	2.5	1
Non-vertex background	2	1
Total systematic error	7.3	6.7

Another source of potential systematic uncertainties are secondary interactions of produced hadrons in detector material, which may lead to additional photon production mainly via the decay of neutral mesons. As for the contamination from hadrons, this non-vertex background becomes important at very low  $p_t$ . Especially for these low- $p_t$  photons the detection via conversion may prove very useful (see next section).

The major contributions to the expected systematic uncertainty on the direct photon measurement are summarized in Table 6.99. Estimates of the error on  $\gamma$ ,  $\pi^0$  and  $\eta$  detection are based on simulation studies with the PHOS detector and on experimental experience within the WA98 experiment.

**6.9.3. Low-mass lepton pairs.** The measurement of correlated  $e^+e^-$  pairs provides alternative experimental means to measure the photon spectrum, in particular at very low  $p_t$  where the background in real photon measurement is large. It has the advantage of providing a measurement of better quality because neutrons, which constitute a main background in calorimetric measurement, do not contribute to the background. In addition, the topographic selection of the lepton pairs provides an almost background-free measurement. The price to pay is that lepton pairs are produced with a reduced cross section which can, however, be partially recovered by the larger acceptance coverage of the central barrel tracking system of ALICE ( $|\eta| \leq 1.4$  and full azimuth) as compared to the acceptance covered by PHOS ( $|\eta| \leq 0.12$  and  $\Delta\varphi \leq 100^\circ$ ). The main contributions to the dilepton spectrum in this mass region are from the following processes:

1. conversion of real photons in the material of the ALICE beam pipe, ITS and TPC;
2. production of virtual photons;
3. Dalitz decay of  $\eta$ -mesons.

We shall examine next the contribution of each of these processes to the dielectron spectrum expected to be measured by ALICE.

**6.9.3.1. Conversion electron pairs.** Photons produced in the collision can be converted into dielectron pairs when passing through the ALICE vertex tracker. The material budget between the interaction point and the first half of the TPC (conversions occurring in the second half of the TPC can hardly be identified through  $V^0$  reconstruction) and for straight tracks perpendicular to the detector surface is 0.2% radiation length for the Be beam-pipe, 7% for ITS [1] and 1.75% for the TPC [393]. This amount of material leads to a photon conversion probability,  $P_c$ , of 6.3% [1035]. Electrons are tracked and identified by the ALICE central tracking system, TPC and TRD. The track-finding efficiency at the trigger level  $\varepsilon_T$  is 63% (including acceptance) for a charged particle rapidity density of 4000 [836]. The identification efficiency  $\varepsilon_{ID}$  is 90% with a charged pion rejection factor of 100 for electrons with transverse momentum larger than 3 GeV/c [836]. Conversion pairs are further identified by their displaced vertex

**Table 6.100.** Values of the various efficiencies entering the calculation of the conversion electrons identification.

		$\varepsilon_T$	$\varepsilon_{ID}$	$\varepsilon_M$	$\varepsilon_V^0$	$\varepsilon_{geo}$
Central Barrel	A–A	0.63	0.90	0.85	0.80	–
	pp	0.90	0.90	0.85	1.00	–
PHOS	AA	–	0.30–0.80 <sup>a</sup>	0.95	–	0.03
	pp	–	0.30–0.95	0.95	–	0.03

<sup>a</sup>From 1 GeV/c to 20 GeV/c electrons.

(between the interaction point and half of the TPC) with an efficiency  $\varepsilon_{V^0}$ , and by applying an invariant mass cut  $\varepsilon_M$  at two sigma from zero,  $0 < M_{e^+e^-} < 0.04 \text{ GeV}/c^2$ . The efficiency  $\varepsilon_{CB}$  for conversion pair detection and identification with the central tracking system is thus

$$\varepsilon_{CB} = P_c \times \varepsilon_T^2 \times \varepsilon_{ID}^2 \times \varepsilon_M \times \varepsilon_{V^0}.$$

The values of the various efficiency parameters are summarized in Table 6.100.

The main source of background in this measurement is due to charged pions misidentified as electrons by the TRD detector and which by chance form, with another particle identified as an electron, from the high multiplicity environment, a correlated pair with zero invariant mass and a displaced vertex. To estimate this contribution to the low-mass dielectron measurement, the NLO pQCD prediction for  $\pi^0$  production [1036], multiplied by 2, was taken. The combinatorial contribution to the invariant-mass region of interest was evaluated for a charged particle density of 4000 at mid-rapidity; among those, 80% are charged pions. For the measurement with the central barrel detectors (TPC and TRD) the TRD electron PID reduces the charged-pions background by a factor of 100. The overall reduction by the global central tracking is 1000, making use of the TPC identification capability through  $dE/dx$  measurement. In addition, the cut on  $V^0$  reduces this contribution by 90%.

PHOS can complement the measurement of conversion electrons in the low-energy part of the photon spectrum. It is taking advantage of a lower contamination level in the particle identification but at the cost of much reduced statistics because of the limited acceptance. The electron identification efficiency that can be achieved by combining the PHOS and CPV identification capabilities varies from 30% at 1 GeV/c to 80% at 20 GeV/c [1037]. The contamination due to any particle wrongly identified as an electron stays below the 2% level. The acceptance factor  $\varepsilon_{geo}$  of PHOS is 3% of  $4\pi$  ( $|\eta| < 0.12$ ,  $\Delta\varphi = 100^\circ$ ). The efficiency  $\varepsilon_{PHOS}$  for conversion-pair detection and identification with PHOS is thus

$$\varepsilon_{PHOS} = P_c \times \varepsilon_{ID}^2(p_t) \times \varepsilon_{geo}^2 \times \varepsilon_M.$$

The values of the various efficiency parameters are summarized in Table 6.100. The overall efficiency varies from  $1.1 \times 10^{-7}$  at  $p_t^{e^+e^-} = 1 \text{ GeV}/c$  to  $1.6 \times 10^{-5}$  at  $p_t^{e^+e^-} = 20 \text{ GeV}/c$ . The main source of background in this measurement is due to wrongly identified charged hadrons which by chance correlate at zero invariant mass.

The statistics that can be accumulated within a standard year of data taking ( $\mathcal{L}_{int}^{AA} = 0.5 \times 10^{33} \text{ cm}^{-2}$ ,  $\mathcal{L}_{int}^{pp} = 10^{37} \text{ cm}^{-2}$ ) was calculated similarly to Eq. (6.153) for pp collisions and for the 5% most-central Pb–Pb collisions at  $\sqrt{s_{NN}} = 5.5 \text{ TeV}$ :

$$\frac{dN^{e^+e^-}}{dp_t} = \mathcal{L}_{int} \times \int_{\Delta y} \frac{d^2\sigma_{AA}^{e^+e^-}}{dp_t dy} dy, \quad (6.159)$$

$$\frac{d^2\sigma_{AA}^{e^+e^-}}{dp_t dy} = \langle T_{AA} \rangle \times \sigma_{AA}^{geo} \times f_C \times \frac{d^2\sigma_{pp}^\gamma}{dp_t dy} \times \varepsilon_{CB/PHOS}. \quad (6.160)$$

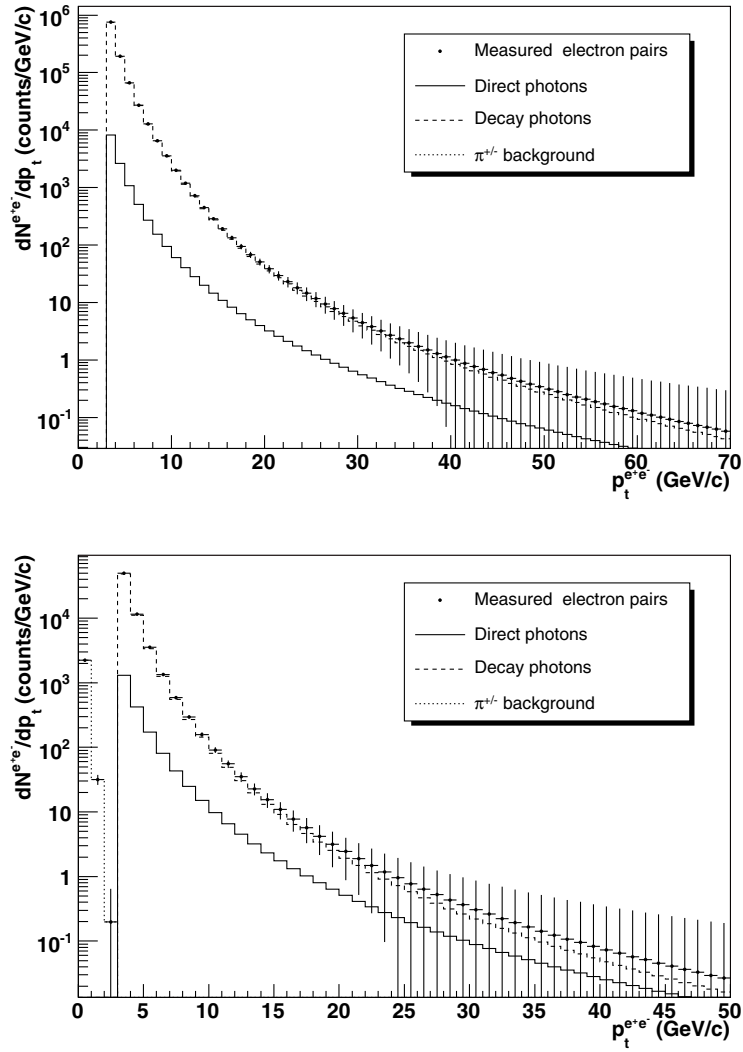


**Figure 6.425.** Photon spectrum reconstructed in the ALICE central tracking system (TPC and TRD) from the measurement of conversion electron pairs in pp at  $\sqrt{s} = 5.5$  TeV (top) and central Pb–Pb at  $\sqrt{s_{NN}} = 5.5$  TeV (bottom) collisions at LHC energies. Photons convert in the ITS material and the electron pairs are detected and identified by the ALICE central tracking system (TPC and TRD). Electron pairs with invariant mass  $0 < M_{e^+e^-} < 0.04$  GeV/ $c^2$  were considered. The statistics correspond to one standard year of data taking. The error bars indicate statistical errors only.

The pp prompt-photon spectrum was taken from NLO pQCD predictions, see Section 6.9.1.2. The decay photon spectrum was calculated from a NLO pQCD prediction from the ratio  $\gamma_{\text{prompt}}/\pi^0$  as discussed in Section 6.9.1.2. A quenching factor of 5 for  $\pi^0$  was assumed for Pb–Pb collisions as indicated by the RHIC data.

These estimates for pp and central Pb–Pb collisions (see Fig. 6.425 for the central barrel acceptance and Fig. 6.426 for the PHOS acceptance) indicate that statistically significant data can be collected, within the estimation of the detectors performance discussed above, for conversion electron-pairs transverse momenta below 25 (40) GeV/ $c$  in the central barrel

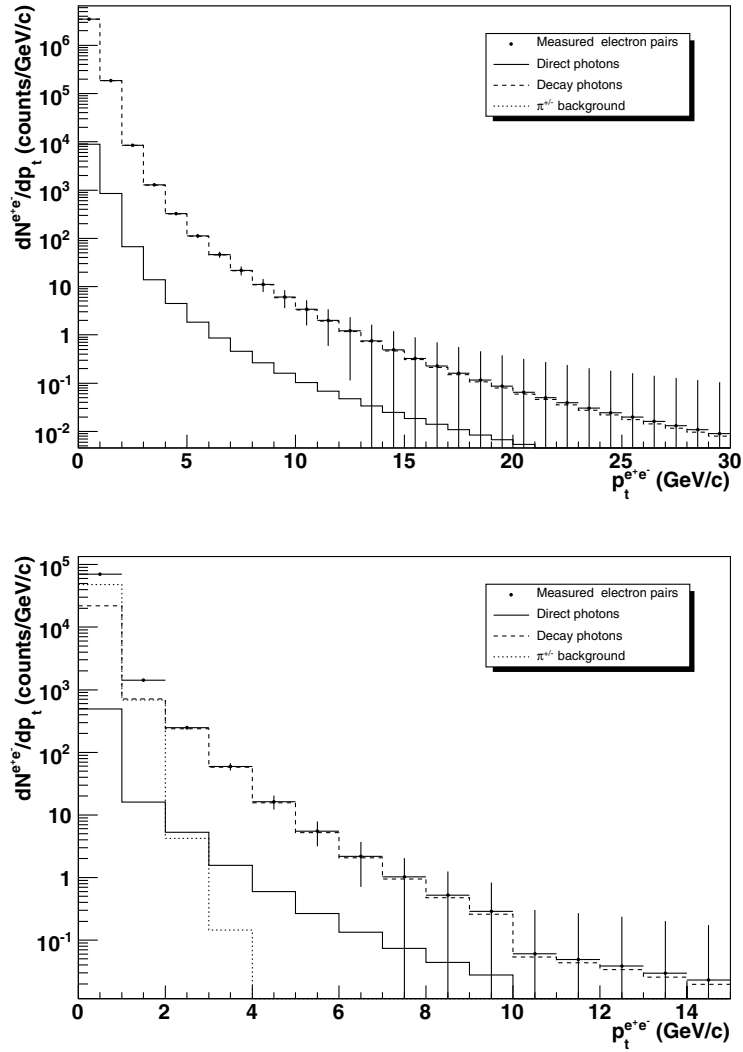


**Figure 6.426.** Photon spectrum reconstructed in PHOS from the measurement of conversion electron pairs in pp at  $\sqrt{s} = 5.5$  TeV (top) and in central Pb–Pb collisions at  $\sqrt{s_{NN}} = 5.5$  TeV (bottom). Photons convert in the ITS material and the electron pairs are detected and identified by PHOS. Electron pairs with invariant mass  $0 < M_{e^+e^-} < 0.04$  GeV/ $c^2$  were considered. The statistics correspond to one standard year of data taking. The error bars indicate statistical errors only. In the pp spectrum, the contribution from the charged pions is out of scale.

detectors and below 7 (15) GeV/ $c$  in PHOS for Pb–Pb (pp) collisions. The expected signal-to-background ratio changes with increasing  $p_t$  from  $2 \times 10^{-2}$  to  $2 \times 10^{-1}$  ( $10^{-2}$  to  $2 \times 10^{-1}$ ) for the central barrel measurement and from  $10^{-2}$  to  $3 \times 10^{-2}$  ( $3 \times 10^{-3}$  to  $2 \times 10^{-2}$ ) for the PHOS measurement in Pb–Pb (pp) collisions.

**6.9.3.2. Virtual photons.** Because of the dominant contribution of decay photons (mainly  $\pi^0 \rightarrow \gamma\gamma$  and  $\eta \rightarrow \gamma\gamma$ ) to the measured photon spectrum, one may consider instead of real photon production, the emission of virtual photons (lepton pairs). Considering, for example, electron pairs in the mass range  $M_{e^+e^-} = [0.2, 0.6]$  GeV/ $c^2$ , part of this background can be

eliminated: the lepton pairs from the Dalitz decays of the  $\pi^0$  and most of the  $\eta$  are below this mass range; the vector mesons decay  $\rho, \omega, \phi \rightarrow e^+e^-$  populates a higher mass range.

From the theoretical point of view, the production rate of low-mass lepton pairs at relatively large transverse momentum is very similar to that of real photons. A rough estimate of Drell–Yan pair production, integrated over a given mass range, is given [1038], with a good accuracy, by the simple relation

$$\frac{d\sigma^{e^+e^-}}{dp_t dy} \simeq C_{e^+e^-} \alpha \frac{d\sigma^\gamma}{dp_t dy}, \quad (6.161)$$

where  $C_{e^+e^-} \sim 0.3$  for  $0.2 \text{ GeV}/c^2 < M_{e^+e^-} < 0.6 \text{ GeV}/c^2$ , valid in the range  $2 \text{ GeV}/c < p_t < 100 \text{ GeV}/c$ , and  $C_{e^+e^-} \sim 0.2$  for  $1 \text{ GeV}/c^2 < M_{e^+e^-} < 3 \text{ GeV}/c^2$ , valid in the range  $4 \text{ GeV}/c < p_t < 100 \text{ GeV}/c$ . These estimates refer only to the prompt production mechanism.

The statistics which can be accumulated in a standard year of data taking with the ALICE central tracking system (Fig. 6.427 and with PHOS (Fig. 6.428) for pp and central Pb–Pb collisions was estimated as in the previous section combining Eqs (6.159), (6.160) and (6.161). Significant statistics can be accumulated with the ALICE central barrel tracking detectors for dielectrons  $p_t$  up to about 11 GeV/c in pp and up to about 8 GeV/c in Pb–Pb. The signal to background ratio rises with  $p_t$  from 3 to 20 in the Pb–Pb measurement and from 5 to 20 in the pp measurement. With PHOS, the poor efficiency to cleanly identify electrons in the large charged pions background does not allow one to perform any significant measurement in Pb–Pb. In pp the PHOS acceptance limits the measurement to transverse momenta below 2 GeV/c with a signal-to-background ratio of about 4. The main background in this measurement comes, in Pb–Pb collisions, from charged-pions wrongly identified as electrons by the TRD. The final estimates (see Fig. 6.427) were obtained with the same assumption as the one used to calculate the background to the conversion electrons measurement but with the appropriate invariant mass range. The results indicate that in the low-mass dielectron spectrum wrongly identified charged pions contribute at the same level as electrons from virtual photons, the latter becoming dominant beyond 5 GeV/c. The signal-to-background for the measurement with the central tracking system, respectively PHOS, ranges from 0.1, respectively 0.001, to 1.0, respectively 0.02, in Pb–Pb when increasing the transverse momentum and is close to 1 in pp.

**6.9.3.3. Dalitz electron pairs.** For low-invariant-mass dielectrons, the background to the measurement of dielectrons from the decay of massive photons, comes mainly from the  $\pi^0$  and  $\eta$  Dalitz decay,

$$\begin{aligned} \pi^0 &\rightarrow e^+e^- + \gamma, \\ \eta &\rightarrow e^+e^- + \gamma. \end{aligned}$$

The branching ratio of other decay channels of  $\pi^0$  and  $\eta$  involving electron pairs is small compared to the Dalitz branching ratio of 1.2% and 1.6%, respectively, for  $\pi^0$  and  $\eta$ . The differential branching ratio for Dalitz decay for a dilepton mass  $M$  is [1039]

$$\frac{d\Gamma^{(a)}}{dM} = \frac{4\alpha}{3\pi} \frac{\Gamma_{(a)\rightarrow 2\gamma}}{M} \left(1 - \frac{M^2}{m_a^2}\right) \left(1 + \frac{2m_e^2}{M^2}\right) \left(1 - \frac{4m_e^2}{M^2}\right)^{1/2},$$

where the index  $a$  refers to  $\pi^0$  or  $\eta$  meson.

In the dielectron invariant-mass region,  $M_{e^+e^-} = [0.2, 0.6] \text{ GeV}/c^2$ , where the virtual photon analysis is performed, only the  $\eta$  Dalitz decay is contributing (see Fig. 6.429). This  $\eta$  Dalitz contribution has been estimated from NLO pQCD cross section prediction for the

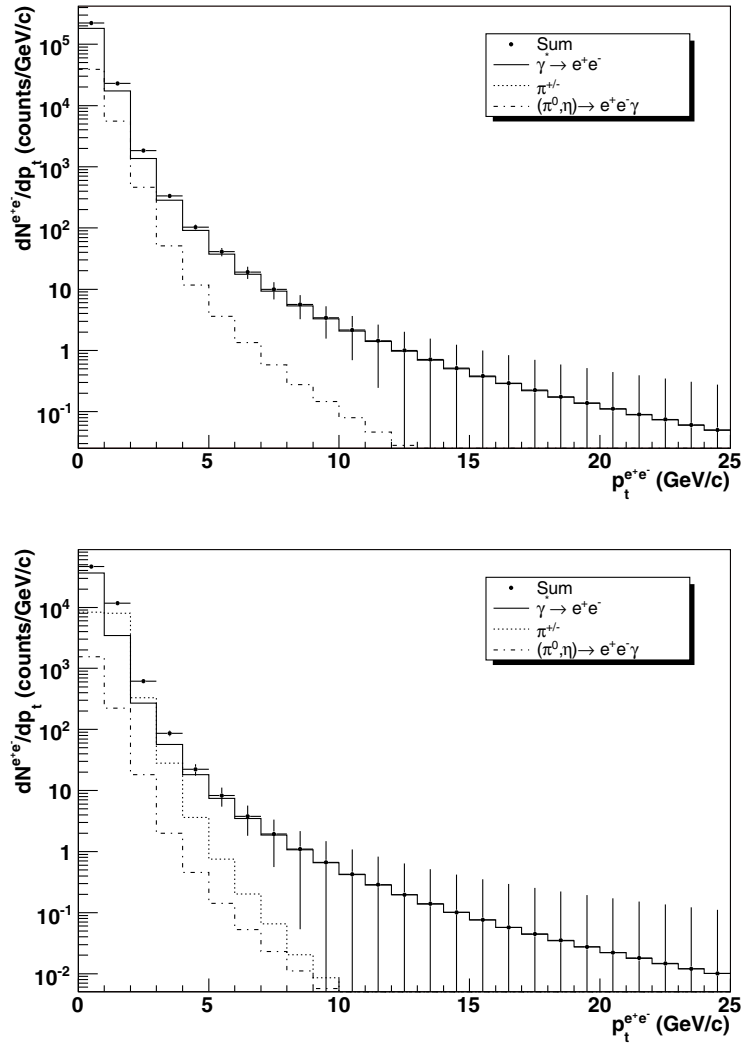


**Figure 6.427.** Virtual photon spectrum reconstructed from the measurement in pp at  $\sqrt{s} = 5.5$  TeV (top) and in central Pb–Pb collisions at  $\sqrt{s_{NN}} = 5.5$  TeV (bottom) collisions of electron pairs with mass in the range 0.2 and 0.6 GeV/ $c^2$ . Electron pairs are detected and identified by the ALICE central tracking system (TPC and TRD). The statistics represent one standard year of data taking. The error bars indicate statistical errors only. In the pp spectrum, the contribution from Dalitz decay is out of scale.

$\pi^0$  production [1036] and applying transverse mass scaling  $\eta/\pi^0 = 0.45$  which was shown to be valid at RHIC for all centralities. The contribution from neutral mesons Dalitz decay (see Fig. 6.427) is about one order of magnitude below the virtual photon signal in pp and Pb–Pb collisions.

This preliminary study indicates that the measurement of electron pairs, either from the conversion of photons or from Drell–Yann pairs, will provide an interesting alternative to the photon measurement as it is almost background free. However, statistics will limit such measurements in the low- $p_t$  domain of the photon spectrum.

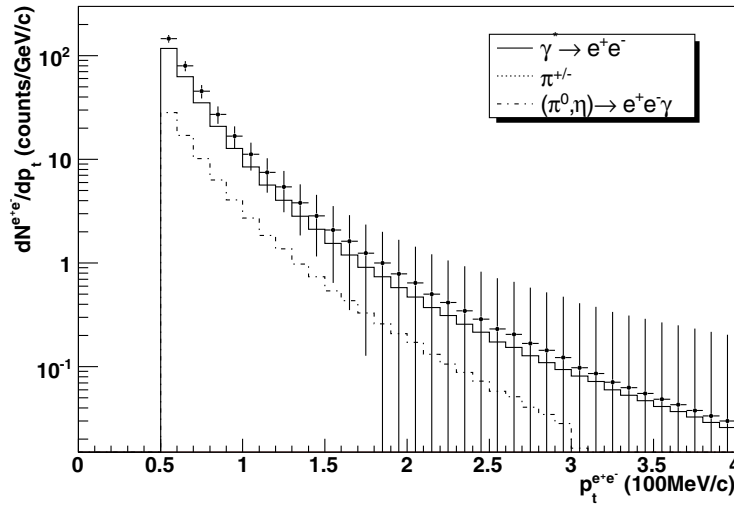


**Figure 6.428.** Virtual photon spectrum reconstructed from the measurement in pp collisions of electron pairs with mass in the range 0.2 and 0.6  $\text{GeV}/c^2$ . Electron pairs are detected and identified by PHOS. The statistics represent one standard year of data taking. The error bars indicate statistical errors only. The contribution from the  $\eta$ -Dalitz decay is out of scale.

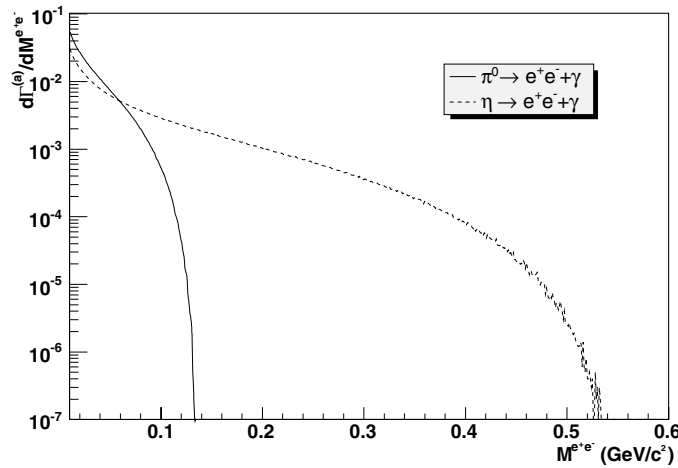


**Figure 6.429.** Differential branching ratio for Dalitz decay of  $\pi^0$  and  $\eta$  meson as a function of the dielectron invariant mass.

**6.9.4. Photon-jet correlations.** Because of the large cross sections available for hard processes at LHC, exclusive jet measurements will be within reach. In particular, jet topology (jet shape, jet *heating*, fragmentation functions, etc.) will be measured to study the redistribution of the energy of the jet traversing the nuclear medium in Pb-Pb collisions [1040]. Such studies require the identification of jets and the measurement of the parton or jet energy, ideally before and after quenching, as accurately as possible. A very attractive method of performing these studies is to tag jets with prompt photons emitted in the opposite direction to the jet direction. The dominant processes for such events are  $g + q \rightarrow \gamma + q$  (Compton) and  $q + \bar{q} \rightarrow \gamma + g$  (annihilation), although recent theoretical studies show that

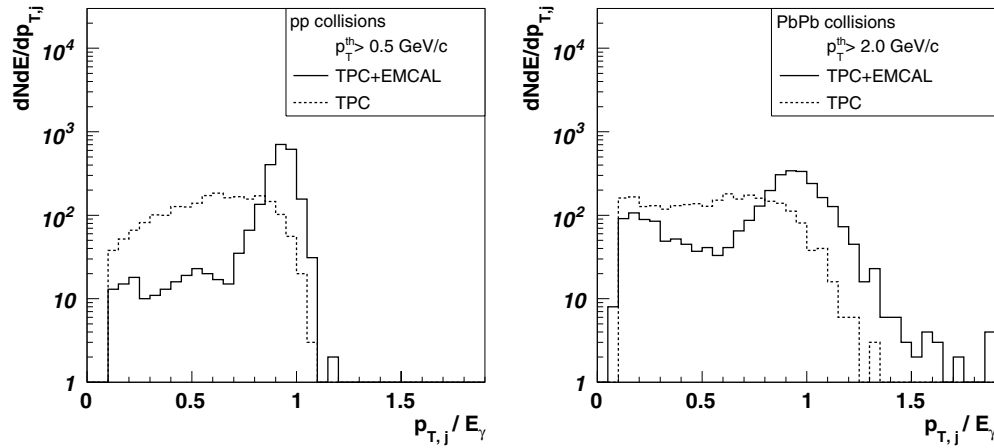


**Figure 6.430.** Distribution of the ratio  $p_{t,j}/E_{\gamma}$  for 40 GeV  $\gamma$ -jet events simulations in the case of pp (left) and Pb-Pb (right) collisions. A jet cone of  $R = 0.3$  and a jet particle threshold of  $p_t > 0.5$  GeV/c are assumed for pp and  $p_t > 2.0$  GeV/c for Pb-Pb collisions. Results for the setups without EMCal (dashed line) and with EMCal (solid line) are given.

for jets with transverse momentum smaller than 50 GeV/c the higher order bremsstrahlung process contributes significantly to the photon spectrum [979]. Photons emerge almost unaltered from the dense strongly-interaction medium and provide a measurement of the original energy and direction of the parton emitted in the opposite direction. Medium effects will be identified through modifications of the fragmentation function, i.e., the redistribution of the jet energy rather than by its reduction.

**6.9.4.1. Experimental method.** A  $\gamma$ -tagging algorithm was developed [980] to identify photon-jet events and to reconstruct the hadron jet features in both pp and Pb-Pb collisions. The steps of the algorithm are the following:

1. Search in each event for the most energetic prompt photon identified in PHOS.
2. Search for the jet leading particle (charged hadron or neutral pion with the highest  $p_t$  value) detected by the central tracking system or EMCal and emitted almost back-to-back to the photon in azimuthal angle, i.e., with  $\Delta\phi$  close to  $180^\circ$ ,  $0.9\pi < \Delta\phi < 1.1\pi$ . An additional condition to be satisfied by the leading particle is that its  $p_t$  value must be at least 10% of the photon energy.
3. Reconstruct the jet as the ensemble of all particles contained inside the cone defined by Eq. (6.151) with the axis aligned along the leading particle direction. We have taken here  $R = 0.3$  and 0.5 GeV/c as the particle  $p_t$  threshold.
4. Finally, the event is identified as a photon-jet event if the value of the ratio of the reconstructed energies of the jet to the prompt photon energy is in a pre-defined window. A photon-jet event observed in the set-up including EMCal is well identified if the ratio  $p_{t,j}/E_{\gamma}$  is close to one, as displayed in Fig. 6.430 for 40 GeV jets. In the case of Pb-Pb collisions, the background is very important and the  $p_{t,j}/E_{\gamma}$  distributions are wide and peak at values greater than one. A higher particle-momentum threshold,  $p_t > 2$  GeV/c, is required to calculate the energy of the jet in order to recover the correlation. Two different values for the lower  $p_{t,j}/E_{\gamma}$  limits are required for this ratio, depending on the experimental set-up:  $0.3 < p_{t,j}/E_{\gamma} < 1.2$  for the configuration without EMCal and  $0.8 < p_{t,j}/E_{\gamma} < 1.2$  for the configuration with EMCal.

**Table 6.101.** TPC, EMCal and PHOS detector acceptances, and energy and position resolutions. The physical TPC  $\eta$  acceptance is larger ( $|\eta| < 0.9$ ), but we select this lower value to ensure a good track matching. Azimuthal angles are given in the ALICE global reference system.

Detector	$ \eta $	$\varphi_{\min}$	$\varphi_{\max}$	$\sigma_E/E$ (%)	$\sigma_{\text{pos}}$
PHOS	0.12	220°	320°	1–1.5	0.8–2.5 cm
TPC	0.7	0°	360°	2	1.1°
EMCal	0.7	60°	180°	1–1.5	0.8–2.5 cm

The jet reconstruction algorithm fails for jets with  $p_t < 10 \text{ GeV}/c$  because the ratio  $p_{t,j}/E_\gamma$  suffers from large fluctuations. Such jets are excluded from the analysis.

**6.9.4.2. Expected performances.** The  $\gamma$ -jet tagging algorithm was tuned for two experimental configurations of ALICE: (i) Charged particles are detected in the central tracking system and neutral particles in EMCal<sup>31</sup>; this configuration is labelled as ‘TPC+EMCal’; (ii) Only the central tracking system is available and consequently only charged particles can be detected; this configuration is labeled as ‘TPC’. The acceptances, the energy and position resolutions of all the detectors used to evaluate the performances are reported in Table 6.101. Using the event simulation as described in Section 6.9.1.3, the jet selection efficiency, defined as the ratio of the number of identified  $\gamma$ -tagged jets to the number of prompt photons found in PHOS was calculated. The efficiency for the configuration with EMCal is about 30%. For the configuration without EMCal we obtain an efficiency of 40–50%, because of: (i) the wider selection range, implying a lower identification quality; and (ii) the larger acceptance in azimuth of the central tracking system as compared to that of EMCal. We have also applied the  $\gamma$ -jet algorithm to jet-jet events in order to estimate the contamination level. If no prompt photon identification is performed in PHOS, only about 10% of the events are accepted in the setup with EMCal, because of its small acceptance. Taking the full acceptance of the TPC, the value rises to 40–50%. These are similar results for both pp and Pb–Pb collisions.

**Fragmentation functions.** A satisfactory method of studying quantitatively the interaction of jets with the medium is to investigate how the produced hadrons are distributed in phase space [1040], i.e., to measure the jet fragmentation function. The experimental fragmentation function is the distribution of charged hadrons within jets as a function of the variable  $z$ , defined for hard processes with a  $\gamma$ -jet pair in the final state as  $z = p_t/E_\gamma$ . Jet fragmentation functions to be measured in a standard year of LHC running for both pp and Pb–Pb collisions were studied for identified  $\gamma$ -jet events in the energy range from 20 to 100 GeV. The fragmentation functions obtained for jet-jet events misidentified as  $\gamma$ -jet events were also studied. Figure 6.431 shows the fragmentation function in pp and Pb–Pb collisions. The following conclusions are drawn:

- For pp collisions, we obtain a signal ( $\gamma$ -jet) to background (jet-jet) ratio of about 20 in the configuration without EMCal and near to 100% background rejection for the setup with EMCal. Prompt photon identification reduces the statistics of  $\gamma$ -jet events to about 10%.
- Concerning Pb–Pb collisions, the contribution from the heavy-ion collision underlying event was eliminated statistically in the final distributions by subtracting a pseudo-fragmentation function calculated outside the cone of the leading particle. The final

<sup>31</sup> The EMCal detector is not yet an approved project and will not be available, at least complete, in the beginning of the LHC operation.

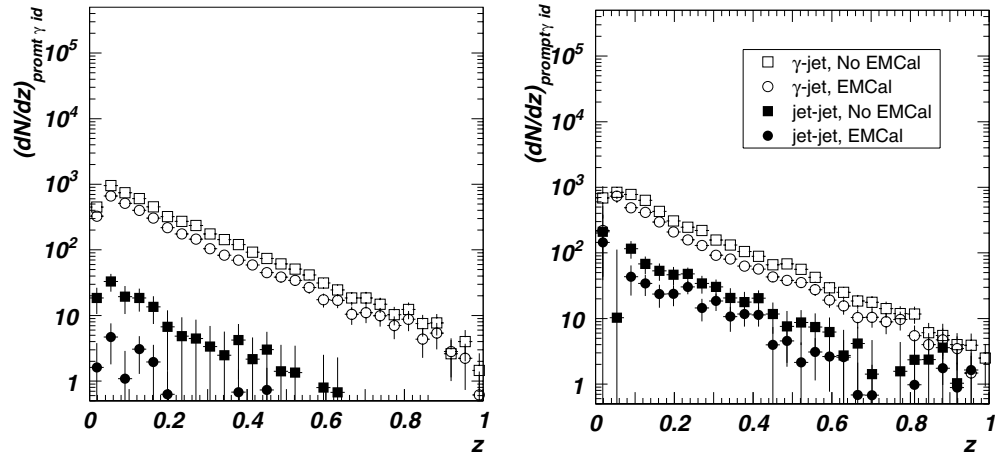


**Figure 6.431.** Fragmentation function for  $\gamma$ -jet and jet-jet events with energy larger than 20 GeV for a standard year run in pp (left) and Pb-Pb (right) collisions. The figures show the fragmentation functions for prompt photons identified in PHOS by medium purity SSA and ICM. The background from the heavy-ion collision was statistically subtracted. Statistical errors are shown.

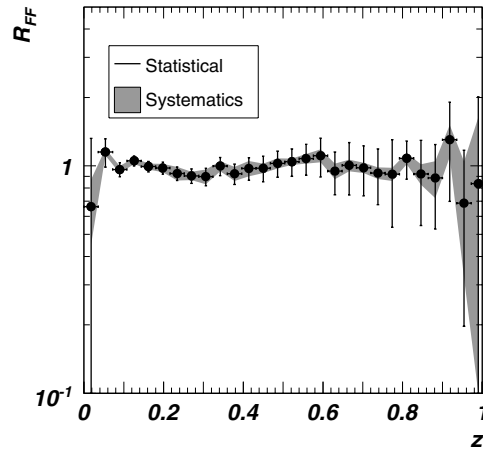


**Figure 6.432.** Ratio of the fragmentation functions of  $\gamma$ -tagged jets with energy larger than 20 GeV for Pb-Pb collisions scaled by Eq. (6.153) to pp collisions detected in the central tracking system and EMCAL. The shaded region represents the systematic error due to the contamination from jet-jet events. Similar ratio and systematics are obtained without EMCAL.

signal-to-background ratio obtained is about 4 in the case without EMCAL and rises to about ten with EMCAL. Prompt photon identification reduces the statistics of  $\gamma$ -jet events to about 60%.

To evaluate the sensitivity of photon-tagged jet fragmentation functions to nuclear medium modifications, we calculated the nuclear modification factor  $R_{FF}$ . This factor is defined as the ratio of the fragmentation function measured in AA collisions to the fragmentation function measured in pp collisions scaled to the number of binary NN collisions, both fragmentation functions calculated for the same beam luminosity and running

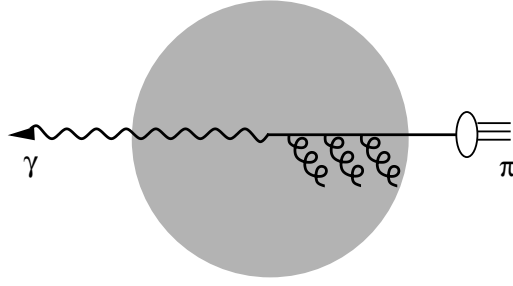


**Figure 6.433.** Schematic description of photon–pion production in heavy-ion collisions. The pion is produced by the collinear fragmentation of a hard parton which has lost some energy while going through the medium; the hard photon escapes the medium without any strong interaction.

time. This factor is equal to one in the absence of nuclear effects, as observed over the entire  $z$  range (Fig. 6.432). The statistical and systematic errors indicate that in the range  $0.1 < z < 0.5$  variations of the  $R_{FF}$  larger than 5% can be measured for both set-ups. We have also considered the case where hadrons from jet events are quenched by a factor 5, the systematic error is below 5% for both set-ups. However, the measurement of the nuclear modification factor with an accuracy better than 5% is limited by the statistics of one year of data taking.

We may still consider another approach in which the prompt photon is detected in EMCal and jets are detected by the central tracking system<sup>32</sup>. In such a setup, and considering similar prompt photon identification features in PHOS and EMCal, the prompt photon detection would be enhanced by a factor 7 and consequently the statistical errors would be reduced by a factor 2.6.

**6.9.5. Photon–pion momentum correlations.** The momentum imbalance  $z_{\gamma\pi} = -(\mathbf{p}_t \cdot \mathbf{p}_{t\pi}) / p_{t\gamma}^2$  spectrum between a hard prompt photon and a much softer (but still hard) hadron produced in hadronic collisions may allow for the determination of the hadron fragmentation function,  $D_i^h(z \simeq z_{\gamma\pi})$ . The photon transverse momentum balances that of the parton  $i$  which fragments into the hadron, to leading order in  $\alpha_s$  (see Fig. 6.433). At least this two-body kinematics may be a valid picture when higher order corrections remain small. Moreover, the fixed order calculations should not be reliable at large  $z_{\gamma\pi}$  because of the large logarithms  $\alpha_s \ln^2(1 - z_{\gamma\pi})$  and  $\alpha_s \ln(1 - z_{\gamma\pi})$  due to soft and collinear gluon emissions which need to be resummed to all orders. This triggered a recent phenomenological study of various pion–photon and photon–photon correlations in heavy-ion collisions at LHC energy [1041].

In order to probe efficiently the pion fragmentation function through the  $\gamma - \pi^0$  momentum imbalance spectrum, sufficiently asymmetric cuts  $p_{t\pi}^{\text{cut}} \ll p_{t\gamma}^{\text{cut}}$  are required to make the range covered in the  $z$  fragmentation variable as wide as possible. In addition, the pion momentum needs to be hard enough to stay within the perturbative regime while the photon momentum should not be too large to maintain reasonable counting rates:

$$\Lambda_{\text{QCD}} \ll p_{t\pi}^{\text{cut}} \ll p_{t\gamma}^{\text{cut}} \ll \sqrt{s}/2. \quad (6.162)$$

In the following, unless otherwise indicated, we choose the cuts  $p_{t\pi}^{\text{cut}} = 5 \text{ GeV}/c$  and  $p_{t\gamma}^{\text{cut}} = 25 \text{ GeV}/c$  for the LHC.

As an illustration, we discuss four distributions in Fig. 6.434; the pion transverse momentum  $p_{t\pi}$ , the photon transverse momentum  $p_{t\gamma}$ , the  $\gamma - \pi^0$  invariant mass  $m_{\pi\gamma}$ , and

<sup>32</sup> It is not advisable to use PHOS as a detector of jet neutral particles because of its reduced acceptance.

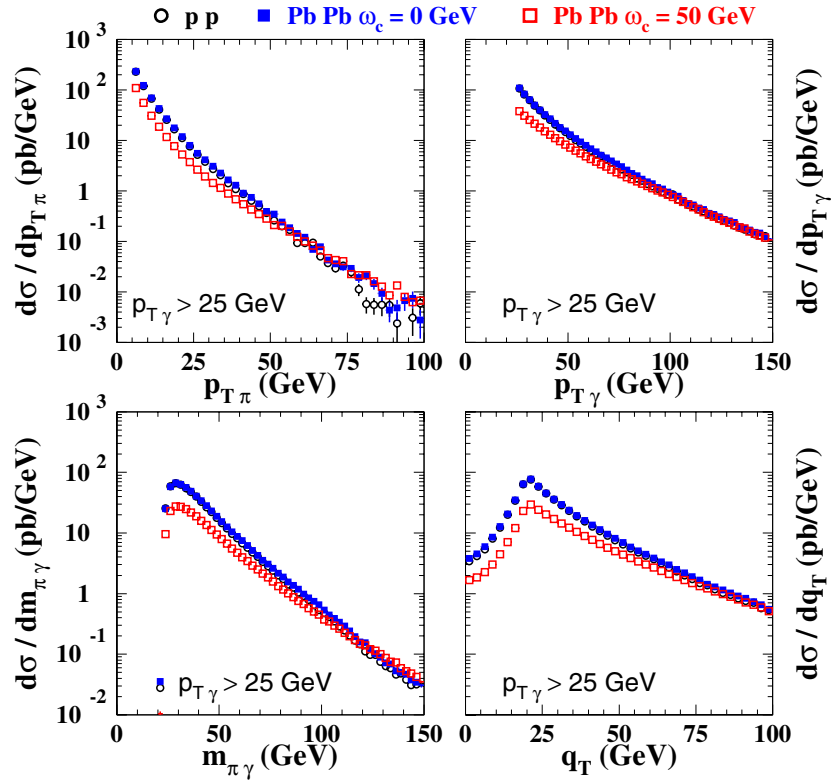


**Figure 6.434.** The four distributions in  $\gamma - \pi^0$  production defined in the text for pp (open dots, hidden by the Pb–Pb points without energy loss) and Pb–Pb (no energy loss: black squares; with energy loss: open squares) at  $\sqrt{s} = 5.5$  TeV. Both the photon and the pion are produced at rapidity  $[-0.5, 0.5]$  and the following cuts are imposed:  $p_{T\gamma} > 25$  GeV/c and  $p_{T\pi} > 5$  GeV/c.

the transverse momentum of the pair  $q_t$ , calculated for pp and Pb–Pb collisions. In Pb–Pb, the calculation included either shadowing and no energy loss, or shadowing and energy loss using  $\omega_c = 50$  GeV.

A small antishadowing effect can be observed at large transverse momenta or at high invariant mass due to the fact that the kinematics then becomes sensitive to partons in the nuclei with larger  $x$  values. Conversely, energy-loss effects are quite visible particularly at the low- $p_t$  values of the pion or the photon. On the other hand, to produce a pion at high transverse momentum requires a parton with large  $k_T$  for which the energy loss is expected to be smaller. We observe, accordingly, that the spectrum in Pb–Pb collision tends to approach the pp spectrum as  $p_{T\pi}$  increases. The medium effects are also particularly visible in the spectrum as a function  $p_{T\gamma}$ : as long as the photon is produced directly, the  $p_{T\gamma}$  spectrum reflects the energy of the parton,  $k_T = p_{T\gamma}$ , which eventually fragments into the pion. Again, the quenching will be maximal for small  $p_{T\gamma}$  (small  $k_T$ ) while at asymptotic energies, parton energy loss will have no observable consequence. Similar behaviour is observed in the invariant-mass distribution: small masses correspond to low  $k_T$  partons and therefore lead to a stronger suppression.

More interesting is the  $q_t$  spectrum which exhibits a maximum when the pion and the photon transverse momenta lie just above the imposed kinematic threshold, which is located

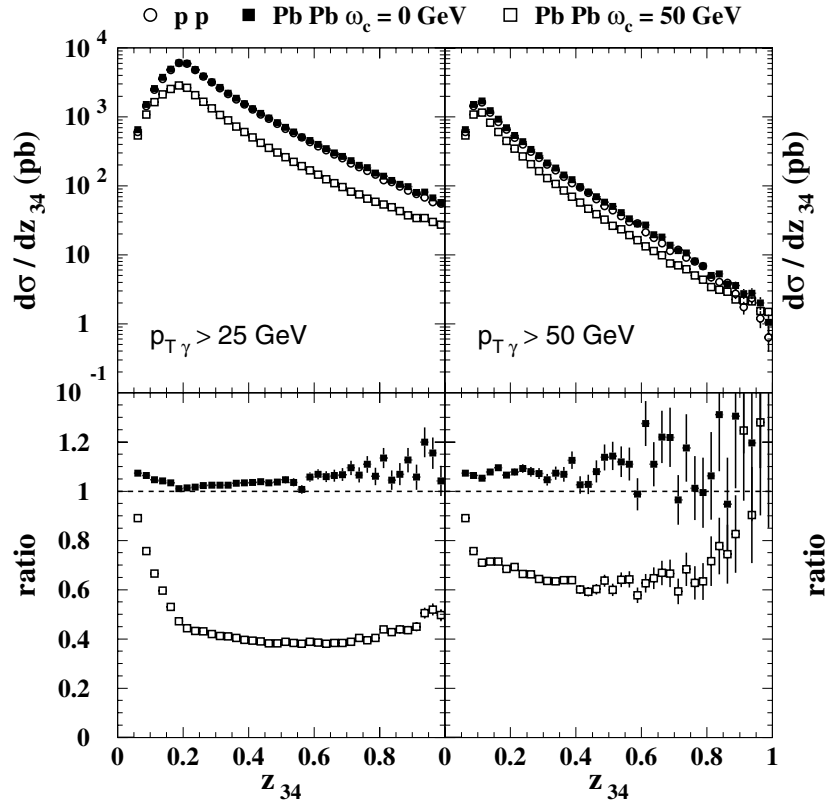


**Figure 6.435.** The  $z_{\gamma\pi}$  distribution in  $\gamma - \pi^0$  production for pp (open dots) and Pb–Pb scattering (no energy loss: black squares; with energy loss: open squares) at  $\sqrt{s} = 5.5$  TeV. Both the photon and the pion are produced at rapidity  $[-0.5, 0.5]$  and the following cuts are imposed:  $p_{T\gamma} > 25$  GeV/c and  $p_{T\pi} > 5$  GeV/c (left) and  $p_{T\gamma} > 50$  GeV/c and  $p_{T\pi} > 5$  GeV/c (right). Bottom: The same distributions normalized to the pp case.

at the difference between the  $p_{T\gamma}$  and the  $p_{T\pi}$  cut, 20 GeV/c. Above 20 GeV/c, the distribution is reminiscent of the  $p_{T\gamma}$  and the  $m_{\pi\gamma}$  distribution and, in particular, the larger the  $q_t$  the weaker the energy-loss effect. Similarly, the energy-loss effects will tend to be smaller at very small  $q_t \ll 20$  GeV/c as the pion transverse momentum and thus the double fragmentation contribution—less affected by the medium—increases with decreasing  $q_t$ . Therefore, we expect the medium effects to be maximal for  $q_t$  roughly around the difference of the transverse momentum cuts.

Figure 6.435 shows the momentum-imbalance spectrum for a photon momentum cut of  $p_{T\gamma}^{\text{cut}} = 25$  GeV/c (left) and  $p_{T\gamma}^{\text{cut}} = 50$  GeV/c (right). As anticipated, its shape is reminiscent of the pion fragmentation function for  $z_{\gamma\pi} \gtrsim p_{T\pi}^{\text{cut}}/p_{T\gamma}^{\text{cut}}$ . In particular, the strong medium effects expected at large  $z$  are clearly seen in this distribution (see the ratio, Figure 6.435, bottom). Note that the quenching factor does not vanish at very large  $z_{\gamma\pi}$  because of the double fragmentation process which is dominant in this kinematic region. This spectrum is nevertheless particularly interesting to determine experimentally fragmentation functions and hence to probe how the dynamics of fragmentation is modified by the hot and dense medium.

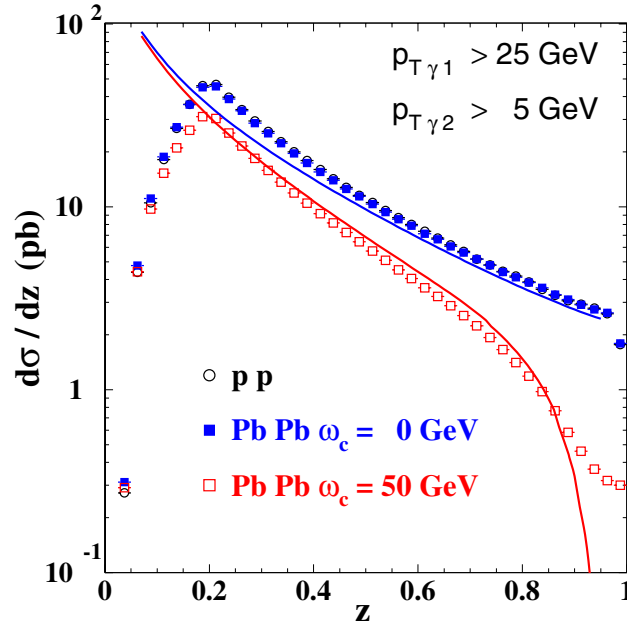


**Figure 6.436.** The  $z$  distribution in  $\gamma$ - $\gamma$  production for pp (open dots) and Pb-Pb scattering (no energy loss: black squares; with energy loss: open squares) at  $\sqrt{s_{NN}} = 5.5$  TeV. Both photons are produced at rapidity  $[-0.5, 0.5]$  and the following cuts are imposed:  $p_{T,\gamma} > 25$  GeV/ $c$  and  $p_{T,\gamma} > 5$  GeV/ $c$ . The solid lines represent the photon fragmentation functions calculated without energy loss (upper curve) and with energy loss (lower curve).

A more spectacular example can be seen in the  $\gamma$ - $\gamma$  momentum imbalance spectrum (Fig. 6.436). In this channel, the one-fragmentation component (one direct and one fragmentation photon) is dominant and the correspondence between the vacuum or the medium-modified fragmentation function (i.e. the theoretical input) and the momentum imbalance spectrum (i.e. the observable) becomes even more obvious. This effect is evidenced by superimposing the fragmentation functions used in the perturbative calculation (rescaled by an arbitrary factor) to the leading-order distribution. Above the ratio of the imposed transverse momentum cuts (here  $z \geq 0.2$ ), a perfect matching is observed between vacuum or medium-modified fragmentation function and the respective imbalance spectra<sup>33</sup>. This is a clear indication that such momentum correlations in the double inclusive  $\gamma - \pi^0$  and  $\gamma$ - $\gamma$  production provides a unique access to the fragmentation physics and, thereby, to a deeper understanding of the underlying energy loss mechanism in QCD media.

Finally let us come to the counting rates expected at the LHC. The number of events is given by Eqs (6.152) and (6.153). Gamma-pion cross sections typically range from 1 to  $10^2$  pb/GeV which would correspond roughly to  $N = 3 \times 10^2 - 3 \times 10^5$  events/GeV. Similarly, one expects  $dN/dz \simeq 3 \times 10^3 - 3 \times 10^5$  events per month in ALICE. These numbers, however, do not take into account the acceptance effects in the ALICE detector.

<sup>33</sup> The appearance of the 2-fragmentation component spoils the agreement above  $z \geq 0.9$ .

### 6.10. Ultra-peripheral collisions

Heavy ions accelerated at the LHC are surrounded by strong electromagnetic fields. Electromagnetic interactions may occur in heavy-ion interactions at any impact parameter. However, in collisions where the nuclei overlap, the strong (hadronic) interactions dominate, and it becomes impossible to distinguish the electromagnetic interactions. This section will therefore only deal with such collisions in which the ions do not interact strongly. This roughly corresponds to impact parameters,  $b$ , larger than twice the nuclear radius,  $R_A$  ( $b > 2R_A$ ). Clearly, these events will have a very different topology compared with the central, hadronic interactions normally considered in ALICE. They will thus require different trigger and analysis techniques but will also broaden the physics potential of ALICE.

*6.10.1. Physics of ultra-peripheral collisions.* The electromagnetic field of one of the nuclei in an ultra-peripheral collision corresponds to a spectrum of equivalent photons impinging on the other (target) nucleus. The quasi-real photons may interact with the target in a variety of ways and provide an opportunity at the LHC to study photonuclear and photon-nucleon interactions at energies higher than at any existing accelerator.

One can identify two classes of ultra-peripheral collisions depending on whether the target nucleus remains intact or breaks up. Examples of ‘elastic’ interactions (i.e. no breakup) include two-photon interactions and photonuclear interactions without colour transfer. The latter can be mediated by exchange of two-gluons or by exchange of the phenomenological particle known as the Pomeron. Photonuclear interactions leading to the breakup of the target include photoproduction of jets and heavy quarks.

There have also been proposals to use ultra-peripheral collisions to search for more exotic processes. Examples of this are investigation of the  $\gamma WW$ -coupling through two-photon production of  $W$ -pairs, searches for the Higgs boson, two-photon production of supersymmetric charginos and sleptons, and a direct determination of the electric charge of the top quark. The following three sections will discuss exclusive vector meson production, two-photon interactions, and photon-induced partonic processes in more detail. Two recent reviews of the physics of ultra-peripheral collisions can be found in [1042, 1043].

*6.10.1.1. Vector meson production.* The cross section for exclusive vector meson production in nucleus–nucleus collisions,  $A + A \rightarrow A + A + V$ , is very large at the collision energies of RHIC and the LHC (Fig. 6.437). This can be understood from the Vector Meson Dominance (VMD) model. According to VMD, the interaction of a photon with a hadronic or nuclear target is preceded by a fluctuation of the photon into a virtual vector meson. The scattering amplitude can then be written as the product of the probability of finding the photon in the vector meson state with the scattering amplitude for the  $V + A$  interaction:

$$\frac{d\sigma}{dt}(\gamma A) = \sum_V \frac{4\pi\alpha}{f_V^2} \frac{d\sigma}{dt}(VA). \quad (6.163)$$

Here,  $f_V$  is the photon vector meson coupling, and  $t$  is the momentum transfer from the target nucleus or nucleon squared. The sum is over all applicable vector meson states. The photon vector meson couplings are constrained from data on the semi-leptonic decay widths,  $\Gamma_{V \rightarrow e^+e^-}$ .

For the low and intermediate mass vector mesons ( $\rho$ ,  $\omega$ ,  $\phi$ ), the nuclear momentum transfer can be treated as exchange of a meson or a Pomeron, and the vector meson is produced through  $\gamma$ -Pomeron (or  $\gamma$ -meson) fusion. The cross section in photon–proton interactions,  $\gamma + p \rightarrow V + p$ , exhibits a characteristic increase with the centre-of-mass energy,  $W_{\gamma p}$ , to the power  $W_{\gamma p}^{0.22}$  for these mesons.

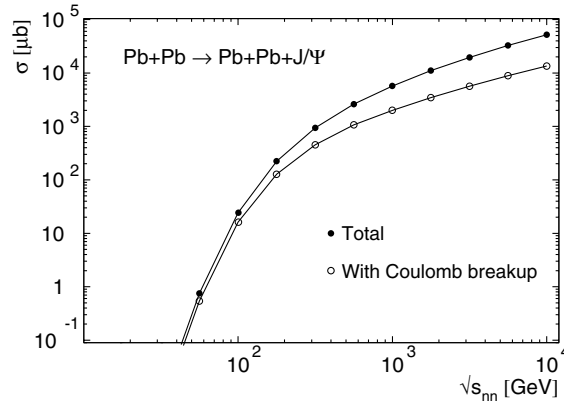


**Figure 6.437.** Cross section for exclusive  $J/\psi$  production in Pb–Pb interactions as a function of the collision energy. The open symbols show the cross section when one or both of the nuclei are broken up by Coulomb excitation. From Refs. [1044, 1045].

The cross section for photoproduction of heavy vector mesons ( $J/\psi$  and  $\Upsilon$ ) has been calculated from QCD (two-gluon exchange) by Ryskin [1046]. The scattering amplitude is then

$$\left. \frac{d\sigma(\gamma p \rightarrow Vp)}{dt} \right|_{t=0} = \frac{\alpha_s^2 \Gamma_{ee}}{3\alpha M_V^2} 16\pi^3 [xg(x, M_V^2/4)]^2. \quad (6.164)$$

Two other calculations have considered the use of relativistic wave functions, off-diagonal parton distributions, and NLO contributions [1047, 1048]. Although the approaches differ, the final results are in good agreement. The cross section for  $\Upsilon(1S)$  production scales roughly as  $W_{\gamma p}^{1.7}$ , while the cross section for  $J/\psi$  exhibits a slower increase with energy  $\propto W_{\gamma p}^{0.8}$ .

The cross section for heavy vector meson production depends on the gluon density,  $g(x, Q^2)$ , to the second power and is therefore a very sensitive probe of the nuclear gluon distribution. A 30% reduction in the nuclear gluon density due to shadowing would roughly halve the cross section. Production of  $J/\psi$  and  $\Upsilon$  at mid-rapidity in Pb–Pb collisions at the LHC corresponds to a gluon  $x$  of  $5 \times 10^{-4}$  and  $2 \times 10^{-3}$ , respectively.

The cross section to produce a vector meson in a nucleus–nucleus collision is obtained through a convolution of the photonuclear cross section with the equivalent photon spectrum [1049, 1050]:

$$\sigma(A + A \rightarrow A + A + V) = 2 \int_0^\infty \frac{dn}{dk} \sigma_{\gamma A \rightarrow VA}(k) dk. \quad (6.165)$$

The 2 takes into account the fact that both ions can act as photon emitter and target. The resulting total cross sections for  $J/\psi$  and  $\Upsilon$  are summarized in Table 6.102. The table also includes the cross section for coherent  $\rho^0$ -meson production, for comparison.

In interactions at small impact parameters, the probability is high that the nuclei will exchange one or more additional photons. The most probable effect of these photons is that the nucleus is excited to a giant dipole resonance and decays by emitting one or a few neutrons. These neutrons can be detected in zero degree calorimeters. The exchange of multiple photons factorizes, leading to an reduction in the photon spectrum when vector mesons are produced in coincidence with nuclear breakup [1045]. The total cross section for exclusive  $J/\psi$  production

**Table 6.102.** Vector meson cross sections and production rates in one ALICE year ( $10^6$  s), from [1044, 1050]. The cross section for  $\Upsilon(1S)$  is calculated without nuclear shadowing; the range corresponds to the uncertainty in the measured  $\gamma$  + proton cross section. See the references for further details.

Final state	Pb–Pb		Ca–Ca	
	$\sigma$	rate (per $10^6$ s)	$\sigma$	rate (per $10^6$ s)
$\rho^0$	5200 mb	$2.6 \times 10^9$	120 mb	$4.8 \times 10^9$
$J/\psi$	32 mb	$1.6 \times 10^7$	$390 \mu\text{b}$	$1.6 \times 10^7$
$\Upsilon(1S)$	150–500 $\mu\text{b}$	80000–250 000	2–8 $\mu\text{b}$	80000–320 000

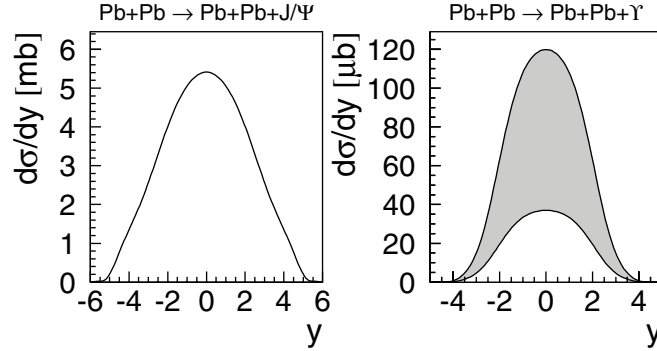


**Figure 6.438.** Calculated rapidity distributions for  $J/\psi$  and  $\Upsilon$  production in Pb–Pb interactions at the LHC [1050].

and the cross section with photonuclear breakup is plotted in Fig. 6.437 as a function of collision energy for Pb–Pb collisions.

By changing variables and differentiating, Eq. 6.165 for one photon emitter/target combination can be written

$$\frac{d\sigma}{dy} = k \frac{dn}{dk} \sigma_{\gamma A \rightarrow \nu A}(k). \quad (6.166)$$

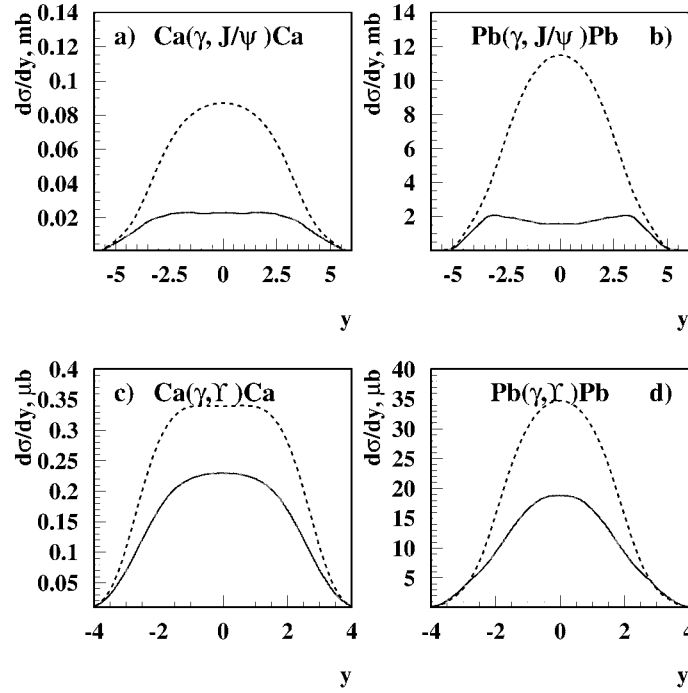
Here,  $y$  is the rapidity of the produced vector meson. If the photon spectrum,  $dn/dk$ , is known, the differential cross section  $d\sigma/dy$  is thus a direct measure of the photonuclear vector meson cross section. At mid-rapidity, the kinematics is unambiguous because of symmetry. Away from  $y = 0$ , the different photon emitter/target configurations give different contributions. If this ambiguity can be resolved, significantly lower values of gluon  $x$  can be probed.

In Eq. 6.165, the cross sections for both target nuclei are added. In general, the amplitudes will interfere, and this leads to a modification of the vector meson transverse momentum spectrum [1051]. The interference does, however, not affect the total cross sections significantly.

The rapidity distributions for  $J/\psi$  and  $\Upsilon$  in Pb–Pb interactions, as calculated in [1050], are shown in Fig. 6.438. These calculations are based on parametrisations of the measured  $\gamma$ –proton vector meson cross sections. For comparison, the results from the calculations in Refs. [1049, 1052] are listed (for two colliding systems) in Table 6.103. Both the estimates obtained in the Leading Twist Approximation (LTA) and in the Impulse Approximation (IA) [1049, 1052] are presented in the Table (more details on these calculations can be found in [1053]). Due to the leading twist shadowing, the cross sections obtained in the LTA are smaller than those predicted by the impulse approximation. For Pb–Pb collisions, the  $\Upsilon$  cross

**Table 6.103.** Total cross sections of  $J/\psi$  and  $\Upsilon$  coherent production in ultra-peripheral collisions at the LHC.

Colliding ions	Ca–Ca , $\gamma = 3500$		Pb–Pb , $\gamma = 2700$	
Quarkonium	$J/\psi$	$\Upsilon$	$J/\psi$	$\Upsilon$
Impulse	0.6 mb	1.8 $\mu$ b	70 mb	133 $\mu$ b
Leading Twist	0.2 mb	1.2 $\mu$ b	15 mb	78 $\mu$ b

**Figure 6.439.** Rapidity distributions for  $J/\psi$  and  $\Upsilon$  coherent production in ultra-peripheral Ca–Ca and Pb–Pb collisions at LHC calculated with the leading twist shadowing based on H1 parametrisation of gluon density (solid curves) and in the Impulse Approximation (dashed curves).

section is suppressed by a factor of about 2, while the suppression of the  $J/\psi$  cross section is much stronger, by about a factor of 5. The cross section for the  $J/\psi$  in Table 6.102 is between the IA and LTA results. The cross section for the  $\Upsilon$  is a bit higher in Table 6.102 than in the IA and LTA approximations, but for the  $\Upsilon$  the uncertainty in the measured  $\gamma$ -proton cross section is higher.

It is worth noting that, in principle, multiple eikonal-type rescatterings due to gluon exchanges could also result in a suppression of vector meson production. However, the suppressions arising from this mechanism are significantly smaller (by a factor of  $\approx 2$ ) than those due to leading twist shadowing, at least for  $x \leq 0.001$ .

The rapidity distributions for coherent  $J/\psi$  and  $\Upsilon$  production with Ca and Pb beams obtained with the LTA and with the IA are presented in Fig. 6.439. The comparison of these distributions indicates that quarkonia suppression due to the leading twist shadowing is very strong at mid-rapidity. In the forward rapidity region covered by the Muon Spectrometer ( $2.5 \leq y \leq 4.0$ ) the suppression is smaller, but a significant difference in the rapidity distributions is still present, at least for the  $J/\psi$ .

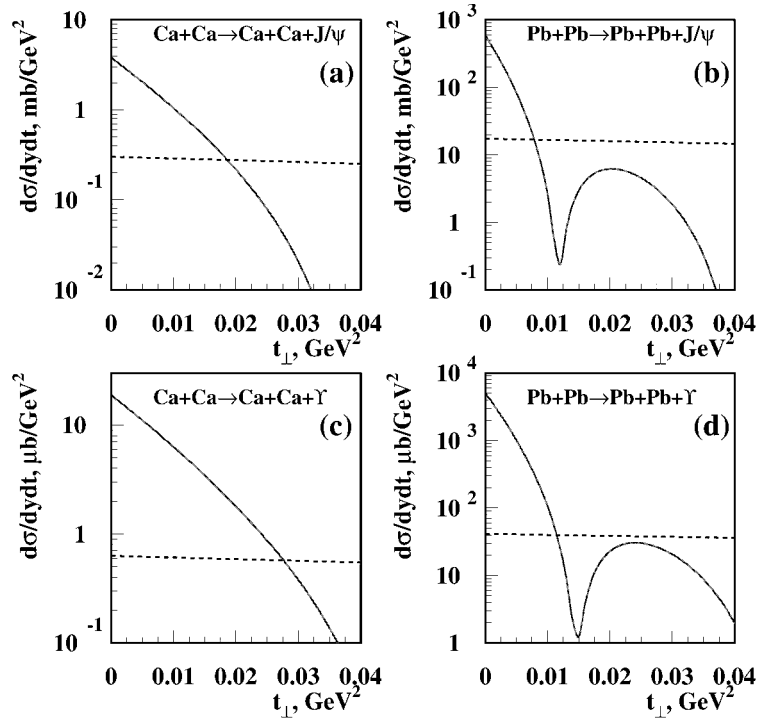


**Figure 6.440.** Momentum transfer distributions for  $J/\psi$  and  $\Upsilon$  coherent (solid curves) and incoherent (dashed curves) production in ultra-peripheral Ca–Ca and Pb–Pb collisions at LHC.

The momentum transfer distributions (at rapidity  $y=0$ ) for coherent  $J/\psi$  and  $\Upsilon$  production with Ca and Pb beams obtained with the impulse approximation are shown in Fig. 6.440. The same figure also shows the distributions for incoherent production estimated in Refs. [1049, 1052] in the impulse approximation. While the momentum transfer distributions for the incoherent process are flat, the ones for coherent production show a typical peaked shape which makes the latter process dominant in the low momentum transfer region.

**6.10.1.2. Two-photon interactions.** Particles can also be produced in ultra-peripheral collisions via a two-photon interaction. In principle any pair of fermions can be produced via  $\gamma\gamma \rightarrow f\bar{f}$ . A quark/anti-quark-pair can appear either as a bound state (meson) or fragment into two jets of hadrons. Since the virtual photons emitted by heavy nuclei are nearly real, only scalar and tensor mesons will be produced in two-photon interactions.

Two-photon production of mesons and of meson- and baryon-pairs is a sensitive probe of the internal hadron structure. For standard  $q\bar{q}$ -mesons, the quark model can predict the relative two-photon widths ( $\Gamma_{\gamma\gamma}$ ) with good accuracy. For exotic states, in particular glueballs, one expects either a strongly reduced coupling to two-photons or none at all.

However, when comparing the two-photon production cross sections of scalar and tensor mesons with those of photoproduced vector mesons, one finds that the two-photon cross sections are lower by a factor of  $\sim 100$  for mesons of comparable mass [1042]. The vector mesons will thus be a serious background to scalar or tensor mesons produced in two-photon interactions. For example, the cross section for two-photon production of the  $\eta_c$  meson will be of the same order of magnitude as photoproduction of a  $J/\psi$  followed by the decay  $J/\psi \rightarrow \eta_c + \gamma$  (Branching ratio 1.3%).

**Table 6.104.** Cross sections for two-photon production of lepton pairs for different cuts on the invariant mass of the pair, calculated within the equivalent photon approach.

Selection	$\sigma(\text{Pb} + \text{Pb} \rightarrow \text{Pb} + \text{Pb} + \text{ll})$	
	$e^+e^-$	$\mu^+\mu^-$
Total	223 kb [1057]	2.0 b
$m_{\text{inv}} > 1.5 \text{ GeV}$	140 mb	45 mb
$m_{\text{inv}} > 6.0 \text{ GeV}$	2.8 mb	1.2 mb

Similarly, the two-photon production of jets and heavy quarks is a sensitive probe of the partonic sub-structure of the photon. However, the rates for processes  $\gamma\gamma \rightarrow q\bar{q}$  are only fractions of the corresponding processes in which the photon interacts with a parton in the target (e.g.  $\gamma g \rightarrow q\bar{q}$ ) [1054]. This will make detection and identification of these two-photon processes very difficult.

A two-photon process which can be studied is two-photon production of lepton pairs. This has been shown by both the STAR [1055] and PHENIX [1056] Collaborations at RHIC, and also by fixed target experiments at the SPS and AGS.

The total cross section for  $e^+e^-$ -pairs is huge (Table 6.104). In fact, the probability of producing an  $e^+e^-$ -pair in a grazing nuclear collision ( $b \approx 2R$ ) is near one, and lowest-order perturbative calculations break down. Higher order calculations must include the possibility for producing multiple pairs in a single event. Observing such multiple pairs would provide a unique opportunity to study strong field QED, but since most pairs have invariant masses of about  $\sim 100 \text{ MeV}$  or less at the LHC, this is experimentally very difficult. The production of high-mass  $e^+e^-$ -pairs and  $\mu^+\mu^-$ -pairs is believed to be well described by leading order calculations. It has therefore been suggested to use this process for luminosity monitoring. Lepton pairs with invariant masses around the  $J/\psi$  or  $\Upsilon$  mass will furthermore be an important background to photonuclear vector meson production, as discussed below.

The cross sections for two-photon production of  $e^+e^-$ - and  $\mu^+\mu^-$ -pairs for different cuts on the invariant masses of the pairs are listed in Table 6.104.

*6.10.1.3. Partonic interactions.* A photon from the electromagnetic field of one of the nuclei may interact with a parton in the target nucleus. The basic processes are  $\gamma + g \rightarrow q + \bar{q}$  and  $\gamma + q \rightarrow g + q$ . In the second process, the  $q$  can be replaced by a  $\bar{q}$  from the sea. The partonic cross sections can be calculated from perturbative QCD, and to leading order they are proportional to the strong coupling constant  $\alpha_s(Q^2)$ , evaluated at scale  $Q^2 = m_q^2 c^2 + p_t^2$ . Calculations can thus be performed for the production of heavy quarks via  $\gamma + g \rightarrow q + \bar{q}$  [1054, 1058, 1059], and for di-jet production [1060, 1061].

The total cross sections for heavy quark production are listed in Table 6.105. It is worth noting that the cross section for  $c\bar{c}$ -pairs is as large as 1 barn. The cross sections are peaked near threshold, and mid-rapidity production of  $c\bar{c}$ - and  $b\bar{b}$ -pairs therefore mainly probes  $x$  values of  $\sim 5 \times 10^{-4}$  and  $\sim 3 \times 10^{-3}$ , respectively. The cross sections are dominated by direct photon-gluon fusion and therefore directly probes the nuclear parton distributions. See Ref. [1054] for a discussion of the sensitivity to different parametrisations of the nuclear shadowing.

Photonuclear production of top quarks would be an interesting probe for a direct determination of the electric charge of the top quark [1062]. The existing data from Fermilab do not exclude an exotic state with charge  $\frac{4}{3}e$  instead of the expected  $\frac{2}{3}e$ . The statistics from a  $10^6 \text{ s}$  run, however, seems to be insufficient (Table 6.105).

**Table 6.105.** Cross sections and production rates for  $\gamma + g \rightarrow q\bar{q}$  in one ALICE year ( $10^6$  s), from [1054, 1062].

Final state	Pb–Pb		Ar–Ar	
	$\sigma$	rate (per $10^6$ s)	$\sigma$	rate (per $10^6$ s)
$\gamma + g \rightarrow c\bar{c} + X$	1050 mb	$5.5 \times 10^8$	14 mb	$5.6 \times 10^8$
$\gamma + g \rightarrow b\bar{b} + X$	4.7 mb	$2.3 \times 10^6$	$70 \mu\text{b}$	$2.8 \times 10^6$
$\gamma + g \rightarrow t\bar{t} + X$	0.3 nb	–	29 pb	( $\sim 1$ )

Calculations for the photonuclear production of jets have only been performed recently [1060, 1061]. Resolved processes are believed to be more important for jets than for heavy quark production, and this makes the cross sections less sensitive to the parton distributions [1060], but photonuclear jet production should still be a sensitive probe of low- $x$  nonlinear QCD dynamics [1061].

Both photonuclear heavy quark and jet production lead to the breakup of the target nucleus. This makes the event topology different from that in exclusive interactions, where a very clean signal can be obtained from the coherence requirement when the entire event is reconstructed. There are to date no experimental data on photon–parton interactions in heavy-ion collisions. The events are, however, characterised by a gap in rapidity, void of particles, between the photon emitting nucleus and the produced final state. This distinguishes the photon–parton events from hadronic interactions and may allow for experimental identification.

**6.10.2. Results from lower energy.** The virtual photon spectrum extends up to a maximum energy of  $\sim \gamma\hbar c/R_A$ , where  $\gamma$  is the Lorentz factor of the beam. For coherent and exclusive processes, this means that the maximum mass of the final state will be given by  $\sim 2\gamma\hbar c/R_A$ , where  $\gamma$  is the Lorentz factor in the centre-of-mass system. At the SPS and RHIC, this is 0.8 GeV and 6.0 GeV, respectively, for heavy ions (Au or Pb). The particle production is significant only at energies well below this value. Thus, from purely kinematical reasons, the particle production in ultra-peripheral collisions before the start-up of RHIC was in practice restricted to  $e^+e^-$ -pairs.

Results from the SPS with sulphur beams [1063, 1064] on two-photon production of free  $e^+e^-$ -pairs were found to be in agreement with lowest order QED calculations. Charge changing reactions, where a lead nucleus is transformed into bismuth and a negative pion ( $\gamma + \text{Pb} \rightarrow \text{Bi} + \pi^-$ ), have also been studied [1065]. The results are in agreement with electromagnetic excitation calculations.

At RHIC, the first results on particle production in ultra-peripheral collisions were obtained by the STAR Collaboration on exclusive production of  $\rho^0$  mesons [1066]. The production was studied both exclusively and with Coulomb breakup of both nuclei. The latter happens if two additional photons with very low energy are exchanged in the same event that produced the vector meson.

The rapidity and transverse mass of the  $\rho^0$  for interactions at  $\sqrt{s_{\text{NN}}} = 200$  GeV is shown in Fig. 6.441. The measured cross section and rapidity distribution are in good agreement with the calculations [1044, 1045].

As mentioned above, STAR has also measured the production of  $e^+e^-$ -pairs in interactions with Coulomb breakup [1055]. The results were found to be in good agreement with lowest order perturbation theory. The pair  $p_t$  distribution deviated from the Weizsäcker–Williams virtual photon approach, showing that the virtual photon mass was important in that kinematical regime.

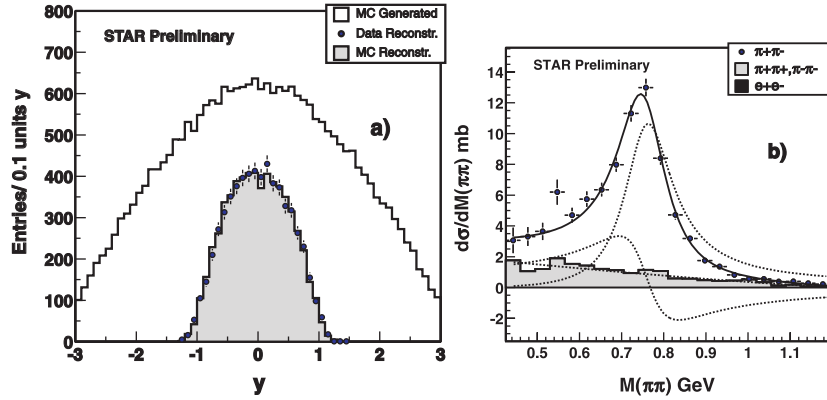


**Figure 6.441.** Rapidity (a) and invariant mass (b) distributions for coherent  $\rho^0$  production in Au–Au interactions accompanied by mutual Coulomb breakup at  $\sqrt{s_{NN}} = 200$  GeV, by the STAR Collaboration [1068]. The dashed curves in (b) correspond to a relativistic Breit–Wigner function and a Söding interference term; the solid curve is the sum of the two. The dash–dotted curve describes the background from incoherent interactions.

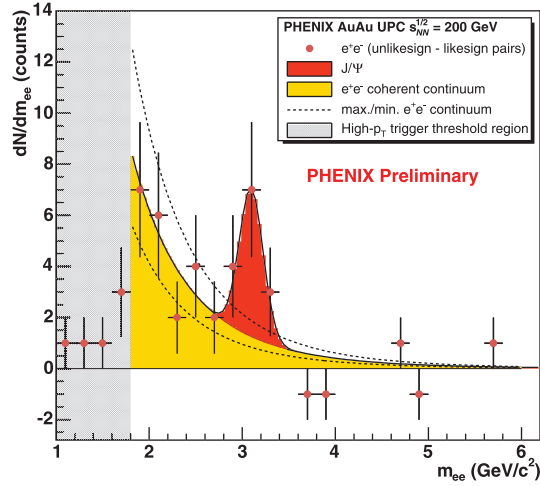


**Figure 6.442.** Invariant mass distribution of  $e^+e^-$ -pairs in coherent  $\text{Au} + \text{Au} \rightarrow \text{Au} + \text{Au}^* + e^+e^-$  reactions measured by the PHENIX Collaboration [1056]. The distribution can be explained by the sum of a continuum contribution from  $\gamma\gamma \rightarrow e^+e^-$  and decays of  $J/\psi \rightarrow e^+e^-$ .

Recently, the PHENIX Collaboration presented the first preliminary results on exclusive  $J/\psi$  production in Au+Au collisions at RHIC [1056]. The electron/positrons from the decay  $J/\psi \rightarrow e^+e^-$  were measured by the electromagnetic calorimeters in the PHENIX central tracking arms. The electromagnetic calorimeters were used in coincidence with the zero-degree calorimeters for triggering on events where a high-mass  $e^+e^-$ -pair was produced in coincidence with Coulomb breakup of one or both nuclei.

The measured  $J/\psi$  cross section is  $d\sigma(y=0)/dy = 44 \pm 16(\text{stat.}) \pm 18(\text{syst.}) \mu\text{b}$ . The main background is continuum production of  $e^+e^-$ -pairs from two-photon interactions. The electron–positron invariant mass distribution is shown in Fig. 6.442.

The mutual Coulomb breakup of the beam nuclei without particle production has also been studied at RHIC [1067].

The first results from RHIC have shown that it is possible to trigger on and identify ultra-peripheral interactions in the high-multiplicity environment of relativistic heavy-ion interactions. So far, only exclusive interactions have been studied, and the identification has been based on reconstructing the entire event and using the summed  $p_t$  of all the tracks as signature for coherence. The measured cross sections have generally been found to be in agreement with expectations. This shows that the photon spectrum is fairly well understood, and that information on the photonuclear cross section can be extracted. The increased energy at the LHC will greatly enhance the physics potential.

One example where it is easy to show that LHC will provide new insights is photoproduction of  $\Upsilon$ . This has been studied in  $\gamma$ -proton interactions at HERA. The accumulated data amounts to less than 50 events in total (H1 and ZEUS). ALICE should have a unique opportunity to improve the existing measurements.

*6.10.3. Ultra-peripheral collisions in ALICE.* The two classes of ultra-peripheral collisions mentioned above ('elastic' and 'inelastic') will require different analysis and trigger techniques. For exclusive vector meson production, the identification is based on reconstructing the entire event (the two tracks from the decay), and identifying the coherent production through the low pair- $p_t$ . The  $\gamma$ -parton interactions must be identified based on the presence of a rapidity gap between the photon emitting nucleus and the produced particles. The method of using rapidity gaps is a standard technique in diffractive interactions at hadron colliders, but it has not been used in heavy-ion experiments so far.

*6.10.3.1. Trigger schemes.* The very different topology of ultra-peripheral interactions compared with central nucleus-nucleus collisions leads to different trigger requirements. For hadronic interactions, it is possible to use the charged-particle multiplicity in a region of phase space outside the acceptance of the central barrel as trigger. This is not possible for ultra-peripheral interactions, which are characterised by gaps, several units of rapidity wide, void of produced particles. To detect the ultra-peripheral events it is necessary to have a low-level trigger sensitive to the production of a few charged particles around mid-rapidity.

In ALICE the Time-of-Flight (TOF) detector is a natural candidate to address this task. The fast response of the multigap resistive plate chambers (MRPC), the large area covered ( $|\eta| < 1$ ) and the high segmentation, makes the TOF well suited for triggering at Level 0 in the central region. Taking advantage of the FPGAs implemented in the hardware, the TOF trigger has a high flexibility, allowing the selection of a large variety of event topologies. The segmentation used by the trigger can be decided at software level, allowing a minimum of 48 pads ( $\approx 500 \text{ cm}^2$ ) per TOF cell.

A reduced signal from the TOF (an 'OR' of several cells) can be used as pretrigger for the ALICE Transition Radiation Detector (TRD). A division of each ALICE azimuthal sector into 16 segments in  $z$ -direction and into 2 segments in azimuthal direction is currently under discussion. Such a scheme leads to 32 cells per azimuthal sector, hence to a total of 576 cells covering all of the central barrel. A trigger bit is derived from each cell depending on whether a track is seen within the cell. A Trigger Bit Logic Unit (TBLU) takes the 576 bits as input and generates a Level 0 signal which is sent to CTP. In this TBLU, the 576 bits are examined for coincidences generated by the track topologies of interest. In addition, coincidences or anti-coincidences of T0, V0-counters can be required at this level. Such a coincidence definition corresponds to a rapidity gap requirement as discussed above.

A possible trigger scheme for exclusive vector meson production is described below:

**Pretrigger for TRD:** The TRD pretrigger signal is taken from the output of the TBLU. Every Level 0 signal of TBLU is sent to TRD as pretrigger signal.

**Level 0:** The TOF Level 0 multiplicity coupled with a suitable topology cut (see next section) will provide a trigger for exclusive events with exactly two charged tracks in the central barrel. The different TBLU output bits carry the information of track multiplicity as well as of empty rapidity gap  $1.6 < |\eta| < 3.9$ . Level 0 triggers are asserted or rejected in the CTP by examining information of the Si-pixel detector. Dark triggers generated by TBLU will be mostly empty in the Si-pixel detector. The information from Si-pixel will therefore eliminate the dark rate considerably at Level 0.

**Level 1:** For the  $J/\psi \rightarrow e^+e^-$  and  $\Upsilon \rightarrow e^+e^-$  decay channels, the main trigger cut at this level will be the identification of one electron and one positron in the TRD. If a more accurate measurement of the multiplicity in the central barrel is available, it could be used to select events with exactly two charged tracks. Information from the zero-degree calorimeters may be used to select events with or without Coulomb breakup.

**High-level trigger:** The high-level trigger may be used to require exactly two tracks from the primary vertex in the TPC with opposite charge. Using the reconstructed momenta, a cut on the summed  $p_t$  of the tracks can be applied. This is highly efficient in suppressing the background from incoherent events. Some of the pions from the decay of the coherently produced  $\rho^0$  could be misidentified as electrons in the TRD at level one. Due to the extremely high rate for  $\rho^0$  production, it might be necessary to apply a cut on invariant mass in the High-level trigger to remove these events.

A similar scheme for  $\gamma$ -parton events is:

**Level 0:** Asymmetric signal in the V0 counters, in other words a low or intermediate multiplicity signal in the counter on one side and no signal in the counter on the opposite side, supplemented by a low-multiplicity trigger from a detector in the central arm, e.g. the time-of-flight.

**Level 1:** The ZDC on the same side as the rapidity gap should be empty. The signal in the ZDC on the opposite side should be low.

**High-level trigger:** The photonuclear events will occur with high rates and only a small fraction of them will be interesting. In addition, the asymmetric signature used in the lower trigger levels are satisfied by beam-gas interactions as well. The high-level trigger will be needed to reject beam-gas events and to select the interesting photonuclear events. This selection could involve identification of open charm.

*6.10.3.2. Trigger backgrounds.* When triggering on ultra-peripheral collisions, the most important parameter to face is the fake trigger rate (FTR), due to combinatorial background. The signal is characterised by a few tracks in an otherwise empty detector. The key ingredient when computing the FTR for the TOF Level 0 trigger is the MRPC noise, the measurement of which, performed in the CERN PS-T10 area, gave  $0.5 \text{ Hz cm}^{-2}$ . Such noise is due to ionizing particles in the chamber, while the fraction coming from the Front End Electronics noise is just few percent (this was measured by switching off the MRPC high voltage). An estimate of the noise that the TOF will experience when running in ALICE is not straightforward: the main sources of background will be the beam-gas collision, the beam mis-injection and the neutron delivered by the Pb-Pb interactions itself. Although the TOF does not contain materials with large neutrons absorption cross section, the TRD, placed in the neighbourhood, makes use of a gas mixture containing Xe (85%), whose isotope Xe-135 has a neutron absorption cross

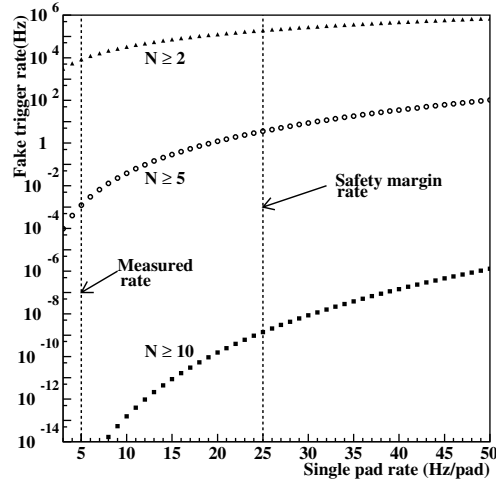


Figure 6.443. Level 0 fake trigger rate as a function of the single pad rate.

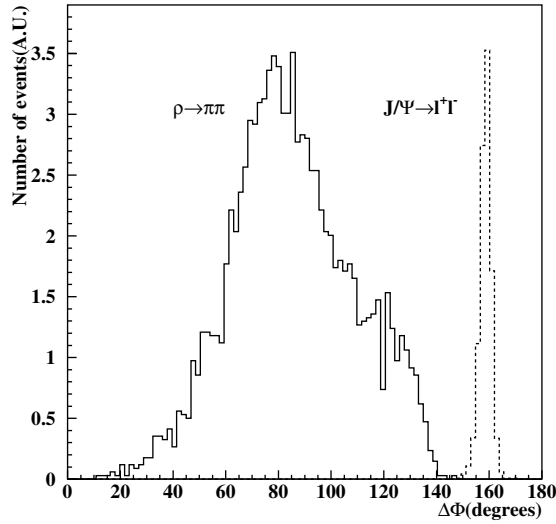


Figure 6.444. Difference in the azimuthal angle between the decay products in the  $J/\psi \rightarrow l^+l^-$  and  $\rho \rightarrow \pi\pi$  decay.

section of few millions of barns. As a safety margin we will use for the prediction reported below a MRPC noise of  $2.5 \text{ Hz cm}^{-2}$ , a factor 5 larger than the measured one.

Figure 6.443 shows the FTR as a function of the rate in the TOF single pad, whose area is approximately  $10 \text{ cm}^2$ . The FTR, when selecting a number of fired cells  $N_{\text{cell}} \geq 5$  is  $\simeq 1 \text{ Hz}$ , while the FTR for  $N_{\text{cell}} = 2$  is  $200 \text{ kHz}$ . Such high rate, unmanageable also at Level 0, can be further reduced by using the vector meson decay topology. We simulated the  $J/\psi \rightarrow l^+l^-$  and the  $\rho \rightarrow \pi\pi$  decay, using the ‘starlight’ Monte Carlo code [1069]. The particles produced in the decay were traced in an empty cylinder in a  $B = 0.5 \text{ T}$  magnetic field. We found an efficiency for containing both the decay products of  $\varepsilon_{\text{cont}}^{J/\psi} = 16.7\%$  and  $\varepsilon_{\text{cont}}^{\rho} = 8.3\%$  respectively. Figure 6.444 shows the distribution of the difference between the  $\varphi$  angles of the two particles produced in the decay, in the plane orthogonal to the beam axis. Although smeared by the

**Table 6.106.** Expected yields within the geometrical acceptance of the ALICE central barrel for Pb–Pb interaction.

Meson	Production Rate (per $10^6$ s)	Decay mode	B.R.	Geometrical Acceptance	Rate (per $10^6$ s)
$\rho^0$	$2.6 \times 10^9$	$\pi^+\pi^-$	100%	7.9%	$2 \times 10^8$
$J/\psi$	$1.6 \times 10^7$	$e^+e^-$	5.93%	16.4%	150 000
$\Upsilon(1S)$	80 000–250 000	$e^+e^-$	2.38%	23.6%	400–1400

magnetic field, a clear topology is still evident: for the leptons from  $J/\psi$  decay, by selecting only pairs of cells in a  $150^\circ \leq \Delta\varphi \leq 170^\circ$  window, the FTR can be reduced by a factor 18, while for the pions from  $\rho$  decay, by selecting only the cell pairs in a  $70^\circ \leq \Delta\varphi \leq 110^\circ$  window, the FTR can be reduced by a factor 9, while keeping 60% of the signal.

A further FTR reduction can be obtained for both vector mesons decay considering that in Pb–Pb interaction, despite a bunch crossing length of 125 ns, the TTC will distribute a 40 MHz clock. Since the OR signal has a 20 ns length, we can align this signal so that the positive edge of the TTC clock is well inside it. By enabling the latching only in the edge effectively corresponding to the bunch crossing and vetoing the latching in the four remaining edges, we can reduce the noise by a factor 5. In the combinatorial background, for  $N_{\text{cell}} = 2$ , this reflects in a factor 25, giving:

$$\text{FTR}_{\text{L0}} < 200 \text{ kHz} / 18 / 25 = 440 \text{ Hz} \quad \text{for the } J/\psi \rightarrow l^+l^- \text{ decay} \quad \text{and} \quad (6.167)$$

$$\text{FTR}_{\text{L0}} < 200 \text{ kHz} / 9 / 25 = 880 \text{ Hz} \quad \text{for the } \rho \rightarrow \pi\pi \text{ decay.} \quad (6.168)$$

Such FTR at L0 level has to be compared with the genuine  $J/\psi \rightarrow l^+l^-$  rate:

$$\text{Rate}_{J/\psi} = \mathcal{L} \cdot \sigma \cdot \varepsilon_{\text{cont}}^{J/\psi} \cdot \Gamma = 5 \times 10^{26} \text{ cm}^{-2} \text{ s}^{-1} \cdot 32 \text{ mb} \cdot 0.167 \cdot 0.12 = 0.32 \text{ Hz} \quad (6.169)$$

and with that of  $\rho \rightarrow \pi\pi$  rate:

$$\text{Rate}_\rho = \mathcal{L} \cdot \sigma \cdot \varepsilon_{\text{cont}}^\rho \cdot \varepsilon_\Phi = 5 \times 10^{26} \text{ cm}^{-2} \text{ s}^{-1} \cdot 5200 \text{ mb} \cdot 0.083 \cdot 0.6 = 120 \text{ Hz.} \quad (6.170)$$

The TOF can tag at Level 0 several meson decays: a detailed study on the selection capability in each UPC channel is undergoing.

**6.10.3.3. Expected rates in the central tracking arm.** The expected yields of vector mesons and lepton pairs from two-photon interactions were estimated from the geometrical acceptance of the ALICE central barrel and muon arm. Events were generated from a Monte Carlo model based on the calculations in [1044, 1069, 1070]. The rate calculations were performed with a beam luminosity of  $5 \times 10^{26} \text{ cm}^{-2} \text{ s}^{-1}$  for Pb–Pb collisions.

The geometrical acceptance of the ALICE central barrel is defined as  $|\eta| < 0.9$  and  $p_t > 0.15 \text{ GeV}/c$ , and for the muon arm  $2.5 \leq \eta \leq 4.0$  and  $p_t > 1.0 \text{ GeV}/c$  is used. It is required that both tracks are within the acceptance for the event to be reconstructed.

For the TRD, a trigger cut of  $p_t > 3.0 \text{ GeV}/c$  will be necessary in central collisions. It is not clear if this would be necessary for ultra-peripheral events. If it is, then it would preclude measurements of coherently produced  $J/\psi$ 's, which all have transverse momenta  $< 100 \text{ MeV}/c$ . The rates for  $e^+e^-$ -pairs are calculated with cuts in  $p_t$  of both 0.15 and 3.0  $\text{GeV}/c$ .

The calculations for vector mesons are summarized in Table 6.106, and the calculations for lepton pairs are shown in Tables 6.107 and 6.108.

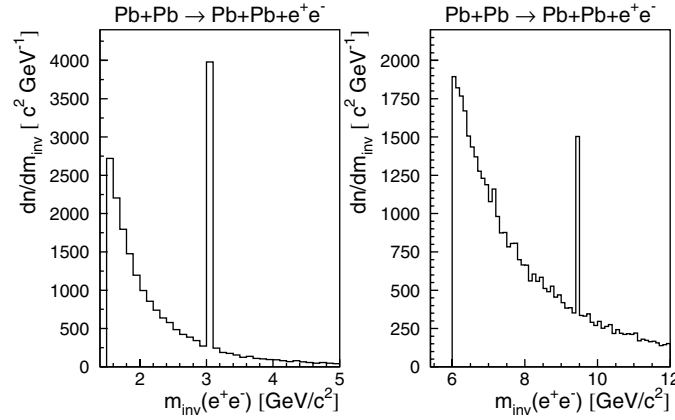
The rates for the  $J/\psi$  seem high enough for an early measurements in ALICE. For example, a luminosity of 5% of the design luminosity would give about 500 reconstructed

**Table 6.107.** Expected yields within the geometrical acceptance of the ALICE central barrel for two-photon production of  $e^+e^-$ -pairs.

Pb + Pb $\rightarrow$ Pb + Pb + $e^+e^-$ , $m_{\text{inv}} > 1.5$ GeV		
Selection	Geometrical Acceptance	Rate (per $10^6$ s)
All	100%	$7 \times 10^7$
$ \eta  < 0.9$ , $p_t > 0.15$ GeV	1.0%	$7 \times 10^5$
$ \eta  < 0.9$ , $p_t > 3.00$ GeV	0.02%	14 000

**Table 6.108.** Expected yields within the geometrical acceptance of the ALICE muon arm for two-photon production of  $\mu^+\mu^-$ -pairs.

Pb + Pb $\rightarrow$ Pb + Pb + $\mu^+\mu^-$ , $m_{\text{inv}} > 1.5$ GeV		
Selection	Geometrical Acceptance	Rate (per $10^6$ s)
All	100%	$2.2 \times 10^7$
$2.2 \leq \eta \leq 4.0$ , $p_t > 1.0$ GeV	0.26%	60 000

**Figure 6.445.** Invariant mass distributions for  $e^+e^-$ -pairs from two-photon interactions and decays of coherently produced  $J/\psi$ 's, where both the  $e^+$  and  $e^-$  are within the geometrical acceptance of the central barrel. The left figure shows the expected yield after  $2 \times 10^4$  s at the design luminosity (corresponding to an integrated luminosity of  $10 \mu\text{b}^{-1}$ ). The right figure is for  $2 \times 10^6$  s ( $1000 \mu\text{b}^{-1}$ ). Only the natural widths of the vector mesons have been included.

$J/\psi$ 's in a 24-hour run. A  $10^6$  s run with Pb–Pb would be sufficient to improve the statistics of photoproduced  $\Upsilon$ 's from HERA significantly.

The expected yield of  $e^+e^-$ -pairs in the central barrel with  $m_{\text{inv}} > 1.5$  GeV for a  $2 \times 10^4$  s run at the design luminosity is shown in Fig. 6.445 (left). The corresponding plot for  $m_{\text{inv}} > 6.0$  GeV for a  $2 \times 10^6$  s run is shown in Fig. 6.445 (right).

**6.10.3.4. Background sources in the central tracking arm.** The experience from RHIC is that coherent events can be identified with good signal to background ratios when the entire event is reconstructed and a cut is applied on the summed transverse momentum of the event. The amount of background from incoherent processes can be estimated by reconstructing events with two tracks of the same charge, e.g.  $\pi^+\pi^+$  or  $\pi^-\pi^-$  if the signal is  $\rho^0 \rightarrow \pi^+\pi^-$  [1066]. For heavy vector mesons, the main background will most likely be lepton pairs produced

in two-photon interactions (since these are produced in coherent interactions, they are not rejected by a cut on the pair- $p_t$ ) [1071].

The following sources of background have, nevertheless, been investigated: peripheral A–A interactions, incoherent  $\gamma$ –A interactions and cosmic muons. These sources were considered for a similar study in STAR [1070].

The contributions from cosmic muons to the trigger was non-negligible in STAR since the scintillator counters used in the central trigger barrel surrounded the TPC and covered a large area. Measurements from L3 + Cosmics which also used scintillators surrounding a large volume (the L3 magnet) saw a cosmic rate about a factor of five lower than calculated for STAR. Note that L3 is situated about 100 m below the surface of the earth. In STAR, the rate of cosmic triggers were reduced by a topology cut on the zenith angle. If the Si-Pixel detector is used for triggering, the area that is susceptible to cosmic muon triggers is much reduced.

Peripheral A–A interactions have been studied with FRITIOF 7.02 [1072]. 5000 peripheral events have been processed. The impact parameter  $b$  was in the range [13,20] fm, corresponding to about 25% of the inelastic cross section. Of these events, 435 (9%) fulfilled the condition that the number of charged tracks in the central barrel,  $n_{\text{TPC}}$  should be in the range:  $1 < n_{\text{TPC}} \leq 5$  and 97 (2%, corresponding to a cross section of about 40 mb) had  $n_{\text{TPC}} = 2$ . This latter number is then an order of magnitude lower than the cross section for  $\rho$  production. Furthermore, the pair- $p_t$  distribution is completely different from the one expected from the signal.

Incoherent photonuclear interactions might be an important background at the trigger level, and for inclusive events also at the analysis level. The direct photon–parton interactions constitute only a small fraction of the total photon–nucleus cross section. The bulk of the cross section is explained by the generalized vector meson dominance model, where the photon first fluctuates to a vector meson ( $\rho^0$ ) which subsequently interacts with the target inelastically. Since the energy spectrum of virtual photons is peaked at energies much lower than the beam energies, these interaction will resemble interactions between the beam nucleus and a hadron nearly at rest.

The total photonuclear cross section can be calculated by integrating over the virtual photon energy spectrum

$$2 \int_{k_{\min}}^{\infty} \sigma_{\gamma A}(k) \frac{dn}{dk} dk. \quad (6.171)$$

The 2 takes into account that each nucleus can act as both photon emitter and target. With a minimum photon energy cut-off  $k_{\min} = 10$  GeV in the rest frame of the target nucleus, and assuming a constant total cross section  $\sigma_{\gamma\text{Pb}} = 15$  mb [1073], this is 44 b. 50000  $\gamma$ –Pb events have been simulated under these conditions with the DTUNUC 2.2 event generator [1073]. 1595 (3%) of these fulfilled the acceptance criteria:  $1 < n_{\text{TPC}} \leq 5$ . This corresponds to a cross section of 1.4 b.

*6.10.3.5. Expected rates in the muon arm.* Coherent quarkonium photoproduction in ultra-peripheral ion collisions has a clearly distinguishable signature: a muon pair should be detected, and nothing else. The useful Level 0 component for this purpose is the muon trigger provided by the Muon Spectrometer in the forward rapidity region. Recently, it has been decided to equip PHOS with the electronics needed to provide a Level 0 trigger. The PHOS covers approximately 10% of the ALICE barrel solid angle, so it will always fire in the most central ALICE events. By combining the muon arm trigger with a veto on either PHOS or the TOF Level 0 signal, events with muon production in the forward direction and abnormally

**Table 6.109.** Expected rates for  $J/\psi$  photoproduction in Pb–Pb collisions (running time  $10^6$  s). The mass bin to estimate the the background was taken as  $\Delta M = 0.25 \text{ GeV}/c^2$ .

	LTA	S/B	Significance	IA/LTA
muon arm	25 000	5	150	2.28
muon barrel	21 400	0.5	80	6.19

**Table 6.110.** Expected rates for  $\Upsilon$  photoproduction in Pb–Pb (running time  $10^6$  s). The mass bin to estimate the background was taken  $\Delta M = 0.5 \text{ GeV}/c^2$ .

	LTA	S/B	Significance
muon arm	25	0.36	2.5
muon barrel	60	0.03	1.3

**Table 6.111.** Expected rates for  $J/\psi$  and  $\Upsilon$  photoproduction for Ar–Ar (running time  $10^6$  s, beam luminosity  $4 \times 10^{28} \text{ cm}^{-2} \text{ s}^{-1}$ ).

	LTA $J/\psi$	LTA $\Upsilon$
muon arm	25 000	33
muon barrel	13 000	72

low multiplicity will be selected at Level 0. We note that the trigger system of the muon arm will allow to select the reaction in two different configurations:

- ‘muon arm’: both muons are detected in the muon arm
- ‘muon barrel’: one muon is detected in the muon arm, the other in the central barrel.

At trigger Level 1 different detectors can be used to improve the selection of ultra-peripheral collisions, for example applying the veto from the outer rings of the V0 detectors.

The expected counting rates were estimated using the AliRoot simulation code [1074]. In the AliRoot simulation we assume that once the muon passed through the detector (10 tracking chambers + 4 trigger chambers of the muon spectrometer and/or has hits both in ITS and TPC), the detector response could be successfully analysed. The resulting acceptances are of the order of 5% and 2% for  $J/\psi$  and  $\Upsilon$ , respectively.

The counting rates (in LTA approach) expected in a Pb–Pb data taking period ( $10^6$  s) for  $J/\psi$  and  $\Upsilon$  photoproduction are given in Table 6.109 and 6.110, respectively. The corresponding counting rates for Ar–Ar collisions are shown in Table 6.111.

In Table 6.109 and 6.110, the signal to background ratios (S/B) and statistical significances ( $S/\sqrt{S+B}$ ) are also given. Note, that background level in [1053] was underestimated. The background is caused by muon pair production in  $\gamma\text{--}\gamma$  collisions (generated according to the distributions taken from [1075]). The angular distribution of the muon pair (which is highly peaked in forward direction) explains difference in S/B ratio in the cases mentioned above. The mass bins used to compute S/B and significance (see caption of Table 6.109 and 6.110) are larger than those quoted for central collisions; they were derived from the results of the AliRoot simulations taking into account the poor knowledge of the quarkonia decay vertex. Approximately 85–90% of the quarkonia reconstructed mass spectrum are within these limits.

The background from muon pairs produced in two-photon interactions will be a problem mainly for the  $\Upsilon$ . The situation is different for  $J/\psi$ : in this case the rate is large (about 1000 detected resonances per day) and both the signal to background ratio and the significance are

sufficient for clean measurement of the phenomenon. In the last column of Table 6.109 the ratios of the  $J/\psi$  rates obtained in the IA and LTA are displayed. The large value of this ratio (about 6) for the muon barrel indicates that the rates measured in this configuration are very sensitive to the reaction mechanism, allowing to explore the transition from nuclear colour transparency to the regime of colour opacity. The smaller value of the ratio for the Muon Arm configuration suggests that measurements of muon pairs in the Muon Spectrometer would be sensitive to gluon density functions.

*6.10.3.6. Background sources in the muon arm.* The first source of background is represented by the incoherent production of heavy quarkonia. As discussed above (see Fig. 6.440) the coherent and incoherent processes show completely different momentum transfer distributions. This feature, together with the fact that incoherent production can be accompanied by neutrons emitted in the ZDC acceptance, means that the two processes can be experimentally identified and studied separately.

Another source of physical background is muon pair production in  $\gamma\text{-}\gamma$  interactions. The total cross section for this process is large, and, as shown in Tables 6.109 and 6.110, the yield in the mass range of interest can also be significant.

Finally, we note that coherent production of heavy quarkonia can also occur in strong (pomeron–pomeron) interactions. The cross sections for this process are expected to be small. However, a more accurate evaluation of this contribution still has to be performed.

## 6.11. Cosmic-ray physics

*6.11.1. Contributions of ALICE to cosmic-ray physics.* The use of high energy collider experiments for cosmic-ray (CR) physics was pioneered during the LEP era by the L3 and ALEPH Collaborations [1076, 1077]. As ALICE intends to use a CR trigger for calibration and alignment of the central detectors, we have explored the possibilities of the experiment to contribute to CR physics, and to make genuine measurements in this field.

There are two main aspects where ALICE could contribute to CR physics. The first would lead to a better understanding of nuclear interactions at very high energy, a point that is fundamental to the description of CR interactions in the atmosphere. In this subject ALICE is unique because it has been designed to track and identify a very large number of charged particles created in pp, pA and A–A collisions event by event. The detailed measurements of the secondaries from the collisions of pp up to Pb–Pb interactions will be used to tune and test the hadronic interaction models at the highest energy attainable using accelerators.

The second aspect is the direct contribution to CR physics which may be accessible with ALICE. The excellent tracking performance of the TPC (described in Section 6.11.5.3), with its precise measurement of the particle momenta, improved by the utilization of other detectors like the TRD and TOF, can be usefully exploited in order to study muons produced after the interaction between a primary CR with a nucleus of the atmosphere. The capability to track very high densities of muons and measure their energy up to 1–2 TeV permits a new approach to the analysis of CR events previously unexploited. A (partially existing) surface array above ALICE, measuring in coincidence observables connected with the energy of the primary, the core and the direction of the extensive air shower, could be used to improve the characterization of the cosmic events.

In the following sections we describe in detail these two aspects and mention briefly the use of atmospheric muons in the calibration and alignment of specific detectors.

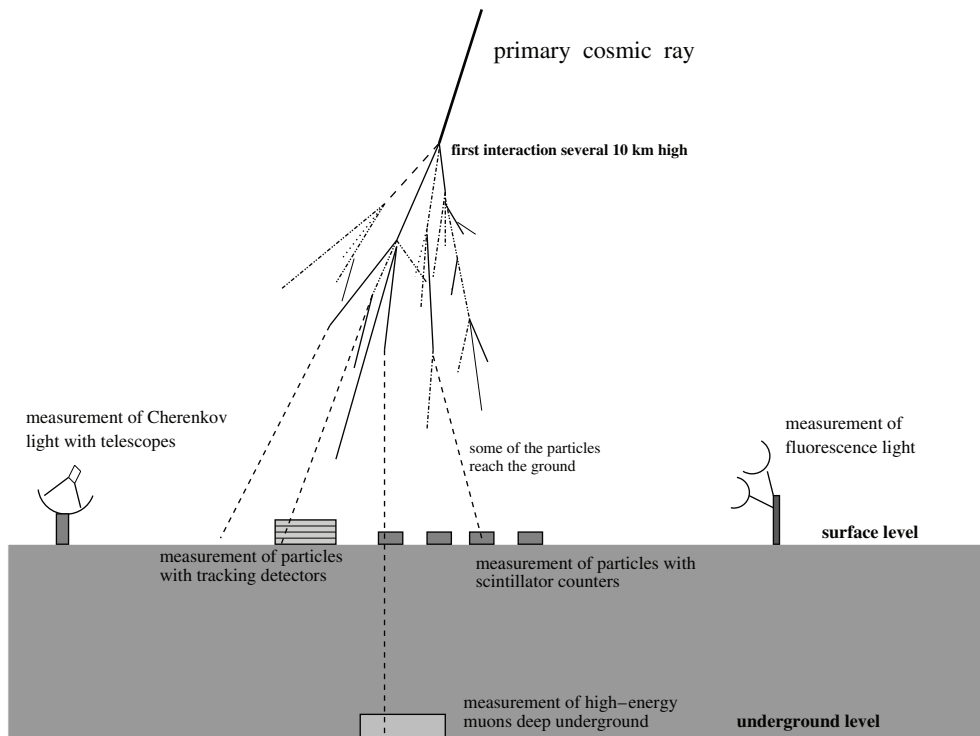


**Figure 6.446.** Pictorial view of an EAS.

**6.11.2. Hadronic interaction models in cosmic rays.** In Chapter 1 of PPR Volume I [3] it was explained that at energies above  $E \simeq 10^{14}$  eV CR measurements are indirect. The primary CR is detected through the shower of particles created by its interaction with a nucleus of the atmosphere. This cascade of particles, developing in the atmosphere, is called Extensive Air Shower (EAS) and it is shown in a pictorial view in Fig. 6.446.

Usually surface arrays of very large dimensions measure only some specific particles of an EAS, while underground apparatus detect only the energetic muons. The identification of the primary CR through measurements of the shower observables, detected at the altitude of the experiment, requires a comparison between experimental data and simulated events. The complicated development of a EAS and the fact that the standard CR experiments sample only a small fraction of the shower particles make sophisticated Monte Carlo simulations at very high energy a necessity. Obtaining a reliable reconstruction of the mass, energy and direction of the primary particle from measured quantities is a challenge for these analyses. This can be done only on a statistical basis by measuring a number of observables and requires a good understanding of the shower cascade and detector performance. While the electromagnetic cascade is well understood, most of the uncertainties in shower simulations arise from the hadronic interactions. In particular the inelastic cross section, the inelasticity, the production of secondary particles and the diffractive processes for proton–air or nucleus–air interactions have to be well understood in order to obtain a good simulation of the shower development. At present, some quantities and processes are poorly known at TeV energies, and for energies involved in indirect measurements several quantities are extrapolated by orders of magnitude.

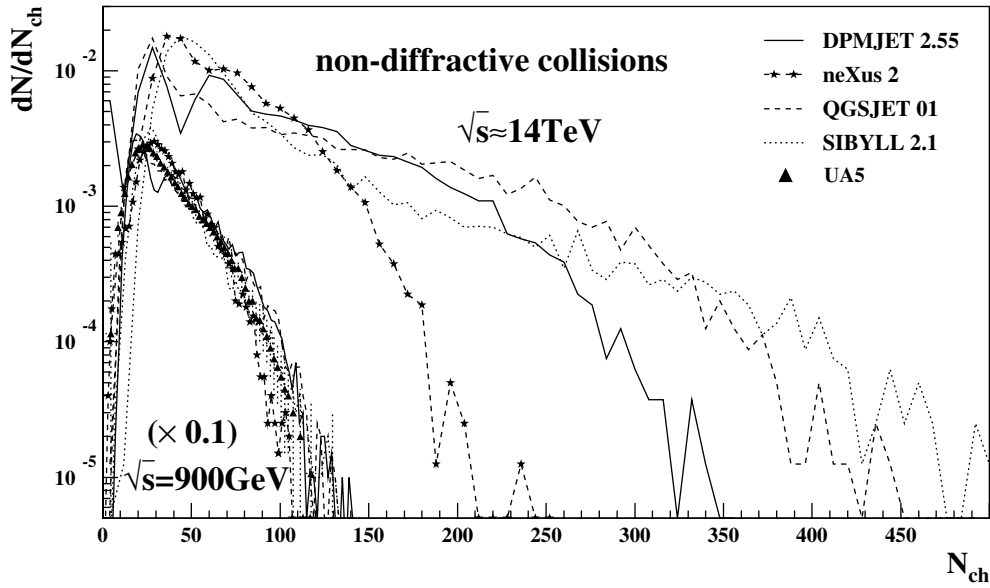


**Figure 6.447.** Multiplicity distribution of charged particles obtained with different hadronic interaction models at the UA5 and LHC energies.

The hadronic interactions are usually described in Monte Carlo programs by phenomenological models tuned to accelerator data at lower energies. Over the past few years, the CR community has adopted the CORSIKA code [1078] as simulation program for EAS development. It is a fully stochastic and four dimensional air-shower generator that contains several hadronic interaction models such as VENUS [1079], QGSJET [1080], DPMJET [1081], HDPM [1082], SIBYLL [1083], neXus [1084], among others, based on the Dual Parton Model (DPM). The first three models adopt concepts of relativistic quantum field theory according to the Gribov–Regge theory. SIBYLL contains the DPM approach with minijet production calculated from QCD, while HDPM, now considered obsolete, parametrizes the  $p\bar{p}$  collider data extrapolating to higher energies and using phenomenological extensions for nucleus interactions. neXus is an evolution of VENUS with the treatment of minijets; only these last two models introduce secondary interactions.

All models tune the free parameters by comparing the simulations to the available experimental data from  $p\bar{p}$ , ep, and heavy ion collisions. The parameters are usually adjusted at the Tevatron energy, i.e. around  $E \sim 10^{15}$  eV, or to  $p\bar{p}$  collisions at  $\sqrt{s} = 630$  or 900 GeV. The extrapolation of some physical quantities, up to LHC energy ( $\sqrt{s} = 14$  TeV), leads to considerable differences among the various interaction models. A detailed comparison of them was performed in [1085]. Figure 6.447 shows the charged particle multiplicity distributions in  $p\bar{p}$  collisions at  $\sqrt{s} = 900$  GeV for non-diffractive events. The distributions obtained by all the models are in good agreement with the experimental data taken by UA5 experiment [1086]. In the same figure, large differences are clearly visible among the various models when these distributions are extrapolated to pp collisions at the LHC ( $\sqrt{s} = 14$  TeV).

The p–air inelastic cross section and the inelasticity have a great influence on the shower development. The inelasticity corresponds to the fraction of energy of the interacting particle converted into the production of secondary particles. It governs the position of the

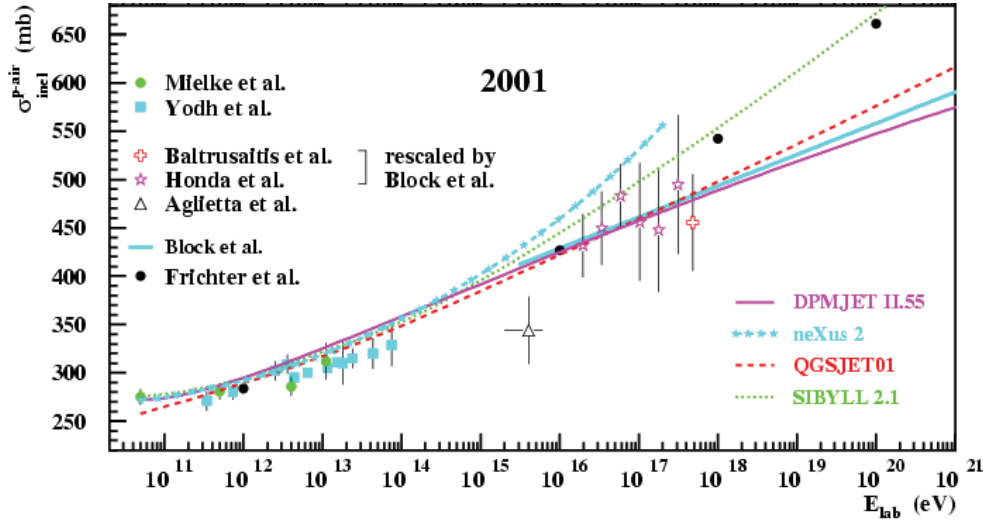


Figure 6.448. p–air inelastic cross section: measurements and theoretical calculations.

maximum number of particles reached by the shower. The inelastic cross section determines the average altitude in the atmosphere in which the first interaction occurs. A change of either of these quantities drastically changes the longitudinal development of the shower. Each model estimates the p–air cross section  $\sigma^{\text{p-air}}$  starting from the  $\sigma^{\text{pp}}$  measured in collider experiments, assuming a random distribution of the nucleons in the air nuclei and using the Glauber model. As we can see from Fig. 6.448, the calculation of  $\sigma^{\text{p-air}}$  leads to different results in the various models starting to diverge at energies relevant for cosmic rays at the knee ( $E > 10^{15}$  eV). A precise measurement of the pp cross section as foreseen by the TOTEM experiment [1087] at LHC will allow a better extrapolation of the  $\sigma^{\text{p-air}}$  to energies above the knee.

Knowledge of the collisions at very high energies, particularly of the secondaries emitted in the forward direction, is fundamental to the improvement of the interaction models for CR physics. Most of the energy is concentrated in this kinematic region, i.e. at very high rapidity or large Feynman- $x$ , strongly influencing the longitudinal development of the EAS. Unfortunately, none of the LHC experiments are particularly well suited to measuring particle production in the very forward region. The tracking capabilities and particle identification of ALICE in the central rapidity region and the multiplicity measurements down to  $\eta = 5$  ( $\theta = 0.7^\circ$ ), can at least be used to constrain hadronic interaction models and extrapolations can relate the different kinematic regions. The ALICE centre of mass energy of  $\sqrt{s} = 14$  TeV corresponds to a proton of  $E \sim 10^{17}$  eV interacting with a fixed nucleon target. The energy of the CR knee is at about  $E = 3 \times 10^{15}$  eV. For the first time, a large energy region above the knee will be explored with the LHC. As well as testing hadronic models at very high energy, accelerator measurements should clarify definitively whether the knee is generated by a change in the properties of the hadronic interactions or if it is due to astrophysical sources. This is one of the important issues debated over the last 40 years which remains unresolved.

A number of accelerator measurements can contribute to the improvement of the the knowledge of hadronic interactions in the energy range relevant for CRs. The hadron spectra for pp and pA minimum bias interactions in the Feynmann- $x$  region  $0.1 < x_F < 0.8$  are fundamental to a precise estimation of the average proton inelasticity and the position of

the shower maximum. The diffractive region is also of great importance but is inaccessible using the current set of experiments. Hadron spectra in the region  $0 < x_F < 0.1$ , where the measurements of ALICE are optimized are useful for providing the number of muons produced in the shower. The relevant measurements are the pseudo-rapidity distributions of identified hadrons. Hadron transverse momentum distributions for low  $p_t$  values ( $< 5 \text{ GeV}/c$ ) are useful for shower experiments using emulsion chambers and hadronic calorimeters.

The study of the A–A interactions is of considerable interest and in particular the nitrogen–nitrogen collisions, since nitrogen and oxygen are the most abundant nuclei in the atmosphere and the C–N–O group is very abundant at the knee energies. The opportunity to study hadron spectra in pp and pA collisions and also to divide these spectra in intervals of centrality can provide consistency checks of model predictions. The asymmetric interaction proton–nitrogen is also considered to be very important.

*6.11.3. The ALICE environment.* Before describing the direct contributions of ALICE to CR physics it is necessary to analyse the effects of the environment on atmospheric muons, and to clarify the differences with the standard CR underground detectors. The flux of cosmic muons is shielded at the ALICE location by 30 metres of rock. This is sufficient to stop all electrons and hadrons created at the surface, leaving only muons with energies above approximately 15 GeV. The magnet yoke and coils also act as additional absorbers. This threshold is much lower than for large underground experiments, which usually detect muons in the TeV region. Correspondingly, a much higher rate is expected.

The rock composition over the experiment is known from the geological surveys made for the L3 experiment. The surface above the ALICE location is flat within a radius of at least 200 metres from the centre of the apparatus, so its effect on the muon absorption and energy loss can be accurately evaluated. In contrast, underground laboratories located below large mountains have to cope with the poorly known overall composition of the rock, and with difficult energy loss corrections which depend on zenith and azimuth angle. A description of the ALICE environment and a first evaluation of its effects on cosmic muons is given below.

*6.11.3.1. Location of the ALICE set-up.* Measurements of CRs in underground experiments require detailed knowledge of the detectors involved and the environment around them. Significant physical effects of the material between ground level and the apparatus include energy loss of muons, scattering, and interactions. All these effects should be carefully simulated for a correct reconstruction of the physical information. The relevant aspects of the ALICE environment are:

- The structure of the main experimental hall underground, including the tunnels, shafts and any other large mechanical structure around the detector at the underground level.
- The composition of the rock below the ground level for a sufficiently large area (a circle of radius of about 200 m) around the ALICE location.

A general view of the CERN LHC Point-2, where the experiment will be installed is shown in Fig. 6.449, while the main parameters are summarized in Table 6.112.

The location and size of the main experimental underground cavern is known from the LEP project. The main accelerator tunnel is inclined by 1.39% with respect to ground level. The rock over the detector, up to the ground level, may be modeled by a uniform thickness of sub-alpine Molasses, whose composition and properties are reported in Table 6.113 [1088].

*6.11.3.2. Effects on atmospheric muons.* The effects of the environment on muons was simulated to explore the type and sensitivity of possible CR measurements within ALICE.

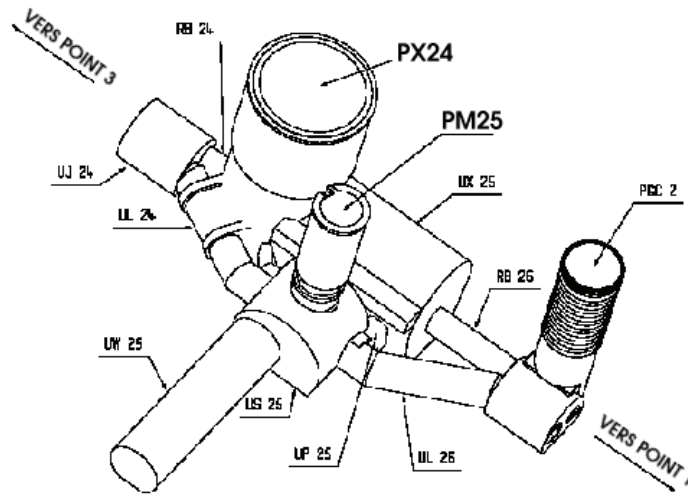


**Figure 6.449.** General view of LHC Point-2.

**Table 6.112.** Main parameters of LHC Point-2, where ALICE will be installed.

Latitude	46.15° N
Longitude	6.02° E
Altitude	449 m a.s.l.
Location of vertex detector	44.8 m underground
Rock thickness over the detector	30 m (approx. 290 rad.lengths)
Lower muon energy threshold	approx. 15 GeV
Orientation of the z-axis	North-West to South-East, about 37.5° w.r.t. North

**Table 6.113.** Composition of sub-alpine Molasses over the ALICE detector. The mean mass number of this material is 23.64, with a density of 2.40 g cm<sup>-3</sup>.

element	H	C	O	Na	Mg	Al	Si	K	Ca	Fe
percentage %	0.8	4.3	48.5	0.7	4.2	3.7	21.5	2.3	10.0	4.0

The average energy threshold  $E_{\mu_{th}}$ , for muons reaching the central magnet after crossing the rock is  $E_{\mu_{th}} \simeq 14\text{--}15$  GeV. Muons crossing the two shafts PX24 and PM25 have a lower threshold as shown in Fig. 6.450, in which the energy loss in the rock is plotted for different azimuth angles. The behaviour of the energy loss with zenith angle is shown in Fig. 6.451. Muons with large zenith angles cross a greater amount of rock and lose more energy; for example the threshold for  $\theta = 50^\circ$  is around 25 GeV. At particular angles, muons travel along the shafts and lose only a small fraction of their energy. This effect is clearly visible in Fig. 6.451, showing that it occurs preferably for zenith angle around  $20^\circ\text{--}40^\circ$ .

Muons crossing the rock change direction due to multiple scattering. This introduces an error in the measurement of the muon direction that has to be added to the tracking error. The distribution of the angular deviation in the space  $\Delta\Psi$  from the direction at surface level for muons with  $p_\mu = 50$  GeV/ $c$  is plotted in Fig. 6.452. At this energy the r.m.s. of the angular deviation due to the rock is around  $\sigma = 0.3^\circ$ . The dependence of the r.m.s. of the angular deviation on the muon energy is plotted in Fig. 6.453.

Energy loss and multiple scattering change the properties of muons reaching the experiment affecting both the flux and the shape of the energy spectrum. To analyse these

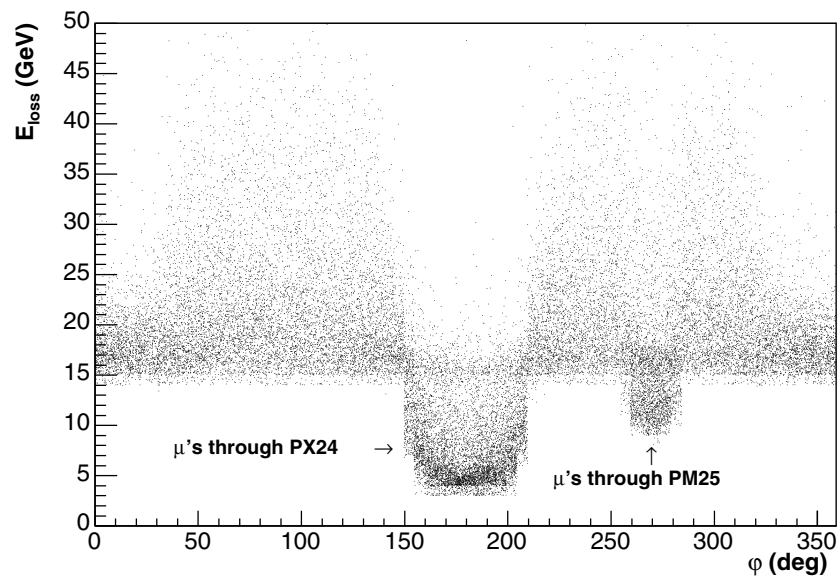


**Figure 6.450.** Energy loss by the muons crossing the rock above ALICE and reaching the upper octant of the central magnet, at different azimuth angles. The effect of the shafts PX24 and PM25 is clearly visible. The location of these two shafts is shown in Fig. 6.449.

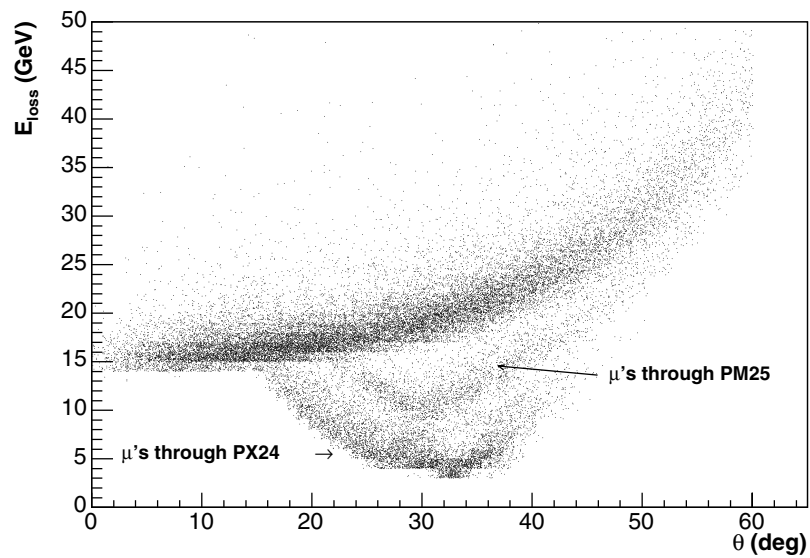


**Figure 6.451.** Energy loss by the muons crossing the rock above ALICE and reaching the upper octant of the central magnet, at different zenith angles. The effect of the rock and of the two shafts PX24 and PM25 is clearly visible.

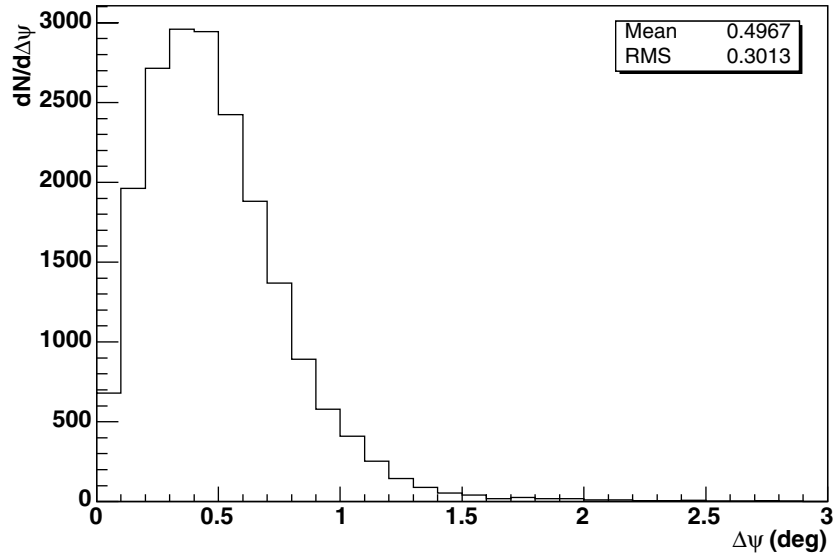


**Figure 6.452.** Angular deviation in space between muon direction at surface and on the upper octant of the central magnet for muons with  $p_\mu = 50 \text{ GeV}/c$ .

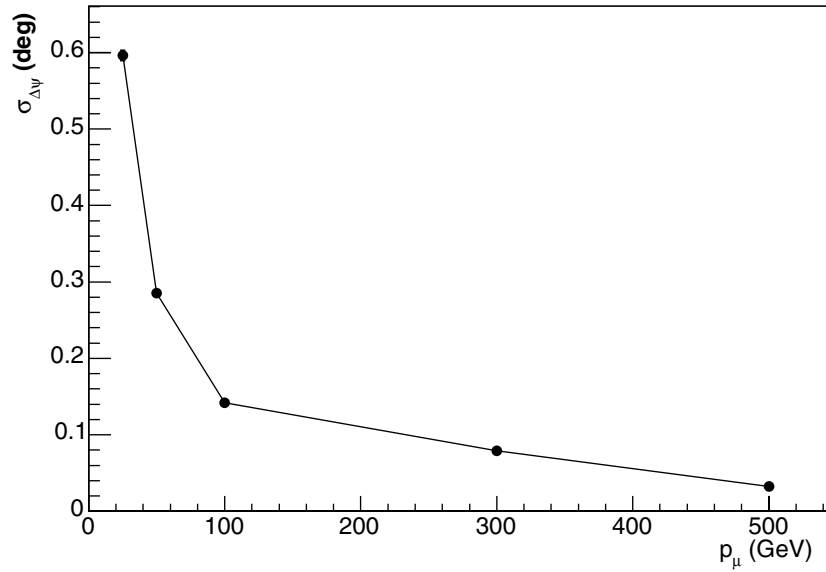


**Figure 6.453.** The r.m.s. of the angular deviation between muon direction at surface and on the upper octant of the central magnet as a function of its momentum.

effects, atmospheric vertical muons ( $0^\circ < \theta < 20^\circ$ ) were generated with the shape of the momentum spectrum and angular distribution given in [1089]. A comparison of the inclusive muon momentum distribution at surface level and of the muons reaching the central magnet is presented in Fig. 6.454 showing the cut-off at low momenta.

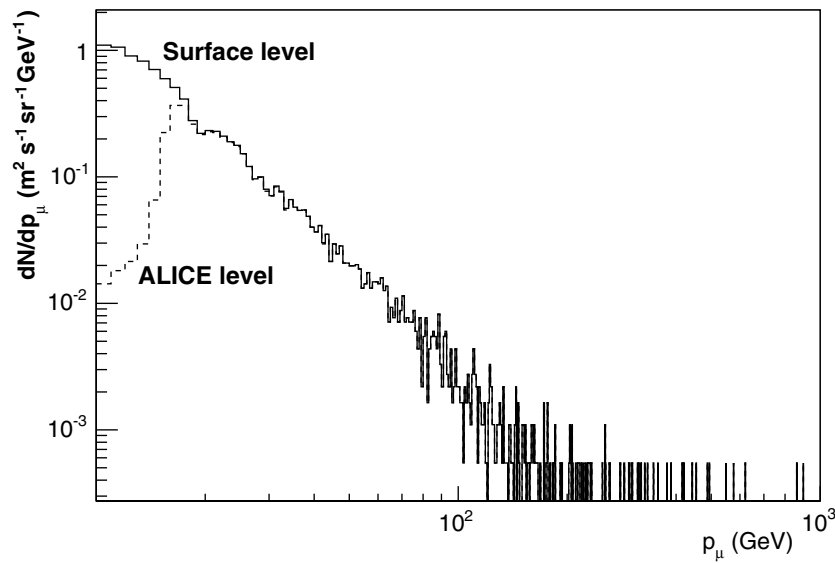


**Figure 6.454.** Muon spectrum at surface level compared with the spectrum of the muons reaching the upper octant of the ALICE central magnet. Only vertical muons are considered.

*6.11.4. Physics topics of interest.* The CR topics which can be addressed in ALICE depend not only on the environment as described above, but also on the trigger conditions and on the live time of the data taking. In principle, a complete coverage of the three upper octants of the central magnet with scintillators (around 200 m<sup>2</sup>) would guarantee the best conditions for triggering atmospheric muons. However, the trigger rate would be of the order of 450 Hz for single muons, which is unacceptable during ALICE data taking.

The coverage currently foreseen for calibration purposes (about 10 m<sup>2</sup> centred above the TPC) would lead to single muon rates of the order of 30 Hz.

An accurate measurement of the energy spectrum and charge ratio of vertical muons in the energy range up to  $E = 1\text{--}2$  TeV can only be performed if a single muon trigger is implemented. Given the size and rate limitations in ALICE, it will be difficult to improve on the statistics taken by the L3 + C experiment ( $> 10^{10}$  CR triggers [1090]).

A multi-muon trigger considerably reduces the acquisition rate also for large surfaces of trigger detectors. Preliminary measurements performed in the experimental cavern have given a coincidence rate (two muons) of 0.027 Hz for a configuration of two  $20 \times 20$  cm<sup>2</sup> scintillator pads placed at a distance of 20 cm from centre to centre. With a distance of 95 cm the coincidence rate has decreased to 0.0021 Hz. These values indicate a level of few Hz of acquisition rate also for large trigger surface when the trigger request is at least two muons, a rate acceptable also during standard data taking. For all these reasons the study of muon bundle seems the most promising topic, while inclusive muon measurements will be limited to vertical events.

*6.11.4.1. The trigger background due to pp interactions.* The CR trigger will deliver a signal during the operation of the LHC beam, and, as explained in the previous paragraph, a cosmic rate of a few Hz is expected for multi-muon events. We have, therefore, to evaluate the level of contamination to this trigger coming from standard pp or heavy-ion interactions, to decide

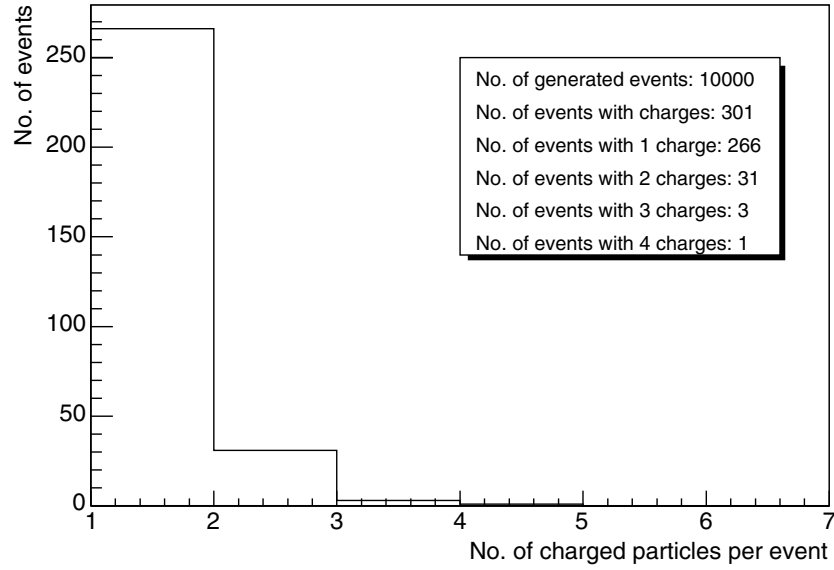


**Figure 6.455.** Number of charged particles per event reaching a  $25 \text{ m}^2$  area above the magnet due to standard pp interactions.

the strategy of the data taking and to estimate its live time. A pp interaction rate of about 200 kHz is foreseen during operation with proton beams at  $3 \times 10^{30} \text{ cm}^{-2} \text{ s}^{-1}$  luminosity. In order to calculate the rate of the fake triggers for cosmic muons at this luminosity we have simulated 10000 minimum bias pp standard events. The number of charged particles per event reaching the external part of the upper octant of the magnet, in an area of  $5 \times 5 \text{ m}^2$  centred above the TPC, is shown in Fig. 6.455. We can see that about 3% of the events give a charged particle in this area, therefore we foresee a fake trigger rate due to pp interactions of the order of 6 kHz for single muon and 600 Hz for multi-muon trigger. This rate does not allow for the use of ACORDE in stand-alone mode. The use of an anticoincidence with V0, T0 and Pixel Detectors can reject the contamination from pp interactions. This anticoincidence will reduce the live time of the cosmic data taking to the level of around 25–30% of the pp run time. In one year of data taking the pp run will be active for  $10^7 \text{ s}$  while the heavy-ion run will last  $10^6 \text{ s}$ . In addition, the empty bunch-crossing time slots, not occupied by particles, will be opened for CR trigger. We estimate, therefore, a live time of about 30 days for cosmic run in one year of LHC operation. Assuming a rate of about 1 Hz for the multi-muon trigger, more than  $2.5 \times 10^6$  events can be taken in one year.

**6.11.4.2. Muon bundles.** ALICE is particularly well adapted to observe underground multi-muon events, which are of interest to investigate the composition of very high energy CRs and to search for exotic CR events.

The transverse size of muon bundles, their number and their energy distribution are sensitive to the mass of the primary nucleus inducing the EAS. A previous analysis of muon bundles from CRs has been done at LEP using the ALEPH detector [1077]. Multi-muon events observed in the  $16 \text{ m}^2$  ALEPH TPC detector with a momentum cut-off of  $70 \text{ GeV}/c$  have been found to be in good agreement with the simulations for multiplicities  $2 < N_\mu < 40$ . In particular, the comparison with the QGSJET CORSIKA simulation for proton and iron

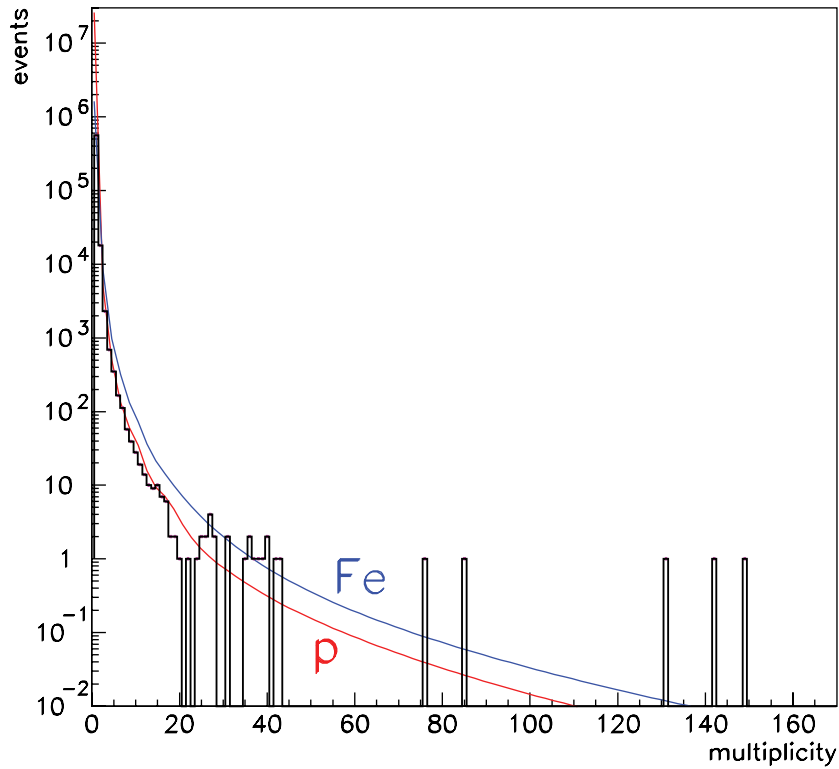


**Figure 6.456.** Multiplicity distribution of muons from the ALEPH-TPC in the CosmoLEP experiment. Data are compared to CORSIKA simulations for p and Fe primary particles. In evidence the five events with highest multiplicity.

primary particles demonstrated that the proton curve describes the observed data well over several orders of magnitude up to muon multiplicities  $N_\mu = 20$ . This indicates that the primary spectrum is dominated by light elements at energies corresponding to these multiplicities. At larger multiplicities there is evidence of a transition to the iron curve. Iron induced showers are more effective in producing muons since they interact higher in the atmosphere and also produce larger pion multiplicities. However, there are five events (see Fig. 6.456) with unexpected large multiplicities  $N_\mu$  (up to 150) which cannot be explained, even assuming pure iron primaries. The highest multiplicity event was actually recorded in only half of the TPC volume because of data overflow. It should also be mentioned that anomalous high multiplicity muon bundle events were also reported by the BUST [1091] and Kolar Gold Fields [1092] experiments.

A number of speculative interpretations of anomalous muon bundles are proposed in the literature, relating them to the existence of Strange Quark Matter (SQM) (see [1093, 1094]) or the formation of Quark–Gluon Plasma (QGP), e.g. in iron–air collisions at the highest energies [1095].

The topology of such muon bundle events can easily be recognized by the ALICE experiment. The fine granularity of the TPC will provide very good pattern-recognition, tracking resolution and momentum determination of the multi-muon events as shown in Section 6.11.5.3. The analysis of the muon bundles will contribute to the understanding of

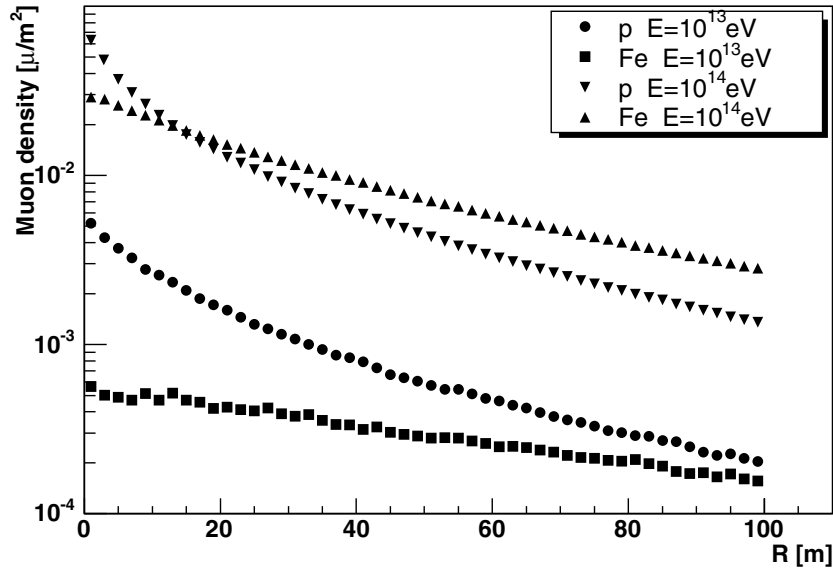


**Figure 6.457.** Lateral distributions of muons reaching ALICE due to p and Fe primaries with  $E = 10^{13}$  and  $10^{14}$  eV.

the composition of very high energy CRs as explained in Section 6.11.4.3 and this might well deliver exciting surprises.

**6.11.4.3. Muon bundles in ALICE.** In order to understand the characteristics of multi-muon events in ALICE we simulated showers produced by the atmospheric interaction of the two extreme types of primary CRs : protons (p) and iron nuclei (Fe) representing the light and the heavy component. The simulations were developed using the CORSIKA code with QGSJET as the hadron interaction model. As a first step, only vertical primaries with four fixed energies,  $E = 10^{13}$ ,  $10^{14}$ ,  $10^{15}$  and  $10^{16}$  eV per element, were simulated to get information on CRs below and around the knee.

Knowledge of the topology of muons crossing the detectors for different primaries and energies is fundamental to understand which kind of measurements can be done with our apparatus. The average lateral distribution of muons (muon density vs distance from the shower centre) reaching the ALICE experiment gives us preliminary information on the maximum muon density and their spatial location. These lateral distributions obtained for p and Fe primaries are shown in Fig. 6.457 for the lower energies and in Fig. 6.458 for the higher ones. We see that at high energies ( $E \geq 10^{15}$  eV) the muon density of the core is independent of the primary, while at lower energies the muons in the core produced by protons have higher probability of reaching the experiment because their energies are higher than muons coming from iron. The maximum density of the core (taken in this analysis as a circle of 2 m of radius around the centre of the shower), is expected to be around  $0.6 \mu/m^2$  for  $E = 10^{15}$  eV (just below the knee), increasing to around  $6 \mu/m^2$  for  $E = 10^{16}$  eV (above the knee). Extrapolating these distributions we estimate a muon density around  $60 \mu/m^2$  for primaries with  $E = 10^{17}$  eV, a density easily measurable with the ALICE TPC as explained in Section 6.11.5.3.

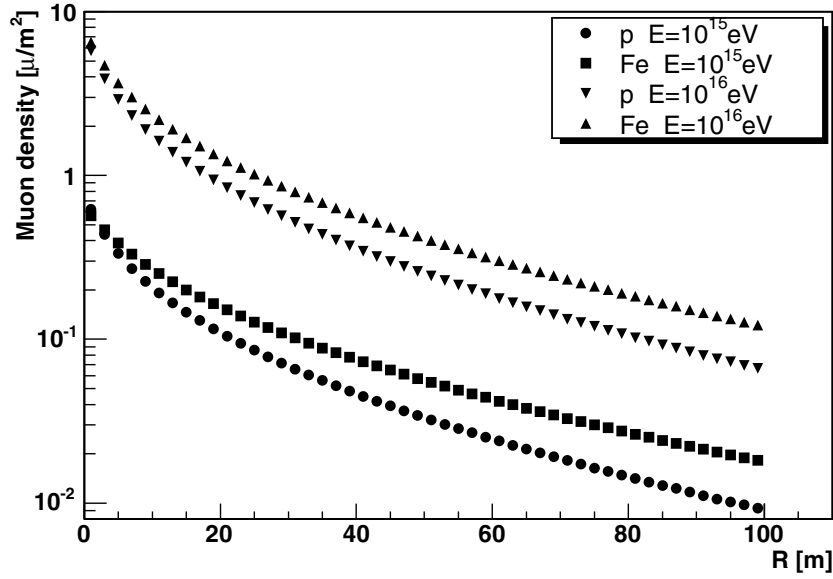


**Figure 6.458.** Lateral distributions of muons reaching ALICE due to p and Fe primaries with  $E = 10^{15}$  and  $10^{16}$  eV.

The TPC is not large enough to study the lateral distribution of the muons but it can be used to measure the density and the energy of the muons crossing the active volume. The measurement of the average energy of the muons detected in the core, for different number of muons in the core  $N_{\mu}^{\text{core}}$ , is shown in Fig. 6.459 for p and Fe with  $E = 10^{15}$  eV. This correlation has the potential to distinguish among the various components of CRs, and a new approach to composition studies can be developed. We see that at low values of  $N_{\mu}^{\text{core}}$  the difference between the average energy of muons due to p ( $\langle E_{\mu} \rangle \simeq 1.1$  TeV) and Fe ( $\langle E_{\mu} \rangle \simeq 0.5$  TeV) is very large, slightly decreasing with the number of muons. This approach was never adopted in the past because CR standard underground detectors are very large in size but do not use magnetic fields to track the muons. The precision of the energy measurement in ALICE introduces new opportunities that still need to be investigated.

As explained in Section 6.11.4, the trigger rate is a crucial aspect because a low trigger rate (few Hz) does not affect the standard data taking of ALICE with either pp or with Pb–Pb collisions, while a higher rate requires to run in a dedicated mode. Most of the atmospheric muons crossing ALICE are created from p or He primaries of energy below  $E = 10^{13}$  eV. A cut in the number of muons strongly decreases the trigger rate and allows an efficient selection of events with higher energies. To evaluate quantitatively the total number of muons reaching ALICE and their dependence with the energy a second sample of simulated events was produced. Showers created by proton primaries in the energy range  $10^{12} < E < 10^{17}$  eV and within the zenith angular range  $0^{\circ} < \theta < 60^{\circ}$  were analysed. Supposing all cosmic rays are due to protons (light elements), an energy spectrum given by

$$\frac{dF}{dE} = 0.225 (E[\text{TeV}])^{-2.7} [\text{m}^2 \text{ s sr TeV}]^{-1}$$

was adopted where  $F$  is the CR flux and 0.225 is its value at  $E = 1$  TeV [1096].

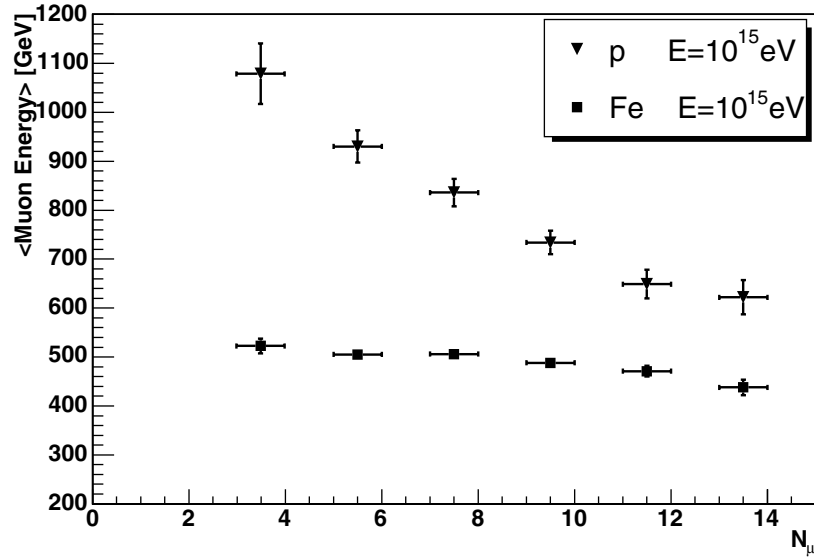


**Figure 6.459.** Average energy of muons in the core for different number of muons in the core. Proton and Fe primary at  $E = 10^{15}$  eV have been simulated.

The number of muons reaching the upper octant of the central magnet in a  $5 \times 5$  m<sup>2</sup> surface centred above the TPC was estimated simulating primary protons in three bins of energy,  $10^{12} < E < 10^{13}$  eV,  $10^{13} < E < 10^{14}$  eV and  $10^{14} < E < 10^{15}$  eV. The distribution of the CR muon multiplicity in 30 days of data taking is shown in Fig. 6.460. We see that a trigger requirement of at least two muons instead of a single muon reduces the number of events by a factor 300 and cuts most of the low energy events. A more severe cut demanding at least five muons selects mostly events with energy above  $E = 10^{14}$  eV, i.e. the region usually analysed with indirect measurements.

The total muon multiplicity distribution in 30 days of data is given in Fig. 6.461 where the contributions of the different ranges of energy are also shown. No knee in the energy flux is taken into account, so this distribution can be considered as an upper limit. In 30 days we do not expect events with muon multiplicity higher than one hundred for proton primaries.

In Fig. 6.462 we compare the muon multiplicity due to pure proton primaries (light elements) with the multiplicity given by pure iron components (heavy elements). Also for pure iron we do not expect events with multiplicity over one hundred in 30 days of data taking. These multiplicities can be easily detected with the ALICE TPC, providing in just one year of running a confirmation of the high multiplicity events observed by ALEPH.

The two curves (light and heavy elements), differing only by less than a factor two, demonstrate the difficulty in separating the CR spectrum into light and heavy components. A detailed analysis of the muon energy may improve significantly the discrimination power concerning CR composition.

**6.11.4.4. Other measurements with atmospheric muons.** Atmospheric muons are created during the development of a shower and constitute the most abundant charged CR component reaching the Earth's surface. They provide valuable information on the primary CR fluxes as well as on the interaction mechanisms of high-energy particles in the

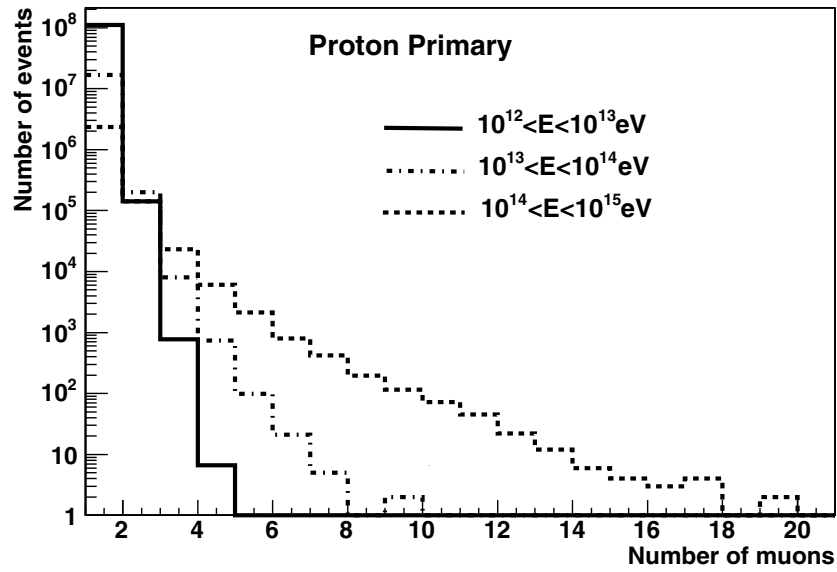


Figure 6.460. Muon multiplicity distribution in ALICE in 30 days of data taking in three ranges of energy for the primary.

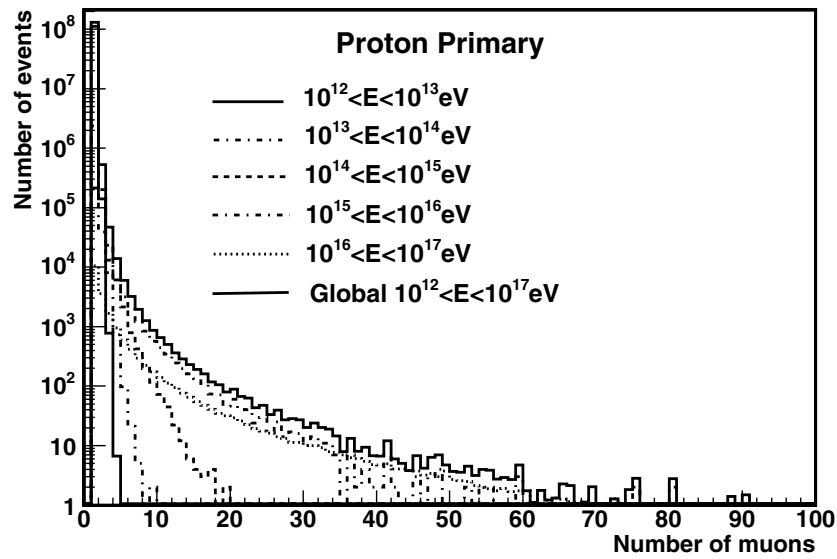


Figure 6.461. Muon multiplicity distribution in ALICE in 30 days of data taking. The contribution of each range of energy is plotted. The all-particle spectrum is assumed to contain only protons.

atmosphere. Muon measurements are also a powerful means of calibration of the atmospheric neutrino calculations. Available results show discrepancies of up to 15–20% in the absolute normalization of the muon fluxes and differences in the observed energy spectra. In Ref. [1089] a compilation and a detailed analysis of all published measurements from 1950

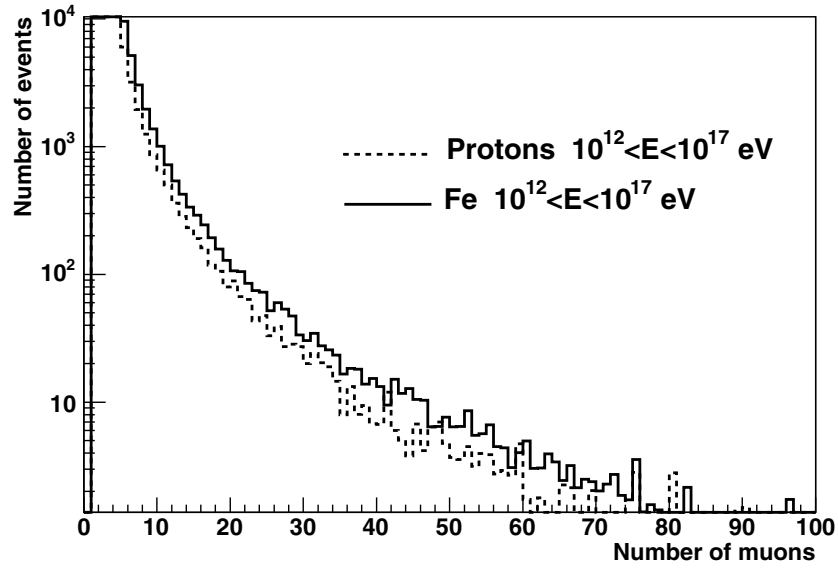


Figure 6.462. Comparison of the muon multiplicity distribution in ALICE in 30 days of data taking for pure proton and pure iron composition.

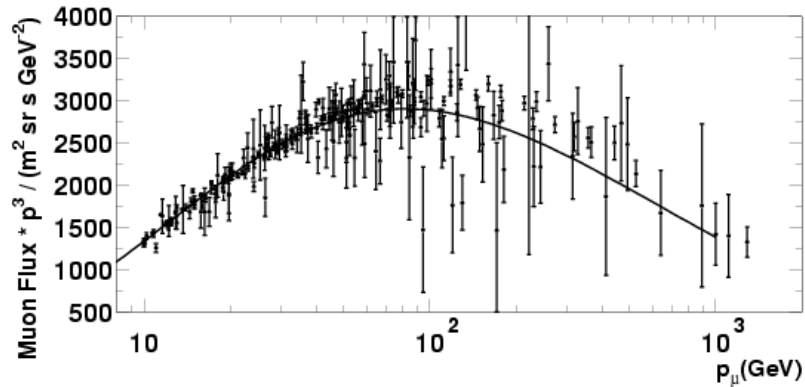


Figure 6.463. Experimental data of vertical atmospheric muon flux and the fitted curve.

until 1999 on vertical atmospheric muon flux and charge ratio is presented. We show in Fig. 6.463, a collection of the experimental data on the muon flux, and the curve obtained by fitting them. The results are mainly concentrated in the range below 100 GeV, while above it few detections were performed and these have large errors.

Only recently, a detailed measurement of the inclusive muon spectrum from 20 GeV up to 3 TeV and the ratio of fluxes of positive to negative muons ( $\mu^+/\mu^-$ ) with errors of a few percent have been obtained with the L3+C experiment [1090]. Final results on the muon spectrum in eight angular bins ranging from  $0^\circ$  to  $58^\circ$  have been reported. The comparison of their results for vertical muons to low momentum experiments like BESS [1097], CAPRICE [1098], MASS [1099] demonstrates a good agreement for both shape and absolute flux normalization of the muon spectrum in the range 40–100 GeV. The

situation is not so clear at higher energies. Only two previous experiments measured an absolute spectrum at high energies; the Kiel spectrum [1100] agrees with the shape of L3 + C, but not with the normalization, while the MARS spectrum [1101] disagrees significantly both in shape and normalization.

A new measurement with ALICE on vertical muons would clarify this situation making use of the powerful tracking capabilities and the high statistics that the experiment can produce in several years of data taking. The measurements have to be carried out over an energy range as wide as possible, especially extending them to high energies (1–2 TeV) where the results are not in agreement among the various experiments. The upper limit is imposed by the intensity of the magnetic field and by the precision of the tracking system. Our first investigation shows that, with a magnetic field intensity of  $B = 0.2$  T, the maximum muon momentum measurable with an error smaller than 50% is 400 GeV/ $c$ . This momentum is extended to at least 1 TeV with a magnetic field intensity of  $B = 0.5$  T, as explained in Section 6.11.5.3.

The search for gamma-ray emission from point sources at TeV and PeV energies is one of the main tools used to understand the origin of high energy CRs. In the eighties several collaborations reported gamma-ray emissions up to very high energies ( $E > 100$  TeV) from Cygnus X-3, a binary system composed of a neutron star and a red giant [1102–1105]. These positive results, however, were not confirmed by more recent measurements [1106, 1107]; this calls into question their statistical significance, but may instead be due to source variability.

In the past, it was proposed to identify gamma ray sources, measuring the rate and the direction of high-energy muons reaching underground detectors, although gamma-rays create showers with approximately 30 times less muons than showers produced by proton primaries [1108]. The capacity of ALICE to seek these sources using standard analysis, as performed with EAS arrays or underground detectors, are limited because of the small surface of the TPC. The search for point-like sources performed by the ALEPH experiment [1077] seems a more appropriate approach for ALICE, although less quantitative than standard searches. With this approach the direction of the events with an high multiplicity of muons have to be transformed into galactic coordinates to verify whether they point to known photon sources. The events analysed by ALEPH did not point to known gamma sources in our galaxy or nearby galaxies, but the statistics was quite poor. A new measurement with ALICE, could gather a ten times larger sample in one year of operation (30 days of live time).

*6.11.4.5. Large area coincidence experiments.* The lateral distribution of muons reaching ALICE presented in Fig. 6.458 indicates that most of the muons are confined to less than few hundred metres in radius also for high energy primaries ( $E = 10^{16}$  eV). Higher energy primaries have a very low rate and are usually investigated at ground level by large detector arrays, while due to the muon momentum cut-off of underground apparatus it is very improbable to observe them in large spread underground experiments such as in the configuration of the LHC experiments. The observation of some time correlated events in CRs over large distances are therefore unexpected and could help to understand the interaction of high energy cosmic nuclei with matter at astrophysical distances. This requires a comparison between the observed and expected rate of standard showers. Also multi-muon events, not explained by shower simulations, may point out the importance of astrophysical radiation originating at large distances, from cosmic beam-dumps [1109], from interactions with interstellar matter or other sources. Even the largest underground detectors are unable to detect these correlations, which are spread-out over much larger distances.

Proposals were made to measure coincidence events between the four LEP experiments, using additional counter arrays mounted around the LEP ring. A pilot experiment was carried out [1110] with the ALEPH detector (for which the muon energy threshold was about 70 GeV)

and five scintillator stations located up to a distance of 1150 m. Double coincidence rate was measured between stations as far apart as 526 m, and triple coincidences were also observed. The double coincidence rate as a function of distance between two stations was compared with Monte Carlo simulations and found in agreement with the hypothesis of a unique large energetic shower originating in the atmosphere.

These experiments can also be carried out by the large LHC detectors, if a suitable CR trigger and a common timing system are implemented. These events can be correlated off-line by using the universal time recorded independently by each experiment for each CR event.

*6.11.5. Use of the TOF and TPC for the detection of atmospheric muons.* The trigger for the detection of cosmic muons is mainly obtained with the ACORDE detector, which is composed of several scintillator counters located in the three upper octants of the central magnet. The arrangement of these counters can be easily changed in order to obtain the most convenient geometry for specific measurements. A detailed description of the ACORDE detector for cosmic triggers was given in PPR Volume I [3]. The TOF can also be used in coincidence with ACORDE or in stand-alone mode to trigger on cosmic muons. In the next paragraph the performance of the TOF as a trigger detector is described.

The central part of the ALICE detector, especially the main tracking device, the TPC, can be used as a cosmic muon spectrograph, due to the large volume and tracking capabilities. The TPC may be tuned to reconstruct cosmic muons with a good resolution ( $\sigma_p/p < 50\%$  at 1 TeV) up to TeV energies, which is better than other CR experiments employing magnetic spectrometers. Also the charge state of the muons traversing the TPC, may be measured up to high energies. An example of a multi-muon event recorded with a TPC sector during tests with atmospheric muons at surface level is given in Fig. 6.464. As we can see, atmospheric muons have a high degree of parallelism and the topology of these events is very different from standard heavy-ion collisions. An initial evaluation of the performance of the TPC detecting cosmic muons is described below. In addition to the TPC, the TRD can be used to both increase the sensitive area (by approximately a factor of two) and to improve the momentum resolution. Its performance for CR physics has however not yet been studied in the simulations.

*6.11.5.1. Use of the TOF as a cosmic trigger.* Because of its fine segmentation (more than  $10^5$  independent channels), fast time response ( $\sim 40$  ps), relatively low noise and large area ( $141 \text{ m}^2$ ), the TOF can give a very significant contribution to the cosmic muon trigger. In addition to their interest for CR physics, these muons provide unique tool to calibrate and align the detectors during commissioning.

The design and the optimization of a cosmic trigger requires a dedicated Monte Carlo simulation, to maximize the signal to noise background ratio and to improve the trigger efficiency.

Cosmic muons at ground level were produced by the COSMOS [1111] event generator and transported through the rock ( $\rho = 2.40 \text{ g cm}^{-3}$ ) by the FLUKA [1112] simulation code. The folding of the cosmic muon flux with the TOF geometry, was made by a simple Monte Carlo, implementing a rough geometry of the TOF. The present study was originally performed to optimize the cosmic trigger for the detector commissioning, assuming the ALICE magnet is switched off.

The L3 + C Collaboration [1090] provided several measurements on the cosmic muons features in the ALICE pit: the muon rate, the angular and the momentum distribution were carefully measured. We used these results as a benchmark for our Monte Carlo.

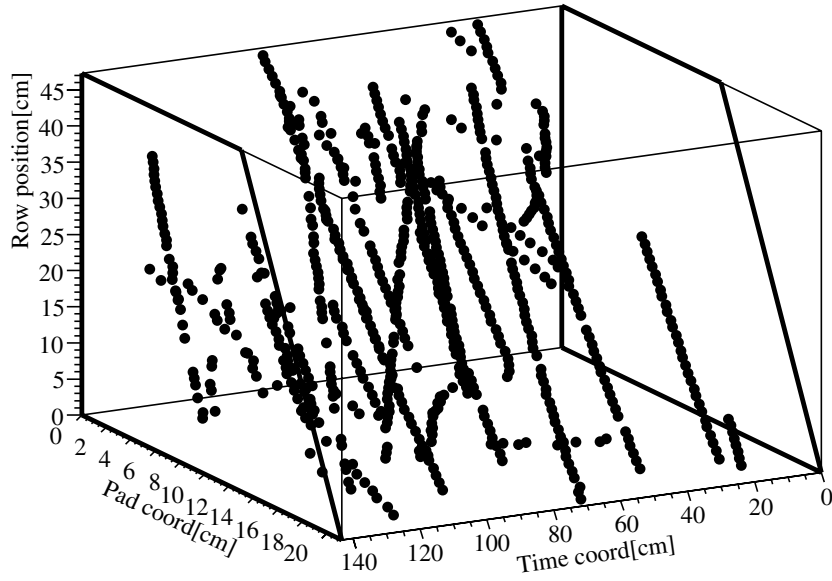


**Figure 6.464.** A multi-muon event taken by the TPC during test with atmospheric muons at surface level.

The TOF trigger is organized in two layers. The first one is made of 72 Local Trigger Modules (LTM), reading the information of the Front End electronics. Each LTM is a VME module sending 24 bits to the second trigger layer, the Cosmic and Topology Trigger Module (CTTM). The bit transmission is made in parallel, so that a fast trigger decision can be released within 800 ns, matching the ALICE L0 timing requirement. The flexibility of the system provided by several FPGAs allows the choice of trigger segmentation at software level, and in the finest configuration any trigger channel is the OR of 96 pads ( $\simeq 900 \text{ cm}^2$  given the area of a single pad of  $9.25 \text{ cm}^2$ ).

The simplest cosmic muon trigger one can propose is based on a single track crossing the TOF. Although the TOF noise level is quite low,  $\simeq 5 \text{ Hz/pad} = 0.54 \text{ Hz cm}^{-2}$ , such a topology would give an unmanageable fake trigger rate. In fact, both the upper (Supermodules 0–8) and the lower (Supermodules 9–17) part of the TOF (hereafter TOF-TOP and TOF-BOTTOM), each made by  $\simeq 78500$  pads, whose area is  $9.25 \text{ cm}^2$ , is expected to give a background rate of:

$$R = 5 \times 7.85 \times 10^4 \sim 395 \text{ kHz.} \quad (6.172)$$

Requiring a coincidence between the TOF-TOP and TOF-BOTTOM in a time window as short as of 50 ns, the total fake trigger rate would be

$$R_{\text{fake}} = \frac{(395 \times 10^3 \times 50 \times 10^{-9})^2}{50 \times 10^{-9}} \simeq 8 \text{ kHz.} \quad (6.173)$$

Since the cosmic muon rate in the TOF is a few  $\text{Hz m}^{-2} \text{ sr}^{-1}$ , such a trigger could be useful only when used in coincidence with another detector, for instance ACORDE. Supposing that the second detector, to be combined with the TOF, has the same fake trigger rate, their coincidence within 50 ns would be  $R_{\text{fake}} \simeq 6 \text{ Hz}$ , which is well below the genuine muon trigger rate.

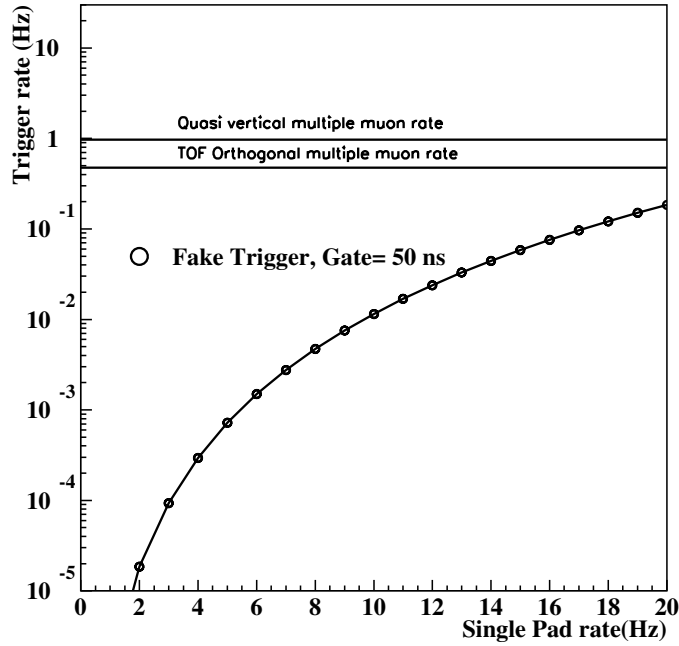


**Figure 6.465.** Multiple muon fake trigger rate as a function of the single pad rate. The genuine muon trigger rate is also shown for quasi-vertical and ‘back-to-back’ events.

An interesting possibility for the TOF in stand-alone mode is offered by the multiple muon events. The multiple muon event rate depends both on the underground depth and on the detector geometry. Considering that the angle between multiple muons is quite small,  $\sigma_{2\mu} \leq 0.2^\circ$  [1090], the parallelism helps to reduce the accidental background. Keeping in mind that the cosmic muon angular distribution in the ALICE pit follows a  $\cos^x\theta$  law, where  $x \simeq 2$  [1113], a straightforward approach is to focus on quasi-vertical multiple muons ( $\theta \leq 20^\circ$ ), triggered via a coincidence between corresponding TOF modules. Considering the OR of a TOF module, made of about 2000 pads, the background rate for this quasi-vertical multiple muon trigger is

$$R_{\text{fake}} = \frac{45 \times (45 - 1) \times (50 \times 10^{-9} \times 2000 \times 5)^4}{2 \times 50 \times 10^{-9}} \simeq 10^{-3} \text{ Hz}, \quad (6.174)$$

which is three orders of magnitude smaller than the rate of real quasi-vertical multiple muon events. While any coincidence of TOF-TOP and of TOF-BOTTOM channels will mimic a single track, at least four aligned channels are required to fake a quasi-vertical multiple muon event.

Another possibility is offered by multiple muons, in which each muon hits two TOF modules placed at  $\Delta\varphi = 180^\circ$  (back-to-back) and at the same position along the  $z$ -axis. Such topology relies on muons orthogonal to the TOF pads and is therefore very interesting for the TOF calibration.

Figure 6.465 shows the expected multiple muon fake trigger rate as a function of the single pad rate; the rates of the quasi-vertical and TOF orthogonal multiple muons are also shown.

**6.11.5.2. Muon reconstruction in the TPC.** Pattern recognition and reconstruction in ALICE is done by a Kalman filter algorithm [1114], which is able to handle the huge multiplicity

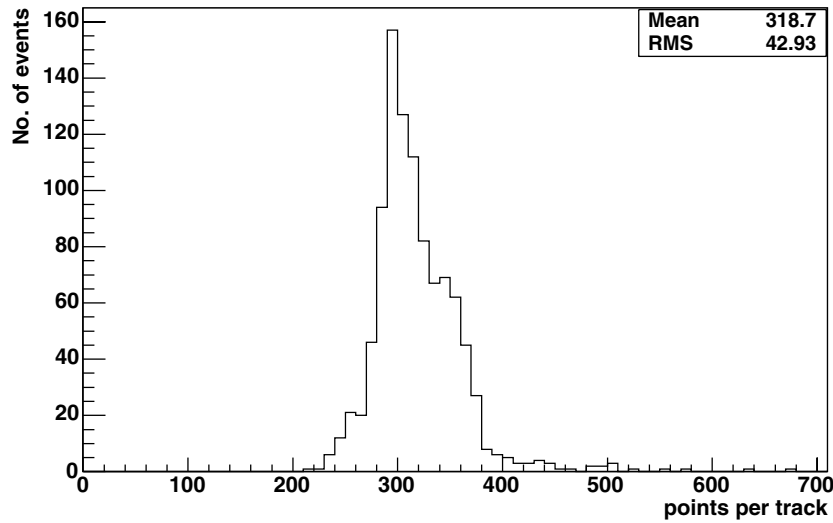


**Figure 6.466.** Distribution of the number of points in the TPC for 100 GeV/ $c$  single negative muons traversing the centre of the detector.

expected in central Pb–Pb collisions at LHC energies. Most of the tracks originating from standard collision events in ALICE come from the primary vertex, located along the beam axis. Cosmic muons are different in this respect, since they can emerge from any point and can traverse the detector at any angle. The energy of such muons is much larger than the average energy of the particles produced in a heavy-ion collision. Another important difference is related to the track multiplicity, which is very small in the case of cosmic muons (typically single tracks with an admixture of multi-muon events at the few per cent level). The standard Kalman filter technique, which is adapted to collision events, is not directly suitable for cosmic muon reconstruction, and an appropriate software was developed for this application. In the following paragraph, we report preliminary results obtained within the framework of the AliRoot package.

Figure 6.466 shows the distribution of the number of space points reconstructed in the TPC for events containing each a single negative muon of 100 GeV/ $c$ , traversing the tracking device in a small cone around the vertical. Most of the events give a number of points between 250 and 450. The average number of points for such tracks is around 320. Some events produce secondary tracks which result in a larger number of points. These are generally cut due to their distance from the main track and to  $\chi^2$  considerations.

The pattern recognition is optimized to handle these space points and recognize those belonging to the main tracks. The information is passed onto the track fitting procedure, which provides the best estimates for transverse momentum, polar and azimuthal angles of the particle, as well as its charge state. To evaluate the intrinsic performance of the main tracking detector, the TPC, as far as momentum and angle resolution and charge state confusion are concerned, monoenergetic single muons were generated in a cone around the vertical axis. A magnetic field  $B = 0.5$  T was used.

For single muons, no special pattern recognition is needed. However, given the possibility of also handling multi-muon events, a variant of the Hough transform was investigated. Basically, for a set of  $N$  points, the  $N(N - 1)/2$  possible pairs define an equivalent number

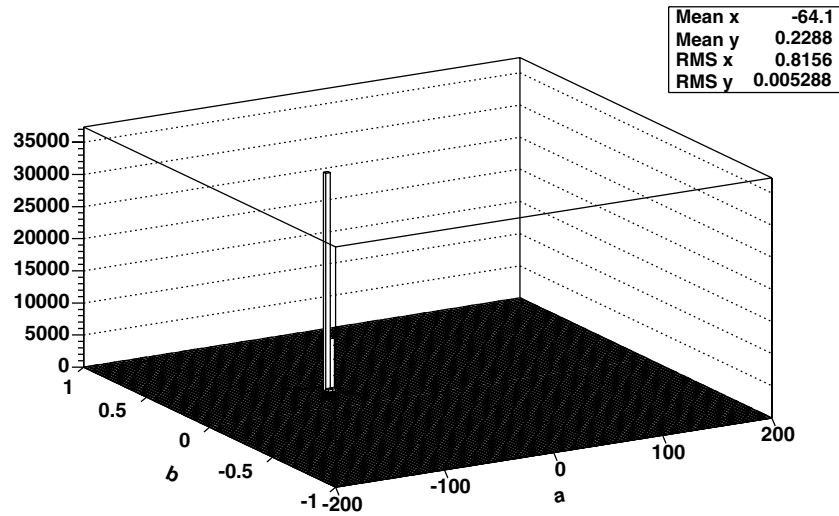


**Figure 6.467.** The line parameters  $a$ ,  $b$  of each line connecting any pair of points are accumulated in a matrix, to identify peaks defining the main tracks.

of lines  $z = a + by$  in the  $yz$  plane. For each pair, the line parameters  $a$  and  $b$  are accumulated in a matrix and a search is made to look for peaks which identify the main tracks. Some cuts are introduced in the procedure to avoid connections among points which are too close or directions incompatible with the detector geometry. For example, Fig. 6.467 shows the Hough plot obtained for a single muon. In case of multi-muon events, a general implementation of the Hough transform would imply five parameters, namely the parameters  $a$ ,  $b$  of the line in the  $yz$  plane and an additional set of three parameters in the transverse plane (for instance the centre and radius of curvature of the track). A five-dimensional matrix accumulator is not easy to manage; in our case, since muon bundles are made of nearly parallel tracks with highly energetic muons, the average slope in the  $xy$  plane is extracted event by event and an additional Hough parameter for each data point is defined as the intercept of the line passing through the point and having the common slope of the bundle.

This is done with the specific purpose of assigning the point to a track, since the muon density is expected to be very low in comparison to the standard pattern recognition with beam events. Once the main tracks are identified, additional conditions are imposed during reconstruction. Due to the large momentum of the cosmic muons being reconstructed, a simple model may be assumed to parametrize each track. In the transverse ( $xy$ ) plane a circular arc is assumed, with a fixed radius of curvature, since the amount of material traversed is very small and the energy loss is negligible. The  $yz$  projection of the track can be fitted by a straight line to a good approximation. Points lying outside a given distance from the fitted straight line in the  $yz$  plane are rejected. Also events which give an abnormal number of space points in the TPC in comparison to the average number of expected points per track are neglected, as well as tracks which have a very large  $\chi^2$  either in the  $yz$  plane or in the  $xy$  plane. After rejection of those points which lie outside a specified distance from the straight  $yz$  line, the points may be fitted in the  $xy$  plane, to extract the radius of curvature and the sign of the track. Several methods can be employed for this procedure. Here we used a parabolic fit  $x = ay^2 + by + c$ . The osculator circle was then assumed to represent the track. The polar and

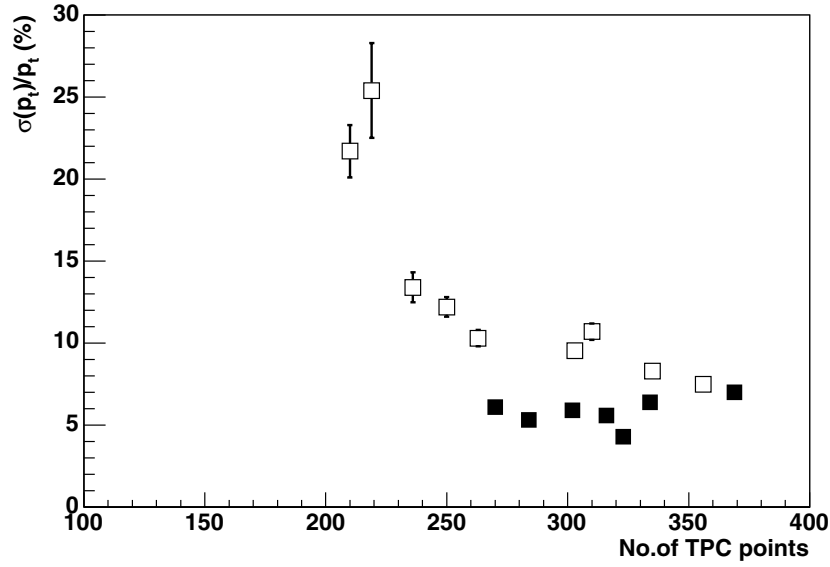


**Figure 6.468.** Transverse momentum resolution for 100 GeV/c cosmic muons tracked in the TPC with a magnetic field  $B = 0.5$  T vs number of points in the TPC.

azimuthal angles of the cosmic muon were derived by the tangent to the circle at the upper edge point.

**6.11.5.3. Results on muon reconstruction.** According to the procedure described in the previous section, the transverse momentum, the polar and azimuthal angles were reconstructed, after imposing cuts on the  $\chi_{\text{lin}}^2$  in the  $yz$  linear fit, on the  $\chi_{\text{par}}^2$  in the  $xy$  parabolic fit, on the number of points and on distance between each point and the fitted straight line in the  $yz$  plane. The tracking performance and  $p_t$  resolution depend on the track topology inside the TPC. The resolution depends both on the number of measured points (track length) and on whether such points originate from a single segment, or come from two separate segments. The latter case occurs when one segment is in the upper part of the TPC and the other one in the lower part, as in the case for muons traversing the TPC in the very central region. To give a preliminary estimate of the dependence of the  $p_t$  resolution upon such parameters, a set of simulations of vertical muons with 100 GeV/c momentum was carried out. The  $x$  or  $z$  values of the injection point  $(x, y, z)$  were systematically changed to vary the track length in the TPC. The transverse momentum resolution as a function of the number of points in the TPC is reported in Fig. 6.468. The black squares are obtained for tracks which traverse the TPC in the central volume (radius less than 90 cm from the beam interaction point), while the white squares refer to muon tracks which do not traverse the ITS. As seen, for the central volume the resolution is nearly constant, whereas the performance is degraded for tracks which cross the TPC near the edges. The problem however will be further investigated in the future, due to the introduction of inclined tracks, which may result in a larger number of points even for those tracks which do not pass through the ITS volume.

In the following analyses of the TPC performance we simulate muons traversing the central volume of the detector. Fig. 6.469 shows the resolution for 100 GeV/c negative muons traversing the TPC in a  $20^\circ$  cone around the vertical direction. A magnetic field  $B = 0.5$  T

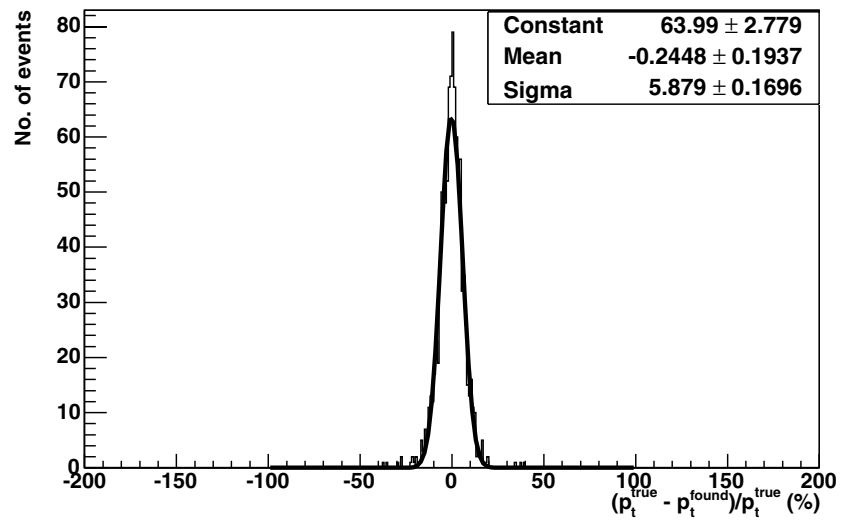


**Figure 6.469.** Transverse momentum resolution for 100 GeV/c cosmic muons tracked in the TPC with a magnetic field  $B = 0.5$  T.

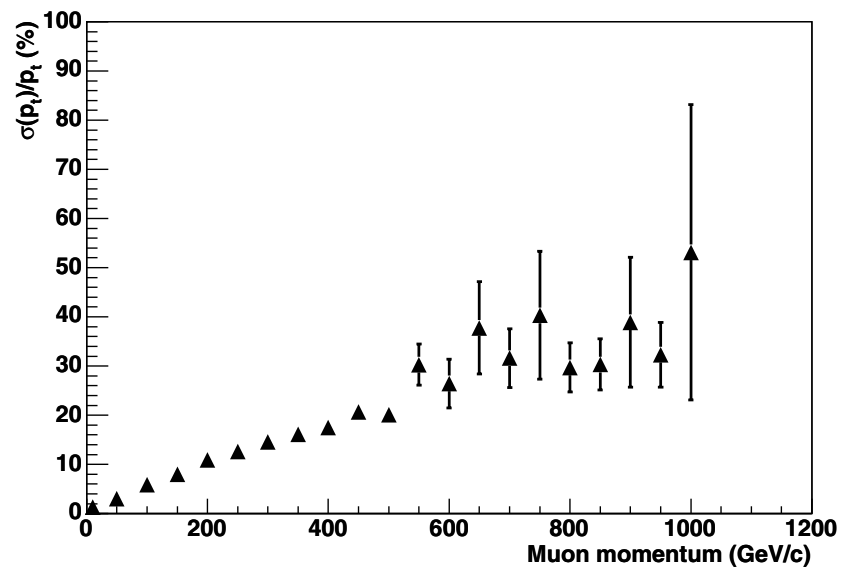


**Figure 6.470.** Transverse momentum resolution of muons as a function of the muon momentum for  $B = 0.5$  T.

was assumed throughout. A value of  $\sigma$  of 5.9% is obtained. With increasing the energy of the muons, the distribution of the  $p_t$  difference is no longer Gaussian, and exhibits a long tail on one side. In such cases the r.m.s. of the distribution is larger than the  $\sigma$ .

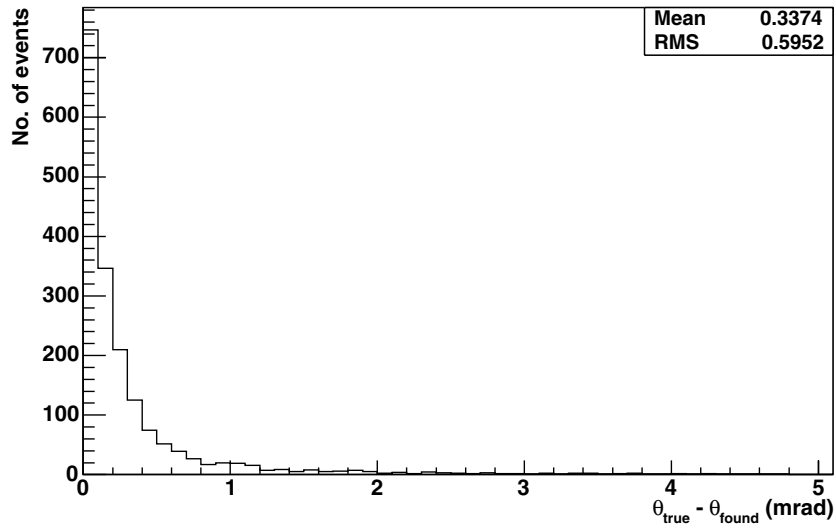


**Figure 6.471.** Overall angular resolution for 100 GeV/ $c$  cosmic muons.

A systematic set of simulations was carried out, for cosmic muons between 10 GeV and 1 TeV to analyse the degradation of the resolution with the energy. For each incident momentum 1000 events were generated and tracked. Figure 6.470 shows the transverse momentum resolution as a function of the incoming muon momentum. The results reported here show that a reasonable resolution can still be obtained at energies as high as 1 TeV. Due to the large tail in the reconstructed momentum especially at higher momenta, the average reconstructed momentum is higher than the true one.

The angular resolution shows a weak dependence on the muon momentum in the range of interest. The overall angular resolution for 100 GeV/ $c$  muons is reported in Fig. 6.471.

The probability of assigning an incorrect charge to a muon increases with its momentum. In Fig. 6.472 is shown the ratio  $N_{\text{mis}}/N_{\text{found}}$  between the number of misidentified particles and the number of found particles, as a function of the muon momentum. Up to energies of the order of 1 TeV, the ratio  $N_{\text{mis}}/N_{\text{found}}$  is lower than 7%.

These results show that with a magnetic field of 0.5 T the ALICE TPC is suitable to reconstruct single muons with an error  $\sigma_p/p < 50\%$  up to energies of the order of 1 TeV. This performance is comparable to those obtained by the L3+C Collaboration and will be further improved by the information provided by the TOF and TRD.

Concerning the detection of multi-muon events, which are the main interest for CR physics in ALICE, additional simulations were carried out to check the separation between neighbouring tracks and the achievable muon density. Figure 6.473 shows the efficiency (found tracks/generated tracks) for events with two parallel tracks, separated by a distance  $d$  ( $d = 4, 5, 6$  and  $20$  cm), as a function of the threshold parameter which allows the identification of peaks in the Hough matrix. The results show that with a suitable choice of the threshold parameter, the efficiency stays close to 100% even if the tracks are separated by 6 cm, decreasing to about 90% for a separation of 5 cm, and to 75% at 4 cm. These results indicate that a muon density of 200/m<sup>2</sup> can be measured with almost a 100% efficiency.

A demonstration of the capabilities of the TPC in tracking high density of muons, is shown in Fig. 6.474, where we see a multi-muon event of high multiplicity taken from the TPC during test with atmospheric muons at surface level.

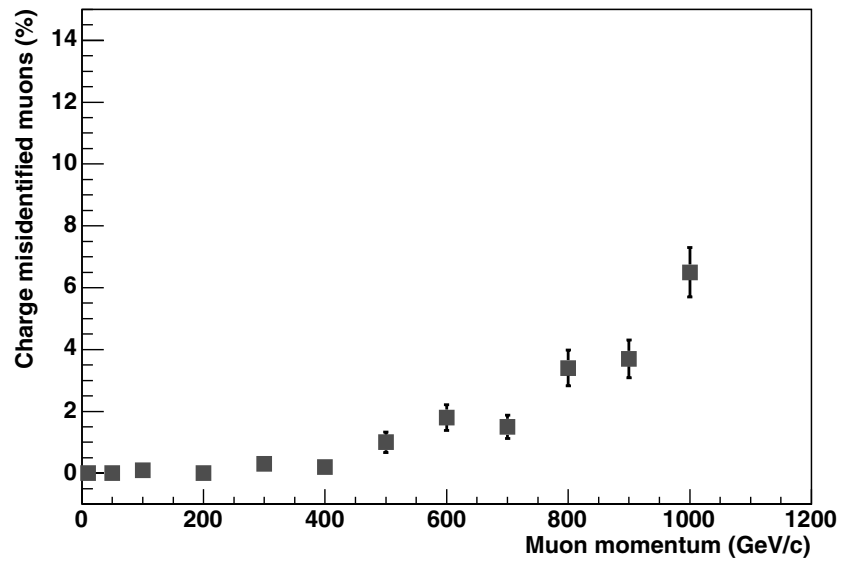


**Figure 6.472.** The ratio between the number of charge misidentified and the number of found muons is reported as a function of the muon momentum for  $B = 0.5$  T.

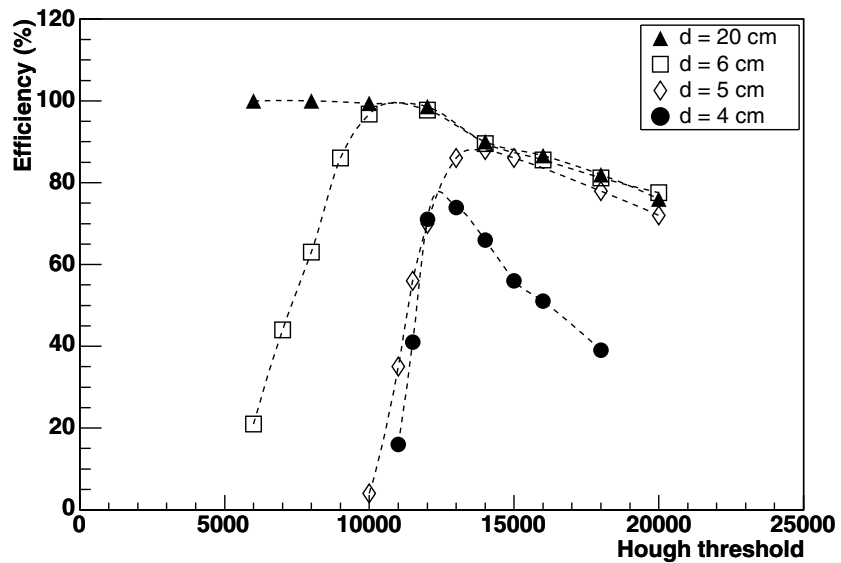


**Figure 6.473.** Reconstruction efficiency for muon events with two parallel tracks, as a function of the threshold parameter in the Hough transform, and for different values of the distance between close tracks.

*6.11.6. Use of atmospheric muons for ALICE detector alignment and calibration.* Atmospheric muons can be used to test and align the different ALICE detectors before final installation and after the installation at Point-2. While the flux of CRs is isotropic, the flux and energy of CR muons depends on the zenith angle because of the different path length in the atmosphere and the rock overburden.

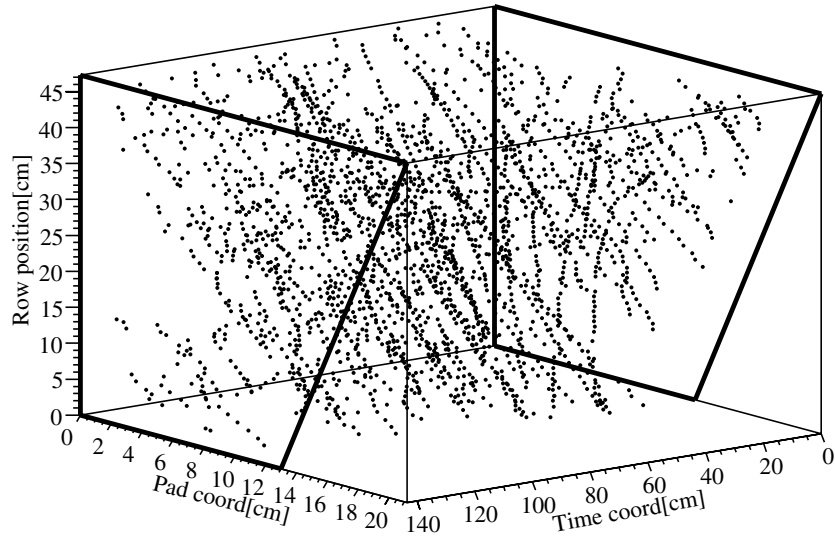


**Figure 6.474.** A multi-muon event of high multiplicity taken from the TPC during test with atmospheric muons at surface level.

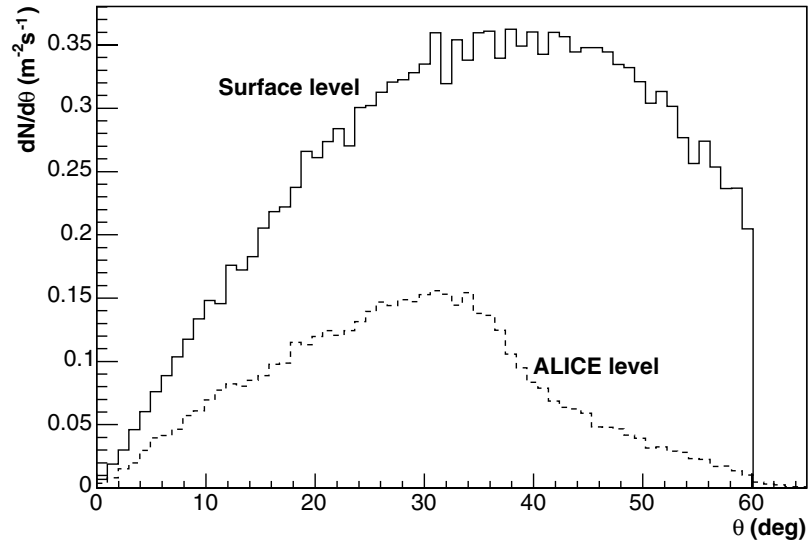


**Figure 6.475.** The zenith angular distribution for muons above  $p_\mu = 10 \text{ GeV}/c$  at surface level and at ALICE depth.

The zenith angle ( $\theta$ ) dependence at surface level was parametrized in the form [1089]

$$\frac{dF}{d \cos \theta} = 1 + a(p) \cdot (1 - \cos \theta),$$

where  $F$  is the flux and  $a(p)$  is a coefficient that depends on the muon momentum  $p$ . The zenith angular distribution for muons with momentum larger than  $p_\mu = 10 \text{ GeV}/c$  at surface

level and at ALICE depth is shown in Fig. 6.475. From this figure and the coverage of the CR trigger chambers, we can estimate the time necessary to calibrate and align any given detector in ALICE.

For most of the detectors cosmic muons provide an adequate flux for basic check of their operation and rough survey of their position in space. A special case is represented by the HMPID, which is direction sensitive. The HMPID is sensitive to particles reaching its radiator from the direction of the beampipe. When the magnetic field is set to 0.5 T, a small fraction of muons crossing ALICE within  $10^\circ$  from the vertical are bend into the direction of the HMPID and enter the detector within an angle of  $\pm 35^\circ$ . Based on a rough calculation of the detector acceptance and taking into account the atmospheric muon flux the resulting rate is about 0.01 muon/s. These particles can be used for monitoring or calibration purposes.

## 7. Conclusions

First ideas for a dedicated heavy ion experiment at the LHC date back to 1990 and the conceptual design of ALICE was laid down in a Letter of Intent in early 1993. This was well before really heavy ions become available for the first time at CERN with the Pb beam at the SPS end of 1994. The focus at the time was on soft and semi-hard processes involving mass and momentum scales of at most 10 GeV.

The physics of ultra-relativistic heavy ions has evolved very substantially since then, and with it the capabilities of the ALICE experiment. Without compromising the performance at low momenta, the physics reach has been extended by about an order of magnitude. It now ranges from a precision measurement of the bulk of the matter created in heavy-ion collisions, with typical momenta below 500 MeV, to heavy quark physics, quarkonia spectroscopy and jet measurements well above 100 GeV.

An extended R&D period has preceded the detector construction and significantly advanced the limits of detector technology, leading to a number of novel solutions specifically adapted to the difficult environment of Pb–Pb collisions at the LHC. In parallel, a large effort went into the offline framework to prepare a modern software capable of reconstructing and analysing the complex heavy ion data in a distributed computing environment. With its state-of-the-art general purpose heavy-ion detector now being assembled, the ALICE collaboration is very much looking forward to meet the physics challenge of LHC when the first collisions will become available.

**ALICE Collaboration**

**Alessandria, Italy**, Facoltà di Scienze dell'Università and INFN: P Cortese, G Dellacasa, L Ramello and M Sitta.

**Aligarh, India**, Physics Department, Aligarh Muslim University: N Ahmad, S Ahmad, T Ahmad, W Bari, M Irfan and M Zafar.

**Amsterdam, The Netherlands**, National Institute for Nuclear and High Energy Physics (NIKHEF): M Botje, P G Kuijer and R Snellings.

**Athens, Greece**, University of Athens, Physics Department: A Belogianni, P Christakoglou<sup>1</sup>, P Ganoti, A Petridis, F Roukoutakis, M Spyropoulou-Stassinaki and M Vassiliou.

**Bari, Italy**, Dipartimento di Fisica dell'Università and Sezione INFN: G E Bruno, I A Cali, M Caselle, G De Cataldo, D Di Bari, D Elia, R A Fini, B Ghidini, V Lenti, V Manzari, A Mastroserio, F Minafra, E Nappi, F Navach, C Pastore, V Patichio, D Perrino, F Posa, R Santoro, I Sgura and G Volpe.

**Bari, Italy**, Politecnico and Sezione INFN: F Corsi, D De Venuto, U Fratino, C Marzocca and A Tauro.

**Beijing, China**, China Institute of Atomic Energy: X Li, Z Liu, S Lu, Z Lu, Q Meng, B Sa, J Yuan, J Zhou and S Zhou.

**Bergen, Norway**, Department of Physics and Technology, University of Bergen: J Alme, S Bablok, A Klovning, J Nystrand, B Pommeresche, M Richter, D Röhrich, K Ullaland and H Yang<sup>2</sup>.

**Bergen, Norway**, Bergen University College, Faculty of Engineering: H Helstrup, K F Hetland, B Kileng and K Røed.

**Bhubaneswar, India**, Institute of Physics: R K Choudhury, S Dash, D P Mahapatra, D Mishra, S C Phatak and R Sahoo.

**Birmingham, United Kingdom**, School of Physics and Space Research, University of Birmingham: L Daniel, D Evans, G T Jones, P Jovanović, A Jusko<sup>3</sup>, J B Kinson, R Platt, R Lietava, J D Tapia Takaki and O Villalobos Baillie.

**Bologna, Italy**, Dipartimento di Fisica dell'Università and Sezione INFN: A Alici, S Antinori, P Antonioli, S Arcelli, G Bari, M Basile, G Cara Romeo, L Cifarelli, F Cindolo, D Falchieri, A Gabrielli, E Gandolfi, D Hatzifotiadou, G Laurenti, M L Luvisetto, A Margotti, M Masetti, R Nania, F Noferini, F Palmonari, A Pesci, G Sartorelli, E Scapparone, G Scioli, G P Vacca, G Valenti, G Venturi, M C S Williams, C Zampolli and A Zichichi.

**Bratislava, Slovakia**, Comenius University, Faculty of Mathematics, Physics and Informatics: V Černý, R Janik, L Lúčan, M Pikna, J Pišút, N Pišútová, B Sitár, P Strmeň, I Szarka and M Zagiba.

**Bucharest, Romania**, National Institute for Physics and Nuclear Engineering: C Aiftimiei, V Catanescu, C I Legrand, M Petrovici, A Pop, C Schiaua and V Simion.

<sup>1</sup> Now Marie Curie Fellow at Physics Department, CERN, Geneva, Switzerland.

<sup>2</sup> On leave from Institute of Particle Physics, Huazhong Normal University, Wuhan, China.

<sup>3</sup> On leave from Institute of Experimental Physics, Košice, Slovakia.

**Budapest, Hungary**, KFKI Research Institute for Particle and Nuclear Physics, Hungarian Academy of Sciences: G Barnaföldi, L Boldizsár, E Dénes, Z Fodor, E Futó, T Kiss, P Lévai, G Pála and J Zimányi.

**Cagliari, Italy**, Dipartimento di Fisica dell'Università and Sezione INFN: I Atanassov, S Basciu, C Cicalo, A De Falco, M Floris, A Masoni, D Mura, G Puddu, S Serci, E Siddi and G Usai.

**Catania, Italy**, Dipartimento di Fisica dell'Università and Sezione INFN: A Badalà, R Barbera, G Lo Re, A Palmeri, G S Pappalardo, A Pulvirenti and F Riggi.

**CERN, Switzerland**, European Organization for Nuclear Research: G Anelli, I Augustin<sup>4</sup>, A Augustinus, J Baechler, J A Belikov<sup>5</sup>, L Betev, A Boccardi, R Brun, M Burns, P Buncic<sup>6</sup>, R Campagnolo, M Campbell, F Carena, W Carena, F Carminati, S Chapeland, C Cheshkov, P Chochula, P Christiansen, A Colla<sup>7</sup>, J Conrad, B F Correia Belbute, M Davenport, J de Groot, A Di Mauro, R Divià, C Engster, S Evrard, C W Fabjan, L Feng, D Flierl, F Formenti, U Fuchs, A García López, A Gheata, M Gheata<sup>8</sup>, C González-Gutiérrez, R Grosso<sup>7</sup>, M Gruwe, H-A Gustafsson<sup>9</sup>, H Hoedelmoser, P Hristov, M Ivanov, L Jirden, C Jorgensen, A Junique, S Kapusta<sup>10</sup>, W Kickinger, W Klempt, A Kluge, L Leistam, J P Lo, M López Noriega, C Lourenço, I Makhlyueva, J-C Marin, P Martinengo, D Meunier-Picard, M Meoni<sup>11</sup>, M Morel, A Morsch, B Mota, H Muller, L Musa, T K Nayak<sup>12</sup>, P Nilsson, D Nouais<sup>13</sup>, F Osmic, D Perini, R Pestotnik, A Peters<sup>6</sup>, V Pinto Morais, S Popescu, F Rademakers, J-P Revol, P Riedler, W Riegler, K Šafařík, K Schossmaier, J Schukraft, Y Schutz<sup>14</sup>, P A Silva Loureiro, C Soos<sup>15</sup>, G Stefanini, D Swoboda, M Tadel, H Taureg, M Tavlet, P Tissot-Daguette, C Torcato de Matos, P Vande Vyvre and J-P Vanuxem.

**Chandigarh, India**, Physics Department, Panjab University: M M Aggarwal, A K Bhati, A Kumar, M Sharma and G Sood.

**Clermont-Ferrand**, France, Laboratoire de Physique Corpusculaire (LPC), IN2P3-CNRS and Université Blaise Pascal: A Baldit, V Barret, N Bastid, G Blanchard, J Castor, P Crochet, F Daudon, A Devaux, P Dupieux, P Force, S Grigoryan<sup>16</sup>, F Guerin, R Guernane, C Insa, F Jouve, J Lecoq, F Manso, P Rosnet, L Royer, P Saturnini and G Savinel.

**Columbus, USA**, Department of Physics, Ohio State University: T J Humanic, I V Kotov, M Lisa, B S Nilsen and D Truesdale.

**Columbus, USA**, Ohio Supercomputer Centre: D Johnson.

**Copenhagen, Denmark**, Niels Bohr Institute: I Bearden, H Bøggild, C H Christensen, J J Gaardhøje, K Gulbrandsen, B S Nielsen and G Renault.

<sup>4</sup> Now at Gesellschaft für Schwerionenforschung (GSI), Darmstadt, Germany.

<sup>5</sup> On leave from JINR, Dubna, Russia.

<sup>6</sup> Supported by EGEE.

<sup>7</sup> On leave from INFN CNAF, Bologna, Italy.

<sup>8</sup> National Institute for Physics and Nuclear Engineering, Bucharest, Romania.

<sup>9</sup> On leave from Division of Experimental High Energy Physics, University of Lund, Lund, Sweden.

<sup>10</sup> On leave from Comenius University, Faculty of Mathematics, Physics and Informatics, Bratislava, Slovakia.

<sup>11</sup> Now at INFN, Sezione di Firenze, Firenze, Italy.

<sup>12</sup> On leave from Variable Energy Cyclotron Centre (VECC), Kolkata, India.

<sup>13</sup> On leave from INFN, Sezione di Torino, Turin, Italy.

<sup>14</sup> On leave from Laboratoire de Physique Subatomique et des Technologies Associées (SUBATECH), Ecole des Mines de Nantes, IN2P3-CNRS and Université de Nantes, Nantes, France.

<sup>15</sup> On leave from Budapest University, Budapest, Hungary.

<sup>16</sup> On leave from Yerevan Physics Institute, Yerevan, Armenia.

**Cracow, Poland**, Henryk Niewodniczanski Institute of Nuclear Physics, High Energy Physics Department: J Bartke, E Gładysz-Dziaduś, E Kornaś, M Kowalski, A Rybicki and A Wróblewski<sup>17</sup>.

**Darmstadt, Germany**, Gesellschaft für Schwerionenforschung (GSI): A Andronic<sup>18</sup>, D Antonczyk, E Badura, R Bailhache, E Berdermann, P Braun-Munzinger, O Busch, M Ciobanu<sup>18</sup>, P Foka, U Frankenfeld, C Garabatos, H Gutbrod, C Lippmann, P Malzacher, A Marín, D Miśkowiec, S Radomski, H R Schmidt, K Schwarz, S Sedykh, R S Simon, D Soyk, H Stelzer, M Stockmeier, G Tziledakis and D Vranic, J Wiechula.

**Darmstadt, Germany**, Institut für Kernphysik, Technische Universität: U Bonnes, I Kraus and H Oeschler.

**Frankfurt, Germany**, Institut für Kernphysik, Johann Wolfgang Goethe Universität: H Appelshäuser, C Blume, T Dietel, M Gaździcki, M Hartig, M Kliemant, S Kniege, T Kolleger, F Kramer, S Lange, C Loizides, M Ploskon, R Renfordt, W Sommer, R Stock and H Ströbele.

**Gatchina, Russia**, St Petersburg Nuclear Physics Institute: Ya Berdnikov, V Ivanov, A Khanzadeev, N Miftakhov, V Nikoulin, V Polyakov, E Rostchin, V Samsonov, O Tarasenkova, V Tarakanov and M Zhalov.

**Havana, Cuba**, Centro de Aplicaciones Tecnológicas y Desarrollo Nuclear (CEADEN): E López Torres, A Abrahantes Quintana and R Díaz Valdes.

**Heidelberg, Germany**, Kirchhoff Institute for Physics: T Alt V Angelov, J Cuveland, M Gutfleisch, S Kalcher, V Lindenstruth, R Panse, C Reichling, R Schneider, T Steinbeck H Tilsner G Tröger and A Wiebalck.

**Heidelberg, Germany**, Physikalisches Institut, Ruprecht-Karls Universität: C Adler, D Emschermann, P Glässel, N Herrmann, W Ludolphs, T Mahmoud, J Mercado, J Milosevic, K Oyama, I Rusanov, R Schicker, P Shukla, H C Soltveit, J Stachel, B Vulpescu, B Windelband and S Yurevich.

**Hiroshima, Japan**, Hiroshima University (Associate member): K Shigaki and T Sugitate.

**Jaipur, India**, Physics Department, University of Rajasthan: R Raniwala and S Raniwala.

**Jammu, India**, Physics Department, Jammu University: S K Badyal, R Bala, A Bhasin, A Gupta, V K Gupta, S Mahajan, L K Mangotra, B V K S Potukuchi and S S Sambyal.

**JINR, Russia**, Joint Institute for Nuclear Research: P G Akichine, V A Arefiev, Ts Baatar<sup>19</sup>, B V Batiounia, V F Chepurinov, S A Chernenko, V K Dodokhov, O V Fateev, A G Fedunov, M Haiduc<sup>20</sup>, D Hasegan<sup>20</sup>, V G Kadychevsky, G Kharadze<sup>21</sup>, B Khurelbaatar<sup>19</sup>, E K Koshurnikov, V L Lioubochits, V I Lobanov, L V Malinina, Y I Minaev, M Nioradze<sup>22</sup>, P V Nomokonov, Y A Panebrattsev, V N Penev, V G Pismennaya, T A Pocheptsov, I Roufanov, G S Shabratova, V Shestakov<sup>23</sup>, A I Shklovskaya, A S Sorin, M K Suleimanov, Y Tevzadze<sup>22</sup>, R Togoo<sup>19</sup>, A S Vodopianov, V I Yurevich, Y V Zanevsky, S A Zaporjets and A I Zinchenko.

<sup>17</sup> Cracow Technical University, Cracow, Poland.

<sup>18</sup> On leave from National Institute for Physics and Nuclear Engineering, Bucharest, Romania.

<sup>19</sup> Institute of Physics and Technology, Mongolian Academy of Sciences, Ulaanbaatar, Mongolia.

<sup>20</sup> Institute of Space Sciences, Bucharest, Romania.

<sup>21</sup> Institute of Physics, Georgian Academy of Sciences, Tbilisi, Georgia.

<sup>22</sup> High Energy Physics Institute, Tbilisi State University, Tbilisi, Georgia.

<sup>23</sup> Research Centre for Applied Nuclear Physics (RCANP), Dubna, Russia.

**Jyväskylä, Finland**, Department of Physics, University of Jyväskylä and Helsinki Institute of Physics: J Äystö, M Bondila, V Lyapin, M Oinonen, T Malkiewicz, V Ruuskanen, H Seppänen, W Trzaska and S Yamaletkinov.

**Kangnung, Republic of Korea**, Kangnung National University: H T Jung, W Jung, D-W Kim, H N Kim, J S Kim, K S Lee and S-C Lee.

**Karlsruhe, Germany**, Institut für Prozessdatenverarbeitung und Elektronik (IPE) (Associate member): T Blank and H Gemmeke.

**Kharkov, Ukraine**, National Scientific Centre, Kharkov Institute of Physics and Technology: G L Bochek, A N Dovbnya, V I Kulibaba, N I Maslov, S V Naumov, V D Ovchinnik, S M Potin and A F Starodubtsev.

**Kharkov, Ukraine**, Scientific and Technological Research Institute of Instrument Engineering: V N Borshchov, O Chykalov, L Kaurova, S K Kiprich, L Klymova, O M Listratenko, N Mykhaylova, M Protsenko, O Reznik and V E Starkov.

**Kiev, Ukraine**, Department of High Energy Density Physics, Bogolyubov Institute for Theoretical Physics, National Academy of Sciences of Ukraine: I Kadenko, Y Martynov, S Molodtsov, Y Sinyukov and G Zinovjev.

**Kolkata, India**, Saha Institute of Nuclear Physics: P Bhattacharya, S Bose, S Chatterjee, S Chattopadhyay, D Das, I Das, A K Dutt-Mazumder, N Majumdar, S Mukhopadhyay, S Pal, L Paul, P Roy, A Sanyal, S Sarkar, P Sen, S K Sen, B C Sinha and T Sinha.

**Kolkata, India**, Variable Energy Cyclotron Centre: Z Ahammed, P Bhaskar, S Chattopadhyay, D Das, S Das, M R Dutta Majumdar, M S Ganti, P Ghosh, B Mohanty, P K Netrakanti, S Pal, R N Singaraju, V Singhal, B Sinha, and Y P Vijoyi.

**Köln, Germany**, University of Applied Sciences Cologne, Communications Engineering (Associate member): G Hartung and T Krawutschke.

**Košice, Slovakia**, Institute of Experimental Physics, Slovak Academy of Sciences and Faculty of Science, P J Šafárik University: J Bán, M Bombara, A Dirner, M Hnatič, I Králik, A Kravčáková, F Kriváň, M Krivda, G Martinská, B Pastirčák, L Šándor, J Urbán and J Vrláková.

**Legnaro, Italy**, Laboratori Nazionali di Legnaro: M Cinausero, E Fioretto, G Prete, R A Ricci and L Vannucci.

**Lisbon, Portugal**, Departamento de Física, Instituto Superior Técnico: P Branco, R Carvalho, J Seixas and R Vilela Mendes.

**Lund, Sweden**, Division of Experimental High Energy Physics, University of Lund: A Oskarsson, L Osterman, I Otterlund and E A Stenlund.

**Lyon, France**, Institut de Physique Nucléaire de Lyon (IPNL), IN2P3-CNRS and Université Claude Bernard Lyon-I: B Cheynis, L Ducroux, J Y Grossiord, A Guichard, P Pillot, B Rapp and R Tieulent.

**Mexico City and Mérida, Mexico**, Centro de Investigación y de Estudios Avanzados del IPN, Universidad Nacional Autónoma de México, Instituto de Ciencias Nucleares, Instituto de Física: J R Alfaro Molina, A Ayala, E Belmont Moreno, J G Contreras, E Cuautle, J C D'Olivo, I Domínguez, A Flores, V Grabski, G Herrera Corral, M Linares, M I Martínez,

A Martínez Dávalos, A Menchaca-Rocha, L M Montaña Zetina, L Nellen, G Paic<sup>24</sup>, J del Pino, P Reyes, A Sandoval<sup>25</sup>, J Solano, S Vergara and A Zepeda.

**Moscow, Russia**, Institute for Nuclear Research, Academy of Science: V A Feshchenko, M B Golubeva, V G Gorlychev, F F Guber, O V Karavichev, T L Karavicheva, E V Karpechev, A B Kurepin, A I Maevskaya, V V Marin, I A Pshenichnov, V I Razin, A I Reshetin, K A Shileev and N S Topil'skaia.

**Moscow, Russia**, Institute for Theoretical and Experimental Physics: A N Akindinov, V Golovine, A B Kaidalov, M M Kats, I T Kiselev, S M Kisselev, E Lioubelev, M Martemianov, A N Martemianov, P A Polozov, V S Serov, A V Smirnitski, M M Tchoumakov, I A Vetlitski, K G Volochine, L S Vorobiev and B V Zagreev.

**Moscow, Russia**, Russian Research Center Kurchatov Institute: D Aleksandrov, V Antonenko, S Beliaev, S Fokine, M Ippolitov, K Karadjev, I Koutcheriaev, V Lebedev, V I Manko, T Moukhanova, A Nianine, S Nikolaev, S Nikouline, O Patarakine, D Peres-souanko, I Sibiriak, A Tsvetkov, A Vasiliev, A Vinogradov and I Yushmanov.

**Moscow, Russia**, Moscow Engineering Physics Institute: V A Grigoriev, V A Kaplin and V A Loginov.

**Mumbai, India**, Indian Institute of Technology (Associate member): B K Nandi and R Varma.

**Mumbai, India**, Bhabha Atomic Research Centre (BARC) (Associate member): V Chandratre and V Kataria.

**Münster, Germany**, Institut für Kernphysik Westfälische Wilhelms Universität: C Baumann, R Glasow, H Gottschlag, J F Grosse-Oetringhaus, N Heine, C Klein-Bösing, K Reygers, R Santo, W Verhoeven, J Wessels and A Wilk.

**Nantes, France**, Laboratoire de Physique Subatomique et des Technologies Associées (SUBATECH), École des Mines de Nantes, IN2P3-CNRS and Université de Nantes: L Aphecetche, R Berny, S Bouvier, G Conesa-Balbastre, Z Conesa-del-Valle, J P Cussonneau, H Delagrangé, M Dialinas, Ch Finck, B Erasmus, M Germain, F Lefèvre, L Luquin, G Martínez, Ch Renard, C Roy and A Tournaire.

**Novosibirsk, Russia**, Budker Institute for Nuclear Physics: A R Frolov and I N Pestov.

**Oak Ridge, USA**, Oak Ridge National Laboratory: T Awes.

**Omaha, USA**, Creighton University: M Cherney and Y Gorbunov.

**Orsay, France**, Institut de Physique Nucléaire (IPNO), IN2P3-CNRS and Université de Paris-Sud: L Bimbot, V Chambert, A Charpy, M P Comets, P Courtat, S Drouet, P Edelbruck, B Espagnon, I Hřivnáčová, R Kunne, Y Le Bornec, M Mac Cormick, J Peyré, J Pouthas, S Rousseau, C Suire, N Willis and T Wu<sup>2</sup>.

**Oslo, Norway**, Department of Physics, University of Oslo: L Bravina, G Løvhøiden, B Skaali, T S Tveter and T Vik.

<sup>24</sup> Department of Physics, Ohio State University, Columbus, USA.

<sup>25</sup> On leave from Gesellschaft für Schwerionenforschung (GSI), Darmstadt, Germany.

**Padua, Italy**, Dipartimento di Fisica dell'Università and Sezione INFN: F Antinori, A Dainese, R Dima, D Fabris, J Faivre, M Lunardon, M Morando, S Moretto, A Pepato, E Quercigh, F Scarlassara, G Segato, R Turrisi and G Viesti.

**Pohang, Republic of Korea**, Pohang University of Science and Technology, Department of Physics and Pohang Accelerator Laboratory: J Choi.

**Prague, Czech Republic**, Institute of Physics, Academy of Science: A Beitlerova, J Mareš, K Polák and P Závada.

**Prague, Czech Republic**, Czech Technical University, Faculty of Nuclear Sciences and Physical Engineering: V Petráček, M Pachr and L Škoda.

**Protvino, Russia**, Institute for High Energy Physics: M Yu Bogolyubsky, G V Khaoustov, Yu V Kharlov, N G Minaev, V S Petrov, B V Polichtchouk, S A Sadovsky, V A Senko, A S Soloviev, P V Stolpovsky and V A Victorov.

**Puebla, Mexico**, Benemérita Universidad Autónoma de Puebla: A Fernández Téllez, E Gamez Flores, R López-Ramírez, A Ortiz-Velázquez, C Pagliarone<sup>26</sup>, S Román-López, G Tejada-Muñoz, A Vargas and L Villaseñor Cendejas

**Řež u Prahy, Czech Republic**, Academy of Sciences of Czech Republic, Nuclear Physics Institute: D Adamová, S Kouchpil, V Kouchpil, A Kugler, M Šumbera and V Wagner.

**Rome, Italy**, Dipartimento di Fisica dell'Università 'La Sapienza' and Sezione INFN: S Di Liberto, M A Mazzoni, F Meddi and G M Urciuoli.

**Rondebosch, South Africa**, University of Cape Town: J Cleymans, G de Vaux, R W Fearick, A Szostak and Z Z Vilakazi.

**Saclay, France**, Centre d'Études Nucléaires, DAPNIA: M Anfreville, A Baldisseri, B Becker, H Borel, J Castillo, J-L Charvet, M Combet, J Gosset, P Hardy, S Herlant, F Orsini, Y Pénichot, H Pereira, F M Staley and M Usseglio.

**Salerno, Italy**, Dipartimento di Fisica 'E R Caianiello' dell'Università and Sezione INFN: A De Caro, D De Gruttola, S De Pasquale, A Di Bartolomeo, M Fusco Girard, G Grella, C Guarnaccia, M Guida, G Romano, S Sellitto, R Silvestri and T Virgili.

**Sarov, Russia**, Russian Federal Nuclear Center (VNIIEF): V Basmanov, D Budnikov, V Demanov, V Ianowski, R Ilkaev, L Ilkaeva, A Ivanov, A Khlebnikov, A Kouryakin, E Mikhailov, S Nazarenko, V Pavlov, S Philchagin, A Punin, V Punin, S Poutevskoi, A Rybin, I Selin, M Smetanin, A Telnov, S Treskov, O Vikhlyantsev, I Vinogradov, A Vyushin, N Zavyalov, S Zhelezov and A Zhitnik.

**Split, Croatia**, Technical University of Split, Faculty of Electrical Engineering, Mechanical Engineering and Naval Architecture (FESB): S Gotovac, E Mudnic and L Vidak.

**St Petersburg, Russia**, V Fock Institute for Physics of St Petersburg State University: A G Asryan, M A Braun, D A Derkach, G A Feofilov, S N Igolkin, A S Ivanov, R S Kolevatov, A A Kolojvari, V P Kondratiev, P A Naumenko, T A Toulina, F F Valiev, V V Vechernin and L I Vinogradov.

<sup>26</sup> On leave from Università degli Studi di Cassino and INFN, Pisa, Italy.

**Strasbourg, France**, Institut de Recherches Subatomiques (IReS), IN2P3-CNRS and Université Louis Pasteur: J Baudot, D Bonnet, J P Coffin, M Estienne, B Hippolyte, C Kuhn, J R Lutz and R Vernet.

**Tokyo, Japan**, University of Tokyo (Associate member): H Hamagaki and K Ozawa.

**Trieste, Italy**, Dipartimento di Fisica dell'Università and Sezione INFN: V Bonvicini, O Borysov<sup>27</sup>, L Bosisio, M Bregant, P Camerini, G Contin, F Faleschini, E Fragiaco, N Grion, G Margagliotti, S Piano, I Rachevskaya, A Rachevski, R Rui and A Vacchi.

**Turin, Italy**, Dipartimenti di Fisica dell'Università and Sezione INFN: B Alessandro, R Arnaldi, S Bagnasco, G Batigne, S Beolè, E Bruna, P Cerello, E Chiavassa, O Cobanoglu, S Coli, E Crescio, N De Marco, P De Remigis, A Ferretti, M Gagliardi, M Gallio, L Gaudichet, R Gemme, G Giraud, P Giubellino, M Idzik, S Martoiu, A Marzari Chiesa, M Masera, G Mazza, P Mereu, M Monteno, A Musso, C Oppedisano, A Piccotti, F Poggio, F Prino, L Riccati, A Rivetti, E Scapparini, D Stocco, F Tosello, L Toscano, G Travaglia, E Vercellin, A Werbrouck, R Wheadon and F Yermia.

**Tsukuba, Japan**, University of Tsukuba (Associate member): Y Miake and S Esumi.

**Utrecht, The Netherlands**, Subatomic Physics Department, Utrecht University and National Institute for Nuclear and High Energy Physics (NIKHEF): J J F Buskop, A P De Haas, C Ivan, R Kamermans, A Mischke, G Nooren, C J Oskamp, Th Peitzmann, E Simili, O Sokolov, A Van Den Brink and N Van Eijndhoven.

**Wako-shi, Japan**, RIKEN (Associate member): H Enyo, K Fujiwara, H Kano and H Onishi.

**Warsaw, Poland**, Soltan Institute for Nuclear Studies: A Deloff, T Dobrowolski, K Karpio, M Malek, H Malinowski, K Redlich<sup>28</sup>, T Siemiarczuk, G Stefanek<sup>29</sup>, L Tykarski and G Wilk.

**Warsaw, Poland**, University of Technology, Institute of Physics: Z Chajecki, H Gos, M Janik, M Jedynek, A Kisiel, T J Pawlak, W S Peryt, J Pluta, P Skowronski, M Slodkowski, P Szuba and T Traczyk.

**Worms, Germany**, University of Applied Sciences Worms, ZTT (Associate member): E S Conner and R Keidel.

**Wuhan, China**, Institute of Particle Physics, Huazhong Normal University: X Cai, H T Ding, H Liu, X R Wang, H Y Yang, Z B Yin and D C Zhou.

**Wuhan, China**, Huazhong University of Science and Technology, Electronic and Information Engineering: X Cao, Q Li, Y Z Liu, G Su, L Tan, and G X Zhu.

**Yerevan, Armenia**, Yerevan Physics Institute: M Atayan, A Grigoryan, H Gulkanyan, A Harutyunyan, A Hayrapetyan, V Kakoyan, M Poghosyan and G Sargsyan.

**Zagreb, Croatia**, Ruder Bošković Institute: T Antčić, K Kadija and T Susa.

<sup>27</sup> On leave from Department of High Density Physics, Kiev, Ukraine.

<sup>28</sup> Institute of Theoretical Physics, University of Wrocław, Wrocław, Poland and Physics Department, CERN, Geneva, Switzerland.

<sup>29</sup> Institute of Physics, Pedagogical University, Kielce, Poland.

## External Contributors

F Arleo<sup>30</sup>, N Armesto<sup>31</sup>, P Aurenche<sup>32</sup>, L Benhabib<sup>33</sup>, A Bogdanov<sup>34</sup>, N Borghini<sup>30</sup>, N Carrer<sup>30</sup>, T Csörgő<sup>35</sup>, S Gupta<sup>36</sup>, U W Heinz<sup>37</sup>, P M Jacobs<sup>38</sup>, R Lednicky<sup>39</sup>, J Letessier<sup>40</sup>, S Mrówczyński<sup>41</sup>, J Rafelski<sup>42</sup>, J Ranft<sup>43</sup>, D Silvermyr<sup>44</sup> and U A Wiedemann<sup>30</sup>.

## Acknowledgments

The ALICE Collaboration would like to acknowledge the contributions by M Cacciari, V Greco, A Giovannini, V Koch, Th Kuhr, S Pratt, C A Salgado, M L Mangano, P Saiz, M Thoma, D Treleani, R Ugoccioni and R Vogt and thank them for fruitful discussions.

In addition, the Collaboration wishes to thank all the administrative and technical staff involved during the preparation of the Physics Performance Report Volume II and in particular the ALICE secretariat, M Connor, U Genoud Prachex and C Herve; the CERN Desktop Publishing Service, in particular S Leech O'Neale, J Tierney and C Vanoli; the CERN Photo Service, in particular M Brice; and the personnel of the CERN printshop.

<sup>30</sup> Physics Department, CERN, Geneva, Switzerland.

<sup>31</sup> Universidade de Santiago de Compostela, Santiago de Compostela, Spain.

<sup>32</sup> Laboratoire d'Annecy-le-Vieux de Physique Théorique LAPTH, Annecy-le-Vieux, France.

<sup>33</sup> Université Paris Sud, Orsay, France.

<sup>34</sup> Moscow Physical Engineering Institute, Moscow, Russia.

<sup>35</sup> KFKI Research Institute for Particle and Nuclear Physics, Budapest, Hungary.

<sup>36</sup> Tata Institute of Fundamental Research, Mumbai, India.

<sup>37</sup> Ohio State University, Columbus, Ohio, USA.

<sup>38</sup> Nuclear Science Division, Lawrence Berkeley National Laboratory, Berkeley, California, USA.

<sup>39</sup> Laboratory for High Energies, JINR, Dubna, Russia.

<sup>40</sup> Laboratoire de Physique Théorique et Hautes Energies, Université de Paris 6 et 7, Paris, France.

<sup>41</sup> Institute of Physics, Swietokrzyska Academy, Kielce and Soltan Institute for Nuclear Studies, Warsaw, Poland.

<sup>42</sup> Department of Physics, University of Arizona, Tucson, Arizona, USA.

<sup>43</sup> Fachbereich Physik, Universität Siegen, Siegen, Germany.

<sup>44</sup> Oak Ridge National Laboratory, Oak Ridge, Tennessee, USA.

## References

- [1] ALICE Collaboration 1999 *Technical Design Report of the Inner Tracking System* CERN/LHCC 99-12
- [2] Morsch A 2001 Contribution to the PPR Meeting, CERN, April 19–20, 2001, and private communication
- [3] ALICE Collaboration 2004 ALICE: Physics Performance Report, Volume I *J. Phys. G: Nucl. Part. Phys.* **30** 1517
- [4] Badalà A *et al* 2001 ALICE-INT-2001-11
- [5] Bustreo N *et al* 2001 ALICE-INT-2001-13
- [6] Badalà A *et al* 2001 ALICE-INT-2001-26
- [7] Badalà A, Barbera R, Lo Re G, Palmeri A, Pulvirenti A, Pappalardo G S and Riggi F (ALICE Collaboration) 2002 *Nucl. Instrum. Methods A* **485** 100
- [8] Dainese A and Maserà M 2003 ALICE-INT-2003-27
- [9] Karimäki V 1997 CMS Note 1997/051
- [10] Billoir P 1984 *Nucl. Instrum. Methods A* **225** 352
- [11] Belikov I, Ivanov M and Šafařík K 2005 ALICE-INT-2005-036
- [12] Riedler P *et al* 2003 *Proc. VERTEX2003 Workshop (Lake Windermere, UK, 2003)* *Nucl. Instrum. Methods A* at press
- [13] Nilsson P *et al* (ALICE SPD Collaboration) 2004 *Nucl. Instrum. Methods A* **535** 424
- [14] Elia D *et al* 2005 ALICE-INT-2005-007
- [15] Elia D *et al* 2005 ALICE-INT-2005-011
- [16] Riedler P *et al* 2003 *Nucl. Instrum. Methods A* **501** 111
- [17] Conrad J and Nilsson P 2005 ALICE-INT-2005-003
- [18] Caliandro R, Dinapoli R, Fini R A and Virgili T 2002 *Nucl. Instrum. Methods A* **482** 619
- [19] Caliandro R *et al* 2000 ALICE-INT-2000-23
- [20] Caliandro R *et al* 2001 ALICE-INT-2001-05
- [21] Barbera R *et al* 2001 ALICE-INT-2001-48
- [22] Batyunya B and Zinchenko A 1994 ALICE-INT-1994-11
- [23] Batyunya B and Zinchenko A 1994 ALICE-INT-1994-31
- [24] Bruno G E *et al* 2005 ALICE-INT-2005-022
- [25] Pulvirenti A, Badalà A, Barbera R, Lo Re G, Palmeri A, Pappalardo G S and Riggi F 2004 *Nucl. Instrum. Methods A* **533** 543
- [26] Peterson C 1989 *Nucl. Instrum. Methods A* **279** 537  
Denby B H 1988 *Comput. Phys. Commun.* **49** 429
- [27] Freeman J A and Skapura D M 1991 *Neural Networks: Algorithms, Application and Programming Techniques* (Reading, MA: Addison Wesley)
- [28] Peterson C and Anderson J R 1988 *Complex Syst.* **2** 59–89
- [29] Morsch A, <http://home.cern.ch/~morsch/AliGenerator/AliGenerator.html>
- [30] Kindziuk P *et al* 1999 ALICE-INT-1999-34
- [31] Belikov I, Ivanov M and Šafařík K 2005 ALICE-INT-2005-037
- [32] Dainese A and Turrisi R 2003 ALICE-INT-2003-28
- [33] ALICE Collaboration 1995 *Technical Proposal*, CERN/LHCC 95-71
- [34] ALICE Collaboration 1999 *Technical Design Report of the Dimuon Forward Spectrometer* CERN/LHCC 99-22
- [35] Mathieson E 1988 *Nucl. Instrum. Methods A* **270** 602
- [36] Chabratova G *et al* 2003 ALICE-INT-2003-006
- [37] Shepp L A and Vardi Y 1982 *IEEE Trans. Med. Im.* **1** 113
- [38] Lucy L B 1974 *Astron. J.* **79** 745
- [39] Richardson W H 1972 *J. Opt. Soc. Am. A* **62** 55
- [40] D’Agostini G 1995 *Nucl. Instrum. Methods A* **362** 487
- [41] Kolganova E A, Ososkov G A and Kosarev E L 2000 *Nucl. Instrum. Methods A* **443** 464
- [42] Wang X N and Gyulassy M 1991 *Phys. Rev. D* **44** 3501
- [43] Billoir P and Qian S 1990 *Nucl. Instrum. Methods A* **294** 219
- [44] ALICE Collaboration 1996 *The Forward Muon Spectrometer—Addendum to the ALICE Technical Proposal* CERN/LHCC 96-32
- [45] Cussonneau J P *et al* 2002 *Proc. XVI Int. Baldin Seminar on High Energy Physics Problems (Dubna, 2002)* pp 68–75
- [46] Chabratova G *et al* 2003 ALICE-INT-2003-002
- [47] Fruhwirth R 1987 *Nucl. Instrum. Methods A* **262** 444

- [48] Chabratova G *et al* 2003 ALICE-INT-2003-053
- [49] Alt T *et al* (ALICE Collaboration) 2004 *J. Phys. G: Nucl. Part. Phys.* **30** S1097  
Vestbø A 2004 *PhD Thesis* University of Bergen
- [50] Adler C *et al* (STAR Collaboration) 2003 *Nucl. Instrum. Methods A* **499** 778
- [51] Hough P 1959 Machine analysis of bubble chamber pictures *Int. Conf. on High Energy Accelerators and Instrumentation (CERN)*
- [52] Cheshkov C 2005 ALICE-INT-2005-024
- [53] Dainese A 2003 *PhD Thesis* University of Padova *Preprint* [nucl-ex/0311004](#)
- [54] Finck Ch *et al* 2005 ALICE-INT-2005-012 version 1.0
- [55] Manso F 2002 ALICE-INT-2002-04 version 1.0
- [56] Standard Performance Evaluation Corporation (SPEC) 2005 SPEC CPU 2000 V1.2,  
<http://www.spec.org/cpu2000/index.html>
- [57] Battyunya B 1998 ALICE-INT-1998-49
- [58] ALICE Collaboration 1999 *A Transition Radiation Detector, Technical Proposal, Addendum 2* CERN/LHCC 99-13
- [59] ALICE Collaboration 2001 *Technical Design Report of the ALICE Transition Radiation Detector* CERN/LHCC 2001-021
- [60] Andronic A *et al* (ALICE Collaboration) 2004 *Nucl. Instrum. Methods A* **519** 508 (*Preprint* [physics/0310122](#))
- [61] Andronic A (ALICE TRD Collaboration) 2004 *Nucl. Instrum. Methods A* **522** 40 (*Preprint* [physics/0402131](#))
- [62] Fabjan C W and Struczinski W 1975 *Phys. Lett. B* **57** 483
- [63] Busch O *et al* (ALICE TRD Collaboration) 2004 *Nucl. Instrum. Methods A* **522** 45 (*Preprint* [physics/0404106](#))
- [64] Holder M and Suhr H 1988 *Nucl. Instrum. Methods A* **263** 319
- [65] Adler C *et al* (ALICE Collaboration) 2005 *Nucl. Instrum. Methods A* **552** 364
- [66] Arcelli S *et al* 2005 ALICE-INT-2005-044
- [67] Gyulassy M and Wang X N 1994 *Comput. Phys. Commun.* **83** 307 (*Preprint* [nucl-th/9502021](#))
- [68] Bengtsson H U and Sjostrand T 1987 *Comput. Phys. Commun.* **46** 43
- [69] Brun R, Bruyant F, Maire M, McPherson A and Zanarini P 1985 *Geant3 User Guide* CERN Data Handling Division DD/EE/84-1, <http://www.info.cern.ch/asdoc/geantold/GEANTMAIN.html>
- [70] ALICE Collaboration 2002 *Addendum to the Technical Design Report of the Time of Flight System* CERN/LHCC 2002-16, Addendum to ALICE TDR 8, 24 April 2002
- [71] Akimov A V *et al* 2004 *Nucl. Instrum. Methods A* **532** 611  
Akimov A V *et al* 2004 *Nucl. Instrum. Methods A* **533** 74
- [72] Antonioli P 2003 A 20 ps TDC readout module for the ALICE Time of Flight system: design and test results *Proc. 9th Workshop on Electronics for LHC Experiments (29 September–3 October 2003, Amsterdam)* CERN-2003-006, LHCC-G-061
- [73] Radomski S *et al* 2003 ALICE-INT-2003-008
- [74] Velkovska J (PHENIX Collaboration) 2002 *Nucl. Phys. A* **698** 507 (*Preprint* [nucl-ex/0105012](#))
- [75] ALICE Collaboration 1998 *Technical Design Report of the High Momentum Particle Identification Detector* CERN/LHCC 98-19
- [76] Di Bari D *et al* 2005 ALICE-INT-2005-043
- [77] Barbosa J *et al* 2000 ALICE-INT-2000-6
- [78] Di Bari D (ALICE Collaboration) 2003 *Nucl. Instrum. Methods A* **502** 300
- [79] Di Mauro A 1998 ALICE-INT-1998-34
- [80] Cozza D *et al* (ALICE Collaboration) 1999 *Nucl. Phys. A* **661** 702
- [81] Aguilar-Benitez M *et al* 1991 *Z. Phys. C* **50** 405
- [82] ALICE Collaboration 1999 *Technical Design Report of the Photon Spectrometer (PHOS)* CERN/LHCC 99-4
- [83] Blick A M *et al* 2000 ALICE-INT-2000-21
- [84] Apeheteche L *et al* 2002 ALICE-INT-2002-02
- [85] Apeheteche L *et al* (PHENIX Collaboration) 2003 *Nucl. Instrum. Methods A* **499** 521
- [86] Delagrèze H *et al* 2001 ALICE-INT-2001-01
- [87] Camard X *et al* 2001 ALICE-INT-2001-27
- [88] Brun R, Hansroul M and Kubler J 1979 *Preprint* CERN DD/EE/79-5
- [89] Conesa G *et al* 2005 ALICE-INT-2005-053
- [90] Aggarwal M M *et al* 2002 *Nucl. Phys. A* **698** 135

- [91] Lonnblad L, Peterson C and Rognvaldsson T 1992 *Comput. Phys. Commun.* **70** 167  
Peterson C, Rognvaldsson T and Lonnblad L 1993 *Preprint* LU-93-29  
Peterson C, Rognvaldsson T and Lonnblad L 1994 *Preprint* CERN-TH.7315/94, Geneva
- [92] Lonnblad L, Peterson C and Rognvaldsson T 1990 *Phys. Rev. Lett.* **65** 1321
- [93] Lonnblad L, Peterson C and Rognvaldsson T 1991 *Nucl. Phys. B* **349** 675
- [94] Bhat P, Lonnblad L, Meir K and Sugano K 1990 *Proc. 1990 DPF Summer Study in High Energy Physics (Colorado)*
- [95] Scabai I, Czako F and Fodor Z 1990 ITP Budapest report 477
- [96] Maggipinto T *et al* 1997 *Preprint* BARI-TH/268-97, Bari
- [97] Aseev A A *et al* 2002 *Preprint* IHEP 2002-3, Protvino
- [98] Bitjukov S I *et al* 1981 *Preprint* IHEP 81-45, Serpukhov
- [99] Bogolyubsky M Yu, Kharlov Yu V and Sadovsky S A 2003 ALICE-INT-2003-037
- [100] Minaev N G 1994 *Preprint* IHEP 94-142, Protvino
- [101] Reid E C and Heath H F 2000 CMS Note 2000/063, Geneva
- [102] Conesa G *et al* 2005 ALICE-INT-2005-16
- [103] ALICE Collaboration 1999 *Technical Design Report for the Photon Multiplicity Detector* CERN/LHCC 99-32
- [104] ALICE Collaboration 2003 *Technical Design Report for the Photon Multiplicity Detector, Addendum-1* CERN/LHCC 2003-038
- [105] Back B B *et al* (PHOBOS Collaboration) 2000 *Phys. Rev. Lett.* **85** 3100 (*Preprint* hep-ex/0007036)  
Back B B *et al* (PHOBOS Collaboration) 2002 *Phys. Rev. Lett.* **88** 022302 (*Preprint* nucl-ex/0108009)
- [106] Takahashi Y and Dake S (JACEE Collaboration) 1987 *Nucl. Phys. A* **461** 263
- [107] Viyogi Y P 2005 *Proc. 5th Int. Conf. on Physics and Astrophysics of Quark Gluon Plasma (Salt Lake City, Kolkata, India, 2005)* *Preprint* nucl-ex/0510079
- [108] Adams J *et al* (STAR Collaboration) 2005 *Phys. Rev. Lett.* **95** 062301 (*Preprint* nucl-ex/0502008)
- [109] Caliendo R, Conrad J, Contreras G, Demarco N, Fini R A, Gallio M, Jorgensen C, Karpechev E, Kurepin A, Maevskaia A, Masera M, Monteno M, Noferini F, Oppedisano C, Scomparin E, Sikler F and Virgili T 2005 *Event Characterization in ALICE* ALICE-INT-2005-034
- [110] Satz H 2001 *Nucl. Phys. B Proc. Suppl.* **94** 204
- [111] Kharzeev D E and Nardi M 2001 *Phys. Lett. B* **507** 121
- [112] Bjorken J D 1983 *Phys. Rev. D* **27** 140
- [113] Hagedorn R 1983 *Riv. Nuovo Cimento* **6** 1
- [114] Giubellino P, Kiselev S, Klempt W, Morsch A, Paic G, Revol J-P and Safarik K 2000 *Day One Proton-Proton Physics with the ALICE Central Detector* ALICE-INT-2000-28
- [115] For a review, see Giovannini A 2001 *Proc. New Frontiers in Soft Physics and Correlations on the Threshold of the Third Millennium* 2001 *Nucl. Phys. B Proc. Suppl.* **92** 3
- [116] Aggarwal M M *et al* (WA98 Collaboration) 2001 *Eur. Phys. J. C* **18** 651
- [117] Antinori F *et al* (NA57 Collaboration) 2005 *J. Phys. G: Nucl. Part. Phys.* **31** 321
- [118] Sikler F *et al* (NA49 Collaboration) 1999 *Nucl. Phys. A* **661** 45
- [119] Abreu M C *et al* (NA50 Collaboration) 2002 *Phys. Lett. B* **530** 43
- [120] Adcox K *et al* (PHENIX Collaboration) 2001 *Phys. Rev. Lett.* **86** 3500
- [121] Adler C *et al* (STAR Collaboration) 2001 *Phys. Rev. Lett.* **87** 112303
- [122] Bearden I G *et al* (BRAHMS Collaboration) 2001 *Phys. Lett. B* **523** 227
- [123] 2004 *Forward Detectors: FMD, T0, V0 Technical Design Report* ALICE-DOC-2004-010
- [124] 1999 *Zero-Degree Calorimeter Technical Design Report* CERN/LHCC 99-5
- [125] 2005 *Computing Technical Design Report* CERN/LHCC 2005-18
- [126] Bialas A *et al* 1976 *Nucl. Phys. B* **111** 461
- [127] Glauber R J 1959 *Lectures in Theoretical Physics* vol 1 (New York: Interscience) p 315
- [128] de Jager C W *et al* 1974 *At. Data Nucl. Data Tables* **14** 485
- [129] Back B B *et al* (PHOBOS Collaboration) 2002 *Phys. Rev. C* **65** 31901R
- [130] Oppedisano C 2002 *PhD Thesis* Università di Torino, ALICE-INT-2002-08
- [131] Wang X N and Gyulassy M 2001 *Phys. Rev. Lett.* **86** 3496
- [132] Brun R, Bruyant F, Maire M, McPherson A C and Zanarini P 1985 *GEANT3 User Guide* CERN Data Handling Division DD/EE/84-1, <http://www.info.cern.ch/asdoc/geantold/GEANTMAIN.html>
- [133] Baltz A J *et al* 1998 *Nucl. Instrum. Methods A* **417** 1
- [134] Pshenichnov I A *et al* 2001 *Phys. Rev. C* **64** 024903
- [135] Schuttauf A *et al* (ALADIN Collaboration) 1996 *Nucl. Phys. A* **607** 457
- [136] Appelshauer H *et al* (NA49 Collaboration) 1998 *Eur. Phys. J. A* **2** 383

- [137] Schlagheck H *et al* (WA98 Collaboration) 1999 *Nucl. Phys. A* **661** 337
- [138] Adams J *et al* (STAR Collaboration) 2004 *Phys. Rev. Lett.* **92** 062301
- [139] Alt C *et al* (NA49 Collaboration) 2003 *Phys. Rev. C* **68** 034903
- [140] Benecke J *et al* 1969 *Phys. Rev.* **188** 2159
- [141] Crawford H *et al* 2003 *STAR ZDC-SMD proposal* STAR Note SN-0448
- [142] Chiavassa E *et al* 1995 *Nucl. Instrum. Methods A* **367** 267
- [143] Poskanzer A M and Voloshin S A 1998 *Phys. Rev. C* **58** 1671
- [144] Armesto N *et al* 2000 *Int. J. Mod. Phys. A* **15** 2019
- [145] Ahle L *et al* 2000 *Phys. Lett. B* **476** 1
- [146] Kharzeev D and Levin E 2001 *Phys. Lett. B* **523** 79
- [147] Virgili T 2005 *1st Italian Workshop on ALICE Physics* (<http://alicemeeting.ct.infn.it/programma.php>)
- [148] Caliendo R, Fini R A and Virgili T 2002 *Measurement of multiplicity and  $dN/d\eta$  using the ALICE Silicon Pixel Detector* ALICE-INT-2002-43
- [149] Back B B *et al* (PHOBOS Collaboration) 2003 *Phys. Rev. Lett.* **91** 052303
- [150] Sjostrand T *et al* 2001 *Comput. Phys. Commun.* **135** 238
- [151] Moraes A, Buttar C and Dawson I 2005 ATLAS Note ATL-PHYS-PUB-2005-007
- [152] Giovannini A and Ugoccioni R 2002 *Global event properties in proton–proton physics with ALICE* Internal Note DFT-29-2001, Univ. di Torino (*Preprint hep-ph/0203215*)
- [153] Ugoccioni R and Giovannini A 2005 *J. Phys. Conf. Ser.* **5** 199
- [154] Conrad J, Contreras J G and Jorgensen C E 2005 *Minimum bias triggers in proton–proton collisions with the VZERO and Silicon Pixel detectors* ALICE-INT-2005-030
- [155] Morsch A 2005 Talk given at ALICE Club, June 2005
- [156] Arnison G *et al* (UA1 Collaboration) 1982 *Phys. Lett. B* **118** 173
- [157] Bocquet G *et al* (UA1 Collaboration) 1996 *Phys. Lett. B* **366** 434
- [157] Breakstone A *et al* 1983 *Phys. Lett. B* **132** 458
- [157] Breakstone A *et al* 1983 *Phys. Lett. B* **132** 463
- [157] Breakstone A *et al* 1987 *Phys. Lett. B* **183** 227
- [158] Alexopoulos T *et al* (E735 Collaboration) 1990 *Phys. Rev. Lett.* **64** 991
- [158] Alexopoulos T *et al* (E735 Collaboration) 1993 *Phys. Rev. D* **48** 984
- [159] Acosta D *et al* (CDF Collaboration) 2002 *Phys. Rev. D* **65** 072005
- [160] Lattes C M G *et al* 1980 *Phys. Rep.* **65** 151
- [161] Wang X N and Hwa R C 1989 *Phys. Rev. D* **39** 187
- [161] Wang X N and Gyulassy M 1992 *Phys. Lett. B* **282** 466
- [162] Basile M *et al* 1980 *Phys. Lett. B* **92** 367
- [162] Basile M *et al* 1980 *Phys. Lett. B* **95** 311
- [162] Basile M *et al* 1981 *Nuovo Cimento A* **65** 400
- [162] Basile M *et al* 1981 CERN-EP/81-147
- [162] Basile M *et al* 1982 *Nuovo Cimento A* **67** 244
- [162] Basile M *et al* 1983 *Nuovo Cimento A* **73** 329
- [162] Basile M *et al* 1984 *Nuovo Cimento A* **79** 1
- [163] Groom D E *et al* 2000 *Eur. Phys. J. C* **15** 1
- [163] Biebel O *et al* 2001 *Preprint hep-ph/0109282* and experimental references therein
- [163] Benecke J 1976 *Nucl. Phys. B* **76** 29
- [163] Morse W M 1977 *Phys. Rev. D* **15** 66
- [163] Breakstone A *et al* 1984 *Phys. Rev. D* **30** 528
- [163] Alner G J *et al* (UA5 Collaboration) 1986 *Phys. Lett. B* **167** 476
- [163] Ansrage R E *et al* (UA5 Collaboration) 1989 *Z. Phys. C* **43** 357
- [164] Back B B *et al* (PHOBOS Collaboration) 2003 (*Preprint nucl-ex/0301017*)
- [165] Alner G J *et al* (UA5 Collaboration) 1986 *Z. Phys. C* **33** 1
- [165] Thome W *et al* 1977 *Nucl. Phys. B* **129** 365
- [166] Armesto N 2005 *J. Phys. Conf. Ser.* **5** 219
- [167] Gurtu A *et al* 1974 *Phys. Lett. B* **50** 391
- [168] Faessler M A *et al* 1979 *Nucl. Phys. B* **157** 1
- [169] Andersson B, Otterlund I and Stenlund E 1978 *Phys. Lett. B* **73** 343
- [170] Chemakin I *et al* (E910 Collaboration) 1999 *Phys. Rev. C* **60** 024902
- [171] Braune K *et al* 1982 *Z. Phys. C* **13** 191
- [172] Siklér F 2003 *Preprint hep-ph/0304065*
- [173] Oppedisano C, Gallio M and Scomparin E 2005 ALICE-INT-2005-051

- [174] Dabrowska A *et al* 1993 *Phys. Rev. D* **47** 1751
- [175] Bass S A, Gyulassy M, Stöcker H and Greiner W 1999 *J. Phys. G: Nucl. Part. Phys.* **25** R1
- [176] Satz H 2000 *Rep. Prog. Phys.* **63** 1511
- [177] Shuryak E V 1984 *Phys. Rep.* **115** 151
- [178] Cleymans J, Gavai R V and Suhonen E 1986 *Phys. Rep.* **130** 217
- [179] Stock R 1999 *Phys. Lett. B* **456** 277
- [180] Stock R 1999 *Prog. Part. Nucl. Phys.* **42** 295
- [181] Stachel J 1999 *Nucl. Phys. A* **654** 119c
- [182] Heinz U 2001 *Nucl. Phys. A* **685** 414
- [183] Heinz U 1999 *Nucl. Phys. A* **661** 140
- [184] Baier R, Mueller A H, Schiff D and Son D T 2001 *Phys. Lett. B* **502** 51
- [185] Gribov L V, Levin E M and Ryskin M G 1983 *Phys. Rep.* **100** 1
- [186] Mueller A H and Qiu J 1986 *Nucl. Phys. B* **268** 427
- [187] Eskola K J, Kajantie K, Ruuskanen P and Tuominen K 2000 *Nucl. Phys. B* **570** 379
- [188] McLerran L and Venugopalan R 1994 *Phys. Rev. D* **49** 2233
- [189] McLerran L and Venugopalan R 1994 *Phys. Rev. D* **49** 3352
- [190] McLerran L and Venugopalan R 1994 *Phys. Rev. D* **50** 2225
- [191] Cleymans J and Redlich K 1999 *Phys. Rev. C* **60** 054908
- [192] Cleymans J, Oeschler H and Redlich K 1999 *Phys. Rev. C* **59** 1663
- [193] Cleymans J, Oeschler H and Redlich K 2001 *Phys. Lett. B* **485** 27
- [194] Becattini F, Cleymans J, Keranen A, Suhonen E and Redlich K 2001 *Phys. Rev. C* **64** 024901
- [195] Redlich K and Tounsi A 2002 *Eur. J. Phys. C* **24** 589
- [196] Schmitz W *et al* (CERES Collaboration) 2002 *J. Phys. G: Nucl. Part. Phys.* **28** 1861
- [197] Braun-Munzinger P and Stachel J 2002 *J. Phys. G: Nucl. Part. Phys.* **28** 1971
- [198] Becattini F 2002 *J. Phys. G: Nucl. Part. Phys.* **28** 1553
- [199] Braun-Munzinger P, Heppel I and Stachel J 1999 *Phys. Lett. B* **465** 15
- [200] Akkelin S V, Braun-Munzinger P and Sinyukov Yu M 2002 *Nucl. Phys. A* **710** 439
- [201] Braun-Munzinger P, Magestro D, Redlich K and Stachel J 2001 *Phys. Lett. B* **518** 41
- [202] Xu N and Kaneta M 2002 *Nucl. Phys. A* **698** 306
- [203] Broniowski W and Florkowski W 2001 *Phys. Rev. Lett.* **87** 272302
- [204] Cleymans J and Redlich K 1998 *Phys. Rev. Lett.* **81** 5284 and references therein
- [205] Adler C *et al* (STAR Collaboration) 2001 *Phys. Rev. Lett.* **87** 182301
- [206] Adams J *et al* (STAR Collaboration) 2004 *Phys. Rev. Lett.* **92** 112301
- [207] Wiedemann U A and Heinz U 1999 *Phys. Rep.* **319** 145 and references therein
- [208] Tomasik B, Wiedemann U A and Heinz U 2000 *Nucl. Phys. A* **663** 753
- [209] Nix J R 1998 *Phys. Rev. C* **58** 2303
- [210] Barz H W, Bertsch G, Kusnezov D and Schulz H 1991 *Phys. Lett. B* **254** 315
- [211] Barz H W, Friman B L, Knoll J and Schulz H 1992 *Nucl. Phys. A* **545** 259
- [212] Braun-Munzinger P, Stachel J, Wessels J P and Xu N 1995 *Phys. Lett. B* **344** 43
- [213] Braun-Munzinger P, Stachel J, Wessels J P and Xu N 1996 *Phys. Lett. B* **365** 1
- [214] Braun-Munzinger P and Stachel J 1996 *Nucl. Phys. A* **606** 320
- [215] Sollfrank J *et al* 1997 *Phys. Rev. C* **55** 392
- [216] Huovinen P *et al* 2001 *Phys. Lett. B* **503** 58 and references therein
- [217] Kabana S and Minkowski P 2001 *New J. Phys.* **3** 4
- [218] Wroblewski A 1985 *Acta Phys. Polon. B* **16** 379
- [219] Anisovich V V and Kobrinsky M N 1974 *Phys. Lett. B* **52** 217
- [220] Karsch F, Laermann E and Peikert A 2001 *Nucl. Phys. B* **605** 579
- [221] Blaizot J P, Iancu E and Rebhan A 2001 *Phys. Rev. D* **63** 065003
- [222] Karsch F, Redlich K and Tawfik A 2003 *Eur. J. Phys. C* **29** 549
- [223] Hagedorn R 1971 *Thermodynamics of Strong Interactions* CERN Report 71-12
- [224] Shuryak E V 1972 *Phys. Lett. B* **42** 357
- [225] Redlich K and Turko L 1980 *Z. Phys. C* **5** 201
- [226] Rafelski J and Danos M 1980 *Phys. Lett. B* **97** 279
- [227] Hagedorn R and Redlich K 1985 *Z. Phys. C* **27** 541
- [228] Letessier J and Rafelski J 2000 *Int. J. Mod. Phys. E* **9** 107
- [229] Torrieri G, Steinke S, Broniowski W, Florkowski W, Letessier J and Rafelski J 2005 *Comput. Phys. Commun.* **167** 229
- [230] Rafelski J and Letessier J 2006 *Eur. J. Phys. C* **45** 61

- [231] Braun-Munzinger P, Redlich K and Stachel J 2004 *Quark–Gluon Plasma 3* ed R C Hwa and X-N Wang (Singapore: World Scientific) pp 491–599
- [232] Andronic A, Braun-Munzinger P and Stachel J 2006 *Nucl. Phys. A* **772** 167 (Preprint [nucl-th/0511071](#))
- [233] Adams J *et al* (STAR Collaboration) 2005 *Nucl. Phys. A* **757** 102
- [234] Zschieche D *et al* 2001 *Nucl. Phys. A* **681** 34
- [235] Rafelski J and Hagedorn R 1981 *Proc. Int. Symp. Statistical Mechanics of Quarks and Hadrons* (Amsterdam: North-Holland) p 253
- [236] Rafelski J 1982 *Phys. Rep.* **88** 331
- [237] Koch P, Müller B and Rafelski J 1986 *Phys. Rep.* **142** 167
- [238] Rafelski J 1991 *Phys. Lett. B* **262** 333
- [239] Andersen E *et al* (WA97 Collaboration) 1999 *Phys. Lett. B* **449** 401
- [240] Antinori F *et al* (NA57 Collaboration) 2002 *Nucl. Phys. A* **698** 118
- [241] Šandor L *et al* (NA57 Collaboration) 2004 *J. Phys. G: Nucl. Part. Phys.* **30** S129
- [242] Caines H *et al* (STAR Collaboration) 2005 *J. Phys. G: Nucl. Part. Phys.* **31** S1057
- [243] Hamieh S, Redlich K and Tounsi A 2000 *Phys. Lett. B* **486** 61
- [244] Becattini F 1996 *Z. Phys. C* **69** 485
- [245] Becattini F and Heinz U 1997 *Z. Phys. C* **76** 269
- [246] Becattini F 1999 *J. Phys. G: Nucl. Part. Phys.* **25** 287
- [247] Margetis S, Šafařík K and Villalobos Baillie O 2000 *Annu. Rev. Nucl. Part. Sci.* **50** 299
- [248] Greiner C 2003 *AIP Conf. Proc.* **644** 337
- [249] Huovinen P and Kapusta J L 2004 *Phys. Rev. C* **69** 014902
- [250] Braun-Munzinger P, Stachel J and Wetterich C 2004 *Phys. Lett. B* **596** 61
- [251] Cleymans J, Förster A, Oeschler H, Redlich K and Uhlig F 2004 *Phys. Lett. B* **603** 146
- [252] Hartnack C, Oeschler H and Aichelin J 2003 *Phys. Rev. Lett.* **90** 102302  
Hartnack C, Oeschler H and Aichelin J 2004 *Phys. Rev. Lett.* **93** 149903 (erratum)
- [253] Blume C *et al* (NA49 Collaboration) 2002 *Nucl. Phys. A* **698** 104
- [254] Harris J *et al* (STAR Collaboration) 2002 *Nucl. Phys. A* **698** 64
- [255] Cassing W 1999 *Nucl. Phys. A* **661** 468
- [256] Greiner C 2002 *J. Phys. G: Nucl. Part. Phys.* **28** 1631
- [257] Weber H, Bratkovskaya E L, Cassing W and Stöcker H 2003 *Phys. Rev. C* **67** 014904
- [258] Gazdzicki M and Roehrich D 1995 *Z. Phys. C* **65** 215
- [259] Gazdzicki M and Gorenstien M I 1999 *Acta Phys. Polon. B* **30** 2705
- [260] Braun-Munzinger P, Cleymans J, Oeschler H and Redlich K 2002 *Nucl. Phys. A* **697** 902
- [261] Gavai R V and Gupta S 2002 *Phys. Rev. D* **65** 094515
- [262] Adler C *et al* (STAR Collaboration) 2002 *Phys. Rev. C* **66** 061901
- [263] Retière F *et al* (STAR Collaboration) 2004 *J. Phys. G: Nucl. Part. Phys.* **30** S335
- [264] Asakawa M and Ko C M 1994 *Phys. Lett. B* **322** 33
- [265] Asakawa M and Ko C M 1994 *Phys. Rev. C* **50** 3064
- [266] Pisarski R D and Wilczek F 1984 *Phys. Rev. D* **29** 338
- [267] Shuryak E V 1991 *Nucl. Phys. A* **525** 3
- [268] Letessier J *et al* 2001 *J. Phys. G: Nucl. Part. Phys.* **27** 427
- [269] Alt C *et al* (NA49 Collaboration) 2005 *Phys. Rev. Lett.* **94** 052301
- [270] Torrieri G and Rafelski J 2001 *Phys. Lett. B* **509** 239
- [271] Markert C 2005 *J. Phys. G: Nucl. Part. Phys.* **31** S897
- [272] Andersson B, Gustafson G, Ingelman G and Sjöstrand T 1983 *Phys. Rep.* **97** 31
- [273] Bocquet G *et al* 1996 *Phys. Lett. B* **366** 447
- [274] Alexopoulos T *et al* 2002 *Phys. Lett. B* **528** 43
- [275] Paic G and Skowronski P K 2005 *J. Phys. G: Nucl. Part. Phys.* **31** 1045
- [276] Antinori F *et al* (NA57 Collaboration) 2004 *J. Phys. G: Nucl. Part. Phys.* **30** 823
- [277] Redlich K 2002 *Nucl. Phys. A* **698** 94
- [278] van Hecke H, Sorge H and Xu N 1999 *Nucl. Phys. A* **661** 493
- [279] Bugaev K *et al* 2002 *Phys. Lett. B* **544** 127
- [280] Gorenstein M I *et al* 2002 *Phys. Rev. Lett.* **88** 132301
- [281] Adams J *et al* (STAR Collaboration) 2004 *Phys. Rev. Lett.* **92** 182301
- [282] Kolb P and Heinz U 2004 *Quark–Gluon Plasma 3* ed R C Hwa and X-N Wang (Singapore: World Scientific) p 634 and references therein
- [283] Huovinen P 2002 *AIP Conf. Proc.* **610** 571
- [284] Teaney D, Lauret J and Shuryak E 2001 *Phys. Rev. Lett.* **86** 4783

- [285] Hirano T 2005 *Preprint* [nucl-th/0510005](#)
- [286] Schnedermann E, Sollfrank J and Heinz U 1993 *Phys. Rev. C* **48** 2462
- [287] Retière F and Lisa M A 2004 *Phys. Rev. C* **70** 044907
- [288] Barannikova O *et al* (STAR Collaboration) 2004 *Preprint* [nucl-ex/0403014](#)
- [289] Schweda K 2005 *Preprint* [nucl-ex/0510004](#)
- [290] Bruno G E *et al* (NA57 Collaboration) 2005 *J. Phys. G: Nucl. Part. Phys.* **31** S127
- [291] Speltz J *et al* (STAR Collaboration) 2005 *Preprint* [nucl-ex/0512037](#)
- [292] Salur S *et al* (STAR Collaboration) 2005 *Preprint* [nucl-ex/0509036](#)
- [293] Xu N 2005 *Nucl. Phys. A* **751** 109
- [294] Adcox K *et al* (PHENIX Collaboration) 2002 *Phys. Rev. Lett.* **88** 242301
- [295] Adler S S *et al* (PHENIX Collaboration) 2004 *Phys. Rev. C* **69** 034909
- [296] Chujo T *et al* (PHENIX Collaboration) 2003 *Nucl. Phys. A* **715** 151
- [297] Sakaguchi T *et al* (PHENIX Collaboration) 2003 *Nucl. Phys. A* **715** 757
- [298] Lamont M A C *et al* (STAR Collaboration) 2004 *J. Phys. G: Nucl. Part. Phys.* **30** S963
- [299] Mironov C *et al* (STAR Collaboration) 2005 *J. Phys. G: Nucl. Part. Phys.* **31** S1195
- [300] Hwa R C and Yang C B 2002 *Phys. Rev. C* **66** 025205
- [301] Hwa R C and Yang C B 2003 *Phys. Rev. Lett.* **90** 212301
- [302] Hwa R C and Yang C B 2004 *Phys. Rev. C* **70** 024905
- [303] Greco V, Ko C M and Lévai P 2003 *Phys. Rev. Lett.* **90** 202302
- [304] Greco V, Ko C M and Lévai P 2003 *Phys. Rev. C* **68** 034904
- [305] Fries R J, Bass S A, Müller B and Nonaka C 2003 *Phys. Rev. Lett.* **90** 202303
- [306] Fries R J, Bass S A, Müller B and Nonaka C 2003 *Phys. Rev. C* **68** 044902
- [307] Biró T S, Lévai P and Zimányi J 1995 *Phys. Lett. B* **347** 6
- [308] Biró T S, Lévai P and Zimányi J 1999 *Phys. Rev. C* **59** 1574
- [309] Biró T S, Lévai P and Zimányi J 1999 *J. Phys. G: Nucl. Part. Phys.* **25** 311
- [310] Csizmadia P and Lévai P 2000 *Phys. Rev. C* **61** 031903
- [311] Csizmadia P and Lévai P 2002 *J. Phys. G: Nucl. Part. Phys.* **28** 1997
- [312] Csizmadia P and Lévai P 2005 *Acta Phys. Hung. A* **22** 371
- [313] Biró T S, Lévai P and Zimányi J 2002 *J. Phys. G: Nucl. Part. Phys.* **28** 1561
- [314] Biró T S, Lévai P and Zimányi J 2005 *J. Phys. G: Nucl. Part. Phys.* **31** 711
- [315] Lévai P and Heinz U 1998 *Phys. Rev. C* **57** 1879
- [316] Fries R J and Müller B 2004 *Eur. J. Phys. C* **34** S279
- [317] Molnar D and Voloshin S A 2003 *Phys. Rev. Lett.* **91** 092301
- [318] Wang X-N 1998 *Phys. Rev. C* **58** 2321
- [319] Vitev I and Gyulassy M 2003 *Nucl. Phys. A* **715** 779
- [320] Vitev I and Gyulassy M 2002 *Phys. Rev. C* **65** 041902R
- [321] Vitev I and Gyulassy M 2002 *Phys. Rev. Lett.* **89** 252301
- [322] Abreu P *et al* (DELPHI Collaboration) 2000 *Eur. J. Phys. C* **17** 207
- [323] Christiansen *et al* 2005 *Performance Test of the ALICE TPC IROC Module at the PS* ALICE-INT-2005-029
- [324] Christiansen *et al* 2005 *Stragglng Functions and PID Capabilities of the ALICE TPC* ALICE-INT-2005-030
- [325] Shao M, Barannikova O, Dong X, Fisyak Y, Ruan L, Sorensen P and Xu Z 2006 *Nucl. Instrum. Methods A* **558** 419 (*Preprint* [nucl-ex/0505026](#))
- [326] Adcox K *et al* (PHENIX Collaboration) 2004 *Phys. Rev. C* **69** 024904
- [327] Dunlop J C *et al* (STAR Collaboration) 2005 *Preprint* [nucl-ex/0510073](#)
- [328] Bearden I G *et al* (BRAHMS Collaboration) 2005 *Phys. Lett. B* **607** 42
- [329] Sjöstrand T *et al* 2003 *Pythia 6.3 Physics and Manual* *Preprint* [hep-ph/0308153](#)
- [330] Cuautle E and Paic G 2005 *Study of the pion and proton production in pp collisions at 14 TeV* ALICE-INT-2005-027
- [331] Srivastava D K 2001 *Eur. J. Phys. C* **22** 129
- [332] Apehceche L *et al* 2002 ALICE-INT-2002-02
- [333] Adler C *et al* (STAR Collaboration) 2001 *Phys. Rev. Lett.* **87** 262301  
Adler C *et al* (STAR Collaboration) 2001 *Phys. Rev. Lett.* **87** 279902
- [334] Adler S S *et al* (PHENIX Collaboration) 2005 *Phys. Rev. Lett.* **94** 122302
- [335] Anticic T *et al* 2004 *Phys. Rev. C* **69** 024902
- [336] Armstrong T A *et al* (E864 Collaboration) 2000 *Phys. Rev. Lett.* **85** 2685
- [337] Rafelski J and Letessier J 2004 *J. Phys. G: Nucl. Part. Phys.* **30** S1
- [338] <http://morsch.home.cern.ch/morsch/generator.html>

- [339] Heinz U and Jacob M 2000 *Preprint nucl-th/0002042*
- [340] Adler S S *et al* (PHENIX Collaboration) 2003 *Phys. Rev. Lett.* **91** 072303
- [341] Adams J *et al* (STAR Collaboration) 2003 *Phys. Rev. Lett.* **91** 072304
- [342] Kopeliovich B Z and Zakharov B G 1989 *Z. Phys. C* **43** 241
- [343] Kopeliovich B Z and Povh B 1999 *Phys. Lett. B* **466** 321
- [344] Garvey G T, Kopeliovich B Z and Povh B 2001 *Comments. Mod. Phys. A* **2** 47
- [345] Witt R 2005 *J. Phys. G: Nucl. Part. Phys.* **31** S863
- [346] Bellwied R 2005 *J. Phys. G: Nucl. Part. Phys.* **31** S675
- [347] Heinz M 2005 *J. Phys. G: Nucl. Part. Phys.* **31** S1011
- [348] Heinz M 2005 *Preprint nucl-ex/0505025*
- [349] Vernet R *et al* 2005 *Topological identification of strange and multi-strange particles with the ALICE detector in Pb–Pb collisions at  $\sqrt{s_{NN}} = 5.5$  TeV* ALICE-INT-2005-042
- [350] Gaudichet L *et al* 2005 *Reconstruction of decay vertices of strange particles in pp collisions in ALICE* ALICE-INT-2005-041
- [351] Sjöstrand T, Lönnblad L and Mrenna S 2001 *Preprint hep-ph/0108264*
- [352] Wang X-N and Gyulassy M 1992 *Phys. Rev. D* **45** 844
- [353] Wang X-N 1997 *Phys. Rev.* **280** 287
- [354] Wang X-N 1999 *Nucl. Phys. A* **661** 609
- [355] Adler C *et al* (STAR Collaboration) 2002 *Phys. Rev. Lett.* **89** 092301
- [356] Adcox K *et al* (PHENIX Collaboration) 2002 *Phys. Rev. Lett.* **89** 092302
- [357] Andronic A and Braun-Munzinger P 2004 *Lecture Notes in Physics* vol 625 (Berlin: Springer) p 35
- [358] Dainese A and Masera M 2003 ALICE-INT-2003-27
- [359] Badalà A *et al* 2001 ALICE-INT-2001-11
- [360] Bustreo N *et al* 2001 ALICE-INT-2001-13
- [361] ATLAS Collaboration 2005 Internal Note ATLAS-INT-2005-07
- [362] Adams J *et al* (STAR Collaboration) 2004 *Phys. Rev. Lett.* **92** 052302
- [363] Sorensen P R 2005 *Preprint nucl-ex/0510052*
- [364] Rapp R and Wambach J 2000 *Adv. Nucl. Phys.* **25** 1
- [365] Brown G E and Rho M 1991 *Phys. Rev. Lett.* **66** 2720
- [366] Marin A *et al* (CERES Collaboration) 2004 *J. Phys. G: Nucl. Part. Phys.* **30** S709
- [367] Shuryak E V and Brown G E 2003 *Nucl. Phys. A* **717** 322
- [368] Adams J *et al* (STAR Collaboration) 2004 *Phys. Rev. Lett.* **92** 092301
- [369] Platt R and Villalobos Baillie O 2005 *Reconstruction of the  $\rho^0$  signal in Pb–Pb collisions* ALICE-INT-2005-040
- [370] Wang X-N and Gyulassy M 1992 *Phys. Rev. Lett.* **68** 1480
- [371] Albrecht H *et al* (ARGUS Collaboration) 1994 *Z. Phys. C* **61** 1
- [372] Pei Y J 1996 *Z. Phys. C* **72** 39
- [373] Blobel V *et al* (Bonn–Hamburg–Munich Collaboration) 1974 *Phys. Lett. B* **48** 73
- [374] Singer R *et al* 1976 *Phys. Lett. B* **60** 385
- [375] Drijard D *et al* 1981 *Z. Phys. C* **9** 293
- [376] Chliapnikov P V *et al* (Soviet–CERN Collaboration) 1980 *Nucl. Phys. B* **176** 303
- [377] Winkelmann F C *et al* 1975 *Phys. Lett. B* **56** 101
- [378] Rafelski J and Muller B 1982 *Phys. Rev. Lett.* **48** 1066
- [379] Bass S A *et al* 1999 *Nucl. Phys. A* **661** 205
- [380] Shor A 1985 *Phys. Rev. Lett.* **54** 1122
- [381] Koch P *et al* 1990 *Z. Phys. C* **47** 477
- [382] Lissauer D and Shuryak E V 1991 *Phys. Lett. B* **253** 15
- [383] Johnson S C *et al* 2001 *Eur. J. Phys. C* **18** 645
- [384] ALICE Collaboration 1995 *Technical Proposal CERN/LHCC 95-71, LHCC/P3* (15 December 1995)
- [385] Afanasev S V *et al* (NA49 Collaboration) 2000 *Phys. Lett. B* **491** 59
- [386] Xu Z 2002 *Nucl. Phys. A* **698** 607
- [387] Adler C *et al* (STAR Collaboration) 2002 *Phys. Rev. C* **65** 041901R
- [388] Friese V 2002 *Nucl. Phys. A* **698** 487
- [389] Batyunya B *et al* 1997 Internal Note/SIM ALICE/97-26
- [390] Akindinov A *et al* 2006 *Eur. J. Phys. C* **45** 669 (*Preprint hep-ph/0601204*)
- [391] De Caro A *et al* 2003 ALICE-INT-2003-067
- [392] Batyunya B *et al* 2005 *Part. Nucl. Lett.* **2** 72

- [393] ALICE Collaboration 2000 *Time Projection Chamber, Technical Design Report*, CERN/LHCC 2000-001, ALICE TDR 7 (7 January 2000)
- [394] ALICE Collaboration 2000 *Time of Flight System, Technical Design Report* CERN/LHCC 2000-12, ALICE TDR 8 (16 February 2000)
- ALICE Collaboration 2002 *Time of Flight System, Technical Design Report, Addendum* CERN/LHCC 2002-016, Addendum to ALICE TDR 8 (24 April 2002)
- [395] Sjöstrand T 1994 *Comput. Phys. Commun.* **82** 74
- [396] Caines H 2002 *Nucl. Phys. A* **698** 112
- [397] Antinori F 2004 *J. Phys. G: Nucl. Part. Phys.* **30** S725
- [398] Seto R K *et al* (E917 Collaboration) 1999 *Nucl. Phys. A* **661** 506
- [399] Beardner I G *et al* (NA44 Collaboration) 1997 *Phys. Rev. Lett.* **78** 2080
- [400] Adler C *et al* (STAR Collaboration) 2001 *Phys. Rev. Lett.* **86** 4778
- [401] De Caro A 2004 The ALICE TOF (Time-Of-Flight): a powerful detector for relevant observables in nucleus-nucleus collisions at LHC *PhD Thesis* University of Bologna  
<http://alice.sa.infn.it/PhDthesisAdeCaro.ps.gz>
- [402] Fachini P 2004 *J. Phys. G: Nucl. Part. Phys.* **30** S735
- [403] Rapp R 2001 *Phys. Rev. C* **63** 054907
- [404] Fachini P *et al* (STAR Collaboration) 2002 *J. Phys. G: Nucl. Part. Phys.* **28** 1599
- [405] Zhang H *et al* (STAR Collaboration) 2004 *J. Phys. G: Nucl. Part. Phys.* **30** S577
- [406] Adams J *et al* (STAR Collaboration) 2005 *Phys. Rev. C* **71** 064902
- [407] Badalà A, Barbera R, Lo Re G, Pappalardo G S, Pulvirenti A and Riggi F 2005 *Study on reconstruction of  $K^*$  (892)<sup>0</sup> signal in ALICE using PHYTIA and HIJING event generators* ALICE-INT-2005-039
- [408] Badalà A *et al* 2004 *Nucl. Instr. Meth. A* **534** 189
- [409] Eidelman S *et al* (Particle Data Group) 2004 Review of Particle Physics *Phys. Lett. B* **592** 1
- [410] Jaffe R L 1977 *Phys. Rev. Lett.* **38** 195  
Jaffe R L 1977 *Phys. Rev. Lett.* **38** 617
- [411] Donoghue J F, Golowich E and Holstein B R 1986 *Phys. Rev. D* **34** 3434
- [412] Paganis S D, Hoffmann G W, Longacre R S, Ray R L, Tang J-L and Udagawa T 2000 *Phys. Rev. C* **62** 024906
- [413] Schaffner-Bielich J, Mattiello R and Sorge H 2000 *Phys. Rev. Lett.* **84** 4305
- [414] Sorge H, Berenguer M, Stöcker H and Greiner W 1992 *Phys. Lett. B* **289** 6
- [415] Sorge H 1995 *Phys. Rev. C* **52** 3291
- [416] Takahashi H *et al* (KEK-PS E373 Collaboration) 2001 *Phys. Rev. Lett.* **87** 212502
- [417] Kuhn C (ALICE Collaboration) 2004 *NATO Advanced Study Institute 'Structure and Dynamics of Elementary Matter' (Kemer, Turkey) NATO Science Series II* (Berlin: Springer) p 166
- [418] Goldhaber G, Goldhaber S, Lee W Y and Pais A 1960 *Phys. Rev.* **120** 300
- [419] Kopylov G I and Podgoretsky M I 1972 *Sov. J. Nucl. Phys.* **15** 219  
Kopylov G I and Podgoretsky M I 1972 *Yad. Fiz.* **15** 392
- [420] Kopylov G I 1974 *Phys. Lett. B* **50** 472
- [421] Hanbury Brown R and Twiss R Q 1954 *Phil. Mag.* **45** 663
- [422] Hanbury Brown R and Twiss R Q 1956 *Nature* **178** 1046
- [423] Bertsch G, Gong M and Tohyama M 1988 *Phys. Rev. C* **37** 1896
- [424] Pratt S 1986 *Phys. Rev. D* **33** 1314
- [425] Chapman S, Scotto P and Heinz U W 1995 *Phys. Rev. Lett.* **74** 4400
- [426] Heinz U W, Hummel A, Lisa M A and Wiedemann U A 2002 *Phys. Rev. C* **66** 044903
- [427] Wiedemann U A 1998 *Phys. Rev. C* **57** 266
- [428] Vitev I 2004 *J. Phys. G: Nucl. Part. Phys.* **30** S791
- [429] Makhlin A N and Sinyukov Y M 1987 *Yad. Fiz.* **46** 637
- [430] Makhlin A N and Sinyukov Y M 1988 *Z. Phys. C* **39** 69
- [431] Csorgo T and Lorstad B 1995 *Nucl. Phys. A* **590** 465
- [432] Csorgo T and Lorstad B 1996 *Phys. Rev. C* **54** 1390
- [433] Sinyukov Y M 1994 *Nucl. Phys. A* **566** 589
- [434] Wiedemann U A, Scotto P and Heinz U W 1996 *Phys. Rev. C* **53** 918
- [435] Sinyukov Y M, Akkelin S V and Tolstykh A Y 1996 *Nucl. Phys. A* **610** 278
- [436] Akkelin S V and Sinyukov Y M 1995 *Phys. Lett. B* **356** 525
- [437] Sinyukov Y M 1989 *Nucl. Phys. A* **498** 151
- [438] Sinyukov Y, Lednicky R, Akkelin S V, Pluta J and Erasmus B 1998 *Phys. Lett. B* **432** 248
- [439] Anchishkin D, Heinz U W and Renk P 1998 *Phys. Rev. C* **57** 1428

- [440] Lisa M A, Heinz U W and Wiedemann U A 2000 *Phys. Lett. B* **489** 287
- [441] Pratt S 1984 *Phys. Rev. Lett.* **53** 1219
- [442] Pratt S, Csoergoe T and Zimanyi J 1990 *Phys. Rev. C* **42** 2646
- [443] Heinz U W and Jacak B V 1999 *Ann. Rev. Nucl. Part. Sci.* **49** 529
- [444] Pratt S *et al* 1994 *Nucl. Phys. A* **566** 103
- [445] Rischke D H and Gyulassy M 1996 *Nucl. Phys. A* **608** 479
- [446] Adams J *et al* (STAR Collaboration) 2005 *Phys. Rev. C* **71** 044906
- [447] Lisa M A *et al* (E895 Collaboration) 2000 *Phys. Rev. Lett.* **84** 2798
- [448] Adcox K *et al* (PHENIX Collaboration) 2002 *Phys. Rev. Lett.* **88** 192302
- [449] Eskola K J, Honkanen H, Niemi H, Ruuskanen P V and Rasanen S S 2005 *Phys. Rev. C* **72** 044904
- [450] Lisa M A (E895 Collaboration) 1999 *Nucl. Phys. A* **661** 444
- [451] Soltz R A, Baker M and Lee J H 1999 *Nucl. Phys. A* **661** 439
- [452] Ganz R (NA49 collaboration) 1999 *Nucl. Phys. A* **661** 448
- [453] Lisa M A *et al* (E895 Collaboration) 2000 *Phys. Lett. B* **496** 1
- [454] Adams J *et al* (STAR Collaboration) 2004 *Phys. Rev. Lett.* **93** 012301
- [455] Bearden I G *et al* (NA44 Collaboration) 2001 *Phys. Rev. Lett.* **87** 112301
- [456] Bearden I G *et al* (NA44 Collaboration) 2001 *Phys. Lett. B* **517** 25
- [457] Adams J *et al* (STAR Collaboration) 2003 *Phys. Rev. Lett.* **91** 262301
- [458] Adams J *et al* (STAR Collaboration) 2003 *Phys. Rev. Lett.* **91** 262302
- [459] Bekele S (STAR Collaboration) 2004 *J. Phys. G: Nucl. Part. Phys.* **30** S229
- [460] Renault G (STAR Collaboration) 2004 *Preprint hep-ex/0404024*
- [461] Chaloupka P 2005 *Preprint nucl-ex/0510064*
- [462] Adamova D *et al* (CERES Collaboration) 2003 *Phys. Rev. Lett.* **90** 022301
- [463] Magestro D (STAR Collaboration) 2005 *J. Phys. G: Nucl. Part. Phys.* **31** 265
- [464] Lisa M A, Pratt S, Soltz R and Wiedemann U 2005 *Ann. Rev. Nucl. Part. Sci.* **55** 357
- [465] Chajeckı Z (STAR Collaboration) 2005 *Preprint nucl-ex/0511035*
- [466] Humanic T J 1998 *Phys. Rev. C* **57** 866
- [467] Humanic T J 2003 *Nucl. Phys. A* **715** 641
- [468] Ray R L and Longacre R S 2000 *Preprint nucl-ex/0008009*
- [469] Ray L and Hoffmann G W 1996 *Phys. Rev. C* **54** 2582
- [470] Lednicky R and Lyuboshits V L 1982 *Sov. Nucl. J. Phys.* **35** 770
- [471] Skowronski P K *et al* 2005 ALICE-INT-2005-026
- [472] Skowronski P K *et al* 2005 ALICE-INT-2005-031
- [473] Batyunya B V *et al* 2005 ALICE-INT-2005-045
- [474] Bowler M G 1988 *Z. Phys. C* **39** 81
- [475] Zajc W A *et al* 1984 *Phys. Rev. C* **29** 2173
- [476] Barz H W 1999 *Phys. Rev. C* **59** 2214
- [477] Bowler M G 1991 *Phys. Lett. B* **270** 69
- [478] Retiere F (STAR Collaboration) 2001 *Preprint nucl-ex/0111013*
- [479] Stavinsky A V *et al* (CLAS Collaboration) 2004 *Phys. Rev. Lett.* **93** 192301
- [480] Chakrabarty S, Raha S and Sinha B 1992 *Mod. Phys. Lett. A* **7** 927
- [481] Srivastava D K and Kapusta J I 1993 *Phys. Lett. B* **307** 1
- [482] Srivastava D K and Kapusta J I 1993 *Phys. Rev. C* **48** 1335
- [483] Timmermann A, Plumer M, Razumov L and Weiner R M 1994 *Phys. Rev. C* **50** 3060
- [484] Peressounko D 2003 *Phys. Rev. C* **67** 014905
- [485] Paic G, Skowronski P K and Tomasik B 2004 *Preprint nucl-th/0403007*
- [486] Albajar C *et al* (UA1 Collaboration) 1989 *Phys. Lett. B* **226** 410
- [486] Albajar C *et al* (UA1 Collaboration) 1989 *Phys. Lett. B* **229** 439
- [487] Alexopoulos T *et al* 1993 *Phys. Rev. D* **48** 1931
- [488] Wang X N 2004 *Phys. Lett. B* **579** 299
- [489] Dokshitzer Y L, Khoze V A, Mueller A H and Troian S I 1991 *Basics of Perturbative QCD* Editions (Gif-sur-Yvette, France: Editions Frontières)
- [490] Kopeliovich B Z 1990 *Phys. Lett. B* **243** 141
- [491] Wiedemann U A 2004 *J. Phys. G: Nucl. Part. Phys.* **30** S649
- [492] Reisdorf W and Ritter H G 1997 *Ann. Rev. Nucl. Part. Sci.* **47** 663
- [493] Herrmann N, Wessels J P and Wienold T 1999 *Ann. Rev. Nucl. Part. Sci.* **49** 581
- [494] Danielewicz P, Lacey R and Lynch W G 2002 *Science* **298** 1592
- [495] Ollitrault J Y 1992 *Phys. Rev. D* **46** 229

- [496] Danielewicz P 1999 *Nucl. Phys. A* **661** 82
- [497] Rischke D H 1996 *Nucl. Phys. A* **610** 88
- [498] Ollitrault J Y 1998 *Nucl. Phys. A* **638** 195
- [499] ALICE Collaboration 2005 *Anisotropic flow in ALICE EDMS Id 682449* ALICE-INT-2005-046 v.1
- [500] Lee K S, Heinz U W and Schnedermann E 1990 *Z. Phys. C* **48** 525
- [501] Voloshin S and Zhang Y 1996 *Z. Phys. C* **70** 665
- [502] Danielewicz P and Odyniec G 1985 *Phys. Lett. B* **157** 146
- [503] Wilson W K, Lacey R, Ogilvie C A and Westfall G D 1992 *Phys. Rev. C* **45** 738
- [504] Ollitrault J Y 1993 *Phys. Rev. D* **48** 1132
- [505] Ollitrault J Y 1997 *Preprint nucl-ex/9711003*
- [506] Danielewicz P 1995 *Phys. Rev. C* **51** 716
- [507] Borghini N, Dinh P M and Ollitrault J Y 2001 *Phys. Rev. C* **63** 054906
- [508] Dinh P M, Borghini N and Ollitrault J Y 2000 *Phys. Lett. B* **477** 51
- [509] Borghini N, Dinh P M and Ollitrault J Y 2000 *Phys. Rev. C* **62** 034902
- [510] Kovchegov Y V and Tuchin K L 2002 *Nucl. Phys. A* **708** 413
- [511] Borghini N *et al* 2002 *Phys. Rev. C* **66** 014901
- [512] Wang S *et al* 1991 *Phys. Rev. C* **44** 1091
- [513] Adcox K *et al* (PHENIX Collaboration) 2002 *Phys. Rev. Lett.* **89** 212301
- [514] Borghini N, Dinh P M and Ollitrault J Y 2001 *Phys. Rev. C* **64** 054901
- [515] Borghini N, Dinh P M and Ollitrault J Y 2002 *Phys. Rev. C* **66** 014905
- [516] Borghini N 2003 *Eur. Phys. J. C* **30** 381
- [517] Bhalerao R S, Borghini N and Ollitrault J Y 2003 *Nucl. Phys. A* **727** 373
- [518] Borghini N, Bhalerao R S and Ollitrault J Y 2004 *J. Phys. G: Nucl. Part. Phys.* **30** S1213
- [519] Yang C N and Lee T D 1952 *Phys. Rev.* **87** 404
- [520] Lee T D and Yang C N 1952 *Phys. Rev.* **87** 410
- [521] Miller M and Snellings R 2003 *Preprint nucl-ex/0312008*
- [522] Agakichiev G *et al* (CERES/NA45 Collaboration) 2004 *Phys. Rev. Lett.* **92** 032301
- [523] Bastid N *et al* (FOPI Collaboration) 2005 *Phys. Rev. C* **72** 011901
- [524] Appelshauer H *et al* (NA49 Collaboration) 1998 *Phys. Rev. Lett.* **80** 4136
- [525] Poskanzer A M *et al* (NA49 Collaboration) 1999 *Nucl. Phys. A* **661** 341 (*Preprint nucl-ex/9906013*)
- [526] Nikolaev S *et al* (WA98 Collaboration) 2003 *Nucl. Phys. A* **715** 579
- [527] Agakichiev G *et al* (CERES Collaboration) 1998 *Nucl. Phys. A* **638** 467
- [528] Abreu M C *et al* (NA50 Collaboration) 1999 *Nucl. Phys. A* **661** 345
- [529] Lacey R A (PHENIX Collaboration) 2002 *Nucl. Phys. A* **698** 559 (*Preprint nucl-ex/0105003*)
- [530] Adler S S *et al* (PHENIX Collaboration) 2003 *Phys. Rev. Lett.* **91** 182301
- [531] Park I C *et al* (PHOBOS Collaboration) 2002 *Nucl. Phys. A* **698** 564
- [532] Back B B *et al* (PHOBOS Collaboration) 2002 *Phys. Rev. Lett.* **89** 222301
- [533] Manly S *et al* (PHOBOS Collaboration) 2003 *Nucl. Phys. A* **715** 611
- [534] Ackermann K H *et al* (STAR Collaboration) 2001 *Phys. Rev. Lett.* **86** 402
- [535] Snellings R J M (STAR Collaboration) 2002 *Nucl. Phys. A* **698** 193
- [536] Adler C *et al* (STAR Collaboration) 2002 *Phys. Rev. Lett.* **89** 132301
- [537] Adler C *et al* (STAR Collaboration) 2002 *Phys. Rev. C* **66** 034904
- [538] Adler C *et al* (STAR Collaboration) 2003 *Phys. Rev. Lett.* **90** 032301
- [539] Snellings R (STAR Collaboration) 2004 *Heavy Ion Phys.* **21** 237
- [540] Adams J *et al* (STAR Collaboration) 2005 *Phys. Rev. C* **72** 014904
- [541] Adams J *et al* (STAR Collaboration) 2005 *Preprint nucl-ex/0510053*
- [542] Snellings R J M *et al* 2000 *Phys. Rev. Lett.* **84** 2803
- [543] Csernai L P and Rohrich D 1999 *Phys. Lett. B* **458** 454
- [544] Csernai L P *et al* 2005 *Acta Phys. Hung. A* **22** 181
- [545] Brachmann J *et al* 2000 *Phys. Rev. C* **61** 024909
- [546] Sorge H 1997 *Phys. Lett. B* **402** 251 (*Preprint nucl-th/9701012*)
- [547] Pinkenburg C *et al* (E895 Collaboration) 1999 *Prepared for Centennial Celebration and Meeting of the American Physical Society (Combining Annual APS General Meeting and the Joint Meeting of the APS and the AAPT, Atlanta, GA, 20–26 March 1999)*
- [548] Chung P *et al* (E895 Collaboration) 2002 *Phys. Rev. C* **66** 021901
- [549] Voloshin S A and Poskanzer A M 2000 *Phys. Lett. B* **474** 27
- [550] Esumi S *et al* (CERES Collaboration) 2002 SFIN (Institute of Physics, Belgrade), year XV, Series A: Conferences, No. A2

- [551] Ray R L (STAR Collaboration) 2003 *Nucl. Phys. A* **715** 45 (Preprint [nucl-ex/0211030](#))
- [552] Esumi S (PHENIX Collaboration) 2003 *Nucl. Phys. A* **715** 599 (Preprint [nucl-ex/0210012](#))
- [553] Snellings R J M, Poskanzer A M and Voloshin S A 1999 Preprint [nucl-ex/9904003](#)
- [554] Bleicher M and Stoecker H 2002 *Phys. Lett. B* **526** 309 (Preprint [hep-ph/0006147](#))
- [555] Heinz U W 2001 *AIP Conf. Proc.* **602** 281
- [556] Zhang B, Gyulassy M and Ko C M 1999 *Phys. Lett. B* **455** 45
- [557] Molnar D and Gyulassy M 2001 Preprint [nucl-th/0102031](#)
- [558] Lin Z w and Ko C M 2002 *Phys. Rev. C* **65** 034904
- [559] Zabrodin E *et al* 2004 Preprint [hep-ph/0403022](#)
- [560] Heiselberg H and Levy A M 1999 *Phys. Rev. C* **59** 2716
- [561] Kolb P F *et al* 2001 *Phys. Lett. B* **500** 232
- [562] Bhalerao R S *et al* 2005 *Phys. Lett. B* **627** 49
- [563] Back B B *et al* (PHOBOS Collaboration) 2005 *Phys. Rev. Lett.* **94** 122303
- [564] Hirano T 2002 *Phys. Rev. C* **65** 011901
- [565] Hirano T and Tsuda K 2002 *Phys. Rev. C* **66** 054905
- [566] Teaney D, Lauret J and Shuryak E V 2001 Preprint [nucl-th/0110037](#)
- [567] Teaney D, Lauret J and Shuryak E V 2001 *Phys. Rev. Lett.* **86** 4783
- [568] Hirano T 2005 Talk given at the Workshop on QGP Thermalization (QGPTH05, Vienna) Private communication
- [569] Teaney D 2003 *Phys. Rev. C* **68** 034913
- [570] Wang X N 2001 *Phys. Rev. C* **63** 054902
- [571] Gyulassy M, Vitev I and Wang X N 2001 *Phys. Rev. Lett.* **86** 2537
- [572] Gyulassy M *et al* 2002 *Phys. Lett. B* **526** 301
- [573] Borghini N, Dinh P M and Ollitrault J Y 2001 Preprint [hep-ph/0111402](#)
- [574] Blaizot J P 2002 *Nucl. Phys. A* **698** 360
- [575] Voloshin S A 2003 *Nucl. Phys. A* **715** 379
- [576] Kolb P F *et al* 2001 *Nucl. Phys. A* **696** 197
- [577] Nonaka C *et al* 2005 *J. Phys. G: Nucl. Part. Phys.* **31** S429
- [578] Nonaka C, Fries R J and Bass S A 2004 *Phys. Lett. B* **583** 73
- [579] Lin Z w and Ko C M 2002 *Phys. Rev. Lett.* **89** 202302
- [580] Greco V and Ko C M 2005 Preprint [nucl-th/0505061](#)
- [581] Kolb P F *et al* 2004 *Phys. Rev. C* **69** 051901
- [582] Adams J *et al* (STAR Collaboration) 2005 *Phys. Rev. Lett.* **95** 122301
- [583] Kolb P F, Sollfrank J and Heinz U W 1999 *Phys. Lett. B* **459** 667
- [584] Teaney D and Shuryak E V 1999 *Phys. Rev. Lett.* **83** 4951
- [585] Kolb P F 2003 *Phys. Rev. C* **68** 031902
- [586] Huovinen P 2005 *Nucl. Phys. A* **761** 296
- [587] Borghini N and Ollitrault J Y 2005 Preprint [nucl-th/0506045](#)
- [588] Kolb P F, Sollfrank J and Heinz U W 2000 *Phys. Rev. C* **62** 054909
- [589] Hirano T, Heinz U W, Kharzeev D, Lacey R and Nara Y 2005 Preprint [nucl-th/0511046](#)
- [590] Radomski S and Foka P 2002 *GeVSim MC event generator* ALICE-INT-2002-031
- [591] <http://www-nsd.lbl.gov/nsd/annual/ydc/nsd1999/rmc/html/STARflow99.html>
- [592] Raniwala R, Raniwala S and Viyogi Y P 2000 *Phys. Lett. B* **489** 9
- [593] CERN/LHCC 2003-038, Addendum 1 to ALICE TDR 6
- [594] Morsch A *et al* 2001 ALICE-INT-2001-22
- [595] Aggarwal M M *et al* 2005 ALICE-INT-2005-047
- [596] Heiselberg H 2001 *Phys. Rep.* **351** 161
- [597] Van Hove L 1982 *Phys. Lett. B* **118** 138
- [598] Stephanov M A, Rajagopal K and Shuryak E V 1998 *Phys. Rev. Lett.* **81** 4816
- [599] Barducci A, Casalbuoni R, De Curtis S, Gatto R and Pettini G 1989 *Phys. Lett. B* **231** 463
- [600] Berges J and Rajagopal K 1999 *Nucl. Phys. B* **538** 215
- [601] Halasz M A, Jackson A D, Shrock R E, Stephanov M A and Verbaarschot J J M 1998 *Phys. Rev. D* **58** 096007
- [602] Stephanov M A, Rajagopal K and Shuryak E V 1999 *Phys. Rev. D* **60** 114028
- [603] Philipsen O 2005 *Proc. Sci., 23rd Int. Symp. on Lattice Field Theory (LAT2005, Dublin, Ireland, July 2005)* PoS(LAT2005)016, [http://pos.sissa.it/archive/conferences/020/016/LAT2005\\_016.pdf](http://pos.sissa.it/archive/conferences/020/016/LAT2005_016.pdf)
- [604] Liu Q j and Trainor T A 2003 *Phys. Lett. B* **567** 184
- [605] Tannenbaum M J (PHENIX collaboration) 2004 *J. Phys. G: Nucl. Part. Phys.* **30** S1367

- [606] Anselm A A and Ryskin M G 1991 *Phys. Lett. B* **266** 482
- [607] Blaizot J P and Krzywicki A 1992 *Phys. Rev. D* **46** 246
- [608] Bjorken J D, Kowalski K L and Taylor C C 1993 *Presented at 7th Les Rencontres de Physique de la Vallée d'Aoste: Results and Perspectives in Particle Physics (La Thuile, Italy, 7–13 March 1993)* SLAC-PUB-6109
- [609] Rajagopal K and Wilczek F 1993 *Nucl. Phys. B* **399** 395
- [610] Mohanty B and Serreau J 2005 *Phys. Rep.* **414** 263
- [611] Stock R 1994 *Prepared for NATO Advanced Study Workshop on Hot Hadronic Matter: Theory and Experiment (Divonne-les-Bains, France, 27 June–1 July 1994)*
- [612] Anticic T *et al* (NA49 Collaboration) 2004 *Phys. Rev. C* **70** 034902
- [613] Appelshauser H *et al* (NA49 Collaboration) 1999 *Phys. Lett. B* **459** 679
- [614] Afanasev S V *et al* (NA49 Collaboration) 2001 *Phys. Rev. Lett.* **86** 1965
- [615] Rybczynski M *et al* (NA49 Collaboration) 2005 *J. Phys. Conf. Ser.* **5** 74
- [616] Alt C *et al* (NA49 Collaboration) 2004 *Phys. Rev. C* **70** 064903
- [617] Alt C *et al* (NA49 Collaboration) 2005 *Phys. Rev. C* **71** 034903
- [618] Afanasiev S V *et al* (NA49 Collaboration) 2002 *Phys. Rev. C* **66** 054902
- [619] Gazdzicki M *et al* (NA49 Collaboration) 2004 *J. Phys. G: Nucl. Part. Phys.* **30** S701
- [620] Christakoglou P, Petridis A and Vassiliou M (NA49 Collaboration) 2005 *Preprint nucl-ex/0510045*
- [621] Aggarwal M M *et al* (WA98 Collaboration) 2002 *Phys. Rev. C* **65** 054912
- [622] Aggarwal M M *et al* (WA98 Collaboration) 1998 *Phys. Lett. B* **420** 169
- [623] Nayak T K *et al* (WA98 Collaboration) 1998 *Nucl. Phys. A* **638** c249
- [624] Aggarwal M M *et al* (WA98 Collaboration) 2001 *Phys. Rev. C* **64** 011901
- [625] Aggarwal M M *et al* (WA98 Collaboration) 2003 *Phys. Rev. C* **67** 044901
- [626] Adamova D *et al* (CERES Collaboration) 2003 *Nucl. Phys. A* **727** 97
- [627] Adcox K *et al* (PHENIX Collaboration) 2002 *Phys. Rev. C* **66** 024901
- [628] Adler S S *et al* (PHENIX Collaboration) 2004 *Phys. Rev. Lett.* **93** 092301
- [629] Adcox K *et al* (PHENIX Collaboration) 2002 *Phys. Rev. Lett.* **89** 082301
- [630] Adams J *et al* (STAR Collaboration) 2003 *Phys. Rev. C* **68** 044905
- [631] Pruneau C A (STAR Collaboration) 2004 *Preprint nucl-ex/0401016*
- [632] Ahammed Z (STAR Collaboration) 2002 *Pramana* **60** 993
- [633] Westfall G D (STAR Collaboration) 2004 *J. Phys. G: Nucl. Part. Phys.* **30** S345
- [634] Das S (STAR Collaboration) 2005 *Preprint nucl-ex/0503023*
- [635] Adams J *et al* (STAR Collaboration) 2005 *Phys. Rev. C* **71** 064906
- [636] Adams J *et al* (STAR Collaboration) 2003 *Phys. Rev. Lett.* **90** 172301
- [637] Wozniak K *et al* (PHOBOS Collaboration) 2004 *J. Phys. G: Nucl. Part. Phys.* **30** S1377
- [638] Back B B *et al* (PHOBOS Collaboration) 2005 *Preprint nucl-ex/0509027*
- [639] Fodor Z and Katz S D 2002 *J. High Energy Phys.* **JHEP03(2002)014**
- [640] Fodor Z and Katz S D 2004 *J. High Energy Phys.* **JHEP04(2004)050** (*Preprint hep-lat/0402006*)
- [641] Allton C R *et al* 2002 *Phys. Rev. D* **66** 074507 (*Preprint hep-lat/0204010*)
- [642] D'Elia M and Lombardo M P 2003 *Phys. Rev. D* **67** 014505
- [643] de Forcrand P and Philipsen O 2002 *Nucl. Phys. B* **642** 290
- [644] Gavai R V and Gupta S 2003 *Phys. Rev. D* **68** 034506
- [645] Allton C R, Ejiri S, Hands S J, Kaczmarek O, Karsch F, Laermann E and Schmidt C 2003 *Phys. Rev. D* **68** 014507
- [646] Gavai R V, Gupta S and Mukherjee S 2005 *Phys. Rev. D* **71** 074013 (*Preprint hep-lat/0412036*)
- [647] Cleymans J 2002 *J. Phys. G: Nucl. Part. Phys.* **28** 1575, and private communication
- [648] Gottlieb S A, Liu W, Toussaint D, Renken R L and Sugar R L 1987 *Phys. Rev. Lett.* **59** 2247
- [649] Gavai R V, Gupta S and Majumdar P 2002 *Phys. Rev. D* **65** 054506
- [650] Bernard C *et al* (MILC Collaboration) 2005 *Phys. Rev. D* **71** 034504
- [651] Blaizot J P, Iancu E and Rebhan A 2001 *Phys. Lett. B* **523** 143
- [652] Vuorinen A 2003 *Phys. Rev. D* **68** 054017
- [653] Chakraborty P, Mustafa M G and Thoma M H 2003 *Phys. Rev. D* **68** 085012
- [654] Koch V, Majumder A and Randrup J 2005 *Phys. Rev. Lett.* **95** 182301
- [655] Gavai R V and Gupta S 2006 *Phys. Rev. D* **73** 014004 (*Preprint hep-lat/0510044*)
- [656] Ejiri S, Karsch F and Redlich K 2006 *Phys. Lett. B* **633** 275 (*Preprint hep-ph/0509051*)
- [657] Gavai R V and Gupta S 2005 *Phys. Rev. D* **72** 054006
- [658] Liao J and Shuryak E V 2006 *Phys. Rev. D* **73** 014509
- [659] Becattini F, Gazdzicki M and Sollfrank J 1998 *Nucl. Phys. A* **638** 403

- [660] Shuryak E V and Stephanov M A 2001 *Phys. Rev. C* **63** 064903
- [661] Mohanty B, Alam J-e and Nayak T K 2003 *Phys. Rev. C* **67** 024904
- [662] Gazdzicki M and Mrowczynski S 1992 *Z. Phys. C* **54** 127
- [663] Mahapatra D P, Mohanty B and Phatak S C 2002 *Int. J. Mod. Phys. A* **17** 675
- [664] Zaranek J 2002 *Phys. Rev. C* **66** 024905
- [665] Mrowczynski S 2002 *Phys. Rev. C* **66** 024904
- [666] Mrowczynski S and Shuryak E V 2003 *Acta Phys. Polon. B* **34** 4241
- [667] Heiselberg H and Vischer A P 1998 *Phys. Lett. B* **421** 18
- [668] Heiselberg H and Jackson A D 1998 *Preprint nucl-th/9809013*
- [669] Mrowczynski S 1998 *Phys. Lett. B* **439** 6
- [670] Bolokhov P A, Braun M A, Feofilov G A, Kondratiev V P and Vechernin V V 2002 ALICE-INT-2002-20
- [671] Liu F, Tai A, Gazdzicki M and Stock R 1999 *Eur. Phys. J. C* **8** 649
- [672] Stodolsky L 1995 *Phys. Rev. Lett.* **75** 1044
- [673] Shuryak E V 1998 *Phys. Lett. B* **423** 9
- [674] Mrowczynski S 1993 *Phys. Lett. B* **314** 118
- [675] Mrowczynski S and Thoma M H 2000 *Phys. Rev. D* **62** 036011 (*Preprint hep-ph/0001164*)
- [676] Asakawa M, Heinz U W and Muller B 2000 *Phys. Rev. Lett.* **85** 2072
- [677] Jeon S and Koch V 2000 *Phys. Rev. Lett.* **85** 2076
- [678] Capella A, Ferreira E G and Kaidalov A B 1999 *Eur. Phys. J. C* **11** 163
- [679] Geiger K 1995 *Phys. Rept.* **258** 237
- [680] Amelin N S, Stauba E F, Csernai L P, Toneev V D, Gudima K K and Strottman D 1991 *Phys. Rev. Lett.* **67** 1523
- [681] Baym G and Heiselberg H 1999 *Phys. Lett. B* **469** 7
- [682] Werner K 1993 *Phys. Rept.* **232** 87
- [683] Schnedermann E and Heinz U W 1992 *Phys. Rev. Lett.* **69** 2908
- [684] Siemens P J and Rasmussen J O 1979 *Phys. Rev. Lett.* **42** 880
- [685] Wilk G and Wlodarczyk Z 2000 *Phys. Rev. Lett.* **84** 2770
- [686] Tsallis C 1988 *J. Statist. Phys.* **52** 479
- [687] Alberico W M, Lavagno A and Quarati P 2000 *Eur. Phys. J. C* **12** 499
- [688] Utyuzh O V, Wilk G and Wlodarczyk Z 2001 *Preprint hep-ph/0103273*
- [689] Korus R, Mrowczynski S, Rybczynski M and Wlodarczyk Z 2001 *Phys. Rev. C* **64** 054908
- [690] Gavin S 2004 *Phys. Rev. Lett.* **92** 162301
- [691] Pruneau C, Gavin S and Voloshin S 2002 *Phys. Rev. C* **66** 044904
- [692] Mohanty B, Alam J e, Sarkar S, Nayak T K and Nandi B K 2003 *Phys. Rev. C* **68** 021901
- [693] Kliemant M, Lungwitz B and Gazdzicki M 2004 *Phys. Rev. C* **69** 044903
- [694] Kapusta J I and Mekjian A 1986 *Phys. Rev. D* **33** 1304
- [695] Roland C *et al* (NA49 Collaboration) 2004 *J. Phys. G: Nucl. Part. Phys.* **30** S1381
- [696] Roland C (NA49 Collaboration) 2005 *J. Phys. G: Nucl. Part. Phys.* **31** S1075
- [697] Bleicher M *et al* 1999 *J. Phys. G: Nucl. Part. Phys.* **25** 1859
- [698] Bialas A 2004 *Phys. Lett. B* **579** 31
- [699] Jeon S and Koch V 1999 *Phys. Rev. Lett.* **83** 5435
- [700] Jeon S and Pratt S 2002 *Phys. Rev. C* **65** 044902
- [701] Bleicher M, Jeon S and Koch V 2000 *Phys. Rev. C* **62** 061902
- [702] Bialas A 2002 *Phys. Lett. B* **532** 249 (*Preprint hep-ph/0203047*)
- [703] Mitchell J T 2004 *J. Phys. G: Nucl. Part. Phys.* **30** S819
- [704] Koch V, Bleicher M and Jeon S 2002 *Nucl. Phys. A* **698** 261  
Koch V, Bleicher M and Jeon S 2002 *Nucl. Phys. A* **702** 291
- [705] Bass S A, Danielewicz P and Pratt S 2000 *Phys. Rev. Lett.* **85** 2689
- [706] Drijard D *et al* (ACCDHW Collaboration) 1980 *Nucl. Phys. B* **166** 233
- [707] Brandelik R *et al* (TASSO Collaboration) 1981 *Phys. Lett. B* **100** 357
- [708] Acton P D *et al* (OPAL Collaboration) 1993 *Phys. Lett. B* **305** 415
- [709] Bozek P 2005 *Phys. Lett. B* **609** 247
- [710] Pratt S and Cheng S 2003 *Phys. Rev. C* **68** 014907
- [711] Ehehalt W and Cassing W 1996 *Nucl. Phys. A* **602** 449
- [712] Cheng S *et al* 2004 *Phys. Rev. C* **69** 054906
- [713] Bozek P, Broniowski W and Florkowski W 2005 *Acta Phys. Hung. A* **22** 149 (*Preprint nucl-th/0310062*)
- [714] Florkowski W, Bozek P and Broniowski W 2004 *Heavy Ion Phys. A* **21** 49

- [715] ALICE Collaboration 2003 *Addendum to the ALICE Technical Design Report of the Photon Multiplicity Detector (PMD)* CERN-LHCC-2003-038
- [716] Gavin S, Gocksch A and Pisarski R D 1994 *Phys. Rev. Lett.* **72** 2143
- [717] Gavin S and Muller B 1994 *Phys. Lett. B* **329** 486
- [718] Kapusta J I and Vischer A P 1997 *Z. Phys. C* **75** 507
- [719] Digal S, Ray R, Sengupta S and Srivastava A M 2000 *Int. J. Mod. Phys. A* **15** 2269
- [720] For an extensive review on “centauros” and related phenomena, see: Gładysz-Dziaduś E 2001 INP Report No. 1879/PH, Cracow
- [721] Brooks T C *et al* (MiniMax Collaboration) 1997 *Phys. Rev. D* **55** 5667
- [722] Alber T *et al* (NA49 Collaboration) *Prepared for 25th Int. Symp. on Multiparticle Dynamics (Stara Lesna, Slovakia, 12–16 September 1995)*
- [723] Pratt S 1993 *Phys. Lett. B* **301** 159
- [724] Akkelin S V and Sinyukov Y M 1999 *Nucl. Phys. A* **661** 613
- [725] Gavin S and Kapusta J I 2002 *Phys. Rev. C* **65** 054910
- [726] Gavin S 2002 *Preprint nucl-th/0204064*
- [727] Kapusta J I and Srivastava A M 1995 *Phys. Rev. D* **52** 2977
- [728] Kapusta J I and Wong S M H 2001 *Phys. Rev. Lett.* **86** 4251
- [729] Wong S M H and Kapusta J I 2003 *Nucl. Phys. A* **715** 573
- [730] Charng Y Y, Ng K W, Lin C Y and Lee D S 2002 *Phys. Lett. B* **548** 175
- [731] Nandi B K, Mishra G C, Mohanty B, Mahapatra D P and Nayak T K 1999 *Phys. Lett. B* **449** 109
- [732] Nandi B K, Nayak T K, Mohanty B, Mahapatra D P and Vijoyi Y P 1999 *Phys. Lett. B* **461** 142
- [733] Mohanty B, Nayak T K, Mahapatra D P and Vijoyi Y P 2004 *Int. J. Mod. Phys. A* **19** 1453
- [734] Graps A 1995 *IEEE Commun. Sci. Eng.* **2** 50
- [735] Takagi F 1984 *Phys. Rev. Lett.* **53** 427
- [736] Das A C and Vijoyi Y P 1996 *Phys. Lett. B* **380** 437
- [737] Aggarwal M M, Bhatia V S, Das A C and Vijoyi Y P 1998 *Phys. Lett. B* **438** 357y
- [738] Aggarwal M M (WA98 Collaboration) 2003 *Pramana* **60** 987
- [739] Leonidov A and Ostrovsky D 2001 *Phys. Rev. C* **63** 037901
- [740] Leonidov A *Preprint* BNL-NT-00/12
- [741] Leonidov A and Ostrovsky D 2000 *Eur. Phys. J. C* **16** 683  
Leonidov A and Ostrovsky D 2002 *Phys. Atom. Nucl.* **65** 886  
Leonidov A and Ostrovsky D 2002 *Yad. Fiz.* **65** 918–29
- [742] Leonidov A and Ostrovsky D 2000 *Phys. Rev. D* **62** 094009
- [743] Capella A and Krzywicki A 1978 *Phys. Rev. D* **18** 4120
- [744] Capella A, Sukhatme U, Tan C I and Tran Thanh Van J 1979 *Phys. Lett. B* **81** 68
- [745] Capella A, Sukhatme U, Tan C I and Tran Thanh Van J 1994 *Phys. Rept.* **236** 225
- [746] Kaidalov A B 1982 *Phys. Lett. B* **116** 459
- [747] Kaidalov A B and Ter-Martirosian K A 1982 *Phys. Lett. B* **117** 247
- [748] Braun M A and Pajares C 1992 *Phys. Lett. B* **287** 154
- [749] Amelin N S, Braun M A and Pajares C 1993 *Phys. Lett. B* **306** 312
- [750] Braun M A and Pajares C 2004 *Phys. Lett. B* **603** 21
- [751] Amelin N S, Armesto N, Pajares C and Sousa D 2001 *Eur. Phys. J. C* **22** 149
- [752] Amelin N S, Armesto N, Pajares C and Sousa D 2000 *String Fusion Model: PSM-1.0 User's Manual*
- [753] Braun M A, Del Moral F and Pajares C 2002 *Phys. Rev. C* **65** 024907 (*Preprint hep-ph/0105263*)
- [754] Armesto N, Pajares C and Sousa D 2002 *Phys. Lett. B* **527** 92 (*Preprint hep-ph/0104269*)
- [755] Braun M A, Pajares C and Ranft J 1999 *Int. J. Mod. Phys. A* **14** 2689
- [756] Nardi M and Satz H 1998 *Phys. Lett. B* **442** 14
- [757] Amelin N S, Armesto N, Braun M A, Ferreiro E G and Pajares C 1994 *Phys. Rev. Lett.* **73** 2813
- [758] Braun M A and Pajares C 2000 *Eur. Phys. J. C* **16** 349
- [759] Braun M A, Kolevatov R S, Pajares C and Vechernin V V 2004 *Eur. Phys. J. C* **32** 535
- [760] Braun M A and Pajares C 2000 *Phys. Rev. Lett.* **85** 4864
- [761] Braun M A, Pajares C and Vechernin V V 2000 *Phys. Lett. B* **493** 54
- [762] Braun M A, Pajares C and Vechernin V V 2001 ALICE-INT-2001-16
- [763] Kolevatov R S and Vechernin V V 2005 *Preprint hep-ph/0501179*  
Kolevatov R S and Vechernin V V 2005 *Preprint hep-ph/0502069*

- [764] Feofilov G 2002 *Experimental Studies of Long-Range Forward-Backward  $P_t$  and Multiplicity Correlations at ALICE, Reports at XVI International Baldin Seminar on High Energy Physics Problems (Dubna, Russia, June 10–15, 2002)*  
Feofilov G 2004 *Proc. Workshop on the Quantum Field Theory and High Energy Physics (QFTHEP2004, St. Petersburg, June 17–22, 2004)*  
Feofilov G *et al* 2004 *Proc. ISHEPP XVII, Relativistic Nuclear Physics and Quantum Chromodynamics (Dubna, Russia, September 27–October 2, 2004)* p 59
- [765] Vechernin V V and Kolevatov R S 2003 *Preprint hep-ph/0305136*
- [766] Glauber R J and Matthiae G 1970 *Nucl. Phys. B* **21** 135
- [767] Wong C Y 1994 *Introduction to High-Energy Heavy-Ion Collisions* (Singapore: World Scientific)
- [768] Dokshitzer Yu L and Kharzeev D E 2001 *Phys. Lett. B* **519** 199 (*Preprint hep-ph/0106202*)
- [769] Armesto N, Salgado C A and Wiedemann U A 2004 *Phys. Rev. D* **69** 114003 (*Preprint hep-ph/0312106*)
- [770] Djordjevic M and Gyulassy M 2003 *Phys. Lett. B* **560** 37 (*Preprint nucl-th/0302069*)
- [771] Djordjevic M and Gyulassy M 2004 *Nucl. Phys. A* **733** 265 (*Preprint nucl-th/0310076*)
- [772] Eskola K J, Honkanen H, Kolhinen V J, Qiu J w and Salgado C A 2003 *Nucl. Phys. B* **660** 211 (*Preprint hep-ph/0211239*)
- [773] Eskola K J, Kolhinen V J and Vogt R 2004 *Phys. Lett. B* **582** 157 (*Preprint hep-ph/0310111*)
- [774] Dainese A, Vogt R, Bondila M, Eskola K J and Kolhinen V J 2004 *J. Phys. G: Nucl. Part. Phys.* **30** 1787 (*Preprint hep-ph/0403098*)
- [775] Kwiecinski J, Martin A D and Stasto A M 1997 *Phys. Rev. D* **56** 3991 (*Preprint hep-ph/9703445*)
- [776] Kutak K and Kwiecinski J 2003 *Eur. Phys. J. C* **29** 521
- [777] Gotsmann E, Levin E, Maor U and Naftali E 2005 *Preprint hep-ph/0504040*
- [778] Baines J *et al* 2006 Subgroup contribution to the proceedings of the HERA and the LHC Workshop *Preprint hep-ph/0601164*
- [779] Eskola K J, Kolhinen V J and Salgado C A 1999 *Eur. Phys. J. C* **9** 61 (*Preprint hep-ph/9807297*)
- [780] Accardi A *et al* 2004 Subgroup contribution to the CERN Report 2004-009 *Preprint hep-ph/0308248*
- [781] Kharzeev D and Tuchin K 2004 *Nucl. Phys. A* **735** 248 (*Preprint hep-ph/0310358*)
- [782] Paver N and Treleani D 1982 *Nuovo Cim. A* **70** 215
- [783] Strikman M and Treleani D 2002 *Phys. Rev. Lett.* **88** 031801 (*Preprint hep-ph/0111468*)
- [784] Abe F *et al* (CDF Collaboration) 1997 *Phys. Rev. Lett.* **79** 584  
Abe F *et al* (CDF Collaboration) 1997 *Phys. Rev. D* **56** 3811
- [785] Cattaruzza E, Fabbro Del A and Treleani D 2004 *Phys. Rev. D* **70** 034022 (*Preprint hep-ph/0404177*)
- [786] Gyulassy M and Wang X N 1994 *Nucl. Phys. B* **420** 583 (*Preprint nucl-th/9306003*)
- [787] Baier R, Dokshitzer Yu L, Mueller A H, Peigné S and Schiff D 1997 *Nucl. Phys. B* **483** 291 (*Preprint hep-ph/9607355*)
- [788] Baier R, Dokshitzer Yu L, Mueller A H, Peigné S and Schiff D 1997 *Nucl. Phys. B* **484** 265 (*Preprint hep-ph/9608322*)
- [789] Zakharov B G 1996 *JETP Lett.* **63** 952 (*Preprint hep-ph/9607440*)
- [790] Wiedemann U A 2000 *Nucl. Phys. B* **588** 303 (*Preprint hep-ph/0005129*)
- [791] Salgado C A and Wiedemann U A 2003 *Phys. Rev. D* **68** 014008, <http://csalgado.home.cern.ch/csalgado> (*Preprint hep-ph/0302184*)
- [792] Gyulassy M, Lévai P and Vitev I 2000 *Nucl. Phys. B* **571** 197 (*Preprint hep-ph/9907461*)
- [793] Gyulassy M, Lévai P and Vitev I 2000 *Phys. Rev. Lett.* **85** 5535 (*Preprint nucl-th/0005032*)
- [794] Gyulassy M, Lévai P and Vitev I 2001 *Nucl. Phys. B* **594** 371 (*Preprint nucl-th/0006010*)
- [795] Dainese A, Loizides C and Paic G 2005 *Eur. Phys. J. C* **38** 461 (*Preprint hep-ph/0406201*)
- [796] Eskola K J, Honkanen H, Salgado C A and Wiedemann U A 2005 *Nucl. Phys. A* **747** 511 (*Preprint hep-ph/0406319*)
- [797] Accardi A *et al* 2004 Subgroup contribution to the CERN Report 2004-009 *Preprint hep-ph/0310274*
- [798] Mustafa M G, Pal D, Srivastava D K and Thoma M H 1998 *Phys. Lett. B* **428** 234 (*Preprint nucl-th/9711059*)
- [799] Lin Z W and Vogt R 1999 *Nucl. Phys. B* **544** 339 (*Preprint hep-ph/9808214*)
- [800] Dokshitzer Yu L, Khoze V A and Troian S I 1991 *J. Phys. G: Nucl. Part. Phys.* **17** 1602
- [801] Dainese A 2005 *J. Phys. G: Nucl. Part. Phys.* **31** S589 (*Preprint hep-ph/0501292*)
- [802] Armesto N, Dainese A, Salgado C A and Wiedemann U A 2005 *Phys. Rev. D* **71** 054027 (*Preprint hep-ph/0501225*)
- [803] Adams J *et al* (STAR Collaboration) 2003 *Phys. Rev. Lett.* **91** 172302 (*Preprint nucl-ex/0305015*)
- [804] Hwa R C and Yang C B 2003 *Phys. Rev. C* **67** 064902
- [805] Adler S S *et al* (PHENIX Collaboration) 2005 *Phys. Rev. C* **72** 024901 (*Preprint nucl-ex/0502009*)

- [806] Laue F *et al* (STAR Collaboration) 2005 *J. Phys. G: Nucl. Part. Phys.* **31** S27
- [807] Greco V, Ko C M and Rapp R 2004 *Phys. Lett. B* **595** 202 (Preprint [nucl-th/0312100](#))
- [808] Vogt R 2003 *Int. J. Mod. Phys. E* **12** 211 (Preprint [hep-ph/0111271](#))
- [809] Mangano M, Nason P and Ridolfi G 1992 *Nucl. Phys. B* **373** 295
- [810] Cacciari M, Frixione S, Mangano M L, Nason P and Ridolfi G 2004 *J. High Energy Phys.* [JHEP07\(2004\)033](#) (Preprint [hep-ph/0312132](#))
- [811] Adams J *et al* (STAR Collaboration) 2005 *Phys. Rev. Lett.* **94** 062301 (Preprint [nucl-ex/0407006](#))
- [812] Tai A *et al* (STAR Collaboration) 2004 *J. Phys. G: Nucl. Part. Phys.* **30** S809 (Preprint [nucl-ex/0404029](#))
- [813] Cacciari M, Nason P and Vogt R 2005 *Phys. Rev. Lett.* **95** 122001 (Preprint [hep-ph/0502203](#))
- [814] Kelly S *et al* (PHENIX Collaboration) 2004 *J. Phys. G: Nucl. Part. Phys.* **30** S1189 (Preprint [nucl-ex/0403057](#))
- [815] Acosta D *et al* (CDF Collaboration) 2003 *Phys. Rev. Lett.* **91** 241804 (Preprint [hep-ex/0307080](#))
- [816] Frixione S, Nason P and Webber B R 2003 *J. High Energy Phys.* [JHEP08\(2003\)007](#) (Preprint [hep-ph/0305252](#))
- [817] Abreu M C *et al* (NA50 Collaboration) 2000 *Eur. Phys. J. C* **14** 443
- [818] NA60 Collaboration 2000 NA60 Proposal, CERN/SPSC 2000-010 <http://na60.cern.ch/www>
- [819] Scomparin E *et al* (NA60 Collaboration) 2005 *Proc. Quark Matter 2005*, *Nucl. Phys. A* at press
- [820] Adler S S *et al* (PHENIX Collaboration) 2005 *Phys. Rev. Lett.* **94** 082301 (Preprint [nucl-ex/0409028](#))
- [821] Adler S S *et al* (PHENIX Collaboration) 2006 *Phys. Rev. Lett.* **96** 032301 (Preprint [nucl-ex/0510047](#))
- [822] Djordjevic M, Gyulassy M, Vogt R and Wicks S 2006 *Phys. Lett. B* **632** 81 (Preprint [nucl-th/0507019](#))
- [823] Armesto N, Cacciari M, Dainese A, Salgado C A and Wiedemann U A 2005 *Phys. Lett. B* **637** 362 (Preprint [hep-ph/0511257](#))
- [824] Martin A D, Roberts R G, Stirling W J and Thorne R S 1998 *Eur. Phys. J. C* **4** 463
- [825] Lai H L *et al* (CTEQ Collaboration) 2000 *Eur. Phys. J. C* **12** 375
- [826] Emel'yanov V, Khodinov A, Klein S R and Vogt R 2000 *Phys. Rev. C* **61** 044904 (Preprint [hep-ph/9909427](#))
- [827] Lai H L *et al* (CTEQ Collaboration) 1997 *Phys. Rev. D* **55** 1280 (Preprint [hep-ph/9606399](#))
- [828] Bedijian M *et al* 2004 Subgroup contribution to the CERN Report 2004-009 Preprint [hep-ph/0311048](#)
- [829] Pumplin J *et al* (CTEQ Collaboration) 2002 *J. High Energy Phys.* [JHEP07\(2002\)012](#) (Preprint [hep-ph/0201195](#))
- [830] Corcella G, Knowles I G, Marchesini G, Moretti S, Odagiri K, Richardson P, Seymour M H and Webber B R 2001 *J. High Energy Phys.* [JHEP01\(2001\)010](#) (Preprint [hep-ph/0011363](#))  
Corcella G, Knowles I G, Marchesini G, Moretti S, Odagiri K, Richardson P, Seymour M H and Webber B R 2002 Preprint [hep-ph/0201195](#)  
Marchesini G, Webber B R, Abbiendi G, Knowles I G, Seymour M H and Stanco L 1992 *Comput. Phys. Commun.* **67** 465
- [831] Norrbin E and Sjöstrand T 2000 *Eur. Phys. J. C* **17** 137
- [832] Carrer N and Dainese A 2003 ALICE-INT-2003-019 Preprint [hep-ph/0311225](#)
- [833] Barate R *et al* (ALEPH Collaboration) 2000 *Eur. Phys. J. C* **16** 597
- [834] Carrer N, Dainese A and Turrise R 2003 *J. Phys. G: Nucl. Part. Phys.* **29** 575  
Carrer N, Dainese A and Turrise R 2002 ALICE-INT-2002-005
- [835] Grosso R 2004 *PhD Thesis* Università degli Studi di Trieste
- [836] ALICE Transition Radiation Detector, *Technical Design Report* CERN/LHCC 2001-021
- [837] ALICE Collaboration 2004 ALICE: Physics Performance Report, Volume I *J. Phys. G: Nucl. Part. Phys.* **30** 1517 (Chapter 4)
- [838] Dainese A and Carrer N 2003 ALICE-INT-2003-011
- [839] TOTEM *Total cross section, elastic scattering and diffractive dissociation at the LHC: Technical Proposal* CERN/LHCC 99-007; LHCC-P-5
- [840] Dainese A 2004 *Eur. Phys. J. C* **38** 495 (Preprint [nucl-ex/0312005](#))
- [841] Antinori F, Dainese A, Lunardon M and Turrise R 2005 ALICE-INT-2005-033
- [842] *A Transition Radiation Detector for Electron Identification within the ALICE Central Detector—Addendum to ALICE Proposal* CERN/LHCC 99-13
- [843] Mahmoud T *et al* (ALICE Collaboration) 2003 *Nucl. Instrum. Meth. Phys. Res. A* **502** 127
- [844] Sandoval A (TRD off-line coordinator) 2004 private communication
- [845] Albajar C *et al* (UA1 Collaboration) 1988 *Phys. Lett. B* **213** 405
- [846] Albajar C *et al* (UA1 Collaboration) 1991 *Phys. Lett. B* **256** 121
- [847] Crochet P, Guernane R, Morsch A and Vercellin E 2005 ALICE-INT-2005-018

- [848] Abbaneo D *et al* (ALEPH Collaboration, CDF Collaboration, DELPHI Collaboration, L3 Collaboration, OPAL Collaboration and SLD Collaboration) 2001 SLAC-PUB-9500, CERN-EP-2001-050, *Preprint hep-ex/0112028*
- [849] Peterson C, Schlatter D, Schmitt I and Zerwas P M 1983 *Phys. Rev. D* **27** 105
- [850] Boudjemline K *et al* 2002 SUBATECH-2002-30
- [851] Sjöstrand T 1982 *Comput. Phys. Commun.* **27** 243
- [852] Agakichiev G *et al* 1998 *Phys. Lett. B* **422** 405
- [853] Angelis A L S *et al* 2000 *Eur. Phys. J. C* **13** 433
- [854] Faivre J 2006 *Eur. Phys. J. C* to appear
- [855] Chilingarov A *et al* 1979 *Phys. Lett. B* **83** 136
- [856] Akesson T *et al* 1996 *Z. Phys. C* **72** 429
- [857] Crochet P *et al* 2000 ALICE-INT-2000-01
- [858] Frixione S and Mangano M L 2004 *J. High Energy Phys.* **JHEP05(2004)056**
- [859] Vogt R 2001 *Phys. Rev. C* **64** 044901
- [860] Alessandro B *et al* (NA50 Collaboration) 2005 *Eur. Phys. J. C* **39** 335 and references therein (*Preprint hep-ex/0412036*)
- [861] Abreu M C *et al* (NA50 Collaboration) 2000 *Phys. Lett. B* **477** 28
- [862] Arnaldi R *et al* 1998 *Nucl. Instrum. Meth. A* **411** 1
- [863] Alessandro B *et al* 2002 *Nucl. Instrum. Meth. A* **493** 30
- [864] Satz H 1999 *Nucl. Phys. A* **661** 104 (*Preprint hep-ph/9908339*)
- [865] Capella A and Sousa D 2003 *Preprint nucl-th/0303055*
- [866] Maiani L, Piccinini F, Polosa A D and Riquer V 2005 *Nucl. Phys. A* **748** 209 (*Preprint hep-ph/0408150*)
- [867] Baldit A *et al* 2000 CERN-SPSC-2000-010
- [868] Arnaldi R *et al* (NA60 Collaboration) 2005 *Proc. 18th Quark Matter Conference (Budapest, Hungary, 4–9 August 2005)* at press
- [869] Digal S, Fortunato S and Satz H 2004 *Eur. Phys. J. C* **32** 547 (*Preprint hep-ph/0310354*)
- [870] Thews R L, Schroedter M and Rafelski J 2001 *Phys. Rev. C* **63** 054905 (*Preprint hep-ph/0007323*)
- [871] Braun-Munzinger P and Stachel J 2000 *Phys. Lett. B* **490** 196 2000 (*Preprint nucl-th/0007059*)
- [872] Andronic A, Braun-Munzinger P, Redlich K and Stachel J 2003 *Phys. Lett. B* **571** 36 (*Preprint nucl-th/0303036*)
- [873] Gorenstein M I, Kostyuk A P, Stoecker H and Greiner W 2001 *Phys. Lett. B* **509** 277 (*Preprint hep-ph/0010148*)
- [874] Ko C M, Zhang B, Wang X N and Zhang X F 1998 *Phys. Lett. B* **444** 237 (*Preprint nucl-th/9808032*)
- [875] Braun-Munzinger P and Redlich K 2000 *Eur. Phys. J. C* **16** 519 (*Preprint hep-ph/0001008*)
- [876] Pereira Da Costa H (PHENIX Collaboration) 2005 *Preprint nucl-ex/0510051*
- [877] Digal S, Petreczky P and Satz H 2001 *Phys. Rev. D* **64** 094015 (*Preprint hep-ph/0106017*)
- [878] Gunion J F and Vogt R 1997 *Nucl. Phys. B* **492** 301 (*Preprint hep-ph/9610420*)
- [879] Baier R, Schiff D and Zakharov B G 2000 *Ann. Rev. Nucl. Part. Sci.* **50** 37 (*Preprint hep-ph/0002198*)
- [880] Crochet P and Braun-Munzinger P 2002 *Nucl. Instrum. Meth. A* **484** 564 (*Preprint nucl-ex/0106008*)
- [881] Crochet P 2005 *Preprint nucl-ex/0510017*
- [882] Barger V D, Keung W Y and Phillips R J N 1980 *Phys. Lett. B* **91** 253
- [883] Chen C 2003 *Proc. 9th Int. Conf. on B-Physics at Hadron Machines (Beauty 2003, Pittsburgh, PA, 14–18 October 2003)* *AIP Conf. Proc.* **722** 67
- [884] Bishai M (CDF Collaboration) 2003 *Proc. 4th Int. Symp. on LHC Physics and Detectors (LHC 2003, Batavia, IL, 1–3 May 2003)* <http://www-cdf.fnal.gov/physics/conferences/2003.html>
- [885] Acosta D *et al* (CDF Collaboration) 2002 *Phys. Rev. Lett.* **88** 161802
- [886] Grigoryan S 2002 ALICE-INT-2002-06
- [887] Grigoryan S 2005 Meeting of the ALICE Physics Working Group 3, 11 April 2005 <http://indico.cern.ch/conferenceDisplay.py?confId=a051590>
- [888] Grandchamp L, Lumpkins S, Sun D, van Hees H and Rapp R 2005 *Preprint hep-ph/0507314*
- [889] ALICE Zero Degree Calorimeters, Technical Design Report, CERN/LHCC 99-5
- [890] Gavin S, McGaughey P L, Ruuskanen P V and Vogt R 1996 *Phys. Rev. C* **54** 2606
- [891] Kampf B, Pavlenko O P and Gallmeister K 1998 *Phys. Lett. B* **419** 412 (*Preprint hep-ph/9712293*)
- [892] Emel'yanov V, Khodinov A, Klein S R and Vogt R 1999 *Phys. Rev. C* **59** 1860 (*Preprint hep-ph/9809222*)
- [893] Vogt R 1999 *Phys. Rep.* **310** 197
- [894] Baur G *et al* (CMS Collaboration) 2000 CMS Note 2000/060
- [895] Kostyuk A P, Gorenstein M I and Greiner W 2001 *Phys. Lett. B* **519** 207 (*Preprint hep-ph/0103057*)
- [896] Shuryak E V 1992 *Phys. Rev. Lett.* **68** 3270

- [897] Geiger K 1993 *Phys. Rev. D* **48** 4129
- [898] Golam Mustafa M, Pal D and Kumar Srivastava D 1998 *Phys. Rev. C* **57** 889 (Preprint [nucl-th/9706001](#))
- [899] Butsyk S A 2005 Preprint [nucl-ex/0510010](#)
- [900] Abreu M C *et al* (NA50 Collaboration) 1999 *Phys. Lett. B* **450** 456
- [901] Gosset J, Baldisseri A, Borel H, Staley F and Terrien Y 2000 *Eur. Phys. J. C* **13** 63 (Preprint [nucl-ex/9906002](#))
- [902] Dumonteil E and Crochet P 2005 ALICE-INT-2005-02
- [903] Matsui T and Satz H 1986 *Phys. Lett. B* **178** 416
- [904] Eskola K J 2002 *Nucl. Phys. A* **702** 249 (Preprint [hep-ph/0111223](#))
- [905] Blaizot J P and Ollitrault J Y 1996 *Phys. Rev. Lett.* **77** 1703 (Preprint [hep-ph/9606289](#))
- [906] Karsch F and Petronzio R 1988 *Z. Phys. C* **37** 627
- [907] Wong C Y 2005 *Phys. Rev. C* **72** 034906 (Preprint [hep-ph/0408020](#))
- [908] Wong C Y 2005 Preprint [hep-ph/0509088](#)
- [909] Alberico W M, Beraudo A, De Pace A and Molinari A 2005 *Phys. Rev. D* **72** 114011 (Preprint [hep-ph/0507084](#))
- [910] Grigoryan S *et al* 2006 ALICE Internal Note (in preparation)
- [911] Heiselberg H and Mattiello R 1999 *Phys. Rev. C* **60** 044902
- [912] Wang X N and Yuan F 2002 *Phys. Lett. B* **540** 62 (Preprint [nucl-th/0202018](#))
- [913] ALICE addendum to Technical Proposal—The Forward Muon Spectrometer CERN/LHCC 96-32, LHCC/P3 addendum 1, 1996
- [914] Stocco D 2005 Tesi di Laurea, Specialistica in Fisica Delle Interazioni Fondamentali, Università di Torino, Italy, unpublished
- [915] Grosse-Oetringhaus J F 2005 *Diploma Thesis* University of Münster
- [916] Hanson G *et al* 1975 *Phys. Rev. Lett.* **35** 1609
- [917] Barber D P *et al* 1979 *Phys. Rev. Lett.* **43** 830
- [918] Bjorken J D Preprint FERMILAB-PUB-82-059-THY
- [919] Thoma M H and Gyulassy M 1991 *Nucl. Phys. B* **351** 491
- [920] Braaten E and Thoma M H 1991 *Phys. Rev. D* **44** 1298
- [921] Wang X-N, Gyulassy M and Plümer M 1995 *Phys. Rev. D* **51** 3436
- [922] Adcox K *et al* (PHENIX Collaboration) 2002 *Phys. Rev. Lett.* **88** 022301
- [923] Adler C *et al* (STAR Collaboration) 2002 *Phys. Rev. Lett.* **89** 202301
- [924] Adler C *et al* (STAR Collaboration) 2003 *Phys. Rev. Lett.* **90** 082302
- [925] Salgado C A and Wiedemann U A 2004 *Phys. Rev. Lett.* **93** 042301
- [926] Shuryak E V 2002 *Phys. Rev. C* **66** 027902
- [927] Affolder T *et al* (CDF Collaboration) 2001 *Phys. Rev. D* **64** 032001
- Affolder T *et al* (CDF Collaboration) 2002 *Phys. Rev. D* **65** 039903
- [928] Christie W B and Shesternanov K 1995 STAR Note 196
- Henry W 2004 *J. Phys. G: Nucl. Part. Phys.* **30** S1287
- [929] Cormier T M 2004 *Eur. Phys. J. C* **34** S333
- [930] Morsch A 2005 *J. Phys. G: Nucl. Part. Phys.* **31** S597
- [931] Frixione S, Kunszt A and Signer A 1996 *Nucl. Phys. B* **467** 399
- [932] Frixione S 1997 *Nucl. Phys. B* **507** 295
- [933] Frixione S and Ridolf G 1997 *Nucl. Phys. B* **507** 315
- [934] Armesto N private communications
- [935] Sjostrand T 1985 *Phys. Lett. B* **157** 321
- [936] Bengtsson M, Sjostrand T and van Zijl M 1986 *Z. Phys. C* **32** 67
- [937] Sjostrand T and van Zijl M 1987 *Phys. Rev. D* **36** 2019
- [938] Eskola K J, Kolhinen V J and Ruuskanen P V 1998 *Nucl. Phys. B* **535** 351
- [939] Loizides C 2005 *PhD Thesis* Frankfurt/Main Preprint [nucl-ex/0501017](#)
- [940] Loizides C 2005 *J. Phys. Conf. Ser.* **27** 226
- [941] Borghini N and Wiedemann U A 2005 CERN-PH-TH-2005-100, BI-TP/2005/20, Preprint [hep-ph/0506218](#)
- [942] Lokhtin I P and Snigirev A M 2000 *Eur. Phys. J. C* **16** 527
- [943] AliRoot <http://www.cern.ch/ALICE/Projects/offline/aliroot/Welcme.html>
- [944] Dawson I, Buttar C and Moraes A 2004 *Czech. J. Phys. A* **54** 221
- [945] Pronko A (CDF Collaboration) 2005 *Acta Phys. Polon. B* **36** 451
- [946] Affolder T *et al* (CDF Collaboration) 2002 *Phys. Rev. D* **65** 092002
- [947] Field R D, [http://www.phys.ufl.edu/rfield/cdf/tunes/rdf\\_tunes.html](http://www.phys.ufl.edu/rfield/cdf/tunes/rdf_tunes.html)

- [948] Abbott B *et al* 1997 Fermilab-Pub-97-242-E  
Abbott B 1994 *PhD Thesis* Purdue University, unpublished  
Abachi S *et al* (D0 Collaboration) 1995 *Phys. Lett. B* **357** 500
- [949] Wiedemann U A 2001 *Nucl. Phys. A* **690** 731
- [950] Noferini F private communications
- [951] Brun R, Bruyant F, Maire M, McPherson A C and Zanarini P 1985 GEANT3 User Guide, CERN Data Handling Division DD/EE/84-1 <http://wwwinfo.cern.ch/asdoc/geantold/GEANTMAIN.html>
- [952] Arnison G *et al* (UA1 Collaboration) 1983 *Phys. Lett. B* **132** 214
- [953] Blyth S-L 2005 Jet studies in ultra-relativistic heavy-ion collisions with the ALICE detectors at the LHC *MSc Thesis, Preprint nucl-ex/0510065*
- [954] Blyth S-L *et al* 2005 A universal jet finding algorithm for heavy-ion collisions at the LHC applied to the ALICE experiment *Nucl. Instrum. Methods* at press
- [955] Contreras J G, López Noriega M and Morsch A 2005 ALICE-INT-2005-035
- [956] Mischke A and Jacobs P 2005 ALICE-INT-2005-50
- [957] ALICE Collaboration 2004 *ALICE Forward Detector TDR*, CERN/LHCC 2004-025
- [958] Appelshäuser H and Ploskon M 2005 ALICE-INT-2005-49
- [959] Adler S S *et al* (PHENIX Collaboration) 2003 *Phys. Rev. Lett.* **91** 072301
- [960] Magestro D (STAR Collaboration) 2005 *Preprint nucl-ex/0510002*
- [961] Arleo F, Aurenche P, Conesa-Balbastre G, Delagrangé H, Kharlov Y, Peitzmann T and Schutz Y 2005 ALICE-INT-2005-032
- [962] Jalilian-Marian J, Orginos K and Sarcevic I 2001 *Phys. Rev. C* **63** 041901 (*Preprint hep-ph/0010230*)
- [963] Wong C and Wang H 1998 *Phys. Rev. C* **58** 376
- [964] Papp G, Lévai P and Fai G 1999 *Phys. Rev. C* **61** 0219021
- [965] Zakharov B G 2004 *JETP Lett.* **80** 1–6
- [966] Aurenche P *et al* 1993 *Nucl. Phys. B* **399** 34  
Aurenche P *et al* 1999 *Eur. Phys. J. C* **9** 107
- [967] Arleo F *et al* 2004 *Photon Physics in heavy-ion collisions at the LHC* CERN Yellow Report 2004-009, *Preprint hep-ph/0311131*
- [968] Eskola K J, Kolhinen V J and Salgado C A 1999 *Eur. Phys. J. C* **9** 61–68
- [969] Eskola K J, Kolhinen V J and Ruuskanen P V 1998 *Nucl. Phys. B* **535** 351–371
- [970] Gordon L E and Vogelsang W 1993 *Phys. Rev. D* **48** 3136
- [971] Lai H-L and Li H-N 1998 *Phys. Rev. D* **58** 114020
- [972] Laenen E, Sterman G and Vogelsang W 2000 *Phys. Rev. Lett.* **84** 4296  
Laenen E, Sterman G and Vogelsang W 2001 *Phys. Rev. D* **63** 114018
- [973] Lai H L *et al* 1997 *Phys. Rev. D* **55** 1280–1296
- [974] Pumplin J *et al* 2002 *J. High Energy Phys.* **JHEP07(2002)012**
- [975] Kniehl B A, Kramer G and Potter B 2000 *Nucl. Phys. B* **582** 514–536
- [976] Bourhis L, Fontannaz M and Guillet J P 1998 *Eur. Phys. J. C* **2** 529–537
- [977] ALICE Collaboration 2004 ALICE: Physics Performance Report, Volume I *J. Phys. G: Nucl. Part. Phys.* **30** 1517 (Chapter 3)
- [978] Conesa G *et al* 2005 *Nucl. Inst. Meth. A* **537** 363–367
- [979] Arleo F *et al* 2004 *J. High Energy Phys.* **JHEP11(2004)009**
- [980] Conesa G *et al* 2005 ALICE-INT-2005-014
- [981] Sjostrand T *et al* 2001 *Preprint hep-ph/0108264*
- [982] Gluck M *et al* 1995 *Z. Phys. C* **67** 433–448
- [983] Gyulassy M and Wang X-N 1994 *Comput. Phys. Commun.* **83** 307–331
- [984] Shuryak E V 1978 *Yad. Fiz.* **28** 796  
Shuryak E V 1978 *Sov. Nucl. J. Phys.* **28** 408
- [985] Kajantie K and Miettinen H I 1981 *Z. Phys. C* **9** 341
- [986] Halzen F and Liu H C 1982 *Phys. Rev. D* **25** 1842
- [987] Kajantie K and Ruuskanen P V 1983 *Phys. Lett. B* **121** 352
- [988] Sinha B 1983 *Phys. Lett. B* **128** 91
- [989] Hwa R C and Kajantie K 1985 *Phys. Rev. D* **32** 1109
- [990] Staadt G, Greiner W and Rafelski J 1986 *Phys. Rev. D* **33** 66
- [991] Neubert M 1989 *Z. Phys. C* **42** 231
- [992] Gale C and Kapusta J I 1991 *Nucl. Phys. B* **357** 65
- [993] Kapusta J I, Lichard P and Seibert D 1991 *Phys. Rev. D* **44** 2774
- [994] Baier R *et al* 1992 *Z. Phys. C* **53** 433

- [995] Aurenche P *et al* 1998 *Phys. Rev. D* **58** 085003
- [996] Steffen F D and Thoma M H 2001 *Phys. Lett. B* **510** 98 (Preprint [hep-ph/0103044](#))
- [997] Arnold P, Moore G D and Yaffe L G 2001 *J. High Energy Phys.* **JHEP11(2001)057**  
Arnold P, Moore G D and Yaffe L G 2001 *J. High Energy Phys.* **JHEP12(2001)009**
- [998] Karsch F, Laermann E, Petreczky P, Stickan S and Wetzorke I 2001 Preprint [hep-lat/0110208](#)
- [999] Biró T S *et al* 1993 *Phys. Rev. C* **48** 1275
- [1000] Baier R *et al* 1997 *Phys. Rev. D* **56** 2548
- [1001] Carrington M E, Defu H and Thoma M H 1999 *Eur. Phys. J. C* **7** 347
- [1002] Traxler C T and Thoma M H 1996 *Phys. Rev. C* **53** 1348
- [1003] Mustafa M G and Thoma M H 2000 *Phys. Rev. C* **62** 014902
- [1004] Karsch F 1988 *Z. Phys. C* **38** 147
- [1005] Xiong L, Shuryak E and Brown G E 1992 *Phys. Rev. D* **46** 3798
- [1006] Song C 1993 *Phys. Rev. C* **47** 2861
- [1007] Kim J K *et al* 1996 *Phys. Rev. D* **53** 4787
- [1008] Nadeau H, Kapusta J I and Lichard P 1992 *Phys. Rev. C* **45** 3034  
Nadeau H, Kapusta J I and Lichard P 1993 *Phys. Rev. C* **47** 2426
- [1009] Rapp R and Wambach J 2000 *Adv. Nucl. Phys.* **25** 1 (Preprint [hep-ph/9909229](#))
- [1010] Gallmeister K, Kämpfer B and Pavlenko O P 2000 *Phys. Rev. C* **62** 057901
- [1011] Zakharov B G 2004 *JETP Lett.* **80** 1–6
- [1012] Zakharov B G 1996 *JETP Lett.* **63** 952–957
- [1013] Zakharov B G 1997 *JETP Lett.* **65** 615–620
- [1014] Turbide S, Gale C, Jeon S and Moore G 2005 *Phys. Rev. C* **72** 014906
- [1015] Arnold P, Moore G D and Yaffe L G 2002 *J. High Energy Phys.* **JHEP06(2002)030**
- [1016] Clare R B and Strottman D 1986 *Phys. Rep.* **141** 177
- [1017] Huovinen P, Ruuskanen P V and Sollfrank J 1999 *Nucl. Phys. A* **650** 227
- [1018] Geiger K 1995 *Phys. Rep.* **258** 376
- [1019] Wang X N 1997 *Phys. Rep.* **280** 287
- [1020] Dumitru A and Rischke D H 1999 *Phys. Rev. C* **59** 354
- [1021] Srivastava D K, Mustafa M G and Müller B 1997 *Phys. Rev. C* **56** 1064
- [1022] Aggarwal M M *et al* (WA98 Collaboration) 2000 *Phys. Rev. Lett.* **85** 3595
- [1023] Huovinen P and Ruuskanen P V 2006 in preparation
- [1024] Srivastava D K and Sinha B 2001 *Phys. Rev. C* **64** 034902
- [1025] Alam J *et al* 2001 *Phys. Rev. C* **63** 021901
- [1026] Srivastava D K 1999 *Eur. Phys. J. C* **10** 487
- [1027] Peressounko D Y and Pokrovsky Y E 2000 Preprint [hep-ph/0009025](#)
- [1028] Steele J V, Yamagishi H and Zahed I 1997 *Phys. Rev. D* **56** 5605
- [1029] Aggarwal M M *et al* (WA98 Collaboration) 2004 *Phys. Rev. Lett.* **93** 022301
- [1030] Turbide S, Rapp R and Gale C 2004 *Phys. Rev. C* **69** 014903
- [1031] Adler S S *et al* (PHENIX Collaboration) 2005 *Phys. Rev. Lett.* **94** 232301 (Preprint [nucl-ex/0503003](#))
- [1032] Hammon N *et al* 1998 *Phys. Rev. C* **57** 3292
- [1033] Jeon S, Jalilian-Marian J and Sarcevic I 2003 *Nucl. Phys. A* **715** 35 (Preprint [nucl-th/0211084](#))
- [1034] Aggarwal M M *et al* (WA98 Collaboration) 2000 Preprint [nucl-ex/0006007](#)
- [1035] Hagiwara K *et al* (Particle Data Group) 2002 Review of Particle Physics *Phys. Rev. D* **66** 010001 (pp 201–2)
- [1036] *Photon Physics in Heavy-Ion Collisions at the LHC* CERN Yellow Report 2004-009 407
- [1037] Conesa G, Delagrange H, Diaz J, Kharlov Y and Schutz Y 2005 ALICE-INT-2005-016
- [1038] Aurenche P, Baier R and Fontannaz M 1988 *Phys. Lett. B* **209** 375
- [1039] Cleymans J, Redlich K and Satz H 1991 *Z. Phys. C* **52** 571
- [1040] Salgado C A and Wiedemann U A 2004 *Phys. Rev. Lett.* **93** 42301
- [1041] Arleo F, Aurenche P, Belghobsi Z and Guillet J-P 2004 *J. High Energy Phys.* **JHEP11(2004)009**
- [1042] Bertulani C A, Klein S R and Nystrand J 2005 *Ann. Rev. Nucl. Part. Sci.* **55** 271 (Preprint [nucl-ex/0502005](#))
- [1043] Baur G, Hencken K, Trautmann D, Sadovskiy S and Kharlov Y 2002 *Phys. Rep.* **364** 359 (Preprint [hep-ph/0112211](#))
- [1044] Klein S and Nystrand J 1999 *Phys. Rev. C* **60** 014903 (Preprint [hep-ph/9902259](#))
- [1045] Baltz A J, Klein S R and Nystrand J 2002 *Phys. Rev. Lett.* **89** 012301 (Preprint [nucl-th/0205031](#))
- [1046] Ryskin M G 1993 *Z. Phys. C* **57** 89
- [1047] Frankfurt L L, McDermott M F and Strikman M 1999 *J. High Energy Phys.* **JHEP02(1999)002** (Preprint [hep-ph/9812316](#))
- [1048] Martin A D, Ryskin M G and Teubner T 1999 *Phys. Lett. B* **454** 339 (Preprint [hep-ph/9901420](#))

- [1049] Frankfurt L, Guzey V, Strikman M and Zhalov M 2003 *J. High Energy Phys.* **JHEP08(2003)043** (Preprint [hep-ph/0304218](#))
- [1050] Klein S R and Nystrand J 2004 *Phys. Rev. Lett.* **92** 142003 (Preprint [hep-ph/0311164](#))
- [1051] Klein S R and Nystrand J 2000 *Phys. Rev. Lett.* **84** 2330 (Preprint [hep-ph/9909237](#))
- [1052] Klein S R and Nystrand J 2003 *Phys. Lett. A* **308** 323 (Preprint [quant-ph/0206060](#))
- [1052] Frankfurt L, Strikman M and Zhalov M 2002 *Phys. Lett. B* **540** 220 (Preprint [hep-ph/0111221](#))
- [1053] Nikulin V and Zhalov M 2003 *ALICE-INT-2003-043*
- [1054] Klein S R, Nystrand J and Vogt R 2002 *Phys. Rev. C* **66** 044906 (Preprint [hep-ph/0206220](#))
- [1055] Adams J *et al* (STAR Collaboration) 2004 *Phys. Rev. C* **70** 031902 (Preprint [nucl-ex/0404012](#))
- [1056] d'Enterria D (PHENIX Collaboration) 2006 *Poster presented at Quark Matter 2005 (Budapest, 5–10 August 2005)* (Preprint [nucl-ex/0601001](#))
- [1057] Alscher A, Hencken K, Trautmann D and Baur G 1997 *Phys. Rev. A* **55** 396 (Preprint [nucl-th/9606011](#))
- [1058] Baron N and Baur G 1993 *Phys. Rev. C* **48** 1999
- [1059] Greiner M, Vidovic M, Hofmann C, Schafer A and Soff G 1995 *Phys. Rev. C* **51** 911
- [1060] Vogt R 2004 Preprint [hep-ph/0407298](#)
- [1061] Strikman M, Vogt R and White S 2006 *Phys. Rev. Lett.* **96** 082001 (Preprint [hep-ph/0508296](#))
- [1062] Klein S R, Nystrand J and Vogt R 2001 *Eur. Phys. J. C* **21** 563 (Preprint [hep-ph/0005157](#))
- [1063] Vane C R *et al* 1992 *Phys. Rev. Lett.* **69** 1911
- [1064] Baur R *et al* (CERES/NA45 Collaboration) 1994 *Phys. Lett. B* **332** 471
- [1065] Scheidenberger C *et al* 2004 *Phys. Rev. C* **70** 014902
- [1066] Adler C *et al* (STAR Collaboration) 2002 *Phys. Rev. Lett.* **89** 272302 (Preprint [nucl-ex/0206004](#))
- [1067] Chiu M, Denisov A, Garcia E, Katzy J and White S 2002 *Phys. Rev. Lett.* **89** 012302 (Preprint [nucl-ex/0109018](#))
- [1068] Meissner F (STAR Collaboration) 2003 *Nucl. Phys. A* **715** 522 (Preprint [nucl-ex/0210028](#))
- [1069] Klein S and Nystrand J STAR Note 347 (available at <http://www.star.bnl.gov/>)
- [1070] Nystrand J and Klein S (STAR Collaboration) 1998 Preprint [nucl-ex/9811007](#)
- [1071] Nystrand J 2005 *Nucl. Phys. A* **752** 470 (Preprint [hep-ph/0412096](#))
- [1072] Pi H 1992 *Comput. Phys. Commun.* **71** 173
- [1073] Engel R, Ranft J and Roesler S 1997 *Phys. Rev. D* **55** 6957 (Preprint [hep-ph/9610281](#))
- [1074] *AliRoot* <http://www1.cern.ch/ALICE/Projects/offline/aliroot/Welcome.html>
- [1075] Hencken K *et al* 1996 Preprint IHEP 96-38 Protvino
- [1076] Adriani O *et al* 2002 *Nucl. Instrum. and Methods. A* **488** 209
- [1077] Avati V *et al* 2003 *Astropart. Phys.* **19** 513
- [1078] Heck D *et al* 1998 Report FZKA 6019 <http://www-ik.fzk.de/corsika/>
- [1079] Werner K 1993 *Phys. Rep.* **232** 87
- [1080] Kalmykov N N and Ostapchenko S S 1993 *Yad. Fiz.* **56** 105
- [1081] Ranft J 1995 *Phys. Rev. D* **51** 64
- [1082] Capdevielle J N *et al* 1992 Report KfK 4998, Kernforschungszentrum Karlsruhe
- [1083] Fletcher R S *et al* 1994 *Phys. Rev. D* **50** 5710
- [1084] Drescher H J *et al* 2001 *Phys. Rep.* **350** 93
- [1085] Heck D 2003 *Nucl. Phys. B Proc. Suppl.* **122** 451–4
- [1086] Alner G J *et al* (UA5 Collaboration) 1987 *Phys. Rep.* **154** 247
- [1087] Avati V *et al* 2003 *Eur. Phys. J. C* **34** s255
- [1088] Richard-Serre C 1971 Technical Report CERN 71–18
- [1089] Hebbeker T and Timmermans C 2002 *Astropart. Phys.* **18** 107
- [1090] Achard P *et al* (L3 Collaboration) 2004 *Phys. Lett. B* **598** 15
- [1091] Bakatanov V N *et al* 1998 *Phys. Atom. Nucl.* **61** 1507
- [1092] Adarkar H *et al* 1991 *Phys. Lett. B* **267** 138
- [1093] Rybczynski M, Wlodarczyk Z and Wilk G 2002 *Acta Phys. Polonica. B* **33** 277
- [1094] Rybczynski M, Wlodarczyk Z and Wilk G 2001 *Nucl. Phys. B Proc. Suppl.* **97** 85
- [1095] Ridky J 2000 Preprint [hep-ph/0012068](#)
- [1096] Hörandel J R 2003 *Astropart. Phys.* **19** 193
- [1097] Sanuki T *et al* (BESS Collaboration) 2002 *Phys. Lett. B* **581** 272
- [1098] Boezio M *et al* (CAPRICE Collaboration) 2003 *Phys. Rev. D* **67** 72003
- [1099] De Pascale M P *et al* 1993 *Geophys. J. Res.* **98** 3501
- [1100] Allkofer O, Carstensen K and Dau W D 1971 *Phys. Lett. B* **36** 425
- [1101] Ayre C *et al* 1975 *J. Phys. G: Nucl. Phys.* **1** 584

- 
- [1102] Samorsky M and Stamm W 1983 *Astrophys. J. L* **17** 268
  - [1103] Lloyd-Evans J *et al* 1983 *Nature* **305** 784
  - [1104] Morello C *et al* 1990 *Nuovo Cimento C* **13** 453
  - [1105] Keno A 1990 *Phys. Rev. Lett.* **64** 1628
  - [1106] Aglietta M *et al* 1995 *Astropart. Phys.* **3** 1
  - [1107] Cronin J W *et al* 1992 *Phys. Rev. D* **45** 4385
  - [1108] Halzen F *et al* 1997 *Phys. Rev. D* **55** 4475
  - [1109] Barwick S *et al* 1991 *J. Phys. G: Nucl. Part. Phys.* **18** 225
  - [1110] Taylor C *et al* CERN/LEPC99-5
  - [1111] <http://cosmos.n.kanagawa-u.ac.jp/kasahara/ResearchHome/cosmosHome/index.html>
  - [1112] Fassó A, Ferrari A, Ranft J and Sala P R 2001 FLUKA: Status and Prospective for Hadronic Applications  
*Proc. Monte Carlo 2000 Conference (Lisbon)* ed A Kling, F Barao, M Nakagawa, L Tavora and P Vaz  
(Berlin: Springer) pp 955–60
  - [1113] Grieder P K F 2001 *Cosmic Rays at Earth* (Amsterdam: Elsevier)
  - [1114] Billior P and Qian S 1990 *Nucl. Instrum. Methods A* **294** 219